MOLECULAR BEAM EPITAXY 1996

Proceedings of the Ninth International Conference on Molecular Beam Epitaxy

Malibu, California, USA, 5–9 August 1996

Part 2
Sections IX–XVIII

Edited by:

Y.-C. Kao

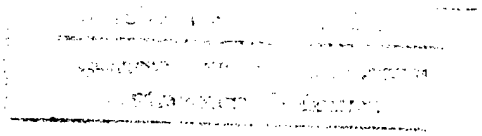

North-Holland

MOLECULAR BEAM EPITAXY 1996

PROCEEDINGS OF THE NINTH INTERNATIONAL CONFERENCE ON
MOLECULAR BEAM EPITAXY
MALIBU, CALIFORNIA, USA, 5–9 AUGUST 1996

PART 2
Sections IX–XVIII

Edited by:
Y.-C. Kao
Texas Instruments, USA

DTIC QUALITY INSPECTED 2

ELSEVIER

Amsterdam – Lausanne – New York – Oxford – Shannon – Tokyo

19970815 029

Copyright © 1997 Elsevier Science B.V. All rights reserved

This journal and the individual contributions contained in it are protected by the copyright of Elsevier Science B.V., and the following terms and conditions apply to their use:
Photocopying
Single photocopies of single articles may be made for personal use as allowed by national copyright laws. Permission of the Publisher and payment of a fee is required for all other photocopying, including multiple or systematic copying, copying for advertising or promotional purposes, resale, and all forms of document delivery. Special rates are available for educational institutions that wish to make photocopies for non-profit educational classroom use.
In the USA, users may clear permissions and make payment through the Copyright Clearance Center Inc., 222 Rosewood Drive, Danvers, MA 01923, USA. In the UK, users may clear permissions and make payment through the Copyright Licensing Agency Rapid Clearance Service (CLARCS), 90 Tottenham Court Road, London W1P 0LP, UK. In other countries where a local copyright clearance centre exists, please contact it for information on required permissions and payments.
Derivative works
Subscribers may reproduce tables of contents or prepare lists of articles including abstracts for internal circulation within their institutions.
Permission of the Publisher is required for resale or distribution outside the institution.
Permission of the Publisher is required for all other derivative works, including compilations and translations.
Electronic storage
Permission of the Publisher is required to store electronically any material contained in this journal, including any article or part of an article.
Contact the Publisher at the address indicated.
Except as outlined above, no part of this publication may be reproduced, stored in a retrieval system or transmitted in any form or by any means, electronic, mechanical, photocopying, recording or otherwise, without prior written permission of the Publisher.

No responsibility is assumed by the Publisher for any injury and/or damage to persons or property as a matter of products liability, negligence or otherwise, or from any use or operation of any methods, products, instructions or ideas contained in the material herein. Although all advertising material is expected to conform to ethical (medical) standards, inclusion in this publication does not constitute a guarantee or endorsement of the quality or value of such product or of the claims made of it by its manufacturer.

⊗ The paper used in this publication meets the requirements of ANSI/NISO Z39.48-1992 (Permanence of Paper)

Reprinted From:
JOURNAL OF CRYSTAL GROWTH 175/176 (1997) Part 2

The Manuscripts of the Proceedings were
received by the Publisher: mid-September 1996/late-January 1997

PRINTED IN THE NETHERLANDS

ELSEVIER

Journal of Crystal Growth 175/176 (1997) 689–695

JOURNAL OF CRYSTAL GROWTH

Low-threshold injection lasers based on vertically coupled quantum dots

V.M. Ustinov[a,*], A.Yu. Egorov[a], A.R. Kovsh[a], A.E. Zhukov[a], M.V. Maximov[a], A.F. Tsatsul'nikov[a], N.Yu. Gordeev[a], S.V. Zaitsev[a], Yu.M. Shernyakov[a], N.A. Bert[a], P.S. Kop'ev[a], Zh.I. Alferov[a], N.N. Ledentsov[1,b], J. Böhrer[b], D. Bimberg[b], A.O. Kosogov[1,c], P. Werner[c], U. Gösele[c]

[a] *A.F. Ioffe Physico-Technical Institute, Politekhnicheskaya 26, St. Petersburg 194021, Russian Federation*
[b] *Institut für Festkörperphysik, Technische Universität Berlin, Hardenbergstrasse 36, D-10623 Berlin, Germany*
[c] *Max-Planck-Institut für Mikrostrukturphysik, Weinberg 2, D-06120 Halle, Germany*

Abstract

We have fabricated and studied injection lasers based on vertically coupled quantum dots (VECODs). VECODs are self-organized during successive deposition of several sheets of (In,Ga)As quantum dots separated by thin GaAs spacers. VECODs are introduced in the active region of a GaAs–AlGaAs GRIN SCH lasers. Increasing the number of periods (N) in the VECOD leads to a remarkable decrease in threshold current density ($\sim$ 100 A/cm^2 at 300 K for $N = 10$). Lasing proceeds via the ground state of the quantum dots (QD) up to room temperature. Placing the QD array into an external AlGaAs–GaAs quantum well allows us to extend the range of thermal stability of threshold current density ($T_0 = 350$ K) up to room temperature. Using (In,Ga)As–(Al,Ga)As VECODs in combination with high temperature growth of emitter and waveguide layers results in further reduction of threshold current density (60–80 A/cm^2, 300 K) and increase in internal quantum efficiency (70%). Room temperature continuous wave operation (light output 160 mW per mirror) and lasing via the states of QDs up to $I = (6–7)\, I_{th}$ have been demonstrated.

PACS: 42.55.P; 42.60; 42.60.L; 68.55.B; 68.55.J; 78.55.C

Keywords: Molecular beam epitaxy; Injection lasers; Quantum dots

1. Introduction

Application of quantum dots (QDs) as an active region in a semiconductor injection laser should lead to ultra low threshold current density and extremely high thermal stability, due to delta function density of states [1]. However, complete practical realization of these theoretical predictions still remains a challenge owing to severe technological problems in synthesizing absolutely uniform defect-free dense arrays of objects exhibiting three-dimensional quantum confinement in an appropriate

* Corresponding author. Fax: +7 812 247 8640; e-mail: vmust@beam.Ioffe.rssi.ru.

[1] On leave from A.F.Ioffe Physico-Technical Institute.

0022-0248/97/$17.00 Copyright © 1997 Elsevier Science B.V. All rights reserved
PII S0022-0248(96)01021-4

higher bandgap matrix. In the present work we use the method of direct QD formation based on a self-organization process at the initial stages of strained layer (In,Ga)As-on-GaAs heteroepitaxy [2, 3]. The quantum pyramids formed under appropriate deposition conditions exhibit a delta function like density of states, good structural perfection, reasonable size uniformity, and intense room temperature (RT) luminescence [3]. Introducing these (In,Ga)As QDs in the active region of a GRIN SCH GaAs-(Al,Ga)As laser allowed us to realize lasing via the ground state of quantum dots at low temperatures. Threshold current density was found to be practically temperature insensitive in the temperature range up to $\sim$ 100 K [4]. However, at higher temperatures we observed the steep increase in the threshold current density accompanied by a blue shift of lasing wavelength. Room temperature lasing energy was close to optical transition energy in wetting layer (WL) [5]. In the present work we report on important improvements in lasing characteristics due to modification of the structure design and molecular beam epitaxy (MBE) growth regimes. We will show that using the concept of vertically coupled quantum dots (VECODs) [6, 7], high temperature growth of emitter and waveguide layers, and the effect of external quantum well or AlGaAs barriers on energy spectrum of a quantum dot lead to remarkable reduction in threshold current density, ground state lasing and $T_0 = 350$ K up to room temperature, and continuous wave (CW) operation of quantum dot injection laser at 300 K.

2. Experimental procedure

The samples studied were grown by solid-source molecular beam epitaxy using a Riber-32P MBE machine. InGaAs QDs and a 100 Å GaAs covering layer were grown at 490, the rest of the structures (except for the cases specially indicated) were grown at 600°C. Reflection high-energy electron diffraction (RHEED) patterns were monitored during the growth. Formation of dots started after the deposition of approximately 11 Å thick $In_{0.5}Ga_{0.5}As$ layer and led to the transformation of a streaky RHEED pattern to a spotty one typical for the three-dimensional growth mode.

The structures for optical and transmission electron microscopy (TEM) studies were grown on GaAs (1 0 0) semi-insulating substrates. QDs were inserted into the middle of a 0.2 μm thick GaAs layer confined by 10 period AlAs (20 Å) / GaAs (20 Å) superlattices.

The laser structures were grown on (1 0 0) Si-doped GaAs substrates. They were composed of 1.5 μm thick $Al_{0.4}Ga_{0.6}As$ emitters, 0.4 μm GRIN waveguide region and 0.6 μm contact layer. The lasers were fabricated in a four cleaved facet or a shallow stripe ($W = 60$ μm) geometry. Laser characteristics were studied under pulsed (pulse duration 100 ns, pulse frequency 5 kHz) and CW excitation in the 80–300 K temperature range.

TEM studies were performed on a high voltage JEOL JEM 1000 (1 MV) microscope.

PL was excited with an Ar^+ laser and detected with a cooled Ge photodetector. Calorimetric absorption (CAS) spectra were taken at 500 mK.

3. VECOD lasers

3.1. Structural and optical properties of vertically coupled quantum dots

Vertically coupled (In,Ga)As/GaAs quantum dots are formed as the result of successive deposition of (In,Ga)As quantum dot sheets and thin GaAs spacers. The mechanisms of VECOD formation for the cases when the GaAs spacer is thicker or thinner than the QD height are discussed in details in Refs. [6, 7], respectively. Typical cross section TEM image of a 3-period VECOD structure is given in Fig. 1. The dot density is approximately 10^{11} cm^{-2}. Each dot is well separated from the others and is composed of three individual InAs islands stacked in vertical direction. Since the GaAs spacers are very thin, the wavefunctions of neighboring islands are essentially overlapped and each VECOD can be considered as a one unified quantum-mechanical object. PL data in favor of this assumption is reported in [8]. It is important that no dislocations or large relaxed clusters are formed.

Fig. 2a shows typical PL and CAS spectra of a VECOD structure [9]. At low excitation densities PL spectrum contains intense line due to ground

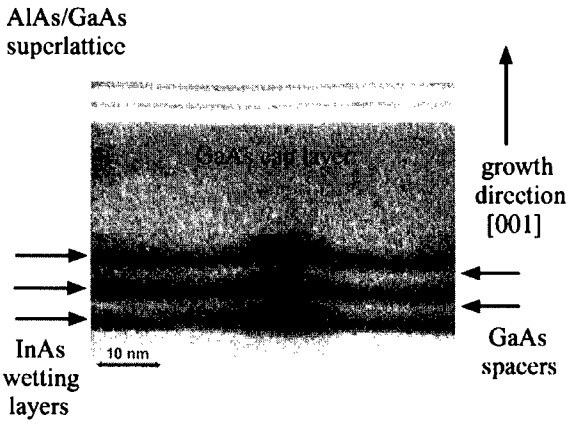

Fig. 1. Cross-section TEM images of the 3-period VECOD composed of 5 Å InAs and 50 Å GaAs layers.

state exciton transition. Increasing the excitation density or observation temperature leads to the appearance of additional peaks due to transitions involving WL states [9]. The indicated PL lines shift toward long wavelengths with increasing the temperature following the GaAs bandgap. Ground- and excited-state peaks in the PL spectrum well agree to similar peaks in calorimetric absorption spectrum indicating the presence of high-density uniform QDs.

Fig. 2b shows PL spectra of structures with different number of QD sheets, N, under high excitation density. One can see that the sample with $N = 1$ demonstrates considerable saturation of luminescence associated with the ground-state transition in a QD, and an intense line due to transitions involving WL states is observed. For the $N = 3$ sample the effect of saturation of ground-state luminescence is pronounced to a less extent, and no saturation is observed for the $N = 6$ sample which is extremely important for laser applications [9].

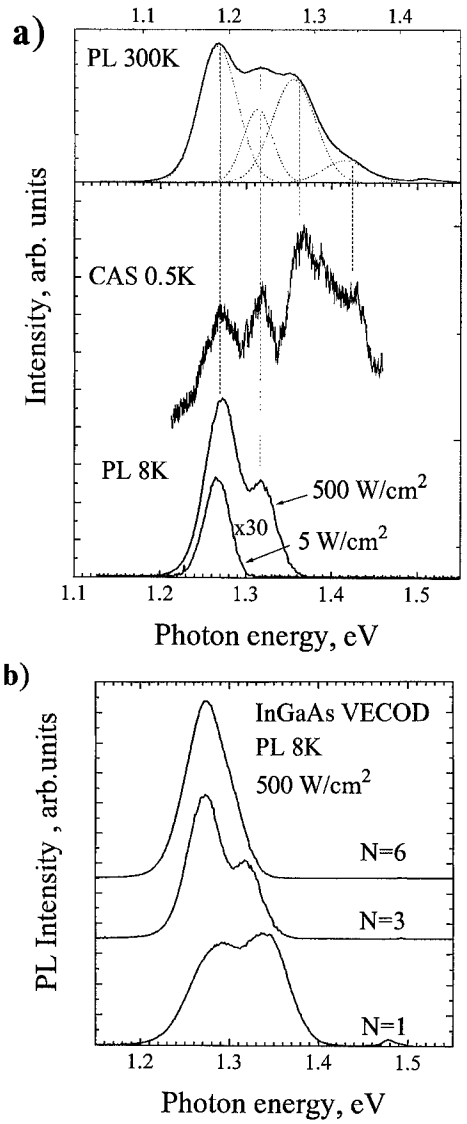

Fig. 2. PL and CAS spectra of the 3-period VECOD structure (a) and PL spectra under high excitation density of 1-, 3-, and 6-period VECODs (b).

3.2. Lasing characteristics

Remarkable progress in PL properties of VECODs as compared to single-sheet QDs led to important improvements in corresponding lasing characteristics. Fig. 3 shows the near-threshold electroluminescence (EL) spectrum of a laser structure based on the $N = 3$ VECOD. Lasing starts at the long-wavelength side of EL peak and the lasing wavelength is in the vicinity of the PL maximum recorded under low excitation density in the entire 77–300 K temperature range. Fig. 4 represents the temperature dependences of lasing wavelength for the VECOD and single-sheet QD based lasers. One can see that these dependences are essentially

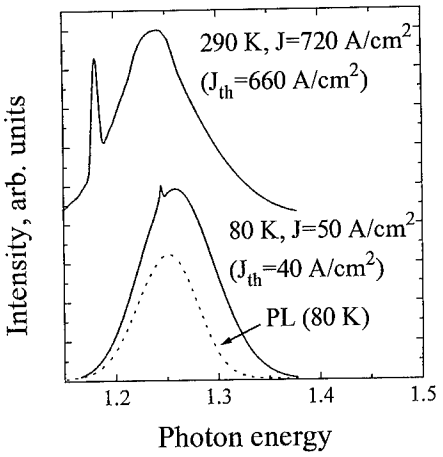

Fig. 3. PL (dashed curve) and electroluminescence spectra of a VECOD laser at 80 and 300 K.

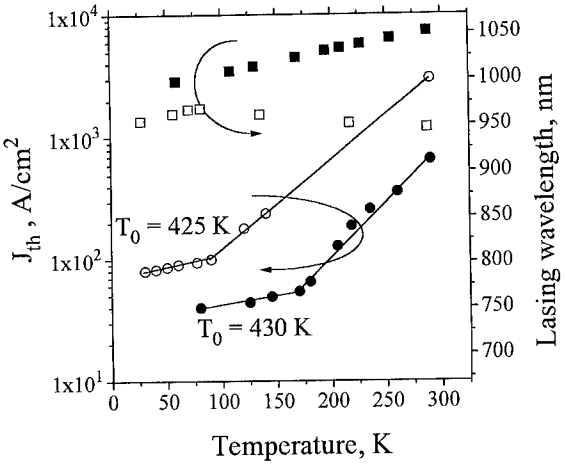

Fig. 4. Temperature dependence of lasing wavelength and threshold current density for the three-period VECOD (solid squares and circles) and single-sheet QD lasers (open squares and circles).

different. Unlike the case of the single-sheet QD laser, the wavelength of the VECOD laser follows the temperature dependence of the GaAs bandgap. Taking into account the lack of ground-state PL saturation described above we may conclude that in VECOD structures lasing proceeds via the ground state of quantum dot up to room temperature.

The threshold current density (J_{th}) in a VECOD gradually decreases with the number of QD sheets. For InGaAs QDs it decreases approximately one order of magnitude from 950 A/cm^2 ($N = 1$) to 98 A/cm^2 ($N = 10$) most probably due to the increase in optical confinement factor. The range of J_{th} thermal stability is extended up to 140–150 K in VECOD lasers, as shown in Fig. 4. The reason for this is presumably the increase in localization energy of carriers in VECODs [8]. It is worth mentioning that low-temperature J_{th} also decreases with N reaching the value as low as 18 A/cm^2 (120 K, $N = 10$).

Differential efficiency (η_D) for the structures studied increases with increasing N, Fig. 5a [10]. However, only moderate values of η_D were measured for the structure with $N = 10$. The reason for this is the relatively low internal quantum efficiency (η_i) characteristic for these structures. Linear extrapolation of the $1/\eta_D$-vs-cavity length (L) dependence (Fig. 5b) gives the value of $\eta_i \approx 0.5$. It means that a significant number of the carriers recombine nonradiatively, most probably in the GaAs layer covering the VECODs which is grown at low substrate temperature (490°C).

Improving the quality of layers adjacent to the QDs through the structure heat-treatment and increasing the separation between energy levels in QDs and barriers through inserting QDs in AlGaAs/GaAs QW or directly in AlGaAs matrix are considered below.

3.3. *Effect of heat treatment on structural and optical properties of (In,Ga)As–GaAs quantum dots*

A possible way to reduce the concentration of point defects due to low-temperature growth is to perform a post-growth annealing. Moreover, high-temperature AlGaAs growth ($\sim$ 700°C) is essential for light emitting devices based on the AlGaAs–GaAs heterostructures to ensure good device performance and operation lifetime.

TEM studies have shown that indium composition in QDs decreases with increasing the lateral dot size, while the dot shape remains essentially the same. This leads to the noticeable blue shift of the PL peak position, as shown in Fig. 6. The increase in integrated PL intensity is presumably due to annealing of the point defects in the process of heat treatment [11].

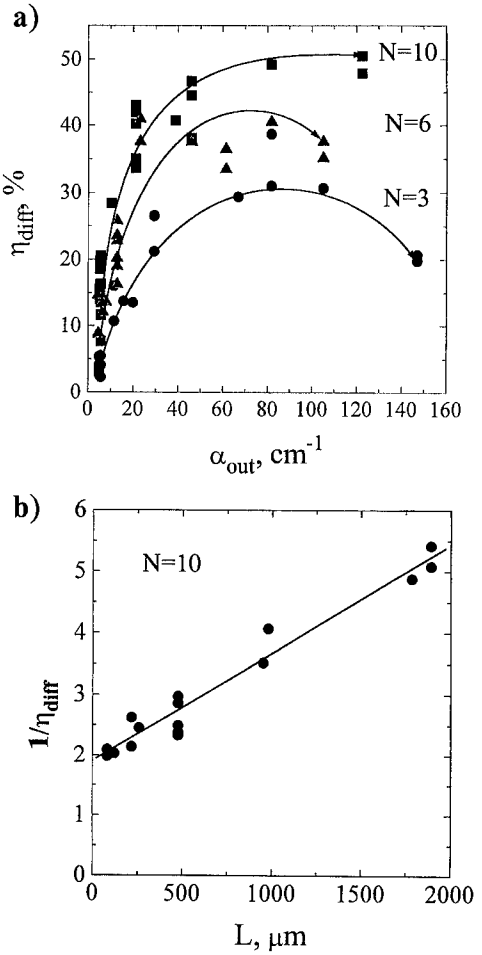

Fig. 5. Differential efficiency vs. output losses for the VECOD lasers (a) and reciprocal differential efficiency vs. cavity length (b).

Room temperature values of J_{th} for the QD laser with AlGaAs layers grown at 700°C are significantly lower than those for the 600°C one: 250 and 700 A/cm^2, respectively. We attribute this to the reduction in the concentration of point defects in a low-temperature GaAs covering QDs due to annealing during the deposition of upper layers of laser structure.

3.4. *Effect of external quantum well and algaas barriers on characteristics of (In,Ga)As QD lasers*

Inserting the InAs QD array into an external AlGaAs/GaAs quantum well (QW) is a possible

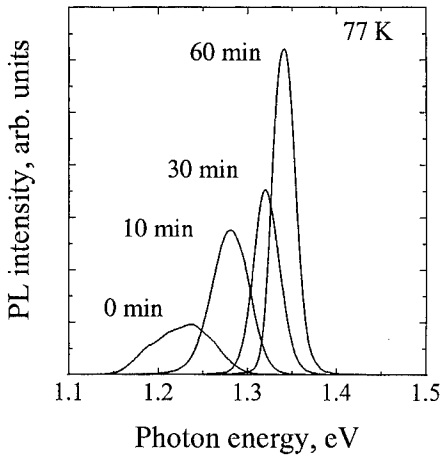

Fig. 6. 77 K PL spectra of the structure containing 3-sheet InAs VECOD for various annealing periods.

way to increase the localization energy of the QD relative to the WL and the GaAs matrix. Calculations within the zero radius potential approximation [12] show that in this case, the WL level shifts stronger than the QD level because the latter is more localized than the former. Moreover, the three-dimensional density of states in GaAs is replaced by the two-dimensional one. These features should lead to the extension of the range of high temperature stability of the threshold current density.

In Fig. 7 we show temperature dependence of J_{th} for the laser whose active region consists of three 100 Å AlGaAs/GaAs QWs separated by 50 Å barriers with the InAs QDs in the middle of each well. The three-well design of the recombination region was chosen to increase optical confinement factor. It is clearly seen that the temperature dependence of J_{th} is described by $T_0 = 350$ K in the entire 77–300 K range, whereas the typical value for an InGaAs QW laser is 130–150 K.

Another way to increase carrier localization energy in a QD is to increase the barrier height. Calculations show that when the GaAs matrix is substituted by AlAs, the energy separation between electron (hole) levels in QD and WL is drastically increased [13]. In our experiments we used (In,Ga)As–$Al_{0.15}Ga_{0.85}As$ quantum dots as the active region and $Al_{0.8}Ga_{0.2}As$ emitters. The growth

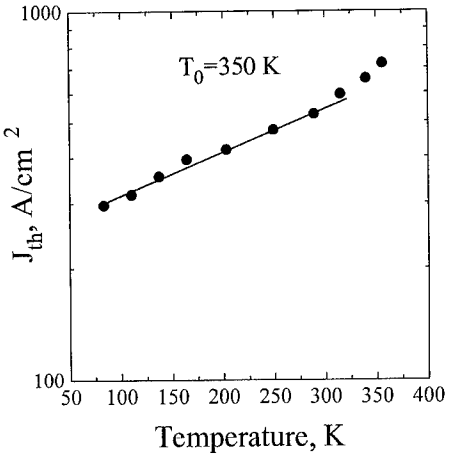

Fig. 7. Temperature dependence of threshold current densities for the laser based on QDs in external quantum well (see in the text).

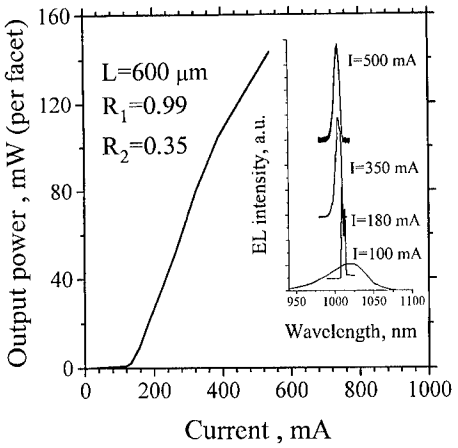

Fig. 8. Light output vs. injection current and EL spectra at various injection currents for the laser containing 10-period (In,Ga)As VECOD.

of the emitter and waveguide layers at 700°C allowed us to overcome the problem of poor crystalline quality of (Al,Ga)As grown at 490°C through point defect annealing similar to the case of GaAs matrix described above. Injection lasers based on (In,Ga)As–(Al,Ga)As VECODs show RT threshold current density as low as 63 A/cm^2 and internal quantum efficiency as high as 70%.

3.5. Room temperature continuous wave (CW) operation

The considerable reduction in threshold current density allowed us to realize RT CW operation of a QD injection laser. In this work we report on characteristics of the VECOD laser based on 10 sheet (In,Ga)As QDs separated by 50 Å GaAs spacers. We used 60 μm wide laser diodes. Light output vs. current characteristics, spontaneous electroluminescence, and lasing spectra at various pumping currents are shown in Fig. 8. The maximum power per facet obtained was 160 mW and the differential efficiency was 45%. The lasing spectrum is somewhat broadened and only slightly shifted toward short wavelengths with increasing pumping current. Consequently, lasing proceeds via the states of quantum dots up to $I = (6–7)\, I_{th}$, maximum value of CW operation achieved in the present experiment.

4. Conclusions

Injection lasers based on vertically coupled quantum dots have been shown to exhibit considerable advantages over the single-sheet quantum dot lasers studied previously. They demonstrate remarkable reduction in threshold current density with increasing number of dot sheets (100 A/cm^2, $N = 10\,300$ K) and extended range of thermal stability due to increase in optical confinement factor and carrier localization energy. An external AlGaAs/GaAs quantum well increases the separation between the energy levels in the quantum dots, wetting layer, and GaAs matrix, leading to further extension of the range of J_{th} thermal stability up to room temperature. T_0 as high as 350 K was obtained in the entire 77–300 K range. Inserting (In,Ga)As QDs into an AlGaAs matrix in combination with high-temperature growth of emitter and wavequide layers allowed us to obtain RT threshold current density as low as 60–80 A/cm^2 and internal quantum efficiency as high as 70%. Room temperature CW operation of QD injection laser and lasing via the states of quantum dots up to $I = (6–7)\, I_{th}$ have been demonstrated.

Acknowledgements

This work is supported by INTAS (Grant 94-1028), Volkswagen Foundation, and Russian Foundation for Fundamental Research (Grant 96-02-17824).

References

[1] Y. Arakawa and H. Sakaki, Appl. Phys. Lett. 40 (1982) 939.
[2] P.M. Petroff and S.P. Den Baars, Superlattice Microstruct. 15 (1994) 15.
[3] N.N. Ledentsov, M. Grundmann, N. Kirstaedter, O. Schmidt, R. Heitz, J. Bohrer, D. Bimberg, V.M. Ustinov, V.A. Schukin, P.S. Kop'ev, Zh.I. Alferov, S.S. Ruvimov, A.O. Kosogov, P. Werner, U. Richter, U. Gosele and J. Heidenreich, Sol. State. Electron. 40 (1996) 785.
[4] N. Kirstaedter, N.N. Ledentsov, M. Grundmann, D. Bimberg, U. Richter, S.S. Ruvimov, P. Werner, J. Heydenreich, V.M. Ustinov, M.V. Maximov, P.S. Kop'ev and Zh.I. Alferov, Electron Lett. 30 (1994) 1416.
[5] D. Bimberg, N.N. Ledentsov, M. Grundmann, N. Kirstaedter, O.G. Schmidt, M.H. Mao, V.M. Ustinov, A.Yu. Eegorov, A.E. Zhukov, P.S. Kop'ev, Zh.I. Alferov, S.S. Ruvimov, U. Gosele and J. Heydenreich, Phys. Status Solidi (b) 194 (1996) 159.
[6] Q. Xie, A. Madhukar, P. Chen and N. Kobayashi, Phys. Rev. Lett. 75 (1995) 2542.
[7] N.N. Ledentsov, V.A. Schukin, M. Grundmann, N. Kirstaedter, J. Bohrer, O. Schmidt, D. Bimberg, V.M. Ustinov, A.Yu. Egorov, A.E. Zhukov, P.S. Kop'ev, S.V. Zaitsev, Zh.I. Alferov, A.I. Borovkov, A.O. Kosogov, S.S. Ruvimov, P. Werner, U. Gosele and J. Heydenreich, Phys. Rev. B 54 (1996) 8743.
[8] V.M. Ustinov, A.Yu. Egorov, A.E. Zhukov, N.N. Ledentsov, M.V. Maksimov, A.F. Tsatsul'nikov, N.A. Bert, A.O. Kosogov, P.S. Kop'ev, Zh.I. Alferov and D. Bimberg, Proc. MRS 1995 Fall Meeting, Boston, USA (1995).
[9] M.V. Maksimov, Yu.M. Shernyakov, S.V. Zaitsev, N.Yu. Gordeev, A.Yu. Egorov, A.E. Zhukov, P.S. Kop'ev, A.O. Kosogov, A.V. Sakharov, N.N. Ledentsov, V.M. Ustinov, A.F. Tsatsul'nikov, Zh.I. Alferov, J. Bohrer and D. Bimberg, Semiconductors 31 (1997), in press.
[10] S.V. Zaitsev, N.Yu. Gordeev, V.M. Ustinov, A.E. Zhukov, A.Yu. Egorov, M.V. Maksimov, A.F. Tastsul'nikov, N.N. Ledentsov, P.S. Kop'ev, D. Bimberg and Zh.I. Alferov, Semiconductors (1996), to appear.
[11] A.E. Zhukov, A.Yu. Egorov, A.R. Kovsh, V.M. Ustinov, M.V. Maksimov, A.F. Tsatsul'nikov, N.N. Ledentsov, N.Yu. Gordeev, S.V. Zaitsev and P.S. Kop'ev, Abstracts of Int. Symp. on Nanostructures: Physics and Technology, St. Petersburg (1996) p. 137.
[12] A.R. Kovsh, M.A. Odnoblyudov, A.Yu. Egorov, A.E. Zhukov, V.M. Ustinov, A.F. Tsatsul'nikov, M.V. Maksimov, N.N. Ledentsov and P.S. Kop'ev, Abstracts of Int. Symp. on Nanostructures: Physics and Technology, St. Petersburg (1996) p. 286.
[13] M. Grundmann, O. Stier and D. Bimberg, Phys. Rev. B 52 (1995) 11969.

ELSEVIER

Journal of Crystal Growth 175/176 (1997) 696–701

JOURNAL OF CRYSTAL GROWTH

Overgrowth of InGaAs quantum dots formed by alternating molecular beam epitaxy

Richard P. Mirin*,[1], James P. Ibbetson, John E. Bowers, Arthur C. Gossard

Electrical and Computer Engineering Department and QUEST, University of California, Santa Barbara, California 93106, USA

Abstract

Alternating molecular beam epitaxy is used to grow InGaAs quantum dots on (1 0 0) GaAs by utilizing the Stranski–Krastanow growth transition. A growth pause during the overgrowth with GaAs that is used to bury the quantum dots improves the photoluminescence intensity and line width compared to continuous growth of GaAs. The optimum thickness of GaAs to grow at the quantum dot growth temperature of 515°C is 9.0 nm. Multiple layers of quantum dots have been grown, and transmission electron micrographs show vertical alignment between the layers. Intensity-dependent, room-temperature photoluminescence shows that excited-state luminescence can be reduced by using multiple layers of quantum dots, but growing too many layers leads to degradation of the photoluminescence intensity.

Keywords: Quantum dots; Indium gallium arsenide; MBE

1. Introduction

Molecular beam epitaxy (MBE) is generally used to grow heterostructures of III–V semiconductors because of the atomically flat interfaces that are required for quantum well structures and devices. However, highly lattice-mismatched layers grown by MBE do not grow in a layer-by-layer fashion. Instead, these lattice-mismatched layers grow in the layer-plus-island (Stranski–Krastanow) growth mode due to a reduction in the strain energy from the island formation. The islands formed are quantum-sized, and this layer-plus-island growth mode has been successfully used to grow arrays of quantum dots (QDs) in the In(Ga)As/GaAs system [1–5], as well as many other III–V semiconductor combinations.

Several groups have recently demonstrated room-temperature operation of QD lasers [6–8] with just a single layer of QDs. Just as in quantum well (QW) lasers, though, it is desirable to obtain higher gain by stacking multiple layers of QDs. Multiple layers of QDs have also recently been demonstrated [1, 9–11], and QD lasers and vertical cavity lasers have been formed with multilayer structures [12, 13]. However, little attention has

* Corresponding author.

[1] Present address: Optoelectronics Division, National Institute of Standards and Technology, 325 Broadway, Boulder, Colorado 80303, USA.

0022-0248/97/$17.00 Copyright © 1997 Published by Elsevier Science B.V. All rights reserved
PII S0022-0248(96)00870-6

been paid to the *overgrowth and burial* of these strained, nonplanar QDs [14], although it has been shown that it is possible to have rough interfaces at subsequent layers due to the underlying islands [9]. Furthermore, the overgrowth thickness has been shown to be very important in determining the structural and optical properties of thin InAs QWs on GaAs [15]. Thus, this GaAs overgrowth is important not only for smoothing the surface so that multiple layers of QDs can be grown with good layer-to-layer uniformity, but also for minimizing the number of nonradiative defects, as is required for optimal devices. Strong interaction between layers via roughness or strain fields can lead to vertical alignment of islands [9–11]. However, this interaction can also lead to layer-to-layer nonuniformity. In this paper, we will describe our experimental techniques for improving the optical properties of QDs and the QD uniformity, both within a single layer and layer-to-layer.

2. Continuous growth versus growth pause

2.1. Sample growth

The samples are grown on semi-insulating, (1 0 0) GaAs substrates in a Varian Gen II MBE machine equipped with an EPI valved arsenic cracking cell. The As_2 flux is kept constant throughout the growth and has a beam equivalent pressure (BEP) of 9.0×10^{-6} Torr. This BEP is converted to an arrival rate of about 2.0 ML/s of atomic arsenic by measuring As-induced reflection high-energy electron diffraction (RHEED) oscillations on a Ga-saturated, GaAs surface [16]. A 0.25 μm GaAs buffer is grown at 590°C at a rate of about 0.93 ML/s. The sample is then cooled to 515°C under As_2 flux for the growth of the InGaAs quantum dots.

The shutter sequence for the growth of the InGaAs is as follows: 0.265 ML In, 2.0 ML As, 0.62 ML Ga, 3 s growth pause, and 6.0 ML As. This cycle is repeated 20 times, giving an epilayer that nominally has 30% In mole fraction and a thickness of 17.7 ML. The 2D–3D RHEED transition occurs between 7.1 and 8.0 ML of deposition. The actual In mole fraction of the quantum dots is larger than 30%, though, due to In segregation to the growth front under these growth conditions.

GaAs is then deposited using conventional MBE (simultaneous beams of Ga and As_2). Samples CG (continuous growth) and GP (growth pause) have 8.0 nm of GaAs deposited at the InGaAs growth temperature of 515°C. Then, the substrate temperature of sample CG is raised to 590°C while an additional 50 nm of GaAs is deposited. Sample GP has a growth pause under As_2 flux in order to raise the substrate temperature to 570°C. When the temperature reaches 570°C, an additional 50 nm of GaAs is deposited while the temperature is increased to 590°C. Both samples then have 50 nm of $Al_{0.4}Ga_{0.6}As$ and 50 nm of GaAs deposited at 590°C.

2.2. Optical characterization

Room-temperature photoluminescence (RTPL) spectra from samples CG and GP are shown in Fig. 1. The peak emission wavelength from sample CG is at about 1260 nm, compared to about 1220 nm from sample GP. The full-width at half-maximum (FWHM) from sample CG is 60.0 meV versus 41.5 meV for sample GP. The peak emission intensity from sample GP is about 3 times that of sample CG. The integrated PL intensity from sample GP is almost double that of sample CG.

The shift in peak emission wavelength between the two samples can be attributed to In segregation into the GaAs overgrowth, and possibly In evaporation, during the growth pause while the sample

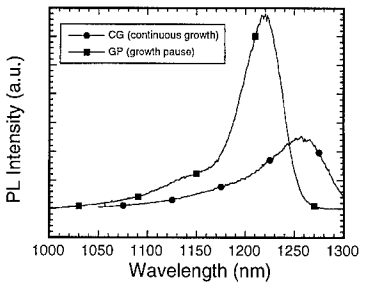

Fig. 1. Room-temperature photoluminescence spectra show the differences between continuous growth and a growth pause to raise the substrate temperature during the overgrowth of InGaAs islands.

temperature is raised to 570°C. Indium segregation leads to shallower confinement, and the ground state of the electron is raised in energy as the electron becomes more characteristic of the barrier, thus blue-shifting the emission wavelength.

Since the surface is nonplanar due to the InGaAs islands, the 8.0 nm of GaAs will not uniformly bury the islands. When the substrate temperature is raised above about 540°C, In near the surface may evaporate from the islands. Note that is especially important on the non-(1 0 0) oriented sidewalls of the islands, as it has been shown that In segregation is enhanced along these directions [15]. As the In evaporates, the islands become smaller, and the bandgap of the island increases due to the larger Ga mole fraction. The consequence of the smaller islands is that the quantization energy increases, and the emission wavelength decreases. As the bandgap increases, the emission wavelength decreases. Thus, In segregation and evaporation from the islands qualitatively explains the decrease in emission wavelength from sample GP.

3. Optimization of overgrowth thickness

3.1. Sample growth

Three samples are grown to determine the optimum thickness of the low-temperature (515°C) GaAs overgrowth layer immediately adjacent to the InGaAs islands. Samples OG3, OG6, and OG12 have the same epilayer structure as sample GP, except the thickness of GaAs grown at 515°C is 3.0, 6.0, and 12.0 nm, respectively. Next comes a growth pause under As_2 flux while the substrate temperature is raised to 570°C. Then, additional GaAs is deposited to give a total of 58 nm for each sample. Finally, 50 nm of $Al_{0.4}Ga_{0.6}As$ and 50 nm of GaAs are deposited at 590°C.

3.2. Optical characterization

RTPL spectra from these three samples are shown in Fig. 2. OG6 has the highest peak intensity of the three samples. The integrated intensity from OG6 and OG12 is approximately equal, and both are about twice the integrated intensity of OG3.

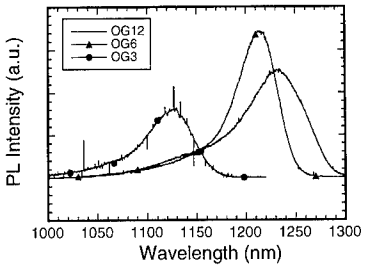

Fig. 2. Room-temperature photoluminescence spectra show the variations in intensity and peak position as a function of the thickness of GaAs that is deposited at the InGaAs island growth temperature of 515°C.

The FWHM of OG6 is only 42 meV, compared to 53 meV from OG3 and 60 meV from OG12. The peak emission wavelength from OG12 is at 1234 nm, compared to 1213 nm from OG6 and 1129 nm from OG3.

As with the previous example, the wavelength shift can be attributed to In segregation and evaporation. It is likely that In evaporation has occurred in OG3, with its thin (3.0 nm) GaAs overgrowth, since the wavelength shifts by about 100 nm compared to OG12. The wavelength shift between OG12 and OG6 is only about 20 nm, so it is unclear if this is due only to segregation or if evaporation is also occurring.

A second set of samples is grown in order to further study the effect of the overgrowth. In this set of samples, the identical epilayer structure is used, and the low temperature overgrowth thicknesses used are 4.5, 6.0, 7.5, and 9.0 nm. The sample with the 9.0 nm overgrowth has a peak intensity three times greater than any of the other samples, and a FWHM that is only 38 meV, whereas all the other samples have line widths of at least 45 meV. Thus, we conclude that 9.0 nm is the optimum thickness of GaAs to grow at the InGaAs quantum dot temperature of 515°C.

4. Multiple quantum dot layers

4.1. Sample growth

The same alternating MBE technique described above is also used to grow multiple layers of QDs.

Samples M17-1 and M17-2 have one and two layers of 17.7 ML $In_{0.3}Ga_{0.7}As$ QDs, respectively. The GaAs barrier in the two layer sample is 25.0 nm. The first 9.0 nm are grown at the InGaAs growth temperature of 515°C. Then there is a growth pause while the substrate temperature is increased to 570°C, and the remaining 16.0 nm of GaAs are deposited as the substrate temperature is increased from 570°C to 590°C. The temperature is then decreased to 515°C to grow the second layer of QDs. Samples M13-1, -3, and -5 have one, three, and five layers of 13.3 ML $In_{0.3}Ga_{0.7}As$ QDs, respectively. The same growth procedure used for M17-2 is used for the samples with multiple layers of QDs. The 2D–3D RHEED transition occurs between 7.1 and 8.0 ML for the first two layers, but occurs between 6.2 and 7.1 ML for the subsequent three layers for the five layer sample.

4.2. Optical characterization

RTPL spectra at various pump powers are shown for M17-1 (Fig. 3a) and M17-2 (Fig. 3b). The lowest pump power is approximately 0.22 mW, and the highest pump power is approximately 169 mW. Note that the vertical scales differ by one order of magnitude, with the single QD layer sample showing greater intensity. This is not the case for a similar group of InGaAs QW samples, where the double QW sample has much brighter luminescence than does the single QW sample.

At 0.22 mW pump power, M17-1 has a peak emission wavelength of 1250 nm and a FWHM of about 51 meV. However, as the pump power is increased the line width increases rapidly as excited-state luminescence becomes more pronounced. At a pump power of about 27 mW, the ground-state luminescence is saturated and the excited-state luminescence intensity surpasses that of the ground state.

At 0.22 mW pump power, M17-2 has a peak emission wavelength of 1276 nm and a FWHM of about 28 meV. This line width is improved compared to M17-1. It has been predicted theoretically that subsequent layers will have improved uniformity [17]. However, there is some ambiguity in this case because the intensity has degraded sharply compared to the single layer of QDs, which suggests that the second layer of QDs in M17-2 has nonradiative defects. Also, the carrier concentration is lower in M17-2 than in M17-1 because M17-2 has two layer of QDs. Since state-filling effects are very strong in these samples, as indicated by the excited-state luminescence, a lower carrier concentration should lead to a narrower line width.

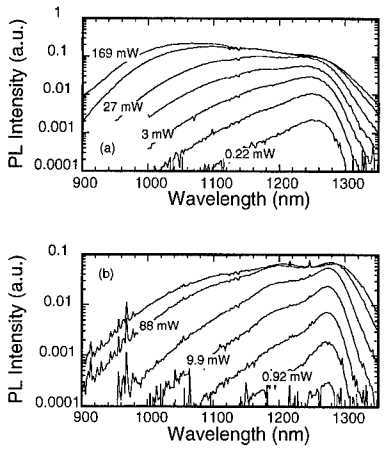

Fig. 3. (a) Intensity-dependent, room-temperature PL from a single layer of 17.7 ML InGaAs quantum dots. Note the strong state-filling effects at high pump powers. (b) Intensity-dependent, room-temperature PL from two layers of 17.7 ML InGaAs quantum dots, separated by a 25 nm GaAs barrier. The emission intensity is much weaker than the single layer sample (note the difference in vertical scales).

RTPL spectra at various pump powers are shown for M13-1 (Fig. 4a), M13-3 (Fig. 4b), and M13-5 (Fig. 4c). The peak emission wavelength at low pump power from M13-1, -3, and -5 is at 1154, 1188, and 1180 nm, respectively. The peak intensity and the integrated intensity from the three layer QD sample is comparable to that of the single layer QD sample. However, both of these quantities are decreased in the five-layer QD sample. The line width from M13-1 is slightly lower than that of M13-3 at low pump power, but increases more rapidly as the excitation power is increased and excited-state luminescence becomes more pronounced. The line shape remains approximately constant for the three-layer QD sample over the range of pump powers used in this experiment. The line width of the five-layer QD sample increases

rapidly as the pump power increases, and several shoulders are observed around the main peak.

The shift in peak emission wavelength from the multilayer samples indicates some layer-to-layer nonuniformity. This correlates with the RHEED observations that the 2D–3D transition occurs when fewer monolayers have been deposited for subsequent layers, which indicates either insufficient smoothing by the GaAs barrier or strain-field interaction with the surface. This allows the islands to grow taller than the previous layers, and thus have lower quantization energy and longer wavelength emission. The relatively poor intensity of the five-layer sample suggests that nonradiative defects have been introduced into the uppermost layers of QDs, which should be the tallest layers and thus have the longest emission wavelength Consequently, the peak emission wavelength from the five-layer sample is about the same as that of the three-layer sample.

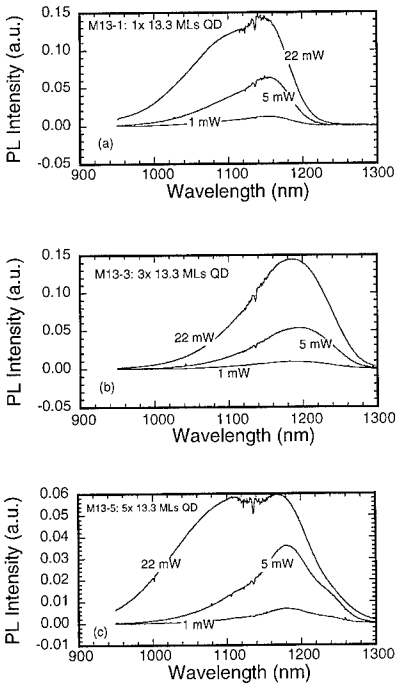

Fig. 4. (a) Intensity-dependent, room-temperature PL from a single layer of 13.3 ML InGaAs quantum dots. (b) Intensity-dependent, room-temperature PL from three layers of 13.3 ML InGaAs quantum dots. (c) Intensity-dependent, room-temperature PL from five layers of 13.3 ML InGaAs quantum dots. Note the drop in emission intensity.

4.3. Transmission electron microscopy

Transmission electron microscopy (TEM) images of M13-1, -3, and -5 are shown in Fig. 5a–Fig. 5c, respectively. The images are taken under two-beam, (2 0 0) dark field conditions to maximize chemical contrast. The multiple layers samples both show vertical alignment of the islands, as has been demonstrated by others [1, 9–11]. The starting surface for each dot layer appears to be flat, so it is likely that the strain field from the underlying islands interacts with the surface to cause this alignment [10].

The subsequent layers of islands get progressively larger, both in the vertical direction and in the lateral direction. This agrees with the RHEED observations that subsequent layers undergo the 2D–3D transition at a slightly lower deposited thickness. It also agrees with the PL spectra, which show a longer emission wavelength for multiple layer samples. Finally, the TEM image of the five-layer sample shows some unusual contrast directly under some of the island stacks. This contrast is not observed in the one-layer and three-layer samples. No threading dislocations are observable under

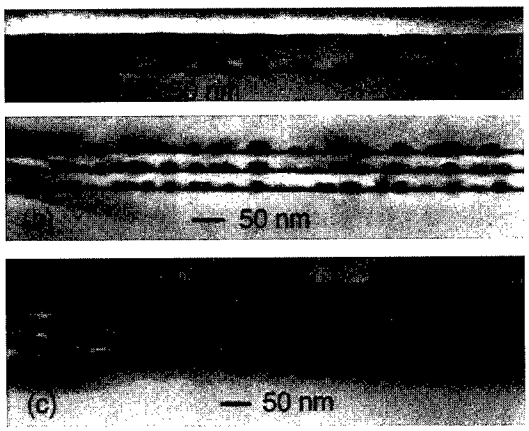

Fig. 5. (a) (2 0 0), dark field TEM image of a single layer 13.3 ML InGaAs sample. (b) (2 0 0), dark field TEM image of a three layer, 13.3 ML InGaAs sample. (c) (2 0 0), dark field TEM image of a five layer, 13.3 ML InGaAs sample.

various beam conditions, but we speculate that this contrast is caused by some defects that are also the cause of the reduced emission intensity from the five-layer sample.

5. Conclusions

We have demonstrated that the overgrowth of GaAs on highly nonplanar, strained InGaAs islands plays an important role in determining the optical properties of these islands. A growth pause after partial burial of the islands improves the PL intensity and line width from the array of islands. There is an optimum thickness of this overgrowth that prevents excess In evaporation from the islands, but still allows high-quality GaAs to be deposited. Multiple layers of QDs have been studied by RHEED, PL, and TEM. The RHEED transition gives a good indication of the layer-to-layer uniformity from the QDs. PL peak emission wavelengths and TEM images correlate with the RHEED observations. Although the formation of islands provides some strain relief, there is still a limit to the number of layers of QDs that can be stacked, as indicated by the decrease in PL intensity and the defects seen from some multilayer samples. The number of layers that can be deposited depends on the composition and thickness of the islands. These results have important consequences for the growth of quantum dot lasers and multilayer quantum dot lasers.

Acknowledgements

The authors would like to thank John English and Tom Reynolds for providing technical assistance. This research is supported by the National Science Foundation's Center for Quantized Electronic Structures (QUEST), Grant No. DMR91-20007.

References

[1] L. Goldstein, F. Glas, J. Marzin, M. Charasse and G. LeRoux, Appl. Phys. Lett. 47 (1985) 1099.
[2] M. Tabuchi, S. Noda and A. Sasaki, in: Science and Technology of Mesoscopic Structures, Eds. S. Namba, C. Hamaguchi and T. Andoin (Springer, Tokyo, 1992) p. 379.
[3] D. Leonard, M. Krishnamurthy, C. Reaves, S. Denbaars and P. Petroff, Appl. Phys. Lett. 63 (1993) 3203.
[4] J. Moison, F. Houzay, F. Barthe, L. Leprince, E. André and O. Vatel, Appl. Phys. Lett. 64 (1994) 196.
[5] R. Mirin, J. Ibbetson, K. Nishi, A. Gossard and J. Bowers, Appl. Phys. Lett. 67 (1995) 3795.
[6] N. Kirstaedter, N. Ledentsov, M. Grundmann, D. Bimberg, V. Ustinov, S. Ruvimov, M. Maximov, P. Kop'ev, ZH. Alferov, U. Richter, P. Werner, U. Gösele and J. Heydenreich, Electron. Lett. 30 (1994) 1416.
[7] K. Kamath, P. Bhattacharya, T. Sosnowski, T. Norris and J. Phillips, Electron. Lett. 32 (1996) 1374.
[8] R. Mirin, A. Gossard and J. Bowers, Electron. Lett. 32 (1996) 1732.
[9] J. Yao, T. Andersson and G. Dunlop, J. Appl. Phys. 69 (1991) 2224.
[10] Q. Xie, A. Madhukar, P. Chen and N. Kobayashi, Phys. Rev. Lett. 75 (1995) 2542.
[11] G. Solomon, J. Trezza, F. Marshall and J. Harris, Jr., Phys. Rev. Lett. 76 (1996) 952.
[12] D. Bimberg, N. Ledentsov, M. Grundmann, N. Kirstaedter, O. Schmidt, M. Mao, V. Ustinov, A. Egorov, A. Zhukov, P. Kopev, Zh. Alferov, S. Ruvimov, U. Gosele and J. Heydenreich, Jpn. J. Appl. Phys. 35 (1996) 1311.
[13] H. Saito, K. Nishi, I. Ogura, S. Sugou and Y. Sugimoto, Appl. Phys. Lett. 69 (1996) 3140.
[14] Q. Xie, P. Chen, A. Kalburge, T. Ramachandran, A. Nayfonov, A. Konkar and A. Madhukar, J. Crystal Growth 150 (1995) 357.
[15] M. Ilg, M. Isabel Alonso, A. Lehmann, K. Ploog and M. Hohenstein, J. Appl. Phys. 74 (1993) 7189.
[16] J. Neave, B. Joyce and P. Dobson, Appl. Phys. A 34 (1984) 179.
[17] J. Tersoff, C. Teichert and M. Lagally, Phys. Rev. Lett. 76 (1996) 1675.

ELSEVIER

Journal of Crystal Growth 175/176 (1997) 702–706

JOURNAL OF CRYSTAL GROWTH

Self-assembling InP quantum dots for red lasers

K. Eberl[a,*], A. Kurtenbach[a], M. Zundel[a], J.Y. Jin-Phillipp[b], F. Phillipp[b], A. Moritz[c], R. Wirth[c], A. Hangleiter[c]

[a] *Max-Planck-Institut für Festkörperforschung, Heisenbergstrasse 1, D-70569 Stuttgart, Germany*
[b] *Max-Planck-Institut für Metalforschung, Heisenbergstrasse 1, D-70569 Stuttgart, Germany*
[c] *Physikalisches Institut, University Stuttgart, Pfaffenwaldring 57, D-70569 Stuttgart, Germany*

Abstract

Self-assembling InP quantum dots are prepared by solid source molecular beam epitaxy. The dots have a diameter of 15 to 50 nm and a height of 5 to 15 nm depending on the nominally deposited InP layer thickness between 1.5 and 7 ML. Transmission electron microscopy measurements are presented to provide information about the structural properties. The InP quantum dots are embedded in $Ga_{0.52}In_{0.48}P$ lattice matched to the GaAs (1 0 0) substrate and show a strong and narrow photoluminescence at room temperature in the visible range. Laser structures are prepared with one layer of InP quantum dots within a 160 nm thick $Ga_{0.52}In_{0.48}P$ waveguide region. 0.7 μm thick AlInP layers are used as cladding layers below and above the waveguide. We observe lasing of the InP quantum dots at room temperature in optically pumped cleaved samples with a length of 500 μm.

Quantum dots based on III/V semiconductor heterostructures are interesting for fundamental research and future device applications. The discrete energy spectrum in zero-dimensional systems promises advantages especially for laser diodes [1]. The concept of self-assembling quantum dots is based on the Stranski–Krastanov growth mode in strained layer heteroepitaxy of materials with a large lattice mismatch [2]. This method offers the possibility to prepare extremely small quantum dots in a simple process without lithography. The materials which have been investigated mainly are InAs and InGaAs on GaAs or AlGaAs [3–9], and InP on $Ga_{0.52}In_{0.48}P$ [9–12].

We are interested in the preparation of InP/$Ga_{0.52}In_{0.48}P$ quantum dots. $Ga_{0.52}In_{0.48}P$ is lattice matched to the GaAs substrate and has a direct band gap at 1.95 eV at 4 K. The lattice mismatch of InP to $Ga_{0.52}In_{0.48}P$ is 3.7%. We have already demonstrated that the energy of the photoluminescence (PL) from the InP islands is adjustable by the amount of InP. An energy shift is observed from 1.85 to 1.53 eV as the nominally deposited thickness increases from 2 monolayers (ML) to 10 ML [11]. Intense PL is obtained even at room temperature as shown in Fig. 2, which makes

* Corresponding author. Tel.: 49 (0)711 689 1312; fax: 49 (0)711 689 1010; email: eberl@servix.mpi-stuttgart.mpg.de.

0022-0248/97/$17.00 Copyright © 1997 Elsevier Science B.V. All rights reserved
PII S0022-0248(96)00813-5

it a promising material system for quantum dot laser diodes. The open question is how much does the size distribution of the dots deteriorate the laser properties, and what is the influence of the wetting layer. In this contribution we report on the preparation of optically pumped self-assembling InP/$Ga_{0.52}In_{0.48}P$ quantum dot laser structures which emit in the visible range at room temperature.

The samples were grown on GaAs (1 0 0) substrates by solid source molecular beam epitaxy (MBE). The phosphorus compounds were prepared by using a GaP decomposition source which provides a very clean and stable P_2 beam [13]. For all samples a 200 nm thick GaAs buffer layer was deposited on semi-insulating GaAs substrates at a temperature of $T_s = 580°C$. The $Ga_{0.52}In_{0.48}P$, $Al_{0.51}In_{0.49}P$ and InP layers were deposited at a substrate temperature of $T_s = 470°C$ with a beam equivalent P_2 pressure of about 5×10^{-6} Torr. The growth rate for InP and $Ga_{0.52}In_{0.48}P$ was 0.5 and 1 ML, respectively.

Fig. 1 shows a plan view transmission electron microscopy (TEM) image from an InP/$In_{0.52}Ga_{0.48}P$ quantum dot structure. One layer of dots with nominally 3 ML InP is grown on top of a 50 nm $Ga_{0.52}In_{0.48}P$ layer. The dots are overgrown by another 50 nm thick $Ga_{0.52}In_{0.48}P$ cap layer. The larger dark spots clearly show the InP island formation. Misfit dislocations have not been detected in this and in other cross-sectional TEM micrographs for the 2 and 3 ML InP dot samples [14]. The size of the islands is 20 to 30 nm in diameter and the density is about 5×10^{10} cm^{-2}. This is comparable to the data obtained from atomic force microscopy from 3 ML islands directly on the surface of a $Ga_{0.52}In_{0.48}P$ layer.

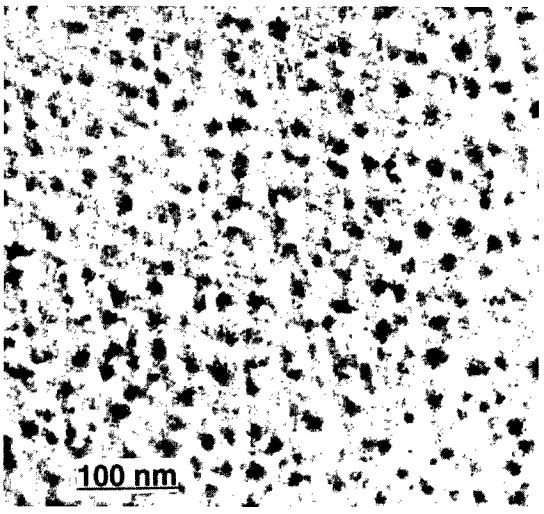

Fig. 1. TEM plan view micrograph from an InP/$Ga_{0.52}In_{0.48}P$ quantum dot structure. The dot layer with nominally three ML InP is embedded in 50 nm $Ga_{0.52}In_{0.48}P$ grown on GaAs (1 0 0) substrate. The size of the InP dots is about 20 to 30 nm in diameter and the density is about 5×10^{10} cm^{-2}.

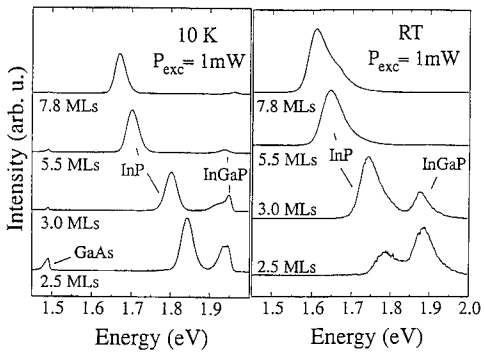

Fig. 2. PL spectra measured at (a) 10 K and (b) room temperature (RT) for samples with InP islands embedded in $Ga_{0.52}In_{0.48}P$. The nominal InP thickness is 2.5, 3, 5.5 and 7.8 ML. The typical PL line width is 30 meV at 10 K and 60 meV at RT.

Fig. 2 shows PL spectra measured at (a) 10 K and (b) room temperature (RT) for samples with InP islands embedded in the middle of a 400 nm thick $Ga_{0.52}In_{0.48}P$ layer. The measurements were performed using the 514.5 nm line of an Ar+ laser for excitation. The excitation density was 1 W/cm^2. The nominal InP thickness is 2.5, 3, 5.5 and 7.8 ML. In the low-temperature spectra we observe three peaks originating from the GaAs buffer layer (close to 1.5 eV), the $Ga_{0.52}In_{0.48}P$ barrier layer (close to 1.95 eV) and the InP dot peak. The typical PL line-width for the dots is 30 meV at 10 K and 60 meV at RT. The InP dot luminescence shifts with the increasing nominal layer thickness, which indicates the increasing size of the InP islands. At the same time the integrated intensity increases significantly against the PL signal from the

$Ga_{0.52}In_{0.48}P$ barrier layer. At 10 K the InP dot peak is a factor of 35 more intense than the $Ga_{0.52}In_{0.48}P$ peak. The strong blue shift of the InP dot PL against bulk InP is essentially due to the confinement effect and the compressive strain within the island.

A shift of the PL energy with increasing nominal layer thickness was also observed for MBE grown InAs dots on GaAs [15]. In contrast to this, MOCVD grown $InP/Ga_{0.52}In_{0.48}P$ structures show an energetically constant PL at 1.64 eV for InP coverages above 2.5 ML [12]. Beside this they observe another PL line around 1.9 eV. The reason of the different results for MBE and MOCVD grown samples is probably the higher surface diffusion in the MOCVD process which leads to the formation of larger islands. Especially for the $InP/Ga_{0.52}In_{0.48}P$ material system there seems to be a pronounced 2-fold size distribution. In comparison to MOCVD grown self-assembling InP dots on $Ga_{0.52}In_{0.48}P$ it seems that the MBE samples prepared at relatively low temperatures provides a more homogeneous size distribution and smaller dots with higher confinement energy.

The room temperature PL spectra in Fig. 2b show an asymmetric shoulder towards higher energies. For ideal quantum dots with a large energy separation between ground state and excited states the line width should not depend on temperature. Possible explanations for the observed broadening of the line width are phonon scattering processes, electron–light hole transitions, and transitions to higher excited states within individual islands. The existence of an excited state has already been reported in photoreflectance measurements on these samples [14]. Another possible mechanism is thermal reemission of carriers from larger dots into coupled smaller dots. Phonon assisted coupling of dots with different size has been observed in resonant time resolved PL measurements [16].

To summarize, the PL properties of the InP quantum dot samples are the following: The PL energy is in the visible range and can be varied by adjusting the nominal InP layer thickness. The integral intensity is very high and dominates even at room temperature for dots formed from 3 ML InP or more. Consequently, the $InP/Ga_{0.52}In_{0.48}P$ self-assembling quantum dot system is a promising candidate for laser diodes.

After carefully optimizing the growth parameters in order to get maximum PL intensity and minimum line width we prepared laser structures for optical gain measurements and optical pumping. The 3 ML InP dots are used for the laser structures because they provide a strong PL signal at room temperature and because they are very small and have a high density within one layer of dots as shown in Fig. 1. Fig. 3 shows a cross-sectional TEM micrograph from an $InP/Ga_{0.52}In_{0.48}P$ quantum dot laser structure with 0.9 μm thick $Al_{0.51}In_{0.49}P$ cladding layers. The 120 nm thick $Ga_{0.52}In_{0.48}P$ waveguide contains one layer of nominally 3 ML InP quantum dots. During the InP deposition the self-assembling islands are formed on top of a 1 to 1.5 ML thick wetting layer. The inset in the upper left corner shows a magnification of the dot layer which is right in the middle of the waveguide. The laser structure is grown on a GaAs substrate and covered with a 50 nm thick GaAs cap layer. The quantum dot related PL from this sample is observed at 1.76 eV with a FWHM of 60 meV at room temperature. The line width at 4.2 K is 28 meV. Optical gain measurements have been reported in Ref. [17].

We have optically pumped a cleaved sample similar to the one shown in Fig. 3 with a cavity length of 500 μm. The waveguide in this sample was 160 nm and the thickness of the cladding layers was 0.7 μm. Fig. 4a shows the intensity of the optical output as a function of the pumping intensity for the peak energies of the quantum dots (QD) and the wetting layer (WL). The wetting layer was not observed in PL; however, it is clearly identified in the gain measurements [17]. Fig. 4b shows the corresponding emission spectrum for 43 kW/cm^2 pumping intensity at room temperature. Above a pumping intensity of about 25 kW/cm^2 the optical output of the quantum dots increases due to lasing activity while the emission from the wetting layer remains relatively weak. The threshold of this laser structure is comparable to values obtained in the same experimental set-up with GaInP/AlGaInP double quantum wells in a similar structure.

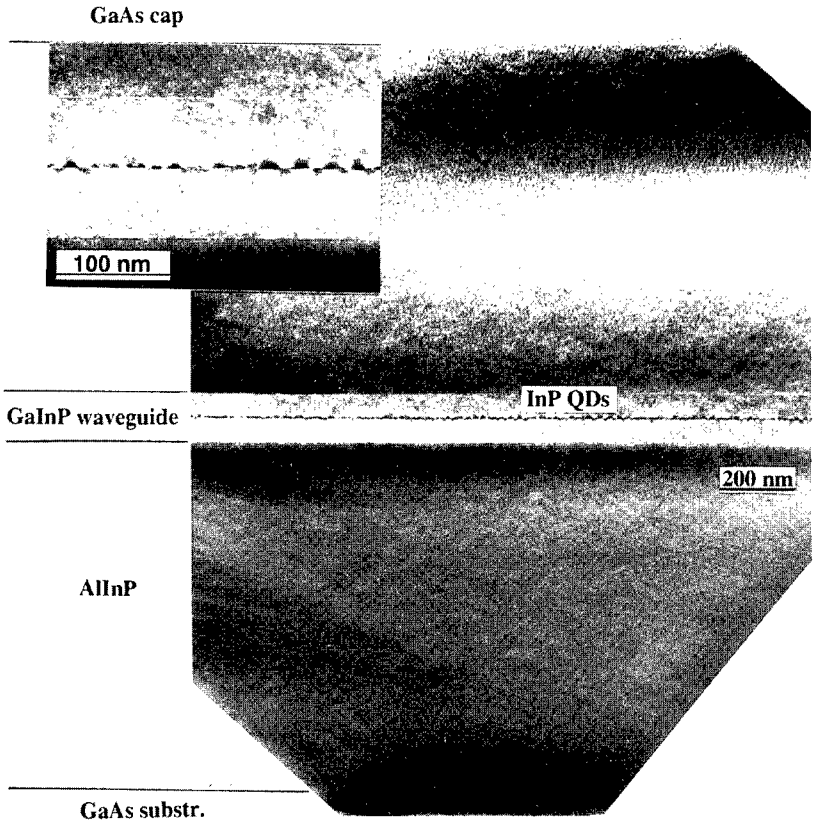

Fig. 3. TEM micrograph from a InP/$Ga_{0.52}In_{0.48}P$ quantum dot laser structure with $Al_{0.51}In_{0.49}P$ cladding layers. The 120 nm thick $Ga_{0.52}In_{0.48}P$ waveguide contains one layer of nominally three ML InP quantum dots. The inset show a magnification of the dot layer.

The behaviour of getting stimulated emission from both the wetting layer and the dots can be explained only if the carriers are not in thermal equilibrium. One explanation is spatial separation of the dots and the wetting layer. A thinner or vanishing wetting layer around the dots has been observed for InAs dots [15]. The consequence of that would be a separated transition rate from the waveguide into the dots and the wetting layer. Further details about the optical characterisation of the laser structure are given in Ref. [17].

In summary, we have demonstrated lasing activity from InP quantum dots at room temperature. This is the first quantum dot laser structure based on InP/$Ga_{0.52}In_{0.48}P$. The observation of an intense laser line from the InP quantum dots is surprising, considering that self-assembling dots have a relatively broad size distribution and that the active volume is extremely small compared to a quantum well laser. Future experiments will concentrate on the introduction of several layers of dots into the waveguide and on removing the wetting layer by in situ etching techniques as demonstrated in Ref. [18].

Acknowledgements

The authors would like to thank K. Tötemeyer and C. Lange for technical assistance, and K. von Klitzing for continuously supporting this work. We acknowledge the financial support by the Bundesministerium für Bildung Wissenschaft und Technologie within the program of quantum structure systems based on III/V semiconductors.

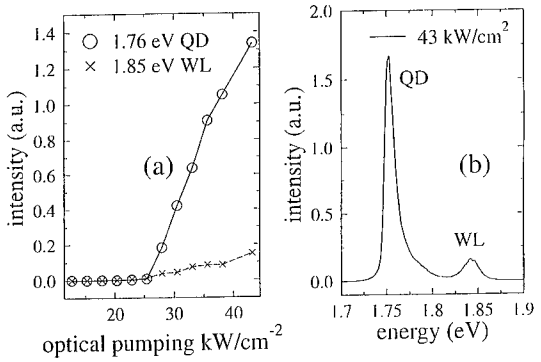

Fig. 4. (a) Intensity of the optical output as a function of the pumping intensity for InP dots/$Ga_{0.52}In_{0.48}P/Al_{0.51}In_{0.49}P$ laser structures with 5 0 0 μm length. (b) shows the corresponding emission spectrum for 43 kW/cm^2 pumping intensity (QD: quantum dots, WL: wetting layer. The measurements are performed at room temperature.

References

[1] M. Asada, Y. Miyamoto and Y. Suematsu, IEEE J. Quantum Electron. QE-22 (1986) 1915.
[2] K. Eberl, P.M. Petroff and P. Demeester, Eds., Low Dimensional Structures Prepared by Epitaxial Growth or Regrowth on Patterned Substrates, NATO ASI Series E, Applied Science, Vol. 298 (Kluwer, Dordrecht 1995).
[3] J.Y. Marzin, J.M. Gerard, D. Barrier and G. Bastard, Phys. Rev. Lett. 73 (1994) 716.
[4] P.M. Petroff and S.P. Den Baars, Superlattice Microstruct. 15 (1994) 15.
[5] J. Oshinowo, S. Tsukamoto, M. Nishinoka and Y. Arakawa, Appl. Phys. Lett. 64 (1994) 1221.
[6] R. Nötzel, T. Fukui, H. Hasegawa, J. Temmyo and T. Tamamura, Appl Phys. Lett. 65 (1994) 2854.
[7] Q. Xie, A. Madhukar, P. Cheng and N. Kobayashi, Phys. Rev. Lett. 75 (1995) 2542.
[8] G. Solomon, J. Trezza, A. Marshall and J. Harris, Phys. Rev. Lett. 76 (1996) 952.
[9] D. Bimberg, N. Ledentsov, M. Grundmann, N. Kirchstaedter, O.G. Schmidt, M.H. Mao, V. Ustinov, A. Egorov, A. Zhukov, P. Kopev, Z. Alferov, S.S. Ruvimov, U. Gösele and J. Heydenreich, Jpn. J. Appl. Phys. 35 (1996) 1311.
[10] D. Leonard, K. Pond and P.M. Petroff, Phys. Rev. B 50 (1994) 11687.
[11] A. Kurtenbach, K. Eberl and T. Shitara, Appl. Phys. Lett. 66 (1995) 361.
[12] W. Seifert, N. Carlsson, P. Castrillo, A. Peterson, M.E. Pistol and L. Samuelson, Appl. Phys. Lett. 65 (1994) 3093.
[13] T. Shitara and K. Eberl, Appl. Phys. Lett. 65 (1994) 356.
[14] A. Kurtenback, C. Ulrich, N.Y. Jin-Phillipp, F. Noll, K. Eberl, K. Syassen and F. Phillipp, J. Electron. Mater. 25 (1996) 395.
[15] J.M. Gerard et al., in: Low Dimensional Structures Prepared by Epitaxial Growth or Regrowth on Patterned Substrates, NATO ASI Series E, Applied Science, Eds. K. Eberl, P.M. Petroff and P. Demeester, Vol. 298 (Kluwer, Dordrecht 1995), p. 35.
[16] A. Kurtenbach, W.W. Rühle and K. Eberl, Solid State Commun. 96 (1995) 265.
[17] A. Moritz, R. Wirth, A. Hangleiter, A. Kurtenbach and K. Eberl, Appl. Phys. Lett. 69 (1995) 212.
[18] T. Kaneko, T. Säger and K. Eberl, Mater. Res. Soc. Symp. Proc. 405 (1996).

ELSEVIER

Journal of Crystal Growth 175/176 (1997) 707–712

JOURNAL OF CRYSTAL GROWTH

Increased size uniformity through vertical quantum dot columns

G.S. Solomon[a,*], S. Komarov[b], J.S. Harris, Jr.[b], Y. Yamamoto[a]

[a] *Edward L. Ginzton Laboratory, Stanford University, Stanford, California 94305-4085, USA*
[b] *Solid State Laboratory, Stanford University, Stanford, California 94305-4055, USA*

Abstract

The effects of stacking strain-induced InAs quantum dot layers on the size uniformity and density of dots in the upper most layer have been investigated using single-dot layers, and stacks of 10 and 20 quantum dot layers with a 56 Å space region of GaAs. In these multilayered structures dots from different layers are aligned in vertical columns. X-ray diffraction indicates diffraction from a superlattice of InAs and GaAs, where the InAs contribution to the diffraction is from the quantum well region which is an integral part of the dot formation process. Thus, these quantum well regions remain intact and planar throughout the stacking process. The quantum well thickness is estimated to be 1.9 InAs monolayers. Atomic-force microscopy indicates the dot density decreases with dot layers, while the average dot height and in-plane dot diameter increase with dot layers. The uniformity of dot height and in-plane diameter also increases with stacking of dot layers as has been predicted [J. Tersoff, C. Teichert and M.G. Lagally, Phys. Rev. Lett. 76 (1996) 1675].

PACS: 68.65. + g; 78.66.Fd; 81.15.Hi

Keywords: Self-assembly; InAs; Quantum dots

The precise monolayer (ML) control of current epitaxial crystal growth techniques and the highly developed understanding of the III–V and group IV semiconductors has led to a well-controlled heterointerface and a quantum well (QW) structure that has had a dramatic impact in semiconductor research and mainstream semiconductor technology. The heterointerface control is responsible for the 1-D carrier confinement in the growth direction, and while a significant effort has been concentrated towards extending this control to 2-D and 3-D confinements with quantum wires and quantum dots, the results have been encouraging but not resounding. This is generally so because lithography techniques are needed for increased confinement and the resolution in lithography is not of the monolayer-like resolution available through epitaxial growth techniques. Recently, a purely epitaxial technique has been used to produce quantum dots in the InAs/GaAs [1] and Ge/Si [2] semiconductor systems. This technique

* Corresponding author.

0022-0248/97/$17.00 Copyright © 1997 Published by Elsevier Science B.V. All rights reserved
PII S0022-0248(96)01227-4

utilizes the strain-induced islanding of the Stranski–Krastonow (SK) growth mode in which the growth surface islands, compensating an increase in energy due to extra surface for a decrease in accumulated strain energy. Unfortunately, the large surface migration processes common in SK growth lead to large inhomogeneous island size distributions so that the spectral features are broadened with respect to QWs, and the narrow, atomic-like transitions are lost in the ensemble broadening. This research is still active and with the fine tuning of growth processes which were needed in the development of successful QW technology, the inhomogeneous broadening can be reduced.

We have extended the strain-induced growth of quantum dots by layering the quantum dots, separating them by spacer layers of GaAs. Transmission-electron microscopy results show that the dots from different layers are arranged in vertical columns [3, 4]. Furthermore, photoluminescence results indicate that the dots within these columns are electronically coupled [4], and this coupling can be adjusted by varying the GaAs spacer layer [5]. A surprising consequence of this layering process was recently discovered by Tersoff et al. [6]. The layering process should decrease the size distribution of the top layer dot ensemble as the layering process continues. We believe that the combination of electronic coupling within the columns and a decreased size variation in the upper dot layers will lead to an improved strain-induced dot system with interesting new features.

In this paper we investigate the structural ordering of the quantum dot columns. Single, 10, and 20 dot layers are investigated each with 50 Å of GaAs spacer layers. Using X-ray diffraction (XRD), we find that the wetting layer continues to be present as the dot layers are stacked, and these wetting layers and GaAs spacer layers are uniform enough to combine to produce superlattice diffraction. Atomic-force microscopy (AFM) is used to investigate the size distribution as various numbers of quantum dot layers are deposited. We observe an increase in the average height and in-plane diameter of the dots, resulting in slightly more hemispherical dots after 20 dot layers are deposited. A decrease in the size variation of the dots with increasing number of quantum dot layers is also seen, as well as an ordering of dots in the (1 0 0) direction.

The crystal growth was conducted using a Gen II MBE machine with GaAs and InAs growth rates of 0.1 μm/h. The As flux consists of cracked As_4 (As_2) and the V/III flux ratio was 9. The substrate growth temperature was 460°C measured by band edge absorption. A 2500 Å GaAs buffer layer was used and deposited at 600°C. The InAs island layers consist of the equivalent of 3 layer-by-layer MLs of InAs. In the vertically stacked quantum dot layers the GaAs thickness between adjacent dot layers is approximately 56 Å, measured by TEM. X-ray diffraction was conducted using a Philips 4 crystal X-ray diffractometer. A Digital Nanoscope II atomic-force microscopy was used to image the surface structure and these measurements were conducted in ambient conditions.

In Fig. 1 XRD results are shown for a sample consisting of 10 InAs dot layers. Superlattice diffraction resulting from a supercell consisting of the GaAs spacer and the InAs are observed. Peaks for the $n = 0, \pm 1$, and ± 2 reflections are present where the (0 0 4)GaAs substrate peak resides

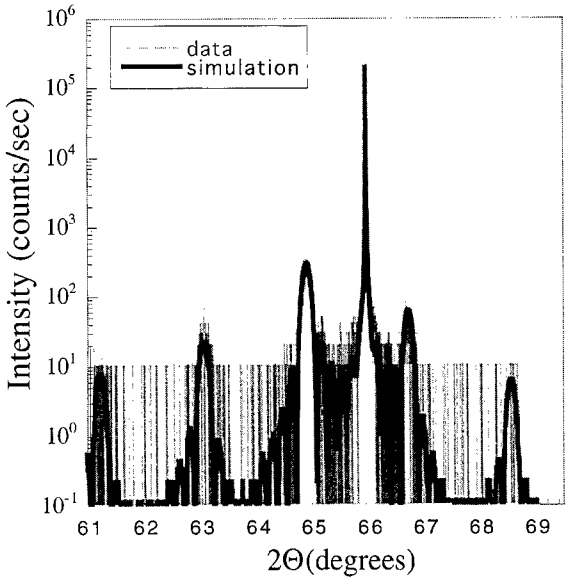

Fig. 1. X-ray diffraction of 10 periods of 3 MLs of InAs and 56 Å of GaAs. Superlattice diffraction indicates an InAs thickness of only 1.9 MLs and is due to the InAs wetting layer region and not the InAs dots.

between the $n = 0$ and $n = 1$ reflections. When fit using a dynamical diffraction model the diffraction in Fig. 1 results in a strained InAs thickness of 1.9 MLs ($\pm$ 0.2 MLs) and a GaAs thickness of 52 Å. Our interpretation of these results is that only the wetting layers of the dots–wetting-layer system are contributing to the superlattice diffraction. Since Fig. 1 represents symmetric diffraction about the (0 0 4)GaAs reflection, the dot regions, with their varying InAs and GaAs vertical sections, should not contribute to superlattice diffraction. The only extensive regions with periodic structure in the growth direction are the regions of the sample without InAs dots where only the wetting layers are present. The best fit to the XRD data occurs when the majority of the InAs is distributed over approximately 9 Å. This diffusion of InAs in GaAs has been observed by other researchers in thin InAs quantum wells in GaAs [7]. This measured value of 1.9 MLs is close to the 1.8 MLs wetting layer thickness observed by other researchers [8] using reflection high energy electron diffraction (RHEED). The RHEED measurements determined the equivalent amount of material deposited leading to the dot transition, while this XRD measurement determines the wetting layer thickness after the dot transition. Because the transition to island growth results in a overall change in the surface topology, it is interesting to note that at least in the regions observed in this type of XRD, the wetting thickness is unchanged by the transition to islanding.

It is of interest to know how the stacking of these InAs dot layers changes the size distribution of the dot ensemble. AFM images of the InAs dot surface are shown in Fig. 2. In these images the growth was terminated after the deposition of the InAs dot layer. Although this is necessary to directly observe the dots, the GaAs layer that normally covers these InAs dots modifies the structure of the dots. In addition, the AFM measurement is done ex situ in an ambient environment and adsorbed materials, as well as the effects of the AFM tip lead to some additional measurement error. In Fig. 2a, the surface topology after a single layer of InAs dots is observed with the AFM. The dots are approximately 40 Å high (in the growth direction) and 200 Å in the in-plane direction. In Fig. 2b, the surface topology after 20 layers of InAs dot layers have been deposited is shown. The dots height and in-plane diameter have increased. The dot density is decreased between the single layer and 20 layer samples from 8.4 to 5.7×10^{10} dots/cm^2. In addition to the decreased island density two other features are apparent in Fig. 2. First, in the 20 layers sample the dots are aligned in the (1 0 0) directions. This alignment is different from the alignment of dots along the (1 1 0) directions observed in single dot layer samples, which is due to steps on the growth surface. Second, there is new surface roughness present in the 20 layers sample.

The decrease in dot density with stacking of individual quantum dot layers, has been predicted if the initial dot density is higher than some equilibrium value which minimizes the overlapping strain fields of the adjacent dots [6]. If the dot density is large then the strain fields of two adjacent dots overlap and only one dot will form above the dots and spacer layer. In the opposite case in which the initial dot density is lower than some equilibrium value, dots will form above the lower dots as well as in the regions where no dots are found below the spacer region. If an equilibrium state can result, the strain field should be periodic over the growth surface, assisting surface diffusion, and the nearest-neighbor distance between nucleating dots will be constant, resulting in uniform nutrient fields for each dot, and thus a more uniform size distribution. Since we have adjusted our growth parameters to increase the dot density in single InAs dot layer samples [9] for optoelectronics applications it is not surprising, in the context of the above discussion, that the dot density should decrease with layering. We believe that the density of dots in an isolated dot layer is determined by the uniformity of the wetting layer [9]. If the wetting layer was ideally uniform then the transition from layer-by-layer growth to island growth would occur uniformly over the surface, leading to a dense array of dots with competing nutrient fields. We believe that this is a local minimum which reduces surface diffusion and even though the dots density is large in the single layer, late stage ripening, the growth of larger dots at the expense of smaller ones, is inhibited. The stacking of dot layers overcomes this problem. The more uniformly periodic strain fields which lead to

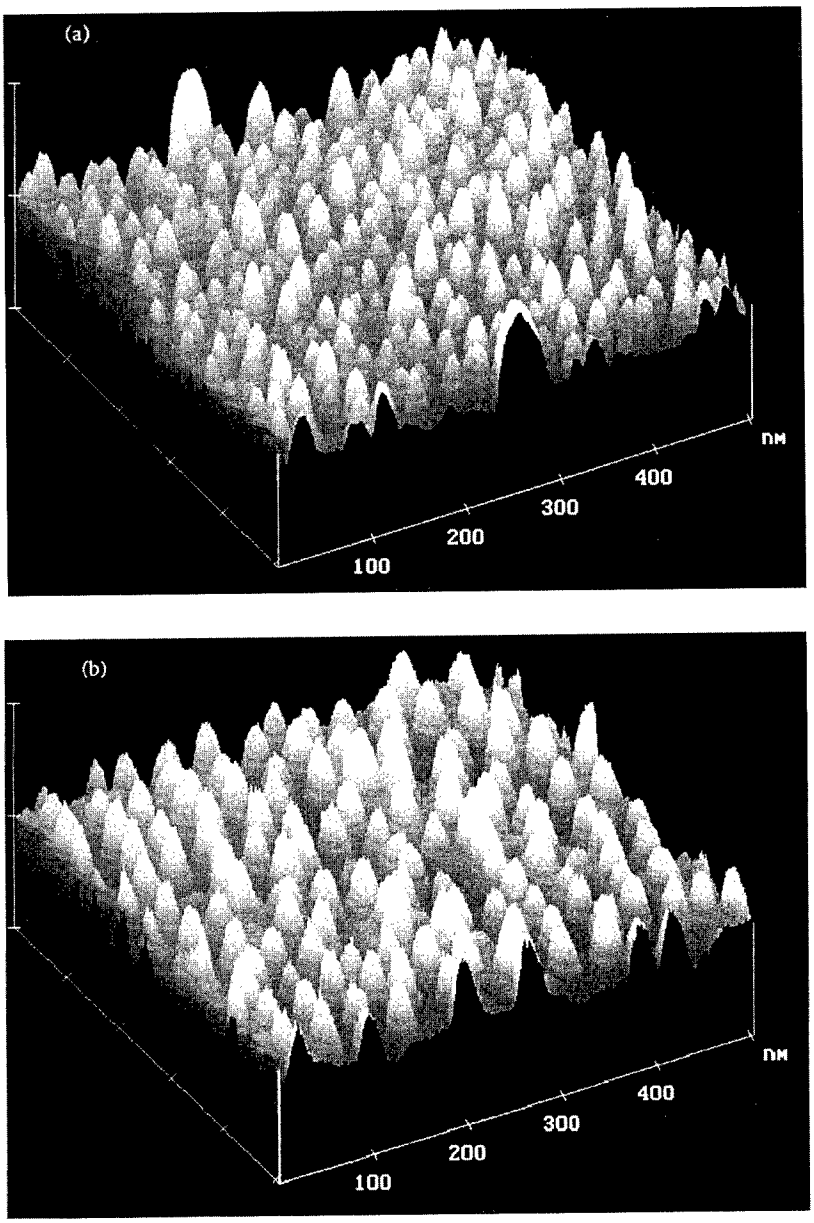

Fig. 2. Atomic-force microscopy of the InAs dot surface where in (a) a single layer of InAs dots have been deposited and in (b) 20 layers of InAs dots have been deposited with 56 Å of GaAs between the dot layers.

the reduced InAs dot density should also lead to a more uniform dot size distribution. This is indeed observed and discussed below.

A statistical evaluation of the AFM images in Fig. 2 is shown in Figs. 3 and 4 . In Fig. 3, a comparison of the variation in height in the single and 20 layers samples is shown. The average height increases from 43 Å in the single sample to 65 Å in the 20 layers sample. The FWHM of the dot height is reduced from 17 to 10 Å between the single and

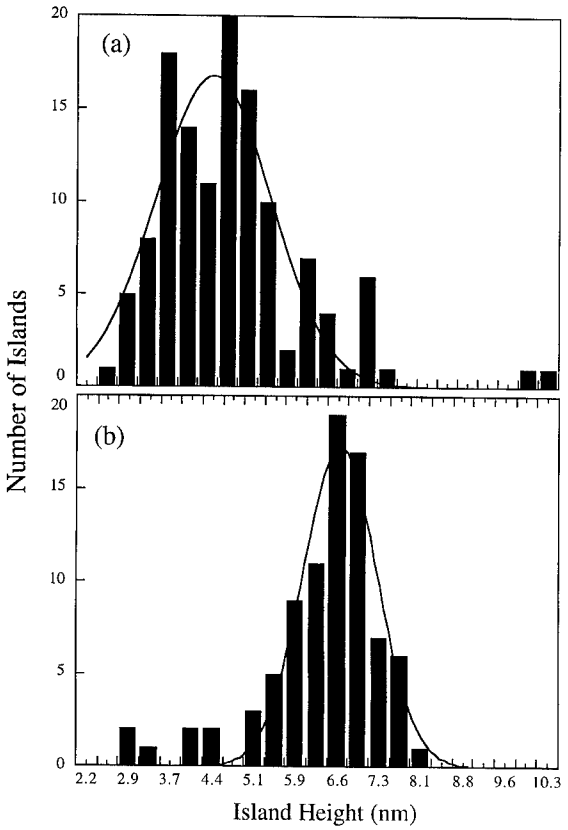

Fig. 3. Height variations determined from AFM, where (a) is for the single dot layer case and (b) is for the 20 layers dots/56 Å GaAs spacer case. With layering, the average height of the dots has increased and the FWHM has decreased.

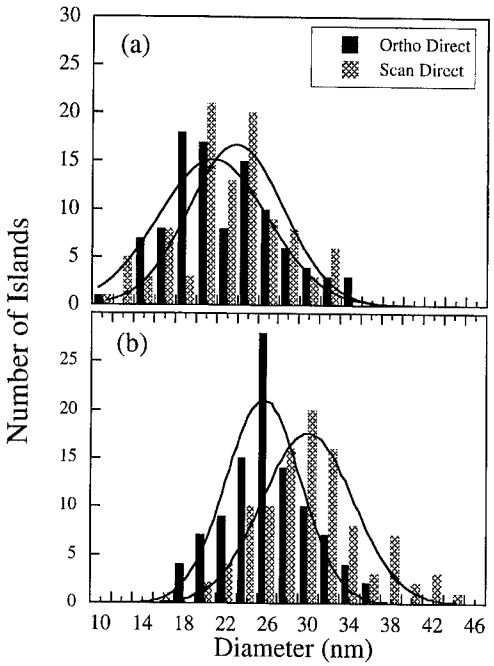

Fig. 4. In-plane dot diameter variations determined from AFM, where (a) represents the single layer case and (b) represents the 20 dot layers/56 Å GaAs spacer case. The average in-plane diameter increases and the FWHM of the in-plane diameter is reduced in the 20 layers stacked case.

20 layers samples even though the average dot height has increased in the 20 layers sample. In Fig. 4, a comparison of the variation in the in-plane dot diameter between the two samples is shown. The in-plane area is not circular but elliptical and the two differently shaded regions in Fig. 4 represent the orthogonal directions with maximum and minimum values. Similar to the average dot height, the dot in-plane diameter has increased after 20 dot layers. The average in-plane diameter of the single dot layer is 218 Å, while the average in-plane diameter after 20 dot layers is 273 Å. The distribution of the in-plane diameter has also narrowed in the 20 dot layer structure. The FWHM of the diameter distribution is reduced from 50 Å (single layer) to 41 Å (20 dot layers). There is a small but observable difference between the height increase and diameter increase in the 20 layer dot distribution. The average height increases more than the average diameter so that the ratio of the height to in-plane radius changes from 0.4 to 0.48 after 20 layers, indicating that these dots are more hemispherical. The increase in the dot height and diameter is in agreement with the reduced island density observed in Fig. 2. Since the dot density is reduced and the wetting layer thickness is unchanged (Fig. 1), the dot size must increase. The reduction in the size variation in height and diameter is due to the more uniform local dot environment resulting from stacking of the dot layers. Since the strain field in the dot layers becomes periodically more uniform with each dot layer, dots are nucleated with more uniform nearest-neighbor distances and hence more uniform nutrient fields. These more uniform surroundings lead to more uniform dots size.

In conclusion, we have shown that the stacking of quantum dot layers with a GaAs spacer layer can be used to reduce the large size distribution in

strain-induced InAs quantum dot layers. Using XRD, we show that through the layering process the wetting layer structure is maintained and remains flat. The 20 layer dot structure produces less dense dot arrays than the single dot structure, and the dots at the top of the 20 layers structure are larger and more uniform than the isolated single dot layer. This increased uniformity has been predicted and is due to the elimination of dot columns with overlapping strain field. Thus, these vertically aligned dot columns are interesting experimentally because of new effects such as electronic coupling within a column, as well as a mechanism to increase the size uniformity of the InAs dots.

This work is support by the ERATO Quantum Fluctuation Project and ARPA/ONR through contract number N00014-93-1-1375.

References

[1] J. Shigetomi, K. Fuwa, S. Shimizu and H. Yamakawa, J. Crystal Growth 111 (1991) 110.
[2] Y.-W. Mo, D.E. Savage, B.S. Swartzentruber and M.G. Lagally, Phys. Rev. Lett. 65 (1990) 1020.
[3] Q. Xie, A. Madhukar, P. Chen and N.P. Kobayashi, Phys. Rev. Lett. 75 (1995) 2542.
[4] G.S. Solomon, J.A. Trezza, A.F. Marshall and J.S. Harris, Jr., Phys. Rev. Lett. 76 (1996) 952.
[5] G.S. Solomon, Y. Yamamoto and J.S. Harris, Jr., J. Vac. Technol. B 14 (1996) 2208.
[6] J. Tersoff, C. Teichert and M.G. Lagally, Phys. Rev. Lett. 76 (1996) 1675.
[7] O. Brandt, K. Ploog, L. Tapfer, M. Hohenstein, R. Bierwolf and F. Phillipp, Phys. Rev. B 45 (1992) 8443.
[8] D. Leonard, M. Krishnamurthy, C.M. Reaves, S.P. Denbaars and P.M. Petroff, Appl. Phys. Lett. 63 (1993) 3203.
[9] G.S. Solomon, J.A. Trezza and J.S. Harris, Jr., Appl. Phys. Lett. 66 (1995) 3161.

ELSEVIER

Journal of Crystal Growth 175/176 (1997) 713–719

JOURNAL OF CRYSTAL GROWTH

Self-assembled structures of closely stacked InAs islands grown on GaAs by molecular beam epitaxy

Yoshiaki Nakata*, Yoshihiro Sugiyama, Toshiro Futatsugi, Naoki Yokoyama

Fujitsu Laboratories Ltd., 10-1 Morinosato-Wakamiya, Atsugi 243-01, Japan

Abstract

Closely stacked Stranski–Krastanow (S–K) growth islands were investigated. InAs islands of nominal 1.8 monolayer thickness were grown periodically with GaAs intermediate layers of less than 3 nm by molecular beam epitaxy. Reflection high-energy electron diffraction and atomic force microscopy revealed that S–K growth islands were formed even with stacked intervals of 2 nm, but the upper island size expanded slightly as the number of stacked layers increased. Transmission electron microscopy revealed that upper islands grew closely just on the lower islands aligning vertically on the first layer islands. Drastic decrease in photoluminescence full-width at half-maximum less than 30 meV was obtained from this structure.

1. Introduction

Low-dimensional carrier-confined nano-structures such as quantum wires and dots are of great interest in high-performance electronic and photonic device applications [1–3]. For precise fabrication of these structures, much attention has been paid to self-organizing and self-assembling phenomena in epitaxial growth. In particular, Stranski-Krastanow (S–K) growth islands formed at the initial stage in the highly mismatched hetero-epitaxy is one of the most promising structures [4, 5]. Both theoretical and experimental studies have shown these islands to be coherent and dislocation-free [6–8]. Attempts to fabricate quantum dot lasers [9–12] and wavelength-domain-multplication (WDM) optical memories [13] using S–K growth InAs islands on GaAs have been reported. However, the luminescence from these S–K growth islands were broad – the reported full-width at half-maximum (FWHM) of photoluminescence (PL) from InAs islands on GaAs were typically about 80 meV [14–16], showing large fluctuation in island size. Islands of such size fluctuation are applicable to WDM memories [3], but often lead to a decrease of optical gain in the lower-order subbands and an increase of threshold current in lasers [11]. According to our estimation, if we can achieve a PL FWHM of around 20 meV, lasing at the ground state can be realized even in as-cleaved devices [11]. Broadening of luminescence was mainly due to fluctuation in island size. Since the

* Corresponding author. Fax: + 81 462 508844; e-mail: nakata@qed.flab.fujitsu.co.jp.

0022-0248/97/$17.00 Copyright © 1997 Elsevier Science B.V. All rights reserved
PII S0022-0248(96)00814-7

S–K growth islands previously produced were disk-like, 20–25 nm in diameter and 3–5 nm in height [17], the broadening of luminescence were possibly dominated by fluctuation in island height. Therefore, if island height can be accurately controlled, luminescence broadening should be greatly reduced.

Recently, in stacked structures, vertical alignment of S–K growth islands due to strain induced by lower-layer islands was reported [15, 16, 18]. In these structures, if the upper islands could be stacked closely just on the lower-layer islands with fairly thin intermediate layers, due to vertical extension of wave function over islands [12], the effective island height can be controlled by the number of stacked layer, while keeping island diameter and density almost the same as those of the first-layer islands.

In this paper, we describe closely stacked S–K growth InAs islands grown with thin GaAs intermediate layers on (0 0 1) GaAs substrates. The structure was evaluated by reflection high-energy electron diffraction (RHEED), atomic force microscopy (AFM), transmission electron microscopy (TEM). We demonstrate highly reduced PL FWHMs of smaller than 30 meV.

2. Growth of closely stacked island structure

We stacked InAs islands with GaAs intermediate layers of less than 3 nm thickness by conventional molecular beam epitaxy (MBE) using metallic In, Ga, Al and As_4 as the source materials. The substrates used were (0 0 1) oriented GaAs. Before growth, the substrates were thermally cleaned at about 680°C for 1 min under an As pressure of 1.2×10^{-5} Torr. Stacked InAs islands were grown on a GaAs (100 nm)/AlGaAs (200 nm)/GaAs (400 nm) buffer layer and covered with a GaAs (50 nm)/AlGaAs (50 nm)/GaAs (100 nm) cap layer. The substrate temperature for growth of InAs islands was 510°C and was 650°C for growth of the buffer layer. They were monitored by a pyrometer calibrated by melting of In–Al alloys. The nominal InAs thickness for island formation was fixed at about 1.8 monolayer (ML). The nominal thickness of GaAs intermediate layers was set at 2 and 3 nm. Prior to and following InAs island growth, the sample was annealed for 2 and 1 min, respectively. The growth rates of InAs and GaAs were approximately 0.1 and 0.75 μm/h. For the 1.8 ML InAs growth, it took about 18 s. The As pressure used for InAs island growth was 6×10^{-6} Torr, and for buffer layer growth was 1.2×10^{-5} Torr. These were measured by an ion gauge at the substrate position. We used two As cells both set at 6×10^{-6} Torr and changed the As pressure abruptly at the interface by switching one of these cells on and off.

During the growth of the buffer layer, surface was As-stabilized 2×4 reconstruction, and then transited $c(4 \times 4)$ reconstruction while the substrate temperature dropped to 510°C. Fig. 1a is the [1 1 0] azimuthal RHEED pattern obtained before InAs growth. The $\frac{1}{2}$ ordered fractional reflections were clearly observed. Just after InAs growth started, the fractional order reflections disappeared immediately, and the transition from streaks to spots started as the growth of InAs reached around 1.6 ML, indicating a two-dimensional (2D) growth transited to a three-dimensional (3D) island growth then. Fig. 1b is obtained after 1.8 ML InAs growth. The RHEED pattern recovered gradually to streaky as the growth of the subsequent GaAs intermediate layer started, although the fractional ordered reflections previously observed were barely visible during growth of the 2 to 3 nm thick GaAs intermediate layer. Fig. 1c is the RHEED pattern obtained after a 3 nm thick GaAs intermediate layer grown over the 1st island layer. By supplying InAs to such surface, the streaky pattern transformed to a spot pattern, but the transition time, (or in terms of the critical InAs thickness for the 2D growth to 3D island growth transition) was shorter (smaller) than for the growth of 1st layer island. Fig. 1d shows RHEED intensity transition observed at the area indicated by a square in the inset patterns during the growth of InAs islands. The 3rd- and 5th-layer islanding started when the growth of InAs reached about 1.0 ML, which is about 63% of the 1st-layer islanding. Presumably, the strain induced by the lower-layer islands or segregation of In atoms in the lower-layer islands affected subsequent islanding. However, the transition of growth mode from a 2D growth to a 3D island growth, and the existence of wetting layers as

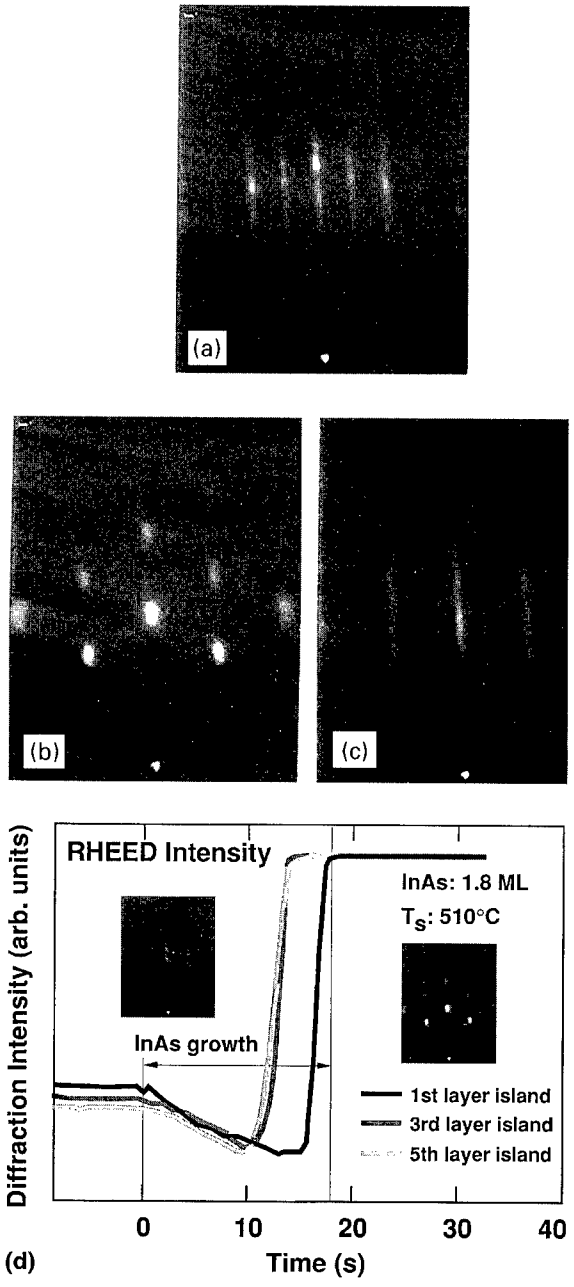

Fig. 1. (1 1 0) azimuthal RHEED patterns (a) before, and (b) after 1.8 ML of InAs growth, and (c) after the 3 nm thick GaAs intermediate layer growth. (d) RHEED intensity transition during the growth of the 1st, 3rd and 5th InAs island layers observed at the point indicated by a square in the inset RHEED pattern.

will be shown later in TEM evaluation both indicate that S–K growth islands were formed even on such thin GaAs intermediate layers. Therefore, the formation of coherent and dislocation-free islands can be expected also in these stacked structures.

3. Evaluation of closely stacked island structure

3.1. Structural features

We evaluated island size and density by ex situ AFM operated in the ambient atmosphere (air). Fig. 2a–Fig. 2d show AFM images of the islanding surfaces at (a) the 1st, (b) the 3rd, (c) the 5th and (d) the 10th layers stacked at 3 nm intervals. We note that these images refer to different epilayers grown under the same conditions. The scanned area is $250 \times 250\ nm^2$. It is evident from these images that islands form even at 3 nm stacking intervals. The upper-layer islands, however, expanded slightly as the number of stacked layers increased. Fig. 3 shows the island size dependence on the number of stacked layers. The average diameter of the 10th-layer islands was about 33 nm which was 140% larger than the 1st-layer islands (about 24 nm in diameter), while the island density decreased from $1 \times 10^{11}\ cm^{-2}$ for the 1st-layer islands to $8 \times 10^{10}\ cm^{-2}$ for the 10th-layer islands.

In order to clarify the structural features, we examined them by TEM. Fig. 4 is a (1 1 0) cross-sectional TEM image of a 5-stacked island structure grown at 2 nm intervals. Each island layer was accompanied by a wetting layer, indicating that the upper-layer islands formed by S–K growth as did the 1st-layer islands. The upper-layer islands grew close just on the lower-layer islands, aligning vertically with the 1st-layer islands. These islands were stacked almost in columnar of about 22 nm in diameter and 13 nm in height shown in the image as dark megaphone-like strained regions. Islands in individual layer were seen to be spatially isolated in the vertical direction, but the distance between the bottom of the upper-layer islands and the top of the lower-layer islands was seen to be 3 to 4 ML or less, which is so thin that the wave functions can be distributed along the vertical column. This

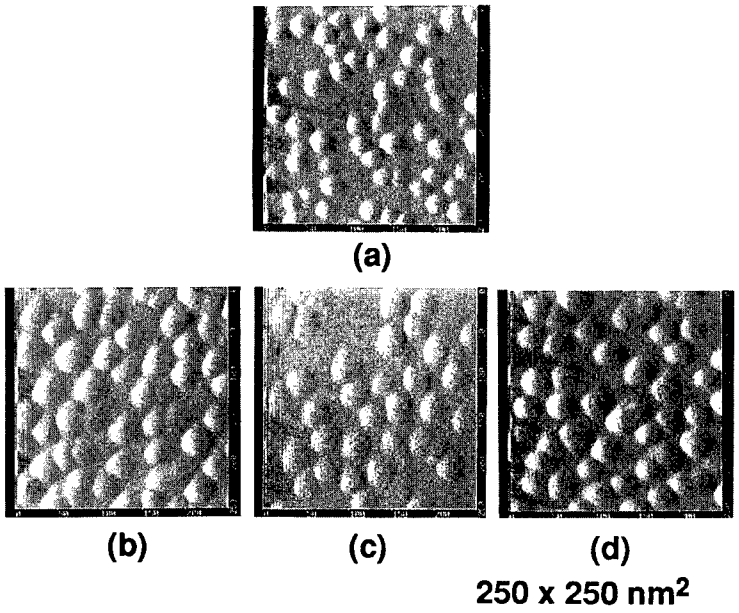

Fig. 2. AFM images of InAs islanding surfaces of (a) the 1st layer, (b) the 3rd layer, (c) the 5th layer, and (d) the 10th layer stacked at 3 nm thick GaAs intervals.

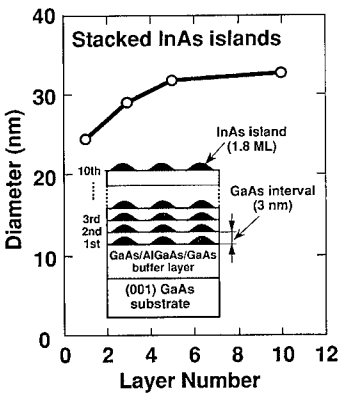

Fig. 3. Dependence of InAs island diameter on number of stacked layers measured from AFM images.

implies that the islands were electronically coupled, behaving as a single quantum dot. We note here that similar structure was first reported in a InAs/GaAs short period superlattice grown using atomic layer epitaxy (ALE) technique [19].

Fig. 5 is a plan view of TEM image obtained from a 5-stack island structure grown at 2 nm intervals. The density of the islands was 8×10^{10} cm^{-2}. This value agreed well with the AFM results. Fluctuation of the lateral size seemed to be smaller than for a single island layer. Although we attempted precise control in the vertical dimension of the islands, somehow uniform lateral dimension was achieved in these closely stacked structures as reported previously [12, 20].

3.2. PL properties

We evaluated the PL properties of these structures at 77 K. Fig. 6 shows the PL spectra of a single island layer and closely stacked 3- and 5-layer island structures grown at 3 nm intervals. The broad PL spectrum of a single island layer transformed to the sharper spectra with the number of stacked layers increased. The peak energy shifted to the lower energy by about 90 meV. This energy shift can be ascribed to reduction of quantum size effects due to the increase in effective island heights.

Fig. 4. (1 1 0) cross-sectional TEM image of a 5-layer stacked InAs island grown at 2 nm GaAs intervals.

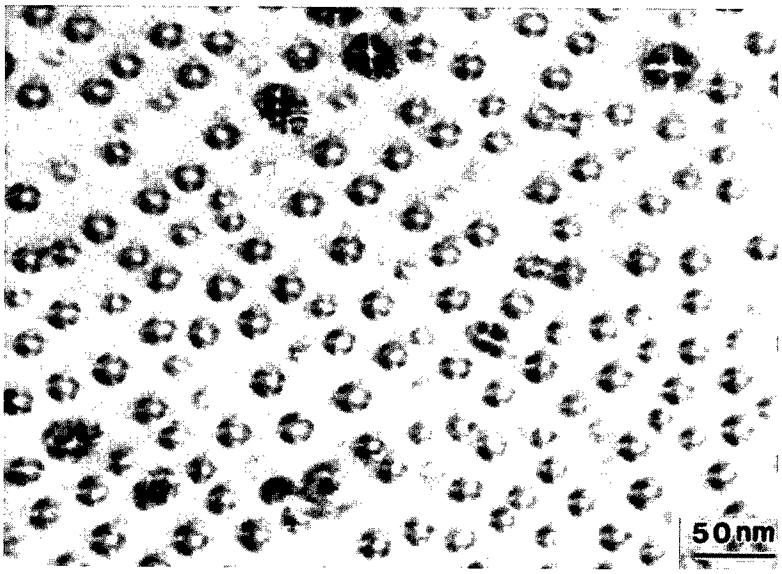

Fig. 5. Plan view of TEM image obtained from a 5-layer stacked InAs island structure grown at 2 nm GaAs intervals.

The FWHM of the 5-layer stacked structure was 27 meV. This is less than one-third of the single island layer structure. The peak intensity was about three times higher compared to the single island layer structure. We also obtained an FWHM of 24 meV from a 5-stack island structure grown at 2 nm intervals [21]. These narrow FWHMs are attributable mainly to the suppression of relative island size fluctuation in the vertical direction accompanied possibly by the high uniformity of lateral dimension as shown in Fig. 5. We also confirmed that PL FWHM was independent on temperature, and that diamagnetic energy shift of the PL was considerably small (less than 3 meV even at 12 T). Fig. 7 shows diamagnetic shift of PL peak at 4.2 K. Magnetic field was applied

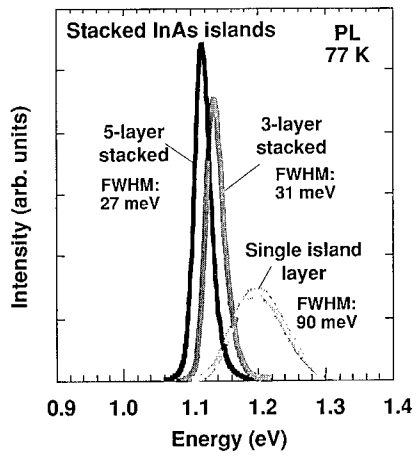

Fig. 6. PL spectra of a InAs single island layer structure, and a 3-layer and a 5-layer stacked InAs island structures grown at 3 nm GaAs intervals as measured at 77 K.

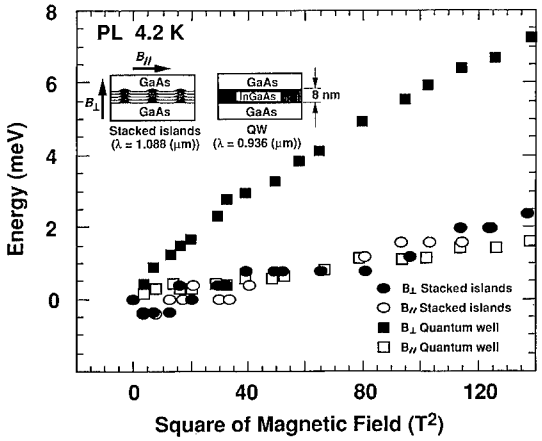

Fig. 7. Diamagnetic shifts of PL peak energy at 4.2 K.

perpendicular and parallel to the sample surfaces. Diamagnetic shifts in an $In_{0.18}Ga_{0.82}As$ (8 nm thick)/GaAs quantum well emitting at 0.94 μm are superimposed. We found that the diamagnetic energy shifts in closely stacked islands was considerably smaller than that in the quantum well. These results indicate that three-dimensional quantum confined structures were formed. Although we have demonstrated laser oscillations at room temperature from the quantum dots grown by usual S–K growth InAs islands, lasing was not at ground state in as-cleaved devices, and threshold current was much higher than expected [11]. Those optical features obtained here are expected to improve these laser characteristics.

4. Summary

Closely stacked InAs islands were grown with fairly thin intermediate layers on (0 0 1) GaAs substrates. RHEED and TEM results revealed that S–K growth islands formed even at stacked intervals of 2–3 nm. The upper-layer islands formed closely just on the lower-layer islands aligning vertically on the first-layer islands. Although island of adjacent layers appeared to be spatially isolated, the separation was so small (3–4 ML or less) that the islands can be electronically coupled, behaving effectively as a single quantum dot. We confirmed that for these stacked structures, three-dimensional quantum confined structures were formed, and PL FWHM decreased drastically to 27 meV and the peak intensity increased to about three times of a single island layer structures. These improved properties are expected to be useful for laser applications.

Acknowledgements

We would like to thank M. Sugawara, H. Shoji and K. Mukai for PL measurements and helpful discussions and Professor S. Muto of Hokkaido University for fruitful discussion. We also thank T. Nakamura and H. Ishikawa for encouragement throughout this work.

References

[1] Y. Arakawa and H. Sakaki, Appl. Phys. Lett. 40 (1982) 939.
[2] H. Sakaki, Jpn. J. Appl. Phys. 28 (1989) L134.
[3] S. Muto, Jpn. J. Appl. Phys. 34 (1995) L210.
[4] D. Leonard, M. Krishnamurthy, C.M. Reaves, S.P. Denbaars and P.M. Petroff, Appl. Phys. Lett. 63 (1993) 3203.
[5] J.-Y. Marzin, J.-M. Gerard, A. Israel, D. Barrier and G. Bastard, Phys. Rev. Lett. 73 (1994) 716.
[6] S. Guha, A. Madhukar and K.C. Rajkumar, Appl. Phys. Lett. 57 (1990) 2110.

[7] D.J. Eaglesham and M. Cerullo, Phys. Rev. Lett. 64 (1990) 1943.
[8] B.J. Spencer, P.W. Voorhees and S.H. Davis, Phys. Rev. Lett. 67 (1991) 3696.
[9] N. Kirstaedter, N.N. Ledentsov, M. Grundmann, D. Binberg, V.M. Ustinov, S.S. Ruvimov, M.V. Maximov, P.S. Kop'ev, Zh.I. Alferov, U. Richter, P. Werner, U. Gosele and J. Heydenreich, Electron. Lett. 30 (1994) 1416.
[10] H. Shoji, K. Mukai, N. Ohtsuka, M. Sugawara, T. Uchida and H. Ishikawa, IEEE Photon. Technol. Lett. 12 (1995) 1385.
[11] H. Shoji, Y. Nakata, K. Mukai, Y. Sugiyama, M. Sugawara, N. Yokoyama and H. Ishikawa, Jpn. J. Appl. Phys. 35 (1996) L903.
[12] D. Binberg, N.N. Ledentsov, M. Grundmann, N. Kirstaedter, O.G. Schmidt, M.H. Mao, V.M. Ustinov, A.Yu. Egarov, A.E. Zhukov, P.S. Kopev, Zh.I. Alferov, S.S. Ruvimov, U. Gosele and J. Heydenreich, Jpn. J. Appl. Phys. 35 (1996) 1311.
[13] K. Imamura, Y. Sugiyama, Y. Nakata, S. Muto and N. Yokoyama, Jpn. J. Appl. Phys. 34 (1995) L1445.
[14] A. Tackeuchi, Y. Nakata, S. Muto, Y. Sugiyama, T. Inata and N. Yokoyama, Jpn. J. Appl. Phys. 34 (1995) L405.
[15] G.S. Solomon, J.a. Trezza, A.F. Marshall and J.S. Harris Jr., Phys. Rev. Lett. 76 (1996) 952.
[16] Y. Sugiyama, Y. Nakata, K. Imamura, S. Muto and N. Yokoyama, Jpn. J. Appl. Phys. 35 (1996) 1320.
[17] J.M. Moison, F. Houzay, F. Barth, L.L. Leprince, E. Andre and O. Vatel, Appl. Phys. Lett. 64 (1994) 196.
[18] Q. Xie, A. Madhukar, P. Chen and N.P. Kobayashi, Phys. Rev. Lett. 75 (1995) 2572.
[19] K. Mukai, N. Ohtsuka, M. Sugawara and S. Yamazaki, Jpn. J. Appl. Phys. 33 (1994) L1710.
[20] J. Tersoff, C. Teichert and M.G. Lagally, Phys. Rev. Lett. 76 (1996) 1675.
[21] Y. Sugiyama, Y. Awano. N. Yokoyama, Y. Nakata and T. Futatsugi, Jpn. J. Appl. Phys., submitted.

ELSEVIER

Journal of Crystal Growth 175/176 (1997) 720–724

JOURNAL OF CRYSTAL GROWTH

Room temperature luminescence from self-organized $In_xGa_{1-x}As/GaAs$ ($0.35 < x < 0.45$) quantum dots with high size uniformity

K. Kamath*, P. Bhattacharya, J. Phillips

Solid State Electronics Laboratory, Department of Electrical Engineering and Computer Science, University of Michigan, Ann Arbor, Michigan 48109, USA

Abstract

Self-organized growth of $In_xGa_{1-x}As/GaAs$ quantum dots (QD) for $0.5 < x$ are studied by time-integrated, time-resolved and temperature-dependent photoluminescence (PL). Low-temperature photoluminescence demonstrates that the critical composition 'x' needed for the formation of 3D islands is between 0.3 and 0.35. This is also supported by reflection high-energy electron diffraction (RHEED) measurements and agrees well with our theoretical predictions that a misfit of $> 2\%$ is needed, from thermodynamic considerations, for the onset of 3D growth. The presence of fine excitonic features superimposed on the emission peaks confirms that the second peak observed in the PL spectra of quantum dots is from an excited state transition. We believe that the saturation of the ground-state emission observed under moderately high excitation photon densities is due to the long decay time constant (~ 2.2 ns) as measured by time-resolved photoluminescence. Temperature variation of luminescence intensity shows a sharper decay for the ground-state emission than for the excited-state emission. Room-temperature luminescence is thus dominated by the excited state emission. Broad area lasers made from separate confinement heterostructure (SCH) laser structures with $In_{0.4}Ga_{0.6}As$ quantum dots as the active region showed lasing from excited state, with $J_{th} = 650$ A/cm^2, and the single-mode ridge lasers gave a modulation bandwidth of 5 GHz at $2.5I_{th}$.

PACS: 68.55.Bd

Keywords: Molecular beam epitaxy; Self-organized growth; Quantum dot; Luminescence; Laser

1. Introduction

Formation of three-dimensional (3D) islands during the molecular beam epitaxial (MBE) growth of highly strained layers, either in the Vollmer–Weber growth mode (direct formation of 3D islands) or in the Stranski–Krastanow growth mode (where growth changes from layer-by-layer to 3D islands) have been studied extensively. Although the formation of islands was observed in highly strained (7%) InAs/GaAs superlattices when

* Corresponding author.

0022-0248/97/$17.00 Copyright © 1997 Elsevier Science B.V. All rights reserved
PII S0022-0248(96)00815-9

the thickness of InAs is more than 2 monolayers (ML) [1], it was predicted that a lattice mismatch of more than 2% is enough, from thermodynamic considerations, to form coherent 3D islands [2]. This corresponds to an In composition of ~30% in the InGaAs/GaAs system. Most of the work in this system has been on binary InAs [3–5] or ternary $In_{0.5}Ga_{0.5}As$ [6–8] on GaAs. We have studied the formation of 3D islands for indium composition <50%. In the InGaAs/GaAs system the formation of 3D island occurs by the Stranski–Krastanow growth mode, wherein the initial layer-by-layer (2D) growth degenerates into 3D islands. The thickness of the initial 2D wetting layer before the onset of 3D growth depends on the strain in the growing layer. It has been reported that in the case of InAs on GaAs the wetting layer is 1.57 ML thick [9], whereas for $In_{0.5}Ga_{0.5}As$ it is 4 ML [6]. A thicker wetting layer, obtained by reducing the In composition, is expected to provide efficient carrier injection into the 3D quantum dots eliminating the problems associated with large relaxation time constants in pure quantum boxes.

Here we report results of a photoluminescence (PL) study of $In_xGa_{1-x}As/GaAs$ quantum dots for $x < 0.5$. Change in the reflection high-energy electron diffraction (RHEED) spectra from 2D to 3D pattern is used in conjunction with the PL results to estimate the minimum composition x required for the formation of 3D islands. Dependence of PL spectra on excitation intensity and temperature was also studied. Time-resolved PL measurements were made to get an insight into the carrier dynamics in these quantum dots. Broad area and single-mode lasers made from an SCH laser structure with InGaAs QDs in the active region were fabricated and analyzed.

2. Experimental procedure

Heterostructures grown for PL measurements consist of a single layer of $In_xGa_{1-x}As$ ($x = 0.3$, 0.35, 0.4 and 0.45) with 0.1 μm GaAs on each sides. A superlattice buffer was grown in all the samples, to smoothen the growth front, before growing the actual structures. Growth rate of GaAs was 0.72 μm/h and that of InGaAs was 1 ML/s. Substrate temperatures used were 620°C and 520°C for GaAs and InGaAs, respectively, and the V/III flux ratio was maintained at ~5. The number of monolayers for the transition of the RHEED spectra from streaky (2D) to spotty (3D) pattern were found to be 6, 8 and 11 for $x = 0.45$, 0.4 and 0.35, respectively. No transition in RHEED spectrum was observed for $x = 0.3$ even after a growth of 20 ML, indicating that no quantum dots are formed. Thicknesses of the grown layers were 8, 10, and 15 ML for $x = 0.45$, 0.4, and 0.35, respectively. A sample with 15 ML quantum well with $x = 0.30$ was also grown for comparing the PL emission from QW and QDs.

Photoluminescence spectra were measured at different temperatures from 16 K to room temperature. A 632.8 nm HeNe laser with a variable attenuator was used as an excitation source. A 0.75 m scanning spectrometer, liquid-nitrogen-cooled photomultiplier, and lock-in amplification were employed to scan the emission spectra with a resolution of better than 0.1 nm. For time-resolved measurements a Ti-saphire laser was used as the excitation source and the spectrally dispersed time-resolved image was obtained with a 0.5 m monochromator, Hamamatsu streak camera, and a high-speed CCD camera. The temporal resolution of the system is 27 ps.

Broad-area and single-mode lasers were fabricated from an SCH laser structure with $In_{0.4}Ga_{0.6}As$ self-organized quantum dots as the active layer. The laser emission spectra were scanned with 1 m spectrometer, thermoelectrically cooled Ge-detector and a Boxcar averager. Modulation bandwidth measurements were made with HP8350B sweep oscillator and HP8593A spectrum analyzer.

3. Results and discussion

Photoluminescence spectra from quantum dots are expected to be broader than those from quantum wells due to the statistical nature of size fluctuation of a large number of quantum dots sampled. The spectral shape is found to be approximately Gaussian for low excitation. At higher excitation levels, contributions from excited-state transitions

gives rise to a second peak due to the saturation behavior of the ground-state transition [5]. Fig. 1 shows the PL spectra obtained from two different samples at various excitation levels. At higher excitation levels, the excited state transition peak at around 1.24 eV is observed in the sample with $In_{0.35}Ga_{0.65}As$ layer, indicating the formation of self-organized quantum dots, whereas there is only a slight broadening of the excitonic emission in the sample with a $In_{0.3}Ga_{0.7}As$ layer as is expected for a 2D quantum well. We can thus infer that the critical In composition for the onset of 3D growth is between 0.3 and 0.35 for our growth conditions, which is also supported by our RHEED studies. This agrees very well with our earlier theoretical predictions [2] that a strain of $>2\%$ is necessary for the formation of 3D islands in the Stranski–Krastanow growth mode. The energy separation between the two peaks of the $In_{0.35}Ga_{0.65}As$ sample is 62 meV. Moreover, there are fine excitonic features superimposed on the emission peaks from QDs, which represent groups of dots with identical dimensions. This is clearly resolved by a derivative spectrum in Fig. 2. The overall linewidth of the ground-state emission of the QDs is 33 meV, which is lower than the 40–50 meV normally reported. This indicates the high degree of uniformity in the QD size. The fine structure is observed in the PL emission from both the ground-state and the excited-state transitions. This provides the argument to preclude the possibility of contribution from wetting layer emission. Furthermore, the transition energy for the wetting layer is estimated to be around 1.358 eV for this structure which is very different from the observed 1.24 eV for the second peak. We have observed that decreasing the growth temperature ($<500°C$)

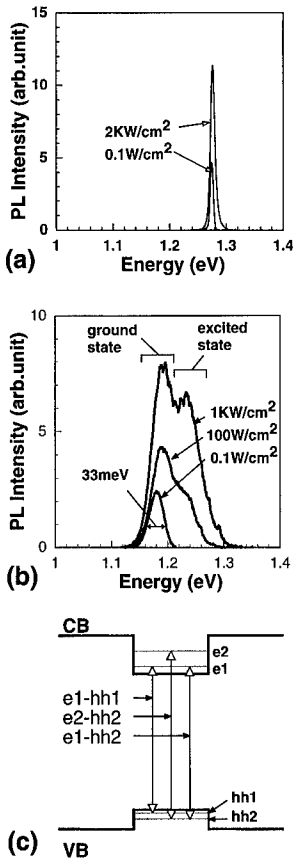

Fig. 1. PL spectra (a) from GaAs/(15ML)$In_{0.3}Ga_{0.7}As$/GaAs and (b) fromGaAs/(15ML)$In_{0.35}Ga_{0.65}As$/GaAs at various excitation levels. (c) potential well and different transitions in self-organized quantum dots.

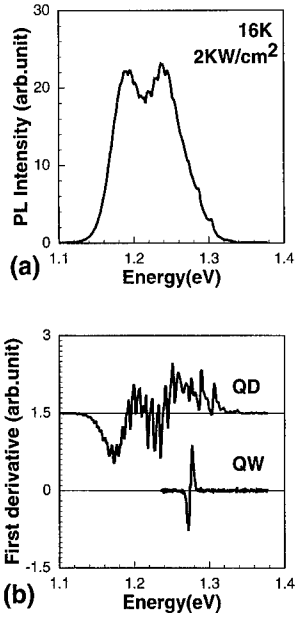

Fig. 2. Sharp peaks superimposed on the excitonic emission from quantum dots observed in PL spectrum (a) and resolved by a derivative spectrum (b). The derivative spectrum for the quantum-well emission peak of Fig. 1a is also shown for comparison.

decreases the size of the quantum dots (<20 nm base width), at the same time decreasing the PL intensity. Growth at a higher temperature improves the PL intensity and increases the size of the quantum dots, ultimately resulting in a large size fluctuation for >550°C. We have used a substrate temperature of 520°C for the best PL intensity, and we expect the base width of the quantum dots to be 20–30 nm. Theoretical calculations [10] assuming a biaxial strain tensor predict a second energy level in the conduction band for these dimensions. The excited-state emission can be either from e1–hh2 transition, which is not forbidden in the pyramidal shape of these type of quantum dots [5], or from e2–hh2 transition, which is possible only in relatively large quantum dots. These transitions are shown in Fig. 1c. The measured energy difference of 62 meV, between ground-state and excited-state transitions, is found to agree with the energy difference between e1-hh1 and e2–hh2 in QDs with a pyramidal base width of 21 nm and a height of 10 nm. The calculations also indicate that the e1–hh2 transition is very weak, compared to the e2–hh2 transition.

The temperature dependence of the PL intensity from $In_{0.35}Ga_{0.65}As/GaAs$ QDs is shown in Fig. 3 for both low and high excitation conditions. The wavelength-integrated intensity remains constant upto about 75 K and then decays due to the ionization of the localized exciton [11]. The intensity of the ground-state emission drops off dramatically, whereas the excited-state transition first decays at a fast rate, followed by a slow decay till room temperature. The fast decay indicates non-radiative transitions associated with a defect level while the slow decay of the excited state reflects the normal thermal quenching. The room-temperature PL spectrum (Fig. 4) is dominated by the excited-state transition since the ground-state transition saturates at much lower excitation levels than that at low temperatures. This implies that if we have such QDs in the active region of a laser, the gain provided by the ground-state transition, before it saturates, may not be sufficient for the onset of lasing. We have made broad-area lasers from an SCH laser structure with $In_{0.4}Ga_{0.6}As$ QDs in the active region, which had a threshold current density of 650 A/cm^2 for 1 mm cavity length. The emission spectra from these lasers showed [12] that the ground-state transition saturates with increasing injection current and lasing indeed takes place from the excited state transition.

In order to study the carrier dynamics in these quantum dots, we have made low-temperature time-resolved PL measurements. Fig. 5 shows the time-resolved PL intensity at different wavelengths obtained from spectrally dispersed image at 8 K. It is found that the decay time constants for the ground state and excited state are ~2.2 ns and ~200 ps, respectively. The rise time of the signal is limited by the resolution of the system to 27 ps. We believe that the slow decay of the ground state may be responsible for the saturation behavior observed in the time-integrated PL measurements. It is interesting to note that the excited state has an order of magnitude shorter decay time constant than the ground state. This predicts a better high-speed performance of the lasers emitting from excited states

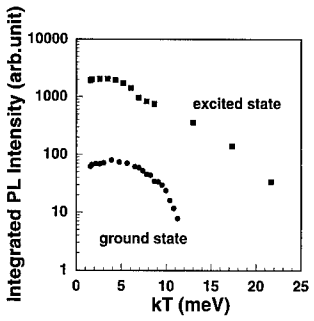

Fig. 3. Temperature variation of the wavelength-integrated intensity for the ground-state and excited-state transition.

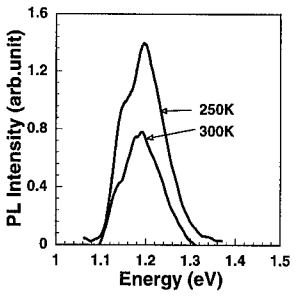

Fig. 4. PL spectra at room temperature (300 K) and at 250 K from $In_{0.35}Ga_{0.65}As/GaAs$ QD structure.

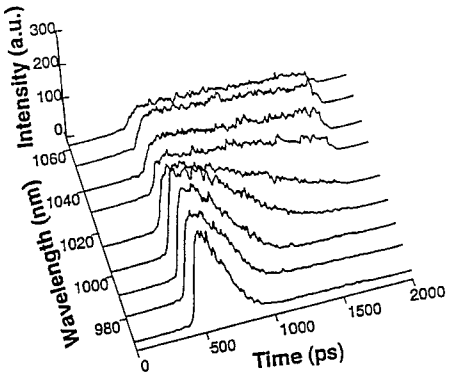

Fig. 5. Spectrally dispersed, time-resolved PL intensity recorded at 8 K from $In_{0.35}Ga_{0.65}As/GaAs$ self-organized quantum dots.

compared to that from ground states. We made single-mode ridge lasers in the ground–signal–ground configuration for bandwidth measurement. The threshold current was relatively high, around 30 mA for a cavity length of 415 μm, which we hope to bring down by optimizing the growth conditions and by having multiple layers of coupled quantum dots. The measured bandwidth was around 5 GHz for a current of $2.5I_{th}$. Increasing the current further reduced the optical power and the bandwidth due to heating. We believe that higher bandwidths can be obtained by having lower threshold current levels.

4. Conclusion

We have found the critical composition for the formation of self- organized quantum dots in $In_xGa_{1-x}As/GaAs$ system to be $0.3 < x < 0.35$. This agrees well with our earlier theoretical prediction that a lattice mismatch of $>2\%$ is necessary, from thermodynamic consideration, for the growth of 3D islands. Photoluminescence measurements show the saturation of the ground-state transition in quantum dots giving emission due to excited-state transition at high excitation levels. The temperature variation of the integrated intensity shows a slower variation for the excited state transition than for the ground-state transition, indicating that the ground-state transition saturates at much lower excitation levels at higher temperatures. Time-resolved measurements show that this may be due to the large decay time constant (~ 2.2 ns) for the ground state. Broad area lasers fabricated from an SCH laser structure with $In_{0.4}Ga_{0.6}As$ QDs as the active layer showed that the lasing occurs from excited states with $J_{th} = 650\ A/cm^2$, which has a photoluminescence decay time constant of 200 ps. A modulation bandwidth of 5 GHz measured with a single-mode ridge laser at a current level of $2.5I_{th}$ indicates that phonon bottleneck problem is not significant for the laser operating from excited-state transition.

Acknowledgements

The authors thank Professor J. Singh and J. Hongtao for useful discussions. The work is supported by the Army Research Office (URI Program) under Grant No. DAAL03-92-G0109.

References

[1] L. Goldstein, F. Glas, J.Y. Marzin, M.N. Charasse and G. LeRoux, Appl. Phys. Lett. 47 (1985) 1099.
[2] P.R. Berger, K. Chang, P. Bhattacharya, J. Singh and K.K. Bajaj, Appl. Phys. Lett 53 (1988) 684.
[3] P. Chen, Q. Xie, A. Madhukar, L. Chen and A. Konkar, J. Vac. Sci. Technol. B 12 (1994) 2568.
[4] Y. Nabetani, T. Ishikawa, S. Noda and A. Sasaki, J. Appl. Phys. 76 (1994) 347.
[5] M. Grundmann, N.N. Ledentsov, O. Stier, D. Bimberg, V.M. Ustinov, P.S. Kop'ev and Zh.I. Alferov, Appl. Phys. Lett. 68 (1996) 979.
[6] D. Leonard, M. Krishnamurthy, C.M. Reaves, S.P. Denbaars and P.M. Petroff, Appl. Phys. Lett. 63 (1993) 3203.
[7] D. Leonard, S. Farard, K. Pond, Y.H. Zhang, J.L. Merz and P.M. Petroff, J. Vac. Sci. Technol. B 12 (1994) 2516.
[8] H. Shoji, K. Mukai, N. Ohtsu, M. Sugawara, T. Uchida and H. Ishikawa, Photon. Technol. Lett. 7 (1995) 1385.
[9] N.P. Kobayashi, T.R. Ramachandran, P. Chen and A. Madhukar, Appl. Phys. Lett. 68 (1996) 3299.
[10] J.Singh and J. Hongtao, private communication.
[11] D.I. Lubyshev, P.P. Gonzalez-Borrero, E. Marega, Jr., E. Petitprez, N. La Scala, Jr. and P. Basmaji, Appl. Phys. Lett. 68 (1996) 205.
[12] K. Kamath, P. Bhattacharya, T. Sosnovski, T. Norris, and J. Phillips Electron. Lett. 32 (1996) 1374.

ELSEVIER

Journal of Crystal Growth 175/176 (1997) 725–729

JOURNAL OF CRYSTAL GROWTH

Growth and characterization of self-organized InSb quantum dots and quantum dashes

T. Utzmeier*, J. Tamayo, P.A. Postigo, R. García, F. Briones

Inst. de Microelectrónica de Madrid, CNM, CSIC, Serrano 144, E-28006 Madrid, Spain

Abstract

We have grown self-organized InSb quantum dots on semi-insulating InP (0 0 1) substrates by molecular beam epitaxy. The size dependency of the uncapped InSb quantum dots on the nominal thickness of the deposited InSb was studied by atomic force microscopy. The dot size has a pronounced minimum at about 2.2 monolayers of InSb. After a nominal thickness of 3.2 monolayers we observe a drastic change of the dot shape, from quantum dots to quantum dashes. From thereon the dots grow in a quasi-cylindric shape aligned in the (1 1 0) direction. The photoluminescence emission of a series of quantum dots was studied, the emission energy being independent of the dot size. When the dots partially relax, the photoluminescence is blue-shifted, which can be explained by a type-II band alignment.

There have been extensive studies on the formation of self-organized quantum-dots (QD) by several growth techniques, such as molecular beam epitaxy (MBE) [1–3], metal-organic chemical vapor deposition [4] and metal-organic vapor-phase deposition [5]. One of the remaining problems of the self-organization of the QDs is the inhomogeneity of the island sizes that broaden the observed PL peaks, and their random distribution over the surface. Also the dot geometry has been studied on (0 0 1) and other surfaces [6].

In this paper we present the growth of InSb QDs on semi-insulating InP (0 0 1) substrates grown by MBE in a pulsed mode, where the group V element is pulsed to enhance the group III surface migration. The self-organized dots were studied by atomic force microscopy (AFM) and photoluminescence measurements. Samples were grown in a conventional solid-source MBE system. After desorption of the InP (0 0 1) oxide at 490°C, we grew a 500 ML thick InP buffer layer, giving a streaky (2×4) reconstruction in the reflection high-energy electron diffraction (RHEED) pattern. Afterwards, the InSb layer was deposited. The surface stoichiometry during growth was controlled by measuring the surface reflection difference signal of the (1 1 0) and (1 − 1 0) directions using a HeNe laser (641.3 nm) at normal incidence to detect the absorption of In-dimers at the growth front reported elsewhere [6]. The InP buffer as well as the InSb islands were grown at a rate of 0.5 ML/s at a growth temperature of 400°C. The growth rate was calibrated by means of RHEED oscillations. After the deposition of 1.2 ML of InSb we observe

* Corresponding author.

0022-0248/97/$17.00 Copyright © 1997 Elsevier Science B.V. All rights reserved
PII S0022-0248(97)00816-0

the typical growth mode transition from two-dimensional layer-by-layer growth to three-dimensional island growth, indicated by the onset of a spotty RHEED pattern. This "critical thickness" is very small and it is not quite sure if the islands grow in the Stransky–Krastanow or in the Volmer–Weber mode, i.e. whether they have a wetting-layer or not. During and after the annealing, the samples were kept under Sb flux until the temperature has fallen below 300°C to ensure that no Sb was lost from the surface.

We took atomic force microscope (AFM) images from various spots on each sample, in order to detect a possible inhomogeneity of the dot sizes over the sample. Typical variations of the mean size in different regions of the same sample were less than 15%. The island size and shape of the uncapped QDs were studied by means of AFM. Fig. 1 shows InSb islands of a sample with nominal thickness of 2 ML. The InSb QDs seem to be randomly distributed and have a quite homogeneous size. Their density amounts to 1×10^{10} QDs per cm^2. The size distribution for the dot diameter has a mean value of 24 ± 4 nm. The height distribution has a mean value of 6 ± 3 nm. (The error values given here and in the following refer to standard deviations of the distributions.) We grew further samples from nominal InSb thicknesses of 1.4–2.8 ML. The statistics of these samples can be seen in Fig. 2 (left part). At small nominal InSb thicknesses the dot diameter is about 80 ± 3 nm and decreases strongly with increasing number of InSb monolayers. The dot height is similarly affected by the nominal InSb layer thickness. The dot density shows opposite behavior. As the diameter reaches its minimum at 2.2 ML, the density has a maximum of 4×10^{10} cm^{-2}. After further InSb deposition up to 2.8 ML of InSb, the dot volume rises again, while the density declines. The surprising feature is that the curve in Fig. 2 shows a minimum. The behavior of the dot sizes and density versus the number of InSb monolayers can be explained qualitatively by material exchange processes. At the onset of the 3D growth, when the QD-density is still low, the islands grow more or less independently from each other. Because the mean inter-dot distance diminishes very quickly (about a factor 3 within 0.4 ML) after the first 3D formation, the QDs interact with each other, exchanging material until they reach their optimal

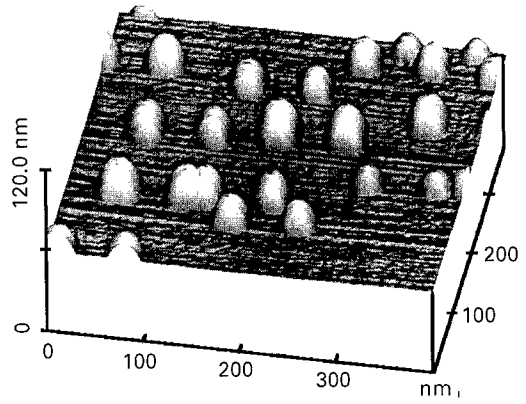

Fig. 1. AFM image of a sample with 2 ML of InSb on InP substrate. The QDs seem to be randomly distributed and have a quite homogenous size. The density amounts to 1×10^{10} cm^{-2}. The mean diameter and height can be seen in Fig. 2.

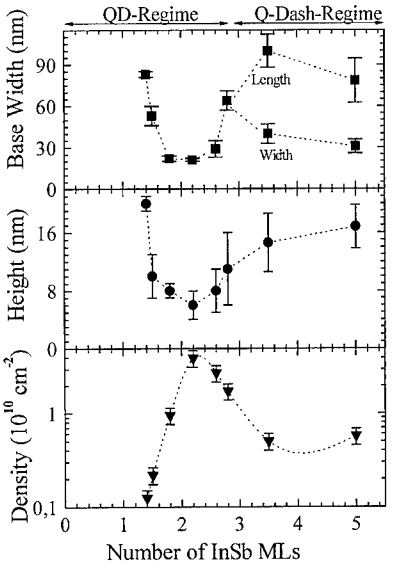

Fig. 2. Statistics on diameters, heights and dot density for various InSb thicknesses. The statistics are made on uncapped samples by AFM. A minimum in size can be observed at around 2.2 ML, where the density is highest. On the right-hand side the quantum dash regime can be seen. Here the islands grow in a quasi-cylindrical shape (see also Fig. 3). The curve for the diameter devides into a curve for length and one for width, respectively. The lines are only a guide for the eye.

size, which is smaller because in this way the surface area is enhanced, which is energetically favorable because this partially relaxes the strain without the formation of dislocations. Similar bahavior has been reported for InAs QDs on GaAs [7, 8]. One has to remember that the samples are grown in an enhanced migration mode. This optimal size seems to be reached at 2.2 ML. Once achieving the optimal size, further InSb deposition results in new island growth, because from then on, the QDs not only interact by material exchange but also through the elastic strain field around each dot (remember the InP substrate next to a QD is expanded) results in a repulsive force between them [9]. Therefore, once having reached the minimum dot distance at 2.2 ML, further deposition can only result in growth of bigger dots, but not more. Furthermore, the density declines with bigger dots because the repulsive force rises with the dot size, which enhances the inter-dot spacing.

If we deposit more than 3.2 ML of InSb we observe a drastic change of the dot geometry (Fig. 3). The QDs no longer have a round shape, but an elongated one. After that point, the QDs maintain their quasi-cylindric shape in all samples with more than 3.2 ML of InSb forming quantum dashes (Q-dash). All Q-dashes are aligned along the (110) direction and their length to width ratio is approximately 2.5. The main Q-dash size is 100 nm long and 40 nm wide, but there are also some bigger ones with length 125 nm and width 66 nm (Fig. 3a). In regions where there is an enhanced surface roughness of the InP substrate, the dots grow all along it. This roughness cannot be explained by the growth conditions because they were the same for all samples (Fig. 1 does not show this roughness), but might be an evidence for an anisotropic strain field due to the Q-dashes, due to the different dimension in length and width. For that reason, we do not believe that the origin of this preferred growth in the (110) direction lies in the surface morphology, but vice versa. Our assumption is supported by the fact that the Q-dashes can grow closer to each other in the lateral than in the longitudinal direction, probably because the repulsive train field in the substrate, originated by the QDs, depends in each direction on the square of the corresponding QD-dimension in that direction. The relative frequencies of the lateral inter-dash spacing w and the longitudinal inter-dash spacing l of the Q-dashes on one sample can be seen in Fig. 4. There are minimum values for w and l of

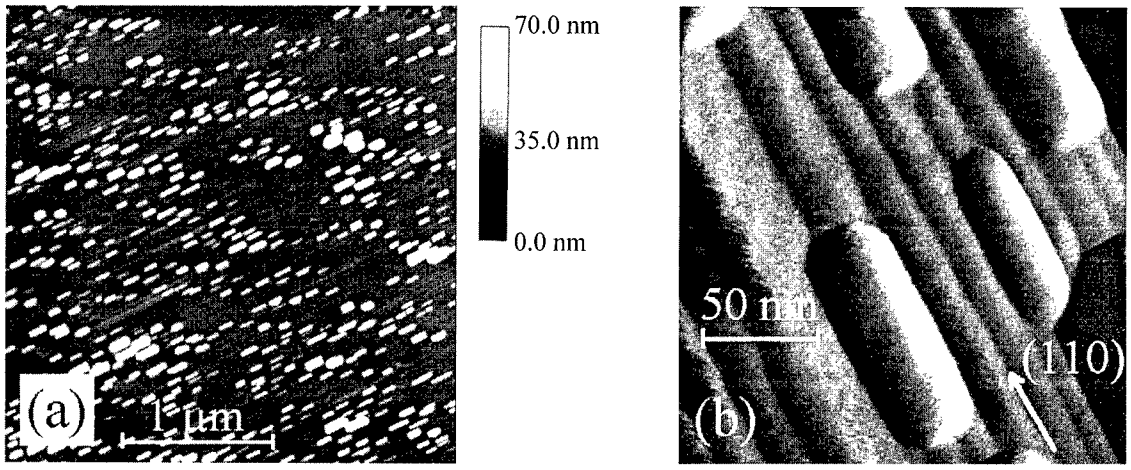

Fig. 3. AFM images of a sample with 3.5 ML of InSb. Image (a) was taken in the height mode, while image (b) was taken in the error signal mode to emphasize the dash edges. The circular QDs have transformed to rectangular quantum dashes. The longer edge lies along the (1 1 0) direction and is about 2.5 times longer than the other one (b). On the left-hand side (a) a higher number of quantum dashes can be seen with dimensions of 100×40 nm, but there are also a few bigger ones, measuring 125×66 nm.

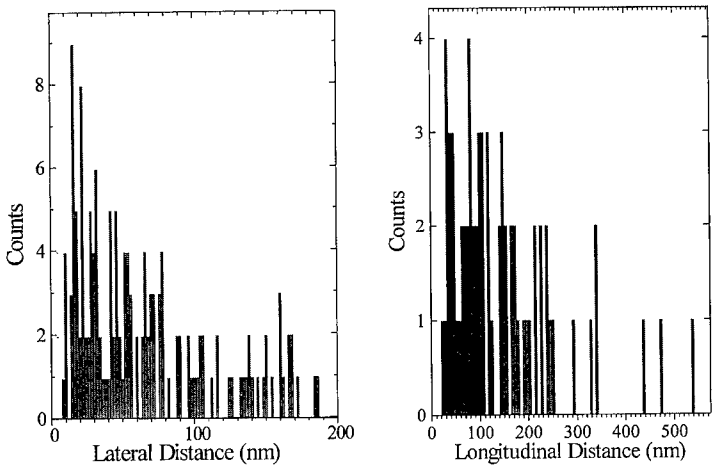

Fig. 4. Statistics on the longitudinal and the lateral spacings between quantum dashes. For the longitudinal distribution we only measured the distance of exactly collinear islands. Both, the longitudinal and the lateral spacings have a minimum value of 23 and 7 nm, respectively.

7 and 23 nm, respectively. The quotient, $l/w = 3.3$, that should depend on the square of the longitudinal and the lateral size of the islands, is somewhat smaller than the theoretical value of 6.3. Assuming an exponential distribution, we obtain a quotient of the mean ranges of the repulsive forces of 2, which is closer to l/w, but the difference to the theoretical value could mean a slight amount of relaxation through dislocations at the interface in the (1 1 0) direction. Only a very small percentage of the Q-dashes are really orientated collinear with others, most of them are displaced with respect to their next neighbors due to the higher strain in that direction, which supports the model of an anisotropic strain field. Thus, the minimum surface energy in the Q-dash regime is obtained with a non-collinear geometry as shown in Fig. 3a. According to Tersoff [10], when the quantum dots pass a critical size, they grow in order to minimize their energy in the dash geometry, as observed in our samples. But his model does not explain why we cannot observe "infinite" large islands instead of many short ones and why the (1 1 0) direction is preferred. Furthermore, we can observe a distribution of the island widths, while the model predicts a constant width. On the other hand, the width distribution is much narrower than the length distribution, suggesting a preferred width value. The constant width in that model is also calculated at constant height, which is probably not the case as seen in Fig. 2, although the error bars are relatively large. Another explanation for the non-constant width could be that wider Q-dashes are formed by two individual ones growing together, which was actually observed on a few occasions on AFM images. In order to understand this unexplained behavior, one has to include the different energies of the different crystal surfaces of the Q-dashes and the interaction of different islands through their strain field in the substrate material.

We studied the photoluminescence of these samples at 12 K, exciting with a Ar^+-laser. The spectra of three samples with 2, 2.8, and 10 ML of InSb dots, respectively, are shown in Fig. 5. The peak at 1.4 eV is attributed to InP, the other two peaks that can be seen at about 1 and 1.2 eV are attributed to two QDs. As more InSb is grown the peak at 1 eV loses intensity, while the one at 1.2 eV gains. Furthermore, the observed blue-shift with growing dot sizes is quite contrary to the expected behavior. The confinement effect of bigger dots should be smaller than that of the smaller ones and therefore a red-shift is expected. But this behavior can be explained supposing a type-II band alignment between the compressed InSb QDs and the InP matrix. Because of the strain applied to the QDs, the InSb

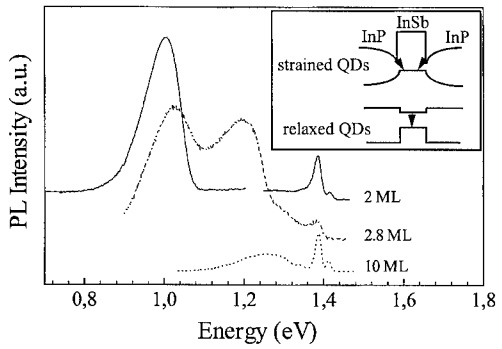

Fig. 5. PL spectra of samples with 2, 2.8 and 10 ML of InSb, respectively. Two peaks at 1 and 1.2 eV can be observed. The one at 1 eV is attributed to strained QDs, while the other one at 1.2 eV is attributed to partially relaxed ones. The inset shows the proposed band alignment for these two cases.

conduction band rises above the InP. On the other side also the InP next to a QDs is expanded, which reduces its band gap in a way that a deep well at the InP/InSb interface is formed in the InP, as seen in the inset of Fig. 5. A type-II alignment has been observed, for example, in GaSb/GaAs QDs [11]. So, when the QD is strained, its emission should be indirect in real space. When the dot reaches a size sufficient to relax, all the strain disappears and a type-I band alignment is obtained again. Therefore, the peak at 1 eV should come from compressed QDs and the other one at 1.2 from partially relaxed ones. In this manner, one can explain why the emission energy of the strained QDs does not shift until about 2.5 ML InSb, although the dot-sizes differ significantly.

The initial stages of growth of InSb QDs on InP substrate have been studied by AFM. typical QD formation can be observed until a InSb thickness of 3.2 ML. From thereon, the quantum-dots drastically change their shape forming Q-dashes along the (110) direction. This behavior can qualitatively be understood, taking into account the elastic energy and surface energy of the QDs and the kinetics of the growth predominantly at the island edges and the repelling force between the islands due to their anisotropic strain field in the substrate. PL measurements of samples with 2–10 ML of InSb reveal that in the strained state, the band alignment between the QDs and the InP matrix material is of type II.

The authors would like to acknowledge the financial support from the European Union (HCM, network CT930349).

References

[1] D. Leonard, M. Krishnamurty, C.M. Reaves, S.P. Denbaar and P.M. Petroff, Appl. Phys. Lett. 63 (1993) 3203.
[2] J.M. Moison, F. Horzay, L. Leprince, E. André and O. Vatel, Appl. Phys. Lett. 64 (1994) 196.
[3] J.-Y. Marzin, J.-M. Gerard, A. Izrael and D. Barrier, Phys. Rev. Lett. 73 (1994) 716.
[4] M. Kimatura, M. Nishioko, J. Oshinowo and Y. Arakawa, Appl. Phys. Lett. 66 (1995) 3663.
[5] R. Nötzel, J. Temmyo, A. Kozen, T. Tamamura, T. Fukui and H. Hasegawa, Appl. Phys. Lett. 66 (1995) 2525.
[6] F. Briones and A. Ruiz, J. Crystal Growth 111 (1991) 194.
[7] J.M. Grárd, J.B. Génin, J. Lefebvre, J.M. Moison, N. Lebouché and F. Marthe, J. Crystal Growth 150 (1995) 351.
[8] A. Ponchet, A. Le Corre, H. L'Haridon, B. Lambert and S. Salaün, Appl. Phys. Lett. 67 (1995) 1850.
[9] L.C.A. Stoop and J.H. Van Der Merwe, J. Crystal Growth 24 (1974) 289.
[10] J. Tersoff and R.M. Tromp, Phys. Rev. Lett. 70 (1993) 2782.
[11] F. Hatami, N.N. Ledentsov, M. Grundmann, J. Böhrer, F. Heinrichsdorf, M. Beer, D. Bimberg, S.S. Ruminov, P. Werner, U. Gösele, J. Heydenreich, U. Richter, S.V. Ivanov, B.Ya. Meltser, P.S. Kop'ev and Zh.I. Alferov, Appl. Phys. Lett. 67 (1995) 656.

ELSEVIER

Journal of Crystal Growth 175/176 (1997) 730–735

JOURNAL OF CRYSTAL GROWTH

MBE growth of novel GaAs/n-AlGaAs field-effect transistor structures with embedded InAs quantum traps and their transport characteristics

G. Yusa[a,*], H. Sakaki[b,c]

[a] *Institute of Industrial Science, University of Tokyo, 7-22-1 Roppongi, Minato-ku, Tokyo 106, Japan*
[b] *Research Center for Advanced Science and Technology, University of Tokyo 4-6-1 Komaba, Meguro-ku, Tokyo 153, Japan*
[c] *Quantum Transition Project, JRDC, Park Bldg. 4F, 4-7-6 Komaba, Meguro-ku, Tokyo 153, Japan*

Abstract

Novel GaAs/n-AlGaAs FETs structures have been grown by molecular beam epitaxy (MBE) by placing InAs quantum dots near the channel. We show that the threshold voltage can be shifted by the trapping or detrapping of electrons in these dots. The number of electrons trapped by each InAs dot is estimated to be one or two, representing the finiteness of quasi-stable trap states. The concentration of trapped electrons at 4.2 K is identical to that at 77 K, suggesting that trapped electrons stay in the ground level up to relatively high temperatures.

1. Introduction

Owing to the development of semiconductor technology, it has recently become possible to fabricate laterally-defined nano-structures, such as quantum wires and dots [1–6]. Especially properties of zero-dimensional electrons confined in quantum dot structures have attracted a wide attention because of their importance both in physics and device applications, such as nonlinear transport devices [2, 3], improved laser performance [4] and ultra-high-density of semiconductor memory devices.

One of the promising methods to form 10 nanometer (nm)-scale dots is to use the Stranski–Krastanov mode of epitaxial growth. In this approach, a material such as InAs or InGaAs is deposited on a lattice mismatched GaAs substrate beyond its critical thickness to form very small dot structures [5, 6]. In addition to these systems, InP dots on InGaP [7] and InSb/GaSb/AlSb dots on GaAs [8] so on have been formed by molecular beam epitaxy (MBE)[5, 6] and metalorganic chemical vapor deposition (MOCVD) [11]. Structures of these self-assembled dots have been studied to find out the dot formation process [5, 6] as well as the strain distribution [9, 10]. Optical properties have been also studied to clarify quantum states in these dots [12, 13] and also explore the possibility of quantum dot lasers which are expected to have

* Corresponding author. E-mail: yusa@kyokusho.rcast.u-tokyo.ac.jp.

0022-0248/97/$17.00 Copyright © 1997 Published by Elsevier Science B.V. All rights reserved
PII S0022-0248(96)00927-X

superior properties over quantum well lasers [4]. Other new insights have been also obtained on details of quantum states by using such methods as capacitance spectroscopy [14], far-infrared spectroscopy [15], and the resonant tunneling spectroscopy of electrons via InAs quantum dots [16].

Although much work has been done on the carrier confinement in the core part of quantum dots, a small number of papers have dealt with trapping and detrapping process of electrons and the subsequent influence of the dot-induced potential on the electron transport. In this paper, we report on the MBE growth on GaAs/n-AlGaAs inverted heterojunctions (inverted HEMT), in which InAs dots are embedded near the electronic channels and investigate how InAs quantum dots serve as electron trap centers for two-dimensional electron gas.

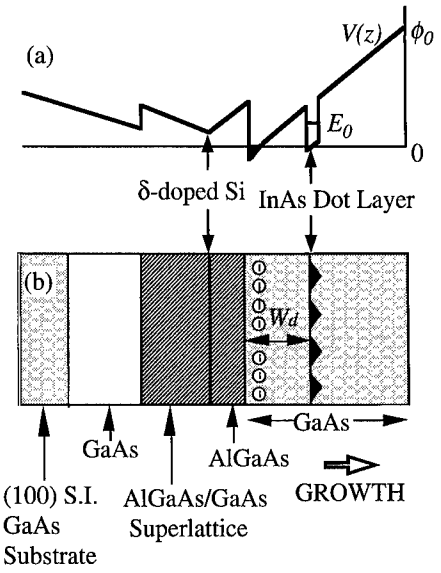

Fig. 1. Schematic illustration of the conduction band diagrams (a) and the composition profile (b) of the dot-embedded GaAs/n-AlGaAs modulation doped field-effect transistors.

2. Growth and sample fabrication

First, to prepare selectively-doped GaAs/n-AlGaAs inverted heterostructures of Fig. 1, we grew by MBE a 200 nm GaAs buffer layer on a semiinsulating GaAs (1 0 0) substrate, and then 11 periods of a 20 nm $Al_{0.25}Ga_{0.75}As$ and 2 nm GaAs layer at the substrate temperature T_s of 600°C. At this point, 1×10^{12} cm^{-2} Si was δ-doped so as to minimize deleterious effects of DX centers [17]. The growth rates for GaAs and $Al_{0.25}Ga_{0.75}As$ are 0.954 and 1.28 ML/s, respectively. We grew a rather thick (70 nm) undoped $Al_{0.25}Ga_{0.75}As$ spacer layer to avoid the degradation of electron mobility [18] that may be induced by the segregation of Si atoms toward the sample surface. Then a GaAs channel layer was deposited to the total thickness of 600 nm. During this phase of growth, InAs quantum dots were formed by the following procedure; after growing a 200 nm-thick GaAs spacer layer, the substrate temperature was decreased immediately to 450°C. Then 1.75 ML InAs was deposited with the rate of 0.1 ML/s to form dot structures. We monitored the growth of InAs by reflection high-energy electron diffraction (RHEED) to confirm the formation of dots [19] when the streaky (2×4) reconstruction pattern transformed to a spotty pattern, as soon as the dots are formed. Then 2.5 nm GaAs was grown at 450°C without interruption to cover the dots. Then the substrate temperature was heated up again to 600°C for further overgrowth of a 400 nm-thick GaAs. Note that InAs dots of this sample S1 are 200 nm from the heterointerface, suggesting that strain effects of dots are negligible. In addition, the ground level of InAs is well above the Fermi level as shown in Fig. 1 unless the surface potential is lowered by the gate electrode.

In advance, another sample of nearly identical structure was prepared except that GaAs overgrowth was dispensed. Atomic force microscopy (AFM) was performed on this sample in air to show that 1.75 ML InAs deposited under our growth condition results in dot structures of typically 5 nm in average height and 20 nm in average diameter at the bottom. Their average concentration is about $5–10 \times 10^{10}$ cm^{-2}. We also prepared, for comparison, two more samples, S2 and S3, in which we inserted a 1 ML InAs and no InAs layer, respectively. These three samples were grown in one day.

We processed these wafers to produce field-effect transistors by forming an Al gate, Hall voltage probes, as well as the source and drain electrodes. The carrier concentration N_s and mobility μ of two-dimensional electron gas (2DEG) were measured as a function of the gate voltage V_g by using the Hall effect [20].

3. Transport and trapping properties

First, we measured N_s and μ of all three samples at 4.2 K in the dark and the results are plotted in Fig. 2. Note in Fig. 2a that the threshold voltages of all three samples S1 (filled circle), S2 (solid line) and S3 (dashed line) are about -0.6 V, from which N_s increases linearly up to $V_g = 0.8$ V. Note that the slopes dN_s/dV_g of these three samples are almost the same. The slope is determined by the gate capacitance between the gate and the channel and is 20 nF/cm^2 for all samples, which agrees well with the designed value.

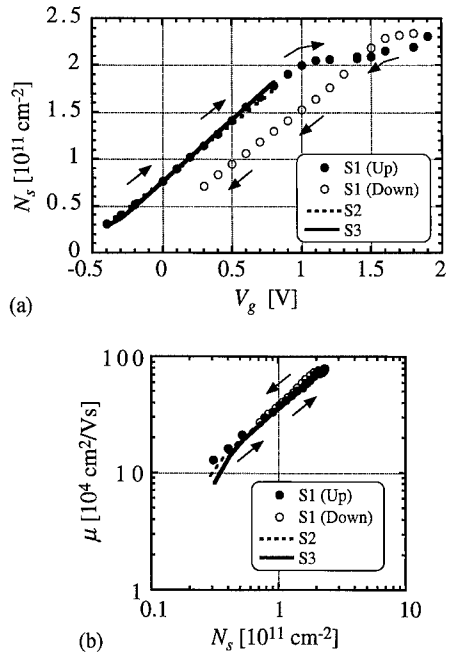

Fig. 2. The concentrations N_s of electrons is plotted as a function of the gate-source voltage (a) and the mobilities μ dependence on N_s (b) of three FETs measured at 4.2 K.

Electron mobilities μ were also measured for V_g between -0.5 V and $+0.8$ V. μ–N_s characteristics are shown in Fig. 2b. Note that S1, S2 and S3 show nearly identical characteristics. This proves that InAs dots play small roles in this region, since InAs dots are well displaced from the 2DEG channel. Hence, the electrons scarcely overlap with the cores of InAs dots and a surrounding strain induced by lattice mismatched InAs. Note that the observed dependence of μ on N_s suggests that the dominant scatterers for all samples are a small number of the coulombic charges coming from background impurities or other impurities originating from nominally δ-doped Si in the AlGaAs [21]. Note here also that μ of electrons are more than 70×10^4 cm^2/V·s at 4.2 K at $N_s \sim 2 \times 10^{11}$/cm^2 in GaAs/AlGaAs inverted heterojunctions, which indicates very good quality of our MBE growth [18, 22].

Once V_g exceeds 0.8 V, leakage current begins to flow between the gate and the channel. This anomalous region will be discussed later. As mentioned earlier, the gate leakage current remains small for $V_g < 0.8$ V. This is reasonable as the Schottky barrier of n-GaAs is about 0.8 eV. For $V_g \geqslant 0.8$ V, the leakage substantially increases in sample S2 and S3, while it remains rather low in sample S1. The electron concentration N_s of sample S1 stays constant for $V_g \geqslant +0.8$ V, indicating that the gate electric field is screened by some charges. This saturation of N_s and reduction of the leakage current in S1 is due to the appearance of an extra potential barrier, which is induced by the trapping of electrons by InAs dots. This situation is shown in Fig. 3a and Fig. 3b. When the potential of the surface layer is pulled down by the gate bias ($V_g = 0.8$ V) as in Fig. 3b, some electrons will be trapped by the dots, which raises the potential. This charging process of dots prevents the leakage current for the gate voltage range between $+0.8$ V and $+1.9$ V. When V_g exceeds $+1.9$ V the leakage current begins to flow again, since the InAs dots are then fully occupied.

In reducing V_g from $+1.9$ V, N_s of S1 is found to decrease with the same slope, as shown by open circles in Fig. 2. The N_s–V_g characteristics are shifted by 4.5×10^{10} cm^{-2}. This shift is due to the discontinuous change of electric field δF, which is

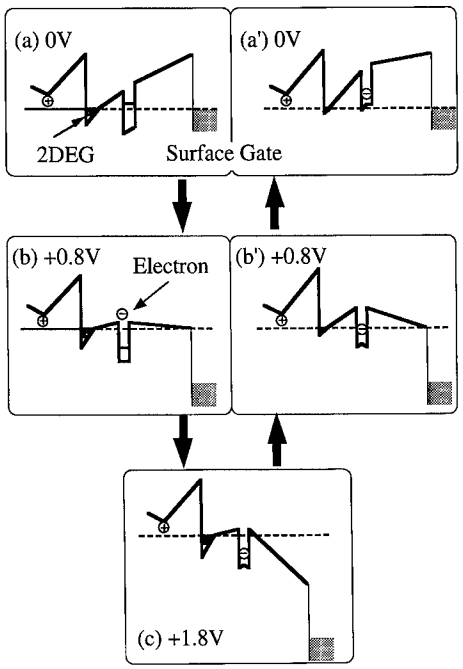

Fig. 3. Illustration of the potential profile of a dot-inserted modulation doped FET at various values of V_g. (a)–(c) show how an empty dot is charged by one electron when V_g increases, while (a') and (b') show the band diagram after the dot is charged up with the electron.

induced by the trapped charges in the InAs dot layer. As shown in Fig. 3c, δF can be expressed as

$$\delta F \equiv F_2 - F_1 = \frac{\delta V}{W_{GaAs}}, \tag{1}$$

where W_{GaAs} is the thickness ($= 0.4\ \mu m$) of the upper surface GaAs layer and δV is the voltage shift of N_s–V_g characteristics. From such data, we can estimate the number, N_{Dot}, of captured electrons in InAs quantum dots, using Gauss's law.

$$N_{Dot} = \frac{\varepsilon_0 \varepsilon_{GaAs} \delta F}{e}, \tag{2}$$

where $\varepsilon_0\ \varepsilon_{GaAs}$ is the permittivity of GaAs, e is the elementary charge. Fig. 2a gives a value of $\delta V = 0.371$ V, from which we find that N_{Dot} is $6.56 \times 10^{10}\ cm^{-2}$.

Since the density D_{Dot} of InAs dots in our sample is estimated to be $(5–10) \times 10^{10}\ cm^{-2}$, the density,

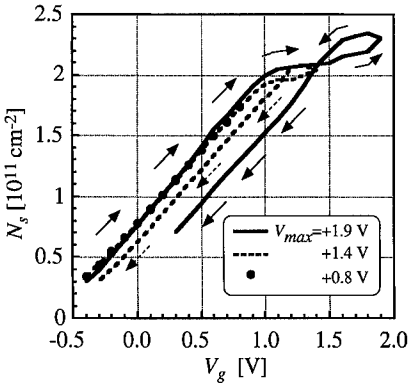

Fig. 4. The concentrations N_s of electrons in the channel of the dot embedded FET measured changing the three different maximum gate-source voltage V_{max} at 4.2 K.

N_{Dot}, of trapped electrons in the dots is very close to D_{Dot}. This indicates that the dots are charged by one or two electrons.

To clarify trapping mechanisms, we measured the N_s–V_g characteristics at 4.2 K for three different maximum gate voltages, V_{max}. Incidentally, measurements were done at 4.2 K but after each measurement, the sample was heated up to room temperature and exposed to a usual room light in order to discharge InAs dots. Fig. 4, N_s shows the result.

When V_g is decreased from $V_{max} = 0.8$ V (indicated by ○), no shift in N_s is observed, suggesting that InAs quantum dots capture such a small number of electrons that no potential charging effect is observed. As Fig. 4 shows, N_s–V_g relation for $V_{max} = +1.9$ V makes a loop and crosses at $V_g = +1.4$ V. However, N_s–V_g relation for $V_{max} = +1.4$ V does not agree with that for $V_{max} = +1.9$ V. This means that to fully occupy dots with electrons, electrons must be injected by applying excess gate bias. Since the saturation of N_s observed in a region of $V_g = +1.0 - +1.9$ V results from the band bending at InAs dot layer as shown in Fig. 3, one can assume that in this region one or two extra electrons can be trapped at excited levels of InAs dots. Indeed, it has been theoretically and experimentally shown that some electrons can occupy not only the ground state but the excited levels in the dots [14, 23]. When reducing

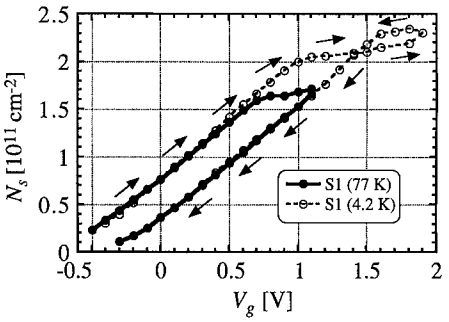

Fig. 5. The concentrations N_s of electrons in the channel of the dot embedded FET measured as a function of the gate-source voltage at two different temperature 4.2 and 77 K.

V_{max} electrons in the excited levels may be discharged, since these electrons in the excited levels can be detrapped more easily than those in the ground level even at 4.2 K. When V_g is decreased from $V_{max} = 1.4$ V, relatively small N_s shift is observed, indicating that not all the InAs dots are occupied. The estimated number of trapped electron is 4.31×10^{10} cm^{-2}, using Eq. (1) and Eq. (2)

N_s–V_g characteristics were also studied at 77 K. The result is shown in Fig. 5. It is clear that both the slope dN_s/dV_g and the shift of the gate threshold δV_s at 77 K are almost the same as those of 4.2 K, suggesting that the number of trapped electrons is almost unchanged. Note that a loop is observed only at 4.2 K, as shown in Fig. 4. Although the enhancement of V_{th} is attributed to the existence of a barrier at 4.2 K, the details of this charging and discharging processes, including a loop at 4.2 K in this region, will be published elsewhere. Since the barrier around the dot is quite high ($\sim$ 100 meV) [15, 19], electrons trapped in the ground level cannot be thermally activated even at 77 K. The rate of tunnel escape process is also expected to be small, since the surrounding GaAs barrier is quite thick. Hence, the reduction of N_s persists even if V_g is biased at -1.0 V, at which the density of 2DEG almost vanishes.

4. Conclusions

We have studied MBE growth of InAs dots and the effects of InAs quantum dots inserted in a novel FET structure and demonstrated that the InAs dots work as electron trap centers, in a region where the wave function of 2DEG hardly overlaps the InAs dots or strain region. Although μ of electrons is not degraded by inserted InAs dots, the electron concentration, N_s at a given gate voltage V_g is found to be reduced once a positive V_g beyond 1.0 V is applied, shifting the threshold voltage of this novel FET device. From the reduction of N_s in the channel, we have shown that each InAs dot captures one or two electrons. We have shown that the number of trapped electrons in InAs dots is dependent on the maximum voltage applied to the gate. This effect was observed at both 77 and 4.2 K, suggesting that electrons captured in the ground state are not detrapped at 77 K. If the structure is optimized, this quantum trap (QT) FET may well function at higher temperatures and serve as a novel memory device.

Acknowledgements

One of the authors (G.Y.) would like to thank the Japan Society for the Promotion of Science for Young Scientists for the partial financial support. Part of this work was supported by a Grant-in-Aid for Scientific Research from the Ministry of Education, Science, Sports, and Culture, Japan.

References

[1] H. Sakaki, Surf. Sci. 267 (1992) 623.
[2] H. Sakaki, K. Wagatsuma, J. Hamasaki and S. Saito, Thin Solid Films 267 (1976) 497.
[3] H. Sakaki, Jpn. J. Appl. Phys. 28 (1989) L314.
[4] Y. Arakawa and H. Sakaki, Appl. Phys. Lett. 40 (1982) 939.
[5] D. Leonard, M. Krishnamurthy, C.M. Reaves, S.P. Denbaars and P.M. Petroff, Appl. Phys. Lett. 63 (1993) 3203.
[6] J.M. Moison, F. Houzay, F. Barthe, L. Leprince, E. Andre and O. Vatel, Appl. Phys. Lett. 64 (1994) 196.
[7] J. Ahopelto, A.A. Yamaguchi, K. Nishi, A. Usui and H. Sakaki, Jpn. J. Appl. Phys. 32 (1993) L32.
[8] R. Brian, R. Bennett, R. Magno and B.V. Shanabrook, Appl. Phys. Lett. 68 (1996) 505.
[9] Q. Xie, P. Chen and A. Madhukar, Appl. Phys. Lett. 65 (1994) 2051.
[10] Q. Xie, P. Chen and A. Madhukar, Phys. Rev. Lett. 75 (1995) 2542.

[11] J. Oshinowo, M. Nishioka, S. Ishida and Y. Arakawa, Appl. Phys. Lett. 65 (1994) 1421.
[12] J.-Y. Marzin, J.-M. Gérard, A Izraë, D. Barrier and G. Bastard, Phys. Rev. Lett. 73 (1994) 716.
[13] M. Grundmann, J. Christen, N.N. Ledentsov, J. Böhrer, D. Bimberg, S.S. Ruvimov, P. Werner, U. Richter, U. Gösele, J. Heydenreich, V.M. Ustinov, A.Yu. Egorov, A.E. Zhukov, P.S. Koe'ev and Zh.I. Alferov, Phys. Rev. Lett. 74 (1995) 4043.
[14] G. Medeiros-Ribeiro, D. Leonard and P.M. Petroff, Appl. Phys. Lett. 66 (1995) 1767.
[15] H. Drexler, D. Leonard, W. Hansen, J.P. Kotthaus and P.M. Petroff, Phys. Rev. Lett. 73 (1994) 2252.
[16] M. Nairhiro, G. Yusa, Y. Nakamura, T. Noda and H. Sakaki, 12th Int. Conf. on the Application of High Magnetic Fields in Semiconductor Physics, Wurzburg, 1996, July.
[17] E. Muñoz, E. Calleja, I. Izpura, F. García, A.L. Romero, J.L. Sánchez-Rojas, A.L. Powell and J. Castagné, J. Appl. Phys. 73 (1993) 4988.
[18] L. Pfeiffer, E.F. Schubert, K.W. West and C.W. Magee, Appl. Phys. Lett. 58 (1991) 2258.
[19] H. Sakaki, G. Yusa, T. Someya, Y. Ohno, T. Noda, H. Akiyama, Y. Kadoya and H. Noge, Appl. Phys. Lett. 67 (1995) 3444.
[20] G. Yusa and H. Sakaki, Electron. Lett. 32 (1996) 491.
[21] K. Hirakawa and H. Sakaki, Phys. Rev. B 33 (1986) 155.
[22] Dojin Kim, A. Madhukar, Ke-Zhong Hu and Wei Chen, Appl. Phys. Lett. 56 (1990) 1874.
[23] M. Grundmann, N.N. Ledentsov, O. Stier, D. Bimberg, V.M. Ustinov, P.S. Kop'ev and Zh. I. Alferov, Appl. Phys. Lett. 68 (1996) 979.

ELSEVIER

Journal of Crystal Growth 175/176 (1997) 736–740

JOURNAL OF CRYSTAL GROWTH

In situ RHEED control of direct MBE growth of Ge quantum dots on Si (0 0 1)

V.A. Markov*, A.I. Nikiforov, O.P. Pchelyakov

MBE Department, Institute of Semiconductor Physics, Russian Academy of Sciences, Siberian Branch, 630090 Novosibirsk, Russian Federation

Abstract

RHEED studies of the morphological transformation of germanium layers during their MBE growth on the Si(0 0 1) surface were carried out. Zero-streak profiles analysis were used to control the formation of coherent and dislocated germanium islands at the film thickness of more than 5 and 8 monolayers (ML), respectively. The dislocation-free islands formed at the first stage (4–8 ML) of the morphological transformation were employed for designing the structures with the self-organized Ge quantum dots. The effects of charge and size quantization of hole transport, such as the Coulomb blockade and the resonance hole tunneling through the discrete energy levels in the quantum dots were observed in these structures.

PACS: 68.35.Bs; 85.30.Vw

Keywords: Germanium; Silicon; MBE; RHEED; Quantum dots

1. Introduction

In the recent years direct synthesis of low-dimensional GeSi structures has received considerable attention. The self-organization of 3D Ge islands on silicon according to Stranski–Krastanow's growth mechanism was used for the first time in Refs. [1–3] to produce a layer of quantum dots as small as 10 nm in diameter. A lot of quantum-sized effects were observed in heterostructures containing quantum dots [1–3]. This approach was widely used later to make GeSi dot structures as well as III–V and II–VI ones. A direct growth allows obtaining of smaller quantum dots against those obtained by lithographic methods. Additionally, the direct synthesis makes it possible to overcome numerous technological problems in designing quantum-sized structures. During the synthesis of the quantum dot structures, it is important to know sizes of the 3D germanium islands and to be able to control in situ the process of their formation. In this connection, the present work was aimed at RHEED studies of the morphological transformations in germanium-on-silicon layers and of the

* Corresponding author. Fax: + 7 3832 357 502; e-mail: markov@isp.nsc.ru.

0022-0248/97/$17.00 Copyright © 1997 Elsevier Science B.V. All rights reserved
PII S0022-0248(96)01180-3

direct growth of the structures containing self-organized quantum dots.

2. Experimental details

Germanium on silicon films were grown using a MBE installation "Katun-C" equipped with two e-beam evaporators for germanium and silicon and two Knudsen cells for doping. Si (0 0 1) wafers of 60 mm diameter were used as substrates. The growth process was controlled in situ using the RHEED technique (20 kV). Diffraction patterns and intensity variations versus time at separate points and along the given profiles were recorded by using a computer-aided TV system "FOTON-4". In the present work variations in intensity profiles versus time were studied along (0 0) streak in the [1 1 0] azimuth. The shortest recording interval for one intensity profile was 0.5 s. The Ge growth rate was measured through observation of RHEED oscillations of specular beam, it was equal to about 0.01 nm/s.

3. RHEED control of quantum dots formation

The initial stages of germanium growth on the Si (0 0 1)-(2 × 1) surface were studied by observing variations in the diffraction patterns and the intensity profiles. From the onset, there were observed RHEED oscillations (Fig. 1a) each period of which corresponded to filling of one monolayer (ML) of $a/4$ (0.14 nm) thickness. At the film thickness of 4–6 ML, highly smeared bulk spots appeared in the diffraction pattern (Fig. 2a). In the literature, such a pattern is accounted for by the formation of germanium clusters shaped as a tetrahedral pyramid with the side orientation of {1 0 5} type (the so-called *hut-clusters*) [4, 5]. According to Refs. [5, 6], there are no misfit dislocations in the clusters, and the strain relaxation in them proceeds due to deformation of the silicon substrate. Fig. 3a presents germanium hut-clusters formed upon growth of the 7 ML film.

The thickness of 5 ± 0.3 ML of the Ge film corresponding to the formation of the smeared bulk spots was determined by analyzing profiles (Fig. 4a,

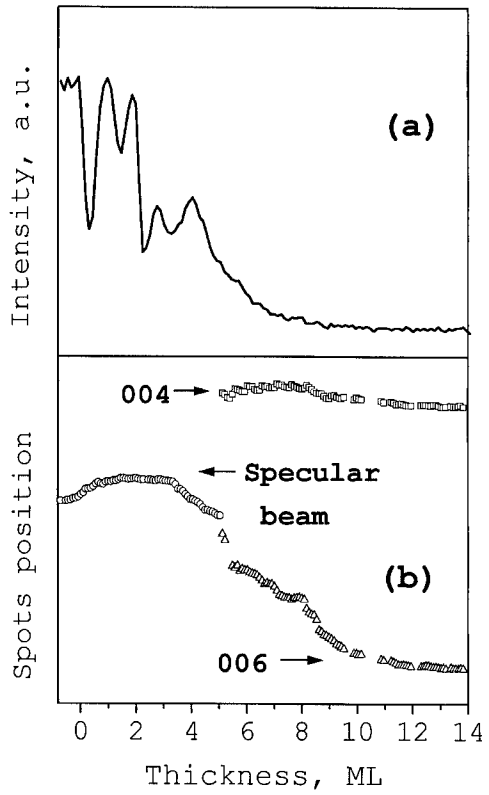

Fig. 1. Specular beam intensity (a) and spot positions in a zero-streak intensity profile (b) versus thickness of Ge/Si (0 0 1) film during it's growth (azimuth [1 1 0]). Arrows show specular beam and real bulk spots positions. Diffraction angle is shown in accordance with RHEED-patterns (Fig. 2).

b). The specular beam is divided into two. As the film grows, they transfer towards the bulk diffraction positions. The most spectacular is the transfer observed for the (0 0 6) beam. The nature of this transfer is not clearly understood now; we assign it to the redistribution of intensities of electron beams reflected by the free silicon surface and by the surface of germanium {1 0 5} planes facing the hut-clusters. The bulk beam is a superposition of electron beams reflected by the surfaces of these two types. Two of these reflections are of large half-widths due to the small cluster size and, thus, are merged into one spot in the diffraction pattern. As germanium is deposited, the cluster grows and

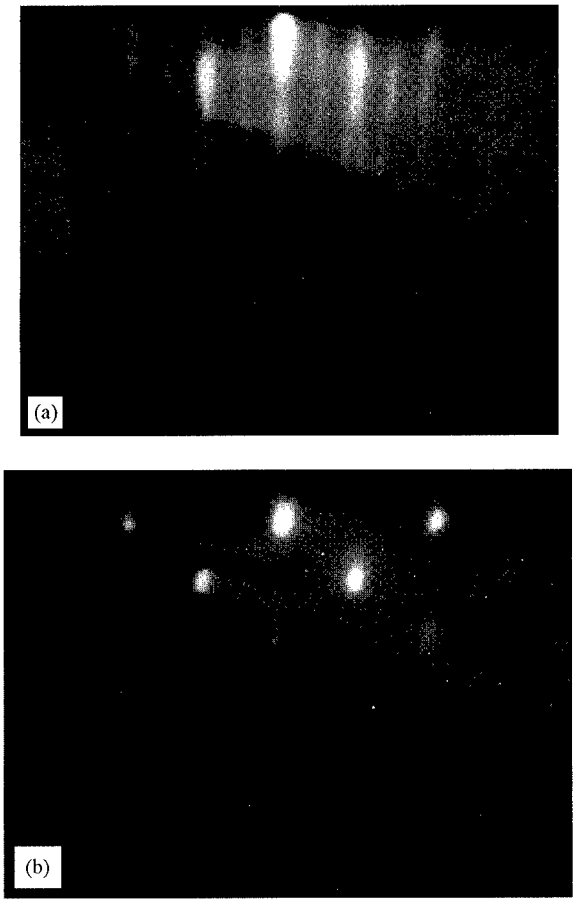

Fig. 2. RHEED-patterns after 7(a) and 12(b) ML Ge growth on Si (0 0 1) surface (400°C, azimuth [1 1 0]).

the intensity of the beam reflected by the {1 0 5} plane increases. On the other hand, the cluster-free Si (0 0 1) surface area decreases, which results in a lower intensity of the specular beam. As a consequence, the bulk spot is shifted from the original position of the specular beam towards the range of large angles.

A similar behavior of bulk spots was observed by us at the growth temperature range of 200–600°C. The beams move more readily at high growth temperatures, probably, due to a larger size of the clusters and a higher rate of their plane growth. The data on profile analysis of RHEED patterns used to elucidate dynamics of the growth of 3D germanium islands will be reported elsewhere.

When the thickness is above 8–10 ML, the diffraction pattern changes gradually (Fig. 2b). According to Refs. [4–6], now it is attributed to the formation of germanium islands with misfit dislocations faced by {1 1 3} planes. When the thickness is above 7.5–8 ML, bright and narrow spots, assigned to bulk diffraction on the islands, appear in the intensity profiles close to the bulk diffraction position (Fig. 4). This is clearly seen after splitting the (0 0 6) spot into two Gaussians (Fig. 4c and Fig. 4d). The wide spot assigned to reflection from {1 0 5} planes disappears rather quickly. For example, it reduces to one-sixth height when the thickness increases by 2 ML only (Fig. 4c and Fig. 4d). The small width of the bulk reflections indicates a markedly larger size of the dislocated islands against the size of the hut-clusters. The latter assumption is supported by the TEM studies of a Ge film of 12 ML thickness (Fig. 3b). The islands with dislocations are formed at a later stage of the morphological reconstruction, and their size (50 nm) is considerably larger than that of the hut-clusters (below 20 nm).

Hence, the germanium hut-cluster films are preferable to design structures with smaller quantum dots. Additionally, the absence of misfit dislocations allows defect-free layers to be grown at the quantum dot surface, which is of importance for development of structures for electric physical measurements. Notice that analysis of intensity profiles in the RHEED pattern makes it possible to detect islands with dislocations before the diffraction pattern changes. Therefore, the formation of large 3D islands incorporating misfit dislocations can be prevented.

4. Direct growth of quantum dot structures

To study tunnel current through the 3D germanium hut-clusters, we grew the structures consisting of the following layers (in order of growth from the p^+-Si (0 0 1) substrate):

- a base electrode p^+-$Ge_{0.7}Si_{0.3}$, 17 nm;
- a tunnel barrier Si, 8 nm;

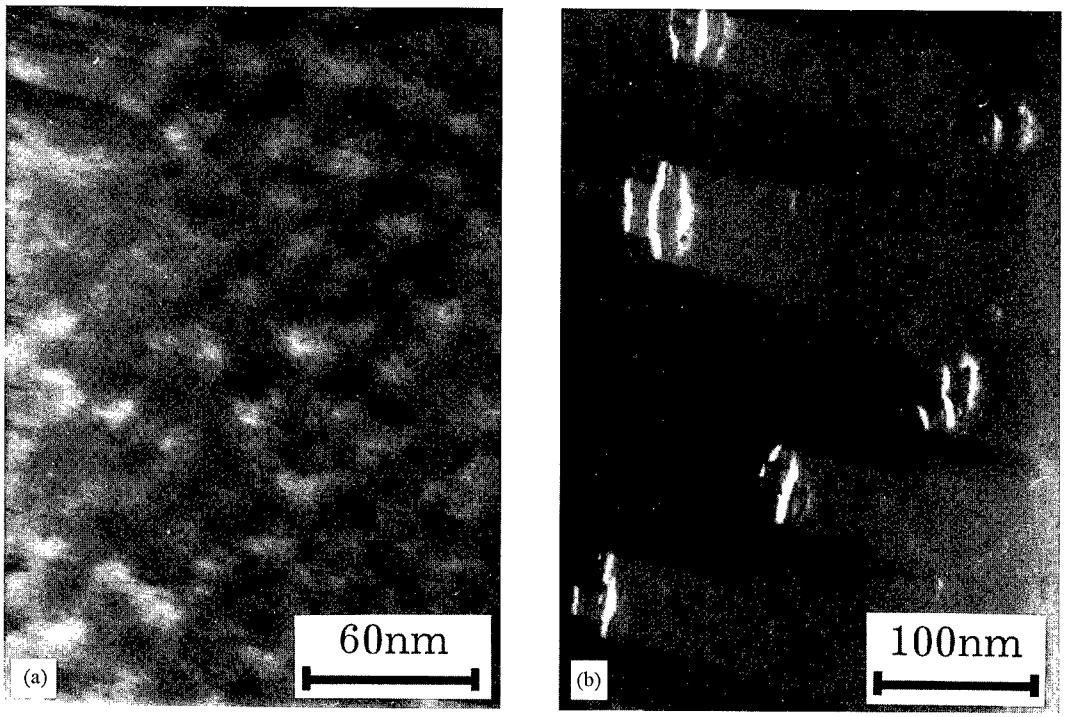

Fig. 3. Transmission electron microscopy (TEM) planar view of Ge/Si (0 0 1) films with thicknesses 7(a) and 12(b) ML (400°C).

- a layer of isolated Ge islands, 1 nm (average thickness);
- a tunnel barrier Si, 16 nm;
- a counter electrode p^+-$Ge_{0.7}Si_{0.3}$, 17 nm;
- an amorphous p^+-Ge contact layer, 500 nm

The layers were processed into mesas of 200–500 μm diameter. Indium ohmic contacts were linked with the substrate and top contact. The differential transversal conductivity $G = dI/dU$ was measured at 4.2 K and conductivity oscillations were observed. Transversal conductivity versus bias voltage for a sample grown at 400°C is shown in Fig. 5. The observed peaks were explained in terms of resonant tunneling of holes through individual energy levels in quantum dots. A splitting of peaks into doublets is observed due to Coulomb blockade of holes transport [2]. The positions of the doublets calculated in accordance with Ref. [7] are indicated by arrows in Fig. 5. The dot sizes used for calculation were obtained from the TEM image (Fig. 3a) with a diameter of 19 nm and height of 30 nm (on the assumption of cylinder-shaped dots). The general consistency between the theory and experimental data is apparent. Details on studies of electrical and optical properties of the grown GeSi heterostructures were given in our previous papers [1–3, 8].

5. Conclusions

It was shown that in situ analysis of intensity profiles in the RHEED pattern is more effective, compared to visual examination of its variations, for the control of the morphological transformation of germanium films on the Si (0 0 1) surface. The thickness of formation of dislocation-free hut-clusters (5 ML) and plastically relaxed 3D germanium islands (8 ML) was determined.

The structures containing self-organized quantum dots of germanium were grown in a direct manner. Effects of size quantization of the hole energy spectrum and Coulomb blockade of hole transfer were observed for these structures.

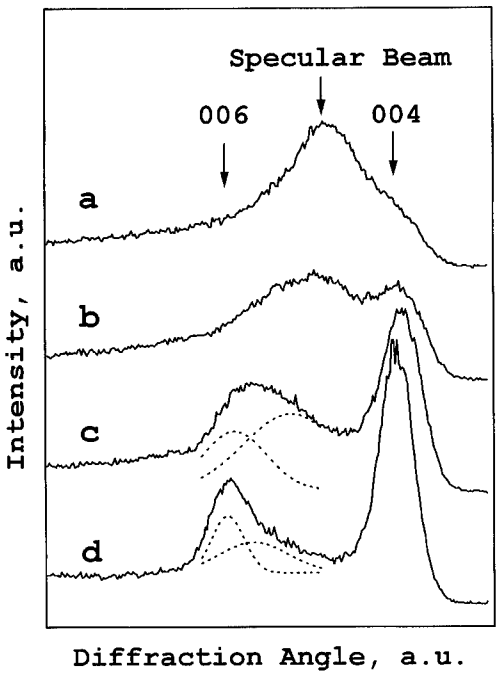

Fig. 4. Zero-streak intensity profiles in RHEED pattern during Ge/Si (0 0 1) films growth at 400°C. Film thickness are 4.6(a), 5.3(b), 8.6(c) and 11.1(d) ML.

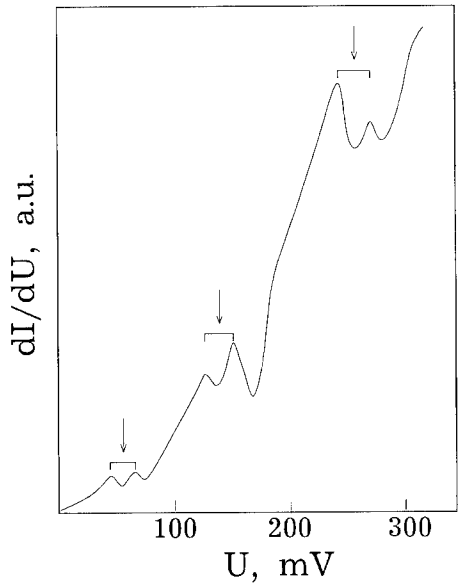

Fig. 5. Transversal differential conductivity versus bias voltage for a structure (see the text) grown at 400°C [2].

Acknowledgements

This work was supported by the Russian State Scientific and Engineering Programs on Promising Technologies on Micro- and Nanoelectronics (Project 129/57/2) and on Physics of Solid State Nanostructures (Project 2-011). The authors are thankful to A.K. Gutakovskii for the TEM results presented in this paper.

References

[1] A.I. Yakimov, V.A. Markov, A.V. Dvurechenskii and O.P. Pchelyakov, Phil. Mag. 65 (1992) 701.
[2] A.I. Yakimov, V.A. Markov, A.V. Dvurechenskii and O.P. Pchelyakov, J. Phys.: Condens. Matter 6 (1994) 2573.
[3] A.I. Yakimov, V.A. Markov, A.V. Dvurechenskii and O.P. Pchelyakov, Pis'ma Zh. Eksp. Teor. Fiz. 63 (1996) 423.
[4] C. Tatsuyama, T. Terasaki, H. Obata, T. Tanbo and H. Ueba, J. Crystal Growth 115 (1991) 112.
[5] Y.-O. Mo, D.E. Savage, B.S. Swartzentruber and M.G. Laggaly, Phys. Rev. Lett. 65 (1990) 1020.
[6] D.J. Eaglesham and M. Cerullo, Phys. Rev. Lett. 64 (1990) 1943.
[7] B. Su, V.J. Goldman, M. Santos and M. Shayegan, Appl. Phys. Lett. 58 (1991) 747.
[8] A.B. Talochkin, V.A. Markov, A.I. Nikiforov and O.P. Pchelyakov, Pis'ma Zh. Eksp. Teor. Fiz. 64 (1996) 203.

ELSEVIER

Journal of Crystal Growth 175/176 (1997) 741–746

JOURNAL OF CRYSTAL GROWTH

Growth controlled fabrication and cathodoluminescence study of 3D confined GaAs volumes on non-planar patterned GaAs(0 0 1) substrates

A. Konkar*, H.T. Lin, D.H. Rich, P. Chen, A. Madhukar

Photonic Materials and Devices Laboratory, Department of Materials Science and Engineering, University of Southern California, Los Angeles, California 90089-0241, USA

Abstract

We report on (a) the effect of growth interruption on the growth profile evolution in growth on non-planar patterned mesa tops via substrate-encoded size-reducing epitaxy (SESRE) and (b) the optical behavior of isolated 3D-confined GaAs volumes as well as 3D-confined GaAs volumes coupled with 1D-confined quantum wells (QWs) fabricated by SESRE. Steady-state excitation and time-resolved cathodoluminescence (CL) are used for these optical studies.

Keywords: Patterned substrate; Growth interruption; Quantum boxes; Time-resolved cathodoluminescence

1. Introduction

The fabrication of semiconductor structures with electronic states confined in more than one dimension is a subject of much activity in recent years. Of the various approaches to the fabrication of such structures, in situ, one-step growth approaches are promising since the structures thus fabricated are expected to be devoid of the problems of damage and contamination. Substrate-encoded size-reducing epitaxy [1] is one such in situ approach in which the differential growth rates on various facets and inter-facet adatom migration are exploited to reduce the mesa top size from as-patterned length scales (typically 1 μm) down to the nanoscale (< 100 nm) regime. One of the critical issues in this approach is the growth condition dependence of the growth profile evolution. Previous studies [1–3] of the growth condition dependence of the growth profile evolution have been limited to the case of continuous growth. In this paper we report on some findings on the effect of growth interruption on the growth on stripe mesas on GaAs(0 0 1). Additionally, 3D confined GaAs volumes synthesized on < 1 0 0 > oriented square mesas [3] via SESRE are examined via steady state as well as time-resolved CL studies to shed light on carrier dynamics of significance to carrier collection

* Corresponding author.

0022-0248/97/$17.00 Copyright © 1997 Elsevier Science B.V. All rights reserved
PII S0022-0248(96)00973-6

efficiency in isolated or communicating 3D-confined volumes.

2. Experimental procedure

GaAs (0 0 1) $\pm$ 0.1° substrates were patterned via conventional photolithography followed by wet chemical etching. The effect of growth interruption was studied for growth on stripe mesas oriented along the $\langle 1\,0\,0\rangle$ and $[1\,\bar{1}\,0]$ directions, with mesa width of $\sim$1 μm and depth of $\sim$0.5 μm. The growth interruption used in these experiments has a duration of $\sim$120 s. GaAs layers of 45 ML thickness followed by 5 ML AlGaAs marker layers were grown to reveal the growth profile evolution. Square mesas for the fabrication of 3D-confined GaAs volumes were patterned along $\langle 1\,0\,0\rangle$ directions. The details of the substrate preparation, MBE growth procedures and the growth profile evolution for 3D-confined GaAs volumes have been given in an earlier paper [3]. For the samples with interacting 3D-confined GaAs volumes and 2D-confined GaAs QWs, the MBE growth consisted of a size-reducing buffer of four periods of [175 ML $Al_{0.25}Ga_{0.75}As$/525 ML GaAs] followed by a 40 period multiple quantum well (MQW) composed of [40 ML $Al_{0.25}Ga_{0.75}As$/20 ML GaAs]. For the sample containing isolated 3D-confined GaAs volumes, the growth consisted a size-reducing buffer composed of 16 period of [5 ML $Al_{0.25}Ga_{0.75}As$/195 ML GaAs] followed by 100 ML $Al_{0.25}Ga_{0.75}As$/20 ML GaAs/200 ML $Al_{0.25}Ga_{0.75}As$ and capped by 50 ML GaAs.

The CL studies were performed with a modified JEOL-840A scanning electron microscope (SEM) with a 0.25 m monochromator. Time-resolved CL experiments were performed with the method of delayed coincidence in an inverted single photon counting mode with a time resolution of $\sim$100 ps [4]. Electron beam pulses of 50 ns width and a frequency 1 MHz were used for excitation for the time-resolved studies.

3. Results and discussion

3.1. Effect of growth interruption on the growth profile evolution

In Fig. 1 are presented the transmission electron microscope (TEM) images showing the growth profile evolution on stripe mesas along the $[1\,\bar{1}\,0]$ (parallel to the As dimer direction; panels (a) and (b)) and the [0 1 0] (at 45° to the As dimer direction; panels (d) and (e)) directions for different temperatures. The As_4 pressure is kept constant at 4.8×10^{-6} Torr and the GaAs growth rate at

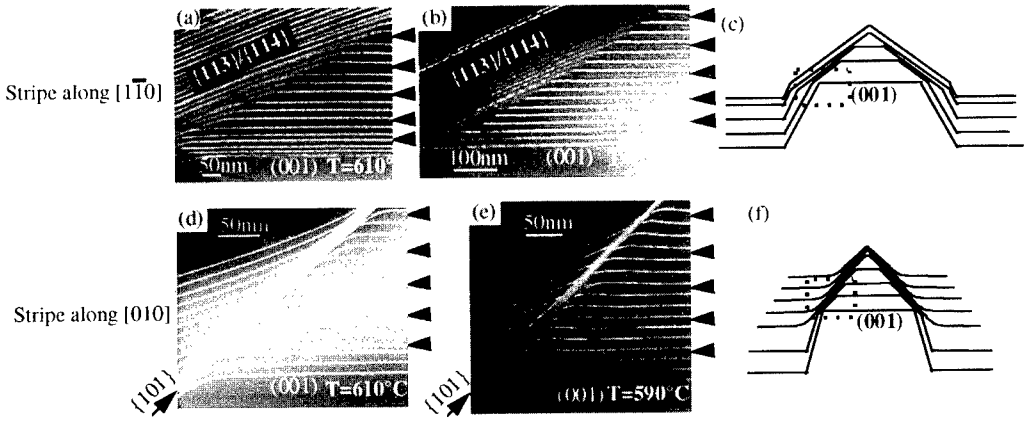

Fig. 1. TEM images of growth on stripe mesas: (a) and (b) along $[1\,\bar{1}\,0]$ direction, (d) and (e) along [0 1 0] direction. Schematic drawings of the growth profile evolution are shown in panels (c) and (f) for the stripe mesas along $[1\,\bar{1}\,0]$ and [0 1 0] directions, respectively.

0.5 ML/s. Only a portion of the mesa top and sidewalls is shown in these images corresponding to the area marked by the dotted rectangle in the schematic drawings in panels (c) and (f). The thin white lines are the AlGaAs markers which delineate the growth profile. The arrows indicate the GaAs layers in which growth was interrupted.

In the case of the growth on stripe mesas along the $[1\,\bar{1}\,0]$ direction, layer thickness on the mesa top (sidewall) for the GaAs layers in which the growth was interrupted is found to be higher (lower) than the preceding and following layers. This implies that migration of Ga atoms from the sidewalls to the mesa top continues in the absence of Ga delivery. Careful measurements of these layer thicknesses for the growth at 610°C indicate that more than 1 ML worth of material migrated from the sidewalls. This indicates that during growth interruption it is not only the initial adatoms on the sidewalls but the atoms that were incorporated into the sidewalls during the growth also migrate to the mesa top. The effect of interruption on the growth profile evolution becomes less significant when the substrate temperature is lowered to 590°C. The flat morphology on the mesa top as evidenced by the AlGaAs markers implies that the migration length of the adatoms on the mesa top, perpendicular to the stripe direction, is larger than half the mesa width (i.e. the migration length is at least ~ 0.5 μm for the growth condition used).

Unlike the above case, in the case for the growth on stripe mesas along [0 1 0] direction at 610°C the thickness on the mesa top of the GaAs layers for which the growth was interrupted is found to be lower than the preceding and following layers (which is evident for the first two interruptions in panel (d)). This implies that in this case Ga atoms migrate in the opposite direction, i.e. from the mesa top to the sidewalls in the absence of Ga delivery. Moreover, a curved morphology is present at the intersection of the mesa top and sidewalls for the GaAs layers with growth interruption. Again, the effect of interruption on the growth profile evolution becomes less significant when the substrate temperature is lowered to 590°C.

3.2. CL studies of 3D-confined GaAs volumes

3.2.1. Interacting 3D-confined GaAs volumes and 1D-confined quantum wells (QWs)

Fig. 2 shows a TEM image of a typical square mesa containing interacting 3D-confined GaAs volumes (dark regions) on the mesa top below pinch-off and 1D-confined GaAs QWs on the {101} sidewalls. The area-averaged CL spectra, taken from a region $\sim 1\ \mu m \times 1\ \mu m$ centered on the mesa top [5], at various sample temperatures are shown in Fig. 3. The spatial region responsible for the identifiable peaks in Fig. 3 can be inferred from the spatially resolved monochromatic CL images and the SEM image shown in Fig. 4. The luminescence from p1 and p2 is primarily from QWs grown on sidewalls away from mesa top while p3 is localized about the mesa top and hence is from thick 3D-confined GaAs volumes just below the pinch-off region. Peak p4 is similarly identified to be from the underlying bulk-like GaAs in the size-reducing buffer.

The peak intensity decrease of p1 relative to p2 and p3 with increasing temperature seen in Fig. 3 indicates thermal re-emission of carriers from thinner QWs (p1) and their subsequent transport and recombination in the thicker QW (p2) and the 3D-confined volumes (p3). Further insight into these thermalization effects is gained from the time-delayed CL measurements. The intensity of peaks p1–p4 (I_{pi}) as a function of time (t) for both decay and onset stages is shown in Fig. 5a and b, respectively. The onset rate r, defined as $\Delta \ln(I_{pi})/\Delta t$,

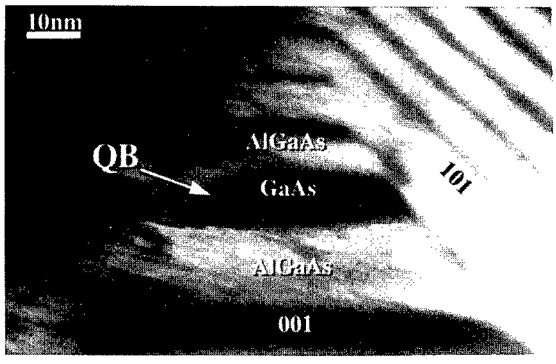

Fig. 2. TEM image of a 20 ML GaAs/40 ML AlGaAs multiple QW growth on the mesa top.

is the slowest for p4 (see Fig. 5b) reflecting the large distances (~0.5 μm) that the hot carrier must traverse before recombining in the thick bulk-like GaAs layers in the size-reducing buffer. These relative rates are also observed in Fig. 5c from the peak intensity ratios. The initial decay time τ_1 measured from the slopes in the $\ln(I_{pi})$ versus time transients shown in Fig. 5a increases in the order p1, p2 and p3 implying the enhanced thermal re-emission of carriers in the QWs (p1 and p2) to feed continuously the larger 3D-confined GaAs volumes represented by p3, as the system proceeds towards equilibrium.

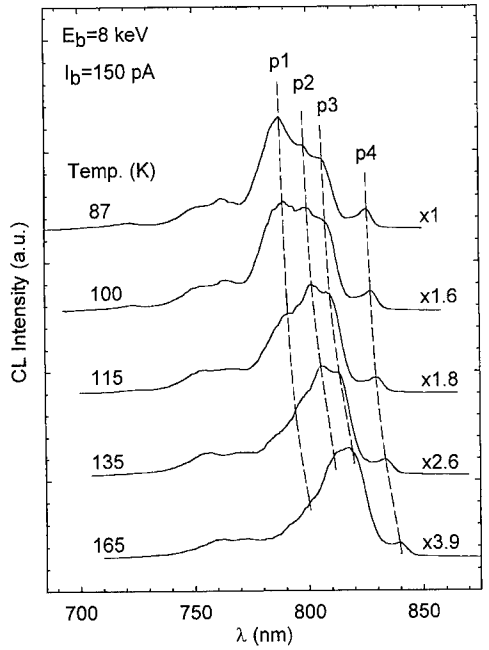

Fig. 3. Constant excitation CL spectra taken at various temperatures. The peak shifts for p1 to p4 with temperature are shown by dashed lines.

3.2.2. *Isolated 3D-confined GaAs volumes*

Fig. 6a shows a TEM image of growth of the SQW on the square mesa top. As seen in the figure, the mesa top size at the start of the GaAs well deposition is ~120 nm. The thickness of the GaAs layer on the mesa top (~11 nm) is higher compared to the deposition thickness (~5.7 nm) due to adatom migration from the {1 0 1} sidewalls to the (0 0 1) mesa top. Negligible GaAs growth on the {1 0 1} sidewalls in the vicinity of the 3D-confined volume is observed indicating good lateral confinement.

Results from CL imaging and spectroscopy are shown in Fig. 6 (panels (c) and (d)) and Fig. 7, respectively. The monochromatic CL images (Fig. 6) show that the high energy peak seen in the spectra shown in Fig. 7 is associated with 3D-confined GaAs volume and the low energy peak has its origin in the bulk-like GaAs in the size-reducing buffer layer. The CL spectra from the

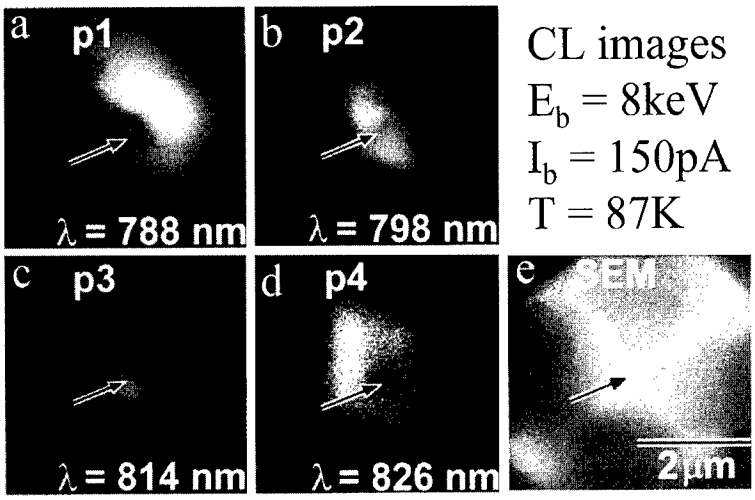

Fig. 4. Monochromatic CL images at various wavelengths (a)–(d), and (e) SEM image. The arrow tips point to the mesa apex position. CL imaging conditions are indicated in the upper right corner.

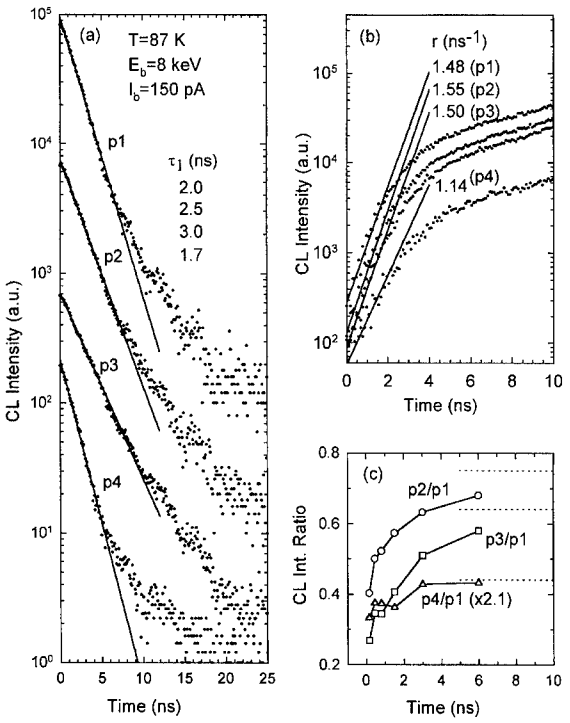

Fig. 5. CL transients for peaks p1–p4: (a) the decay curves with linear fits for the initial ~ 6 ns of decay; (b) the onset curves with linear fits for the first ~ 2 ns; (c) CL peak intensity ratios p2/p1, p3/p1, and p4/p1.

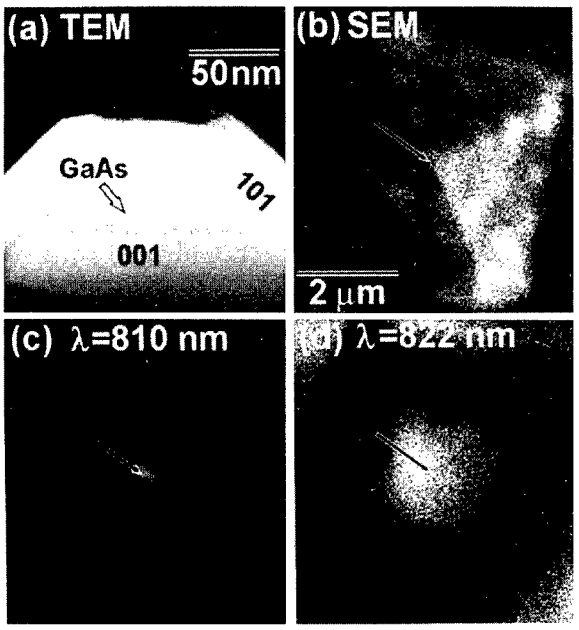

Fig. 6. (a) TEM, (b) SEM, and monochromatic CL images at (c) $\lambda = 810$ nm and (d) $\lambda = 822$ nm taken with an electron beam of $E_b = 8$ keV and $I_b = 150$ pA at $T = 87$ K. The length scale for the CL images (c) and (d) is indicated in the SEM image. The arrow tips in (b)–(d) point to the mesa apex position.

non-patterned planar region (not shown) shows a peak at $\lambda = 778$ nm at 87 K which is associated with the SQW deposition. The red shift of the CL peak from well deposition on the mesa top with respect to that from the planar region is attributed to interfacet adatom migration induced GaAs thickness enhancement on the mesa top. The temperature dependence of the CL spectra (see Fig. 7) shows that the ratio of the peak intensity of the 3D-confined to bulk-like GaAs decreases with increasing temperature ($T < 90$ K) indicating good carrier confinement in these 3D-confined volumes. The reversal of this trend for temperatures beyond 90 K is under investigation.

Strong evidence for 3D confinement of the high energy peak in the CL spectra comes from the results of excitation current dependence. Fig. 8 shows a plot of the full width at half maximum (FWHM) versus the excitation current for the peaks from the mesa top 3D confined GaAs volume (labeled mesa) and the corresponding GaAs/AlGaAs single QW (SQW) in the planar region (labeled planar) of the same sample. The FWHM of the SQW on the planar region increases from ~6.7 to ~9.6 meV as I_b increases from 10 pA to 5 nA, whereas the FWHM of the 3D-confined region increases by a factor of almost 3 for the same increase of I_b. This enhanced peak width broadening reflects rapid phase-space-filling in the 3D-confined GaAs volume.

4. Conclusion

The role of growth interruption during SESRE on patterned stripe mesas is examined for the first time and found to reveal remarkable continued interfacet migration during growth interruption.

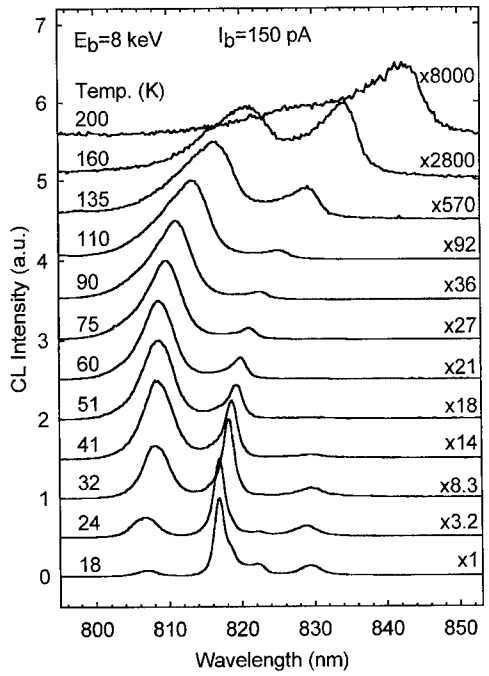

Fig. 7. Constant excitation CL spectra taken at various temperatures in 18 K $\leqslant$ T $\leqslant$ 200 K. range.

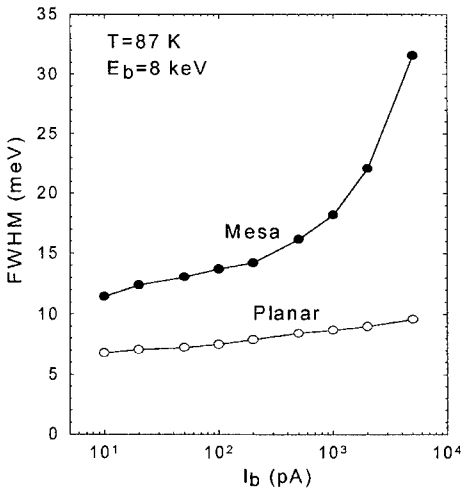

Fig. 8. Full width at half maximum (FWHM) of CL peaks originating from the 3D-confined GaAs volume and the GaAs/AlGaAs single QW (denoted as mesa and planar, respectively) as a function of excitation current.

Temperature-dependent and time-resolved CL experiments on coupled 3D-confined volumes grown by SESRE reveal carrier feeding from sidewall quantum wells to the 3D-confined volumes. Isolated confined 3D volumes show the expected phase-space-filling behavior.

Acknowledgements

This work was supported by AFOSR, ONR, and NSF (RIA-ECS).

References

[1] A. Madhukar, K.C. Rajkumar and P. Chen, Appl. Phys. Lett. 62 (1993) 1547; A. Madhukar, Thin Solid Films 231 (1993) 8.
[2] See, for example: M. Lopez and Y. Nomura, J. Crystal Growth 150 (1995) 68, and references therein.
[3] A. Konkar, K.C. Rajkumar, Q. Xie, P. Chen, A. Madhukar, H.T. Lin and D.H. Rich, J. Crystal Growth 150 (1995) 311.
[4] D. Bimberg, H. Munzel, A. Steckenborn and J. Christen, Phys. Rev. B 31 (1985) 7788.
[5] D.H. Rich, H.T. Lin, A. Konkar, P. Chen and A. Madhukar, Appl. Phys. Lett. 69 (1996) 665.

ELSEVIER

Journal of Crystal Growth 175/176 (1997) 747–753

JOURNAL OF CRYSTAL GROWTH

Manipulating InAs island sizes with chemical beam epitaxy growth on GaAs patterns

Mark S. Miller*, Lars Landin, Søren Jeppesen, Anders Petersson, Ivan Maximov, Bernhard Kowalski, Lars Samuelson

Department of Solid State Physics, Lund University, Box 118, 221 00 Lund, Sweden

Abstract

We demonstrate the manipulation of InAs island size through growth on patterned GaAs substrates. Using chemical beam epitaxy, we deposited islands on patterns consisting of concentric circular trenches. One sample was left uncapped for atomic force microscopy, and another was capped with GaAs for micro-photoluminescence. Luminescence images taken at particular energies show that at different orientations along the circular arcs, the islands have different luminescence energies and thus different sizes. In correlating the island distributions found by atomic force microscopy images with the luminescence, we conclude that the InAs islands that form in high-density one-dimensional chains are smaller than those that are not in chains.

PACS: 73.20.Dx; 73.61.Ey; 78.66.Fd; 81.15.Ef

1. Introduction

The small defect-free islands that form at the early stages of compressively strained epitaxial growth may be interesting for single-electron or single-hole devices. For the case of InAs on GaAs, the islands that form on top of a thin wetting layer after one to two monolayers of growth are pyramidally shaped, having 12–25 nm wide bases, and 3–6 nm heights [1, 2]. These islands have a deep conduction-band potential well which may contain only a single bound state [4]. Many groups have reported such islands on flat substrates grown with molecular beam epitaxy [3, 5–10], metalorganic chemical vapor deposition [11, 12], and chemical beam epitaxy [13]. When island-containing layers are separated by thin GaAs layers, the islands align vertically [3, 14], and may be placed closely enough together to couple the conduction band states [15–17, 23]. Such stacked islands could be at the heart of electrical devices.

The individual stacks may possibly be contacted because island position can be controlled by growing on lithographically patterned GaAs substrates [18]. The islands form selectively in the patterned features, displaying a clear dependence on local surface orientation. The number of islands in small holes varies approximately as the square of the hole diameter [19]. A selectivity ratio has been defined

* Corresponding author. E-mail: mark.miller@ftf.lth.se.

0022-0248/97/$17.00 Copyright © 1997 Published by Elsevier Science B.V. All rights reserved
PII S0022-0248(96)01219-5

Fig. 1. Atomic force micrograph of InAs islands grown in circular GaAs trenches. The height data are displayed with simulated illumination from the left, and the trenches are narrow to the upper left and curve down and widen to the lower right.

as the ratio of the island density in the holes to the density away from the pattern, with a ratio of more than 1000 reported [19]. The minimum center-to-center period reported for chains of islands many microns long was 33 nm [18]. When capped with GaAs the islands on patterns retain their quantum dot luminescence properties. Other reports on island growth in patterns include InAs islands aligned on intentionally bunched step edges [20], InAs islands grown on etched gratings that showed surface orientation and deposition shadowing effects [21], and InP and InAs islands grown on corrugations formed by W-wire overgrowth that showed surface orientation and alignment effects [22].

We report here that for a given set of growth conditions the island size depends on the size and orientation of patterned features. InAs islands were formed on two GaAs substrates patterned with sets of concentric circular trenches. One sample was left uncapped for atomic force microscopy (AFM) and the other was capped with GaAs for microscopic photoluminescence (μPL). The island linear density seen by AFM in the trench varies with angle around the trench. In μPL the island luminescence energy also varies with angle around the circles. This demonstrates that not only can patterns be used to position islands, but may as well be used to engineer the island sizes.

2. Sample growth and experimental details

The chemical beam epitaxy machine, of our own design, uses pressure-regulated sources without a carrier gas. The precursors are triethylgallium, trimethylindium, and tertiary-butylarsine, with the tertiary-butylarsine thermally cracked to As_2. The data we present here are from growths 941230A, an uncapped sample, and 941230B, a GaAs-capped sample. Arrays of sets of seven concentric circles were defined in (1 0 0)GaAs substrates with electron beam lithography and wet etched to a depth of 100 nm. The radial pitch of the circles is 1.25 μm. A GaAs buffer layer of 100 nm was grown before depositing approximately 1.5 monolayers of InAs at 493°C. More detailed growth conditions are given in Ref. [18]. The InAs island density outside of the patterned area of the uncapped sample was $2 \times 10^7\ cm^{-2}$. The buffer layer growth was very orientation-dependent.

We operated our AFM in a constant force mode. Our transmission-electron microscopy measurement on islands grown under similar condition showed approximately pyramidal islands of 4 nm height and 20 nm base. Our estimate of the AFM tip radius is 80 nm, using the ≈ 50 nm apparent island width and assuming a spherical tip and a 4 nm high sharp point for the island. The data we present here have been leveled and flattened, and are displayed to simulate oblique illumination, but are otherwise unprocessed. The PL data were taken at 5 K using the 488 nm line of an Ar^+ laser for excitation. The luminescence signal was either dispersed with a monochromator and detected with a Ge detector for spectra or was directed through interference filters into a CCD camera for imaging. Image integration times were from 1 to 10 s.

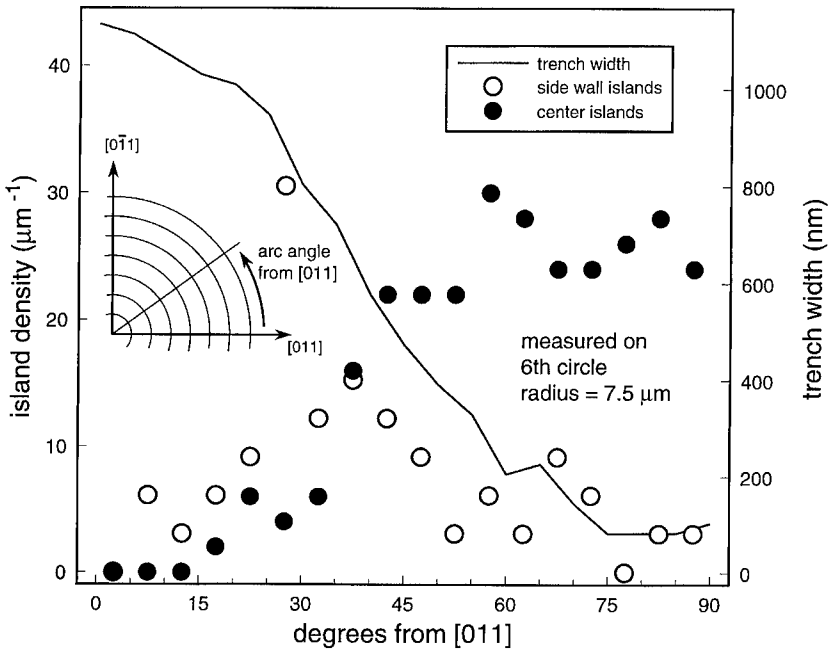

Fig. 2. Linear island densities and trench width as functions of arc angle measured at the circle center and with respect to the [0 1 1] direction. The center islands are those aligned in the center of the trench, and the wall islands are those that have otherwise formed on the side wall of the trench. The inset depicts the meaning of arc angle.

3. Atomic force microscopy

An AFM micrograph of InAs islands formed in circular arcs on the uncapped sample is given in Fig. 1. Illumination of the data surface is from the left. Here we will refer to the position along the circular arcs by giving the angle measured at the circle center, increasing counterclockwise from the [0 1 1] direction. Only angles from the first quadrant are discussed because the circles are symmetric. This geometric definition is depicted schematically in an inset to Fig. 2. While the as-etched circles were formed with anisotropic etching, the buffer layer growth was very orientation-dependent. Where the trenches run in the [0 1 1] direction, at 90° arc angle, they are almost closed off, and those in the [0 $\bar{1}$ 1] direction, at 0° arc angle, are very wide and have even contributed GaAs to the (1 0 0) ridge top between them. At positions along the arcs from 30 to 60°, the trench side walls have several shallow pockets with characteristic sizes of 0.25 μm.

The InAs islands have formed very selectively in the etched and overgrown trenches. For the narrow portions of the arcs from about 45 to 90°, the islands are concentrated in dense chains in the center of the trenches. A high proportion of the pockets on the side walls, perhaps originating from lithographic irregularities, have single or few islands in them. At angles from 30° down to 0° along the arcs, some InAs islands and roughness can be seen in the trenches. The roughness is perhaps due to partially formed islands. The islands and roughness below 30° are scattered and not clearly associated with the trench center.

We have measured the trench width and counted the island density as functions of angle and plotted the results in Fig. 2. The data are from the next to the outermost circle of the pattern, a portion of which is visible in the upper right quarter of Fig. 1. The radius of the circle is 7.5 μm. The islands have been put into two classifications for the counting: those aligned in the trench center and those on the trench side walls, including those in shallow

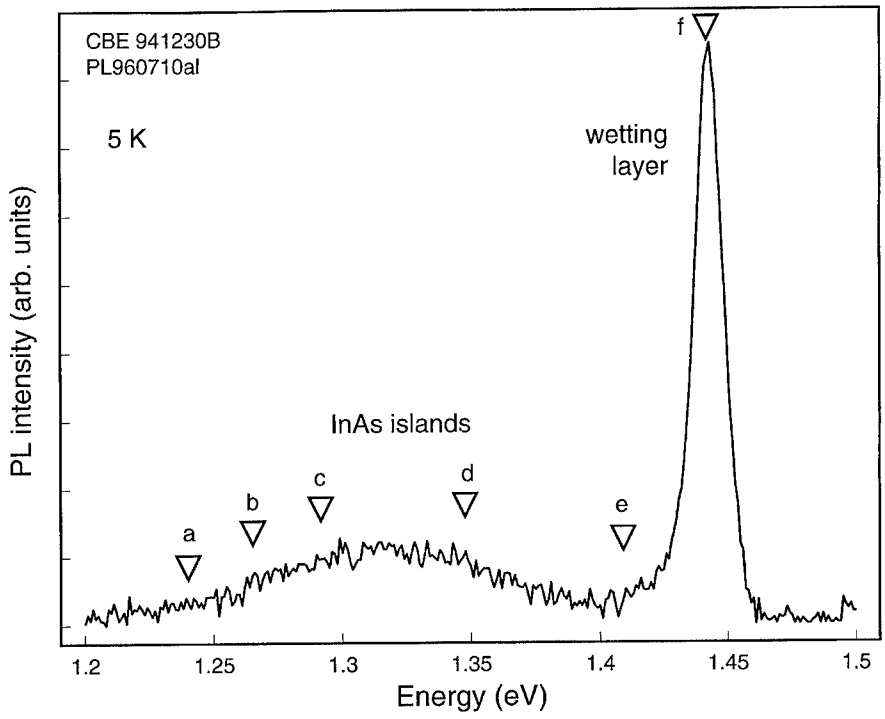

Fig. 3. Photoluminescence spectrum of islands grown in circular trenches and capped with GaAs. The six markers indicated the energies at which the images of Fig. 4 were made.

pockets. The resulting counts are plotted as 1D densities along the arc. The centered island chains are seen at linear densities above 20 μm^{-1} for trench widths of 600 nm and less. The centered chains essentially begin to disappear for angles below 45°. The islands on the trench side walls are seen over the whole arc length, though have the highest density from 30 to 45°, in the region with the most side wall pockets.

4. Micro-photoluminescence

The broad area photoluminescence from the circles on the capped sample, given in Fig. 3, shows the typical features of a low- to medium-density InAs island sample. The tall peak at 1.440 eV is from the approximately one-monolayer-thick wetting layer, and the low broad peak at 1.32 eV is from the InAs islands.

Fig. 4 shows six μPL images taken at the energies indicated by the markers (a)–(f) in the spectrum of Fig. 3. The overall nonuniformity in intensity from each image is due to the nonuniformity of the exciting laser spot. The four lower energy images, from 1.240 to 1.348 eV in Fig. 4a–Fig. 4d, have luminescence coming almost exclusively from the sets of concentric circles. At the imaging energy of 1.409 eV, Fig. 4e, the luminescence principally comes from the circles, but a substantial amount of intensity also comes from the unpatterned areas between the sets of circles. The highest energy image, Fig. 4e, taken with the wetting layer luminescence is approximately complementary to the island images.

The angular distribution of the luminescence is different for each of the images in Fig. 4. For the images of island PL, Fig. 4a–Fig. 4d, most of the intensity is above some angle with respect to [0 1 1]. In the image taken at the intermediate

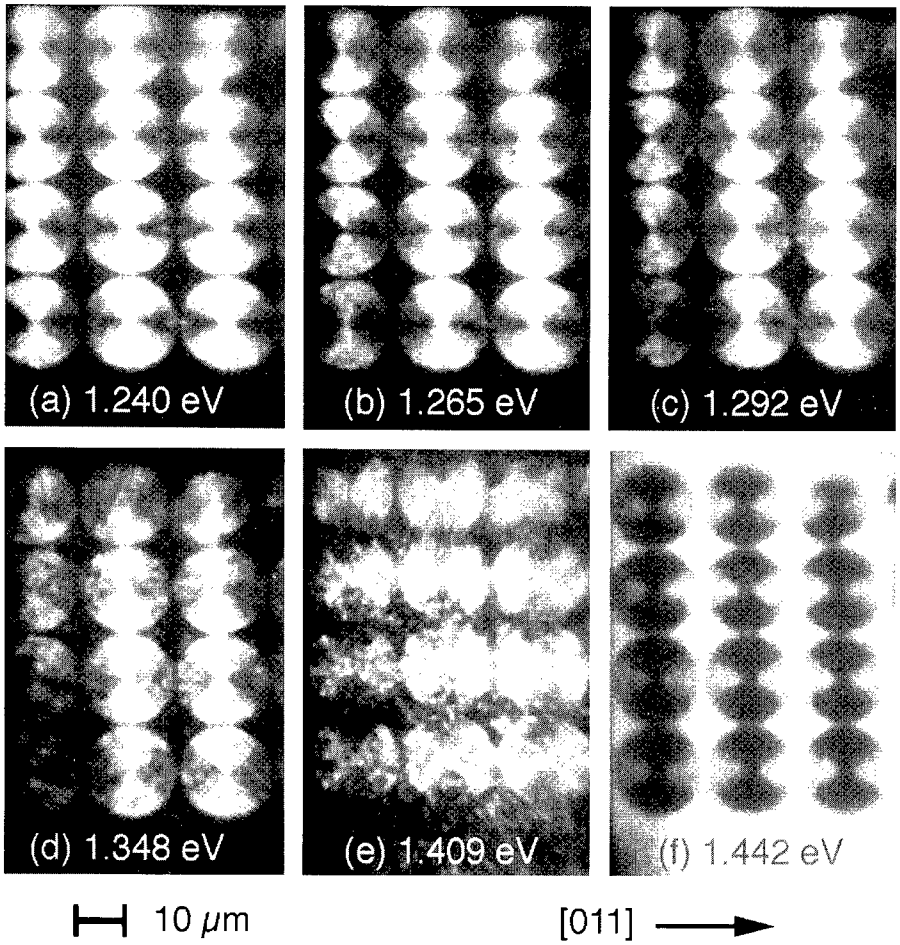

Fig. 4. Micro-photoluminescence images of InAs islands formed in sets of concentric circular trenches. The energies of the images are marked in the spectrum of Fig. 3 and correspond to luminescence from (a)–(d) the islands, (e) structures intermediate between islands and wetting layer, and (f) the wetting layer. The intensity patterns from the islands and wetting layers are complementary.

energy of 1.409 eV, Fig. 4e, the intensity shows an "X" pattern near 32°, and most of the intensity within the circles comes from lower angle regions. Essentially, all of the wetting layer luminescence from the patterned area, Fig. 4f, comes from regions below an angle of approximately 30°. Here we will characterize each image by the angle of the edge that defines the upper or lower limit of the luminescing region. The energy of the images are plotted in Fig. 5 versus the angles which characterize the edges of the luminescing regions. Two points are plotted for the image of Fig. 4a because two edges are seen. The luminescence edge of a seventh image at 1.319 eV which is not shown in Fig. 4 is also plotted.

5. Discussion

The AFM and μPL images may be combined to draw some conclusions about which islands are luminescing at what energies. From the island density distributions plotted in Fig. 2, it is seen that center island chains are principally at angles higher than 40°, but the side wall islands are distributed to much lower angles, down through 20°. The

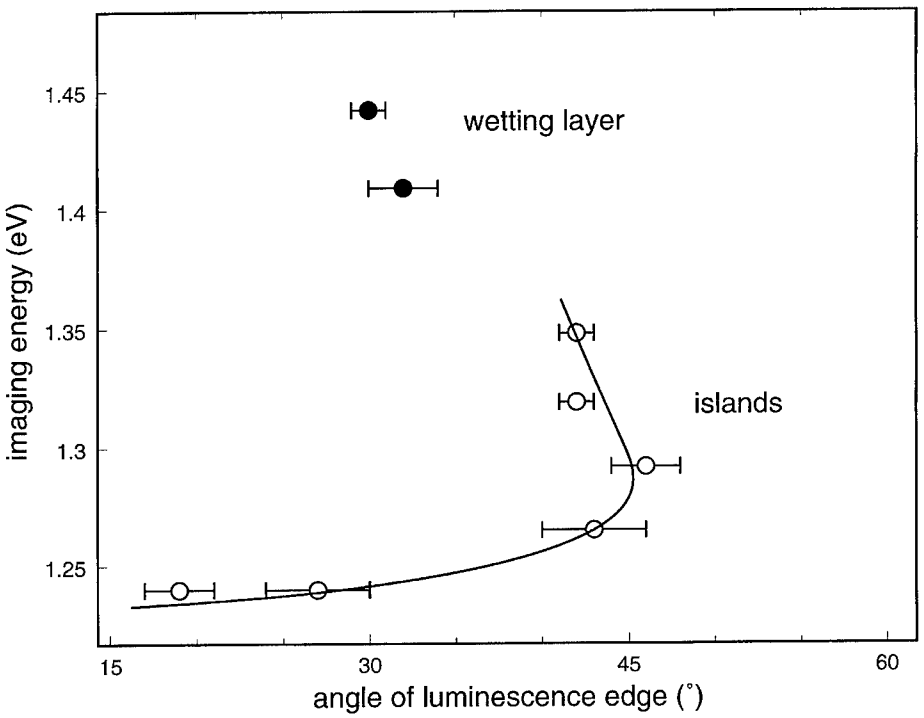

Fig. 5. The imaging detection energies of Fig. 4 versus the angle of luminecsence measured from the [0 1 1] direction. The line drawn for the edges of the island luminescence regions is a guide to the eye. This plot indicates that changing the pattern, here the angle and trench width, changes the island size, which is seen in the changing luminescence energies. The arc angle is depicted in the inset to Fig. 2.

luminescence edges in the images taken at energies between 1.26 and 1.35 eV are at angles above 40°, but the luminescence edge of the images taken at 1.24 eV extends down to approximately 20°. We therefore infer that the center-chained islands are smaller and luminesce at the higher energies than the side wall islands which can be larger and luminesce at the lower energies.

The "X" shaped pattern seen at 32° in the image taken at the intermediate energy of 1.409 eV seems to mark the boundary between the center island chain luminescence and the wetting layer luminescence. This is the angle below which the chains thin out and disappear, and may be considered as some sort of phase boundary for the condensation of the InAs islands into 1D chains.

In this study we have not attempted to determine island size from AFM measurements, which are highly complicated by tip-island convolution effects. On a flat substrate, we estimate our vertical resolution to be about 2 InAs monolayers for these islands that are 10–15 monolayers high. Our lateral resolution of the shape differences, though, is no better than 5 nm. Together, these lead to an uncertainty in the volume of around 50%. On the tilted faces of the patterned features, the uncertainties are greater because different islands on different local orientations will be measured with different portions of the tip.

A principal conclusion that we reach using the data of this paper, and especially those of Fig. 5, is that for a given set of growth conditions, the island size can be manipulated by changing the size and orientation of etched and overgrown patterns. Here the changing size and orientation are the trench width and angle. The indication of changing island size is the measured change in luminescence-energy distribution characterized by the angle of the edge of the luminescing region. Thus, in Fig. 5, the independent variable is the pattern and the dependent variable is the size. Unfortunately, while these circular patterns provide an existence proof of

manipulating island size with patterns, these patterns do not lend themselves well to separating the independent influences of trench orientation and width on island formation.

Acknowledgements

This work was carried out within the Nanometer Structures Consortium, with funding from the Swedish Engineering and Science Councils (TFR, NFR) and NUTEK. We wish to thank Mats-Erik Pistol for many useful and stimulating discussions.

References

[1] J.M. Gérard, in: Confined Electrons and Photons New Physics and Applications, Eds. E. Burnstein and C. Weisbuch (Plenum, New York, 1995) p. 357.
[2] D. Leonard, K. Pond and P.M. Petroff, Phys. Rev. B 50 (1994) 11687.
[3] L. Goldstein, F. Glas, J.Y. Marzin, M.N. Charasse and G.L. Roux, Appl. Phys. Lett. 47 (1985) 1099.
[4] M. Grundmann, O. Stier and D. Bimberg, Phys. Rev. B 52 (1995) 11969.
[5] S. Guha, A. Madhukar and K.C. Rajkumar, Appl. Phys. Lett. 57 (1990) 2110.
[6] D. Leonard, M. Krishnamurthy, C.M. Reaves, S.P. Denbaars and P.M. Petroff, Appl. Phys. Lett. 63 (1993) 3203.
[7] J.M. Moison, F. Houzay, F. Barthe and L. Leprince, Appl. Phys. Lett. 64 (1994) 196.
[8] J.-Y. Marzin, J.-M. Gérard, A. Izraël, D. Barrier and G. Bastard, Phys. Rev. Lett. 73 (1994) 716.
[9] G.S. Solomon, J.A. Trezza and J.S. Harris, Appl. Phys. Lett. 66 (1995) 991.
[10] Y. Nabetani, T. Ishikawa, S. Noda and A. Sasaki, J. Appl. Phys. 76 (1994) 347.
[11] R. Nötzel, J. Temmyo and T. Tamamura, Nature 369 (1994) 131.
[12] J. Oshinowo, M. Nishioka, S. Ishida and Y. Arakawa, Appl. Phys. Lett. 65 (1994) 1421.
[13] M.S. Miller, S. Jeppesen, B. Kowalski, I. Maximov and L. Samuelson, J. Crystal Growth 164 (1996) 345.
[14] Q. Xie, A. Maduhukar, P. Chen and N.P. Kobayashi, Phys. Rev. Lett. 75 (1995) 2542.
[15] G.S. Solomon, J.A. Trezza, A.F. Marshall and J.S. Harris, Phys. Rev. Lett. 76 (1996) 952.
[16] M.S. Miller, S. Jeppesen, B. Kowalski, M.-E. Pistol, K. Georgsson and L. Samuelson, J. Appl. Phys. 80 (1996) 3360.
[17] Z.I. Alferov et al., Semiconductors 30 (1996) 194.
[18] S. Jeppesen, M. Miller, D. Hessman, B. Kowalski, I. Maximov and L. Samuelson, Appl. Phys. Lett. 68 (1996) 2228.
[19] S. Jeppesen, M.S. Miller, B. Kowalski, I. Maximov and L. Samuelson, Superlattices Microstruct., in press.
[20] M. Kitamura, M. Nishioka, J. Oshinowo and Y. Arakawa, Appl. Phys. Lett. 66 (1995) 3663.
[21] D.S.L. Mui, D. Leonard, L.A. Coldren and P.M. Petroff, Appl. Phys. Lett. 66 (1995) 1620.
[22] W. Seifert, N. Carlsson, S. Jeppesen, M. Miller, M.-E. Pistol, L.E. Wernersson and L. Samuelson, Proc. IEEE 7th Int. Conf. on Indium Phosphide and Related Materials, Sapporo (1995) p. 17.
[23] Y. Sugiyama, Y. Nakata, S. Muto and N. Yokoyama, Jpn. J. Appl. Phys. 35 (1996) 1320.

ELSEVIER

Journal of Crystal Growth 175/176 (1997) 754–759

JOURNAL OF CRYSTAL GROWTH

Self-organized quantum dot structures in strained $(GaP)_n(InP)_m$ short period superlattices grown on GaAs (N 1 1) by gas-source MBE

S.J. Kim, H. Asahi*, M. Takemoto, K. Asami, J.H. Noh, S. Gonda

The Institute of Scientific and Industrial Research, Osaka University, 8-1 Mihogaoka, Ibaraki, Osaka 567, Japan

Abstract

$(GaP)_n(InP)_m$ short-period superlattices (SLs) are grown on GaAs (N 1 1) (N = 2–5) and (1 0 0) substrates by gas-source molecular beam epitaxy. Scanning tunneling microscopy and transmission electron microscopy observations show that the SLs grown on GaAs (N 1 1)A have lateral-composition-modulated dot/columnar structures with a lateral period of about 10–20 nm, while wire structures are formed on GaAs (1 0 0). Quantum dots formed in $(GaP)_n(InP)_m$ SL/$In_{0.49}Ga_{0.51}P$ multilayers by self-organization exhibit strong 77 K photoluminescence (PL) with a narrow full-width at half-maximum of about 40 meV. Anomalous temperature variation of PL peak energy is also observed in these self-organized structures.

PACS: 68.65. + g; 78.55.Cr

Keywords: Self-organized quantum dot; GaP/InP superlattice; Gas source MBE; TEM; STM; PL

1. Introduction

Low-dimensional structures such as quantum wires (QWRs) and quantum dots (QDs) are attracting great interest for novel device applications and physical studies. Progress in the fabrication of high-quality QWR/QD structures using self-organized growth method has supplied opportunities for detailed experimental studies on two/three-dimensional quantum confinement structures [1–4].

Recently, we have reported the substrate-orientation dependence of lateral composition modulation in the $(GaP)_n(InP)_n$ superlattices (SLs) grown by gas-source molecular beam epitaxy (MBE) [5]. We have shown that the formed structures of the SLs grown on GaAs (1 0 0), and (3 1 1)A and (4 1 1)A are wire and dot structures, respectively, by transmission electron microscopy (TEM) observation. On the other hand, we have found that the

* Corresponding author. E-mail: asahi@sanken.osaka-u.ac.jp.

0022-0248/97/$17.00 Copyright © 1997 Elsevier Science B.V. All rights reserved
PII S0022-0248(96)01008-1

$(GaP)_1(InP)_1$ SLs grown on GaAs (1 1 1) have strong CuPt-type ordering and exhibit a band-gap reduction as large as 321 meV (large red-shift), compared with the band gap of disordered InGaP of the same average composition.

In this paper, we report the scanning tunneling microscopy (STM) and TEM observations on the high density of self-organized structures formed in the $(GaP)_n(InP)_m$ SLs grown on GaAs(N 1 1)A by gas source MBE. We also describe the TEM and photoluminescence (PL) results on the self-organized QD structures fabricated by growing $(GaP)_n(InP)_m$ SL/$In_{0.49}Ga_{0.51}P$ multilayers.

2. Experimental procedure

$(GaP)_n(InP)_m$ SLs and $(GaP)_n(InP)_m$ SL/$In_{0.49}Ga_{0.51}P$ multilayer QD structures ($n \leqslant m$) were grown by gas source MBE. Elemental Ga, In and thermally cracked AsH_3, PH_3 were used as group III and group V sources, respectively. Reflection high-energy electron diffraction (RHEED) intensity oscillations were used to calibrate GaP and InP growth rates (GaP: 3.3 s/ML; InP: 3.7 s/ML). Both SLs and QD structures were grown at 420–460°C after the growth of 300 nm GaAs buffer layer at 600°C. AsH_3 and PH_3 flow rates were 1.0 and 1.2 sccm, respectively. Samples for STM observation were doped with Si and the carrier concentrations were 2×10^{18} cm^{-3}. Formed structures were investigated by STM, TEM and PL measurements. Electrically etched tungsten (W) tips were used as a STM probe in this study. TEM observation was performed to compare with the STM image. Both the 325 nm line of a He–Cd laser (19 mW) and 488 nm line of an Ar^+ laser (70 mW) were used in the PL measurement as excitation sources.

3. Results and discussion

3.1. STM and TEM observation of self-organized structures in $(GaP)_n(InP)_m$ SLs

TEM images (not shown) for 0.3 μm-thick $(GaP)_n(InP)_n$ SLs grown on GaAs (1 0 0) substrates showed lateral wire composition modulation (formation of the Ga-rich and In-rich regions) with a lateral period of about 10–20 nm and a lateral wire length of over 200 nm along the [0 1 1] and [0 1 $\bar{1}$] directions, respectively, as observed by Hsieh et al. [1]. The length of the lateral wire structures was increased by the growth on vicinal (1 0 0) substrates. This composition modulation is probably due to the island formation along the [0 1 $\bar{1}$] direction during growth, which is primarily determined by the direction of the group V dimer bonds related to the migration direction [1].

Plan-view TEM observations on the 0.3 μm-thick $(GaP)_2(InP)_2$ SLs grown on GaAs (N 1 1)A revealed the lateral periodic composition modulation (dot structures) with a period of 10–20 nm, along both the [0 1 $\bar{1}$] and [$\bar{k}$ l m] directions ([0 1 1] equivalent direction on the (1 0 0) plane). Both (0 1 1) and (0 1 $\bar{1}$) cross-sectional TEM images showed columnar structures with a lateral period of about 10–20 nm [3]. They are oriented along the [1 0 0] direction for $N \geqslant 4$ or [2 1 1] direction for $N \leqslant 3$. It is noteworthy that on the (1 0 0) surface the lateral periodic composition modulation occurs only along the [0 1 1] direction (wire structures), while on the (N 1 1)A surfaces the lateral periodic composition modulation occurs along the [0 1 $\bar{1}$] direction as well as along the [$\bar{k}$ l m] direction. The dot/columnar structures observed here are not considered to be caused by spinodal decomposition because the structures caused by spinodal decomposition were observed along the [0 1 0] and [0 0 1] equivalent directions [6, 7]. The cross-sectional TEM images for the SLs grown on (1 1 1)A and (1 1 1)B substrates revealed that the lateral composition modulation does not occur and that the quasi-perfect monolayer SL is formed until $n \leqslant 4$. PL peak energies were also greatly dependent on the substrate orientation and monolayer number n [5].

Thirty six periods of $(GaP)_{1.5}(InP)_{1.88}$ SLs and $(GaP)_2(InP)_{2.5}$ SLs were here grown on GaAs(3 1 1)A and GaAs(4 1 1)A substrates at 460°C, and were studied by STM and TEM. Fig. 1 shows their STM ((a) and (c)) and plan-view TEM ((b) and (d)) images. These images indicate the formation of uniform high-density dot structures along the [$\bar{k}$ l m] and [0 1 $\bar{1}$] directions. The dot periods and the observed structures in STM and

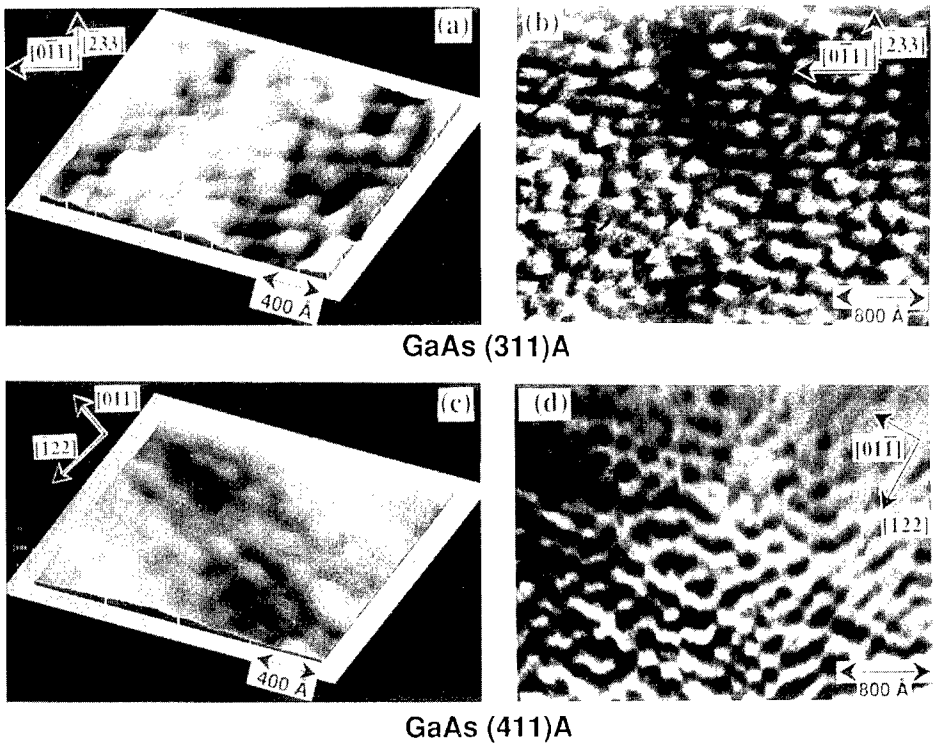

Fig. 1. (a) STM and (b) dark-field plan-view TEM images for the $(GaP)_2(InP)_{2.5}$ SLs grown on GaAs (3 1 1)A. (c) STM and (d) dark-field plan-view TEM images for the $(GaP)_{1.5}(InP)_{1.88}$ SLs grown on GaAs (4 1 1)A. STM image was obtained with a sample bias of -3.49 and -4.39 V, respectively, in constant current mode.

plan-view TEM images are nearly the same. The dot period studied by STM observation increased with increasing n and m. Scanning tunneling spectroscopy (STS) measurement showed that the voltage width for the $dI/dV = 0$ at bright region was narrower than that at dark region, suggesting that they correspond to the In-rich region and the Ga-rich region, respectively, and showing the band-gap variation due to lateral composition modulation.

In these SLs the dot (columnar) structure densities were larger than 10^{11} cm^{-2}. These results indicate the promising potential for the fabrication of high-density quantum dot (QD) structures by growing $(GaP)_n(InP)_m$ SL/InGaP multilayers, as shown in the next subsection. High density of QD structures are favorable for obtaining high optical gain and therefore low threshold current density in laser diodes.

3.2. *Quantum dots formed in $(GaP)_n(InP)_m$ SL/$In_{0.49}Ga_{0.51}P$ multilayers*

Self-organized QWR and QD structures were grown on GaAs (1 0 0) and (N 1 1)A, respectively. The grown structures consist of (i) a 300 nm-thick $In_{0.49}Ga_{0.51}P$ buffer layer, (ii) 5 cycles of $(GaP)_n(InP)_m$ SL (18 periods, about 20 nm) layers and $In_{0.49}Ga_{0.51}P$ (20 nm) layers and (iii) a 300 nm-thick $In_{0.49}Ga_{0.51}P$ top layer, as shown in Fig. 2a.

Both (0 1 1) and (0 1 $\bar{1}$) cross-sectional TEM images show lateral composition modulation, indicating QD structure formation in the $(GaP)_{1.5}(InP)_{1.88}$ SL layer regions grown on GaAs (4 1 1)A substrate, as shown in Fig. 2b and Fig. 2c. The QWR structures were formed in the SL grown on GaAs (1 0 0) substrates for the same structures.

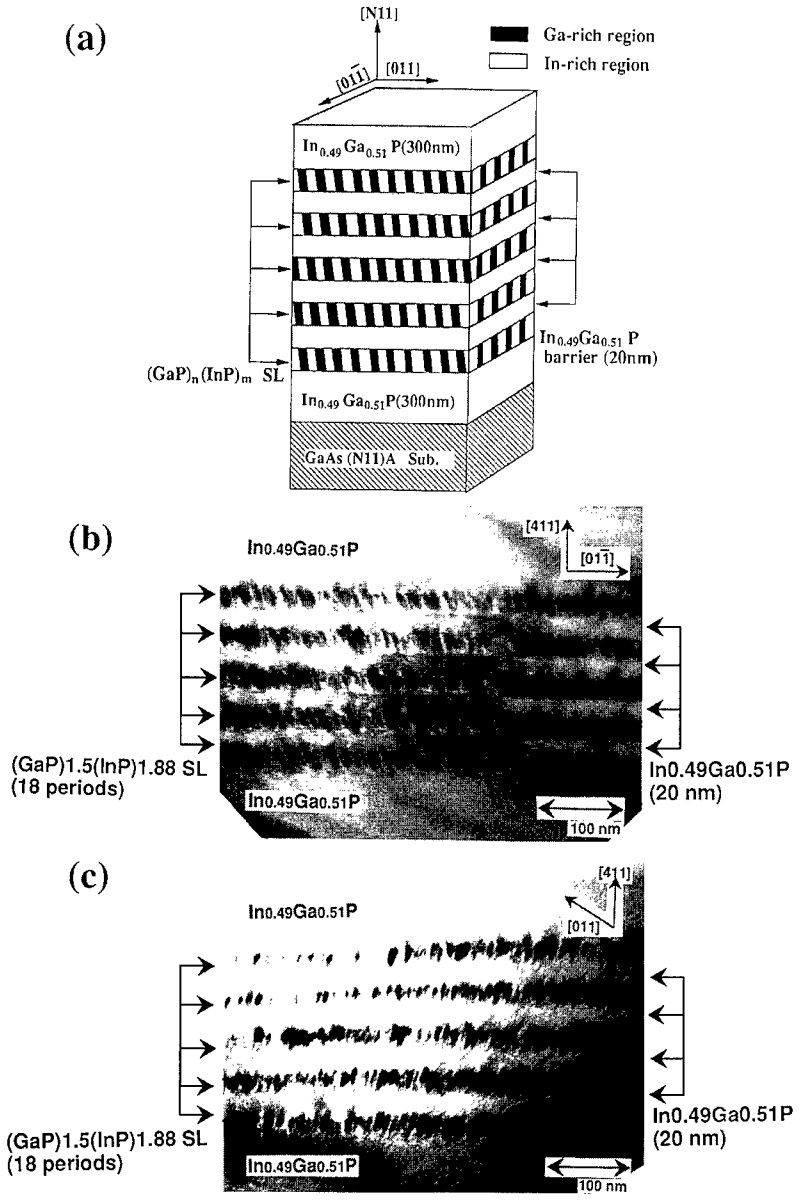

Fig. 2. (a) Schematic diagram of the quantum dot structures formed in the $(GaP)_n(InP)_m$ SL/$In_{0.49}Ga_{0.51}P$ multilayers grown on GaAs (N 1 1). (b) and (c): bright-field cross-sectional TEM images for (0 1 1) and (0 1 $\bar{1}$) planes, respectively. Both (0 1 1) and (0 1 $\bar{1}$) cross-sectional TEM images exhibit lateral dot structures due to lateral periodic composition modulation.

PL spectra at 77 K for the QDs grown on (N 1 1)A are shown in Fig. 3. The full width at half-maximum (FWHM) for the QDs are about 39–98 meV. For the QDs on (3 1 1)A the best PL intensity and FWHM were obtained. PL peak energy variation with growth temperature at 420–460°C was very small, though PL intensity increased with increasing growth temperature.

By increasing the deviation percentage of the SL periodicity ΔT [8],

$$\Delta T = (\text{SL period} - Ia_0)/Ia_0,$$

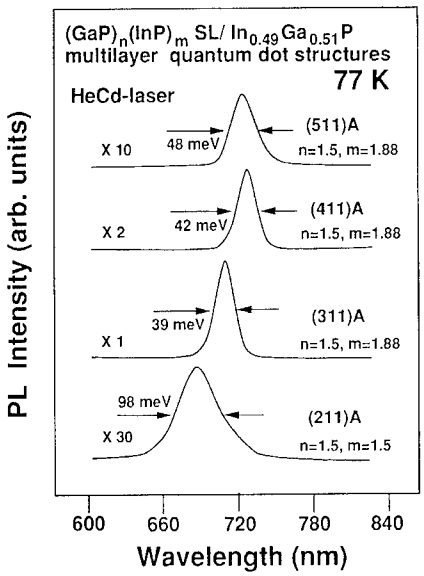

Fig. 3. PL spectra at 77 K for the self-organized quantum dots (QDs) formed in the $(GaP)_{1.5}(InP)_{1.5}$ SL and $(GaP)_{1.5}(InP)_{1.88}$ SL/$In_{0.49}Ga_{0.51}P$ multilayers grown on GaAs (N 1 1)A.

the PL peak energy of the QDs showed a larger red-shift due to larger lateral composition modulation in the $(GaP)_n(InP)_m$ SL region, where SL period $= (n + m)a_0/2$, $n = I =$ integer and the GaAs lattice constant $a_0 = 5.6533$ Å.

The PL peak energy for the QDs was higher than that for the QWRs. The PL intensity of the QDs was stronger than that of QWRs. The PL intensity for the QDs formed in $(GaP)_2(InP)_{2.5}$ SL/$In_{0.49}Ga_{0.51}P$ multilayers was three orders of magnitude stronger than that of QWRs. However, the PL intensity of the QWRs for the $(GaP)_{1.5}(InP)_{1.88}$ SL was two orders of magnitude stronger than that for the $(GaP)_2(InP)_{2.5}$ SL.

3.3. Temperature dependence of PL peak energy

We have observed anomalous temperature dependence of the PL peak energy for these QDs. Fig. 4a shows the temperature variation of the PL spectrum for QDs formed in the $(GaP)_{1.5}(InP)_{1.88}$ SL/$In_{0.49}Ga_{0.51}P$ multilayers grown on GaAs (3 1 1)A. FWHM is less than 40 meV below 80 K, though it decreases with increasing temperature due to tunneling effect between neighbor quantum states up to 45 K. At temperatures over 80 K it increases further, the origin of which is not known at present. Similar temperature variation of

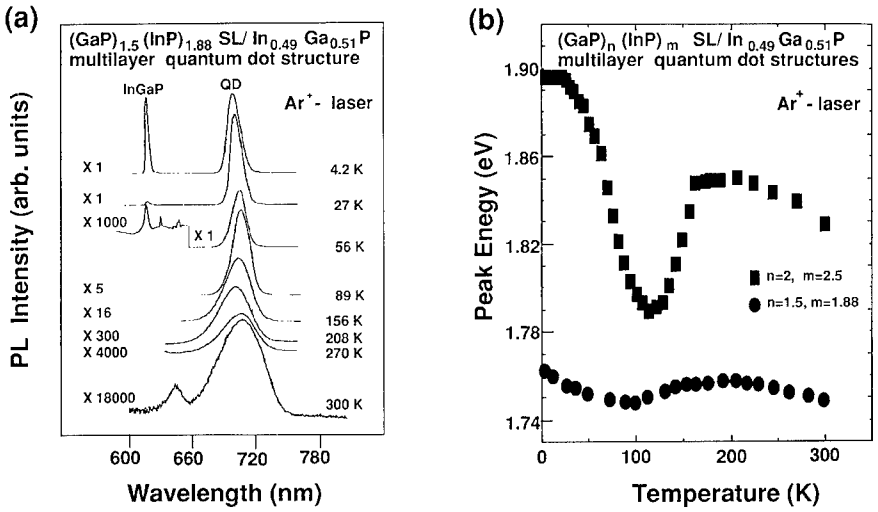

Fig. 4. Temperature dependences of (a) PL spectra and (b) PL peak energies for the QDs formed in the $(GaP)_{1.5}(InP)_{1.88}$ SL and $(GaP)_2(InP)_{2.5}$ SL/$In_{0.49}Ga_{0.51}P$ multilayer grown on GaAs (3 1 1)A.

FWHM was also observed for the QDs formed in the $(GaP)_2(InP)_{2.5}$ SL.

With increasing temperature the PL peak energy for the $(GaP)_{1.5}(InP)_{1.88}$ SL decreases rapidly in the low-temperature region, has a minimum at about 100 K, then increases in the range of 100–190 K, and has a relatively small but normal temperature variation over 200 K, as shown by closed circles in Fig. 4b. Much more pronounced temperature variation was also observed for the QDs of the $(GaP)_2(InP)_{2.5}$ SL. PL peak energy has a minimum at about 120 K, then increased in the range of 125–175 K, and had a normal temperature variation over 200 K, as shown by quadrangles in Fig. 4b. The temperature variation of PL intensity observed in these QDs is similar to those observed for the InAs QD structures formed on GaAs by the Stranski–Krastanov mode MBE [2]. On the other hand, the PL peak energy for the QWRs on GaAs (1 0 0) showed very small temperature variation up to 120 K. The origin of these anomalous temperature variations is not known at present, but the existence of the strained ordered structures in the $(GaP)_n(InP)_m$ SL regions may play a role. Similar anomalous temperature variation of the PL peak energy to that for the QDs was observed for the ordered alloy of InGaP grown by MOVPE [9, 10]. The anomalous temperature variation of PL peak energy observed here is much larger than those observed for the InGaP ordered alloy [9, 10].

4. Summary

$(GaP)_n(InP)_m$ SLs were grown on GaAs (N 1 1) and (1 0 0) substrates by gas-source MBE. STM and TEM observations showed that the quantum dot/columnar structures were formed in the SLs grown on GaAs (N 1 1)A substrates by the lateral periodic composition modulations both along the [0 1 $\bar{1}$] direction and the [0 1 1] equivalent direction with a lateral period of 10–20 nm. The surface densities of these dot structures were larger than 10^{11} cm^{-2}.

Quantum dots were fabricated by growing $(GaP)_n(InP)_m$ SL/$In_{0.49}Ga_{0.51}P$ multilayers on GaAs (N 1 1)A substrates by self-organization. Strong 77 K PL with a narrow FWHM of about 40 meV were observed for these QDs grown on GaAs(3 1 1)A. Anomalous temperature variation of the PL peak energy was observed in all of these self-organized structures.

Acknowledgements

The authors would like to thank T. Ishibashi for the technical support and useful discussion on TEM measurement. This work was supported in part by a Grant-in-Aid for Scientific Research on Priority Area from the Ministry of Education, Science, Sports and Culture and by the Research and Development Association for Future Electron Devices.

References

[1] K.C. Hsieh, J.N. Baillargen and K.Y. Cheng, Appl. Phys. Lett. 57 (1990) 2244.
[2] D.I. Lubyshev, P.P. González-Borrero, E. Marega, Jr., E. Petitprez, N. La Scala, Jr. and P. Basmaji, Appl. Phys. Lett. 68 (1996) 205.
[3] A. Tackeuchi, Y. Nakata, S. Muto, Y. Sugiyama, T. Inata and N. Yokoyama, Jpn. J. Appl. Phys. 34 (1995) L405.
[4] K. Mukai, N. Ohtsuka, H. Shogi and M. Sugawara, Appl. Phys. Lett. 68 (1996) 3013.
[5] S.J. Kim, H. Asahi, M. Takemoto, K. Asami and S. Gonda, Jpn. J. Appl. Phys. 35 (1996) 4225.
[6] P. Henoc, A. Izrael, M. Quillec and H. Launois, Appl. Phys. Lett. 40 (1982) 963.
[7] O. Wada, S. Isozumi and S. Komiya, Jpn. J. Appl. Phys. 23 (1984) L241.
[8] P.J. Pearah, A.C. Chen, A.M. Moy, K.C. Hsieh and K.Y. Cheng, IEEE J. Quantum Electron. 30 (1994) 608.
[9] M. Kondow, S. Minagawa, Y. Inoue, T. Nishino and Y. Hamakawa, Appl. Phys. Lett. 54 (1989) 1760.
[10] B.T. McDermott, K.G. Reid, N.A. El-Masry, S.M. Bedair, W.M. Duncan, X. Yin and H. Pollak, Appl. Phys. Lett. 56 (1990) 1172.

ELSEVIER

Journal of Crystal Growth 175/176 (1997) 760–764

JOURNAL OF CRYSTAL GROWTH

Intersubband absorption from $In_{0.26}Ga_{0.74}As/GaAs$ quantum dot superlattice

Dong Pan[a,*], Y.P. Zeng[a], J.M. Li[a], C.H. Zhang[a], M.Y. Kong[a], H.M. Wang[a], C.Y. Wang[a], J. Wu[1,b]

[a] *Material Center, Institute of Semiconductor, Chinese Academy of Science, P.O. Box 912, Beijing 100083, People's Republic of China*
[b] *Beijing Laboratory of Electron Microscopy, Chinese Academy of Science, P.O. Box 2724, Beijing 100080, People's Republic of China*

Abstract

We have grown a high-quality 20 period InGaAs/GaAs quantum dot superlattice with a standard structure typically used for quantum well infrared photodetector. Normal incident absorption was observed around 13–15 μm. Potential applications for this work include high-performance quantum dot infrared detectors.

Keywords: Quantum dot; Intersubband absorption; Quantum dot infrared photodetector

1. Introduction

Zero-dimensional (0D) quantum dots (QD) structures have attracted much interest in recent years due to their δ-function-like density of states, strong carrier localization, large exciton binding energies, and enhanced oscillator strength [1–3]. High-quality quantum dot can be self-formed in situ in Stranski–Krastanow growth mode without resorting to any substrate patterning process [4–11].

The growth of quantum dot superlattice has also been of much interest [9, 10]. The formation mechanism of quantum dots needs to be further investigated, such as the complex indium migration dynamics in the process of self-organization growth and the formation of wetting layer. On the other hand, very high detectivity quantum dot infrared photodetector can be achieved by using intersubband transition taking place between bound levels in quantum dot. The discrete levels in quantum dots hinder carrier relaxation toward the ground state and thus a very long carrier lifetime [12–14]. This is called the "phonon bottleneck effect". Unlike the conventional GaAs/AlGaAs QWIPs that require a coupler (e.g. gratings) to couple the normal incident radiation [15], the intersubband transition in quantum dot can be induced by the normal incident radiation due to the localized state in quantum dots. Hence, the intersubband absorption quantum dot infrared photodetector (QDIP)

* Corresponding author.
[1] Also at: Institute of Semiconductor, Chinese Academy of Science, People's Republic of China.

0022-0248/97/$17.00 Copyright © 1997 Elsevier Science B.V. All rights reserved
PII S0022-0248(96)01010-X

has a great advantage over the conventional GaAs/AlGaAs QWIP.

Quantum dot multilayer is required for enhencing infrared absorption. High-quality InGaAs/GaAs QDs have been difficult to grow due to dislocation occurring with increasing layer thickness. Presently, there have been only a few reports on high-quality InGaAs/GaAs quantum dot superlattice [9, 10]. In Stranski–Krostanow growth mode, initial growth starts two dimensionally in the layer-by-layer mode, but after a certain thickness is reached, islands form spontaneously and a very thin 2D wetting layer is left behind the islands. If the growth is allowed to continue beyond the initial island formation stage, misfit dislocations start forming at the island edges [4, 12]. Therefore, the dislocation-free InGaAs/GaAs quantum dots require that the growth be interrupted immediately after the formation of the islands but before the islands reach a size for which strain relaxation and misfit dislocation occurs [4]. The superlattice is a more complex system than the single layer and dislocation easily occurs in the process of quantum dot growth.

Using lower indium fraction permits the thicker layer without dislocations, and the island formation may be completely controlled by growth condition. In the paper, we have grown a high-quality 20 period InGaAs/GaAs quantum dot supperlattice (QDS) with low indium fraction ($x = 0.26$). The normal incident infrared absorption can be observed at 13–15 μm.

2. Experimental proceudre

The InGaAs/GaAs QDS was grown by molecular beam epitaxy (Riber-32P) on semi-insulting GaAs (1 0 0) substrate. The structure of InGaAs/GaAs QDS is very similar to the conventional QWIP. The layers consisted of, a 1.3 μm buffer layer, a 1.0 μm n^+ contact layer, a 20 period InGaAs/GaAs quantum dot arrays, and a 1.0 μm GaAs and 200 nm AlGaAs ($x = 0.04$) top contact layer. The InGaAs layers and the contact layers were Si-doped with doping concentrations of 1×10^{18} cm^{-3}, and δ-doping for InGaAs layer. The growth rate for GaAs was 2.83 A/s. The indium fraction in InGaAs is about 0.26–0.28, which is determined by reflection high-energy electron diffraction oscillations and equivalent beam pressure. The quantum dots were self-formed by the coherent relaxation into islands of InGaAs between undoped GaAs layers. The actual amount of indium incorporated in the dots is difficult to measure or calculate due to the complex dynamics of the atoms during island formation.

The cross-sectional transmission electron micrograph (TEM), low-temperature photoluminescence and X-ray double-crystal diffraction have been used to measure the structural and optical properties for quantum dot superlattice. The infrared absorption was measured for QDS by using a Fourier transform infrared (FTIR) spectrometer at room temperature, which was carried out under two modes: multipass 45° wave guide and normal incident mode. These measured results are presented in Figs. 1–6.

3. Result and discussion

Fig. 1 shows the cross-sectional TEM micrograph of the quantum dot array. A 20 period defect-free quantum dot array is clearly shown. Using cross sectional view TEM results, statistics on the QD size can be extracted. Fig. 2 shows these results. It shows that the average size of quantum dots is 28 nm (diameter), 7 nm (height) and 0.26, height to diameter ratio. It is worth noting that the actual size of quantum dot is smaller than the one measured by TEM because the distributions measured by TEM are affected by strain which tends to overestimate the size. Fig. 3 shows the low-temperature (10 K) photoluminescence (PL) spectrum of QDS. A strong luminescence peak around 1.25 eV is observed. The peak PL intensity dependence of excitation power is also presented in Fig. 3 and it is noted that there is no saturation of intensity, which indicates that island-attributed PL is not due to defects or impurities. The dot peaks have a full-width at half-maximum of about 53 meV, which is due to the size fluctuation of quantum dots. These results are in good agreement with the present reports for quantum dots [2–4]. It is worth noting that the vertical correlation of quantum dot is not

Fig. 1. Cross-sectional view of quantum dot superlattice.

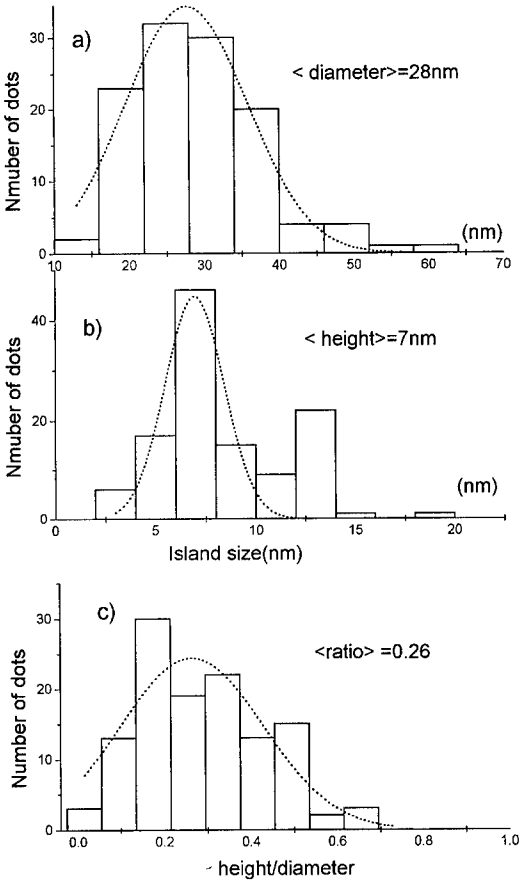

Fig. 2. Histogram of dot (islands) measured from cross-sectional TEM micrograph and fit with a Gaussian curve: (a) the island diameter; (b) the island height; (c) the ratio of the height to diameter.

obvious in our sample, which is due to the thicker spacer layer (34 nm). This observation agrees with a report by Xie [10]. Fig. 4 shows the measured X-ray double-crystal rock curve. Over ten satellite peaks are observed, indicative of good structural quality. The period of superlattice is calculated to 34 nm. The quantum dot superlattice structure is shown schematically in Fig. 5.

As measured in the conventional QWIPs, we measure the infrared spectrum of quamtum dot array using Brucker IFS-120HR FTIR in a multi-pass 45° wave-guide configuration [15], as seen in Fig. 6(a). Strong absorption peaks are observed at 13–14 μm with a 13 mev FWHM. Fig. 6b shows the measured infrared absorption spectrum under the normal incident radiation. The obvious absorption peaks around 14–15 μm with a 11 mev can be observed. Compared with that measured in a multi-pass 45° wave-guide configuration, the peaks is shifted to the lower energy, which is similar to the

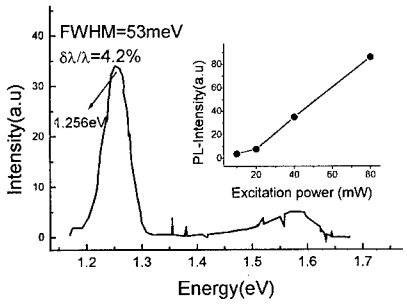

Fig. 3. Low-temperature (10 K) photoluminescence spectra of sample. The insets show the PL intensity dependence of excitation power and it is noted that there is no saturation of intensity, which indicates that island-attributed PL is not due to defects or impurities.

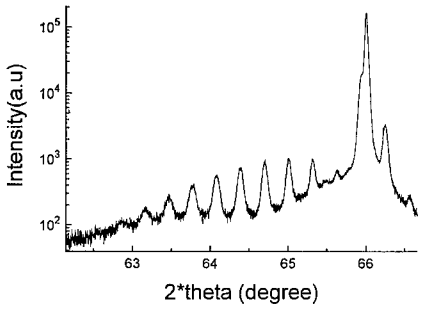

Fig. 4. The measured (0 0 4) Bragg reflection spectra of sample.

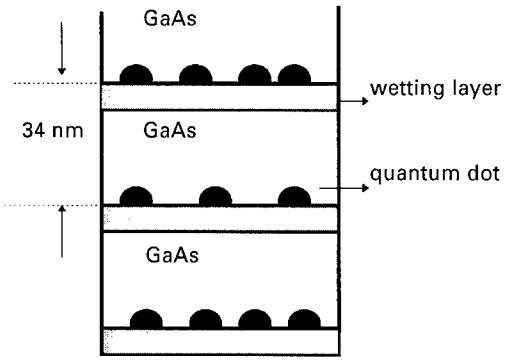

Fig. 5. The schematic diagram of quantum dot superlattice.

depolarization effect in normal incident absorption InGaAs/GaAs quantum well [16]. The measured multi-peak structure may be due to the different size of quantum dots, as seen in the PL results.

Since we do not know accurate In content in islands, it is impossible to calcualte the energy level for the quantum dot superlattice. The observed intersubband absorption probably results from either quantum dots or quantum well (wetting layer) since the normal incident intersubband transition is possible in InGaAs/GaAs QWs [16, 17]. However, the narrow absorption line width suggests that the absorption takes place between the bound levels in low-dimensional material. Based on the norminal growth parameters, it is impossible to find such the intersubband transition from bound level to bound level in quantum well (the bound-to-continuum instead) [15, 18]. In particular, the normal infrared absorption can be directly observed without using a mutlipass 45° waveguide and polarization configuration. In the

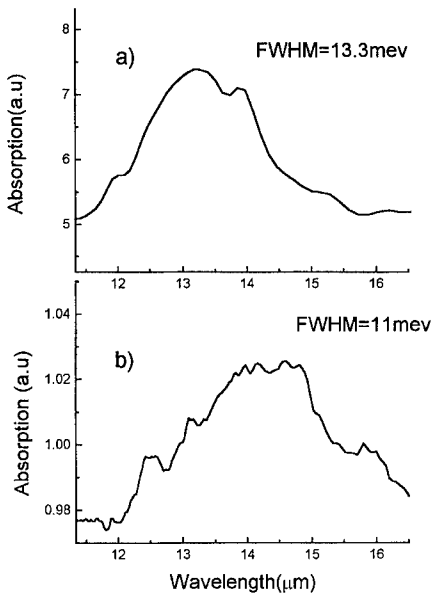

Fig. 6. The measured infrared absorption from quantum dot superlattice: (a) in a multipass 45 wave-guide configuration; (b) under normal incident radiation.

case of quantum well, the normal incident absorption is so weak that it is difficult to observe without using waveguide [15]. Hence, the 13–15 μm infrared absorption results from the intersubband transition in quantum dots. To the author's knowledge, this is the first report that the normal incident infrared absorption can be observed from the QDS. Since the detectivity is proportional to carrier lifetime, the quantum dot infrared photodetector can be predicated to have much higher sensitivity than the quantum well infrared photodetector (QWIPs).

4. Conclusion

We report for the first time, the infrared absorption around the wavelength of 13–15 μm from 20 period dislocation-free InGaAs/GaAs quantum dot superlattice (QDS) with the low In fraction ($x = 0.26$). It opens a way to high sensitivity quantum dot infrared photodetectos. The QDS has been investigated by the transmission electron micrograph, low-temperature photoluminesccence and X-ray double-crystal diffraction. The transmission

electron micrograph reveals that the size distribution of quantum dots: ~ 28 nm in diameter and 7–15 nm in height. A strong luminescence peak is observed around ~ 1.25 eV from 10 K photoluminescence. The superlattice period is 34 nm.

References

[1] Y. Arakawa and H. Sakaki, Appl. Phys. Lett. 40 (1982) 939.
[2] L. Brus, IEEE. J. Quantum Electron. 22 (1986) 1909.
[3] H. Sakaki, Jpn. J. Appl. Phys. 28 (1989) L314.
[4] R. Leon, P.M. Petroff, D. Leonard and S. Fafard, Science 67 (1995) 1996.
[5] D. Leonard, M. Krishnamurthy, C.M. Reaves, S.P. Denbaars and P.M. Petroff, Appl. Phys. Lett. 63 (1991) 3203.
[6] R. Leon, S. Fafard and D. Leonard et al., Appl. Phys. Lett. 67 (1995) 521.
[7] S. Fafard, Z. Wasilewski, J. McCaffrey and S. Raymond, Appl. Phys. Lett. 68 (1993) 991.
[8] M. Grundmann, N.N. Kendentosv, O. Stier, D. Dimberg, V.M. Ustinov, P.S. Kopev and Zh.I. Alferov, Appl. Phys. Lett. 68 (1996) 979.
[9] J. Tersoff, C. Teichert and M.G. Lagally, Phys. Rev. Lett. 76 (1996) 675.
[10] Q. Xie, A. Madhukar, P. Chen and N.P. Kobayashi, Phys. Rev. Lett. 75 (1995) 2542.
[11] S. Guha, A. Madhukar and K.C. Rajkumar, Appl. Phys. Lett. 57 (1990) 2110.
[12] K. Mukai, N. Ohtsuka, H. Shoji and M. Sugawara, Appl. Phys. Lett. 68 (1996) 3013.
[13] H. Benisty, C.M. Sotomayor and C. Weisbuch, Phys. Rev. B 44 (1991) 10945.
[14] U. Bockelamnn and G. Bastard, Phys. Rev. B 42 (1990) 8947.
[15] B.F. Levine, J. Appl. Phys. 74 (1993) R1.
[16] H.S. Li, R.P.G. Karunasri, Y.W. Chen and K.L. Wang, J. Vac. Sci. Technol. B 11 (1993) 922.
[17] G. Karunasiri, J.S. Park, J. Chen, R. Shih, J.F. Scheihing and M.A. Dodd, Appl. Phys. Lett. 67 (1995) 2600.
[18] S.D. Gunapala, K.M.S.V. Bandara, B.F. Levine, G. Sarusi, J.S. Park, T.L. Lin, W.T. Pike and J.K. Liu, Appl. Phys. Lett. 64 (1994) 3431.

ELSEVIER

Journal of Crystal Growth 175/176 (1997) 765–770

JOURNAL OF CRYSTAL GROWTH

Molecular-beam epitaxy of self-assembled InAs quantum dots on non-(1 0 0) oriented GaAs

P.P. González-Borrero*, E. Marega, Jr., D.I. Lubyshev, E. Petitprez, P. Basmaji

Instituto de Física de São Carlos, Universidade de São Paulo, CP 369, 13960-970 São Carlos, SP, Brazil

Abstract

In this paper we report optical properties of InAs quantum dots (QD) grown by molecular-beam epitaxy on GaAs (2 1 1)A, (*n* 1 1)A/B, where *n* is 1, 5 and 7, and on reference (0 0 1) substrates. The photoluminescence (PL) spectra reveal differences in amplitude, integral luminescence, peak position and shape. Temperature dependence indicates an additional lateral confinement on (0 0 1), (*n* 1 1)B, (2 1 1)A and (1 1 1)A substrates. Our results also show an enhancement of QD onset thermal quenching energy by a factor of ~ 3 for these orientations, when compared with the reference quantum well. PL polarization measurements show strong in-plane dependence caused by the quantum dot's structural anisotropy. However, the structure grown on (5 1 1)A and (7 1 1)A surfaces does not exhibit QD formation.

PACS: 73.20.Dx; 78.55. – m; 68.55.Bd

Keywords: Quantum dots; Self-assembled; High-index; MBE

1. Introduction

The growth of strained films has become a field of intense study in recent years. In particular, InGaAs/GaAs and InAs/GaAs systems have been intensively investigated due to the possibility of producing nearly defect-free quantum dot (QD) structures. These structures are a result of the Stranski–Krastanow (SK) growth mode [1]. Such a growth mode starts two-dimensionally; after a certain critical thickness is reached, islands are formed spontaneously, and a thin wetting layer is left below the islands. The main QD parameters, such as size distribution, lateral size, height and form, are dependent on the mechanism of stress relaxation of the two-dimensional layer (2D) to three-dimensional (3D) islands. Such quantum dots have mainly been obtained by molecular-beam epitaxy (MBE) [2, 3] or metalorganic chemical vapor deposition (MOCVD) [4, 5], with (0 0 1)-orientation substrates. Few works studying QD formation on GaAs high-index surfaces have been reported [5, 6]. During MBE growth these high-index planes break up into periodic arrays of nanometer scale facets, thus lowering the surface energy. This microscopic surface morphology represents the

* Corresponding author. Fax: + 55 16 2713616; e-mail: gonzalez@ ifqsc.sc.usp.br.

0022-0248/97/$17.00 Copyright © 1997 Elsevier Science B.V. All rights reserved
PII S0022-0248(96)01182-7

equilibrium surface structure, and is generally stable during growth. Therefore, the lateral periodicity is fixed for a certain crystallographic orientation [7, 8]. Such periodicity might influence the indium adatom kinetics, resulting in different stress relaxation for each surface. These conditions determine the growth mode for each orientation.

In this work, we used high-index GaAs surfaces to study the formation of self-assembled InAs quantum dots on (n 1 1)A/B planes. Photoluminescence (PL) results indicate QD formation for all orientations except (5 1 1)A and (7 1 1)A. PL polarization measurements suggest the presence of developed microfacets on QDs.

2. Experimental procedure

The samples were grown by MBE technique, using a Meca 2000 system, on GaAs reference (0 0 1), (2 1 1)A and (n 1 1)A/B (where n is 1, 5 and 7) substrates. Growth process was monitored in situ by means of reflection high-energy electron diffraction (RHEED) (15 kV). The substrates were degreased and etched ex situ, then soldered side by side with indium on a molybdenum holder and immediately transfered to the sample load-lock system. After transfer to the MBE growth chamber, the surface oxide had been thermally desorbed by heating the substrate wafers to $\sim 580°C$ under an arsenic flux. An As_4 background pressure of 9×10^{-6} Pa was used during structure growth. Then, the substrate temperature T_s was raised to 620°C and samples were outgassed for 5 min. After this, T_s was lowered to 600°C and a 80 nm GaAs/AlAs (2/2 nm) superlattice was grown, followed by a 0.5 μm GaAs buffer layer. During the last 0.1 μm buffer layer, T_s was decreased to 500°C to grow a 3 nm $In_{0.2}Ga_{0.8}As$ reference quantum well (QW) and the remainder of the structure. The gallium- and indium-cell temperatures were kept constant during T_s variations. In order to compare optical properties, the QW was grown with the same nominal estimated thickness as the InAs quantum dots [9] and separated from them by a 100 nm GaAs layer. In order to finish the structure, a 50 nm GaAs cap layer was grown. The growth rates of GaAs and InAs determined by the RHEED oscillation technique were, respectively, 0.23 and 0.061 nm/s on GaAs(0 0 1) plane. Since T_s (500°C) was below critical temperature for starting indium reevaporation, we assumed these growth rates to be the same for all orientations. Interface smoothing was carried out, using growth interruption, during 1 min before and 3 min after InAs deposition. During these growth interruptions, growth was stopped momentarily by closing the gallium and indium cells for a specified duration, while the arsenic cell was always kept open to maintain an excess arsenic pressure condition. The QD nucleation was directly observed by RHEED on (0 0 1) surface, when the pattern changed from streaky to spotty. We observed that the growth mode was 2D during the deposition of the first three monolayers (ML) and later it changed to 3D (SK mode). Afterwards three InAs ML were deposited for QD formation. The surface morphology of the (1 1 1)A and (2 1 1)B orientations was hazy due to choice of growth parameters for optimum quality of the (0 0 1) planes. The other planes showed a mirrorlike surface. The photoluminescence measurements were performed at 16 K in a closed-cycle He cryostat using a 514.5 nm line of Ar^+ laser. The average excitation density was 150 W/cm^2. A photomultiplier mounted on a 0.5 m monochromator was adapted for detection of PL signal in lock-in mode.

3. Results and discussion

Fig. 1 shows PL spectra at 16 K for all orientations. Concerning just the reference quantum well (QW) PL signal, we have observed that the peak position and the full width at half-maximum (FWHM) depend on crystallographic orientation. Such an effect has already been reported in Ref. [10]. For (0 0 1), (n 1 1)B, (2 1 1)A and (1 1 1)A surfaces, an additional peak has been detected at around 1.35 eV. This peak is attributed to the quantum dot formation on each orientation. High QD PL efficiency was obtained for (0 0 1) and (7 1 1)B surfaces, where QD–QW integrated PL intensity ratio is 3.2 and 1.9, respectively. In the other planes this ratio was one order of magnitude smaller. Peak positions, FWHM, and the integral

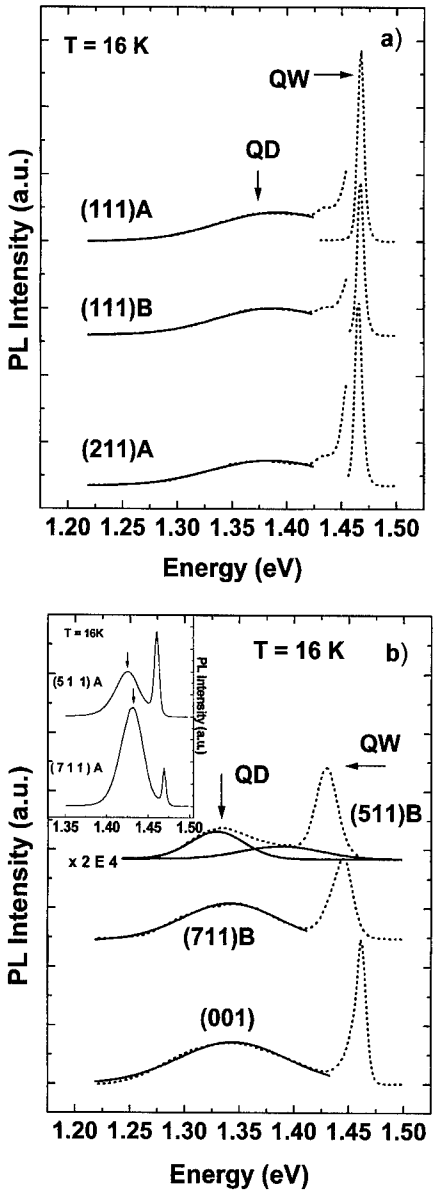

Fig. 1. PL spectra of (a) (1 1 1)A/B, (2 1 1)A, and (b) (5 1 1)B, (7 1 1)B, and (0 0 1) samples (dotted lines). Solid line represents Gaussian fitting for QDs, indicating formation of QDs with one predominant size. The inset in (b) shows the PL spectra for (5 1 1)A and (7 1 1)A surfaces, where grown the structure does not exhibit QD formation.

intensity ratios QD/QW for all samples are listed in Table 1. For each orientation the QD peak can be fitted by one Gaussian shape. In the case of (5 1 1)B plane, fitting is done by two Gaussians. The Gaussian with high-energy peak was attributed to the contribution of wetting layer to PL signal. We also measured QD PL excitation density dependence in the range of 10–10^3 W/cm^2 (T = 16 K) in order to deduce the density of stress-related defects in the QDs. The result shows linear dependence (not shown here), indicating a low defect density on QD interfaces. The inset of Fig. 1b exhibits PL spectra for (5 1 1)A and (7 1 1)A planes. The arrows indicate an unexpected peak of an additional structure, with energy position higher than the QD. We believe that this PL characteristic is related to a two-dimensional layer (QW) formed after the stress relaxation of a critical InAs layer. An enhancement of the FWHM of this PL signal is observed in comparison to reference QW. This increase is probably due to the formation of dislocations or related defects as a result of stress relaxation. Non-QD formation on (5 1 1)A has previously been reported [5, 10].

In order to obtain additional information about the QD properties, measurements of PL temperature dependence were carried out. Fig. 2 displays the (7 1 1)B PL spectra. The QW PL intensity decreases drastically when the temperature changes from 16 to 70 K, contrary to that of QDs, which persists up to $\sim$ 160 K. This persistence at high temperatures is related to the increase of oscillator strength due to additional lateral confinement [11, 12]. In addition, an unusual large red shift for QD peak position ($\sim$ 0.1 eV) is observed when temperature oversteps $\sim$ 45 K for all orientations. The rate of energy decrease with temperature is about two or three times higher than InAs band gap decrease rate. In order to explain this red shift and reduction of FWHM (see below), a model involving exciton recombination and thermal activation and transfer has recently been proposed [13]. In our case, this model does not describe completely our experimental data because the Gaussian shape of QD PL peak is maintained as temperature raises [14]. Another possible explanation is related to a temperature dependence of electron effective mass in InAs. Because the quantization energy of an electron–hole pair in the QD is higher by about a factor of 4 than that in the QW, this causes a greater change in the quantization

Table 1
Peak energy (in eV), FWHM (in eV), and QD–QW wavelength integrated PL (IPL) intensity ratio for all orientations at 16 K

Orientation	Quantum dot		Quantum well		IPL_{QD}/IPL_{QW}
	F_P	FWHM	E_P	FWHM	
(0 0 1)	1.338	~ 123	1.461	~ 12	~ 3.2
(7 1 1)B	1.344	~ 102	1.444	~ 23	~ 1.9
(5 1 1)B	1.330	~ 58	1.430	~ 24	~ 0.1
(2 1 1)A	1.381	~ 128	1.466	~ 7	~ 0.1
(1 1 1)A	1.392	~ 136	1.468	~ 6	~ 0.1
(1 1 1)B	1.387	~ 132	1.468	~ 6	~ 0.2

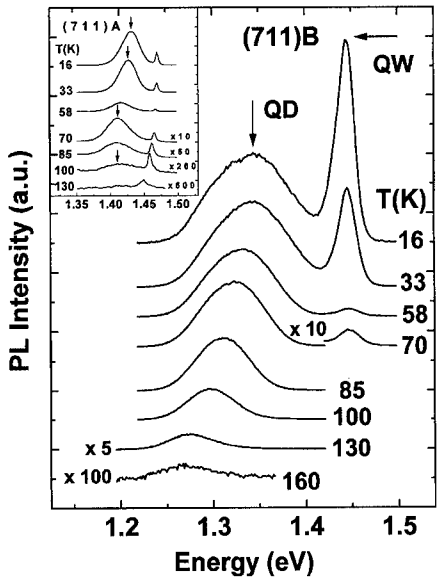

Fig. 2. (7 1 1)B and (7 1 1)A (inset) PL temperature dependence. The arrow in the inset indicates presence of an unexpected peak (see text).

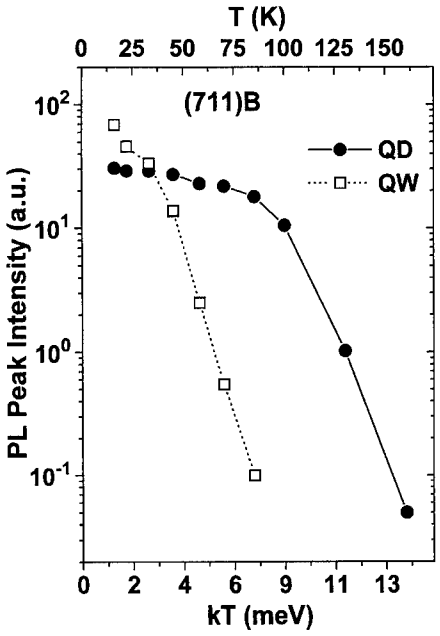

Fig. 3. QW and QD peak amplitude thermal energy dependence for (7 1 1)B plane. The QW peak is thermally quenched at ~ 1.5 meV, whereas the QD peak persists up to ~ 4 meV (see Table 2).

energy of the QD relative to that of the QW when the effective mass is changed [15]. The inset of Fig. 2 shows PL temperature dependence for (7 1 1)A surface. We can see that the behavior of the unexpected peak, indicated with arrow, is different from the (7 1 1)B QD. This dependence also suggests the existence of stress-related defects, and lack of relationship between peak and QD formation.

Fig. 3 exhibits QD and QW PL intensities shown in Fig. 2 as a function of the thermal energy. From similar plots for all orientations, we extracted the value for thermal quenching energy (E_Q). Further, by plotting the logarithm of wavelength-integrated PL values versus $1/kT$, we determined activation energy (E_A) of thermionic emission.

Table 2
Thermal quenching energy (E_Q) and electron–hole emission activation energy (E_A) values in meV for all orientations

Orientation	E_Q		E_A	
	QD	QW	QD	QW
(0 0 1)	~ 6	~ 2	~ 47	~ 24
(7 1 1)B	~ 4	~ 1.5	~ 52	~ 22
(5 1 1)B	~ 6	~ 2	~ 40	~ 28
(2 1 1)A	~ 6	~ 2	~ 28	~ 20
(1 1 1)A	~ 6	~ 2	~ 27	~ 19
(1 1 1)B	~ 6	~ 2	~ 32	~ 23

E_A and E_Q values are summarized for all orientations in Table 2. We observed that QD's E_Q is about 3 times larger than QW's. E_A values observed for QD are about 1.4–2.4 times higher than for QW, suggesting suppression of electron-hole emission from QDs to GaAs barrier, due to a binding energy increase. Activation energy of unexpected peak of (5 1 1)A and (7 1 1)A surfaces was also determined. The E_A values are around 18 and 24 meV for (5 1 1)A and (7 1 1)A orientations, respectively. For (5 1 1)A plane, this value is almost the same as for reference QW (17 meV). In the case of (7 1 1)A, activation energy is 1.3 times higher than that for the reference QW (19 meV). Taking into account temperature dependence, power density dependence of peak position and intensity, as well as activation energy values, we attributed the unexpected peak, already referred to, to the emission of a 2D layer.

Fig. 4 exhibits an unexpected effect present in PL FWHM as a function of temperature for (7 1 1)B, (2 1 1)A, (1 1 1)A/B orientations. In the case of QDs, an unusual decrease of FWHM was detected for Gaussian-shaped emissions from 16 to 85 K for (1 1 1)B, 100 K for (1 1 1)A and (2 1 1)A, and 130 K for (7 1 1)B planes, respectively. This effect was reported in Ref. [14] and described in terms of suppression of non-predominant size QD emissions, and persistence of predominant size emissions present at the center of a Gaussian shaped PL function. In Ref. [13] as noted above, another model was proposed to explain this reduction of FWHM.

QD PL polarization dependence measurements were also carried out to determine probable structural anisotropy of QDs in-plane. Fig. 5 shows the angular dependence of normalized PL peak intensity for (0 0 1), (7 1 1)B and (5 1 1)B orientations. These planes demonstrate a strong polarization effect. A maximum of PL intensity has been set for PL component when polarization angle is zero, occurring when polarization is parallel to the following crystallographic directions: $[\bar{2}\,7\,7]$ for (7 1 1) plane, $[\bar{2}\,5\,5]$ for (5 1 1)B and $[1\,\bar{1}\,0]$ for

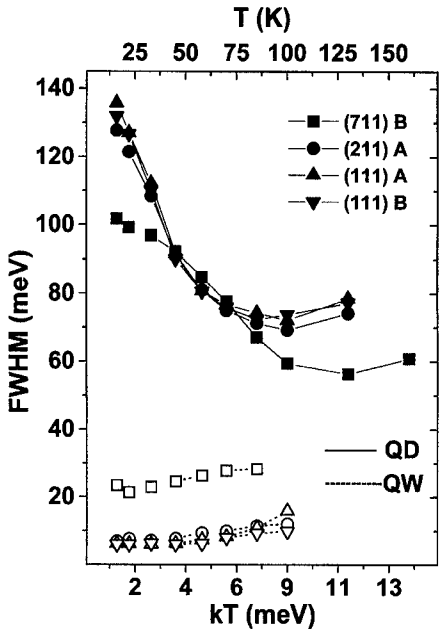

Fig. 4. QW (open symbols) and QD (closed symbols) PL FWHM temperature dependence of (7 1 1)B (square), (2 1 1)A (circle), (1 1 1)A (up triangle), and (1 1 1)B (down triangle) samples.

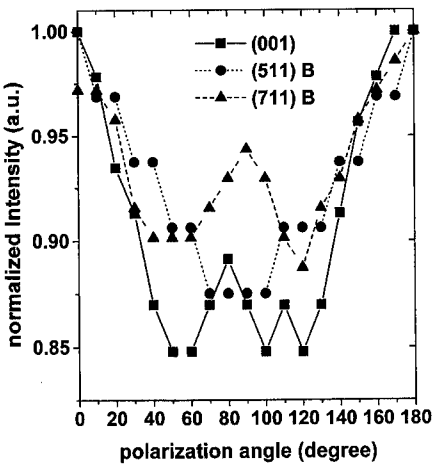

Fig. 5. Angular dependence of normalized PL intensity for (0 0 1) (square), (5 1 1)B (circle), and (7 1 1)B (up triangle) oriented samples. The crystallographic directions, corresponding to the zero value of the polarization angle, are [1 $\bar{1}$ 0] for (0 0 1), [$\bar{2}$ 5 5] for (5 1 1)B and [$\bar{2}$ 7 7] for the (7 1 1) plane.

(0 0 1), respectively. Based on our results, we believe that QDs grown on these oriented planes have well-developed microfacet configuration. Similar results have been reported for InAs QD on (0 0 1) [16] and InGaAs QD on high-index surfaces [6].

4. Conclusions

Optical properties of self-organized InAs quantum dots grown on high-index GaAs substrates have been investigated. Such properties are strongly dependent on substrate orientations. Quenching energy for QDs is around three times higher than for reference QW. Dependence of optical characteristics with temperature is related to an increase of exciton binding energy and activation energy for thermionic emission, due to additional lateral confinement. Our results show an unusual decrease of FWHM with temperature, suggesting suppression of non-predominant size QD emissions and persistence of those of predominant size. Non-QD formation was detected on (7 1 1)A and (5 1 1)A orientations. For such surfaces, an unexpected peak related to a two-dimensional layer was observed. These results suggest that another growth mechanism predominates in such A surfaces as a result of stress relaxation.

Acknowledgements

The support of CNPq and FAPESP is gratefully acknowledged.

References

[1] I.N. Stranski and L. Von Krastanow, Akad. Wiss. Lit. Mainz Math.-Natur Kl. 11b 146 797 (1939).
[2] D. Leonard, M. Krishnamurthy, C.M. Reaves, S.P. Denbaars and P.M. Petroff, Appl. Phys. Lett 63 (1993) 3203.
[3] P. Chen, Q. Xie, A. Madhukar, Li Chen and A Konkar, J. Vac. Sci. Technol. B 12 (1994) 2568.
[4] J. Oshinowo, M. Nishioka, S. Ishida and Y. Arakawa, Appl. Phys. Lett 65 (1994) 1421.
[5] R. Nötzel, T. Fukui, H. Hasegawa, J. Temmyo and T. Tamamura, Appl. Phys. Lett 65 (1994) 2854.
[6] D.I. Lubyshev, P.P. González-Borrero, E. Marega, Jr., E. Petitprez and P. Basmaji, J. Vac. Sci. Technol. B 14 (1996) 2212.
[7] R. Nötzel, N.N. Ledentsov, L. Däweritz, K.H. Ploog and M. Hohenstein, Phys. Rev. B 45 (1992) 3507.
[8] R. Nötzel, L. Däweritz and K.H. Ploog, Phys. Rev. B 46 (1992) 4736.
[9] Q. Xie, A. Konkar, A. Kalburge, T.R. Romachandran, P. Chen, R. Cartland, A. Madhukar, H.T. Lin and D.H. Rich, J. Vac. Sci. Technol. B 13 (1995) 642.
[10] P.P. González-Borrero, D.I. Lubyshev, E. Marega Jr., E. Petitprez and P. Basmaji, J. Crystal Growth 169 (1996) 424.
[11] G.W. Bryant, Phys. Rev. B 37 (1988) 8763.
[12] M. Sugarawa, N. Okazaki, T. Fujii, Ph and S. Yamazaki, Phys. Rev. B 48 (1993) 8848.
[13] Z.Y. Xu, Z.D. Lu, Z.L. Yuan, X.P. Yang, B.Z. Zheng, J.Z. Xu, W.K. ge, Y. Wang and L.L. Chang, Superlattice Microstruct. 20 (1996).
[14] D.I. Lubyshev, P.P. González-Borrero, E. Marega, Jr., E. Petitprez, N. La Scala, Jr. and P. Basmaji, Appl. Phys. Lett. 68 (1996) 205.
[15] D.I. Lubyshev, Yu.A. Pusep, P.P. González-Borrero, E. Marega Jr., E. Petiprez, N. La Scala Jr. and P. Basmaji, unpublished.
[16] Y. Nabetani, T. Ishikawa, S. Noda and A. Sasaki, J. Appl. Phys. 76 (1994) 347.

ELSEVIER

Journal of Crystal Growth 175/176 (1997) 771–776

JOURNAL OF CRYSTAL GROWTH

InAs/GaAs self-assembled quantum dots grown by ALMBE and MBE

A. Bosacchi, P. Frigeri, S. Franchi*, P. Allegri, V. Avanzini

CNR-MASPEC Institute, Via Chiavari 18a, I-43100 Parma, Italy

Abstract

We have studied the effect of different growth schemes of structures with InAs/GaAs self-assembled dots on the size of dots and, then, on their PL features. Lower confining layers, dots and upper confining layers were grown by different techniques (ALMBE and MBE), at different growth temperatures and by using growth interruptions. Both AFM and PL show that the ALMBE is particularly suited to grow relatively large dots with sharp size distributions at relatively large InAs coverages without incurring dot coalescence. Moreover, the low temperature ALMBE growth of caps reduces the interaction between dots and caps. The control of dot sizes and of dot/cap interaction results in PL emissions shifted towards the spectral windows of photonic interest. In particular, structures with ALMBE dots and with optimized confining layers show a significantly bright emission at 1.26 μm at 300 K.

PACS: 68.55

Keywords: Quantum dots; MBE; ALMBE

1. Introduction

Self-assembled dots originating from deposits of highly strained materials on lattice-mismatched substrates are very simple systems which show low-dimensionality effects that can be exploited both for applications and for fundamental studies on semiconductor physics and crystal growth [1–3]. Among the most important parameters of the dot populations, there are the island size and its distribution; the size determines the luminescence emission energy from the dots, while the size distribution affects the full widths at half maximum (FWHMs) of the transitions. InAs/GaAs dots generally have dimensions such that their emission occurs at $\leqslant 1$ μm at low temperatures; therefore, in order to have room temperature (RT) emissions within the spectral windows of photonic interest, such as the 1.3 μm one, the dot sizes should be substantially increased, in order to reduce the extent of carrier confinement. Emissions at 1.24 μm at RT have been obtained from structures with

* Corresponding author. Fax: + 39 521 269 209; e-mail: franchi@prmasp.bo.cnr.it.

0022-0248/97/$17.00 Copyright © 1997 Elsevier Science B.V. All rights reserved
PII S0022-0248(96)01031-7

almost-coalesced dots and, then, with reduced carrier confinement [4]. However, uncontrolled coalescence as a tool for increasing the dot dimensions should be avoided, since it may result in the formation of dots which include misfit dislocations, that drastically reduce the PL efficiency [5]. The achievement of FWHMs lower than the thermal energy at room temperature ($kT \sim 25$ meV) is of paramount importance so as not to spoil the advantages of the zero- dimensionality of the structures.

While MBE and MOVPE are widely used for the preparation of dot structures, new growth techniques are investigated [6–8] since they may give interesting benefits. Atomic layer MBE (ALMBE, also termed as migration enhanced epitaxy, MEE [9]) is considered interesting since the alternate supply of anions and cations gives rise to a significant increase of cation surface migration. It is expected that this feature would result in sharper size distributions of larger dots, since it may cause the selective enlargement of existing dots, instead of the continuous nucleation of new small islands. Moreover, the enhanced migration of cations allows the growth of InGaAs alloys at low temperatures where the In segregation towards the growth front is substantially minimized [10]; this should reduce the interaction of quantum dots with the upper confining layers in structures intended for luminescence; such an interaction may reduce the dimensions of dots and substantially modify their shape [11].

The aim of this work is to study: (i) how the sizes and the size distribution of self-assembled InAs/GaAs quantum dots are affected by the growth technique (MBE or ALMBE), (ii) how the growth parameters and procedures of the upper confining layers influence the interaction between the dots and the caps, and then, the dot dimensions and the photoluminescence (PL) emission energies and (iii) which are the design and preparation parameters that give efficient PL at 300 K in the spectral windows of photonic interest.

2. Experimetal details

The InAs/GaAs dot structures were grown by MBE and ALMBE under different conditions and with different InAs coverages θ; they consist: (i) of GaAs buffer layers, (ii) of InAs dots, and (iii), only in the case of the structures intended for PL studies, of GaAs upper confining layers. The buffer layers were generally grown by MBE at 580°C; then the growth was interrupted for 210 s to lower the growth temperature to that required for the dot deposition. The dots were deposited at 460°C either by MBE or ALMBE. The upper confining layers were grown after interruptions of 210 s by ALMBE (at 360°C or 460°C) or by MBE; in the latter case, 5 ML of GaAs were deposited at 360°C so as to limit In segregation [10] and, then, the effects on dot morphology due to dot interaction with caps; the topmost 10 nm of the caps were grown at temperatures increasing up to 580°C.

As_4/Ga and As_4/In beam equivalent pressure ratios of ~ 12 and ~ 45 were used; the In and Ga fluxes were adjusted for InAs and GaAs growth rates of 0.12 and 2.8 ML/s, respectively; during ALMBE, the growth rate was set at 0.2 ML/cycle and the As supply time was chosen so as to give a sharp (2×4) surface reconstruction at the end of the As cycle. The substrates were radiatively heated at growth temperatures T_g measured by a suitable optical pyrometer for $T_g \geqslant 450$°C and by a thermocouple (TC) not in direct contact with the substrate for $T_g < 450$°C. For $T_g < 450$°C, the TC readings were corrected by the difference (~ 200°C) between the TC and the optical pyrometer values measured at $T_g > 450$°C. The coverages were determined by using the growth rate measured by observing the 2D–3D growth transition on a calibration substrate just before the preparation of the dots under investigation and by assuming that the transition takes place at an InAs coverage $\theta_{tr} = 1.6$ ML. This value is consistent with that deduced from the measurement of the growth rate by means of RHEED oscillations; moreover, it is very close to that (1.57 ML) determined by very careful experiments described in Ref. [12], under slightly different conditions; it should be recalled, however, that the values of θ_{tr} are not very sensitive to growth conditions [5].

The PL spectra were taken in the temperature range 10–300 K with a spectral resolution of 0.5 meV, and were excited by the blue line of an Ar^+ laser, using power densities as small as 0.5 W/cm^2.

Topographic images of uncapped dots were taken by contact-mode Atomic Force Microscopy (AFM) under constant probe force conditions. The measurements were performed using silicon nitride cantilevers and tips with curvature radii of ~20 nm. Then, the images were analyzed in order to derive the mean lateral size and the height distributions of dots. In the analysis, the convolution effects of AFM tips were not taken into account, but they are the same for all the lateral size distributions discussed here.

3. Results and discussion

Let us compare first dots grown by ALMBE and by MBE at temperatures of 460°C. In Fig. 1a and Fig. 1b we show the AFM images of dots grown by ALMBE and MBE at 460°C, respectively, with InAs coverages of 3.0 ML. It is very interesting to note that for relatively large coverages the dots grown by MBE tend to coalesce more extensively than the ALMBE ones, and that the uncoalesced dots have larger lateral size when they are grown by ALMBE. Further details can be deduced by the inspection of Fig. 2 where we show the distribution of lateral sizes of dots grown with InAs coverages of 2.4 and 3.0 ML. The main results are that: (i) for both coverages the dots grown by ALMBE have mean lateral sizes larger than that of the MBE counterparts (19 versus 14 nm and 21 versus 16 nm, for $\theta = 2.4$ and 3.0 ML, respectively) and (ii) the lateral size distributions are always sharper in the case of ALMBE dots. Moreover, also the height distribution (not shown here) are peaked at larger values of θ when ALMBE dots are considered (4.2 versus 2.8 nm and 5.0 versus 3.8 nm, for $\theta = 2.4$ and 3.0 ML, respectively). The coalescence of MBE dots for $\theta = 3.0$ ML can be also deduced from the analysis of Fig. 2 that shows that MBE dots have a lateral size distribution with a tail and a possible small peak at large lateral sizes (~50 nm); these features are completely absent in the case of ALMBE dots. The data relative to structures with different coverages (not presented here) show that the coalescence of dots begins at coverages of ~2.4 ML and of ~3.6 ML, for MBE and ALMBE, respectively. The value relative to MBE is close to that

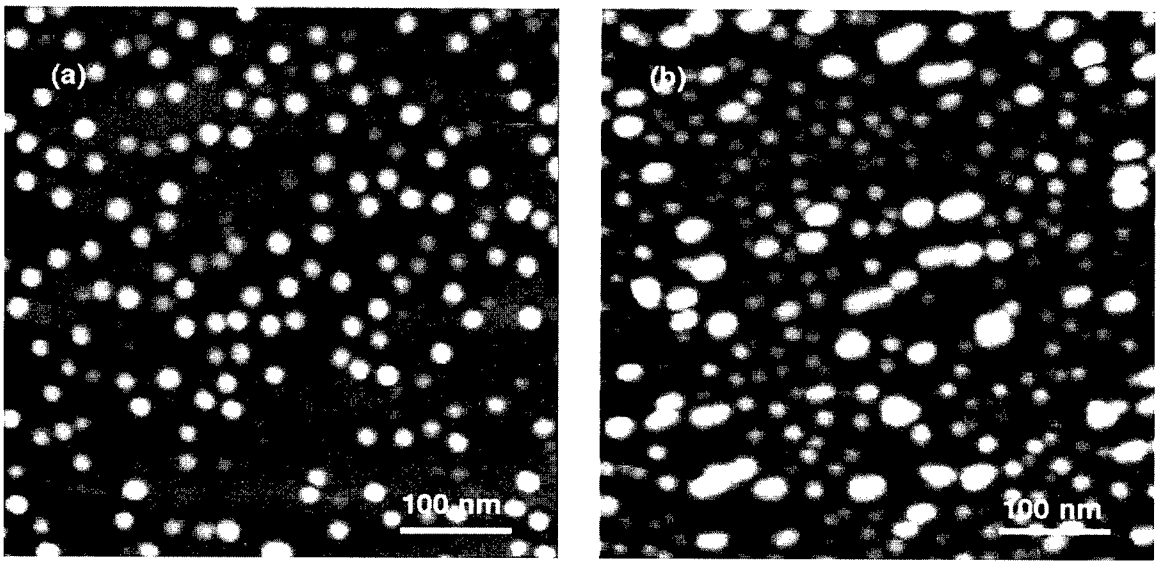

Fig. 1. AFM micrograph of InAs/GaAs dots grown by ALMBE (panel a) and by MBE (panel b) at 460°C. The InAs coverage is 3.0 ML. The dots have been deposited on a MBE GaAs layer grown at 580°C, after a 210 s interruption. The ALMBE dots have been grown in 15 ALMBE cycles. The image has been obtained by a tip with a 20 nm radius.

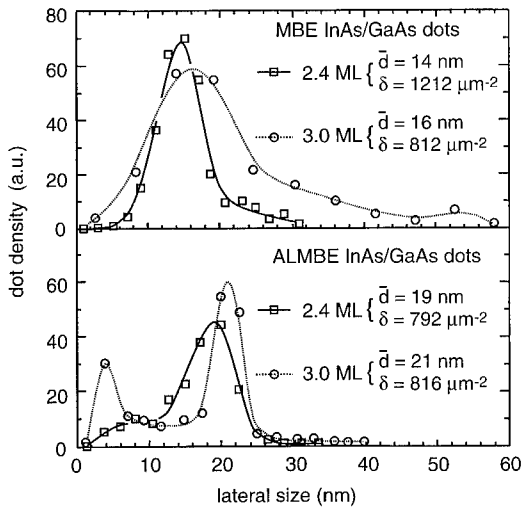

Fig. 2. Distributions of lateral sizes of dots grown by MBE and ALMBE with InAs coverages of 2.4 and 3.0 ML. The dots have been prepared under the conditions described in the caption of Fig. 1. The most frequent lateral size ($\bar{d}$) and the dot density (δ) are also given. In the analysis of AFM images the convolution effect due to the 20 nm radius of the AFM tip is not taken into account.

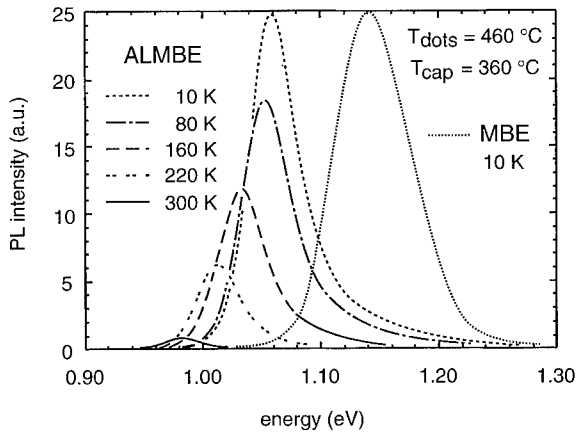

Fig. 3. Photoluminescence spectra of InAs/GaAs quantum dots grown by ALMBE and by MBE at 460°C with InAs coverages of 3.0 ML; in both cases (ALMBE and MBE dots) the upper confining layers have been prepared at 360°C by ALMBE and the dots have been deposited on a MBE GaAs layer grown at 580°C, after a 210 s interruption. The spectral resolution and the excitation power are 0.5 meV and 0.5 W/cm^2, respectively.

(2.18 ML) very recently measured by Madhukar and coworkers [12]. For ALMBE dots and $\theta \sim 3.0$ ML, a distribution of tiny dots (with mean lateral size of $\sim$4 nm) shows up, which is absent at lower coverages and in MBE structures.

The size features discussed so far have implications also on the PL of dot structures; by comparing different sets of samples grown by both techniques at 460°C and capped with GaAs layers grown by ALMBE at 360°C, we observe that the photoluminescence (PL) of ALMBE dots have (Fig. 3): (i) energies smaller and (ii) FWHMs narrower than those of the corresponding MBE ones; these features are consistent with the larger lateral sizes and heights (at the same ML coverages) of ALMBE dots and with their sharper size distributions. This observation is particularly interesting since it suggests that ALMBE is a viable technique for the growth of relatively large dots, suitable for the fabrication of photonic devices.

Let us now turn our attention to the effects of growth conditions of the upper confining layers on the PL properties of self-assembled dots. Therefore, we compare first structures with dots grown by MBE at 460°C with coverages of 2.0 ML and with caps prepared either by MBE (at 360°C for 5 ML and then at 580°C) or by ALMBE at 360°C. While in the former case the PL emission is at $\sim$1.26 eV at 10 K, the ALMBE capped structures have emissions at energies lower by $\sim$0.1 eV. This observation suggests that growing caps by MBE results in a substantial modification of dots, even if we grew the first 5 ML of the GaAs cap at sufficiently low temperatures to reduce the effects of In segregation [10], if the low-temperature grown layer was thick enough to cover the dots. On the other hand, the PL FWHMs of ALMBE capped structures are somewhat larger ($\sim$70 meV) than that of the MBE counterparts ($\sim$50 meV), thus suggesting that the conditions following the growth of dots affect their size uniformity.

Then, we consider the effect of the growth temperature (360°C versus 460°C) of ALMBE caps on ALMBE dots deposited at 460°C with InAs coverages of 2.4 ML. The results show that the emission energies are 1.04 and 1.25 eV for caps deposited at 360°C and 460°C, respectively, thus suggesting that the ALMBE growth of caps at relatively high

temperatures affects the size dots and, consequently, increases the confinement of carriers.

As for the bottom confining layers, we observe that much more efficient luminescence is obtained from dot structures where the MBE growth of buffers at relatively high temperatures (580°C) is followed by an interruption of 210 s to lower the growth temperature to that required for the dot deposition. Other schemes investigated were the deposition of thin ALMBE layers grown at the temperatures used for the ALMBE preparation of dots at 460°C, with and without growth interruptions prior to the deposition of dots.

In Fig. 3, we show the PL spectra at different temperatures of structures grown under the optimum conditions found in this work; the structures consist of MBE bottom confining layers followed by growth interruptions, ALMBE dots deposited at 460°C with InAs coverages of 3.0 ML and ALMBE caps grown at 360°C (for comparison we report the 10 K spectrum of a similar structure, but with the dots deposited by MBE); the interesting feature is that we observe a significantly bright PL at 300 K at 1.26 μm, excited by power densities as small as 0.5 W/cm^2. This is a result of great interest for the photonic exploitation of quantum dot structures in the 1.3 μm spectral window.

4. Conclusions

We have studied the effect of different growth schemes of structures with InAs/GaAs self-assembled dots on: (i) the size of dots and (ii) their PL features. The results show that ALMBE is very effective in growing relatively large dots at relatively large InAs coverages without incurring dot coalescence, that may result in the formation of misfit dislocations. Moreover, we have shown that the growth of the upper confining layer by ALMBE at low temperatures (360°C) gives rise to a much lesser interaction between dots and caps (and, then, in a lesser decrease of the dot effective size) than the other investigated schemes, such as the growth by ALMBE (at 460°C) or by MBE (5 ML at 360°C and 10 nm at 580°C). The larger dot lateral size and the lower reduction of dot size due to cap–dot interaction results in dot structures emitting at lower energies and, then, more suited for photonic applications. For instance, structures with MBE dots/MBE caps, MBE dots/ALMBE caps and ALMBE dots/ ALMBE caps and with InAs coverages of 3 ML have 10 K emissions at 1.01, 1.08 and 1.17 μm, respectively. The last structure has an intense 300 K emission at 1.26 μm. Our results show that the advantage of ALMBE in growing dot structures is twofold since the enhanced cation surface migration (i) results in larger dots with sharper size distributions since it allows the selective enlargement of existing dots, instead of the continuous nucleation of new small islands, and (ii) allows the growth at lower temperatures where the cap–dot interaction that reduces the effective dimensions of the dots and modify their shape is substantially decreased.

Acknowledgements

The work has been partially supported by the CNR PS "Materiali e Dispositivi per Optoelettronica e Microelettronica".

References

[1] J.Y. Marzin, J.M. Gérard, O. Cabrol, B. Jusserand and B. Sermage, Nuovo Cimento D 17 (1995) 1285; J.M. Gérard, in: Confined Electron and Photon New Physics and Applications, Eds. C. Weisbuch and E. Burstein, NATO ASI Series (Plenum, New York, 1994).
[2] D. Bimberg, N.N. Ledentsov, M. Grundmann, N. Kirstaedter, O.G. Schmidt, M.H. Mao, V.M. Ustinov, A.Y. Egorov, A.E. Zhukov, P.S. Kopev, Z.I. Alferov, S.S. Ruvimov, U. Gosele and J. Heydenreich, Phys. Status Solidi (b) 194 (1996) 159.
[3] A. Madhukar, J. Crystal Growth 163 (1996) 149.
[4] A. Tackeuchi, Y. Nakata, S. Muto, Y. Sugiyama, T. Inata and N. Yokoyama, Jpn. J. Appl. Phys. (1995) L405.
[5] A. Sasaki, J. Crystal Growth 160 (1995) 27.
[6] G.E. Tsyrlin, A.O. Golubok, S.Y. Tipisev and N.N. Ledentsov, Semiconductors 29 (1995).
[7] N.N. Ledentsov, P.D. Wang, C.M.S. Torres, A.Y. Egorov, M.V. Maximov, V.M. Ustinov, A.E. Zhukov and P.S. Kopev, Phys. Rev. B 50 (1994) 12171.
[8] K. Mukai, N. Ohtsuka, H. Shoji and M. Sugawara, Appl. Phys. Lett. 68 (1996) 3013.

[9] For a review, see: Y. Horikoshi, Semicond. Sci. Technol. 8 (1993) 1032.
[10] See, for example: A. Bosacchi, F. Colonna, S. Franchi, P. Pascarella, P. Allegri and V. Avanzini, J. Crystal Growth 150 (1995) 185, and references therein.
[11] X.W. Lin, J. Washburn, Z. Liliental-Weber, E.R. Weber, A. Sasaki, A. Wakahara and Y. Nabetani, Appl. Phys. Lett. 65 (1994) 1677.
[12] N.P. Kobayashi, T.R. Ramachandran, P. Chen and A. Madhukar, Appl. Phys. Lett. 68 (1996) 3299.

ELSEVIER

Journal of Crystal Growth 175/176 (1997) 777–781

JOURNAL OF CRYSTAL GROWTH

Formation of self-organized $In_{0.5}Ga_{0.5}As$ quantum dots on GaAs by molecular beam epitaxy

Jen-Inn Chyi[a,*], Tzer-En Nee[b], Ching-Ting Lee[b], Jia-Lin Shieh[a], Jen-Wei Pan[a]

[a] *Department of Electrical Engineering, National Central University, Chung-Li 32054, Taiwan, ROC*
[b] *Institute of Optical Sciences, National Central University, Chung-Li 32054, Taiwan, ROC*

Abstract

Self-organized $In_{0.5}Ga_{0.5}As$ quantum dots have been successfully grown on vicinal GaAs substrates by molecular beam epitaxy. The density of the quantum dots can be changed by nucleating the dots under different As overpressure. Substrate tilt angle of 15° results in much larger dot size and density than that of 4° due to the closely spaced step edges on the surface. Through investigations of the dots grown on $In_{0.1}Ga_{0.9}As$ buffer, the strain energy of the buffer layer is also found to be an important factor that affects the size and density of the quantum dots.

PACS: 68.55.Bd; 68.55.Jk

Keywords: Quantum dots; Step-bunching; Molecular beam epitaxy

1. Introduction

Semiconductor quantum dots is an area of great interest for low-dimensional quantum physics and devices. Since ex situ processes such as lithography, etching, and regrowth cannot avoid the surface effects, process-induced damages, and rough heterostructure interface, which seriously deteriorate the properties of the quantum dot structures, the formation of self-organized quantum dots during epitaxial growth becomes one of the key techniques for the realization of high-quality quantum devices. This technique basically relies on the lattice strain and/or the bunched steps to induce coherent island growth at the edge of the terraces. Both molecular beam epitaxy (MBE) [1, 2] and metalorganic vapor-phase epitaxy (MOVPE) [3, 4] have been successfully used to demonstrate the strain-induced self-organization. Since the quantum dots formed by this method do not suffer from the adverse effects mentioned above, a number of InGaAs and InAs quantum dot lasers have been realized [5, 6]. Nevertheless, further efforts have to be made to lead to the performance as expected. The control of size, density, and arrangement of the quantum dot

* Corresponding author. Fax: + 886 3 425 5830; e-mail: chyi@mbox.ee.ncu.edu.tw.

0022-0248/97/$17.00 Copyright © 1997 Elsevier Science B.V. All rights reserved
PII S0022-0248(96)01034-2

is one of the essential tasks for this purpose. In this work, we have investigated the effects of several growth parameters, such as As overpressure, substrate tilt angle, strained buffer layer, on the formation of $In_{0.5}Ga_{0.5}As$ self-organized quantum dots on GaAs by molecular beam epitaxy. The factors that influence the nucleation of InGaAs quantum dots on GaAs are discussed.

2. Experimental procedure

The samples investigated were grown by solid-source molecular beam epitaxy. Vicinal GaAs substrates (4° and 15° towards (1 1 1)A) were used in this work for comparison. The surface reconstruction during growth was monitored by reflection high-energy electron diffraction (RHEED). After oxide desorption, a 200 nm thick GaAs buffer layer was grown in the step-flow regime, i.e. low V/III flux ratio at 580°C, which led to the (3×1) surface reconstruction. In order to enhance the step-bunching effect, which facilitates the formation of self-organized quantum dots, the GaAs buffer was annealed at 580°C for 30 min before the substrate temperature was lowered to 520°C for the deposition of InGaAs quantum dots. The resultant step edges, running parallel to the $[1\,\bar{1}\,0]$ direction, were found to be uniformly distributed over a large area as shown in Fig. 1. When the substrate temperature was reduced to 520°C, the RHEED pattern changed from (3×1) to (2×4). The $In_{0.5}Ga_{0.5}As$ quantum dots were then grown with interruptions corresponding to 0.5 monolayer (ML) of $In_{0.5}Ga_{0.5}As$ and 5 s of As_4 irradiation for each period. The growth was stopped as the RHEED pattern transformed from a streaky pattern to a spotty pattern, indicating the presence of three-dimensional islands on the growing surface. In this work, quantum dots were formed after the deposition of 5 ML of $In_{0.5}Ga_{0.5}As$ at a growth rate of 0.5 ML/s. It was found that a thicker layer was needed to form the quantum dots if lower growth rate was used. The $In_{0.5}Ga_{0.5}As$ quantum dots were investigated using atomic force microscopy (AFM). The AFM images were taken in the contact mode with a scan rate of typically 1 Hz.

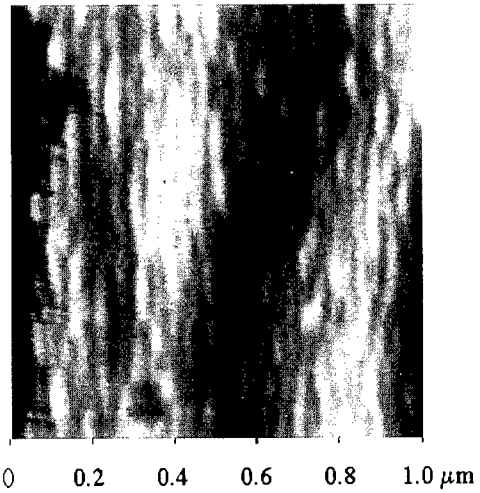

Fig. 1. Atomic force micrograph of the bunched steps formed on 4°-off (1 0 0) GaAs substrate.

3. Results and discussion

Images taken by AFM show that the self-organized $In_{0.5}Ga_{0.5}As$ quantum dots are formed spontaneously at the edge of the terraces. Shown in Fig. 2a is the image of the quantum dots formed on the 4°-off substrate at 520°C. The central blurry area is caused by successive measurements. The size of these well-organized InGaAs quantum dots is about 25 nm in diameter and 3 nm in height. A lower density of quantum dots, as shown in Fig. 2b, can be obtained by commencing the growth under an As-free condition, i.e. when the As shutter remains closed during the annealing and the cooling steps. The dot density decreased from about 3.6×10^{10} to 1.2×10^{10} cm^{-2}, while the size remains about the same. This is attributed to the longer diffusion length at the growing surface for the group III adatoms under low As background conditions. The effect of the diffusion length was also examined by growing the quantum dots using alternating (In, Ga) and As_4 beams. This growth scheme is supposed to enhance the migration of the group III adatoms on the growing surface, and leads to two-dimensional growth. No quantum dots, except for the bunched steps, were observed when the total thickness of the InGaAs was about

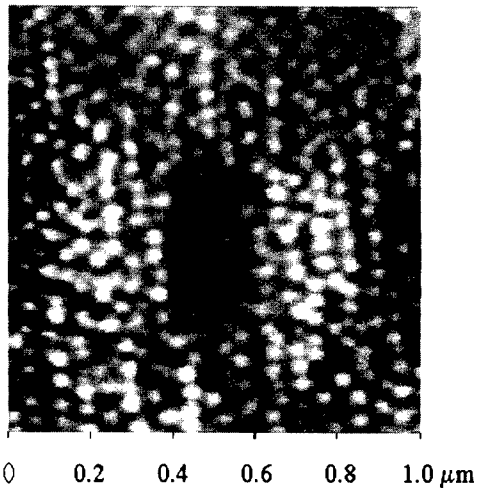

Fig. 2. Atomic force micrograph of the MBE grown InGaAs quantum dots on 4°-off (1 0 0) GaAs substrate with (a) As shutter open and (b) As shutter closed before the growth.

7.5 ML. It can be concluded that more deposition is needed to form quantum dots in this growth scheme because the wetting layer is thicker in this case.

However, the dots grown on the 15°-off substrate exhibit significantly different characteristics as compared with the dots on the 4°-off substrate.

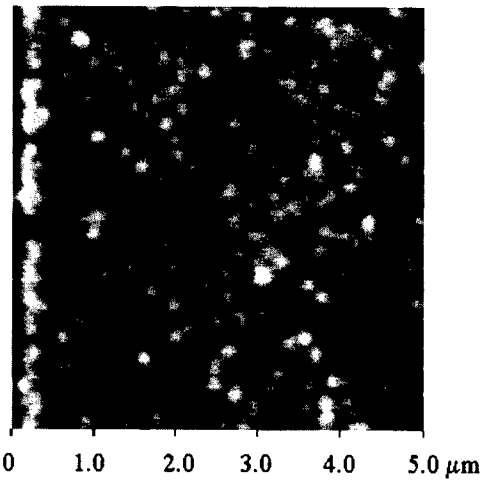

Fig. 3. Atomic force micrograph of the MBE grown InGaAs quantum dots on 15°-off (1 0 0) GaAs substrate.

Fig. 3 shows the AFM images of the quantum dots formed on these two substrates side-by-side after the deposition of 3.5 ML of InGaAs at a growth rate of 0.7 ML/s. The size of the dots on the 15°-off substrate is about 190 nm, which is much larger than that of the dots on the 4°-off substrate. It is believed that the smaller distance between the terrace edges on the 15°-off substrate limits the diffusion of the adatoms during the growth and a large number of nucleation sites was provided for the formation of three-dimensional islands. Therefore, the dots thus formed have larger size due to their energetically favorable surface configuration. Since their size is larger than the terrace, the dots overlap with each other and lose their regularity.

We have also studied the effects of surface strain on the formation of quantum dot since the nucleation of quantum dot is closely related to the surface energy which may be modified by lattice strain. Fig. 4 shows the AFM images of the $In_{0.5}Ga_{0.5}As$ quantum dots formed on a 15 nm thick pseudomorphic $In_{0.1}Ga_{0.9}As$ buffer and a 0.2-μm-thick strain-relaxed $In_{0.1}Ga_{0.9}As$ buffer, respectively. These dots were formed by depositing 5 ML of $In_{0.5}Ga_{0.5}As$ at 520°C. Obviously, the pseudomorphic $In_{0.1}Ga_{0.9}As$ buffer results in higher dot density, even higher than that for the dots grown on GaAs buffer. This is attributed to the higher

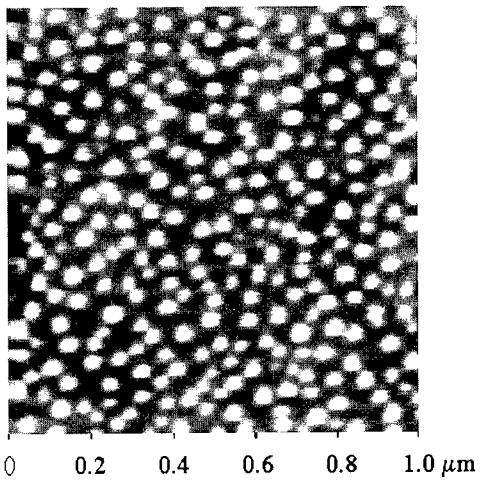

Fig. 4. Atomic force micrograph of the MBE grown InGaAs quantum dots on (a) 15 nm-thick pseudomorphic $In_{0.1}Ga_{0.9}As$ and (b) 0.2 μm-thick strain-relaxed $In_{0.1}Ga_{0.9}As$ buffer layers.

strain energy stored in the pseudomorphic layer, which facilitates three-dimensional growth. This $In_{0.1}Ga_{0.9}As$ pseudomorphic layer plays the same role as the wetting layer in the Stranski–Krastanov growth mode often observed in the growth of (In, Ga)As quantum dots on GaAs. Using such a strained buffer layer, quantum dots of smaller size and high density can be obtained as compared to

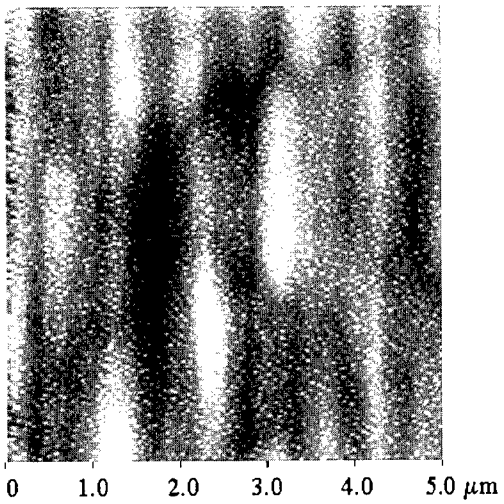

Fig. 5. Atomic force micrograph of the MBE grown InGaAs quantum dots on 0.2 μm-thick strain-relaxed $In_{0.1}Ga_{0.9}As$ buffer layers showing the modulation of dot density by the cross-hatch patterns.

the case of direct growth on GaAs. This might be beneficial for the realization of low-threshold quantum dot lasers since both quantum confinement and gain region are increased, although the dots do not seem to be well-organized. On the other hand, the density for the dots grown on the relaxed buffer is slightly lower than that for the direct growth while the dot size is about the same. It implies that the lattice mismatch between $In_{0.1}Ga_{0.9}As$ and $In_{0.5}Ga_{0.5}As$ is the dominant factor in the dot nucleation process. More interestingly, it was found that the dot density on the relaxed buffer is modulated by the cross-hatching resultant from strain relaxation. As shown in Fig. 5, higher dot density is observed at the top region of the hatch. This is closely related to the lower surface energy at the top of the hatch [7]. Since most of the adatoms are driven towards the more energetically favorable region, the nucleus of quantum dots, the dot density is enhanced at this region. Similar behavior has also been observed for the growth of vertically stacked InAs quantum dots on GaAs where the dots beneath provide lower surface energy for the successive nucleation of InAs dots [8]. Therefore, perfect vertically aligned quantum dot structure is spontaneously formed.

4. Conclusion

Self-organized $In_{0.5}Ga_{0.5}As$ quantum dots have been grown on vicinal (1 0 0) GaAs by molecular beam epitaxy. Parameters that affect the configuration of the quantum dots, such as substrate tilt angle, As background pressure, and the strain in the buffer layer, have been investigated. The associated surface strain energy and free energy for the adatoms are the key factors in the formation of the quantum dots. The size and density of the quantum dots can be varied accordingly for various applications.

Acknowledgements

The authors thank the support of MBE laboratory of Optical Science Center, NCU. This work was partly supported by the National Science Council under contract No. NSC85-2215-E-008-022.

References

[1] D. Leonard, K. Pond and P.M. Petroff, Phys. Rev. B 50 (1994) 11687.
[2] D. Bimberg, M. Grundmann, N.N. Ledentsov, S.S. Ruvimov, P. Werner, U. Richter, J. Heydenreich, V.M. Ustinov, P.S. Kop'ev and Z.I. Alferov, Thin Solid Films 267 (1995) 32.
[3] M. Kitamura, M. Nishioka, J. Oshinowo and Y. Arakawa, Appl. Phys. Lett. 66 (1995) 3663.
[4] R. Notzel, J. Temmyo, T. Tamamura, T. Fukui and H. Hasegawa, Jpn. J. Appl. Phys. 34 (1995) L872.
[5] H. Shoji, K. Mukai, N. Ohtsuka, M. Sugawara, T. Uchida and H. Ishikawa, IEEE Photon. Technol. Lett. 7 (1995) 1385.
[6] N. Kirstaedter, N.N. Ledentsov, M. Grundmann, D. Bimberg, V.M. Ustinov, S.S. Ruvimov, M.V. Maximov, P.S. Kop'ev, Zh.I Alferov, U. Richter, P. Werner, U. Gosele and J. Heydenreich, Electron. Lett. 30 (1994) 1416.
[7] I.V. Markov, Crystal Growth for Beginners (World Scientific, New Jersey, 1995) ch. 4, p. 405.
[8] G.S. Solomon, J.A. Trezza, A.F. Marshall and J.S. Harris, Jr., Phys. Rev. Lett. 76 (1996) 952.

ELSEVIER

Journal of Crystal Growth 175/176 (1997) 782–786

JOURNAL OF CRYSTAL GROWTH

MBE growth and magnetotunnelling transport properties of a single GaAs/AlAs/GaAs barrier incorporating InAs quantum dots

M. Henini*, I.E. Itskevich, T. Ihn, P. Moriarty, A. Nogaret, P.H. Beton, L. Eaves, P.C. Main, J.R. Middleton, J.S. Chauhan

Department of Physics, University of Nottingham, Nottingham NG7 2RD, UK

Abstract

We describe the growth and investigation of a novel type of structure in which self-organised InAs quantum dots are incorporated in the AlAs tunnelling barrier of an n–i–n single-barrier GaAs/AlAs/GaAs heterostructure. The low-temperature current–voltage curves exhibit a series of pronounced peaks which are absent in a control sample grown without InAs in the barrier. By studying their behaviour in a magnetic field B, we attribute these peaks to single-electron tunnelling through single discrete zero-dimensional states of individual InAs dots in the barrier.

1. Introduction

The fabrication of low-dimensional structures, such as quantum dots or wires, has been intensively pursued in recent years in order to realize novel devices using confinement effects. One of the promising fabrication methods is to use self-organised three-dimensional structures which are formed during the initial stage of heteroepitaxy growth in lattice-mismatched systems, called the Stranski–Krastanov (SK) growth mode. In the SK growth mode the mismatched epitaxy is initially accommodated by biaxial compression in a layer-by-layer (2D) growth region, traditionally called the wetting layer. After deposition of a few monolayers the strain energy increases and the development of islands (3D) becomes more favourable than planar growth. In the III–V semiconductor material system, SK growth has been used to grow InAs islands on GaAs and it has been shown that the size fluctuation of dots is relatively small ($\leqslant 10\%$) and the small dots and surrounding host matrix are dislocation-free and strained coherently with GaAs. It has been reported that the InAs growth mode changes from 2D to 3D upon the deposition of less than 2 ML of InAs. To date, studies have been limited to the optical properties of self-organised InAs quantum dots on GaAs.

In this paper we describe the growth of a novel type of structure in which the dots are incorporated in the AlAs tunnelling barrier of an n–i–n single

*Corresponding author. Fax: +44 115 951 5180; e-mail: ppzmh@ppn1.nott.ac.uk.

0022-0248/97/$17.00 Copyright © 1997 Elsevier Science B.V. All rights reserved
PII S0022-0248(96)01035-4

barrier GaAs/AlAs/GaAs heterostructure. This type of structure provides us with a novel means of studying the quantum dots by magnetotunnelling spectroscopy.

2. Experimental procedure

The epitaxial layers were deposited by molecular beam epitaxy (MBE) using a Varian Gen II system on 2 in (1 0 0) n^+-GaAs substrate oriented within $\pm 0.5°$. The preparation of the MBE machine followed the method adopted previously to give optimum quality of material [1]. Prior to loading, the substrates were cleaned using a 5 min ultrasonic degrease in Summa-Clean followed by a 5 h soak in Summa-Develop. Both solutions are commercially available choline etches [2]. The wafers were rinsed in deionised water and spun dry before being mounted onto Mo blocks with In. The substrates were then heated in the growth chamber at 600°C for 30 min in order to desorb the thin oxide film on the substrates.

The sample consisted of the following layers, in order of growth from the substrate: (i) a 1 μm thick buffer layer of GaAs doped at $n = 4 \times 10^{18}$ cm^{-3}; (ii) 100 nm of GaAs, $n = 2 \times 10^{16}$ cm^{-3}; (iii) a 100 nm thick spacer layer of undoped GaAs; (iv) an undoped AlAs barrier of thickness 5.1 nm; (v) 1.8 monolayers of InAs; (vi) an undoped AlAs barrier of thickness 5.1 nm; (vii) a 100 nm thick spacer layer of undoped GaAs; (viii) 100 nm of GaAs, $n = 2 \times 10^{16}$ cm^{-3}; and (ix) a 0.5 μm top contact layer of GaAs, $n = 4 \times 10^{18}$ cm^{-3}. The growth temperature was 550°C as monitored by a pyrometer, except during the growth of InAs when the temperature was lowered to 520°C. The growth rates are one monolayer/s (ML/s) for GaAs, 0.5 ML/s for AlAs and 0.066 ML/s for InAs. The formation of InAs islands was monitored by RHEED, and the average thickness of InAs deposited is 1.8 ML. A control sample without the InAs layer was also grown. The size and density of InAs quantum dots were estimated by SEM and STM from samples of the same design but with the growth terminated after depositing the InAs layers. The STM samples were capped with a thick arsenic layer before they were transferred to a separate UHV STM chamber.

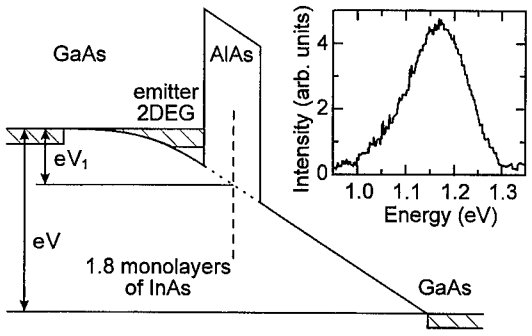

Fig. 1. A schematic energy band diagram of the sample under an applied voltage V. Inset: photoluminescence spectrum from the sample at 4.2 K.

During growth the GaAs surfaces showed a (2×4) reconstruction. The samples were rotated during growth to improve uniformity. After growth, the epitaxial surfaces were examined, using a Nomarski phase-contrast optical microscope and were found to be mirror smooth and nearly defect-free.

The graded doping in the contact layers and the undoped spacer layers adjacent to the barrier are thought to improve the performance of the devices by reducing dopant diffusion into the region close to the barrier during growth, thus reducing the number of bound impurity scatterers.

The epitaxial layers were processed into circular mesas of various diameters ranging from 30 to 400 μm by means of photolithography and wet-etching techniques. Au and AuGe were evaporated and alloyed to form ohmic contacts.

A schematic band diagram of the device under an applied bias V is shown in Fig. 1. Because of the low doping in the regions close to the barrier, an applied bias produces a 2DEG in an accumulation layer adjacent to the emitter barrier.

3. Results and discussion

The current–voltage characteristics $I(V)$, recorded for a 100 μm diameter mesa in the absence of magnetic field, are shown in Fig. 2. Forward and reverse bias correspond to electron flow from and to the substrate, respectively. An $I(V)$ curve for the

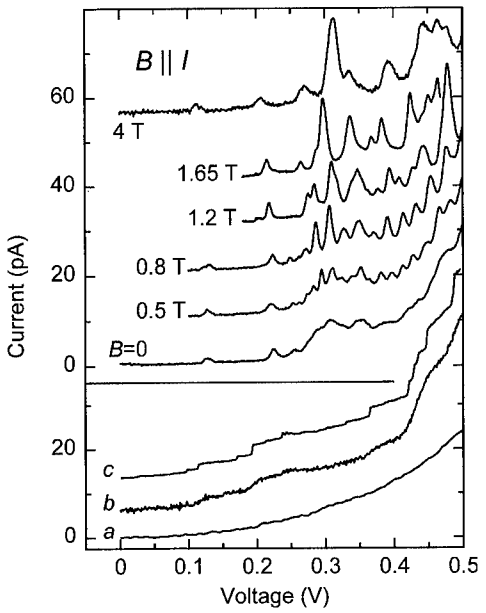

Fig. 2. The $I(V)$ characteristics of a 100 μm diameter mesa. Lower: (a) control sample; (b) for $B = 0$ in reverse bias at 4.2 K and (c) at 0.35 K. Upper: $I(V)$ in forward bias at 4.2 K at various $B \| I$. Curves are offset.

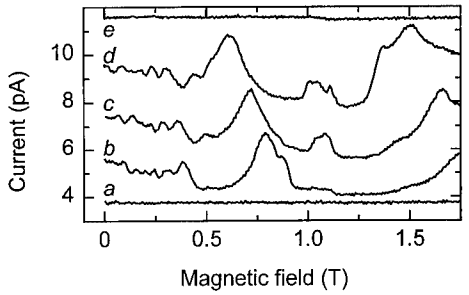

Fig. 3. $I(B)$ characteristics at various V: (a) 105 mV, (b) 114 mV, (c) 115 mV, (d) 116 mV, (e) 130 mV. Curves are offset.

control sample is also shown for comparison. Both devices have a very high impedance ($\sim 10^{12}\ \Omega$) around zero bias and exhibit a monotonically increasing background current. In addition, pronounced, low-current (a few pA) peaks, superimposed on the background current, are observed for the InAs quantum dot device for forward bias above 100 mV at 4.2 K. The peaks are absent in reverse bias at 4.2 K, where there is only indistinct structure. The asymmetry in the $I(V)$ characteristics in forward and reverse bias as shown in Fig. 2 results from the asymmetry of dot positions in the AlAs layer. The dots are grown on the centre plane of the barrier, but the AlAs layer covering the dots is effectively thinner due to the size and shape of the dots, and thus has a higher tunnelling probability than the AlAs layer on the substrate side. Thus, for reverse bias the tunnelling rate out of the dots is much smaller than the rate of tunnelling into the dots from the accumulation layer. On lowering the temperature to 0.4 K, the structure in reverse bias evolves into a set of distinct steps. The $I(V)$ curve of the control sample has no structure in either bias direction but the background current is of similar magnitude.

The peaks in $I(V)$ arise from resonant tunnelling through states in the barrier, and our observations indicate that these states are associated with the incorporation of InAs in the barrier. We have also examined the effect of magnetic field on the tunnelling current in forward bias in order to confirm that the discrete (zero-dimensional) electron states of InAs quantum dots in the barrier are the states through which the resonant tunnelling occurs. For B applied parallel to the current, the $I(V)$ curves change qualitatively as shown in Fig. 2. At fields as low as 0.4 T a series of narrow peaks arises in the curves. The peaks diverge in bias and their number falls with increasing B up to 3–4 T. Increasing B from 4 to 12 T causes the peaks to shift to lower bias with little change in shape.

Fig. 3a shows examples of $I(B)$ at constant bias V_0. If V_0 is equal or close to the bias at which a peak occurs, there are pronounced oscillations in $I(B)$. Their maxima and minima shift to smaller B with increasing V_0. The $I(B)$ curves exhibit no structure at V_0 just below or above a peak in $I(V)$.

The energy spectrum of the 2DEG in the emitter-accumulation layer splits into a set of discrete Landau levels for B normal to the sample plane. Therefore, we attribute the sharp peaks in $I(V)$ to the Landau quantisation of the 2DEG in the emitter which is consistent both with the peak divergence with increasing B and with their shift to lower V. As to the oscillations in $I(B)$, these behave quite differently from magneto-oscillations earlier reported in single-barrier tunnelling devices [3], for

which the maxima should shift to higher B with increasing V_0. In our case the maxima in $I(B)$ occur when the magnetic field brings an occupied Landau level in the 2DEG in resonance with the energy levels in the barrier. In effect, both $I(V)$ and $I(B)$ probe the density of states (DOS) of the 2DEG in the emitter accumulation layer.

To estimate the size of the resonant states in the barrier, we have used the diamagnetic shift of peaks in $I(V)$ in magnetic fields applied normal to the current, i.e. parallel to the barrier plane. Applying $B \perp I$ up to 11 T causes no qualitative change in the $I(V)$ characteristics at 4.2 K. Their evolution is shown in Fig. 4a. The peak current values fall with increasing B for the lower-voltage peaks. The peak positions shift to lower voltage quadratically in B, as shown in Fig. 4b.

The variation in peak voltage is determined by the relative diamagnetic shifts of the electron state in the 2DEG and the resonant state in the barrier. Within the uncertainty in the values of parameters used, we estimate the size of the resonant barrier state to be $\approx (10 \pm 5)$ nm. This value is fully consistent with the size of InAs quantum dots measured by SEM and STM on samples of the same design but with the growth terminated after depositing the InAs layers. The samples for STM measurements were arsenic-capped in the growth chamber before being transferred to a separate STM chamber where arsenic desorption and imaging took place. From SEM and STM imaging we estimated the density of dots as $\approx 2 \times 10^{11}$ cm^{-2}, with a dot size $\approx (10 \times 10)$ nm^2. We therefore conclude that the peaks in $I(V)$ originate from the tunnelling through the electron states of the self-organised InAs dots incorporated in the barrier.

The observed decrease of peak amplitude with increasing $B \perp I$ in Fig. 4a is qualitatively similar to that reported recently for magnetotunnelling into donor states [4]. As will be discussed in another paper, this provides a separate estimate for the spatial extent of the dot wave function which is consistent with the above value.

A PL spectrum of our tunnel structure, recorded with Ge detector at He–Ne laser excitation ($\lambda = 6328$ Å) is shown in the inset of Fig. 1. The spectrum exhibits a broad line with a maximum few hundred meV below the GaAs band-gap energy.

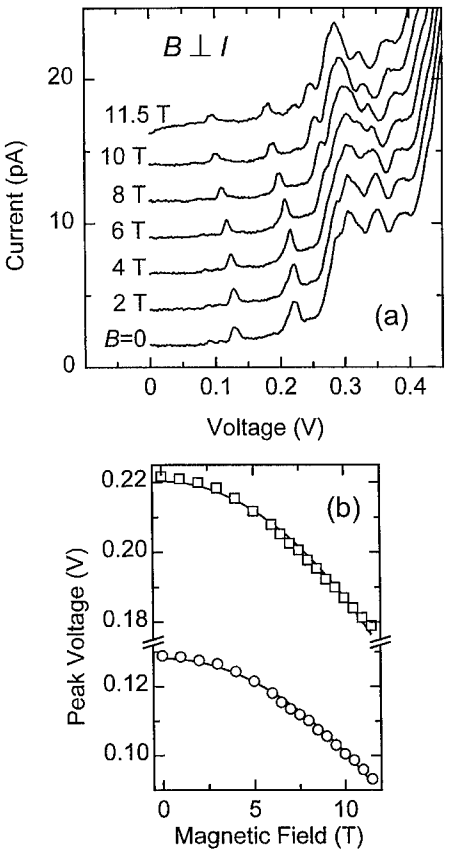

Fig. 4. (a) $I(V)$ characteristics at various $B \perp I$. Curves are offset. (b) Diamagnetic shift of lower voltage peaks in $I(V)$. Solid lines are parabolic fits.

The line corresponds to the emission from the dot ensemble and is similar to that reported by other groups [5–7].

We now discuss why we are able to resolve tunnelling through only a few single dots rather than a broad tunnelling peak due to the ensemble of dots, about 10^7 dots in a typical mesa, in analogy with the broad lines observed in PL. To understand this, note that the PL spectrum from the sample (Fig. 1) suggests that for the majority of dots the electron ground energy level is below the conduction band edge E_c, in agreement with capacitance spectroscopy studies [8]. These levels are unavailable for energy-conserving tunnelling processes. We observe tunnelling through extremal dots with electron level energies above E_c. Such dots can arise

due to fluctuations in size (30–40%), shape and strain or possible Al alloying of dots. Our picture implies that a fraction of dots should be charged at zero bias, in order to align the chemical potentials of the dot ensemble and the collector and emitter n-doped contact layers. The accumulation of the 2DEG is followed by dot discharge when the device is biased, which contributes strongly to the leverage factor dependence on voltage.

4. Conclusion

We have fabricated novel resonant tunnelling devices with buried InAs quantum dots and demonstrated resonant tunnelling through single zero-dimensional states of individual InAs dots in the barrier. The MBE technique coupled with SK growth provides us with a novel means of producing 0D tunnel structures in which we can freely potential vary the tunnel barrier heights and widths, and the alloy composition of the dots. It should also be possible to produce stacked dot structures [9] and dot structures in different index substrate planes.

Acknowledgements

We are grateful to M. Steer and M.S. Skolnick for help with PL measurements and for useful discussions. This work is supported by EPSRC (UK). I.E.I. and L.E. acknowledge the Royal Society and EPSRC for research fellowships.

References

[1] M. Henini, P.J. Rodgers, P.A. Crump, B.L. Gallagher and G. Hill, J. Crystal Growth 150 (1995) 451.
[2] Summa-clean and Summa-develop are brand name products of Mallinckrodt Inc. (Science Products Division).
[3] F.W. Sheard, L. Eaves and G.A. Toombs, Phys. Scr. T 19 (1987) 179.
[4] J.-W. Sakai, T.M. Fromhold, P.H. Beton, L. Eaves, P.C. Main and F.W. Sheard, Phys. Rev. B 48 (1993) 5664.
[5] J.-Y. Marzin, J.M. Gerard, A. Izrael, D. Barrier and G. Bastard, Phys. Rev. Lett. 73 (1994) 716.
[6] R. Heitz, M. Grunmann, N.N. Lendenstov, L. Eckey, M. Veit, D. Bimberg, V.M. Ustinov, A.Y. Egorov, A.E. Zhukov, P.S. Kop'ev and Z.I. Alferov, Appl. Phys. Lett. 68 (1996) 361.
[7] M. Grundmann, N.N. Lendenstov, O. Stier, D. Bimberg, V.M. Ustinov, P.S. Kop'ev and Z.I. Alferov, Appl. Phys. Lett. 68 (1996) 979.
[8] G. Medeiros-Ribeiro, D. Leonard and P.M. Petroff, Appl. Phys. Lett. 66 (1995) 1767.
[9] G.S. Solomon, J.A. Trezza, A.F. Marshall and J.S. Harris, Phys. Rev. Lett. 76 (1996) 952.

ELSEVIER

Journal of Crystal Growth 175/176 (1997) 787–792

JOURNAL OF CRYSTAL GROWTH

Selective MBE growth of GaAs wire and dot structures using atomic hydrogens and their electronic properties

T. Noda[a,*], Y. Nagamune[b], Y. Ohno[a], S. Koshiba[c], H. Sakaki[a,b,c]

[a] *Institute of Industrial Science, University of Tokyo, 7-22-1 Ropppongi, Minato-ku, Tokyo 106, Japan*
[b] *Electrotechnical Laboratory, 1-1-4 Umezono, Tsukuba-shi, Ibaraki 305, Japan*
[c] *Quantum Transition Project, JRDC, Park Bldg. 4F, 4-7-6 Komaba, Meguro-ku, Tokyo 153, Japan*

Abstract

The selective growth of GaAs wire and dot structures by molecular beam epitaxy in the presence of atomic hydrogen was studied on a GaAs substrate with stripe and window shaped SiN_x mask patterns. It was found that 20 nm ridges were successfully formed on long stripe patterns but the ridge width increased substantially when grown on short stripes of less than several μm. This is ascribed to the longitudinal migration of Ga flowing from the two ends of a stripe to its central zone. The incorporation of Si dopants into a 0.3 μm-wide wire was achieved. Negative magnetoresistance and conductance fluctuations indicative of the one-dimensional nature of electrons were observed. On a 2×2 μm square window pattern, a pyramidal structure with two-fold symmetry was formed, on which a GaAs dot with the lateral dimension of 100 nm was grown. Photoluminescence (PL) spectra from this dot exhibited a shoulder structure 15 meV, suggesting the filling of several discrete levels and the slow relaxation of carriers.

1. Introduction

The fabrication of 10–100 nm scale quantum wires (QWIs) and quantum dots (QDs) is important not only for device applications but also for the physics of low dimensional systems. Among various methods, selective area growth of nanostructures using SiN_x or SiO_2 mask patterns is attractive. Indeed, both metalorganic chemical vapour deposition [1–6] and molecular beam epitaxy (MBE) with the assistance of atomic hydrogen [7] have been used to produce nearly damage-free nanostructures.

The characterization of such selectively grown QWIs has been mostly done by optical methods since transport characterization requires the formation of electrical contacts and the introduction of dopants. Since various facets appear in the selective growth due to the migration of atoms from one plane to another, the shape of nanostructures is strongly influenced by boundary conditions of crystal growth including the presence of end zones for electrical contacts. It is thus indispensable to clarify these facets interaction to form quantum structures suitable for transport studies.

* Corresponding author. E-mail: noda@kyokusho.rcast.u-tokyo.ac.jp.

0022-0248/97/$17.00 Copyright © 1997 Elsevier Science B.V. All rights reserved
PII S0022-0248(96)01199-2

In this work we investigate structural features and electronic properties of *n*-GaAs wires and dots prepared by the selective MBE growth using thermally cracked atomic hydrogen [8]. Specifically, we discuss the effect of longitudinal diffusion of Ga atoms in short stripe patterns bound by two wide patterns for electrical contacts and also on a GaAs substrate with window patterns.

2. Sample prepartion

Patterns were made into a 50 nm thick SiN_x film deposited on a (1 0 0) semi-insulating GaAs substrate by using electron-beam lithography and wet chemical etching. Fig. 1a and Fig. 1b illustrate patterns for wires and dots, respectively. In Fig. 1a, stripe window is parallel to $\langle 0\,1\,1\rangle$ and is connected to 40 μm wide windows on both ends. In Fig. 1b, a 2×2 μm square window pattern is aligned along $\langle 0\,1\,0\rangle$ and $\langle 0\,0\,1\rangle$.

A GaAs substrate with these patterns was first cleaned in MBE chamber by exposing atomic hydrogen for 30 min at the substrate temperature T_s of 350°C [8]. Then, a 10 nm GaAs was deposited to smoothen the surface at T_s of 590–600°C. We raised T_s by 10–20°C and then deposited a 900 nm thick GaAs buffer layer for wire structure or a 300 nm buffer for dot structure. By this time, relatively sharp ridge structures were formed, as schematically shown in Fig. 2. Then, 10 periods of a superlattice (SL) buffer layer were grown consisting of a 5 nm AlGaAs and a 1.5 nm GaAs with 10 s of growth interruption (GI). At this point a 6 nm thick GaAs QW structure was formed which had a 5 nm AlGaAs barrier and 7 nm AlGaAs barrier on the bottom side and top side of the QW, respectively. A 60 nm Si-doped AlGaAs layer was further deposited with the donor density of 5.5×10^{17} cm^{-3} to supply electrons and the growth was completed by a 10 nm thick GaAs capping layer. During the MBE growth, thermally cracked atomic hydrogens were supplied [9] with the sample heating block rotating at the rate of 15 rpm. The cracking cell was set at about 1600°C and the hydrogen flux was 0.90 cm^3. The growth rate was 0.24 μm/h for GaAs and 0.10 μm/h for AlAs. The flux ratio As_4/Ga was 5–6. The mole fraction of Al in AlGaAs was 0.29. In this growth condition, Ga atoms impinging onto SiN_x masks desorbed efficiently with the assistance of atomic hydrogen. However, Al containing materials such as AlGaAs are hard to desorb and, therefore, form polycrystals on masks, as shown in Fig. 2.

3. Fabrication of GaAs wire structures

Fig. 2a–Fig. 2c show SEM images of a sample grown on a 1.6 μm-wide stripe pattern of Fig. 1a. Note that the growth took place selectively in the window region although a little amount of polycrystalline AlGaAs was deposited on SiN_x mask regions. The central portion of the ridge wire

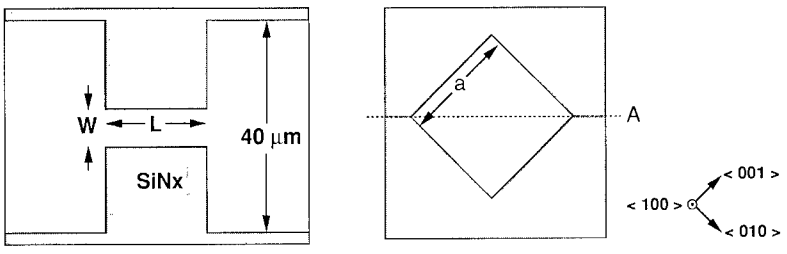

Fig. 1. Schematic illustrations of SiN_x mask patterns for the fabrication of wire (a) and dot (b) structures. A stripe pattern in the wire pattern is parrallel to $\langle 0\,1\,1\rangle$. The dimensions of the stripe window are 0.8–1.6 μm in width and 1–6 μm in length. A square pattern in the dot pattern is aligned along $\langle 0\,1\,0\rangle$ and $\langle 0\,0\,1\rangle$ with a size of 2 μm.

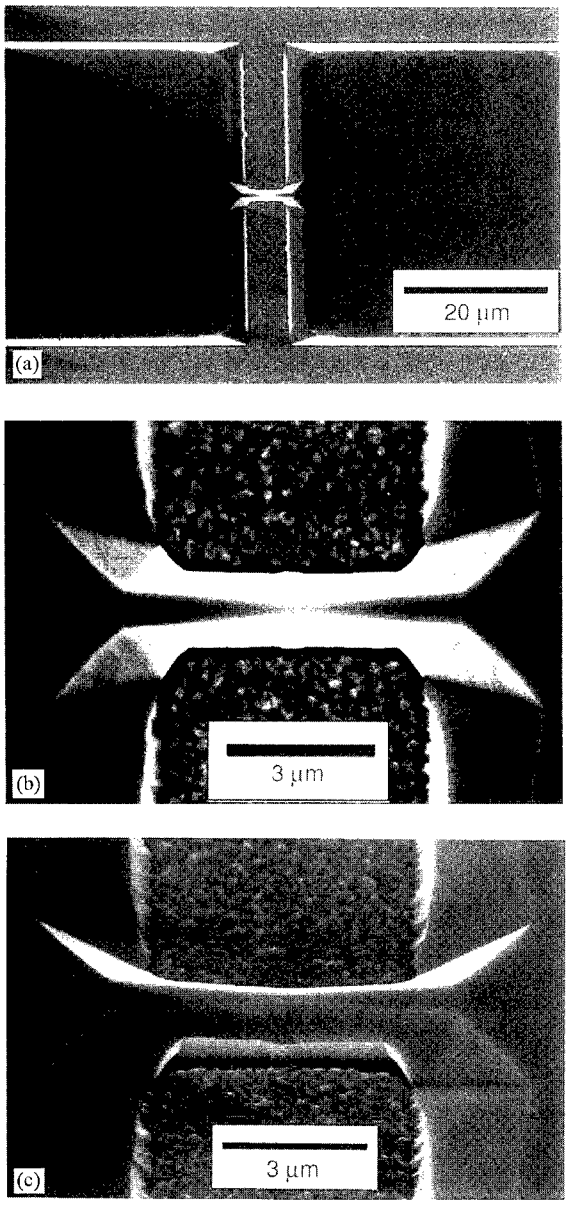

Fig. 2. SEM images of a short wire grown on the pattern of Fig. 1a: (a) Top view image of the sample, and b and c magnified images seen from the top and from a direction tilted 33° from the top. Composite facets develop at boundaries between the wire region and the two 40 μm wide lead regions.

consists of two (1 1 1)B side planes, a top (1 0 0) plane, which are commonly found in the facet structures grown on mesa running along the ⟨0 1 1⟩ direction. In the cross-over regions where the wire meets with the 40-μm wide lead regions, more complicated facets were found. In the case of long stripes 20 nm scale ridges were successfully formed since the ridge tends to sharpen due to the up-flow of Ga from the two (1 1 1)B side facets to the top (1 0 0) facet [10]. In short stripes, however, the self-narrowing process was found to be suppressed. This is because the diffusion of Ga is strongly modified by the presence of wide regions on both ends of stripes.

We then examined how the final ridge width depends on the stripe length. The ridge width in the central part of wires was measured and shown as a function of L in Fig. 3. Here the original width W of stripes was 1.6 μm. The width was found to widen exponentially as L decreases, indicating that the diffusion of Ga along the stripe direction plays an important role in determining the ridge shape. The ridge width decreases by a factor of $1/e$ every-time L increases by 3 μm. Note that this figure is close to the reported diffusion length on (1 1 1)B plane [10]. We found also that the amount of GaAs incorporated on ridge regions was somewhat greater than the amount deposited, indicating the in-flow of materials. Hence, the dominant process which prevents the sharpening of ridges is the longitudinal flow of materials from the stripe ends to the stripe center.

Next, we studied transport properties of a series of 3 μm long selectively doped GaAs wires at 1.6 K. In Fig. 4, the magnetoresistance of four wire samples A–D are shown for the width W_c of wire channel ranging from 0.3 to 1.1 μm. The original stripe width W is also indicated in the figures. For comparison, the data on a 40 μm-wide ordinary two-dimensional electron gas (2DEG) sample E are also shown. Note that the zero-field resistance depends on the wire width. In our samples, electrons accumulate mainly on the top (1 0 0) plane, since the QW on the (1 1 1) facet is too thin to accomodate electrons. Very strong Shubnikov-de Haas (SdH) oscillations seen in Fig. 4 for $B > 1$ T in all samples originate from the 2DEG flowing in the 40 μm wide lead regions. In contrast, the resistance of samples for $B < 1$ T depend on the stripe widths W and display distinct negative magnetoresistances (NMR) especially in sample A. This NMR is indicative of a weak localization effect in quasi-1D

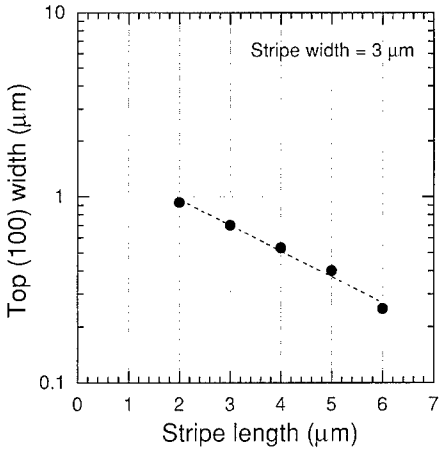

Fig. 3. The widths of ridges measured in the middle part of stripe vs the stripe lengths L. The width of stripes is fixed at 1.6 μm.

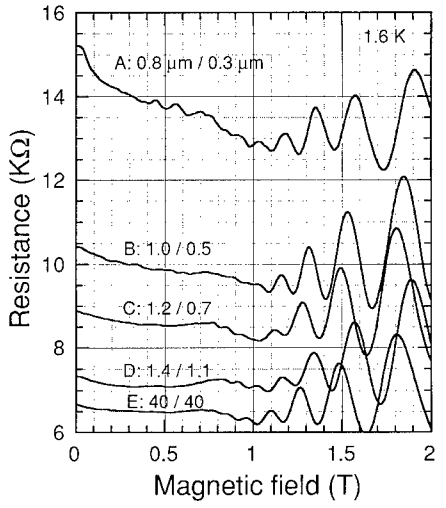

Fig. 4. Two-terminal magnetoresistances measured at 1.6 K on a series of samples grown on 3 μm-long stripes. The widths W of original stripe patterns and the estimated channel widths W_c are indicated in the figure. As W decreases, the zero-field resistance increases and displays negative magnetoresistance with distinct fluctuation.

system. In sample A, random oscillatory fluctuations on NMR were reproducibly observed. This may be related to a kind of universal conductance fluctuation (UCF), although its amplitude is far less than that expected from theory. The presence of junctions [11] and/or the geometrical inhomogenity of wires may reduce the interference of wavefunctions and UCF, though more study is necessary to conclude this.

Next we discuss the quality of sample A. The mobility μ and the electron concentration N_s of 2DEGs of a 6 nm thick GaAs QW grown simultaneously on a flat substrate were studied by Hall effect and found to be $4.7 \times 10^{11}\,\mathrm{cm}^{-2}$ and $3.4 \times 10^{4}\mathrm{cm}^2/(\mathrm{V\,s})$ at 4.2 K. These values are close to those derived from the SdH oscillations of Fig. 4. On the basis of these values, the resistance of sample E is calculated to be 6 kΩ as the 40 μm-wide 2DEG channel stretches about 250 μm to both ends. This value is close to the zero-field resistance of sample E.

Since the zero-field resistance of sample A is 15.3 kΩ, the resistance of the wire region is estimated to be about 8.5 kΩ. If we assume N_s in the wire region to be comparable to that of 2DEG and take account of the wire geometry (3 μm in length and 0.3 μm in width), μ is estimated to be about $2 \times 10^{4}\ \mathrm{cm}^2/(\mathrm{V\,s})$. This value is almost half of 2DEG, probably due to the presence of inhomogenities of the wire geometry. We expect that the quality of wires can be further improved by optimizing the growth conditions.

4. Fabrication of GaAs dot structures

By using a window pattern of Fig. 1b, we grew a pyramidal facet structure and then a crescent shaped GaAs dot on its top. Fig. 5a shows an SEM image taken from the top, and Fig. 5b is the cross-sectional view of the structure seen after cutting along the line A of Fig. 1b. Note that the symmetry of a pyramidal dot structure is not fourfold but twofold although a pyramidal structure tends to exhibit fourfold symmetry as the growth proceeds. In this pyramidal structure, facet planes with indices higher than (1 1 0) are formed. One can also see that crescent shaped GaAs dots with 100 nm width and 30 nm thickness, sandwitched by AlGaAs, are successfully formed.

PL spectra of GaAs dots at 15 K are shown in Fig. 6 at various excitation powers. The main peak

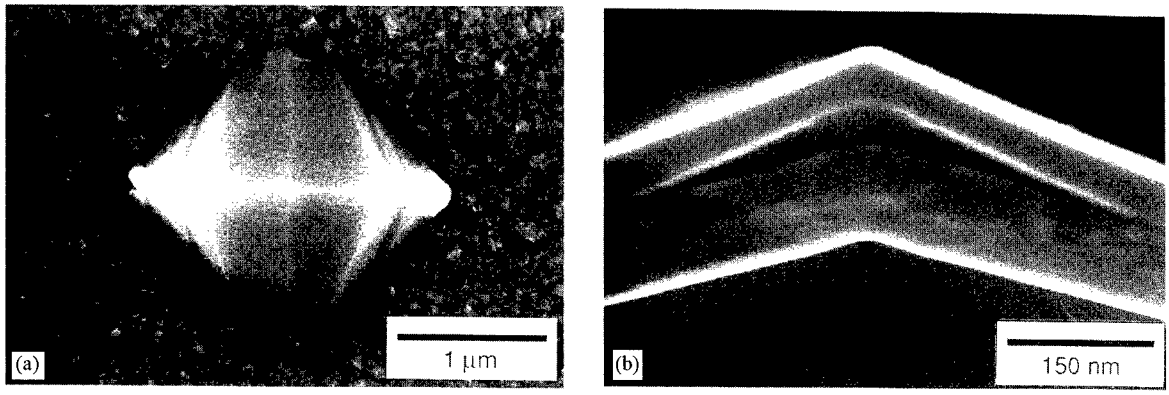

Fig. 5. SEM images of a GaAs dot: (a) top view and (b) cross-sectional view cut along line A in Fig. 1b. A crescent shaped GaAs dot, sandwiched by AlGaAs, is formed.

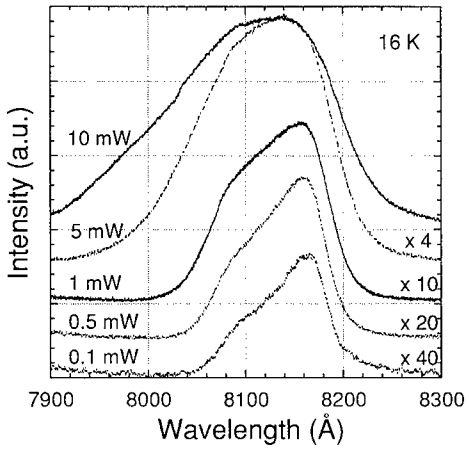

Fig. 6. PL spectra of the GaAs dot with a lateral size of 100 nm measured at 16 K at various excited laser power levels. The data are shifted for clarity.

is located at 1.520 eV, which is 6 meV higher than that of the bulk GaAs. This is close to the energy shift expected in 30 nm thick QWs. At 1.535 eV, a shoulder is located 15 meV higher than the main peak. Broad spectra with a shoulder unexpectedly survived even at excitation powers lower than 1 meV, corresponding to the excitation power density of ~ 1 W/cm. This fact suggests electron accumulation and the slow relaxation of photogenerated carriers in GaAs dots.

5. Conclusions

In conclusion, we have fabricated GaAs wire and dot structures by MBE with assistance of atomic hydrogen. We have found that the interfacet interaction is modified by the presence of leads and that the longitudinal diffusion suppresses the sharpening process of ridges particularly in short stripe patterns.

Acknowledgements

We thank Dr. Tsujino for the support of optical measurements. This work is supported by the Grant-in-Aid from the Ministry of Education and by the Research Development Corporation of Japan.

References

[1] E. Kapon, D.M. Hwang and R. Bat, Phys. Rev. Lett. 63 (1989) 430.
[2] S. Tsukamoto, Y. Nagamune, M. Nishioka and Y. Arakawa, J. Appl. Phys. 71 (1992) 533.
[3] C.S. Tsai, J.A. Lebens, C.C. Ahn, A. Nouhi and K.J. Vahala, Appl. Phys. Lett. 60 (1992) 240.
[4] S. Tsukamoto, Y. Nagamune, M. Nishioka and Y. Arakawa, J. Appl. Phys. 62 (1993) 49.
[5] K. Kojima, K. Mitsunaga and K. Kyuma, Appl. Phys. Lett. 55 (1989) 882.

[6] E. Kapon, K. Kash, E.M. Clausen, jr., D.M Hwang and E. Colas, Appl. Phys. Lett. 60 (1992) 477.
[7] T. Sugaya, M. Kaneko, Y. Okada and M. Kawabe, Jpn. J. Appl. Phys. 32 (1993) L1834.
[8] T. Sugaya and M. Kawabe, Jpn. J. Appl. Phys. 30 (1991) L402.
[9] T. Sugaya, Y. Okada and M. Kawabe, Jpn. J. Appl. Phys. 31 (1992) L713.
[10] S. Koshiba, Y. Nakamura, M. Tsuchiya, H. Noge, H. Kano, Y. Nagamune, T. Noda and H. Sakaki, J. Appl. Phys. 76 (1994) 4138.
[11] G. Edwards, A. Grincwajg and D. Ferry, Jpn. J. Appl. Phys. 34 (1995) 4348.

ELSEVIER

Journal of Crystal Growth 175/176 (1997) 793–798

JOURNAL OF CRYSTAL GROWTH

Molecular beam epitaxial growth of InGaAs/InGaAsP quantum wires on V-grooved InP substrates with (1 1 1) sidewalls

J. Wang*, D.A. Thompson, B.J. Robinson , J.G. Simmons

Centre for Electrophotonic Materials and Devices, McMaster University, Hamilton, Ontario, Canada, L8S 4L7

Abstract

Bulk InGaAsP and InGaAs/InGaAsP quantum well structures have been grown by gas source molecular beam epitaxy on V-grooved InP substrates having (1 1 1)A and (1 1 1)B sidewalls. The growth of the InGaAsP layer in a (1 1 1)A V-groove results in a flat and wide bottom, which rules out the possibility of the formation of InGaAs/InGaAsP quantum wires (QWRs). However, the growth of the InGaAsP layer in (1 1 1)B V-grooves results in a sharper bottom so that crescent-shaped InGaAs/InGaAsP quantum wells are formed such that QWR behaviour is possible. Transmission electron microscopy shows that the crescent-shaped InGaAs layer has a very large thickness variation at the V-groove bottom and that all layers at the V-groove bottom are free of extended defects. The photoluminescence from different spatial regions of the sample has been identified using a selective etching technique. Two peaks are associated with the QWRs at V-groove bottom, with the higher energy one apparently being from the second lateral subband transition. The energy separation between these two peaks is consistent with values calculated from the measured thickness variation. Consistent with QWR behaviour, the photoluminescence is polarized, with a stronger signal along the wire direction than perpendicular to the wire direction.

PACS: 68.55.Bd

Keywords: Quantum wire; V-groove; MBE; InGaAsP; InGaAs; Polarization

1. Introduction

Growth onto V-grooved substrates has been demonstrated to be one of most promising ways, among various techniques, to make quantum wires (QWR) [1]. QWR lasers with very low threshold currents have been grown onto V-grooved GaAs substrates [1, 2]. However, much less progress has been made on InP based-materials, even though they are very important to telecommunication applications. To our knowledge, neither QWR laser structures nor InGaAs/InGaAsP QWRs have been successfully grown on V-grooved InP substrates [3, 5]. One difficulty arises from a sidewall

* Corresponding author. Fax: + 1 905 527 8409; e-mail: wangj4@mcmail.cis.mcmaster.ca.

0022-0248/97/$17.00 Copyright © 1997 Published by Elsevier Science B.V. All rights reserved
PII S0022-0248(96)00951-7

diffusive flux and increased incorporation of group III adatoms in the V-groove bottoms. Consequently, a planarization develops as the growth of buffer and barrier layers proceeds, making QWR formation impossible. A second difficulty arises due to the differential migration of indium over gallium, resulting strain development and possible relaxation generated defects [1, 3–6]. Nevertheless, InGaAs/InP quantum wire formation was recently reported on V-grooves with (1 1 1)A sidewalls [7]. For a laser structure, however, InGaAsP barrier or waveguiding layers with sufficient thicknesses have to be grown. Such InGaAsP layers need to be defect-free and V-groove bottoms must be sharp before the growth of the quantum well layer [3, 4]. The subsequent quantum wire layer should form a crescent-shape profile and also be free of defects. In this work, using gas source molecular beam epitaxy (GSMBE) we have grown quaternary and quantum well structures on V-grooves with both (1 1 1)A and (1 1 1)B sidewalls, which are expected to show different growth behaviour. Transmission electron microscopy (TEM) has been used to examine layer morphology and to determine the dimensions of the crescent-shaped InGaAs/InGaAsP quantum wells in (1 1 1)B V-grooves. Based on the measured quantum well thickness variation, a simple quantum wire model has been used to estimate lateral subband separations. Optical characterizations, including spatially resolved photoluminescence (PL) and PL polarization, have also been performed on the InGaAs/InGaAsP quantum wires.

2. Experimental procedure

V-grooves with both (1 1 1)A and (1 1 1)B sidewalls were chemically etched in (1 0 0) InP substrates. V-grooves with (1 1 1)A sidewalls were etched using $2HBr : 2H_3PO_4 : 1K_2Cr_2O_7$ as an etchant and SiO_2 as a V-groove etching mask, with patterns of 1 μm wide openings aligned along the [0 $\bar{1}$ 1] direction. V-grooves with (1 1 1)B sidewalls were obtained using an etch solution of $5HCl : 1H_3PO_4$, with 1 μm wide photoresist mask openings aligned along the [0 1 1] direction [8].

A bulk InGaAsP quaternary layer and an InGaAs/InGaAsP quantum well structure were grown by GSMBE on the V-groove etched substrates. The quaternary layer has a nominal composition of $In_{0.72}Ga_{0.28}As_{0.61}P_{0.39}$ (with a bandgap wavelength of 1.3 μm) and a nominal thickness of 40 nm. In the quantum well structure, the InGaAs layer is lattice-matched to InP and nominally 1.2 nm thick; the lower and upper InGaAsP barrier layers, also having a composition of $In_{0.72}Ga_{0.28}As_{0.61}P_{0.39}$, are nominally 20 nm thick. All InGaAs and InGaAsP layers were grown at a growth rate of 1 μm/h, a substrate temperature of 450°C and a V/III flux ratio of 2.6. Along with the quaternary and ternary layers, InP layers were also grown, under conditions giving sharp V-groove bottoms and smooth morphology [9], to serve as buffer and capping layers in the above structures. Buffer layers were 50 nm thick, while capping layer thicknesses varied from 50 to 500 nm.

Cross-sectional TEM was used to examine layer morphology and any extended defect structures. Conventional low temperature (15 K), top-emission PL measurements were performed on the quantum well structure samples using a 488 nm Ar^+ laser with a spot diameter of about 250 μm which typically covered 20 grooves. The sample was selectively etched [7] with the planar (1 0 0) regions and upper parts of sidewalls removed, (i.e. all but the bottom $\sim$ 1.5 μm of sidewalls was removed). The polarization of photoluminescence originating from quantum well in the V-groove bottom region was also investigated, with the backside of the sample mechanically polished and optically excited by a cw YAG laser. The 1.06 μm YAG laser light passed through the InP substrates and selectively pumped the InGaAsP and InGaAs layers. The spectra were calibrated with respect to the polarization response of the PL system.

3. Results and discussion

Fig. 1 is the TEM image of the InGaAsP layer, sandwiched between InP buffer and capping layers, grown on a (1 1 1)A V-groove. It shows no extended defects present at the V-groove bottom, but a dramatic planarization at the V-bottom region is evident. After the growth of the InP buffer layer, the V-groove bottom is faceted with (3 1 1) planes and

is only 20 nm wide. Subsequently, the top surface becomes flat and expands to 80 nm width after the growth of the InGaAsP layer. This result implies that the growth behaviour of an InGaAsP layer in a (1 1 1)A V-groove is an obstacle to the formation of QWRs. This is further demonstrated by Fig. 2, which is the TEM image of a 3-quantum well structure grown on a (1 1 1)A V-groove. It is seen that all three InGaAs layers are wide, having no significant thickness variation to produce lateral quantum confinement. Thus, InGaAs/InGaAsP QWRs cannot be obtained in a (1 1 1)A V-groove, even though InGaAs/InP QWRs have been achieved in such a type of V-groove [7].

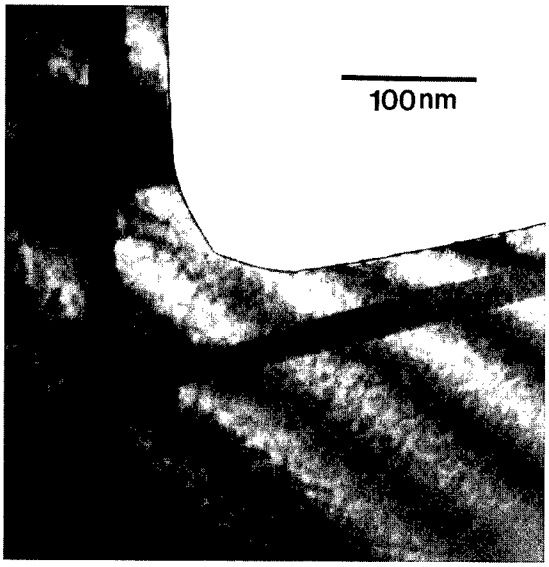

Fig. 1. The cross-sectional TEM image of InP/InGaAsP/InP structure at the bottom of the (1 1 1)A V-groove.

In contrast, the InP and InGaAsP layers grown on a (1 1 1)B V-groove show different layer morphology, as shown in Fig. 3. The V-groove bottom is flat and small (about 30 nm wide) after the growth of the InP buffer layer. However, the subsequent InGaAsP quaternary layer evolves during growth such that its top surface in the V-groove bottom is sharper, i.e. it develops into a rounded bottom with a small radius of curvature. This feature indicates that the InGaAsP growth behaviour on a (1 1 1)B V-groove is different from that on a (1 1 1)A V-groove, in a way which could be used for quantum-wire formation. The causes for the different growth behaviour of InGaAsP on (1 1 1)A and (1 1 1)B V-grooves and the cause for

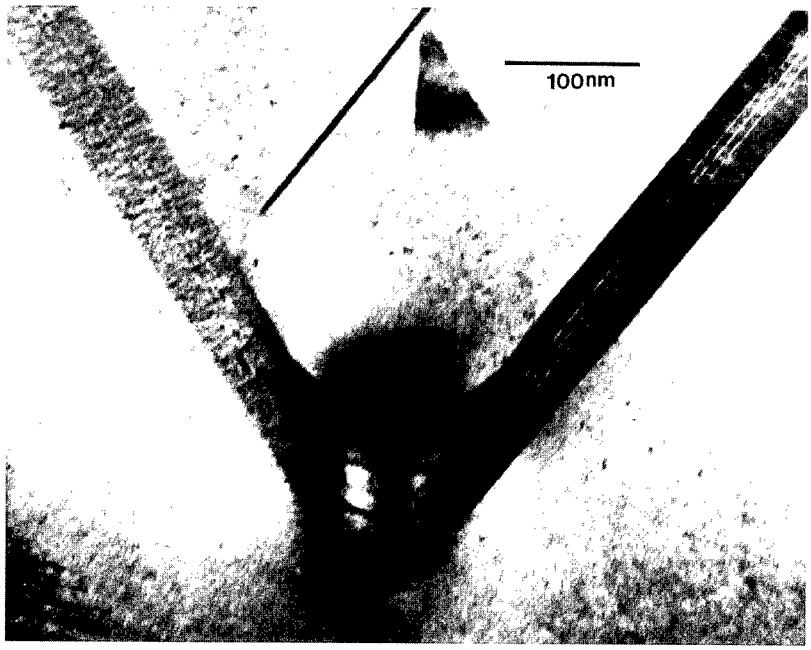

Fig. 2. The cross-sectional TEM image of InGaAs/InGaAsP 3 quantum well structure at the bottom of the (1 1 1)A V-groove.

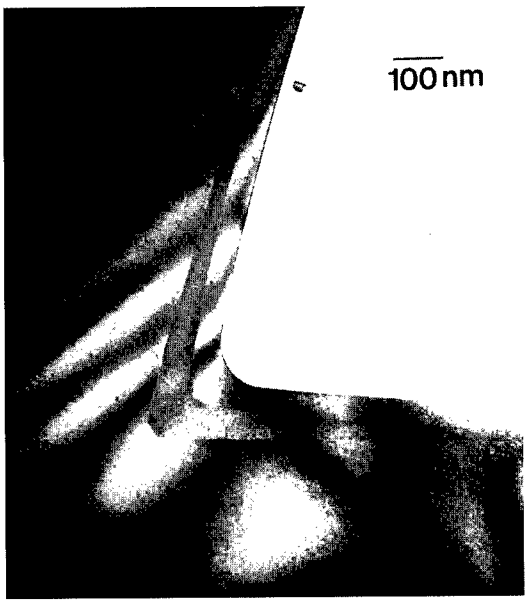

Fig. 3. The cross-sectional TEM image of InP/InGaAsP/InP structure at the bottom of the (1 1 1)B V-groove.

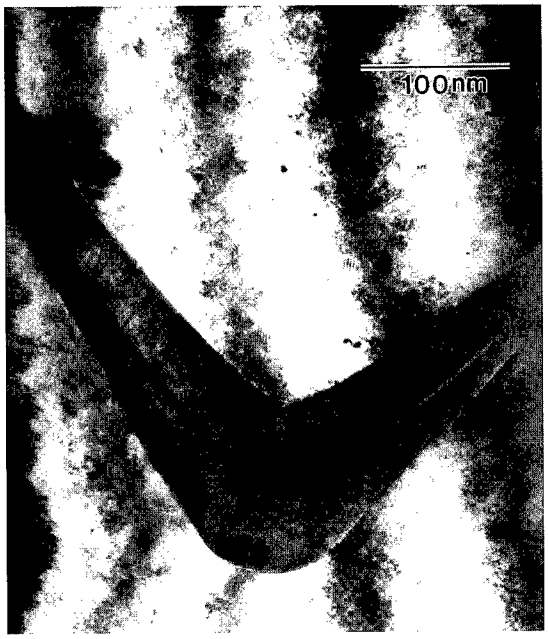

Fig. 4. The cross-sectional TEM image of InGaAs/InGaAsP single quantum well structure at the bottom of the (1 1 1)B V-groove, showing a crescent-shaped InGaAs/InGaAsP quantum wire.

the different growth behavior of InGaAsP to that of InP are not currently understood.

Fig. 4 is the TEM image of a InGaAs/InGaAsP quantum well structure grown on a (1 1 1)B V-groove. As seen in the image, all ternary and quaternary layers at V-groove bottoms are free of any extended defects. Moreover, the InGaAs layer at the V-groove bottom clearly shows a crescent-shape. The thickness is about 7 nm at the center of V-bottom, which is nearly 6 times the nominal thickness on a planar (1 0 0) region and more than 10 times the estimated thickness on the sidewall, indicating a significant group III adatom migration to the bottom from the sidewalls. The physical width of the crescent-shaped InGaAs region is about 50 nm. A big thickness variation in such a small width is an indication of possible quantum wire formation. Furthermore, even the top of upper InGaAsP layer is sharp, which implies promise for the formation of multiple InGaAs/InGaAsP QWRs.

To estimate the lateral quantum confinement for the InGaAs/InGaAsP QWR, a simplified lateral one-dimensional parabolic potential model was used, which neglects band intermixing and is similar to that used for GaAs/AlGaAs QWRs [1, 10, 11] and InGaAs/InP QWRs [7]. This involves determining the InGaAs layer thickness at different positions from the TEM images and calculation of the associated confinement energies with a conventional quantum well calculation. The confinement energy distributions follow parabolic shapes near the center of the wire, for which the lateral subband separations are calculated to be 17, 5.7 and 22.2 meV for electrons, heavy holes and light holes respectively. The effective widths, W_{eff}, of the wire for electrons, heavy holes and light holes are 22, 13.6 and 20 nm, respectively [1, 10, 11]. These subband separations are slightly higher than those reported on InGaAs/InP QWR grown on (1 1 1)A V-grooves [7] and are about the same as those obtained on GaAs/AlGaAs QWRs [1, 11]. The larger light-hole subband separation compared to that of electrons is due to the valence band offset being larger than the conduction band offset. For the InP-based system, the ratio of conduction band offset to valence band offset is taken as 40/60, while the ratio for GaAs/AlGaAs is 60/40. The different band offset ratios result in different

relative subband separations among electrons, heavy holes and light holes between the InGaAs/InGaAsP and GaAs/AlGaAs systems. Therefore, there is less lateral confinement for electrons and larger lateral confinement for holes in the InGaAs/InGaAsP system compared to the GaAs/AlGaAs system [1, 11].

Conventional low temperature photoluminescence was carried out on the InGaAs/InGaAsP QWR sample grown on (1 1 1)B V-grooves to examine the optical properties of the QWRs. Fig. 5a is the spectrum from the patterned region of the as-grown sample, displaying multiple peaks, at 0.756, 0.776, 0.892, 0.946 eV (with a shoulder at 0.93) and 0.982 eV. To resolve the spectrum spatially a selective etching technique, as described in reference [7], was used. Fig. 5b is the PL spectrum obtained with top planar (1 0 0) regions and upper sidewalls removed, showing that the PL peaks at 0.946 and 0.892 eV have been removed. Therefore, it is concluded that these peaks are originating from either the top (1 0 0) surfaces or upper sidewalls where there exists a composition variation and a quantum well thickness variation. The peak at 0.982 eV is assigned to the lower part of the sidewalls, which region has a high energy due to a thinner quantum well thickness than the (1 0 0) regions. The peaks at 0.756 and 0.776 eV are from quantum wires at the V-groove bottoms. Their low energies, compared to that on the planar region, are consistent with the composition (about 70% In) as measured by energy dispersive X-ray analysis. The full width at half maximum of the peak at 0.756 eV is about 15 meV, which is narrower not only than that of the quantum well peak on the non-patterned (1 0 0) region but also than that of InGaAs/InP QWRs grown on (1 1 1)A V-grooves [7]. It seems that a broad peak with a high energy tail which was observed in Ref. [7] is resolved into two peaks in the spectra in the present work. The peak at 0.756 eV is from the QWR ground energy levels (1e-1hh), while the peak at 0.776 eV is assumed to be from the higher QWR subband transition (2e–2hh). The 20 meV separation between these two peaks is consistent with estimated energy separations (22.7 meV) between 1e-1hh and 2e–2hh transitions. The low PL intensity from QWRs, compared to that of quantum wells on the lower part of sidewalls, is due to its small size. The size of the lower part of sidewalls is about 60 times of that of QWRs. This suggests that carrier diffusion from sidewalls to the QWRs is not significant.

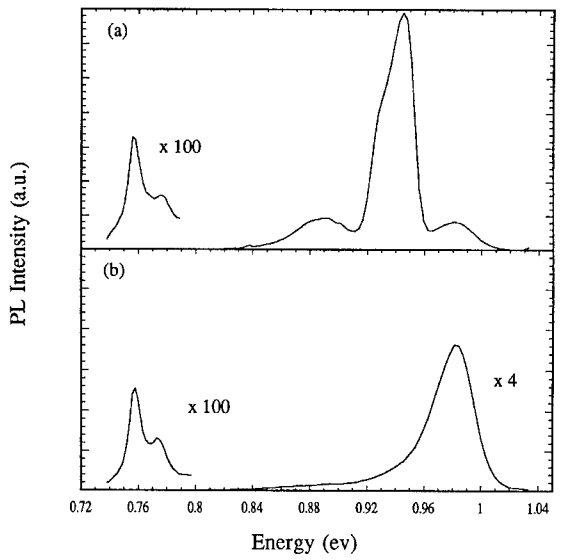

Fig. 5. Photoluminescence spectra at 15 K: (a) a sample before selective etching; (b) a sample with quantum well on a (1 0 0) planar region and upper sidewalls partially wet-etched away.

This study suggests that the appearance of the second QWR subband transition with PL spectra is related to bandfilling, because the relative intensity of the 2e–2hh subband transition with respect to that of the ground level transition increases with pumping power and sample temperature. A similar phenomenon has been observed in GaAs/AlGaAs QWRs where the band-filling argument was experimentally supported by magneto-PL and time-resolved PL measurements [11, 12]. The band-filling effects are believed to be associated with a sharp QWR density of states and small subband separations.

Polarization has also been used to characterize the QWRs in this work. Fig. 6 shows the PL spectra polarized along, and normal to, the wire direction at a given spot. It is seen that the PL intensity is strongly polarized, with the signal along the wire direction being more than twice that perpendicular to the wire direction. This polarization behaviour results from heavy-hole transitions

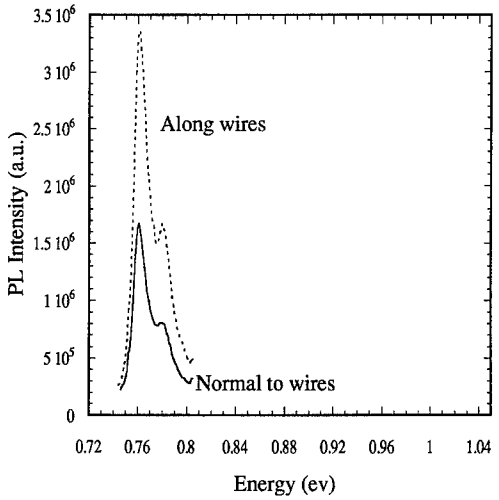

Fig. 6. Polarization of quantum wire photoluminescence at a temperature of 15 K.

of QWRs [13–15]. The InGaAs wire is sufficiently strained and thin that the light-hole band is separated from the heavy-hole band, and the transitions observed in the PL spectra are associated with heavy holes.

4. Conclusions

In summary, the growth of InGaAsP in (1 1 1)A V-grooves in InP results in a significant planarization development and flat V-bottoms; thus, InGaAs/InGaAsP QWRs cannot be obtained in (1 1 1)A V-grooves. In contrast, the growth of an InGaAsP layer in (1 1 1)B V-grooves leads to a sharper bottom, in which InGaAs/InGaAsP quantum wires have been achieved. The QWRs are defect free and crescent-shaped. A significant thickness variation across a small width results in subband separations comparable to those achieved in the GaAs-based system. The existence of lateral subbands has been demonstrated in PL spectra and also supported by polarization measurements. The subband separation observed in PL spectra is consistent with a calculated value based on the wire geometry observed by TEM.

Acknowledgements

We thank S.A. McMaster for help on MBE operation. This work was supported by the Ontario Centre for Materials Research and the Natural Sciences and Engineering Research Council of Canada.

References

[1] E. Kapon, in: Epitaxial Microstructure, Ed. A.C. Gossard (Academic Press, New York, 1994) p. 259.
[2] S. Tiwari, G.D. Pettit, K.R. Milkove, F. Legoues, R.J. Davis and J.M. Woodall, Appl. Phys. Lett. 64 (1994) 3536.
[3] R. Bhat, E. Kapon, S. Simhony, E. Colas, D.M. Hwang, N.G. Stoffel and M.A. Koza, J. Crystal Growth 107 (1991) 716.
[4] R. Bhat, E. Kapon, J. Werner, D.M. Hwang, N.G. Stoffel and M.A. Koza, App. Phys. Lett. 56 (1990) 863.
[5] N.J. Bulitka, A. Gupta, B.J. Robinson, D.A. Thompson, G.C. Weatherly and J.G. Simmons, Mat. Res. Soc. Symp. Proc., Vol. 326 (1993) 183.
[6] Y.M. Galeuchet, P. Roentgen and V. Graf, Appl. Phys. Lett. 53 (1988) 2638.
[7] J. Wang, B.J. Robinson, D.A. Thompson and J.G. Simmons, Appl. Phys. Lett. 67 (1996) 1358.
[8] J. Wang, D.A. Thompson, J.G. Simmons, M. Boumerzoug, M. Boudreau and P. Mascher, J. Electrochem. Soc. 142 (1995) 593.
[9] J. Wang, B.J. Robinson, D.A. Thompson and J.G. Simmons, J. Crystal Growth (1996), in press.
[10] E. Kapon, D.M. Hwang and R. Bhat, Phys. Rev. Lett. 63 (1989) 430.
[11] R. Rinaldi, M. Ferrara, R. Cingolani, U. Marti, D. Martin, F. Morier-Gemoud, P. Ruterana and F.K. Reinhart, Phys. Rev. B 50 (1994) 11795.
[12] A.C. Maciel, J.F. Ryan, R. Rinaldi, R. Cingolani, M. Ferrara, U. Matri, D. Martin, F. Morier-Gemound and F.K. Reinhart, Semicond. Sci. Technol. 9 (1994) 893.
[13] P.C. Sercel and K.J. Vahala, Phys. Rev. B 44 (1991) 5681.
[14] T. Sugaya, M. Kaneko, Y. Okada and M. Kawabe, Jpn. J. Appl. Phys. 32 (1993) L1834.
[15] W. Pan, H. Yaguchi, K. Onabe, K. Wada, Y. Shiraki and R. Ito, J. Crystal Growth 145 (1994) 702.

ELSEVIER

Journal of Crystal Growth 175/176 (1997) 799–803

JOURNAL OF CRYSTAL GROWTH

Vertically stacked quantum wires fabricated by an in situ processing technique

M. López-López[a,*], Tomonori Ishikawa[b]

[a] *Departamento de Física, Centro de Investigación y de Estudios Avanzados del IPN, Apartado Postal 14-740, México 07000 DF, México*
[b] *Optoelectronics Technology Research Laboratory, 5-5 Tohkodai, Tsukuba, Ibaraki 300-26, Japan*

Abstract

We have fabricated vertically stacked structures consisting of two arrays of AlGaAs/GaAs quantum wires using a processing technique conducted under an ultra-high vacuum or in a controlled ambient, called in situ electron beam (EB) lithography. In this technique a thin GaAs oxide layer was selectively formed on a clean GaAs surface by EB-stimulated oxidation in an oxygen atmosphere, and then used as a mask material to define mesa stripes by Cl_2 gas etching. Subsequently, ridge structures were formed on the mesa stripes by the MBE growth of a GaAs layer. The first array of quantum wires was formed on the top of the ridges by the growth of an AlGaAs/GaAs quantum well. Then, these wire structures were buried and the surface was flattened out by the growth of a thick GaAs layer. The second array of quantum wires was successively formed by a second pattern and regrowth process. The successful fabrication of these structures was confirmed by cathodoluminescence measurements at 77 K.

1. Introduction

During the fabrication process of nanostructures, in particular when dealing with III–V compound semiconductors, unintentional contamination of the processed surfaces must be minimized, since this would severely deteriorate the electrical and optical properties of the resulting structures. Several approaches have been proposed in order to synthesize nanostructures, like quantum wires and boxes, with interfaces free of contaminants. One of the most promising methods to fabricate such nanostructures is the epitaxial growth on pre-pattern substrates [1–6]. However, so far, the patterning step has been carried out using conventional lithographic techniques using organic resists and under air-exposure conditions, which yields to unavoidable contamination. Furthermore, this method is presently limited in the sense that the final array is ultimately determined by the initial patterned structure. Great flexibility would be achieved if substrate patterning and regrowth could be realized successively, and as many times as required without exposing the wafer to air using an in situ processing technique [7].

In this direction, in the last few years we have been developing a technique called "in situ electron-beam (EB) lithography" [8], in which lateral

* Corresponding author.

0022-0248/97/$17.00 Copyright © 1997 Published by Elsevier Science B.V. All rights reserved
PII S0022-0248(96)00886-X

patterning and molecular beam epitaxy (MBE) are conducted sequentially, without exposing the sample to air. In this technique an ultrathin GaAs oxide layer is selectively formed on a clean GaAs surface by EB-stimulated oxidation under a controlled oxygen atmosphere [9], and then it is used as a mask material against subsequent Cl_2 gas etching. In this way in-situ patterning of the underlying GaAs layer is achieved, then the oxide mask is thermally removed, and the MBE regrowth step on a clean patterned substrate is carried out. In this work, to show the great flexibility of this technique we have fabricated vertically stacked structures consisting of two arrays of quantum wires. The high quality of these structures is demonstrated by cathodoluminescence measurements.

2. Experimental system

Fig. 1 shows a schematic illustration of the ultra-high vacuum (UHV) multichamber system used to perform the in situ EB lithography process. Seven chambers, for sample loading, sample exchange, preheating, MBE, surface treatments, analysis, and etching are connected by UHV tunnels, so that samples loaded into the system can be transferred from one chamber to another without exposure to air. The base pressure of the system is better than 1.3×10^{-7} Pa, except for the loading chamber. An EB gun column placed on the top of the etching chamber is used for the patterning. The EB gun was designed so as to obtain a small EB diameter at a high current density by using a high-brightness Zr/O/W thermal field emitter [8]. The entire etching chamber is made of iron in order to shield the EB from any fluctuations in the environmental magnetic fields. This chamber is also equipped with a gas introduction system with a thin stainless-steel nozzle in order to supply O_2 gas to the sample surface along with EB irradiation.

3. Fabrication of vertically stacked quantum wires

The process used to fabricate quantum wires is illustrated in Fig. 2. First, in order to obtain a clean GaAs surface a 500 nm thick buffer layer was

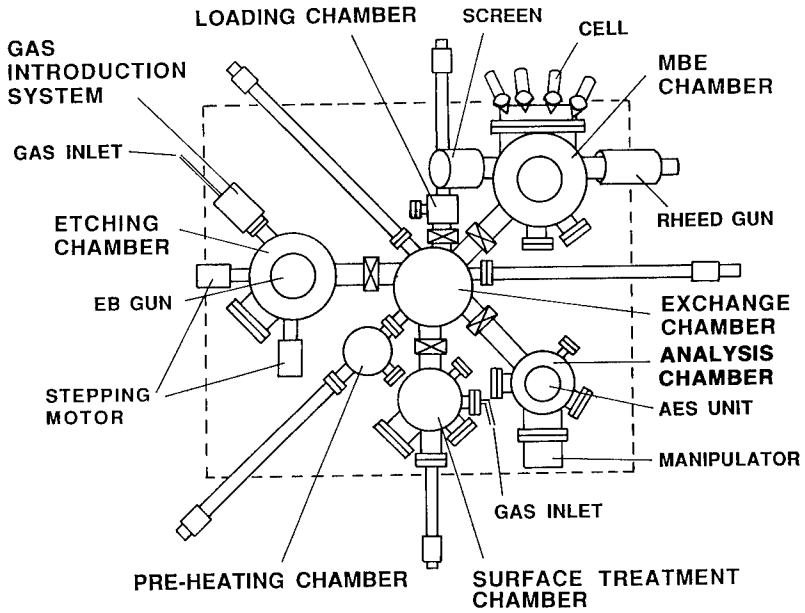

Fig. 1. Schematic illustration of the UHV multichamber system used in this work. The chambers for etching, MBE, preheating, surface treatment, surface analysis, and sample loading are connected to the sample exchange chamber through vacuum tunnels.

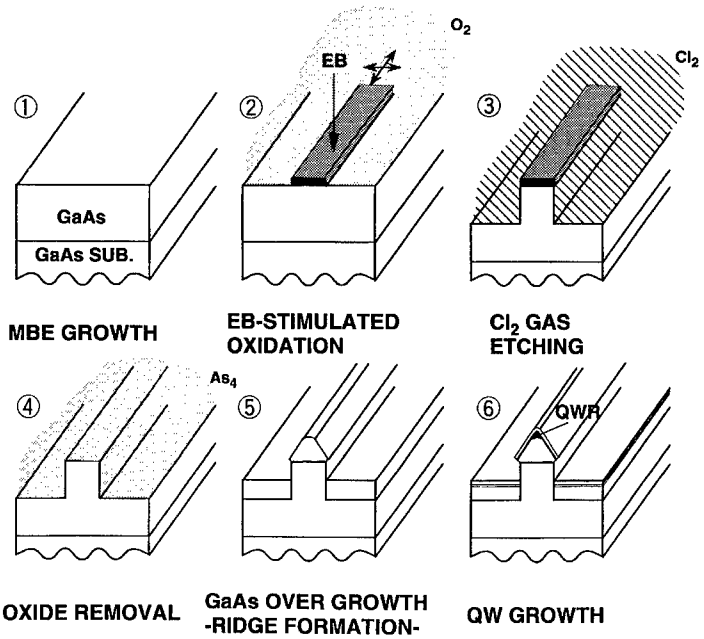

Fig. 2. Process sequence of in situ patterning and regrowth used to define the first array of wires. This array was buried in a 500 nm thick GaAs layer. Then, the second array of wire structures was successively formed by a second pattern and regrowth process using steps (2)–(6).

grown by MBE on a GaAs(001) substrate misoriented 2° towards the [1 1 0] direction (Fig. 2(1)). Under an As pressure the sample was cooled down to room temperature, and then it was transferred to the etching chamber. Then, O_2 was gradually introduced into the etching chamber through the nozzle up to reach an O_2 pressure of 2.66×10^{-4} Pa. In order to locally enhance the O_2 pressure the nozzle was placed at a distance of 400 μm from the sample surface. Using a pattern generator a 25 kV-EB with a beam current of 4 nA was raster-scanned over the surface at room temperature so as to selectively form a thin GaAs oxide-mask layer by EB-stimulated oxidation with a total dose of 6×10^{18} electrons/cm^2 (Fig. 2(2)). Here it is worth to mention that we have used slightly misoriented GaAs(0 0 1) substrates because more resistant oxide masks can be obtained on this kind of substrates [9]. The O_2 gas was evacuated from the etching chamber to obtain a pressure of less than 1.3×10^{-6} Pa. Then, the substrate temperature was increased to 150°C, and Cl_2 gas was introduced to the chamber to perform the etching step at a Cl_2 gas pressure of 6.6×10^{-3} Pa. We have found, in a study using in situ Auger electron spectroscopy and reflection high-energy electron diffraction, that stoichiometric etching is realized and smooth As-stabilized surfaces are obtained under these etching conditions, which are excellent for the regrowth of high-quality quantum wells [10]. The etching time used here was 5 min, in this way mesa-stripe structures oriented along the [1 $\bar{1}$ 0] direction having a width of 200 nm, and 300 nm depth were defined (Fig. 2(3)). We used the [1 $\bar{1}$ 0] mesa direction because the Cl_2 etching produces normal-type mesa stripes exhibiting (311)A slanting planes along this direction, which can be easily buried during the regrowth step. The etching chamber was evacuated to about 1.3×10^{-7} Pa, and then the sample was transferred back to the MBE chamber. In order to remove the oxide mask the substrate temperature was increased to 620°C in an As flux, it was kept at this temperature for 20 min to complete the desorption of the oxide mask (Fig. 2(4)). Then, for the

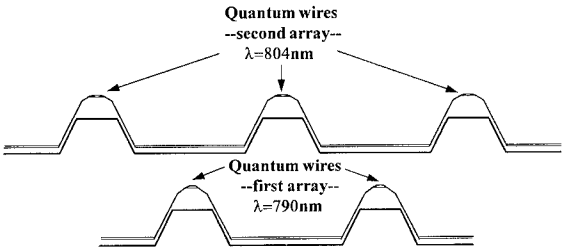

Fig. 3. Schematic illustration of the vertically stacked structure consisting of two arrays of wires.

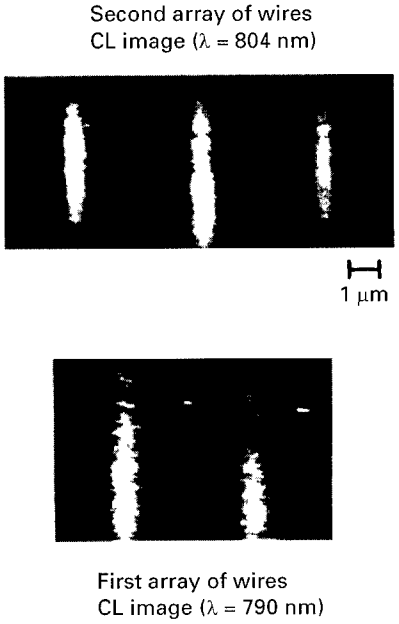

Fig. 4. Spatially resolved CL images showing the emission from the first ($\lambda = 790$ nm) and second ($\lambda = 804$ nm) array of wire structures.

regrowth step the substrate temperature was lowered to 600°C. The mesa-top width was reduced during the growth of a 200 nm thick GaAs buffer layer, due to the migration of Ga atoms from the (311)A sidewalls to the top (001) surface. In this way narrow ridge structures were formed on the mesas (Fig. 2(5)). Then, a 3.5 nm thick GaAs quantum well with 20 nm thick $Al_{0.3}Ga_{0.7}As$ barriers was grown, quantum wires at the top of the ridges were formed directly in this step because of the slow growth rate on the sidewalls compared to that on the mesa top (Fig. 2(6)). Subsequently, these wire structures were buried, and the surface was flattened out by the growth of a 500 nm thick GaAs layer. Then, the second array of wire structures was successively formed by a second pattern (EB-stimulated oxidation and Cl_2 gas etching), and regrowth process. In order to obtain wire structures emitting at a different wavelength from the first array, a different quantum well width of 5 nm was grown during the formation of the second array of wires.

Fig. 3 shows a schematic illustration of the final structure. Cathodoluminescence (CL) measurements on this structure were performed at 77 K, using a 10 keV electron beam with 1 nA current as an excitation source. We found that the first and second array of wire structures emitted at 790 and 804 nm, respectively. Fig. 4 shows spatially resolved CL images taken at a selected wavelength of 790 nm (bottom image) and 804 nm (upper image), showing the emission from the first and second array of wire structures, respectively. These results show the feasibility of fabricating optically active stacked structures by using in situ EB lithography, thus showing the great potential of this technique.

4. Conclusion

We succeeded in fabricating vertically stacked structures consisting of two arrays of quantum wires by in situ EB lithography. Since the patterning and regrowth can be repeated as many times as required without exposing the wafer to air, this all-UHV processing technique is very promising for fabricating arbitrarily designed arrays of low dimensional structures.

Acknowledgements

This work was carried out in collaboration with Dr. N. Tanaka and Dr. I. Matsuyama. The authors would like to express their gratitude to Dr. M. Tamura, Dr. Y Katayama, and Dr. I. Hayashi for continuous support of this work.

References

[1] E. Kapon, M.C. Tamargo and D.M. Hwang, Appl. Phys. Lett. 50 (1987) 347.
[2] A. Madhukar, Thin Solid Films 231 (1993) 8.
[3] S. Koshiba, H. Noge, H. Akiyama, T. Inoshita, Y. Nakamura, A. Shimizu, Y. Nagamune, M. Tsuchiya, H. Kano, H. Sakaki and K. Wada, Appl. Phys. Lett. 64 (1994) 363.
[4] T. Röhr, H. Kratzer, G. Böhm, W. Klein, G. Tränkle and G. Weimann, J. Crystal Growth 150 (1995) 306.
[5] T. Shitara, M. Tornow, A. Kurtenbach, D. Weiss, K. Eberl and K.v. Klitzing, Appl. Phys. Lett. 66 (1995) 2385.
[6] Y. Liu, S. Shimomura, N. Sano, K. Gamo, A. Adachi and S. Hiyamizu, Semicond. Sci. Technol. 8 (1993) 2197.
[7] M. Hong, J. Crystal Growth 150 (1995) 277.
[8] T. Ishikawa, N. Tanaka, M. López and I. Matsuyama, J. Vac. Sci. Technol. B 13 (1995) 2777.
[9] M. López, N. Tanaka, I. Matsuyama and T. Ishikawa, Jpn. J. Appl. Phys. 34 (1995) L1024.
[10] N. Tanaka, M. López, I. Matsuyama and T. Ishikawa, J. Vac. Sci. Technol. B 13 (1995) 2250.

ELSEVIER

Journal of Crystal Growth 175/176 (1997) 804–808

JOURNAL OF CRYSTAL GROWTH

UHV-AFM study of MBE-grown 10 nm scale ridge quantum wires

S. Koshiba[a,*], Ichiro Tanaka[a], Y. Nakamura[a], I. Kamiya[a], T. Someya[b], T. Ngo[a], H. Sakaki[a,b]

[a] *Quantum Transition Project*[1], *JRDC, 4-7-6-4F Komaba, Meguro-ku, Tokyo 153, Japan*
[b] *University of Tokyo, 4-6-1 Komaba, Meguro-ku, Tokyo 153, Japan*

Abstract

We evaluate the shape of ridge quantum wires (RQWIs) with nm-scale resolution by using SEM and ultra-high-vacuum (UHV) AFM system which is connected to MBE chamber. This MBE-AFM system provides us a detailed information about the evolution of size and uniformity of ridges grown under various conditions. In this report, we investigate systematically how the growth temperature T_s and As flux affect the width and morphology of GaAs ridge structure. The results show that a very sharp and uniform GaAs ridge structures ($W < 10$ nm) can be obtained. On the basis of this understanding, we fabricated the ridge quantum wire of 10 nm width.

PACS: 61.16.Ch; 68.55.Jk; 81.05.Eu; 81.15.Hi

Keywords: MBE; UHV-AFM; Ridge structure; Quantum wire

1. Introduction

Facet formation by epitaxial growth on a patterned substrate has been explored with great interests as a promising method to organize nanometer size structures [1–5]. We have earlier reported successful growth of 16 nm-wide RQWIs by MBE [6–10]. Their lifetime of photoluminescence has shown a unique temperature dependence indicative of one-dimensional excitons [11]. For their device applications the structural uniformity and the width control of the wire are extremely important.

In this work, we evaluate the shape of RQWIs with nm-scale resolution by using ultra-high-vacuum (UHV) AFM system which is connected to our MBE chamber. This MBE-AFM system provides us systematic and detailed information about the time evolution of the size and uniformity of ridges grown under various growth conditions with nanometer resolution.

* Corresponding author. Fax: + 81 3 3460 9026; e-mail: koshiba@kyokusho.rcast.u-tokyo.ac.jp.

[1] As of October 1, 1996, Quantum Transition Project is run by Japan Science and Technology Corporation (JST).

0022-0248/97/$17.00 Copyright © 1997 Elsevier Science B.V. All rights reserved
PII S0022-0248(96)01204-3

Previously, we have shown that the ridge width (W) can be controlled by adjusting the growth temperature (T_s) [12]. However, variation of T_s affects not only the width W, but also the uniformity of ridges. For example, the ridge grown at T_s of 515°C is quite narrow ($W < 10$ nm), but its morphology is poor. Since a very sharp GaAs ridge with good uniformity is indispensable with a RQWI of 10 nm width, a better growth condition must be explored. In this report, we investigate the effects of not only T_s but also of As flux to show that a very sharp and uniform ridge structures ($W < 10$ nm) can be obtained.

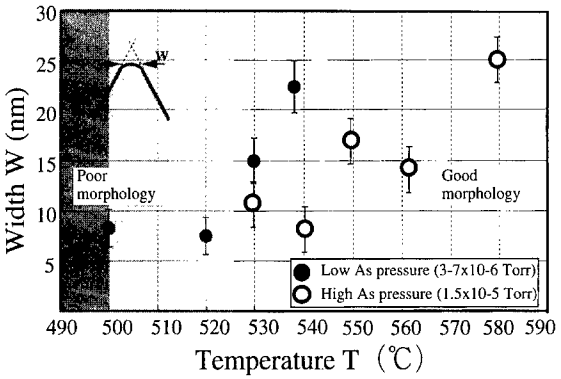

Fig. 1. The width W of GaAs ridges measured as a function of substrate temperature T_s. Solid circles are for the MBE growth with low As flux and blank circles are for high As flux.

2. Experimental procedure

GaAs(0 0 1) wafers were patterned by photo lithography and etched by a reactive ion etcher using $SiCl_4$. The width and height of mesa were about 1.6 and 2–3 μm, respectively. To form a ridge structure a 2.5 μm thick GaAs layer was grown at the substrate temperatures T_s of 560°C. Then the GaAs and AlAs layers were alternatively grown at various T_s under the As_4 beam equivalent pressure ranging from 2×10^{-6} to 3×10^{-5} Torr. The growth rates of GaAs and AlAs were 0.25 and 0.10 μm/h, respectively. The width W of ridge structure was measured by UHV-AFM and cross-sectional SEM [14, 15]. By UHV-AFM we can evaluate the ridge width W and especially its morphology, without exposing the sample to the air. Hence, we can study effects of growth parameters on a single sample. As AFM is influenced by the finiteness of tip radius, each tip was characterized by SEM and the actual ridge width W was determined by the deconvolution of the raw AFM data. Then the ridge width W was also evaluated by SEM using reflected electron mode.

Fig. 1 is the width W of the GaAs ridges thus determined as a function of T_s. Solid circles are for low As flux, while blank circles are for high As flux. The width W increases with increasing T_s, but the use of high As flux is effective in reducing W, especially at high T_s (>530°C). Note that W can be as narrow as 8 nm even at 540°C if high As flux is used. As for the mechanism of increase in width W at high growth temperature T_s, we previously reported that the frequent dissociation of Ga atoms followed by re-arrangement process at the summit of the ridge plays a key role [8]. Hence, the use of high As flux and/or low T_s seems effective in suppressing this dissociation process of Ga atoms.

Variation of T_s influences the morphology of ridge structure. For example, when T_s is lowered to 520°C or below, the width W becomes less than 10 nm, but the (1 1 1)B surface and the (1 $\bar{1}$ 0) sidewall surface which stands vertically along the mesa stripe direction get rough. In such a case, the (1 $\bar{1}$ 0) side surfaces have some blistered facet structures, which indicates that a substantial amount of Ga will be incorporated there. The surface of (1 1 1)B nearby also has random facet structures. Fig. 2 shows the AFM scan of a sample grown at 515°C. Note that step bunching is clearly observed on the (1 1 1)B surface [13]. Note also that (1 1 1)B surface has an anomalous recess where the ridge width loses its uniformity. In the region where the ridge is uniform, the (1 $\bar{1}$ 0) surface is quite flat. There the growth rate on the (1 $\bar{1}$ 0) surface is very low, and the mesa width does not increase so much. Hence the smoothness of the ridge top is strongly correlated with the smoothness of the nearby (1 1 1)B and (1 $\bar{1}$ 0) surfaces.

Next, we grew another sample at $T_s = 560$°C, while As flux was increased to 1.5×10^{-5} for small width W. Fig. 3a shows the AFM image of this sample right after the growth, which indicates that

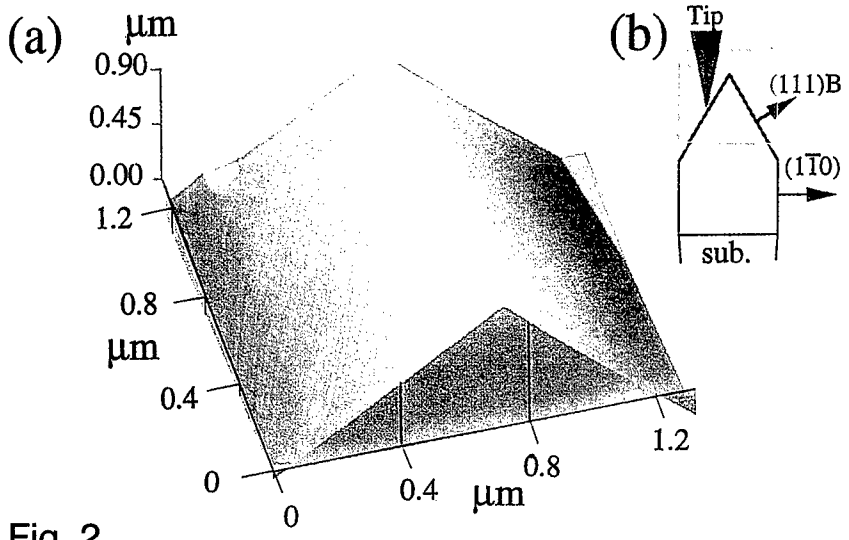

Fig. 2

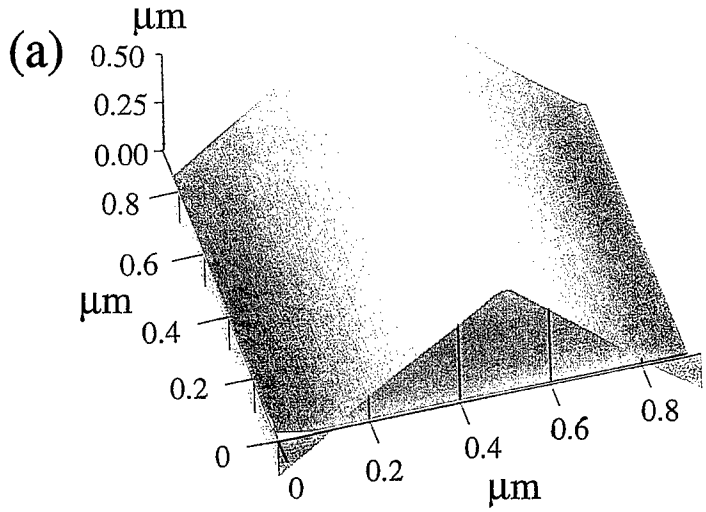

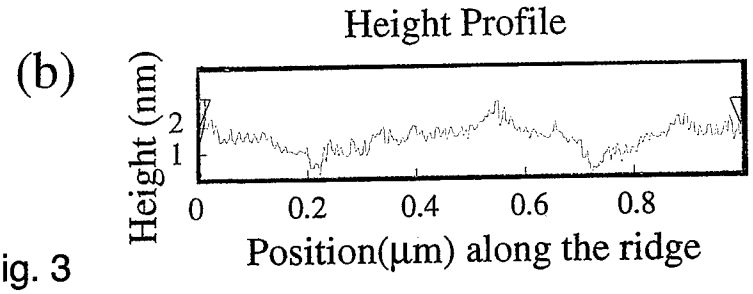

Fig. 3

Fig. 2. (a) AFM image of a GaAs ridge structure grown at 515°C. (b) the shaded area indicates the zone where UHV-AFM measurement was done.

Fig. 3. (a) AFM image of a GaAs ridge structure grown at 560°C. (b) the height distribution of the ridge structure along the ridge top.

a sharp ridge of 15 nm width was uniformly formed. Fig. 3b shows the height distribution along the ridge and indicates that the roughness is quite small within ± 1 nm for the entire region ($>1\ \mu m^2$) measured. The planes forming the ridge are almost as flat as the surface of GaAs grown on a (0 0 1) substrate grown under the optimum condition.

Moreover, we have grown at 540°C a stack of three RQWIs consisting of 12 nm GaAs layers and 4 nm thick AlAs barrier layers on top of the ridge structure. Fig. 4 is its cross-sectional SEM micrograph where GaAs layers appear as bright layers and AlAs as dark and thin layers. Note that all three RQWIs have almost the same width ($W \sim 10$ nm) and height, indicating that the shape of the ridge grown under this condition is stable and reproducible.

Next we discuss the ways to fabricate 10 nm scale RQWI structures. To achieve a strong lateral confinement of carriers in RQWIs, one must form a uniform and narrow ridge structure of AlGaAs or AlAs with the width of less than 30 nm which functions as a bottom barrier. Then one must form on its top a thin GaAs quantum well (QW) in such a way that the resultant GaAs ridge is even narrower than the bottom ridge structure. As described before, the first condition has already been achieved. However, the second requirement is even harder to meet, because this GaAs ridge tends to be broader than that of AlAs ridges if grown under the same condition. Hence, we attempted to control the ridge width W first by varying the growth temperature T_s. The shrinkage of ridge width was achieved as T_s was lowered from 580 to 530°C. Its effect was marginal, due to the limited range of acceptable growth temperature and due to the short growth time of GaAs.

Next we examined the effect of controlling As flux. To change the As flux quickly, we prepared two As sources, a conventional K-cell source A,

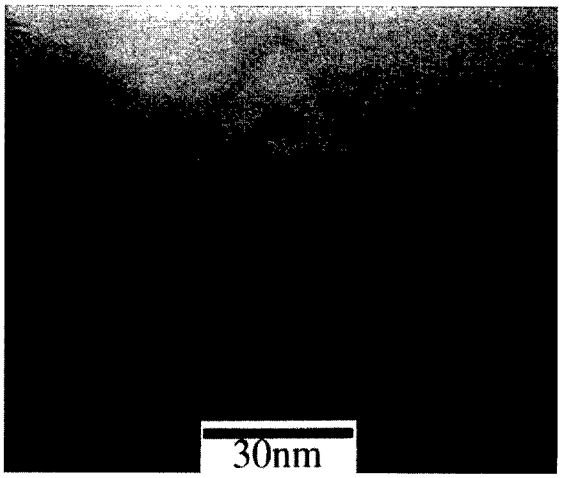

Fig. 4. An SEM micrograph of the stacked ridge quantum wires.

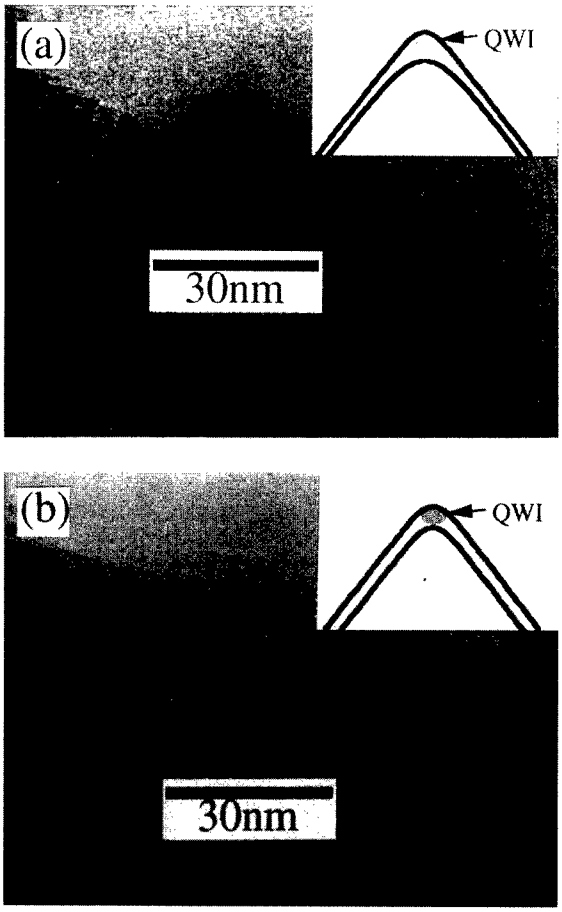

Fig. 5. SEM micrographs of GaAs ridge quantum wires bound by two AlAs barriers (dark stripes) grown at 560°C under two different As fluxes. A Slight widening of the angle between two (1 1 1)B facets is due to the positional drift of samples in SEM equipment.

and a valved K-cell source B. First we grew a GaAs ridge at 560°C with a low As flux ($\sim 2 \times 10^{-6}$ Torr) from source B. After the formation of a broad GaAs ridge, we covered the surface by a thin AlAs layer of 3 nm thickness to preserve the shape. Then we increased the As flux to $\sim 3 \times 10^{-5}$ Torr by opening the shutter of source A and loosening the valve of source B. Under this high As flux, we grew a GaAs QW layer of 8 nm thickness and a 5 nm thick AlAs layer. Fig. 5a is the cross-sectional SEM image of this RQWI structure. Note that a sharp RQWI is sandwiched between two AlAs barrier layers. Note that the GaAs layer on the top of ridge is thicker than that on the (1 1 1)B. Hence, electrons are expected to be confined strongly in the wire of 10 nm width × 8 nm height. Fig. 5b shows the cross-section of a RQWI grown under an As flux of $\sim 1.5 \times 10^{-5}$ Torr. As the thickness of a GaAs layer on (1 1 1)B is about 3 nm, and is smaller than that of Fig. 5b, the quantized energy of electrons in the side QW on (1 1 1)B of Fig. 5a is 220 meV, which is higher than that of Fig. 5b by 100 meV. Hence, electrons in the RQWI of Fig. 5a will be tightly confined.

3. Conclusions

From the morphological study of MBE-grown GaAs ridge structures by UHV-AFM and cross-sectional SEM, we have shown that the increase of As flux is quite effective in reducing the ridge width down to 10 nm even at high substrate temperatures. As a result, the condition to form very narrow GaAs and AlAs ridges with good morphology has been clarified. Very narrow and uniform ridge quantum wire structures, including the stacked wires have been successfully grown by optimizing both the substrate temperature and the As flux.

Acknowledgements

We thank Professor Y. Shiraki of University of Tokyo and Professor P.M. Petroff of University of California Santa Barbara for their cooperation in our project. This work was partially supported by Grant-in-Aid for Scientific Research from the Ministry of Education, Science, and Culture, Japan.

References

[1] E. Kapon, D.M. Hwang and R. Bhat, Phys. Rev. Lett. 63 (1989) 430.
[2] T. Fukui and S. Ando, Electron. Lett. 25 (1989) 410.
[3] S. Tsukamoto, Y. Nagamune, M. Nishioka and Y. Arakawa, Appl. Phys. Lett. 62 (1993) 49.
[4] Y. Nomura, Y. Morishita, S. Goto, Y. Katayama and T. Isu, Appl. Phys. Lett. 64 (1994) 1123.
[5] X.Q. Shen and T. Nishinaga, Jpn. J. Appl. Phys. 32 (1994) L1117.
[6] S. Koshiba, Y. Nakamura, M. Tsuchiya, H. Noge, H. Kano, Y. Nagamune, T. Noda and H. Sakaki, J. Appl. Phys. 76 (1994) 4138.
[7] S. Koshiba, H. Noge, H. Akiyama, Y. Nakamura, Shimizu and A.H. Sakaki, in: Gallium Arsenide and Related Compounds 1992, Inst. Phys. Conf. Ser. 129, Eds. T. Ikegami, F. Hasegawa and Y. Takeda (IOP, Bristol, 1993) p. 931.
[8] S. Koshiba, H. Noge, H. Akiyama, T. Inoshita, Y. Nakamura, A. Shimizu, Y. Nagamune, M. Tsuchiya, H. Sakaki and K. Wada, Appl. Phys. Lett. 64 (1994) 363.
[9] S. Koshiba, H. Noge, H. Ichinose, H. Akiyama, Y. Nakamura, T. Inoshita, T. Someya, K. Wada, A. Shimizu and H. Sakaki, Solid State Electron. 37 (1994) 729.
[10] S. Koshiba, H. Noge, Y. Nakamura, H. Akiyama, T. Inoshita, H. Ichinose, K. Wada, R. Hull and H. Sakaki, Nanostructures and Quantum Effects, Springer Series of Material Science 31 (Springer, Heidelberg, 1994) p. 213.
[11] H. Akiyama, S. Koshiba, T. Someya, K. Wada, H. Noge, Y. Nakamura, T. Inoshita, A. Shimizu and H. Sakaki, Phys. Rev. Lett. 72 (1994) 924.
[12] S. Koshiba, T. Noda, H. Noge, Y. Nakamura, H. Ichinose, T. Shitara, D.D. Vvedensky and H. Sakaki, J Crystal Growth 150 (1995) 322.
[13] Y. Nakamura, Ichiro Tanaka, Norishige Takeuchi, S. Koshiba, H. Noge and H. Sakaki, Jpn. J. Appl. Phys. 35 (1996) 4038.
[14] I. Tanaka, S. Koshiba and H. Sakaki, in: Proc. Int. Conf. on Quantum Devices and Circuits 96, to be published.
[15] S. Koshiba, Ichiro Tanaka, Y. Nakamura, H. Noge and H. Sakaki, Appl. Phys. Lett. 70 (1997) 883.

ELSEVIER

Journal of Crystal Growth 175/176 (1997) 809–813

JOURNAL OF CRYSTAL GROWTH

Improved optical qualities of $GaAs/Al_{0.3}Ga_{0.7}As$ tilted T-shaped quantum wires fabricated by glancing-angle molecular beam epitaxy

N. Tomita[a,*], T. Kishi[1,a], K. Takekawa[a], K. Fujita[b], T. Watanabe[b], A. Adachi[c], S. Shimomura[a], S. Hiyamizu[a]

[a] *Faculty of Engineering Science, Osaka University, Machikaneyama, Toyonaka, Osaka 560, Japan*
[b] *ATR Optical and Radio Communications Research Laboratories, Seika-cho, Soraku-gun, Kyoto 619-02, Japan*
[c] *Nissin Electric Co. Ltd., Umezu-Takase-cho, Ukyo-ku, Kyoto 615, Japan*

Abstract

High-quality $GaAs/Al_{0.3}Ga_{0.7}As$ tilted T-shaped quantum wires (tilted T-QWRs) were fabricated with a two-step growth of molecular beam epitaxy (MBE), which consists of glancing-angle MBE growth of $GaAs/Al_{0.3}Ga_{0.7}As$ multi-quantum well (MQW) layer (five 6.6 nm thick GaAs wells) on a reverse-mesa etched (1 0 0) GaAs substrate and MBE over growth of $GaAs/Al_{0.3}Ga_{0.7}As$/single-quantum well (SQW) (7.3 nm well width) on a (1 1 1)B facet. This new technique enable us to fabricate lots of tilted T-QWRs over a large area of a GaAs substrate surface. Full-width-at-half-maximum (FWHM) of a cathodoluminescence (CL) peak from the tilted T-QWRs was reduced down to 10 meV at 78 K, which is almost comparable with those of GaAs/AlGaAs T-QWRs fabricated by the cleaved-edge overgrowth.

Keywords: GaAs; $Al_{0.3}Gd_{0.7}As$; Glancing-angle MBE; T-shaped quantum wire; (1 1 1)B facet; Selective growth

1. Introduction

Recently, low-dimensional semiconductor structures such as quantum wires (QWRs) and quantum dots (QDs) have been intensively investigated because of their novel optical properties [1–3]. Pfeiffer et al. [4] fabricated $GaAs/Al_{0.3}Ga_{0.7}As$T-shaped QWRs (T-QWRs) by the cleaved edge overgrowth (CEO) method. In this method, a GaAs quantum well (QW) layer and an $Al_{0.3}Ga_{0.7}As$ barrier layer are overgrown on a (1 1 0) cleaved plane of a $GaAs/Al_{0.3}Ga_{0.7}As$ multi-quantum well (MQW) layer grown on a (1 0 0) GaAs substrate by MBE. Therefore, the cross-sectional dimension of the T-QWRs can be precisely controlled in the atomic scale and high quality T-QWRs have been obtained [4, 5]. These T-QWRs, however, are fabricated only on a very limited area of the cleaved

* Corresponding author. Fax: +81 6 845 4632; e-mail: tomi@aquarius.mp.es.osaka-u.ac.jp.

[1] Present address: Sumitomo Electric Co. Ltd., Itami, Hyougo 664, Japan.

0022-0248/97/$17.00 Copyright © 1997 Elsevier Science B.V. All rights reserved
PII S0022-0248(96)00952-9

surface of the MQW layer and it is difficult to apply the T-QWRs to electric or optical devices.

In order to find some solutions of this problem, we have attempted to fabricate GaAs/$Al_{0.3}Ga_{0.7}As$ tilted T-shaped QWRs (tilted T-QWRs) using (1 1 1)B facet planes, instead of the (1 1 0) cleaved plane, preferentially grown on a reverse-mesa etched GaAs substrate by glancing-angle molecular beam epitaxy (GA-MBE) [6–8]. In this case, many tilted T-QWRs can be easily fabricated on a lot of mesa stripes along [1 1 0] direction on a large area of a (1 0 0) GaAs substrate. During GA-MBE growth (no substrate rotation), the preferentially formed (1 1 1)B facet planes are not directly exposed to both Ga and Al beams due to a self-shadowing effect [6]. After the GA-MBE growth of a GaAs/$Al_{0.3}Ga_{0.7}As$ MQW layer, a cross-section of the MQW structure appears on the (1 1 1)B facet plane when we choose a growth condition where the inter-facet migration of Ga and Al atoms do not occur from the (1 0 0) surface to the (1 1 1)B facet. GaAs/$Al_{0.3}Ga_{0.7}As$ tilted T-QWRs are fabricated by overgrowing a GaAs QW layer and an $Al_{0.3}Ga_{0.7}As$ barrier layer on the (1 1 1)B facet plane by a normal MBE with rotating the substrate just after the GA-MBE growth [6, 7]. In the previous work [6], we observed strong cathodoluminescence (CL) at 78 K from 20 GaAs/$Al_{0.3}Ga_{0.7}As$ tilted T-QWRs formed with a GaAs/$Al_{0.3}Ga_{0.7}As$ MQW of the well width of $L_W = 5.4$ nm on the (1 0 0) plane and a GaAs/$Al_{0.3}Ga_{0.7}As$ QW of $L_w = 4.6$ nm on the (1 1 1)B facet, but the full-width-at-half-maximum (FWHM) of the CL peak from the tilted T-QWRs was as large as 61 meV which is mainly due to not optimized conditions for both GA-MBE growth and overgrowth on (1 1 1)B facets. Recently, we reduced this FWHM value down to 19 meV by using improved growth conditions but the CL peak from the tilted T-QWRs was observed only as a shoulder next to the large CL peak from GaAs/$Al_{0.3}Ga_{0.7}As$ QWs on the (1 0 0) plane [7]. This FWHM was still about twice as large as those of GaAs/$Al_{0.3}Ga_{0.7}As$ T-QWRs (10 meV [4], 4–7 meV [5]) fabricated by the CEO method, which is mainly due to smaller size of GaAs/$Al_{0.3}Ga_{0.7}As$ tilted T-QWRs (4.4 nm-wide MQW on the (1 0 0) plane and 4.5 nm-wide QW on the (1 1 1)B facet). In this paper, we report on much improved CL spectra from GaAs/$Al_{0.3}Ga_{0.7}As$ tilted T-QWRs with a little bit larger size fabricated on a reverse-mesa etched (1 0 0) GaAs substrate by the two-step growth (GA-MBE/MBE).

2. Fabrication of GaAs/$Al_{0.3}Ga_{0.7}As$ tilted T-QWRs

The structure of the fabricated sample is shown in Fig. 1a. A GaAs/$Al_{0.3}Ga_{0.7}As$ (87 nm/4.3 nm, 20 periods) superlattice buffer, an $Al_{0.3}Ga_{0.7}As$ layer (87 nm) and a GaAs layer (6.6 nm) were grown on a reverse-mesa etched GaAs (1 0 0) substrate by GA-MBE ($T_s = 630°C$, V/III = 25). Next, a GaAs/$Al_{0.3}Ga_{0.7}As$ (6.6 nm/17 nm, 4 periods) MQW layer and an $Al_{0.3}Ga_{0.7}As$ barrier layer (47 nm) were grown by GA-MBE ($T_s = 570°C$, V/III = 25) to reduce the inter-facet migration of Ga atoms [8]. Finally, a GaAs/$Al_{0.3}Ga_{0.7}As$

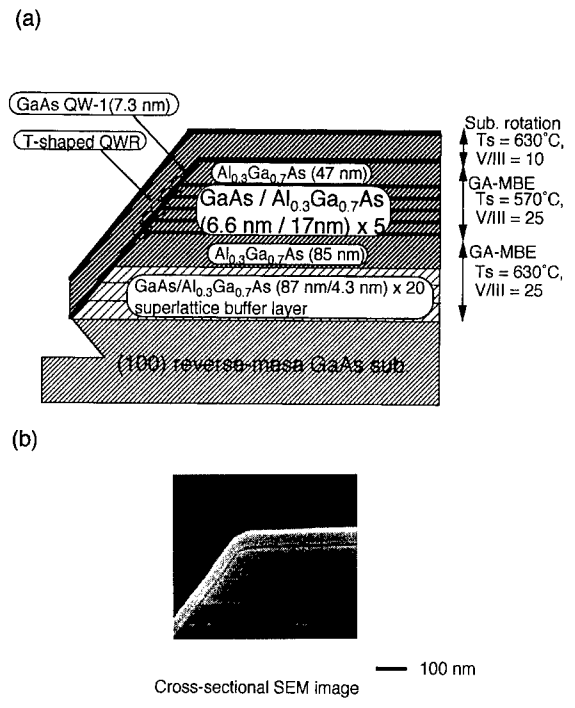

Fig. 1. Sample structure of GaAs/$Al_{0.3}Ga_{0.7}As$ tilted T-QWRs (a) and its cross-sectional SEM image (b).

(7.3 nm/51 nm) SQW and a 12 nm-thick GaAs cap layer were overgrown on the (1 1 1)B facet under the optimized overgrowth condition on the (1 1 1)B facet (T_s = 630°C, V/III = 10) to obtain high optical quality of a GaAs/$Al_{0.3}Ga_{0.7}As$ SQW with rotating the substrate at 60 rpm [7]. Fig. 1b shows the cross-sectional SEM image of the grown sample. Five tilted T-QWRs were successfully fabricated at the junction region of MQW on the (1 0 0) plane and the SQW on the (1 1 1)B facet plane.

3. CL measurements

A CL spectrum of the GaAs/$Al_{0.3}Ga_{0.7}As$ tilted T-QWRs at 78 K is shown in Fig. 2, which was obtained when a focused electron beam (0.2 μm diameter, 7 keV) excited the (1 1 1)B facet region (the tilted T-QWR region). CL peaks at 787 nm and at 795 nm come from the GaAs/$Al_{0.3}Ga_{0.7}As$ MQW on (1 0 0) plane and from the GaAs/$Al_{0.3}Ga_{0.7}As$ SQW on the (1 1 1)B facet, respectively. These MQW on the (1 0 0) plane and SQW on the (1 1 1)B facet form the tilted T-QWRs at their cross regions. The luminescence from the tilted T-QWRs was observed at 803 nm. This peak energy was 1.544 eV which is 31 meV lower than that of the MQW on (1 0 0) plane and is 15 meV lower than that of the SQW on the (1 1 1)B facet plane. This red-shift is caused by the weaker confinement of carriers of the tilted T-QWRs. A peak at 817 nm comes from the edge of the SQW on the (1 0 0) plane which was formed with a thicker QW due to the surface migration of Ga atoms from (1 1 1)B facet plane to (1 0 0) plane when the GaAs/$Al_{0.3}Ga_{0.7}As$ SQW was overgrown on the (1 1 1)B facet. As can be seen in Fig. 2, all these CL peaks are well resolved.

In order to investigate the optical qualities of the tilted T-QWRs fabricated by the two-step growth of GA-MBE / MBE, we measured CL spectra with changing the intensity of the exciting electron beam as shown in Fig. 3. The CL peaks from the T-QWRs were clearly observed in all cases. In the case of a weak electron beam (1×10^{-9} A), the peak from the SQW on the (1 1 1)B facet plane does not become clear, while that from the tilted T-QWRs is still clear, implying that almost all of electrons and holes excited in the (1 1 1)B facet region diffuse into the tilted T-QWR regions and radiatively recombine there. With increasing the exciting

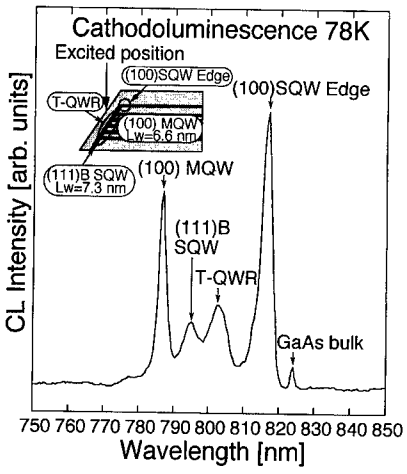

Fig. 2. CL spectrum (78 K) observed in the GaAs/$Al_{0.3}Ga_{0.7}As$ T-QWRs sample when the (1 1 1)B facet region is excited by the electron beam.

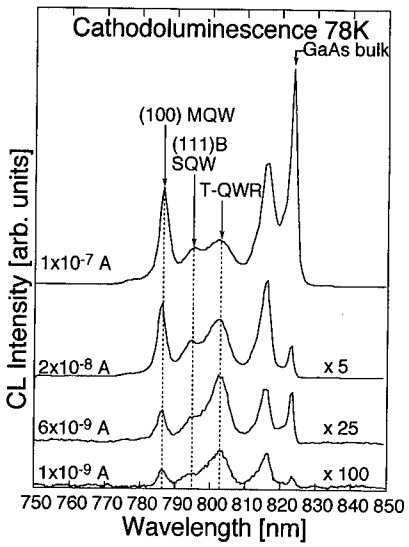

Fig. 3. CL spectra (78 K) observed in the GaAs/$Al_{0.3}Ga_{0.7}As$ T-QWRs. Excitation intensities are changed from 1×10^{-9} to 1×10^{-7} A.

electron beam, the luminescence from the SQW on the (1 1 1)B facet become clear and FWHM of the peak from the T-QWRs become larger. It is partly due to the band filling effect in the tilted T-QWRs. In the case of the low exciting intensity (1×10^{-9}–6×10^{-9} A), FWHM of the peak from the T-QWRs is 10 meV, which is about half of that (19 meV) of previous GaAs/$Al_{0.3}Ga_{0.7}As$ tilted T-QWRs [7], and is almost comparable with those (10 meV [4], 4 – 7 meV [5]) of GaAs/$Al_{0.3}Ga_{0.7}As$ T-QWRs fabricated by the CEO method.

4. Calculation of electron and hole states in the T-QWRs

In order to understand quantitatively the optical properties of the tilted T-QWRs, we calculated states of electrons and holes in the GaAs/$Al_{0.3}Ga_{0.7}As$ tilted T-QWRs based on the finite element method (FEM). The advantage of FEM is that the eigenenergy and eigenstates of carriers confined in a volume with an arbitrary shape can be calculated without any approximation in principle. We take the direction perpendicular to the (1 0 0) substrate surface as the z-axis. The y-axis is taken to be parallel to the tilted T-QWRs (i.e. [1 1 0] direction) and the x-axis is taken to be perpendicular to the tilted T-QWRs in (1 0 0) plane, respectively. In the effective-mass approximation, the envelope wave function of conduction electrons in the GaAs/$Al_{0.3}Ga_{0.7}As$ tilted T-QWR is of the form $e^{iky}\Psi(x, z)$, where $\Psi(x, z)$ satisfies the 2D Schrödinger equation given by

$$-\frac{\hbar^2}{2m_e^*}\left(\frac{\partial^2\Psi}{\partial x^2}+\frac{\partial^2\Psi}{\partial z^2}\right)+U_c\Psi=E_e\Psi, \tag{1}$$

where $\hbar$ is the Plank's constant, E_c is an eigenenergy of an electron confined in the tilted T-QWR. In Eq. (1), $m_e^*(x, z)$ is a position-dependent effective mass of an electron. In the GaAs and $Al_{0.3}Ga_{0.7}As$ regions, we used the effective masses of $m_e^*=0.067m_0$ and $m_e^*=0.071m_0$, respectively, where m_0 is the static mass of an electron. The conduction-band offset of 225 meV was used for $U_c(x, z)$. The Schrödinger equation for holes is given by

$$-\frac{\hbar^2}{2m_h^*}\left(\frac{\partial^2\Psi}{\partial x^2}+\frac{\partial^2\Psi}{\partial z^2}\right)+U_v\Psi=E_h\Psi. \tag{2}$$

The valence band off-set of 131 meV was used for $U_v(x, y)$. We used the common hole mass (m_h^*) of $0.45m_0$ for GaAs and $Al_{0.3}Gs_{0.7}As$ regions. In this calculation, the electron–hole Coulomb interaction was neglected.

Fig. 4a shows $|\Psi|^2$ of an electron confined in the tilted T-QWR: the contours are lines of constant probability ($|\Psi|^2=0.2, 0.4,..., 0.8$) for electrons. The contour map of $|\Psi|^2$ is given in Fig. 4 b. The top of calculated $|\Psi|^2$ slightly shifts from the crosspoint of the QW on (1 0 0) plane and the QW on (1 1 1)B facet due to effectively thinner width of the $Al_{0.3}Ga_{0.7}As$ barrier on the (1 0 0) QW layer near the T-shaped region. In this calculation, we obtained a red-shift of 22 meV for recombination energy in the tilted T-QWRs from the corresponding MQW transition. The observed red-shift is about 31 meV. The difference (9 meV) between the observed and calculated red-shifts is considered to

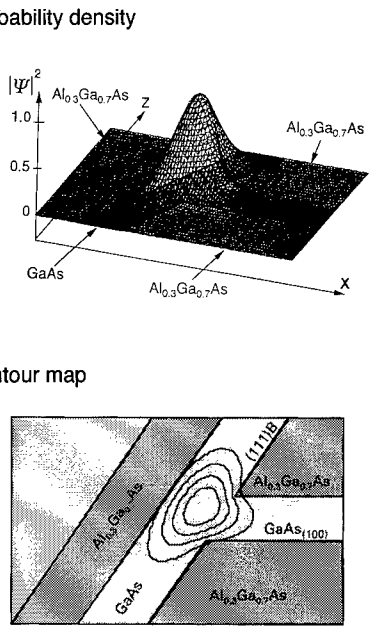

Fig. 4. Calculated probability density $|\Psi|^2$ (a) and contour map of $|\Psi|^2$ (b) for a electron confined in the tilted T-QWRs.

equal to an excess part of the exciton binding energy for the one-dimensional structure (the tilted T-QWR). Taking into account of an exciton binding energy of 11 meV for the 6.6 nm wide MQW, we obtain an exciton binding energy of 20 meV for the tilted T-QWRs, which agrees well with the value (17 meV) obtained for a GaAs/AlGaAs T-QWR by Wegscheider et al. [9].

5. Conclusion

$GaAs/Al_{0.3}Ga_{0.7}As$ tilted T-QWRs (6.6 nm wide MQW on the (1 0 0) plane and 7.3 nm wide SQW on the (1 1 1)B facet plane) were successfully fabricated by the two-step MBE growth (GA-MBE/MBE). Well-resolved CL peaks from the MQW on (1 0 0) plane, the SQW on (1 1 1)B facet plane, and the tilted T-QWRs were observed. FWHM of the CL peak from the tilted T-QWRs was as small as 10 meV at 78 K, which is comparable with those (10 meV [4], 4–7 meV [5]) of $GaAs/Al_{0.3}Ga_{0.7}As$ T-QWRs fabricated by the CEO method. Electron and hole states in the T-QWR was investigated with the use of the finite element method (FEM). The binding energy of excitons in the $GaAs/Al_{0.3}Ga_{0.7}As$ tilted T-shaped QWRs is estimated to 19 meV by comparing with calculated recombination energies and the observed CL peak energies for the MQW and the tilted T-QWRs.

Acknowledgements

This work is supported in part by a Grant-in-Aid for Scientific Research on Priority Area, "Quantum Coherent Electronics" from the Ministry of Education, Science, Sports and Culture.

References

[1] Y. Arakawa and H. Sakaki, Appl. Phys. Lett. 40 (1982) 939.
[2] L. Bányai, I. Galbraith, C. Ell and H. Haug, Phys. Rev. B 36 (1987) 6099.
[3] S. Schmitt-Rink, D.A.B. Miller and D.S. Chemla, Phys. Rev. B 35 (1987) 8113.
[4] L. Pfeiffer, K.W. West, H.L. Sörmer, J.P. Eisenstein, K.W. Baldwin, D. Gershoni and J. Spector, Appl. Phys. Lett. 56 (1990) 1697.
[5] T. Someya, H. Akiyama and H. Sakaki, Phys. Rev. Lett. 74 (1995) 3664.
[6] S. Shimomura, K. Inoue, M. Tanaka, N. Tomita, A. Adachi, M. Fujii, T. Yamamoto, T. Watanabe, N. Sano, K. Murase and S. Hiyamizu, Solid-State Electron. 37 (1994) 597.
[7] N. Tomita, M. Tanaka, T. Saeki, K. Fujita, T. Watanabe, T. Higuchi, N. Sano, A. Adachi, S. Shimomura and S. Hiyamizu, J. Vac. Sci. Technol. B 14 (1996) 3550.
[8] M. Tanaka, N. Tomita, T. Higuchi, S. Shimomura, A. Adachi, N. Sano and S. Hiyamizu, J. Crystal Growth 150 (1995) 388.
[9] W. Wegscheider, L.N. Pferffer, M.M. Dignam, A. Pinczuk, K.W. West, S.L. McCall and R. Hull, Phys. Rev. Lett. 71 (1993) 4071.

ELSEVIER

Journal of Crystal Growth 175/176 (1997) 814–818

JOURNAL OF CRYSTAL GROWTH

High-density GaAs/$(GaAs)_2(AlAs)_2$ quantum wires naturally formed on (7 7 5)B-oriented GaAs substrates by molecular beam epitaxy

M. Higashiwaki[a,*], M. Yamamoto[a], S. Shimomura[a], A. Adachi[b], S. Hiyamizu[a,c]

[a] *Faculty of Engineering Science, Osaka University, Toyonaka, Osaka 560, Japan*
[b] *Nissin Electric Co. Ltd., Umezu-takase-cho, Ukyo-ku, Kyoto 615, Japan*
[c] *Research Center for Extreme Materials, Osaka University, Toyonaka, Osaka 560, Japan*

Abstract

GaAs/$(GaAs)_2(AlAs)_2$ quantum wires (QWRs) were naturally formed in a thin GaAs/$(GaAs)_2(AlAs)_2$ quantum well (QW) with a regularly corrugated AlAs/GaAs upper interface (a period of 12 nm) and a flat GaAs/AlAs lower interface grown on (7 7 5)B-oriented GaAs substrates by molecular beam epitaxy. The QWRs were formed side by side with an extremely high density of 8×10^5 QWRs/cm, which is the same to that of the previous GaAs/AlAs QWRs grown on the (7 7 5)B substrate (the highest density of QWRs ever reported [8]). A photoluminescence from the QWRs formed in the QW with an average well width (L_w) of 2.1 nm, which have a cross section of about 12×2 nm^2, showed a strong polarization dependence (the polarization degree $P \equiv [(I_{\parallel} - I_{\perp})/(I_{\parallel} + I_{\perp})] = 0.21$). The polarization degree is about twice as large as that of the previous GaAs/AlAs QWRs with an average L_w of 3.3 nm grown on the (7 7 5)B substrate. This improvement of the polarization degree is mainly due to the further reduced QW width, which results in an improved one-dimensional confinement of carriers in the present QWRs.

1. Introduction

Recently, low-dimensional quantum structures such as quantum wires (QWRs) and quantum dots (QDs) have attracted much interest from the viewpoints of low-dimensional physics and device applications, and many endeavors have been devoted to fabricate these structures. The confinement of carriers in QWRs or QDs gives rise to sharp peaks in the density of states, and it is expected to realize high efficient lasers with a low threshold current and a reduced temperature dependence of threshold current by using QWRs or QDs [1, 2]. Among many fabrication techniques of QWRs, molecular beam epitaxy (MBE) [3–6] and metalorganic chemical vapor deposition [7] on high index planes with multi-atomic steps of GaAs crystals are very promising, because the fabrication techniques are very simple and QWRs can be formed without any fabrication damage. When we studied optical properties of GaAs/AlAs quantum wells (QWs) grown on GaAs substrates with various tilted

* Corresponding author. Fax: +81 6 8454632; e-mail: higashi@d310.mp.es.osaka-u.ac.jp.

0022-0248/97/$17.00 Copyright © 1997 Elsevier Science B.V. All rights reserved
PII S0022-0248(96)00861-5

angles from the (1 1 1)B plane toward the (1 1 0) plane by MBE, we eventually found that the GaAs/AlAs QWRs structure is naturally formed on GaAs substrates with an off-angle of 8.5° from the (1 1 1)B plane [(7 7 5)B-oriented GaAs substrates] in 1995. And we have reported the GaAs/AlAs QWRs grown on the (7 7 5)B GaAs substrate by MBE [8]. The GaAs/AlAs QWRs on the (7 7 5)B substrate were naturally formed in a 3.3 nm thick GaAs/AlAs QW with a corrugated AlAs/GaAs upper interface (lateral period 12 nm and vertical amplitude 1.2 nm) and a flat GaAs/AlAs lower interface. Density of the QWRs was very high (8×10^5 QWRs/cm), but the one-dimensional confinement of carriers was rather weak. It is difficult to reduce the GaAs well width further in order to enhance the one-dimensional confinement of carriers for the GaAs/AlAs QWs, because the ground energy level of electrons in the QW approaches the X band edge of the AlAs barrier layer with decreasing L_w down to about 3 nm.

In this paper, we study to avoid the X-band edge problem by using $(GaAs)_2(AlAs)_2$ short-period superlattice (SPS) barriers instead of AlAs barriers and improve the one-dimensional confinement of carriers in the GaAs/$(GaAs)_2(AlAs)_2$ QWRs grown on (7 7 5)B GaAs substrates by MBE.

2. Fabrication of QWRs

Samples in this study were grown by a Nissin RB-2001G MBE system. V/III pressure ratio was 9 (14) for GaAs (AlAs), and growth rates of GaAs and AlAs were 1.0 μm/h. The (7 7 5)B GaAs substrate was degreased and etched using a sulfuric acid etchant ($H_2SO_4 : H_2O_2 : H_2O = 5 : 1 : 1$) before loading into the growth chamber, and they were thermally cleaned at a substrate temperature (T_s) of 650°C for 15 min in As_4 atmosphere (10^{-6} Torr) just before MBE growth.

The surface of GaAs grown on the (7 7 5)B GaAs substrate can be changed between a flat surface and a corrugated surface by controlling the substrate temperature. The surface of GaAs becomes flat at $T_s = 540$–580°C and corrugates above $T_s = 640$°C, while the surface of AlAs is always flat above $T_s = 540$°C.

Fig. 1 shows a schematic illustration of the GaAs/$(GaAs)_2(AlAs)_2$ QWRs structure grown on the (7 7 5)B GaAs substrate. The GaAs/$(GaAs)_2(AlAs)_2$ QWRs structure on the (7 7 5)B substrate was fabricated as follows. First, a 25-period (30 nm thick) $(GaAs)_2(AlAs)_2$ SPS barrier layer was grown on a 800 nm-thick GaAs/AlAs buffer layer at $T_s = 580$°C (Fig. 2a). Second, the

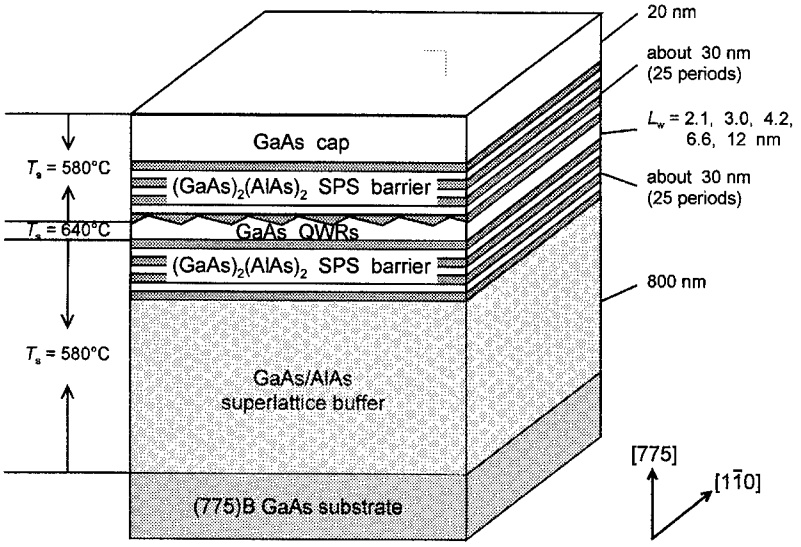

Fig. 1. Schematic illustration of GaAs/$(GaAs)_2(AlAs)_2$ QWRs grown on (7 7 5)B GaAs substrate.

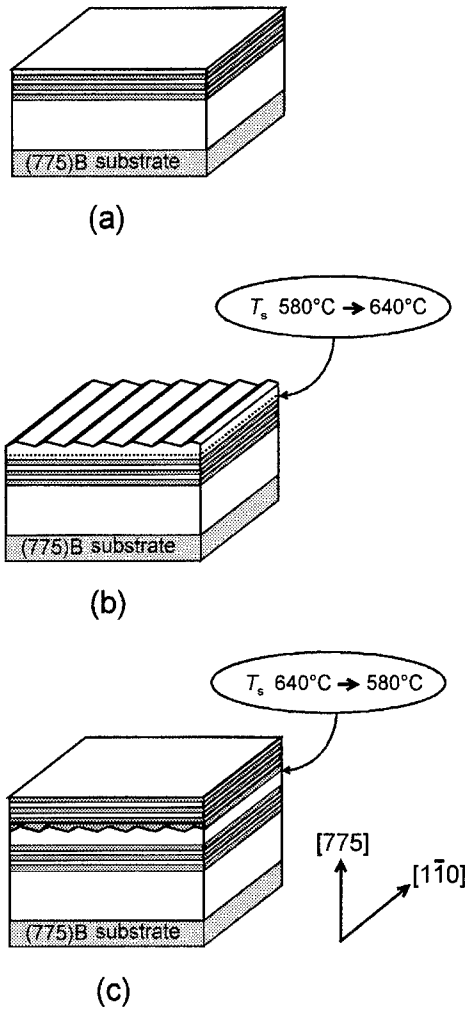

Fig. 2. Fabrication process of $GaAs/(GaAs)_2(AlAs)_2$ QWRs grown on (7 7 5)B GaAs substrate.

substrate temperature was raised to 640°C, and a GaAs QW (QWRs) layer was grown on the structure at $T_s = 640$°C (Fig. 2b). Regular corrugation with very straight step edges along [1 $\bar{1}$ 0] direction is formed. Lateral period and vertical amplitude of the corrugation is 12 and 1.2 nm by cross-sectional transmission electron microscopy. Details of the corrugation have been reported previously in Ref. [8]. Third, $(GaAs)_2(AlAs)_2$ SPS barrier was grown after reducing the substrate temperature from 640 to 580°C. The surface turned to be flat again [Fig. 2c]. The corrugated interface results in a periodic modulation of the well width in the QW. Therefore, lateral confinement effect of carriers arises and QWRs are naturally formed at the thick parts in the $GaAs/(GaAs)_2(AlAs)_2$ QW grown on the (7 7 5)B substrate. After repeating second and third processes with changing QW layer thickness (L_w), a 20 nm thick GaAs cap layer was finally grown on the structure. Hence, high-density $GaAs/(GaAs)_2(AlAs)_2$ QWRs were fabricated using the interesting MBE growth characteristics of GaAs and AlAs on the (7 7 5)B GaAs substrate. Average well widths (L_w) were 2.1, 3.0, 4.2, 6.6 and 12 nm, respectively.

3. Photoluminescence measurements

We measured photoluminescence (PL) at 14 K not only from the $GaAs/(GaAs)_2(AlAs)_2$ QWs (including QWRs) grown on the (7 7 5)B GaAs substrate but also from $GaAs/(GaAs)_2(AlAs)_2$ QWs grown on a (1 0 0) GaAs substrate at $T_s = 640$°C without any growth interruptions. The samples were excited by a He–Cd laser beam with a power of 2 mW and a beam diameter of about 200 μm.

Fig. 3 shows PL spectra at 14 K from the QWs (QWRs) on the (7 7 5)B substrate and the QWs on the (1 0 0) substrate for two different polarization directions. For the sample on the (7 7 5)B substrate, a solid line shows the PL spectrum from the QWs for the polarization parallel to the QWRs ([1 $\bar{1}$ 0] direction), and a dotted line shows that for the polarization perpendicular to the QWRs ([5 5 $\overline{14}$] direction). PL peaks at 670, 707, 741, 776 and 804 nm are from the QWRs with average L_w of 2.1, 3.0, 4.2, 6.6 and 12 nm on the (7 7 5)B substrate, respectively. For the reference QWs grown on the (1 0 0) substrate, a solid line shows PL spectrum for the polarization parallel to the cleaved surface ([0 1 1] direction), and a dotted line shows that for the polarization perpendicular to the cleaved surface ([0 $\bar{1}$ 1] direction).

Full-width at half-maximum of the PL peak from the QWRs with an average L_w of 2.1 nm on the (7 7 5)B substrate was 30 meV, while that from the QW with a L_w of 2.1 nm on the (1 0 0) substrate was 20 meV. The integrated PL intensity from the QWRs on the (7 7 5)B substrate was almost

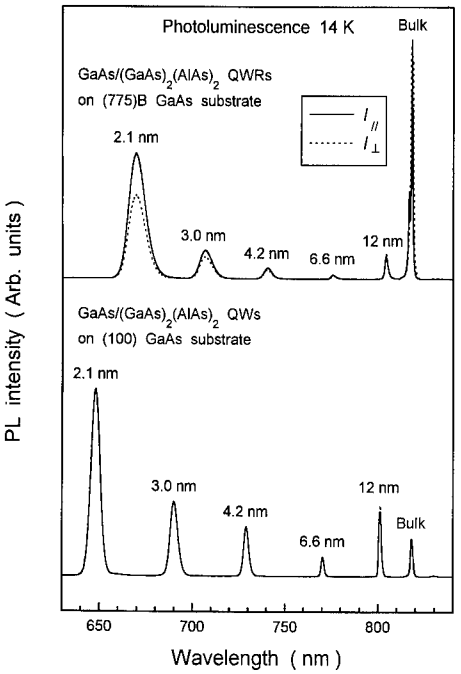

Fig. 3. Polarized PL spectra (14 K) from GaAs/$(GaAs)_2(AlAs)_2$ QWs (including QWRs) grown on (7 7 5)B GaAs substrate and conventional GaAs/$(GaAs)_2(AlAs)_2$ QWs grown on (1 0 0) GaAs substrate.

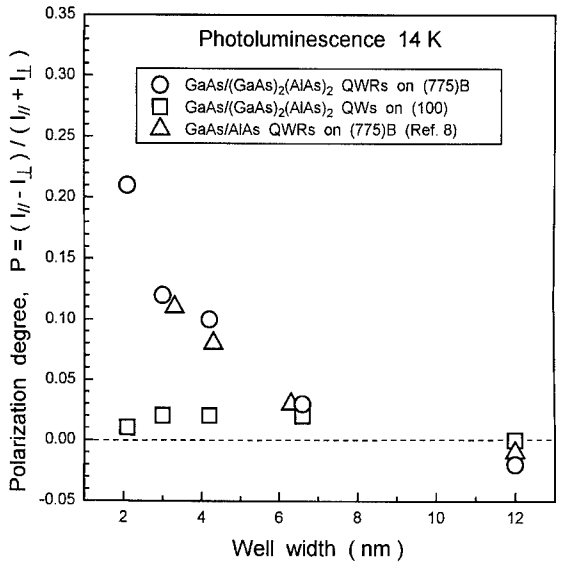

Fig. 4. Polarization degree, $P \equiv [(I_{\parallel} - I_{\perp})/(I_{\parallel} + I_{\perp})]$, for GaAs/$(GaAs)_2(AlAs)_2$ QWs (QWRs) grown on (7 7 5)B GaAs substrate, GaAs/$(GaAs)_2(AlAs)_2$ QWs grown on (1 0 0) GaAs substrate and previous GaAs/AlAs QWs (QWRs) grown on (7 7 5)B GaAs substrate [8] as a function of average well width L_w.

the same as that from the QW on the (1 0 0) substrate. These results indicate that the GaAs/$(GaAs)_2(AlAs)_2$ QWRs grown on the (7 7 5)B substrate had high optical quality.

The polarization degree, $P \equiv [(I_{\parallel} - I_{\perp})/(I_{\parallel} + I_{\perp})]$, of PL peaks from the GaAs/$(GaAs)_2(AlAs)_2$ QWs (QWRs) on the (7 7 5)B substrate, the GaAs/$(GaAs)_2(AlAs)_2$ QWs on the (1 0 0) substrate and the previous GaAs/AlAs QWs (QWRs) grown on the (7 7 5)B substrate [8] are plotted as a function of L_w in Fig. 4. With decreasing L_w from 12 to 2.1 nm, the polarization anisotropy of PL from the QWs (QWRs) on the (7 7 5)B substrate monotonously increases. The PL peak from the QWRs with the average L_w of 2.1 nm on the (7 7 5)B substrate exhibits the strongest polarization dependence ($P = 0.21$). On the other hand, the polarization dependence is constantly almost zero for the QWs on the (1 0 0) substrate. These results are in good agreement with theoretical investigations that PL from a QWR is polarized parallel to the wire direction [9, 10]. The polarization degree of PL from the QWRs with the average L_w of 2.1 nm on the (7 7 5)B substrate was about twice as large as that ($P = 0.11$) from the previous GaAs/AlAs QWRs with an average L_w of 3.3 nm grown on the (7 7 5)B substrate [8]. These results indicate that lateral confinement effect of carriers due to the corrugated interface is actually much enhanced by decreasing L_w down to 2.1 nm, and high-density GaAs/$(GaAs)_2(AlAs)_2$ QWRs with a considerably strong one-dimensional confinement of carriers are realized on the (7 7 5)B substrate by MBE.

Using the finite element method (FEM), we also calculated the envelope wave functions ψ for ground energy levels of electrons and heavy holes in the GaAs/$Al_{0.5}Ga_{0.5}As$ QW with an average L_w of 2.1 nm, which is almost equivalent to the GaAs/$(GaAs)_2(AlAs)_2$ QWRs with the average L_w of 2.1 nm grown on the (7 7 5)B substrate. This FEM calculation showed that the envelope wave function of electrons spreads rather laterally beyond the boundary of the QWR, but that of heavy holes is clearly localized within the QWR.

The high-density QWRs are formed in a GaAs/$(GaAs)_2(AlAs)_2$ N-multi-layer structure grown on the (7 7 5)B substrate, then they are expected to be applied to semiconductor lasers with extremely high-density QWRs ($8N \times 10^5$ QWRs/cm).

4. Conclusion

GaAs/$(GaAs)_2(AlAs)_2$ QWRs were naturally formed in a thin GaAs/$(GaAs)_2(AlAs)_2$ QW with a regularly corrugated AlAs/GaAs upper interface (a period of 12 nm) and a flat GaAs/AlAs lower interface grown on (7 7 5)B-oriented GaAs substrates by MBE. The density of the QWRs was as high as 8×10^5 QWRs/cm. The PL peak at $\lambda = 670$ nm from the QWRs formed in the QW with an average well width of 2.1 nm, which have a cross section of about 12×2 nm^2, showed a strong polarization dependence (the polarization degree $P \equiv [(I_{\parallel} - I_{\perp})/(I_{\parallel} + I_{\perp})] = 0.21$). The observed degree of polarization is about twice as large as that ($P = 0.11$) from the previous GaAs/AlAs QWRs with an average well width of 3.3 nm on the (7 7 5)B substrate [8]. In addition, the integrated PL intensity from the GaAs/$(GaAs)_2(AlAs)_2$ QWRs was as large as that from the corresponding 2.1 nm QW grown on the (1 0 0) GaAs substrate. These results imply that the GaAs/$(GaAs)_2(AlAs)_2$ QWRs grown on the (7 7 5)B substrate have high potential for applications in optical devices.

Acknowledgements

This work is supported in part by a Grant-in-Aid for Scientific Research on Priority Areas, "Quantum Coherent Electronics" from Ministry of Education, Science, Sports and Culture.

References

[1] Y. Arakawa and H. Sakaki, Appl. Phys. Lett. 40 (1982) 939.
[2] Y. Arakawa and A. Yariv, IEEE J. Quantum Electron. 22 (1986) 1887.
[3] K. Inoue, K. Kimura, K. Maehashi, S. Hasegawa, H. Nakashima, M. Iwane, O. Matsuda and K. Murase, J. Crystal Growth 127 (1993) 1041.
[4] M. Takeuchi, K. Shiba, K. Sato, H.K. Huang, K. Inoue and H. Nakashima, Jpn. J. Appl. Phys. 34 (1995) 4411.
[5] R. Nötzel, N.N. Ledentsov, L. Däweritz and K. Ploog, Phys. Rev. B 45 (1992) 3507.
[6] R. Nötzel, D. Eissler and K. Ploog, J. Crystal Growth 127 (1993) 1068.
[7] S. Hara, J. Motohisa, T. Fukui and H. Hasegawa, Jpn. J. Appl. Phys. 34 (1995) 4401.
[8] M. Higashiwaki, M. Yamamoto, T. Higuchi, S. Shimomura, A. Adachi, Y. Okamoto, N. Sano and S. Hiyamizu, Jpn. J. Appl. Phys. 35 (1996) 606.
[9] C.R. McIntyre and L.J. Sham, Phys. Rev. B 45 (1992) 9443.
[10] A.A. Yamaguchi and A. Usui, J. Appl. Phys. 78 (1995) 1361.

ELSEVIER

Journal of Crystal Growth 175/176 (1997) 819–824

JOURNAL OF CRYSTAL GROWTH

Growth of GaInAsP quantum wire heterostructures using the strain-induced lateral-layer ordering process

A.M. Moy, A.C. Chen[1], K.Y. Cheng*, L.J. Chou, K.C. Hsieh

Department of Electrical and Computer Engineering and the Microelectronics Laboratory, University of Illinois at Urbana-Champaign, Urbana, Illinois 61801, USA

Abstract

We present a generalized strain-balance theory on the strain-induced lateral-layer ordering (SILO) process, where various combinations of short-period superlattice (SPS) constituents are used to fabricate novel quantum wire (QWR) heterostructures. Based on the theory, we have fabricated two sets of QWRs in the GaInP and GaInAsP material systems with emission wavelengths of 6200 Å and 1 μm, respectively. Growth of $(GaP)_2/(InP)_1$ SPS was used to create QWRs on $GaAs_{0.66}P_{0.34}$-based substrates. Also, QWRs were formed using $(GaP)_{2.2}/(InAs)_1$ SPS on GaAs substrates. In both these cases, the monolayer pairings of the SPS constituents were unequal. Transmission electron microscopy and polarized photoluminescence spectroscopy confirm the formation of QWRs. These results support the validity of the generalized theory of the SILO process.

1. Introduction

The development of semiconductor quantum wires (QWR) has been driven by the theoretically predicted improvements in performance over quantum well (QW) devices, as well as the scientific aspect of exploring new concepts in engineering. While current efforts into creating QWRs include etch and regrowth [1], growth on patterned substrates [2], and cleaved edge overgrowth [3], the strain-induced lateral-layer ordering (SILO) process has proven itself to be a simple and reliable technique for QWR formation [4]. The in situ SILO technique can use standard (1 0 0) on-axis or vicinal substrates [5], creates lateral composition modulation perpendicular to the growth direction, and applies to a wide range of growth conditions. It also avoids damage at interfaces because no pre- or post-growth processing is required. The SILO technique uses localized strain within short-period superlattices (SPS) to drive atomic migration, resulting in lateral quantum wells (LQW) formed in the [1 1 0] direction. Combined with common QW fabrication methods, which confine charge carriers in the (1 0 0) growth direction, this technique creates two-dimensionally confined QWRs.

A key factor of the SILO technique is that the strain balance is maintained through the SPS layer. That is, the layers which comprise the SPS have

* Corresponding author.

[1] Present address: Science Center, Rockwell International, Thousand Oaks, CA 91358, USA.

0022-0248/97/$17.00 Copyright © 1997 Elsevier Science B.V. All rights reserved
PII S0022-0248(96)01033-0

alternating compressive and tensile strain, with respect to the growth substrate. Thus, while the strain within the SPS can be large, the net strain is finite and near zero. This near-zero overall strain is significant so that defects due to lattice relaxation are minimized. Previous efforts utilizing the SILO process studied the formations of QWRs through the growth of $(GaP)_m/(InP)_n$ SPS on GaAs [6] and $(GaAs)_m/(InAs)_n$ SPS on InP [7]. In order to fulfill the nearly balanced strain requirement in these material systems, only near-equal monolayer pairings of the SPS ($m \approx n$) could be studied. As a consequence, photonic devices fabricated using the SILO process exist in limited wavelength domains.

In this study, we have generalized the strain-balance concept in the SILO process where the monolayer pairs of the SPS are not equal ($m \neq n$) and yet still satisfy the near-zero net strain condition. This is demonstrated by the growth of $(GaP)_2/(InP)_1$ SPS on a $GaAs_{0.66}P_{0.34}$ substrate. Additionally, QWR formation is also explored using $(GaP)_{2.2}/(InAs)_1$ SPS grown on GaAs. Polarized emission from these samples was observed near 6200 Å and 1 μm, respectively. Thus, this study provides important evidence about the validity and versatility of the SILO process as it is applied to QWR formation in a wide selection of materials.

2. Theory

Realizing one-dimensionally confined structures in semiconductors has been routinely explored and exploited in the past 20 years. Typically, these fabricated QWs confine carriers in the growth direction. A more difficult challenge has been to create two-dimensionally confined QWRs. For this type of structure, composition variation of the alloy must occur simultaneously in two orthogonal directions.

In an effort to create viable QWRs in semiconductors, the SILO process was developed [8]. This growth technique is an in situ method for forming LQWs in the growth plane through molecular beam epitaxy growth. The basic technique of the SILO process is based on the deposition of alternating thin layers of two different materials to form a SPS, where each of the layers is strained with respect to the growth substrate. This nearly strain balanced structure, however, is tensile for one of the layers and compressive for the other. During the growth of this SPS, the localized finite net strain that exists can trigger spinodal decomposition [9] or induce a morphological instability [10] on the surface. This will cause atoms in the alloy to migrate in a plane perpendicular to the growth direction. As predicted by Glas, once the composition modulation is initiated, it is stable and propagates as growth continues [11]. In previous studies, this modulation has always been observed to occur in the [1 1 0] direction, creating LQWs. When combined with larger band-gap material in the growth direction via standard QW growth methods, somewhat uniform arrays of QWRs are formed. The key factor of the SILO process is that the strain in each of the alternating layers is opposite in sign but nearly equal in magnitude. Thus, the SPS as a whole has minimal strain, and defects due to lattice relaxation or critical thickness boundaries are not induced.

Previous studies have explored the growth of $(GaP)_m/(InP)_n$ SPS on GaAs substrates to create $Ga_xIn_{1-x}P$ QWRs [6]. The lattice mismatch between GaP/GaAs and InP/GaAs is approximately equal in magnitude (~4%), but opposite is sign. By growing this superlattice using the condition that $m \approx n$ on GaAs, the tensile and compressive strain forces within the SPS region compensate each other to provide a near-zero global strain (ΔS). Similarly, $(GaAs)_m/(InAs)_n$ SPS has been grown on InP substrates to create $Ga_xIn_{1-x}As$ QWRs [7]. In this case also, the condition $m \approx n$ was used. Thus, because of the nature and magnitude of the strain that exists in the SPS using the aforementioned material systems, only the case of using nearly equal monolayer pairing ($m \approx n \approx 2$) has been previously studied. While success has been achieved in creating QWRs in these systems, the necessity to fulfill the balanced strain conditions has also limited the wavelength ranges for photonic devices fabricated via the SILO process.

The near strain balanced conditions of the SILO process in general are not limited to the case of $m \approx n$. Consider the general SPS consisting of $(A)_m/(B)_n$ grown on a substrate with a lattice

constant a_0, where A and B are arbitrary semiconductor alloys. The amount of mismatch between the SPS and substrate can be characterized using the equation

$$\Delta T \equiv \frac{\text{SPS period} - N(a_0/2)}{N(a_0/2)},$$

where SPS period $= (ma_A + na_B)/2$, N is the nearest integer of $(m + n)$, and a_A and a_B are the lattice constants of the SPS constituent layers. In order for strain balance to occur within the SPS, the lattice constant of the substrate (a_0) must be between the constants of the constituents (a_A and a_B). The global strain can be calculated using the relation

$$\Delta S \equiv |m\,\Delta a_A + n\,\Delta a_B|,$$

where $\Delta a_A = (a_A - a_0)/a_0$ and $\Delta a_B = (a_B - a_0)/a_0$. The only necessary constraint of the SILO process is therefore that ΔS and ΔT are small but finite ($\sim 5\%$). This condition provides the strain to drive the atomic migration within the alloy, and yet maintains the near lattice match of the SPS as a whole [8]. The number of monolayers used in the SPS need not be equal, provided that the proper substrates and SPS constituents are used.

3. Experimental procedure

To verify the generalized strain-balance theory, two QWR heterostructures were created using the SILO process with $m \neq n$ in the SPS layers. The first was $[(GaP)_2/(InP)_1$ SPS]/AlGaInP grown on $GaAs_{0.66}P_{0.34}$ substrates. This substrate, commonly employed for light-emitting diode fabrication, uses vapor-phase epitaxy to compositionally grade GaAs to GaAsP on a (1 0 0) oriented GaAs substrate [12]. Each of the 5 SPS QW grown consisted of 12 pairs of the binary constituents, with QWs separated by 100 Å $Al_{0.15}Ga_{0.53}In_{0.32}P$ barriers. The second QWR structure was $[(GaP)_m/(InAs)_n$ SPS]/GaAs grown on (1 0 0) oriented GaAs. The QWR region consisted of 5 SPS QWs, where 12 pairs of $(GaP)_{2.2}/(InAs)_1$ SPS made up each well, separated by 75 Å GaAs barriers. Surrounding this QWR region above and below was 2500 Å of lattice-matched $Ga_{0.52}In_{0.48}P$. Lateral modulation in the [1 1 0] direction within the SPS regions, along with the barrier materials in the [0 0 1] direction, create the two-dimensionally confined QWRs.

Samples were grown using a gas-source molecular beam epitaxy system, with elemental In and Ga group III sources, and thermally cracked AsH_3 and PH_3 group V sources [13]. Both a cryogenic and turbomolecular pump were used to evacuate the growth chamber. Growth rates of individual effusion cells were calibrated using reflection high-energy electron diffraction intensity oscillations.

The structural and optical properties of the QWR samples were characterized using transmission electron microscopy (TEM) and polarized photoluminescence (PPL) spectroscopy, respectively. Excitation for the PPL measurements was performed using the 5145 Å line of an Ar ion laser. The photoluminescence (PL) emission signal was measured using a 0.5 m focal length grating spectrometer and a liquid-nitrogen-cooled Ge detector, using the lock-in technique. Samples were mounted in an evacuated cold finger type cryostat. To determine the polarization of the emission, PPL additionally employed a polarization analyzer. This analyzer was rotated so that its axis could be oriented either parallel or perpendicular to the QWR direction. Also, a depolarizer was employed to remove any anisotropic effects of the spectrometer grating. The polarization value (ρ) for the PPL was calculated using the equation $\rho = (I_{\parallel} - I_{\perp})/(I_{\parallel} + I_{\perp})$, where $I_{\parallel}$ is the PL peak intensity measured with the polarizer axis parallel to the QWR direction, and $I_{\perp}$ is the PL peak intensity measured with the polarizer axis perpendicular to the QWR direction.

4. Results and discussion

In TEM images of both samples, a uniform contrast appears across the SPS region in the [1 1 0] cross section (not shown), while strong dark and light fringes are seen in the $[\bar{1}\,1\,0]$ cross-section. The dark field $[\bar{1}\,1\,0]$ cross-sectional TEM image

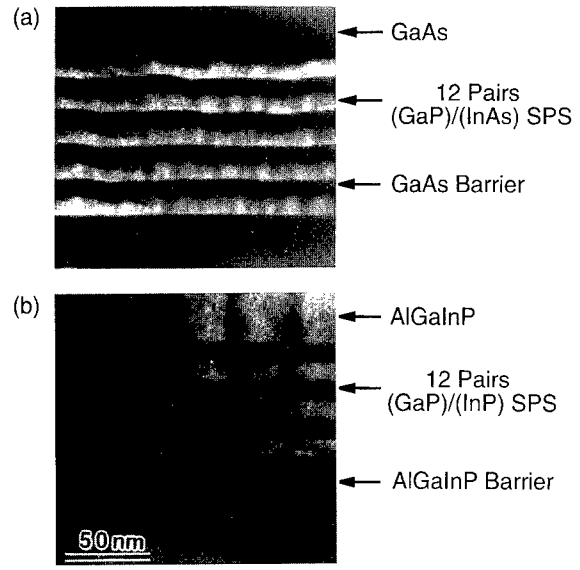

Fig. 1. The [$\bar{1}$ 1 0] dark field cross-sectional transmission electron microscopy images of the (a) [$(GaP)_{2.2}/(InAs)_1$ SPS]/GaAs QWRs on GaAs substrate and (b) [$(GaP)_2/(InP)_1$ SPS]/AlGaInP QWRs on $GaAs_{0.66}P_{0.34}$ substrate.

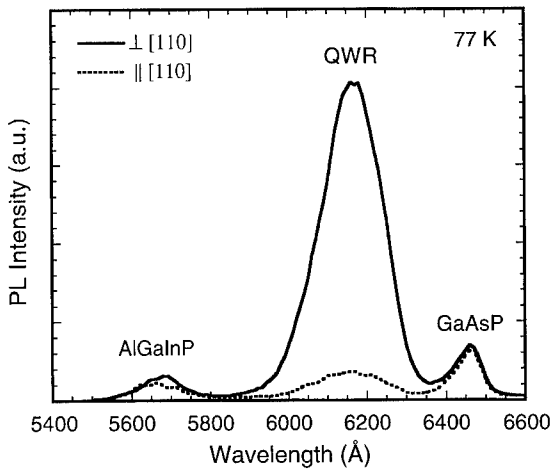

Fig. 2. Polarized photoluminescence (PPL) emission at 77 K from QWRs created using $(GaP)_2/(InP)_1$ SPS on a $GaAs_{0.66}P_{0.34}$ substrate. The solid and dashed lines denote the orientation of the polarization analyzer with respect to the [1 1 0] direction for the PPL measurement.

of a QWR structure using a [$(GaP)_{2.2}/(InAs)_1$ SPS]/GaAs is shown in Fig. 1a. Fig. 1b displays the [$\bar{1}$ 1 0] cross section of the QWRs formed using $(GaP)_2/(InP)_1$ SPS and $Al_{0.15}Ga_{0.53}In_{0.32}P$. The light fringes correspond to the higher-energy band-gap material. The 5 QWs existing in the [0 0 1] direction are clearly visible. Lateral modulation occurs in the [1 1 0] direction, the same direction as was observed in previous SILO studies using equal monolayer pairings [6, 7]. The atomic segregation forms wires which lie in the [$\bar{1}$ 1 0] direction, and the lateral periodicity of the QWR in the [1 1 0] direction is on the order of ~150–200 Å. The interface non-uniformity apparent in the $(GaP)_{2.2}/(InAs)_1$ SPS sample is most likely a result of the non-optimal source switching scheme used, where As and P intermixing in the lattice can affect the surface roughness [14]. The general layout of the cross section that the images display is similar to that seen in other instances of the QWRs formed by the SILO process [6, 7].

Fig. 2 displays the PPL spectrum of the [$(GaP)_2/(InP)_1$ SPS]/AlGaInP QWRs at 77 K. As seen in this figure, evidence of the QWR formation is clearly present due to the highly polarized nature of the PL emission ($\rho = 0.84$), with its peak wavelength near 6200 Å. As a reference, the spectra from the surrounding AlGaInP and the GaAsP substrate are shown and are seen to be nominally polarized. For this application of the SILO process, the global strain is $\Delta S = 0.36\%$ and the mismatch between the SPS and the substrate is $\Delta T = 0.12\%$. The room-temperature PPL spectra for the [$(GaP)_{2.2}/(InAs)_1$ SPS]/GaAs based QWRs are shown in Fig. 3. The emission from this structure, near 1.02 μm, is also highly polarized, with a value $\rho = 0.67$. Using the strain calculations described in a previous section, strain values for this structure are $\Delta S = 0.7\%$ and the SPS/substrate mismatch is $\Delta T = 6.6\%$. The observed luminescence intensity and degree of polarization is comparable to the previous studies of SILO produced QWRs.

It is evident from the periodic fringes in the cross-sectional TEM micrographs and the strong polarization of the PPL spectra that QWRs have been formed in these two heterostructures [15]. These results, in combination with previously reported QWR formation using SPS with equal number monolayer pairings, verify the generalized strain-balance theory and its relation to lateral

composition modulation through the SILO process. Indeed, this method has been employed to generate QWRs across numerous material systems and substrates. Fig. 4 summarizes the distinct emission wavelength regimes from visible to near infrared where the SILO technique has thus far been used to create QWRs [6, 7].

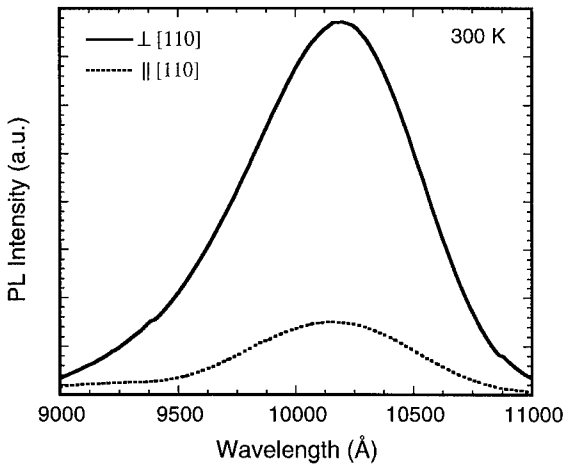

Fig. 3. The room-temperature PPL emission from QWRs created using $(GaP)_{2.2}/(InAs)_1$ SPS on a GaAs substrate. The solid and dashed lines denote the orientation of the polarization analyzer with respect to the [1 1 0] direction for the PPL measurement.

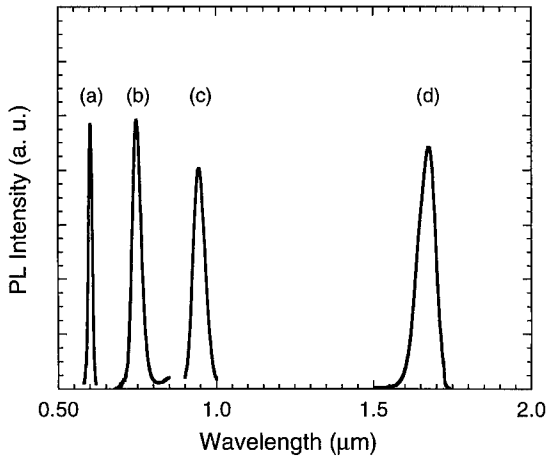

Fig. 4. Observed PL spectra of QWR emission from material systems and substrates formed by the SILO process: (a) $(GaP)_2/(InP)_1$ SPS on $GaAs_{0.66}P_{0.34}$, (b) $(GaP)_2/(InP)_2$ SPS on GaAs, (c) $(GaP)_2/(InAs)_1$ SPS on GaAs, and (d) $(GaAs)_2/(InAs)_2$ SPS on InP.

5. Conclusion

Due to the restrictions of certain material systems, previous endeavours into QWR formation by using the SILO process with this technique have used equal monolayer pairings within the SPS. In this paper, we presented a generalized theory of the SILO process where the required number of monolayer pairings within the SPS to maintain strain-balanced conditions has been established. The data gathered for this report provide evidence for the theory's generality by its extension into new material systems (GaInAsP on GaAs and GaInP on GaAsP) as well as new growth schemes (non-equal monolayer SPS pairings). A number of QWR heterostructures with a wide range of PL emissions from visible to near-infrared have been demonstrated. It is therefore seen that the SILO technique is a versatile tool to create functional QWRs in semiconductors.

Acknowledgements

Funding for this research was provided by the National Science Foundation (NSF-ECD-89-43166 and DMR-89-20538) and the Joint Services Electronics Program (N00014-96-1-0129).

References

[1] Y. Miyake, H. Hirayama, S. Tamura, S. Arai, M. Asada, Y. Miyamoto and Y. Suematsu, IEEE J. Quantum Electron. 29 (1993) 2123.
[2] E. Kapon, D.M. Hwang and R. Bhat, Phys. Rev. Lett. 63 (1989) 430.
[3] W. Wegscheider, L. Pfeiffer, M. Dignam, A. Pinczuk, K. West and R. Hull, Semicond. Sci. Technol. 9 (1994) 1933.
[4] P.J. Pearah, A.C. Chen, A.M. Moy, K.C. Hsieh and K.Y. Cheng, IEEE J. Quantum Electron. 30 (1994) 608.
[5] A.C. Chen, A.M. Moy, L.J. Chou, K.C. Hsieh and K.Y. Cheng, Appl. Phys. Lett. 66 (1995) 2694.
[6] A.C. Chen, A.M. Moy, P.J. Pearah, K.C. Hsieh and K.Y. Cheng, Appl. Phys. Lett. 62 (1993) 1359.
[7] S.T. Chou, K.Y. Cheng, L.J. Chou and K.C. Hsieh, Appl. Phys. Lett. 66 (1995) 2220.

[8] K.Y. Cheng, K.C. Hsieh and J.N. Baillargeon, Appl. Phys. Lett. 60 (1992) 2892.
[9] K.C. Hsieh and K.Y. Cheng, Mater. Res. Soc. Proc. 379 (1995) 145.
[10] B.J. Spenser, P.W. Voorhees and S.H. Davis, J. Appl. Phys. 73 (1993) 6955.
[11] F. Glas, J. Appl. Phys. 62 (1987) 3201.
[12] A.C. Chen, A.M. Moy and K.Y. Cheng, J. Vac. Sci. Technol. B 13 (1995) 762.
[13] A.M. Moy, A.C. Chen, S.L. Jackson, X. Liu, K.Y. Cheng, G.E. Stillman and S.G. Bishop, J. Vac. Sci. Technol. B 11 (1993) 826.
[14] A.M. Moy, A.C. Chen, K.Y. Cheng, L.J. Chou and K.C. Hsieh, unpublished.
[15] K.Y. Cheng, K.C. Hsieh, J.N. Baillargeon and A. Mascarenhas, Proc. 1991 Int. Symp. GaAs and Related Compounds, Inst. Phys. Series 120, Seattle, WA, USA (1992) pp. 589–594.

ELSEVIER

Journal of Crystal Growth 175/176 (1997) 825–832

JOURNAL OF CRYSTAL GROWTH

MBE growth of high-power InAsSb/InAlAsSb quantum-well diode lasers emitting at 3.5 μm

G.W. Turner*, M.J. Manfra, H.K. Choi, M.K. Connors

Lincoln Laboratory, Massachusetts Institute of Technology, Lexington, Massachusetts 02173-9108, USA

Abstract

Molecular beam epitaxy (MBE) has been employed for the growth of strained quantum-well laser structures on InAs substrates. These lasers consist of compressively strained InAsSb wells, tensile-strained InAlAsSb barriers, and lattice-matched AlAsSb cladding layers. Broad-stripe lasers, with emission at wavelengths between 3.2 and 3.55 μm, have exhibited cw power of 215 mW/facet at 80 K, pulsed threshold current density as low as 30 A/cm^2 at 80 K, characteristic temperatures (T_0) between 30 and 40 K, and maximum pulsed operating temperature of 225 K. Ridge-waveguide lasers have cw threshold current of 12 mA at 100 K, and a maximum cw operating temperature of 175 K. In this paper we will present some of the key issues regarding the MBE growth of such high-power lasers on InAs and discuss future directions for improved device performance.

PACS: 68.55.Bd; 42.55.Px

1. Introduction

A number of different approaches are actively being investigated with the goal of obtaining high-performance mid-infrared (3–5 μm) diode lasers that are capable of high-power cw operation at room temperature. These include laser structures based on conventional electron–hole recombination in quantum-well (QW) and superlattice active regions of either Type I [1] or Type II [2] band alignment, and quantum cascade structures which are based on unipolar intersubband transitions [3]. All of these approaches attempt to overcome limitations, such as nonradiative Auger recombination, that are increasingly important for room-temperature operation of long-wavelength diode lasers. We have previously reported Type I multiple-quantum-well (MQW) diode lasers, grown by molecular beam epitaxy (MBE) on GaSb substrates, consisting of active regions of compressively strained InAsSb wells and tensile-strained InAlAsSb barriers, and lattice-matched AlAsSb cladding layers. Such lasers emitted at 3.9 μm and operated cw up to 128 K [4].

In this paper, we describe our investigation of similar strained MQW diode lasers, based on active regions of InAsSb wells and InAlAsSb barriers, and AlAsSb cladding layers, but grown by MBE on

* Corresponding author.

0022-0248/97/$17.00 Copyright © 1997 Published by Elsevier Science B.V. All rights reserved
PII S0022-0248(96)01030-5

InAs substrates. These laser structures are grown with epitaxial compositions adjusted to (a) achieve the desired strains and Type I band alignments in the active region materials and (b) maintain lattice matching of the cladding layers to the InAs substrate. The reasons for investigating such QW structures on InAs substrates will be explained and the resultant performance of high-power, mid-infrared diode lasers will be discussed. We will also describe some of the MBE growth issues which were found to influence the characteristics of these long-wavelength diode lasers.

2. Experimental procedure

The InAsSb QW lasers were grown in a solid-source EPI Gen II 3 in MBE system, equipped with two Sb_4 sources, an EPI valved As cracking source used to provide As_2 flux, and conventional ion pumps. InAs(100) n-type substrates were prepared by either (a) solvent cleaning and chemical etching in a 4:1:7 $H_2SO_4:H_2O_2:H_2O$ solution, followed by In-bonding for typical substrate material, or (b) directly loaded into a solderless block containing an Al_2O_3 backing plate for 2 in epi-ready substrate material. After careful UHV outgassing and oxide desorption of the substrates in an As_2 flux, the following layers were grown: n^+-InAs buffer, ~ 2.0 μm n-$AlAs_{0.16}Sb_{0.84}$ lower cladding, MQW active region consisting of 150 Å compressively strained $InAs_{0.935}Sb_{0.065}$ wells and 300 Å tensile-strained $In_{0.85}Al_{0.15}As_{0.9}Sb_{0.1}$ barriers, ~ 2.0 μm p-$AlAs_{0.16}Sb_{0.84}$ upper cladding, and 500 Å p^+-GaSb cap layer. These values give approximately 0.45% strain in the wells and 0.27% strain in the barriers, with the strain–thickness product in wells and barriers set to approximately the same value in an attempt to achieve a strain-balanced active region. A cross-section of the laser structure is shown in Fig. 1. Be was used as the p-type dopant and GaTe was the source for Te as an n-type dopant. Hall measurements of nominally undoped InAsSb and InAlAsSb layers grown on semi-insulating GaAs substrates yielded n-type conductivity, as was observed for growth of the related alloys on GaSb. Since the active regions used for this work were undoped, the p–n junction was formed at the active-layer/upper-cladding interface. The two Sb_4 effusion cells allowed some optimization of the III/V ratio for each alloy, when used in conjunction with the valved As_2 source. The buffer and cladding layers were grown at ~ 0.8–0.9 μm/h, and the QW active regions were grown at slightly lower growth rate. The substrate temperature was controlled at 520°C for the lower cladding, 430°C for the QW

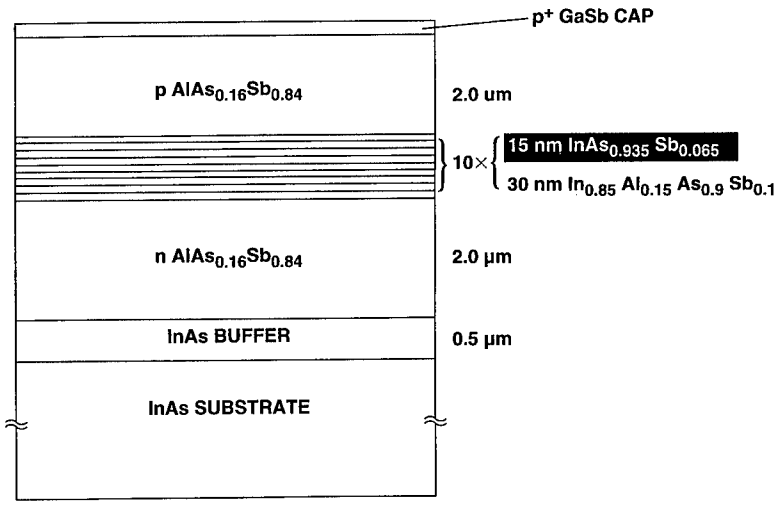

Fig. 1. Cross section of InAs QW laser structure.

active region, and reduced to 490°C for the upper cladding and GaSb cap layer. As will be shown below, this reduction in upper cladding temperature was necessary to prevent degradation of the active regions. As previously reported [5], the necessity of precise control of composition, strain, and lattice parameter required a number of test growths and calibration procedures.

After dismounting of the In-bonded samples, the In-alloyed region on the back side of the InAs wafer was removed by etching in HNO_3, making sure that the wafer surface was protected during the etching process. Samples grown on the 2 in epi-ready substrates did not require this additional step, as there was no apparent degradation of the back side of the InAs substrate at the growth temperatures used. The surfaces of the InAs substrates were characterized by atomic force microscopy (AFM), and the epitaxial layers were characterized by photoluminescence spectroscopy, double-crystal X-ray diffraction (DCXRD), and Auger microprobe chemical analysis. The complete MBE-grown laser wafers exhibited excellent surface morphology, and especially for the epi-ready 2 in substrates, very good yields of laser diodes with consistent characteristics were obtained across the entire wafer.

To evaluate laser performance, broad-stripe lasers 100–250 μm wide were fabricated by using SiO_2 patterning. For both n and p contacts, non-alloyed Ti/Pt/Au was used. Ridge-waveguide lasers, 8 μm wide, were fabricated from some wafers using reactive ion etching in a BCl_3/Ar plasma to define the ridges. Lasers were mounted junction-side up on Cu heat sinks using In, and loaded into a dewar for low-temperature I–V and L–I measurements.

3. Results

Because of the desire to grow complete laser structures on large-area, nonbonded substrates, epi-ready InAs material was evaluated by AFM. Fig. 2 shows a comparison between conventional InAs material and epi-ready material from two different vendors, with the respective samples taken directly from the vendor's packaging to the AFM apparatus. The remarkable smoothness of the epi-ready InAs surface was also confirmed by a comparison of reflection high-energy electron diffraction images obtained before oxide desorption in the growth chamber. In the AFM image of the epi-ready samples there is some evidence of atomic structure on the as-received surface, and this structure was determined to be crystallographically oriented by AFM scanning in different directions.

A key reason for the consideration of the growth of strained InAsSb/InAlAsSb QW active regions on InAs substrates is the presence of a large predicted miscibility gap for the InAlAsSb barrier material [6]. As shown in Fig. 3, changing from GaSb to InAs substrates increases the predicted region of stable growth for InAlAsSb from a maximum Al content of less than 6% to approximately 15%. Increasing the Al content in the InAlAsSb barrier material is important to improve both the conduction and the valence band offset in the active region, for improved carrier confinement and enhanced laser performance [7]. Although these theoretical predictions of regions of stable growth for the InAlAsSb alloy are strictly valid for equilibrium growth conditions, our previous experience with the nonequilibrium, MBE growth of InAsSb/InAlAsSb QWs on GaSb substrates confirmed the practical difficulty of increasing the Al content in this barrier alloy, while still maintaining high-quality QWs.

As an indication of the quality of $InAs_{0.935}Sb_{0.065}/In_{0.85}Al_{0.15}As_{0.9}Sb_{0.1}$ strained MQWs that can be grown on InAs substrates by MBE, Fig. 4 shows a comparison of a 10-well test structure grown on an InAs buffer layer. The excellent agreement between the actual DCXRD data and the simulated diffraction curve shows high structural perfection in the MQW test structure. For these QW structures, the best results were obtained with an As_2 interruption at each well/barrier interface. While the use of InAs substrates permits the growth of high-quality MQW active regions, the growth of the $AlAs_{0.16}Sb_{0.84}$ lattice-matched cladding region becomes more difficult, since this alloy now contains $\sim$ 2X as much arsenic as was the case for the lattice-matched cladding alloy grown on GaSb, and is near a region of

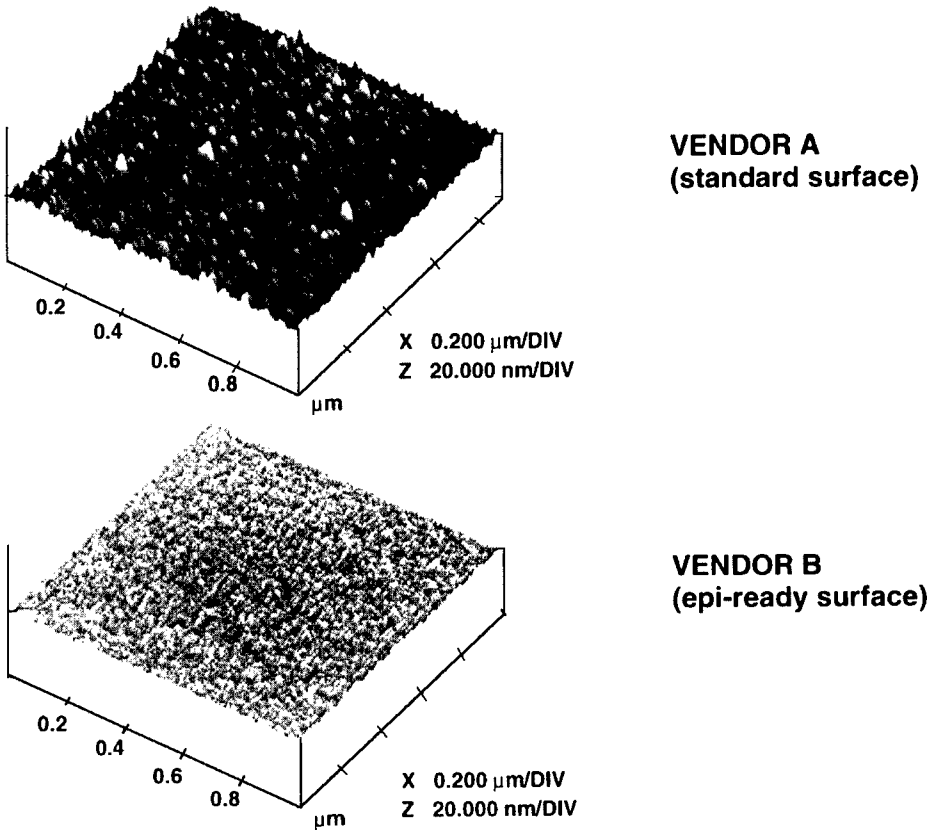

Fig. 2. Atomic force micrograph of conventional and epi-ready substrates.

alloy miscibility [8]. In spite of this difficulty, high-quality n- and p-type AlAsSb alloys were grown on InAs. In addition, as was found with the growth on similar structures on GaSb, the transition from Sb-dominated growth in the lower cladding to As-dominated growth in the active regions (and the reverse transition to the upper cladding) was best achieved by enhancing Sb-like interfaces and suppression of As-like interfaces in these transition regions. This observation has also been reported for the growth of InAs/AlSb quantum wells [9].

A more challenging problem with the growth of complete MQW laser structures on InAs was the degradation of the active region caused by the overgrowth of the upper cladding layer at the increased growth temperature necessary for the good-quality material. To investigate this effect, a MQW test structure, similar to that in Fig. 4, was furnace annealed in a sealed ampoule for various times, and DCXRD scans were taken after the annealing. Fig. 5 shows the results of these experiments, where annealing at 530°C for 3 h (a typical growth time for the upper cladding) completely obliterated the satellite structure, while annealing at 510°C for 3 h resulted in less degradation of the satellite structure. A growth temperature of 490°C was chosen as a reasonable compromise between optimizing upper cladding layer electrical and optical quality and active layer degradation.

Broad-stripe diode lasers fabricated from these structures showed emission near 3.4 μm, with pulsed current density as low as 30 A/cm^2 at 80 K, and characteristic temperatures in the range 30–40 K. By measuring devices with cavity lengths of 500, 1000 and 1500 μm the internal quantum efficiency and internal loss coefficient are estimated to be

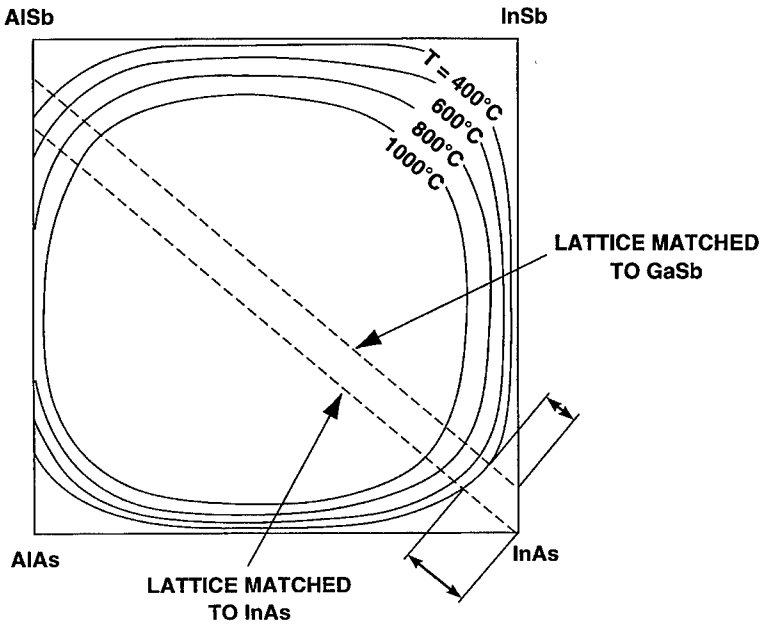

Fig. 3. Calculated alloy stability curves for In–Al–As–Sb system (from Ref. 6). The two dotted lines represent alloys matched to GaSb and InAs.

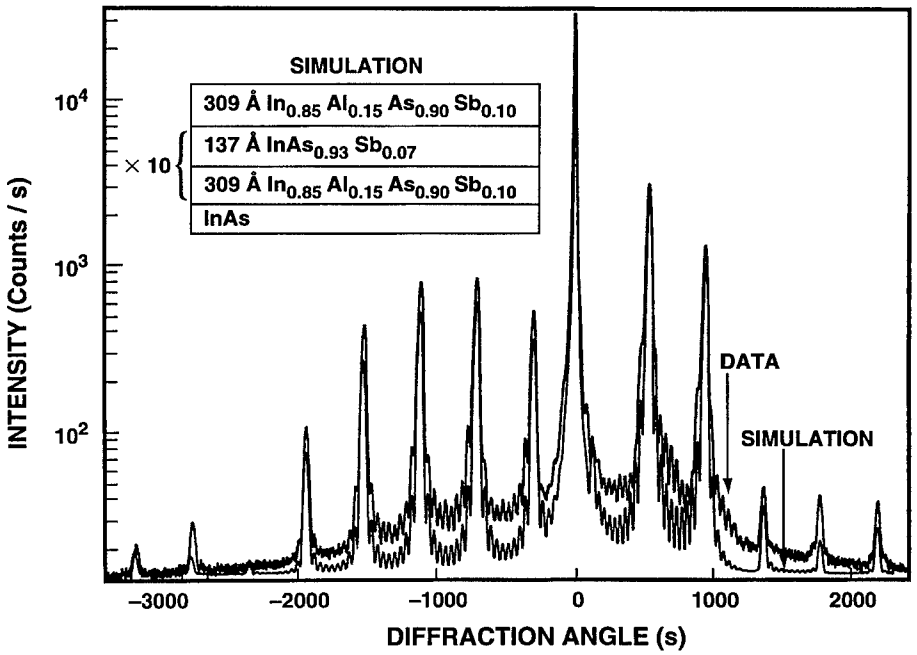

Fig. 4. DCXRD scan and simulation of InAsSb/InAlAsSb QW test structure grown on InAs.

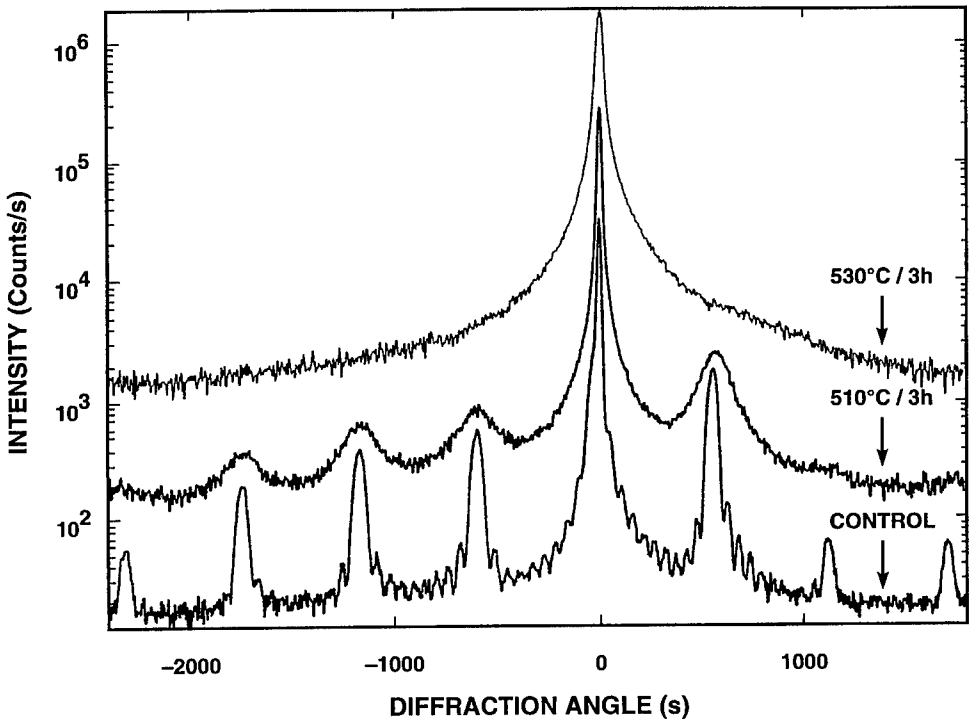

Fig. 5. DCXRD comparison of annealed QW test structures: (a) control sample, (b) after annealing at 510°C for 3 h, and (c) after annealing at 530°C for 3 h.

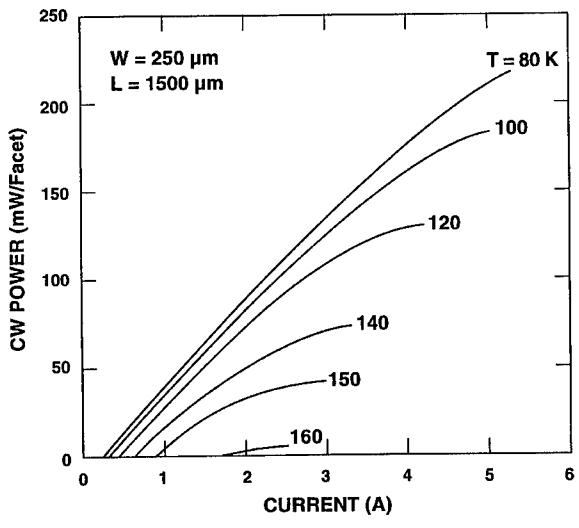

Fig. 6. CW output power versus current for QW broad-area device at various temperatures.

63% and 9 cm^{-1}, respectively. Fig. 6 shows the cw power versus current of a 1500 μm device at several temperatures. At 80 K the maximum cw output power is 215 mW/facet, limited by junction heating. The maximum output power decreases with temperature, and at 150 K it is ~ 35 mW/facet. The operating voltage at the maximum power is ~ 4 V at 80 K. This surprisingly large operating voltage (more than 10 times the photon energy) is caused by the presence of large internal heterobarriers, as seen in the band offset diagram, Fig. 7. Substantially higher output power would be expected if these large operating voltages can be reduced by incorporating graded interfaces in the laser structure. Lasers with different active layer QW structures have been evaluated and emission wavelengths at 80 K of 3.21–3.38 μm have been observed. For a laser with 80 K emission at 3.21 μm, emission wavelength versus temperature is

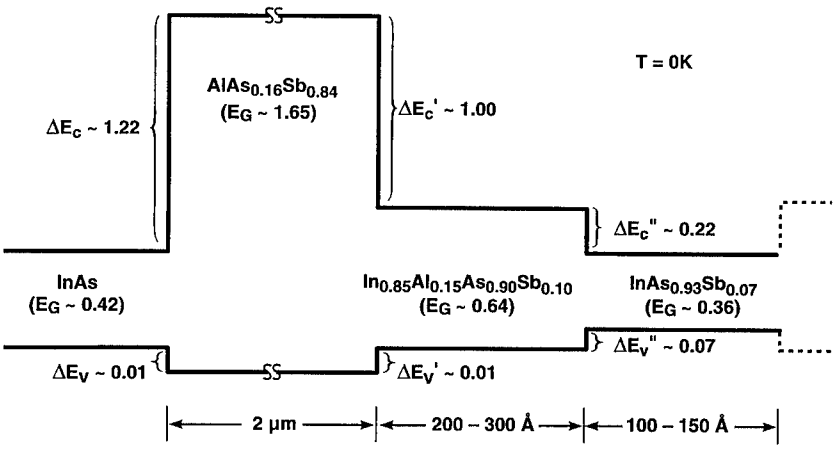

Fig. 7. Band offset diagram of InAsSb/InAlAsSb QW laser on InAs.

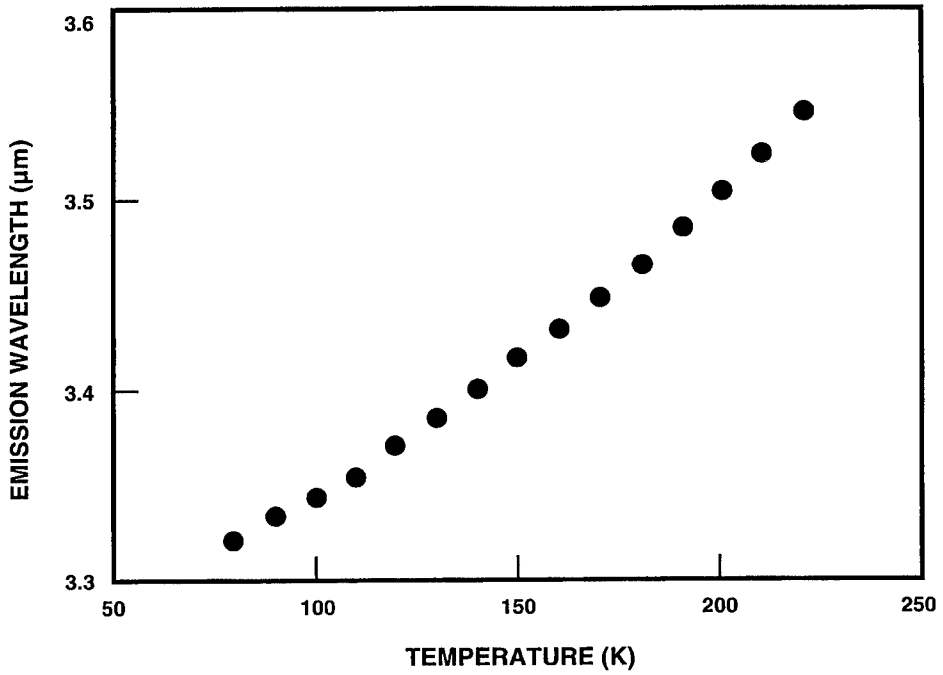

Fig. 8. Emission wavelength versus temperature for broad-area QW laser.

shown in Fig. 8. At low temperatures the wavelength shifts at ~ 1 nm/K, gradually increasing to ~ 2 nm/K at 220 K. Ridge-waveguide lasers 8 μm wide exhibited CW threshold current of 12 mA at 100 K and maximum cw operating temperature of 175 K. Additional details on laser performance are reported elsewhere [10].

4. Discussion

Impressive diode laser performance has been obtained at ~ 3.5 μm with strained InAsSb/InAlAsSb MQW structures grown on InAs. The use of InAs substrates has enabled the growth of InAlAsSb barriers with increased Al content, which in turn

lead to the development of improved QW active regions. The use of InAs substrates, however, further complicated the growth of lattice-matched AlAsSb cladding layers. Although we have not fully optimized the present laser structures, we are confident that by incorporating graded regions to reduce heterobarrier offsets, we can obtain improved performance with reduced operating voltage. With these complex laser structures, careful attention to the growth issues such as strain and lattice matching, thermal effects, and chemistry at interfaces is required for optimum performance.

5. Summary

We have demonstrated that MBE growth on InAs substrates is capable of producing high-performance InAsSb/InAlAsSb QW diode lasers with emission near 3.5 μm. Further improvements in device structures should lead to even higher performance lasers.

Acknowledgements

The authors would like to thank D.L. Spears for helpful discussions, D.R. Calawa, J.W. Chludzinski, M.K. Connors, L.M. Eriksen, L. Krohn, W.L. McGilvary and P.M. Nitishin for technical assistance, and K.J. Challberg for manuscript editing. The authors would like to acknowledge R. Dawson and Y.-H. Zhang for the suggestion to evaluate epi-ready InAs wafers. This work was sponsored by the Phillips Laboratory, Department of the Air Force.

References

[1] G.W. Turner, H.K. Choi and H.Q. Le, J. Vac. Sci. Technol. B 13 (1995) 699.
[2] T.C. Hasenberg, D.H. Chow, A.R. Kost, R.H. Miles and L. West, Electron. Lett. 31 (1995) 275.
[3] J. Faist, F. Capasso, D.L. Sivco, C. Sirtori, A.L. Hutchinson and A.Y. Cho, Science 264 (1994) 553.
[4] H.K. Choi and G.W. Turner, J. Appl. Phys. Lett. 67 (1995) 332.
[5] G.W. Turner, H.K. Choi, D.R. Calawa, J.V. Pantano and J.W. Chludzinski, J. Vac. Sci. Technol. B 12 (1994) 1266.
[6] K. Onabe, NEC Res. Dev. 72 (1984) 1.
[7] H.K. Choi and G.W. Turner, Phys. Scr., to be published.
[8] H.C. Casey and M.B. Panish, in: Heterostructure Lasers, Part B (Academic Press, New York, 1978) p. 25.
[9] G. Tuttle, H. Kroemer and J.H. English, J. Appl. Phys. 67 (1990) 3032.
[10] H.K. Choi, G.W. Turner, M.J. Manfra and M.K. Connors, J. Appl. Phys. Lett 68 (1996) 2936; H.K. Choi, G.W. Turner and M.J. Manfra, Electron. Lett. 32 (1996) 1296.

ELSEVIER

Journal of Crystal Growth 175/176 (1997) 833–837

JOURNAL OF CRYSTAL GROWTH

Microstructural properties of $InAs/InAs_xSb_{1-x}$ superlattices and $InAs_xSb_{1-x}$ ordered alloys grown by modulated molecular beam epitaxy

Y.-H. Zhang[1,a,*], A. Lew[b], E. Yu[b], Y. Chen[c]

[a] *Hughes Research Laboratories, 3011 Malibu Canyon Road, Malibu, California 90265, USA*
[b] *Department of Electrical Engineering and Computer Science, University of California at San Diego, La Jolla, California 92093, USA*
[c] *Lawrence Berkeley Laboratary, University of California, Berkeley, California 94720, USA*

Abstract

Modulated molecular beam epitaxy (MMBE) has been demonstrated to be useful in controlling group-V alloys such as $InAs_xSb_{1-x}$ and $AlAs_xSb_{1-x}$. Further studies of the MMBE grown $InAs_xSb_{1-x}$ ordered alloys and $InAs/InAs_xSb_{1-x}$ superlattices by using cross-sectional scanning tunneling microscopy show well defined interfaces between $InAs_xSb_{1-x}$ ordered alloys and InAs. Clear composition modulation is observed in the $InAs_xSb_{1-x}$ ordered alloy layers. Transmission electron diffraction and microscopy, X-ray diffraction, and low temperature photoluminescence experiments show no obvious sign of CuPt orderings. These results suggest that MMBE provides a possible means to bypass the ordering problem of $InAs_xSb_{1-x}$ random alloys.

PACS: 81.15.Hi; 61.16; 78.66 − w; 68.65. + g

Keywords: MBE; InAs; InAsSb; InSb; STM; TEM

Control of alloy composition of group-V alloys has been problematic for molecular beam epitaxy (MBE). The problem is even more acute for the epitaxial growth of $InAs_xSb_{1-x}$ random alloys due to the spontaneous CuPt-orderings [1–3]. Such orderings result in substantial bandgap shrinkage [1, 2]. Due to the spontaneous nature of these orderings, it is difficult to accurately and reproducibly control the desired bandgap for optoelectronic device application. Previously, we reported a straightforward and accurate means of controlling the incorporation of As and Sb by rapidly alternating As_2 and Sb fluxes, i.e. modulated MBE (MMBE), for As/Sb group-V alloys [4]. In this paper we will present some latest results of the atomic-scale crystalline properties of the MMBE grown $InAs_xSb_{1-x}$ ordered alloys and superlattices (SL) using cross-sectional scanning tunneling microscopy (STM), transmission electron diffraction and microscopy (TED and TEM), X-ray

[1] Present address: Electrical Engineering Department, Arizona State University, Tempe, Arizona 85287, USA.

* Corresponding author.

0022-0248/97/$17.00 Copyright © 1997 Elsevier Science B.V. All rights reserved
PII S0022-0248(96)01201-8

diffraction, and optical spectroscopy. These results show that MMBE provides not only a better control of the composition but also a possible way to bypass the problems of spontaneous CuPt orderings in $InAs_xSb_{1-x}$ random alloys.

The samples used in the present study were grown by MMBE with a conventional solid-source MBE system equipped with cracking As and Sb cells. The growth rate for all the epilayers was kept around 0.50 μm/h while the growth temperatures were kept around 480–500°C measured by both a calibrated pyrometer and a thermocouple. Different from conventional MBE, MMBE uses a straightforward and accurate means of controlling the incorporation of As and Sb by rapidly modulating As_2 and Sb beams during growth. This method will be referred to as MMBE later on. By exploiting this method, the MBE growth yields $InAs_xSb_{1-x}$ ordered alloys (or InAs/InSb short-period SLs) rather than random alloys. Detailed discussion of MMBE has been published in Ref. [4].

Three types of samples are used for present study. The first sample (Sample A) is a 172 Å-InAs/52 Å$InAs_{0.76}Sb_{0.24}$ SL grown on an InAs substrate. Each of the 53 Å $InAs_{0.76}Sb_{0.24}$ layer consists of 4 periods of nominal 7.8 Å InAs/5.2 Å InSb SL structures. The second sample (Sample B) is a laser structure consisting of an InAs/$InAs_{0.924}Sb_{0.076}$ SL active region. The details of the whole laser structure can be found in Ref. [5]. The third type of samples (Sample C and D) has a 3000 Å $InAs_xSb_{1-x}$ ordered-alloy layer consisting of 250-period 12 Å InAs/InSb short-period SL. This layer is sandwiched by two 200 Å InAs layers grown on GaSb substrates.

The group-V interfaces, such as As/Sb interfaces, have been the topic of extensive study. It has been reported that the interface quality has strong impact on the material structural properties. Since the compositions of ordered alloys are controlled by the shutter duty cycle, it is extremely helpful to understand the detailed atomic structural properties of MMBE-grown samples. Cross-sectional STM can perfectly serve this purpose.

STM experiments for this study focused on Sample A. Fig. 1a shows a constant-current cross-sectional STM image of a single $InAs_{0.76}Sb_{0.24}$ ordered-alloy layer surrounded by InAs layers within a 172 Å InAs/52 Å $InAs_{0.76}Sb_{0.24}$ superlattice. Topographic contrast across the $InAs_{0.76}Sb_{0.24}$ layer, averaged over approximately 200 individual line scans corresponding to this image, is plotted in Fig. 1b. Several features in the structure of the ordered alloy layer and the InAs/$InAs_{0.76}Sb_{0.24}$ interfaces may be noted. Contrast between the InAs and $InAs_{0.76}Sb_{0.24}$ is clearly visible, with the interfaces between the layers appearing abrupt to within ~1–2 monolayers. The four-period ordered structure within the $InAs_{0.76}Sb_{0.24}$ alloy layer arising from the MMBE growth technique is also evident, with the bright regions corresponding to the InSb-like layers.

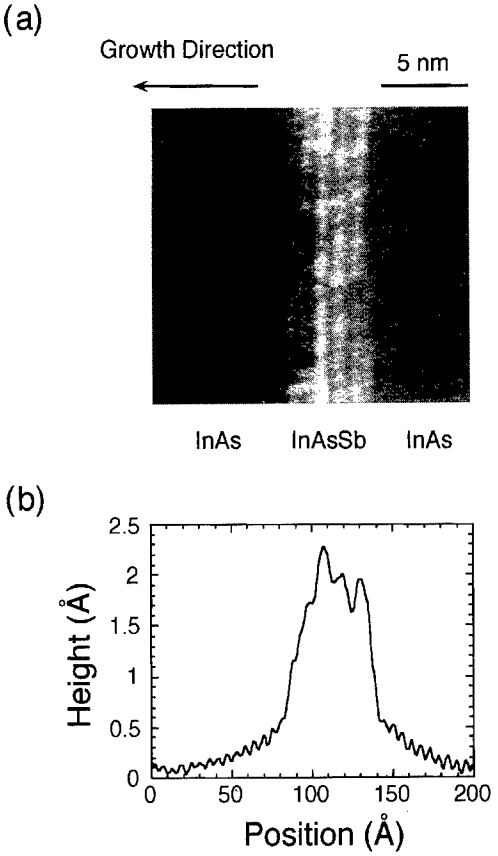

Fig. 1. (a) A high-resolution constant-current cross-sectional STM image of a single $InAs_{0.76}Sb_{0.24}$ ordered-alloy layer surrounded by InAs. (b) An averaged topographic line scan of the layer and the surrounding InAs layers.

From the topographic line scan, an increase in contrast, corresponding to increasing Sb content, is observed from the first to the third InSb-like layer. This was seen consistently with different cleaved samples and tips, and suggests that the presence of As cross incorporation is most severe at the start of the $InAs_{0.76}Sb_{0.24}$ growth, and decreases as the layer is grown. An asymmetry in interface abruptness is also observed, with the $InAs_{0.76}Sb_{0.24}$-on-InAs interface appearing atomically abrupt and the InAs-on-$InAs_{0.76}Sb_{0.24}$ interface appearing to be graded over 1–2 monolayers. We believe this grading arises from segregation of Sb on the wafer surface during the $InAs_{0.76}Sb_{0.24}$ growth, and incorporation of the segregated Sb into the subsequently grown InAs layer. A detailed discussion of the STM studies may be found in Ref. [6].

TED study of InAs/$InAs_{0.924}Sb_{0.076}$ SL active region in a laser structure (Sample B) reveals additional detailed information about the structure properties of the SL. The sample is examined in a [1 1 0] cross-section direction perpendicular to the [0 0 1] growth direction. TED diffraction pattern of the InAs/$InAs_{0.924}Sb_{0.076}$ SL active region is shown in Fig. 2. Only zinc-blende reflections appear on the TED image. Special attention is paid to the possible reflections caused by CuPt orderings. No reflection spots at half the distance between (0 0 0) and {1 1 1} reflection spots are visible, indicating that there is no detectable CuPt orderings in the studied InAs/$InAs_{0.924}Sb_{0.076}$ SL. The absence of CuPt orderings is further confirmed by photoluminescence study of MMBE grown thick $InAs_{0.9}Sb_{0.1}$ ordered-alloy layers almost lattice matched to GaSb substrates. Close lattice match of the epitaxial layer to the substrate allows one to determine the composition more accurately. In this case, no residual or local strains exist, excluding many uncertainties such as the determination of compositions and residual strains.

$InAs_{0.9}Sb_{0.1}$ ordered-alloy layers lattice matched to GaSb substrates are used for PL experiments. The average compositions of these layers are determined by X-ray diffraction measurements. As an example, the X-ray diffraction spectrum of Sample D is plotted in Fig. 3a. A distinct sharp X-ray diffraction peak is observed for the 3000 Å $InAs_{0.931}Sb_{0.069}$ layer. The small peak on the large angle side is the diffraction from the two 200 Å InAs layers. The average strain in the $InAs_{0.931}Sb_{0.069}$ layer is 3.0E-3. Taking into account the layer thickness of only 3000 Å, the epitaxial layer is coherently strained based on the model given in Ref. [7].

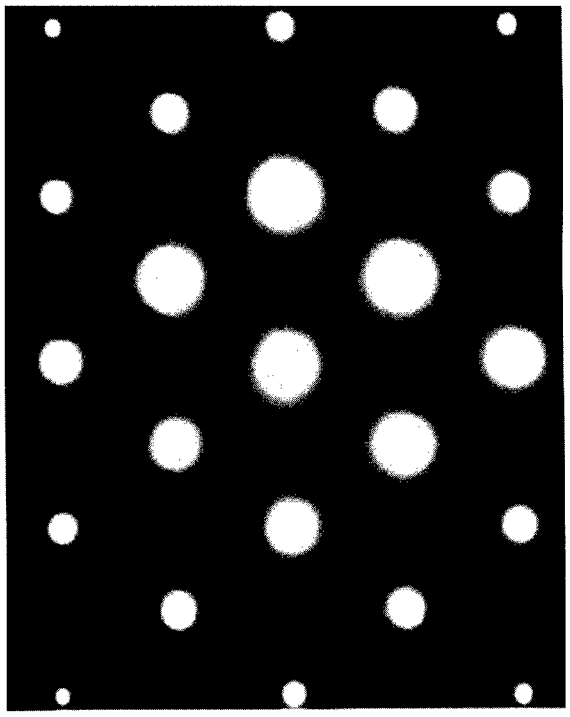

Fig. 2. TED pattern of the InAs/$InAs_{0.924}Sb_{0.076}$ SL active region in a midwave infrared laser structure.

The low temperature PL spectrum for the same sample (Sample D) is plotted in Fig. 3b. The bandgaps of free standing $InAs_xSb_{1-x}$ random alloys as a function of temperature and alloy composition are given by [8]

$$E_g(\text{Cal.}) = 0.411 - \frac{3.4\times10^{-4}\,T^2}{210+T} - 0.876\cdot(1-x) + 0.70(1-x)^2 + 3.4\times10^{-4}(1-x)x\,T^2.$$

By taking into account the strain effects [9], the calculated bandgaps [E_g(Cal.)] of samples C and D are listed in Table 1 together with sample parameters and PL peak positions. FTIR photoluminescence excitation study of similar samples has revealed that there is a very small Stokes

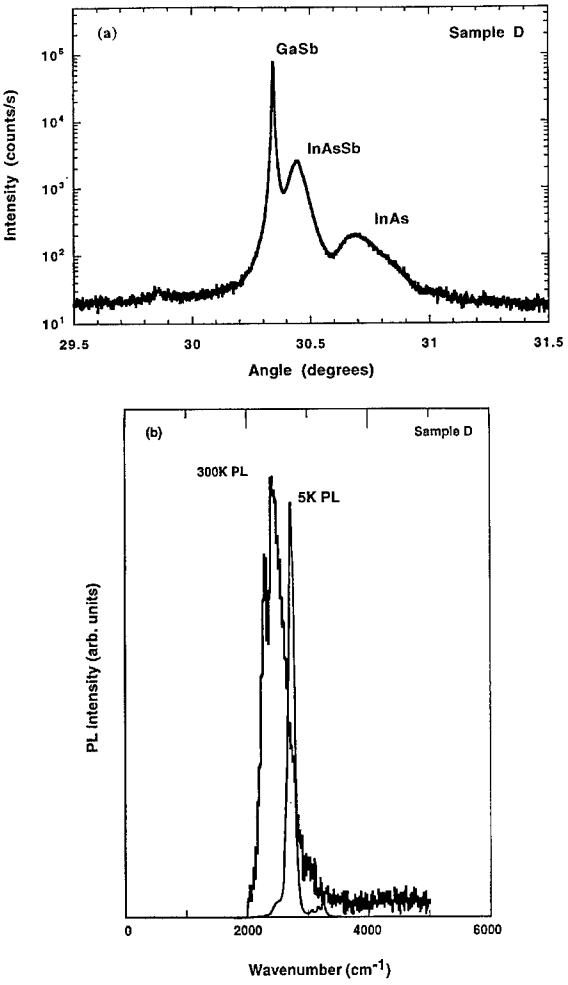

Fig. 3. (a) A high-resolution X-ray diffraction spectrum of a single $InAs_{0.93}Sb_{0.07}$ ordered-alloy layer (Sample D) grown on GaSb substrate. (b) PL spectra of the $InAs_{0.93}Sb_{0.07}$ ordered-alloy layer taken at different temperatures.

(5–7 meV) shift between PL peaks and the bandgaps for similar samples at low temperatures (~10 K) [10]. Such Stokes shift for low temperature PL peak is mainly due to localization of photogenerated carriers. At room temperature the photogenerated carriers are delocalized. Therefore, the room temperature PL peak reveals more directly the bandgap. One can see from Table 1 that the agreement between the measured bandgaps with the calculated ones are very good, confirming the absence of CuPt orderings in the As rich $InAs_xSb_{1-x}$ ($x \sim 0.9$) ordered alloys.

It has been evidenced by TEM and optical spectroscopy studies that there is strong CuPt orderings in $InAs_xSb_{1-x}$ random alloys. These orderings can be clearly observed for even As-rich alloys ($x > 0.9$) [3] and reaches maximum when $x = 0.5$ [11]. In comparison with these facts, we believe that the absence of CuPt orderings in the ordered alloys is mainly due to the following reasons: First, the ordered alloys consist mainly of binary–binary short-period InAs/InSb SL. As shown in the STM images the interfaces are well defined although some atomic intermixing exists. These MMBE introduced artificial ordering along growth direction probably hinders the formation of spontaneous CuPt orderings. Second, CuPt ordering is maximum at lower growth temperature (< 400°C) [11]. At higher growth temperatures (> 400°C), MBE grown $InAs_xSb_{1-x}$ alloy layers show uniform compositions. The samples used in the present study are grown at 480°–500°C. At such high growth temperatures, it is not expected to have CuPt orderings even for MBE grown $InAs_xSb_{1-x}$ random alloys.

Table 1
Comparison of experimental and calculated results for samples C and D; x gives the average InAs mole fraction in $InAs_xSb_{1-x}$ ordered alloys while E_g(Exp.) and E_g(Cal.) are the measured and calculated bandgaps, respectively

Sample	x	PL peak (meV)	Stocks shifts (meV)	E_g(Exp.) (meV)	E_g(Cal.) (meV)	ΔE_g (meV)
C	0.934	341 (10 K)	6	347	355	8
		301 (300 K)	–	301	301	0
D	0.931	342 (10 K)	6	348	353	5
		297 (300K)	–	297	299	2

In summary, STM and TED studies have demonstrated excellent atomic-scale structural properties of modulated MBE grown $InAs_xSb_{1-x}$ ordered alloys and superlattices. These alloys ($x \sim 0.9$) do not show any sign of CuPt orderings in TED images. No obvious bandgap shrinkage beyond experiment errors has been observed. MMBE technique thus does provide a way to avoid CuPt orderings in As-rich $InAs_xSb_{1-x}$ alloys.

References

[1] H.R. Jen, K.Y. Ma and G.B. Stringfellow, Appl. Phys. Lett. 54 (1989) 1154.
[2] S.R. Kurtz, L.R. Dawson, R.M. Bielfeld, D.M. Follstaedt and B.L. Doyle, Phys. Rev. B 46 (1992) 1909.
[3] D.M. Follstaedt, R.M. Biefeld, S.R. Kurtz, L.R. Dawson and K.C. Baucom, Narrow Gap Semiconductors 1995, Proc. Int. Conf. on Narrow Gap Semiconductors, Ed. J.L. Reno (Institute of Physics Publishing, London, 1995) p. 225.
[4] Y.-H. Zhang, J. Crystal Growth 150 (1995) 838.
[5] Y.-H. Zhang, Appl. Phys. Lett. 66 (1995) 118.
[6] A.Y. Lew, E.T. Yu and Y.-H. Zhang, J. Vac. Sci. Technol. B 14 (1996) 2940.
[7] J.W. Matthews and A.E. Blakeslee, J. Crystal Growth 27 (1974) 118.
[8] H.H. Wieder and A.R. Clawson, Thin Solid Films 15 (1973) 217.
[9] S.R. Kurtz, G.C. Osbourn, R.M. Biefeld and R.S. Lee, Appl. Phys. Lett. 53 (1988) 216.
[10] F. Fuchs and Y.-H. Zhang, unpublished.
[11] T.-Y. Seong, A.G. Norman, I.T. Ferguson and G.R. Booker, J. Appl. Phys. 73 (1993) 8227.

ELSEVIER

Journal of Crystal Growth 175/176 (1997) 838–843

JOURNAL OF CRYSTAL GROWTH

Sb-surface segregation and the control of compositional abruptness at the GaAsSb/GaAs interface

Ron Kaspi*, Keith R. Evans[1]

Wright Laboratory, Heterojunction Physics Branch, WL/AADP, Wright Patterson Air Force Base, Ohio 45433, USA

Abstract

Quantitative measurements of Sb surface segregation in pseudomorphic $GaAs_{0.8}Sb_{0.2}$ layers grown on GaAs (0 0 1) using molecular beam epitaxy (MBE) were performed in situ using the line-of-sight mass spectrometry (MS) technique. It was observed that substantial surface accumulation of Sb occurs under normal growth conditions, giving rise to compositional broadening of the GaAsSb on GaAs interface. This compositional grading is found to strongly depend on the growth temperature as well as the presence of Sb at the GaAs film surface prior to the initiation of GaAsSb layer growth. We report the effect to substrate temperature and shutter sequence on the evolution of Sb surface accumulation near the interface and demonstrate that a compositionally abrupt interface can be formed by populating the GaAs surface with an amount of Sb equivalent to that expected on the GaAsSb surface during growth at steady state. Additionally, compositional abruptness at the GaAs on GaAsSb interface can be achieved by a "chemical flashoff" of the surface Sb population during exposure to an incident As_2 flux.

PACS: 07.75. + h; 68.55.Bd; 68.10.Gw

Keywords: Surface segregation; Interfacial broadening; Mass spectroscopy

1. Introduction

Much of the success of III–V semiconductor devices containing antimony, such as infrared photodetectors [1] and lasers [2], depends on the ability to grow precisely tailored heterostructures. A critical component of this is the formation of compositionally abrupt interfaces, especially between arsenide and Sb-containing layers.

The interface between a ternary and a binary III–V alloy is often compositionally broadened due to the surface segregation of the more weakly bound species occupying the shared sublattice of the ternary alloy [3]. Compositional broadening occurs as a result of the gradual buildup or decay of surface accumulation of this species near the intended interface. For example, in pseudomorphic InGaAs/GaAs heterostructures grown by molecular beam epitaxy (MBE), the transient buildup of

* Corresponding author.

[1] Present address: Semiconductor Laser International, 421 E. Main St Endicott, NY 13760, USA.

0022-0248/97/$17.00 Copyright © 1997 Elsevier Science B.V. All rights reserved
PII S0022-0248(96)00948-7

the surface segregated "In floating layer" on InGaAs occurs at the expense of In incorporation into the film near the InGaAs on GaAs interface [4–10]. This results in an In-deficient graded InGaAs region which can be extensive at normal growth conditions. Similarly, the GaAs on InGaAs interface is broadened by the incorporation of the "In floating layer" in the InGaAs layer into the GaAs overlayer [5, 8]. Studies performed to date on interfacial broadening in III–V heterostructures have almost exclusively addressed group-III atom segregation (e.g., Ga on AlGaAs, In on InGaAs, In on InGaP), while little is known about Sb surface segregation and compositional broadening at the GaAs/GaAsSb interface. However, Sb surface segregation during GaAsSb growth can be expected since Sb is considerably more volatile than As [11]. For example, Sb surface segregation on InAs has been observed [12]. Very few in situ techniques allow quantitative measurement of surface accumulation to be made. We take advantage of the fact that a static $GaAs_{0.8}Sb_{0.2}$ film surface containing a surface segregated population of Sb is unstable when exposed to an incident arsenic flux [13]. Under these conditions, an efficient As/Sb exchange reaction results in the removal of the Sb surface population by desorption. We have performed precise desorption measurements to quantify the "Sb floating layer" using the line-of-sight mass spectrometry (MS) technique and monitored its evolution near the $GaAs_{0.8}Sb_{0.2}$ on GaAs interface. The data demonstrate that the compositional grading at this interface can be eliminated when the Sb population at the GaAs starting is properly controlled. We also propose to take advantage of the As/Sb exchange to eliminate the "Sb floating layer" in order to form a more abrupt GaAs on GaAsSb interface.

2. Experimental procedure

Film growth and in situ measurements were performed in a Varian Gen-II MBE chamber equipped with a quadrupole mass spectrometer (QMS) mounted onto the center port in the source flange, directly facing the wafer as described in detail elsewhere [14]. The line-of-sight of the ionizing region of the QMS was limited to approximately the central $\frac{1}{2}$ of the radiatively heated 2 in diameter wafer. A variety of $GaAs_{0.8}Sb_{0.2}$ surfaces were carefully prepared by pseudomorphic growth on GaAs (001) using cracked As_2 and Sb_2 beams at substrate temperatures T_s ranging between 325°C and 515°C. The $GaAs_{0.8}Sb_{0.2}$ growth rate was 0.75 ML/s, and the entire incident antimony flux ($J(Sb_2)$ = 0.15 ML/s) was incorporated (i.e., unity Sb sticking coefficient throughout the T_s range) to give the nominal Sb-mole fraction, $x(Sb) = 0.2$.

The surface accumulated population of antimony Θ^{Sb} was measured using the QMS by quantifying the amount of antimony purged from the surface as a result of As/Sb surface exchange. It was previously shown that the QMS Sb signal from the monomer (mass/q = 121 or 123 amu/e) is propotional to the total Sb-flux leaving the film surface within a wide range of temperatures and surface composition [14]. The QMS Sb signal versus time profile shown in Fig. 1 describes a typical measurement of Θ^{Sb} following the deposition of a thin $GaAs_{0.8}Sb_{0.2}$ layer. Initially, both the As_2 and Sb_s beams are coincident on the static GaAs surface, and a constant QMS Sb signal is observed. At this stage, the QMS Sb signal is proportional to the total antimony desorption rate which is equivalent to the total incident Sb_2 flux of 0.15 ML/s. Based on this measurement, the QMS Sb signal during

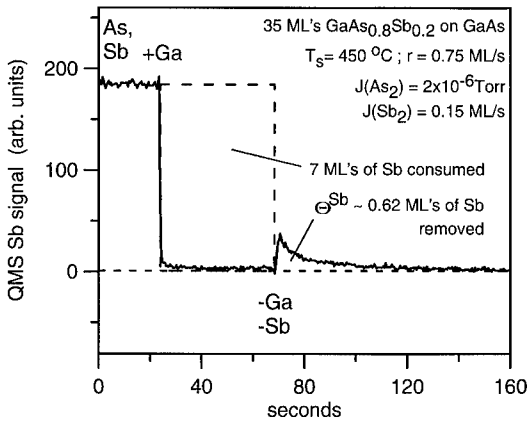

Fig. 1. Evolution of QMS Sb signal as $GaAs_{0.8}Sb_{0.2}$ layer growth is initiated, interrupted, and As/Sb exchange occurs.

the remainder of the experiment can be calibrated with the desorption rate. As shown in Fig. 1, the Sb desorption signal is observed to drop to zero when the Ga cell shutter is opened and alloy growth is initiated, indicating that all of the incident Sb_2 is consumed and the Sb_2 sticking coefficient is indeed unity. In the case shown in Fig. 1, both the Ga and Sb_2 fluxes are interrupted after 35 ML of $GaAs_{0.8}Sb_{0.2}$ growth at $T = 450°C$, and the film surface remains exposed only to the incident As_2 beam. Immediately following the growth interruption, a sharp rise in the QMS Sb signal is observed which is generally followed by a gradual decay. This indicates that antimony is purged from the surface of the film and that the surface becomes slowly depleted of Sb in the presence of the As_2 beam. The area under this feature can be quantified based on the calibration described above, and was measured to be $\sim 0.62 \pm 0.05$ ML for the case shown in Fig. 1. This is considerably larger than the expected 0.2 ML based on x(Sb), verifying substantial Sb surface accumulation in $GaAs_{0.8}Sb_{0.2}$ at these growth conditions. Assuming steady-state conditions are reached after 35 ML of growth, Θ^{Sb} is comparable to ~ 0.79 ML of In measured to accumulate at the surface of a 90 Å thick $In_{0.22}Ga_{0.78}As$ layer deposited on GaAs at the same temperature in a previous study [10].

3. Results

3.1. Evolution of the surface segregated layer

When Θ^{Sb} reaches a steady-state value during film growth, the nominal GaAsSb alloy composition can be attained because the presece of the "Sb floating layer" does not alter the Sb sticking coefficient. However, it is expected that a transient build-up of surface Sb population occurs near the GaAsSb on GaAs interface where Θ^{Sb} is intially zero. In order to measure the evolution of Θ^{Sb} as a function of the distance from the interface, a series of $GaAs_{0.8}Sb_{0.2}$ layers of varying thickness were deposited on GaAs at $T_s = 450°C$. In each case an antimony desorption measurement was performed during As/Sb exchange following growth interruption in a manner similar to that described above. In this series, the GaAs static surface was bathed only in As_2, while Sb_2 was introduced together with Ga to initiate alloy growth. Fig. 2 shows the measured values of Θ^{Sb} as a function of nominal $GaAs_{0.8}Sb_{0.2}$ layer thickness. It is observed that Θ^{Sb} gradually increases from 0.31 ± 0.05 ML after 3 ML of $GaAs_{0.8}Sb_{0.2}$ deposition to 0.62 ± 0.05 ML after 10 ML of $GaAs_{0.8}Sb_{0.2}$ deposition where a steady-state value $\Theta^{Sb}(ss)$ of 0.62 ± 0.05 ML is approached. The observed evolution of Θ^{Sb} suggests that the nominal value of x(Sb) = 0.2 is not reached until nearly 30 Å from the interface, and that the graded GaAsSb layer at the interface is deficient in Sb. Based on the measured value of Θ^{Sb} after 3 ML of $GaAs_{0.8}Sb_{0.2}$ growth, the average Sb mole fraction in the first 3 ML of the alloy is ~ 0.10, significantly lower than the intended value of 0.2.

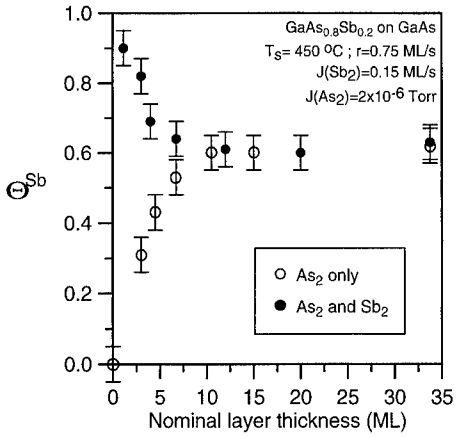

Fig. 2. Sb surface accumulation as a function of the proximity to the intended interface. The effect of two different shutter sequences is shown.

The GaAsSb on GaAs interface can also be formed using an alternative shutter sequence: the GaAs static surface is bathed in both As_2 and Sb_2 prior to opening the Ga shutter to initiate GaAsSb as described in Fig. 1. In this case, a steady-state surface population of Sb is already present at the GaAs surface and can be expected to influence the evolution of Θ^{Sb} when growth is initiated. A series of Θ^{Sb} values measured over incrementally thicker $GaAs_{0.8}Sb_{0.2}$ layers deposited on GaAs in this

manner is also shown in Fig. 2. It was observed that Θ^{Sb} is initially large ($\Theta^{Sb} = 0.90 \pm 0.05$ ML after ~ 1 ML deposition of $GaAs_{0.8}Sb_{0.2}$) and decays to the steady-state value of ~ 0.62 ML after nearly 10 ML of alloy deposition. The lack of Sb desorption signal during the growth of the $GaAs_{0.8}Sb_{0.2}$ layer implies that the excess Sb at the film surface near the interface is incorporated into the film. This results in a compositionally graded GaAsSb layer at the interface which contains excess Sb in contrast to the result of the previously described shutter sequence. Assuming that the observed reduction in Θ^{Sb} within the first 3 ML of $GaAs_{0.8}Sb_{0.2}$ is homogeneously incorporated into the alloy, the Sb mole fraction adjacent to the interface is ~ 0.25, significantly higher than the intended value of 0.2.

3.2. Control of compositional abruptness

The evolution of Θ^{Sb}, as demonstrated above, depends strongly on the amount of Sb at the initial surface prior to the depositon of the GaAsSb layer. It has been previously demonstrated that if a surface accumulated population equivalent in size to the steady-state value on the ternary alloy surface can be maintained at the initial static surface, then the transient behavior of Θ near the interface, thus compositional grading, can be eliminated [9, 10]. The fact that we can populate the starting surface in excess of Θ^{Sb}(ss) as shown in Fig. 2 suggests that the surface Sb population on GaAs, Θ^{Sb}(GaAs), can be matched to Θ^{Sb}(ss) on GaAsSb under appropriate conditions.

To search for growth conditions where Θ^{Sb}(ss) = Θ^{Sb}(GaAs), the effect of T_s on Θ^{Sb}(ss) and Θ^{Sb}(GaAs) was studied. A series of $GaAs_{0.8}Sb_{0.2}$ layers were deposited on GaAs at $325 < T_s < 515$°C using the same incident fluxes, and Θ^{Sb}(ss) was measured. The layer thickness in each case was 35 ML in order to ensure that steady-state conditions were achieved. It was observed that Θ^{Sb}(ss) is as large as 1.20 ± 0.05 ML at $T_s = 515$°C, and is reduced to 0.36 ± 0.05 ML at $T_s = 325$°C, as plotted in Fig. 3. Also shown in Fig. 3 are the measured values of Θ^{Sb}(GaAs) for a range of T_s.

In this case, Θ^{Sb}(GaAs) was measured by blocking off the incident Sb_2 flux on the GaAs static surface irradiated by both As_2 and Sb_2, and attributing the decay of the QMS Sb signal to the surface buildup of antimony. We observe the general trend that Θ^{Sb}(ss) increases with T_s while Θ^{Sb}(GaAs) decreases with T_s, and that a crossover point exists where Θ^{Sb}(ss) = Θ^{Sb}(GaAs).

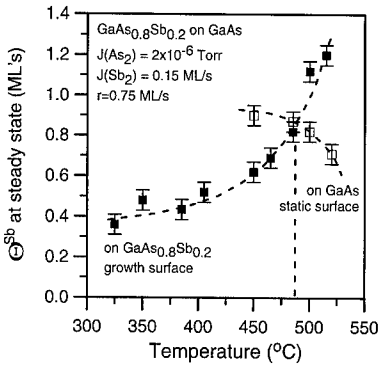

Fig. 3. Sb surface accumulation as a function of substrate temperature for both the GaAsSb growth surface and the GaAs static starting surface. The crossover point is near $T_s \sim 485$°C.

Data shown in Fig. 3 indicate that, given the incident fluxes used, a crossover point where Θ^{Sb}(GaAs) = Θ^{Sb}(ss) exists near $T_s = 485$°C. As is generally observed for surface segregating species, Θ^{Sb}(ss) increases with increasing T_s; however, Θ^{Sb}(GaAs) has an inverse relationship with T_s. Θ^{Sb}(GaAs) is observed to decrease from 0.90 ± 0.05 ML at $T_s = 450$°C to 0.71 ± 0.05 ML at $T_s = 520$°C. Both of these trends are expected since surface segregation is kinetically limited [7, 15] while the stoichiometry on a static surface is not.

To measure the evolution of Θ^{Sb} on $GaAs_{0.8}Sb_{0.2}$ layers near the interface when Θ^{Sb}(GaAs) is matched to Θ^{Sb}(ss), a set of $GaAs_{0.8}Sb_{0.2}$ surfaces were prepared at $T_s = 485$°C. In situ measurements of Θ^{Sb} using line-of-sight mass spectrometry as described earlier is shown in Fig. 4. It is observed that Θ^{Sb} remains constant at a value of 0.82 ± 0.05 ML throughout the region near the $GaAs_{0.8}Sb_{0.2}$ on GaAs interface. The lack of a transient in Θ^{Sb} indicates that Sb is incorporated into the film at the steady-state level and the Sb-deficient region near the interface is eliminated.

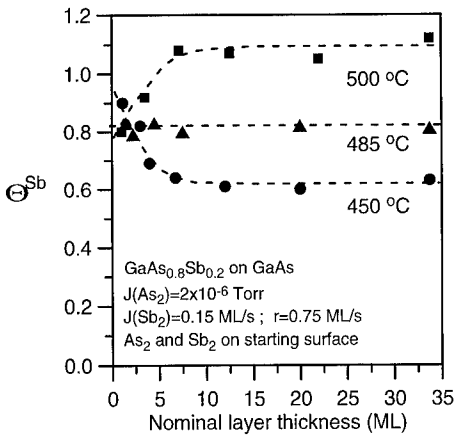

Fig. 4. The evolution of Θ^{Sb} within film thickness when Θ^{Sb} is less than, equal to, and greater than Θ^{Sb} (GaAs) at $T_s = 450$, 485, and 500°C, respectively.

The formation of a compositionally abrupt GaAs on GaAsSb interface, on the other hand, necessitates the elimination of the "Sb-floating layer" prior to the deposition of GaAs. As demonstrated in Fig. 1, we propose to achieve this by interrupting the growth at this interface to expose the surface to the incident As_2 flux. This will ensure that the Sb population at the GaAsSb surface will be purged so that GaAs growth can proceed without surface riding and incorporation of Sb.

4. Discussion

Following the kinetic model of surface segregation developed by Muraki [7] in which only the exchange between the top GaAsSb monolayer and the "Sb floating layer" is allowed, a segregation ratio R can be assigned. R is defined as the fraction of Sb atoms at the top layer which segregate to the floating layer after each new monolayer of growth, and is given by $1 - [x(\mathrm{Sb})/\Theta^{Sb}(\mathrm{ss})]$. R is measured to be 0.76 at $T_s = 485$°C in these experiments, and is comparable to the values reported for In in InGaAs ($0.78 < R < 0.85$) at similar growth temperatures [6, 10].

The growth temperature determined to be necessary to eliminate compositional grading near the $GaAs_{0.8}Sb_{0.2}$ on GaAs interface is specific to the incident fluxes and growth rate used, as well as nominal x(Sb) in the alloy. Based on the results of previous investigations of In surface segregation on InGaAs [5, 10, 16], it is expected that Θ^{Sb}(ss) will increase as x(Sb) is increased. However, it is not clear whether T_s will have to decrease to yield $\Theta^{Sb}(\mathrm{GaAs}) = \Theta^{Sb}(\mathrm{ss})$ for larger x(Sb). This is because Θ^{Sb}(GaAs) is also expected to increase as a larger incident Sb_2 flux is employed to give a larger x(Sb). It is clear, however, that arbitrary choices of growth parameters can result in interfacial broadening for which the magnitude and the direction of the compositional grading is not known. Heterostructures for devices which depend on compositionally abrupt interfaces can therefore benefit from such experiments to fine-tune the growth parameters.

These qualitative effects of segregation are expected in other alloy systems; thus compositional grading in InAsSb, AlAsSb and quaternary III–III–AsSb layers near the binary III–As interface is expected.

5. Conclusion

Line-of sight mass spectrometry was used to investigate Sb surface segregation on $GaAs_{0.8}Sb_{0.2}$ during MBE growth by quantifying the desorbed antimony as a result of As/Sb surface exchange. It was observed that size of the surface segregated Sb population at steady state increases with T_s, and that its evolution near the $GaAs_{0.8}Sb_{0.2}$ on GaAs interface results in compositional broadening. We have developed a growth approach based on controlling the surface Sb population which is expected to result in compositionally more abrupt interfaces than can be obtained by standard MBE growth. Our data suggests that the compositional grading can be eliminated when the shutter sequencing and T_s is precisely chosen so that Θ^{Sb}(GaAs) is well matched to Θ^{Sb}(ss).

Acknowledgements

We gratefully acknowledge Mr. E.N. Taylor for his expert technical assistance and C.I. Huang for

his support. This work was performed at Wright Laboratory, Avionics Directorate, under Air Force Contract No. F33615-95-C1619, with partial support from the Air Force Office of Scientific Research.

References

[1] D.H. Chow, R.H. Miles, C.W. Nieh and T.C. McGill, J. Crystal Growth 111 (1991) 683.
[2] Y.-H. Zhang, Appl. Phys. Lett. 66 (1995) 118.
[3] J.M. Moison, C. Guille, F. Houzay, F. Barthe and M. Van Rompay, Phys. Rev. B 40 (1989) 6149.
[4] J.-M. Gerard, Appl. Phys. Lett. 61 (1992) 2096.
[5] J. Nagle, J.P. Landesman, M. Larive, C. Mottet and P. Bois, J. Crystal Growth 127 (1993) 550.
[6] H. Toyoshima, T. Niwa, J. Yamazaki and A. Okamoto, Appl. Phys. Lett. 63 (1993) 821.
[7] K. Muraki, S. Fukatsu, Y. Shiraki and R. Ito, J. Crystal Growth 127 (1993) 513.
[8] J.F. Zheng, J.D. Walker, M.B. Salmeron and E.R. Weber, Phys. Rev. Lett. 72 (1994) 2414.
[9] J.-M. Gerard and C. d'Anterroches, J. Crystal Growth 150 (1995) 467.
[10] R. Kaspi and K.R. Evans, Appl. Phys. Lett. 67 (1995) 819.
[11] M. Yano, M. Ashida, A. Kawaguchi, Y. Iwai and M. Inoue, J. Vac. Sci. Technol. B 7 (1989) 199.
[12] M.W. Wang, D.A. Collins, T.C. McGill, R.W. Grant and R.M. Feenstra, J. Vac. Sci. Technol. B 13 (1995) 1689.
[13] M. Yano, H. Yokose, Y. Iwai and M. Inoue, J. Crystal Growth 111 (1991) 609.
[14] R. Kaspi and K.R. Evans, J. Crystal Growth, in press.
[15] O. Dehaese, X. Wallart and F. Mollot, Appl. Phys. Lett. 66 (1995) 52.
[16] H. Toyoshima, T. Niwa, J. Yamazaki and A. Okamoto, J. Appl. Phys. 75 (1994) 3908.

ELSEVIER

Journal of Crystal Growth 175/176 (1997) 844–848

JOURNAL OF CRYSTAL GROWTH

MBE growth of Si-doped InAlAsSb layers lattice-matched with InAs

Makoto Kudo*, Tomoyoshi Mishima

Central Research Laboratory, Hitachi, Ltd., 1-280, Higashi-Koigakubo, Kokubunji-shi, Tokyo 185, Japan

Abstract

The two-dimensional electron gas concentration in InAs channel modulation-doped heterostructures can be controlled by using an $In_{0.5}Al_{0.5}As_{0.56}Sb_{0.44}$ quaternary alloy – doped with Si as a donor – as an electron-supplying layer. When lattice-matched with InAs, an electron concentration of more than 4×10^{18} cm^{-3} was obtained in the quaternary layer. The two-dimensional electron gas concentration of an undoped-$In_{0.5}Al_{0.5}As_{0.56}Sb_{0.44}$/undoped-InAs heterostructure was 7×10^{11} cm^{-2} and that of a Si-doped $In_{0.5}Al_{0.5}As_{0.56}Sb_{0.44}$/undoped-InAs heterostructure was 1.24×10^{12} cm^{-2}. The electron mobility was low, though, due to the roughness of the heterointerface. If the interface can be made smooth, however, $In_{0.5}Al_{0.5}As_{0.56}Sb_{0.44}$ will be a useful material for forming the electron-supplying layer of InAs channel modulation-doped heterostructures.

PACS: 68.55.Bd; 73.61.Ey

Keywords: Two-dimensional electron gas; Modulation-doped heterostructures; InAs channel; Electron-supplying layer

1. Introduction

Al(Ga)(As)Sb/InAs heterostructures have been widely studied for future high-frequency field effect transistor (FET) applications because of their very high electron mobility which exceeds 20 000 cm^2/V·s at room temperature (RT) [1–6]. In this material system, two-dimensional electron gas (2DEG) concentrations of the order of 10^{12} cm^{-2} are known to accumulate in the InAs layer even though no layers are intentionally doped. In this heterostructure, the 2DEG concentration can be changed by changing the top barrier thickness [7, 8]. However, it is hard to control the concentration without changing the top barrier thickness, because n-type doping of Al(Ga)Sb is difficult. The Si, which behaves only as a donor for (Al)GaAs, turns into partially compensated acceptors in GaSb and AlSb [9]. Although column VI materials, such as S, Se, and Te, become donors for GaSb and AlSb [9], the vapor pressure of these materials is too high for accurate control of the doping concentration in MBE. Chow et al. reported that Si-modulation-doped InAs/AlSb

* Corresponding author. Fax: + 81 423 27 7679; e-mail: mkudo@crl.hitachi.co.jp.

0022-0248/97/$17.00 Copyright © 1997 Elsevier Science B.V. All rights reserved
PII S0022-0248(96)00935-9

superlattices yield controllable n-type carrier concentration up to 1×10^{18} cm^{-3} [10]. However, for FET application, more than 3×10^{18} cm^{-3} of carrier concentration is thought to be required.

To overcome these problems, we propose the use of a Si-doped $In_{0.5}Al_{0.5}As_{0.56}Sb_{0.44}$ layer as an electron-supplying layer lattice-matched on the InAs channel in this paper. We have found that Si behaves as a donor in $In_{0.5}Al_{0.5}As_{0.56}Sb_{0.44}$ through our investigation of the electronic properties of Si-doped $In_{0.5}Al_{0.5}As_{1-x}Sb_x$ ($x < 0.5$). Finally, we demonstrate here that the 2DEG concentration in the InAs layer can be controlled by changing the Si-doping concentration in the $In_{0.5}Al_{0.5}As_{0.56}Sb_{0.44}$ electron-supplying layer.

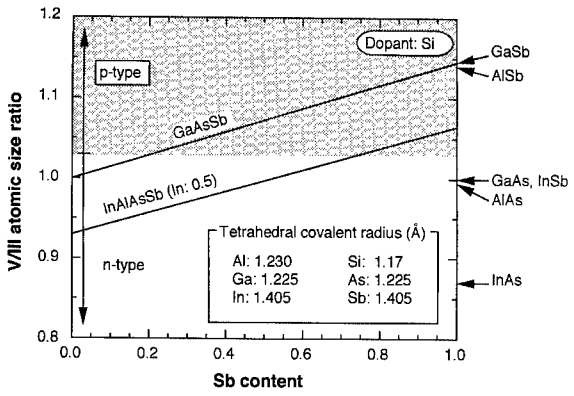

Fig. 1. Experimental and predicted site occupations depending on the V/III atomic size ratio. The tetrahedral covalent radius of the element, which is listed inside the graph, is used as the atomic size.

2. Predicted site occupation of Si in InAlAsSb

According to the prediction by Pindoria et al., Si occupies the site by replacing the largest atom in III–V compounds under normal growth conditions (i.e., usually a group-V flux rich condition) [11]. The most direct confirmation of this size effect comes from the observed gradual shift from n-type to p-type in Si-doped $GaAs_{1-x}Sb_x$ [12]. When the Sb content is below 0.2, the Si-doped $GaAs_{1-x}Sb_x$ layers are n-type. When the Sb content is above 0.25, on the other hand, the Si-doped $GaAs_{1-x}Sb_x$ layers become p-type. The experimental site occupation, which depends on the V/III atomic size ratio (the Sb content), for $GaAs_{1-x}Sb_x$ is shown in Fig. 1. The tetrahedral covalent radius of the element is used as the atomic size [13]. As shown, the transition from n-type to p-type occurs at a V/III atomic size ratio of about 1.03. The predicted site occupation, which depends on the Sb content of the Si-doped $In_{0.5}Al_{0.5}As_{1-x}Sb_x$, is also shown in Fig. 1. If we assume that the n/p-type transition of Si-doped $In_{0.5}Al_{0.5}As_{1-x}Sb_x$ occurs at the same V/III atomic size ratio as $GaAs_{1-x}Sb_x$, we can predict that Si-doped $In_{0.5}Al_{0.5}As_{1-x}Sb_x$ will be n-type when the Sb content is below 0.7. Since the Sb content of $In_{0.5}Al_{0.5}As_{1-x}Sb_x$ lattice-matched with InAs is 0.44, Si-doped $In_{0.5}Al_{0.5}As_{0.56}Sb_{0.44}$ will be n-type and can be used as a electron-supplying layer for InAs channel modulation-doped heterostructures.

Therefore, we have decided to concentrate on studying a Si-doped $In_{0.5}Al_{0.5}As_{1-x}Sb_x$ alloy ($x < 0.5$) for use as electron-supplying layers of InAs channel modulation-doped heterostructures.

3. Material growth and characterization

All samples for this study were grown with a conventional solid-source MBE system. After thermal cleaning of semi-insulating (1 0 0) GaAs substrates at 600°C in an As_4 flux, we successively grew an undoped $In_{0.5}Al_{0.5}As$ layer (300 nm), an undoped $In_{0.5}Al_{0.5}As_{1-x}Sb_x$ layer (1 μm), a Si-doped $In_{0.5}Al_{0.5}As_{1-x}Sb_x$ layer (110 nm, Si concentration: 7.3×10^{18} cm^{-3}), and an undoped $In_{0.5}Al_{0.5}As_{1-x}Sb_x$ layer (110 nm). The substrate temperature was fixed at 350°C. The growth rate of the $In_{0.5}Al_{0.5}As(Sb)$ layer was about 1.2 μm/h. The As_4 pressure at the sample position was fixed at 1×10^{-5} Torr, and the Sb_4 pressure was varied from 0 to 9.6×10^{-7} Torr. The Al and In content was calibrated by double-crystal X-ray diffraction (DXRD) using an $In_{0.52}Al_{0.48}As$ layer grown on an InP substrate. Two $In_{0.5}Al_{0.5}As_{0.56}Sb_{0.44}$/InAs heterostructures were also grown, one modulation-doped and one undoped (see Fig. 2). An AlSb/InAs heterostructure was also grown as a reference.

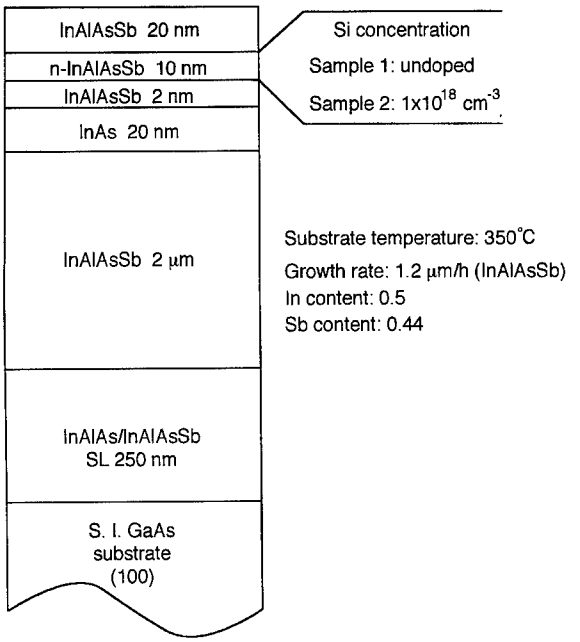

Fig. 2. A schematic diagram of the InAlAsSb/InAs (modulation-doped) heterostructure.

The mobility and free electron concentration of the samples were evaluated by the conventional van der Pauw method at RT (297 ± 3 K).

The $In_{0.5}Al_{0.5}As_{0.56}Sb_{0.44}$/InAs heterointerface quality was investigated directly by transmission electron microscopy (TEM).

4. Results and discussion

The lattice constant and Sb content of $In_{0.5}Al_{0.5}As_{1-x}Sb_x$ as a function of the Sb_4 beam pressure is shown in Fig. 3. The lattice-matching with InAs is given at an Sb beam pressure of about 9×10^{-7} Torr.

The free electron concentration and mobility of Si-doped $In_{0.5}Al_{0.5}As_{1-x}Sb_x$ as a function of the Sb content is shown in Fig. 4. The Si-doping concentration was fixed at 7.3×10^{18} cm^{-3}. All layers showed n-type conduction as we predicted in Section 2. The free electron concentration decreases from 5.76×10^{18} to 4.21×10^{18} cm^{-3} as the Sb content increases from 0 to 0.47. The discrepancy

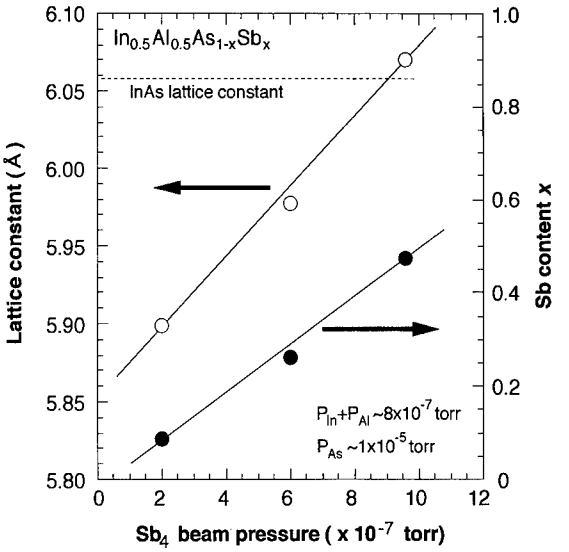

Fig. 3. The lattice constant and Sb content of $In_{0.5}Al_{0.5}As_{1-x}Sb_x$ as a function of the Sb_4 beam pressure. The growth temperature was fixed at 350°C.

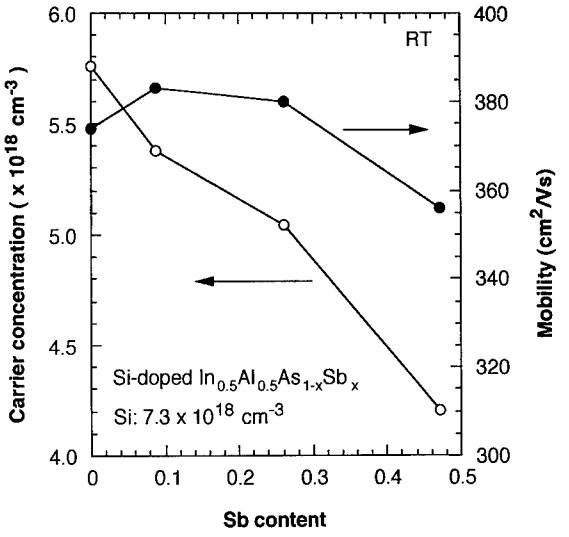

Fig. 4. The free electron concentration and mobility of $In_{0.5}Al_{0.5}As_{1-x}Sb_x$ as a function of Sb content. The free electron concentration and mobility of a Si-doped $In_{0.52}Al_{0.48}As$ layer grown on an InP substrate as a reference were 6.9×10^{18} cm^{-3} and 360 cm^2/V·s, respectively.

between the doping concentration and the free electron concentration at the Sb content of 0 is due to dislocations in the epitaxial layer, because there is a large mismatch in the lattice constants of the

Table 1
Hall measurement of InAs channel heterostructures

Barrier/buffer materials	Si concentration (cm^{-3})	Mobility ($cm^2/V \cdot s$)	Sheet carrier concentration (cm^{-2})
InAlAsSb	Undoped	3800	7.00×10^{11}
InAlAsSb	1×10^{18}	4600	1.24×10^{12}
AlSb/AlGaSb	Undoped	14100	4.73×10^{12}

GaAs substrate and the $In_{0.5}Al_{0.5}As$ epitaxial layer. When we grew Si-doped $In_{0.52}Al_{0.48}As$ on an InP substrate as a reference, an electron concentration of $6.9 \times 10^{18}\ cm^{-3}$ was obtained. By improving the buffer layer quality, larger electron concentration can be obtained on GaAs substrates [14].

The mobilities, on the other hand, were almost constant and remained between 356 and 383 $cm^2/V \cdot s$. These values are comparable with that of the reference $In_{0.52}Al_{0.48}As$ grown on an InP substrate at the same doping concentration (360 $cm^2/V \cdot s$).

These results indicate that $In_{0.5}Al_{0.5}As_{0.56}Sb_{0.44}$ is a suitable material for use as the electron-supplying layer for InAs channel modulation-doped heterostructures.

We then grew two InAlAsSb/InAs heterostructures (Fig. 2). The InAlAsSb layer of sample #1 was intentionally left undoped and the InAlAsSb layer of sample #2 was Si-doped at a concentration of $1 \times 10^{18}\ cm^{-3}$. An AlSb/InAs heterostructure was also grown as a reference. The result of the Hall measurement is listed in Table 1. The 2DEG concentrations of the undoped and Si-doped modulation-doped heterostructures were $7 \times 10^{11}\ cm^{-2}$ and $1.24 \times 10^{12}\ cm^{-2}$, respectively. This is the first time that the 2DEG concentration in InAs channel modulation-doped heterostructures has been controlled by Si-doping using a lattice-matched electron-supplying layer. The mobility, however, was very small compared with that of the AlSb/InAs heterostructure. We believe this is due to the rough heterointerface between the InAlAsSb and the InAs.

To investigate the roughness of the InAlAsSb/InAs heterointerface, we used TEM (Fig. 5). As you can see in the TEM micrograph, the

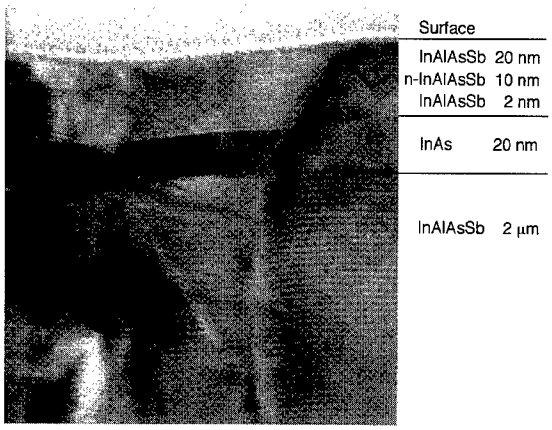

Fig. 5. Cross-sectional TEM micrograph of an InAlAsSb/InAs modulation-doped heterostructure. The stripes parallel to the growth plane in the InAlAsSb layer might be due to the substrate rotation. The rotation rate evaluated from this TEM micrograph was almost same with that we usually set for substrate rotation.

InAlAsSb/InAs heterointerface was very rough and many dislocations were observed. This suggests that the surface smoothing effect of InAlAsSb is weaker than that of an AlGaAsSb material system. When an AlGaAsSb material system was used as a buffer layer in an InAs channel heterostructure, very high mobility (over 20000 $cm^2/V \cdot s$) was obtained even without using a superlattice as a smoothing layer [6]. So we must improve the buffer layer quality of InAlAsSb/InAs material systems to obtain a smooth interface and high mobility.

5. Conclusions

The 2DEG concentration in InAs channel heterostructures can be controlled by using a Si-doped $In_{0.5}Al_{0.5}As_{0.56}Sb_{0.44}$ quaternary alloy as an electron-supplying layer. Under growth conditions suitable for lattice-matching with InAs, an electron concentration of more than $4 \times 10^{18}\ cm^{-3}$ was obtained in the Si-doped $In_{0.5}Al_{0.5}As_{0.56}Sb_{0.44}$ quaternary layer. The 2DEG concentration of the

undoped-$In_{0.5}Al_{0.5}As_{0.56}Sb_{0.44}$/undoped-InAs heterostructure was $7 \times 10^{11}\,cm^{-2}$ and that of the Si-doped $In_{0.5}Al_{0.5}As_{0.56}Sb_{0.44}$/undoped-InAs heterostructure was $1.24 \times 10^{12}\,cm^{-2}$. This is the first time that the 2DEG concentration in InAs channel heterostructures has been controlled by Si-doping. The mobility, however, was lower than that of the AlSb/InAs heterostructure due to the rough heterointerface. This indicates that $In_{0.5}Al_{0.5}As_{0.56}Sb_{0.44}$ will be a suitable material for use as the electron-supplying layer for InAs channel modulation-doped heterostructures as soon as the buffer layer quality can be improved.

References

[1] L.F. Luo, R. Beresford, W.I. Wang and H. Munekata, Appl. Phys. Lett. 55 (1989) 789.
[2] G. Tuttle, H. Kroemer and J.H. English, J. Appl. Phys. 67 (1990) 3032.
[3] J.D. Werking, C.R. Bolognesi, L.-D. Chang, C. Nguyen, E.L. Hu and H. Kroemer, IEEE Electron Device Lett. 13 (1992) 164.
[4] X. Li, K.F. Longenbach, Y. Wang and W.I. Wang, IEEE Electron Device Lett. 13 (1992) 192.
[5] K. Yoh, K. Kiyomi, M. Yano and M. Inoue, J. Crystal Growth 127 (1993) 29.
[6] N. Kuze, K. Nagase, S. Muramatsu, S. Miya, T. Iwabuchi, A. Ichii and I. Shibasaki, J. Crystal Growth 150 (1995) 1307.
[7] C. Nguyen, B. Brar, H. Kroemer and J.H. English, Appl. Phys. Lett. 60 (1992) 1854.
[8] S. Ideshita, A. Furukawa, Y. Mochizuki and M. Mizuta, Appl. Phys. Lett. 60 (1992) 2549.
[9] S. Subbanna, G. Tuttle and H. Kroemer, J. Electron. Mater. 17 (1988) 297.
[10] D.H. Chow, Y.H. Zhang, R.H. Miles and H.L. Dunlap, J. Crystal Growth 150 (1995) 879.
[11] G. Pindoria, R.A.A. Kubiak, S.M. Newstead and D.P. Woodruff, Surf. Sci. 234 (1990) 17.
[12] J.H. Zhao, A.Z. Li, J. Jeong, D. Wong, J.C. Lee, M.L. Milliman, T.E. Schlesinger and A.G. Milnes, J. Vac. Sci. Technol. B 6 (1988) 627.
[13] V. Swaminathan and A.T. Macrander, Materials Aspects of GaAs and InP based Structures, (Prentice Hall, Englewood Cliffs, 1991).
[14] For example, by using a step graded buffer: T. Mishima, K. Higuchi, M. Mori and M. Kudo, J. Crystal Growth 150 (1995) 1230.

ELSEVIER

Journal of Crystal Growth 175/176 (1997) 849–852

JOURNAL OF CRYSTAL GROWTH

Molecular beam epitaxial growth of GaInSbBi for infrared detector applications

Q. Du*, J. Alperin, W.I. Wang

Department of Electrical Engineering, Columbia University, New York, New York 10027, USA

Abstract

The growth of a new quaternary semiconductor alloy GaInSbBi suitable for 8–12 μm infrared detector applications by molecular beam epitaxy is reported for the first time. By the introduction of Ga into the InSbBi alloy, the following have been achieved: (1) enhancement of Bi incorporation, (2) improved lattice-matching to InSb, and (3) suppression of multiple-phase growth and improved surface morphology. The dependence of Bi content and surface morphology on growth temperature and substrate orientation has been investigated. Significant improvement in surface morphology is achieved for films grown on large angle off-axis substrates including (3 1 1)A and (5 1 1)A. Infrared absorption measurements performed at 77 K indicate that a cutoff wavelength as long as 10.7 μm was achieved. The principles demonstrated in this work are quite general and can be applied to other quaternary material systems containing N, P, As, and Sb such as GaInTlSb and GaInAsN to cover a wide range of band gaps.

PACS: 78.65.Fa; 68.55.Bd

Keywords: Molecular beam epitaxy; Fourier transform infrared spectroscopy; Infrared detector

The $InSb_{1-x}Bi_x$ material system has undergone much investigation in recent years due to its potential application in 8–12 μm infrared detectors as the band gap can be varied from that of InSb (~ 0.23 eV at $T = 0$ K) to a metallic phase with increasing x. Joukoff and Jean-Louis first reported the growth of bulk $InSb_{1-x}Bi_x$ using the Czochralski technique [1]. However, a solid solubility limit of 2.6 mol% InBi was found due to the different crystal structures of InSb (zincblende) and InBi (tetragonal). Subsequently, nonequilibrium growth techniques such as multi-target sputtering [2–4] and molecular beam epitaxy (MBE) [5, 6], were employed in order to increase Bi incorporation. Although Bi content appeared to have been enhanced from secondary ion mass spectroscopy (SIMS) measurements, poor growth morphology and the formation of multiple phases were shown to degrade the material quality. All previous results [5–9] showed no indication of an extension of a clear band-edge absorption to a longer wavelength. Most likely, the Bi measured by SIMS was not incorporated in the crystal lattice.

* Corresponding author.

0022-0248/97/$17.00 Copyright © 1997 Elsevier Science B.V. All rights reserved
PII S0022-0248(96)01231-6

Given the covalent atomic radii of In, Sb and Bi (1.44, 1.40, and 1.46 Å, respectively), it is clear that the lattice constant of the epilayer is increased with increased Bi content, thus increasing the lattice mismatch to the InSb substrates. As a result, Bi, the largest atom, is squeezed out of its lattice site in the lattice-mismatched layer; therefore,inducing the formation of a second phase and limiting the Bi content.

In this work, we report the growth and optical properties of $Ga_{0.04}In_{0.96}Sb_{0.97}Bi_{0.03}$ films grown by MBE on InP substrates and demonstrate that increased Bi content in high-quality crystals can be achieved by the incorporation of Ga into the InSbBi alloy. In addition, (3 1 1)A and (5 1 1)A-oriented growth is shown to increase the incorporation of Bi and improve surface morphology further.

In our experiments, Ga was incorporated into the InSbBi alloy in order to reduce the lattice constant and improve the lattice match to InSb (the covalent atomic radius of Ga is 1.26 Å, which is much smaller than that of Sb and Bi). Although the introduction of Ga to InSb increases the band gap, the increase is minimal for a low Ga content due to the band gap narrowing near the InSb end of the ternary alloy (the band gap for $Ga_xIn_{1-x}Sb$ is given as $0.172 + 0.139x + 0.415x^2$ at 300 K). In addition, film composition can be easily controlled by MBE as GaInSb is a group III alloy with only one group V element. This technique of "lattice compensation" is widely applicable and may also be applied to other narrow gap compounds, such as adding Ga to InTlSb and InAsN.

The dependence of surface morphology on substrate orientation is best understood when one considers the surface bonding structure of various substrate orientations [10]. The atoms on the (1 0 0) surface each has one double-dangling bond, while each (1 1 1)A surface atom has one single-dangling bond. The (5 1 1)A surface (16° off (1 0 0) toward (1 1 1)A), as shown in Fig. 1, is composed of both single- and double-dangling bond sites as the flat (1 0 0) terrace consists of two terrace atoms, each with double-dangling bonds, and one step-edge atom with one single-dangling bond. For (n 1 1)A-oriented substrates, the step-edge group III atom has a very stable configuration [10], providing a favorable bond-site for Sb and Bi. We have

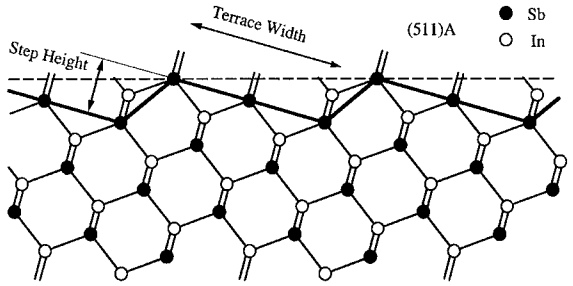

Fig. 1. (5 1 1)A InSb viewed along the [0 $\bar{1}$ 1] direction. The heavy line highlights the (1 0 0) terrace structure.

previously demonstrated that AlGaAs grown on the (n 1 1)-A oriented substrates exhibited superior electrical and optical properties [10].

In our experiments, we observed that the large angle off-axis substrates (i.e., (3 1 1)A and (5 1 1)A) were critical for the incorporation of Bi in the films and for sustaining two-dimensional crystal growth. Although Bi content did not increase significantly for the (3 1 1)A and (5 1 1)A-oriented films as compared to the (1 0 0)-oriented films, the surface morphology for (3 1 1)A and (5 1 1)A is significantly superior, most likely due to the absence of multiple phases. Most importantly, all GaInSbBi films grown on the (1 0 0)-orientation did not show an extension of the cutoff wavelength. Only films grown on (3 1 1)A and (5 1 1)A exhibited a band-edge that was clearly extended to longer wavelengths.

$Ga_xIn_{1-x}Sb_{1-y}Bi_y$ films were grown in a Varian Gen II MBE system on (1 0 0), (3 1 1)A, and (5 1 1)A InP substrates using Sb_4 and Bi sources. The InP substrates were chemically etched with a $H_2SO_4 : H_2O_2 : H_2O$ (5 : 1 : 1) solution, mounted on Mo-blocks and then loaded into the chamber. In order to accommodate the large lattice mismatch between the GaInSbBi film and the InP substrate, a 1 μm AlSb intermediate buffer layer was grown at 500°C, followed by a 1 μm InSb epilayer grown at 400°C. The substrate temperature was measured by an infrared pyrometer. Then the $Ga_{0.04}In_{0.96}Sb_{1-x}Bi_x$ films were grown at a growth rate of 0.5 μm/h. The Sb/In flux ratio was maintained near unity in order to produce a mirror-smooth InSb buffer layer surface [11], while the Ga/In flux ratio was used to control the Ga

content. Reflection high-energy electron diffraction (RHEED) was employed in order to provide in situ monitoring, enabling the maintenance of a slightly Sb-rich condition which is necessary to prevent the formation of metal droplets.

The dependence of the surface morphology and optical absorption of GaInSbBi films on growth temperature was investigated for the substrate temperature range 300 and 380°C. Within this range of substrate temperature investigated, a higher growth temperature was found to result in a superior surface morphology, which was also evidenced from the streaky RHEED patterns during crystal growth indicating a two-dimensional nucleation. Lower substrate temperatures often resulted in more spotty RHEED patterns possibly due to the lower surface mobility of adatoms at lower temperatures. However, optical absorption measurements using Fourier transform infrared spectroscopy (FTIR) indicated that the GaInSbBi films grown at lower substrate temperatures exhibited an absorption edge at longer wavelengths (corresponding to an increased Bi content). This indicated that the sticking coefficient of Bi is higher at lower substrate temperatures, which is consistent with previous reported results [5, 6].

The Sb flux was varied during the growth of the GaInSbBi films in order to investigate the nucleation competition between Sb and Bi. Our results indicated that an Sb-rich condition resulted in a nearly-zero Bi sticking coefficient, while an Sb-deficient condition (i.e. Sb/(Ga + In) ratio slightly less than unity) enhanced the Bi incorporation. Again, this is consistent with previously reported results [5, 6].

The FTIR spectrum at 77 K (Fig. 2) indicated an extended absorption wavelength, 10.7 μm, for $Ga_{0.04}In_{0.96}Sb_{1-x}Bi_x$ films grown under Sb-deficient conditions. In addition, two absorption regions were observed, corresponding to the InSb and $Ga_{0.04}In_{0.96}Sb_{1-x}Bi_x$ films. Based on a 36 meV decrease in energy gap per atomic percentage of Bi increase [12], Bi content was estimated to be roughly 3% (Fig. 3).

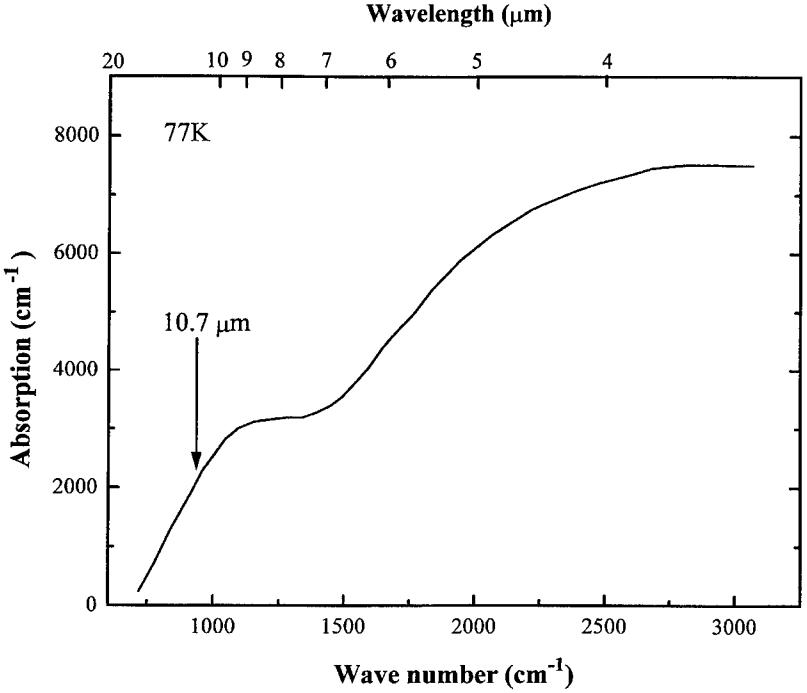

Fig. 2. The 77 K absorption spectrum of a $Ga_{0.04}In_{0.96}Sb_{0.97}Bi_{0.03}$(5 1 1)A film.

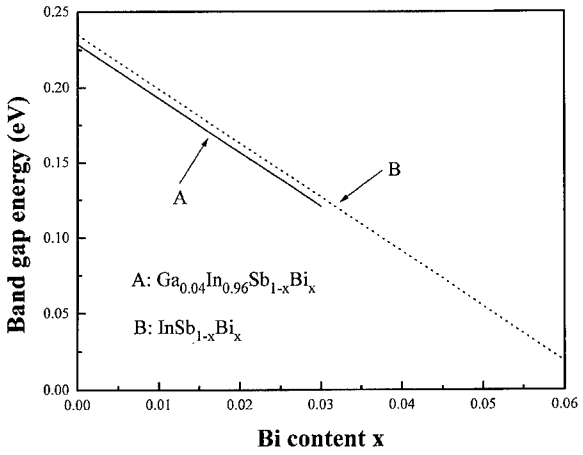

Fig. 3. The calculated band gap of GaInSbBi based on linear interpolation of binary compound semiconductors at 77 K.

In conclusion, $Ga_{0.04}In_{0.96}Sb_{0.97}Bi_{0.03}$ suitable for 8–12 μm infrared detector applications has been grown by MBE on (1 0 0), (3 1 1)A and (5 1 1)A InP substrates. The FTIR results indicate that a cutoff wavelength as long as 10.7 μm has been achieved for films grown on the (3 1 1)A and (5 1 1)A orientation but not for (1 0 0). Also, significant improvement in surface morphology was observed for films grown on (3 1 1)A and (5 1 1)A. The principles demonstrated in this work are quite general and can be applied to other quaternary material systems containing N, P, As, and Sb such as GaInTlSb and GaInAsN to cover a wide range of tunable band gaps.

This work was supported by the Air Force Office of Scientific Research.

References

[1] B. Joukoff and A.M. Jean-Louis, J. Crystal Growth 12 (1972) 169.
[2] J.L. Zilko and J.E. Greene, Appl. Phys. Lett. 33 (1978) 254.
[3] J.L. Zilko and J.E. Greene, J. Appl. Phys. Lett. 51 (1980) 1549.
[4] J.L. Zilko and J.E. Greene, J. Appl. Phys. Lett. 51 (1980) 1560.
[5] K. Oe, S. Ando and K. Sugiyama, Jpn. J. Appl. Phys. 20 (1981) L303.
[6] A.J. Noreika, W.J. Takei, M.H. Francombe and C.E.C. Wood, J. Appl. Phys. 53 (1982) 4932.
[7] T.P. Humphreys, P.K. Chiang, S.M. Bedair and N.R. Parikh, Appl. Phys. Lett. 53 (1988) 142.
[8] K.Y. Ma, Z.M. Fang, D.H. Jaw, R.M. Cohen and G.B. Stringfellow, Appl. Phys. Lett. 55 (1989) 2420.
[9] Z.M. Fang, K.Y. Ma, R.M. Cohen and G.B. Stringfellow, J. Appl. Phys. 68 (1990) 1187.
[10] W.I. Wang, E.E. Mendez, Y. Iye, B. Lee, M.H. Kim and G.E. Stillman, J. Appl. Phys. 60 (1986) 8134; K.F. Longenbach and W.I. Wang, Appl. Phys. Lett. 59 (1991) 2427; I. W. Tao, C. Schwartz and W.I. Wang, J. Vac. Sci. Technol. B 10 (1992) 838.
[11] L.K. Li, Y. Hsu and W.I. Wang, J. Vac. Sci. Technol. B 11 (1993) 872.
[12] A.M. Jean-Louis, B. Ayrault and J. Vargas, Phys. Status Solidi 34 (1969) 341.

ELSEVIER

Journal of Crystal Growth 175/176 (1997) 853–859

JOURNAL OF CRYSTAL GROWTH

Large mismatch heteroepitaxy of InSb on Si(1 1 1) substrates using CaF_2 buffer layers

W.K. Liu[a,*], X.M. Fang[b], J. Winesett[a], Weiluan Ma[a], Xuemei Zhang[a], M.B. Santos[a], P.J. McCann[b]

[a] *Department of Physics and Astronomy, University of Oklahoma, Norman, Oklahoma 73019, USA*
[b] *School of Electrical, Engineering and Laboratory for Electronic Properties of Materials, University of Oklahoma, Norman, Oklahoma 73019, USA*

Abstract

The results of initial attempts to grow large lattice-mismatched InSb/Si structures using CaF_2 buffer layers are reported. Substrate temperatures in the range of 300–400°C were used and MBE growth was initiated by opening the In and Sb shutters simultaneously, producing In-terminated InSb(1 1 1)-A surfaces on Si(1 1 1) substrates. High structural quality was confirmed by reflection high-energy electron diffraction, electron channeling and high-resolution X-ray diffraction. Electron mobility as high as 65 000 $cm^2/(V\,s)$ for a density of $\sim 2\times 10^{16}\,cm^{-3}$ was measured at room temperature for an 8 μm-thick InSb layer grown on CaF_2/Si(111).

1. Introduction

The maturity of integrated circuit technology and the availability of low-cost, rugged, large-area wafers have made Si the most attractive substrate material for semiconductor thin film growth. With advancements in molecular beam epitaxy (MBE) technology, heteroepitaxy has been achieved on Si substrates with a lattice mismatch as large as 20% [1–12]. InSb has the smallest bandgap, highest intrinsic electron mobility and lowest electron effective mass of all binary III–V compounds. These characteristics make InSb-based structures candidates for infrared devices, high speed transistors and magnetic field sensors. Monolithic integration of InSb devices on Si substrates thus offers advantages in microelectronics and infrared detector array fabrication.

Compared to heteroepitaxy of GaAs on Si ($\sim$ 4% mismatch) and CdTe on Si ($\sim$ 19% mismatch), very little has been reported on heteroepitaxy of InSb on Si [8–13]. The main challenges in the growth of InSb on Si stem from the large lattice mismatch (> 19%), the different thermal expansion coefficients ($\alpha_{InSb} \approx 2\alpha_{Si}$ at 300 K) and antiphase domain (APD) formation (polar on nonpolar growth for (0 0 1) and (1 1 1) orientations). Tilted substrates [9–11], In pre-deposition [8] and the insertion of various buffer layers [8, 10–14] have been used to alleviate some of these problems.

* Corresponding author. Fax: + 1 405 325 7557; e-mail: wliu@phyast.ou.edu.

0022-0248/97/$17.00 Copyright © 1997 Elsevier Science B.V. All rights reserved
PII S0022-0248(96)00912-8

Group IIa fluoride layers have been widely used as buffers for the growth on Si of CdTe [1–3] (whose lattice constant is close to that of InSb) and PbSe [7, 15, 16]. As evident from Fig. 1, the ~ 19% lattice mismatch between InSb and Si can be reduced through graded layers of CaF_2 and BaF_2. Recently, thin InSb films have been grown on Si substrates using a BaF_2/InSb/BaF_2 sandwich-type buffer [10].

MBE growth of high quality CaF_2 and BaF_2 films on Si substrates has been demonstrated by several groups [16]. The CaF_2/Si(1 1 1) interface was found to be primarily Ca–Si bonds with a neutral overlayer containing complete F^-–Ca2 + –F^- triple layers [18, 19]. The CaF_2(0 0 1) surface has a perpendicular dipole moment and the repeat unit consists of Ca^{2+}–F^- double layers [17]. It may therefore be possible to grow APD-free InSb on these polar CaF_2 surfaces. Moreover, fluoride layers are also known to be effective in relieving thermal mismatch stress in heteroepitaxial systems through gliding dislocations [7, 16, 17, 20]. Their low elastic stiffness coefficients, particularly that of BaF_2, can also provide additional strain relief via plastic deformation [20–22].

Although the fluorides have much larger thermal expansion coefficients than Si, fluoride films cooled to room temperature after high temperature growth on Si generally do not contain cracks [17]. For thick CdTe/CaF_2/Si structures, near vanishing strain was measured in the CdTe layer and the CaF_2/Si interface is believed to be responsible for the strain relief of the entire structure [7]. The low substrate temperatures used for InSb growth should also help to minimize thermal mismatch problems in InSb/CaF_2/Si structures.

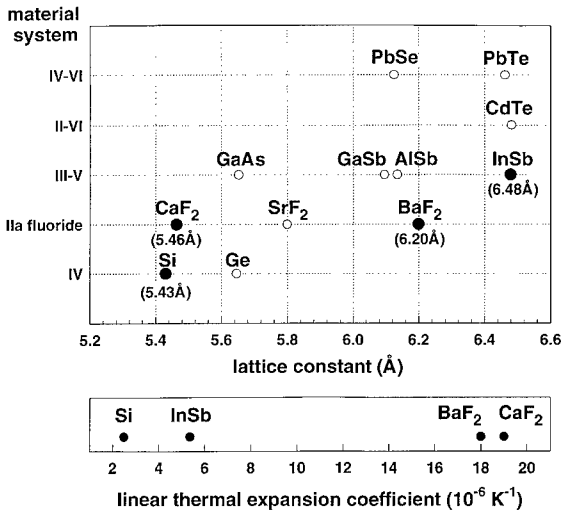

Fig. 1. Lattice constants and thermal expansion coefficients of various material systems related to this work.

In this article, we explore the relatively new use of group IIa fluoride buffer layers in the MBE growth of InSb on Si(1 1 1) substrates. Detailed reflection high-energy electron diffraction (RHEED) and scanning electron microscopy (SEM) studies on the initial growth of this heteroepitaxial system are presented. The interfacial properties are investigated using X-ray photoelectron spectroscopy (XPS), the crystalline quality is confirmed using high-resolution X-ray diffraction and the electrical properties of the InSb films are characterized using Hall-effect measurements.

2. Experimental procedure

MBE growth of InSb/fluoride/Si structures was carried out in an Intevac Gen II system with an analysis chamber and two growth chambers: one for fluoride growth and the other for InSb growth. Three-inch diameter Si(1 1 1) substrates (Silicon Sense, Inc.) were cleaned using the Shiraki method [23] and the passivating oxide was thermally desorbed in the fluoride growth chamber at 1100°C, producing well-defined Si(1 1 1)-(7 × 7) RHEED patterns. Substrate temperatures (T_{sub}) were measured by a thermocouple located at the center of the substrate heater and could differ from real sample temperatures by as much as 100°C.

A high-purity polycrystalline CaF_2 source was evaporated from a graphite-coated PBN crucible while a background pressure of ~ 10^{-10} Torr was maintained. The Si substrate was rotated at 10 rpm and heated to 700°C. Typically, 1000 Å of CaF_2 was deposited at ~ 10 Å/min. This growth rate corresponded to a beam equivalent pressure of ~ 7×10^{-8} Torr. Details of fluoride growth on Si substrates have been reported elsewhere [24].

Following fluoride deposition, the samples were cooled to room temperature and transferred under

ultra-high vacuum to another growth chamber for subsequent InSb deposition using solid elemental sources of In (7 N, Nikko Kyodo) and Sb (6.5 N, Dowa). In most cases, a thin nucleation layer (2000 Å thick) was first grown at a low growth rate ($\sim$ 0.1 ML/s) and a low temperature ($\sim$ 300°C) to reduce the concentration of crystal defects at the interface [25, 26]. A T_{sub} from 350°C to 400°C, a growth rate of $\sim$ 0.65 ML/s and an Sb_4 to In beam equivalent pressure ratio of $\sim$ 3 were used for growth of the active layer. Growth rates were inferred from RHEED intensity oscillations observed during InSb growth on GaAs(0 0 1) substrates. Growth was interrupted occasionally in the early stages to improve crystallinity and surface smoothness.

A Varian electron gun was operated at 9.5 keV and an angle of incidence between 1° and 3° to monitor the RHEED patterns. Digitized images of these patterns were obtained using a CCD camera and a data acquisition system developed by *k*-Space Associates, Inc. We have previously demonstrated that RHEED characterization, in spite of the known effects of electron-beam-induced fluorine desorption, can be used to study fluoride surfaces [24]. Electron beam irradiation time on the fluoride layers was kept to a minimum and RHEED patterns recorded at the initial InSb growth stages were taken from previously unexposed areas. These precautions prevent modification of the starting surface by the electron beam and ensure that the observed diffraction features reflect actual growth morphology.

An adjoining analysis chamber was used to conduct XPS experiments at room temperature, thereby eliminating complications associated with the use of capping layers and exposure to atmosphere. The analysis chamber was equipped with a VG100AX hemispherical analyzer and an XR3E2 dual-anode X-ray source used in conjunction with a VGX900 data acquisition system (Fisons Instruments). The base pressure of this chamber was kept below 10^{-9} Torr during the experiments. XPS spectra arising from In 3d, Sb 3d, Ca 2p and F 1s transitions were obtained by running the Al $K\alpha_{1,2}$ source ($h\nu$ = 1486.6 eV) at a 15 keV potential and a 10 mA emission current. The constant analyzer energy mode was used with a pass energy of 20 eV.

SEM micrographs were obtained using a JEOL JSM880 system (15 kV potential, $\sim$ 10 nA emission current) and electron channeling patterns were taken at a 20° scan angle and a 25 kV potential. X-ray diffraction data (ω–2θ scans) were obtained using a Philips Materials research diffractometer operated with a 4-bounce Ge(2 2 0) incident-beam monochrometer.

3. Results and discussion

Fig. 2 illustrates the evolution of the RHEED patterns during the growth of $InSb/CaF_2/Si(1\ 1\ 1)$. The smooth transition from the Si(1 1 1)-(7 × 7) to the CaF_2(1 1 1)-(1 × 1) surface reconstruction (Fig. 2a and Fig. 2b) provides evidence that CaF_2 growth proceeds two-dimensionally. Parallel epitaxy is confirmed by comparing the electron channeling pattern of the bare Si substrate with one taken after growth of the CaF_2 film (Fig. 3a and Fig. 3b). The six-fold symmetry characteristic of (1 1 1)-oriented layers is found in both patterns. Fewer details are observed in the CaF_2 pattern as a result of a higher defect density in the CaF_2 layer than in the Si substrate.

Subsequent growth of InSb was initiated by exposing the CaF_2 layer to In and Sb fluxes simultaneously. The emergence of more closely spaced InSb-related spots in the RHEED pattern (Fig. 2c) indicated that nucleation took place via the formation of 3D epitaxial islands, as expected from the large lattice mismatch. The cloudy appearance of the sample's surface arose from the high density of dislocations at the interface. As growth proceeded, CaF_2 diffraction streaks weakened until disappearing after deposition of $\sim$ 10 ML of InSb (Fig. 2d). Meanwhile, the InSb diffraction features became brighter and 1/2-order spots began emerging in both the[1 $\bar{1}$ 0] and [1 $\bar{1}$ 2] azimuths (Fig. 2d). At an equivalent layer thickness of $\sim$ 25 ML, 1/2-order streaks could be clearly seen (Fig. 2e). The reflectance of the surface also improved at this stage but was not uniform across the 3 in. wafer. The coalescence of differently-sized islands with differing degrees of strain relaxation, and hence different lattice constants [27], may explain these observations. After depositing 1000 Å of InSb,

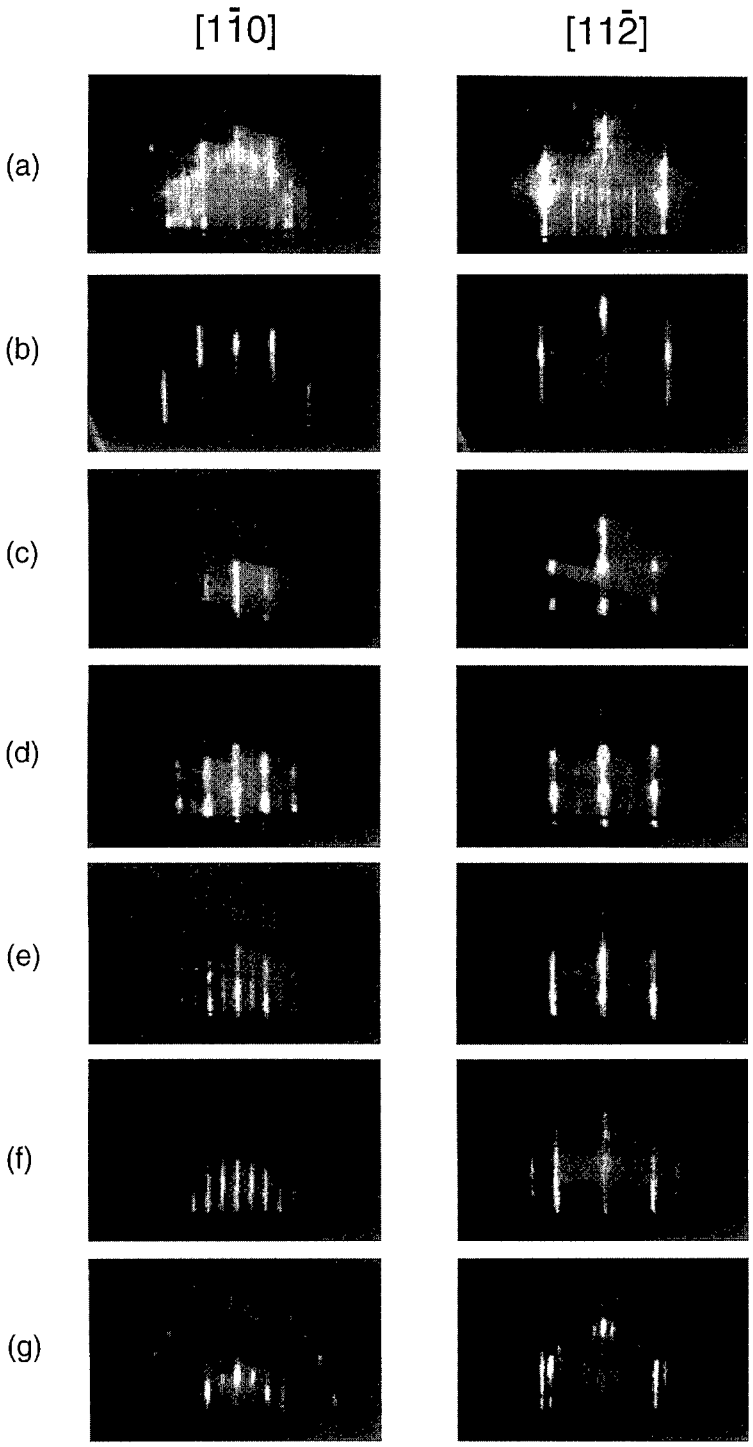

Fig. 2. Evolution of RHEED patterns during the growth of InSb/CaF_2/Si(1 1 1): (a) Si(1 1 1)-(7 × 7); (b) 1000 Å CaF_2(1 1 1)-(1 × 1); initial growth of InSb: (c) ~ 2 ML, (d) ~ 10 ML, (e) ~ 25 ML; after the growth of a 0.4 μm film showing (f) well-defined InSb(1 1 1)-(2 × 2) and (g) static InSb(1 1 1)-(2 × 6) surface reconstructions.

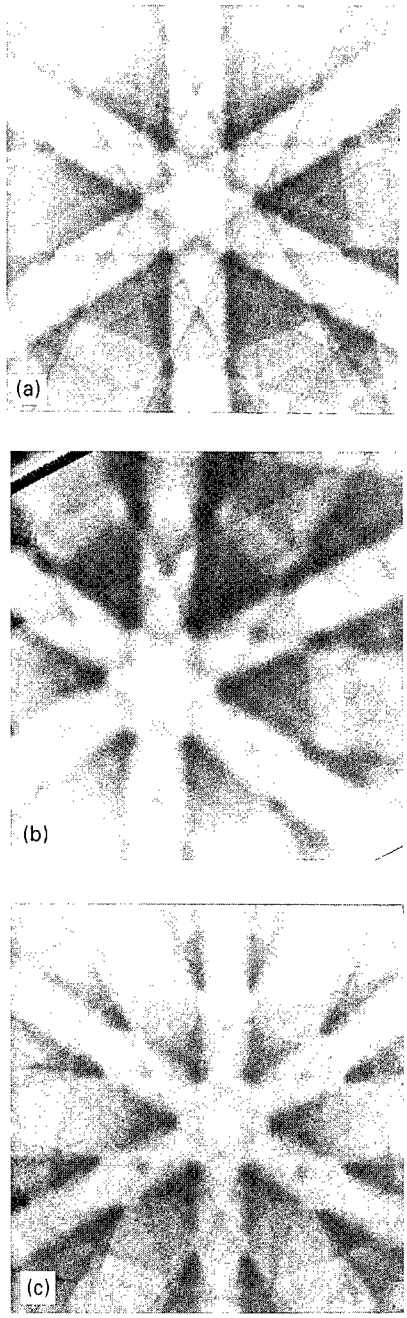

Fig. 3. Electron channeling patterns (25 kV, 20° scan angle) showing the replication of 6-fold symmetry in (a) Si(111) substrate, (b) ~ 1000 Å CaF_2/Si(1 1 1) and (c) 8 μm thick InSb/CaF_2/Si(1 1 1).

growth was interrupted while the substrate temperature was raised to 375°C before further growth resumed. Fig. 2f shows a well-defined (2 × 2) RHEED pattern for a 4000 Å InSb film. It is worth noting that InSb films grown without the low-temperature, low-growth-rate buffer appeared less smooth but more uniform. Increasing the initial growth temperature above 375°C also roughened the surface. When growth was terminated and the substrate temperature lowered under an Sb flux, a change from (2 × 2) In-stabilized to (2 × 6) Sb-stabilized surface reconstruction was observed (Fig. 2g). This transition was reversible and is characteristic of an In-terminated InSb(1 1 1)A surface [28, 29]. This behavior differs from that of GaAs grown on CaF_2/Si(1 1 1), where an As-terminated (1 1 1)B surface is produced [30].

XPS spectra of In 3d, Sb 3d, Ca 2p and F 1s signals were taken at various stages of growth. Within the resolution limit of our XPS system (~ 1 eV), no interfacial products were detected. The normalized photoemission intensities of the substrate peaks decrease and the epilayer peaks increase exponentially with increasing InSb coverage. The composition of the InSb film appears stoichiometric throughout the growth.

The crystalline quality, epitaxial orientation and surface morphology of the epilayer were further investigated using SEM and optical microscopy. Non-uniformity in film thickness is detected under SEM by the presence of curved growth steps on an otherwise fairly smooth surface. Optical micrographs taken under Nomarski interference contrast revealed the presence of features related to stacking faults (Fig. 4). Their density was found to increase dramatically with growth temperature. The initial low-temperature, low-growth-rate buffer also helped reduce the density of these defects. Occasionally, extended cracks along the ⟨1 1 0⟩ directions were observed hundreds of microns apart in films thicker than several microns. Also, sawtooth-shaped microcracks were observed to be most pronounced around defects and can be attributed to the pinning of strain-relieving misfit dislocations [17]. The sharpness and six-fold symmetry of the electron channeling pattern for an 8 μm InSb film (Fig. 3c) is similar to that of the underlying CaF_2/Si layer (Fig. 3b). This indicates that {1 1 1} parallel

epitaxy is achieved and that the InSb layer is not twinned. The high crystalline quality indicated by the channeling pattern was confirmed by X-ray diffraction measurements where the full width at half maximum for the InSb layer was 125 arcsec. This value is comparable to that reported for material systems with similar lattice mismatch such as CdTe/Si [2].

To assess the electrical properties of the InSb layers, Hall-effect measurements were carried out at room temperature and 77 K. The results for InSb layers with different growth parameters are summarized in Table 1. Note that variations in the electrical properties were detected across each wafer due to the non-uniform epitaxial growth expected in a system with such a large lattice mismatch. In general, smoother areas yielded higher electron mobilities. All samples were found to be n-type with room-temperature mobilities in the 10^4 cm^2/(V s) range. Electron mobility as high as 65 000 cm^2/(V s) ($n \approx 2 \times 10^{16}$ cm^{-3}) was obtained in an 8 μm film grown with a 0.3 μm low-temperature, low-growth-rate buffer. This compares favorably to the best room-temperature values reported to date for heteroepitaxial InSb films [8, 11, 12, 31, 32]. The 77 K mobilities, however, were at least an order of magnitude lower than the room temperature values. Similar behavior has been reported for other InSb-on-Si structures and is attributed to electron scattering from dislocations arising from both lattice and thermal strains [8, 10]. A conversion to p-type conduction at low temperature, previously reported for InSb films grown on BaF_2 substrates and attributed to thermal strain [33], was not observed.

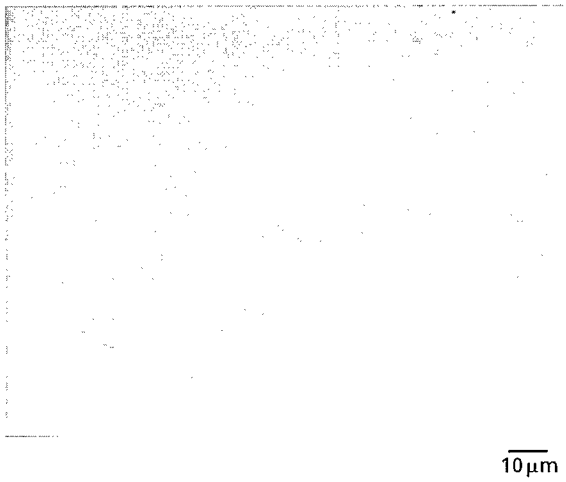

Fig. 4. Nomarski micrograph of an 8 μm thick InSb/CaF_2/Si(1 1 1) film revealing the presence of stacking-fault-related features.

It has been reported that only a very narrow growth window exists for optimal GaAs/CaF_2 films grown on on-axis Si(1 1 1) substrates [30, 34, 35]. The stringent requirement for optimal growth, however, can be relaxed by growing on off-axis substrates [34, 35]. In addition, the initial nucleation of GaAs can be improved by the formation of an As layer on the CaF_2/Si(1 1 1) surface [30, 36, 37]. The epitaxial quality of InSb/CaF_2/Si(1 1 1) may also be improved by applying an Sb soak prior to growth on off-axis substrates.

Table 1
Electrical properties of InSb/fluoride/Si structures studied in this work

Sample	Structure	Growth parameters[a]	μ_{RT} (cm^2/(V s)), n_{RT} (cm^{-3})	$\mu_{77\,K}$ (cm^2/(V s)), $n_{77\,K}$ (cm^{-3})
S139	InSb/CaF_2/Si(1 1 1)	$d_a \approx 2$ μm, $d_b \approx 0.1$ μm, $T_{sub} = 375$°C	24 500–28 500; $n = 2.0 \times 10^{16}$ cm^{-3}	–
S140	InSb/CaF_2/Si(1 1 1)	$d_a \approx 3$ μm, $d_b \approx 0$ μm, $T_{sub} = 375$°C	13 000; $n = 1.9 \times 10^{16}$ cm^{-3}	–
S141	InSb/CaF_2/Si(1 1 1)	$d_a \approx 5$ μm, $d_b \approx 0.2$ μm, $T_{sub} = 350$°C	29 020; $n = 1.7 \times 10^{16}$ cm^{-3}	1686; $n = 2.3 \times 10^{15}$ cm^{-3}
S144	InSb/CaF_2/Si(1 1 1)	$d_a \approx 8$ μm, $d_b \approx 0.3$ μm, $T_{sub} = 350$°C	48 647–65 518; $n \approx 2.0 \times 10^{16}$ cm^{-3}	4715; $n = 1.6 \times 10^{15}$ cm^{-3}

[a] d_a: thickness of active InSb layer, d_b: thickness of low-temperature, low-growth rate InSb buffer.

4. Conclusions

Epitaxial growth of InSb on large lattice-mismatch Si(1 1 1) substrates was achieved by MBE using CaF_2 buffer layers. Structural and room-temperature electrical data indicate that Si(1 1 1) can be used as an alternative substrate for InSb growth. However, detailed study of the influence of growth parameters such as substrate orientation, shutter opening sequence, flux ratio, growth temperature and buffer layer thickness on the crystalline quality need to be done before the prospect of growing vertically stacked single-crystal narrow-gap compound semiconductor/insulator/Si structures can be realized.

Acknowledgements

The authors thank Matthew Johnson for helpful discussion, Bill Chissoe for the SEM studies and Joel Young for technical support. This work is supported by the NSF through grants OSR-9108771, OSR-9550478 and ECS-9410015.

References

[1] Y. Lo, R.N. Bicknell, T.H. Myers, J.F. Schetzina and H.H. Stadelmaier, J. Appl. Phys. 54 (1983) 4248.
[2] H. Zogg and S. Blunier, Appl. Phys. Lett. 49 (1986) 1531.
[3] A.N. Tiwari, W. Floeder, S. Blunier, H. Zogg and H. Weibel, Appl. Phys. Lett. 57 (1990) 1108.
[4] A.N. Tiwari, S. Blunier and H. Zogg, Appl. Phys. Lett. 60 (1992) 621.
[5] R. Sporken, S. Sivananthan, K.K. Mahavadi, G. Monfroy, M. Boukerche and J.P. Faurie, Appl. Phys. Lett. 55 (1989) 1879.
[6] J.P. Faurie, R. Sporken, S. Sivananthan and M.D. Lange, J. Crystal Growth 111 (1991) 698.
[7] H. Zogg, S. Blunier and J. Masek, J. Electrochem. Soc. 136 (1989) 775.
[8] J.-I. Chyi, D. Biswas, S.V. Iyer, N.S. Kumar, H. Morkoc, R. Bean, K. Zanio, H.-Y. Lee and Haydn Chen, Appl. Phys. Lett. 54 (1989) 1016.
[9] G.E. Franklin, D.H. Rich, Hawoong Hong, T. Miller and T.-C. Chiang, Phys. Rev. B 45 (1992) 3426.
[10] H.C. Lu, H.R. Fetterman, C.J. Chen, C. Hsu and T.M. Chen, Solid-State Electron. 36 (1993) 533.
[11] L.K. Li, Y. Hsu and W.I. Wang, J. Vac. Sci. Technol. B 11 (1993) 872.
[12] S.V. Ivanov, A.A. Boudza, R.N. Kutt, N.N. Ledentsov, B. Ya. Meltser, S.S. Ruvimov, S.V. Shaposhnikov and P.S. Kop'ev, J. Crystal Growth 156 (1995) 191.
[13] T. Sudersena Rao, J.B. Webb, D.C. Houghton, J.M. Baribeau, W.T. Moore and J.P. Noad, Appl. Phys. Lett. 53 (1988) 51.
[14] W. Dobbelaere, J. De Boeck and G. Borghs, Appl. Phys. Lett. 55 (1989) 1856.
[15] H. Zogg and M. Hüppi, Appl. Phys. Lett. 47 (1985) 133.
[16] H. Zogg, C. Maissen, S. Blunier, S. Teodoropol, R.M. Overney, T. Richmond and J.W. Tomm, Semicond. Sci. Technol. 8 (1993) S337.
[17] Leo J. Schowalter and Robert W. Fathauer, CRC Critical Reviews in Solid State and Material Sciences 15 (1989) 367 and references therein.
[18] F.J. Himpsel, F.U. Hillebrecht, G. Hughes, J.L. Jordan, U.O. Karleson, F.R. McFeely, J.F. Morar and D. Rieger, Appl. Phys. Lett. 48 (1986) 596.
[19] Marjorie A. Olmstead, R.I.G. Uhrberg, R.D. Bringans and R.Z. Bachrach, J. Vac. Sci. Technol. B 4 (1986) 1123.
[20] H. Zogg, Appl. Phys. Lett. 49 (1986) 933.
[21] S. Blunier, H. Zogg, C. Maissen, A.N. Tiwari, R.M. Overney, H. Haefke, P.A. Buffat and G. Kostorz, Phys. Rev. Lett. 68 (1992) 3599.
[22] P.W. Sullivan, R.F.C. Farrow and G.R. Jones, J. Crystal Growth 60 (1982) 403.
[23] A. Ishizaka and Y. Shiraki, J. Electrochem. Soc. 133 (1986) 666.
[24] X.M. Fang, P.J. McCann and W.K. Liu, Thin Solid Films 272 (1996) 87.
[25] G.M. Metze and A.R. Calawa, Appl. Phys. Lett. 42 (1983) 818.
[26] K. Ishida, M. Akiyama and S. Nichi, Jpn. J. Appl. Phys. 25 (1986) L288.
[27] S.J. Rosner, S.M. Koch and J.S. Harris, Jr., Appl. Phys. Lett. 42 (1986) 1764.
[28] A.J. Noreika, M.H. Francombe and C.E.C. Wood, J. Appl. Phys. 52 (1981) 7416.
[29] T. Nakada, T. Ikeda, M. Yata and T. Osaka, Surf. Sci. 222 (1989) L825.
[30] W. Li, T. Anan and L.J. Schowalter, J. Crystal Growth 135 (1994) 78.
[31] J.-I. Chyi, S. Kalem, N.S. Kumar, C.W. Litton and H. Morkoc, Appl. Phys. Lett. 53 (1988) 1092.
[32] J.R. Söderström, M.M. Cumming, J.-Y. Yao and T.G. Andersson, Semicond. Sci. Technol. 7 (1992) 337.
[33] John L. Davis, Thin Solid Films 192 (1990) 111.
[34] H. Mizukami, K. Tsutsui and S. Furukawa, Jpn. J. Appl. Phys. 30 (1991) 3349.
[35] W. Li, T. Thundat, T. Anan and L.J. Schowalter, J. Vac. Sci. Technol. B 13 (1995) 670.
[36] W. Li, T. Anan and L.J. Schowalter, J. Vac. Sci. Technol. B 12 (1994) 1067.
[37] W. Li, T. Thundat, T. Anan and L.J. Schowalter, Appl. Phys. Lett. 65 (1994) 595.

ELSEVIER

Journal of Crystal Growth 175/176 (1997) 860–867

JOURNAL OF CRYSTAL GROWTH

Indium antimonide doped with manganese grown by molecular beam epitaxy

D.L. Partin*, J. Heremans , C.M. Thrush

Physics and Physical Chemistry Department, General Motors Research & Develoment Center, Warren, Michigan 48090-9055, USA

Abstract

Indium antimonide is of interest for infrared detecting and emitting devices and for magnetic field sensors. In this study, indium antimonide doped with manganese and grown by molecular beam epitaxy was investigated. Secondary ion mass spectroscopy (SIMS) was used to show that the incorporation of manganese is near unity over a wide range of manganese concentrations. Manganese is observed to be an acceptor with a dopant efficiency which follows a power law in which the hole density is proportional to the manganese concentration raised to the power α. The power α depends on the growth temperature; at 300°C, $\alpha = 0.86$ and at 360°C, $\alpha = 0.78$. Lightly manganese doped samples have transport dominated by electrons at low temperatures due to hole freeze out, followed by holes at intermediate temperatures and finally by intrinsic electrons at high temperatures. Additional SIMS studies showed that manganese diffuses relatively slowly in indium antimonide.

Keywords: Dopant; Diffusion; Magnetoresistor

1. Introduction

Indium antimonide is of interest for magnetic position sensors, transistors, infrared detectors and infrared emitters. InSb has a narrow energy band gap of 0.18 eV and a very large phonon limited mobility of 78 000 $cm^2 V^{-1} s^{-1}$ at 300 K. In general, these devices require well-controlled donor and acceptor impurities. Studies of acceptors in epitaxial films have included the p-type dopants Zn [1], Cd [1], Be [2–4], and to some extent C [5]. Of these dopants, Zn and Cd have generally been the preferred dopants for InSb films grown by metal organic chemical vapor deposition (MOCVD), partially because of environmental concerns about volatile beryllium compounds. Be has been the p-type dopant most frequently used in InSb films grown by molecular beam epitaxy (MBE) despite some problems such as a doping efficiency of about 0.5 or less and a tendency to rapidly migrate toward the growing InSb film surface. Carbon produces highly compensated material which may be p-type at cryogenic temperatures [5].

* Corresponding author. Fax: +1 81 986 3091; e-mail: dpartin@cmsa.gmr.com.

0022-0248/97/$17.00 Copyright © 1997 Elsevier Science B.V. All rights reserved
PII S0022-0248(96)00916-5

Manganese has not been previously studied in epitaxial InSb films to our knowledge. However, bulk InSb crystals doped with manganese have been investigated [6, 7]. It was found to be a monovalent acceptor with an ionization energy which varied from 9.5 meV at low Mn concentrations to zero at a Mn concentration of about 1×10^{17} cm^{-3}. The solubility was about 5×10^{18}–1×10^{19} cm^{-3}. Thus, it was the aim of the current work to examine the properties of Mn doped InSb films grown by molecular beam epitaxy.

2. Experimental techniques

We have previously reported on the growth of InSb by MBE [8, 9]. The equipment and growth techniques used were similar in the present case. The MBE source ovens contained indium, antimony, and manganese, all of 99.9999% purity or higher. The antimony source was not cracked, and thus consisted mostly of Sb_4. The vacuum during deposition was $\sim 1 \times 10^{-9}$ Torr. A temperature stabilized quartz crystal deposition monitor could be moved into the growth position before or after growth to measure the fluxes of In, Sb, and Mn. The Sb/In flux ratio (corrected to equivalent atomic fluxes) was 1.3 during these growths. Secondary ion mass spectroscopy (SIMS) studies were done at the University of Western Ontario using a Cameca IMS-3f instrument.

3. Experimental results: growth issue

The flux of manganese at the sample position vs. the inverse Mn oven temperature was very linear for Mn fluxes corresponding to $\sim 1 \times 10^{18}$–1×10^{20} Mn cm^{-3} (at an InSb growth rate of 1 μm/h) and Mn fluxes at lower oven temperatures were found by extrapolation. Such data allows absolute impinging flux calculations. Measurements of the In and Sb fluxes before and after each growth are much easier since their fluxes are several orders of magnitude larger. A sequence of Mn-doped InSb films was grown at a substrate temperature of 300°C or 360°C and with various Mn fluxes. These films were analyzed with SIMS to determine the ratio $^{55}Mn/^{121}Sb$. These data are shown in Fig. 1. The straight line is a fit that assumes a linear relationship between the impinging Mn flux and the Mn incorporated into the film. This appears to be a good assumption for all except the highest Mn fluxes in films grown at the higher (360°C) substrate growth temperature. Since the solid solubility of Mn in bulk InSb crystals was found to be about 5×10^{18}–1×10^{19} cm^{-3} [6], the fact that incorporation of Mn at 360°C is no longer linear with Mn flux above these levels suggests that a bulk solubility limit is being reached. However, at 300°C the Mn fully incorporates in the bulk of the film. This implies that a metastable solid solution is attained or possibly that an Mn-rich phase has precipitated in the bulk of the films. However, there is a "missing mass" problem for the heavily doped films grown at 360°C. Presumably, the missing Mn either reevaporated from the InSb surface during growth or

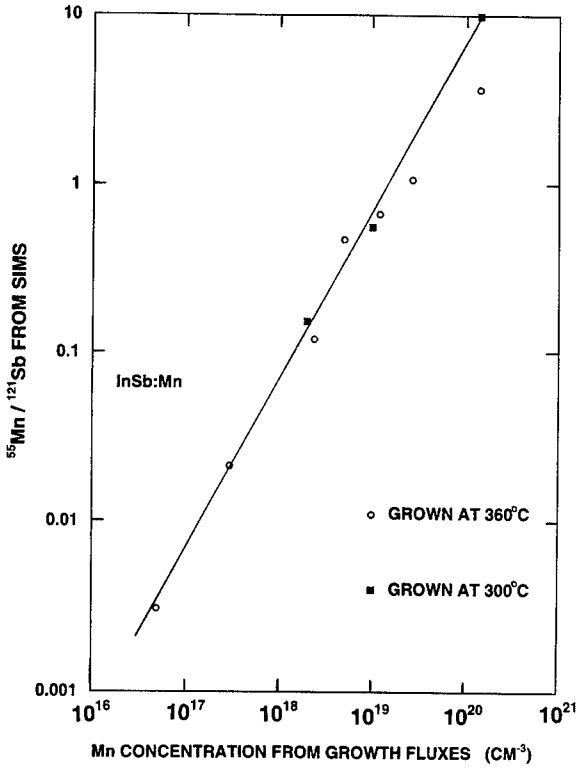

Fig. 1. The isotope ratio $^{55}Mn/^{121}Sb$ determined for several Mn-doped InSb films grown at two different substrate growth temperatures.

surface segregated on the growing surface. This latter possibility was examined immediately after growth by transferring a film under vacuum to an analytical chamber which had an Auger electron spectrometer. The Auger spectrum of a film grown at 360°C and doped with Mn at a concentration 1.5×10^{20} cm^{-3} showed about 0.1 monolayer of Mn on the surface. While this is a non-negligible amount, it is far less than the amount that appears to be missing from the bulk of the film as shown in Fig. 1. This suggests that a significant amount of Mn reevaporates from the InSb surface at a substrate temperature of 360°C and at large Mn concentrations. This reevaporation may involve rejection of some of the Mn from the bulk because of solid solubility limitations resulting in a buildup of Mn on the surface, enhancing the probability of reevaporation of an Mn-rich specie.

An important criterion for a dopant is that it should have an acceptably low solid state diffusion coefficient at the sample growth temperature. To study Mn diffusion, an InSb film was grown at 360°C which consisted of 1000 nm of undoped material followed by 100 nm doped at $N_{Mn} = 2.4 \times 10^{18}$ cm^{-3}

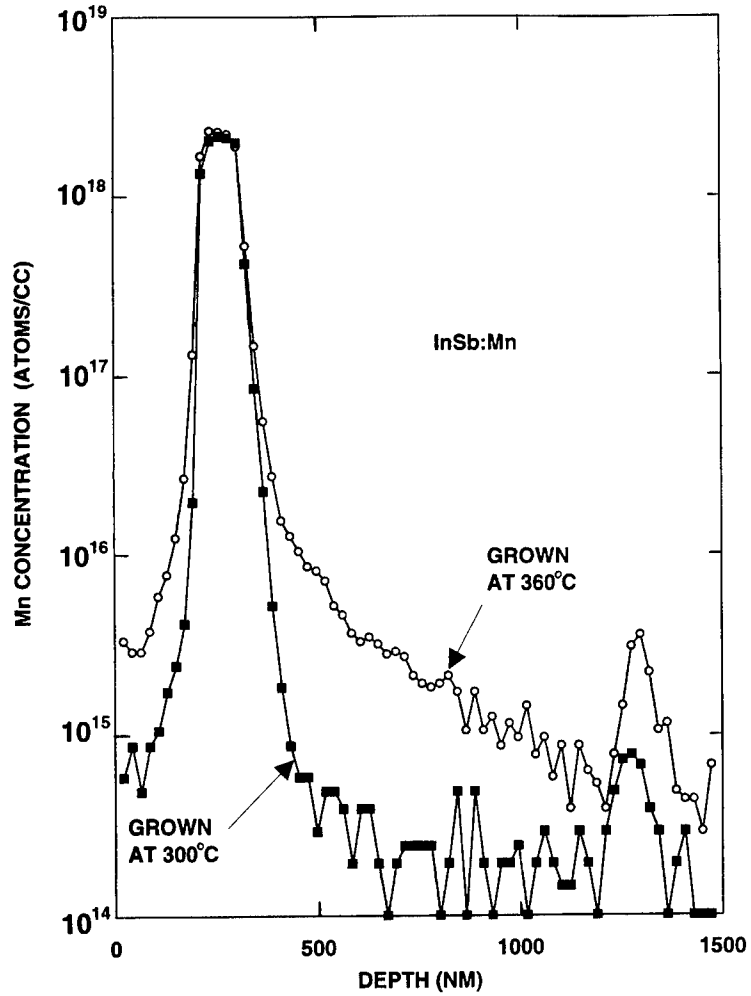

Fig. 2. SIMS depth profile of Mn in InSb grown at 300°C or at 360°C. Only the region between 200 and 300 nm was intentionally doped.

which in turn was followed by 200 nm of undoped material. A nominally identical film was grown at 300°C for comparison. SIMS depth profiles of ^{55}Mn in these films are shown in Fig. 2. In general, a very well-defined Mn-doped layer is observed in each film, as expected. A small Mn peak is also observed at the InSb/substrate interface. This may be caused by leakage of Mn flux around the Mn oven shutter before growth. Ion bombardment effects may play a role in broadening the profiles, but the fact that a much broader peak is seen for the sample grown at 360°C at low Mn concentration implies a solid state diffusion mechanism. Further data is needed to quantitatively study the diffusion mechanism. The diffusion profiles appear to have approximately symmetrical shapes down to low Mn concentrations. This is much different from the case of Be diffusion in InSb in which anomalously large diffusion toward the surface is seen at high concentrations at the higher growth temperatures. Thus Mn is relatively easy to control and it incorporates well in InSb except at the highest concentrations. It diffuses slowly except at low concentration at 360°C.

4. Experimental results: transport studies

Hall effect and magnetoresistivity data were acquired from 2 to 473 K on all samples. The samples were photolithographically defined mesas of the epitaxial films shaped as six-probe Hall bars. The DC Hall resistivity and magnetoresistivity were calculated as the averages over the two polarities of magnetic field and current. In the lowest-doped samples, electrons dominate transport at the lowest temperatures, holes at intermediate temperatures, and intrinsic electrons at high temperatures. Evidence for two and even three-carrier conduction is thus visible in the field dependence of the Hall resistivity and magnetoresistivity near the n-to-p and p-to-n transition temperatures. The

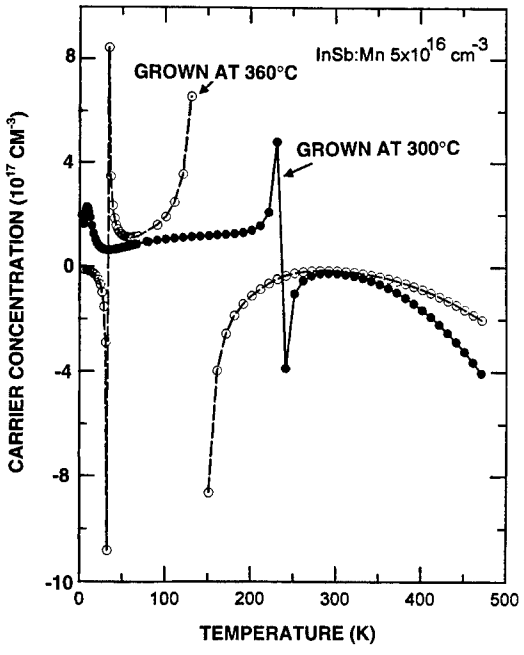

Fig. 3. The carrier concentration of two manganese-doped films as a function of temperature inferred from the inverse of the Hall coefficient (from Fig. 5). Positive values refer to holes and negative values to electrons.

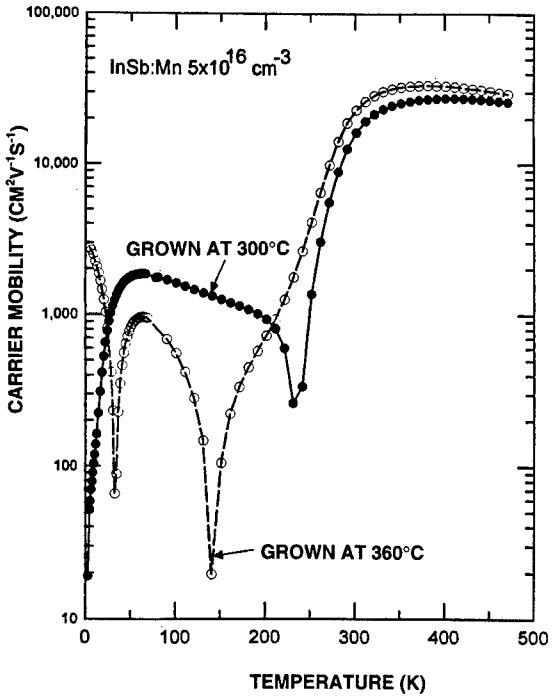

Fig. 4. The mobility of carriers for two InSb films both doped with manganese at a concentration of 5×10^{16} cm^{-3}.

highest-doped samples exhibit negative magnetoresistance because of magnetic scattering. This further complicates the analysis of the data in terms of multi-carrier conduction. For this report, we choose to use only the low-field data ($\mu B \ll 1$, where μ is the mobility of the carrier with the highest mobility). Thus, we used 0.065 T $\geqslant B$ for $T < 70$ K, and 0.036 T $\geqslant B$ for 70 K $< T <$ 473 K. From these low-field data, we compute the density and mobility of these high-mobility carriers, which dominate the electrical transport.

The approximate density of the high-mobility carrier (> 0 for holes, < 0 for electrons), obtained by simply using the inverse of the Hall coefficient, is shown in Fig. 3 for two InSb films both doped with manganese at a concentration 5×10^{16} cm^{-3}. The divergences near the n-to-p and p-to-n transitions are unphysical, because multi-carrier conduction dominates in that regime. Conduction is only dominated by holes in an intermediate temperature range for the sample grown at 360°C. Holes freeze out allowing electrons to dominate conduction below 33 K in this sample because the Mn acceptor level is above the valence band edge [6]. These electrons apparently are caused by residual donors as unintentional background impurities. Electrons

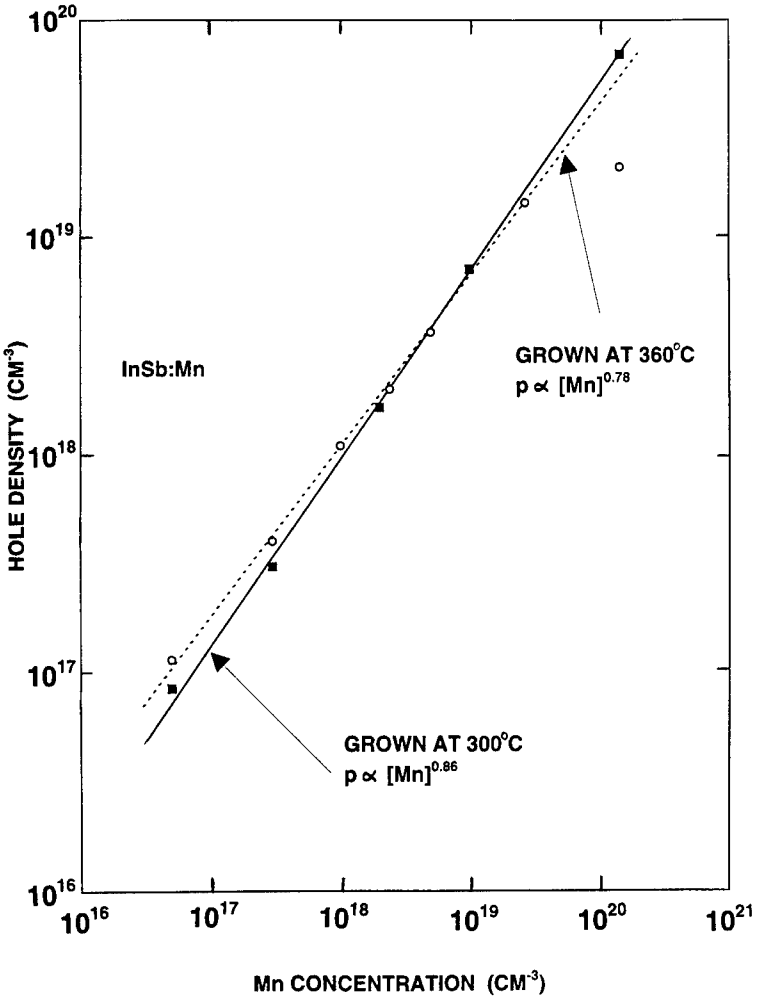

Fig. 5. The hole density versus manganese concentration measured at 64 K for two film growth temperatures.

again dominate conduction above 142 K because of the high density of intrinsic carriers. A somewhat similar behavior is observed for the sample grown at 300°C, except that the holes only partially freeze out at low temperatures. The mobility of carriers for these same two samples is shown in Fig. 4. One noteworthy feature is that the high temperature electron mobilities approach 30 000 $cm^2 V^{-1} s^{-1}$ at 470 K, which is close to the value 34 600 $cm^2 V^{-1} s^{-1}$ which we attain in undoped InSb films at this temperature. This implies that this concentration of Mn (5×10^{16} cm^{-3}) does not scatter electrons very strongly at this temperature.

The low-temperature n-to-p transition does not occur in samples with higher Mn concentrations because the ionization energy of the Mn level decreases with Mn concentration [6]. It can be seen in Fig. 3 that at an intermediate temperature, near 64 K, the hole density is reasonably temperature-independent (the curve for $T_{growth} = 360°C$ in Fig. 3 is the worst case). Therefore, we assume that the hole concentration at 64 K represents the saturation hole density induced by the Mn-doping.

The hole densities and mobilities of Mn-doped InSb at 64 K are shown in Figs. 5 and 6, respectively. We observe a power-law relationship, $p \sim [Mn]^{\alpha}$,

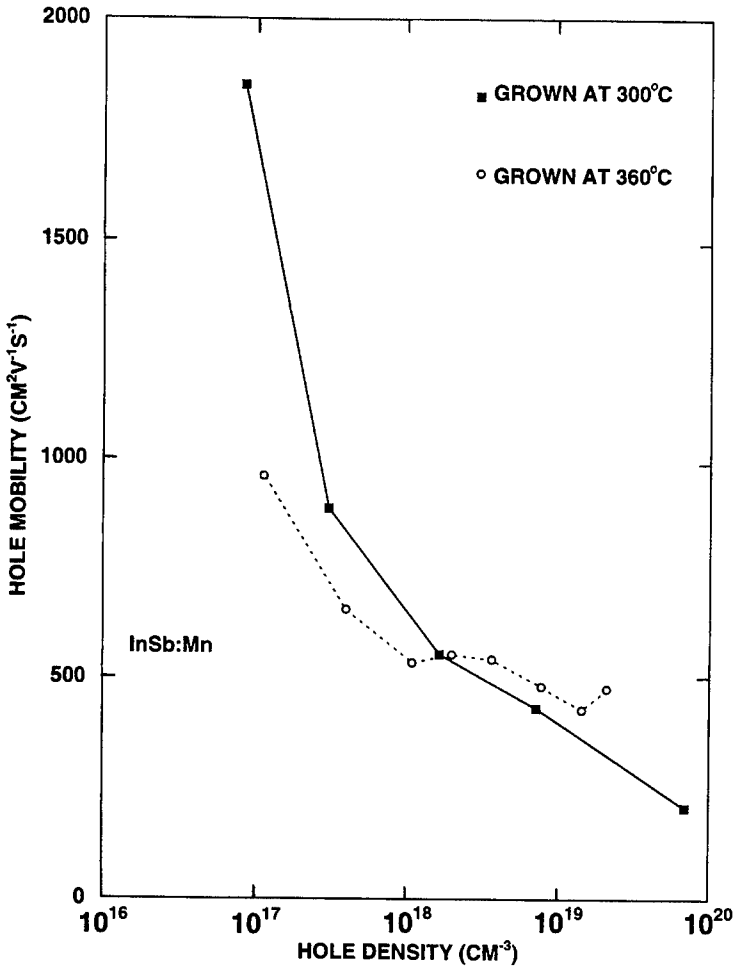

Fig. 6. The hole mobility versus hole density measured at 64 K for two film growth temperatures.

which is closer to linear for films grown at 300°C ($\alpha = 0.86$) than for films grown at 360°C ($\alpha = 0.78$). Our films had a linear relationship between Mn incorporation and the Mn flux during growth except at Mn levels near 10^{20} cm^{-3} (see Fig. 1). Thus, except at the highest Mn levels, the sub-linear relationship in Fig. 5 cannot be explained by problems with Mn incorporation in the InSb film. Since manganese was previously found to be a monovalent acceptor in InSb bulk crystals, our results suggest that the lattice site at which manganese incorporates is dependent upon on growth parameters. Films grown at 360°C had a less linear relationship between Mn and hole densities. This result is rather similar to one recently reported for Mn incorporation in InAs [10]. In that study, it was reported that MBE-grown InAs films had Mn on the In lattice sites for low growth temperatures (near 200°C) or at low concentrations (below 1 at%). Thus, we speculate that the increasingly sub-linear dependence of hole density on Mn concentration in InSb at higher film growth temperature may imply that an increasing fraction of Mn atoms are not occupying the normal In lattice sites where Mn acts as a normal acceptor impurity in InSb. The hole mobility at 64 K is shown as a function of the hole density at that temperature in Fig. 6.

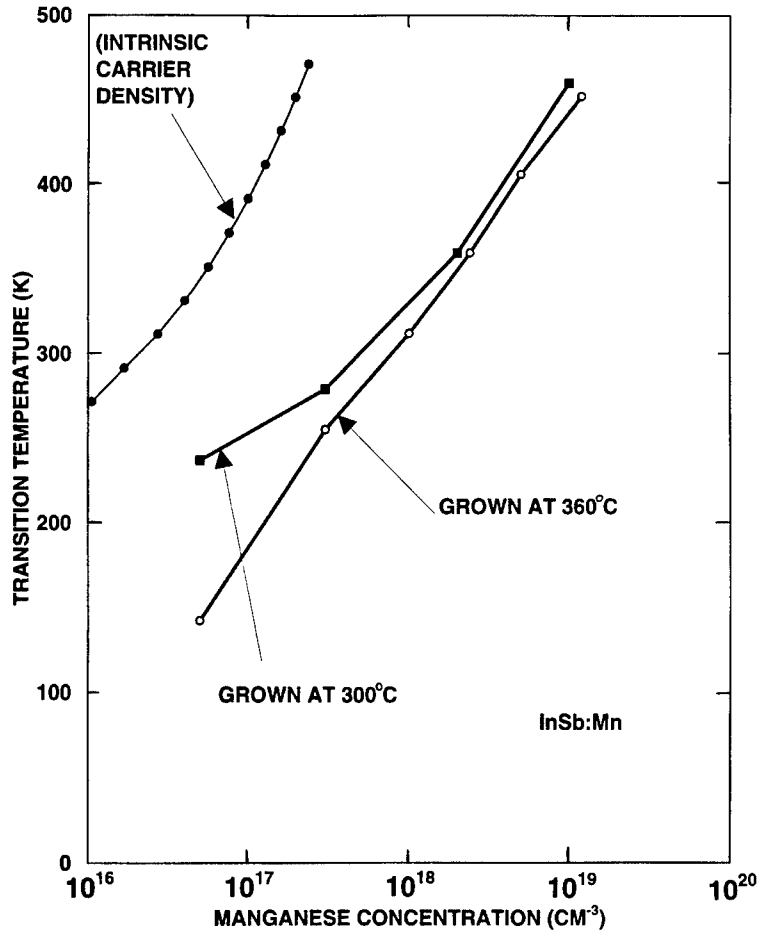

Fig. 7. Transition temperature above which conduction is dominated by electrons versus manganese concentration. The intrinsic carrier density (determined from an undoped InSb film) is also shown versus temperature on the same axes.

The above discussion was based upon transport measurements at 64 K. Transport measurements were made over the range 2–473 K. As the temperature was increased, the dominant carrier type changed from holes to electrons. The transition temperature at which this occurred is shown in Fig. 7 as a function of Mn concentration and film growth temperature. This transition is caused by the dependence of the intrinsic electron density on temperature and by the fact that electrons have about two orders of magnitude higher mobility than holes in InSb. Thus, when the intrinsic electron density is over an order of magnitude lower than the Mn concentration, the intrinsic electrons will begin to dominate conduction. We determined the intrinsic electron density from an InSb undoped film which was grown under conditions similar to those used in the current study. It was 2.8 μm thick, and had a low temperature background electron density of about 1×10^{15} cm^{-3}. Over the temperature range for which data are shown in Fig. 7 (271–471 K), the electron mobility in our undoped InSb film decreased from 66 000 to 34 600 cm^2 V^{-1} s^{-1}. These electron mobilities are roughly two orders of magnitude higher than the hole mobilities generally measured for Mn-doped InSb in this temperature range.

Thus, manganese has been shown to be a useful, well-controlled acceptor dopant for InSb grown by molecular beam epitaxy. While only films grown by molecular beam epitaxy have been studied so far, it appears to be feasible to grow InSb films by metal organic chemical vapor deposition (MOCVD) which are doped with manganese using a compound such as tricarbonyl manganese. This has not yet been studied.

References

[1] R.M. Biefeld, S.R. Kurtz and I.J. Fritz, J. Electron. Mater. 18 (1989) 775.
[2] T. Ashley, A.B. Dean, C.T. Elliott, G.J. Pryce, A.D. Johnson and H. Willis, Appl. Phys. Lett. 66 (1995) 481.
[3] T. Ashley, C.T. Elliott, N.T. Gordon, R.S. Hall, A.D. Johnson and G.J. Pryce, Appl. Phys. Lett. 64 (1994) 2433.
[4] P.E. Thompson, J.L. Davis, M.J. Yang, D.S. Simons and P.H. Chi, J. Appl. Phys. 74 (1993) 6686.
[5] T.S. Rao, J.B. Webb, Y. Beaulieu, J.L. Brebner, J.P. Noad and J. Jackman, J. Vac. Sci. Technol. A 7 (1989) 1215.
[6] M.Y. Dashevskii, V.S. Ivleva, L.Y. Krol, I.N. Kurilenko, L.B. Litvak-Gorskaya, R.S. Mitrofanova and E.Y. Fridlyand, Sov. Phys. Semicond. 5 (1971) 757.
[7] F.F. Kharakhorin, M.F. Poluboyarkova, V.G. Vinogradova and V.L. Kheifets, Sov. Phys. Semicond. 2 (1968) 678.
[8] D.L. Partin, J. Heremans and C.M. Thrush, J. Appl. Phys. 71 (1992) 2328.
[9] D.L. Partin, J. Heremans and C.M. Thrush, J. Crystal Growth 111 (1991) 614.
[10] Y.L. Soo, S.W. Huang, Z.H. Ming and Y.H. Dao, Phys. Rev. B 53 (1996) 4905.

ELSEVIER

Journal of Crystal Growth 175/176 (1997) 868–872

JOURNAL OF CRYSTAL GROWTH

Molecular beam epitaxial growth of high electron mobility InAs/AlGaAsSb deep quantum well structures

Naohiro Kuze[a,*], Hiromasa Goto[a], Masahiro Matsui[a], Ichiro Shibasaki[a], Hiroyuki Sakaki[b]

[a] *Central Laboratory, Asahi Chemical Industry Co., Ltd., 2-1 Samejima, Fuji, Shizuoka 416, Japan*
[b] *RCAST, The University of Tokyo, 4-6-1 Komaba, Meguro, Tokyo 153, Japan*

Abstract

We investigated InAs deep quantum well structures made from InAs/AlGaAsSb materials on GaAs substrates by molecular beam epitaxy. By accurately controlling As_4/Sb_4 and As_4/In beam flux ratios, we were able to grow the high-quality crystals of AlGaAsSb and InAs. Very high electron mobility of more than 32,000 cm^2/Vs were obtained at room temperature. It was found that the optimum beam-equivalent-pressure (BEP) ratio of As_4/In for growing an InAs quantum well layer is 110 to get the highest electron mobility. Moreover, a strong photoluminescence (PL) peak of AlGaAsSb band-edge emission at 10 K was observed around 1.2 eV. We determined that the optimum As_4/Sb_4 BEP ratio is 6.7 for AlGaAsSb from the full width at half-maximum of PL peaks and electrical characteristics. We also observed the blue shifted PL of AlGaAsSb as the As_4/Sb_4 BEP ratio decreased.

1. Introduction

The InAs/AlGaAsSb material system is of interest for its high electron mobility and large conduction band offset of ~ 1.3 eV at the InAs/AlGaAsSb heterojunction. Fig. 1 shows a schematic cross section and energy band diagram of InAs deep quantum well structures (DQWs). In recent years, the InAs/AlSb quantum well (QW) system has been studied by several groups [1–5]. Bolognesi et al. [5] achieved high electron mobilities of 33 000 $cm^2/V\,s$ in the InAs/AlSb system, using a nucleation layer, buffer layers as thick as a few microns of AlSb, smoothing superlattices, and InSb-like interface controls. However, InAs/AlSb materials have a disadvantage for use in practical devices because AlSb easily becomes oxidized during the device fabrication process.

We proposed new InAs DQWs, made from InAs/AlGaAsSb materials, which are reliable enough for practical use [6, 7]. In our InAs DQWs, the InAs QW layer is sandwiched between quaternary AlGaAsSb buffer/barrier layers that are lattice-matched to InAs because of the introduction of As. Furthermore, Ga is incorporated into the buffer/barrier layers to suppress the oxidation of

* Corresponding author. Fax: + 81 545 62 3089; e-mail: a8212678@ut.asahi-kasei.co.jp.

0022-0248/97/$17.00 Copyright © 1997 Elsevier Science B.V. All rights reserved
PII S0022-0248(96)00975-X

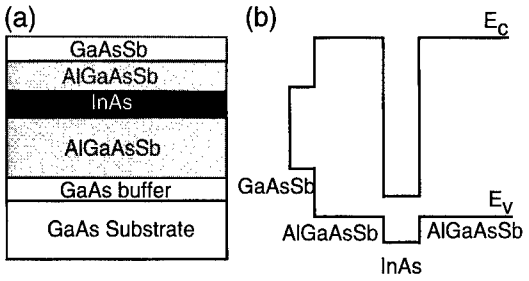

Fig. 1. (a) Schematic cross section and (b) energy band diagram of InAs /$Al_{0.5}Ga_{0.5}AsSb$ DQWs.

the antimonide layers. Our InAs DQWs consist of five simple layers, including a submicron-thick AlGaAsSb layer. Although neither superlattices nor interface controls are employed during the growth of InAs DQWs, very high electron mobilities of more than 30 000 $cm^2/V\,s$ have been obtained [8]. Moreover, we have applied InAs DQWs to Hall sensors as a practical device and have obtained high sensitivities, small dependence of input resistance on temperature, and good reliability [7].

In this paper, we report on the As_4/In beam-equivalent-pressure (BEP) ratio dependence of electrical characteristics of InAs DQWs. We also discuss the optimum As_4/Sb_4 BEP ratio during the growth of AlGaAsSb buffer/barrier layers from the full width at the half-maximum (FWHM) of the photoluminescence (PL) peak of AlGaAsSb band-edge emission at 10 K.

2. Experimental procedure

All samples were grown on semi-insulating GaAs (1 0 0) substrates in a specially modified VG Semicon V100 MBE system, equipped with elemental group III and group V solid sources, the latter producing As_4 and Sb_4 beams.

The growth was initiated with a 150 nm GaAs buffer layer at a substrate temperature of 580°C. The substrate temperature was measured by an optical pyrometer during the entire time of the InAs DQWs growth. Following the growth of a 600 nm $Al_{0.5}Ga_{0.5}AsSb$ buffer/barrier layer at 540°C, 15 nm of not-intentionally doped InAs, a 10 nm of $Al_{0.5}Ga_{0.5}AsSb$, and a 5 nm of GaAsSb cap layer were grown. $Al_{0.5}Ga_{0.5}AsSb$ barriers and GaAsSb cap layer were not intentionally doped. The As content y in $Al_{0.5}Ga_{0.5}As_ySb_{1-y}$ lattice-matched to InAs is 0.12. The energy gap of $Al_{0.5}Ga_{0.5}As_{0.12}Sb_{0.88}$ is about 1.36 eV. The substrate temperature was gradually decreased to 450°C prior to the start of the InAs growth and held there for the remainder of the growth [7]. The Al/Ga ratio was calibrated by measuring the reflection high-energy electron diffraction (RHEED) oscillation of AlAs and GaAs. The BEPs for In and Sb_4 were measured just under the substrate holder using the movable ion gauge before raising the arsenic temperature. The BEP of As_4 was the average of measurements before and after the growth. The growth rate of AlGaAsSb was 800 nm/h. The growth rate of InAs changed from 400 to 1000 nm/h when the V/III ratio was investigated by changing In temperature.

The morphology of the InAs surface grown on AlGaAsSb buffer/barrier layer was analyzed by high-resolution scanning electron microscopy (HRSEM). The electron mobilities at room temperature were determined by van der Pauw measurement. PL spectra were measured at 10 K using a Ge detector cooled to 77 K. A 488.0 nm line of an Ar^+ laser was used as a pump source with an excitation density of 5 W/cm^2.

3. Results and discussion

The surface structure of the grown epilayers was analyzed in situ by RHEED patterns during the entire time of the InAs DQWs growth. As soon as the AlGaAsSb growth was initiated on the GaAs surface, the streaked (2 × 4) RHEED pattern became spotty instantly because of a 7% lattice mismatch between the GaAs and AlGaAsSb. However, the strain relaxation of AlGaAsSb was very fast and the spot RHEED pattern turned into a strongly streaked (1 × 3) pattern after growing only a 35 nm thick of AlGaAsSb layer [8]. After 600 nm of AlGaAsSb growth, the InAs layer was grown without growth interruption and interface control. Just after the InAs layer growth started, the RHEED pattern changed from a streaked (1 × 3) to a weakly

streaked (1 × 1) pattern. This indicates that the InAs layer two-dimensionally grew on the AlGaAsSb buffer layer. We also confirmed that the InAs layer on AlGaAsSb grew two-dimensionally by atomic force microscopy, as reported in Ref. [8]. The strongly streaked (1 × 3) pattern recovered as soon as the top AlGaAsSb barrier layer started to grow. This streaked (1 × 3) pattern did not change until the end of the GaAsSb cap layer growth.

We studied the As_4/In BEP ratio dependence of electron mobility during the InAs QW layer growth. The As_4/In BEP ratio was changed from 85 to 220 by changing the In cell temperature. In Fig. 2 the electron mobility at room temperature is shown as a function of As_4/In BEP ratio. The highest electron mobility of 27 000 cm^2/V s was obtained by using the As_4/In BEP ratio of 110 at an In flux of about $J_{In} = 1.0 \times 10^{14}$ atoms/cm^2 s. We have to control As_4/In BEP between 95 and 120 to get a higher electron mobility than 25 000 cm^2/V s. The surface morphology was observed by HRSEM after 3 ML growth of InAs on the AlGaAsSb surface. Fig. 3a and Fig. 3b show the HRSEM images of samples grown at As_4/In BEP ratios of 110 and 220, respectively. The morphology of the InAs grown at the ratio of 1 1 0 was smoother than that at the ratio of 2 2 0. We speculate that In atoms may be able to migrate more easily under relatively lower arsenic pressure. If the As_4 flux increases, In atoms may be covered with As atoms before In atoms migrate well on the surface. In contrast, if the As_4 flux is lower than the optimum BEP ratio of 1 1 0, In atoms may start to coalesce and form In droplets.

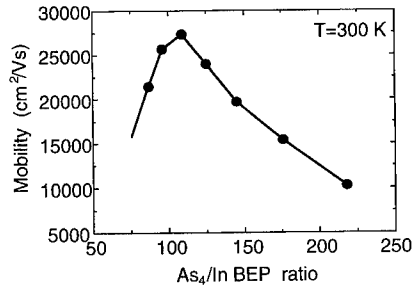

Fig. 2. The electron mobility dependence for InAs DQWs as a function of As_4/In BEP ratio. The As_4/Sb_4 BEP ratio was constant at 8.5. The As content y in $Al_{0.5}Ga_{0.5}As_ySb_{1-y}$ was 0.02.

The As_4/Sb_4 BEP ratio during the AlGaAsSb growth was also investigated. The As_4/Sb_4 BEP ratio was changed from 6 to 12 by changing Sb_4 cell temperature. The As_4 BEP was kept at 1.80×10^{-5} Torr during the growth of the InAs DQWs layers. Fig. 4 shows the FWHM of the PL peak from AlGaAsSb as a function of the As_4/Sb_4 BEP ratio. The PL spectra from InAs DQWs were dominated by a single strong peak around 1.2 eV, corresponding to the band-edge emission of the $Al_{0.5}Ga_{0.5}AsSb$ layer at 10 K, as shown in Fig. 4b. It was found that there is a minimum FWHM of the sample grown by using an As_4/Sb_4 BEP

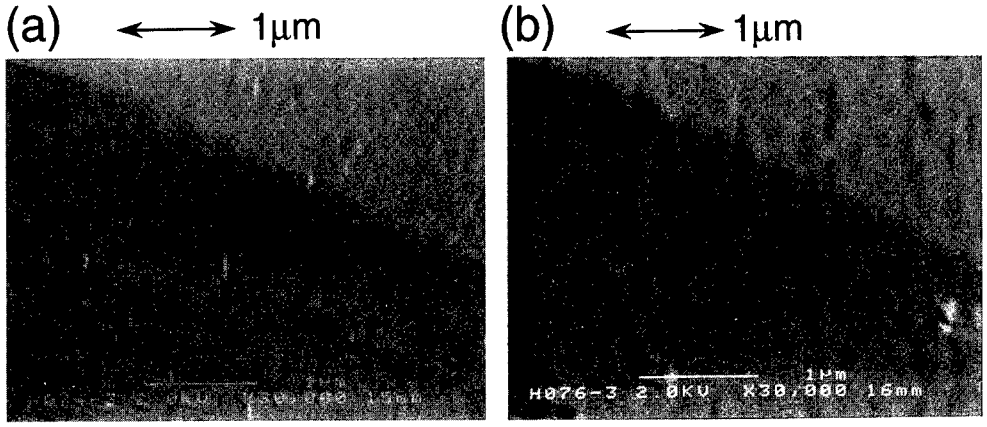

Fig. 3. HRSEM images of the surface after 3 ML growth of InAs on AlGaAsSb at As_4/In BEP ratio of (a) 110 and (b) 220.

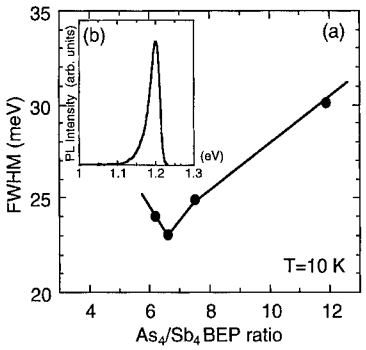

Fig. 4. (a) FWHM of PL spectra peak of AlGaAsSb band-edge emission at 10 K as a function of As_4/Sb_4 BEP ratio. The As_4/In BEP ratio was constant at 110. (b) PL spectrum of the sample grown at the As_4/Sb_4 BEP ratio of 6.7. The As content y in $Al_{0.5}Ga_{0.5}As_ySb_{1-y}$ was 0.01.

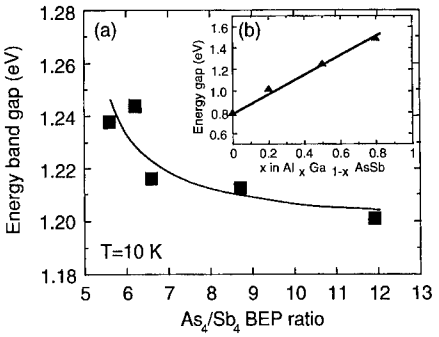

Fig. 5. (a) AlGaAsSb band gap as a function of As_4/Sb_4 BEP ratio. (b) $Al_xGa_{1-x}AsSb$ energy band gap as a function of Al content x.

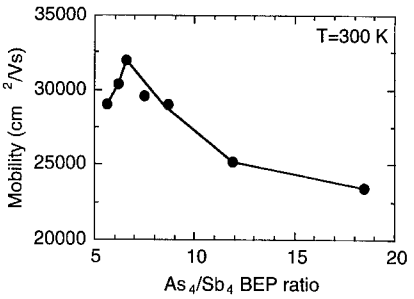

Fig. 6. Room temperature mobility dependence for InAs DQWs as a function of As_4/Sb_4 BEP ratio. The As_4/In BEP ratio was constant at 110.

ratio of 6.7 at an Sb_4 flux of about $J_{Sb} = 8.9 \times 10^{14}$ atoms/cm^2 s.

Moreover, we also investigated the PL peak shift of AlGaAsSb band-edge emission as a function of the As_4/Sb_4 BEP ratio. As the Sb_4 flux increased, the As content y in $Al_xGa_{1-x}As_ySb_{1-y}$ decreased and y was almost zero at the As_4/Sb_4 ratio of 5.5, which was confirmed by X-ray diffraction. If the Sb ratio increases in AlGaAsSb at a constant Al/Ga ratio, the energy band gap should decrease. However, the photon energy increased from 1.20 to 1.24 eV at 10 K as the As_4/Sb_4 BEP ratio decreased from 12 to 5.5, as shown in Fig. 5a. This indicates that the $Al_xGa_{1-x}AsSb$ energy gap increased because of the change in the Al/Ga ratio as the Sb_4 beam flux increased. In order to estimate the change in the Al/Ga ratio in AlGaAsSb, we grew calibration samples changing x in $Al_xGa_{1-x}AsSb$ from 0 to 0.8 at a constant As_4/Sb_4 BEP ratio. Fig. 5b shows the energy band gap of $Al_xGa_{1-x}AsSb$ as a function of x. We can estimate that the Al content x increases from 0.44 to 0.48 as the As_4/Sb_4 BEP ratio decreases from 12 to 5.5. The reason the x changes as the As_4/Sb_4 BEP ratio changes may be explained as follows. The heats of formation ($-\Delta H_f$, spectroscopy) of AlSb, GaSb, AlAs, and GaAs are, respectively, 20.3, 9.5, 17.3, and 16.3 kcal/mol [9]. We speculate that AlSb is thermodynamically more stable than GaSb and the stability of AlAs is almost the same as GaAs. Therefore, AlSb may be formed more easily than GaSb during the growth of AlGaAsSb as the Sb flux increases. Further studies are required to clear the dependence of electron mobility on Al/Ga ratio in AlGaAsSb of InAs DQWs.

Furthermore, we evaluated the crystalline quality of AlGaAsSb by the X-ray diffraction rocking curves. The minimum FWHM of 600 arcsec was also observed at the As_4/Sb_4 BEP ratio of 6.7. Since we reduced the substrate temperature from 540°C to 450°C before growing the InAs QW layer, the FWHM of AlGaAsSb was suppressed to 600 arcsec.

Finally, we measured the Hall mobility of these samples at room temperature. We found that the mobility curve had a maximum of 32 000 cm^2/V s at the As_4/Sb_4 BEP ratio of 6.7, as shown in Fig. 6.

For a 6.7 As_4/Sb_4 BEP ratio growth, an electron mobility of 90 000 $cm^2/V\,s$ at 77 K was obtained. The typical carrier densities and sheet resistances at room temperature were in the ranges of 0.9–$1.1 \times 10^{12}\,cm^{-2}$ and 185–250 Ω, respectively. The not-intentionally doped InAs DQWs have remarkably high electron sheet concentrations of the order of $10^{12}\,cm^{-2}$. We can reproducibly grow the InAs DQWs with high electron mobility of more than 30,000 $cm^2/V\,s$ by maintaining the As_4/Sb_4 BEP ratio at 6.7 and As_4/In BEP ratio at 110.

4. Conclusion

To improve the electron mobility of InAs DQWs, we have to grow high-quality crystals of AlGaAsSb buffer/barrier layers and the InAs QW layer. By accurately controlling As_4/Sb_4 for the AlGaAsSb layer growth and As_4/In for the InAs QW layer growth in InAs DQWs, we have obtained very high electron mobility of more than 32 000 $cm^2/V\,s$ at room temperature. The optimum BEP ratios of As_4/Sb_4 and As_4/In are 6.7 and 110, respectively, from the electrical and optical characterizations of InAs DQWs. We believe that InAs/AlGaAsSb DQWs, with their high electron mobility, are promising materials for high-speed electronic devices and magnetic sensor applications.

Acknowledgements

The authors thank Dr. Kohichi Mori at Asahi Chemical Industry for his continuous encouragement.

References

[1] G. Tuttle, H. Kroemer and J.H. English, J. Appl. Phys. 65 (1989) 5239.
[2] K. Yoh, T. Moriuchi, M. Yano and M. Inoue, J. Crystal Growth 111 (1991) 643.
[3] S. Ideshita, A. Furukawa, Y. Mochizuki and M. Mizuta, Appl. Phys. Lett. 60 (1992) 2549.
[4] H. Munekata, L. Esaki and L.L. Chang, J. Vac. Sci. Technol. B 5 (1987) 809.
[5] C.R. Bolognesi, H. Kroemer and J.H. English, J. Vac. Sci. Technol. B 10 (1992) 877.
[6] K. Nagase, S. Muramatsu, N. Kuze, T. Iwabuchi, A. Ichii, M. Toyama and I. Shibasaki, in: Digest of Technical Papers; Late News, Transducers '93 (1993).
[7] N. Kuze, K. Nagase, S. Muramatsu, S. Miya, T. Iwabuchi, A. Ichii and I. Shibasaki, J. Crystal Growth 150 (1995) 1307.
[8] N. Kuze, H. Goto, S. Miya, S. Muramatsu, M. Matsui and I. Shibasaki, Mater. Res. Soc. Symp. Proc. Vol. 399 (1996) 165.
[9] J.C. Phillips, Bonds and Bands in Semiconductors (Academic Press, New York, 1973) ch. 8, Table. 8.2.

ELSEVIER

Journal of Crystal Growth 175/176 (1997) 873–876

JOURNAL OF CRYSTAL GROWTH

MBE growth and characterization of high-quality GaInAsSb/AlGaAsSb strained multiple quantum well structures

A.Z. Li[a,*], Y. Zhao[a], Y.L. Zheng [a], G.T. Chen[b], G.P. Ru[a], W.Z. Shen[c], J.Q. Zhong[a]

[a] *State Key Laboratory of Functional Materials for Informatics, Shanghai Institute of Metallurgy, Chinese Academy of Sciences, Shanghai 200050, People's Republic of China*

[b] *Shanghai Institute of Optical and Fine Mechanics, Chinese Academy of Sciences, Shanghai 201800, People's Republic of China*

[c] *Shanghai Institute of Technical Physics, Chinese Academy of Sciences, Shanghai 200083, People's Republic of China*

Abstract

Molecular beam epitaxial growth and characterization of GaInAsSb/AlGaAsSb strained multiple quantum wells (MQWs) have been investigated. Optimization for the growth have been studied by characterizing the MQWs with double-crystal X-ray rocking curve, photoluminescence (PL) and absorption measurements and evaluating laser diode performance. Up to the fifth-order the satellite peak is resolved in rocking curves, and asymmetric distribution of satellite peaks is found which indicates large strain in quantum well structures. PL and absorption measurements at different temperatures show the high quality of GaInAsSb/AlGaAsSb multiple quantum wells grown under optimized conditions. The full-width of half-maximum of a PL peak as narrow as 9.0 meV is achieved at 4 K, and room-temperature PL and well-resolved excitonic absorption peaks are observed in the MQW structures. By using the GaInAsSb/AlGaAsSb MQWs as active layers in laser diodes, pulsed operation at room temperature with emission at 2.05 μm has been obtained.

1. Introduction

The GaInAsSb/AlGaAsSb quaternary systems have recently been receiving much attention, due to their potential application as semiconductor diode lasers with emission wavelength in the range 2–4 μm [1–6]. High-performance GaInAsSb/AlGaAsSb quantum well (QW) lasers grown by molecular beam epitaxy (MBE) has been demonstrated [4–6]. The recombination of photoexcited carriers in GaInAsSb/AlGaAsSb QW is a process of vital importance for the optoelectronic devices based on those quaternary QW structures. Photoluminescence (PL) has so far been an important characterization tool for the recombination process as well as for assessing the QW quality. We previously reported the PL characteristics in GaInAsSb/AlGaAsSb QW system [7–9]. On the

* Corresponding author. Fax: + 86 21 62513510; e-mail: azli@fudan.ihep.ac.cn.

0022-0248/97/$17.00 Copyright © 1997 Published by Elsevier Science B.V. All rights reserved
PII S0022-0248(96)00976-1

other hand, the employment of strained QW in devices extends the choice of compatible materials and greatly increases the ability to control their optical and electronic properties. Recent investigations show that the strained multiple-QW (MQW) laser diodes may be far superior to those with conventional unstrained MQW structures in operational characteristics [10]. PL, though may detect the strain, cannot extract the strain straightforward, for the energy of PL peak depends on well width, barrier height as well as strain. Instead, double-crystal X-ray rocking curve (DCXRC) analysis has been proven to be a sensitive characterization method for investigating period thickness, alloy composition and strain in MQWs [11]. In this paper we report MBE growth, DCXRC, PL and absorption characterization of GaInAsSb/AlGaAsSb strained MQW structures and demonstration of GaInAsSb/AlGaAsSb MQW laser diodes.

2. Experimentals procedure

The GaInAsSb/AlGaAsSb MQW structures were grown in a home-made conventional solid-source MBE system. Uncracked As_4 and Sb_4 were used as the As and Sb sources. The substrate temperature was measured by a thermocouple. The compositions of epilayers were determined by electron microprobe analysis, while layer thicknesses were estimated from the growth rate. They were also confirmed further by DCXRC measurements.

DCXRC measurements were performed on a computer-controlled high-resolution X-ray double-crystal diffractometer. (1 0 0)-oriented GaAs crystal was used as the first crystal to diffract Cu $K_{\alpha 1}$ X-radiation from a normal focus Cu tube run at 35 kV, 20 mA in spot-focus mode.

PL and absorption measurements were performed on a Nicolet 800 Fourier transform infrared spectrometer over the temperature range of 4 K to room temperature (290 K). PL measurements have been carried out using an Ar-ion (514.5 nm) laser for excitation and a liquid-nitrogen-cooled InSb detector, while the absorption spectra were also detected by an InSb photodiode with a tungsten lamp focused onto the sample. The optical measurements were made with a resolution of 4 cm^{-1}.

3. Results and discussion

3.1. MBE growth and DCXRC characterization

The GaInAsSb/AlGaAsSb MQW structures were grown on (1 0 0) Te-doped GaSb substrates. Prior to the growth of the GaInAsSb/AlGaAsSb MQW, a 1.0 μm-thick n^+-GaSb buffer layer was firstly grown at a calibrated real temperature of 500°C. After 10 min interruption, GaInAsSb/AlGaAsSb MQW was grown at 500–520°C under As, Sb-rich condition with the growth rate ranging from 0.7 to 1.0 μm/h. The growth process was controlled by a computer and in-situ monitored by reflection high-energy electron diffraction (RHEED). Several MQW samples grown at different temperatures and with different growth rates were characterized by DCXRC measurements.

Fig. 1 shows the (4 0 0) rocking curve of a 20-period $Ga_{0.75}In_{0.25}As_{0.02}Sb_{0.98}$ (10 nm)/$Al_{0.16}Ga_{0.84}As_{0.02}Sb_{0.98}$ (30 nm) MQW, which was grown at 510°C with growth rate of 0.8 μm/h. The solid line is the measured rocking curve while the solid line with dots is the theoretical one simulated by Speriosu's model [11]. In the measured curve, in addition to the GaSb substrate peak, seven satellite peaks could be clearly seen, indicating high quality of the GaInAsSb/AlGaAsSb MQW structure. The satellite peak spacing yields an average quantum well period thickness

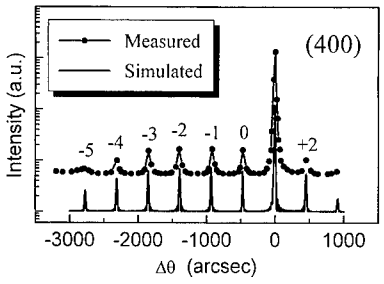

Fig. 1. Experimental and simulated (400) rocking curves for a 20-period $Ga_{0.75}In_{0.25}As_{0.02}Sb_{0.98}$ (10 nm)/$Al_{0.16}Ga_{0.84}As_{0.02}Sb_{0.98}$ (30 nm) MQW.

41.9 ± 0.2 nm, in good agreement with the nominal value 40.0 nm. Speriosu's simulation identifies each satellite peak and up to the fifth-order satellite peak of the MQW can be resolved in the measured rocking curve. GaInAsSb/AlGaAsSb MQWs grown at temperatures higher than 520°C or lower than 500°C or with growth rates higher than 0.9 μm/h show fewer and weaker satellite peaks in rocking curves. Notice the asymmetry of the envelope of those satellite peaks, which indicates the existence of considerable strain in the QW. To investigate the strain further, (1 1 5) DCXRC measurements have been carried out, for perpendicular strain $\varepsilon_\perp$ will be more sensitive in asymmetric diffractrometry than symmetric one. Fig. 2 shows the (1 1 5) rocking curve for the same GaInAsSb/AlGaAsSb MQW. Besides the asymmetry of the envelope of the satellite peaks, the figure even shows the disappearance of the zeroth-order peak in the rocking curve, which strongly indicates large strain in the MQW. With detailed simulation, the biaxial strain parallel to and uniaxial strain perpendicular to the plane of the interface is determined as $\varepsilon_\parallel = 3.31 \times 10^{-3}$ and $\varepsilon_\perp = 3.14 \times 10^{-3}$, respectively. These values are less than lattice mismatch $\Delta a/a$ (~ 1%), which could be attributed to the distribution of compressive and tensile strain in the well and barrier. And the coherence factor is also determined to be as high as 0.97, indicating that the mismatch in the QW is accommodated mainly by the strain.

3.2. *Photoluminescence and absorption measurements*

Fig. 3 shows the PL spectrum at 4 K for that GaInAsSb/AlGaAsSb MQW sample grown under optimized conditions. From the figure, a single PL peak is observed, corresponding to the recombination between the first electron subband and the first heavy-hole subband (E_1–HH_1). The full-width at half-maximum (FWHM) of 9.0 meV (4 K) and 13.0 meV (10 K), the best result yet reported in this quaternary system, indicates the good optical quality of the MQW. Fig. 4 shows the PL and absorption spectra at different temperatures for another sample, 20-period $Ga_{0.75}In_{0.25}As_{0.04}Sb_{0.96}$ (10 nm)/$Al_{0.22}Ga_{0.78}As_{0.02}Sb_{0.98}$ (30 nm) MQW.

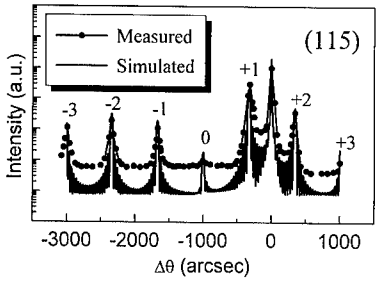

Fig. 2. Experimental and simulated (115) rocking curves for the 20-period $Ga_{0.75}In_{0.25}As_{0.02}Sb_{0.98}$ (10 nm)/$Al_{0.16}Ga_{0.84}As_{0.02}Sb_{0.98}$ (30 nm) MQW.

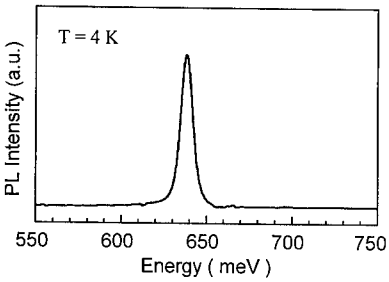

Fig. 3. Photoluminescence spectra of $Ga_{0.75}In_{0.25}As_{0.02}Sb_{0.98}$ (10 nm)/$Al_{0.16}Ga_{0.84}As_{0.02}Sb_{0.98}$ (30 nm) MQW. The excitation power density was 100 mW/cm^2.

In PL spectra a single PL peak, corresponding to E_1–HH_1 recombination, is observed throughout the temperature region of the measurements (4–290 K), with FWHM of 12.1 meV at 4 K and 22.1 meV at 290 K. While in the absorption spectra, additional excitonic absorption structures (E_1–LH_1 and E_2–HH_2) appear at lower temperatures due to the increase of the overlap integral of electron and hole wave functions. The sharp rise in the highest energy portion of the absorption spectra is due to absorption in GaSb substrate. Furthermore, small Stokes shift between the PL and absorption peaks is found at any temperature. This fact, along with strong luminescence and well-resolved excitonic absorption peaks observable at room temperature, undoubtedly demonstrates the high quality of the MQW structures. The detailed analysis of the optical characteristics of the GaInAsSb/AlGaAsSb MQWs can be found elsewhere [7, 8]. By using the high-quality

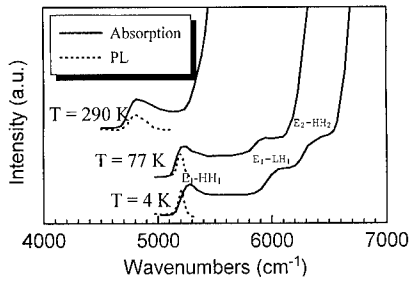

Fig. 4. Infrared absorption and photoluminescence spectra of $Ga_{0.75}In_{0.25}As_{0.04}Sb_{0.96}$ (10 nm)/$Al_{0.22}Ga_{0.78}As_{0.02}Sb_{0.98}$ (30 nm) MQW at different temperatures. The excitation power density was 100 mW/cm^2 for the PL measurements.

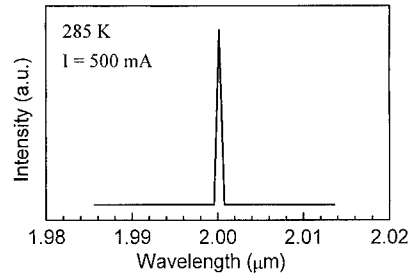

Fig. 5. Emission spectrum for a GaInAsSb/AlGaAsSb MQW laser diode operating pulsed at 285 K.

GaInAsSb/AlGaAsSb MQWs as active layers, GaInAsSb/AlGaAsSb MQW laser diodes have been fabricated through broad area stripe laser processing. Fig. 5 shows the emission spectrum for a GaInAsSb/AlGaAsSb MQW laser diode. Room-temperature pulsed operation with stable threshold current density lower than 900 A/cm^2 has been achieved. The peak wavelength of lasing is 2.05 μm and the FWHM of the peak is 0.6 nm.

4. Conclusion

High-quality GaInAsSb/AlGaAsSb strained MQWs have been successfully grown by MBE. Both structural and optical qualities of those MQWs have been characterized by DCXRC, PL and absorption measurements. Up to the fifth-order, satellite peak of MQW is observed in a rocking curve, and large strain exists in the QW structure. The FWHM of a PL peak as narrow as 9.0 meV is achieved at 4 K, and room-temperature PL and well-resolved excitonic absorption peaks are observed in the MQW structures. By using the high-quality GaInAsSb/AlGaAsSb MQWs as active layers, room-temperature pulsed operation laser diodes with emission at 2.05 μm and threshold current density lower than 900 A/cm^2 have been fabricated.

Acknowledgements

This work was supported by the National Advanced Technology Committee and the State Science and Technology Committee under Project A of National Climb Plan of China. The authors would like to thank Mr. G. Tong for his assistant in DCXRC measurements and simulations. Thanks is also given to Mr. C.C. Li and J. Hu for their technical assistance.

References

[1] T.H. Chiu, W.T. Tsang, J.A. Ditzenberger and J.P. van der Ziel, Appl. Phys. Lett. 49 (1986) 1051.
[2] S.J. Eglash, H.K. Choi and G.W. Turner, J. Crystal Growth 111 (1991) 669.
[3] H.K. Choi and S.J. Eglash, J. Quantum Electron. QE-27 (1991) 1555.
[4] H.K. Choi and S.J. Eglash, Appl. Phys. Lett. 61 (1992) 1154.
[5] G.W. Turner, H.K. Choi, D.R. Calawa, J.V. Pantano and J.W. Chludzinski, J. Vac. Sci. Technol. B 12 (1994) 1266.
[6] H. Lee, P.K. York, R.J. Menna, R.U. Martinelli, D.Z. Garbuzov, S.Y. Narayan and J.C. Connolly, Appl. Phys. Lett. 66 (1995) 1942.
[7] W.Z. Shen, S.C. Shen, W.G. Tang, Y. Zhao and A.Z. Li, J. Appl. Phys. 78 (1995) 5696.
[8] W.Z. Shen, S.C. Shen, W.G. Tang, Y. Zhao and A.Z. Li, Appl. Phys. Lett. 67 (1995) 3432.
[9] W.Z. Shen, Y. Chang, S.C. Shen, W.G. Tang, Y. Zhao and A.Z. Li, J. Appl. Phys. 79 (1995) 2139.
[10] M. Watanabe, J. Rennie, M. Okajima and G. Hatakoshi, Appl. Phys. Lett. 63 (1993) 1486.
[11] V.S. Speriosu and T. Vreeland, Jr., J. Appl. Phys. 56 (1984) 1591.

ELSEVIER

Journal of Crystal Growth 175/176 (1997) 877–882

JOURNAL OF CRYSTAL GROWTH

MBE growth of GaInAsSb p/n junction diodes for thermophotovoltaic applications

Parvez N. Uppal[a,*,1], Greg Charache[b], Paul Baldasaro[b], Brian Campbell[b], Stephen Loughin[c], Stefan Svensson[d,1], David Gill[e,1]

[a] *Sanders, A Lockheed Martin Company, NHQ6-1551, 65 Spit Brook Road, Nashua, New Hampshire 03061, USA*
[b] *Lockheed Martin, P.O. Box 1072, Schenectady, New York 12301, USA*
[c] *Lockheed Martin Astro Space, P.O. Box 8555, Philadelphia, Pennsylvania 19101, USA*
[d] *ARL, AMSRL-PS-PB, 2800 Powder Mill Rd., Adelphi, Maryland 20783, USA*
[e] *National Semiconductor, 10810 Guilford Rd., Suite 111, Annapolis Junction, Maryland 20701, USA*

Abstract

This paper reports recent progress in the development of quaternary III–V thermophotovoltaic (TPV) devices based on MBE grown $Ga_xIn_{1-x}As_ySb_{1-y}$. TPV is of great interest for a variety of applications (1st and 2nd NREL Conf. on Thermophotovoltaic Generation of Electricity, AIP Conf. Proc. 321 (1994), 358 (1995)). The objective of this work is to develop a TPV cell which is "tunable" to the emission spectrum of a heated blackbody, at temperatures in the range of 1200–1473 K. One aspect of this "tuning" is to match the band gap, E_{gap}, of the photovoltaic device to the peak output of the heat source. An advantage of the quaternary III–V semiconductor systems is that devices can be fabricated by molecular beam epitaxy on a suitable binary substrate, such as GaSb or InAs, and the band gap and lattice constant can be adjusted more or less independently, to match requirements. Quaternary cells, with band-gaps in the 0.5–0.72 eV range, have been fabricated and tested. For 0.54 eV devices we obtained open circuit voltage $V_{OC} = 0.3$ V and short circuit current $I_{SC} = 1.5$ A/cm^2 under infrared illumination of a 1200 K blackbody. Under high illumination levels the V_{OC} and I_{SC} ranged from 0.5 V at 3 A/cm^2 for 0.72 eV devices to 0.31 V at 1.2 A/cm^2 for 0.5 eV devices, indicating good photovoltaic device characteristics over the range of bandgaps. The diode ideality factor for 0.54 eV devices ranged from 2.45 at low illumination indicating tunneling-dominated dark current, to 1.7 at high illumination intensity indicating recombination-generation dominated dark currents.

1. Introduction

Thermophotovoltaic (TPV) devices have a wide variety of applications [1, 2]. The elements of a TPV system include an emitter which is a heat source coupled to a blackbody radiator, a spectral control element (band-pass filter) and a photovoltaic converter which is matched to the blackbody and spectral control element. A schematic for a TPV system is shown in Fig. 1.

Fig. 2 compares the power emitted by a blackbody at various temperatures and compares the

* Corresponding author. Fax: + 1 603 885 1074.

[1] Work done at Lockheed Martin Laboratories, Baltimore, Maryland 21227, USA.

0022-0248/97/$17.00 Copyright © 1997 Published by Elsevier Science B.V. All rights reserved
PII S0022-0248(96)00977-3

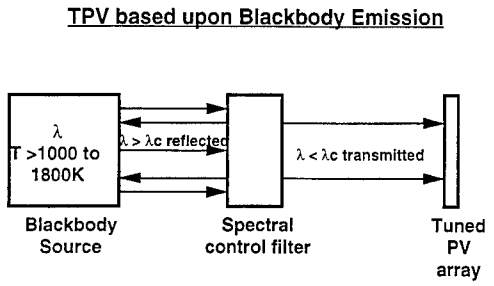

Fig. 1. Schematic diagram of a TPV system based upon blackbody emission.

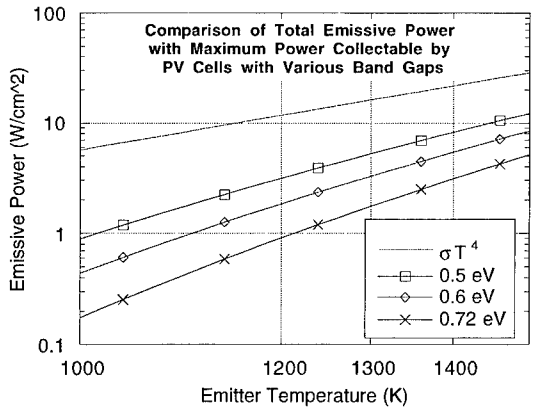

Fig. 2. Comparison of total emissive power with maximum power collectable by PV cells with various bandgaps.

power at wavelengths shorter than the cut-off wavelengths for GaSb, and two lower bandgaps. The three lower curves represent the maximum power available for conversion by cells with those bandgaps without taking into consideration any factors limiting their conversion efficiency. It must be pointed out that a high efficiency PV diode is only one aspect of demonstrating an efficient TPV system, an effective spectral control device is critical to obtain high overall system efficiency. As an example, for a 1200 K blackbody, almost 70% of the blackbody power density lies below the bandgap of a 0.5 eV bandgap PV cell. This requires an efficient band-pass filter which reflects most of the radiation below the semiconductor bandgap out to 10 μm back to the blackbody to recycle the photons and allows maximum transmittance above the semiconductor bandgap for the PV cell to convert.

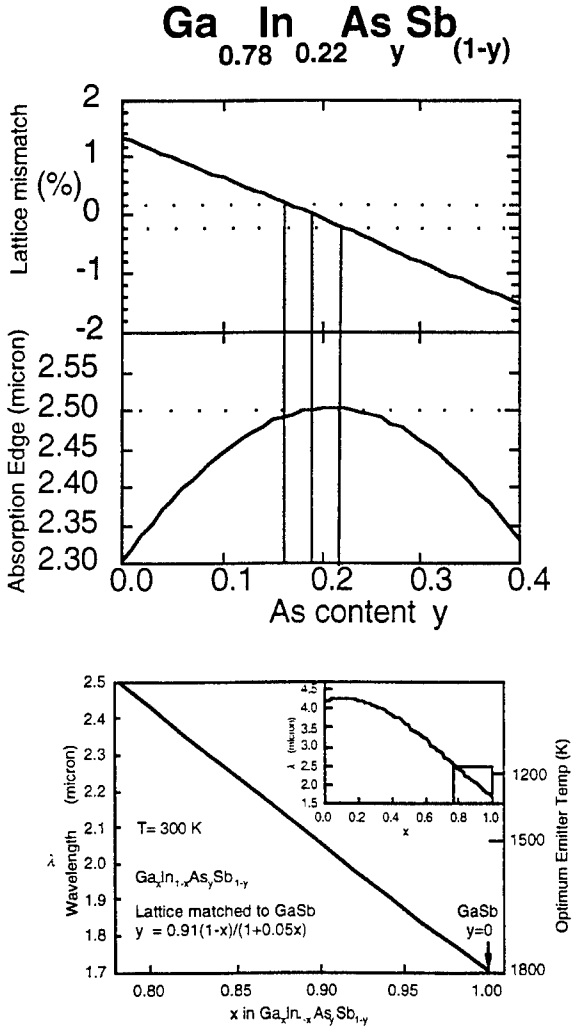

Fig. 3. Shows the GaInAsSb bandgap and lattice constant change as a function of In and As. It can be seen from the figure that the Group III ratios have a much stronger effect on the bandgap than changing the Group V ratios.

Among the unique advantages of the quaternary GaInAsSb system are that the bandgap and the lattice constant can be adjusted to match the requirements. Fig. 3 shows the alloy composition and the bandgap range of interest lattice matched to GaSb.

In this paper we present recent progress on obtaining large area (1 cm × 1 cm) variable bandgap GaInAsSb PV cell lattice matched to GaSb substrates with bandgaps between 0.72 eV and 0.5 eV.

2. Material growth

The material used for the fabrication of the GaInAsSb TPV devices was grown using a Varian Gen II MBE system. 2 in n-type ($1–2 \times 10^{17} cm^{-3}$) exact (0 0 1) oriented GaSb substrates were used. The oxide on these wafers was desorbed in situ in the MBE system. The wafers were heated to about 400°C, then the Sb_4 shutter was opened, the oxide was observed to come off at temperatures in the 525–535°C range as monitored by the pyrometer. An n+ ($\sim 5 \times 10^{18}$ cm^{-3}) 100 nm GaSb buffer layer was grown to smooth the surface and improve the RHEED pattern. During the GaSb growth the substrate temperature was dropped to 500°C and growth of GaInAsSb was initiated. This formed the base region of the TPV device and had a thickness of 5 μm and an n-type doping density of 2×10^{17} cm^{-3}. Next the p-type emitter and p-type GaSb (300 Å) window layer were grown with a doping density of $1–2 \times 10^{18}$ cm^{-3}. Fig. 4 shows a typical device structure.

In order to obtain the correct bandgap, Ga and In ratios were adjusted. To obtain the lattice constant match with the substrate, As and Sb ratios were adjusted. The GaInAsSb devices were lattice matched to within 0.05% with the substrate. When the mismatch exceeded 0.1% the wafer was observed to bend. The wafers bent in a convex shape with a plus (larger than the substrate-excess Sb) mismatch. The wafers were observed to bend in a concave shape with a negative (smaller than the substrate-excess As) mismatch. This bending of wafers was much worse in the case of InAs substrates, because InAs is a softer material than GaSb. To relieve the lattice mismatch strain quaternary GaInAsSb appears to deform the substrate instead of relieving strain by the formation of dislocations. This is presumably due to the alloy hardening effect of the second group V in the films. Due to this alloy hardening effect, the layer finds it energetically difficult to produce and propagate dislocations and hence bends to relieve the strain. This bending of the wafers took place at the growth temperature and could be observed through the view port, this rules out the bending due to any coefficient of thermal expansion mismatch. To further investigate the possibility of lattice mismatch related bending peculiar to the GaInSb material system we grew the ternary GaInSb (with the same Ga and In ratio as in the quaternary) on GaSb, we did not observe any bending despite a much larger mismatch (> 0.5%). This indicates that in the mixed arsenide–antimonide quaternaries strain relaxation proceeds differently as compared to the ternaries, and can have important device implications. Further investigations using TEM are needed on the GaInAsSb quaternary system.

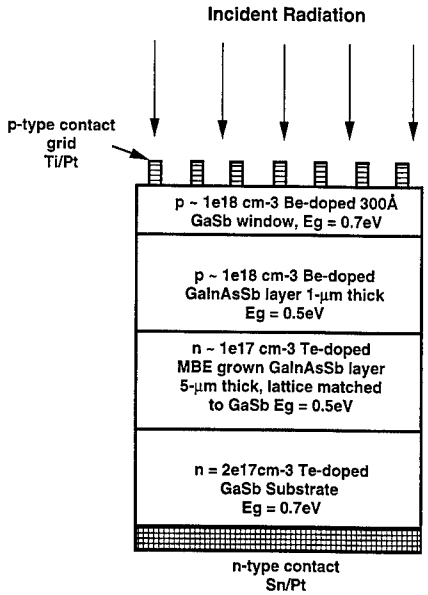

Fig. 4. Cross-section of a TPV device.

3. Device fabrication and characterization

1 cm × 1 cm mesa diodes were fabricated using chemical etching, the mesa diodes had a single 1mm wide central busbar for making electrical contact to the devices. The busbar was connected to grid lines 0.45 cm long 100 μm apart and 10 μm wide. Front metallization was done by evaporating Ti and Pt in an e-beam evaporator and then depositing a 5 μm thick Au or Al to obtain a low resistance contact for high current densities. For bottom Ohmic contact a thick Sn/Pt or Sn/Au was used. A 0.2 μm Silicon Nitride layer on top was used as an antireflection coating.

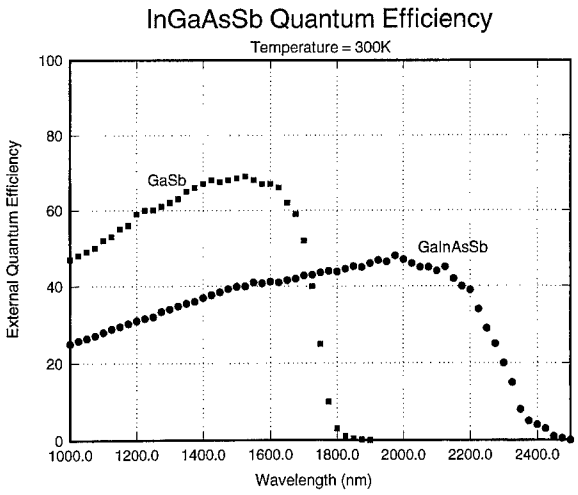

Fig. 5. External quantum efficiency as a function of wavelength for a typical GaSb and a GaInAsSb device.

The diodes were tested under dark and under blackbody illuminated conditions. Fig. 5 shows an external quantum efficiency versus wavelength for a typical device. The figure shows a comparison for a typical GaSb and GaInAsSb device. The fall off at short wavelengths indicates high surface recombination, pointing to the need for an effective front surface passivation or a high bandgap window layer. A softer roll off in quantum efficiency at wavelengths near the band edge indicates the absence of an effective back surface field. Adding these two layers to the devices will considerably improve their performance.

Fig. 6 shows comparison of a typical I–V characteristics from a GaInAsSb and GaSb PV diodes under similar low light level illumination conditions. As is to be expected the short circuit current is higher for the lower bandgap device. The I–V characteristics point to the need for better ohmic contacts and this is an area which is under current investigation. Some of series resistance in the GaInAsSb devices could be due to a heterostructure barrier between GaInAsSb and GaSb [3]. The conduction and valence band discontinuities between GaSb and GaInAsSb are 0.24 and -0.1 eV, respectively. This is particularly troublesome and needs to be reduced by degenerately doping the junction or by bandgap grading.

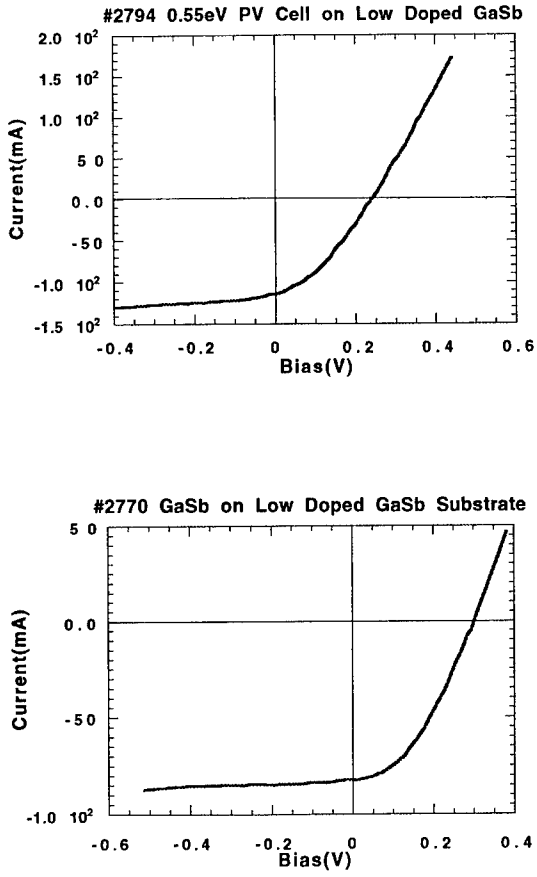

Fig. 6. I–V characteristics for a GaSb and a 0.55 eV GaInAsSb device.

Fig. 7 shows the PV short circuit current density versus the blackbody temperature. It can be observed that for low temperature (1200 K) TPV applications the narrow gap (0.54 eV) cells are the answer because they offer more than three times the current density as compared to the GaSb (0.73 eV) cells.

Fig. 8 plots the measured short circuit current density vs the open circuit voltage. Assuming the ideal diode relation

$$I_{SC} = I_0[\exp\{qV_{OC}/nkT\} - 1],$$

where I_{SC} is the short circuit current, I_0 is the dark current, V_{OC} is the open circuit voltage, n is the diode ideality factor, k is the Boltzmann constant and T is the temperature.

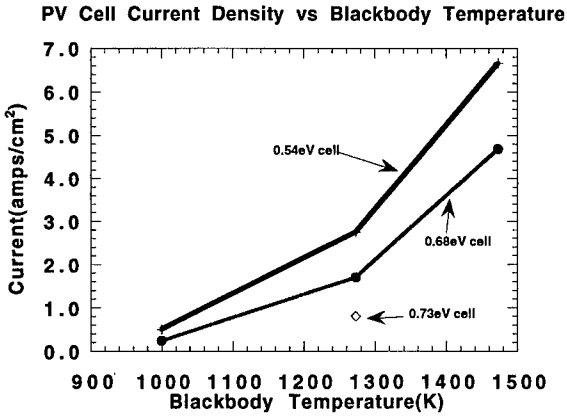

Fig. 7. Shows the PV cell current density as a function of blackbody temperature.

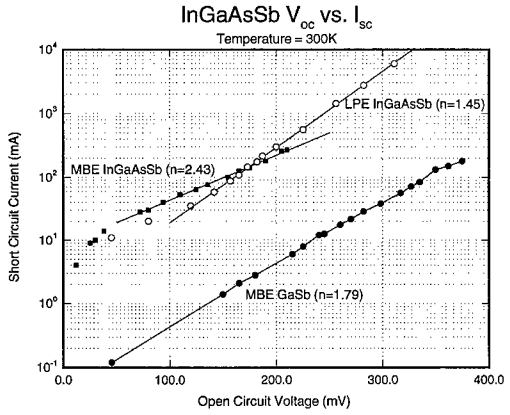

Fig. 8. Comparison of GaSb and GaInAsSb cell open circuit voltage versus short circuit current.

There are four potential dark current mechanisms: diffusion ($n = 1$), bulk recombination/regeneration ($n = 2$), surface recombination ($n = 2$) and band to band tunneling ($n > 2$). In Fig. 8 we plotted the I_{SC} versus V_{OC} and fitted the ideal diode equation assuming a single dominant dark current mechanism. We found it useful to compare the data for our MBE grown GaInAsSb and GaSb diodes and JX Crystal LPE grown cells. At low current injection conditions MBE grown devices show a diode ideality factor of 2.43, indicating band to band tunneling, LPE devices on the other showed a combination of diffusion and generation/recombination dark current. This difference could be due

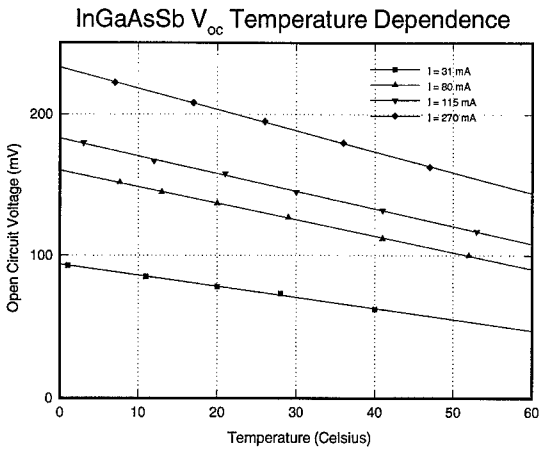

Fig. 9. Open circuit voltage dependence of GaInAsSb cells on temperature.

to a lower base doping for the LPE grown cells. Lower base doping leads to a lower V_{OC}. MBE cells show a higher V_{OC} at a lower I_{SC} (this is very desirable) as compared to LPE cells. This data leads us to conclude that at the high current levels required for TPV device operation, higher base doping is advantageous even though higher ideality factors are observed. Thus GaInAsSb diodes are more efficient energy convertors at high illumination levels. Some of the dark current could also be due to a lack of surface passivation. Use of an effective passivant or a high bandgap window layer will also reduce the dark current.

Fig. 9 plots V_{OC} versus T for MBE grown GaInAsSb cells. This is done for various I_{SC} values. This data also helps determine the differences in the dominant dark current mechanisms. From low to high illumination levels the V_{OC} decreases linearly with temperature. The difference in the slope dV_{OC}/dT between very low injection levels and higher injection levels indicate that at lower current levels the current is a combination of tunneling and some other mechanism, for higher injection levels once the tunneling barrier has been overcome the dark current mechanism is almost entirely due to tunneling [4], this is indicated by a relatively small change in the dV_{OC}/dT slope. It will be interesting to measure dV_{OC}/dT for even higher injection levels to see if other dark current mechanisms become dominant.

4. Conclusions

We have presented data on the current status of lattice matched GaInAsSb TPV devices and pointed out the areas in which improvements or device design changes are needed. Quaternary lattice matched TPV devices are very promising for thermal power conversion and offer superior performance due to potentially higher long term reliability and higher open circuit voltages and currents than lattice mismatched InGaAs/InP devices.

References

[1] 1st NREL Conf. on the Thermophotovoltaic Generation of Electricity, Copper Mountain, CO, AIP Conf. Proc. 321 (1994).
[2] 2nd NREL Conf. on the Thermophotovoltaic Generation of Electricity, Copper Mountain, CO, AIP Conf. Proc. 358 (1995).
[3] M.P. Mikhailova and A.N. Titkov, Semicond. Sci. Technol. 9 (1994) 1279.
[4] G.W. Charache, J.L. Egley, L.R. Danielson, D.M. Depoy, P.F. Baldasaro, B.C. Campbell, S. Hui, L.M. Fraas and S.J. Wojtczuk, 25th Photovoltaic Specialists Conf., Crystal City, VA, 13–17 May, 1996.

ELSEVIER

Journal of Crystal Growth 175/176 (1997) 883–887

JOURNAL OF CRYSTAL GROWTH

Molecular-beam-epitaxial growth of $Ga_{1-x}In_xSb$ on GaAs substrates

J.H. Roslund*, O. Zsebők, G. Swenson , T.G. Andersson

Department of Physics, Chalmers University of Technology and Göteborg University, S-412 96 Gothenburg, Sweden

Abstract

Molecular beam epitaxy has been used to grow $Ga_{1-x}In_xSb$ in the entire compositional range. Good Hall mobility values were obtained, but the surfaces were rough and exhibited square defects. The X-ray diffraction Bragg peaks in the middle of the compositional range were broadened due to the disorder inherent in the alloy. A small inclination of the epitaxial layers with respect to the substrate was also found in this region.

1. Introduction

Presently there is much interest in antimony-containing III–V semiconductors. For example, $Ga_{1-x}In_xSb$ has been used in the active region of mid-infrared diode lasers [1, 2], in far-infrared strained-superlattice detectors [3] and resonant tunnelling devices [4].

This paper reports molecular-beam-epitaxial growth and characterization of $Ga_{1-x}In_xSb$ alloy layers. Although it is clearly related to $In_xGa_{1-x}As$, this alloy has not been as extensively studied. Low growth temperatures are of particular interest since $InAs/Ga_{1-x}In_xSb$ superlattices are grown with the highest structural quality at 390–410°C [5].

The first epitaxial growths of $Ga_{1-x}In_xSb$ were made by liquid phase epitaxy [6, 7]. Since then the alloy has been grown by molecular beam epitaxy (MBE) [8, 9], metalorganic vapour-phase epitaxy (MOVPE) [10, 11] and metalorganic molecular beam epitaxy (MOMBE) [12, 13]. Much emphasis has been put on the optical properties, but also on structural characterization, mainly for lower In concentrations.

2. Experimental procedure

2.1. Growth

A series consisting of more than thirty 4-μm-thick $Ga_{1-x}In_xSb$ layers, spanning the entire compositional range, was grown on (0 0 1)-oriented semi-insulating GaAs substrates. Both unintentionally doped and Si-doped samples were grown in a modified Varian 360 system with arsenic and antimony cracking cells and standard effusion cells for gallium and indium. The cracking temperatures of the V-sources were kept at 1200°C. In situ

* Corresponding author.

0022-0248/97/$17.00 Copyright © 1997 Elsevier Science B.V. All rights reserved
PII S0022-0248(96)00978-5

cleaning began by pre-heating the substrates in ultra-high vacuum. This was followed by thermal desorption of the native oxide in the growth chamber. The normal procedure during this step is to stabilize the surface under an arsenic flux. Recent studies have shown, however, that arsenic is easily incorporated in antimonides in non-negligible amounts [14, 15]. Therefore the possibility to desorb the oxygen under an antimony flux was tested. As compared to desorption under arsenic, the process seemed more sudden and it was also noted that it seemed to occur at 20–30°C lower temperature. This could be due to a bombardment effect caused by the greater mass of antimony. However, with no further independent means to measure the temperature, it was difficult to establish this point with certainty, and hence all growth temperatures reported in this paper assume that the desorption occurred at the regular temperature of 583°C.

Since most of the growth temperatures were below 500°C, where the optical pyrometer loses its accuracy, substrate temperatures were estimated assuming a linear relationship between the actual temperature and the reading of a thermocouple mounted in non-contact position on the back side of the substrate holder.

Growth rates were calculated from reflection high-energy electron diffraction (RHEED) oscillations prior to growth. The In molar fraction, x, of the alloy was determined in advance by calculating

$$x = \left[1 + \left(\frac{a_{\mathrm{InAs}}}{a_{\mathrm{GaSb}}}\right)^3 \frac{v_{\mathrm{GaSb}}}{v_{\mathrm{InAs}}}\right]^{-1}, \quad (1)$$

where a_{InAs} is the lattice constant of InAs and v_{InAs} is the growth rate it has at the chosen In source temperature, and analogously for a_{GaSb} and v_{GaSb}. In most cases, this gave excellent agreement with the values determined from X-ray diffraction. The surface properties were continuously monitored by RHEED. The $Ga_{1-x}In_xSb$ grew under a (1×3) reconstruction for $x < 0.4$ and a (2×3) for $x > 0.4$.

2.2. Analysis

X-ray rocking curves were measured in a high-resolution X-ray diffractometer equipped with a Cu $K\alpha_1$ X-ray source and a four Ge-crystal monochromator set in the (2 2 0) position. Rocking curves were obtained by scanning through the (0 0 4) reflection of the sample. Information on the lattice constants parallel and perpendicular to the surface were obtained by measuring the angles of incidence giving the Bragg peak for the (1 1 5) and $(\bar{1}\,\bar{1}\,5)$ reflections. From this, the equlibrium lattice constant and the residual strain can be found [16].

Surface analysis was performed by optical microscopy, surface profiling in a Tencor Alpha-Step 500 and scanning electron microscopy (SEM).

Electrical properties were assessed by measuring the resistivity, ρ, and the Hall constant, R_{H}, in the square van der Pauw arrangement on $3 \times 3\ \mathrm{mm}^2$ samples in a magnetic field of 0.4 T. The Hall carrier concentration was obtained from $n_{\mathrm{H}} = 1/eR_{\mathrm{H}}$ and the Hall mobility from $\mu_{\mathrm{H}} = R_{\mathrm{H}}/\rho$ [17].

Optical measurements were made by Fourier transform photoluminescence (FTPL). The excitation source was a 514.5 nm Ar-ion laser. The sample was kept in a He cryostat and the luminescence was analysed with a Fourier transform spectrometer equipped with an InSb detector.

3. Results

All of the X-ray rocking curves exhibited the substrate's Bragg peak and a wider peak originating from the 4-μm-thick overlayer. In some cases the position of the latter depended on the incident azimuth of the X-ray, indicating that the epitaxial layer is inclined with respect to the substrate. This inclination was hardly noticeable for alloy compositions close to the binaries but increased to about 300 arcsec for $Ga_{0.6}In_{0.4}Sb$. The width of the Bragg peak associated with the $Ga_{1-x}In_xSb$ layer increases in the middle of the compositional range. There was also a strong anisotropy revealing itself in different full widths at half maximum (FWHMs) for X-rays incident in different azimuths. Fig. 1 shows the FWHM of the epilayer peak with X-rays incident along the $[1\,\bar{1}\,0]$ azimuth for samples grown at 430°C. The peaks are broader than for $In_xGa_{1-x}As$ samples grown at near-group-III stabilized conditions. The residual strain in the $Ga_{1-x}In_xSb$ layers was of the order 0.1%, which is comparable to $In_xGa_{1-x}As$ of similar thickness [18].

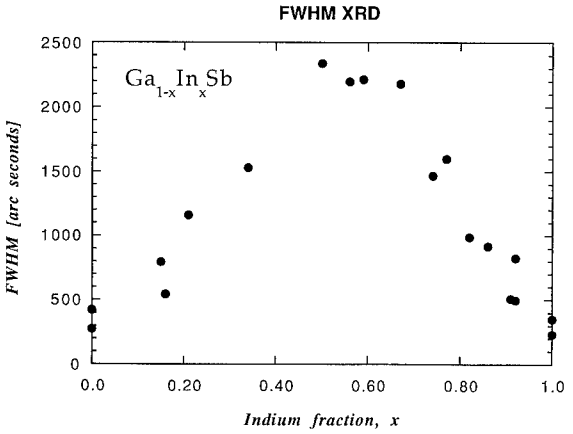

Fig. 1. Full width at half maximum of the (0 0 4) Bragg peak from the $Ga_{1-x}In_xSb$ layer in X-ray diffraction as a function of the In content in the alloy. The middle of the range shows significant broadening attributable to the disorder in the alloy.

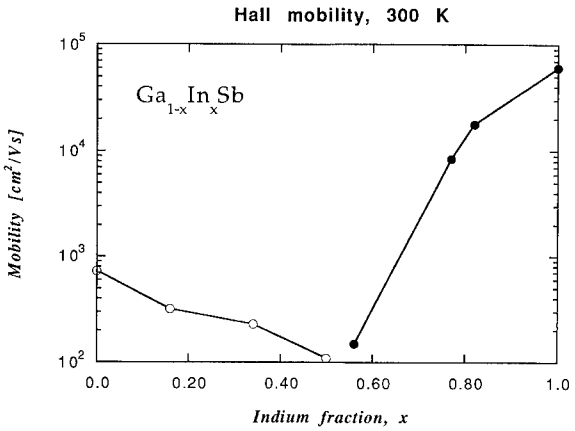

Fig. 2. Hall mobility at room temperature for unintentionally doped $Ga_{1-x}In_xSb$ layers. p-type samples are denoted by open symbols and n-type by solid. The mobility is suppressed in the middle of the range due to the disorder.

Fig. 2 shows the Hall mobility measured on the unintentionally doped samples. $Ga_{1-x}In_xSb$ is p-type for $x < 0.55$ and n-type for higher values. A temperature-dependent measurement revealed that the low electron mobility of the sample at $x = 0.56$ is in fact a hole mobility. Just below room temperature the sample has a cross-over from p-type to n-type and the sample appears n-type in the Hall effect measurement due to the large ratio of electron-to-hole effective masses, although the conductivity is still dominated by the holes.

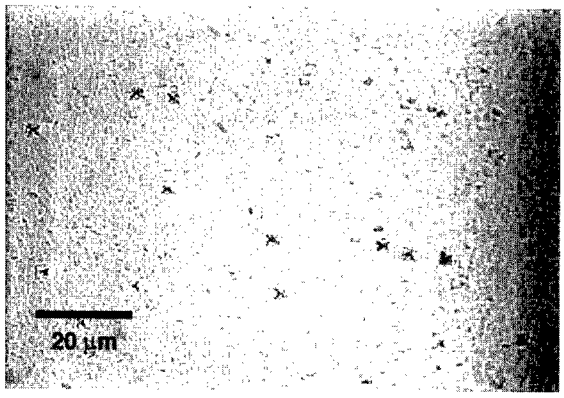

Fig. 3. Typical optical micrograph of the surface morphology for $Ga_{0.6}In_{0.4}Sb$: Si grown at 430°C.

Fig. 3 shows a typical optical micrograph of the surface morphology of $Ga_{0.6}In_{0.4}Sb$. The surface analysis showed that the surfaces particularly in the middle of the compositional range were very rough and covered with square defects. The sides of the squares were aligned along the $< 1\,1\,0 >$ directions. Many samples also exhibited pyramid-like defects protruding 100–200 nm from the surface. Fig. 4 shows two kinds of pyramid-shaped defects. The sample in Fig. 4a had been excessively heated during the oxide desorption and was the only sample which showed this type of fully grown pyramid. Most other samples exhibited the collapsed pyramid structure in Fig. 4b. It is also noteworthy that the sample in Fig. 4a had a much more narrow Bragg peak than other samples in its compositional range.

There was a strong correlation between alloy composition and surface morphology. Close to the binaries the surfaces were very smooth with tall, sharp pyramids of high surface density. In the middle of the compositional range the surfaces were rougher, and the pyramids were always located on top of a square plateau. The pyramids were also flatter here with larger lateral size and of lower density.

Only samples that had been grown at temperatures below 440°C for low In concentrations,

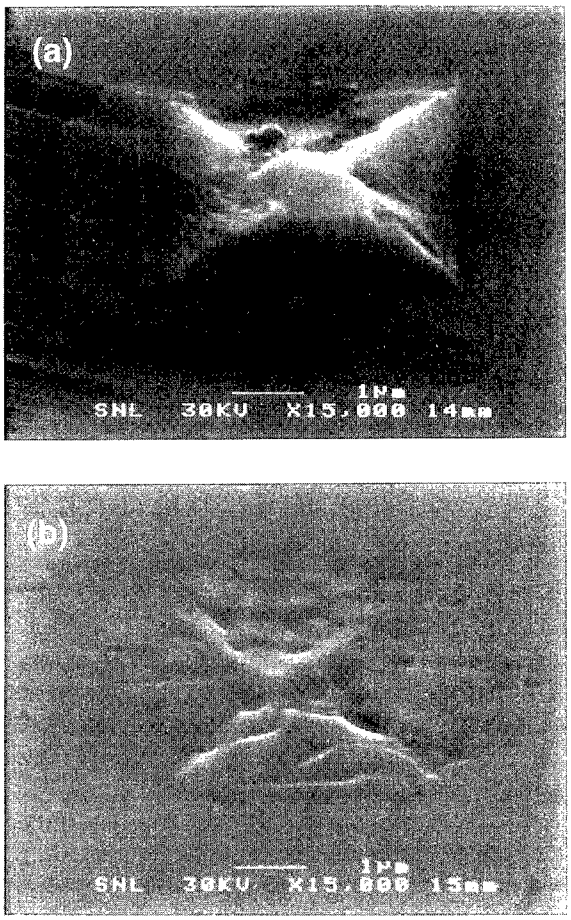

Fig. 4. Different types of pyramid-shaped surface defects seen in secondary-electron imaging SEM: (a) fully grown pyramid (b) collapsed pyramid.

where the surface reconstruction changes from (1×3) to (1×5) as the group-III flux is removed, showed any detectable photoluminescence.

Other III–V antimonides are known to have surface morphologies and FWHMs that are highly sensitive to V/III-ratio and substrate temperature [19, 20]. Fig. 5 shows the measured FWHM for a series of $Ga_{0.6}In_{0.4}Sb$ grown at different temperatures. For low temperatures FWHM is larger for X-rays incident along the [1 $\bar{1}$ 0] azimuth. At approximately 500°C there is a point where the FWHM is isotropic. For higher growth temperatures the [1 1 0] azimuth gives the lowest FWHM. Growth temperatures higher than 530°C resulted in

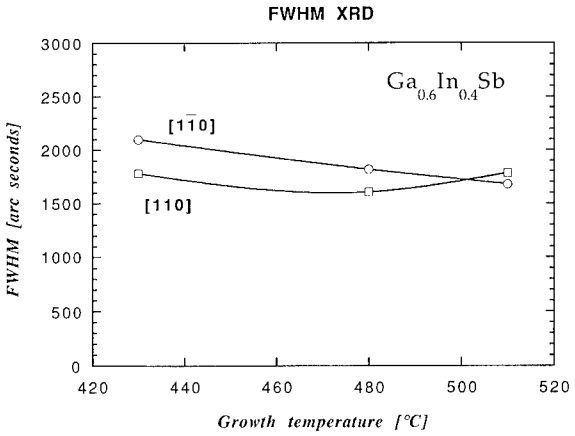

Fig. 5. XRD FWHMs for a series of $Ga_{0.6}In_{0.4}Sb$: Si samples grown at different temperatures. The lines are drawn as guides for the eye.

a dim RHEED pattern during growth and extremely wide Bragg peaks. Back-scattered electron imaging in SEM indicated that these samples are of non-uniform composition. The best FWHMs occurred for growth temperatures in the range 480–500°C, but these peaks are still much broader than normally observed for comparable $In_{0.4}Ga_{0.6}As$.

4. Discussion

The disorder in a III–V solid solution can be divided into two different categories. The first kind of disorder is due to the fact that some Ga atoms have been replaced with In atoms, with different scattering powers for X-rays. The second kind of disorder comes from the difference in bond length between Ga–Sb bonds and In–Sb bonds. Using extended X-ray absorption fine structure (EXAFS) results, Mikkelsen and Boyce discovered that the Ga–As and In–As bond lengths in $In_xGa_{1-x}As$ depend on the alloy composition, but in a fashion that allows the average bond length to obey Vegard's law [21]. These two effects will maximize the disorder and broaden the X-ray FWHM in the middle of the compositional range as seen in Fig. 1.

The XRD anisotropy has also been observed in $In_xGa_{1-x}As$ [22]. It is believed that it is caused by

different probabilities to create dislocations in different directions.

The defects on the surface seem to be related to the start of the growth. We also compared samples where the native oxide had been desorbed under As flux. The density of the pyramid-like defect was lower but not zero. However no improvement in surface roughness could be seen.

Defects aligned along the crystallographic directions have been reported for $Ga_{1-x}In_xSb$ in other studies. Kodama and Parker et al. have noted similar defects which were explained as stacking-fault polyhedra [23, 24].

5. Conclusions

We can conclude that $Ga_{1-x}In_xSb$ grows with a rough surface and has broad XRD Bragg peaks in the investigated temperature region, 400–500°C. The structural quality was seen to improve slightly for $Ga_{0.6}In_{0.4}Sb$ by increasing the growth temperature from 430°C to 480°C. This not unexpected since GaSb is grown with the best quality above 500°C [25].

Acknowledgements

The authors are grateful to Mr. Joakim Dalfors at the University of Linköping for the photoluminescence measurements. Surface analysis was carried out in the Swedish Nanometre Laboratory. This work has been supported by NUTEK (Swedish National Board for Industrial and Technical Development) and NFR (Swedish Natural Science Research Council).

References

[1] D.H. Chow, R.H. Miles, T.C. Hasenberg, A.R. Kost, Y.-H. Zhang, H.L. Dunlap and L. West, Appl. Phys. Lett. 67 (1995) 3700.
[2] R.H. Miles, D.H. Chow, Y.-H. Zhang, P.D. Brewer and R.G. Wilson, Appl. Phys. Lett. 66 (1995) 1921.
[3] I.H. Campbell, I. Sela, B.K. Laurich, D.L. Smith, C.R. Bolognesi, L.A. Samoska, A.C. Gossard and H. Kroemer, Appl. Phys. Lett. 59 (1991) 846.
[4] J. Jimenez, X. Li and W.I. Wang, Appl. Phys. Lett. 64 (1994) 2127.
[5] J.L. Davis, R.J. Wagner, J.R. Waterman, B.V. Shanabrook and J.P. Omaggio, J. Vac. Sci. Technol. B 11 (1993) 861.
[6] A. Joullie, R. Dedies, J. Chevrier and G. Bougnot, Rev. Phys. Appl. 9 (1974) 455.
[7] H. Miki, K. Segawa, M. Otsubo, K. Shirahata and K. Fujibayashi, Jpn. J. Appl. Phys. 17 (1978) 2079.
[8] H. Gotoh, T. Yamamoto and M. Kimata, Jpn. J. Appl. Phys. 21 (1982) L767.
[9] M. Kodama and M. Kimata, J. Crystal Growth 73 (1985) 641.
[10] Y.K. Su, F.S. Juang and T.S. Wu, Jpn. J. Appl. Phys. 30 (1991) 1609.
[11] G. Bougnot, F. Delannoy, F. Pascal, A. Giani, J. Kaokab, J. Bougnot, R. Fourcade, P.J. Walker, N.J. Mason and B. Lambert, J. Crystal Growth 107 (1991) 502.
[12] T. Kaneko, H. Asahi, Y. Okuno and S. Gonda, J. Crystal Growth 95 (1989) 158.
[13] Y. Itani, H. Asahi, T. Kaneko and S. Gonda, J. Appl. Phys. 73 (1993) 1161.
[14] D.H. Chow, R.H. Miles, J.R. Söderström and T.C. McGill, J. Vac. Sci. Technol. B 8 (1990) 710.
[15] J.T. Zborowski, W.C. Fan, T.D. Golding, A. Vigliante, P.C. Chow, H.D. Shih and J.M. Anthony, J. Appl. Phys. 71 (1992) 5908.
[16] M.A.G. Halliwell, M.H. Lyons, S.T. Davey, M. Hockley, C.G. Tuppen and C.J. Gibbings, Semicond. Sci. Technol. 4 (1989) 10.
[17] D.C. Look, Electrical Characterization of GaAs Materials and Devices , (Wiley, Chichester, 1989).
[18] A.V. Drigo, A. Aydinli, A. Carrera, F. Genova, C. Rigo, C. Ferrari, P. Franzosi and G. Salviati, J. Appl. Phys. 66 (1989) 1975.
[19] J.E. Oh, P.K. Bhattacharya, Y.C. Chen and S. Tsukamoto, J. Appl. Phys. 66 (1989) 3618.
[20] J.-I. Chyi, S. Kalem, N.S. Kumar, C.W. Litton and H. Morkoç, Appl. Phys. Lett. 53 (1988) 1092.
[21] J.C. Mikkelsen and J.B. Boyce, Phys. Rev. Lett. 49 (1982) 1412.
[22] M. Grundmann, U. Lienert, J. Christen, D. Bimberg, A. Fischer–Colbrie and J.N. Miller, J. Vac. Sci. Technol. B 8 (1990) 751.
[23] M. Kodama, Phys. Status Solidi (a) 141 (1994) 145.
[24] S.D. Parker, R.L. Williams, R. Droopad, R.A. Stradling, K.W.J. Barnham, S.N. Holmes, J. Laverty, C.C. Philips, E. Skuras, R. Thomas, X. Zhang, A. Staton–Bevan and D.W. Pashley, Semicond. Sci. Technol. 4 (1989) 663.
[25] M. Lee, D.J. Nicholas, K.E. Singer and B. Hamilton, J. Appl. Phys. 59 (1986) 2895.

ELSEVIER

Journal of Crystal Growth 175/176 (1997) 888–893

JOURNAL OF CRYSTAL GROWTH

Stranski–Krastanov growth of InSb, GaSb, and AlSb on GaAs: structure of the wetting layers

B.R. Bennett[1], B.V. Shanabrook, P.M. Thibado[2], L.J. Whitman, R. Magno

Naval Research Laboratory, Washington, DC 20375-5347, USA

Abstract

Thin layers of InSb, GaSb and AlSb were grown on GaAs(0 0 1) by molecular beam epitaxy and characterized in situ with scanning tunneling microscopy. All three materials exhibit a Stranski–Krastanov growth mode. Distinct wetting layers and self-assembled quantum dots are present after deposition of one to four monolayers of (In,Ga,Al)Sb. The wetting layers consist of anisotropic, ribbon-like structures oriented along the [$\bar{1}$ 1 0] direction, with characteristic separations of 40–50 Å. The initial GaAs surface reconstruction affects both the wetting layer structure and the quantum dot density.

1. Introduction

The Stranski–Krastanov (SK) growth mode in strained-layer heteroepitaxy has been recognized for decades [1–3]. In this mode, the deposited layer initially grows as a two-dimensional (2D) wetting layer for at least one monolayer. Then, three-dimensional (3D) islands form on the wetting layer. Recently, there has been considerable interest in using SK growth to deposit coherent islands, known as self-assembled quantum dots (QDs). These QDs have been reported in semiconductor systems including InAs/GaAs, InP/InGaP, and GaSb/GaAs [4–8]. Although QDs with size uniformities on the order of 10% are routinely achieved, many potential applications such as solid-state lasers require more uniform ensembles of QDs. Theoretical work suggests that the uniformity of QDs is related to the structure of the wetting layer, [9–11] but few experimental studies have been reported [12–15]. In this work, we apply in-situ scanning tunneling microscopy (STM) to investigate the structure of wetting layers of GaSb, AlSb and InSb on GaAs (mismatches of 7.8%, 8.5% and 14.6%, respectively) grown by molecular beam epitaxy (MBE). In all three cases, we observe wetting layers composed of 2D islands with anisotropic ribbon-like structure and characteristic inter-island separations of 40–50 Å.

2. Experimental procedure

Experiments were carried out in an interconnected multi-chamber ultra-high vacuum (UHV)

[1] E-mail: bennett@bloch.nrl.navy.mil.

[2] Present address: Department of Physics, University of Arkansas, Fayetteville, Arkansas 72701, USA.

0022-0248/97/$17.00 Copyright © 1997 Published by Elsevier Science B.V. All rights reserved
PII S0022-0248(96)00917-7

facility that includes a III–V solid-source MBE and a surface analysis chamber with STM. All growths were performed on n^+GaAs, oriented to within 0.1° of (0 0 1). Growth temperatures were determined by GaAs band-edge transmission thermometry [16]. First, a GaAs buffer layer 0.5–1.0 μm thick was grown at 580°C (with interrupts) at a growth rate of 1.0 monolayer (ML)/s with the growth monitored by reflection high-energy electron diffraction (RHEED). During the GaAs buffer growth, the RHEED pattern was a streaky (2×4) reconstruction. Before the growth of each antimonide layer, a 3–5 min growth interrupt was performed at 580°C under an As_4 flux, resulting in the appearance of sharp diffraction spots along each streak. A well-ordered (2×4) or $c(4\times4)$ reconstruction was then prepared by alternately lowering the substrate temperature and As flux until the point at which the As valve could be closed without degradation of the RHEED pattern. This technique produces GaAs surfaces with ~ 5000 Å-wide terraces separated by monolayer-height (3 Å) steps [17]. The antimonide layer was grown by migration-enhanced epitaxy with a cation deposition rate of 0.10 ML/s and a V : III flux ratio of approximately 2 : 1. For example, to grow 1.5 ML of InSb, the shutter sequence was: 5 s In, 20 s Sb, 5 s In, 20 s Sb, 5 s In, 20 s Sb. After deposition of the III-Sb monolayers, the sample was held at the growth temperature under an Sb_4 flux for 120 s before cooling. Finally, the sample was transferred under UHV to the STM chamber and imaged at room temperature. All STM images displayed here were acquired in constant-current mode with currents between 0.1 and 1.0 nA and sample biases ranging from −2.0 to −3.2 V. The images are displayed in gray-scale without corrections for thermal drift.

3. Results

Well-ordered surfaces are observed for GaAs(0 0 1)-(2×4) and -$c(4\times4)$, in contrast to the disordered surface revealed by both RHEED and STM after the deposition of 1–4 ML of GaSb, AlSb or InSb. After growth of 1.0 ML of GaSb on GaAs(0 0 1)-$c(4\times4)$ at 490°C, RHEED exhibited primary and half-order streaks along with weak transmission spots in the [1 1 0] direction, and chevrons in the [$\bar{1}$ 1 0] direction [18, 19]. The resulting surface morphology, shown in Fig. 1a, consists of a disordered distribution of 2D islands. The islands are somewhat elongated, with $\leqslant$ 1 ML-deep gaps between them [20]. Note that quantum dots (QDs) have not yet formed at this coverage. After deposition of a total of 3.5 ML GaSb, strong RHEED transmission spots were visible in both the [1 1 0] and [$\bar{1}$ 1 0] directions, indicating 3D growth. The distance between the spots was clearly smaller than the distance between the diffraction streaks, implying that the QDs had formed with a larger in-plane lattice constant than the GaAs substrate. Because ex situ TEM images of QDs on similarly prepared samples do not exhibit Moiré fringes [21], however, this change in lattice constant must not result from the formation of dislocations but rather must arise from the elastic relaxation of the GaSb bonds within the QD. The presence of QDs has been confirmed on similar samples by ex situ AFM, with typical densities of $1\times10^9/cm^2$, heights of 80 Å, and apparent diameters of 400 Å [21]. An STM image of a typical area between QDs is shown in Fig. 1b. (We try to avoid imaging QDs during studies of the wetting layer in order to avoid damage to the STM tip.) At this GaSb coverage, the wetting layer structure exhibits highly anisotropic ribbon-like structures oriented along the [$\bar{1}$ 1 0] direction. The characteristic ribbon separation, computed from the autocorrelation function for this image, is 50 Å in the [1 1 0] direction.

Ribbon-like wetting layers also result from the growth of AlSb on GaAs. We examined 2.0 ML of AlSb deposited on a (2×4) reconstructed GaAs surface at 500°C. After AlSb growth, the RHEED pattern revealed transmission spots superimposed on a (1×3) streak pattern. The resulting surface, shown in Fig. 2, is qualitatively similar to that following the growth of 3.5 ML of GaSb (Fig. 1b), with ribbon-like structures running along the [$\bar{1}$ 1 0] direction. The autocorrelation function yields a characteristic separation of 40 Å. Although not shown in this image, QDs are also present on the surface. Raman spectroscopy measurements of AlSb QDs on GaAs showed a two-mode

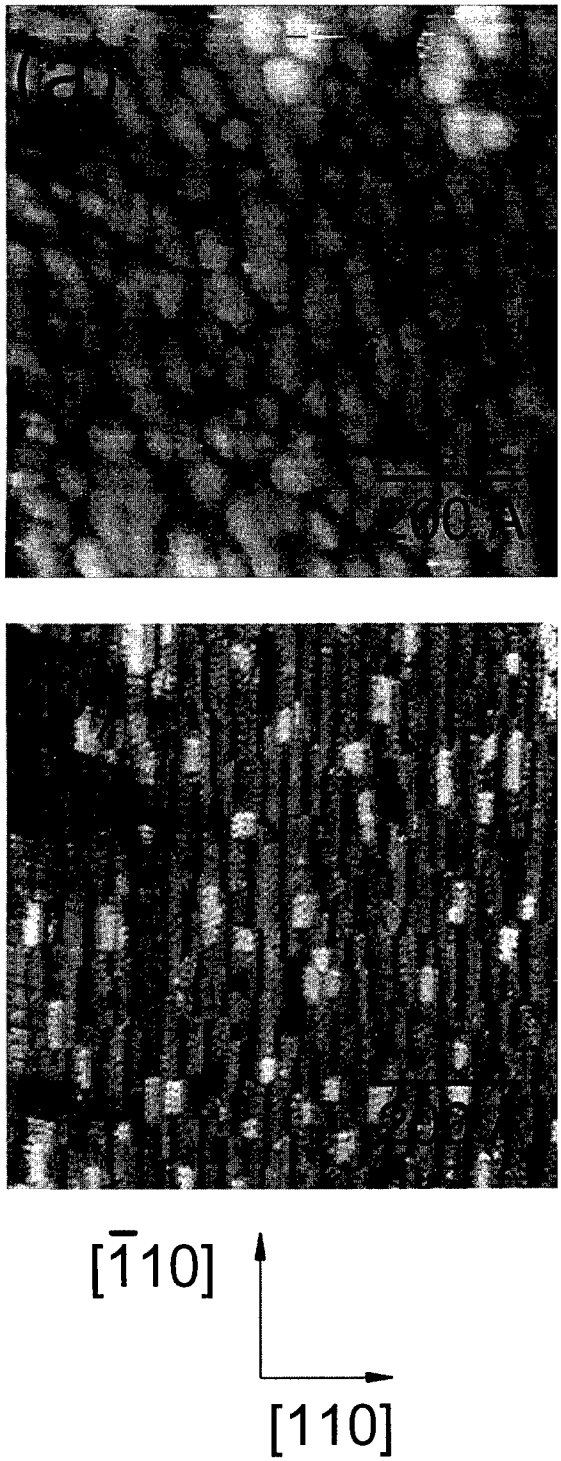

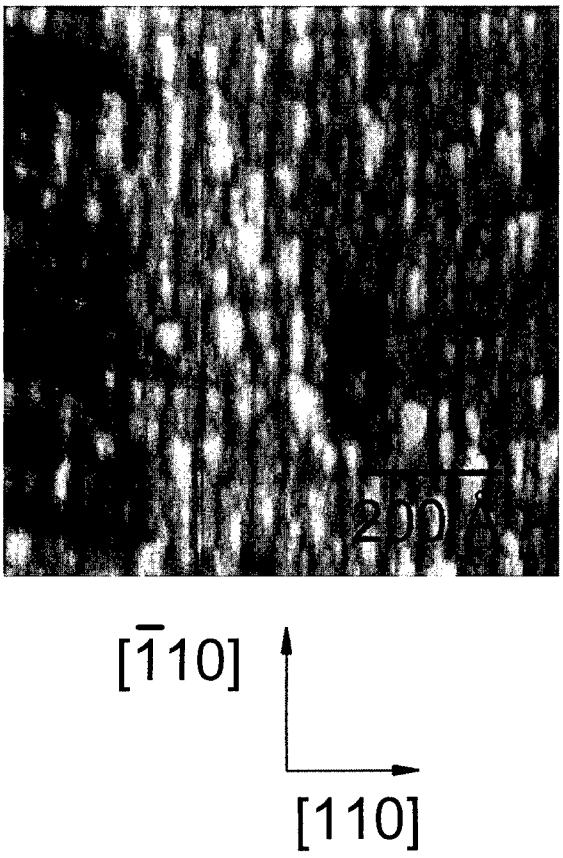

Fig. 2. Filled-state STM image of 2.0 ML of AlSb on GaAs(001)-(2 × 4). The gray-scale height range is approximately 12 Å.

behavior indicating the formation of an AlGaSb alloy due to Ga segregation [22]. Hence, the surface shown in Fig. 2 is more appropriately described as $Al_xGa_{1-x}Sb$.

Using ex situ AFM, we previously observed QDs after as little as 1.5 ML of InSb on GaAs [6]. In this study, we examined 1.5 and 2.0 ML of InSb on GaAs(0 0 1)-c(4 × 4) and 1.5 ML of InSb on GaAs(0 0 1)-(2 × 4) with STM. The substrate temperature during InSb growth was 410°C. In all three cases, RHEED revealed weak transmission spots in

Fig. 1. Filled-state STM images of GaSb on GaAs(001)-c(4 × 4). GaSb coverages are: (a) 1.0 ML and (b) 3.5 ML. The gray-scale height ranges are approximately (a) 8 Å and (b) 10 Å. Quantum dots (not shown) are present on sample (b) but not on (a).

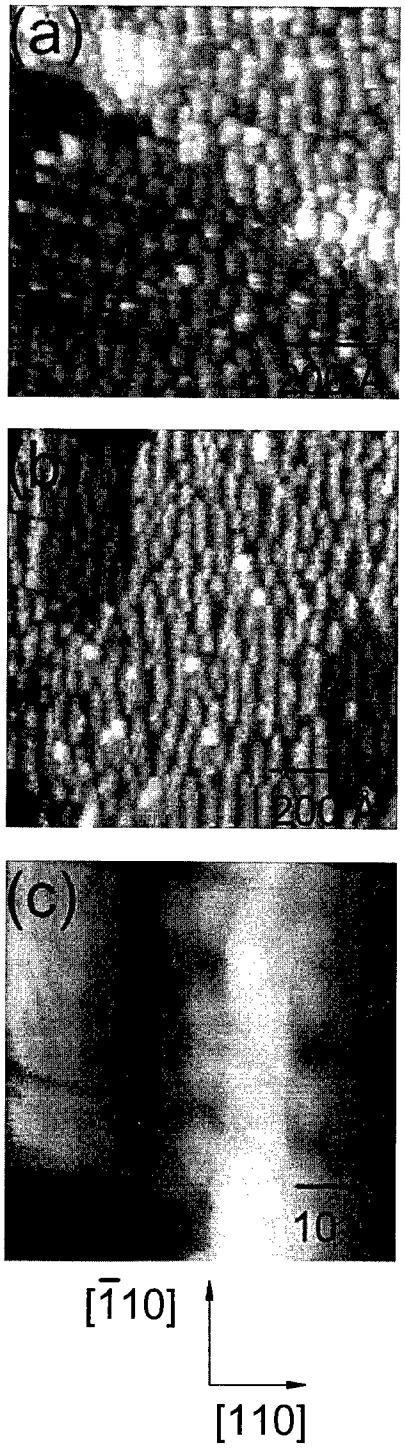

the [1 1 0] direction and chevrons in the [$\bar{1}$ 1 0] direction; STM and AFM confirmed the presence of QDs. In addition to coherent QDs, large dislocated islands were observed for each sample [23]. In Fig. 3a and Fig. 3b we show the STM images acquired between the QDs for 1.5 ML of InSb on GaAs-c(4 × 4) and GaAs-(2 × 4), respectively. Anisotropic ribbon-like structures are present for both initial substrate reconstructions. The characteristic ribbon separations from autocorrelation analyses are 50 Å for growth on GaAs-c(4 × 4) and 40 Å for growth on GaAs-(2 × 4). The characteristic length of the islands in the [$\bar{1}$ 1 0] direction is somewhat shorter for InSb deposition on the GaAs-c(4 × 4) reconstruction. Fig. 3c displays a higher magnification image of 1.5 ML of InSb on GaAs-(2 × 4), revealing atomic-scale structure. The surface appears to have a multilayer structure terminated by dimers (most likely Sb dimers).

4. Discussion

The traditional view of SK growth is that the initial deposition occurs as a continuous wetting layer. Our results, however, suggest a more complicated structure with a discontinuous morphology which may arise from a combination of effects. Both the relative surface energies of the absorbates and substrate, and the mismatch-related strain which may be relieved by the formation of vacancy lines, may play a role. A simple calculation, assuming complete strain relaxation by vacancy arrays, gives a spacing of 12.5 atomic planes or 54 Å for an 8% mismatch (GaSb or AlSb) and 6.8 atomic planes or 31 Å for InSb. These values are comparable to the characteristic separations of the ribbon-like structures found for all three materials.

A few groups have investigated the initial stages of InAs growth on GaAs by in situ STM.

Fig. 3. Filled-state STM images of 1.5 ML of InSb on GaAs: (a) GaAs(0 0 1)-c(4 × 4) starting surface, (b) GaAs(0 0 1)-(2 × 4) starting surface, and (c) higher magnification image of surface in (b). The gray-scale height ranges are approximately (a) 12 Å, (b) 12 Å, and (c) 8 Å. Note the monolayer-height (3 Å) steps visible in (a) and (b).

Bressler-Hill et al. examined submonolayer coverages of InAs grown on GaAs(0 0 1)-(2 × 4) surfaces [12]. They observed 2D InAs islands elongated along the [$\bar{1}$ 1 0] direction – the same direction found in this work. Based upon an examination of the scaling properties of the island size, they concluded that growth along the [$\bar{1}$ 1 0] direction behaves as if it is unstrained while growth in the [1 1 0] direction is quenched by strain. In contrast, Cirlin et al. studied InAs growth on GaAs(0 0 1)-c(4 × 4) and found wire-like structures oriented along the [1 0 0] direction (i.e. 45° from [$\bar{1}$ 1 0]) [15]. Because of the different symmetries of the (2 × 4) and c(4 × 4) reconstructions it is not surprising that for low coverages the features of the wetting layer would be oriented in different directions. We observe some evidence of this behavior in our data. Surfaces with 1.0 ML of GaSb (Fig. 1a) and 1.5 ML of InSb (Fig. 3a) on GaAs-c(4 × 4) are more isotropic than 1.5 ML of InSb (Fig. 3b) and 2.0 ML of AlSb (Fig. 2) on GaAs-(2 × 4), consistent with the more isotropic structure of the c(4 × 4) reconstruction. As indicated in Fig. 1b, however, after additional GaSb is deposited (3.5 ML total), the remnant character of the symmetry of the GaAs-c(4 × 4) surface reconstruction is eliminated and the wetting layer becomes highly anisotropic. The anisotropy of this structure does not appear to arise from kinetic limitations but, rather, is attributed to the direction-dependent strain associated with the dimer-based surface reconstructions of the wetting layers.

In addition to the impact of the reconstruction symmetry on the morphology of the wetting layer, the differences in the amount of As on the surface are also expected to influence the formation of antimonide quantum dots. For example, because the As coverage on a c(4 × 4) reconstruction is 1.75 ML [24], compared to 0.5 ML for a (2 × 4) surface [25], we expect the initial formation of AlAs (GaAs) when Al (Ga) is incident on a GaAs-c(4 × 4) surface. Because this material would not be under strain, the coverage required to form quantum dots could be expected to be larger for the GaSb and AlSb dots grown on the c(4 × 4) reconstruction. This is in agreement with our earlier studies of AlSb QD formation on the c(4 × 4) reconstruction which found that QDs did not form until over 3 ML AlSb had been deposited [6, 22]. This should be contrasted with the current study which shows that QDs form after only 2 ML of AlSb is deposited on the (2 × 4) reconstruction. This issue becomes even more complex for the deposition of InSb QDs on the c(4 × 4) reconstruction, where the initial deposition of In would be expected to form InAs. (The InSb/GaAs mismatch is twice as large as the InAs/GaAs mismatch.) AFM measurements on the samples of Fig. 3 revealed a higher density of both QDs and dislocated islands for the (2 × 4) reconstruction compared to the c(4 × 4) reconstruction.

5. Summary

Epilayers of GaSb, AlSb and InSb, with mismatches of 8–15%, exhibit a Stranski–Krastanov growth mode on GaAs(0 0 1). In situ STM measurements reveal that the wetting layers are not uniform, but consist of anisotropic, ribbon-like structures oriented along the [$\bar{1}$ 1 0] direction, with characteristic separations of 40–50 Å and heights of a few angstroms. These wetting layers coexist with self-assembled quantum dots. The initial GaAs surface reconstruction affects both the wetting layer structure and the QD density.

Acknowledgements

This work was supported by the Office of Naval Research.

References

[1] I.N. Stranski and L. Krastanov, Sitzungsber. Akad. Wiss. Wien, Math.-Naturwiss. K1 IIb 146 (1938) 797.
[2] E. Bauer, Z. Krist. 110 (1958) 372.
[3] R.W. Vook, Opt. Eng. 23 (1984) 343.
[4] P.M. Petroff and S.P. DenBaars, Superlattice Microstruct. 15 (1994) 15, and references therein.
[5] L. Samuelson, N. Carlsson, P. Castrillo, A. Gustafsson, D. Hessman, J. Lindalh, L. Montelius, A. Petersson, M.-E. Pistol and W. Seifert, Jpn. J. Appl. Phys. 34 (1995) 4392.
[6] B.R. Bennett, R. Magno and B.V. Shanabrook, Appl. Phys. Lett. 68 (1996) 505.
[7] E.R. Glaser, B.R. Bennett, B.V. Shanabrook and R. Magno, Appl. Phys. Lett. 68 (1996) 3614.

[8] F. Hatami, N.N. Ledentsov, M. Grundmann, J. Bohrer, F. Heinrichsdorff, M. Beer, D. Bimberg, S.S. Ruvimov, P. Werner, U. Gosele, J. Heydenreich, U. Richter, S.V. Ivanov, B.Ya. Meltser, P.S. Kopev and Zh.I. Alferov, Appl. Phys. Lett. 67 (1995) 656.
[9] C. Priester and M. Lannoo, Phys. Rev. Lett. 75 (1995) 93.
[10] C. Ratsch and A. Zangwill, Surf. Sci. 293 (1993) 123.
[11] C. Ratsch, P. Smilauer, D.D. Vvedensky and A. Zangwill, J. Phys. I France 6 (1996) 575.
[12] V. Bressler-Hill, S. Varma, A. Lorke, B.Z. Nosho, P.M. Petroff and W.H. Weinberg, Phys. Rev. Lett. 74 (1995) 3209.
[13] N.P. Kobayashi, T.R. Ramachandran, P. Chen and A. Madhukar, Appl. Phys. Lett. 68 (1996) 3299.
[14] Q. Xie, N.P. Kobayashi, T.R. Ramachandran, A. Kalburge, P. Chen and A. Madhukar, Mater. Res. Soc. Proc. 379 (1995) 177.
[15] G.E. Cirlin, G.M. Guryanov, A.O. Golubok, S.Ya. Tipissev, N.N. Lenentsov, P.S. Kopev, M. Grundmann and D. Bimberg, Appl. Phys. Lett. 67 (1995) 97.
[16] B.V. Shanabrook, J.R. Waterman, J.L. Davis and R.J. Wagner, Appl. Phys. Lett. 61 (1992) 2338.
[17] P.M. Thibado, E. Kneedler, B.T. Jonker, B.R. Bennett, B.V. Shanabrook and L.J. Whitman, Phys. Rev. B 53 (1996) R10481.
[18] Y. Nabetani, T. Ishikawa, S. Noda and A. Sasaki, J. Appl. Phys. 76 (1994) 347.
[19] R.P. Mirin, J.P. Ibbetson, K. Nishi, A.C. Gossard and J.E. Bowers, Appl. Phys. Lett. 67 (1995) 3795.
[20] P.M. Thibado, B.R. Bennett, M.E. Twigg, B.V. Shanabrook and L.J. Whitman, J. Vac. Sci. Technol. A 14 (1996) 885.
[21] B.R. Bennett, P.M. Thibado, M.E. Twigg, E.R. Glaser, R. Magno, B.V. Shanabrook and L.J. Whitman, J. Vac. Sci. Technol. B 14 (1996) 2195.
[22] B.R. Bennett, B.V. Shanabrook and R. Magno, Appl. Phys. Lett. 68 (1996) 958.
[23] B.R. Bennett, B.V. Shanabrook, E.R. Glaser, R. Magno and M.E. Twigg, Superlattice Microstruct. 21 (1997).
[24] D.K. Biegelsen, R.D. Bringans, J.E. Northrup and L.-E. Swartz, Phys. Rev. B 41 (1990) 5701.
[25] J. Zhou, Q. Xue, H. Chaya, T. Hashizume and T. Sakurai, Appl. Phys. Lett. 64 (1994) 583.

ELSEVIER

Journal of Crystal Growth 175/176 (1997) 894–897

JOURNAL OF CRYSTAL GROWTH

Buffer-dependent mobility and morphology of InAs/(Al,Ga)Sb quantum wells

M. Thomas[a,*], H.-R. Blank[a], K.C. Wong[b], H. Kroemer[a]

[a] *Department of Electrical and Computer Engineering, University of California, Santa Barbara, California 93106, USA*
[b] *Department of Physics, University of California, Santa Barbara, California 93106, USA*

Abstract

We find that the mobility and morphology of InAs/(Al,Ga)Sb quantum wells grown by molecular beam epitaxy on lattice-mismatched GaAs depends strongly on the composition of the buffer layers. Using atomic force microscopy we show that GaSb buffers provide atomically flat interfaces on the scale of the electron Fermi wavelength for the quantum wells. In contrast, AlSb buffers generate a very rough interface on the same scale. Van der Pauw measurements show that this results in a greatly reduced low-temperature mobility for InAs quantum wells grown on AlSb buffers. We propose that the Ga adatoms tend to be more mobile than Al adatoms and therefore smooth out the roughness generated in the nucleation layer. Using a GaSb buffer layer, we have achieved new record mobilities in InAs quantum wells.

PACS: 73.50.Dn; 73.61.Ey

Keywords: Low-field transport and mobility; Piezoresistance; III–V semiconductors

InAs quantum wells are promising for many device applications, including high-speed field effect transistors [1, 2], resonant tunneling diodes [3] or superconducting Josephson field effect transistors [4]. Bulk InAs has an inherently higher mobility than bulk GaAs [5]. One would therefore expect InAs quantum wells (QWs) to achieve higher mobilities than GaAs QWs. However, this has not been the case. Initial problems with growing InAs by MBE included the lattice mismatch with commonly available substrates (Si has a lattice constant $a = 5.43$ Å, GaAs has $a = 5.65$ Å and InP has $a = 5.87$ Å whereas InAs has $a = 6.06$ Å). This was partially overcome by growing a thick buffer layer of GaSb or AlSb on GaAs [6]. The (Al,Ga)Sb is nearly lattice matched to InAs and the buffer layer serves to attenuate the dislocations due to the lattice mismatch with GaAs (7%). Another problem with growing high mobility InAs QWs has been the interface with (Al,Ga)Sb barriers. Since both the group-III and group-V elements change at the interface, there are two possible types of interface

* Corresponding author. Fax: + 1 805 893 3262; e-mail: thomas@nemesis.ece.ucsb.edu.

0022-0248/97/$17.00 Copyright © 1997 Elsevier Science B.V. All rights reserved
PII S0022-0248(96)00920-7

[7]: InSb-like and AlAs-like. It has been found that the InSb-like interface is superior [7]. Even with these improvements, however, the mobility of the InAs QWs does not match that of GaAs/(Al,Ga)As QWs. In earlier work, Nguyen et al. [8], found that a GaSb buffer provided better mobilities in the InAs QW than a mixed GaSb/AlSb buffer. However, they could not provide an explanation for the difference, and did not look at samples with only AlSb in the buffer. In this work, we have further improved the mobility in InAs QWs by optimizing the buffer layer growth. We find that a GaSb buffer provides mobilities in the InAs QW nearly an order of magnitude greater than with an AlSb buffer. We have investigated this effect in detail and we show that it is directly related to the morphology induced by the different compositions of the buffer layer.

We begin all growths on semi-insulating GaAs substrates. To grow the 6.1 Å materials (AlSb, GaSb and InAs), we first provide a nucleation layer of ~ 1 nm AlAs and then grow approximately 80 nm of AlSb. This sequence has been shown [6] to quickly nucleate two-dimensional growth of the 6.1 Å materials. These nucleation layers are grown at 570°C. The buffer layer is then started and the temperature is then lowered, to 530°C. The buffer layer is either GaSb or AlSb of greater than 1 μm thickness. Since the goal of this work is to determine the effect of this buffer layer on the morphology and mobility of InAs QWs, this is the only parameter that is varied. After the buffer layer is grown, the bottom barrier of the QW is grown as an $Al_{0.5}Ga_{0.5}Sb$ digital alloy superlattice, typically 100 nm thick. The digital alloy consists of 2.5 nm GaSb followed by 2.5 nm AlSb, periodically repeated to the necessary thickness. If high electron concentrations are desired in the QW, Te delta-doped layers are inserted in the barriers. 15 nm of InAs is then grown with an InSb-like interface. The samples for AFM measurements are complete at this point. The samples for mobility measurements have a top superlattice barrier on the QW and a surface GaSb cap to prevent Al oxidation.

Immediately after unloading the samples from the MBE system we scan the surface with a Digital Instruments Nanoscope III atomic force microscope. The samples have also been measured after being exposed for several days in the air and show no significant differences in the following results. In Fig. 1a and Fig. 1b we show the surface of the InAs as scanned by AFM. Fig. 1a shows the sample grown on a GaSb buffer, while Fig. 1b shows

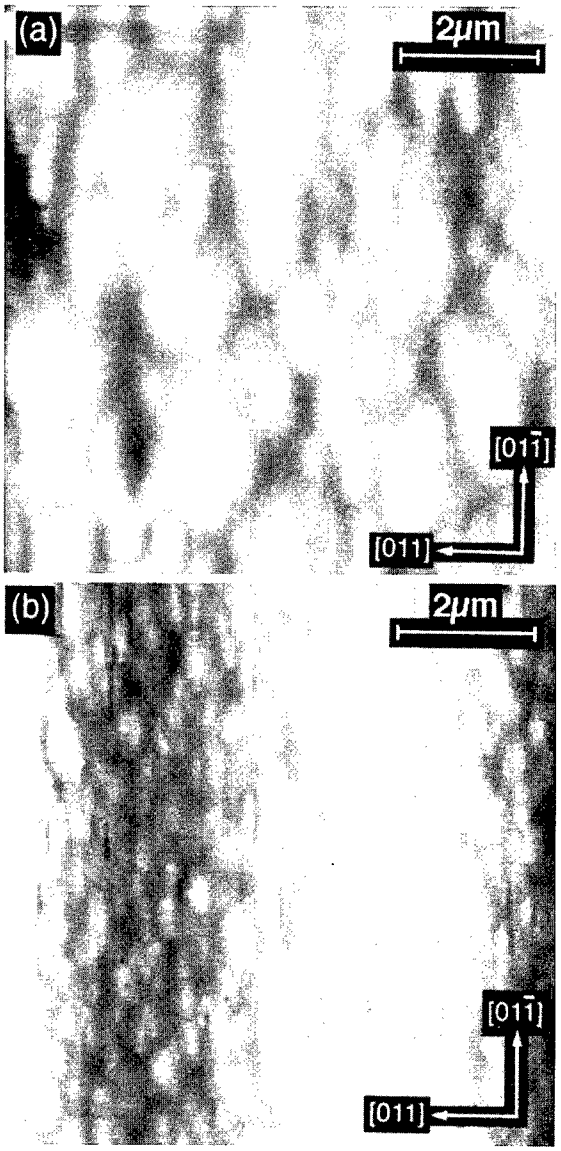

Fig. 1. (a) 8 μm × 8 μm AFM scan of 15 nm InAs surface grown on 1.4 μm GaSb buffer. Slightly anisotropic mounds are visible with lateral dimensions ~ 1 × 1.5 μm and with height ~ 4 nm. (b) 8 μm × 8 μm scan of 15 nm InAs surface on 1.4 μm AlSb buffer showing slightly smaller (~ 0.5 × 0.5 μm) mounds but with the same vertical scale.

a sample grown on an AlSb buffer. On the scale shown, there is very little qualitative difference between the two surfaces. Both show characteristic features about 4 nm in height and with lateral dimensions about 1×1.5 μm. These features are associated with screw dislocations for lattice-mismatched heteroepitaxy [9]. Since the mismatch between buffer and substrate is 7%, dislocations are nucleated in the first few monolayers of growth. However, by growing a thick enough buffer layer, the dislocations can be reduced by several orders of magnitude, to a steady state of $\sim 10^8$ cm^{-2}.

However, on a much smaller scale, we observe a significant difference between the two samples. In Fig. 2a and Fig. 2b, we see the same samples, but scanned at a resolution of 800×800 nm. Fig. 2a, which shows the InAs grown on GaSb buffer, exhibits monolayer steps of InAs (height ~ 0.4 nm) with a lateral width ~ 40 nm. In contrast, Fig. 2b shows the sample with the AlSb buffer, and shows trenches about 4 nm deep, but also with a characteristic lateral scale of about 40×150 nm.

Since the electrons that contribute to conductivity and hence mobility are all at the Fermi surface, only scattering potentials that vary on the order of the Fermi wavelength are important. For our samples, the Fermi wavelength $\lambda_f = (2\pi/n_s)^{1/2}$, varies from 35 to 15 nm (n_s from 5.5×10^{11} to 4.3×10^{12} cm^{-2} in the lowest occupied subband). It is only scattering potentials on this scale that will significantly affect the mobility. Thus the variations shown in Fig. 1a and Fig. 1b do not affect the mobility, since the height fluctuations occur over 500 to 1500 nm, which is more than 10 times λ_f. On the other hand, the variations shown in Fig. 2 should strongly affect the mobility. For the GaSb buffer, the variations are only monolayer steps, and this should correspond to only a small interface scattering potential in the InAs QW. However, for the AlSb buffer, the variations are an order of magnitude greater in height (but still on the same lateral scale) which is a significant fraction of the QW thickness, and so will generate a large scattering potential. Hence, the mobility of the samples with an AlSb buffer should be much less than those with a GaSb buffer because the AlSb grows much rougher.

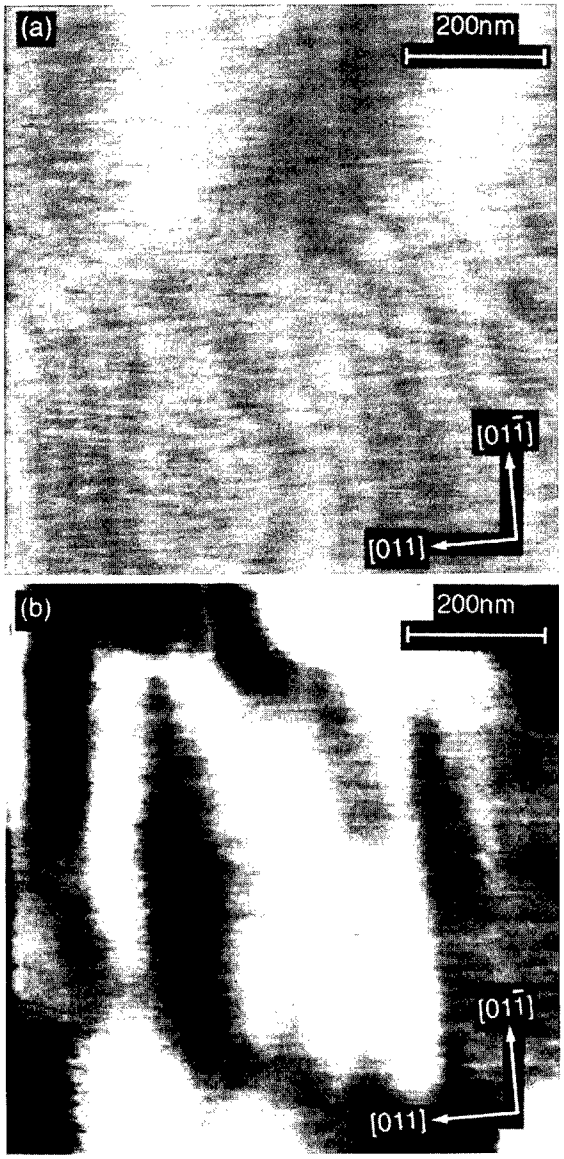

Fig. 2. (a) 800 nm × 800 nm AFM scan of 15 nm InAs grown on GaSb showing monolayer terraces. The average terrace width is 40 nm. (b) 800 nm × 800 nm scan of 15 nm InAs on 1.4 μm AlSb showing very deep trenches (~ 4 nm) on a similar lateral scale as in (a).

To confirm this, we also grew samples for measuring the mobility of the InAs QWs. These samples were identical to those grown for AFM measurements, except that a top barrier superlattice and GaSb cap were grown on the InAs. Van

der Pauw measurements from room temperature to 12 K were performed to determine the mobility and carrier concentration of these samples. The samples with a GaSb buffer had consistently higher mobilities at low temperature than the samples with AlSb. This effect occurred over more than an order of magnitude difference in carrier concentration. The largest difference in mobility occurred for the lowest concentration, $n_s = 5.5 \times 10^{11}$ cm^{-2}. In this case, the mobility for the sample with GaSb buffer (240 000 cm^2/V s) is almost seven times greater than the sample with the AlSb buffer (35 000 cm^2/V s). The Fermi wavelength for this sample is also most comparable to the lateral scale of the roughness. For a concentration of 1.3×10^{12} cm^{-2}, we achieved a record mobility of 944 000 cm^2/V s at 12 K with the GaSb buffer. In contrast, the same concentration but with an AlSb buffer only achieved 244 000 cm^2/V s at 12 K. Similar results were obtained for very high electron concentrations, e.g., $n_s = 7 \times 10^{12}$ cm^{-2}. In this case, the low-temperature mobilities for GaSb and AlSb buffers were 236 000 and 91 000 cm^2/V s, respectively.

The preceding results have been consistently reproduced over a large number of MBE-grown samples. We can rule out impurity scattering from the buffer layer since this layer is 100 nm from the InAs QW. Furthermore, these same results have been obtained with separate charges of Al in the Al source furnace. The effect is also robust with respect to variations in the buffer layer growth temperature over nearly 100°C, with variations in GaSb cap thickness, and with the presence or absence of delta doping sheets.

The large mobilities we can achieve at low temperatures may be attributed primarily to the growth dynamics of AlSb versus GaSb. The AFM scans suggest that GaSb smoothes out the roughness generated due to the lattice mismatch of GaAs and (Al,Ga)Sb. This is possible if the Ga adatoms have a high enough mobility to move around the surface during growth. In contrast, the lower mobility of Al adatoms causes them to stick approximately where they land. Thus AlSb tends to preserve the morphology of the underlying epilayers. This hypothesis is supported by other experiments [9, 10]. The mobilities we have obtained are competitive with the best mobilities achieved in GaAs QWs [11].

We wish to acknowledge useful discussions with Dr. Berinder Brar (now at Texas Instruments, Dallas, TX) and technical assistance from J.H. English. One of us (H.-R.B.) wishes to acknowledge support from the Deutsches Forschungsgemeinschaft. Part of this work was supported by the NSF Science and Technology Center for Quantized Electronic Structures, grant DMR 91-20007 and this work also made use of the MRL Central Facilities supported by the NSF under award DMR 91-23048.

References

[1] C.R. Bolognesi, E.J. Caine and H. Kroemer, IEEE Electron. Dev. Lett. 15 (1994) 16.
[2] B. Brar and H. Kroemer, IEEE Electron. Dev. Lett. 16 (1995) 548.
[3] D.H. Chow and J.H. Schulman, Appl. Phys. Lett. 64 (1994) 76.
[4] T. Akazaki, H. Takayanagi, J. Nitta and T. Enoki, Appl. Phys. Lett. 68 (1996) 418.
[5] O. Madelung, Ed., Semiconductors: Group IV Elements and III-V Compounds (Springer, Heidelberg, 1991) pp. 106, 138.
[6] S. Subbanna, G. Tuttle and H. Kroemer, J. Electron. Mater. 17 (1988) 297.
[7] G. Tuttle, H. Kroemer and J.H. English, J. Appl. Phys. 67 (1990) 3032.
[8] C. Nguyen, B. Brar, C.R. Bolognesi, J.J. Pekarik, H. Kroemer and J.H. English, J. Electron. Mater. 22 (1993) 255.
[9] B. Brar and D. Leonard, Appl. Phys. Lett. 66 (1995) 463.
[10] H.-R. Blank, M. Thomas, K.C. Wong and H. Kroemer, Appl. Phys. Lett. 69 (1996) 2080.
[11] L.N. Pfeiffer, K.W. West, J.P. Eisenstein, K.W. Baldwin and P. Gammel, Appl. Phys. Lett. 61 (1992) 1211.

ELSEVIER

Journal of Crystal Growth 175/176 (1997) 898–902

JOURNAL OF CRYSTAL GROWTH

Molecular beam epitaxy of vertically compact $Al_xGa_{1-x}As$/GaAs laser-HEMT structures for monolithic integration

A. Gaymann*, J. Schaub, W. Bronner, N. Grün, J. Hornung, K. Köhler

Fraunhofer-Institut für Angewandte Festkörperphysik, Tullastrasse 72, D-79108 Freiburg, Germany

Abstract

Vertically compact $Al_xGa_{1-x}As$/GaAs laser structures with $Al_{0.3}Ga_{0.7}As$/AlAs SPSL-cladding layers were grown on top of HEMT structures by MBE and investigated with regard to series resistance. We found an exponential dependence of series resistance R_s with AlAs and $Al_{0.3}Ga_{0.7}As$ SPSL-layer thicknesses at ambient temperature. Laser-HEMT structures for monolithic integration were grown and lasers were processed. For $3 \times 200\ \mu m^2$ 3-QW-lasers, suitable for high-frequency performance, threshold currents of 20 mA and series resistances below 12 Ω were obtained. The slope of the linear regression of the I_{th} values as a function of mesa width yielded a low threshold current density j_{th} of 480 A/cm^2. Reduction of the p-cladding thickness from 600 nm down to 450 nm shows no increase in threshold current density if the p-dopants are kept from diffusing into the active region. This clearly demonstrates that laser structures for monolithic integration can be designed very compact without loosing performance.

1. Introduction

The monolithic integration of laser and electronic circuits represents a promising device technology to meet the growing demand for future information data transfer systems. An ideal semiconductor for short-range optical communication is the GaAs/$Al_xGa_{1-x}As$ system since even sophisticated vertical structures can be routinely grown by molecular beam epitaxy (MBE). However, in the case of monolithic integration, an increased complexity of the layer structure may lead to restrictions for parameters like growth temperatures, doping profiles and layer thicknesses which can result in lower device performance.

Growth of the low-temperature HEMT structure on top of the highly doped cap of the laser structure is excluded since it results in poor high-frequency performance. A processed laser structure overgrown in an second epitaxial run is also excluded due to poor crystal quality of the overgrown layer at the mesa edges [1]. Therefore, we grow the laser structure on top of the HEMT structure. This is done during one epitaxial run. A scheme of the

* Corresponding author. Fax: + 49 761 5159200, e-mail: gaymann@iaf.fhg.de.

0022-0248/97/$17.00 Copyright © 1997 Elsevier Science B.V. All rights reserved
PII S0022-0248(96)00877-9

vertical layer structure is given in Fig. 1. In order to obtain an easy to manufacture HEMT process, a vertically compact design of the laser structure is necessary. This can be achieved by a moderate thickness of the cladding layers with high aluminum content realized by short period $Al_{0.3}Ga_{0.7}As$/AlAs superlattices (SPSLs).

In this paper three points will be addressed: Firstly, the influence of the layer sequence of the SPSLs on the series resistance of the laser diode is studied. Secondly, DC data of lasers grown on top of the HEMT structures are reported. Finally, a successful reduction of p-cladding layer thickness is reported.

2. Growth of heterostructures and results

All samples were grown by MBE on 2 in GaAs substrates in a Varian Modular Gen II. The aluminum content in the ternary compound was $x = 0.3$. Layers with Al mole fractions between 0 and 0.3 were realized by GaAs/$Al_{0.3}Ga_{0.7}As$ short-period superlattices (SPSLs) and those with $x > 0.3$ by $Al_{0.3}Ga_{0.7}As$/AlAs SPSLs. The growth rate for GaAs was 1.25 μm/h. It was controlled by reflection high-energy diffraction (RHEED) before and after the growth. The actual composition of the ternary compound, and by that, the aluminum contents and the growth rates of all other compositions were determined by additional RHEED measurement of the $Al_{0.3}Ga_{0.7}As$ compound. The knowledge of the actual thicknesses of the various layers is important for the wet etching step during laser processing. The As_4/Ga beam equivalent pressure was below 20. Si and Be are used as n- and p-dopants, respectively. Doping concentrations are related to GaAs. Calibration of dopants was done with Hall effect measurements of GaAs layers.

For studying the influence of the AlAs and $Al_{0.3}Ga_{0.7}As$ layer thicknesses in the cladding layers on the series resistance of the laser diode, samples with different SPSL-layer thicknesses were grown. The layer sequence of the test samples was the same as the structure displayed in Fig. 1. The mean Al mole fraction of the cladding layers was 80%. AlAs- and $Al_{0.3}Ga_{0.7}As$-layer thicknesses varied from 2 to 6 nm and 0.8 to 2.4 nm,

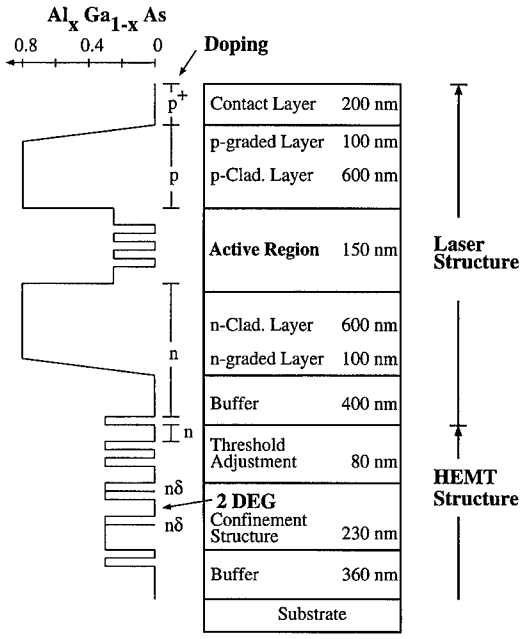

Fig. 1. Layer sequence of the $Al_xGa_{1-x}As$/GaAs laser-HEMT structure for monolithic integration (drawings are not in scale).

respectively. The total thicknesses of the cladding layer was 600 nm. The Be concentration in the p-cladding layer was chosen to 1×10^{18} cm^{-3} to emphasize the effect of the short period layer thicknesses on R_s. Diode mesas with a cavity length of 200 μm and widths from 3 to 32 μm were fabricated by means of wet etching. Electrical contacts were obtained by evaporation of ohmic metals. Series resistance was determined by recording I–V curves of fabricated diodes at ambient temperature. R_s is the differential resistance for diode voltages above 2 V. Fig. 2 shows the measured R_s data for cavity widths of 3 μm (full diamonds) and 16 μm (full triangles). The y-axis is chosen in logarithmic scale. We found an exponential dependence of series resistance R_s on AlAs and $Al_{0.3}Ga_{0.7}As$ SPSL-layer thicknesses. This functional relation can be understood by taking into account tunneling processes of holes through the AlAs barriers. (The vertical hole transport in the cladding layer should be the main contribution to series resistance since vertical electron transport contributes much less to R_s due to the much higher mobility.) Thus, if the AlAs barrier thickness increases the tunneling probability

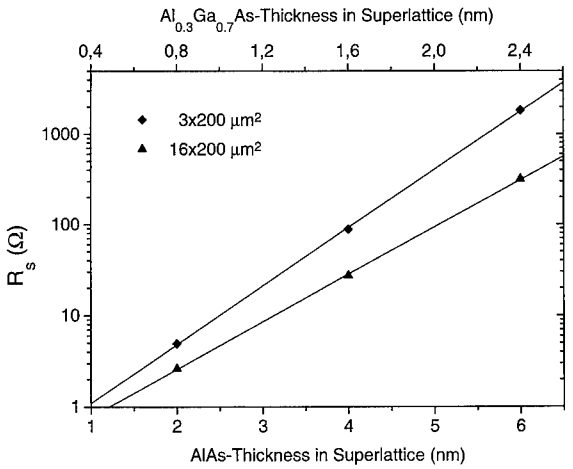

Fig. 2. Series resistances for two different laser mesas as a function of the AlAs-thickness in the $Al_{0.3}Ga_{0.7}As$/AlAs SPSL cladding layers. The mean Al mole fraction of the cladding layers is 80%.

should decrease exponentially, e.g., the series resistance should increase similarly. However, at room temperature not only tunneling processes occur but also vertical transport in the p-doped superlattice driven by thermionic emission is present. With increasing AlAs barrier thickness, the $Al_{0.3}Ga_{0.7}As$ quantum well width increases, too, in order to keep a mean Al mole fraction of 80%. This results in a higher energy difference between QW level and valence band edge. Thus, this second contribution also leads to higher series resistance with thicker AlAs layers since the number of carriers crossing the barriers gets smaller. However, the details of the vertical transport can only be discussed based on results for the temperature dependence of R_s and lies beyond the scope of this paper. As a result, acceptable R_s values can be obtained even with low Be doping of the cladding layers if the thicknesses of the SPSL layers are sufficiently thin.

Laser-HEMT structures for monolithic integration were grown as follows (see Fig. 1): First, the two-sided δ-doped QW HEMT structure was grown at a substrate temperature $T_s = 520°C$ measured by pyrometer. This growth temperature is sufficiently low to suppress Si segregation into the two-dimensional electron gas (2DEG) channel. After growth of a thin etchstop layer the laser structure was grown. The T_s was raised to 660°C for the growth of the n-graded layer, the n-cladding layer and the separate confinement layers with the laser active region. This active region consists of three 7.4 nm thick quantum wells which are separated by 7.2 nm thick $Al_{0.25}Ga_{0.75}As$ barriers. At the beginning of the lower confinement layer, T_s was lowered for the growth of a few monolayers to prevent Si from segregating into the quantum wells. The p-cladding layer and p-graded layer were grown at slightly reduced temperatures of 625°C and 590°C, respectively. Finally, the heavily-doped GaAs cap layer was grown at $T_s = 520°C$.

For the AlAs and $Al_{0.3}Ga_{0.7}As$ layers in the SPSL-claddings of the actual laser-HEMT structure we choose a thickness of 3 nm and 1.2 nm, respectively. These values seem reasonable with regard to a limitation of shuttering times and frequency. The Si-doping concentration of the n-buffer, n-graded layer, and n-cladding layer was $4 \times 10^{18}\,cm^{-3}$.

Resistivities for higher p-doping concentrations were estimated from Fig. 2 on the supposition that the mobility is only weakly dependent on N_{Be} in the considered doping regime and that the p-cladding layer and the p-graded layer contribute most to R_s. In order to obtain a series resistance of 15 Ω the doping concentration of the p-cladding was set to $1 \times 10^{18}\,cm^{-3}$ for the first 300 nm and raised to $2 \times 10^{18}\,cm^{-3}$ for the growth of the remaining 300 nm. This doping profile leads to an effective lowering of Be diffusion into the active region for two reasons. First, the Be concentration is held below the solubility limit of $2 \times 10^{18}\,cm^{-3}$ in $Al_{0.8}Ga_{0.2}As$. Solubility limits of Be in $Al_xGa_{1-x}As$ as a function of Al mole fraction were found in Be doped samples by depth profiling with Secondary Ion Mass Spectrometry [2]. Our investigations have clearly demonstrated the ability of Be to diffuse through the complete p-cladding layer if the intended doping concentration in the cladding layer is beyond these upper limits. It was also shown that in this case this diffusion process cannot be suppressed by using low growth temperatures. As a second point, if the Be concentration is below the solubility limit like in the laser-HEMT structure reported here, Be diffusion can be reduced by lowering the growth temperature T_S. For that

reason T_S values of 625°C and 590°C were chosen for the p-cladding and the p-graded layer, respectively. The p-graded layer was doped with $8 \times 10^{18}\,cm^{-3}$. Laser diodes with fixed cavity length and various widths were processed by means of wet etching and evaporation of ohmic metals. Details of the process technology can be found in Ref. [3]. Finally, laser mirrors were fabricated by either reactive ion etching (RIE) or chemical assisted ion-beam etching (CAIBE). These two methods have proved to be highly reproducible and have yielded $Al_xGa_{1-x}As/GaAs$ lasers with almost the same threshold currents as lasers with cleaved facets.

I_{th} and R_s were determined by on-wafer measurements. Here, R_s is the differential resistance for a diode current 5 mA above threshold. The lasing wavelength was 850 nm. The quality and homogeneity of the laser mirrors were tested by measuring 40 identical lasers which were located on a diameter of the wafer. We found a scattering of the I_{th} data points of less than 10%. Values for I_{th} and R_s for mesa widths between 3 and 32 μm are shown in Fig. 3. For $3 \times 200\,\mu m^2$ 3 QW-lasers we found threshold currents I_{th} below 20 mA and series resistances below 12 Ω. The slope of the linear regression of the I_{th} values yielded a threshold current density j_{th} of 480 A/cm^2. This is almost the same value as obtained for high-speed $Al_xGa_{1-x}As/GaAs$ lasers grown in our laboratory on top of a 1 μm buffer under optimized growth conditions [4]. The DC performance of our laser grown on the HEMT structure can be compared with data from literature and with earlier results. Nichols et al. [5] obtained a threshold current density of 700 A/cm^2 and a series resistance of 50 Ω for a strained GaAs/AlGaAs/GaInAs MQW laser structure grown on top of a MESFET by MOCVD although much thicker cladding layers were used. The circuits operated with bandwidths as high as 3.4 GHz. A similar bandwidth of a MBE grown GaInAs/GaAs MODFET/laser device was reached by Offsey et al. [6]. Typical threshold currents were 80 mA for the $20 \times 800\,\mu m^2$ lasers. Earlier data of monolithic integrated laser-HEMT devices from our laboratory were reported by Hornung et al. in Ref. [7]. Typical results were a threshold current of 28 mA and a series resistance of 22 Ω for a $4 \times 360\,\mu m^2$ laser diode grown on top of a HEMT structure. Laser diodes and driver circuits showed performance up to data rates of 7.4 Gbit/s in a short-range optical data transfer setup. Hence, taking the actual vertical layer structure as a starting point it should be possible to obtain a fully integrated laser-HEMT device exceeding the bandwidth reported in Ref. [7].

Finally, attempts were made to make the laser structure even more compact. Laser-HEMT structures with different p-cladding thicknesses but identical doping profiles were grown. Cladding layers

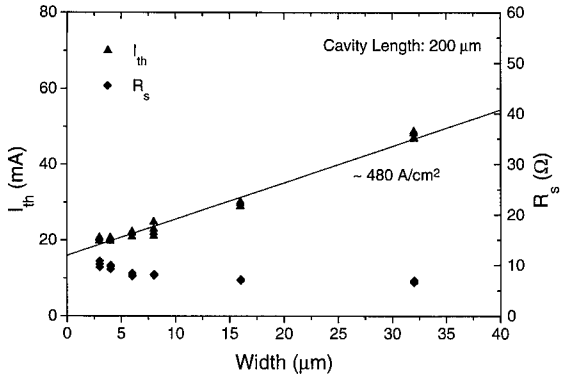

Fig. 3. Threshold currents and series resistances of 3-QW-lasers grown on top of a HEMT structure with mesa widths between 3 and 32 μm and a cavity length of 200 μm.

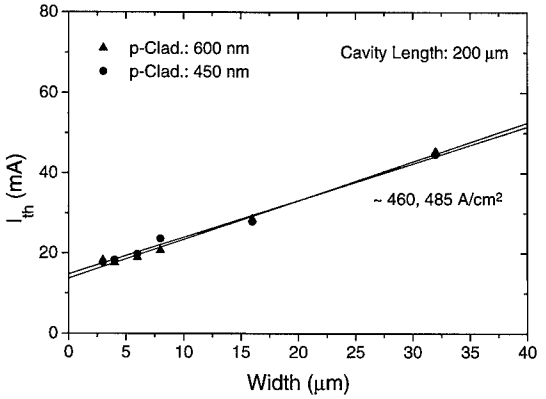

Fig. 4. Threshold currents of 3-QW-lasers grown on top of a HEMT structure with 450 and 600 nm p-cladding thicknesses.

were doped as reported above with the exception of the p-graded and the cap layers which were doped throughout with 2×10^{18} cm^{-3}. This was done to keep Be diffusion into the active region to a minimum. Fig. 4 shows the results for laser diodes with a cavity length of 200 μm and widths between 3 and 32 μm. Threshold current densities below 485 A/cm^2 were found for both p-cladding thicknesses of 600 and 450 nm, respectively. R_s were above 30 Ω as expected. Nevertheless, no increase in j_{th} was observed upon reducing the cladding layer thickness by 150 nm.

3. Conclusion

Vertically compact $Al_xGa_{1-x}As$/GaAs laser structures grown on top of HEMT structures with $Al_{0.3}Ga_{0.7}As$/AlAs SPSL-cladding layers were grown by MBE. We found an exponential dependence of series resistance R_s on AlAs and $Al_{0.3}Ga_{0.7}As$ SPSL-layer thickness at ambient temperature. Laser-HEMT structures suitable for high-frequency performance were grown and processed. A threshold current density of 480 A/cm^2 was reached for a 3-QW-laser grown on top of a low-temperature grown HEMT. Laser-HEMT structures grown with different p-cladding thicknesses showed no increase in threshold current density upon reducing the cladding layer by 150 nm. This clearly demonstrates that laser structures for monolithic integration can be designed even more compact when the p-doping profile is chosen in a way that p-dopants are kept from diffusing into the active region.

Acknowledgements

The authors wish to thank T. Jakobus and his process technology group. Especially, the work of C. Buchgeister, J. Daleiden, S. Klußmann, E. Olander and G. Schilli is acknowledged. The "Bundesministerium für Bildung, Wissenschaft, Forschung und Technologie" is acknowledged for financial support.

References

[1] K. Köhler, Appl. Surf. Sci. 100/101 (1996) 383.
[2] A. Gaymann, M. Maier, W. Bronner, N. Grün and K. Köhler, Mater. Sci. Eng. B, in press.
[3] W. Bronner, J. Hornung, K. Köhler and E. Olander, in: Gallium Arsenide and Related Compounds, Eds. H.S. Rupprecht and G. Weimann (IOP, Bristol, 1994) p. 461.
[4] J.D. Ralston, I. Esquivias, S. Weisser, D.F.G. Gallagher, P.J. Tasker, E.C. Larkins, J. Rosenzweig, H.P. Zappe, J. Fleissner and D.J. As, SPIE Vol. 1680 (1992) 127.
[5] D.T. Nichols, J. Lopata, W.S. Hobson, N.K. Dutta, P.R. Berger, D.L. Sivco and A.Y. Cho, Electron. Lett. 30 (1994) 490.
[6] S.D. Offsey, P.J. Tasker, W.J. Schaff, L. Kapitan, J.R. Shealy and L.F. Eastman, Electron. Lett. 26 (1990) 350.
[7] J. Hornung, Z.-G. Wang, W. Bronner, E. Olander, K. Köhler, P. Ganser, B. Raynor, W. Benz and M. Ludwig, Electron. Lett. 29 (1993) 1694.

ELSEVIER

Journal of Crystal Growth 175/176 (1997) 903–909

JOURNAL OF CRYSTAL GROWTH

MBE growth of quaternary InGaAlAs layers in InGaAs/InAlAs HBTs to improve device performance

T.R. Block*, J. Cowles, L. Tran, M. Wojtowicz, A.K. Oki, D.C. Streit

TRW Electronics and Technology Division, Redondo Beach, California 90278, USA

Abstract

InAlAs/InGaAs HBTs grown on InP substrates can achieve excellent high-frequency performance but suffer from low breakdown and low current gain due to the small InGaAs bandgap. By replacing the InGaAs collector and/or base with a quaternary InGaAlAs layer the device characteristics are improved. Using an InGaAlAs collector the breakdown voltage is found to increase the breakdown voltage of the device from 15 to 23 V. Using such a layer in both the collector and base has the added benefit of increasing the device current gain from 40 to greater than 60. Current gain can be increased even more dramatically to 88 by using a graded InGaAlAs layer in the base. However, the use of InGaAlAs layers was found to increase the device V_{be} voltage and degrade the RF properties somewhat. These parameters can be traded off and optimized for a given application.

PACS: 68.55.Bd; 85.30.Pq; 73.40.Kp

Keywords: MBE; InGaAs; InGaAlAs; Heterojunction bipolar transistor

1. Introduction

InAlAs/InGaAs HBTs grown on InP substrates can provide high-frequency performance useful in many applications. [1, 2]. However, these devices tend to have low breakdown voltage and low current gain. These limitations can be improved by adding a larger bandgap material to either the collector and/or the base of the device [3, 4]. In this paper we report the effects of using InGaAlAs layers for this purpose. The use of this quaternary allows the bandgap to be varied while keeping the layer lattice matched to the InP substrate. When an InGaAlAs layer is used only in the collector the breakdown voltage is increased but complex graded quaternary layers must be grown surrounding the collector layer and a thin, pulse-doped layer must be added to suppress current blocking [5]. This collector structure has been shown to achieve a combination of high-breakdown and high-frequency performance [6]. Alternatively, both the collector and base layers can be grown at a fixed InGaAlAs concentration. In addition to increasing the breakdown voltage, this structure also increases the device current gain, probably due to a reduction

* Corresponding author.

0022-0248/97/$17.00 Copyright © 1997 Elsevier Science B.V. All rights reserved
PII S0022-0248(96)01236-5

in Auger recombination in the base. In this paper we compare these two approaches, and also the use of a graded composition InGaAlAs layer in the base to reduce the base transit time.

2. HBT device structure and growth

The device wafers for this study were grown in a Gen II modular MBE system using nonIndium-bonded 2-in (1 0 0)InP substrates. All the layers in the structures were grown nominally lattice-matched to the InP substrate with a growth rate of 15 nm/min. The InGaAlAs graded layers were graded in composition by continuously varying the Ga and Al concentrations while maintaining a lattice constant equal to that of the InP substrate. Substrate temperatures in the vicinity of 500°C were used for the growth of the different layers. Growth conditions were optimized to reduce any Be diffusion from the base into the emitter. All the layers except the base were doped n-type using a Si doping source.

The wafers grown for this study consisted of variations on two basic profiles shown in Figs. 1 and 2. In Fig. 1 the structure for a pulse-doped InGaAlAs collector with graded InGaAlAs layers and an InGaAs base is shown. This profile consists of an n^+ InGaAs subcollector layer followed by an n^+ InGaAlAs layer graded in composition to the desired InGaAlAs collector composition. The collector layers consist of an n^- InGaAlAs collector layer followed by a 10 nm InGaAlAs layer doped in the mid-10^{17} range to compensate the quasi-field generated by the subsequent InGaAlAs layer graded in composition to the InGaAs base. The base region consisted of an 80 nm InGaAs base doped with Be to a level of 3×10^{19} cm^{-3} and an InGaAs spacer layer. The emitter consisted of a graded InGaAlAs layer, followed by an InAlAs emitter and a heavily Si-doped InGaAs contact layer. The quaternary collector of this device is used to increase the breakdown voltage of the device while the pulse-doping serves to reduce current blocking effects as we described in an earlier publication [5]. With this structure we used Al compositions of $In_{0.53}(Ga_{0.5}Al_{0.5})_{0.47}As$, $In_{0.52}(Ga_{0.25}Al_{0.75})_{0.48}As$, and $In_{0.52}Al_{0.48}As$.

In Fig. 2 is shown the alternate structure which is formed by growing a relatively low Al-composition InGaAlAs layer for both the collector and base, avoiding the need for both the graded-composition layer at the base collector junction and the pulse-doped layer. The aluminum composition of the

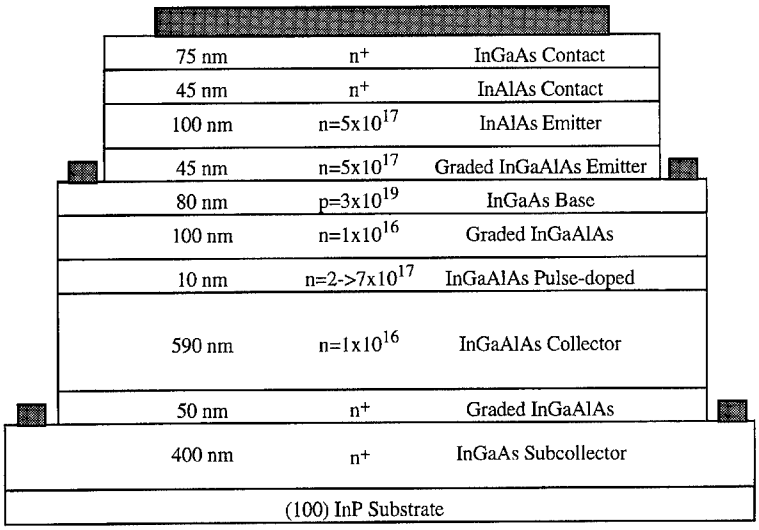

Fig. 1. Schematic cross-section of InP-based, InGaAlAs pulse-doped collector HBT.

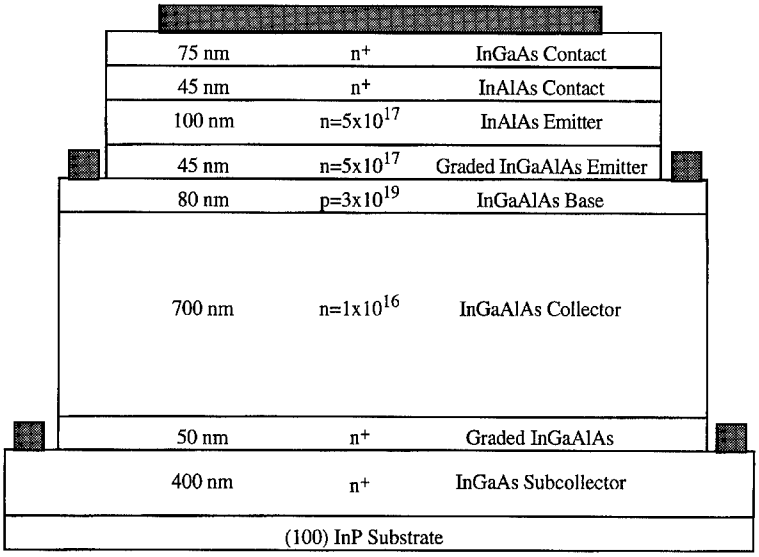

Fig. 2. Schematic cross-section of InP-based, InGaAlAs base and collector HBT.

collector–base layers was chosen to give bandgap energy of 0, 50, 100, and 200 meV greater than InGaAs. This corresponds to Al compositions of $x = 0$, 0.07, 0.15, and 0.29 for $In_{0.53}(Ga_yAl_x)_{0.47}As$ [7]. Except for the $x = 0.29$ wafer, the remainder of the structure is the same as the pulse-doped structure of Fig. 1. For the $x = 0.29$ wafer the Al composition of the initial emitter layer was increased to preserve the step in Al composition at the base–emitter junction.

An additional wafer was grown using the pulse-doped collector layers shown in Fig. 1 but with a graded-composition InGaAlAs base. For this sample the base was graded from $In_{0.53}Ga_{0.47}As$ at the base–collector junction to $In_{0.53}(Ga_{0.83}Al_{0.17})_{0.47}As$ at the base–emitter junction. This results in a built-in quasi-electric field across the base of $\sim$14.5 kV/cm to reduce the electron transit time.

3. Material characterization

After growth, the samples were analyzed with double-crystal X-ray diffraction (DXRD) and Photoreflectance (PR). Representative DXRD spectra for some of these samples is shown in Fig. 3. These spectra indicate very close lattice-matching of all layers, typically to within 100 arcsec of the InP substrate, which corresponds to a difference in composition equivalent to that between $In_{0.530}Ga_{0.470}As$ and $In_{0.525}Ga_{0.475}As$. This extremely accurate and precise control over composition and lattice-constant is made possible by MBE.

Representative PR spectra taken from some of these samples are shown in Fig. 4. As discussed in a previous publication [6], these spectra provide information on both the compositions of the various layers and the built-in electric fields. For the samples with a constant composition base and collector, the spectral region between 0.7 and 1 eV displays an oscillation related to the base-collector junction. This oscillation corresponds to an energy gap in the base of 0.82, 0.86, and 0.98 eV which gives bandgap shifts referenced to $In_{0.53}Ga_{0.47}As$ of approximately 70, 110, and 230 meV, respectively. The remaining oscillations in the spectra arise from the base-emitter layers of the device [8]. The oscillations for Al compositions of 0, 0.07, and 0.15 are all very similar as can be seen in Fig. 4. This is in contrast to the sample with the Al concentration of 0.29 which displays differences due to the alternate emitter grading described above.

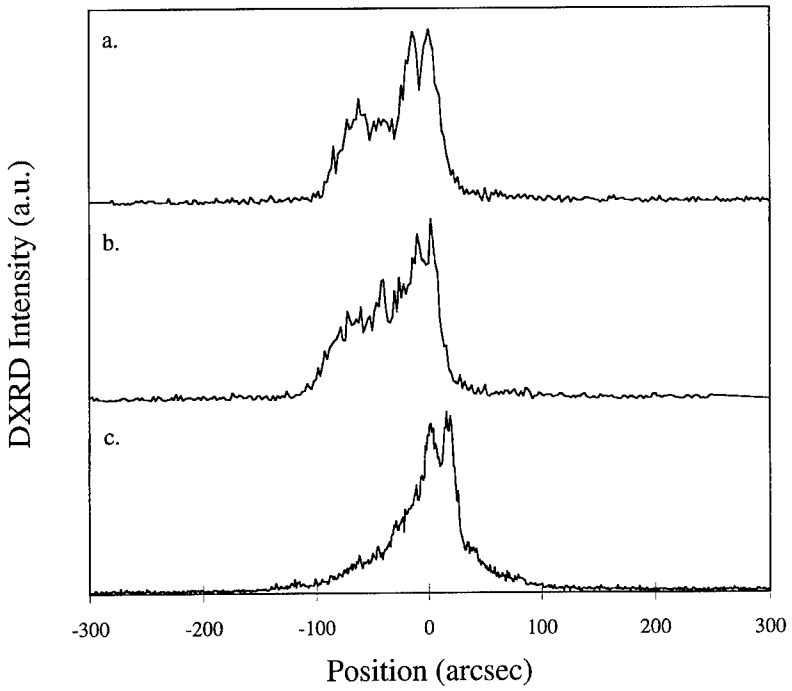

Fig. 3. Representative double-crystal X-ray diffraction spectra from HBT structures: (a) $In_{0.53}(Ga_{0.93}Al_{0.07})_{0.47}As$ base and collector sample, (b) $In_{0.53}(Ga_{0.85}Al_{0.15})_{0.47}As$ base and collector sample, and (c) $In_{0.53}(Ga_{0.83}Al_{0.17})_{0.47}As$ graded base with $In_{0.53}(Ga_{0.5}Al_{0.5})_{0.47}As$ collector. These spectra indicate control of the nominal In composition to 0.530 ± 0.005.

The PR spectra for the graded-composition base device was found to be very similar to the pulse-doped PR spectra. It displayed a high-field oscillation near 0.8 eV associated with the graded base and also displayed collector and emitter oscillations identical to that of a $In_{0.53}(Ga_{0.5}Al_{0.5})_{0.47}As$ collector sample with an InGaAs base.

4. Device performance

The use of InGaAlAs layers in either the collector or in base and collector dramatically improved the DC characteristics of the HBT devices as can be seen in Table 1. The most noticeable improvement is an increase in device breakdown voltage BV_{cbo}. For the pulse-doped collector BV_{cbo} can be increased from 15 V for an InGaAs collector to over 23 V for an InAlAs collector. The devices of Fig. 2 with both a quaternary base and collector showed an even larger increase in breakdown voltage with Al composition as can be seen in Fig. 5. Here BV_{cbo} is again seen to increase to 23 V, but at a composition of only $In_{0.53}(Ga_{0.71}Al_{0.29})_{0.47}As$. This is due to the higher composition at the base–collector junction in these structures compared to the pulse-doped samples.

An additional benefit to be gained by using the InGaAlAs base and collector profile of Fig. 2 is the increase in current gain, from $\beta = 40$ for an InGaAs base to greater than $\beta = 60$ for the $In_{0.53}(Ga_{0.71}Al_{0.29})_{0.47}As$ base plus collector device. We attribute this increase in current gain to a reduction of Auger recombination in the larger bandgap base. In addition, for the $In_{0.53}(Ga_{0.71}Al_{0.29})_{0.47}As$ sample the alternate emitter grading may also be contributing to higher beta. To increase the current gain beyond these levels, the base was compositionally graded from $In_{0.53}Ga_{0.47}As$ to $In_{0.53}(Ga_{0.83}Al_{0.17})_{0.47}As$ over the 80 nm base. The resulting built-in field substantially reduced the base transient time as can

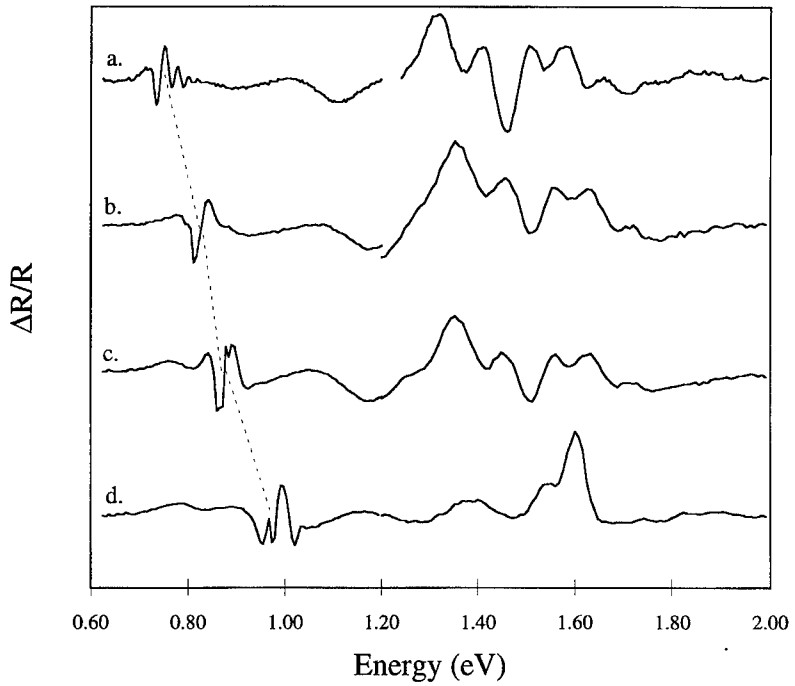

Fig. 4. PR spectra for samples with base and collector compositions of (a) $In_{0.53}Ga_{0.47}As$, (b) $In_{0.53}(Ga_{0.93}Al_{0.07})_{0.47}As$, (c) $In_{0.53}(Ga_{0.85}Al_{0.15})_{0.47}As$, and (d) $In_{0.53}(Ga_{0.71}Al_{0.29})_{0.47}As$. Dashed line highlights the oscillation from the base region.

Table 1
DC parameters for 75 × 75 μm HBT device fabricated from the different profiles

Profile	Peak β	BV_{cbo} (V)	Base sheet (Ω/sq)	V_{be} at 1 μA (V)
$In_{0.53}Ga_{0.47}As$ collector + base	40	15	460	0.320
$In_{0.53}(Ga_{0.93}Al_{0.07})_{0.47}As$ collector + base	43	19	490	0.363
$In_{0.53}(Ga_{0.85}Al_{0.15})_{0.47}As$ collector + base	47	22	545	0.411
$In_{0.53}(Ga_{0.71}Al_{0.29})_{0.47}As$ collector + base	62	23	627	0.509
$In_{0.53}(Ga_{0.50}Al_{0.50})_{0.47}As$ collector	38	20	460	0.320
$In_{0.52}(Ga_{0.25}Al_{0.75})_{0.48}As$ collector	41	21	460	0.343
$In_{0.52}Al_{0.48}As$ collector	40	23.5	460	0.338
$In_{0.53}(Ga_{0.50}Al_{0.50})_{0.47}As$ collector + graded $In_{0.53}(Ga_{0.83}Al_{0.17})_{0.47}As$ base	88	16	480	0.405

be seen from the large increase in current gain to 88.

The breakdown and current gain benefits to be gained from the insertion of the InGaAlAs collector and base layers must be traded off against an increase in the device V_{be}, base sheet resistance, and also a reduction in the RF properties. As can be seen again from Table 1, the addition of Al to the InGaAs base results in an increase in the V_{be} of the devices which scales directly with the increase in bandgap at the base–emitter junction. For the quaternary base and collector devices we see increases in V_{be} of 43, 91, and 189 meV compared to the measured increases in bandgap using PR of 70,

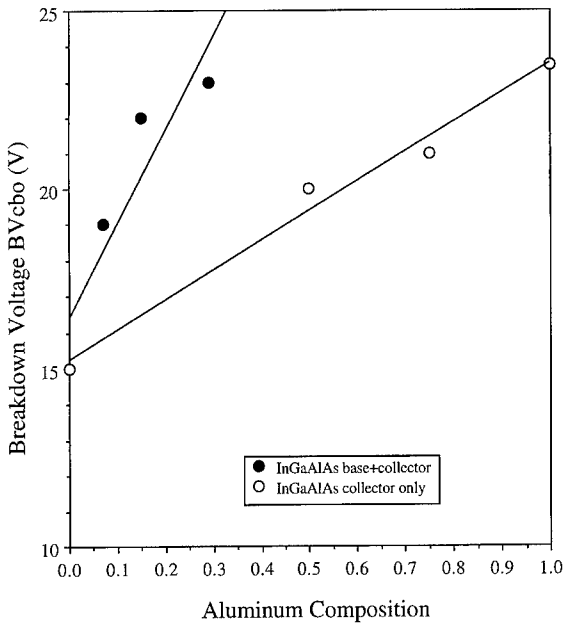

Fig. 5. Variation in BV_{cbo} with aluminum concentration for a 75 × 75 μm HBT device. Closed circles represent InGaAlAs base and collector devices while open circles represent InGaAlAs collector only devices.

110, and 230 meV. For the graded base structure we see an increase in V_{be} of 85 meV for a nominal increase in bandgap of 116 meV at the base–emitter junction. The base sheet resistance also increased from 460 Ω/sq for an InGaAs base to 627 Ω/sq for an $In_{0.53}(Ga_{0.71}Al_{0.29})_{0.47}As$. In terms of base–emitter properties the graded base is clearly superior with close to twice the current gain of the comparable $In_{0.53}(Ga_{0.85}Al_{0.15})_{0.47}As$ base and smaller increases in V_{be} and base sheet resistance.

A major concern in the use of the quaternary InGaAlAs in the collector of the device is the effects of current blocking, which limits the RF performance of the device. Small (1 × 10 μm) dual emitter devices were fabricated to look at the impact of the quaternary collector on RF performance. The resulting performance is shown in Table 2. In Table 2 it can be seen that the addition of any amount of Al results in a drop in both f_T and f_{max}. For the InGaAlAs base and collector samples f_T drops off to 50 GHz compared to 80 GHz for a pure InGaAs base and collector. At the same time the current density at which the f_T curve rolls over also drops substantially from 100 to 35 kA/cm^2. Similar reductions in f_T, f_{max}, and J_{max} can be seen in Table 2 for the InGaAlAs collector only samples.

From these results it is clear that the addition of Al to both the collector and base results in a relatively large degradation of device performance, particularly in decreasing the current at which the f_T curve rolls over. Presumably a lower electron saturation velocity in InGaAlAs compared to InGaAs is the cause of this effect. The plot of f_T with Al concentration shown in Fig. 6 indicates the severity of the decrease in f_T particularly for the quaternary base plus collector structures. Note also that the graded base device contained a $In_{0.53}(Ga_{0.50}Al_{0.50})_{0.47}As$ collector which consequently limited its RF performance. The combination of such a graded base with an InGaAs

Table 2
RF parameters for 1 μm × 10 μm HBT device fabricated from the different profiles

Profile	Peak f_T (GHz)	Peak f_{max} (GHz)	J_{max} at 1.5 V (kA/cm^2)
$In_{0.53}Ga_{0.47}As$ collector + base	80	180	100
$In_{0.53}(Ga_{0.93}Al_{0.07})_{0.47}As$ collector + base	64	130	50
$In_{0.53}(Ga_{0.85}Al_{0.15})_{0.47}As$ collector + base	50	105	35
$In_{0.53}(Ga_{0.71}Al_{0.29})_{0.47}As$ collector + base	50	94	35
$In_{0.53}(Ga_{0.50}Al_{0.50})_{0.47}As$ collector	57	140	45
$In_{0.52}(Ga_{0.25}Al_{0.75})_{0.48}As$ collector	49	–	–
$In_{0.52}Al_{0.48}As$ collector	40	–	–
$In_{0.53}(Ga_{0.50}Al_{0.50})_{0.47}As$ collector + graded $In_{0.53}(Ga_{0.83}Al_{0.17})_{0.47}As$ base	56	126	40

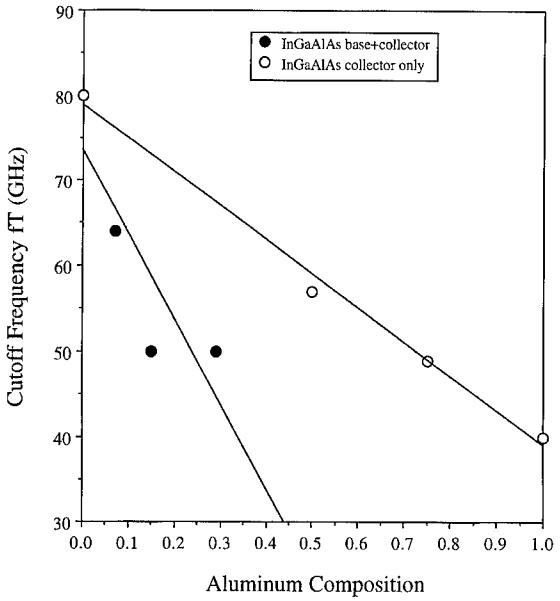

Fig. 6. Variation in f_T with aluminum concentration for a 1×10 μm HBT device. Closed circles represent InGaAlAs base and collector devices while open circles represent InGaAlAs collector only devices.

collector should in principle give good RF performance and high current gain with the tradeoff of lower breakdown and somewhat higher V_{be}.

5. Summary and conclusions

In summary, we presented here the material characteristics and device performance of quaternary InGaAlAs HBT profiles that have optimized different device parameters such as high current gain, high breakdown, and high frequency performance. These complex structures were created using MBE growth with its demonstrated ability to produce complex graded layers with excellent control of lattice-matching to the InP substrate. Photoreflectance spectra were used to determine the post-growth compositions of the layers and to demonstrate the reproducibility of the base–emitter layers. The use of InGaAlAs in the collector only or in both the base and collector was found to substantially increase the breakdown voltage of the device. Use of a quaternary InGaAlAs layer in the base was also found to increase the device current gain compared to an InGaAs base, while a more substantial increase in the gain was achieved by grading the Al composition of the base. These performance benefits were found to come at a cost of an increase in device V_{be} and a degradation of RF performance. This presents the opportunity of tailoring the use of these layers for applications where some tradeoff in V_{be} and RF performance is acceptable and a large advantage is to be gained from higher breakdown and larger current gain.

Acknowledgements

The authors wish to thank and acknowledge the assistance of An-Chih Han, Anita Anderson, Tim Naeole, Veronica Zamora, and Leniza Go in the fabrication and characterization of the various structures.

References

[1] K.W. Kobayashi, L.T. Tran, S. Bui, J. Velebir, D. Nguyen, A.K. Oki and D.C. Streit, IEEE 1993 Microwave and Millimeter-wave Monolithic Circuits Symp. Digest 85 (1993).
[2] K.W. Kobayashi, L.T. Tran, J.C. Cowles, T.R. Block, A.K. Oki and D.C. Streit, IEEE Trans. Microwave Theory Tech. 44 (1996) 739.
[3] M. Hafizi, T. Liu, P.A. Macdonald, M. Lui, P. Chu, D.B. Rensch, W.E. Stanchina and C.S. Wu, Int. Elec. Dev. Mtg. IEDM-93 (1993) 791.
[4] K. Kurishima, H. Nakajima, T. Kobayashi, Y. Matsuoka and T. Ishibashi, Appl. Phys. Lett. 62 (1993) 2372.
[5] J.Cowles, L.Tran, T. Block, D. Streit and A. Oki, 53rd Device Res. Conf., Charlottesville, VA (1995) pp. 84–85.
[6] T.R. Block, M. Wojtowicz, J. Cowles, L. Tran, A.K. Oki and D.C. Streit, J. Vac. Sci. B 14 (1996) 2221.
[7] R.F. Kopf, H.P. Wei, A.P. Perley and G. Livescu, Appl. Phys. Lett. 60 (1992) 2386.
[8] M. Wojtowicz, T.R. Block, D. Pascua, A.-C. Han and D.C. Streit, Proc. 8th InP and Related Materials Conf. (1996) Schwäbisch-Gmünd, Germany, pp. 576–577.

ELSEVIER

Journal of Crystal Growth 175/176 (1997) 910–914

JOURNAL OF CRYSTAL GROWTH

Improved hole transport properties of highly strained $In_{0.35}Ga_{0.65}As$ channel double-modulation-doped structures grown by MBE on GaAs

Makoto Kudo*, Hidetoshi Matsumoto, Takuma Tanimoto, Tomoyoshi Mishima, Isao Ohbu

Central Research Laboratory, Hitachi, Ltd., 1-280, Higashi-Koigakubo, Kokubunji-shi, Tokyo 185, Japan

Abstract

Hole transport properties have been improved by using highly strained $In_{0.35}Ga_{0.65}As$ channel double-modulation-doped heterostructures grown by molecular beam epitaxy. This structure provided both a high mobility of 354 $cm^2/(V\,s)$ and a high sheet hole concentration of $1.23 \times 10^{12}\,cm^{-2}$ at room temperature. Double-modulation-doped field effect transistors with a 0.4-μm gate length and a 20-μm gate width were fabricated. Transconductance of 118 mS/mm, which is about 1.5 times higher than that of single-modulation-doped field-effect transistors, was obtained at room temperature.

1. Introduction

To obtain high performance complementary GaAs-based circuits, which have the potential to provide low power-consumption and high-efficiency operation, improved transconductance in the p-channel field-effect transistors (FETs) is needed. The hole transport properties of GaAs-based p-channel FETs can be improved by using a strained InGaAs layer as a channel due to the strain-induced splitting of the valence band [1]. This splitting decreases the average hole effective mass whose momentum vector is parallel to the channel, and increases the hole mobility. Thus, greater splitting is desired so that a larger concentration of light holes can act as carriers.

To increase the strain-induced separation between light- and heavy-hole bands, the In content of the InGaAs layers needs to be increased. However, growing high quality $In_xGa_{1-x}As$ layers ($x \geqslant 0.3$) on GaAs substrates has been difficult due to the surface segregation of In atoms, even when the layer thickness is less than the critical thickness [2].

Recently, it was reported that the In content of InGaAs layers pseudomorphically grown on GaAs substrates could be raised above 0.3 by optimizing the growth condition [3, 4]. These highly strained layers improved the electron transport properties; mobility of over 6500 $cm^2/(V\,s)$ and sheet electron concentration of $2.94 \times 10^{12}\,cm^{-2}$ were obtained

* Corresponding author. Fax: +81 423 27 7679; e-mail: mkudo@crl.hitachi.co.jp.

0022-0248/97/$17.00 Copyright © 1997 Elsevier Science B.V. All rights reserved
PII S0022-0248(96)00884-6

from highly strained AlGaAs/InGaAs modulation-doped structures [3].

We previously showed that hole transport properties are also improved by using this highly strained layer as a channel of a p-type double-modulation-doped (D-MOD) $Al_{0.39}Ga_{0.61}As$/GaAs/$In_{0.35}Ga_{0.65}As$ heterostructure [5]. We obtained a mobility of 284 $cm^2/(V\,s)$ and a sheet hole concentration of 1.84×10^{12} cm^{-2}.

In this paper, we show that the hole mobility can be further improved by optimizing the growth conditions. We also discuss our results from testing fabricated p-channel double-modulation-doped field-effect transistors (D-MODFETs) that use the highly strained $In_{0.35}Ga_{0.65}As$ layer as a channel.

2. Experimental details

All samples for this study were grown with an ANELVA 850 V conventional solid-source molecular beam epitaxy (MBE) system. Before growing the FET structures, we grew three types of samples to check the quality of the epitaxial layers, whose structures are shown in Fig. 1. The thermal cleaning temperature of the semi-insulating (1 0 0) GaAs substrates was 600°C in an As_4 flux of 1×10^{-5} Torr. The substrate temperature for the growth of the 200-nm-thick undoped GaAs and 100-nm-thick undoped AlGaAs (Al content: 0.39) buffer layers was 580°C. This was reduced to 500°C after growing the buffer layers to suppress the Be surface segregation. After growing a 5-nm-thick p-AlGaAs, a d_{sp}-nm-thick undoped AlGaAs and a 2-nm-thick undoped GaAs layer, the substrate temperature was further reduced to 420°C to suppress the In surface segregation. After growing a 6-nm-thick InGaAs (In content: 0.35) layer and 2-nm-thick undoped GaAs layer, the growth temperature was increased to 500°C and a d_{sp}-nm-thick undoped AlGaAs, a 6-nm-thick p-AlGaAs, and a 10-nm-thick undoped AlGaAs layer, plus a 10-nm-thick p-GaAs cap, were grown at 500°C. The growth temperature was changed with a 2–5-min growth interruption under As_4 flux. The growth temperature of 420°C is optimum for the growth of pseudomorphic $In_xGa_{1-x}As$ layers on GaAs with a high In content of 0.35 [6], and 500°C is the upper limit for the growth of a Be-doped AlGaAs layer in which the segregation and/or diffusion of the Be atom is suppressed to the order of 3–4 monolayers [7]. The Be concentration of the carrier-supplying layer below the channel was 1.5×10^{18} cm^{-3}, while the Be concentration of the carrier-supplying layer above the channel was either 5×10^{18} cm^{-3} (sample 1) or 3×10^{18} cm^{-3} (sample 2 and 3). The thickness of the AlGaAs spacer was 4 nm (sample 1 and 2) or 8 nm (sample 3). The GaAs growth rate was fixed at 1.0 μm/h. The In content was calibrated by photoluminescence (PL) measurements at 77 K using an InGaAs/GaAs single quantum well structure [8] and the Al content was calibrated in the same way using a thick AlGaAs layer.

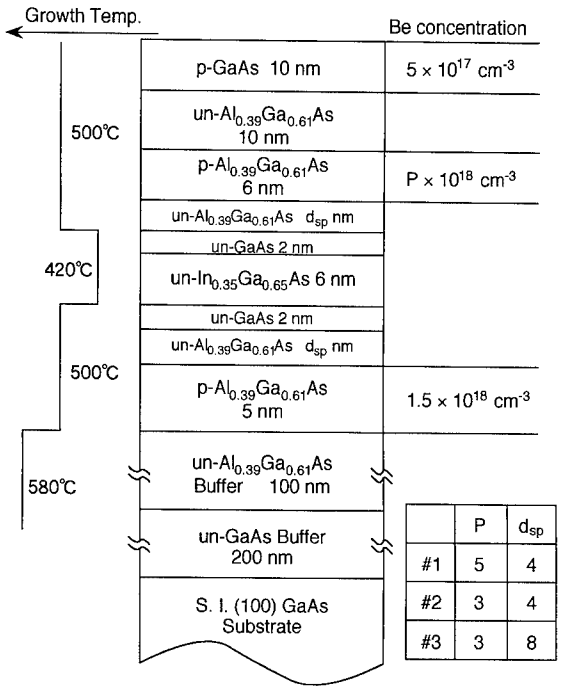

Fig. 1. Schematic cross section of a D-MOD pseudomorphic heterostructure to check the quality of the highly strained channel.

The mobility and sheet hole concentration of these samples were evaluated by the conventional van der Pauw method at room temperature (RT).

The layer structure (from the substrate) of the p-channel D-MODFET consists of 200-nm-thick

undoped GaAs, 100-nm-thick undoped AlGaAs (Al content: 0.39), 4-nm-thick p-AlGaAs (sample 4: 2.1×10^{18} cm^{-3}, sample 5: 4.2×10^{18} cm^{-3}, Notice that doping concentration was increased to cancel the process damage while the gate recess), 3-nm-thick undoped AlGaAs, 2-nm-thick undoped GaAs, 6-nm-thick undoped InGaAs (In content: 0.35), 2-nm-thick undoped GaAs, 3-nm-thick undoped AlGaAs, 4-nm-thick p-AlGaAs (1.5×10^{19} cm^{-3}), 11-nm-thick undoped AlGaAs, 20-nm-thick undoped GaAs, 3-nm-thick undoped AlGaAs and 160-nm-thick p-GaAs (4×10^{19} cm^{-3}).

A single modulation-doped field effect transistor (S-MODFET) was also fabricated as a reference (sample 6). The layer structure was the same as that of the D-MODFET except that the GaAs buffer layer was 300 nm thick, and the 100-nm-thick undoped AlGaAs and the 4-nm-thick p-AlGaAs layers were not grown.

Conventional mesa isolation, nonalloyed ohmic contacts for source and drain, and a double recessed gate process were used in the device fabrication. The gate lengths were 0.4 or 1.75 μm, and the gate width was 20 μm.

3. Results and discussion

The mobility of the D-MOD structure as a function of sheet hole concentration is shown in Fig. 2. The results of previously reported p-channel modulation-doped heterostructures [5, 9, 10] are also plotted for comparison. Very high mobility of 354 cm^2/(V s) was obtained at a sheet hole concentration of 1.23×10^{12} cm^{-2} (sample 3). At a higher concentration of 2.88×10^{12} cm^{-2}, still higher mobility of 276 cm^2/(V s) was obtained (sample 1). As far as we know, these mobilities are the highest yet reported at these hole concentrations. These high mobilities were achieved by individually optimizing the growth temperatures of each layer. This confirms that the Be segregation and/or the diffusion length at 500°C was smaller than the spacer thickness of 4 nm. The discrepancy in the mobility between this work and our previous report [5] is due to the different growth temperature used for the carrier-supplying layer. In our previous report, the growth temperature for the carrier-supplying layer

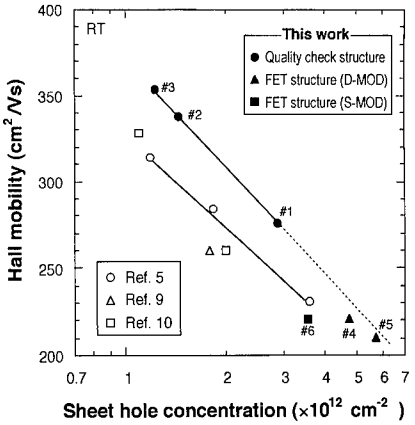

Fig. 2. RT Hall mobility of p-channel modulation-doped pseudomorphic heterostructures as a function of sheet hole concentration. The results of the FET structures (samples 4–6) were measured after removing the 160-nm-thick p-GaAs capping layer by reactive ion etching. The lines are guides for the eyes.

(420°C) appears to have been too low to maintain good crystalline quality in the AlGaAs layers.

The typical current–voltage characteristic of the highly strained InGaAs channel D-MODFET and the extrinsic transconductance and drain current as a function of gate bias at room temperature are shown in Fig. 3. These figures show that this D-MODFET offers good FET characteristics. At a gate length of 0.4 μm, the maximum extrinsic transconductance exceeded 100 mS/mm constantly in the 3-in. wafer used to fabricate the FETs. The highest value of extrinsic transconductance reached in this work was 118 mS/mm at a gate length of 0.4 μm (sample 5). The source resistance was about 5 Ω mm.

The relation between transconductance and gate length is shown in Fig. 4. The results from the S-MODFETs and other p-channel FETs [1, 9–14] are also plotted for comparison. To our knowledge, the transconductance of 118 mS/mm is the highest yet reported. This shows that highly strained D-MODFET structures can be used to improve the performance of p-channel FETs.

Transconductance of 82 mS/mm was obtained for the S-MODFET (sample 6) at a gate length of 0.4 μm. This difference in the transconductances

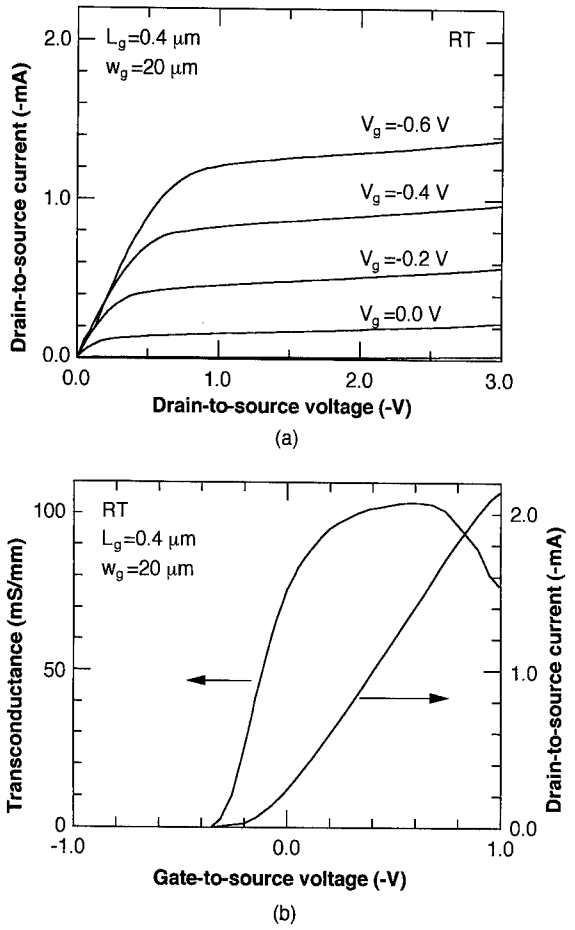

Fig. 3. (a) The typical current–voltage characteristic of the highly strained InGaAs channel D-MODFET, and (b) extrinsic transconductance and drain current as a function of gate bias at RT (sample 4).

between the D-MODFET and the S-MODFET was due to the difference in the maximum carrier concentration that could be accumulated in the channel while maintaining high mobility. It is difficult for S-MOD structures to maintain high mobility (above 260 $cm^2/(V\,s)$) at sheet hole concentrations exceeding $2\times10^{12}\,cm^{-2}$ [5]. The improved carrier confinement in the channel also improved the transconductance of the D-MODFETs, while S-MODFETs do not have a potential barrier below the channel (only a GaAs buffer layer exists between the channel and the substrate).

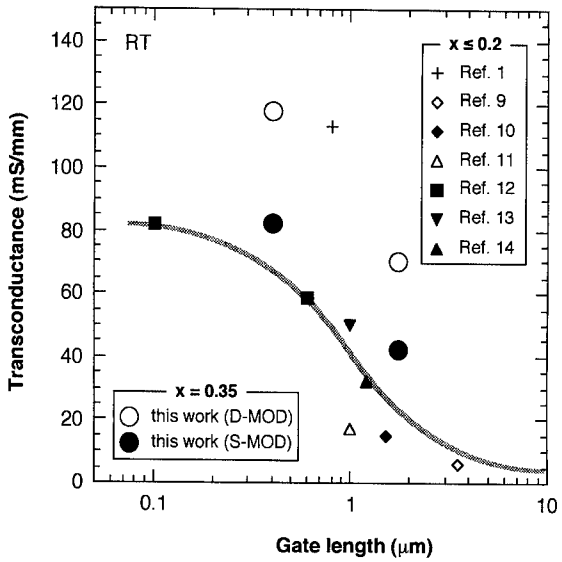

Fig. 4. The relation between transconductance and gate length at RT. The curve is a guide for the eyes.

4. Conclusions

A highly strained $In_{0.35}Ga_{0.65}As$ layer can be used as a channel in p-type AlGaAs/InGaAs D-MOD heterostructures grown on GaAs substrates by MBE. Having grown such a structure, we obtained a high mobility of 354 $cm^2/(V\,s)$ and a high sheet hole concentration of $1.23\times10^{12}\,cm^{-2}$ at room temperature. At a higher concentration of $2.88\times10^{12}\,cm^{-2}$, a still higher mobility of 276 $cm^2/(V\,s)$ was obtained. These high mobilities were achieved by individually optimizing the growth temperatures used for each layer.

The transconductance of a D-MODFETs with a 0.4-μm gate length and a 20-μm gate width reached 118 mS/mm. To our knowledge, this is the highest transconductance yet reported.

Acknowledgements

We wish to express our gratitude to Dr. Tohru Nakamura and Dr. Masanobu Miyao of the Hitachi Central Research Laboratory for their continuous encouragement throughout this study.

References

[1] P.P. Ruden, M. Shur, D.K. Arch, R.R. Daniels, D.E. Grider and T.E. Nohava, IEEE Trans. Electron Devices 36 (1989) 2371.
[2] H. Toyoshima, T. Niwa, J. Yamazaki and A. Okamoto, Appl. Phys. Lett. 63 (1993) 821.
[3] M. Kudo, T. Mishima and M. Washima, Appl. Phys. Lett. 64 (1994) 628.
[4] H. Toyoshima, T. Niwa, J. Yamazaki and A. Okamoto, J. Appl. Phys. 75 (1994) 3908.
[5] M. Kudo, T. Mishima, H. Matsumoto, I. Ohbu and T. Tanimoto, J. Electron. Mater. 25 (1996) 944.
[6] M. Kudo, T. Mishima and M. Washima, J. Crystal Growth 150 (1995) 1236.
[7] E.F. Schubert, J. Vac. Sci. Technol. A8 (1990) 2980.
[8] M. Kudo and T. Mishima, J. Appl. Phys. 78 (1995) 1685.
[9] T.J. Drummond, T.E. Zipperian, I.J. Fritz, J.E. Schirber and T.A. Plut, Appl. Phys. Lett. 49 (1986) 461.
[10] R.T. Hsu, W.C. Hsu, J.S. Wang, M.J. Kao, Y.H. Wu and J.S. Su, Jpn. J. Appl. Phys. 35 (1996) 2085.
[11] C.-P. Lee, H.T. Wang, G.J. Sullivan, N.H. Sheng and D.L. Miller, IEEE Electron Device Lett. EDL-8 (1987) 85.
[12] T. Tanimoto, M. Yamane, S. Goto and Y. Uchida, Trans. IEICE E 73 (1990) 1849.
[13] J.K. Abrokwah, J.-H. Huang, W.J. Ooms and J.A. Hallmark, IEEE Trans. Electron Devices 40 (1993) 278.
[14] A.G. Baca, T.E. Zipperian, A.J. Howard, J.F. Klem and C.P. Tigges, Appl. Phys. Lett. 65 (1994) 752.

ELSEVIER

Journal of Crystal Growth 175/176 (1997) 915–918

JOURNAL OF CRYSTAL GROWTH

MBE growth of double-sided doped InAlAs/InGaAs HEMTs with an InAs layer inserted in the channel

M. Sexl*, G. Böhm, D. Xu, H. Heiß, S. Kraus, G. Tränkle, G. Weimann[1]

Walter-Schottky-Institut, Technische Universität München, D-85748 Garching, Germany

Abstract

InAlAs/InGaAs high electron mobility transistors (HEMTs) with an InAs layer inserted in the $In_{0.53}Ga_{0.47}As$ channel were grown on InP-substrates by solid source molecular beam epitaxy (MBE). By optimizing position, thickness and growth temperature of the InAs layer, the mobility at 300 K has been increased by 47%. HEMTs with a gate length of 0.15 μm showed very high transconductances and cut-off frequencies f_T in excess of 1270 mS/mm and 235 GHz, respectively.

PACS: 81.05.Ea; 81.15.Hi

Keywords: MBE; HEMT; InGaAs; InAlAs; InAs

1. Introduction

InP-based InAlAs/InGaAs high electron mobility transistors (HEMTs) have demonstrated excellent high-frequency and low-noise performance. These are explained by the high electron mobility, saturation drift velocity and sheet carrier density of the InAlAs/InGaAs two-dimensional electron gas (2DEG) system. In this work we investigate InAlAs/InGaAs HEMTs with a thin InAs layer inserted into the InGaAs channel. This structure improves the electron transport properties. We optimized the structure by changing the position, thickness and growth temperature of the InAs layer.

In conventional HEMT structures high contact and sheet resistances in the access regions between alloyed contact and gate electrode can cause large parasitic source and drain resistances. This is effected by the large conduction band discontinuity between the InGaAs cap layer and InAlAs supply layer, forming a barrier in the current flow between these layers. We demonstrate that an additional Si-δ-doping at the interface of the cap and supply layer reduces the barrier heights and lowers the parasitic resistances, leading to excellent DC and RF characteristics.

* Corresponding author. Fax: + 49 89 320 6620; e-mail: mas@e26.physik.tu-muenchen.de.

[1] Now at: Fraunhofer Institut für Angewandte Festkörperphysik, D-79108 Freiburg, Germany.

0022-0248/97/$17.00 Copyright © 1997 Elsevier Science B.V. All rights reserved
PII S0022-0248(96)01203-1

2. MBE growth of InAs

The heterostructures were grown by solid source MBE on Fe-doped semi-insulating (1 0 0) InP epi-ready substrates with growth rates of the lattice matched InAlAs and InGaAs layers around 1 μm/h, and a V/III ratio of 27 (beam equivalent pressure). Recently [1], we have demonstrated that a channel thickness of 12 nm and double sided δ-doping are essential for low output conductance and kink-free I/V characteristics of lattice-matched HEMTs. Therefore, the HEMT structure consists of a 12 nm wide InGaAs channel, in which a strained InAs layer was embedded, Fig. 1a. Si-δ-doping was used in both InAlAs barriers, with a spacer thickness of 5 nm and a donor concentration of 5×10^{12} and 1.5×10^{12} cm^{-2} in the upper and the lower barrier.

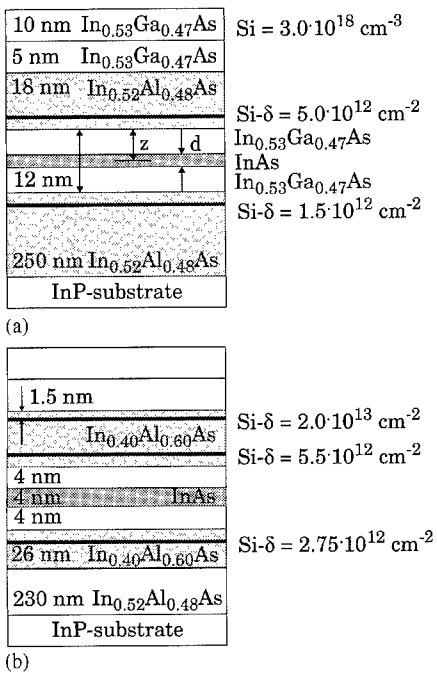

Fig. 1. (a) Layer structure of the conventional double-sided δ-doped HEMT. Sample 1 was grown without InAs for comparison. In sample 2, InAs with 4 nm was symmetrically centered in the InGaAs channel. (b) Modified layer structure for HEMT application: increasing δ-doping concentrations and Al-content in the barriers, introduction of an additional Si-δ-doping at 1.5 nm into the top InAlAs.

The position z of the inserted InAs is the distance between the InAlAs spacer layer and the center of the InAs, ranging from 3 to 9 nm. At two different growth temperatures, 470°C and 420°C, the thickness d of the InAs layer was raised from 2 nm up to 5 nm, keeping the total channel thickness constant.

Hall measurements at 300 and 77 K confirmed the enhanced mobility of the InAs inserted channel HEMT. Fig. 2 shows the correlation between the position z of 2 nm InAs, grown at a substrate temperature of 470°C, and the mobility. The optimized mobility increase was obtained for symmetrically centered InAs layers. Solid lines are plotted to guide the eye, with the assumption that mobility is attributed to scattering due to the ionized impurities and interface roughness of both δ-dopings and interfaces of the channel

$$\frac{1}{\mu} \sim \frac{1}{z} + \frac{1}{t - z}.$$

Compared to the reference sample without InAs, the room temperature mobility is increased from 8500 cm^2 V^{-1} s^{-1} to 10 500 cm^{2}V^{-1} s^{-1} by inserting only 2 nm InAs. Fig. 3 shows the correlation between InAs thickness d, mobility and substrate temperature, where the position is fixed at the center of the channel. For a substrate temperature of 470°C, the largest mobility is achieved for a thickness of 2 nm. It is well known [2] that the critical thickness increases for lower growth temperatures. Therefore, the substrate temperature for

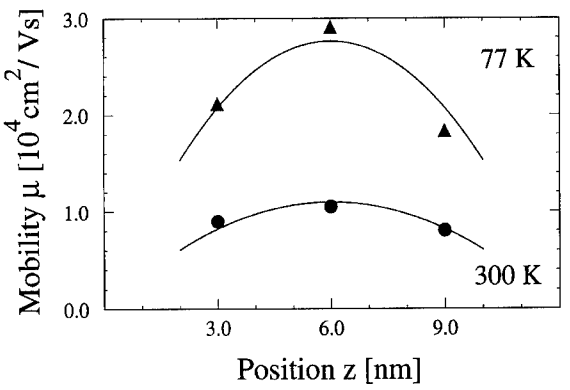

Fig. 2. Correlation between position z of the inserted 2 nm InAs layer and mobility at 77 (triangle) and 300 K (circle).

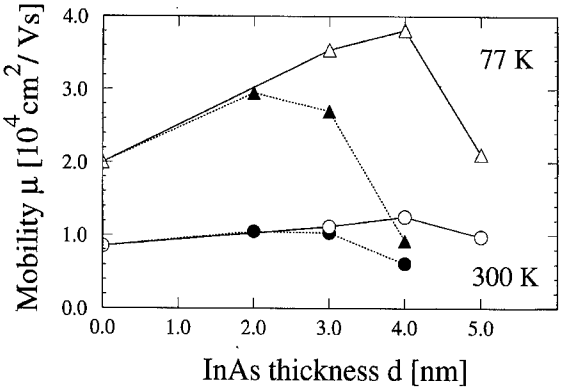

Fig. 3. Correlation between thickness d of the inserted InAs layer ($z = 6$ nm) and mobility at 77 (triangle) and 300 K (circle). Growth temperature was 470°C (dotted lines) and 420°C (solid lines), respectively.

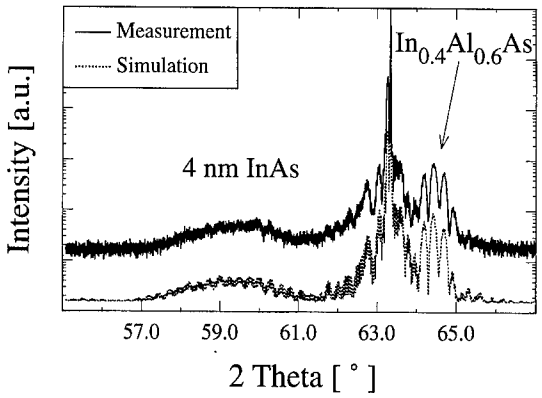

Fig. 4. X-ray diffraction spectra (4 0 0) of the pseudomorphic HEMT (sample no. 3) on InP substrate (solid line: measurement, dotted line: simulation).

the growth of the InGaAs/InAs/InGaAs channel is changed to 420°C. Obviously, the critical thickness is increased, thus allowing successful use of 4 nm InAs resulting in very high mobilities of 38 400 $cm^2 V^{-1} s^{-1}$ and 12 500 $cm^2 V^{-1} s^{-1}$ at 77 K and room temperature, respectively. This mobility is 47% higher than that of the conventional heterostructure without InAs. All these structures had a 2DEG carrier density of around 3.5×10^{12} cm^{-2}.

3. High electron mobility transistor

Thus, having established that, under our growth conditions, 4 nm thick inserted InAs layers give optimized transport properties, we modified the structure for device applications by (i) increasing the δ-doping concentrations to 5.5×10^{12} and 2.75×10^{12} cm^{-2} (ii) increasing the Al-content in the barriers to 0.6 and (iii) introducing an additional Si-δ-doping at the interface of the cap and supply layer, Fig. 1b. This resulted in (i) 2DEG-densities of 5.6×10^{12} cm^{-2} (ii) improved carrier confinement and breakdown voltages and (iii) reduced source and drain resistances.

The control of the different compositions of the strained layers was verified by X-ray diffraction measurements of the HEMT structure, shown in Fig. 4. Simulation of this spectrum using dynamical scattering theory fits the measured curve very well. The appearance of interference fringes and the exact position of the pseudomorphic layers confirm the high material quality.

Shubnikov-de Haas measurements at 4.2 K show that two subbands are occupied with a carrier density of 4.0×10^{12} cm^{-2} in the first and 1.6×10^{12} cm^{-2} in the second subband. Even with this high carrier density, the mobility at 4.2 K is 48 000 $cm^2 V^{-1} s^{-1}$.

HEMTs were fabricated from the conventional heterostructure without InAs, the conventional heterostructure with 4 nm InAs and the modified structure with 4 nm InAs inserted. After wet chemical mesa etching for device isolation, ohmic contacts were formed by evaporation of Ge/Ni/Au/Ge/Ni/Au and annealed at 320°C. Using electron-beam lithography, 0.15 μm T-shaped gates were defined in two layer resist. Gate recess was performed in two steps: first by selective succinic acid etch for the lateral recess definition, second by a nonselective phosphoric acid etch to remove the top Si-δ-doping. The conventional heterostructures are processed in the same way for comparison.

Fig. 5 shows the drain I–V characteristics of the modified structure with an output conductance of 160 mS/mm (at $V_{DS} = 1$ V) and a maximum drain current of 1250 mA/mm. Pinch-off behavior is excellent. However, the drain-source breakdown voltage at high current is rather low (1.5 V). Higher breakdown voltages can be achieved with lower doping levels. This device has a very high current

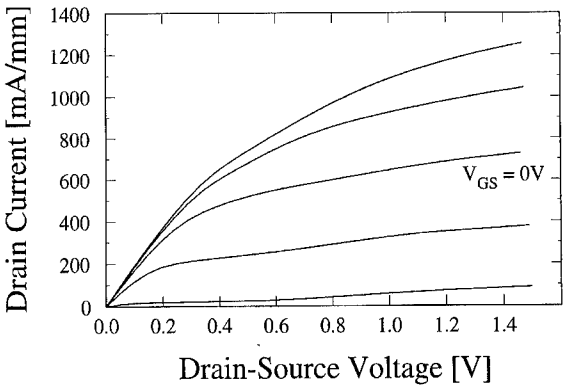

Fig. 5. Drain I–V characteristic of the pseudomorphic HEMT (sample no. 3) at 300 K ($\Delta V_{GS} = 0.25$ V, $L_G = 0.15$ μm, $d_{SD} = 2$ μm)

gain cut off frequency f_T of 235 GHz, the maximum oscillatory frequency f_{max} is measured with 220 GHz, due to the output conductance [1]. The very low source resistance of 0.27 Ω mm causes an extrinsic transconductance of 1270 mS/mm, shown in Fig. 6. These excellent results are achieved by (i) inserting 4 nm InAs and (ii) introducing an additional Si-δ-doping at the interface of the cap and supply layer. By inserting 4 nm InAs in the conventional heterostructures, the extrinsic transconductance is increased from 735 to 945 mS/mm (Fig. 6), the source resistance is reduced from 0.52 to 0.41 Ω mm. The higher mobility in the InAs channel reduces the sheet resistance in the access region between the alloyed contact and gate electrode. The

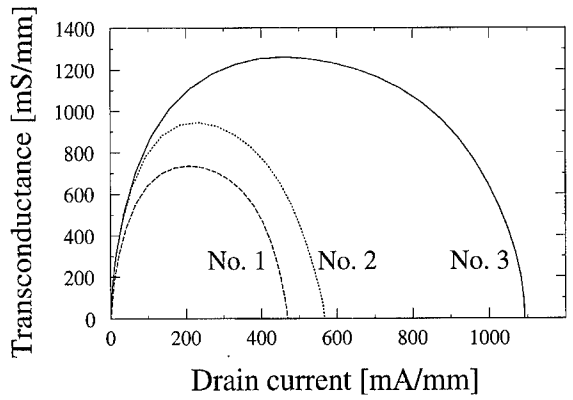

Fig. 6. Extrinsic transconductance $g_{m,ext}$ of lattice matched, 4 nm inserted and Si-δ-doping inserted HEMTs versus drain current density at $V_{DS} = 1$ V.

Table 1
Device characteristics of double-sided δ-doped InAlAs/InGaAs HEMT structures ($g_{m,ext}$: extrinsic transconductance; R_S, R_D: source, drain resistance)

Sample no.	$g_{m,ext}$ (mS/mm)	R_S/R_D (Ω mm)
1	735	0.52/0.48
2	945	0.41/0.43
3	1270	0.27/0.25

Sample no. 1: conventional heterostructure, 12 nm InGaAs channel without InAs.
Sample no. 2: conventional heterostructure, channel with 4 nm InAs.
Sample no. 3: modified heterostructure, 4 nm InAs and Si-δ-doping at the interface of the cap and supply layer.

additional Si-δ-doping reduces the barrier heights between InGaAs cap layer and InAlAs supply layer, so a tunneling current through the barrier is possible [3] and the source resistance is further reduced to 0.27 Ω mm. The effective electron velocity, estimated from the intrinsic transconductance with $V_{DS} = 1$ V, of the InAs-channel heterostructure is 2.50×10^7 cm/s, compared to 1.95×10^7 cm/s without InAs. The HEMT results are summarized in Table 1.

4. Summary

We have demonstrated that symmetrically centered 4 nm InAs layers in a double-sided δ-doped InAlAs/InGaAs HEMT improve the electron transport properties. The mobility is increased by 47% and the effective electron velocity is increased by 30% at 300 K. By introducing an additional Si-δ-doping at the interface of the cap and supply layer, the source resistance is significantly reduced to 0.27 Ω mm, resulting in a very high transconductance of 1270 mS/mm and high cut-off frequencies f_T of 235 GHz.

References

[1] H. Heiß, D. Xu, S. Kraus, M. Sexl, G. Böhm, G. Tränkle and G. Weimann, in: Proc. 8th Int. Conf. on Indium Phosphide and Related Materials, Schwäbisch Gmünd (1996) p. 470.
[2] G.J. Whaley and P.I. Cohen, J. Vac. Sci. Technol. B 6 (1988) 625.
[3] S.J. Lee and C.R. Crowell, Solid State Electron. 288 (1985) 659.

ELSEVIER

Journal of Crystal Growth 175/176 (1997) 919–923

JOURNAL OF CRYSTAL GROWTH

Resonant tunnelling of holes in double barrier heterostructures grown by MBE on (1 1 0) oriented GaAs substrates

M. Henini[a,*], R.K. Hayden[b], T. Takamasu[b], N. Miura[b], L. Eaves[a], G. Hill[c]

[a] *Department of Physics, University of Nottingham, University Park, Nottingham NG7 2RD, UK*
[b] *Institute for Solid State Physics, University of Tokyo, Roppongi, Minato-ku, Tokyo 106, Japan*
[c] *Department of Electronic and Electrical Engineering, University of Sheffield, Mappin Street, Sheffield S1 3JD, UK*

Abstract

Hole tunnelling in Be-doped GaAs/AlAs double barrier quantum well structures, grown by molecular beam epitaxy on the (1 1 0) GaAs surface, have been investigated. Fewer resonances are observed in the current–voltage characteristic of the device than in the characteristics of similar devices grown on (1 0 0) and (3 1 1)A oriented substrates. High magnetic fields are used to examine the anisotropic in-plane energy dispersion of the QW states of the (1 1 0) diode. The dispersion of one of the resonances is found to be much greater than has been observed in (1 0 0) and (3 1 1)A oriented devices.

1. Introduction

There has recently been renewed interest in quantum well (QW) devices in the GaAs/AlAs system grown on substrate orientations other than (1 0 0). However, the (1 1 0) orientation has received much less attention than other orientations, both experimentally [1] and theoretically [2–7]. This is due in part to the difficulties of epitaxial growth on the amphoteric (1 1 0) GaAs surface. There have been several calculations of the valence band structure in such devices [2–6], and they show the anisotropy of the quasi-two-dimensional subbands to be much larger in (1 1 0) oriented systems than in those with (1 0 0) and (1 1 1) orientations.

To date, there have been no experiments to test these theoretical predictions of the valence band structure in the (1 1 0) plane. In this contribution, resonant tunnelling of holes through a (1 1 0) oriented QW is reported, and magnetotunnelling spectroscopy is used to study the valence subband structure. The experimental results are compared with recent theoretical work.

2. Experiment

The structure was grown on a semi-insulating (1 1 0) GaAs substrate misoriented 6° towards the (1 1 1)A face using an Intevac Gen-II molecular beam epitaxy system. The growth was performed at a temperature of 560°C with growth rates for GaAs and AlAs of 1 ML s^{-1} and 0.5 ML s^{-1} respectively,

* Corresponding author.

0022-0248/97/$17.00 Copyright © 1997 Elsevier Science B.V. All rights reserved
PII S0022-0248(96)00885-8

as measured by reflection high-energy electron diffraction. The As/(Ga, Al) beam-equivalent pressure ratio determined by an ionization gauge was approximately 12. On exactly oriented (1 1 0) surfaces, good electrical and optical properties can only be obtained by using low growth temperature (450–500°C), doubling the arsenic overpressure, and halving the gallium flux to 0.5 ML s^{-1}. A misoriented substrate was selected because good surface morphology could be achieved [8] and because the misorientation allows the use of a much higher growth temperature, and standard arsenic overpressure and gallium growth rate, without compromising the quality of the resonant tunnelling devices. Previous devices on (1 0 0) and (3 1 1)A oriented substrates were grown at 630°C [9].

The layer structure of the device is shown in Fig. 1. It consists of a 4.2 nm QW between 5.1 nm AlAs barriers. The upper and lower contact layers are Be-doped and are separated from the barriers by spacer layers. The QW, tunnel barriers and spacer layers are not intentionally doped. The material was processed into circular mesas of 200 μm diameter and contacts formed, using standard wet-etching, photolithography and metallization techniques. Ohmic contacts were made to the top p^+-layer and the p^+-layer immediately above the semi-insulating substrate.

600 nm GaAs	$p=2\times10^{18}$ cm^{-3}	top contact
100 nm GaAs	$p=1\times10^{18}$ cm^{-3}	
100 nm GaAs	$p=5\times10^{17}$ cm^{-3}	
5.1 nm GaAs	NID	spacer
5.1 nm AlAs	NID	tunnel barrier
4.2 nm GaAs	NID	quantum well
5.1 nm AlAs	NID	tunnel barrier
5.1 nm GaAs	NID	spacer
100 nm GaAs	$p=5\times10^{17}$ cm^{-3}	
100 nm GaAs	$p=1\times10^{18}$ cm^{-3}	
3 μm GaAs	$p=2\times10^{18}$ cm^{-3}	lower contact
(110) GaAs	semi-insulating	substrate

Fig. 1. Layer structure of the device considered in the text. The resonant tunnelling structure is formed by the not-intentionally-doped (NID) layers. The substrate is misoriented from the (1 1 0) plane by 6° towards the (1 1 1)A plane.

Fig. 2 shows the $I(V)$ characteristics, at 4.2 K, in various magnetic fields $\boldsymbol{B}$ between 0 and 38 T. Measurements were made with the magnetic field applied parallel to the layer planes along the [1 $\bar{1}$ 0] direction, Fig. 2(a), and along the [0 0 1] direction, Fig. 2(b). In the absence of a magnetic field, only one resonance is directly visible in the $I(V)$ characteristic, at 858 mV. In the presence of a magnetic field, this resonance moves to higher bias and weakens markedly; it is only visible as a weak feature in the differential conductance, dI/dV, for fields above 30 T. In zero magnetic field, there is also a resonant feature at 122 mV, but is only visible as a weak feature in dI/dV. This resonance also moves to higher bias with increasing magnetic field, but increases in strength, so that it is just discernible in the $I(V)$ characteristic at around 300 mV, for $\boldsymbol{B} > 22$ T when $\boldsymbol{B}$ is parallel to [1 $\bar{1}$ 0], and for $B > 31$ T when $\boldsymbol{B}$ is parallel to [0 0 1].

The dependence of the amplitudes of the resonances with magnetic field has been studied previously and has been shown to be different for different peaks [10, 11]. From Fig. 2 it can be seen that the increase in amplitude of the lower bias resonance with magnetic field is particularly marked for $\boldsymbol{B}$ parallel to [1 $\bar{1}$ 0]. When $\boldsymbol{B}$ is applied parallel to the [0 0 1] direction, the amplitude also increases, but less strongly. It can also be seen that this resonance becomes much broader with increasing magnetic field for $\boldsymbol{B}$ parallel to [0 0 1] than for $\boldsymbol{B}$ parallel to [1 $\bar{1}$ 0]. For the higher bias resonance, in both magnetic field orientations, the amplitude decreases rapidly with magnetic field. These effects are typical of the quantum mechanical admixing of light and heavy hole states, and of the complexities of hole resonant tunnelling in high magnetic fields [10, 12, 13].

The complicated dispersion curves of energy versus in-plane wave vector, $\varepsilon(\boldsymbol{k}_{\|})$, of the valence band QW have recently been investigated on similar structures grown on non-(1 0 0) GaAs planes using magnetotunnelling spectroscopy. The correspondence between magnetic field $\boldsymbol{B}$ and $\boldsymbol{k}_{\|}$, and that between applied bias V and the energy ε at which holes are injected into the quantum well can be used to examine the in-plane energy wave vector dispersion curves, $\varepsilon(\boldsymbol{k}_{\|})$, for the QW subbands corresponding to the observed resonances [11]. It has

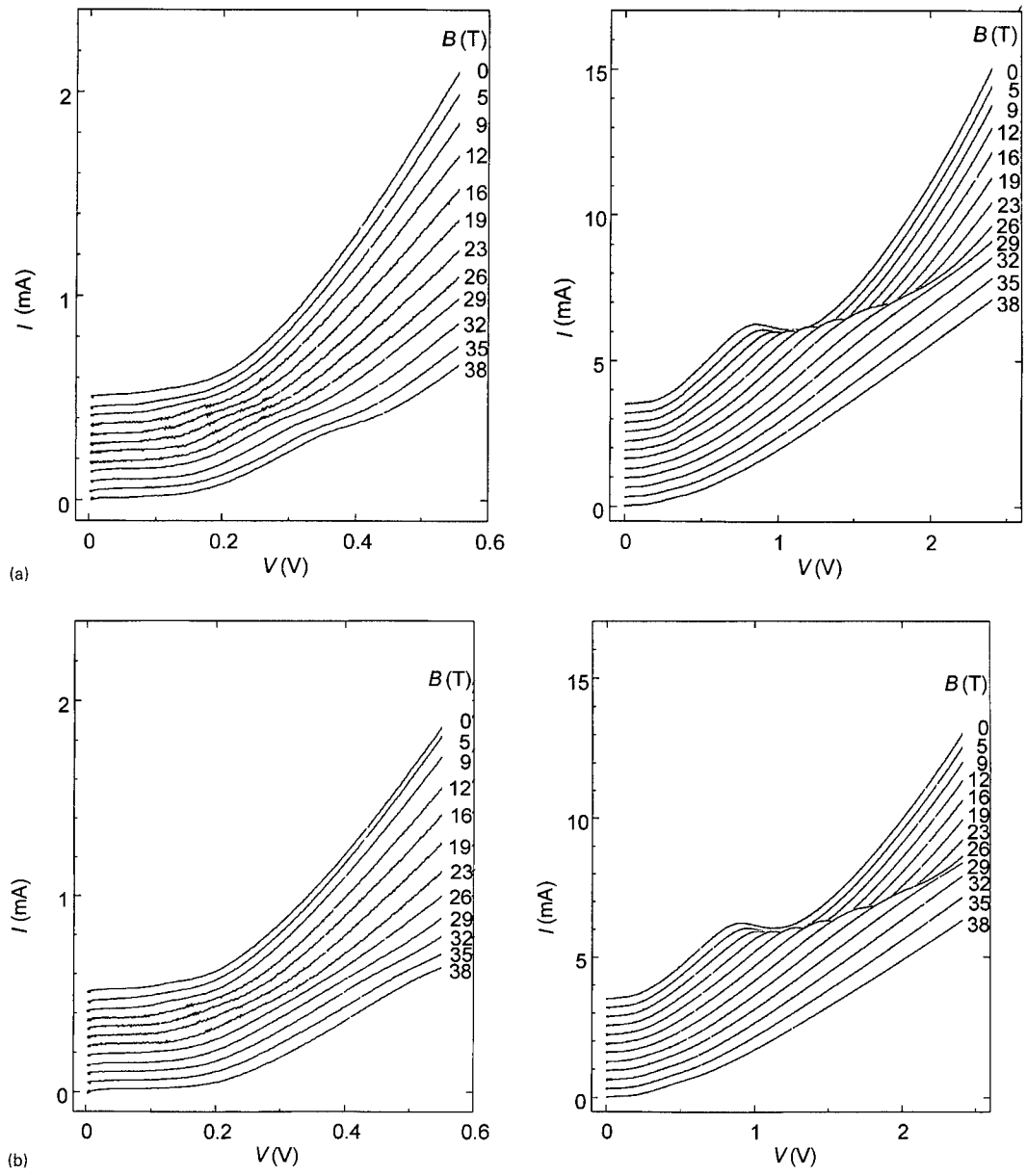

Fig. 2. Current-voltage, $I(V)$, characteristics at 4.2 K of a 200 μm diameter mesa, in various magnetic fields between 0 and 38 T. The magnetic field was applied parallel to the layer planes (a) along the [1 $\bar{1}$ 0] direction and (b) along the [0 0 1] direction. The vertical scales are for the characteristics at 38 T. Other curves are displaced vertically for clarity.

been demonstrated theoretically that for a device with quantum well width $w = 4.2$ nm, magnetic fields $B < 40$ T produce only a small variation from the $\varepsilon(\boldsymbol{k}_{\|})$ dispersion when $B = 0$ [12]. Thus plots of resonant peak voltage position, V_p, as a function of magnetic field $\boldsymbol{B}$, such as those shown in Fig. 3, should qualitatively represent the $\varepsilon(\boldsymbol{k}_{\|})$ curves for these two subbands [10, 12].

The observed anisotropy of the resonances, shown in Fig. 3, is small at low values of $\boldsymbol{B}$ and is

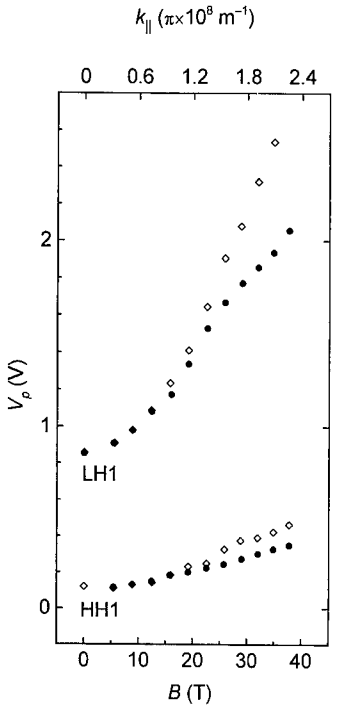

Fig. 3. Plots of resonant peak voltage position, V_p, as a function of magnetic field $\boldsymbol{B}$. Filled circles are for $\boldsymbol{B}$ parallel to [1 $\bar{1}$ 0], corresponding to $\boldsymbol{k}_{\|}$ along [0 0 1]; open diamonds are for $\boldsymbol{B}$ parallel to [0 0 1], corresponding to $\boldsymbol{k}_{\|}$ along [$\bar{1}$ 1 0]. Values of $\boldsymbol{k}_{\|}$ are obtained from the expression $k_{\|} = eB\,\Delta s/h$, where Δs is the average separation between holes in the emitter accumulation layer and in the QW.

only apparent for $B > 15$ T. For some quantum well widths, the anisotropy is expected to be apparent even at very low magnetic fields, for example, for $w < 3.0$ nm [2] and for $w = 10$ nm [6]. However, this anisotropy is sensitive to the device parameters and may not be so significant for intermediate well widths [4].

For both resonances, the anisotropy indicated by the magnetotunnelling measurements presented here is in the reverse sense to that calculated for $w < 3.0$ nm [2], but in the same sense as calculated for $w \geq 5$ nm [3–6]. From the $V_p(\boldsymbol{B})$ curves, it can be seen that both the subbands in this device are higher in hole energy for $\boldsymbol{k}_{\|}$ along [$\bar{1}$ 1 0] than for $\boldsymbol{k}_{\|}$ along [0 0 1].

One of the most noticeable features of Fig. 3, in comparison with previously studied p-type devices on the GaAs/AlAs system, is the very large dispersion of the higher bias resonance. This resonance shifts to higher bias by almost 1.2 V for $\boldsymbol{B}$ parallel to [1 $\bar{1}$ 0], corresponding to $\boldsymbol{k}_{\|}$ along [0 0 1], and by more than 1.6 V for $\boldsymbol{B}$ parallel to [0 0 1], corresponding to $\boldsymbol{k}_{\|}$ along [$\bar{1}$ 1 0]. Theoretically, the subband with the greatest dispersion is expected to be LH1 [4], suggesting that the higher bias resonance corresponds to tunnelling into LH1. However, the observed dispersion is anomalously large, even for LH1.

For this well width, the HH2 and LH1 resonances are expected to be very close at $\boldsymbol{k}_{\|} = 0$. The first resonance in the $I(V)$ characteristic, which is at a much lower bias than the LH1 resonance, is therefore attributed to tunnelling into the HH1 subband of the quantum well. As is the case here, the HH1 resonance is often very weak in the $I(V)$ characteristics of p-type double barrier diodes. Coupling of the quantum well HH1 subband to the light-hole states of the tunnel barriers is known to be poor [14]. Also, at low biases, there is insufficient charge accumulation in the emitter subband, which is mainly for HH1 character, for states with larger $\boldsymbol{k}_{\|}$, and therefore greater light-hole character, to be occupied. This also leads to poor coupling with the light-hole states of the emitter tunnel barrier. Most of the tunnel current passes through light-hole states in the barrier [15], so the combination of these effects gives a very low resonant current density.

The reasons for the absence of a peak corresponding to tunnelling into the HH2 subband, and for the very large dispersion of the higher bias resonance, are unclear. The observation of only two resonances contrasts with the much larger number seen in devices grown on (1 0 0) and (3 1 1)A oriented substrates which were otherwise identical to the one considered here [9]. In those devices, six and seven resonances, respectively, were observed in the $I(V)$ characteristics [10]. Theoretically, a (1 1 0) oriented quantum well is expected to have more bound states, because the heavy-hole quantization effective mass is large [4], see Table 1. As each resonance in the $I(V)$ characteristic corresponds to tunnelling from an emitter accumulation layer into a subband of the quantum well, a larger number of resonances would be expected. In contrast, the light-hole quantization effective mass is

Table 1
Quantization effective masses of holes in GaAs

	⟨1 0 0⟩	⟨3 1 1⟩	⟨1 1 0⟩	⟨1 1 1⟩
$m_{hh}^*(m_e)$	0.38	0.55	0.71	0.95
$m_{lh}^*(m_e)$	0.09	0.08	0.08	0.08

almost isotropic in GaAs. Thus, in principle, the first light-hole resonance should be at similar bias in devices that have different orientation but are otherwise identical. However, differences will occur due to unavoidable variations during device fabrication, such as in dopant density and ohmic contact resistance. The LH1 resonances in the devices presented in Ref. [9] are at 318 mV in the (1 0 0) oriented device and at 310 mV in the (3 1 1)A oriented device. In zero magnetic field, the LH1 resonance of the (1 1 0) device is at 858 mV. This suggests either that the resistance of the contact regions is higher in this (1 1 0) device, or that there is greater charge accumulation in the QW of the device. Both of these effects increase the scaling between V and ε, and may explain why tunnelling into the HH3 subband is also not observed: the increased scaling between V and ε pushes the resonance beyond the available bias range. Note that in p-type resonant tunnelling devices, charge build-up in the quantum well does not necessarily produce resonances with sharp cut-offs [16], in contrast to the effect in n-type devices. The very flat dispersion expected for the HH2 and HH3 subbands [4] would produce very broad weak resonances [8] and, combined with the poor coupling of heavy hole states in the quantum well to light hole states in the barrier, may be another reason why tunnelling into these two subbands is not observed.

3. Summary

Resonant tunnelling of holes into the first heavy hole and light hole subbands of a (1 1 0) oriented quantum well has been observed. The current–voltage characteristics show fewer resonances than are expected from calculations of the valence band states in quantum wells of this orientation. The valence subbands of the quantum well appear to be less anisotropic than expected from some previous theoretical studies.

Acknowledgements

This work is supported by the United Kingdom Engineering and Physical Sciences Research Council, the Japanese Ministry of Education, Science and Culture, and the Japan Society for the Promotion of Science. M.H. wishes to acknowledge the British Council for financial support.

References

[1] L.T.P. Allen, E.R. Weber, J. Washburn and Y.C. Pao, Appl. Phys. Lett. 51 (1987) 670.
[2] M.P. Houng, Y.C. Chang and W.I. Wang, J. Appl. Phys. 64 (1988) 4609.
[3] J.B. Xia, Phys. Rev. B 43 (1991) 9856.
[4] A.T. Meney, Superlattice Microstruct. 11 (1992) 31.
[5] Z. Ikonic, V. Milanovic and D. Tjapkin, Phys. Rev. B 46 (1992) 4285.
[6] G. Shechter, L.D. Shvartsman and J.E. Golub, J. Appl. Phys. 78 (1995) 288.
[7] R.H. Henderson and E. Towe, J. Appl. Phys. 79 (1996) 2029.
[8] K. Tsutsui, H. Mizukami, O. Ishiyama, S. Nakamura and S. Furukawa, Jpn. J. Appl. Phys. 29 (1990) 468.
[9] M. Henini, R.K. Hayden, E.C. Valadares, L. Eaves, G. Hill and M.A. Pate, Semicond. Sci. Technol. 7 (1992) 267.
[10] R.K. Hayden, L. Eaves, M. Henini, E.C. Valadares, O. Kühn, D.K. Maude, J.C. Portal, T. Takamasu, N. Miura and U. Ekenberg, Semicond. Sci. Technol. 9 (1994) 298.
[11] R.K. Hayden, D.K. Maude, L. Eaves, E.C. Valadares, M. Henini, F.W. Sheard, O.H. Hughes, J.C. Portal and L. Cury, Phys. Rev. Lett. 66 (1991) 1749.
[12] G. Goldoni and A. Fasolino, Phys. Rev. B 51 (1995) 9903.
[13] E.C. Valadares, Phys. Rev. B 46 (1992) 3935.
[14] C.Y.P. Chao and S.L. Chaung, Phys. Rev. B 43 (1991) 7027.
[15] J.N. Schulman and Y.C. Chang, Phys. Rev. B 31 (1985) 2056.
[16] R.K. Hayden, L. Eaves, M. Henini, D.K. Maude, J.C. Portal and G. Hill, Appl. Phys. Lett. 60 (1992) 1474.

ELSEVIER

Journal of Crystal Growth 175/176 (1997) 924–929

JOURNAL OF CRYSTAL GROWTH

GaAs/AlAs resonant tunneling diodes with super-flat interfaces grown on (4 1 1)A GaAs substrates by MBE

K. Shinohara[a,*], K. Kasahara[a], S. Shimomura[a], A. Adachi[b], N. Sano[c], S. Hiyamizu[a,d]

[a] *Faculty of Engineering Science, Osaka University, Toyonaka 560, Japan*
[b] *Nissin Electric Co. Ltd., Ukyo-ku, Kyoto 615, Japan*
[c] *Faculty of Science, Kwansei-Gakuin University, Nishinomiya 662, Japan*
[d] *Research Center for Extreme Materials, Osaka University, Toyonaka, Osaka 560, Japan*

Abstract

GaAs/AlAs resonant tunneling diodes (RTDs) with atomically flat GaAs/AlAs interfaces over an entire device area (super-flat interfaces) have been successfully fabricated on a (4 1 1)A GaAs substrate by molecular beam epitaxy (MBE). The (4 1 1)A GaAs/AlAs RTDs exhibited a superior peak-to-valley current ratio ($J_p/J_v = 11.8$ at 80 K) to that (7.5) of RTDs simultaneously grown on a conventional (1 0 0)GaAs substrate. The improved J_p/J_v ratio of the (4 1 1)A RTD is believed to be due to the super-flat GaAs/AlAs interfaces, which significantly reduce the valley current density.

Keywords: (4 1 1)A GaAs substrates; Super-flat interface; GaAs/AlAs RTD

1. Introduction

Formation of atomically flat GaAs/AlGaAs interfaces over a macroscopic area is very important for applications to quantum devices such as GaAs/AlGaAs resonant-tunneling hot-electron transistors (RHETs). GaAs/AlGaAs quantum wells (QWs) grown on (4 1 1)A-oriented GaAs substrates by molecular beam epitaxy (MBE) have been reported to show extremely flat interfaces over a large area ("super-flat interfaces") [1–4]. GaAs/$Al_{0.3}Ga_{0.7}As$ QWs with well width of 2.4 nm grown on the (4 1 1)A substrate show a very narrow photoluminescence (PL) peak (FWHM = 5.5 meV at $\lambda = 709.2$ nm) at 4.2 K [1] whose line width is the same as that for growth-interrupted QWs grown on (1 0 0) GaAs substrates [5]. There always exist two or three PL peaks from a single QW on a conventional (1 0 0) substrate due to the lateral variation of well thickness by ± 1 ML [5, 6], while the GaAs/$Al_{0.3}Ga_{0.7}As$ QWs grown on (4 1 1)A substrates exhibit only one sharp PL peak from each QW over an extraordinarily large area ($\sim 1\ cm^2$), indicating the formation of effectively atomically flat (4 1 1)A GaAs/AlGaAs interfaces over a wafer-size area [2]. These super-flat interfaces

* Corresponding author. Fax: + 81 6 845 4632; e-mail: shino@d310.mp.es.osaka-u.ac.jp.

0022-0248/97/$17.00 Copyright © 1997 Elsevier Science B.V. All rights reserved
PII S0022-0248(96)01012-3

have been applied to $GaAs/Al_{0.3}Ga_{0.7}As$ resonant tunneling diodes (RTDs) which exhibited a better peak-to-valley current ratio ($J_p/J_v = 5.0$ at 77 K) than that (4.1) of a RTD simultaneously grown on (1 0 0) GaAs substrate, but both devices yielded figures of merit inferior to state-of-the-art RTDs because of their thick barrier layers (10 nm) and low barrier height ($Al_{0.3}Ga_{0.7}As$ barriers) [7]. In this paper, we report the successful fabrication of GaAs/AlAs RTDs on (4 1 1)A GaAs substrates by MBE with much improved I–V characteristics due to super-flat interfaces and an improved RTD structure.

2. Experimental procedure

n^+-GaAs substrates with (4 1 1)A and (1 0 0) orientations were degreased and chemically etched by sulfuric acid etchant solution ($H_2SO_4 : H_2O_2 : H_2O = 5 : 1 : 1$) prior to MBE growth. GaAs/AlAs double-barrier resonant tunneling (DBRT) structures were simultaneously grown on these substrates in a Nissin RB-2001G MBE system. The substrate temperature was monitored by a pyrometer, which was calibrated by the melting point of aluminum (660°C). The substrates were rotated at 30 rpm during MBE growth. A 400 nm-thick highly Si-doped n-GaAs layer (1.0×10^{18} cm^{-3}) and a 100 nm-thick n-GaAs layer ($n = 5 \times 10^{17}$ cm^{-3}) were grown at 580°C and V/III ratio of 14 (in pressure) to realize n-GaAs on the (4 1 1)A GaAs substrate which exhibits a low compensation ratio similar to a Si-doped GaAs grown on a (1 0 0) substrate [8]. An undoped AlAs ($L_b = 3$ nm)/GaAs ($L_w = 7$ nm)/AlAs ($L_b = 3$ nm) DBRT structure with 10 nm-thick undoped GaAs spacer layers was grown at 640°C and V/III ratio of 14 in order to form the super-flat (4 1 1)A GaAs/AlAs interfaces [4]. Then 100 nm-thick n-GaAs ($n = 5 \times 10^{17}$ cm^{-3}) and 500 nm-thick n-GaAs ($n = 1.0 \times 10^{18}$ cm^{-3}) were grown at 580°C and V/III ratio of 14. Finally, a heavily Si-doped n-$In_xGa_{1-x}As$ ($x = 0$–0.5, $n = 3.0 \times 10^{19}$ cm^{-3}) contact layer was grown at 520°C to form the non-alloy ohmic contact with AuGe : Ni. Growth rates of GaAs and AlAs were 1.0 μm/h. Mesa structures for RTDs were made by photolithography and wet etching. A SiO_2 film was used for electric isolation and passivation. After opening windows in the SiO_2 film on the top of the mesa structure, nonalloy ohmic contacts of AuGe : Ni were made there.

3. Results and discussion

Fig. 1 shows I–V characteristics (80 K) of the GaAs/AlAs RTDs with a contact area of 120 μm diameter fabricated on the (4 1 1)A (a) and the (1 0 0) GaAs substrates (b). The (4 1 1)A RTD shows a peak current density of 200.2 A cm^{-2} (149.6 A cm^{-2}) at a forward (backward) bias of 0.46 V (−0.36 V), while the (1 0 0) RTD shows the peak current density of 355.7 A cm^{-2} (356.6 A cm^{-2}) at 0.39 V (−0.39 V). The valley current density of the (4 1 1)A RTD is as small as 17.0 A cm^{-2} (13.6 A cm^{-2}) in the forward (backward) bias which is 36% (28%) of that [47.5 A cm^{-2}, (48.3 A cm^{-2})] of the (1 0 0) RTD. Then, the peak-to-valley current ratio (J_p/J_v) becomes 11.8 (11.0) in the forward (backward) bias for the (4 1 1)A RTD which is 57% (49%) larger than that [7.5 (7.4)] of the (1 0 0) RTD. These improved behaviors of peak and valley current densities of (4 1 1)A RTDs with respect to the (1 0 0) RTDs are similar to the case of $GaAs/Al_{0.3}Ga_{0.7}As$ RTDs previously reported [7], but higher peak current density (J_p) and an extremely high peak-to-valley current ratio (J_p/J_v) were achieved for the present (4 1 1)A GaAs/AlAs RTD due to its thin (3 nm) and high (AlAs) barriers. The peak current density (the peak-to-valley current ratio) of the GaAs/AlAs RTD became 5 times (2.4 times) as large as that of the previous $GaAs/Al_{0.3}Ga_{0.7}As$ RTD [7]. The observed peak voltage is 0.46 V for the (4 1 1)A RTD, which is 3.5 times larger than the calculated value (0.13 V) of $2E/e$, where E is the resonant energy in the double-barrier structure at zero bias. This is due to a parasitic resistance at the ohmic contacts in both electrodes.

Fig. 2a shows the peak-to-valley current ratios (J_p/J_v) of the (4 1 1)A and (1 0 0) RTDs as a function of temperature. At 300 K, a value of J_p/J_v (1.4) of the (4 1 1)A RTD is almost the same as that of the (1 0 0) RTD, while it increases more than that of

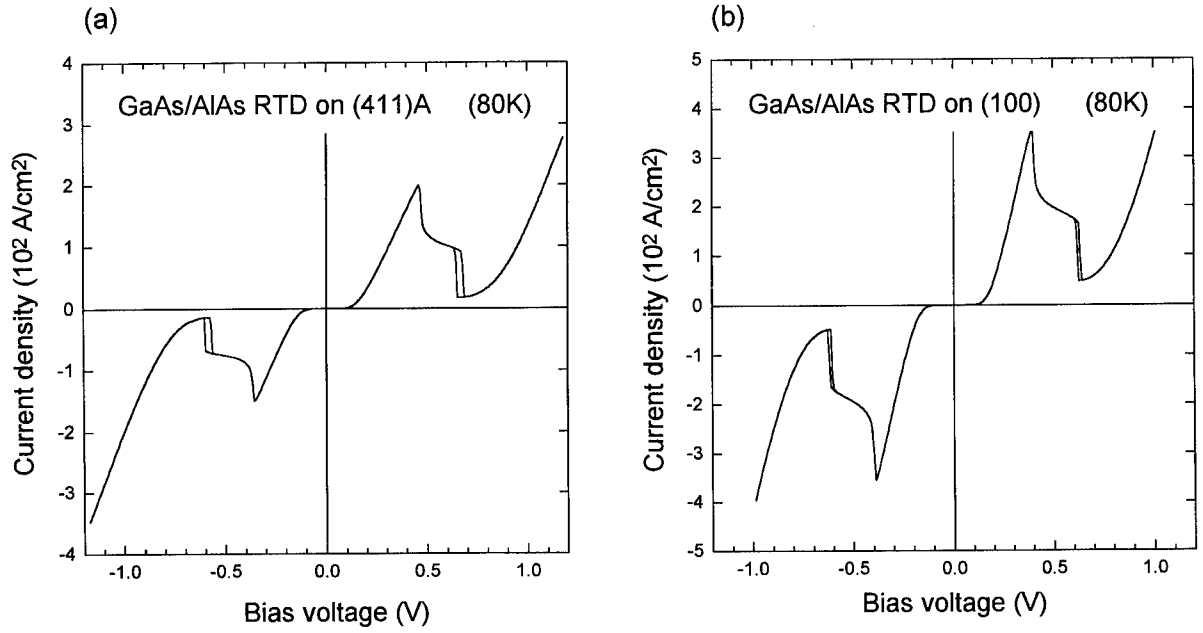

Fig. 1. Current–voltage characteristics of GaAs/AlAs double-barrier resonant-tunneling diodes on the (4 1 1)A GaAs substrate (a) and on the (1 0 0)GaAs substrate (b) with a common contact area of 120 μm diameter.

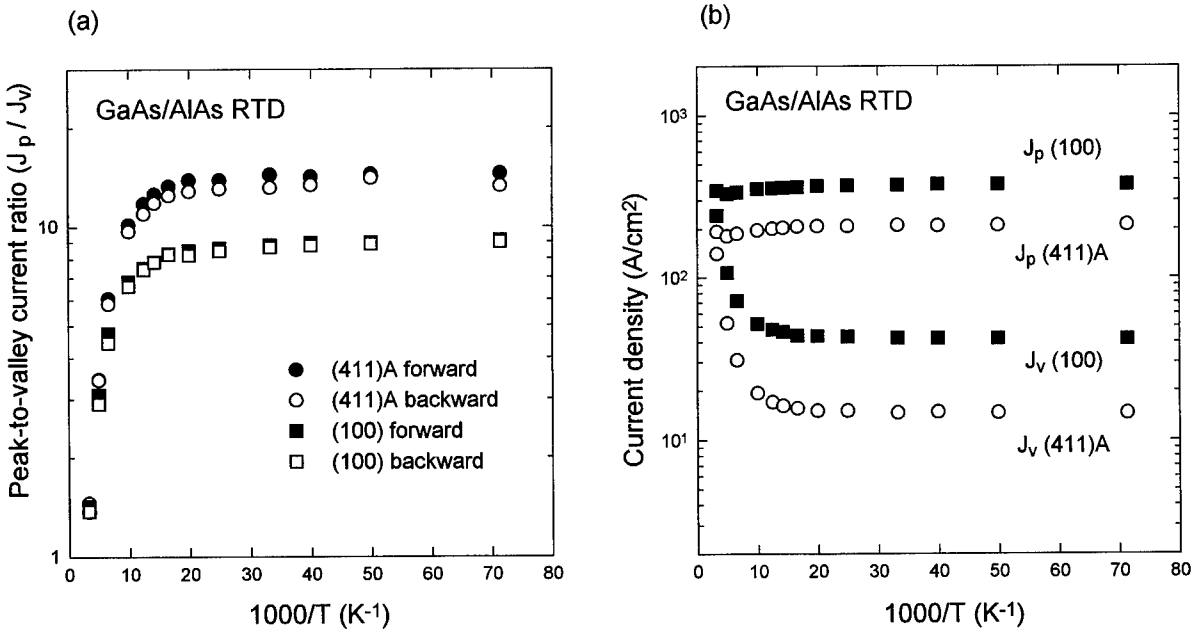

Fig. 2. Temperature dependence of peak-to-valley current ratios (J_p/J_v) (a) and peak current density (J_p) and valley current density (J_v) (b) of GaAs/AlAs double-barrier diodes on the (4 1 1)A and (1 0 0)GaAs substrates.

Table 1
Peak and valley current densities and peak-to-valley current ratios at the forward (backward) bias of GaAs/AlAs RTDs fabricated on (4 1 1)A and (1 0 0) GaAs substrates

Temperature (K)	(4 1 1)A RTD			(1 0 0) RTD		
	J_p (A cm^{-2})	J_v (A cm^{-2})	J_p/J_v	J_p (A cm^{-2})	J_v (A cm^{-2})	J_p/J_v
300	192.8	140.8	1.4	342.9	241.6	1.4
	(144.1)	(98.9)	(1.5)	(342.7)	(249.7)	(1.4)
80	200.2	17.0	11.8	355.7	47.5	7.5
	(149.6)	(13.6)	(11.0)	(356.6)	(48.3)	(7.4)
14	211.2	14.5	14.6	374.8	41.3	9.1
	(160.2)	(12.0)	(13.4)	(373.3)	(41.6)	(9.0)

the (1 0 0) RTD with decreasing temperature and becomes almost constant ($\sim$15) below 50 K. This constant value of J_p/J_v is 67% larger than that ($\sim$9) of the (1 0 0) RTD. Numerical values of the peak and valley current densities (J_p, J_v) and the peak-to-valley current ratio (J_p/J_v) at 300, 80 and 14 K are also listed in Table 1. The peak and valley current densities of the (4 1 1)A and (1 0 0) RTDs are plotted as a function of the temperature in Fig. 2b. The peak current density of the (1 0 0) RTD is almost constant over the whole range of temperature from 14 to 300 K, and it is almost 1.5 times larger than that of the (4 1 1)A RTD. Decrease of the barrier thickness results in increase in the resonance width due to the enhanced transmission coefficient in the off-resonant voltage range which results in the increase of the resonant current. Tsuchiya and his co-workers reported that the resonant current increases by 1.7 times while decreasing the barrier thickness by only 1 ML for GaAs/AlAs RTD with the well width of 7 nm [9]. Since the (4 1 1)A and the (1 0 0) RTDs were grown simultaneously, the average thicknesses of the AlAs barrier layers of both RTDs were the same within the error limit of 1%. The electron concentration of both sides of the double-barrier structure should affect the peak current density, but the electron concentration of *n*-GaAs layers on (4 1 1)A substrate is almost the same as that of the *n*-GaAs layers grown on (1 0 0) substrate because the optimized growth condition was used for growing *n*-GaAs layers with a low compensation ratio on (4 1 1)A substrate [8]. Therefore, the large peak current density of the (1 0 0) RTD is mainly due to the tunneling through the locally thinner regions of the AlAs barriers with the lateral variation of the barrier thickness of ± 1 ML.

The valley current density (J_v) of the (4 1 1)A RTD is much smaller than that of the (1 0 0) RTD over the whole range of the temperature from 14 to 300 K and it is almost constant below 50 K due to the extinction of the thermal current over the barriers. The forward valley current density is 14.5 A cm^{-2} for the (4 1 1)A RTD at 14 K, which is as small as 35% of that (41.3 A cm^{-2}) of the (1 0 0) RTD. We believe that this drastic decrease of J_v for the (4 1 1)A RTD should be due to its superflat interfaces. The interface roughness deteriorates the lateral momentum conservation of electron tunneling through the double-barrier structure. The lateral potential fluctuation caused by the interface roughness scatters electrons to other states with different lateral and longitudinal momentums. Hence, the interface roughness leads to the increase of off-resonant transmissivity, i.e., increase of J_v.

Fig. 3 shows J_p/J_v observed at 77 K as a function of J_p for GaAs/AlGaAs RTDs. An open square and an open circle show J_p/J_v values obtained for the (4 1 1)A and the (1 0 0) RTDs in this study, respectively. J_p/J_v values reported so far for GaAs/AlGaAs RTDs grown on the conventional (1 0 0) GaAs substrates by MBE are also shown (solid squares [9–11], solid triangles [12], solid circles

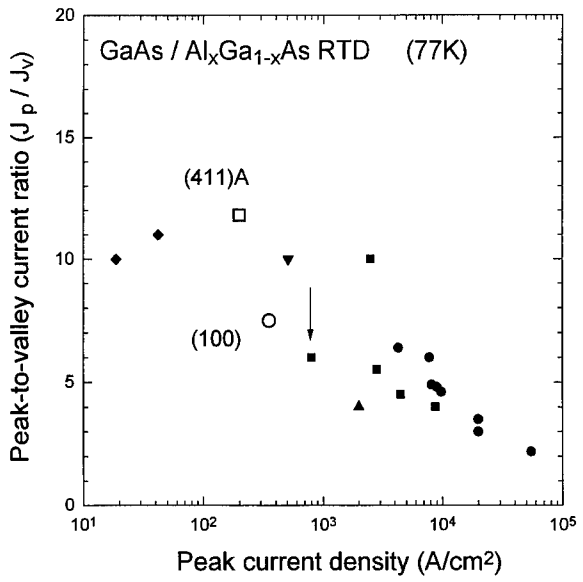

Fig. 3. Peak-to-valley current ratio (J_p/J_v) of the (4 1 1)A RTD (□) and the (1 0 0) RTD (○) as a function of the peak current density. Reported values of J_p/J_v for GaAs/AlGaAs RTDs are also shown by solid squares [9–11], solid triangle [12], solid circles [13, 14], solid inverse triangle [15] and solid diamonds [16].

[13, 14], solid inverse triangle [15] and solid diamonds [16]). As seen in Fig. 3, J_p/J_v tends to decrease with increasing J_p. This negative trend is explained as follows: a higher current density results in a higher concentration of electrons accumulated in a quantum well of a RTD, which may increase the electron–phonon or the electron–electron scattering and may increase the valley current density (J_v). The J_p/J_v value of the (1 0 0) RTD (open circle) is almost on the same level as the previous datum, indicated by an arrow, of a GaAs/AlAs RTD [10] which has almost the same DBRT structure ($L_b = 3$ nm, $L_w = 7$ nm) except for the thickness of the spacer layers ($L_s = 1.5$ nm). On the other hand, the (4 1 1)A RTD has an apparently large J_p/J_v as compared with those of the (1 0 0) RTDs and this improvement is believed to be due to the super-flat interfaces realized on the (4 1 1)A GaAs substrate. RTDs grown on the (4 1 1)A GaAs substrates are expected to be applied to ultra-high speed RHETs because super-uniform and thin barrier layers can be used.

4. Conclusions

GaAs/AlAs double-barrier resonant-tunneling diodes (DBRTDs) with 3 nm-thick barrier layers and a 7 nm-thick well layer have been simultaneously grown on the (4 1 1)A and (1 0 0) GaAs substrates by MBE. Much improved peak-to-valley current ratio (J_p/J_v) was obtained for the (4 1 1)A GaAs/AlAs RTD. This J_p/J_v value achieved for the (4 1 1)A RTD is not only much higher than that of the RTD simultaneously grown on (1 0 0) substrate, but also one of the best data reported for GaAs/AlGaAs RTDs. This result is believed to be due to the super-flat interfaces realized in the (4 1 1)A RTD.

Acknowledgements

This work was supported in part by a Grant-in-Aid for Scientific Research (A) from the Ministry of Education, Science, Sports and Culture.

References

[1] S. Shimomura, A. Wakejima, A. Adachi, Y. Okamoto, N. Sano, K. Murase and S. Hiyamizu, Jpn. J. Appl. Phys. 32 (1993) L1728.
[2] S. Hiyamizu, S. Shimomura, A. Wakejima, S. Kaneko, A. Adachi, Y. Okamoto, N. Sano and K. Murase, J. Vac. Sci. Technol. B 12 (1994) 1043.
[3] S. Shimomura, S. Kaneko, T. Motokawa, K. Shinohara, A. Adachi, Y. Okamoto, N. Sano, K. Murase and S. Hiyamizu, J. Crystal Growth 150 (1995) 409.
[4] S. Shimomura, K. Shinohara, T. Kitada, S. Hiyamizu, Y. Tsuda, N. Sano, A. Adachi and Y. Okamoto, J. Vac. Sci. Technol. B 13 (1995) 696.
[5] M. Tanaka, H. Sakaki, J. Yoshino and T. Furuta, Surf. Sci. 174 (1986) 65.
[6] J.H. Neave, B.A. Joyce, P.J. Dobson and N. Norton, Appl. Phys. A 31 (1983) 1.
[7] S. Shimomura, K. Shinohara, K. Kasahara, T. Motokawa, A. Adachi, Y. Okamoto, N. Sano and S. Hiyamizu, Solid State Electron. 40 (1996) 417.
[8] K. Shinohara, T. Motokawa, K. Kasahara, S. Shimomura, N. Sano, A. Adachi and S. Hiyamizu, Semicond. Sci. Technol. 11 (1996) 125.
[9] M. Tsuchiya and H. Sakaki, Jpn. J. Appl. Phys. 25 (1986) L185.
[10] M. Tsuchiya and H. Sakaki, Appl. Phys. Lett. 50 (1987) 1503.

[11] M. Tsuchiya, H. Sakaki and J. Yoshino, Jpn. J. Appl. Phys. 25 (1985) L466.
[12] T.J. Shewchuk, P.C. Chapin, P.D. Coleman, W. Kopp, R. Fischer and H. Morkoc, Appl. Phys. Lett. 46 (1985) 508.
[13] S. Muto, T. Inata, H. Ohnishi, N. Yokoyama and S. Hiyamizu, Jpn. J. Appl. Phys. 25 (1986) L577.
[14] T. Inata, S. Muto, Y. Nakata, T. Fujii, H. Ohnishi and S. Hiyamizu, Jpn. J. Appl. Phys. 25 (1986) L983.
[15] H. Toyoshima, Y. Ando, A. Okamoto and T. Itoh, Jpn. J. Appl. Phys. 25 (1986) L786.
[16] H.M. Yoo, S.M. Goodnick and J.R. Arthur, Appl. Phys. Lett. 56 (1990) 84.

ELSEVIER

Journal of Crystal Growth 175/176 (1997) 930–934

JOURNAL OF CRYSTAL GROWTH

Photoluminescence characterization of MBE grown AlGaAs/InGaAs/GaAs pseudomorphic HEMTs

M. Wojtowicz*, D. Pascua, A.-C. Han, T.R. Block, D.C. Streit

TRW Electronics and Technology Division, Redondo Beach, California 90278, USA

Abstract

We compare the experimental and theoretical photoluminescence (PL) spectra of power and low-noise pseudomorphic AlGaAs/InGaAs high electron mobility transistor (HEMT) profiles. The modeling approach uses a self-consistent solution between Schrödinger equation and Poisson's equation to calculate the electron and hole energy levels, envelope functions, and concentrations. Results are in good agreement with 4.2 K photoluminescence measurements. PL spectra of the HEMTs show two peaks due to transitions between the e1–hh1 and e2–hh1 channel states. For the low-noise profile, the intensity of the e2–hh1 transition is greater than the e1–hh1 transition intensity while for the power profile, the e1–hh1 transition intensity is greater. The difference in intensities between the low-noise and power profiles is due to differences in the doping of the profiles.

PACS: 85.30.De; 78.55.Cr; 71.25.Tn

Keywords: Photoluminescence; Pseudomorphic; HEMT; InGaAs; pHEMT; MBE

1. Introduction

The need for AlGaAs/InGaAs/GaAs high electron mobility transistor (HEMT) devices for low noise and power microwave circuits continues to increase. In order to reduce costs and ensure a stable supply of epitaxial material, the HEMT device structure must be monitored and screened as close to the growth process as possible. Low temperature photoluminescence (PL) provides a very useful technique to monitor the InGaAs channel material properties, providing the relation between the spectral features and the InGaAs channel material characteristics is understood. In this study we have correlated the 4.2 K PL spectral features from the InGaAs channel region of both a low-noise and a power HEMT profile with their material profile characteristics. The low-noise profile has a single AlGaAs–InGaAs interface whereas the power profile has AlGaAs on both sides of the channel providing two AlGaAs–InGaAs interfaces. For convenience, we will call the low-noise profile a single heterostructure profile and the power

* Corresponding author.

0022-0248/97/$17.00 Copyright © 1997 Elsevier Science B.V. All rights reserved
PII S0022-0248(96)01222-5

profile a double heterostructure profile. Correlating the PL spectral features with channel material characteristics allows us to use PL for monitoring the MBE grown HEMT material to provide consistent material for low-noise and power applications.

Much work has been done on using PL to extract data from HEMT structures. In particular, estimates of the channel interface roughness can be calculated from the full width at half maximum (FWHM) of the 4.2 K PL spectra [1–3] while at higher temperatures the FWHM can give a measure of the channel sheet charge concentration [2, 4, 5]. Also, at 4.2 K, the PL spectral features are very sensitive to channel composition as well as channel width. At higher temperatures, thermal broadening reduces the PL sensitivity to channel conditions. Since the channel conditions are extremely critical to device performance, 4.2 K PL measurements are necessary to ensure material quality. However, 4.2 K PL can only be measured on witness wafer, not actual device wafers. This is not a problem since one witness sample per day per MBE machine is sufficient for us to monitor the material quality once the growth process has stabilized. If the MBE machine has not stabilized then only witness samples are grown. In this paper we compare the theoretical and measured PL spectra of both the single heterostructure and double heterostructure profiles. The differences between the spectra of the two profiles will be identified and explained. We show that the origins of the PL spectral features are the same for both profiles but that differences in the profiles lead to shifts in the energies and intensities of the spectral features.

2. Material profiles and theory

The structures used in this study were grown at TRW by molecular beam epitaxy using Intevac GenII Modular equipment on 3-in (1 0 0) undoped GaAs substrates. The material profiles are shown in Fig. 1. Sheet doping for the double heterostructure profile is $N_s = 3.5 \times 10^{12}\ \mathrm{cm}^{-2}$ at 300 K and $N_s = 3.3 \times 10^{12}\ \mathrm{cm}^{-2}$at 77 K as derived from Hall measurements. For the single heterostructure, the sheet doping is $N_s = 2.5 \times 10^{12}\ \mathrm{cm}^{-2}$ at 300 K and $N_s = 2.3 \times 10^{12}\ \mathrm{cm}^{-2}$ at 77 K. PL measurements

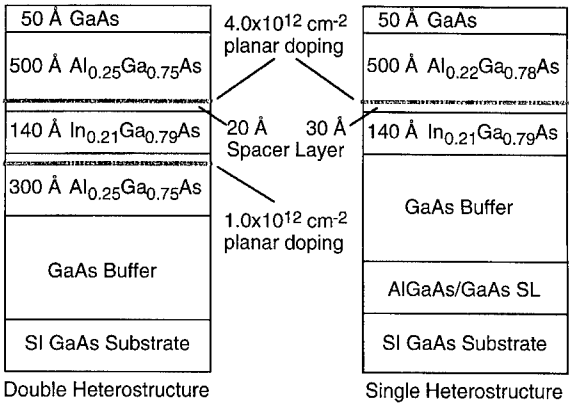

Fig. 1. Single and double heterostructure HEMT material profiles. The primary difference between the two structures is the additional 300 Å AlGaAs buffer region and buffer doping in the double heterostructure profile.

were made using the 514.2 nm line from an Ar^+ laser at an incident power density of $\approx 50\ \mathrm{mW/cm^2}$, a 1-m computer controlled SPEX monochromator, and a Ge detector cooled to 77 K. A lock-in technique was used to reduce noise.

A self-consistent numerical solution of Schrödinger's equation and Poisson's equation was used to solve for the electron and hole energy levels, envelope function, and densities [6]. The solution is based on a finite element analysis that assumes a minimum energy is defined along the z-direction for both the heavy-hole and light-hole valence bands and the conduction band. Spatial variation of the effective mass and dielectric constant are incorporated in the finite element matrix. Excitonic recombination was not considered due to screening and band filling effects. This assumption is confirmed by a lack of exciton luminescence in both the single and double heterostructure spectra. A quasi-static assumption between e–h pair generation and recombination was used to calculate the quasi-Fermi levels and occupational probability. Exchange terms and excitonic effects were neglected due to the high channel carrier concentration [7].

Strain effects were accounted for by appropriately modifying the InGaAs band energy using $c_{11} = 11.24$ dynes/cm and $c_{12} = 5.196$ dynes/cm [8]. The conduction band energy discontinuity is given by $\Delta E_C = 0.70 \Delta E_G$. Table 1 lists the material

Table 1
Material constants used to calculate the quantum well energy levels and wavefunctions

Material	E_G	m_e^*	m_{hh}^*	m_{lh}^*
$Al_{0.22}Ga_{0.78}As$	1.697	0.0763	0.562	0.1010
$Al_{0.25}Ga_{0.75}As$	1.734	0.0778	0.569	0.1030
GaAs	1.422	0.0670	0.520	0.0870
$In_{0.21}Ga_{0.79}As$	1.256[a]	0.0583	0.573	0.0747

[a]This value includes a 44 meV increase in bandgap energy due to strain energy.

parameters used for each layer. We assume midgap Fermi level pinning at the free GaAs surface [9, 10]. Doping segregation effects are modeled by using 20 Å uniformly doped regions with the same total dose [10, 11]. Energy state broadening, an excess e–h pair distribution, and impurity scattering were used to calculate the spectral broadening.

3. Spectral analysis

Fig. 2 shows the energies and wavefunctions for the $n = 1$ and 2 electron states (e1, e2) as well as the $n = 1$ heavy hole state (hh1) for the single heterostructure profile. Fig. 3 shows the energies for the $n = 1$, 2, and 3 electron states (e1, e2, e3) and the wavefunctions for the $n = 1$ and 2 electron states as well as the $n = 1$ heavy hole state (hh1) for the double heterostructure profile. The e3 state is not truly a channel state since the wavefunction is localized in the notch formed by the AlGaAs/GaAs buffer interface. The e3 energy level is shown only for reference since the Fermi energy lies just below this level. Only the $n = 1$ heavy hole state is considered because the excess holes would thermalize to the top of valence band prior to recombining.

Fig. 4 shows representative measured and calculated PL spectra for both profiles. The solid lines show the measured spectra while the dashed lines show the calculated spectra. Both measured and calculated spectra are normalized to the peak amplitude. Good agreement is obtained between the measured and calculated spectra. Two peaks are observed in both structures. The lower energy peak corresponds to the e1–hh1 transition while the higher energy peak corresponds to the e2–hh1 transition. The e2–hh1 peak broadening is less than the $E_F - E_2$ separation, therefore no Fermi edge singularity is seen [12]. In both profiles, the e1 electron state is strongly localized at the front surface side of the well while the e2 state is more weakly localized at the buffer side of the well. In the single heterostructure profile, the ionized donors on the surface side of the channel attract the electrons and repel the holes which reduces the intensity of the e1–hh1 transition relative to the intensity of the e2–hh1 transition. In the double heterostructure profile, the ionized donors on the buffer side of the channel increase the localization of the e2 state to the buffer side of the well, decrease the localization of the e1 state at the front surface side of the well, and repel the holes from buffer side of the well. The effect on the double heterostructure PL spectra

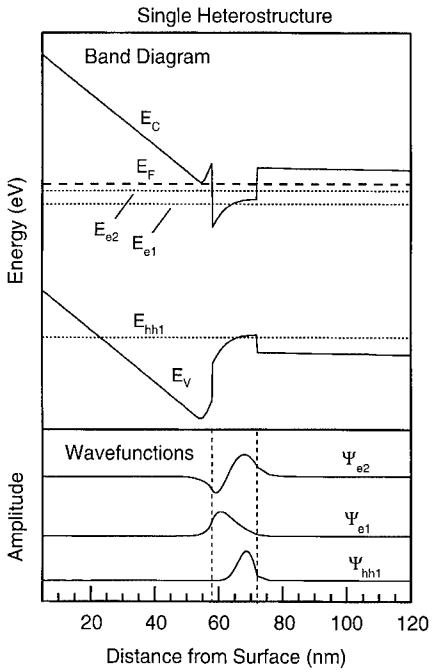

Fig. 2. Conduction band minima, valence band maxima, and electron energy states (top) and the wavefunctions for each energy state (bottom) plotted as a function of position for the single heterostructure device. The dashed vertical lines in the wavefunction plots denote the well boundaries. In this structure, the holes are localized near the buffer edge of the well which results in a stronger overlap between the e2 and hh1 wavefunctions than between the e1 and hh1 wavefunctions.

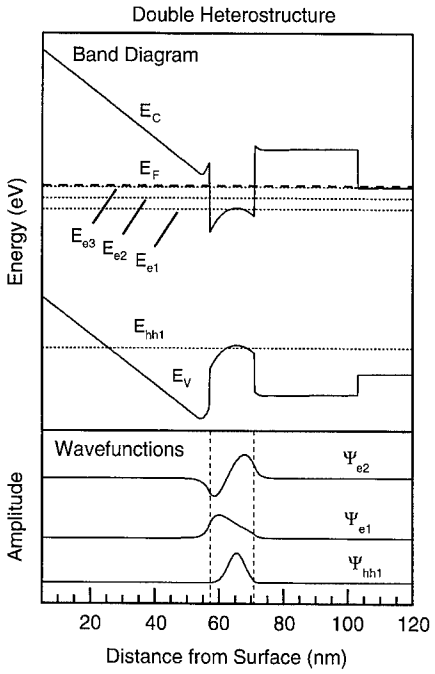

Fig. 3. Conduction band minima, valence band maxima, electron energy states (top) and the wavefunctions for each energy state (bottom) plotted as a function of position for the double heterostructure device. The dashed vertical lines in the wavefunction plots denote the well boundaries. In this structure, the holes are localized near the center of the well which results in a stronger overlap between the e1 and hh1 wavefunctions than between the e2 and hh1 wavefunctions.

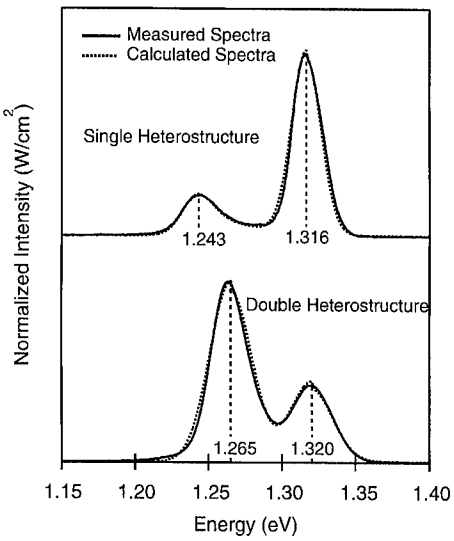

Fig. 4. Comparison of measured and calculated PL spectra for a single and double heterostructure HEMT. Solid lines are measured data and the dotted lines are the calculated spectra. Good agreement is obtained for both structures.

is to decrease the e2–hh1 transition intensity and increase the e1–hh1 transition intensity relative to the single heterostructure profile. The additional donors in the double heterostructure also reduce the energy of the e2 state and increase the energy of the hh1 state. This has the net affect of increasing the e1–hh1 transition energy and decreasing the e2–hh1 transition energy.

Broadening of the PL lineshapes is very complicated but can be generally accounted for by considering the natural spread in the energy states, thermal broadening of the hole distribution, impurity-assisted broadening, and interface roughness. At low excitation power densities and at low temperatures, the spread in energy states and thermal broadening of the holes is small which confines the holes to a very narrow range of momentum ($\boldsymbol{k}$) values near the bottom of the valence band. Therefore, for direct $\boldsymbol{k}$ conserving transitions, the recombining electrons can only come from a narrow range of energies near the bottom of the electron band, emitting photons over a narrow range of energies near the minimum of the electron-to-hole state energies.

Impurity and interface roughness broadening are very similar processes. In these processes, the $\boldsymbol{k}$ conservation is broken by allowing electrons to scatter into intermediate, virtual, states either directly before or after photon emission. High-energy electrons with energies up to the Fermi energy can recombine with holes, emitting a significant number of photons above the minimum electron-to-hole state energies. The transition probability of these higher energy electrons decreases as electron energy increases due to the energy term in the denominator of the transition probability matrices. However, because the density of states increases with energy, the net affect of impurity and interface roughness scattering is to shift the emitted photon distribution toward higher energies [13]. This is seen in the PL spectra as a broadening of the high energy side of the spectral features and an increase in the energy of the peak PL intensities.

In the single heterostructure profile, the PL spectra FWHM is 29.0 meV for the e1–hh1 transition and 27.4 meV for the e2–hh1 transition. The e1–hh1 transition is expected to have a greater FWHM than the e2–hh1 transition because impurity and interface roughness have a greater affect on the e1–hh1 transition than the e2–hh1 transition due to localization of the e1 state at the front AlGaAs–InGaAs interface near the front doping layer. This is also the reason for the high-energy tail in the PL spectra of the e1–hh1 transition. In the double heterostructure profile, the PL spectra FWHM is 33.5 meV for the e1–hh1 transition and 33.0 meV for the e2–hh1 transition. The broadening of the e1–hh1 and e2–hh1 transitions are expected to be similar in the double heterostructure profile since both the e1 and e2 states are localized at an AlGaAs–InGaAs interface near a doping plane.

4. Summary and conclusions

In conclusion, the PL spectra of double and single heterostructure AlGaAs/InGaAs/GaAs HEMT profiles were measured at 4.2 K and compared with the PL spectra calculated using a self-consistent solution of Poisson's and Schrödinger's equations. Two peaks are identified corresponding to transitions between the e1 and e2 conduction band states and the hh1 valence band state confined in the well. In both profiles, the e1 electron state is confined at the front surface side of the well while the e2 state is confined at the buffer side of the well. For the single heterostructure profile, the holes are localized near the buffer side of the well, resulting in a stronger overlap integral between the e2 and hh1 states than between the e1 and hh1 states. However, for the double heterostructure profile, the holes are localized closer to the center of the well due to repulsion by the ionized donors in the buffer. This results in a stronger overlap between the e1 and hh1 states than between the e2 and hh1 states. This shift in the relative intensities is seen in the measured and calculated PL spectra. Now that we understand the origin of the spectral features, we monitor the transition energies and intensities to ensure the uniformity of MBE grown HEMT wafers delivered for processing.

References

[1] M.S. Skolnick, J.M. Rorison, K.J. Nash, D.J. Mowbray, P.R. Tapster, S.J. Bass and A.D. Pitt, Phys. Rev. Lett. 58 (1987) 2130.
[2] A. Dodabalapur, V.P. Kesan, D.R. Hinson, D.P. Neikirk and B.G. Streetman, Appl. Phys. Lett. 54 (1989) 1675.
[3] M.A. Herman, D. Bimberg and J. Christen, J. Appl. Phys. 70 (1991) R1.
[4] H. Brugger, H. Müssig, C. Wölk, K. Kern and D. Heitmann, Appl. Phys. Lett. 59 (1991) 2739.
[5] J.M. Gilprez, J.L. Sánchez-Rojas, E. Muñoz, E. Calleja, J.P.R. David, G. Hill and J. Catagne, Appl. Phys. Lett. 61 (1992) 1225.
[6] G. Bastard and J.A. Brum, IEEE J. Quantum Electron. QE-22 (1986) 1625.
[7] T. Ando, A.B. Fowler and F. Stern, Rev. Mod. Phys. 54 (1982) 437.
[8] Arent et al., J. Appl. Phys. 66 (1989) 1739.
[9] H. Shen, M. Dutta, L. Fotiadis, P.G. Newman, R.P. Moerkirk, W.H. Chang and R.N. Sacks, Appl. Phys. Lett. 57 (1990) 2118.
[10] E.F. Schubert, J.M. Kuo, R.F. Kopf, A.S. Jordan, H.S. Luftman and L.C. Hopkins, Phys. Rev. B 42 (1990) 1364.
[11] L. Pfeiffer, E.F. Schubert, K.W. West and C.W. Magee, Appl. Phys. Lett. 58 (1991) 2258.
[12] M.S. Skolnick, D.M. Whittaker, P.E. Simmonds, T.A. Fisher, M.K. Saker, J.M. Rorison, R.S. Smoth, P.B. Kirby and C.R.H. White, Phys. Rev. B 43 (1991) 7354.
[13] S.K. Lyo and E.D. Jones, Phys. Rev. B 38 (1988) 4113.

ELSEVIER

Journal of Crystal Growth 175/176 (1997) 935–939

JOURNAL OF CRYSTAL GROWTH

Multispectral InGaAs/GaAs/AlGaAs laser arrays by MBE growth on patterned substrates

K. Kamath*, P. Bhattacharya, J. Singh

Solid State Electronics Laboratory, Department of Electrical Engineering and Computer Science, University of Michigan, Ann Arbor, Michigan 48109, USA

Abstract

Multispectral semiconductor laser arrays on single chip is demonstrated by molecular beam epitaxial (MBE) growth of $In_{0.2}Ga_{0.8}As$/GaAs quantum well lasers on GaAs (1 0 0) substrates patterned by dry etching. No regrowth is needed for simple edge emitting lasers. It was observed that the laser characteristics are not degraded by the patterned growth. The shift in the emission wavelength obtained by this method can be controlled by varying the width of the pre-patterned ridges as well as by selecting the regions with different number of vertical sidewalls on both sides. We have also shown that multispectral vertical cavity surface emitting laser (VCSEL) arrays can be made by this technique with a single regrowth.

PACS: 68.55.Bd

Keywords: Molecular beam epitaxy; Patterned growth; Adatom migration; Reactive ion etching; Laser

1. Introduction

Semiconductor laser arrays with spectrally separated emission wavelengths in close spatial proximity are of interest in applications such as wavelength division multiplexing and multi-wavelength optical recording. Two different techniques have been tried with molecular beam epitaxy (MBE) to obtain dual and multiple wavelength laser arrays. In the first approach [1], the laser structure is grown in two steps. In the first step, lower clad and multiple quantum well active layer with different composition and well widths are grown. By selectively etching the quantum wells (QW), regions with different emission wavelengths are defined. The upper clad is then regrown to complete the laser structure. Although laser arrays with multiple emission wavelengths can be obtained by a single regrowth step in this technique, it has a major disadvantage that the regrown interface is in the active region. In the second approach [2], impurity induced intermixing from a doped layer adjacent to the quantum well by post-growth annealing is utilized to realize the change in band gap of the quantum well. This has the advantage

* Corresponding author.

0022-0248/97/$17.00 Copyright © 1997 Elsevier Science B.V. All rights reserved
PII S0022-0248(96)00941-4

that no regrowth is involved. However, only two different wavelengths can be obtained by this method, one without intermixing and one with intermixing. Moreover, the high-temperature anneal used for intermixing might seriously degrade the laser performance. In this paper we present a new technique wherein multiple wavelength laser arrays with close spatial proximity are obtained in a single step growth on patterned substrates.

When an alloy such as InGaAs is grown on a patterned substrate, lateral composition modulation is obtained due to the large difference in surface migration lengths of In (~ 25 μm) [3] and Ga(1–2 μm) [4]. However, most of the earlier work [3–7] was done on patterned substrates with sloping (n 1 1) walls, which are hard to control accurately. We have recently shown that when InGaAs is grown on GaAs (1 0 0) substrates patterned with vertical sidewalls as shown in Fig. 1a, there is a blue shift in the band gap of the material grown on top of the patterns and in the grooves, when the dimensions of the patterns are of the order of migration length of In on GaAs [8, 9]. The measured blue shift in the photoluminescence of $In_{0.2}Ga_{0.8}As$/GaAs quantum wells grown on ridges of different widths is shown in Fig. 1b. This blue shift results from changes in alloy composition and thickness, which in turn are due to the dual effects of growth on the sidewalls, and a large density of kink sites provided by the edges of the patterns to the migrating adatoms. As a result InGaAs with increasing blue shift in the bandgap can be obtained by reducing the pattern dimensions. Moreover, the photoluminescence spectra of quantum wells grown on top of the ridges show linewidths as narrow as those on unpatterned substrates [8]. Therefore, laser structures grown on such patterned substrates are expected to exhibit similar threshold characteristics as those on unpatterned substrates.

Here we present the results of our study on $In_{0.2}Ga_{0.8}As$/GaAs laser arrays with varying emission wavelengths obtained by MBE growth on GaAs substrates patterned by reactive ion etching (RIE). We also explore the possibility of integrating multispectral vertical cavity surface emitting laser (VCSEL) arrays.

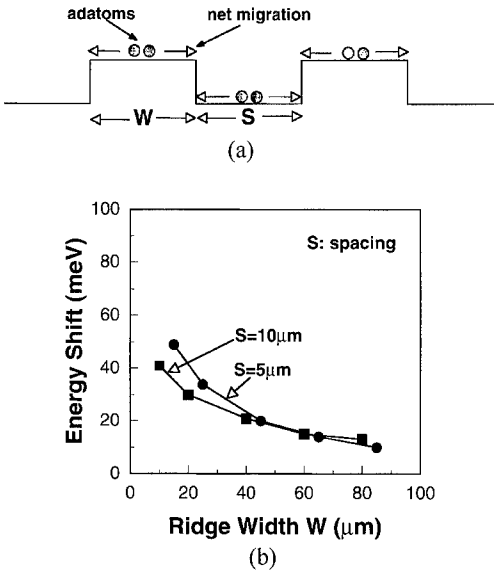

Fig. 1. (a) Schematic illustrating the In adatom migration on a patterned substrate with vertical sidewalls obtained by dry etching (b) dependence of pattern dimensions on the blue shift in the band gap of $In_{0.2}Ga_{0.8}As$/GaAs quantum well grown on ridges.

2. Experimental procedure

Pseudomorphic $In_{0.2}Ga_{0.8}As$/GaAs single quantum well separate confinement heterostructure (SQW-SCH) lasers, as shown in Fig. 2, were grown

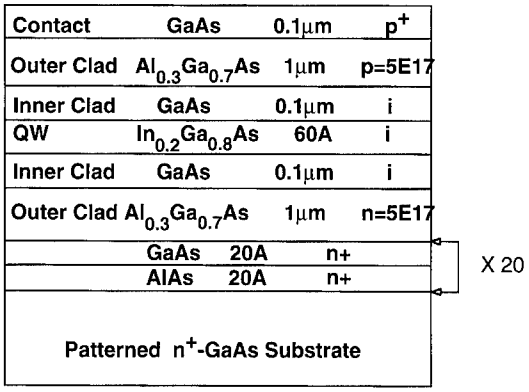

Fig. 2. Structure parameters of the SCH laser grown on GaAs (1 0 0) substrates patterned into 2 μm deep ridges with vertical sidewalls. The layers marked inner clad are the carrier confinement regions.

in a Varian GEN II MBE system. The n^+-GaAs (1 0 0) substrates were patterned into 2 μm deep ridges (width 10–60 μm) having vertical sidewalls, obtained by RIE. The growth rate of GaAs was 0.72 μm/h and the V/III flux ratio ~5. The GaAs and $Al_{0.3}Ga_{0.7}As$ layers were grown at 620°C and the $In_{0.2}Ga_{0.8}As$ layers were grown at 540°C. Silicon and berylium were used as n- and p-type dopants, respectively. Single mode ridge waveguide lasers were fabricated with alloyed Pd/Zn/Pd/Au and Ni/Ge/Au/Ti/Au for p-ohmic and n-ohmic contacts, respectively, and with wet and dry etching.

For the demonstration of multispectral VCSELs, the structures were grown in two growth steps. The bottom distributed Bragg reflector (DBR) mirror with 20 periods of GaAs/AlAs was grown in the first step. Small circular patterns with 12–45 μm diameters were masked by photoresist and the samples were etched by RIE to reach the substrate. A wet etch with $H_2SO_4/H_2O_2/H_2O$ (1 : 8 : 800) was performed before introducing the sample in the MBE system for regrowth. One more period of bottom DBR followed by the active region consisting of single $In_{0.2}Ga_{0.8}As$ QW surrounded by 0.1 μm of GaAs on each side were regrown by MBE. Fig. 3 shows the scanning electronic microscope (SEM) image of such pillars before and after regrowth.

Photoluminescence measurements were made on all the samples at 18 K with 488 nm Ar + laser excitation source, 0.75 m scanning spectrometer, liquid nitrogen cooled photomultiplier, and lock-in amplification. The excitation laser was focused to a spot size (~15 μm) of the order of the size of the patterns.

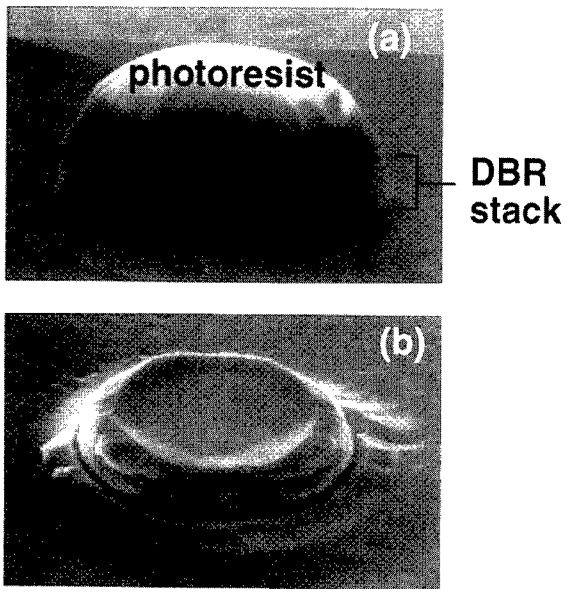

Fig. 3. SEM image of the pillar etched from DBR stack (a) before and (b) after regrowth. The etched pattern before regrowth is shown with the photoresist used as a mask for RIE.

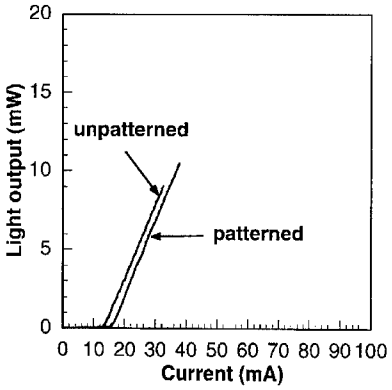

Fig. 4. *L–I* characteristics of the single mode (3 μm) lasers with 500 μm cavity length from patterned and unpatterned regions of the same sample. Clearly, there is no significant degradation in either the threshold current or the differential efficiency.

3. Results and discussion

Single mode lasers (3 μm wide) fabricated from the unpatterned region has a threshold current of 12 mA for a cavity length of 500 μm. The *L–I* characteristics of the lasers from unpatterned and patterned regions of the same laser bar are shown in Fig. 4. There is no significant change in either threshold current or the slope above threshold which indicate that the quality of the material grown on top of the ridges is as good as that on the plane substrates. This corroborates our earlier report that there is no significant difference in the intensity or the line width of the PL emission from the material on unpatterned region and on top of the ridge [8].

The emission spectra obtained from lasers placed at three different regions of the same laser bar are shown in Fig. 5. Laser L0 is located farthest – greater than one migration length of indium adatoms – from the patterns so that there is no contribution from the surface discontinuity at the sidewalls. L1 is close to the patterned ridge and hence has sidewalls on one side. L2 and L3 are from a 20 and 10 μm ridges, respectively, and have sidewalls on both sides. As is evident from Fig. 5b, there is a blue shift in the emission energy of the lasers on top of the patterns compared to laser L0. The blue shift is more for 10 μm ridge compared to 20 μm ridge in agreement with the PL measurements [8]. Also, the amount of blue shift in laser emission wavelength for lasers having 1 sidewall is different from that of 10 and 20 μm ridges. Thus, with a suitable combination of the ridge width and the placing of the lasers, a large number of lasers with closely spaced emission wavelength can be integrated in close spatial proximity. We have observed a maximum shift of 11 nm for a minimum ridge width of 10 μm used in this study.

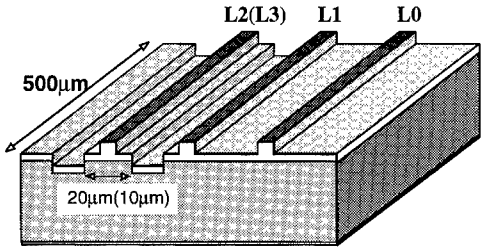

(a)

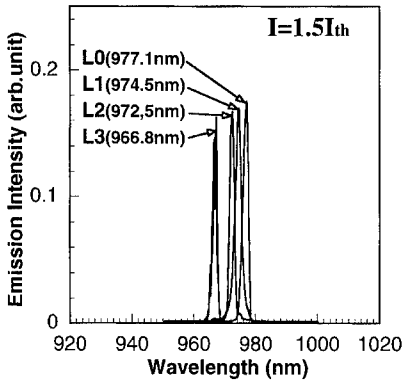

(b)

Fig. 5. (a) Schematic and (b) emission spectra of the multispectral lasers grown on patterned and unpatterned regions. Laser L0 is from an unpatterned region where there is no side wall within a migration length. L1 is close to the patterns and has one sidewall while L2(L3) is on 20(10) μm ridge and hence has two sidewalls.

One of the major benefits of using this technique of patterned growth for obtaining multi-spectral laser arrays is that conventional single mode laser processing is used and no changes in the fabrication steps are necessary. However, its limitation lies in the fact that the maximum wavelength difference that can be obtained is limited. Therefore, we can conclude that this technique is useful in applications where a large number of lasers with relatively small wavelength shift is needed with precise control over wavelength spacing.

Another area where this technique of varying emission wavelengths by pre-patterning the substrates is applicable is in the fabrication of multispectral VCSELs. Multispectral VCSELs have been tried earlier by differential heating across the wafer wherein the growth rate of the DBR stack and therefore the reflection maximum is varied. However, this has not proved to be a very controllable process. Here, we present the possibility of obtaining multispectral VCSELs by growth on patterned substrates. This is done in two growth steps. After growing the bottom DBR stack, circular patterns are formed by RIE and then the VCSEL structure is completed by a regrowth step. The problems associated with regrowth can be partially eliminated by growing one period of the bottom DBR before growing the active layers. This will put the regrown interface in the DBR region rather than in the active region. In order to demonstrate the possibility of obtaining multiple emission wavelengths, PL samples were prepared by a regrowth of single quantum well on the DBR pillars as explained in Section 2. The PL spectra obtained from plane region and from the top of the patterns of two different diameters are shown in Fig. 6. There is a shift of 11 and 46 meV in the emission peak from the QW on top of pillars of diameters 35 and 12 μm, respectively. These spectra were taken after etching off the QW from rest of the region.

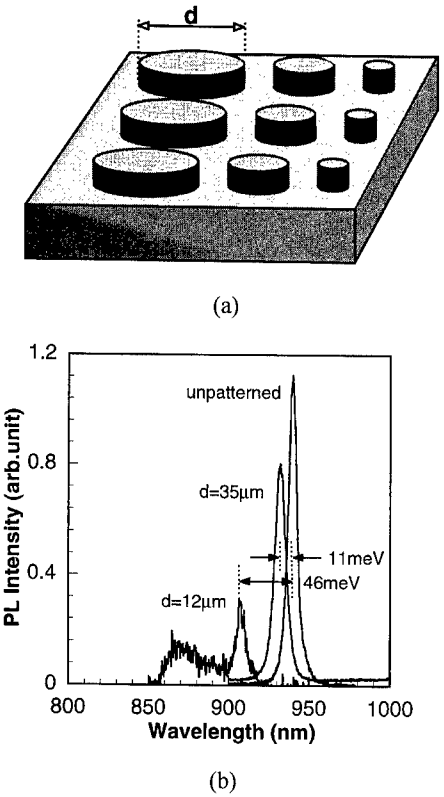

Fig. 6. PL spectra of $In_{0.2}Ga_{0.8}As/GaAs$ QW grown on patterned DBR structure. DBR pillars obtained by RIE is shown schematically in (a). The PL spectra from the QW on top of patterns with 12 and 35 μm diameter are shown in (b) along with the PL spectrum form an unpatterned region of the same sample.

The PL intensity from the 12 μm pattern is less because the excitation laser spot size is larger than the pattern diameter, which is also responsible for the second peak on the higher energy side due to the emission from the sidewalls.

We have thus shown that multispectral VCSEL array can be obtained by patterned growth. However, it should be noted here that such VCSEL arrays can be made only if the emission spectra of all the devices in the array lie within the flat region of the reflection spectrum of the DBR mirror.

4. Conclusion

We have demonstrated multispectral laser arrays by MBE growth on non-planar patterned substrates, without using regrowth. The blue shift obtained in the band gap of the material on top of ridges having *vertical* sidewalls is utilized in integrating lasers with different emission wavelengths. It is found that the characteristics of the lasers on top of the patterns are similar to those on unpatterned substrates indicating that there is no degradation in the behavior of the lasers due to patterned growth. Laser emission spectra show that the blue shift obtained depends on the ridge width of the pre-patterns as well as the number of sidewalls. We have also demonstrated that multispectral VCSEL arrays can possibly be made with a single regrowth step.

Acknowledgements

This work is supported by Advanced Research Projects Agency (COST) under Grant No. MDA 972-94-1-004.

References

[1] K.J. Beernink, R.L. Thornton and H.F. Chung, Appl. Phys. Lett. 64 (1994) 1802.
[2] K.J. Beernink, D. Sun, R.L. Thornton and D.W. Treat, Appl. Phys. Lett. 68 (1996) 284.
[3] D.J. Arent, S. Nilsson, Y.D. Galeuchet, H.P. Meier and W. Walter, Appl. Phys. Lett. 55 (1989) 2611.
[4] M. Hata, T. Isu, A. Watanabe and Y. Katayama, Appl. Phys. Lett. 56 (1990) 100.
[5] S. Nilsson, E. Van Gieson, D.J. Arent, H.P. Meier, W. Walter and T. Foster, Appl. Phys. Lett. 55 (1989) 972.
[6] F.S. Turco, M.C. Hwang, R.E. Nahory, J. Werner, K. Kash and E. Kapon, Appl. Phys. Lett. 56 (1990) 72.
[7] E.M. Clausen, Jr., E. Kapon, M.C. Tamargo and D.M. Hwang, Appl. Phys. Lett. 56 (1990) 776.
[8] K. Kamath, J. Phillips, J. Singh and P. Bhattacharya, J. Vac. Sci. Technol. B 14 (1996) 2313.
[9] J. Phillips, K. Kamath, J. Singh and P. Bhattacharya, Appl. Phys. Lett. 68 (1996) 1120.

ELSEVIER

Journal of Crystal Growth 175/176 (1997) 940–944

JOURNAL OF CRYSTAL GROWTH

MBE growth of high-quality InP for GaInAs/InP heterostructures using incongruent evaporation of GaP

H. Künzel*, J. Böttcher, P. Harde, R. Maessen[1]

Heinrich-Hertz-Institut für Nachrichtentechnik Berlin GmbH, Einsteinufer 37, D-10587 Berlin, Germany

Abstract

The incongruent evaporation of GaP source material using a conventional effusion cell equipped with a PBN scavenger at the orifice is demonstrated as a simple and cost-effective way to generate a pure P_2 molecular beam, suitable for the growth of InP layers in a solid-source MBE system. Low residual carrier concentrations in combination with high mobilities as well as narrow and intense photoluminescence spectra were achieved. While some arsenic incorporation from the growth environment was observed, gallium incorporation is limited to below 0.1% of the group-III lattice sites. n- and p-doping using Si and Be has been investigated. Successful growth of InP/GaInAs heterostructures indicates that the use of the GaP source technique is a viable way for growing AlGaInAs/InP device structures by solid source MBE.

1. Introduction

Long wavelength (1.3–1.6 μm) quantum well lasers based on the $(Al_xGa_{1-x})_{0.48}In_{0.52}As$ rather than the commonly used GaInAsP material system have gained increasing attention recently as they promise superior laser performance in terms of high-temperature operation, high output power and speed as well as low chirp [1–3] due to the larger conduction band offset in these alloys. Concerning the cladding layer material, the ternary $Al_{0.48}In_{0.52}As$ would be the consequent choice, however, due to its better thermal and electrical conductivity, InP is clearly preferable.

This contribution specifically reports on the MBE growth of InP employing a conventional ion-pumped growth system. As high precision control of the phosphorus flux, as offered by valved cracker cells [4], is not necessary when only the binary InP is required, the incongruent evaporation of GaP from a conventional effusion cell equipped with a scavenger at the orifice appears to be a very simple and cost-effective way to generate an extremely pure P_2 molecular beam [5]. Using this technique, the growth of high-quality InP in terms of morphology, electrical and optical characteristics will be presented. Contamination of InP by Ga from the GaP source as well as by As from the growth environment has been analysed. Results on the incorporation of the conventional dopants Si and Be will be described. Subsequently, the growth of abrupt GaInAs/InP heterostructures will be demonstrated, proving the suitability of GaP

* Corresponding author. Fax: + 49 30 31002-558; e-mail: kuenzel@mails.hhi.de.

[1] On leave from: Technical University of Eindhoven, P.O. Box 513, Eindhoven, The Netherlands.

0022-0248/97/$17.00 Copyright © 1997 Elsevier Science B.V. All rights reserved
PII S0022-0248(96)00879-2

source MBE of InP for InP/(Al)GaInAs device structures.

2. Experimental procedure

The InP layers were grown in a conventional MBE system which is exclusively equipped with an ion pump. Except for arsenic, As, conventional effusion cells were used for the group-III and the dopant elements. For As a valved cracker cell was employed (with only the As_4-mode used) to facilitate the rapid switching of the As_4 beam within GaInAs/InP heterostructures. The GaP source material (polycrystalline 6 N) was also evaporated from a conventional cell. The use of the P_2 beam originating from the GaP did not cause any difficulty with the MBE system. Even during warm up of the growth chamber the pressure rise did not exceed 10^{-5} mbar. In addition, opening of the growth chamber did not provoke any firing even without pre-baking. Reduction of the residual Ga beam generated during the GaP evaporation was achieved by the implementation of a multiple diaphragm approach [6]. A custom designed PBN device similar to Ref. [5] was applied. The GaP cell was operated without a shutter, i.e. the P_2 beam was switched on and off simply by variation of the source temperature. Consequently, growth interruptions of up to 5 min with an As_4 stabilising beam impinging on the surface were required at InP/GaInAs and GaInAs/InP interfaces. InP layers were deposited onto epi-ready (100) InP substrates without applying any pre-treatment. The substrate surface was inspected by RHEED during oxide desorption to calibrate the thermocouple reading of the substrate temperature, T_g. Growth was initiated at $T_g = 465°C$, and the sample temperature was subsequently ramped to its final value.

The properties of the MBE-grown InP were assessed with conventional characterisation tools: interference microscopy, 10 K photoluminescence, PL, 300/77 K Hall measurements, double-crystal X-ray diffraction, DCXRD, and secondary-ion mass spectroscopy, SIMS, using an oxygen primary beam.

3. Results

The temperature of the GaP source, T_{GaP}, to deliver an adequate P_2 beam density was determined from an Arrhenius type plot of the P_2 pressure (flux gauge) versus $1/T_{GaP}$. Variation of the cell temperature between 800°C and 865°C results in an increase of the P_2 beam pressure from 1.0×10^{-6} mbar to 8.0×10^{-6} mbar. The chamber pressure increases correspondingly from 0.55×10^{-7} mbar to 1.8×10^{-7} mbar.

3.1. Material characteristics

InP layers were deposited at temperatures between 400°C and 500°C. Inspection by interference contrast microscopy confirmed smooth and featureless surfaces at minimum BEP(P_2/In) ratios between 2 and 10, depending on T_g. The effectiveness of suppressing the residual Ga concentration, originating from the GaP source, by means of the PBN scavenger in front of the cell orifice was studied by SIMS profiling of ^{71}Ga. In Fig. 1, the SIMS profile of a 0.8 μm thick InP layer grown at 420°C shows a strong ^{71}Ga interface peak due to Ga deposition occurring during P_2 stabilisation of the InP substrate during oxide desorption, as well as a low and constant amount of ^{71}Ga incorporated during growth. For the particular V/III ratio applied, a ^{71}Ga concentration of 2×10^{18} cm^{-3} was determined, which corresponds to an overall

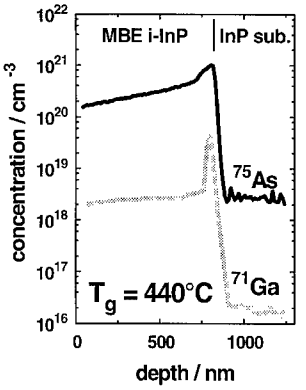

Fig. 1. SIMS depth profiles of residual ^{75}As and ^{71}Ga in an MBE InP layer grown from a GaP source.

amount of ^{71}Ga plus ^{69}Ga of 5×10^{18} cm^{-3}. Thus, only a fraction of 5×10^{-4} of the overall group-III lattice sites is occupied by gallium which is a factor of two lower than previously reported [5].

The dominant contaminant in the InP layer depicted was found to be arsenic. Its concentration exceeds that of residual gallium by roughly two orders of magnitude, thus amounting to several percent. Apart from the accumulation at the layer/substrate interface, related to the formation of an intermediate In(P, As) layer during the oxide desorption process, As incorporation exponentially decreases during growth, which indicates that it is released from any background source. This is not surprising since the MBE system had been extensively used for the growth of AlGaInAs layers in the past. However, by extensive baking of the MBE system As incorporation was dramatically reduced to a level below 0.1%, which lies in the same range as reported for MBE InP growth with valved cracker cells [7, 8]. The high amount of residual As present in Fig. 1 results in some lattice distortion amounting to values even in excess of 1000 ppm with the occurrence of cross-hatching indicating strain relaxation. Successful reduction of residual As by extensive baking gives rise to an X-ray diffration pattern composed of only one InP peak (FWHM : 21 arcsec) revealing a lattice distortion below 50 ppm.

High T_g values and correspondingly lower V/III ratios during deposition were found to favour the reduction of the residual carrier concentration. This is demonstrated in Fig. 2, in which 300 and 77 K Hall data are shown in dependence of the V/III ratio for samples grown at $T_g = 420$°C. In agreement with the decrease of residual carrier concentration down to $1.6/0.6 \times 10^{15}$ cm^{-3} (300/77 K), when reducing the V/III ratio from 6 to 3, a monotonous increase of the 77 K mobility from 20.000 to 50.000 cm^2/V·s was observed as well. At a lower V/III ratio the 300 K carrier concentration drops below 10^{15} cm^{-3}, however, a degradation of mobility as well as surface roughness due to group-V deficient growth are observed in that case.

High optical quality of the MBE-grown InP was obtained, as depicted in Fig. 3 which shows 10 K PL spectra of a layer grown at 420°C in comparison with state-of-the-art MOVPE-grown InP ($T_g = 650$°C). For both epitaxy techniques, the observed dominance of the excitonic near band edge emission indicates high optical quality. The impurity related transitions between 1.40 and 1.37 eV are close to the detection limit. While the linewidth of the MOVPE excitonic emission is as narrow as 2 meV, the MBE grown InP shows a larger line width of 5 meV, due to the higher residual carrier concentration of the particular MBE layer investigated (5×10^{14} cm^{-3} (MOVPE) versus 7×10^{15} cm^{-3} (MBE)). Interestingly, despite the strong blue shift of 12 meV of the emission from MBE InP indicating a relatively high degree of As incorporation (roughly 2% in this case), the integral intensity of the MBE InP is fairly comparable to that of the MOVPE-grown material.

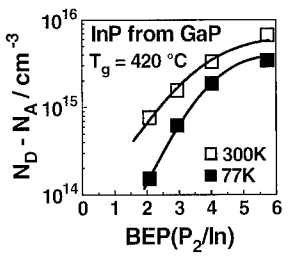

Fig. 2. 300/77 K Hall carrier concentrations of undoped MBE InP in dependence of the P_2/In ratio.

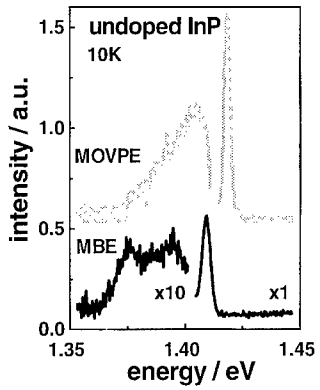

Fig. 3. Comparison of 10 K PL spectra of InP layers grown by MBE using a GaP source and by low-pressure MOVPE.

3.2. Si and Be doping

Studies on n- and p-type doping were performed using the conventional dopants Si and Be and comparing their incorporation behaviour with that in GaInAs. Doping levels between 1×10^{17} and 1×10^{19} cm^{-3} were investigated. Hall carrier concentrations were found to be identical in InP and GaInAs for n- and p-doping over the whole doping level range. Particularly for Be incorporation, the observed Arrhenius-type p versus T_{Be}^{-1} behaviour in combination with the Be concentration, as measured by SIMS, indicate that up to 1×10^{19} cm^{-3} complete activation occurs. The agreement with the GaInAs data suggests 100% Be incorporation in InP. The electrical quality of the n- and p-doped layers compares well with published mobility values obtained in material grown with a valved cracker cell [9]. At a doping concentration of 1×10^{18} cm^{-3} 300 K mobilities of 1750 and 55 cm^2/V·s were obtained for Si- and Be-doping, respectively.

Although Be atoms are known to be prone to acceptor diffusion during growth [10], controlled Be incorporation in InP could be achieved at a reduced T_g of 420°C. This is demonstrated in Fig. 4 by comparing SIMS ^{9}Be profiles of 1.3 μm thick p-InP homogeneously doped to 1.3×10^{19} cm^{-3} (highest Be concentration applied throughout this study) and a p$^+$/p-doped structure (5×10^{18} cm^{-3}/2×10^{17} cm^{-3}) designed for the p-cladding layer of a laser. Even for the highly doped layer only minor movement of Be was detected. The corresponding SIMS profile (a) shows that homogeneous incorporation occurs apart from some depletion observable near the substrate/layer interface, apparently associated with accumulation at the interface, and a constant low-level incorporation in the substrate. The latter appears to be strongly dependent on doping concentration, as demonstrated by comparison with profile (b) in Fig. 4. Reduction of the doping concentration to 5×10^{18} cm^{-3} obviously eliminates Be movement allowing for a very abrupt change in doping concentration to a level of 2×10^{17} cm^{-3}. In addition, no beryllium could be detected in the substrate in this case, hence ruling out any significant Be movement into an active laser region if implemented in a real laser structure.

3.3. GaInAs/InP heterostructures

To further assess the applicability of InP grown from a GaP source to heterostructure devices, we have deposited InP/GaInAs/InP test layers similar to those implemented in optoelectronic devices. SIMS-profiles, presented in Fig. 5, give an impression of the switching ability from As to P and vice versa, confirming that quite abrupt switching is possible. A P concentration drop of nearly three orders of magnitude to a constant low level can be obtained which is determined by the idling temperature of the GaP source operated without a shutter. The As level can also be abruptly changed at the

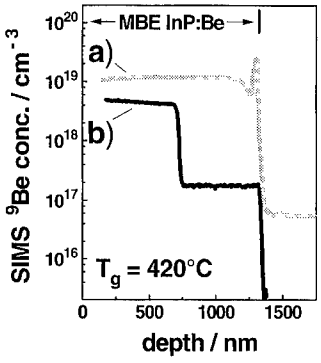

Fig. 4. SIMS ^{9}Be depth profiles of Be-doped MBE p-InP: (a) homogeneously doped p^{++}-InP : Be; (b) p$^+$/p-InP : Be.

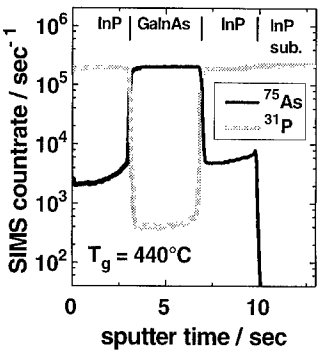

Fig. 5. ^{31}P and ^{75}As depth profiles of a MBE grown InP/GaInAs/InP heterostructure using GaP and As as the group-V source materials.

InP/GaInAs interface, however, as already pointed out, an exponential decay of the As level in InP is observed, ranging from 0.03 in the lower towards 0.01 in the upper InP layer for the specific sample shown. In addition, no substantial P incorporation in GaInAs is observed.

4. Summary

In summary, it has been demonstrated that incongruent evaporation of GaP from a conventional effusion cell equipped with a multiple diaphragm device is a simple and cost effective way to generate a very pure P_2 beam. InP layers of high quality and well-controllable incorporation of dopants, particularly Be, were deposited. Abrupt switching from InP to GaInAs was successfully achieved with no substantial P incorporation in GaInAs. While residual incorporation of Ga in InP was demonstrated to remain at a negligible level below 0.1%, As incorporation from the growth environment is of concern. Nevertheless, levels down to 0.1% are attainable.

Acknowledgements

Part of this work was conducted under contract with Bosch-Telecom GmbH, Backnang, Germany.

References

[1] H. Hillmer, R. Lösch, F. Steinhagen, W. Schlapp, A. Pöcker and H. Burkhard, Electron. Lett. 31 (1995) 1346.
[2] R. Bhat, C.E. Zah, M.A. Koza, B. Pathak, F. Favire, W. Lin, M.C. Wang, N.C. Andreadakis, D.-M. Hwang, T.P. Lee, Z. Wang, D. Darby, D. Flanders and J.J. Hsieh, J. Crystal Growth 145 (1994) 858.
[3] P.J.A. Thijs, T. van Dongen, J.J.M. Binsma and E.J. Jansen, Proc. 8th IPRM, Schwäbisch Gmünd (1996) IEEE Catalog #96CH35930 Library of Congres #96-75713, p. 765.
[4] J.N. Baillargeon, A.Y. Cho, F.A. Thiel, R.J. Fischer, P.J. Pearah and K.Y. Cheng, Appl. Phys. Lett. 65 (1994) 207.
[5] T. Shitara and K. Eberl, Appl. Phys. Lett. 65 (1994) 356.
[6] M.J. Mondry, E.J. Caine and H. Kroemer, J. Vac. Sci. Technol. A3 (1985) 316.
[7] J.C. Harmand, J.P. Praseuth, E. Idiart-Alhor, R. Palla, J.L. Pelouard and M. Quillec, J. Crystal Growth 150 (1996) 1292.
[8] T. Feifel and K. Panzlaff, data presented at the German National MBE Workshop, Stuttgart, 1995, unpublished.
[9] J.N. Baillargeon, A.Y. Cho, R.J. Fischer, P.J. Pearah and K.Y. Cheng, Proc. 7th IPRM, Sapporo (1995) IEEE Catalog #96CH35720 Library of Congres #94-79424, p. 148.
[10] M.B. Panish, R.A. Hamm, D. Ritter, H.S. Luftman and C.M. Cotell, J. Crystal Growth 112 (1994) 343.

ELSEVIER

Journal of Crystal Growth 175/176 (1997) 945–947

JOURNAL OF CRYSTAL GROWTH

Gas-source molecular beam epitaxial growth of low threshold current 1.3 μm InAsP/InGaAsP lasers

P. Thiagarajan*, G.E. Giudice, H. Temkin , G.Y. Robinson

Department of Electrical Engineering, Colorado State University, Fort Collins, Colorado 80523, USA

Abstract

Highly strained InAsP/InGaAsP MQW lasers emitting at 1.3 μm grown by gas-source molecular beam epitaxy with threshold currents of 1.1 mA at 20°C are reported. Lasers with anti-reflection/high-reflection coated facets exhibited slope efficiencies as high as 0.48 mW/mA, output powers of 65 mW, and wall plug efficiencies of 30% at 10 mW.

1. Introduction

InP-based semiconductor lasers operating at 1.3 μm have received much attention due to their increasing role in applications such as fiber-optic communication and optical interconnect systems. These applications require that the semiconductor lasers maintain low threshold currents and high output powers over a wide temperature range. For semiconductor lasers operating at 1.3 μm, separate confinement heterostructure multiple quantum well (SCH-MQW) lasers using compressively strained InAsP wells with either lattice-matched or strained InGaAsP barriers grown on InP have been demonstrated to have superior high-temperature and output power performance over the commonly used InGaAsP/InGaAsP SCH-MQW lasers [1, 2]. We had recently reported on the optimization of growth conditions for high-quality 1.3 μm InAsP/InGaAsP SCH-MQW lasers by gas-source molecular beam epitaxy (GSMBE) [3]. Here we report on InAsP/InGaAsP SCH-MQW lasers for 1.3 μm emission grown by GSMBE with very low threshold currents of 1.1 mA at 20°C and 6.1 mA at 100°C. To our knowledge, these are the lowest threshold currents yet reported for any InGaAsP lasers grown by GSMBE [4–6].

2. Experimental procedure

The InAsP/InGaAsP heterostructures were grown on (1 0 0) n-type InP substrates. Conventional effusion cells were used to provide the In and Ga atomic fluxes, with growth rates of 0.6–1.0 μm/h. AsH_3 and PH_3 were thermally cracked at 800°C to obtain the As_2 and P_2 molecular beams, with flow rates of 2–10 sccm.

A schematic of the epitaxial layer structure used for the InAsP/InGaAsP SCH-MQW laser is

* Corresponding author.

0022-0248/97/$17.00 Copyright © 1997 Elsevier Science B.V. All rights reserved
PII S0022-0248(96)00829-9

shown in Fig. 1. The laser structure consisted of a 1 μm n-type InP cladding layer (1×10^{18} cm^{-3}), the active region, a 1.5 μm p-type InP cladding layer (7×10^{17} cm^{-3}), and finally a 0.2 μm p-type InGaAs contact layer (2×10^{19} cm^{-3}). The active region consisted of six wells of $InAs_{0.45}P_{0.55}$, 4.5 nm thick, with 15 nm InGaAsP barriers with band gap emission of 1.15 μm (denoted as 1.15Q), and 110 nm InGaAsP (1.15Q) separate confinement layers on either side of the MQW region. The InP cladding layers were grown at 460–480°C, while the active region was grown at 430°C, since substrate temperatures between 410 and 430°C were previously determined to be optimum for GSMBE growth of the InAsP/InGaAsP MQWs [3]. Buried heterostructure (BH) lasers were fabricated from the GSMBE wafers with an InP p–n–i–n current blocking structure using MOCVD [7]. For high-reflection coatings alternating layers of SiO_2 and Si were evaporated on the laser facets; for anti-reflection coatings a single layer of SiO_2 was used.

3. Results

The light output versus drive current (L–I) characteristics of BH lasers with a cavity length L of 125 μm and different facet reflectivities (R_1 and R_2) are shown in Fig. 2. For lasers with uncoated facets (i.e., $R_1/R_2 = 29\%/29\%$), a minimum threshold current of 6.5 mA was measured. With a high-reflection coating on the rear facet ($R_2 = 95\%$), the threshold current reduced to 3.0 mA. A low threshold current of 1.1 mA was measured for the 125 μm long lasers with high-reflection coatings on both facets ($R_1/R_2 = 85\%/95\%$).

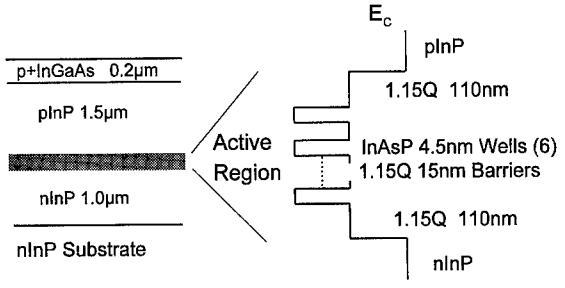

Fig. 1. Schematic diagram of the epitaxial layer structure of the InAsP/InGaAsP SCH-MQW laser.

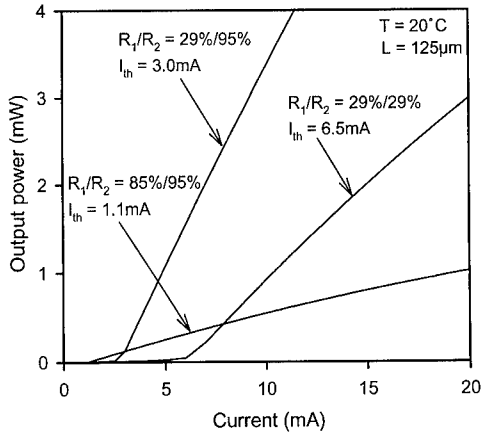

Fig. 2. Light output versus drive current characteristics for 125 μm long buried heterostructure lasers with different facet reflectivities (R_1 and R_2). R_1 is the front facet reflectivity and R_2 is the reflectivity of the rear facet.

The L–I characteristics as a function of temperature for a BH laser with a cavity length of 125 μm and $R_1/R_2 = 85\%/95\%$ was measured. The threshold current increased from 1.1 mA at 20°C to only 6.1 mA at 100°C.

The output power of the lasers was increased by using anti-reflection coatings for the front facet ($R_1 = 10\%$) and high-reflection coating for the rear facet ($R_2 = 95\%$). The L–I characteristics of a 250 μm long and a 750 μm long laser with anti-reflection/high-reflection coated facets are shown in Fig. 3. A maximum output power of 49 and 65 mW were measured for the 250 μm and 750 μm long lasers, respectively, at 20°C. Very high slope efficiencies of 0.48 mW/mA and wall plug efficiencies of 30% at 10mW were observed for devices of 250 μm in length at 20°C.

The maximum output power as a function of device temperature is shown in Fig. 4. The maximum output power dropped from 49 mW at 20°C to 4 mW at 90°C for the 250 μm long laser and from 65 mW at 20°C to 15 mW at 90°C for the 750 μm long laser. Even at these high operating powers and elevated temperatures no catastrophic failure of the lasers were observed in our preliminary evaluation.

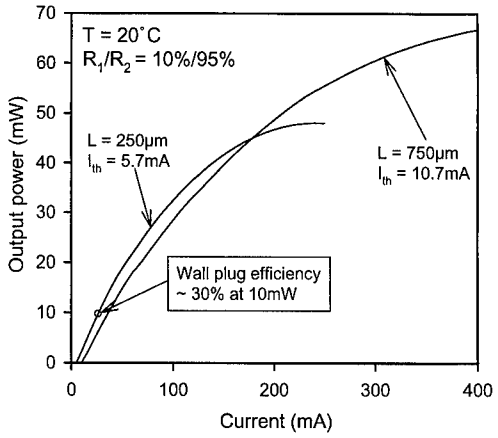

Fig. 3. Light output versus drive current characteristics for a 250 μm long laser and a 750 μm long laser with anti-reflection/high reflection coated facets (R_1/R_2 = 10%/95%).

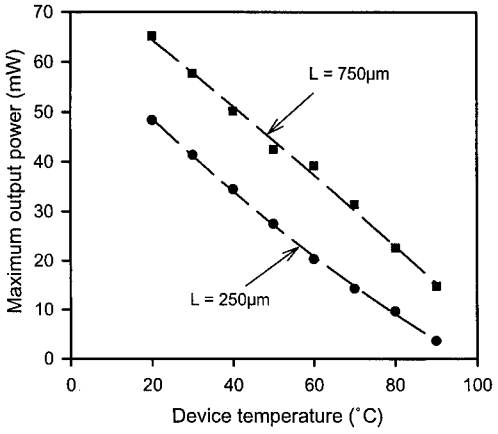

Fig. 4. Maximum output power as a function of device temperature for 250 μm and 750 μm long buried heterostructure lasers with R_1/R_2 = 10%/95%.

4. Summary

In summary, we report low threshold current InAsP/InGaAsP SCH-MQW lasers for 1.3 μm emission grown by GSMBE. Threshold currents as low as 1.1 mA at 20°C and 6.1 mA at 100°C were measured for buried heterostructure lasers with high-reflection coatings on the laser facets. To our knowledge, these are the lowest threshold currents yet reported for InGaAsP lasers grown by GSMBE. Furthermore, external slope efficiencies as high as 0.48 mW/mA with wall plug efficiencies of 30% at 10mW were observed, and a maximum output power of 65 mW at 20°C was achieved.

Acknowledgements

The authors would like to acknowledge R.A. Logan for the MOCVD regrowth. This work was supported by Hanscom Laboratory (No. F19628-93-K-0022) and ARPA.

References

[1] M. Yamamoto, N. Yamamoto and J. Nakano, IEEE J. Quantum Electron. QE-30 (1994) 554.
[2] H. Oohashi, S. Seki, T. Hirono, H. Sugiura, T. Amano, M. Ukei, J. Nakano, M. Yamamoto, Y. Tohmori, M. Fukuda and K. Yokoyama, Electron. Lett. 31 (1995) 556.
[3] P. Thiagarajan, A.A. Bernussi, H. Temkin, G.Y. Robinson, A.M. Sergent and R.A. Logan, Appl. Phys. Lett. 67 (1995) 3676.
[4] G.-J. Shiau, C.-P. Chao, P.E. Burrows and S.R. Forrest, Appl. Phys. Lett. 65 (1994) 892.
[5] J.-L. Liévin, L. Le Gouézigou, D. Bonnevie, F. Gaborit, F. Poingt and F. Brillouet, Appl. Phys. Lett. 60 (1992) 1211.
[6] M. Pessa, T. Hakkarainen, J. Keskinen, K. Rakennus, A. Salokatve, G. Zhang and H. Asonen, SPIE's Int. Conf. on Physical Concepts for Novel Optoelectronic Device Applications, Aachen, Germany, 28 October–2 November (1990).
[7] H. Temkin, D. Coblentz, R.A. Logan, J.M. Vandenberg, R.D. Yadvish and A.M. Sergent, Appl. Phys. Lett. 63 (1993) 2321–2323.

ELSEVIER

Journal of Crystal Growth 175/176 (1996) 948–954

JOURNAL OF CRYSTAL GROWTH

High temperature (Ga)InAsP/high band gap GaInAsP barriers 1.3 μm SL-MQW lasers grown by gas source MBE

Ph. Pagnod-Rossiaux*, F. Gaborit, N. Tscherptner, L. Roux, C. Starck, B. Fernier

Alcatel–Alsthom Recherche, Route de Nozay, F-91460 Marcoussis, France

Abstract

We report on an experimental investigation of the temperature sensitivity of (Ga)InAsP compressively strained multi-quantum well (MQW) 1.3 μm broad area lasers with respect to the amount of strain and barrier band gap. The composition of wells are adjusted to let the strains range from 0.6% to 1.4%, whereas barrier band gap scales from 1.13 to 1.3 eV. Threshold current densities per well for infinite length as low as 60 to 135 A cm^{-2} at 20°C asses for the high quality of the structures grown by gas source MBE. Characteristic temperatures of 80 to 110 K, depending on the barrier band gap, are measured between 20°C and 80°C for 1200 μm long devices.

Keywords: 1.3 μm lasers; Strain-compensated multi-quantum wells; Characteristic temperature

1. Introduction

Low cost, low drive current, wide temperature range [− 40°C, + 80°C] 1.3 μm lasers are key components for large volume fibre to the home applications. In the GaInAsP/InP system, Auger recombination and/or carrier overflow in the barrier and SCH layers, resulting in low characteristic temperature T_0 (40–50 K for short cavity length), have been identified to limit high temperature performances of the devices [1, 2].

The introduction of strain in quantum well lasers is well known to improve threshold current densities through a reduction of both densities of state and nonradiative recombination processes (Auger, inter valence band absorption) [3]. Highly strained (≈1.4%) InAsP 1.3 μm MQWs have been shown to be of interest for low threshold lasers [4, 5]. However, the effect of strain on the temperature sensitivity, as seen from many experimental results, is controversial [3]. As a matter of fact, temperature sensitivity strongly depends on the lasing cavity design parameters, i.e. vertical and lateral confinements, length, facets coating, leading to a large discrepancy of results.

More recently, the benefit of high band gap barriers on the temperature characteristics of devices

* Corresponding author. Fax: + 33 1 69 63 17 85; e-mail:philippe.pagnod@aar.alcatel-alsthom.fr.

0022-0248/97/$17.00 Copyright © 1997 Elsevier Science B.V. All rights reserved
PII S0022-0248(96)00953-0

has been evidenced. Lasing at temperatures in excess of 130°C has been reported with structures including 1.05 μm InGaAsP barriers and SCH layers grown by chemical beam epitaxy (CBE) [6]. To's as high as 117 K between 20°C and 60°C have been shown on 10 InAsP strained-layer multi-quantum well (SL-MQW) with InGaP barriers devices grown by atmospheric pressure metal organic vapor phase epitaxy (AP-MOVPE) [7]. It has to be pointed out that T_0 is not the most relevant parameter regarding high temperature laser operation. From this point of view, threshold current density and external quantum efficiency at 80°C are best suited to characterize the potential of a device structure.

We report on the experimental investigation of both compressive strain in the wells and barrier (lattice-matched or tensile strained) band gap on the temperature characteristics of SL-MQW broad area (BA) lasers grown by gas source MBE (GSMBE).

2. Structure design and growth

The strain in the In(Ga)AsP QWs increases as their Ga concentration (Xw) is reduced. For a wavelength of 1.3 μm and a well width of 8 nm, compressive strain values of 0.6, 1% and 1.4% can be reached with $X_w \approx 0.19$, 0.11 and 0.00, respectively.

The compositions of the barriers have been calculated to meet the following requirements: (i) to let the electron escape energy E_{be} range in a large interval, E_{be} being defined as the difference between the well/barrier conduction bands offset ΔE_c and the 1rst quantized electron level e_1. (ii) To compensate with tensile strain the highly compressive InAsP wells. Tensile strain of about -0.8% is achievable by GS-MBE. Moreover, tensile strain in barriers improves slightly the conduction bands offsets, and thus further increases E_{be}. From those conditions, a maximum $E_{be} \approx 200$ meV is calculated for $Ga_{0.11}InP$ (-0.5%) barriers and $InAs_{0.43}P$ wells. Such values compare favorably with those obtained in the AlGaInAs/InP system [8].

The structures consist of six QWs and seven barriers, both 8 nm thick embeded in thick 1.05 μm lattice-matched GaInAsP SCH layers. The optical confinement factor in all the structures is kept almost constant and nearly equal to that of a previously described structure [9], that showed high quality characteristics at 85°C, hereafter refered as sample 1.

The active stacks are grown on 2″ n-type InP wafers, and are cladded with a 0.5 μm thick n ($[Si] = 2 \times 10^{18}\ cm^{-3}$) type InP buffer and a 0.5 μm p ($[Be] = 1 \times 10^{18}\ cm^{-3}$) type InP layers. The growth is performed under high group V fluxes (PH_3 flow rate $\geqslant 10$ sccm) at temperatures of 480°C to 500°C for the SL-GaInAsP/GaInAsP structures and of 470°C for the InAsP/tensile GaInAsP, in order to improve the tensile material quality [10]. Growth interruptions at each interfaces are necessary to allow for appropriate gas switching. As will be discussed later, such a process is of high importance regarding the control of the composition of low As concentration, high band gap quaternaries barriers.

The structures exhibit high room temperature photo-luminescence (PL) yield with low FWHM (25 to 30 meV) and sharp double crystal X-ray diffraction (DC-XRD) satellite peaks. The analysis of the positions and relative intensities of the satellite peaks, allows a precise measurement of the period of the MQW and the determination of the strain share between wells and barriers. In addition, due to the precise control of the III elements fluxes obtained in MBE, the well and barriers compositions are known with a good precision, as stated by the good agreement between experimental and calculated DC-XRD spectra. As mentioned above, the interface growth interruptions (IGI), for As-free barrier composition, are of major importance regarding the control of materials composition and crystalline quality, as clearly evidenced in Fig. 1. The DC-XRD spectra of two 8 periods InAsP/GaInP MQW are displayed together with their PL intensity maps. Growth interruption times have been increased to reduce arsenic residual incorporation in barriers. Sample B experiences an IGI four times longer than sample A and shows superior PL intensity and homogeneity. The comparison of the rocking curves indicates a lower tension in the barriers of sample A, cancelling the strain compensation effect. On the other hand,

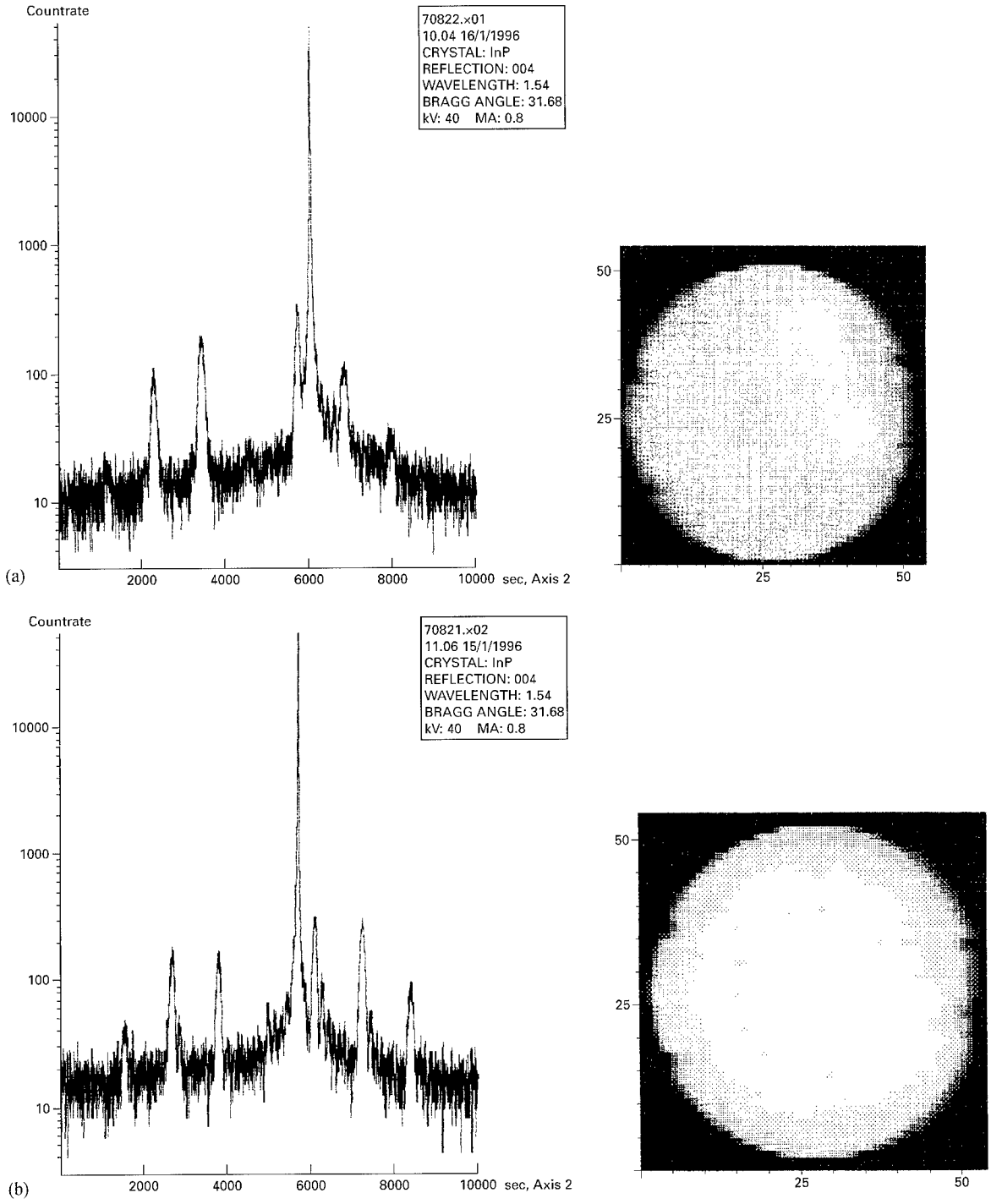

Fig. 1. DC-XRD spectra and PL maps of 8 periods InAsP (8 nm)/$Ga_{0.11}InP$ (8 nm) MQW structures grown with different interface growth interuption (IGI) times: (a): Sample A. (b): Sample B. IGI is 4 times than for sample A.

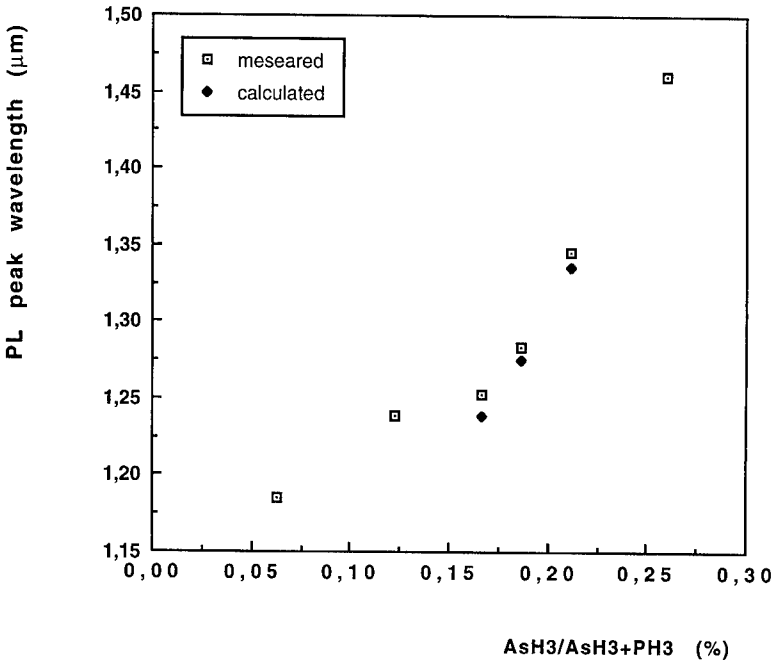

Fig. 2. Measured InAsP/InGaAsP QW PL peak wavelength as a function of the hydrides flow rates ratio used for the growth of InAsP (white squares). Composition parameters deduced from XRD are used for the calculated wavelengths (dark dots).

Table 1
Composition parameters of the studied; X_w (Y_w) and X_b (Y_w) refer to the Ga (As) concentration in wells and barriers, respectively

Sample	Well				Barrier				
	L_w (nm)	X_w	Y_w	ε (%)	L_b (nm)	X_b	Y_b	ε (%)	Gap (μm)
1	8.1	0.2	0.62	0.6	10.2	0.11	0.25	0.03	1.10
2	8.4	0.105	0.54	1.0	8.4	0.105	0.25	0.06	1.05
3	8.0	0	0.43	1.38	8.1	0.19	0.35	−0.2	1.10
4	8.4	0	0.43	1.38	8.4	0.19	0.29	−0.4	1.08
5	8.4	0	0.4	1.28	8.4	0.19	0.18	−0.8	1.015
6	8.5	0	0.44	1.41	8.1	0.105	0.08	−0.5	0.96

XRD rocking curves of 8 periods InP/$Ga_{0.11}$InP superlattices are easily fitted with the measured periods and the Ga concentrations calculated from the calibrated In and Ga flux ratio. We thus conclude to excess arsenic incorporation, decreasing with the duration of the growth interruption.

Using XRD, the arsenic concentration in InAsP can be calculated within ± 1%, resulting in easy control of the PL wavelength of InAsP/GaInAsP MQWs as a function of hydrides flow rates, as shown in Fig. 2. Wavelengths calculated with the compositions determined by XRD are in good agreement with experiment.

Table 1 summarizes the parameters of the structures selected for lasers processing. E_{be} values range from ≈ 70 to ≈ 170 meV for samples 1 to 6, respectively.

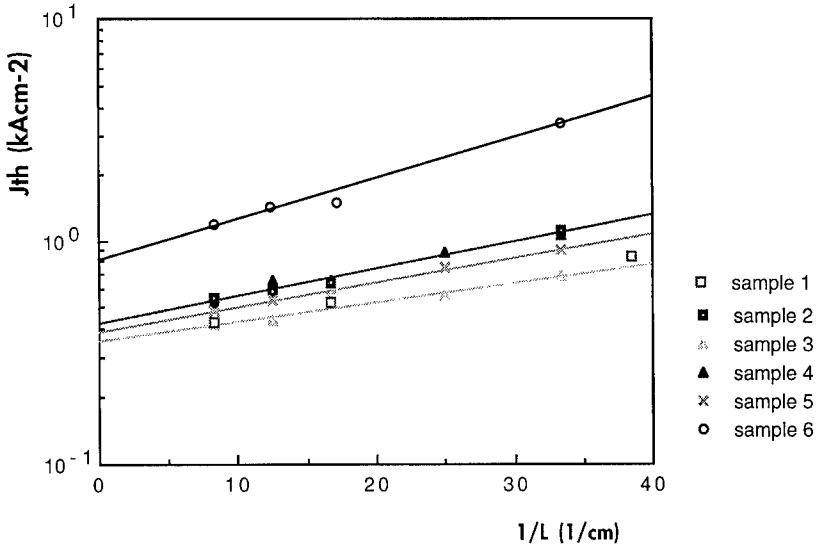

Fig. 3. Threshold current densities at 20°C as a function of inverse cavity length.

3. Device results

The structures are overgrown by GSMBE with p-type InP cladding (2.5 μm, $p = 1 \times 10^{18}$ cm^{-3}) and InGaAs contact (0.3 μm, $p = 3 \times 10^{19}$ cm^{-3}) layers, and are subsequently processed as 100 μm wide BA lasers. Their as-cleaved $L(I)$ characteristics are measured from 20°C to 80°C, for cavity lengths ranging from 300 to 1200 μm. Fig. 3 shows a plot of threshold current densities (J_{th}) at 20°C as a function of inverse cavity lengths. Low J_{th} of 420 to 560 A cm^{-2} are measured on samples 1 to 5 for 1200 μm long lasers. External quantum efficiencies (η_{ext}) ranging from 0.31 to 0.36 W/A are measured for short cavity length (300 μm). Sample 6, with high barrier band gap of $\approx$ 1.29 eV (0.96 μm quaternary), exhibits threshold current densities in excess of 1 kA cm^{-2} for all lengths and poor external efficiencies for short cavity length. Calculation of current distribution in a MQW structure as a function of well number and barrier composition (lattice-matched GaInAsP) shows that inhomogeneous pumping may occur for barrier band gap in excess of 1.24 eV, because of the large valence bands offsets ($\Delta E_v \approx 0.6\ \Delta E_g$) responsible for inhomogeneous hole injection. This effect has been reported by Kito et al. [11] to appear for barrier band gaps between 1.18 and 1.25 eV.

Table 2
Average characteristic parameters J_0, α_{int} (α), η_{int} (η) of broad area lasers at 20°C and 80°C

Sample	20°C			80°C		
	J_0	α	η	J_0	α	η
2	71	5.6	0.73	155	7.9	0.49
3	57	8.7	0.93	125	11	0.52
5	64	6.8	0.90	143	8.9	0.62
6	134	–	–	217	–	–

Internal losses (α_{int}) and quantum efficiencies (η_{int}) calculated from $1/\eta_{ext}$ (L) curves, are displayed in Table 2, as well as threshold current densities per well for infinite length (J_0) at temperature of 20°C and 80°C. Low internal losses of 6 to 11 cm^{-1} are found up to 80°C, demonstrating the high quality of the active material. Such characteristics are among the best reported so far [12–15].

Average characteristic temperatures for 300 and 1200 μm long lasers range from 50 to 80 K and from 60 to 110 K, respectively, depending on the barrier band gap. A variation of T_0 with respect to

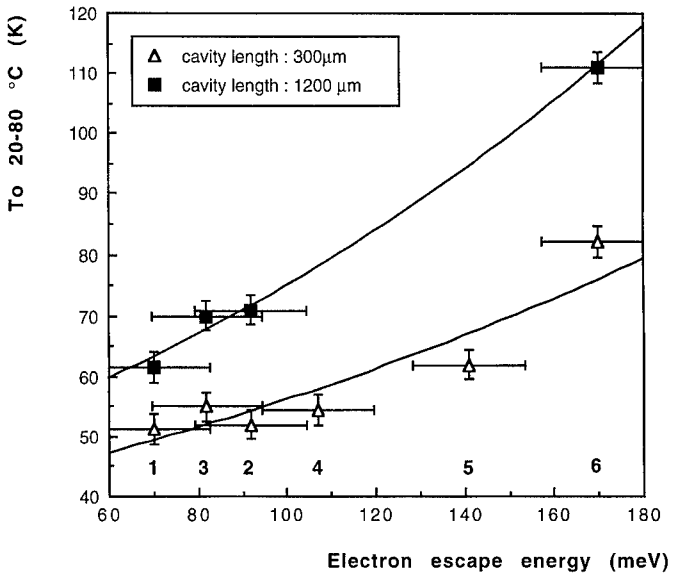

Fig. 4. Characteristic temperature between 20°C and 80°C as a function of the electron escape energy (well to barrier conduction band offset – 1st quantized electron energy).

calculated electron escape energy E_{be} is seen in Fig. 4. Solid lines are exponential fits of the experimental points. A noteworthy improvement of T_0 is seen for E_{be} higher than 140 meV. On the other hand, the comparison of the T_0's measured for samples 1 to 4 indicates a minor influence of strain, in the 0.6–1.4% range, on characteristic temperatures. However, the lowest threshold current densities at 80°C are obtained for the InAsP sample 3, with $T_0 = 55$ K. This clearly demonstrates that T_0 is not the only parameter to be considered for high temperature laser operation.

4. Conclusion

In summary, 1.3 μm In(Ga)AsP SL-MQW broad area lasers, with QWs strains and InGaAsP barrier compositions ranging from 0.6% to 1.4% and from 1.10 to 0.96 μm, respectively, have been grown by GSMBE. Their high quality characteristics have been analyzed at temperatures up to 80°C, as a function of strain and electron escape energy. An improvement of the characteristic temperatures up to 110 K is shown for high band gap barriers, whereas strain does not influence T_0 within the studied range. However, inhomogeneous carrier injection limits the lasing characteristics of devices with band gap barriers higher than ≈ 1.24 eV.

The lowest threshold current densities, at 80°C, of 2 kA cm^{-2} and 0.96 kA cm^{-2} for 300 μm and 1200 μm long cavities and as-cleaved facets has been obtained with an InAsP (1.4%)/1.10 μm GaInAsP (-0.2%) MQW structure, despite a T_0 of 55 K. These results show that the optimization of high temperature laser is a trade-off between low threshold current density at room temperature and T_0.

References

[1] S. Seki, H. Oohasi, H. Sugiura, T. Hirono and K. Yokoyama, Appl. Phys. Lett. 67 (1995) 1054.
[2] A.A. Bernussi, H. Temkin, D.L. Coblentz and R.A. Logan, Appl. Phys. Lett. 66 (1) (1995) 67.
[3] P.J.A. Thijs, L.F. Tiemeijer, J.J.M. Binsma and T. van Dongen, IEEE J. Quantum Electron. 30 (1994) 477.

[4] Ph. Pagnod-Rossiaux, B. Fernier, M. Matabon and L. Goldstein, in: Proc. 7th Eur. MBE Workshop, Bardonecchia, Italy (1993), paper G1.
[5] A. Kasukawa, N. Iwai, T. Namegaya and T. Kikuta, Electron. Lett. 28 (1992) 2351.
[6] H. Oohashi, S. Seki, T. Hirono, H. Suguria, T. Amano, M. Ueki, J. Nakano, M. Yamamoto, Y. Tohmori, M. Fukuda and K. Yokoyama, Electron. Lett. 31 (1995) 556.
[7] A. Ougazzaden, A. Mircea and C. Kazmierski, Electron. Lett. 31 (1995) 803.
[8] C.E. Zah, R. Bhat and T.P. Lee, Proc. 7th Int. Conf. on InP and Related Materials (1995) Paper WA1.1, pp. 14–17.
[9] B. Fernier, F. Gerard, Ph. Pagnod, G. Michaud, G. Ripoche, G. Vendrome and R.M. Capella, Electron. Lett. 31 (1995) 2174.
[10] J.-Y. Emery, C. Starck, L. Goldstein, A. Ponchet and A. Rocher, J. Crystal. Growth 127 (1993) 241.
[11] M. Kito, N. Otsuka, M. Ishino and Y. Matsui, IEEE J. Quantum Electron. 32 (1996) 38.
[12] A. Mathur, J. Osinski, P. Grodzinski and P.D. Dapkus, IEEE Photonics Lett. 7 (1993) 753.
[13] A. Kasukawa, N. Yokouchi, N. Yamanaka and N. Iwai, Electron. Lett. 31 (1995) 1749.
[14] N. Yokouchi, N. Yamanaka, N. Iwai, T. Matsuda and A. Kasukawa, Proc. 7th Int. Conf. on InP and Related Materials, 1995, paper WA2.3, pp. 57–60.
[15] M. Toivonen, A. Salokatve, M. Jalonen, J. Näppi, H. Asonen, M. Pessa and R. Murrison, Electron. Lett. 31 (1995) 797.

ELSEVIER

Journal of Crystal Growth 175/176 (1997) 955–959

JOURNAL OF CRYSTAL GROWTH

MBE grown mid-infrared type-II quantum-well lasers

Chih-Hsiang Lin[a], S.J. Murry[a,*], D. Zhang[a], P.C. Chang[a], Yucai Zhou[a], S.S. Pei[a], J.I. Malin[b], C.L. Felix[b], J.R. Meyer[b], C.A. Hoffman[b], J.F. Pinto[b]

[a] *Space Vacuum Epitaxy Center, University of Houston, Houston, Texas 77204-5507, USA*
[b] *Code 5600, Naval Research Laboratory, Washington, DC 20375, USA*

Abstract

We have employed molecular-beam epitaxy (MBE) for the growth of mid-infrared (MIR) type-II quantum-well laser structures. These lasers consist of strain-balanced InAs/InGaSb/InAs/AlSb type-II quantum wells lattice-matched to the AlSb cladding layers. We have demonstrated optically pumped lasers emitting from 3 to 4.3 μm under pulsed operation. For the 3.2-μm lasers, stimulated emission was observed at temperatures up to 350 K. The characteristic temperature T_0 at operation temperatures above ambient was 68 K. Here, we discuss the optimization of the MBE growth of MIR type-II quantum-well lasers, including substrate temperatures, V/III beam-equivalent pressure ratios, and shutter sequencing for better interface control and laser performance.

PACS: 42.55.P; 81.05.E

Keywords: Infrared; Semiconductor laser; MBE; Quantum well

1. Introduction

Efficient mid-infrared (MIR) diode lasers are highly desirable for a variety of applications including remote sensing, molecular spectroscopy, and environmental monitoring due to the strong characteristic absorption lines of many gas molecules in the MIR range. The detection sensitivity of trace gases is typically higher by two orders of magnitude at the fundamental absorption lines than at overtones in the near infrared (IR). Many commercial and military MIR systems are limited by a lack of adequate optical sources. Recently, significant progress has been achieved towards room-temperature operation for MIR diode lasers, promising compact and inexpensive sources more widely applicable than conventional technology such as optical parametric oscillators (OPOs).

MIR lasers have been demonstrated in a variety of material systems, including IV–VI and II–VI diodes, and III–V devices based on interband or intersubband transitions. Lead-salt IV–VI lasers emitting at wavelengths longer than 3 μm have been commercially available for a number of years. These lasers with emission wavelengths of 4 μm have exhibited pulsed operation at temperatures up to 290 K [1], and cw operation up to 223 K [2].

* Corresponding author.

0022-0248/97/$17.00 Copyright © 1997 Elsevier Science B.V. All rights reserved
PII S0022-0248(96)00830-5

However, they are not expected to produce high output power (> 1 mW) because of the poor thermal conductivity of lead–salt alloys, and the susceptibility to damage. For narrow band gap II–VI semiconductors such as HgCdTe alloys, relatively high powers have been reported [3], but for wavelengths beyond 3 μm the maximum operating temperatures have been ≤ 160 K. It is thus very desirable to develop semiconductor lasers based on III–V alloys, which offer good metallurgical and thermal properties with better-quality substrates readily available.

Room-temperature operation of diode lasers based on InGaAsSb/AlGaAsSb materials have been demonstrated at wavelengths shorter than 2.8 μm [4, 5]. However, the growth of InGaAsSb quaternary alloys with band gaps narrower than 0.37 eV (> 3.4 μm) turns out to be metastable and problematic because of a miscibility gap [6]. Until now, the highest reported operating temperature (T_{max}) of any III–V type-I interband semiconductor laser emitting at wavelengths $\geqslant 3.2$ μm was 225 K [7]. The corresponding characteristic temperatures (T_0) were in the range of 17–30 K for operating temperatures above 120 K. Recently, type-I InAlAs/InGaAs quantum-cascade (QC) lasers based on intersubband transitions had lased up to 320 K at a wavelength of about 5 μm [8]. However, the demonstrated type-I QC lasers had low radiative efficiencies near threshold ($< 10^{-3}$) due to fast optical phonon scattering which led to high threshold current densities and substantial heating.

Recently, we reported an optically- pumped type-II quantum-well (QW) laser operating up to 285 K at 4.1 μm [9]. The characteristic temperature T_0 was 35 K for 170 K $\leqslant T_{op} \leqslant$ 270 K. The active region was composed of 35 periods of undoped InAs/$In_{0.3}Ga_{0.7}Sb$/InAs/AlSb (21 Å/31 Å/21 Å/43Å) multiple quantum wells (MQWs) sandwiched by AlSb cladding layers. The maximum peak output power ($\lambda_{pump} = 1.06$ μm) was about 650 mW at 81 K, while about 250 mW was collected at 170 K. The type-II four-constituent QW structure combines the advantages of good carrier confinement, the potential of significant suppression of non-radiative Auger losses [10, 11], large optical matrix elements, and a two-dimensional density-of-states for both electrons and holes. Here we report results of 3.2-μm lasers and some preliminary results of 4.3-μm lasers. We also discuss key issues regarding the MBE growth of MIR type-II QW lasers, including substrate temperatures, V/III beam-equivalent pressure (BEP) ratios, and shutter sequencing for interface control and laser performance

2. Experimental procedure

The type-II QW lasers were grown in a Riber 32 molecular beam epitaxy (MBE) system on p-type GaSb substrates using an EPI As valved cracker cell and an EPI Sb cracker cell. Growth rates for each layer composition were calibrated to within ± 2% using reflection high-energy electron diffraction (RHEED) and were confirmed by double-crystal X-ray diffraction (DCXRD) measurements. The background doping was low 10^{15} cm^{-3} n-type for InAs and about 2×10^{16} cm^{-3} p-type for GaSb.

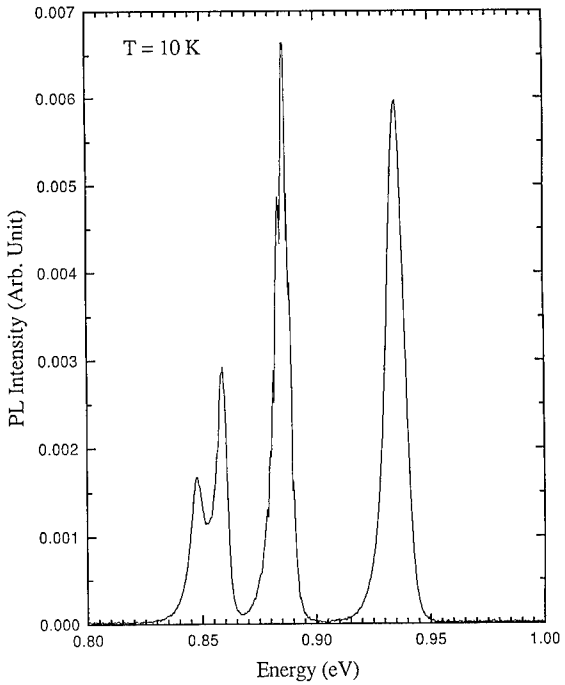

Fig. 1. PL spectrum of the GaSb/AlSb QWs at 10 K with GaSb well thicknesses of 40, 70, 100, 130 Å. The AlSb barrier thickness was 300 Å.

From DCXRD spectra, the background Sb in InAs was about 1.2% and the background As in GaSb was about 3.2%, with the same growth rate and same V/III BEP ratio of 3 for InAs and GaSb. The BEP ON/OFF ratio with the shutter opened or closed was about 8 for As_2, and was about 160 for Sb_1. When the Sb/Ga V/III BEP ratio was increased, the background As in GaSb decreased. However, the background Sb in InAs was not sensitive to the As flux. This implies that the sticking coefficient of background Sb in InAs at 440°C is almost 100%. From photoluminescence (PL) spectra, the material quality of GaSb/AlSb QWs is not sensitive to the Sb/Ga V/III BEP ratio as long as the ratio is larger than 1.8. Fig. 1 shows the 10 K PL spectrum of GaSb/AlSb QWs with GaSb well thicknesses of 40, 70, 100, and 130 Å grown at 500°C. The full-width at half-maximum was 6.1 meV for the 100 Å GaSb well, 6.8 meV for the 70 Å GaSb well, and 9.0 meV for the 40 Å GaSb well.

For the laser samples, the substrate temperature was controlled at 530°C for the bottom AlSb cladding layer, 440°C for the MQW active region to optimize the material quality of InAs and InGaSb wells, and 510°C for the top AlSb cladding layer and GaSb cap to minimize degradation of the underlying layers. The MBE grown laser wafers exhibited excellent surface morphology. The substrate temperature was calibrated by optical pyrometry, the InSb melting temperature (525°C), and the GaSb oxide desorption temperature (575°C to 585°C). During the growth of AlSb cladding layers, we noticed that the RHEED patterns became more and more spotty. After growing 2-μm AlSb, the substrate temperature decreased by about 50 to 70°C as estimated from the optical pyrometry and InAs RHEED patterns, since InAs displays 2×1 RHEED patterns only when the substrate temperature is between 380°C and 470°C [12]. We believe that the decrease of the substrate temperature is due to the large difference in the refractive indices of the GaSb substrate and AlSb.

During the growth, the InGaSb layers in the active region and the AlSb cladding layers displayed good 1×3 RHEED patterns, while the InAs layers exhibited 2×1 patterns with a V/III BEP ratio of 10 using As_4 or 3 using As_2. However, the RHEED patterns for the AlSb barriers in the MQW active region were not as good, since the substrate temperature was about 440°C. We have also noticed that it took about 1.5 monolayers of InAs growth to change the RHEED patterns from 1×3 to 2×1. This suggests that the interface was InSb dominant and that there was some Sb floating on the InGaSb or AlSb surface and got incorporated into the InAs layers, which was subsequently confirmed by the TEM analysis. After the growth of InAs, the sample was exposed to As_2 only for two more seconds. Next, all of the shutters were closed for six seconds to reduce the background As. Then, the Sb shutter was open for two seconds before the growth of InGaSb or AlSb. When we grew InGaSb or AlSb on top of an InAs layer, the RHEED patterns changed from 2×1 to 1×3 right after we opened the Sb shutter. Therefore, the interface quality for InGaSb or AlSb grown on top of InAs is better than that for InAs grown on top of Sb-based materials. The buffer and cladding layers were grown at about 0.85 μm/h, and the InGaSb and AlSb layers in the MQW active region were grown at about 0.7 μm/h.

After characterized by DCXRD and PL, wafers were lapped down to a thickness of 125 μm, and then cleaved to laser bars with cavity lengths on the order of 500 μm. The lasers with uncoated facets were indium heat sunk to a copper cold finger, epitaxial-side-up, and mounted in an Air Products Heli-Tran dewar. The devices were optically pumped over a 90-μm wide strip by 70 ns pulses from a Q-switched 2.06 μm Ho–YAG laser. At this pump wavelength, it is estimated that only about 10% of the incident intensity is absorbed in the active region. The lasing output was collected and focused onto the slit of a $\frac{1}{4}$ m monochromator and measured with an InSb detector.

For the 3.2-μm lasers, the active region is composed of 40 periods of undoped InAs/$In_{0.3}Ga_{0.7}Sb$/InAs/AlSb (17 Å/28Å /17 Å/43Å) MQWs sandwiched between two AlSb cladding layers. The PL line width was about 100 nm at 80 K, and about 180 nm at 300 K. The line width for edge emission above the lasing threshold narrowed to 45 nm at 300 K, which was limited by the instrument resolution. Fig. 2 shows the threshold pump intensity as a function of temperature. The slope of the data in

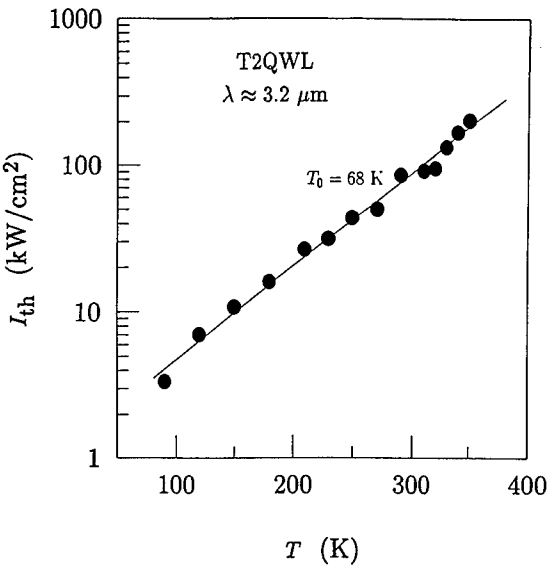

Fig. 2. Threshold pump intensity as a function of temperature for the 3.2-μm laser. The corresponding characteristic temperature was 68 K for the entire temperature range 90–350 K.

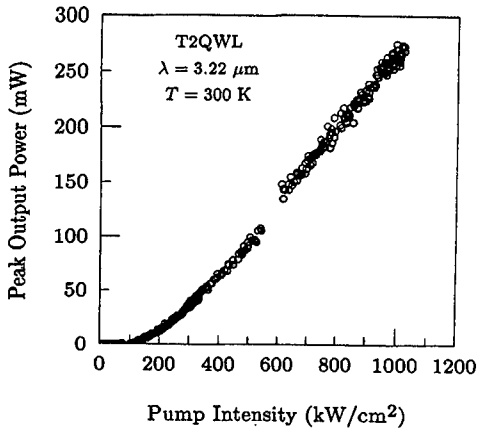

Fig. 3. Peak output power as a function of pump intensity (λ_{pump} = 2.06 μm) at 300 K for the 3.2-μm laser.

Fig. 2 yields a characteristic temperature (T_0) of 68 K over the entire temperature range from 90 to 350 K, which compares favorably with reported values of $T_0 \leqslant 40$ K at temperatures above 210 K for other III–V and IV–VI interband mid-IR lasers. The observed T_{max} of 350 K is the highest ever reported for a semiconductor laser emitting beyond 2.5 μm. Fig. 3 plots the peak output power as a function of pump intensity at 300 K. We find that more than 270 mW is generated at ambient temperature, which represents a significant step toward the realization of practical MIR sources. Correlation of the observed threshold intensities with estimated absorption coefficients and calculated threshold carrier concentrations leads to an estimated Auger coefficient of 5.0×10^{-27} cm^6/s at 300 K [13]. Lasers from a second wafer using conventional As_4 and Sb_4 effusion cells lased only up to 310 K. It is possible that the use of the monomeric Sb source could have reduced the defect-related nonradiative recombination. Further investigations will be performed in the future.

Recently, we have also demonstrated 4.3-μm lasers emitting up to 270 K. The active region composed of 35 periods of undoped InAs/$In_{0.31}Ga_{0.69}Sb$/InAs/AlSb (24 Å/40 Å/24 Å/43) MQWs. The DCXRD spectrum displayed clear satellite peaks which indicated good material quality, even though the MQW active region was lattice-matched to the AlSb cladding layers instead of the GaSb substrate. From the threshold pump intensity as a function of temperature, the characteristic temperature (T_0) was determined to be 36 K over the temperature range 160 K to 270 K. The detailed data will be presented elsewhere.

3. Conclusions

We have demonstrated that MBE is capable of growing high-quality strain-balanced type-II InAs/InGaSb/InAs/AlSb QWs which are well suited for the MIR lasers. Two optically pumped devices incorporating four-constituent MQWs lased at 3.2 μm with the maximum operating temperature of 350 K and a characteristic temperature of 68 K over the entire temperature range 90–350 K, and at 4.3 μm with the maximum operating temperature of 270 K and a characteristic temperature of 36 K. Higher operating temperatures and output powers are expected with further improvements in the material quality of the type-II QW.

Acknowledgements

The authors would like to thank Dr. S.-N.G. Chu at Bell Laboratories of Lucent Technologies for the TEM measurements, and C.-H. Thang and Dr. Alex Freundlich for DCXRD measurements. The work at Univ. of Houston was partially supported by NASA contract No. NAGW-977 and TcSCH. Research at NRL was supported by the Office of Naval Research.

References

[1] D.L. Partin, IEEE J. Quantum Electron. QE-24 (1988) 1716.
[2] Z. Feit, M. McDonald, R.J. Woods, V. Archambault and P. Mak, Appl. Phys. Lett. 68 (1996) 738.
[3] M. Zandian, J.M. Arias, R. Zucca, R.V. Gil and H. Shin, Appl. Phys. Lett. 59 (1991) 1022.
[4] H.K. Choi, S.J. Eglash and M.K. Connors, Appl. Phys. Lett. 63 (1993) 3271.
[5] H. Lee, P.K. York, R.J. Menna, R.U. Martineli, D.Z. Garbuzov, S.Y. Narayan and J.C. Connolly, Appl. Phys. Lett. 66 (1995) 1942.
[6] H.Q. Le, G.W. Turner, S.J. Eglash, H.K. Choi and D.A. Coppeta, Appl. Phys. Lett. 64 (1994) 152.
[7] H.K. Choi, G.W. Turner, M.J. Manfra and M.K. Connors, Appl. Phys. Lett. 68 (1996) 2936.
[8] J. Faist, F. Capasso, J.N. Baillarseon, C. Sirtori, D.L. Sivco, A.L. Hutchinson, S.-N.G. Chu and A.Y. Cho, Appl. Phys. Lett. 68 (1996) 3680.
[9] J.I. Malin, J.R. Meyer, C.L. Felix, J.R. Lindle, L. Goldberg, C.A. Hoffman, F.J. Bartoli, C.-H. Lin, P.C. Chang, S.J. Murry, R.Q. Yang and S.S. Pei, Appl. Phys. Lett. 68 (1996) 2976.
[10] C.H. Grein, P.M. Young and H. Ehrenreich, J. Appl. Phys. 76 (1994) 1940.
[11] E.R. Youngdale, J.R. Meyer, C.A. Hoffman, F.J. Bartoli, C.H. Grein, P.M. Young, H. Ehrenreich, R.H. Moles and D.H. Chow, Appl. Phys. Lett. 64 (1994) 3160.
[12] J.F. Chen and A.Y. Cho, J. Electron. Mater. 22 (1993) 259.
[13] J.R. Meyer, C.A. Hoffman, F.J. Bartoli and L.R. Ram-Mohan, Appl. Phys. Lett. 67 (1995) 757.

ELSEVIER

Journal of Crystal Growth 175/176 (1997) 960–963

JOURNAL OF CRYSTAL GROWTH

Waveguide modulator structures with soft optical confinement grown by the epitaxial shadow mask (ESM) MBE-technique

S. Malzer*, W. Geißelbrecht, U. Hilburger, M. Kneissl, P. Kiesel, R. Mayer, G.H. Döhler

Institut für Technische Physik, Universität Erlangen-Nürnberg, Erwin-Rommel-Strasse 1, D-91058 Erlangen, Germany

Abstract

Excellent selective n- and p-contacts to highly doped and closely adjacent layers in n-i-p-i doping superlattices can be fabricated using the epitaxial shadow mask molecular beam epitaxy (ESM-MBE). With this method the growth within the window of a GaAs/AlGaAs mask obtained by selective wet chemical etching is controlled by the geometrical aspect of the effusion cells relative to the substrate. We demonstrate first results of using ESM-MBE for the in-situ fabrication of waveguide structures, including waveguide modulators. This double hetero p-i-n modulator exhibits a modulation contrast of more than 30 dB (for a 900 μm long device) for a voltage swing of 6.5 V. Propagation losses in the waveguide structure are less than 11 dB/cm and mainly due to free carrier absorption in the waveguide region.

1. Introduction

A key issue for the feasibility of opto-electronic integrated circuits (OEICs) is the possibility of smart integration of active components (laser diode, photodetector) and passive elements (intersection, crossing, coupler) with modulators [1, 2]. Epitaxial regrowth is widely used to fabricate buried ridge laser structures [3] or even vertical cavity surface emitting lasers [4]. Surface selective growth on masked substrates has been demonstrated for opto-electronic device applications [5–7]. The epitaxial shadow mask MBE technique [8] has been shown to yield excellent selective in situ ohmic contacts to the respective n- and p-layers of n-i-p-i doping superlattices. These structures are attractive for applications as (waveguide) modulators because high switching contrast can be achieved with low driving voltages [9]. Another important issue concerns the electro-optical effect used for intensity or phase modulation. Most work in the literature deals with the quantum confined stark effect (QCSE) [10–13] because of the very attractive and pronounced features of the field-dependent excitonic absorption in the quantum wells. Few papers report on the use of the Wannier–Stark localization in superlattices [14, 15] or on the bandfilling effect in electron transfer quantum well modulators [16]. The Franz Keldysh effect (FKE) has been barely used [17] despite of comparable absorption changes and rather simple double hetero p-i-n structures. Photolithographically fabricated ridge waveguide modulators, for example, turned out to be highly

* Corresponding author. Fax: 49 9131 85 7293: e-mail: malzer@physik.uni-erlangen.de.

0022-0248/97/$17.00 Copyright © 1997 Elsevier Science B.V. All rights reserved
PII S0022-0248(96)00954-2

polarization insensitive (in contrast to QCSE modulators) and exhibited a switching contrast of 40 dB (for a 760 μm long device) with propagation losses of less than 0.5 dB/cm without bias [18].

In this paper, we report the fabrication and the results of a double hetero p-i-n waveguide modulator structure grown by the epitaxial shadow mask MBE technique and based on the Franz-Keldysh effect.

2. Experimental procedure

The samples were grown in a Riber 32P machine with a CBr_4 gas line used for p-type doping. An EPI valved cracker cell was used in the As_2 mode ($T_{cracker} = 800°C$) with a V/III-ratio of ≈ 10 for the growth of samples containing AlGaAs layers. A quarter of a 2 in wafer with an epitaxial shadow mask (8 μm $Al_{0.5}Ga_{0.5}As$ and 3 μm GaAs layer on top) was photolithographically patterned into stripes with different widths (> 10 μm). The GaAs layer was etched with an anisotropic etchant ($NH_3OH : H_2O_2 : H_2O = 3 : 1 : 15$) and the AlGaAs layer was then selectively etched with HF. The sample was extensively rinsed in clean water and blown dry before loading back into the MBE chamber. The standard growth position of the Riber 32P was used to have highest symmetry to all the cells. The sample was mounted on the In-free holder and grown under standard conditions ($T_{growth} = 600°C$, growth rate = 1 μm/h, rotation speed = 12 rpm).

Starting with a 1 μm $Al_{0.3}Ga_{0.7}As$ cladding layer, followed by a 1 μm GaAs layer and a 0.5 μm $Al_{0.3}Ga_{0.7}As$ layer on top, a waveguide structure was fabricated in situ. Within the GaAs layer, a δ-n-doped bottom and a δ-p-doped top layer were grown while the rotation was stopped and the sample was properly aligned relative to the doping cells exploiting the shadowing effect for the doping beams [19]. The doping density of the δ-n- and δ-p-layer was $1 \times 10^{13}\ cm^{-2}$ each. (The doping densities were calibrated by Hall measurements of homogeneous doped samples). In Fig. 1, a scanning electron picture of the as grown structure before the mask was removed and a cross section through the waveguide is shown. The GaAs waveguiding layer

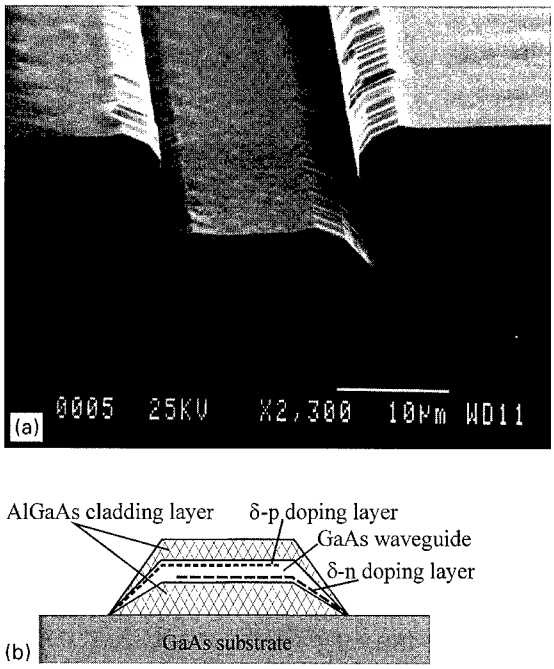

Fig. 1. (a) Cross-sectional view through the waveguide as grown by the epitaxial shadow mask technique. The shadow mask is still on the substrate. (b) Schematic of the layers: a n-δ-doped layer at the bottom and a p-δ-doped on the top of the GaAs layer was grown

becomes gradually thinner at the edges of the structure resulting in soft optical confinement for the optical mode. The defect density on the surface of the waveguide is as low as for growth without a shadow mask. Some (sub-μm) roughness along the edges is still apparent which was transferred from the edges of the mask window.

After the growth, the shadow mask was selectively etched away and ohmic n-(Au/Ge) and p-contacts (Au/Zn) were evaporated to the respective edges. Finally, waveguide devices of about 1 mm length were cleaved.

Transmission experiments were carried out with spectrally dispersed light of a tungsten halogen lamp or with coherent light of a tunable Ti-Sapphire laser coupled into a fiber. The intensity was optionally tuned with a HP 8158 B optical fiber attenuator. The tapered fiber output was aligned to the front end of the waveguide structure while monitoring the output signal of the modulator at

the backside with a CCD camera. The camera was replaced by the Si detector head of a HP 8153 powermeter for measuring the transmitted power.

3. Results and discussion

The devices showed good rectifying behavior but relatively high contact resistance which is probably due to the fact that just one n- and p-δ-doped layer was used which are covered by the 0.5 μm thick undoped AlGaAs top layer. The normalized transmission changes for different wavelengths from 920 to 895 nm in 5 nm wavelength steps are shown in Fig. 2 for a 0.9 mm long and 10 μm wide waveguide structure. A modulation contrast of 30 dB could be achieved with a voltage swing between -6 and $+0.5$ V for the shortest wavelength used. The contrast decreases with increasing wavelength according to the diminishing absorption changes due to the FKE. We mention that in this 10 μm wide waveguide modulator at least one higher mode is propagating. The waveguide losses were determined by measuring the contrast of the Fabry–Perot oscillations of the modes while slowly heating the sample [20]. The relative transmission of a waveguide structure with the length L and the facet reflectivity R is given by

$$T(\varphi) = \frac{(1-R)^2 \mathrm{e}^{-\alpha L}}{(1-R\,\mathrm{e}^{-\alpha L})^2 + 4R\,\mathrm{e}^{-\alpha L}\sin^2(\varphi)} \qquad (1)$$

with $\varphi = 2\pi nL/\lambda$ and the propagation loss α. The temperature dependence of the effective index n is about 4.5×10^{-5} 1/K. The function $T(\varphi)$ is oscillating with φ and from the contrast ratio $k = (T_{max} - T_{min})/(T_{max} + T_{min})$ one can calculate an upper limit for the total losses. Fig. 3 shows the transmission at room temperature as a function of temperature change at the wavelength $\lambda = 923$ nm (solid line) together with calculated loss curves for different absorption values (dashed lines). The best correspondence to the experimental data was found for $\alpha = 2.7$ 1/cm which yields a loss of 11 dB/cm. This seems to be a still rather high value for waveguide modulator structures. But one has to bear in mind that the δ-doping layers lie in the active region and therefore absorption due to free carriers has to be considered. Also, leakage through the relatively thin (1 μm) lower cladding layer might still contribute significantly to the total loss.

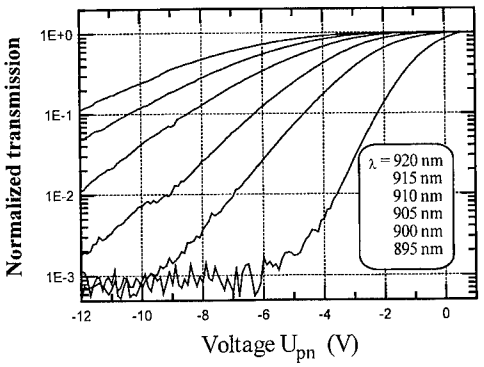

Fig. 2. Normalized transmission changes for different wavelengths between 920 and 895 nm (from left to right) referring to $U_{pn} = +0.5$ V

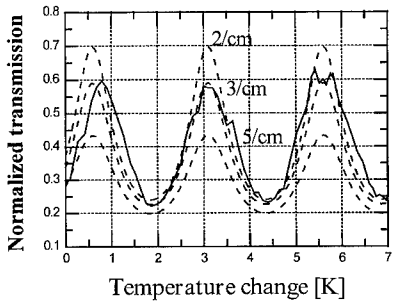

Fig. 3. Measured Fabry–Perot oscillations (solid curves) due to the temperature-dependent change of the refraction index. Calculated patterns (dashed curves) after Eq. (1) are drawn for comparison.

4. Conclusion and perspectives

The fabrication of in-situ structured waveguides has been successfully demonstrated. Even with just one single δ-n and δ-p doping layer in the active layer satisfactory contrast ratios as high as 30 dB have been achieved. The waveguide losses for that structure are still relatively high compared to conventional waveguide structures which is mainly

due to free carrier absorption in the active layer. Further investigations are in progress to improve the results significantly. First, homogeneous doping layers have to be used in the cladding layers. This is made by the "flash-doping" technique, i.e. opening the respective doping shutters for a short time when the sample is properly oriented during continuous rotation [19].

The width of the waveguides has to be reduced also to achieve monomode propagation. This can be done by reducing the width of the shadow mask or by lateral variation of the Al-content. This can be done by the same "flash"-technique mentioned above by opening the Al-shutter for a short period in the proper position to give an increasing Al-content directed outside to the edges in the GaAs waveguiding layer.

Acknowledgements

This work was supported by the Deutsche Forschungsgemeinschaft DFG under grant no. Do356/17-1.

References

[1] T.L. Koch and U. Koren, IEEE J. Quantum Electron. 27 (1991) 641.
[2] M. Suzuki, H. Tanaka, S. Akiba and Y. Kushiro, IEEE J. Lightwave Technol. 6 (1988) 779.
[3] T.A. Strand, B.J. Thibeault, D.S.L. Mui, L.A. Coldren, P.M. Petroff and E.L. Hu, Appl. Phys. Lett. 66 (1995) 1966.
[4] H. Saito, H. Kosaka, M. Sugimoto, I. Ogura, K. Kasahara and Y. Sugimoto, J. Vac. Sci. Technol. B 12 (1994) 2905.
[5] J.M. Hong, J.D. Flood, J.L. Merz, T. Sands and J. Washburn, J. Vac. Sci. Technol. 4 (1986) 629.
[6] Y. Chen, T.H. Chiu, J.E. Zucker and S.N.G. Chu, Appl. Phys. Lett. 62 (1993) 1641.
[7] H. Heinecke, J. Crystal Growth 127 (1993) 126.
[8] K.H. Gulden, X. Wu, P. Kiesel, A. Höfler, M. Kneissl, J.S. Smith and G.H. Döhler, Appl. Phys. Lett. 62 (1993) 3180.
[9] G.W. Yoffe, J. Brübach, F. Karouta, W.C. van der Vleuten, L.M.F. Kaufmann and J.H. Wolter, Appl. Phys. Lett. 63 (1993) 1456.
[10] U. Koren, B.I. Miller, T.L. Koch, G. Eisenstein, R.S. Tucker, I. Bar-Joseph and D.S. Chemla, Appl. Phys. Lett. 51 (1987) 1132.
[11] K. Wakita, Y. Kawamura, M. Nakao and H. Asahi, IEEE J. Quantum Electron. 23 (1987) 2210.
[12] D. Moss, R.L. Williams, M. Dion and D. Landheer, Appl. Phys. Lett. 59 (1991) 3139.
[13] T.C. Huang, Y. Chung, D.B. Young, N. Dagli and L.A. Coldren, IEEE Photon. Technol. Lett. 3 (1991) 141.
[14] F. Devaux, E. Bigan, M. Allovon, J.-C. Harmand, F. Huet, M. Carre and J. Landreau, Appl. Phys. Lett. 61 (1992) 2773.
[15] A.L. Moretti, D.J. Vezzetti, F.A. Chambers, K.A. Stair and G.P. Devane, IEEE Photon. Technol. Lett. 4 (1992) 576.
[16] J.E. Zucker, K.L. Jones, M. Wegener, T.Y. Chang, N.J. Sauer, M.D. Divino and D.S. Chemla, Appl. Phys. Lett. 59 (1991) 201.
[17] C. Rolland, G. Mak, K.L. Prosyk, C.M. Martin and Puetz, IEEE Photon. Technol. Lett. 3 (1991) 894.
[18] B. Knüpfer, P. Kiesel, M. Kneissl, S. Dankowski, N. Linder and G.H. Döhler, IEEE Photon. Technol. Lett. 5 (1993) 1386.
[19] S. Malzer, M. Kneissl, P. Kiesel, K.H. Gulden, X.X. Wu, J.S. Smith and G.H. Döhler, J. Vac. Sci. Technol. B 14 (3) (1996) 2175.
[20] E. Kapon and R. Bhat, Appl. Phys. Lett. 50 (1987) 1628.

ELSEVIER

Journal of Crystal Growth 175/176 (1997) 964–970

JOURNAL OF CRYSTAL GROWTH

The growth and characterization of two new P-type compressively strained layer InGaAs/AlGaAs/GaAs quantum well infrared photodetectors for mid- and long-wavelength infrared detection

J. Chu[a,*], Sheng S. Li[a], Pin Ho[b]

[a] *Department of Electrical and Computer Engineering, University of Florida, Gainesville, Florida 32611, USA*
[b] *Lockheed Martin Electronics Laboratory, Syracuse, New York 13221, USA*

Abstract

Investigation of two p-type compressively-strained layer (PCSL) InGaAs/AlGaAs/GaAs quantum well infrared photodetectors (QWIPs) grown on (1 0 0) semi-insulating (SI) GaAs substrate has been carried out. The first detector uses a step-bound-to-miniband (SBTM) transition scheme for long wavelength infrared (LWIR) detection and has a detection peak at 10.4 μm with a full width at half-maximum bandwidth, $\Delta\lambda/\lambda_p = 20\%$. A responsivity of 28 mA/W was obtained for this detector at $T = 65$ K and $V = 3.0$ V, with a spectral detectivity $D^* = 1.4 \times 10^9$ cm Hz$^{1/2}$ W^{-1} at T = 65 K and $V = 1.0$ V. The detector was under the background limited performance (BLIP) at $T = 40$ K and $V \leqslant 2.0$ V. The second detector is a two-color stacked QWIP composed of a PCSL $In_{0.2}Ga_{0.8}As/Al_{0.3}Ga_{0.7}As$ QWIP for the MWIR detection at $\lambda_p = 4.8$ μm and a PCSL $In_{0.15}Ga_{0.85}As/Al_{0.1}Ga_{0.9}As$ for the LWIR detection at $\lambda_p = 10$ μm. The peak responsivity for the LWIR QWIP was found to be 25 mA/W at $V_b = 2$ V, $T = 40$ K, $\lambda_p = 10$ μm, a FWHM of $\Delta\lambda/\lambda_p = 40\%$, and the calculated detectivity was found to be $D^* = 1.1 \times 10^{10}$ cm Hz$^{1/2}$ W^{-1}. Two response peaks for the MWIR QWIP were found to be at 4.8 and 5.4 μm with maximum responsivities of 12 and 19 mA/W (at $T = 77$ K and $V_b = 5$ V), and spectral bandwidths of 21 and 26%, respectively. The detectivity (D^*) for the MWIR stack determined at $\lambda_p = 5.4$ μm, $V_b = 1.0$ V and $T = 77$ K was found to be 5.5×10^{11} cm Hz$^{1/2}$ W^{-1}.

1. Introduction

In recent years, a great deal of works have been published on the III–V semiconductor quantum well infrared photodetectors (QWIPs) for long wavelength infrared (LWIR) and mid-wavelength infrared (MWIR) focal plane arrays (FPAs) applications. Most of the studies have been centered on the n-type QWIPs [1, 2]. However, for n-QWIPs due to quantum mechanical selection rules, normal incidence absorption is forbidden without the use of metal or dielectric grating couplers. In contrast, the normal incidence absorption is allowed in p-type QWIPs due to the mixing between

* Corresponding author.

0022-0248/97/$17.00 Copyright © 1997 Elsevier Science B.V. All rights reserved
PII S0022-0248(96)01237-7

the off zone-center ($k \neq 0$) heavy-hole and light-hole states [3]. Because of the larger effective mass (hence lower optical absorption coefficient) and the lower hole mobilities, the performance of p-QWIPs are in general lower than n-QWIPs [1, 4]. However, if the biaxial compressive strain is introduced into the quantum well layers of a p-QWIP, then the effective mass of the heavy holes will be reduced, which in turn can improve the overall device performance [5]. In this work, we present a new p-type compressively strained layer step-bound-to-miniband (SBTM) transition InGaAs/AlGaAs/GaAs QWIP for LWIR detection. The need to detect simultaneously two different infrared wavelengths in the MWIR and LWIR bands has led us to design a stacked p-type compressively strained layer (PCSL) QWIP structure with detection peaks in the 3–5 μm MWIR band and 8–14 μm LWIR band. The results of this multicolor stacked QWIP will also be presented in this paper.

2. Design and growth of p-type strained layer QWIPs

First, we report a new p-type SBTM CSL-QWIP grown on a semi-insulating (SI) (1 0 0)GaAs by molecular beam epitaxy (MBE) using InGaAs for the quantum well and AlGaAs/GaAs material system for the superlattice barrier layer. As illustrated in Fig. 1a, the transition scheme for this p-QWIP is from the localized ground bound heavy hole state (HH1) in the wide Be-doped InGaAs quantum well to the resonant coupled miniband of the undoped GaAs/AlGaAs superlattice (SL) barrier. This structure creates a potential difference between the SL barrier region and the quantum well which blocks part of the undesirable tunneling dark current from the heavily doped heavy hole ground state, HH1 [2] in the quantum well. The physical parameters were chosen so that the ground state in the wide InGaAs quantum well is well above the top of the GaAs/AlGaAs SL barrier, and the third excited heavy hole state (HH4) is in resonance with the ground level of the superlattice miniband (SL1) to achieve a higher quantum efficiency. Since the superlattice consists of thin barriers, the photoexcited holes can easily tunnel through the SL barrier layer and transport along the aligned miniband to be collected by the ohmic contacts.

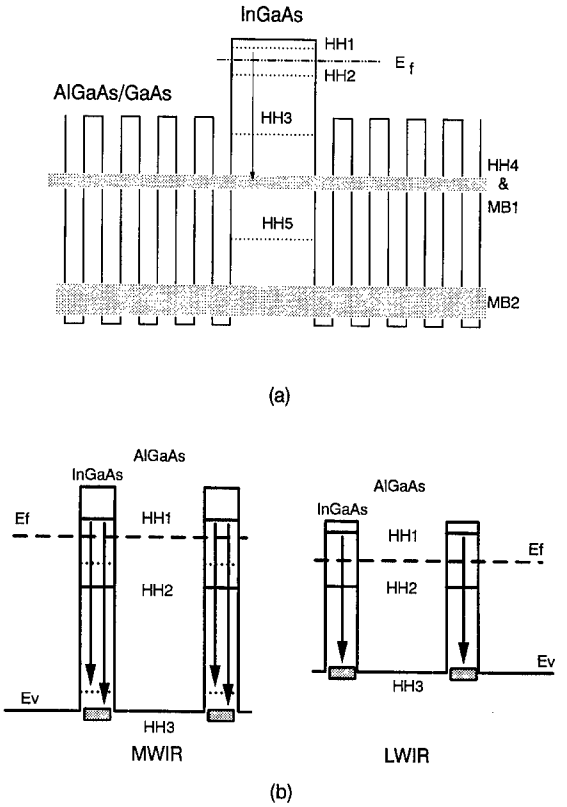

Fig. 1. The energy band diagrams and intersubband transition schemes for (a) a SBTM PCSL-InGaAs/AlGaAs/GaAs QWIP, and (b) a two-color stacked PCSL-InGaAs/AlGaAs QWIP for the MWIR and LWIR detection.

The p-type SBTM CSL-QWIP consists of Be-doped $In_{0.12}Ga_{0.88}As$ quantum wells to populate the ground heavy hole (HH1) state. The quantum well layer is under compressive strain with a lattice mismatch of nearly -0.8%. Surrounding the quantum well layers are the SL barriers of undoped $Al_{0.35}Ga_{0.65}As$ alternating with undoped GaAs quantum wells. The p-type ohmic contacts were formed by using a cap layer and a buffer layer of heavily Be-doped GaAs grown on top of the SBTM QWIP and between the SBTM QWIP and the GaAs substrate, respectively.

The second QWIP studied in this work is a multicolor stacked P-QWIP for the MWIR and

LWIR two-band detection. Fig. 1b shows the energy band diagram of a stacked p-type compressively strained layer (PCSL-) InGaAs/AlGaAs QWIP for the MWIR and LWIR detection. This multicolor QWIP consists of two distinct multiquantum well stacks separated by a common ohmic contact layer and sandwiched between the two (top and bottom) ohmic contact layers. This stacked PCSL- QWIP was grown by the MBE technique on SI (1 0 0)GaAs substrate. The bottom contact consists of a heavily Be-doped GaAs contact layer. On top of the contact, the $Al_{0.3}Ga_{0.7}As/In_{0.2}Ga_{0.8}As$ QWIP layer structure was grown for the MWIR stack. The LWIR QWIP stack was formed by using Be-doped $In_{0.15}Ga_{0.85}As$ quantum wells surrounded with the undoped $Al_{0.1}Ga_{0.9}As$ barrier layers. The whole stack was sandwiched between two thin $Al_{0.1}Ga_{0.9}As$ blocking barriers. Finally, heavily Be-doped GaAs layers were grown for the top and middle ohmic contacts. Both the LWIR and MWIR quantum wells are in biaxial compression. This multicolor stacked QWIP used the bound-to-quasi-bound (BTQB) intersubband transition scheme for detection of MWIR and LWIR radiation.

3. Theoretical considerations

To analyze the performance and characteristics of the two PCSL-QWIPs described above, we performed the theoretical calculations of the energy states in the quantum well and the superlattice barrier regions along with the transmission coefficient, $|T^*T|$, by using the multiple layer transfer matrix method (TMM) [6]. Using linearly interpolated values for the heavy-hole and light-hole effective masses and the bandgap energies at 77 K for GaAs, $Al_{0.35}Ga_{0.65}As$, and $In_{0.12}Ga_{0.88}As$ we determined the intersubband transition wavelengths for the LWIR absorption to occur at a peak wavelength of 10 μm, when the effect of biaxial compressive strain was considered. The induced energy band edge shifts for the conduction band, heavy hole subband, and the light hole subband are given respectively by [7],

$$\Delta E_c = 2c_1 \frac{C_{11} - C_{12}}{C_{11}} \delta_0,$$

$$\Delta E_{hh} = b \frac{C_{11} + C_{12}}{C_{11}} \delta_0,$$

$$\Delta E_{lh} = -\Delta E_{hh} + \frac{(\Delta E_{hh})^2}{2\Delta_0},$$

where c_1 is the combined hydrostatic deformation potential which characterizes the splitting of the Γ_8 valence band under strain, b is the shear deformation potential, C'_{ij}s are the elastic constants, Δ_0 is the spin orbit split-off energy, and δ_0 is the lattice mismatch or the in-plane strain, which is defined as $\delta_0 = (a - a_s)/a$.

Another feature of the p-type QWIPs is the inherently larger quantum efficiency than that of n-QWIPs, which is given by $\eta = P(1 - R)[1 - \exp(-\alpha l)]$.

Given similar absorption coefficients, α, and well thickness, l, the prefactor P is equal to 0.5 for n-QWIPs and 1.0 for p-QWIPs, which gives us a doubling of the quantum efficiency for p-QWIPs. Due to the inherently low absorption coefficients of p-type materials, and the large hole effective mass, compressive strain must be used to reduce the hole effective mass in order to increase the intersubband absorption.

With the inclusion of compressive strain, the mobility of the heavy holes is enhanced by reducing the heavy hole effective mass [5]. Also associated with the presence of compressive strain is the reduction of the in-plane density of states in the InGaAs quantum well. Thus, with a significant lowering of the effective mass of the ground heavy holes, an increase in the absorption coefficient and the corresponding quantum efficiency is expected.

4. Results and discussion

In order to evaluate the performance of the QWIP devices, mesa structure with area of $216 \times 216\ \mu m^2$ was formed on the MBE grown QWIP wafer by wet chemical etching for radiometric and electrical characterization. A narrow ring of Cr/Au film was deposited by E-beam evaporation to create the ohmic contacts. It is noted that in this type of mesa and ring contact structures, the

normal incidence IR radiation is allowed only one pass through the QWIP stack.

For the multicolor stacked QWIP, three mesa structures of different thicknesses were etched to allow separate characterization of the LWIR, MWIR, and the combined stacked QWIP devices. The LWIR QWIP mesa structure was formed using the top and middle ohmic contacts, while the MWIR QWIP mesa structure had the top LWIR stack etched away before the mesa formation. The combined stacked QWIP used the top and bottom ohmic layers for contacts.

The device characterization was performed in a closed cycle helium cryogenic dewar. An HP 4145B semiconductor parameter analyzer was used to measure the dark I–V characteristics and the 300 K background photocurrent. Under dark conditions, holes can be transferred out of the quantum wells and produce the observed dark current mainly due to two mechanisms: the thermionic emisson out of the quantum wells and thermally generated carriers tunneling through the superlattice barriers. Given the high aluminum composition in the SL barrier layers, considerable indium content in the quantum well layers, and the effect of the compressive strain lowering the energy of the heavy hole states, the effective barrier seen by the ground heavy hole states was found to be 299 meV, which should suppress the thermionic emission of hole carriers out of the quantum well. However, due to the heavily doped ohmic contact regions, a large triangle potential might be formed to effectively lower the barrier with increasing thermionic emission, and hence results in a higher dark current than expected. Additional contributions to the higher dark current characteristics might also arise from the higher aluminum content used in the SL barrier layers, which has been attributed to the formation of DX centers in the AlGaAs barrier layers.

Fig. 2 shows the dark I–V curves measured over a wide range of temperatures from 40 to 77 K along with the 300 K background photocurrent (FOV = 180°) curve for the SBTM PCL-QWIP device. Relatively symmetrical I–V characteristics were obtained for this device under postive and negative biases, indicating that the dopant migration effect is negligible in this device. Fig. 3a shows

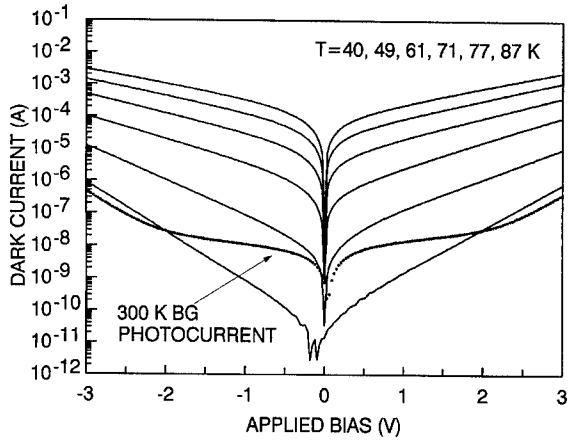

Fig. 2. The dark I–V characteristics for the SBTM PCSL-QWIP as a function of temperature along with the 300 K background photocurrent (FOV 180°).

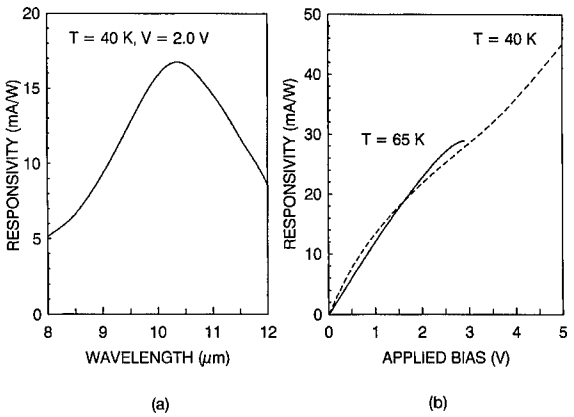

Fig. 3. (a) The photoresponsivity versus wavelength, and (b) responsivity versus applied bias at $T = 40$, 65 K for the SBTM PCSL-QWIP.

the measured photoresponse of the same SBTM PCL-QWIP. A single peak was found at $\lambda_p = 10.4\ \mu m$, which is in good agreement with the calculated value of 10 μm (see Fig. 1a). With a half-peak value at 12 μm, we derived a spectral bandwidth of $\Delta\lambda/\lambda_p = 20\%$. This narrow responsivity bandwidth is consistent with that expected for a bound-to-miniband transition QWIP. A maximum responsivity of 28 mA/W was found at $T = 65$ K and $V_b = +3.0$ V. At an operating temperature of 65 K, the noise spectral density was

measured as 4.0×10^{-26} A^2/Hz at a bias of 1.0 V. Corresponding to this operating point, the measured responsivity at the 10.4 μm peak was found to be 13 mA/W. From the above data, the spectral detectivity of $D^* = 1.4 \times 10^9$ cm Hz$^{1/2}$ W^{-1} was obtained. Note that this is the detectivity achieved by a single pass of the normal incidence IR radiation through the SBTM PCL-QWIP. If the test structure is altered to include the backside thinning and a reflective top contact, then the responsivity will increase substantially. The corresponding detectivity will also increase, since the dark current and the noise spectral density remain constant. The variation of responsivity with applied bias is plotted in Fig. 3b. The results show that the responsivity and hence the photoconductive gain increase linearly with the applied bias at a fixed operating temperature.

The dark I–V characteristic for the MWIR, LWIR, and the combined stacked QWIP measured at $T = 77$ K is shown in Fig. 4a. As expected the dark current of the LWIR QWIP stack is several orders of magnitude higher than the MWIR QWIP stack, due to the exponential dependence of the dark current on the barrier height. As clearly seen in Fig. 4a, most of the voltage drop is across the MWIR stack due to the much larger dynamic resistance of the MWIR stack. Fig. 4b shows the measured I–V curves at $T = 40$, 60, and 77 K for the LWIR QWIP stack. The asymmetry in the dark I–V characteristics observed in this device can be attributed to the dopant migration effect [8].

The spectral responsivity for the MWIR QWIP measured at $V = 5$ V and $T = 77$ K is shown in Fig. 5. The responsivity measurements were performed with the device mounted in a closed cycle helium dewar and illuminated by a blackbody source running through a grating monochrometer and appropriate IR filters. The resulting photocurrent is amplified and detected by a lock-in amplifier. Results of the measurements revealed that two photoresponse peaks were observed in the MWIR band at $\lambda_{p,mw1} = 4.8$ μm and $\lambda_{p,mw2} = 5.4$ μm. The 4.8 μm peak is in excellent agreement with the ground heavy hole (HH1) to second bound heavy hole (HH3) transition calculated by the TMM, which predicts a detection peak at 4.7 μm. The detectivity for this MWIR peak was determined to

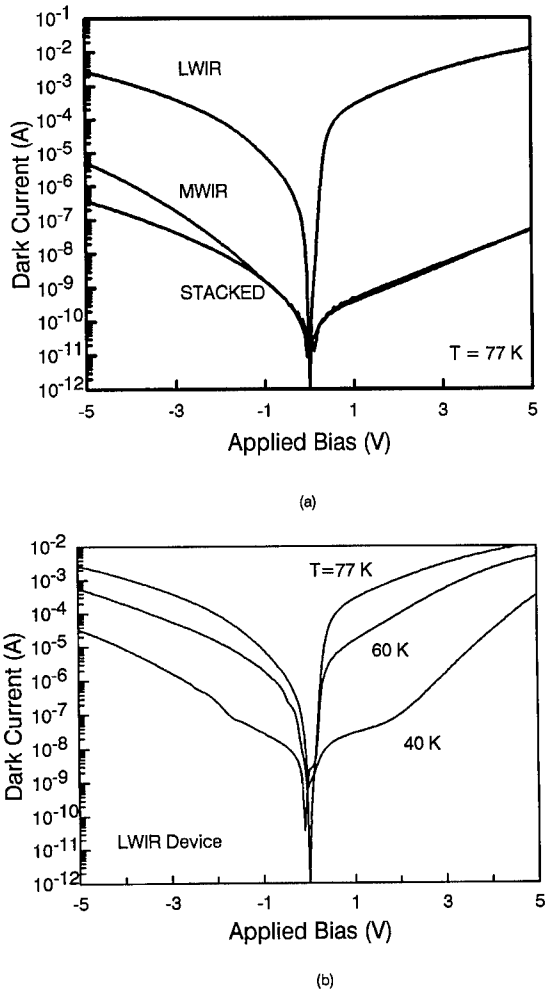

Fig. 4. The dark I–V characteristics for (a) the stacked, MWIR, and LWIR PCSL-QWIP, and (b) the LWIR QWIP for $T = 40$, 60, and 77 K.

be $D^* = 3.3 \times 10^{11}$ cm Hz$^{1/2}$ W^{-1} at $V_b = 1.0$ V and $T = 77$ K. The measured spectral bandwidth for the first MWIR peak was found to be $\Delta\lambda/\lambda_{p,mw1} = 21\%$ and $\Delta\lambda/\lambda_{p,mw2} = 26\%$ for the second peak. The second, longer wavelength peak is attributed to the transition from the HH1 states to the second bound light hole (LH2) states within the quantum well. The calculated responsivity peak for this transition is 5.6 μm, which is also in good agreement with the measured value. The higher responsivity of the 5.4 μm peak is attributed to the

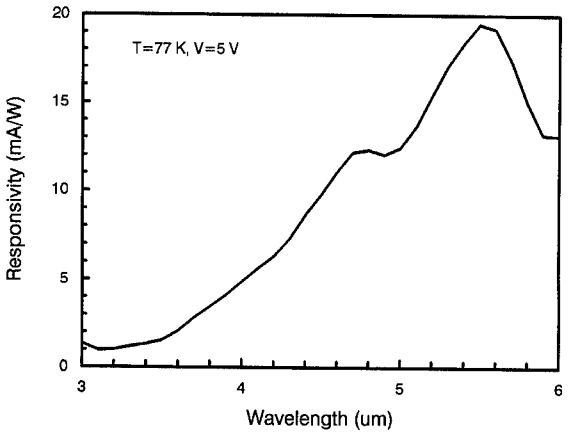

Fig. 5. The spectral responsivity versus wavelength for the MWIR PCSL-QWIP, measured at $T = 77$ K and $V = 5$ V. Two response peaks at 4.8 and 5.4 μm were observed for this device.

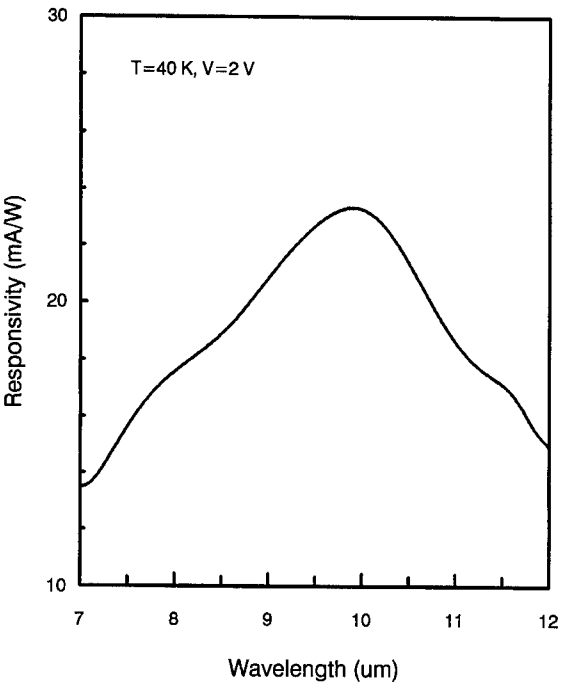

Fig. 6. The spectral responsivity versus wavelength for the LWIR PCSL-QWIP, measured at $T = 40$ K and $V = 2$ V. One response peak at 10 μm was obtained for this device.

higher absorption coefficent inherent with the HH to LH transition [4]. The spectral detectivity for this MWIR peak was found to be 5.5×10^{11} cm $Hz^{1/2}$ W^{-1} at $V_b = 1.0$ V and $T = 77$ K.

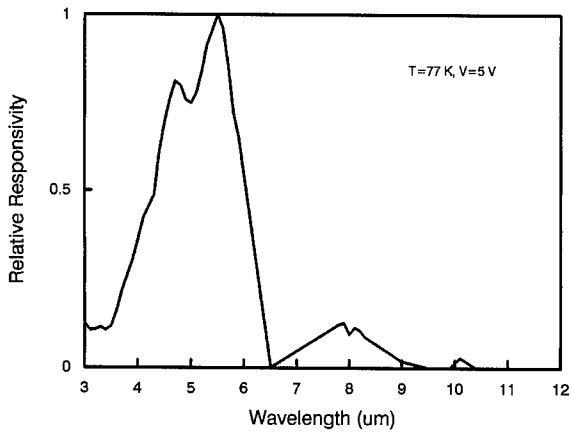

Fig. 7. The relative photoresponse versus wavelength for the combined stacked PCSL-QWIP. Three photoresponse bands were detected in this stacked QWIP.

The responsivity for the LWIR QWIP stack as a function of the wavelength is shown in Fig. 6. A peak detection wavelength at $\lambda_{p,lw} = 10.0$ μm was found for the LWIR QWIP device, which is in excellent agreement with the calculated value of 10 μm from the TMM. The maximum responsivity measured at $T = 40$ K and $V = 2.0$ V was found to be 25 mA/W, with a detectivity of 1.1×10^{10} cm $Hz^{1/2}$ W^{-1} under the same conditions. It is interesting to note that a very broad response with full width at half-maximum bandwidth of 40% was achieved for this device. Fig. 7 shows the relative spectral response of the combined MWIR and LWIR QWIP stack, displaying one dominant response band at MWIR and two smaller response peaks at LWIR bands.

5. Conclusions

In conclusion, we have demonstrated two new p-type compressively strained layer QWIPs using InGaAs/AlGaAs/GaAs material systems for the MWIR and LWIR detection. It is shown that by using the compressive strain in the quantum well and the superlattice barriers, the step bound-to-miniband transition can be achieved, which could be useful in producing a new narrow bandwidth LWIR p-QWIP device. We have also demonstrated that simultaneous two-color two-band

detection can be achieved with strained layer p-type QWIPs by stacking the LWIR and MWIR QWIP devices in series and using a three terminal structure. Given the inherent benefit of normal incidence detection without the use of grating couplers, the simplicity of the p-QWIP design deserves futher investigation. By further optimizing the quantum well doping density, biaxial strain strength, superlattice barrier parameters, and by using a triangle potential blocking layer in the ohmic contact regions for the SBTM p-QWIP, high performance LWIR and MWIR p-QWIPs can be developed for IR imagery applications.

Acknowledgements

The research performed at the University of Florida was sponsored and monitored by the US Air Force Material Command, Phillips Laboratory/VTRP, Kirtland AFB, NM under a subcontract with Maxwell S-Cubed Div., and in part supported by the Defense Advanced Research Project Agency (DARPA) and monitored by the Office of Naval Research under AASERT grant No. N00014-93-1-0827.

References

[1] B.F. Levine, J. Appl. Phys. 74 (8) (1993) R1.
[2] L.S. Yu, Y.H. Wang and S.S. Li, Appl. Phys. Lett. 60 (1992) 992.
[3] Y.-C. Chang and R.B. James, Phys. Rev. B 39 (1989) 12672.
[4] H. Xie, J. Katz and W.I. Wang, Appl. Phys. Lett. 56 (1991) 3601.
[5] K. Hirose, T. Mizutani and K. Nishi, J. Crystal Growth 81 (1987) 130.
[6] A.K. Ghatak, K. Thyagarajan and M.R. Shenoy, IEEE J. Quantum Electron. 24 (1988) 1524.
[7] F.H. Pollack, in: Strained-layer superlattices: physics, Vol. 32, Ed. T.P. Pearsall (1990) p. 17.
[8] H.C. Liu, Z.R. Wailewski and M. Buchanan, Appl. Phys. Lett. 63 (1993) 761.

ELSEVIER

Journal of Crystal Growth 175/176 (1997) 971–976

JOURNAL OF CRYSTAL GROWTH

Large array of GaAs modulators and detectors flip-chip solder bonded to silicon CMOS using InGaP as the selective etch stop for GaAs substrate removal

J.M. Kuo[a,*], Y.C. Wang[a,f], K.W. Goossen[b], L.M.F. Chirovsky[a], S.P. Hui[a], B.T. Tseng[a], J. Walker[b], A.L. Lentine[c], R.E. Leibenguth[d], G. Livescu[a], W.Y. Jan[b], J.E. Cunningham[b], L.A. D'Asaro[a], A. Ron[a,e], D. Dahringer[a], D. Kossives[a], D.D. Bacon[a], R.L. Morrison[c], R.A. Novotny[c], D.B. Buchholz[c], W.E. Mayo[f]

[a] *AT&T Bell Laboratories, Lucent Technologies, Murray Hill, New Jersey 07974, USA*
[b] *AT&T Bell Laboratories, Lucent Technologies, Holmdel, New Jersey 07733, USA*
[c] *AT&T Bell Laboratories, Lucent Technologies, Naperville, Illinois 60566, USA*
[d] *AT&T Bell Laboratories, Lucent Technologies, Breinigsville, Pennsylvania 18031, USA*
[e] *Technion, Israel Institute of Technology, Haifa 32000, Israel*
[f] *Department of Mechanics and Materials Science, Rutgers University, Piscataway, New Jersey 08855, USA*

Abstract

We demonstrate the integration of a large (64 × 68) p-i(MQW)-n GaAs diode array to a silicon CMOS chip, using flip-chip solder bump bonding techniques together with concomitant GaAs substrate removal. The capability of removing a relatively large area of GaAs substrate cleanly and uniformly is attributed to the introduction of a new selective etch stop with a smooth isotropic etchant for the GaAs substrate removal. The presence of the lattice matched $In_{0.49}Ga_{0.51}P$ selective etch stop layer has no detrimental effect on the performance of the GaAs/AlGaAs optical detector/modulator diodes, which gives the chip the large I/O count of 4352.

PACS: 42.79.Ta

Keywords: InGaP; Flip-chip solder bonding; Modulation/detector array

1. Introduction

In recent years, considerable effort has been devoted to the development of the integration of III–V optoelectronics with silicon electronic circuits. This material combination finds many applications in optical computing, optical information processing, and optical interconnect. The optical detector/modulator diodes based on the quantum-confined Stark effect (QCSE) with a GaAs/AlGaAs multiple-quantum-well (MQW) structure are good

* Corresponding author.

0022-0248/97/$17.00 Copyright © 1997 Elsevier Science B.V. All rights reserved
PII S0022-0248(96)01206-7

candidates for the photonic elements of this concept, since they can play the roles of surface normal optical input and/or output (I/O) devices for silicon integrated circuits (IC's) [1]. The integration of two-dimensional arrays of such diodes with Si CMOS circuits is desirable for massive parallelism and connectivity [2].

Possible technologies for achieving large arrays of GaAs/AlGaAs MQW devices on Si CMOS include heteroepitaxial growth, epitaxial lift-off (ELO) and flip-chip bonding. Heteroepitaxial growth of GaAs/AlGaAs modulators on silicon has been demonstrated, [3–5] however, it encounters the problems of the incompatibility of growth and processing technologies [6]. These problems can be alleviated by the technique of epitaxial lift-off [7, 8]. ELO is a process that can free the GaAs epilayers or devices from its growth substrate and reattach them to a new substrate. The high material quality of lattice-matched growth is therefore preserved. The key to the success of this technique is the selective etching of a sacrificial AlAs layer grown between the GaAs substrate and the bottom layer of the device by HF. ELO not only offers the advantage of placing a high-quality single crystalline GaAs film on Si without regard to lattice matching, but also allows GaAs devices and silicon IC's to be independently designed and fabricated for optimum performance. However, there are still some problems to be overcome, e.g. the presence of cracks or strain in the thin layers as well as the handling and adhesion of the thin films [9]. Another approach which is more manufacturable, is the so called flip-chip solder bump bonding technique [1, 2]. In this approach, the hybridization process of GaAs/AlGaAs detector/modulator diodes on silicon includes the chip fabrication, die separation, the alignment, and the solder bump bonding of the GaAs diode array chips onto silicon chips; etching off the optically opaque and thermally straining GaAs substrate; and finishing with the deposition of an anti-reflection coating. This approach offers the same advantages as ELO, but without the drawback of thin-film handling as is required in ELO.

Recently, flip-chip solder bump bonding of GaAs/AlGaAs MQW detector/modulator diodes on Si electronic IC's has been demonstrated by Goossen et al. [1]. In that process, a 1.5 μm thick $Al_{0.3}Ga_{0.7}As$ was used as the selective etch stop for the GaAs substrate removal which was chemically removed by 1 : 100 $NH_4OH : H_2O_2$ using a jet etcher. The low etching selectivity of this etchant limits the usefulness of the $Al_{0.3}Ga_{0.7}As$ as an etch stop layer, because it cannot sufficiently compensate for any etching nonuniformities induced during the removal of a thick substrate. The GaAs chip size for successful substrate removal is therefore limited. Here we report a new selective etch stop approach which greatly increases the etching selectivity and gives uniform final etching results over a larger area compared to the $Al_{0.3}Ga_{0.7}As$ etch stop. We use an $In_{0.49}Ga_{0.51}P$ etch stop layer which is lattice matched to the GaAs substrate and which also acts as a buffer layer in the epitaxial growth. We have also demonstrated that the new $In_{0.49}Ga_{0.51}P$ selective etch stop grown as the buffer layer has no detrimental effect on the performance of the GaAs/AlGaAs modulators. The entire substrate from a 64×68 diode array was removed cleanly with the new selective etch stop without using substrate thinning or jet etching techniques. Uniform photocurrent response across the array demonstrates that the $In_{0.49}Ga_{0.51}P$ layer is indeed a good selective etch stop for GaAs substrate removal for the entire MQW diode array. The new selective etch stop layer thus enhances the manufacturability of the flip-chip solder bump bonding and substrate removal techniques.

2. Device fabrication

The epitaxial layers of the GaAs/AlGaAs p-i(MQW)-n diode structure as shown in Fig. 1 were grown using gas-source molecular beam epitaxy (GSMBE) on a 2″ or 3″ semi-insulating GaAs substrate. A 5000 Å $In_{0.49}Ga_{0.51}P$ layer was first grown, followed by a 1 μm $Al_{0.11}Ga_{0.89}As$ p^+-layer and a 500Å undoped $Al_{0.11}Ga_{0.89}As$ spacer. Then the undoped MQW were grown, which consisted of 95 periods of 85 Å GaAs wells and 35 Å $Al_{0.3}Ga_{0.7}As$ barriers. Finally, a 1000 Å n^+-$Al_{0.11}Ga_{0.89}As$ layer, followed by a 1000 Å n^+-GaAs contact layer. The growth conditions and the switching procedure between AsH_3 and PH_3 gases

can be found elsewhere [10, 11]. Arrays of detector/modulator diodes are produced on the GaAs wafer via a coplanar ion-implantation process [12]. 3 μm thick Sn/Pb solder with dimension of 15 × 15 microns was deposited on both the n and p ohmic contacts of the modulators using 10 μm-thick photoresist and lift-off technique [13]. Each GaAs chip consists of 4352 GaAs/AlGaAs MQW diodes and 8704 solder bumps. The physical size of the GaAs modulator chip is 6.2 mm × 6.2 mm. The complete GaAs chips were then seperated. The CMOS chips (7 mm × 7 mm) designed with 256 16 × 1 switching nodes, each with 16 optical inputs and 1 optical output, were made in the Lucent 1 μm technology. Mating aluminum pads from the modulators were designed on the chips, and Ti–Ni–Au metals were deposited on them to provide a solder-wettable surface. Then solder was deposited on those pads, by a process similar to the one for the GaAs chips. A precision bonder was employed to bond the chips together. A low viscosity epoxy (used to protect the circuitry from the substrate etchant) was flowed between the chips and was cured at 100°C. The bonded chips were then immersed in a H_3PO_4 based etching solution, which dissolves the GaAs substrate at a rate of approximately 3.5 μm/minute isotropically. The dissolution stoped at the $In_{0.49}Ga_{0.51}P$ layer. Selectivity of ~ 290 was obtained. This etchant does not attack Si. Finally, a SiO_x anti-reflection (AR) coating was deposited.

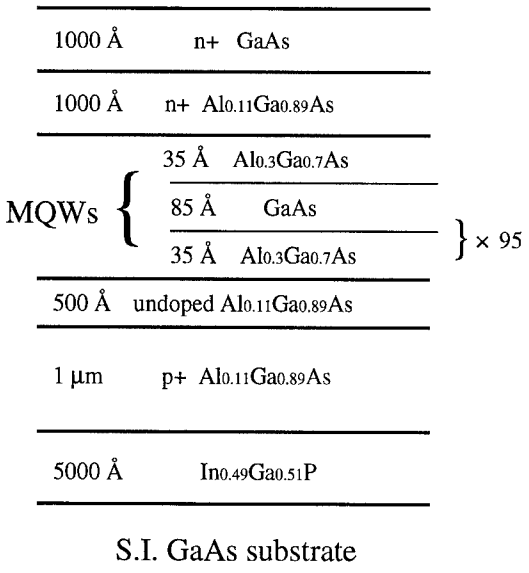

Fig. 1. Structural schematic of the modulator/detector array used in this study.

3. Results and discussion

With the new $In_{0.49}Ga_{0.51}P$ selective etch stop, one question we have to answer first is whether

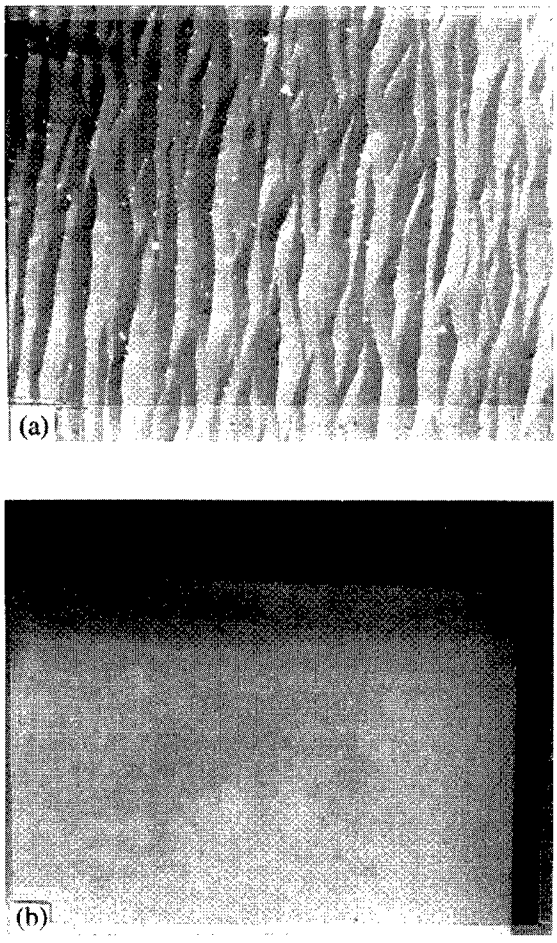

Fig. 2. Nomarski contrast photomicrographs of (a) wavy-finished $In_{0.49}Ga_{0.51}P$ surface caused by non-uniform etching during the GaAs substrate removal process by a H_3PO_4 based etching solution; and (b) smooth $In_{0.49}Ga_{0.51}P$ surface with an isotropic H_3PO_4 etching solution for GaAs substrate removal.

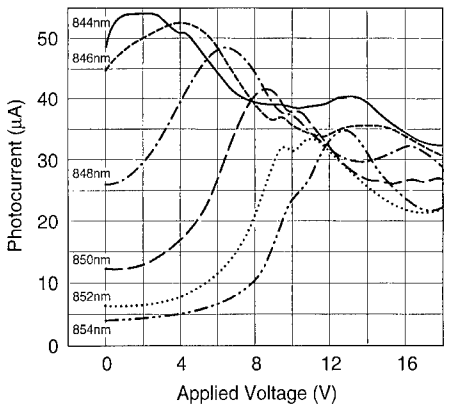

Fig. 3. Photocurrent spectra of a GaAs/AlGaAs MQW modulator without AR coating at several wavelengths under different reverse bias conditions, revealing quantum-confined Stark effect in the modulator.

a mirror-like smooth surface can be obtained after the removal of the GaAs substrate. Wavy-finished $In_{0.49}Ga_{0.51}P$ surfaces, preferentially along the [0 1 1] crystallographic direction, are observed for some etching solutions we tried. The wavy surface is caused by non-uniform etching of the thick GaAs substrate and the attack of $In_{0.49}Ga_{0.51}P$ by the etchant. Therefore, a selective etchant which can etch GaAs uniformly is the key to the success of this approach. Fig. 2 shows the difference of two Nomarski contrast photographs of the $In_{0.49}Ga_{0.51}P$ surface after the removal of GaAs substrate by two different H_3PO_4 based etchants. Strong contrast of the finishing surfaces between the non-uniform and uniform etching solution is clearly revealed. Using the right etchant, we are able to achieve

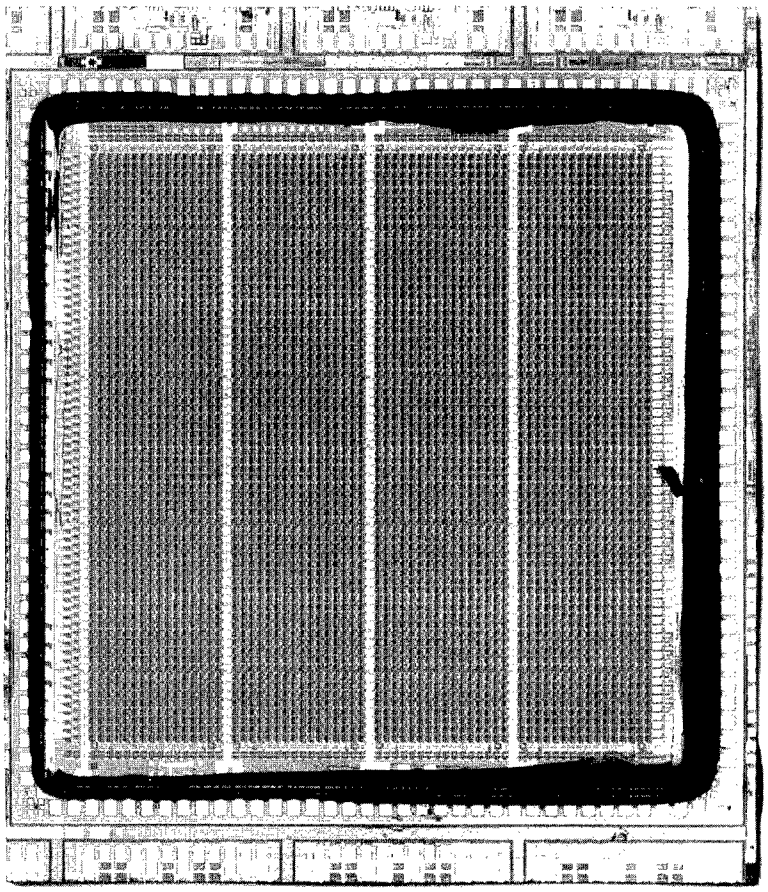

Fig. 4. A finished 64 × 68 GaAs/AlGaAs MQW diode array flip-chip solder bump bonded to silicon CMOS with switching nodes.

a mirror-like $In_{0.49}Ga_{0.51}P$ surface with a 2 in diameter after the removal of the GaAs substrate.

Another important question to be answered is whether the $In_{0.49}Ga_{0.51}P$ has a detrimental effect on the performance of the GaAs/AlGaAs modulators. Fig. 3 shows the photocurrent spectra of a modulator without AR coating at several wavelengths under different reverse bias conditions. As the wavelength increases, the peak of the photocurrent at different wavelength shifts to higher bias voltage. This is an expression of the quantum-confined Stark effect in the GaAs/AlGaAs MQW modulator. At the desired system operation wavelength of 850 nm, a photocurrent change from 12.5 μA to 42 μA for a 0–8.5 V bias swing has been measured. This result is comparable to the best performance of an otherwise identical GaAs/AlGaAs MQW modulator grown with an $Al_{0.3}Ga_{0.7}As$ selective etch stop. A photo of a finished GaAs/AlGaAs MQW diode array bonded to silicon CMOS with switching nodes is shown in Fig. 4. The uniformity of the epitaxial growth and fabrication process is demonstrated through the virtually identical photocurrents measured from the center to the edge of a 2″ wafer as shown in Fig. 5. We also perform a visual test of the 64×68 SEED array by forward biasing the modulators in the light emitting diode (LED) mode. All but 2 out of the 4352 MQW diodes generate light, which is attributed to the improved yield (100%) of the new $In_{0.49}Ga_{0.51}P$ selective etch stop. Missing contacts to the p-type metal cause the imperfect yield of the array. Switching nodes have been tested at rates above 400 Mb/s per channel. System operation from 155 to 208 Mb/s has been demonstrated using this chip. With their high optical signal I/O count, these chips will be the backbone of a 256×256 asynchronous transfer mode (ATM) switching fabric system demonstration performed at 155 Mbit/s data rate per channel.

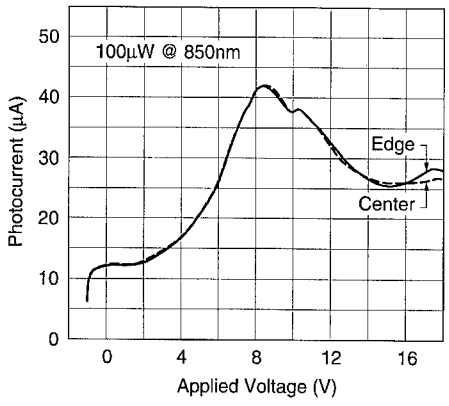

Fig. 5. Virtually identical photocurrents of GaAs/AlGaAs MQW modulators measured from the center to the edge of a 2″ wafer shows the uniformity of the epitaxial growth and fabrication process.

4. Conclusions

We report a new $In_{0.49}Ga_{0.51}P$ selective etch stop which can achieve smooth surface after the GaAs substrate removal. The $In_{0.49}Ga_{0.51}P$ selective etch stop not only has no detrimental effect on the performance of the GaAs/AlGaAs modulators, but also gives more uniform etching over a larger area. This new method improves the yield of GaAs/AlGaAs MQW diodes integrated with silicon CMOS via a flip-chip solder-bonding technique. For a 64×68 diode array, all but 2 out of 4352 diodes generate photocurrent in response to light, which is attributed to the improved yield (100%) of the new selective etch. Switching nodes have been tested at rates above 400 Mb/s per channel. System operation from 155 to 208 Mb/s has been demonstrated using this chip.

Acknowledgements

The authors gratefully acknowledge Y.K. Chen, N.K. Dutta, D.A.B. Miller, D.V. Lang, and H. Kogelnik for their enthusiasm and support of this project.

References

[1] K.W. Goossen, J.A. Walker, L.A. D'Asaro, S.P. Hui, B. Tseng, R. Leibenguth, D. Kossives, D.D. Bacon, D. Dahringer, L.M.F. Chirovsky, A.L. Lentine and D.A.B. Miller, IEEE Photon. Technol. Lett. 7 (1995) 360.

[2] K.W. Goossen, J.E. Cunningham and W.Y. Jan, IEEE Photon. Technol. Lett. 5 (1993) 776.

[3] K.W. Goossen, G.D. Boyd, J.E. Cunningham, W.Y. Jan, D.A.B. Miller, D.S. Chemla and R.M. Lum, IEEE Photon. Technol. Lett. 1 (1989) 304.
[4] P. Barnes, P. Zouganeli, A. Rivers, M. Whitehead, G. Perry, K. Woodbridge and C. Roberts, Electron. Lett. 25 (1989) 995.
[5] K.W. Goossen, J.A. Walker, J.E. Cunningham, W.Y. Jan, D.A.B. Miller, S.K. Tewksbury and L.A. Hornak, Photon. Switching Tech. Dig. 8 (1993) 50.
[6] P. Demeester, I. Pollentier, P. De Dobbelaere, C. Brys and P. Van Daele, Semicond. Sci. Technol. 8 (1993) 1124.
[7] E. Yablonovitch, T. Gmitter, J.P. Harbison and R. Bhat, Appl. Phys. Lett. 51 (1987) 2222.
[8] C. Camperi-Ginestet, M. Hargis, N. Jokerst and M. Allen, IEEE Photon. Technol. Lett. 3 (1991) 1123.
[9] I. Pollentier, P. De Dobbelaere, F. De Pestel, P. Van Daele and P. Demeester, Eur. Solid State Dev. Res. Conf. (1989) 401.
[10] J.M. Kuo and E.A. Fitzgerald, J. Vac. Sci. Technol. B 10 (1992) 959.
[11] J.M. Kuo, H.C. Kuo, J.Y. Cheng, Y.C. Wang, Y. Lu and W.E. Mayo, J. Crystal Growth 158 (1996) 393.
[12] L.A. D'Asaro, L.M.F. Chirovsky, E.J. Laskowski, S.S. Pei, R.E. Leibenguth, T.K. Woodward, M. Focht, A.L. Lentine, M.T. Asom, G. Guth, R.F. Kopf, J.M. Kuo, S.J. Pearton, G.J. Przybylek, F. Ren and L.E. Smith, IEEE Electron Dev. Lett. 13 (1992) 528.
[13] B. Tseng, S.P. Hui, K.W. Goossen, L.A. D'Asaro and J.R. Lothian, The 187th Meeting of The Electrochemical Society, Reno, Nevada (1995).

ELSEVIER

Journal of Crystal Growth 175/176 (1997) 977–982

JOURNAL OF CRYSTAL GROWTH

Molecular beam epitaxy of strain-compensated InGaAs/GaAsP quantum-well intersubband photodetectors

K. Bacher*, S. Massie, M. Seaford[1]

Quantum Epitaxial Designs, Inc., 119 Technology Drive, Bethlehem, Pennsylvania 18015, USA

Abstract

We report on the growth of quantum well intersubband photodetectors (QWIPs) with InGaAs wells grown on GaAs. Arsenic species and substrate temperature were varied to investigate their effects on the photoluminescence (PL) and lattice relaxation of 40 period InGaAs/GaAs QWIP samples. Both PL intensity and lattice relaxation decreased with decreasing substrate temperature – the PL dropping steeply below 500°C and the relaxation dropping gradually below 470°C. In all cases examined, however, the relaxation was at least 33% as measured by asymmetric (1 1 5) five crystal X-ray scans. Introducing a small percentage of phosphorous into the barriers to partially strain-compensate the structure was found to dramatically reduce the lattice relaxation while maintaining the highest PL intensity. Comparison of this strain-compensated InGaAs/GaAsP QWIP with the optimized InGaAs/GaAs QWIP revealed that the dark current was reduced by a factor of 4 while the photocurrent remained virtually unchanged resulting in an increase in the background limited operating temperature by approximately 3 K.

PACS: 62.40. + i; 85.60.Dw; 85.60.Gz

Keywords: Strain compensation; QWIP; MBE; GaAsP; GaAs; InGaAs

Quantum well intersubband photodetectors (QWIPs) are attractive devices for imaging at mid- and long-infrared wavelengths, especially for large staring arrays. The mature III–V material technology used to manufacture these devices results in much lower costs, larger array sizes, higher pixel operability, and better uniformity than are achievable in competing technologies, such as HgCdTe. The excellent uniformity is especially important for large arrays since the array uniformity, rather than the individual detector performance, ultimately limits the minimum resolvable temperature of state of the art arrays [1].

Typically, the active region of a QWIP detector consists of multiple 20–60 Å quantum wells each separated by several hundred angstroms of a wider bandgap barrier material. The absorption process takes place between states located entirely within either the conduction or valence band rather than

* Corresponding author. Fax: + 1 610 861 5273; e-mail: bacher@fast.net.

[1] Present address: Department of Electrical Engineering, Cornell University.

0022-0248/97/$17.00 Copyright © 1997 Elsevier Science B.V. All rights reserved
PII S0022-0248(96)01007-X

between bands, which allows the use of relatively wide bandgap semiconductors, such as GaAs, to detect light at wavelengths greater than 3 μm. The most widely studied QWIPs use GaAs for the quantum wells and AlGaAs for the barriers. Although the near lattice match of these materials at any AlGaAs composition reduces the difficulty of the growth, there are limitations to these devices which can be addressed by using other materials, such as InGaAs.

First, because the detection wavelength is limited by the conduction band offset, the detection wavelength of GaAs/AlGaAs QWIPs with direct AlGaAs barriers is limited to greater than 5.6 μm [2]. Although QWIPs can be made with indirect barriers, they generally experience unusually high dark current relative to the detection wavelength of the device [2, 3]. Using a smaller bandgap material in place of the GaAs well will give a larger band offset and allow detection in the 3–5 μm mid-IR without the need for indirect AlGaAs barriers. Second, the use of deeper wells at longer wavelengths can remove or lower the Al content of the barriers, potentially improving the material quality and carrier transport in the barriers. Finally, several groups have demonstrated normal incidence absorption – supposedly a forbidden transition in n-type QWIPs- using InGaAs quantum wells [4, 5]. The ability to absorb light at normal incidence with an intersubband transition would reduce the processing complexity and eliminate a likely source of non-uniformity by eliminating the need for diffractive gratings in QWIP arrays [6]. Although, strictly speaking, only the later two points are applicable to the present work near 15 μm, it is anticipated that the results will applicable to future work in the 3–5 μm band as well.

The use of InGaAs wells, however, is complicated by the associated lattice mismatch. Even with only 10% In in the wells, Lenchyshyn et. al., saw clear evidence of dislocations arising from the lattice mismatch in 32 period QWIPs [7]. To address this problem of growing a large number of strained quantum wells, we first varied the growth conditions attempting to optimize the material quality.

We grew the multiple quantum well (MQW) region of several QWIP samples, Fig. 1, at substrate temperatures ranging from 430°C to 530°C to assess the effects of substrate temperature on photoluminescence (PL) and lattice relaxation. The top and bottom GaAs layers were grown at 600°C. As_2 was used as the arsenic species since a sample grown at 530°C with As_4 resulted in almost an order of magnitude reduction in the photoluminescence intensity. The substrate thermocouple was calibrated by measuring the spectral position of the bandedge absorption. The calibrated thermocouple was then used to control the substrate temperature during the growth.

After growth, the samples were characterized by room temperature photoluminescence from the quantum wells and asymmetric (1 1 5) 5 crystal X-ray scans to assess the material quality. As can be seen in Table 1, the PL intensity, PL linewidth (FWHM) and lattice relaxation all increase with increasing substrate temperature. The PL peak wavelength was relatively constant near 986 nm indicating no systematic changes in quantum well composition or thickness. The change in PL intensity is most drastic, increasing by a factor of 5 as the growth temperature changed from 470°C to 500°C.

Material	Thickness	Doping	
GaAs	5000 Å	$2x10^{18}$ cm^{-3}	
GaAs	600 Å		
GaAs	510 Å		\ Repeated
$In_{0.2}Ga_{0.8}As$	51 Å	$1x10^{17}$ cm^{-3}	/ 40 Times
GaAs	1110 Å		
GaAs	10000 Å	$2x10^{18}$ cm^{-3}	
GaAs Substrate	-	-	

Fig. 1. QWIP structure to test the effects of growth temperature on material quality.

Table 1
Photoluminescence and X-ray measurements on QWIP samples with MQW region grown at different substrate temperatures

Temperature (°C)	PL			Relaxation (%)
	Intensity (au)	FWHM (meV)	Wavelength (nm)	
430	0.256	26.6	986.5	33
450	0.295	29.5	983.5	35
470	0.335	27.1	982.5	39
500	1.05	28.8	988.5	39
530	1.25	30.0	987.5	39

The relaxation, on the other hand, increased slightly with temperature at lower temperatures, but was constant for temperatures above 450°C. Because the samples grown at 500°C and 530°C had similarly high PL intensities, we believed the smaller linewidth of the sample grown at 500°C indicated slightly better material quality. We acknowledge, however, that the small variation in linewidth and inconsistent point at 450°C might indicate that the FWHM of these samples is limited by variations among the 40 quantum wells in the structure rather than the FWHM of the individual quantum wells. A single quantum well would not have the same degree of relaxation, so it is difficult to verify this by a separate growth. It is interesting to note that although the measured relaxation of all these samples was greater than 30%, cross-hatching was only barely visible under a Nomarski microscope.

Because of the high degree of relaxation evident in these samples, we attempted to improve the material quality through the use of strain-compensation [8]. Adding phosphorous to the GaAs barriers will decrease their lattice constant to compensate for the larger lattice constant of the InGaAs wells. This results in a reduction of the accumulated stress from the large number of quantum wells in the structure.

As has been demonstrated [9, 10], the amount of phosphorous incorporated into $GaAs_{1-x}P_x$ layers is dependent not only on the As to P ratio, but also, because of the preferential incorporation of As, on the As to Ga ratio as well. To determine the As and P fluxes necessary to produce a strain-compensated structure, we grew three samples of the superlattice in Fig. 2 with different As and P fluxes. The structure was designed to have the same ratio of barrier thickness to well thickness as the previous growths, but with a superlattice period small enough so that the 0-order superlattice peak in (0 0 4) X-ray scans would be the first peak to the left of the substrate peak, even in a structure without any phosphorous in the barriers. This allows the X-ray scan to unambiguously determine the 0-order peak and thus amount of phosphorous incorporated into the barriers and degree of strain compensation.

Since we did not want to adjust the As flux during the growth, the minimum As flux examined was still sufficient to maintain As stabilized growth

Material	Thickness	Doping	
GaAsP	200 Å	-	\ Repeated
$In_{0.2}Ga_{0.8}As$	20 Å	-	/ 10 Times
GaAs Substrate	-	-	

Fig. 2. Superlattice to measure by X-ray the degree of strain compensation achieved by incorporating phosphorous into the barrier layers.

for the InGaAs quantum wells at a V : III BEP ratio of approximately 14 : 1. The phosphorous was obtained by heating bulk InP chunks to 524°C–527°C in an As effusion cell. In order to minimize the phosphorous background, we tried to keep the phosphorous flux as small as possible while still strain compensating the structure. Fig. 3 illustrates the effects of changing the As and P fluxes to vary the degree of strain compensation as evidenced by (0 0 4) X-ray diffraction scans. As the tensile strain in the barrier layer is increased, the average superlattice lattice constant approaches that of the substrate. In the X-ray scans, this shows up as a decrease in the separation between the 0-order superlattice peak and the substrate peak. The results are summarized in Table 23. The final case represents a reduction of the average strain by 60% compared to the non-strain-compensated case, indicating 2.3% phosphorous incorporation in the barriers. A more direct measurement of the reduction of the accumulated stress in the samples can be seen in the reduction of wafer warp as measured by a Tropel Autosort also shown in the table.

Although the final condition tested was not completely strain-compensated, we still expected to see a dramatic reduction of the lattice relaxation in a 40 period QWIP. An additional sample of the structure in Fig. 1 was grown except that the central 500 Å of the barriers was $GaAs_{0.977}P_{0.023}$ instead of GaAs. The MQW region was grown at 470°C. The resulting PL FWHM was 29.2 meV and the PL intensity was 1.23 – comparable to the best values in the non-compensated case. The lattice relaxation, however, was reduced from 39% to 5%. With the incorporation of slightly more phosphorous into the barriers, we feel that the relaxation can be eliminated entirely.

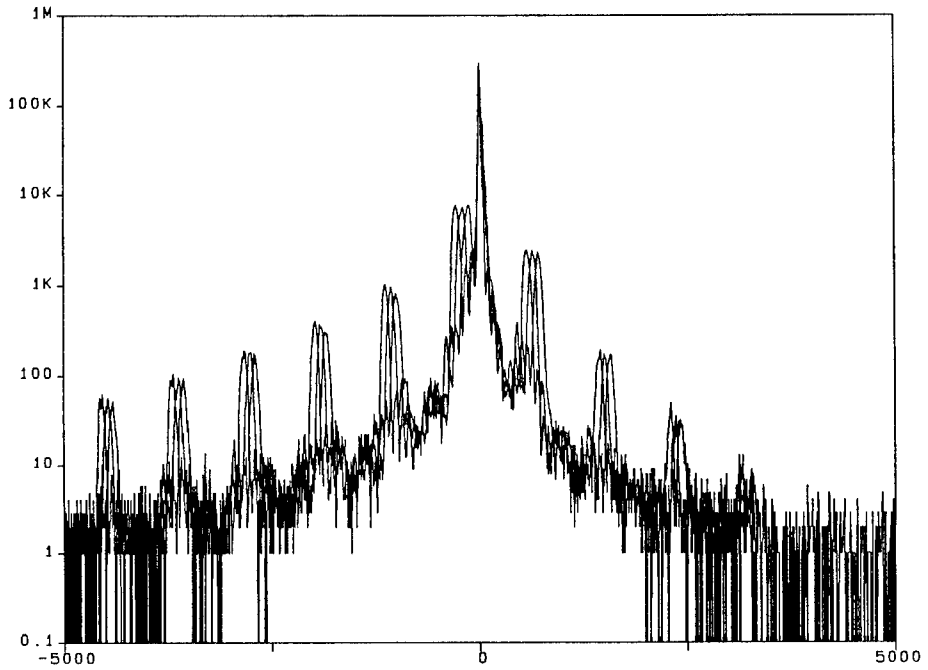

Fig. 3. Five crystal (004) X-ray scans of the superlattice structure in Fig. 2 grown with different As and P fluxes showing varying degrees of strain-compensation. These scans correspond to the data listed in Table 2.

Table 2
Degree of strain compensation measured by the difference in average lattice constant of the superlattice from that of the substrate ($\Delta a/a$); the reduction of accumulated stress as more strain is compensated is also evident in the reduction of wafer warp measured by a Tropel Autosort

BEP (Torr)		SL $\Delta a/a$ (ppm)	Wafer warp (μm)
As	P		
1×10^{-5}	3×10^{-7}	1020	4.8
8×10^{-6}	4×10^{-7}	750	4.4
5×10^{-6}	4×10^{-7}	480	4.2

This reduction of lattice relaxation can be seen qualitatively in (0 0 4) X-ray scans as well. Fig. 4 shows that more superlattice peaks are visible for the strain compensated case and the FWHM of the peaks is reduced from 92 to 28 arcsec. This is very close to the calculated FWHM of the superlattice peaks, assuming no relaxation, of 25 arc-seconds. The (0 0 4) scan of the strain-compensated QWIP also provides quantitative verification of the small relaxation of the strained quantum wells. The two peaks very close together in the center of the scan correspond to the substrate and the top GaAs contact layer. Because of the slightly larger in-plane lattice constant resulting from the very slight relaxation of the multiple quantum wells, the top GaAs layer is under tensile strain and produces the peak on the right. The peak separation is exactly that expected for the measured 25 ppm increase in the in-plane lattice constant of the MQW region. The small linewidth of this strained GaAs peak indicates that excellent crystalline quality is still maintained.

To asses the effects of the relaxation reduction on device performance, we processed QWIP devices from this strain-compensated wafer and the non-compensated wafer grown at 500°C. The dark current at different device temperatures along with the 300 K background photocurrent of typical devices from these wafers are shown in Fig. 5. The photocurrent for these devices is nearly identical, yet the

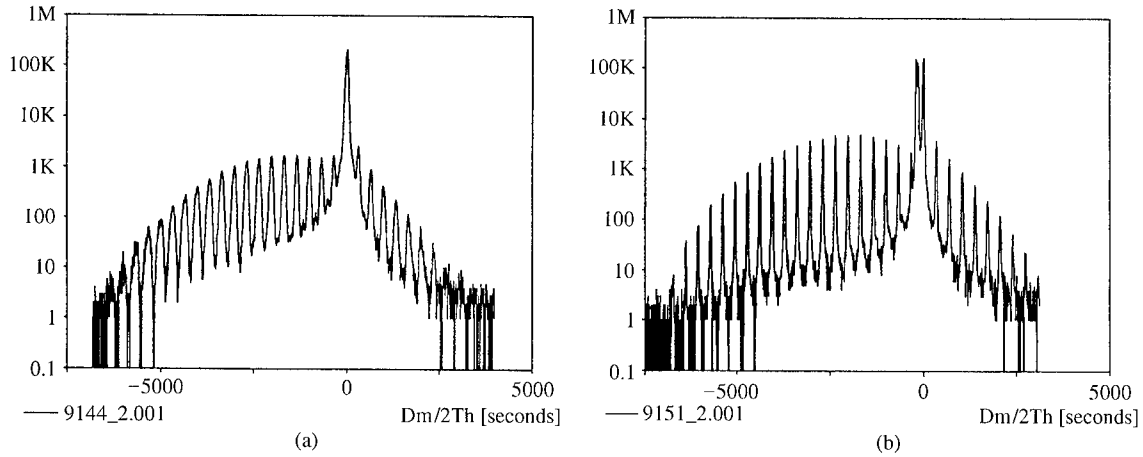

Fig. 4. Five crystal (004) X-ray scans of (a) a non-strain-compensated QWIP and (b) the strain compensated QWIP.

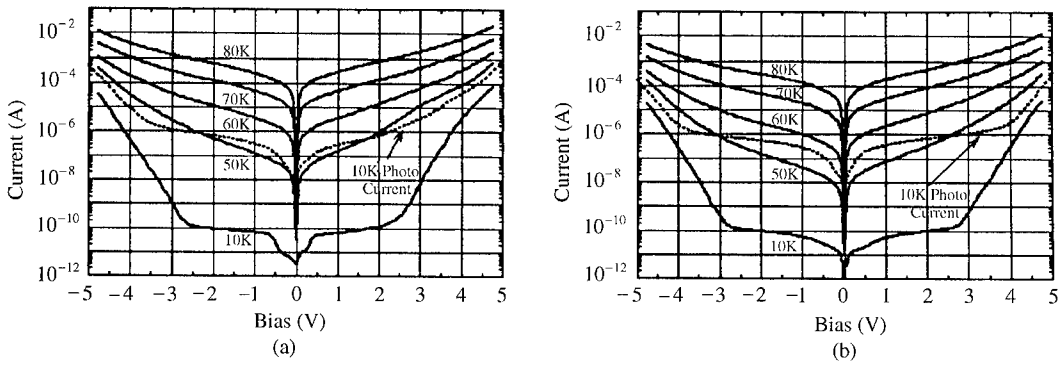

Fig. 5. Dark current and background photocurrent of (a) a non-strain-compensated QWIP and (b) the strain-compensated QWIP.

dark current is reduced by a factor of 4, leading to an increase of about 3 K in the background limited operating temperature of the strain-compensated device. Comparison of the photocurrent spectra of these devices shows only a small decrease in the cutoff wavelength, from 13.9 to 13.7 μm, indicating that the dark current reduction is not just due to an increase in the barrier height resulting from the addition of phosphorous to the barriers.

In conclusion, we have demonstrated the use of strain compensation to reduce the lattice relaxation resulting from the accumulated stress of a large number of strained quantum wells. In 40 period QWIP structures, the relaxation was reduced from greater than 30% to only 5%. Because only partial strain-compensation was used in this sample, it is likely that the relaxation can be eliminated entirely by a slight increase in the phosphorous content of the barrier layers. The improved material quality resulted in a factor of 4 decrease in the dark current and 3 K increase in the background limited operating temperature of QWIPs processed from the strain-compensated material compared to QWIPs processed from the non-compensated material grown.

The authors would like to acknowledge NASA for support of this work under the administration of the Jet Propulsion Laboratory.

References

[1] B. Beck et al., paper presented at the October meeting of the Electrochemical Society, Chicago, II (1995).
[2] B.F. Levine, S.D. Gunapala and R.F. Kopf, Appl. Phys. Lett. 58 (1991) 1551.
[3] H. Schenider, P. Koidl, F. Fuchs, B. Dischler, K. Schwarz and J.D. Ralston, Semicond. Sci. Technol. 6 (1991) C120.
[4] L.H. Peng, J.H. Smet, T.P.E Broekaert and C.G. Fonstad, Appl. Phys. Lett. 61 (1992) 2078.
[5] G. Karunasiri, R. Shih and J. Chen, paper presented at the 53rd Device Research Conf. Charlottesville, VA (1995).
[6] K.L. Tsai, C.P. Lee, J.S. Tsang, H.R. Chen and K.H. Chang, IEEE Electron Dev. Lett. 16 (1995) 49.
[7] L.C. Lenchyshyn, H.C. Liu, M. Buchanan and Z.R. Wasilewski, Semicond. Sci. Technol. 10 (1995) 45.
[8] D.C. Houghton, M. Davies and M. Dion, Appl. Phys. Lett. 64 (1994) 505.
[9] J.R. Arthur and J.J. Lepore, Vac. Sci. Technol. 6 (1969) 545.
[10] C.T. Foxon, B.A. Joyce and M.T. Norris, J. Crystal Growth 49 (1980) 132.

ELSEVIER

Journal of Crystal Growth 175/176 (1997) 983–989

JOURNAL OF CRYSTAL GROWTH

MBE growth and characterization of doped multiple quantum well avalanche photodiodes

H.M. Menkara*, R.N. Bicknell-Tassius, R. Benz, II, C.J. Summers

Advanced Materials Technology Division, Georgia Tech. Research Institute, Atlanta, Georgia 30332-0861, USA

Abstract

In the present study, how certain growth, processing and surface treatment techniques can be used to dramatically lower the dark current behavior of APDs by several orders of magnitude and improve the depletion characteristics of the built-in structures is shown. Through careful dopant calibration, the devices could be grown such that they were essentially fully depleted as grown, even though doping levels in the avalanche region were in the low 10^{18} cm^{-3}. The full depletion characteristics of the APDs were verified using theoretical modeling conducted for devices with similar structure and doping profiles. After processing the devices into mesa diodes, various surface passivation treatments were investigated These include both O_2 plasma and sodium sulfide treatments. Through the application of such treatments, a decrease in the reverse bias dark current by as much as a factor of 1000 was achieved. Dark currents as low as 1 pA were obtained near zero bias. In some APDs, the dark currents increased to only 12 pA at 20% of breakdown. In addition, these devices exhibited extremely high gains, which exceeded 35 000 in some APDs. The effect of the dopant profile in the avalanche region was also investigated. It was found that by the proper choice of dopant density and separation the break down voltage of the devices could be reduced by as much as 25%.

Keywords: MBE; MQW; APD; Dark current; Surface passivation

1. Introduction

Extensive studies have been carried out on multiple quantum well (MQW) structures because of their potential applications in avalanche photodiodes (APDs) and tunneling devices [1]. The MQW structure was first proposed by Chin et al. [2] and Capasso et al. [3] as a method to enhance the electron–hole ionization ratio ($k = \alpha/\beta$) beyond that typically found in bulk semiconductor materials. Later, Blauvelt [4] proposed the doped MQW structure in an attempt to further increase k through the introduction of localized electric field regions throughout the depletion layer. The desire for high performance optical detectors has resulted in several proposed MQW APD structures using different material systems and growth techniques in an attempt to minimize the high levels of inherent dark currents and optimize the APD gain, noise, and bandwidth characteristics. In addition, the

* Corresponding author.

0022-0248/97/$17.00 Copyright © 1997 Elsevier Science B.V. All rights reserved
PII S0022-0248(96)01181-5

recent interest in the use of APDs in imaging systems has necessitated the development of devices with low levels of dark currents and high gains for low light applications. Because of the high frame rate and high pixel density requirements in new imaging systems, it is desirable to provide some front-end gain in the imager to allow operation under low light level conditions. In order to maintain low dark currents and high gains for such applications, methods of minimizing dark current are needed. In addition, the APD must be capable of operating with low power, and low noise.

In previous studies of doped well APD's the results have been clouded by the effects of incomplete depletion of the avalanched region. This incomplete depletion led to premature avalanche breakdown and a voltage dependent gain due to a increased number of active stages as the reverse bias on the structure was increased [5].

Not only have previous studies of these structures been hampered by incomplete depletion, but inadequate surface passivation has lead to large dark currents. A number of techniques have been previously proposed for the passivation of GaAs/AlGaAs device structures. These include wet and plasma surface treatments [6], hydrogen ion-passivation [7], Se [8] and S surface treatments [9, 10].

In the following sections, the effects of careful dopant calibrations, and surface passivation on the properties of doped well MQW avalanche photodiodes will be presented.

2. Experimental technique

The structures that were analyzed were volume- and delta-doped MQW APDs that were grown using molecular beam epitaxy (MBE) in a Varian Gen II system and were fabricated using standard photolithographic techniques. All samples in this study were grown in a solid source Varian Gen II MBE system using solid As_4 as the arsenic species. Samples were grown on $\frac{1}{4}$ of a 2 in n-type GaAs wafer that were briefly etched in 5 : 1 : 1 $H_2SO_4 : H_2O : H_2O_2$ before being indium mounted on a standard molybdenum sample holder. In order to minimize dopant diffusion and segregation, while still maintaining the growth of high quality AlGaAs the temperature was kept near 580°C. A V/III beam equalivant pressure ratio of 15 was employed for all the growth runs.

All APD devices consisted of a 1 μm Be-doped (3×10^{18} cm^{-3}) p^+ top layer, and a 1 μm Si-doped (3×10^{18} cm^{-3}) n^+ back contact layer. In the volume-doped MQW devices, high electric fields were achieved in the GaAs wells of the avalanche region through the introduction of 50 Å of highly doped (3.0×10^{18} cm^{-3}) adjacent p^+ and n^+ layers which resulted in the avalanche region consisting of a series of closely compensated p–n junctions. In the delta-doped APDs, this was accomplished using delta-doped p^+ and n^+ layers with a sheet charge density of $(1\text{–}6) \times 10^{12}$ cm^{-2}, separated by undoped spacer layers ranging from 50 to 150 Å. The MQW region in all structures consisted of 10 sets of alternating layers of GaAs (500 Å) and $Al_{0.42}Ga_{0.58}As$ (500 Å) with 1000 Å periods.

Before the actual APD device structures were grown extensive dopant calibrations were carried out. These included not only the growth and measurement of traditional Hall effect samples, but also the growth and testing of special dopant calibration structures each of which consisted of just an avalanche region, thereby eliminating the effect of flux transients on the measurements. These structures were also measured by Hall effect. In this way the n- and p-type doping could be precisely balanced in the actual device structures, such that even though the dopant concentration in the depletion region were in the 10^{18} cm^{-3} range, they were precisely balanced to insure complete depletion.

Dark current measurements (I–V) on the MQW APD devices were conducted using a fully automated computer-controlled Keithley Source–Measure Unit (SMU) which connects to the device under test using a probe station or an 8-pin test fixture. Both dark and light I–V measurements were completed and the data was then used to calculate the multiplication gain of the device as a function of applied bias. Either electron- or hole-injections could be achieved by focusing the HeNe laser beam inside the p-contact ring at the top p- or the bottom n-layer. Capacitance–voltage measurements (C–V) were made using a computer-controlled HP4277A LCZ meter which can be interfaced with the same

test fixtures used in the current–voltage experiment. The C–V data was then used to calculate the doping concentrations and the depletion width profiles of the structures. C–V modeling was conducted using Silvaco's TCAD and device simulation software. Theoretical C–V solutions were obtained using small signal analysis at a frequency of 1 MHz and with a signal magnitude of 0.03 V, similar to the testing conditions used in the experimental measurements.

3. Results and discussion

In Fig. 1 is shown the C–V results for volume and delta-doped MQW APDs with a built-in 1 μm MQW region and device areas of 1.72×10^{-4} cm^2 and 3.13×10^{-4} cm^2, respectively. The large zero-bias capacitance of the volume-doped APD is an indication of a small initial depletion width due to dopant imbalance in the avalanche region. The dopant calibration for this sample was carried out using only traditional Hall samples. On the other hand, the capacitance for the delta-doped device is more than 50% lower at zero applied bias and remains relatively constant with applied voltage, which indicates that the structure is fully depleted. The theoretical C–V data support this conclusion and shows a very good agreement (to within 0.2 pF) with the measured data. The slight discrepancy between the experimental and theoretical results is due to parasitic capacitance effects and uncertainties in the actual active area of the APD structure. In Fig. 2 is shown the calculated depletion width versus apparent carrier concentration profile obtained using the C–V data presented in Fig. 1. The zero-bias depletion width for the delta-doped device is about 1 μm (full depletion) compared to only

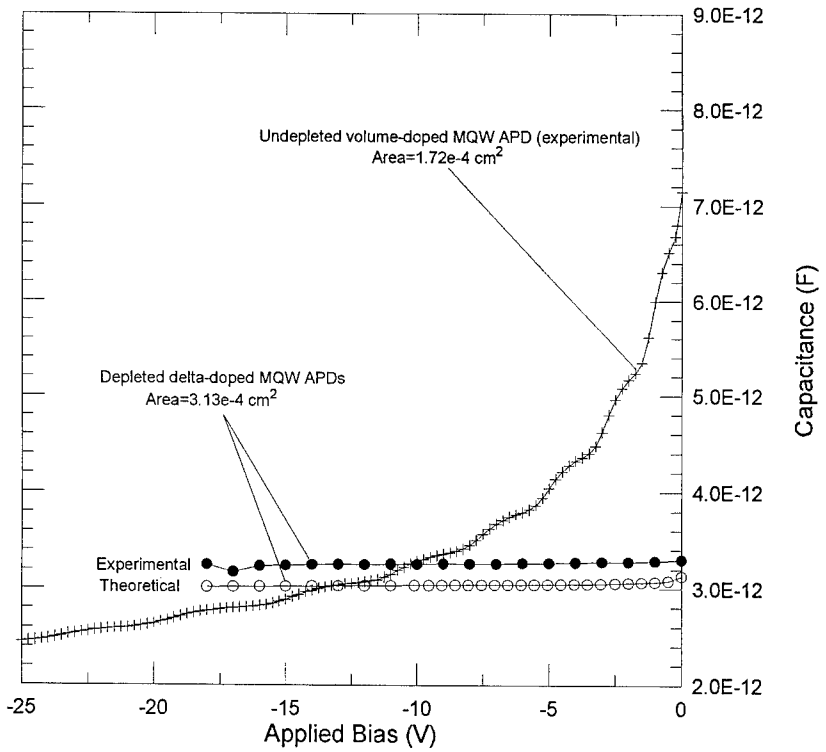

Fig. 1. Experimental and theoretical C–V plots for a delta-doped MQW APD with 1 μm depletion region and a device area of 3.13×10^{-4} cm^2.

0.25 μm for the volume-doped APD. This implies that the p- and n-doping concentrations throughout the delta-doped device are very closely matched resulting in a symmetric electric field profile and a uniform depletion throughout all 10 stages of the MQW structure. This conclusion is supported by the corresponding theoretical data shown in Fig. 2 and by other previously conducted studies [11].

Dark current is one of the main parameters of concern in photodetectors. Dark current analysis and the reduction of dark current are very important for high sensitivity and low noise applications. Not only do large dark currents lead to saturation of read out electronics, but they also have been directly correlated to large low frequency noise and device reliability [12]. Defect centers, heterojunction interface traps, as well as mesa surface leakage can generate high levels of excess dark current and reduce minority-carrier lifetime [13].

In a typical PN junction, the overall dark current is the sum of the bulk and surface components. The bulk component is usually made up of diffusion, generation–recombination, and tunneling currents. The surface component consists of generation–recombination, and leakage shunt currents usually formed at semiconductor and dielectric interfaces [14]. In a MQW device structure with top p and n contacts such as the APDs used in our experiments, there are additional sources of dark current components. These are due to defect centers at the GaAs/AlGaAs interface and most importantly to surface leakage currents along the mesa edge which can contribute significantly to the dark current.

After processing the APD devices into mesa diodes, various surface passivation techniques were investigated. These include both plasma ashing in an O_2 plasma and ammonium sulfide treatments. Through the application of such treatments,

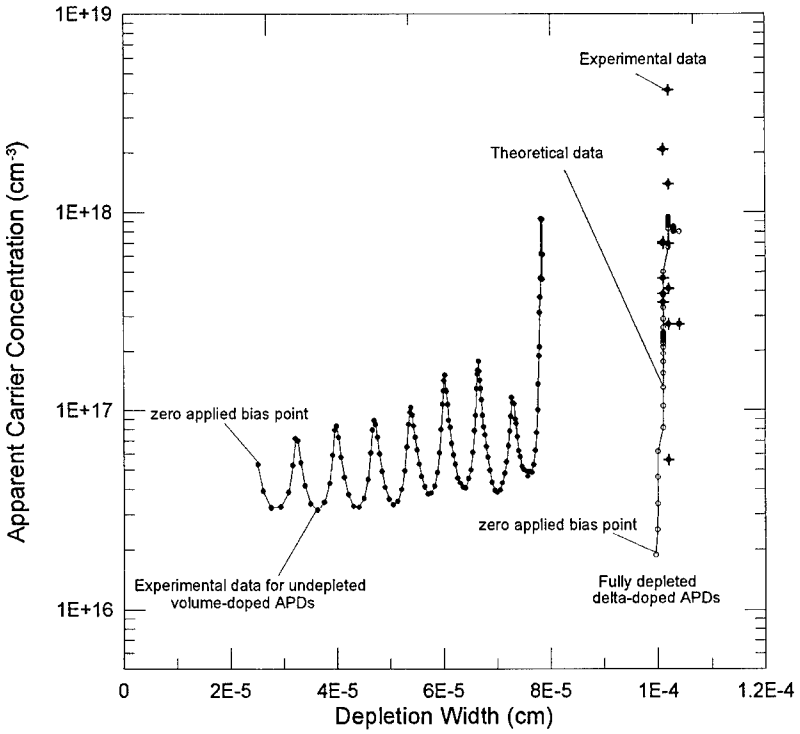

Fig. 2. Experimental and theoretical depletion width profiles versus apparent carrier concentrations for 10-period volume/delta-doped MQW APDs.

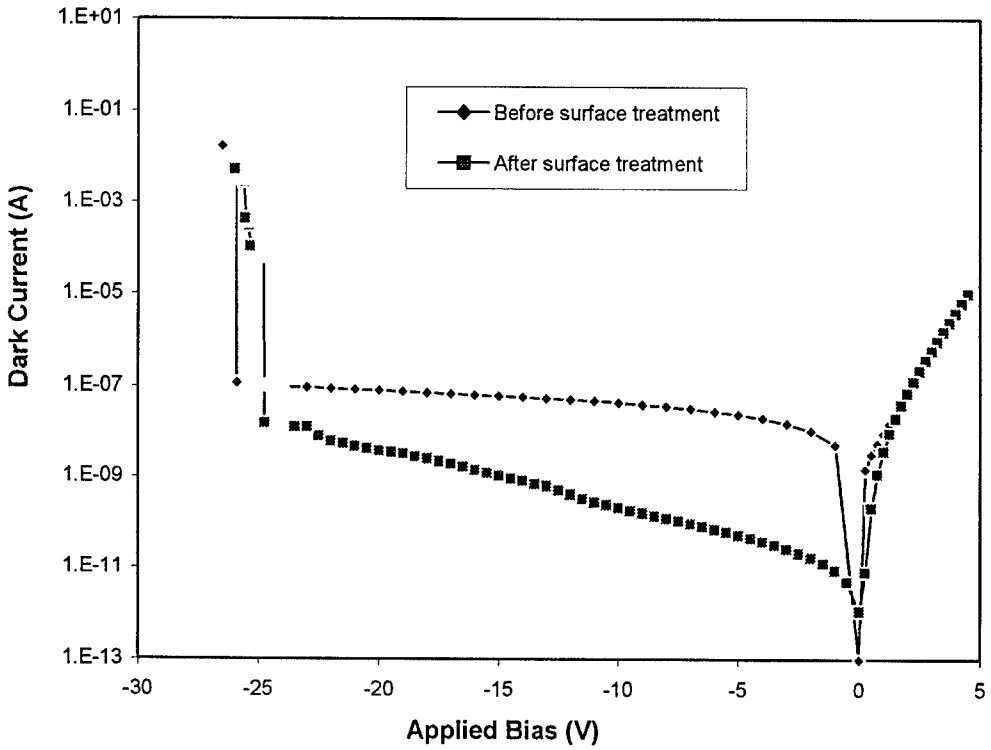

Fig. 3. Dark current reduction in a MQW APD as a result of surface treatment by ammonium sulfide.

a decrease in the reverse bias dark current by as much as a factor of 1000 was achieved in the low bias region. This can be seen in Fig. 3 where the dark current of an APD is plotted both before and after surface treatment by ammonium sulfide. The rapid increase in the dark current at low reverse bias and the large drop in its value achieved by surface treatment are indicative of surface leakage. The leakage in these heterojunction mesa diodes was dominated by generation/recombination currents near the intersection of the mesa surface with the GaAs/AlGaAs depletion region.

As a result of surface treatment, dark currents as low as 1 pA were obtained near zero applied bias. In some APDs, the dark currents increased to only 12 pA at 20% of breakdown. In addition, these devices exhibited extremely high gains which exceeded 10000 as shown in Fig. 4. In most traditional APDs, the presence of high dark currents usually presents a limiting factor preventing the further increase in a device's photocurrent gain beyond the onset of avalanche breakdown. By reducing the dark current in such device, it becomes possible to maintain the dark contribution at levels well below that of the photocurrent. This makes it possible to achieve and sustain high levels of gains well beyond the onset of breakdown.

The effect of the separation between the p- and n-delta doping layers has also been investigated. As shown in Fig. 5 the distance separation between the delta doped layers has a significant effect on the reverse bias at which the onset of breakdown occurs. By decreasing the distance between the delta-doped layers in the avalanche region from 150 to 50 Å the breakdown voltage of the devices could be reduced from more than 28 V to less than 22 V, a decrease of almost 25%.

The separation between the delta-doped layers in these devices could not only be used to reduce the reverse bias breakdown, but also had a significant

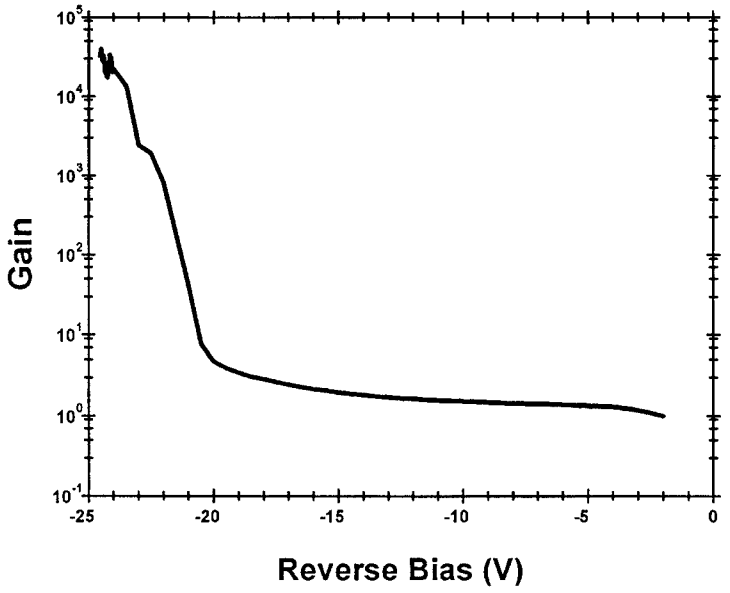

Fig. 4. Gain versus voltage characteristics of a delta-doped MQW APD.

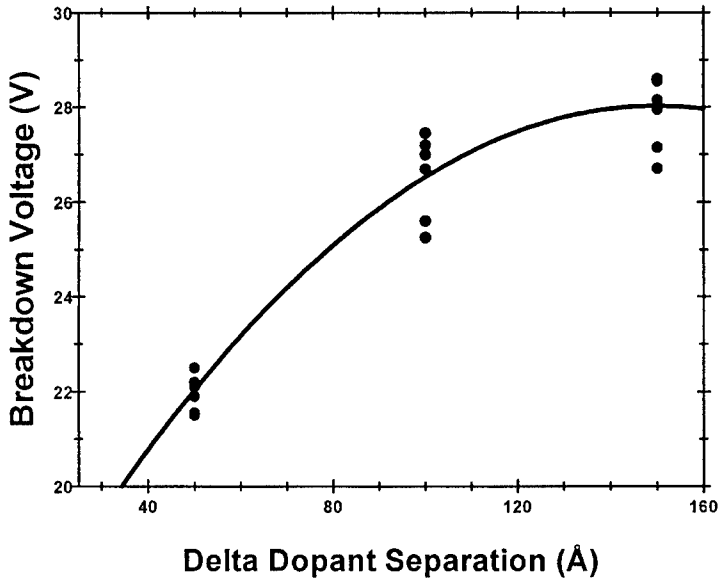

Fig. 5. Dependence of the reverse bias breakdown voltage on the dopant separation in delta-doped MQW APDs.

effect on the dark current in the devices. The effect of the dopant separation on the dark current density at 25% of the reverse bias breakdown is shown in Fig. 6, where the dark current density is shown for a set of delta-doped APDs as a function of the dopant separation. In this figure, it can be seen that by proper choice of the dopant separation the dark current can be reduced by more than a factor of two.

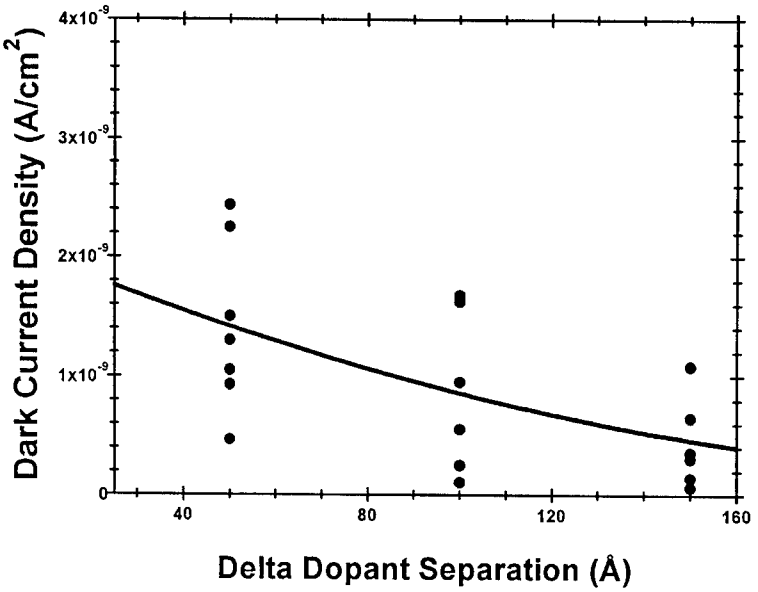

Fig. 6. Dependence of the dark current density on dopant separation in delta-doped MQW APDs.

4. Summary

In summary, it has been shown that by careful MBE dopant calibration and the use of delta-doping, doped well MQW APD's can be grown that are in excellent agreement with theoretical predictions. Through the application of various surface passivation treatments dark current in these devices could be reduced by three orders of magnitude. This reduction in dark current allows the devices to be operated past the onset of break down, and thereby achieve gains greater than 10 000. These low dark currents also allowed for the first time the investigation of the effects of the exact dopant profile on the device properties. It was observed that significant decreases in reverse bias break down and dark current could be achieved by the proper choice of the dopant separation in these delta-doped MQW APDs.

Acknowledgements

This work was sponsored by NASA under contract number NAGW-2753.

References

[1] F. Capasso, in: Semiconductors and Semimetals, Vol. 22, Eds. R.K. Willardson and A.C. Beer (Academic Press, New York, 1985) p. 2.
[2] R. Chin, N. Holoniak, G.E. Stillman, J.Y. Tsang and K. Hess, Appl. Phys. Lett. 16 (1980) 467.
[3] F. Capasso, W.T. Tsang, A.L. Hutchinson and P.G. Williams, Appl. Phys. Lett. 30 (1982) 38.
[4] H. Blauvelt, S. Margalit and A. Yariv, Electron. Lett. 18 (1982) 375.
[5] P. Aristin, A. Torabi, K. Garrison, H.M. Harris and C.J. Summers, Appl. Phys. Lett. 60 (1992) 85.
[6] U. Erben and R. Gründler, Phys. Status Solidi (a) 134 (1992) R41.
[7] Y.-L. Chang, S.I. Yi, S. Shi, E. Hu, W.H. Weinberg and J. Merz, J. Vac. Sci. Technol. B 13 (1995) 1801–1894.
[8] F.S. Turco, C.J. Sandroff, D.M. Hwang, T.S. Ravi and M.C. Tomargo, J. Appl. Phys. 68 (1990) 1038.
[9] H. Oigawa, J.-F. Fan, Y. Nannichi, H. Sugahara and M. Oshima, Jpn. J. Appl. Phys. 30 (1991) L322.
[10] C.J. Sandroff, R.N. Nottenburg, J.-C. Bischoff and R. Bhat, Appl. Phys. Lett. 51 (1987) 33.
[11] H.M. Menkara, B.K. Wagner, and C.J. Summers, Opt. Mater. 16 (1996) 103.
[12] X. Zhao, M.J. Deen and L.E. Tarof, Electron. Lett. 32 (1996) 250.
[13] R.U. Martinelli, T.J. Zamerowski and P. Longway, Appl. Phys. Lett. 53 (1988) 989.
[14] K.R. Linga, G.H. Olsen, V.S. Ban, A.M. Joshi and W.F. Kosonocky, J. Lightwave Technol. 10 (1992) 207.

ELSEVIER

Journal of Crystal Growth 175/176 (1997) 990–993

JOURNAL OF CRYSTAL GROWTH

Low dark current AlGaInAs/InP waveguide photodiodes using hybrid MBE and MOCVD growth

K. Nishikata*, H. Shimizu, K. Hiraiwa, S. Yoshida, N. Yamanaka, M. Irikawa, A. Kasukawa

Yokohama R & D Laboratories, The Furukawa Electric Co., Ltd., 2-4-3 Okano, Nishi-ku, Yokohama 220, Japan

Abstract

Dark current of 7pA with one cleaved facet and 20pA with an anti-reflection coating at the reverse bias voltage of 3 V was obtained for AlGaInAs/InP pin waveguide photodiodes, in which an AlGaInAs absorption layer and optical confinement layers were grown by optimized molecular beam epitaxy and an upper InP cladding layer was grown by metal-organic chemical vapor deposition. This is the lowest known dark current reported for long-wavelength pin waveguide photodiodes to date.

1. Introduction

Hybrid integrated optical modules [1] consisting of a laserdiode (LD), photodiodes (PDs) and a silica-based planar waveguide circuit (PLC), have been proposed as candidates for a low-cost optical module for an access network. As for the photodiodes used in the module, side-illuminated waveguide PDs (WGPDs) are promising since they can be integrated on the PLC in the same way as the LDs integration. The long-wavelength WGPDs with high sensitivity, large optical tolerance and low dark current are suitable for mass production of the optical integrated modules. High sensitivity and large optical tolerance have recently been achieved by using a large multimode waveguide [2] and a thick absorption layer up to 3 μm thickness [3]. This was because the thick absorption layer and thick optical confinement layers of which thickness summed up to 5.5 μm made a large multimode core and reduced the mode-field mismatch between the mode of the incident light and that of the waveguide. Dark current had been, however, very large because it is difficult to grow high-quality thick epitaxial layers and to decrease the leakage current on the sides of high-mesa for the waveguide. This large dark current had been one of problems in the development of the WGPDs.

In order to solve this problem, we optimized molecular beam epitaxy (MBE)-growth conditions and utilized hybrid-growth technique of MBE and metal-organic chemical vapor deposition

* Correponding author. Fax: + 81 45 322 6961; e-mail: knishi@yokoken.furukawa co.jp.

0022-0248/97/$17.00 Copyright © 1997 Elsevier Science B.V. All rights reserved
PII S0022-0248(96)01011-1

(MOCVD). The resulting dark current of the WGPDs was 7 pA with one cleaved facet at a reverse bias voltage of 3 V. This remarkably reduced dark current indicated generation-recombination which subsequently dominated the leakage and the surface-leakage component was eliminated.

2. MBE growth conditions optimization

It is necessary for the WGPDs to grow thick AlGaInAs layers of which thickness sums up to more than 5 μm. When we grow such thick epitaxial layers using MBE, the small defects increase. These defects are typically $4 \times 1\ \mu m^2$ and 20 nm high. These small defects were not observed when we grew the epitaxial layer less than 2 μm thick. These increasing defects are a problem in growing thick AlGaInAs layer, but there are not any previous reports to optimize the growth conditions and solve this problem. Hence, we need to determine the best condition for the growth of thick AlGaInAs. We optimized three conditions namely, growth rate, arsenic pressure (P(As)) and growth temperature (T_g) to suppress the small defects. The examined epitaxial layers were 3 μm thick AlGaInAs with a band-gap wavelength of 1.25 μm. The defect type and density were measured with Nomarski differential interference microscope, scanning electron microscope, and atomic force microscope. The composition of the examined layers was controlled within 50 arcsec in high-resolution X-ray diffraction and the T_g was monitored by a pyrometer.

Figs. 1–3 show the defect densities as a function of the growth rate, the P(As), the T_g, respectively, where the value of P(As) of 1×10^{-5} Torr was accorded with the V/III ratio of 10. The defect density decreases as the growth rate is decreased. With increasing As pressure, the defect density decreases and reaches a minimum at the P(As) of 1×10^{-5} Torr and increases with the P(As) above 1.5×10^{-5} Torr. With increasing T_g, we can see a similar tendency that there is a minimum point of the defect density at the T_g of 460°C. At high growth rate, high As pressure and low temperature, a defect density increase is caused by a decrease in the migration of atoms impinging on the substrate

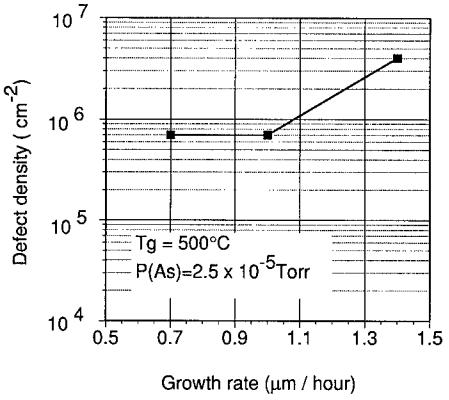

Fig. 1. Defect density variation with growth rate for 3 μm thick AlGaInAs.

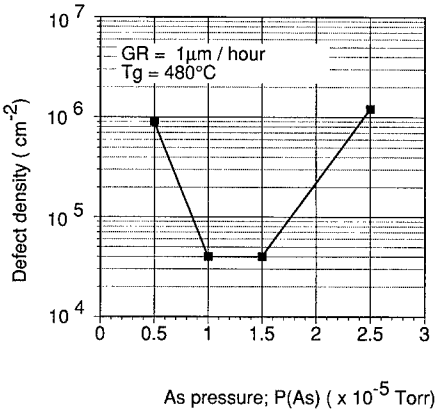

Fig. 2. Defect density as a function of As pressure.

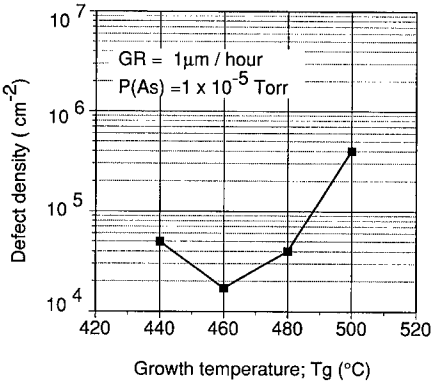

Fig. 3. Defect density as a function of growth temperature.

and a consequent increase in the inhomogeneity of atoms of the group III. The defect increase in the low As pressure and in the high temperature is caused by the increase in indium segregation due to the lack and the desorption of Arsenic.

As a result, with a growth rate of 1.0 μm/h, a V/III ratio of 10 and a T_g of 460°C, we have successfully obtained high-crystalline quality of 3 μm thick AlGaInAs layers with a defect density of 1.5×10^4 cm^{-2}.

3. Design and fabrication of waveguide photodiodes

The waveguide photodiode consists of a p-GaInAsP contact layer, a p-InP clad layer, a p-AlGaInAs optical confinement layer, a 0.4 μm thick undoped AlGaInAs absorption layer with a band-gap wavelength of 1.4 μm, and an n-AlGaInAs optical confinement layer. All layers were lattice matched to the (1 0 0) InP substrate. AlGaInAs epitaxial layers were grown by the optimized MBE and the upper InP cladding and the GaInAsP contact layer were grown by MOCVD. This was because the InP layer proud to be of stable material that had less leakage current than the AlInAs layer used ordinarily in MBE. This was also because we could etch selectively the InP cladding layer and the AlGaInAs layer and then we could obtain the high-mesa structure by a conventional wet etching. The surface made by the wet etching has less dark current than that by a dry etching.

We made a mesa stripe structure of which height was more than 5 μm and buried with polyimid and silicon nitride, as shown in Fig. 4. The junctions were 30, 50 and 100 μm long by 19 μm wide. The cleaved facet was coated with silicon nitride in order to prevent reflecting.

4. Dark current measurements

Fig. 5 shows the dark current in the resulting waveguide PDs at the reverse voltage of 3 V as a function of the absorption-stripe length. The dark currents for devices with one cleaved facet were 7, 10 and 16 pA with the stripe length of 30, 50 and 100 μm, respectively. The dark current with AR coating increased slightly to 20, 24, and 33 pA, respectively. These small values are the lowest reported to date for waveguide photodiodes and are smaller than that of well-designed long-wavelength surface-illuminated pin photodiodes.

Fig. 6 shows an illustration of the sources of dark current. The dark current consists of diffusion current, generation current [4], tunneling current,

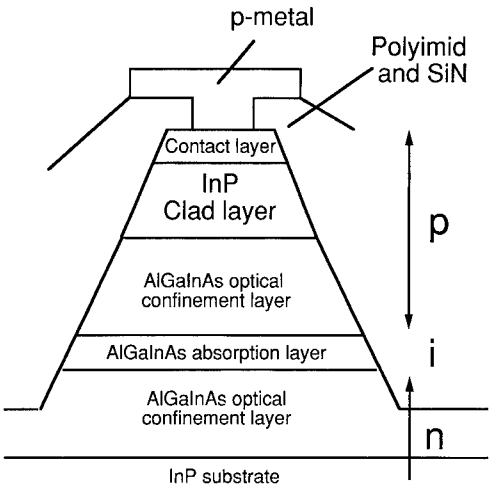

Fig. 4. Device structure of a waveguide photodiode.

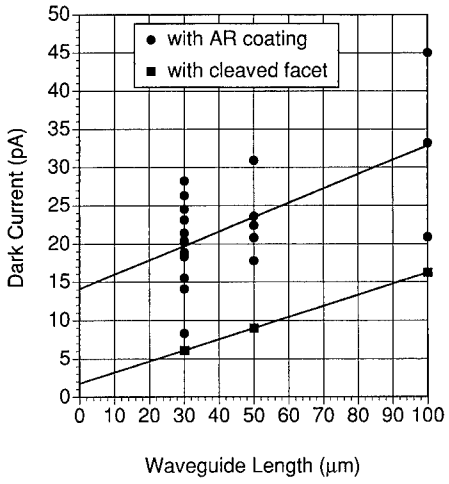

Fig. 5. Resulting dark current of waveguide photodiodes with and without anti-reflection coatings.

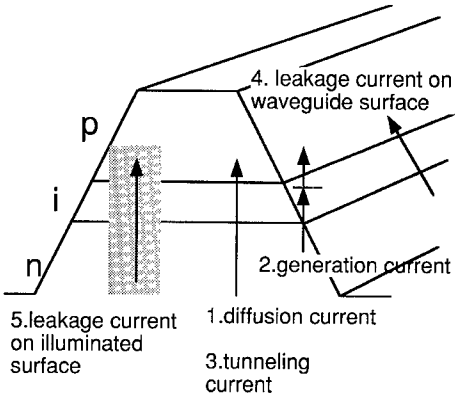

Fig. 6. Illustration of sources of dark current in a waveguide photodiode.

surface leakage currents on the sides of the waveguide and on the illuminated surface. The diffusion current is estimated to be a few pA and the tunneling current is negligible at this low bias voltage.

The dark current value at the stripe length of 0 indicates the leakage on the illuminated surface. Dark current density that originated from the leakage on the illuminated surface can be evaluated to be 0.78 pA/μm. The increase with the stripe length consists of the leakage current originating from the generation-recombination and mesa surface leakage components. The increase rate can be evaluated to be 0.19 pA/μm. These results with the small values indicate that the generation-recombination component dominates and the surface leakage component is eliminated.

5. Conclusions

We optimized the MBE-growth conditions and utilized the hybrid-growth technique of MBE and MOCVD. As a result, we obtained waveguide photodiodes with dark current as low as 7 pA with one cleaved facet, and 20 pA with an anti-reflection coating at a reverse bias voltage of 3 V.

Acknowledgements

The authors would like to thank Dr. S. Kashiwa for his encouragement.

References

[1] Y. Yamada, S. Suzuki, K. Moriwaki, Y. Hibino, Y. Tohmori, Y. Akutsu, Y. Nakasuga, T. Hashimoto, H. Terui, M. Yanagisawa, Y. Inoue, Y. Akahori and R. Nagase, Electron. Lett. 31 (1995) 1366.
[2] K. Kato, S. Hata, J. Yoshida and A. Kozen, IEEE J. Quantum. Electron. 28 (1992) 2728.
[3] K. Nishikata, K. Hiraiwa, H. Shimizu, N. Iwai, N. Yamanaka, M. Irikawa and A. Kasukawa, Proc. 1st Optoelectron. and Commun. Conf., PD2-7, Chiba, Japan (1996).
[4] S.R. Forrest, R.F. Leheny, R.E. Nahory and M.A. Pollack, Appl. Phys. Lett. 37 (1980) 322.

ELSEVIER

Journal of Crystal Growth 175/176 (1997) 994–998

JOURNAL OF CRYSTAL GROWTH

Improved electroabsorption properties in 1.3 μm MQW waveguide modulators by a modified doping profile

X.B. Mei*, K.K. Loi, W.S.C. Chang, C.W. Tu

Department of Electrical and Computer Engineering, University of California, 9500 Gilman Drive, San Diego, La Jolla, California 92093-0407, USA

Abstract

In 1.3 μm electroabsorption (EA) waveguide modulators used for microwave photonic links, we have used a modified doping profile to provide a better confinement of the depletion region in the p–i–n structure under reverse bias, without causing serious free carrier absorption. Theoretical simulation of the electric field distribution and experimental result on surface-normal photocurrent measurement, as well as waveguide measurement, are shown in this paper. An improvement of 29% of the quantum confined Stark effect (QCSE) is obtained, and in the waveguide measurement, 15% improvement of the transmission–voltage slope efficiency is achieved.

1. Introduction

Electroabsorption (EA) modulators based on quantum confined Stark effect (QCSE) in multiple quantum wells (MQWs) are among the most promising candidates for components in microwave photonic links because of their high efficiency, high speed, and low drive voltage. We have demonstrated, in our previous work, high-efficiency 1.3 μm EA waveguide modulators utilizing 11 periods of strain-compensated $InAs_{0.4}P_{0.6}/Ga_{0.13}In_{0.87}P$ MQWs as the active region [1]. More recently, we achieved improved RF efficiency by an optimized structure with 6 MQWs [2]. To achieve a high RF link efficiency, a low waveguide insertion loss and a large slope efficiency in the transmission–voltage (T–V) curves are two of the most desirable characteristics of the modulators. The insertion loss consists of two parts, coupling loss between the waveguide and the fibers and the propagation loss inside the waveguide. In this paper, we report a modified doping profile which increases the slope efficiency while having a low insertion loss.

2. Structure design

An EA modulator is in principle a reverse biased p–i–n structure with the active region in the undoped i-region. The i-region in our structures contains 6 periods of $InAs_{0.4}P_{0.6}/Ga_{0.13}In_{0.87}P$ strain-compensated MQWs with the well and

* Corresponding author. Fax: + 1 619 534 2486; e-mail: xmei@sdcc3.ucsd.edu.

0022-0248/97/$17.00 Copyright © 1997 Elsevier Science B.V. All rights reserved
PII S0022-0248(96)01014-7

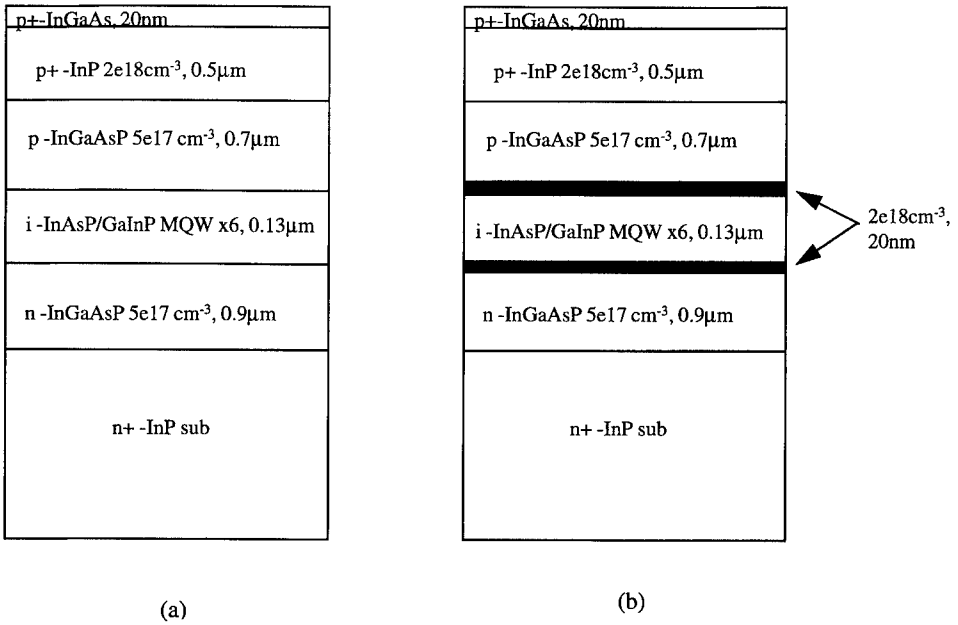

Fig. 1. Layer structures of 1.3 μm waveguide modulators with (a) conventional and (b) modified doping profiles.

barrier thicknesses of 95 and 105 Å, respectively. The EA properties of such MQWs have been reported in detail previously [3]. The active MQW region is sandwiched between a p-doped and an n-doped passive $In_{0.87}Ga_{0.13}As_{0.29}P_{0.71}$ waveguiding layers with a band-gap wavelength of 1.15 μm. A schematic of the structure is shown in Fig. 1a. This structure provides a vertical optical mode size of approximately 2 μm, comparable with the mode size in a lensed fiber, so that the coupling loss is reduced. Notice that the doping level in the p- and n-type waveguiding layers is only 5×10^{17} cm^{-3}, low enough to reduce the propagation loss caused by free-carrier absorption. However, the problem with the above-mentioned structure is that the depletion region extends from the i-region into the guiding layers under revere bias because of the relatively low doping level in these guiding layers and relatively thin i-region (thickness $d_i = 0.13$ μm). The wider depletion region causes a decrease in the electric field (E-field) in the MQWs, and thus the QCSE, at a given bias voltage V_a, resulting in a lower T–V slope efficiency. Our solution to this problem is to insert a highly doped (2×10^{18} cm^{-3}) and thin (200 Å) p^+ (n^+) $In_{0.87}Ga_{0.13}As_{0.29}P_{0.71}$ layer (pulse-doped layer) in the p (n) guiding layer right on the side of the i-region as shown in Fig. 1b. Since the two pulse-doped layers are very thin compared to the waveguide thickness (~1.7 μm), they do not cause serious free carrier absorption.

Fig. 2 is a computer simulation using Simwin 3.2, a Poisson–Schrodinger solver, of the E-field distribution in the structures with and without pulse doping (PD) under a V_a of 3 V. The background doping in the i-region is assumed n-type, 8×10^{15} cm^{-3}, the same as that in our undoped InP epilayer. The built-in potential V_{bi} is 1 V from the simulation. It can be seen that the depletion region extends into the p and n regions in the conventional structure whereas PD provides a better confinement of depletion region within the i-region. Better confinement means that the depletion region is thinner under the same V_a, so a larger E-field (F) can be obtained in the MQWs. Fig. 3 shows three F–V curves from the simulation. Curve (a) is the case that the confinement is perfect, that is, there is no extension of depletion region into

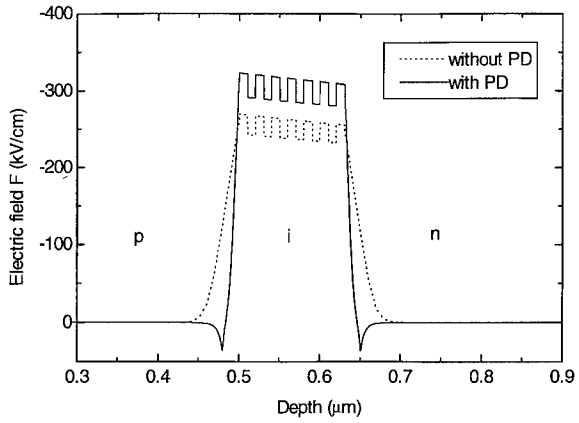

Fig. 2. Computer simulation of e-field distribution in the p–i–n modulator structures with 6 MQWs in the i-region under 3 V reverse bias.

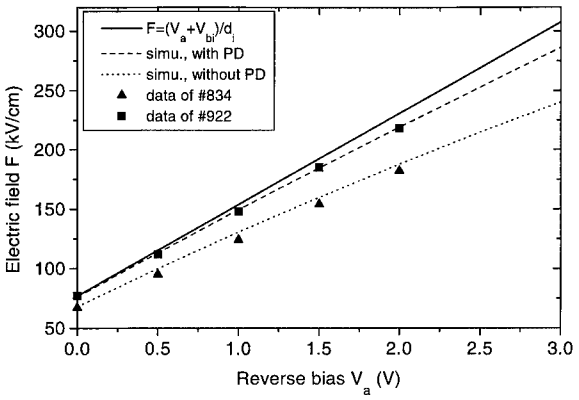

Fig. 3. E-field in the i-region versus reverse bias in p–i–n structures with different doping profiles. The lines are result from computer simulation. The scattered symbols are experimental data.

the p and n regions. Therefore, this curve is a straight line with a slope of $1/d_i$. Curves (b) and (c) are cases with and without PD, respectively. Curve (b) has a larger slope than (c), indicating a thinner depletion region. Under a V_a from 0 to 3 V, F is approximately 20% larger in the structure with PD. From the simulation results, we expect that under a given bias a larger QCSE and a higher T–V slope efficiency in a waveguide modulator employing PD can be obtained.

3. Experimental procedure

The MQW samples were grown in a Varian GEN-II MBE system modified for gas-source MBE growth. Thermally decomposed AsH_3 and PH_3 were used as the group V sources, and elemental In and Ga as the group III sources. Elemental Si and Be were used as n- and p-type dopants, respectively. The growth temperature was 460°C, and the InP growth rate was typically 1 μm/h. The growth rate was determined by intensity oscillations of reflection high-energy electron diffraction (RHEED). The samples were grown on S-doped n^+-InP substrates.

For surface-normal photocurrent measurement, mesas with a 500 μm diameter were defined by wet chemical etching on the sample surface. A ring-shaped AuZn/Cr contact was evaporated onto the p^+-$In_{0.53}Ga_{0.47}As$ cap layer. In was used as the n-type contact on the back side of the substrate. The breakdown voltage of the ring diodes is typically 6 V at 2 μA leakage current. The surface-normal photocurrent measurement was performed at room temperature. A beam of monochromatic light was focused onto the center window of the ring diode, and the photocurrent was amplified with a lock-in amplifier. The reverse electric bias was applied via the ring-shaped electrode and the back contact.

Waveguide modulators were fabricated using CCl_2F_2 reactive ion beam etching. The 2 μm ridge height confines the waveguide mode laterally. The devices are 3 μm in width and 190–230 μm in length. Tapered single-mode fibers were used to couple TE polarized light into and out of the modulator. The measurement was carried out at 1.32 μm wavelength, approximately 27 meV detuned from the zero-bias exciton peak.

4. Results and discussion

For comparison, two waveguide modulator samples, #834 and #922 were grown. The structures are shown in Fig. 1a and Fig. 1b, respectively. #922 has the above-mentioned pulse-doped layers while #834 does not. In Fig. 4 we plot the QCSE energy shift of the $n = 1$ heavy hole exciton peak in

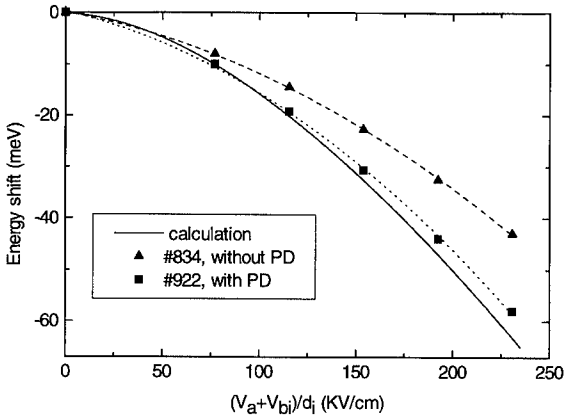

Fig. 4. QCSE versus reverse bias in samples #834 and #922. The solid line is a calculation based on effective well width model

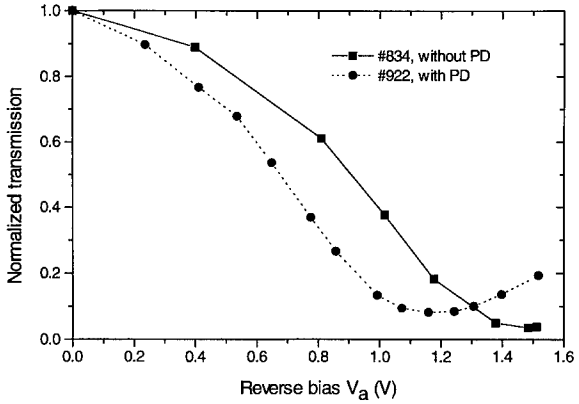

Fig. 5. Electrical-to-optical transfer curves (T–V curves) of waveguide modulators #834 and #922.

samples #834 and #922 against the reverse bias. The solid line is a theoretical calculation based on the effective well width model [4], assuming that the depletion region width equals the i-region width, d_i, and the E-field is uniform across the depletion region and is zero elsewhere. This situation is the ideal case where the confinement of the depletion region is perfect. From Fig. 4, one can see clearly that #922 has a much larger QCSE than #834 under a given bias. At 2 V reverse bias, the difference is as large as 29%. This result indicates that the pulse-doped layers provide a better confinement of the depletion region and therefore increase the efficiency of the bias voltage, as predicted by the simulation shown in Fig. 3. By comparing the experimental QCSE with the calculation value in Fig. 4, we obtained the E-field at each V_a. These E-field values are plotted in Fig. 3 as scattered symbols, together with the simulation result. The experimental data agree with the simulation very well. The E-field in #922 is approximately 20% larger than that in #834, and therefore it is expected to achieve a 20% improvement in the T–V slope efficiency from waveguide measurement.

Fig. 5 shows the electrical-to-optical transfer curves of waveguide modulator devices fabricated on #834 and #922. The slope efficiency is obtained by taking the first derivative of these curves. The highest slope efficiency of #922 is 1.34 V^{-1}, 15% higher than 1.17 V^{-1} of #834. Since the device of #922 is 190 μm in length, 35 μm shorter than #834 due to the fluctuation in cleaving, the contrast ratio of the former is a little smaller than that of the latter as seen in Fig. 4. If #922 had the same device length as #834, the slope efficiency difference would be even higher than 15%, which is in good agreement with the expected value, 20%. #922 exhibits not only a higher slope efficiency but also a lower bias voltage, 0.8 V, to achieve the peak slope efficiency, compared with 1.1V in #834. From the result shown above, a higher RF link efficiency is expected in #922.

5. Conclusions

We have demonstrated an improved performance of waveguide modulators used for microwave photonic links by employing a modified doping profile. The new profile includes two pulse-doped layers on each side of the i-region, which provides a better confinement of the depletion region and increases the efficiency of the reverse bias without causing serious free carrier absorption. Twenty-nine percent improvement in QCSE and 15% improvement in T–V slope efficiency are observed in the pulse-doped sample. Other device performance is still being investigated.

Acknowledgements

This work is supported by the DARPA Optoelectronics Technology Center.

References

[1] K.K. Loi, I. Sakamoto, X.B. Mei, C.W. Tu and W.S.C. Chang, IEEE Photon. Technol. Lett. 8 (1996) 626.

[2] K.K. Loi, X.B. Mei, C.W. Tu and W.S.C. Chang, SPIE Proc. 2844 (1996) (Int. Symp. on Optical Science, Engineering and Instrumentation, Photonics and Radio Frequency, Denver, USA, 1996), to be published.

[3] X.B. Mei, K.K. Loi, H.H. Wieder, W.S.C. Chang and C.W. Tu, Appl. Phys. Lett. 68 (1996) 90.

[4] D.A.B. Miller, D.S. Chemla, T.C. Damen, A.C. Gossard, W. Wiegmann, T.H. Wood and C.A. Burrus, Phys. Rev. B 32 (1985) 1043.

ELSEVIER

Journal of Crystal Growth 175/176 (1997) 999–1003

JOURNAL OF CRYSTAL GROWTH

Investigation of Si-doped p-type AlGaAs/GaAs, AlGaAs/InGaAs quantum well infrared photodetectors and multiquantum wells grown on (3 1 1)A GaAs

Albert Chin[a,*,1], C.C. Liao[a,b], J. Chu[c], S.S. Li[c]

[a] *Department of Electronics Engineering, National Chiao Tung University, Hsinchu, Taiwan, ROC*
[b] *Department of Electrical Engineering, Chung Hua Polytechnic Institute, Hsinchu, Taiwan, ROC*
[c] *Department of Electrical and Computer Engineering, University of Florida, Gainesville, Florida 32611, USA*

Abstract

We have studied two Si-doped p-type quantum well infrared photodetectors (QWIPs) using AlGaAs/GaAs and AlGaAs/InGaAs grown on (3 1 1)A GaAs. The Si-doped AlGaAs/GaAs p-QWIP exhibits a symmetrical dark I–V characteristic at all the measured temperatures from 40 to 120 K. The strained p-type AlGaAs/InGaAs QWIP exhibits a slightly asymmetrical dark I–V characteristic, but is markedly less asymmetrical than that doped with beryllium. The slight asymmetry in dark I–V characteristic and the large blue-shift in responsivity spectra may be due to the thickness modulation observed from TEM and the red-shift of PL peak energy, where PL peak energies from (3 1 1)A AlGaAs/InGaAs multiple quantum wells are red-shifts of 7 and 22 meV to the side-by-side grown (1 0 0).

1. Introduction

P-type quantum well infrared photodetectors (QWIPs) have attracted much attention recently because of the inherent capability of normal incidence radiation and even enhanced intersubband transition [1, 2]. To date, most of the p-type QWIPs reported so far have used either beryllium (Be) or carbon (C) for the dopant species. However, both dopants have serious shortcomings. Be suffers from the problem of fast out-diffusion [3] and asymmetrical *I–V* characteristics measured in p-QWIP [2, 4] while C is not compatible to the normal solid source MBE. Because high p-type concentration has been reported by Si-doped GaAs grown in (3 1 1)A orientation [5], we have studied the Si-doped p-type QWIPs in this orientation. Other advantage of the growth of AlGaAs/GaAs or AlGaAs/InGaAs p-QWIP on (3 1 1)A GaAs is due to the reduced incorporation of deep recombination centers at the quantum well interfaces [6], which may in turn increase the quantum efficiency and improve the device performance. Further reduction of deep recombination centers can be expected in (3 1 1)A orientation because of the very-low diffusion coefficient of Si, and a higher growth

* Corresponding author. Fax: +1 214 995 2770; e-mail: chin@spdc.ti.com.

[1] On sabbatical leave at Semiconductor Process and Design Center, Texas Instruments, Dallas, Texas 75243, USA.

0022-0248/97/$17.00 Copyright © 1997 Published by Elsevier Science B.V. All rights reserved
PII S0022-0248(96)00922-0

temperature can be used to grow the AlGaAs/GaAs multiple quantum wells (MQWs) in p-QWIP. It is well known that a high growth temperature can reduce the oxygen and growth-induced defect [7], while a higher efficiency of photoluminescence (PL) can be obtained.

In this paper, we report the first study of Si-doped p-QWIP grown on (3 1 1)A GaAs. Very symmetrical dark I–V characteristic was obtained in AlGaAs/GaAs p-QWIP, which demonstrates the low diffusion of Si impurity as compared to Be. The strained Si-doped AlGaAs/InGaAs p-QWIP shows a slightly asymmetrical dark I–V characteristic, but is markedly less than that of the same structure by Be-doping.

2. Experimental procedure

The layer structure of AlGaAs/GaAs p-QWIP consists of a 1.0 μm Si-doped GaAs bottom contact layer, 40 periods of 2.8 nm GaAs well with 30 nm $Al_{0.29}Ga_{0.71}As$ barrier, and a 1.0 μm Si-doped GaAs top contact layer. The quantum wells and contact layers are doped with Si to a concentration of 3×10^{18} cm^{-3}. The layer structure for strained AlGaAs/InGaAs p-QWIP is similar to the unstrained AlGaAs/GaAs, except that the quantum well region consists of 20 periods of 5 nm $In_{0.12}Ga_{0.88}As$ well with 50 nm $Al_{0.1}Ga_{0.9}As$ barrier. The growth temperatures were 600 and 550°C for AlGaAs/GaAs and strained AlGaAs/InGaAs p-QWIPs, respectively. A low V/III beam equivalent pressure (BEP) of ~ 10 is used to achieve high p-type doping. We have also grown AlGaAs/GaAs and AlGaAs/InGaAs multiple quantum wells (MQWs) in order to further characterize the quality of quantum well in (3 1 1)A orientation. The AlGaAs/GaAs MQWs consists of a 0.1 μm $Al_{0.29}Ga_{0.71}As$ buffer, 5 periods of 5 nm GaAs well with 20 nm $Al_{0.29}Ga_{0.71}As$ barrier, and a 0.1 μm $Al_{0.29}Ga_{0.71}As$ top layer. The strained AlGaAs/InGaAs MQWs consists of a 0.1 μm $Al_{0.1}Ga_{0.9}As$ buffer, 5 periods of 10 nm $In_{0.12}Ga_{0.88}As$ well with 20 nm $Al_{0.1}Ga_{0.9}As$ barrier, and a 0.1 μm $Al_{0.1}Ga_{0.9}As$ top layer. Photoluminescence (PL) was used to characterize the optical properties of the MQWs. Hall measurement was used to measure the p-type doping for Si-doped (3 1 1)A GaAs. In order to measure the I–V characteristic and the responsivity, the p-QWIPs were processed into 216×216 μm^2 mesas.

3. Results and discussion

Fig. 1 shows the PL spectra for (3 1 1)A AlGaAs/GaAs MQWs grown at 600°C. A (1 0 0) AlGaAs/GaAs MQWs, grown at 550°C, is also shown for comparison. It is well known that significant Be out-diffusion occurs at a growth temperature of 600°C, and for that reason we have chosen the growth temperature of 550°C in (1 0 0) orientation for comparison. PL full-width-at-half-maximum (FWHM) line width of 9.2 and 11.2 meV are measured from an undoped AlGaAs/GaAs MQWs grown on (1 0 0) and (3 1 1)A GaAs, respectively, which indicates sharp interfaces can be obtained in both directions. However, one order of magnitude of PL intensity enhancement was measured from the 600°C grown (3 1 1)A MQWs than that grown on (1 0 0) at 550°C, which suggests better material quality can be achieved in (3 1 1)A direction. The increased PL intensity may be due to the

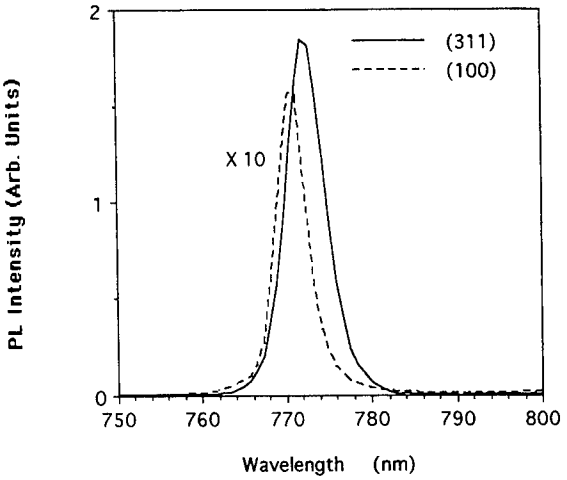

Fig. 1. Low temperature (15 K) PL spectra of AlGaAs/GaAs MQWs grown on (3 1 1)A and (1 0 0) GaAs at 600°C and 550°C, respectively.

improved material quality at a 50°C higher growth temperature or by the inherent lower interface recombination in (3 1 1)A orientation to (1 0 0) [6].

Fig. 2 shows the dark I–V characteristics of AlGaAs/GaAs p-QWIP grown at 600°C. Very symmetrical dark I–V characteristics are observed in both the forward and the reverse bias regions over the entire temperature range from 40 to 120 K, which is markedly improved when compared to Be-doped p-QWIP reported by Levine et al. [1]. The symmetrical I–V characteristic indicates the uniform doping in the quantum wells and the negligible impurity out-diffusion during growth. Similar low out-diffusion of Si impurity is also reported in a heterojunction bipolar transistor by Li et al. [8] even at a high growth temperature of 670°C. It is noticed that the dark current is in the same order to similar structure by Levine et al. [1] of a 4×10^{18} cm^{-3} Be-doped AlGaAs/GaAs p-QWIP with 3 nm well separated by 30 nm $Al_{0.3}Ga_{0.7}As$, which indicates the excellent material quality of p-QWIP grown in (3 1 1)A direction. The measured hole mobility at a hole concentration of 3×10^{18} cm^{-3} is 75 cm^2/(V s), which is comparable to the mobility value of ~ 100 cm^2/(V s) doped by Be [5]. The slightly lower mobility is believed to be due to the compensation effect from the higher V/III BEP ratio. However, a higher As flux is required to grow the AlGaAs and InGaAs layers.

To further reduce the dark current, we have studied the strained AlGaAs/InGaAs p-QWIP with the same device size. Fig. 3 shows the dark I–V characteristic of the AlGaAs/InGaAs p-QWIP grown at 550°C. A low growth temperature of 550°C is chosen to reduce the In re-evaporation from the InGaAs layer. In spite of the expected reduction of dark current, a slight asymmetry was observed under forward and reverse biased conditions. However, the asymmetry is markedly less than that of the Be-doped QWIP. It is unlikely that the asymmetry is due to Si out-diffusion, because the growth temperature is lower than that of AlGaAs/GaAs p-QWIP. Furthermore, in sharp contrast to the Be-doped p-QWIP, the dark current asymmetry is opposite to that from doping migration effect [1].

Fig. 4 shows the measured photo-responsivity spectra of strained AlGaAs/InGaAs p-QWIP doped by Si. A strong absorption peak at 3.7 μm is observed, with a shoulder around 3.0 μm and a small absorption at 5.7 μm. The primary absorption peak at 3.7 μm is much shifted from the designed absorption peak at 10 μm, which may be due to either the mis-estimated parameters in

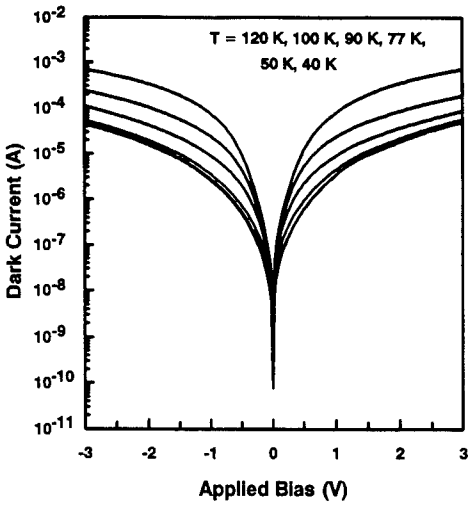

Fig. 2. Dark I–V characteristics of AlGaAs/GaAs p-QWIP measured at different temperatures.

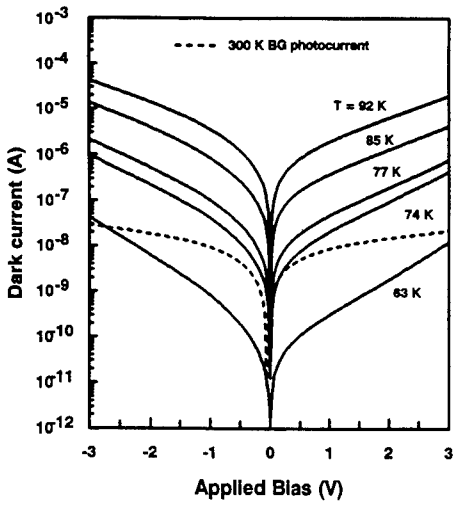

Fig. 3. Dark I–V characteristics of the strained AlGaAs/InGaAs p-QWIP measured at different temperatures.

(3 1 1)A orientation or the formation quantum wires reported by Notzel et al. [9].

We have studied the AlGaAs/InGaAs MQWs to further understand the unusual I–V asymmetry and the blue-shift of absorption wavelength. Fig. 5 shows the PL spectra of the strained AlGaAs/InGaAs MQWs grown on (3 1 1)A and (1 0 0) GaAs at 550°C. Although strong PL intensity was also observed for AlGaAs/InGaAs MQWs grown on (3 1 1)A GaAs, multiple PL transitions were measured with peak energy red-shifts of 7 and 22 meV to that of side-by-side grown (1 0 0) GaAs. We have used cross-sectional transmission electron microscopy (TEM) to study this effect. The PL energy red-shift is due to the growth-induced thickness modulation of quantum wells, which form quasi quantum wires in (3 1 1)A orientation [9]. More detailed study of TEM and the formation of quantum wires will be published elsewhere. Therefore the slight asymmetry in dark I–V characteristic of AlGaAs/InGaAs p-QWIP may be attributed to the thickness modulation. The large blue-shift of peak absorption in responsivity spectra may be also due to the formation of wider quantum wells as observed from TEM and PL.

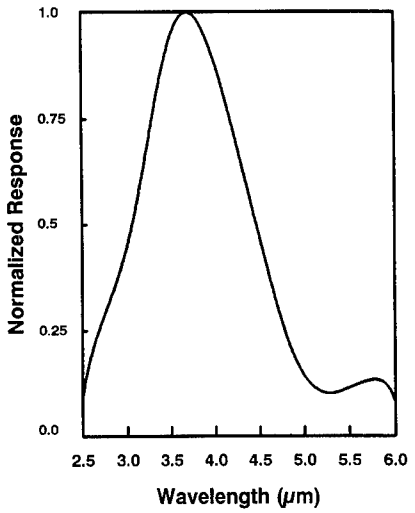

Fig. 4. Normalized responsivity for the strained AlGaAs/InGaAs p-QWIP grown on (3 1 1)A GaAs.

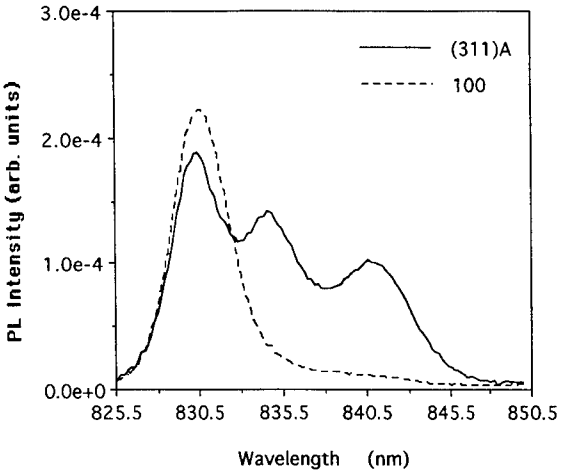

Fig. 5. Low temperature (15 K) PL spectra of the AlGaAs/InGaAs MQWs grown on (3 1 1)A and (1 0 0) GaAs at 550°C.

4. Conclusions

We have demonstrated that the Si can be used as an alternative dopant for p-type QWIP. The highly symmetrical dark I–V characteristic from the AlGaAs/GaAs p-QWIP suggests the negligible dopant migration of Si impurity during growth. The strained p-type AlGaAs/InGaAs QWIP exhibits a lower dark current and a slightly asymmetrical dark current characteristic, but the asymmetry is markedly less than that doped by Be. The asymmetry in the strained p-QWIP is not due to the impurity out-diffusion, because the dark current asymmetry is opposite to that from doping migration. The slight asymmetry in dark I–V characteristic and the large blue-shift in responsivity spectra may be due to the thickness modulation observed from the red-shift of PL peak energy and TEM.

Acknowledgements

The work performed at National Chiao-Tung University in Taiwan was supported by an NSC grant (No.85-2215-E-009-012).

References

[1] B.F. Levine, S.D. Gunapala, J.M. Kao, S.S. Pei and S. Hui, Appl. Phys. Lett. (1991) 1864.
[2] Y.H. Wang, S.S. Li, J. Chu and P. Ho, Appl. Phys. Lett. 64 (1994) 727.
[3] H.C. Liu, R. Wasilewski and M. Buchanan, Appl. Phys. Lett. 63 (1993) 761.
[4] B.F. Levine, J. Appl. Phys. 74 (1993) R1.
[5] K. Agawa, K. Hirakawa, N. Sakamoto, Y. Hashimoto and T. Ikoma, Appl. Phys. Lett. 65 (1994) 1171.
[6] O. Brandt, K. Kanamoto, M. Tsugami, T. Isu and N. Tsukada, Appl. Phys. Lett. 67 (1995) 1885.
[7] P. Krispin, R. Hey and H. Kostial, J. Appl. Phys. 77 (1995) 5773.
[8] W. Li and P.K. Bhattacharya, IEEE Electron. Dev. Lett. 13 (1992) 29.
[9] R. Notzel, N.N. Ledentsov, L. Daweritz and K. Ploog, Phys. Rev. B 45 (1992) 3507.

ELSEVIER

Journal of Crystal Growth 175/176 (1997) 1004–1008

JOURNAL OF CRYSTAL GROWTH

808 nm high-power laser grown by MBE through the control of Be diffusion and use of superlattice

Donghai Zhu*, Zhanguo Wang, Jiben Liang, Bo Xu, Zhanping Zhu, Jun Zhang, Qian Gong, Shengying Li

Laboratory of Semiconductor Materials Science, Institute of Semiconductors, Chinese Academy of Sciences, P.O. Box 912, Beijing 100083, People's Republic of China

Abstract

808 nm high-power laser diodes are grown by MBE. In the laser structure, the combination of Si-doped GRIN (graded-index) region adjacent to n-AlGaAs cladding layer with reduced Be doping concentration near the active region has been used to diminish Be diffusion and oxygen incorporation. As compared with the laser structure which has undoped GRIN region and uniform doping concentration for Si and Be, rsepectively, in the cladding layers, the slope efficiency has increased by about 8%. Typical threshold current density of 300 A/cm^2 and the minimum threshold current density of 220 A/cm^2 for lasers with 500 μm cavity length are obtained. A high slope efficiency of 1.3 W/A for coated lasers with 1000 μm cavity length is also demonstrated. Recorded CW output power at room temperature has reached 2.3 W.

PACS: 42.55.Px; 61.72.Vv; 81.15.Hi; 66.30.Jt

Keywords: High-power; Semiconductor laser; MBE; Quantum well

1. Introduction

High-power laser diodes for the light source of solid-state laser pumping have been extensively investigated [1, 2]. To realize high-power operation, it is needed to achieve a lower operating current and higher quantum efficiency. The performance characteristics of the laser diodes are determined by the quality of the epitaxial layer, laser structure design and the control of growth condition. Beryllium (Be) diffusion plays an important role in the performance of GaAs/AlGaAs laser diodes grown by MBE. Both increased oxygen incorporation and p–n junction displacement are related to Be diffusion [3]. In addition, the Be is believed to be responsible for the failure of laser diode [4]. Although MBE technique can provide better reproducible control over composition, thickness and doping profile in the direction of growth, careful treatments are needed for Be doping. In this paper, we report the MBE growth of GRIN-SCH SQW

* Corresponding author. Fax: + 86 10 62562389; e-mail: dhzhu@red.semi.ac.cn.

0022-0248/97/$17.00 Copyright © 1997 Elsevier Science B.V. All rights reserved
PII S0022-0248(96)01018-4

808 nm high-power laser diodes through the control of Be diffusion. The application of the superlattice buffer is also included.

2. Laser structure and epitaxial growth

The MBE machine used in this experiment is a Riber 32p system. Because the high-power laser diodes operate under crude conditions, it is required to improve the quality of the laser materials. It is believed that the growth of high-quality laser structure by MBE requires a more sophisticated methods than that for MOCVD-grown lasers [5]. In our laser structure, superlattices in GaAs buffer and n-AlGaAs cladding layers were incorporated. The superlattice can bring some benefits such as the reduction in the propagation of defects from substrate, a relief of strain at the interface between high aluminum concentration cladding layer and the substrate [5]. The superlattice also offers additional defense against oxygen incorporation, makes the epitaxial layer flat and improves the quality of the lower interface of the QW [6]. The advantage of superlattice may improve the uniformity of the laser materials which is beneficial to the high-power or broad-area laser diodes. Low aluminum composition AlGaAs layer is introduced as a getter buffer to remove the transient oxygen because impurities including oxygen are released as the Mo holder is heated to higher temperatures.

Fig. 1 is the schematic diagram of GRIN-SCH AlGaAs SQW laser composition profiles. The laser was grown by MBE on an n^+-GaAs substrate. The growth sequence is described as follows: a 1 μm thick n-GaAs buffer layer containing a five-period n-GaAs/$Al_{0.6}Ga_{0.4}As$ (10 nm/10nm) superlattice buffer layer, 0.5 μm thick n-$Al_{0.1}Ga_{0.9}As$ layer, 1.3 μm thick n-$Al_{0.6}Ga_{0.4}As$ cladding layer including a five-period GaAs/$Al_{0.6}Ga_{0.4}As$ (10 nm/10 nm) superlattice; 0.2 μm thick slightly Si doped $Al_xGa_{1-x}As$ confining layer (linearly graded from $x = 0.6$ to 0.3), undoped 10 nm-thick $Al_{0.07}Ga_{0.93}As$ active layer, undoped 0.2 μm thick $Al_xGa_{1-x}As$ confining layer (linearly graded from $x = 0.3$ to 0.6), 1.3 μm thick p-$Al_{0.6}Ga_{0.4}As$ cladding layer, and 0.3 μm thick p^+-GaAs contact layer. Silicon was used as the n-type and beryllium as the p-type dopant. Growth rate was 1.2 μm/h for $Al_{0.6}Ga_{0.4}As$.

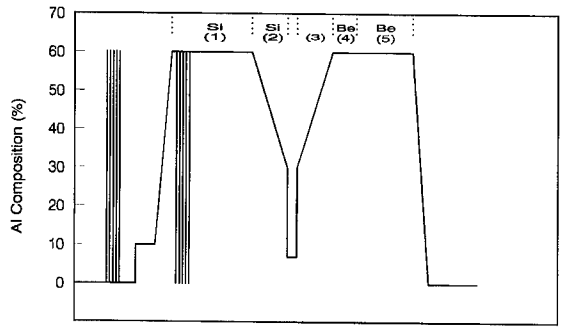

Fig. 1. Schematic composition profiles for the laser structure.

Beryllium has a high diffusivity in AlGaAs/GaAs structure [7]. The unstable behavior of this dopant during crystal growth, as well as during operation of laser diodes make the control of p–n junction difficult and affect the stability of lasers [8, 4]. On the other hand, Naresh Chand et al. [3] reported that compared to undoped AlGaAs layer, the oxygen content is lower in the Si-doped AlGaAs layer and higher in the Be-doped one. Oxygen which forms nonradiative recombination centers degrades the performance and reliability of the laser diodes. The above research results indicate that beryllium doping and diffusion have important effects on the performance of laser diodes. Experimental analysis [3] also shows that the diffusion of Be can be retarded by increasing the doping of n-layer and doping the n-side of the GRIN region. Considering the Be, Si and undoping-related oxygen incorporation, it is reasonable to dope the GRIN region adjacent to the n-AlGaAs cladding layer with Si in order to reduce oxygen content in the active region nd avoid the p–n junction displacement (a separation of p–n junction from the active layer heterojunction).

We adopted tailoring doping profiles in the epitaxial growth. In the laser structure (type I) as shown in Fig. 1, the Si doping concentration in the GaAs buffer and n-AlGaAs cladding layer (1) are 2×10^{18} and $1 \times 10^{18}\ cm^{-3}$, respectively. The GRIN region (2) adjacent to the n-AlGaAs cladding layer was doped with Si to $10^{16}\ cm^{-3}$. GRIN region (3) was undoped. The low Be-doped region

(4) (5×10^{17} cm^{-3}) in the p-AlGaAs cladding layer near the GRIN region at a range of 0.1 μm was adopted. Except for the doping concentration in this region, the Be doping in the p-AlGaAs cladding layer (5) is 8×10^{17} cm^{-3}. The reason for the lower Be-doping concentration near the GRIN region is as follows: First, it is found that undoped AlGaAs spacer layer (as thick as 0.2 μm) is ineffective to prevent Be diffusion [13]. The Be atoms piled up in the middle of the n-side GRIN region by ~60 nm from the QW region (the experimental condition is similar to ours). The distance from the beginning of the diffusion to the pile-up of the Be atoms is about 0.3 μm. Our GRIN region is 0.2 μm for each side. We expected that the lower Be doping region (0.1 μm) plus the 0.2 μm GRIN region might be helpful to prevent Be out-diffusion. Second, the reduced doping concentration proximate to the active region can enhance the external quantum efficiency in a proper laser structure [9]. In order to show the influence of the tailoring doping profiles on the laser performance, another type of laser structure (type II) was grown. In the type-II laser structure, all the GRIN region and active layer are undoped. The n- and p-AlGaAs cladding layers are uniformly doped with Si (1×10^{18} cm^{-3}) and Be (8×10^{17} cm^{-3}). The laser structures of type I and type II differ only by the doping profiles and the rest of the structures is identical. More than ten growths for each structure were carried out.

3. Device fabrication and laser performance

First, 100 μm wide and 500 μm long uncoated lasers were fabricated in order to obtain the parameters reflecting the quality of epitaxial wafer. There is no obvious difference in the threshold current density for the two structures. The typical threshold current density is 300 A/cm^2. The minimum J_{th} is 220 A/cm^2. These values are satisfactory when compared with lasers of similar structure [10, 11], which indicates the high-quality epitaxial materials grown by MBE and fairly low-concentration of nonradiative recombination centers. However, a difference in the slope efficiency exists. Statistical data show that the slope efficiency is 0.84 and 0.78 W/A per facet for type I and type II structures, respectively. Enhancement in the slope efficiency is obtained by about 8% in type I as compared to type II. It was reported that doping modifications had no measurable effect on external quantum efficiency for a structure in which the optical field is tightly confined [9] because there were less changes in the free-carrier absorption. If this is true, for our laser structure (type I) in which the optical field is tightly confined [9], we consider the improvement of slope efficiency as the result of decreased concentration of nonradiative recombination center or the minimizing p–n junction displacement, or both, in type-I structure. The displacement allows majority carrier current flow out of the active layer. The current does not contribute to lasing [14].

Second, dielectric (SiO_2) defined metal-stripe lasers with 100, 200 μm wide stripes and 1000 μm cavity length were also fabricated for type-I structure. High- and low-reflectivity facet coatings were applied to each facet using SiO_2 and Si, which gives the reflectivity of 10% and 90% at the front and rear facets, respectively. Zn diffusion was performed to reduce the contact resistance. Ti/Pt/Au was used for the p-side contact, the n-side contact was formed with AuGe/Ni/Au. Laser chips were mounted on Cu heat sinks with In solder in the junction down configuration.

Typical slope efficiency of these lasers is 1 W/A. Output power versus current characteristics at room temperature under CW operation are shown in Fig. 2. These lasers are different in stripe width and same in the cavity length (1000 μm). Curve (a) represents one of coated lasers with 100 μm stripe width. Curve (b) represents one of coated-laser with 200 μm stripe width. In curve (a), laser can be operated up to 2 W. In curve (b), a high slope efficiency of 1.3 W/A for the coated-front facet alone is demonstrated, recorded CW output power reached 2.3 W. The typical emission wavelength of 100 μm wide stripe laser diodes under 1 W output power was measured to be 808 nm, as shown in Fig. 3.

The temperature dependence of CW light output versus current characteristics for 100 μm stripe laser is depicted in Fig. 4. The temperature dependence of I_{th} is given by

$$I_{th} = I_0 \exp(T/T_0),$$

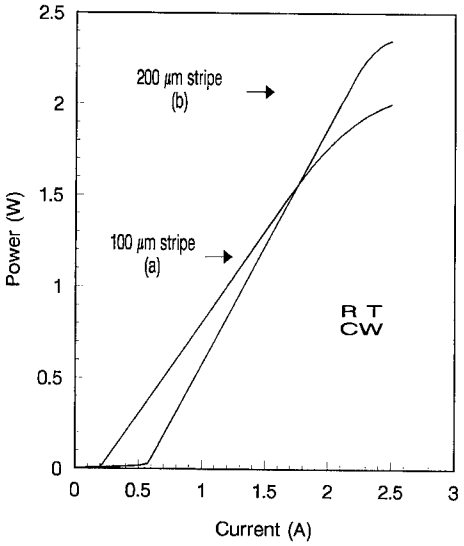

Fig. 2. Light output power vs. current characteristics of the lasers with 100 and 200 μm stripe width.

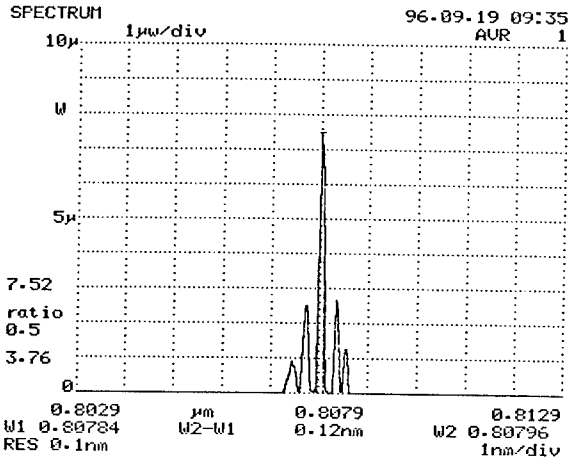

Fig. 3. Typical emission spectrum for the 100 μm × 1000 μm laser devices under output power 1 W at room temperature.

where I_{th} is the threshold current at the temperature T, I_0 is a constant and T_0 is the characteristic temperature. The laser has been operated up to 95°C at 0.5 W under CW operation. The characteristic temperature T_0 is as high as 185 K between 35–85°C and 163 K between 85–95°C, which indicates the good thermal characteristic

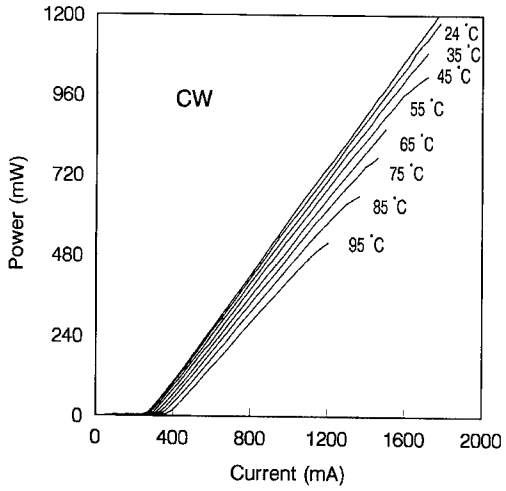

Fig. 4. Light output power vs. current characteristics of the high-power laser at different temperatures under CW conditions.

of the laser structure. Because shorter wavelength AlGaAs/GaAs lasers tend to have a small T_0 [12], this value is relatively high.

In summary, high-power 808 nm-AlGaAs quantum-well lasers are grown by MBE. Both reduced Be doping concentration near the active region and the Si doping in the n-side GRIN region are used to reduce the Be diffusion and oxygen incorporation near the active region. Compared with nontailoring-doping laser structure, the enhancement of the slope efficiency is observed. The minimum threshold-current density of 220 A/cm^2 is obtained. High slope efficiency of 1.3 W/A is demonstrated. Recorded CW output power at room temperature has reached 2.3 W.

Acknowledgements

The authors are grateful for the help from Zujie Fang, Bin Liu, Xiongwei Hu, Caizheng Jin, Xiaojie Wang and Qin Han throughout this work.

References

[1] V.P. Chaly, D.M. Demidov, G.A. Folin, S.Yu. Karpov, V.E. Myachin, Yu.V. Pogorelsdy, I.Yu. Rusanovich, A.P. Shkurku and A.L. Ter-Martirosyan, J. Crystal Growth 150 (1995) 1350.

[2] I. Eliashevich, J. Diaz, H. Yi, L. Wang and M. Razeghi, Appl. Phys. Lett. 66 (1995) 3087.
[3] N. Chand, S.N.G. Chu, A.S. Jordan, M. Geva and V. Swaminathan, J. Vac. Sci. Technol. B 10 (1992) 807.
[4] A. Jakubowicz, A. Oosenbrug and Th. Forster, Appl. Phys. Lett. 63 (1993) 1185.
[5] M.E. Givens, L.J. Mawst, C.A. Zmudzinski, M.A. Emanuel and J.J. Coleman, Appl. Phys. Lett. 50 (1987) 301.
[6] H. Imamoto, F. Sato, K. Imanaka and M. Shimura, Appl. Phys. Lett. 54 (1989) 1388.
[7] P. Enquist, G.W. Wisks and L.F. Eastman, J. Appl. Phys. 58 (1985) 4130.
[8] G.E. Kohnke, M.W. Koch, C.E.C. Wood and G.W. Wicks, Appl. Phys. Lett. 66 (1995) 2786.
[9] R.G. Waters, D.S. Hill and S.L. Yellen, Appl. Phys. Lett. 52 (1988) 2017.
[10] Y. Nagai, K. Shigihara, A. Takami, S. Karakida, Y. Kokubo and A. Tada, IEEE Photon. Technol. Lett. 3 (1991) 97.
[11] C.A. Wang, H.K. Choi and M.K. Connors, IEEE Photon. Technol. Lett. 1 (1989) 351.
[12] L.A. Coldren and S.W. Corzine, in: Diode Lasers and Photonic Integrated Circuits (Wiley, New York, 1995) ch. 2, p. 58.
[13] V. Swaminathan, N. Chand, M. Geva, P.J. Anthony and A.S. Jordan, J. Appl. Phys. 72 (1992) 4648.
[14] P.J. Anthony, J.R. Pawlik, V. Swaminathan and W.T. Wang, IEEE J. Quantum. Electron. QE-19 (1983) 1030.

ELSEVIER

Journal of Crystal Growth 175/176 (1997) 1009–1015

JOURNAL OF CRYSTAL GROWTH

Continuously graded buffers for InGaAs/GaAs structures grown on GaAs

A. Bosacchi[a], A.C. De Riccardis[a], P. Frigeri[a], S. Franchi[a,*], C. Ferrari[a], S. Gennari[a], L. Lazzarini[a], L. Nasi[a], G. Salviati[a], A.V. Drigo[b], F. Romanato[b]

[a] *CNR, MASPEC Institute, Via Chiavari 18a, I-43100 Parma, Italy*
[b] *INFM, Physics Department of Padova University, Via Marzolo 8, I-35131 Padova, Italy*

Abstract

We report on the preparation under optimized conditions and on the study of InGaAs buffers grown on GaAs, intended for MQW structures for 1.3 and 1.5 μm optical operation at 300 K; the buffers have linear, square-root and parabolic composition profiles. They were designed so that MQWs grown atop the buffers are virtually unstrained, unlike those prepared following the conventional approach that are under compressive strain. The results obtained by the concomitant use of TEM, HRXRD, AFM and PL show that, by carefully designing the buffers: (i) the misfit dislocation (MD) profiles and thicknesses of the MD-free regions in the buffers can be predetermined, (ii) active structures atop the buffers are virtually unstrained and have efficient 300 K photoluminescence in the 1.3 and 1.5 μm windows of photonic interest, (iii) the structures have threading dislocation concentrations in the low 10^6 cm^{-2} range and show smooth and symmetric cross-hatchings.

1. Introduction

Lattice mismatched structures have interesting applications in spite of the potentially adverse effects related to strain relaxation, since they allow to extend the range of materials that can be considered and, then, of the properties that can be exploited. Moreover, the accurate control of the resulting strain may give significant advantages, since it can be used as a tool for band engineering. Furthermore, it is of interest to use substrates that, even if mismatched: (i) have higher crystalline perfection and definite electrical, optical and mechanical properties, or (ii) allow the preparation of structures suited for the fabrication of different devices with integrated functions. Structures consisting of InGaAs layers deposited on GaAs substrates are gaining increasing attention for optical modulators based on the quantum-confined Stark effect [1], quantum well infrared detectors [2] and metamorphic high electron mobility transistors [3], 1.3 μm quantum well lasers [4] and non-linear optical devices [5].

* Corresponding author. Fax: + 39 521 269 209; e-mail: franchi@prmasp.bo.cnr.it.

0022-0248/97/$17.00 Copyright © 1997 Elsevier Science B.V. All rights reserved
PII S0022-0248(96)00961-X

Buffer layers with either step-graded or continuously graded compositions have been proposed to (i) relax the strain resulting from lattice mismatch; (ii) bury the misfit dislocations (MD) away from the active part of the structure; (iii) prevent the onset of three-dimensional nucleation; and (iv) reduce the propagation of threading dislocations (TD) towards the active parts of devices [6]. Linearly graded buffers are generally used (with the exception of Refs. [7, 8]), however, we expect that continuously graded buffers with selected composition profiles may give additional benefits, such as the control of the MD profiles within the buffers.

The aim of this work was to evaluate buffers with compositions graded according to (a) linear, (b) square-root and (c) parabolic (with the vertex at the top of the buffer) dependences on the distance from substrates. The experimental results were obtained by the concomitant use of transmission electron microscopy (TEM), high-resolution X-ray diffraction (HRXRD), atomic force microscopy (AFM) and photoluminescence (PL). The results show that by proper buffer designing: (i) the thicknesses of the MD-free regions of buffers can be varied, (ii) the MDs can be concentrated far from the active structures grown atop the buffers, (iii) these structures are virtually unstrained, (iv) the TD concentrations can be reduced in the low 10^6 cm^{-2} range, (v) the structures grown under optimized conditions have smooth and symmetric cross-hatchings and (vi) the MQWs have efficient 300 K photoluminescence in the 1.3 and 1.5 μm spectral windows.

2. Experimental procedure

After careful studies on the optimization of growth conditions, the InGaAs buffers with different composition profiles were grown on semi-insulating (0 0 1) GaAs by solid-source MBE at 400°C using As_2 beams; instead, the InGaAs/GaAs MQWs were grown at 400°C by atomic layer MBE (ALMBE) that allows to select the compositions of the InGaAs wells by only adjusting the In and Ga supply times, without changing the temperature of the cation cells reached at the end of the growth of buffers [9]. Composition grading was obtained by varying the In and Ga cell temperatures in such a way to maintain a growth rate of 0.28 nm/s. Prior to each run, the In and the Ga fluxes were calibrated by RHEED oscillation measurements using InAs and GaAs substrates, respectively. The substrates were radiatively heated at growth temperatures T_g measured by a suitable optical pyrometer for $T_g \geqslant 450$°C and by a thermocouple (TC) for $T_g < 450$°C. For $T_g < 450$°C, the TC readings were corrected by the difference (~ 200°C) between the TC and the optical pyrometer values measured at $T_g > 450$°C. Great care was paid to keep the growing surface temperature at the intended value during growth; this was done by lowering the electrical power to the substrate heater in a controlled way so as to counterbalance the increasing optical power absorbed during the growth of buffers and MQWs. The As_2 beam-equivalent pressure (BEP) was 5.5×10^{-6} Torr, while the As_2/Ga BEP ratio was ~ 9.

TEM observations were carried out by an JEOL 2000FX instrument operating at 200 KeV on (1 1 0) oriented cross sectional samples. The dislocation distribution at the buffer/substrate interfaces and across the buffer layers was studied under bright field, dark field and weak beam conditions using $\boldsymbol{g} = 220$ type scattering vectors. Conventional $\boldsymbol{g} \cdot \boldsymbol{b}$ contrast analyses showed that the majority of the dislocations were 60° type in character. Dark field $\boldsymbol{g} = 200$ type imaging conditions were used for studying the MQW structural quality and thicknesses. Finally, the MQW periods and interface-smoothness were studied in the lattice resolution mode.

High-resolution X-ray diffraction (HRXRD) measurements were performed using a diffractometer fitted with a four-crystal X-ray monochromator. (0 0 4) symmetrical and (3 3 5) asymmetrical CuKα diffraction profiles were used to measure the strain and tilt angle of the MQWs; from these curves we also obtained the average lattice parameters of MQWs parallel and perpendicular to the interfaces, the compositions of the top of buffers and the average compositions and the period of MQWs. A good agreement between MQW periods determined by TEM and HRXRD was found, while the mean compositions of MQWs deduced by HRXRD are close to those determined

by Rutherford back-scattering experiments in selected samples.

Atomic force microscopy (AFM) was carried out under conventional conditions.

The photoluminescence (PL) spectra were taken at 10 and at 300 K with a spectral resolution of 0.5 meV, and were excited by the blue line of an Ar^+ laser, using power densities as small as 0.5 W/cm^2.

3. Design of the structures

According to the existing models on strain relaxation [6, 8, 10, 11] buffers with increasing compositions can be divided into two parts: (i) the one closest to the substrate (up to a distance δ_r from the substrate itself) is fully relaxed, due to the formation of misfit dislocations that have a concentration proportional to the composition gradient, and (ii) the topmost part that (a) is void of misfit dislocations, (b) has a lattice parameter $a(x_r)$, where $x_r = x(\delta_r)$ ($x(\delta)$ giving the dependence of the $In_xGa_{1-x}As$ composition on the distance δ from the substrate and $a(x)$ being the lattice parameter as a function of x), and (c) is under strain in regions where $x(\delta) \neq x_r$. The values of δ_r can be found by means of the equation [8, 10, 11]

$$k_n = \left(\frac{\Delta a}{a}\right)^n \int_{\delta_r}^{\delta_b} (x(\delta) - x(\delta_r))^n \, d\delta \qquad (1)$$

with $n = 1$ [10] or $n = 2$ [8, 11]; $\Delta a/a = 0.07$ is the lattice mismatch between InAs and GaAs, while $k_1 = 0.83$ nm [10], $k_2 = 3.68 \times 10^{-3}$ nm [8, 11] and δ_b is the total thickness of the buffer.

From Eq. (1) it follows that by choosing the composition profile $x(\delta)$ and the thickness δ_b it should be possible to predetermine (i) the thickness $(\delta_b - \delta_r)$ of the MD-free region and (ii) the lattice parameter $a(x_r)$ of the upper part of the buffer; on the other hand, the concentration profile of MDs is determined by the composition profile in the buffers. It is worth noting that if additional structures deposited atop buffers can be considered as single layers with free-standing lattice parameters a_a (and with a mean composition x_a), then, by choosing the composition profile of buffers, the active structures can be put under overall compressive, null or tensile strain, thus affecting their electronic, optical and transport properties. However, if the lattice parameter of the upper part of the buffer is significantly different from that of the active structure ($x_r \neq x_a$), the latter modifies the strain situation of the buffer that cannot be considered as an independent block any more; in that case, Eq. (1) should be used considering the whole structure consisting of buffer and active region.

We designed structures consisting of graded buffers and two types of MQW structures for 1.3 and 1.5 μm optical modulators, thereafter referred to as 1.3 and 1.5 μm MQWs. The 1.5 and 1.3 μm MQWs both have mean compositions $x_{MQW} = 0.34$ and consist of 30.5 periods of 30 and 35 Å GaAs barriers and of 65 and 75 Å thick $In_{0.5}Ga_{0.5}As$ wells, respectively. The buffer structures were designed according to Ref. [8, 11] in order to avoid strain in the MQWs; therefore, the composition profiles with linear, square-root and parabolic profiles were graded in 3000 nm up to values x_m of 0.41, 0.39 and 0.38, respectively, so that $x_m > x_r = x_{MQW}$. It should be noted that this approach is different from that generally used, where the buffer compositions are graded up to the mean compositions of the MQWs ($x_m = x_{MQW}$), thus resulting in MQWs under compressive strain.

4. Results and discussion

Fig. 1 shows a comparison among cross sections of linear, square-root and parabolic buffers; the most interesting features are: (i) it can be clearly seen that the topmost parts of buffers are void of MDs, as predicted by the existing models [6, 8, 10, 11], and as previously observed in Refs. [12, 13], (ii) the thicknesses of MD-free layers increase ranging from linear, square-root and parabolic buffers and are ~ 600 nm for the last ones; the values are in reasonable agreement with the results of Eq. (1) with $n = 2$; (iii) the misfit dislocations have different distributions in buffers with different composition profiles, being almost uniformly distributed (up to x_r) in the linear buffers and strongly accumulated towards the

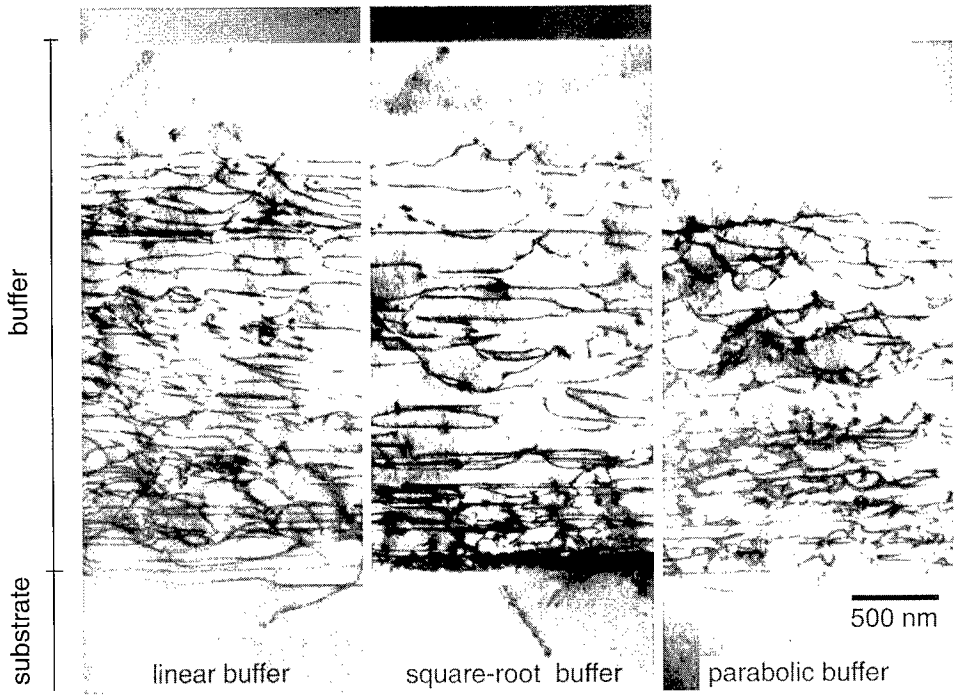

Fig. 1. (1 1 0) oriented cross-sectional TEM micrographs of 3000 nm thick InGaAs buffers (grown on (1 0 0) GaAs), with linear ($0.005 \leqslant x \leqslant 0.41$), square-root ($0.005 \leqslant x \leqslant 0.39$) and parabolic ($0.005 \leqslant x \leqslant 0.38$) composition profiles. $\boldsymbol{g} = 220$ type scattering vectors were used.

substrate/buffer interface in square-root buffers; (iv) as predicted by the strain relaxation models [6], continuous grading of composition results in a relatively low concentration of TDs, that in our buffers is lower than 1×10^6 cm^{-2}.

When MQWs were grown on the buffers, only a few TDs and MDs at the MQW/buffer interface were found by TEM observations; their maximum density ranged between 1.5×10^6 and 4×10^6 cm^{-2} for structures with linear and parabolic buffers, respectively. The thicknesses of the MD-free layers in structures with and without MQWs are approximately the same, thus implying that the MQWs do not contribute to the integral of Eq. (1), and, then, that the MQWs are closely lattice-matched to the topmost part of the buffers ($x_r \sim x_a$). Independent of the type of buffer, the MQWs have the same structural quality and interface smoothness (on atomic scale), as those shown in Fig. 2, relative to a MQW grown on a linear buffer.

As an example, in Fig. 3 we show the (0 0 4) CuKα diffraction profile of a 1.5 μm MQW grown on a square-root buffer; the quality of the structures is assessed by the occurrence of peaks related to MQW periodicity. From the average lattice parameters of MQWs parallel and perpendicular to the interfaces we conclude that the MQWs are nearly lattice matched to the different types of buffers; the In compositions x_m at the top of buffers evaluated by the diffraction profiles are in good agreement with those derived by using the experimental values of the mean composition of MQWs, the thicknesses of the barriers and wells (obtained by TEM observations) and the In and Ga supply times; it is interesting to note that the x_r values obtained by Eq. (1) using the above x_m values are consistent with the strain, whether slightly tensile or compressive, of the MQWs given by HRXRD experiments.

As for the surface smoothness, AFM observations show that both uncapped buffers and MWQs

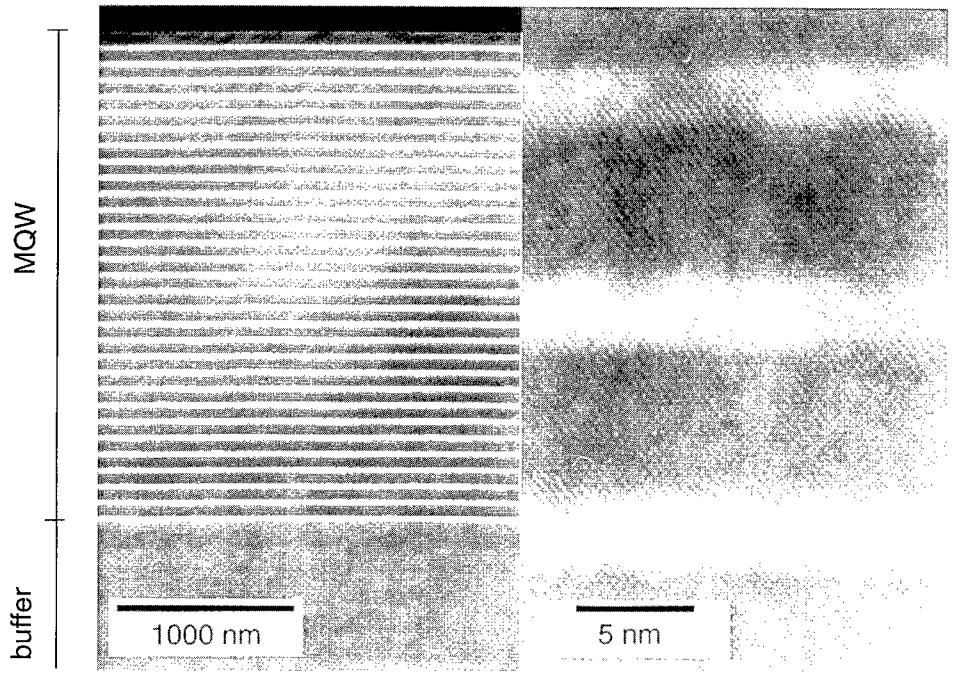

Fig. 2. Dark field, $\boldsymbol{g} = 002$ type (left panel) and bright field zone axis lattice resolution (right panel) micrographs of a 1.5 μm MQW (30 Å GaAs / 65 Å $In_{0.5}Ga_{0.5}As$) grown atop a linearly graded ($0.005 \leqslant x \leqslant 0.41$) InGaAs buffer.

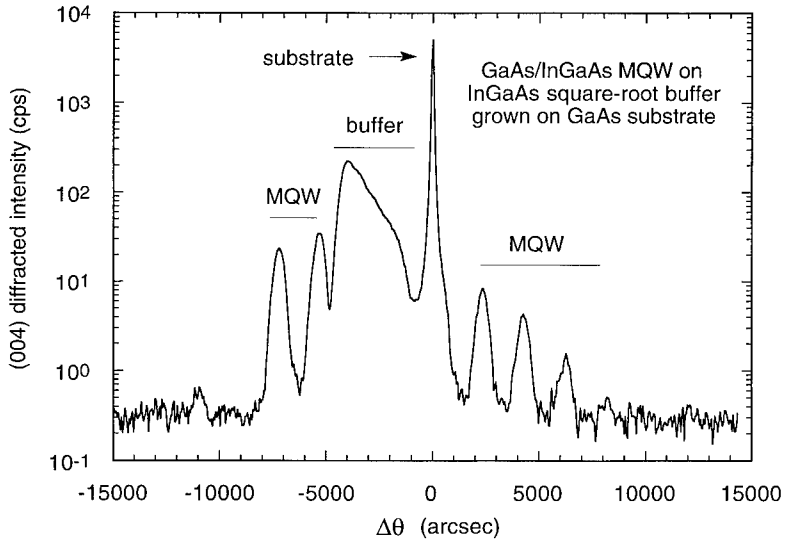

Fig. 3. (0 0 4) CuKα diffraction profile of a 1.5 μm MQW (30 Å GaAs / 65 Å $In_{0.5}Ga_{0.5}As$) grown atop a square-root ($0.005 \leqslant x \leqslant 0.39$) InGaAs buffer.

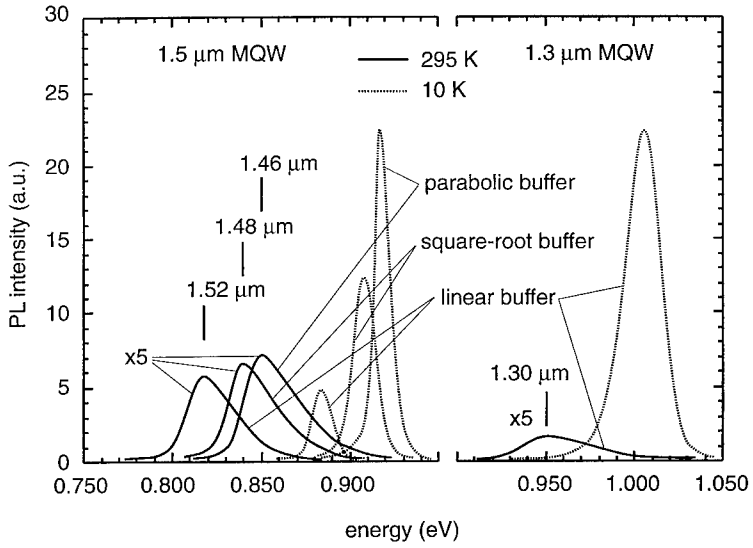

Fig. 4. 10 K and 300 K PL spectra of 1.3 and 1.5 μm MQWs (30 Å GaAs / 65 Å $In_{0.5}Ga_{0.5}As$ and 35 Å GaAs / 75 Å $In_{0.5}Ga_{0.5}As$, respectively), grown on linear ($0.005 \leqslant x \leqslant 0.41$), square-root ($0.005 \leqslant x \leqslant 0.39$) and parabolic ($0.005 \leqslant x \leqslant 0.38$) buffers. The spectral resolution and power densities were 0.5 meV and a 0.5 W/cm^2, respectively.

have small and symmetric cross-hatchings along the two orthogonal $< 1\,1\,0 >$-type directions; the standard deviations of the surface heights (SDSH) depend only slightly on the type of buffer, being, for instance, 3.4 ± 0.3 and 2.6 ± 0.3 nm for linear and parabolic buffers, respectively. The MQWs tend to planarize the surfaces, as can be deduced by the SDSHs of 1.5 μm MQW surfaces that are 2.0 ± 0.3 and 1.4 ± 0.2 nm, for linear and parabolic buffers, respectively.

In Fig. 4 we show the PL spectra at 10 and 300 K of 1.5 and 1.3 μm virtually unstrained MQWs grown on the same buffers as those shown in Fig. 1. It is worth noting that by carefully designing and growing the structures, efficient PL can be obtained at 300 K within or close to the 1.3 and 1.5 μm spectral windows of photonic interest. The PL full-width-at-half-maximums (FWHM) at 10 K relative to the 1.5 μm MQWs (9, 12 and 12 meV, for the parabolic, the square-root and the linear buffers, respectively) are significantly small; this result can be likely related to the design of buffers that virtually do not strain MQWs, unlike the approach that matches the compositions of the tops of buffers to the mean compositions of MQWs. This interpretation may also explain the reduction of the PL FWHMs for increasing x_m up to values larger than x_{MQW} reported in Ref. [14]; our 300 K FWHMs are smaller by a factor of ~ 3–4 than the 77 K FWHMs given in same paper [14].

5. Conclusions

We prepared under optimized conditions and studied InGaAs buffers grown on GaAs, intended for MQW structures for 1.3 and 1.5 μm optical operation at 300 K; the buffers have linear, square-root and parabolic composition profiles. The buffers were designed in such a way that the MQWs grown atop the buffers are virtually unstrained, unlike those prepared following the conventional approach, that are compressively strained. The results obtained by the concomitant use of TEM, HRXRD, AFM and PL show that (i) the MDs profiles and thicknesses of the MD-free regions in the buffers can be predetermined, (ii) the active structures atop buffers are virtually unstrained and have efficient 300 K photoluminescence in the 1.3 and 1.5 μm windows, and (iii) the structures have

TD concentrations in the low 10^6 cm^{-2} range and smooth and symmetric cross-hatchings.

Acknowledgements

The work at MASPEC Institute has been partially supported by the INFN Project RD 23. Thanks are due to P. Allegri, V. Avanzini and M. Scaffardi for technical assistance.

References

[1] S.M. Lord, B. Pezeshki, S.D. Kim and J.S. Harris, Jr., J. Crystal Growth 127 (1993) 759; S.D. Kim, J.A. Trezza and J.S. Harris, Jr., J. Vac. Sci. Technol. B 13 (1995) 1526.
[2] H.C. Chui, E.L. Martinet, M.M. Fejer and J.S. Harris, Jr., Appl. Phys. Lett. 64 (1994) 736; H.C. Chui, S.M. Lord, E. Martinet, M.M. Fejer and J.S. Harris, Jr., Appl. Phys. Lett. 63 (1993) 364.
[3] P. Win, V. Druelle, A. Cappy, Y. Cordier, J. Favre and C. Bouillet, Appl. Phys. Lett. 61 (1992) 922.
[4] T. Uchida, H. Kurakake, H. Soda and S.J. Yamazaki, J. Electron. Mater. 25 (1996) 581; H. Ito and J.S. Harris, Jr., Jpn. J. Appl. Phys. 12A (1994) 6516.
[5] E.L. Martinet, H.C. Chui, G.L. Woods, M.M. Fejer, J.S. Harris, Jr., C.A. Rella, B.A. Richman and H.A. Schwettman, Appl. Phys. Lett. 65 (1994) 2630.
[6] J. Tersoff, Appl. Phys. Lett. 62 (1993) 693.
[7] K. Dettmer, U. Behner and R. Beserman, J. Crystal Growth 157 (1995) 142.
[8] G. Salviati, C. Ferrari, L. Lazzarini, S. Franchi, A. Bosacchi, F. Taiariol, M. Mazzer, C. Zanotti-Fregonara, F. Romanato and A.V. Drigo, Int. Phys. Conf. Series 146 (1995) 337 (1995).
[9] M. Madella, A. Bosacchi, S. Franchi, P. Allegri and V. Avanzini, J. Crystal Growth 127 (1993) 270.
[10] A. Sacedón, F. González-Sanz, E. Calleja, E. Muñoz, S.I. Molina, F.J. Pacheco, D. Araújo, R. García, M. Lourenço, Z. Yang, P. Kidd and D. Dunstan, Appl. Phys. Lett. 66 (1995) 3334.
[11] F. Romanato, Study and characterization of compound semiconductor epitaxial layers, PhD Thesis, University of Padova (1994), unpublished.
[12] A. Bosacchi, A.C. De Riccardis, C. Ferrari, S. Franchi, L. Lazzarini and G. Salviati, MRS Spring Meeting, 8–12 April (1996); S. Francisco, unpublished.
[13] S.D. Kim, H. Lee and J.S. Harris, Jr., J. Crystal Growth 141 (1994) 37.
[14] H.C. Chui and J.S. Harris, Jr., J. Vac. Sci. Technol. B 12 (1994) 1019.

ELSEVIER

Journal of Crystal Growth 175/176 (1997) 1016–1021

JOURNAL OF CRYSTAL GROWTH

Molecular beam epitaxy growth and characterization of $In_xGa_{1-x}As$ ($0.57 \leqslant x \leqslant 1$) on GaAs using InAlAs graded buffer

S.M. Wang[a,*], C. Karlsson[a], N. Rorsman[a], M. Bergh[b], E. Olsson[c], T.G. Andersson[c], H. Zirath[a]

[a] *Department of Microwave Technology, Chalmers University of Technology, S-41296 Göteborg, Sweden*
[b] *Department of Solid State Electronics, Chalmers University of Technology, S-41296 Göteborg, Sweden*
[c] *Department of Physics, Chalmers University of Technology, S-41296 Göteborg, Sweden*

Abstract

$In_xGa_{1-x}As$ ($x \geqslant 0.57$) thin layers were grown on GaAs by molecular beam epitaxy using an InAlAs graded buffer. Surface roughness of the graded buffer decreased with reduced buffer thickness and growth temperature. The InGaAs layers grown on a graded buffer revealed a larger tilting angle, a higher residual strain and electron mobility than those grown directly on GaAs. Increasing the graded buffer thickness above 1.2 μm did not improve the transport properties of InAs. The InAs mobility increased with layer thickness. This was explained by assuming two conducting channels, given $\mu_{300} = 1.8 \times 10^4$ cm^2/(V s) and $\mu_{77} = 5.1 \times 10^4$ cm^2/(V s) for bulk InAs.

PACS: 68.55. – a; 73.61.Ey; 81.15.Hi

Keywords: MBE; InGaAs; InAlAs graded buffer; GaAs

1. Introduction

The presence of threading and misfit dislocations is common in relaxed lattice mismatched semiconductor heterostructures and limits their use in device applications. In the last several years efforts have been made to reduce dislocation densities by first growing a graded alloy buffer [1–9]. In this case the nucleated dislocations glide to sample edges or interface more easily as compared with those in a uniform layer, because of a larger strain force and weaker pinning [10]. By using this technique, dislocation densities as low as 10^6 cm^{-2} and 10^4 cm^{-2} have been reported for Ge on Si [5] and for $In_{0.48}Ga_{0.52}As$ on GaAs [7], respectively. Devices like InAlAs/$In_xGa_{1-x}As$ ($x \geqslant 0.52$) high electron mobility transistors on GaAs [11–13] and

* Corresponding author.

0022-0248/97/$17.00 Copyright © 1997 Elsevier Science B.V. All rights reserved
PII S0022-0248(96)00892-5

$In_xGa_{1-x}P$ light emitting diodes on GaP [14] have been fabricated showing very promising performance. More important, this technique offers the possibility of growing metamorphic "substrates" with adjustable lattice constant. In this work, we report MBE growth and characterization of $In_xGa_{1-x}As$ ($x \geqslant 0.57$) on GaAs using continuously graded InAlAs buffers. Incorporation of Al instead of Ga in the graded buffer is motivated by the fact that it reduces the background carrier density in subsequent layers [3]. The influence of growth temperature and graded buffer thickness on material quality is studied by atomic force microscopy (AFM), double crystal X-ray diffraction (XRD) and Hall effect measurements.

2. Material growth

We used quarter 2 in. semi-insulating (0 0 1) GaAs substrates and In-mounting Mo sample holders (MSHs). Samples were grown under As-rich growth conditions and rotated at 10 rpm in a solid source Varian Gen II MBE system. Each sample consisted of a GaAs buffer (0.1 to 0.5 μm thick) grown at 580°C, a graded $In_xAl_{1-x}As$ buffer and in some samples an $In_xGa_{1-x}As$ bulk layer with the In content the same as the final value of the graded buffer, x_f. During growth of the graded buffer, both In and Al source temperatures were varied linearly. The initial x-value, x_i, was 0.005. For comparison, one sample (#518) with a 1 μm thick $In_xGa_{1-x}As$ graded buffer was grown. The growth temperature, T_g, measured by a pyrometer, varied between 350°C and 480°C for the graded buffers and between 420°C and 500°C for the bulk layers. As the pyrometer measured temperature correctly only above 450°C and use of MSHs would change the pyrometer reading, a temperature calibration procedure was made. Fig. 1 shows the relation between the pyrometer and the thermocouple temperature, T_{tc}, for three MSHs and an In-free sample holder. The T_g-value was calibrated by the oxide desorption temperature of GaAs (583°C). As seen, the T_g-value is about 60–70°C lower for the MSHs than for the In-free holder, indicating heat dissipation of the MSHs. The pyrometer measures a higher T_g-value when the As_2 shutter is open than closed. This is due to reflection of heat radiation from the As_2 cracker (at 1000°C) by the MSH. The reflection is dominant at low T_{tc}-values which sets a minimum pyrometer reading of 520°C. Thus, the correct growth temperature is measured only when the As_2 shutter is closed. In the temperature range used in this work the difference of T_g-values between MSHs was within 10°C. The In content and the growth rate (around 1 μm/h) were calibrated by RHEED oscillations.

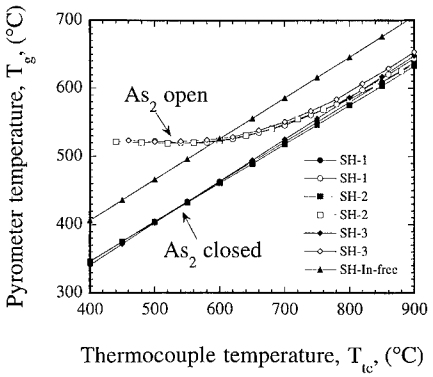

Fig. 1. Temperature calibration for three MSHs and one In-free sample holder.

3. Characterization results and discussions

Atomic force microscopy was used to study the surface properties of the $In_xAl_{1-x}As$ ($x_f = 0.8$) graded buffer layers. We first checked the surface of the GaAs buffer and found that the root-mean-square (rms) roughness value decreased only slightly from 0.36 to 0.30 nm, when the GaAs thickness increased from 0.1 to 0.5 μm. Based on this fact, a 0.1 μm thick GaAs buffer was selected for the AFM samples, in which four samples had a graded buffer thickness, L_{grad}, of 1 μm grown at 300–480°C while two were grown at 350°C with thicknesses of 0.5 and 2 μm, respectively. The corresponding lattice mismatch slope, k, was between 2.9 and 11.5%/μm. All samples were mirror-like to the naked eye and showed random surface morphology under AFM. A typical AFM image is shown in Fig. 2 and the rms roughness values are collected in Fig. 3. The surface becomes more rough with

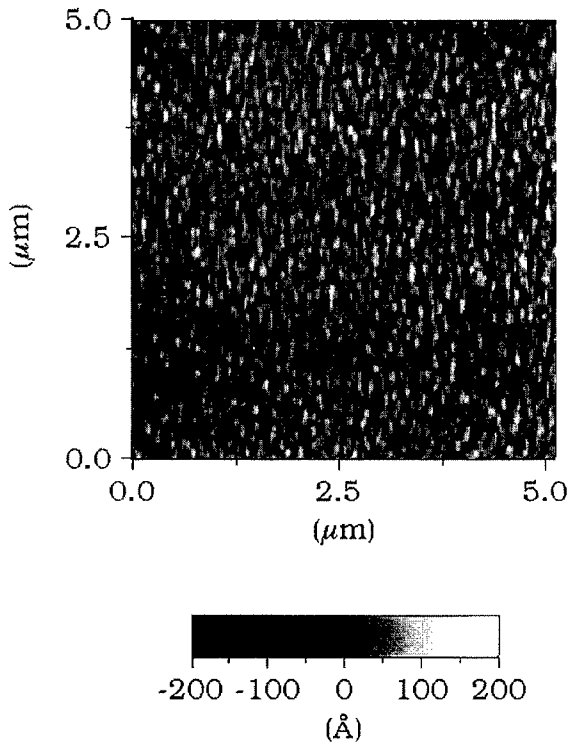

Fig. 2. AFM images of InAlAs graded buffer grown at 350°C.

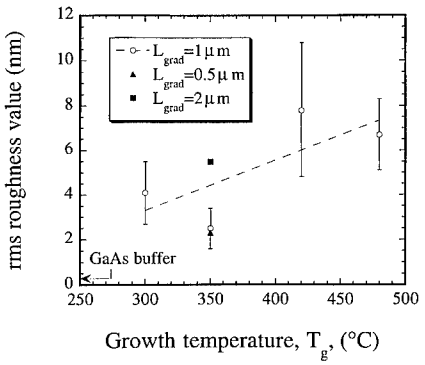

Fig. 3. Summary of rms roughness values measured by AFM.

increasing growth temperature or L_{grad}. This is caused by different local growth rates on the surface after strain relaxation. When a layer relaxes by generation of dislocations or 3D islands, the residual strain is not uniform over the surface. The less strained areas have a lower elastic energy and thus, a relatively higher growth rate. Since at high growth temperatures the adatoms have large kinetic energy and surface diffusion length, they can easily find such areas and form rough surface. For a 1 μm thick InAlAs graded buffer grown at 350°C, a rms roughness value of 2.5 ± 0.9 nm was obtained.

Double crystal XRD was performed in 2 μm thick $In_xGa_{1-x}As$ ($0.57 \leqslant x \leqslant 1$) layers, grown with and without the InAlAs graded buffer. Both symmetric (0 0 4) and asymmetric (1 1 5 ±) diffraction geometry were used and the rocking curves were recorded at four different azimuthal angles. The XRD results are summarized in Table 1. For the InGaAs layers grown directly on GaAs, the alloy peak is narrow and the peak shift with the azimuthal angle is small. However, for the InGaAs layers grown on the graded buffer, the alloy peak is wide and the shift is strong. A typical rocking curve at the (0 0 4) diffraction geometry is shown in Fig. 4. The peak shift with the azimuthal angle indicates a tilting of the $In_xGa_{1-x}As$ layer relative to the GaAs substrate. This implies that the net value of the Burgers vector along the z-direction is not zero. The full-width at half-maximum (FWHM) is wider than that of layers without the graded buffer, indicating a wide distribution of the vertical lattice constant. This can be explained by the two factors: First, continuous alloy grading and non-uniform dislocation density along the z-direction in the InAlAs graded buffer cause a wide distribution of lattice constant. Second, strain could be further relieved in the 2 μm thick InGaAs layer by dislocation formation which broadens the InGaAs peak. In addition, the FWHM is about 2–3 times wider in one direction than in its perpendicular direction in all samples with the graded buffer. We believe that it is related to the asymmetric distribution of dislocations. The values of FWHM listed in Table 1 are for the narrow one.

Both vertical and lateral lattice constants are extracted from the asymmetric (1 1 5 ±) XRD rocking curves. The in-plain residual strain, ε, and the In content are then obtained assuming Vegards law holds. The residual strain in the layers grown on a graded buffer is larger than in layers grown directly on GaAs, which is in line with the Tersoff

Table 1
Summary of XRD results

Sample No.	Misfit slope k (%)	In content x	Tilting angle θ_t (°)	FWHM (mrad)	Residual strain ε (10^{-3})	
					XRD	Tersoff model
541	–	1	0.18	1.6	0.9	–
542	6.0	1	1.74	6.2	1.9	3.5
544	3.0	1	1.35	7.9	1.4	2.6
545	2.0	1	1.19	5.7	1.2	2.2
552	–	0.741	< 0.01	4.2	1.3	–
553	5.3	0.740	0.92	8.9	3.4	3.0
554	–	0.571	< 0.01	6.2	< 0.1	–
557	5.1	0.575	1.01	11.1	0.7	2.7

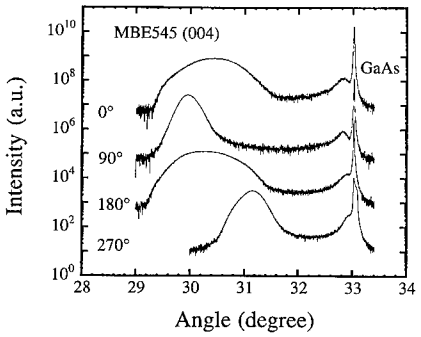

Fig. 4. XRD rocking curve from a 2 μm thick InAs layer grown on a 3.6 μm thick InAlAs graded buffer.

model [10]. The large strain force pushes nucleated dislocations towards sample edges and interface. Thus, the dislocation density is reduced. According to Tersoff [10] the residual strain near the surface is

$$\varepsilon = (2\lambda k/bc)^{1/2}, \quad (1)$$

where λ is the energy per unit length of dislocation, b is the Burgers vector and c is the appropriate elastic constant for biaxial strain. The calculated residual strain is also listed in Table 1. It increases with the misfit slope, in agreement with the observation. However, the calculated ε-values are larger than the measured data except for #553. This is due to further strain relaxation in the 2 μm thick InGaAs layer because of a small lattice mismatch between the graded buffer and the bulk layer. For the InAs samples with $x_f = 0.995$, this lattice mismatch is larger.

A comparative study of electron mobility in samples with and without a graded buffer was made. Since the mobility values depend highly on the cleanness of the MBE system and the growth conditions, we only compare samples grown subsequently under similar growth conditions. The van der Pauw method was used in Hall-effect measurements and all data were measured at a magnetic field of 0.2 T and a current of 10 μA. Table 2 lists electron mobility, μ, and carrier density, n, of the InAs layers using a Hall coefficient of 1.3. Use of a graded buffer increases mobility by 10%–15% at 300 K for both As_4 and As_2 sources. Compared with the InGaAs graded buffer, use of an InAlAs graded buffer reduces background carrier density without significant decrease of mobility. When the L_{grad} is increased from 1.2 to 3.6 μm, the mobility is nearly unchanged at 300 K and decreases slightly at 77 K. Hence, a thick graded buffer does not improve transport properties.

We have also grown InAs layers with different thicknesses on a 1.2 μm thick InAlAs graded buffer. The mobility at 300 K increases from 1.08×10^4 cm^2/(V s) for the 2 μm layer to 1.39×10^4 cm^2/(V s) for the 10 μm layer. The measured conductivity, σ, and Hall factor, R, are shown in Fig. 5. It is well known that for InAs the Fermi level is pinned 0.2 eV above the conduction band minimum [15] and a surface accumulation layer exists with a high sheet electron concentration [16]. Hence, the measured mobility

Table 2
Summary of transport properties from InAs layers with and without InAlAs graded buffer

Sample No.	Description	300 K		77 K	
		μ (10^4 cm^2/(V s))	n (10^{16} cm^{-2})	μ (10^4 cm^2/(V s))	n (10^{16} cm^{-2})
As_4 source, T_g = 420–425°C, d = 3 μm					
501	reference	1.04	2.09	2.45	0.95
518	on 1 μm InGaAs buffer	1.21	4.00	2.20	2.60
519	on 1 μm InAlAs buffer	1.11	1.77	3.10	0.79
520	on 3 μm InAlAs buffer	1.14	1.79	3.60	0.82
As_2 source, T_g = 460–470°C, d = 2 μm					
541	reference, L_{grad} = 0	0.87	2.91	2.50	1.21
542	L_{grad} = 1.2 μm	1.08	2.24	2.92	1.07
544	L_{grad} = 2.4 μm	1.13	2.43	2.85	1.16
545	L_{grad} = 3.6 μm	1.03	2.42	2.69	1.08

is an averaged value due to this parallel conduction. For two conducting channels the σ and R can be expressed by [17]

$$R = \frac{(d_b + d_s)(R_b\sigma_b^2 d_b + R_s\sigma_s^2 d_s)}{(\sigma_b d_b + \sigma_s d_s)^2}, \quad (2)$$

$$\sigma = \frac{(\sigma_b d_b + \sigma_s d_s)}{d_b + d_s}, \quad (3)$$

where subscripts b and s denote bulk and surface layer, respectively, and d is the layer thickness. This is a good assumption here, since no abrupt band offset exists at the interface between the graded buffer and the InAs layer. The best theoretical fits using Eqs. (2) and (3) are shown in Fig. 5 by lines using $\mu_b = 1.8 \times 10^4$ cm^2/(V s), $n_b = 2.7 \times 10^{15}$ cm^{-3} $\mu_s = 8.9 \times 10^3$ cm^2/(V s), $n_s = 4.4 \times 10^{12}$ cm^{-2} at 300 K and $\mu_b = 5.1 \times 10^4$ cm^2/(V s), $n_b = 1.1 \times 10^{15}$ cm^{-3}, $\mu_s = 2.7 \times 10^4$ cm^2/(V s), $n_s = 1.8 \times 10^{12}$ cm^{-2} at 77 K. From this we can estimate the maximum dislocation density. Theoretical calculations have revealed that the lattice scattering limits the 300 K mobility of InAs to be 3.5×10^4 cm^2/(V s) [18]. The mobility due to the ionized impurity scattering in our case is over 1×10^6 cm^2/(V s) and thus negligible. If we assume that among the other scattering mechanisms only dislocation scattering is significant, this gives us 3.7×10^4 cm^2/(V s). The maximum dislocation density can then be calculated [19] to be 4×10^7 cm^{-2}.

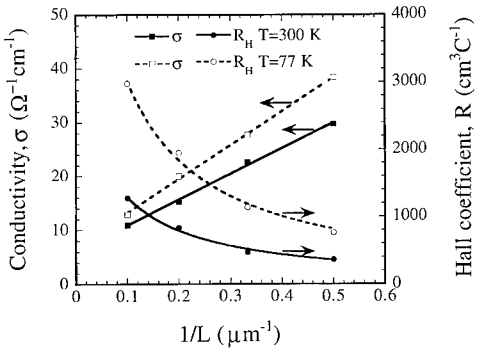

Fig. 5. Measured conductivity and Hall factor as a function of inverse InAs thickness. Lines are theoretical fits.

Fig. 6 shows the transport properties of $In_xGa_{1-x}As$ layer as a function of In content measured at (a) 300 K and (b) 77 K. Again, a higher electron mobility is found in the layers grown on an InAlAs graded buffer. The mobility decreases rapidly when the x-value is reduced from 1. This can be partly explained by the fact that the growth conditions are not optimized for the $In_xGa_{1-x}As$ layers and partly by the increased alloy scattering. For $x = 0.57$, the mobility at 77 K is smaller than at 300 K. To understand the scattering mechanisms behind this abnormal phenomenon, a temperature dependent mobility measurement is necessary.

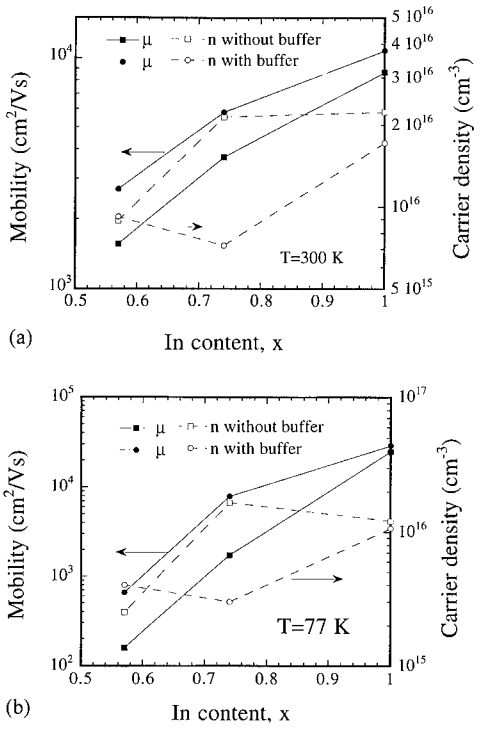

Fig. 6. Electron mobility and carrier density from $In_xGa_{1-x}As$ grown with and without InAlAs graded buffer measured at (a) 300 K and (b) 77 K.

4. Conclusions

We have studied surface, structural and transport properties of MBE grown $In_xAl_{1-x}As$ ($x_f = 0.8$) graded buffers on GaAs and bulk $In_xGa_{1-x}As$ ($0.57 \leqslant x \leqslant 1$) layers with and without such a graded buffer. The surface of the graded buffers revealed random and rough morphology. The rms roughness value increased with growth temperature and graded buffer thickness. A small roughness value of 2–3 nm was obtained for $L_{grad} \leqslant 1$ μm and $T_g \leqslant 350$°C. The $In_xGa_{1-x}As$ layers grown on an InAlAs graded buffer showed a larger tilting angle, a broader FWHM and a higher residual strain as compared with the layers grown directly on GaAs. Transport properties were improved in layers grown on a graded buffer. Increasing the graded buffer thickness did not increase the electron mobility of InAs for $L_{grad} \geqslant 1.2$ μm. The thickness dependent mobility of InAs can be well explained by assuming two conducting channels. The extracted electron mobility of the bulk InAs is 1.8×10^4 cm^2/(V s) at 300 K and 5.1×10^4 cm^2/(V s) at 77 K.

Acknowledgements

Professor E. Kolleberg is acknowledged for his support of this work. The Swedish Research Council for Engineering Science (TFR) is acknowledged for financial support.

References

[1] K. Chang, P. Bhattacharya and R. Lai, J. Appl. Phys. 67 (1990) 3323.
[2] P. Ribas, V. Krishnamoorthy and R.M. Park, Appl. Phys. Lett. 57 (1990) 1040.
[3] K. Inoue, J.C. Harmand and T. Matsuno, J. Crystal Growth 111 (1991) 313.
[4] F.K. LeGoues, B.S. Meyerson and J.F. Morar, Phys. Rev. Lett. 66 (1991) 2903.
[5] F.K. LeGoues, B.S. Meyerson, J.F. Morar and P.D. Kirchner, J. Appl. Phys. 71 (1992) 4230.
[6] J.C.P. Chang, J. Chen, J.M. Fernandez, H.H. Wieder and K.L. Kavanagh, Appl. Phys. Lett. 60 (1992) 1129.
[7] V. Krishnamoorthy, Y.W. Lin and R.M. Park, J. Appl. Phys. 72 (1992) 1752.
[8] S.I. Molina, F.J. Pacheco, D. Araujo, R. Garcia, A. Sacedon, E. Kalleja, Z. Yang and P. Kidd, Appl. Phys. Lett. 65 (1994) 2460.
[9] K. Häusler, K. Eberl and W. Sigle, Semicond. Sci. Technol. 10 (1995) 167.
[10] J. Tersoff, Appl. Phys. Lett. 62 (1993) 693.
[11] N. Rorsman, C. Karlsson, S.M. Wang, H. Zirath and T.G. Andersson, Electron. Lett. 31 (1995) 1292.
[12] M. Chertouk, H. Heiss, D. Xu, S. Kraus, W. Klein, G. Böhm, G. Tränkle and G. Weimann, Microwave Opt. Technol. Lett. 11 (1996) 145.
[13] H. Rhodin, A. Nagy, V. Robbins, C. Su, C. Madden, A. Wakita, J. Raggio and J. Seeger, in: Proc. 1995 IEEE 7th Int. Conf. InP and Related Mater. (1995) p. 73.
[14] T.P. Chin, J.C.P. Chang, K.L. Kavanagh, C.W. Tu, P.D. Kirchner and J.M. Woodall, Appl. Phys. Lett. 62 (1993) 2369.
[15] H.H. Wieder, in: Properties of Lattice-Matched and Strained InGaAs, Ed. P. Bhattacharya (INSPEC, London, 1993) p. 137.
[16] D.L. Partin and J. Heremans, in: Handbook on Semiconductor, Vol. 3A, Ed. S Mahajan (Elsevier, Amsterdam, 1994) p. 420.
[17] R.L. Petritz, Phys. Rev. 97 (1955) 641.
[18] Y.J. Jung, B.H. Kim, H.J. Lee and J.C. Woolley, Phys. Rev. B 26 (1982) 3151.
[19] B. Pödör, Phys. Status Solidi 16 (1966) K167.

ELSEVIER

Journal of Crystal Growth 175/176 (1997) 1022–1027

JOURNAL OF CRYSTAL GROWTH

Improved nucleation and spiral growth of PbTe on BaF_2 (1 1 1)

A.Y. Ueta[1], G. Springholz*, G. Bauer

Institut für Halbleiterphysik, Johannes Kepler Universität Linz, Altenbergstrasse 69, A-4040 Linz, Austria

Abstract

Molecular beam epitaxy of PbTe on BaF_2(1 1 1) is studied by in situ reflection high-energy electron diffraction and atomic force microscopy. It is shown that a 4 monolayer thick EuTe nucleation layer predeposited on the BaF_2 substrate drastically improves the nucleation and coalescence of the PbTe layers. After complete coalescence of the layers, PbTe growth is found to be completely dominated by growth spirals formed around threading dislocations that originate from the growth on the 4.2% lattice-mismatched BaF_2 substrates. Due to annihilation processes, the threading dislocation density rapidly decreases with layer thickness, which results in drastic increase of the 10 K electron mobilities in the layers. Thus, thick PbTe buffer layers are well suited as "virtual" substrates for IV–VI compound multilayers and heterostructures.

PACS: 68.55.Bd; 61.16.Ch; 61.14.Hg; 68.55.Jk

1. Introduction

Advances in epitaxial growth of lead-salt (IV–VI) semiconductors [1] have recently lead to room temperature operation of mid-infrared lead-salt diode lasers in pulsed mode [2] and to cw operation at 223 K [3]. While these devices are usually grown on lead-salt substrates, (1 1 1) oriented BaF_2 has proven to be an excellent alternative as substrate material for lead-salt heterostructures [4]. It is readily available in high crystalline quality and because of the well-matched thermal expansion coefficients no significant degradation of epitaxial layers occurs during thermal cycling. In addition, while lead-salt substrates are always highly conducting, BaF_2 is insulating and optically transparent, which is an essential prerequisite for the study of the electronic properties of heterostructures [5, 6].

In the present work, we carried out a systematic study of molecular beam epitaxy (MBE) of PbTe on BaF_2(1 1 1) using in situ reflection high-energy electron diffraction (RHEED) and ex situ atomic force microscopy (AFM). It is demonstrated that by using a thin EuTe nucleation layer predeposited on the BaF_2 substrate, the 3D nucleation of PbTe can be drastically improved and extremely smooth surfaces can be obtained already after 300 Å layer

* Corresponding author. Fax: + 43 732 2468 9650; e-mail: g.springholz@hlphys.uni-linz. ac.at.

[1] Permanent address: Instituto Nacional de Pesquisas Espaciais-INPE-LAS, 12227-010 São José dos Campos, Brazil.

0022-0248/97/$17.00 Copyright © 1997 Elsevier Science B.V. All rights reserved
PII S0022-0248(96)00985-2

thickness. Due to the 4.2% lattice-mismatch of PbTe relative to the BaF_2 substrate we observe a high density of threading dislocations on these surfaces. These give rise to a spiral type of growth mode during further deposition. While such type of growth mode is well known and understood for bulk crystal growth at low supersaturation [7], it is surprising that this growth mode is also present under MBE conditions far from thermodynamic equilibrium. From AFM and scanning tunneling microscopy we find a very rapid decrease of the threading dislocation density with increasing layer thickness. This decrease is correlated with an increase of the low-temperature electron mobilities in the epitaxial layers by two orders of magnitude, reaching more than 2×10^6 cm^2/V·s for layers larger than 3 μm in thickness.

2. Experimental procedure

Epitaxial growth was carried out in a Riber 1000 MBE system with standard effusion cells for PbTe, Eu, Te_2, and Bi_2Te_3 [5], where the latter was used for n-type doping. Cleaved BaF_2(1 1 1) substrates were baked at 500°C for 15 min prior to epitaxial growth. For PbTe a substrate temperature of 340°C and growth rates of about 1.4 μm/h were used. Additional Te_2 flux was used in order to improve PbTe growth [8]. In situ RHEED was carried out using a 35 keV electron gun and the surface structure of the samples were studied using a Park Scientific Autoprobe CP AFM operated in contact mode. With this, the monolayer step structure could be clearly resolved in air. In situ UHV scanning tunneling microscopy (STM) studies were also performed [9].

3. Nucleation of PbTe on BaF_2 (1 1 1)

Due to the much larger (1 1 1) free surface energies of the lead salts as compared to BaF_2, epitaxial growth always starts in a 3D Vollmer–Weber growth mode, where large triangular-shaped pyramidal islands with low-energy (1 0 0) side facets are formed on the substrate surface [10]. In situ RHEED studies show that coalescence of these islands begins only for layer thicknesses larger than 1000 Å, and a completely streaked RHEED pattern characteristic of a 2D surface is usually restored not before 0.5 μm layer deposition [11, 12]. Therefore, for high-quality lead-salt heterostructures always thick buffer layers have to be deposited on BaF_2. In principle, the same nucleation behavior is observed also for other lead-salt compounds, although it is noted that the coalescence behavior can be quite different for BaF_2 surface areas preirradiated by the RHEED high-energy electron beam.

For MBE growth of the ternary compound $Pb_{1-x}Eu_xTe$ on BaF_2 (1 1 1), however, we found that a complete layer coalescence takes place already at 500 Å layer thickness, even when the Eu content is below 1%. This is a factor of 10 faster as for the pure binary compound. Since such a small Eu content does not change the overall growth properties, the drastic improvement can be only due to a different interaction between Eu and the BaF_2 substrate. Indeed, from separate experiments we find that a few monolayers (ML) of pure EuTe predeposited on BaF_2 just before PbTe growth results in a similar improvement of the coalescence behavior. The pure EuTe compound has the same rock salt crystal structure as the lead-salt compounds and the lattice-mismatch with respect to PbTe is only 2.1%. EuTe is grown using elemental beam flux sources with excess Te_2 flux in order to retain the right stoichiometry of the compound [13].

Fig. 1 shows the RHEED patterns recorded for such a growth sequence. In this case, after the usual substrate preheating procedure, first 4 ML EuTe is deposited on the BaF_2 surface. Instantaneously, the RHEED patterns changes to a 3D transmission diffraction pattern (see Fig. 1), indicating the presence of a 3D growth mode also for the EuTe case. When PbTe is deposited on top of this EuTe nucleation layer, initially, the surface roughens even more, as is indicated by a slight faceting of the diffraction spots (see RHEED patterns for 10 Å PbTe in Fig. 1). Then, however, a rapid smoothening of the surface takes place and already at 50 Å layer thickness the onset of streaking is observed in the RHEED patterns, and very rapidly a completely streaked RHEED pattern is restored (Fig. 1). Thus, already at 200–300 Å PbTe layer

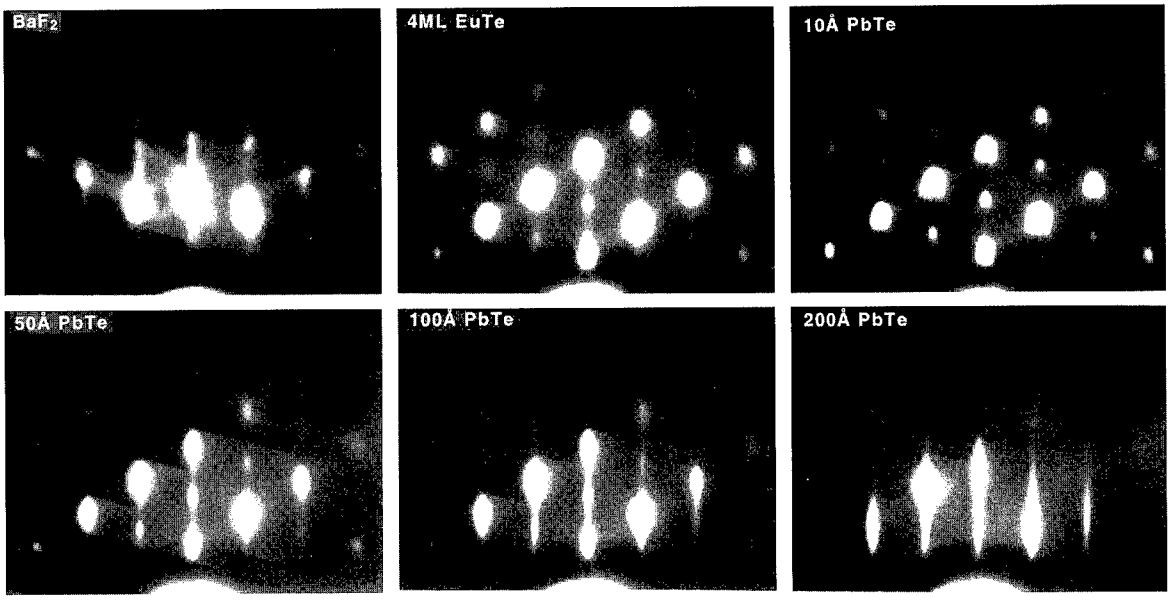

Fig. 1. Sequence of RHEED patterns ([1 1 0] azimuth direction) recorded for PbTe MBE growth on BaF_2(1 1 1) using a 4 ML EuTe nucleation layer. From top left to bottom right: BaF_2 substrate, 4 ML EuTe, 10 Å PbTe, 50 Å PbTe, 100 Å PbTe and 200 Å PbTe.

thickness a smooth 2D epitaxial surface is obtained by this modified growth sequence.

4. Spiral growth and structural properties

AFM images taken after complete coalescence of the PbTe layers show that the epitaxial surface at 500 Å layer thickness is very smooth even on a large length scale (see Fig. 2a). These surfaces consist only of monolayer steps due to epitaxial growth. In addition, detailed STM studies reveal that most of the surface step segments are terminated by threading dislocations (TD), as indicated in Fig. 2b and Fig. 2c by the arrows. These threading dislocations originate from the growth on the 4.2% lattice-mismatched substrate and connect the misfit dislocation segments at the PbTe(EuTe)/BaF_2 interface with the free surface, as shown schematically in Fig. 3.

If one draws a closed loop around a threading dislocation on the surface, there remains a net surface normal displacement of 3.7 Å, which indicates that the threading dislocations are of screw-type character. In the lead-salt compounds, the dislocation Burgers vector is usually of $\frac{1}{2}$[1 1 0] type, which is inclined by 54.7° with respect to the (1 1 1) interface. Therefore, it has 3.72 Å surface normal component, which corresponds exactly to the height of the resulting step on the surface. As evident from Fig. 2b and Fig. 2c, most of the surface steps produced by the TDs are terminated at the other end by a second dislocation with opposite Burgers vector.

Since in our AFM images, we usually do not observe 2D islands nucleated on the epitaxial surface, PbTe growth proceeds in a pure step flow growth mode where deposition of atoms results in a *lateral* growth at the step edges. However, since the end points of these surface steps are *pinned* by the threading dislocations, this lateral step growth eventually leads to the formation of growth spirals on the surface (see Fig. 2), similar as in dislocation-mediated growth of bulk single crystal. As more material is deposited on the surface, the TD density rapidly decreases. Since the diameter of the growth spirals is equal to the spacing of the TDs on the surface, larger and larger

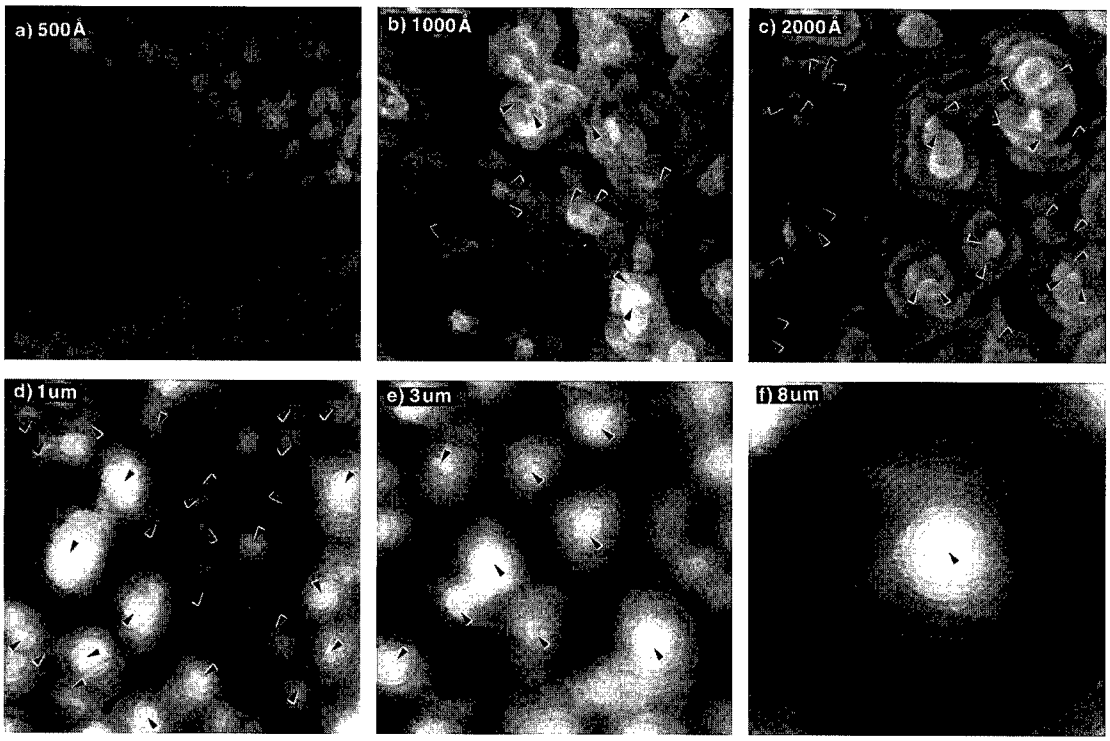

Fig. 2. AFM images of PbTe epitaxial layers with different layer thicknesses deposited on BaF_2(1 1 1) using a 4 ML EuTe nucleation layer. From top left to bottom right: 500 Å PbTe, 1000 Å PbTe, 2000 Å PbTe, 1 μm PbTe, 3 μm PbTe and 8 μm PbTe. Note the different scales of the images which is 4×4 μm^2 for the top row and 8×8 μm^2 for the bottom row. The arrows in the images indicate threading dislocations originating from the growth on the 4.2% lattice-mismatched BaF_2 substrate.

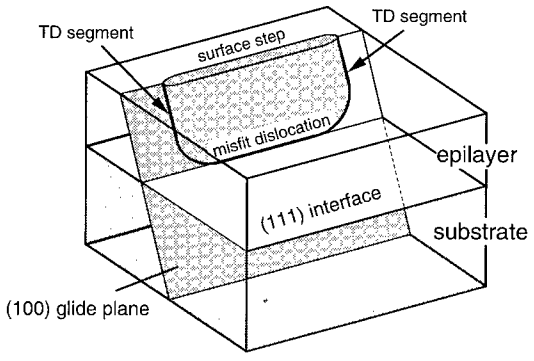

Fig. 3. Schematic illustration of the dislocation configuration.

growth spirals are produced on the surface (see Fig. 2d–Fig. 2f).

At 3 μm layer thickness, the surface is completely covered by large growth spirals, which are typically 2–3 μm apart (Fig. 2e), and at 8 μm thickness spirals with diameter as large as 8 μm are observed (note the different length scales in the AFM images shown in Fig. 2). Since throughout the whole growth process the average step spacing within the spirals remains essentially constant ($\approx$2000 Å, see Fig. 2), the large growth spirals consist of many turns and as a result, the centers of these spirals are elevated by more than 50 Å above the rest of the surface. This gives rise to a gentle overall hillock structure of the PbTe surfaces that is usually observed by Normarski microscopy.

As is evident from Fig. 2, both right- and left-handed growth spirals are observed on the surface. Thus, threading dislocations with different orientations of the Burgers vector are present in the layers. Due to the elastic strain fields of dislocations, dislocations with anti parallel Burgers vector are strongly attracted to each other. As a result, they move

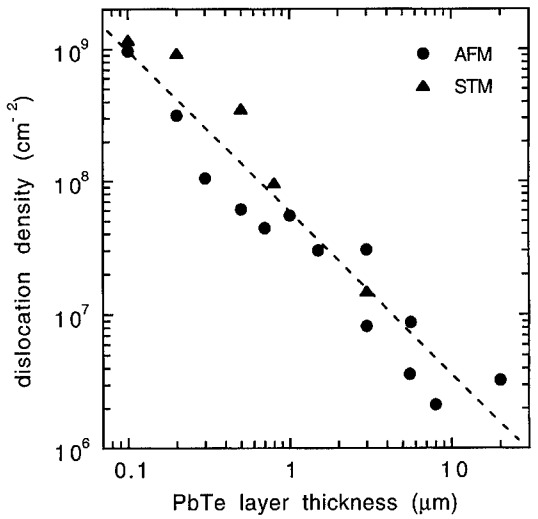

Fig. 4. Threading dislocation density for PbTe layers on BaF_2 as a function of layer thickness, determined by STM (▲) and AFM (•).

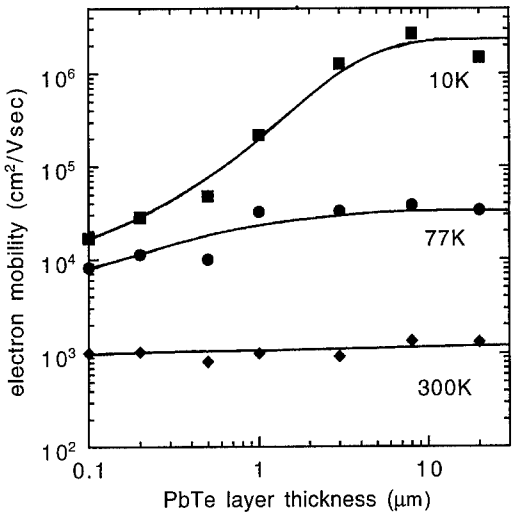

Fig. 5. Electron mobility of PbTe layers on (1 1 1)BaF_2 substrates as a function of layer thickness at 10 (●), 77 (■) and 300 K (◆).

closer and closer together and when they meet annihilate each other, i.e., the threading arms of the misfit dislocations are removed. This is the mechanism responsible to the reduction of the TD density as growth proceeds.

From STM and AFM images taken at various layer thicknesses, we have determined the TD density as a function of layer thickness and the result is shown in Fig. 4. We find a surprisingly rapid decrease of the TD density with increasing layer thickness from above 1.5×10^9 cm^{-2} for 1000 Å layer thickness, to a few times 10^6 cm^{-2} for layers of several μm in thickness, following roughly a power law dependence with a negative exponent of 1.2 (dashed line in Fig. 4). This rapid decrease implies a quite high dislocation mobility at the elevated growth temperatures, which is consistent with recent thermal cycling studies of lead-salt epitaxial layers on Si(1 1 1) substrates [14].

Fig. 5 shows the carrier mobilities of PbTe epitaxial layer as a function of layer thickness obtained from temperature-dependent Hall effect measurements. In this sample series, Bi-doping was used to adjust the n-type carrier concentration to be in the range of the mid-10^{17} cm^{-3}, whereas not intensionally doped layers of less than 0.5 μm in thickness are usually p-type of the order of 10^{18} cm^{-3}. While the phonon-limited room temperature mobility of the layers is essential constant for all layers, we observe a drastic increase of the 10 K mobilities by two orders of magnitude from 2×10^4 for layers of 1000 Å in thickness to above 2×10^6 cm^2/V·s for layers exceeding 3 μm. This rapid increase clearly indicates a strong correlation between carrier mobility and TD density in PbTe epitaxial layers.

5. Conclusions

In conclusion, it was shown that MBE growth of PbTe on BaF_2(1 1 1) substrates can be greatly improved by the use of a thin EuTe nucleation layer predeposited on the BaF_2 substrate. From AFM studies, the surface structure of these layers is found to be determined mainly by threading dislocations originating from the PbTe/BaF_2 interface. This, in combination with persisting step flow growth results in a unique spiral type of growth mode that is usually not observed for strained-layer heteroepitaxy of other semiconductors. Continued growth results in a drastic decrease of the threading dislocation density, leading to significant improvements in the electronic properties of the layers.

Acknowledgements

This work was supported by the Jubiläumsfonds der Österreichischen Nationalbank, FWF (#11557) and BMWVK, Austria and the "Conselho Nacional de Desenvolvimento Cientifico e Tecnologico do Brasil".

References

[1] D.L. Partin, in: Semiconductor and Semimetals, Vol. 33, Eds. R.K. Williams and A.C. Beer (Academic Press, New York, 1991) p. 311.
[2] Z. Shi, M. Tacke, A. Lambrecht and H. Böttner, Appl. Phys. Lett. 66 (1995) 2537.
[3] Z. Feit, M. McDonald, R.J. Woods, V. Archambault and P. Mak, Appl. Phys. Lett. 68 (1996) 738.
[4] H. Holloway, in: Physics of Thin Films, Vol. 11, Eds. G. Hass and M.H. Francombe (Academic Press, New York, 1980) p. 105.
[5] S. Yuan, G. Springholz, G. Bauer and M. Kriechbaum, Phys. Rev. B 49 (1994) 5476.
[6] G. Springholz, G. Ihninger, G. Bauer, M.M. Olver, J.Z. Pastalan, S. Romaine and B.B. Goldberg, Appl. Phys. Lett. 63 (1993) 2908.
[7] W.K. Burton, N. Cabrera and F.C. Frank, Philos. Trans. R. Soc. London A 243 (1951) 299.
[8] G. Springholz, G. Bauer and G. Ihninger, J. Crystal Growth 127 (1993) 302.
[9] G. Springholz, A.Y. Ueta, N. Frank and G. Bauer, Appl. Phys. Lett. 69 (1996) 2822.
[10] H. Clemens, E.J. Fantner, W. Ruhs and G. Bauer, J. Crystal Growth 66 (1984) 251.
[11] H. Clemens, H. Krenn, B. Tranta, P. Ofner and G. Bauer, Superlattice Microstruct. 4 (1988) 591.
[12] J. Fuchs, Z. Feit and H. Preier, Appl. Phys. Lett. 53 (1988) 894.
[13] G. Springholz and G. Bauer, Phys. Rev. B 48 (1993) 10998.
[14] H. Zogg, S. Blunier, A. Fach, C. Maissen, P. Müller, S. Teodoropal, V. Meyer, G. Kostorz, A. Dommann and T. Richmond, Phys. Rev. B 50 (1994) 10801.

ELSEVIER

Journal of Crystal Growth 175/176 (1997) 1028–1032

JOURNAL OF CRYSTAL GROWTH

Molecular beam epitaxy of $Al_{0.48}In_{0.52}As/Ga_{0.47}In_{0.53}As$ heterostructures on metamorphic $Al_xGa_yIn_{1-x-y}As$ buffer layers

M. Haupt*, K. Köhler, P. Ganser, S. Müller, W. Rothemund

Fraunhofer-Institut für Angewandte Festkörperphysik, Tullastrasse 72, D-79108 Freiburg, Germany

Abstract

Ternary $Al_xIn_{1-x}As/Ga_yIn_{1-y}As$ heterostructures with a lattice mismatch up to 4% are grown on GaAs by molecular beam epitaxy. Two buffer layer concepts to compensate the lattice misfit between the $Al_xIn_{1-x}As/Ga_yIn_{1-y}As$ layers and the GaAs substrate using the quaternary $Al_xGa_yIn_{1-y}As$ in a linear graded and two-step graded fashion, respectively, are presented. The Al and Ga content of the ternary layers were chosen to be $x = 0.48$ and $y = 0.47$, respectively, in order to obtain the same heterostructures identical to those grown lattice matched on InP as a reference. The surface morphology and the transport properties of $Al_{0.48}In_{0.52}As/Ga_{0.47}In_{0.53}As$ high-electron mobility transistor structures were studied by atomic force microscopy and Hall measurements, respectively. Optical properties were investigated by low-temperature photoluminescence on quantum well structures. The use of the two step graded buffer layers resulted in three-dimensional layer growth and inferior layer quality. In contrast, the linear graded buffer approach was found to result in superior heterostructure properties due to the two-dimensional growth mode during the whole growth process resulting in the typical cross-hatched surface morphology.

PACS: 61.55; 68.55; 72.00; 72.90; 78.55; 81.15

Keywords: Molecular beam epitaxy; Metamorphic growth; AlInAs/GaInAs heterostructures

1. Introduction

Ternary $Al_{0.48}In_{0.52}As/Ga_{0.47}In_{0.53}As$ heterostructures lattice matched to InP offer a wide range of applications for electronic and optoelectronic devices. This material system is especially suitable for applications in long-wavelength optical-communication range at wavelengths between 1.3 and 1.55 μm. Interesting as well are the high-electron mobility and concentration achieved in modulation-doped $Al_{0.48}In_{0.52}As/Ga_{0.47}In_{0.53}As$ heterostructures for the design of high-speed field effect transistors [1]. InP substrates are generally more expensive than high-quality GaAs substrates, it is therefore desirable to combine the advantages of $Al_{0.48}In_{0.52}As/Ga_{0.47}In_{0.53}As$ heterostructures

* Corresponding author.

0022-0248/97/$17.00 Copyright © 1997 Elsevier Science B.V. All rights reserved
PII S0022-0248(96)01013-5

with the low cost and availability of large GaAs substrates. To achieve successful growth of possible $Al_{0.48}In_{0.52}As/Ga_{0.47}In_{0.53}As$ device structures, the large mismatch between the GaAs substrate and the $Al_{0.48}In_{0.52}As/Ga_{0.47}In_{0.53}As$ high-electron mobility transistor (HEMT) and quantum well (QW) structures has to be accomodated by a suitable epitaxial buffer layer sequence. This resorts to a more complicated growth process. A successful epitaxy of relaxed $Al_xIn_{1-x}As/Ga_yIn_{1-y}As$ on GaAs with good material quality can be achieved by a stepwise or continuous change of the In content (and thus the lattice constant) during growth of a ternary $Al_xIn_{1-x}As$ or $Ga_yIn_{1-y}As$ buffer layer and with different growth temperatures [3–7]. The growth of a relaxed buffer layer sequence provides a 'new substrate', and if the lattice constants of both $Al_xIn_{1-x}As$ and $Ga_yIn_{1-y}As$ were the same, one could grow on this new substrate lattice-matched heterostructures with an *arbitrarily chosen In content*. This work presents two buffer layer concepts to compensate the lattice misfit using the quaternary $Al_xGa_yIn_{1-x-y}As$ in a step and linear graded fashion, respectively. To preserve the advantage of GaAs substrate in terms of epitaxial cost, the buffer thickness was kept at 1 μm. The In content of the layers was chosen to be $1 - x = 0.52$ and $1 - y = 0.53$ in order to have the same heterostructures grown lattice matched on InP as a reference.

2. Experimental procedure

The heterostructures were grown by molecular beam epitaxy (MBE) in a Varian Modular Gen II on 2 in GaAs and InP substrates. The calibration of the growth rates was done by measuring RHEED intensity oscillations and performing beam equivalent pressure measurements before and after growth of the layer structures. With additional X-ray measurements (HRXRD) one is able to determine the composition of the lattice matched layers. Control of the substrate temperature was achieved with an Ircon Mod 2 infrared pyrometer. The substrates, GaAs (Freiberger Inc.) and InP (Sumitomo Inc.) were etched with $H_2O : NH_3OH : H_2O_2$ and

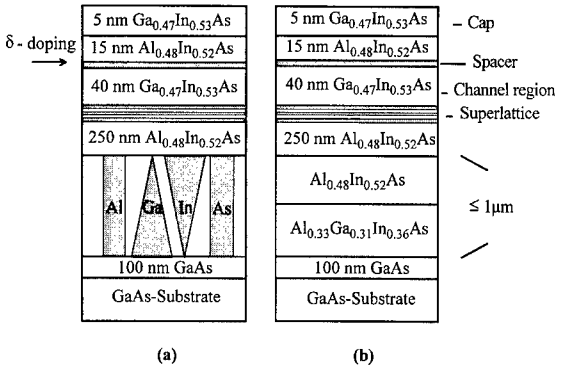

Fig. 1. MBE grown buffer structures for linear (a) and stepwise (b) compensation of the lattice misfit.

$H_2O : HCl : H_2O_2$, respectively, before loading into the MBE system. On top of the buffer structure, which is kept at a thickness of 1 μm, the appropriate structures described below were grown. The growth rate of the buffer layers was 2 μm/h. The HEMT structure has a δ-doping concentration of 5×10^{12} cm^{-2} separated by a 5 nm spacer layer from the 40 nm $Ga_{0.47}In_{0.53}As$ electron channel (Fig. 1). To obtain good morphological and electrical properties, the growth of a superlattice (10×4 nm $Al_{0.48}In_{0.52}As$/4 nm $Ga_{0.47}In_{0.53}As$) prior to growth of the HEMT structure is necessary. The optimum growth temperature of the HEMT structure was at a thermocouple readout of 600°C (pyrometer readout: 530°C) for both, lattice matched growth on InP as well as lattice relaxed growth on GaAs. The quantum well (QW) structure for the optical studies consisted of five quantum wells with well thicknesses of 20, 10, 4, 3 and 1 nm grown at the same optimized growth temperature. Before growing the actual buffer layer for the linear grading beginning with $Al_{0.51}Ga_{0.49}As$, a 100 nm GaAs layer is grown. The grading was performed using computer controlled temperature ramping for Ga and In, finally conforming to the lattice constant of $Al_{0.48}In_{0.52}As$ (Fig. 1a). The step graded buffer consists of two layers beginning with 500 nm of $Al_{0.33}Ga_{0.31}In_{0.36}As$ and continuing with 500 nm of $Al_{0.48}In_{0.52}As$ (Fig. 1b).

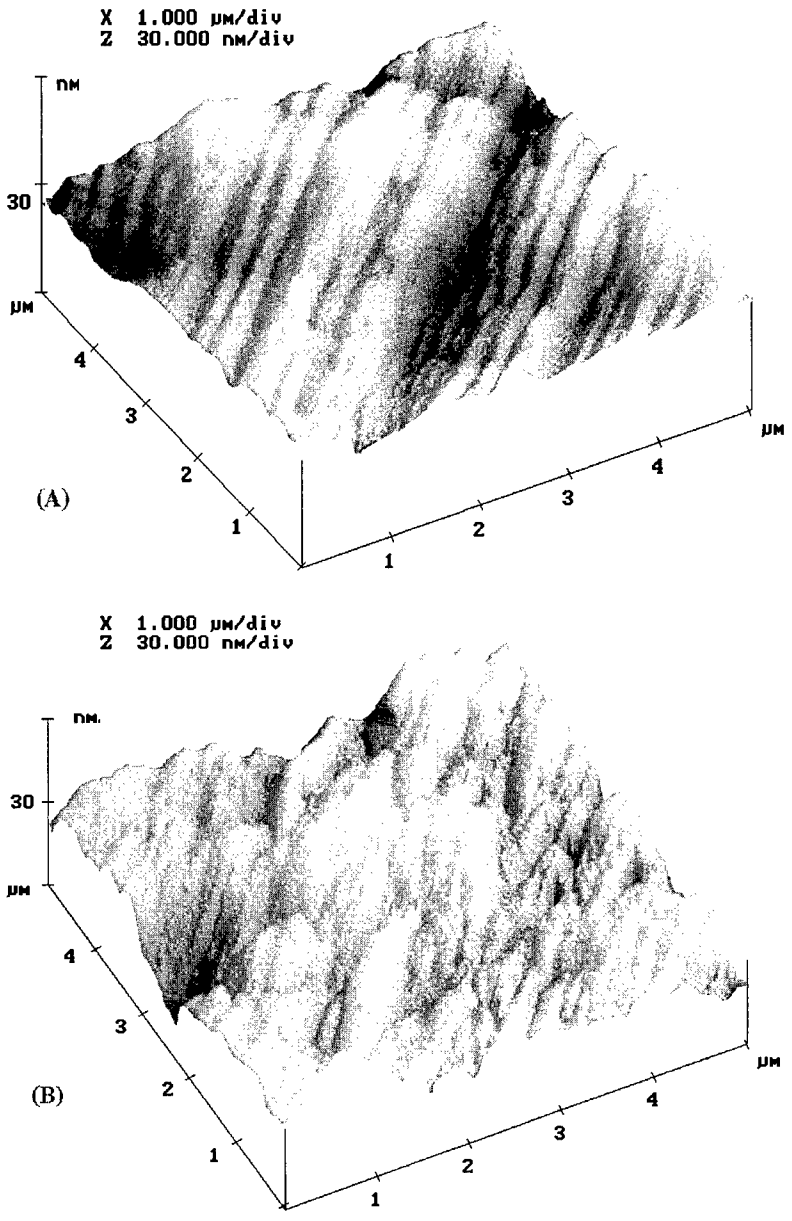

Fig. 2. AFM surface profiles: linearly graded (a) and step graded (b).

3. Results and discussion

Focusing on the surface morphology, Fig. 2a shows an atomic force microscope (AFM) surface plot obtained from a linearly graded HEMT structure. The growth temperature T_B of the buffer for this sample was 400°C (thermocouple readout). One observes a 'cross-hatched' morphology of the surface, which indicates the existence of misfit dislocations with a two-dimensional growth (2D) mode or layer by layer growth still present [8]. The 3D–AFM surface plot shows that the RMS

roughness of the 'cross-hatched' structure in the (0 1 1) direction is significantly higher (RMS value: 2.6 nm) than that of perpendicular to this direction (RMS value: 3.1 nm). For the step-graded buffer the AFM surface plot is shown in Fig. 2b. The morphology of the surface is the result of a three-dimensional (3D) island growth (RMS value: 4.1 nm). An In content of 36% results in a major change of the lattice constant after which no 2D growth of the layers occurs. The 3D growth is caused by the quaternary $Al_{0.33}Ga_{0.31}In_{0.36}As$ having a lattice misfit beyond 2% with respect to GaAs [4]. As shown by Schweizer et al. [2] and Yao et al. [6], it is necessary for 2D growth of the layers to keep the In content clearly below 35%. This requirement cannot be fulfilled with all effusion cell temperatures fixed and with only one intermediate step in the lattice constant. The range between 300°C and 400°C for the buffer growth temperature T_B has been found to yield nearly identical RMS roughness values for both step and linear grading with a slightly better surface morphology of the heterostructure utilizing the linear graded buffer. The lowest RMS roughness value of 2.6 nm was found at a substrate temperature T_B of 350°C for the linear graded buffer [9]. The same HEMT structure grown lattice matched on InP yielded a RMS roughness of 0.2 nm.

Hall mobilities of the HEMT structures with both buffer types for 300 and 77 K are given in Fig. 3. The Hall mobility $\mu_{77\,K}$, plotted as a function of the temperature T_B, apparently shows higher values for the linear-graded structures with a maximum of 38 000 $cm^2/V\,s$ (9800 $cm^2/V\,s$ at 300 K) at 450°C. For the step-graded structures a maximum of 26 000 $cm^2/V\,s$ (9200 $cm^2/V\,s$ at 300 K) at a T_B of 400°C (Fig. 3) is measured. An electron concentration of $3.0 \times 10^{12}\,cm^{-2}$ was measured for all samples. A decrease of the mobilities for T_B below 350°C and above 450°C is observed for both buffer types. The same HEMT structure grown lattice matched on InP yielded an electron mobility of 50 000 $cm^2/V\,s$ at 77 K (11 000 $cm^2/V\,s$ at 300 K), slightly better than the values achieved on the linear-graded buffer. This difference may be attributed to the large increase in surface roughness in the latter case, and therefore to an increase in the interface roughness of the electron channel.

The line width data of a series of $Al_{0.48}In_{0.52}As/Ga_{0.47}In_{0.53}As$ QWs with well widths of 20, 10, 4, 3, and 1 nm are shown in Fig. 4. The superior interface quality of the QWs grown on the linear-graded buffer, compared to the growth on the step-graded buffer, is obvious from the reduced PL line width. Line widths obtained of the structures grown on linear-graded buffer have values between

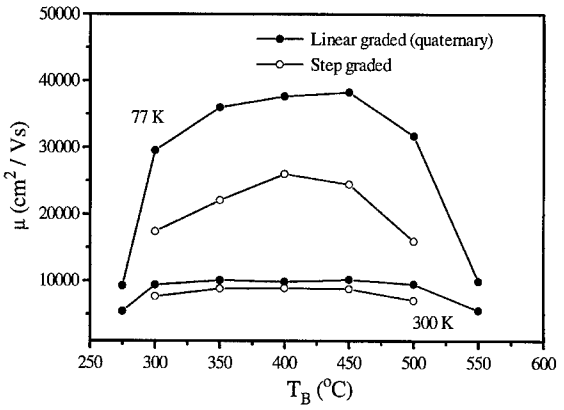

Fig. 3. Hall mobilities at 300 and 77 K of $Al_{0.48}In_{0.52}As/Ga_{0.47}In_{0.53}As$ HEMT structures grown on linear- and step-graded buffers as a function of the buffer-growth temperatures.

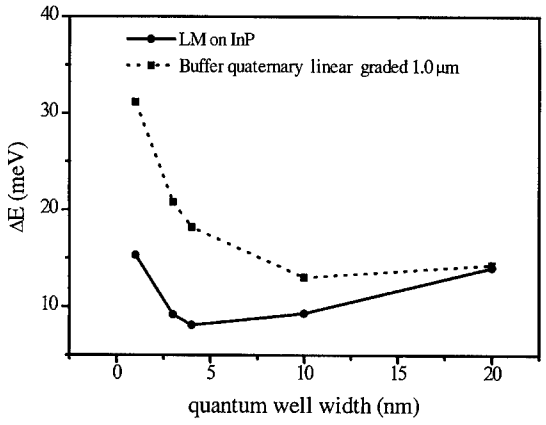

Fig. 4. PL line width data of five quantum wells grown lattice matched on InP and on GaAs with a lattice relaxed linear graded buffer.

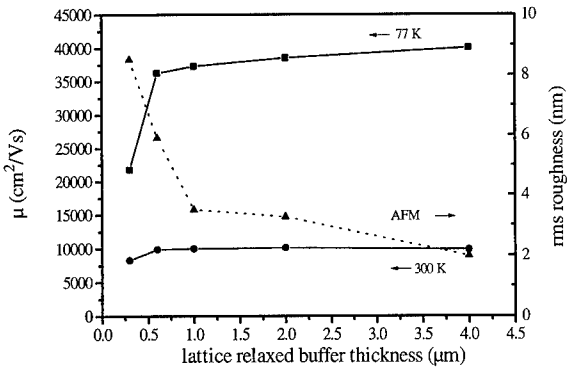

Fig. 5. Electron mobility and RMS surface roughness as a function of the lattice relaxed buffer thickness.

17 and 33 meV (Fig. 4). The same structure grown on step-graded buffer yielded line widths above 35 meV. The maximum intensities of the PL spectra for the QWs grown on linear- and step-graded buffer layers each differ by a factor of ten compared to the QWs grown lattice matched on InP [9]. Together with the Hall mobility data the linear-graded buffer concept yielded results close to those achieved on InP. In addition, $Al_{0.48}In_{0.52}As/Ga_{0.47}In_{0.53}As$ quantum wells grown lattice matched on InP show the lowest line widths in the range of 7–15 meV (Fig. 4) which are comparable to published data [10].

However, after the successful growth of $Al_{0.48}In_{0.52}As/Ga_{0.47}In_{0.53}As$ heterostructures on GaAs which yielded the best results grown on a linear-graded lattice-relaxed buffer an experiment in terms of varying the thickness of the lattice relaxed buffer was performed. Intuitively, one would suggest an increase in electron mobility and a decrease in RMS roughness, respectively, by the use of very thick (2–4 μm) lattice-relaxed buffer layers due to fewer misfit dislocations. As it is clearly observed from Fig. 5, the growth of thicker buffer material only yields a small increase of the electron mobility and a small decease in RMS roughness, respectively, but to a large expense in epitaxial material.

4. Conclusions

Two buffer layer concepts for the lattice relaxed growth of $Al_{0.48}In_{0.52}As/Ga_{0.47}In_{0.53}As$ heterostructures on GaAs have been compared and related to the growth on InP. Electrical data yield the optimum growth temperature of the buffer at 400°C. Based on electrical and optical data, the two buffer concepts in their extreme linear- (Ga and In furnace temperatures are varied) and step-graded form (all furnace temperatures are constant) clearly show that it is favorable to vary the lattice constant during buffer growth *as smoothly as possible*. Increasing the total relaxed buffer thickness up to 4 μm only results into marginal improvements of electrical and morphological properties of the $Al_{0.48}In_{0.52}As/Ga_{0.47}In_{0.53}As$ heterostructures.

References

[1] See, e.g.: T. Fink, B. Raynor, M. Haupt, K. Köhler, J. Braunstein, N. Grün and J. Hornung, J. Vac. Sci. Technol. B 12 (1994) 3332.
[2] T. Schweizer, K. Köhler and P. Ganser, Appl. Phys. Lett. 60 (1992) 469.
[3] H. Masato, T. Masuno and K. Inoue, Jpn. J. Appl. Phys. 30 (1991) 3850.
[4] J. Chen, J.M. Fernandez, S.D. Kim and J.S. Harris, Semicond. Sci. Technol. 7 (1992) 601.
[5] S.M. Lord, B. Pezeshki and J.S. Harris, J. Crystal Growth 127 (1993) 749.
[6] J.Y. Yao, T.G. Anderson and G.L. Dunlop, J. Appl. Phys. 69 (1991) 2224.
[7] T. Mishima, K. Higuchi, M. Mori and M. Kudo, J. Crystal Growth 150 (1995) 1230.
[8] P.J. Goodhew, J. Phys. Chem. Solids 55 (1994) 1107.
[9] M. Haupt, K. Köhler, P. Ganser, S. Emminger, S. Müller and W. Rothemund, Appl. Phys. Lett. 69 (1996) 412.
[10] T. Mishima, J. Kasai, Y. Uchida and S. Takahashi, J. Crystal Growth 95 (1989) 338.

ELSEVIER

Journal of Crystal Growth 175/176 (1997) 1033–1038

JOURNAL OF CRYSTAL GROWTH

Incorporation of As_2 in $InAs_xP_{1-x}$ and its application to $InAs_xP_{1-x}$/InP quantum well structures

M. Hopkinson*, J.P.R. David

Department of Electronic and Electrical Engineering, University of Sheffield, Mappin Street, Sheffield SI 3JD, UK

Abstract

We report studies on the incorporation of arsenic in $InAs_xP_{1-x}$ layers grown on InP substrates by solid-source MBE (SS-MBE) using group V valved cracker sources. Under phosphorus stabilised growth conditions we observe that As_2 is incorporated into $InAs_xP_{1-x}$ with near-unity efficiency up to As fractions (x) of about 0.4. For higher As_2 fluxes the incorporation is increasingly non-linear and the composition saturates at a value of $x \sim 0.8$. Similar behavior has been observed for the growth of $InAs_xP_{1-x}$ on InAs. The results are applied to the growth of $InAs_xP_{1-x}$/In(GaAs)P quantum wells and to graded composition $InAs_xP_{1-x}$ buffer layers. The result indicate excellent potential for optical device applications over the wavelength range 0.9–2.0 μm.

1. Introduction

$InAs_xP_{1-x}$/InP quantum well (MQW) structures have emerged as an important material system for long wavelength optoelectronics, at wavelengths such as 1.06, 1.3 and 1.55 μm [1–4]. A favourable strain-induced valence band splitting and large conduction band discontinuity ($\Delta E_C \sim 0.6$–$0.7\Delta E_G$) offers considerable advantages for lasers and optical modulators. Devices reported include 1.3 μm separate-confinement heterostructure (SCH) lasers with low threshold current density and high characteristic temperature (T_0) [5] and 1.3 μm electroabsorption waveguide modulators [6]. Tensile-strained InGaP can be used to replace InP as the barrier layer, offering increased electron confinement and suppression of strain relaxation in strain-balanced structures. In addition the relative ease which group V compositions can be varied, together with the relatively low strain difference between InAs and InP (+3.2%) makes $InAs_xP_{1-x}$ an attractive system for graded composition buffer layers. The growth of detectors or emitters on strain-relaxed buffer layers offers access to wavelengths beyond that of conventional InP-based heteroepitaxy.

From a more fundamental point of view it is interesting to contrast the properties of $InAs_xP_{1-x}$/InP, where the interface is formed due to substitution on the group V sub-lattice, with group III alloy QW systems and in particular with strained $In_xGa_{1-x}As$/GaAs. Although high quality $In_xGa_{1-x}As$/GaAs QW's have been widely reported there are problems, particularly for high

* Corresponding author. Fax: +44 114 2726391; e-mail: m.hopkinson@sheffield.ac.uk.

0022-0248/97/$17.00 Copyright © 1997 Elsevier Science B.V. All rights reserved
PII S0022-0248(97)01228-6

indium compositions, as a consequence of indium desorption and surface segregation. The effects can alter both indium content and the compositional profile of $In_xGa_{1-x}As$ quantum wells. In contrast the interfacial quality of the group V alloy QW system $InAs_xP_{1-x}/InP$ may be influenced by intermixing or exchange between As and P and the complex incorporation behaviour of As_2 and P_2 makes compositional calibration at first sight seem very diffcult.

2. Experimental procedure

Growth was carried out using a VG V80H MBE system equipped with group III effusion sources and group-V valved cracker cells. Elemental arsenic and red-phosphorus are evaporated at temperatures of 385 and 340°C, respectively, in the evaporation zone of the valved cracker and subsequently cracked by tantalum baffles in a high temperature zone (950°C). Growth was carried out under P-stabilised (2×4) conditions at a temperature of 480–500°C using a P_2 beam equivalent pressure $\approx 5\times10^{-6}$ mbar. For the growth of $InAs_xP_{1-x}$, As_2 was co-evaporated during the growth of InP with the flux controlled by the valved cracker position. The performance characteristics of the EPI VCIII-As source are well documented. We find that the cracker cell provides a stable reproducible As_2 flux at a specific valve position. However steps must be taken to prevent the build-up of arsenic around the cracker zone by regular high temperature outgassing. The addition of a computer controlled servo-motor valve drive enables the flux to be changed from zero to a set value within a timescale ≈ 1 s.

For a fixed evaporation temperature (385°C) we have calibrated the arsenic flux as a function of cracker valve position by performing As-induced Reflection high-energy electron diffraction (RHEED) measurements on gallium terminated GaAs substrates at a temperature of 520°C. The results give a value for the incorporated arsenic flux in terms of monolayers of GaAs/s. The indium flux is measured using 'conventional' group V stabilised RHEED oscillation measurements on InAs. Both the As and In growth rates are modified to take into account the differences between the host lattice constant and InP.

3. Arsenic incorporation in $InAs_xP_{1-x}$

It has long been known that arsenic incorporates much more readily than phosphorus into III–V compounds. The effect was first quantified by Foxon et al. using modulated beam techniques [7] who showed that probability of incorporation of As_4 into GaAs or InAs is up to 50 times higher than that of P_4. The behaviour is attributed to a significantly greater surface lifetime for As_4. Their results suggested a growth scheme for mixed group V alloys, such as $InAs_xP_{1-x}$, in which the supply of the most easily incorporated group V (in this case arsenic) is restricted with respect to the group III flux. The remaining group III sites are then available for incorporation with the weakly incorporated group V (phosphorus), which is provided in excess. The growth scheme has been exploited by Hou and Tu [8] who first suggested the use of As-induced RHEED measurement technique for in situ $InAs_xP_{1-x}$ composition determination.

Fig. 1 shows the relationship between the incident (As/In) ratio and the incorporated arsenic fraction (x) in a series of $InAs_xP_{1-x}/InP$ multi-quantum well (MQW) structures, with (x) determined by post-growth X-ray diffraction analysis of single thin bulk layers and multi-quantum well structures. Two regions are observed; for $x \leqslant 0.4$, As_2 is incorporated with near-unity efficiency, whilst for higher x the dependency is increasingly nonlinear and the $InAs_xP_{1-x}$ composition tends to an asymptotic value of around 0.8. Our results are very similar to those of Hou and Tu [8]. We find the As composition (x) of our layers is relatively invariant of variations in P_2 flux. This is fortunate since the stability of the phosphorus cracker source is not as good as that of the arsenic source. We have also investigated the growth of thin $InAs_xP_{1-x}$ multilayers on InAs substrates, for which we used (As/In) values of up to, and exceeding, unity.

Despite the presence of sufficient As_2 to account for all of the available group III sites, we find that arsenic compositions of between 0.7 and 0.8 are obtained, or conversely that P_2 incorporates into

InAs at fractions of between 0.2 and 0.3. The arsenic fractions are slightly higher than those achieved on InP for similar (As/In) values. The results indicate a rapid reduction in the As_2 sticking coefficient at high surface coverage.

4. Optical properties of multi-quantum well p-i-n diodes

To investigate the optical and electrical properties of $InAs_xP_{1-x}$/InP QW's a number of p-i(MQW)-n structures have been grown with values of arsenic composition from $x = 0.15$–0.66. Table 1 lists the details of several of these structures, grouped together as structures with room temperature exciton peak positions close to the wavelengths 1.06, 1.3 and 1.55 μm. These are the wavelengths of technological interest for optoelectronic devices. All the structures had 80 Å QW thicknesses. The samples differ however in terms of barrier material, barrier thickness and total number of periods. In the absence of strong relaxation, $InAs_xP_{1-x}$ quantum well structures exhibit intense, narrow, room temperature photoluminescence (PL) emission. Fig. 2 shows relative PL data from several samples and emphasizes the wide wavelength range that can be covered by $InAs_xP_{1-x}$ QW's. The data includes for example, samples #1108 and #1125 in Table 1 which provide a comparison between 1.3 μm strained InP and strain-balanced InGaP barriers. The strain balanced 1.55 μm (#1217) is also shown in the figure. PL linewidths as low as 12 meV at room temperature and 3.5 meV at low temperature have been observed in the 1.3 μm structures.

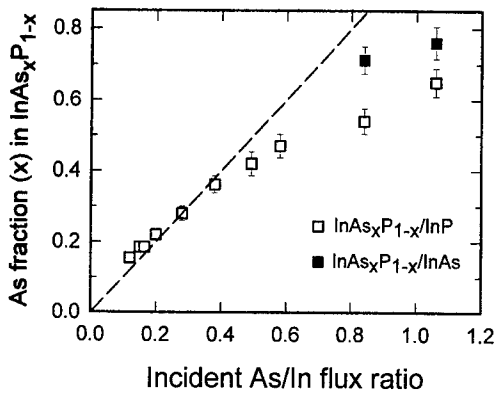

Fig. 1. Incorporated As fraction (x) in $InAs_xP_{1-x}$ as a function of incident flux ratio.

Electrical measurements have been carried out on p^+-i(MQW)-n^+ samples fabricated into 200 μm diameter mesa diodes. Typical reverse leakage values of $I_R < 10$ nA at -30 V are observed in the low strain $\lambda \approx 1.06$ μm samples. For the $\lambda \approx 1.3$ μm samples with InP barriers, barrier thickness $\geqslant 400$ Å and $\leqslant 20$ periods were required to obtain reasonable

Table 1
$InAs_xP_{1-x}$/In(GaAs)P multiquantum well structures

#	d_{Bar} (Å)	Barrier	Periods	x ($InAs_xP_{1-x}$)	Relaxation (%)	300 K Photoluminescence	
						Wavelength (nm)	FWHM (meV)
1207	150	InP	10	0.28	0	1096	18
1208	150	InP	20	0.28	0	1101	19.3
1209	150	InP	30	0.29	29	1113	17.5
1210	150	InP	50	0.28	52	1134	24.9
1108	420	InP	20	0.42	31	1314	26
1117	420	InGaAsP	20	0.41	24	1283	22
1125	420	$In_{0.96}Ga_{0.04}P$	20	0.42	11	1316	18
1216	500	InP	5	0.56	0	1502	20.8
1217	500	$In_{0.92}Ga_{0.08}P$	5	0.56	0	1530	18

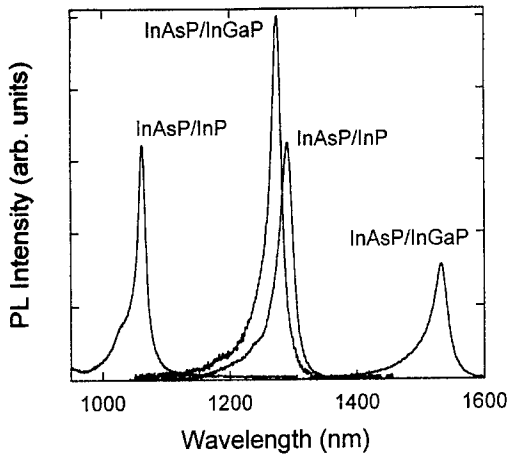

Fig. 2. Room temperature photoluminescence data for InAsP/In(Ga)P MQW structures with $\lambda \sim 1.06$, 1.3 and 1.55 μm. The PL linewidths are in the range 15–20 meV.

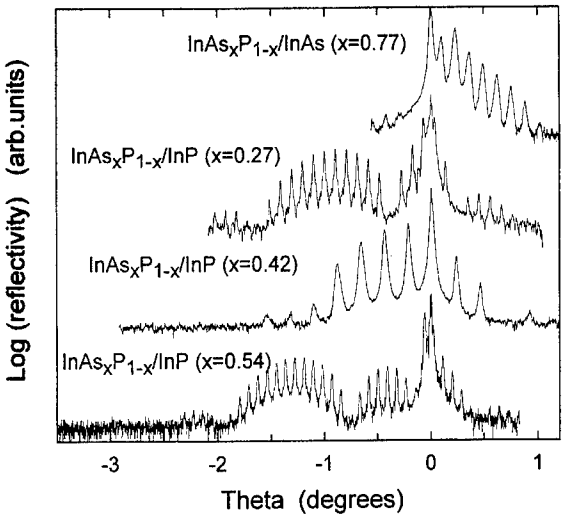

Fig. 3. X-ray diffraction data from $InAs_xP_{1-x}$/InP and $InAs_xP_{1-x}$/InAs multi-quantum well structures.

dark currents. Values of I_R of 1 mA at -10 V are fairly typical of these structures. Strain-balanced $InAs_{0.41}P_{0.69}/In_{0.96}Ga_{0.04}P$ MQWs show I_R values one or two orders of magnitude lower than those with InP barriers.

Although the wavelength of $InAs_xP_{1-x}$ MQW's can be extended to 1.55 μm ($x \sim 0.56$) and the optical properties of these structures are excellent (300 K linewidths of 18–20 meV) the reverse leakage of the devices is rather high. The values are ~ 1 mA at -20 V for the InP barrier structure (#1216) and ~ 50 μA at -20 V for the InGaP barrier sample (#1217). These high reverse leakage values may preclude the use of such structures in applications such as optical modulators.

5. Structural characterisation

High resolution X-ray diffraction has been used to assess well composition and strain relaxation in these samples, using (0 0 4) and high/low incidence asymmetric (1 1 5) reflections. (0 0 4) reflection data from several $InAs_xP_{1-x}$/InP MQW structures is shown in Fig. 3. The data also shows the InAs-based structure, which has thin $InAs_xP_{1-x}$ tensile barriers, and which was described in relation to the As incorporation measurements of Fig. 1. The data shows the excellent structural quality of $InAs_xP_{1-x}$/InP which is at least comparable to $In_xGa_{1-x}As$/GaAs. Values of relaxation obtained from X-ray measurements are given in Table 1. It can be seen that the level of relaxation increases with increased x, with reduced barrier width or with increasing number of periods. Plan view TEM of wedge shaped specimens has been used to image the buffer-MQW, MQW and MQW-cap interface planes of these structures. Even in the most highly relaxed samples no dislocations were observed within the MQW region. Misfit dislocation arrays were present at the buffer-MQW and at the MQW-cap interfaces, with the latter at a much lower density. The behaviour is normal for low strain MQW's, with partial relaxation occurring at the buffer-MQW interface whilst the MQW itself remains coherent [9]. The MQW acts as a single strained layer of average well-barrier composition. The relaxation data can be well explained using the geometrical theory of strain relaxation developed for single strained layers [10]. The model predicts accurately, for example, a critical layer thickness (CLT) of 420 nm for the $InAs_{0.28}P_{0.72}$ As/InP MQW's which have an average strain (ε) = 3.1×10^{-3}. This value of CLT is almost 10 times higher

than that predicted by the Matthews and Blakeslee single-kink model for the same strain value [11].

6. Compositional graded buffer layers

Graded $InAs_xP_{1-x}$ compositions can be easily grown by slowly ramping the position of the arsenic cracker valve, the variation of which is approximately linear with composition. We have grown strain-relaxed p-i-n diode structures on linear graded $InAs_xP_{1-x}$ buffer layers. For the buffer a grading rate of $x = 0.2/\mu m$ was used. The thickness of the buffer layers varies from 2.5 to 4.8 μm. After the buffer layer a step back in composition of $x \approx 0.07$ is performed to cancel the residual strain in the buffer layer. The design scheme for the linear graded buffer follows that of reference [12]. On top of the buffer layer a p-i-n diode is grown at the relaxed $InAs_xP_{1-x}$ composition. The structure is 1.5 μm Si-doped (n^+), 1.5 μm intrinsic region and 0.5 μm Be-doped (p^+) $InAs_xP_{1-x}$. A series of structures has been grown with compositions (x) of 0.32–0.85. The final compositions, as measured by post-growth X-ray analysis, are within $x \approx 0.05$ of the target composition from calibration of the valved cracker source.

Fig. 4 shows room temperature PL from a number of graded p^+-i-n^+ diode structures. The PL peak wavelength reaches 2.32 μm for the highest composition, $x \sim 0.85$. The PL wavelength is in good agreement with the expression $E_g(300\,K) = 1.351 - 1.315x + 0.32x^2$ eV for relaxed $InAs_xP_{1-x}$ layers in reference [13]. Room temperature PL linewidths are typically 35–40 meV. We can further increase the wavelength by growing $In_xGa_{1-x}As$ lattice-matched to the relaxed buffer layer. We have grown $In_{0.17}Ga_{0.83}As$ structures on relaxed $InAs_{0.7}P_{0.3}$ buffer layers which have PL emission at wavelengths $\geqslant 2.5$ μm.

Since the primary interest in such structures is for mid-IR detectors the reverse dark currents need to be fairly low. Analysis of 200 μm mesa diode structures shows a general increase in dark current and degradation in breakdown as the composition in increased. Diodes with $x \approx 0.32$ and 0.42 show dark currents in the range 1–100 nA at −10 V,

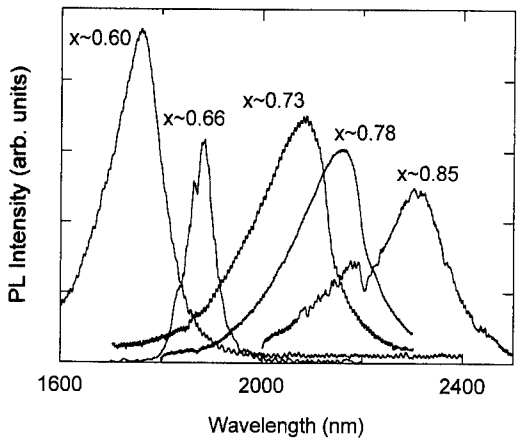

Fig. 4. Room temperature PL of $InAs_xP_{1-x}$ layers grown on strain-relaxed linear-graded buffer layers.

whilst for example for the $x \approx 0.7$ sample the value is in excess of 100 μA for the same voltage. The increase suggests that threading dislocations are not solely confined to the mismatched buffer layer in the higher strain samples and that some further improvement may be required to use these structures in applications such as avalanche photodetectors. For $x < 0.5$ however the performance is quite satisfactory and compares well with previous reports of planar pn diodes grown on generally much thicker buffer layers by MOVPE or VPE techniques [14, 15].

Acknowledgements

The authors would like to thank colleagues M.A. Pate, G. Hill and D.M. Carr (Sheffield), S.K. Haywood and P. Guy (Hull), A. Krier (Lancaster), P.N. Stavrinou (Oxford) and R. Beanland (GEC-Marconi, Caswell) for their assistance in this work.

References

[1] T.K. Woodward, T.H. Chiu and T. Sizer, II, Appl. Phys. Lett. 60 (1992) 2846.
[2] R.P. Schneider, Jr. and B.W. Wessels, J. Electron. Mater. 20 (1991) 1117.
[3] H.Q. Hou and C.W. Tu, J. Electron. Mater. 21 (1992) 137.

[4] J.P.R. David, M. Hopkinson, P.N. Stavrinou and S.K. Haywood, J. Appl. Phys. 78 (1995) 3330.
[5] M. Yamamoto, N. Yamamoto and J. Nakano, IEEE J. Quantum Electron. QE-30 (1994) 554.
[6] X.B. Mei, K.K. Loi, H.H. Wider, W.S.C. Chang and C.W. Tu, Appl. Phys. Lett. 68 (1996) 90.
[7] C.T. Foxon, B.A. Joyce and M.T. Norris, J. Crystal Growth 49 (1990) 132.
[8] H.Q. Hou and C.W. Tu, Appl. Phys. Lett. 60 (1992) 1873.
[9] D.C. Houghton, D.D. Perovic, J.-M. Baribeau and G.C. Weatherly, J. Appl. Phys. 67 (1990) 1850.
[10] D.J. Dunstan, P. Kidd, L.K. Howard and R.H. Dixon, Appl. Phys. Lett. 59 (1991) 3390.
[11] J.W. Matthews and A.E. Blakeslee, J. Crystal Growth 27 (1974) 118.
[12] A. Sacedon, F. Gonzales-Sanz, E. Calleja, E. Munoz, S. Molina, F.J. Pacheco, D. Araujo, R. Garcia, M. Lourenco, Z. Yang, P. Kidd and D.J. Dunstan, Appl. Phys. Lett. 66 (1995) 3334.
[13] R.J. Nicholas, R.J. Stradling and J.C. Ramage, J. Phys. C 12 (1979) 1641.
[14] M.A. di Forte-Poisson, C. Brylinski, J. Di Persio, X. Hugo, B. Vilotitch and C. Le Noble, J. Crystal Growth 124 (1992) 782.
[15] K. Linga, G.H. Olsen, V.S. Ban, A.M. Joshi and W.F. Kosonocky, J. Lightwave Tech. 10 (1992) 1050.

ELSEVIER

Journal of Crystal Growth 175/176 (1997) 1039–1044

JOURNAL OF CRYSTAL GROWTH

Growth of abrupt GaAs/Ge heterointerfaces by atomic hydrogen-assisted molecular beam epitaxy

Yoshitaka Okada[a,*,1], James S. Harris, Jr.[a], Atsushi Sutoh[b], Mitsuo Kawabe[b]

[a] *Solid State Electronics Laboratory, Stanford University, Stanford, California 94305, USA*
[b] *Institute of Materials Science, University of Tsukuba, 1-1-1 Tennodai, Tsukuba Ibaraki, Japan*

Abstract

High-quality epitaxy of GaAs-on-Ge system has been developed at low growth temperatures around 400°C by atomic hydrogen-assisted molecular beam epitaxy (H-MBE). The segregation of Ge is significantly reduced and abrupt GaAs/Ge heterointerface is successfully formed. Using reflection high-energy electron diffraction (RHEED), secondary ion mass spectroscopy (SIMS) and atomic force microscopy (AFM) as characterization tools, it is demonstrated that enhanced layer-by-layer two-dimensional growth mode is realized from the earliest stages of growth and evolution of single-domain (2×4) GaAs(0 0 1) is achieved on vicinal Ge substrates at 400°C by H-MBE technique. The modification of growth mode and consequent improvement in material quality are explained at the simplest level by the surfactant properties of atomic H in MBE growth of GaAs.

PACS: 81.15.Hi; 81.05.Ea; 81.65.Ya; 68.35.Ct; 61.16.Ch

Keywords: MBE; Surfactant-mediated epitaxy; Heteroepitaxy; Atomic hydrogen; Segregation; Growth mode; Surface reconstruction; GaAs-on-Ge; RHEED; AFM; SIMS

1. Introduction

GaAs-on-Ge material is gaining particular interest for application to low-cost, high-efficiency solar cells [1]. Not only is the lattice-mismatch between GaAs and Ge favorably small ($< 0.1\%$), the difference in their thermal expansion coefficients $\Delta\alpha$ is also small. This is in contrast with a more popularly studied GaAs-on-Si system (lattice-mismatch of $\sim 4.0\%$ and $\Delta\alpha \approx 60\%$). However, in GaAs-on-Ge epitaxy, a serious problem of segregation and interdiffusion of Ge and As at the GaAs/Ge heterointerface arises when GaAs is grown on Ge substrates at high temperatures (> 450°C) [2]. Consequently, the initial stages of growth generally proceed by a three-dimensional (3D) islanded growth mode, thereby resulting in the degradation of surface flatness and interface abruptness [3, 4].

In this work, high-quality epitaxy of GaAs-on-Ge is achieved at a lower growth temperature of

* Corresponding author.
[1] Present address: Institute of Materials Science, University of Tsukuba, 1-1-1 Tennodai, Tsukuba, Ibaraki, Japan. Fax: + 81 298 55 7440; e-mail: okada@mat.ims.tsukuba.ac.jp.

0022-0248/97/$17.00 Copyright © 1997 Elsevier Science B.V. All rights reserved
PII S0022-0248(96)01026-3

~400°C by atomic hydrogen-assisted molecular beam epitaxy (H-MBE), in which atomic H is generated by cracking of molecular hydrogen at a hot tungsten filament heated to >1500°C inside the MBE growth chamber. It is shown that Ge segregation is minimized and layer-by-layer two-dimensional (2D) growth mode is realized from the early stages of growth. Previously, we showed that atomic H acts as a surfactant in MBE growth of GaAs, where both the kinetics and energetics of growth can be modified in an accurately controlled manner [5–8]. The modification and control of elementary processes of growth at an atomic scale has historically been difficult to accomplish, until when the concept of surfactant epitaxy was first reported in SiGe/Si heteroepitaxy using As as a surfactant [9]. The use of atomic H is regarded as favorable since self-doping, or auto-doping could be a problem with other surfactant elements, and from a technological viewpoint, it is advantageous that sources of atomic H can be easily installed into MBE systems. Furthermore, irradiation of atomic H during MBE growth brings a number of additionally favorable effects, such as in-situ surface cleaning and inactivation of deep-level defect centers [7, 8]. As a result, layer-by-layer 2D growth and high material quality can be achieved even for the MBE growth of highly lattice-mismatched systems, and are recently reported for GaAs/Si [7, 8], SiGe/Si [9] and other important materials.

Using reflection high-energy electron diffraction (RHEED), atomic force microscopy (AFM) and secondary ion mass spectroscopy (SIMS) as characterization tools, it is demonstrated that H-MBE growth results in significant reductions of Ge segregation and Ge/As interdiffusion in GaAs-on-Ge heteroepitaxy. Hence, atomically smooth surfaces and abrupt GaAs/Ge heterointerfaces are formed as required for a variety of applications. Also the mechanisms responsible for the observed reductions of Ge segregation in H-MBE technique are discussed in terms of surfactant properties of atomic H.

2. Experimental procedure

Continuous generation of atomic H inside our MBE growth chamber was achieved with a self-assembled cracker that fits into one of the effusion cell ports of the chamber. The hydrogen cracker consists of spirally wound tungsten filament, which when heated $\gtrsim$1500°C, dissociates molecular hydrogen into atomic H through catalytic process with cracking ratios of $\gtrsim$1% [10]. The surface structure was monitored by RHEED during the substrate cleaning and growth. The surface morphologies and roughness were characterized by AFM in ambient atmosphere and depth profiles of compositional elements were measured by SIMS with Cs^+ ions with an acceleration voltage of 1 kV.

Vicinal Ge(0 0 1) substrates tilted 2°-off toward [1 1 0] azimuth were arbitrarily chosen for this work. Before the deposition of GaAs, each Ge substrate was first cleaned in the organic solvents followed by a wet-etch in $H_2SO_4 : H_2O_2 : H_2O = 5 : 1 : 1$ in volume. Once placed in the chamber, the native oxide was removed either by atomic H irradiation at ~350°C for 15 min, or by conventional thermal cleaning at 550°C. We found reproducibly that atomic H cleaning results in a more reliable surface with improved flatness than by thermal cleaning [11]. The growth was then carried out under various growth parameters. The growth temperature was varied from 250°C to 600°C, though the temperature of greatest interest was around 400°C in order to minimize the Ge segregation and interdiffusion of Ge and As while achieving as high a material quality as possible. The growth rate was between 0.1 and 1.0 μm/h, and H_2 backpressure was kept constant at 6×10^{-6} Torr by manual control of a variable leak-valve, both during substrate cleaning and MBE growth.

3. Results

Fig. 1 summarizes the changes of RHEED pattern measured for Ge(0 0 1) and GaAs during MBE growth for both with atomic H (H-MBE), and without atomic H, i.e., conventional MBE. The growth temperature and growth rate were 400°C and 0.5 μm/h, respectively. First, the RHEED pattern observed after the substrate cleaning was typically a (2×2) streak or two orthogonal (2×1) reconstructions indicative of double-domain structure regardless of the cleaning method, atomic H or

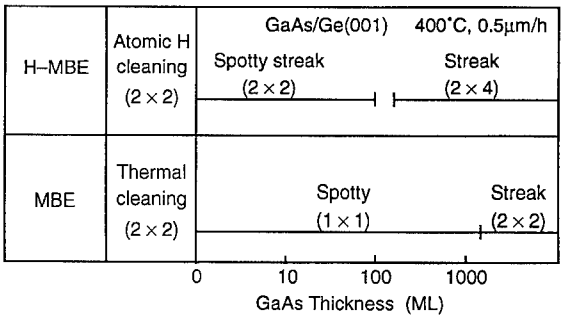

Fig. 1. Changes of RHEED pattern of GaAs(0 0 1) with growth measured for H-MBE and conventional MBE. The growth temperature and growth rate are 400°C and 0.5 μm/h, respectively.

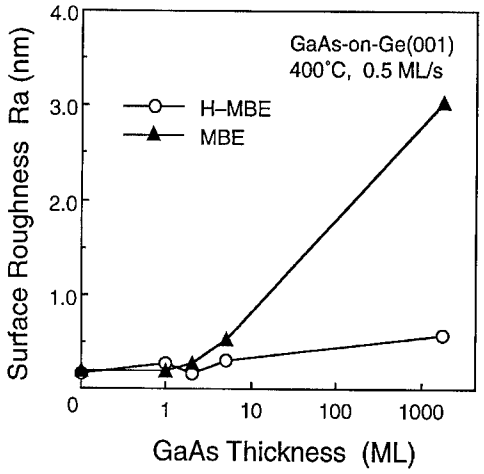

Fig. 2. Average surface roughness measured by AFM. H-MBE gives atomically flat surface of GaAs-on-Ge.

thermal cleaning. But, the streak was sharper and brighter for the atomic H-cleaned samples showing improved surface flatness compared to thermal cleaning. The improvement in surface flatness of Ge substrates after atomic H cleaning was also confirmed by AFM measurements. Second, the RHEED pattern changed from (2 × 2) streak to a spotty (1 × 1) pattern immediately after the onset of MBE growth without atomic H. It gradually recovered to a streaky (2 × 2) pattern after continued growth of ~1200 ML. Third, the RHEED pattern changed from clear (2 × 2) streak to a (2 × 2) spotty streak during ~5 ML deposition for H-MBE case. After the growth of ~150 ML, it recovered to a clear streak pattern, but this time, evolution of single-domain (2 × 4) reconstruction was obtained. As the RHEED results show, streak diffraction pattern is maintained and layer-by-layer 2D growth is enhanced by H-MBE. However, it is noted that RHEED patterns were strongly dependent on the growth rate of GaAs. The recovery to a streak after becoming spotty during the initial stage of deposition was faster for higher growth rates.

Fig. 2 plots the results of average surface roughness measured by AFM for GaAs grown on Ge substrates by H-MBE and MBE. The measurements were performed in air immediately after cooling the samples rapidly down to room temperature. The growth temperature and growth rate were 400°C and 0.5 μm/h, respectively, in both cases. It can be observed that for H-MBE case as marked by open circles, the surface roughness does not increase appreciably with growth and is ~0.6 nm after 1800 ML of deposition, which corresponds to about 2 ML thickness roughness. On the other hand, surface roughing worsens with growth for the MBE sample as marked by closed triangles. The average roughness is as much as ~3.0 nm after 1800 ML deposition, which therefore consist of 3D multilayers of ≳10 ML thickness. Thus, it is shown that the ideal layer-by-layer growth achieved by H-MBE technique as from the RHEED analysis in Fig. 1, also results in significantly improved surface smoothness.

Figs. 3 and 4 show the SIMS depth profiles of compositional atoms, Ge, Ga and As around the GaAs/Ge heterointerface measured for samples grown by H-MBE and MBE, respectively. The growth temperature, growth rate, and film thickness in both cases were 400°C and 0.5 μm/h, and 1.0 μm, respectively. It is clearly observed that Ge segregation into GaAs layer and diffusion of As into Ge substrate are more severe in MBE samples even for a relatively low growth temperature of 400°C. On the other hand, the interface abruptness is significantly improved in H-MBE samples. For example, it is seen that after a fast initial decrease of Ge concentration at the GaAs/Ge interface with a slope of ~7.6 nm/dec, which gives

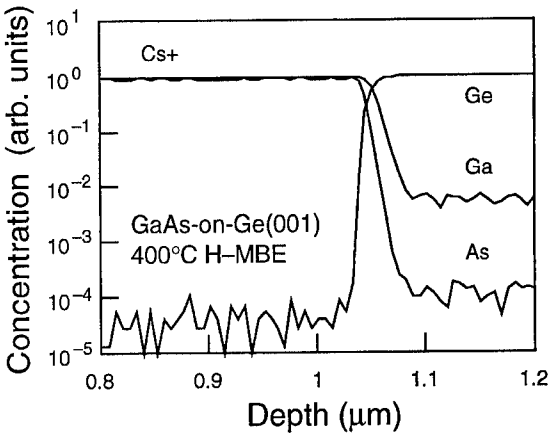

Fig. 3. SIMS depth profiles for the H-MBE sample grown at 400°C.

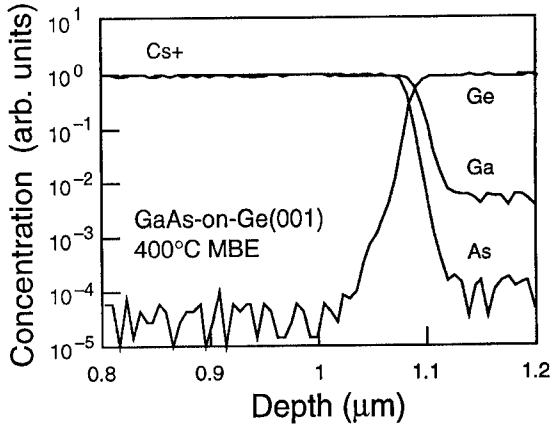

Fig. 4. SIMS depth profiles for the MBE sample grown at 400°C.

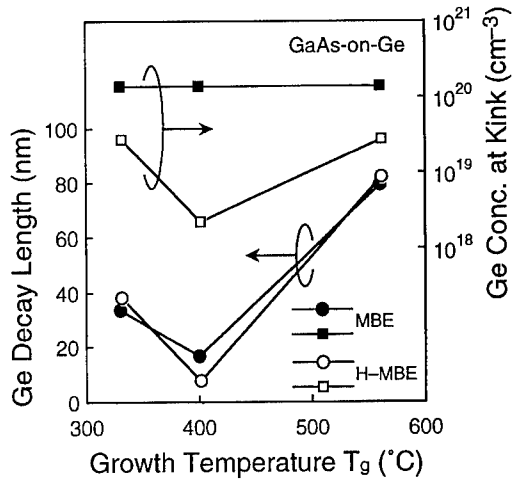

Fig. 5. Ge concentrations at bending point and level-off slopes in SIMS profiles measured for H-MBE and MBE samples in a temperature range of 330 and 560°C.

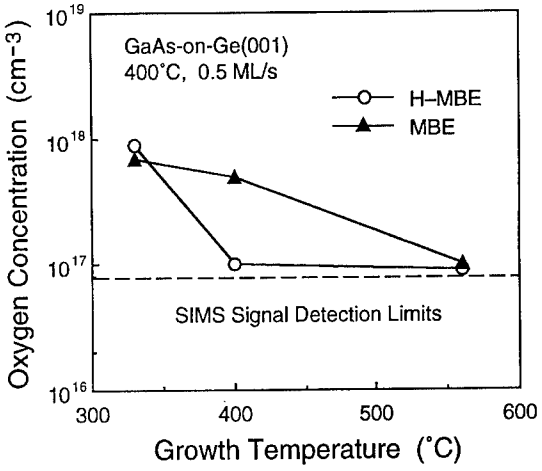

Fig. 6. Temperature dependence of oxygen concentrations in GaAs epilayers grown on Ge by H-MBE and MBE.

the resolution limit of our SIMS measurement, the slope levels off to ~ 17 nm/dec at a concentration of $\sim 1.4 \times 10^{20}\,\mathrm{cm}^{-3}$ at the bending point in the MBE sample. In comparison, the slope is unchanged for the H-MBE sample and Ge concentration drops abruptly down to a measurement limit of $\lesssim 2.2 \times 10^{18}\,\mathrm{cm}^{-3}$. Furthermore, both the Ge concentration at the bending point and level-off slope in the SIMS profiles were found to be smaller for H-MBE samples than for MBE in a temperature range of 330–560°C, as plotted in Fig. 5. It is also noted that the Ge segregation decay length, instead of reducing exponentially with temperature, which one would expect because of kinetic/thermal limitation imposed to segregation process, showed a minimum around 400°C. Lastly, it was observed, as shown in Fig. 6, that irradiation of atomic H during MBE growth reduces oxygen concentration in GaAs layer to below measurement limit of $9.0 \times 10^{16}\,\mathrm{cm}^{-3}$ for H-MBE sample grown at 400°C. Hence, reduction of oxygen-related defect

centers is expected, though a detailed analysis needs to be performed to be more quantitative.

4. Discussion

As presented, Ge segregation and Ge/As interdiffusion are significant even for a low growth temperature of 400°C by MBE. Though the segregation decay length depends strongly on growth conditions such as growth rate, it is shown that Ge segregation can be reduced significantly for the given conditions, by the use of atomic H continuously irradiated on the surface during MBE growth. It is known that segregation process is generally governed by the strength of bonding energy [3], the surface, interface as well as strain energies associated with heteroepitaxy system as a whole [9], and the densities of dislocations and types of defects present in the system. Kroemer also pointed out the importance of charge neutrality fulfillment in polar-on-nonpolar heteroepitaxy [12]. Our aim for introducing atomic H into MBE growth is to try to modify and control the growth mode by modifying the surface energetics and kinetics in such a manner that layer-by-layer 2D nucleation mode would be promoted and hence segregation and interdiffusion be minimized. Such a growth concept known as surfactant epitaxy, is attracting increasing attention in recent years and widely reported for GaAs/Si [7, 8], and SiGe/Si [9] systems.

Recently, we reported on the basic analysis of atomic-scale growth mechanisms for homoepitaxial MBE of GaAs using atomic H as a surfactant [5]. In conventional MBE, the surface free energy of Ge(0 0 1) being lower than the barely As-stabilized GaAs(0 0 1) surface favors 3D islanded growth and Ge segregation and Ge/As interdiffusion are accelerated even for low substrate temperatures. In H-MBE growth of GaAs-on-Ge, it is thought that the effect of reduction of surface energy of H-adsorbed GaAs(0 0 1) is predominant and, consequently, a preference for 2D layer-by-layer growth mode is provided, whereby successfully resulting in atomically smooth and abrupt heterointerfaces as required for a variety of device fabrication. It is also noted that the growth model discussed here should be applicable only in a relatively limited range of growth temperature. This is because the desorption rate of atomic H from GaAs(0 0 1) surface is found to increase rapidly above ~450°C and the growth kinetics becomes thermally limited and crystal quality becomes poor below ~300°C, even though the effectiveness of atomic H is still observable at these temperatures. And this is probably the reason for Ge segregation decay length, as plotted in Fig. 4, to have a minimum point at ~400°C, though additional work is necessary to clarify completely the role of atomic H. Finally, in situ removal of foreign contaminants such as carbon and oxygen during H-MBE also serve to suppress heterogeneous nucleation and formation of impurity-related defect centers.

5. Summary

We have developed high-quality epitaxy of GaAs-on-Ge system at low growth temperatures by H-MBE technique. It is demonstrated that enhanced layer-by-layer 2D growth mode is realized from the earliest stages of MBE growth and single-domain (2 × 4) GaAs(0 0 1) surface is evolved at 400°C by H-MBE. The Ge segregation and Ge/As interdiffusion are reduced and an abrupt GaAs/Ge heterointerface is successfully formed. In H-MBE growth of GaAs-on-Ge, the reduction of surface energy of H-adsorbed GaAs(0 0 1) seems to be the predominant effect that as a result, provides preference for 2D layer-by-layer growth mode. Modification of growth mode and consequent improvements in material quality presented here are explained at the simplest level by the surfactant properties of atomic H in MBE growth of GaAs.

References

[1] R. Venkatasubramanian, M.L. Timmons, J.B. Posthill, B.M. Keyes and R.K. Ahrenkiel, Proc. 23rd IEEE Photovoltaic Specialists Conf., Louisville (1993) p. 691.
[2] N. Chang, J. Klem, T. Henderson and H. Morkoç, J. Appl. Phys. 59 (1986) 3601.
[3] T. Kawai, H. Yonezu, Y. Yamaguchi, M. Lopez, K. Pak and W. Kürner, J. Crystal Growth 127 (1993) 107.
[4] Ching-An Chang, J. Appl. Phys. 53 (1982) 1235.

[5] Y. Okada and J.S. Harris, J. Vac. Sci. Technol. B 14 (1996) 1725.
[6] Y. Okada, T. Fujita and M. Kawabe, Appl. Phys. Lett. 67 (1995) 676.
[7] Y. Okada, H. Shimomura and M. Kawabe, J. Appl. Phys. 73 (1993) 7376.
[8] Y. Okada, S. Ohta, A. Kawabata, H. Shimomura and M. Kawabe, J. Electron. Mater. 23 (1994) 331.
[9] M. Copel, M.C. Reuter, E. Kaxiras and R.M. Tromp, Phys. Rev. Lett. 63 (1989) 632.
[10] A. Sutoh, Y. Okada, S. Ohta and M. Kawabe, Jpn. J. Appl. Phys. 34 (1995) L1379.
[11] Y. Okada, A. Sutoh, M. Kawabe and J.S. Harris, Mater. Res. Soc. Symp. Proc. 399 (1996) 203.
[12] H. Kroemer, J. Crystal Growth 81 (1987) 193.

ELSEVIER

Journal of Crystal Growth 175/176 (1997) 1045–1050

JOURNAL OF CRYSTAL GROWTH

Growth and characterization of In_2Se_3 epitaxial films by molecular beam epitaxy

Tamotsu Okamoto[a,*], Akira Yamada[b], Makoto Konagai[b]

[a] *Research Center for Quantum Effect Electronics, Tokyo Institute of Technology, 2-12-1, O-okayama, Meguro-ku, Tokyo 152, Japan*
[b] *Department of Electrical and Electronic Engineering, Tokyo Institute of Technology, 2-12-1, O-okayama, Meguro-ku, Tokyo 152, Japan*

Abstract

Structural control of In_2Se_3 films was attempted by molecular beam epitaxy (MBE). In_2Se_3 epitaxial films with layered structure based on zincblende structure were successfully grown on (0 0 1)GaAs substrates at low temperatures ($T_g \leqslant 520$°C at VI/III ratio of 10) and at low VI/III ratios (VI/III $\leqslant 30$ at 500°C), and polycrystalline In_2Se_3 films with defect wurtzite structure were grown at high temperatures ($T_g \geqslant 540$°C at VI/III ratio of 10) and high VI/III ratios (VI/III $\geqslant 90$ at 500°C). In the epitaxial In_2Se_3 films with layered structure, the direction of *c*-axis corresponded to [1 $\bar{1}$ 1] and [$\bar{1}$ 1 1] directions in the (0 0 1)GaAs substrates. Furthermore, exciton emission located at around 579 nm was observed in the photoluminescence spectra of the In_2Se_3 films at 4.2 K.

1. Introduction

III_2–VI_3 compound semiconductors have several crystal structures. For example, Ga_2Se_3 has a defect zincblende structure. This structure is basically zincblende structure, but $\frac{1}{3}$ of cation sites are vacant. Up until now, we investigated the molecular beam epitaxial (MBE) growth of Ga_2Se_3 films on (0 0 1)GaAs and (0 0 1)GaP substrates, and it was found that a spontaneous superlattice was formed and the unique properties such as large optical anisotropy were shown by the ordering of the native Ga vacancies in Ga_2Se_3 films [1–6]. On the other hand, In_2Se_3 has two types of crystal structure different from that of Ga_2Se_3, i.e., layered structure (α-phase) and defect wurtzite structure (γ-phase) [7–9]. The layered structure consists of rather loose stacks of covalently bonded layers, including five atomic layers of Se–In–Se–In–Se, by van der Waals force. The basic structure of the layered In_2Se_3 is wurtzite or zincblende structure. Therefore, it is considered that the native In vacancies form planes in every three In planes in the layered In_2Se_3 and the layered In_2Se_3 is a kind of vacancy-ordered structure. Meanwhile, the defect wurtzite structure is basically a wurtzite structure, but $\frac{1}{3}$ of the cation sites are vacant as well as the defect zincblende structure. In this structure, the In vacancies take screw arrangement. Therefore, γ-In_2Se_3 shows large optical rotary power [9]. However, there are no reports on the epitaxial

* Corresponding author. Fax: +81 3 5734 2897; e-mail: okamoto@pe.titech.ac.jp.

0022-0248/97/$17.00 Copyright © 1997 Elsevier Science B.V. All rights reserved
PII S0022-0248(96)00984-0

growth of In_2Se_3 films. In this paper, we attempted the structural control and characterization of In_2Se_3 films on (0 0 1)GaAs substrates, and In_2Se_3 epitaxial films with layered structure based on zincblende structure were successfully grown on (0 0 1)GaAs substrates. This is the first report on the successful growth of In_2Se_3 epitaxial films. Furthermore, we observed an exciton emission located at around 579 nm in the low-temperature photoluminescence spectra of the In_2Se_3 films for the first time.

2. Experimental procedure

In_2Se_3 films were grown on SI-(0 0 1)GaAs substrates by MBE technique using EIKO Engineering Model EV-100. The growth temperature was varied in a range of 450–540°C. VI/III ratio was varied from 5 to 90 by increasing Se beam equivalent pressure (BEP), keeping In BEP constant. In these growth conditions, the growth rate was limited by the supply of In atoms. The growth rate of In_2Se_3 films was around 800 nm/h, and the film thickness was around 800 nm. Before being inserted into the MBE system, the GaAs substrates were degreased, chemically etched in a 3 : 1 : 1 $H_2SO_4 : H_2O_2 : H_2O$ solution at 60 C for 1.5 min. After acid etching, the GaAs substrates were heated at 550 C for 15 min in the growth chamber to remove surface oxides. The [1 1 0] and [1 $\bar{1}$ 0] direction of the GaAs substrates were determined by anisotropic etching. The crystallinity of In_2Se_3 films was characterized by reflection high-energy electron diffraction (RHEED) and Raman spectroscopy. An Ar^+ laser (514.5 nm, 50 mW) was used for Raman spectroscopy. Surface morphology and cross-sectional image were observed by scanning electron microscopy (SEM). Photoluminescence (PL) measurement was carried out at 4.2 K. The 488.0 nm emission line of an Ar^+ laser was used as an excitation light.

3. Results and discussion

First of all, we investigated the effects of VI/III ratio on crystal structure of In_2Se_3. Fig. 1 shows RHEED patterns of In_2Se_3 films for various VI/III ratios. The growth temperature was kept at 500°C. At the VI/III ratios below 30, zincblende-type spots are observed for [$\bar{1}$ 1 0] incidence. This result indicates that epitaxial In_2Se_3 films with zincblende structure were successfully grown on GaAs substrates. For [$\bar{1}$ $\bar{1}$ 0] incidence, spot pattern is not observed. This result is considered to be attributed to the surface morphology, which will be discussed later. On the other hand, at VI/III ratio of 90, spot pattern is not observed. We confirmed by X-ray diffraction that the film prepared at VI/III ratio of 90 was polycrystalline.

In order to clarify the crystal structure of the In_2Se_3 films, we characterized the In_2Se_3 films by Raman spectroscopy. Fig. 2 shows Raman spectra of In_2Se_3 films for various VI/III ratios. At VI/III ratios below 30, a peak located at 108 cm^{-1} is observed. This peak appears at the same wavelength as in the reported Raman spectrum of the bulk α-In_2Se_3 with layered structure [10]. Therefore, In_2Se_3 epitaxial films are found to have layered structure based on zincblende structure. A peak located at around 205 cm^{-1} in the films with VI/III ratios below 30 was also observed in the Raman spectrum of the bulk α-In_2Se_3 [10]. On the other hand, at VI/III ratio of 90, a peak is located at 151 cm^{-1}, which is the same wavelength as observed in the spectrum of the bulk γ-In_2Se_3 with defect wurtzite structure [10]. This result indicates that polycrystalline In_2Se_3 with defect wurtzite structure was obtained under high VI/III ratio conditions. Besides, we investigated the growth of In_2Se_3 films with VI/III ratio below 5. In the growth conditions, the growth rate of In_2Se_3 decreased with decreasing VI/III ratio, and no deposition of In_2Se_3 was observed with VI/III ratio below 1. This result can be considered to be attributed to the reevaporation of In and Se compounds with high vapor pressure such as In_2Se, and is similar to the MBE growth of Ga_2Se_3 films [1].

Furthermore, we observed surface morphology and cross-sectional image of the epitaxial In_2Se_3 film by scanning electron microscopy (SEM). Fig. 3 shows the surface morphology and the (1 1 0) cross-sectional SEM image of the epitaxial In_2Se_3 film grown at 500 C with VI/III ratio of 10. A schematic drawing of (1 1 0) cross-sectional view of the

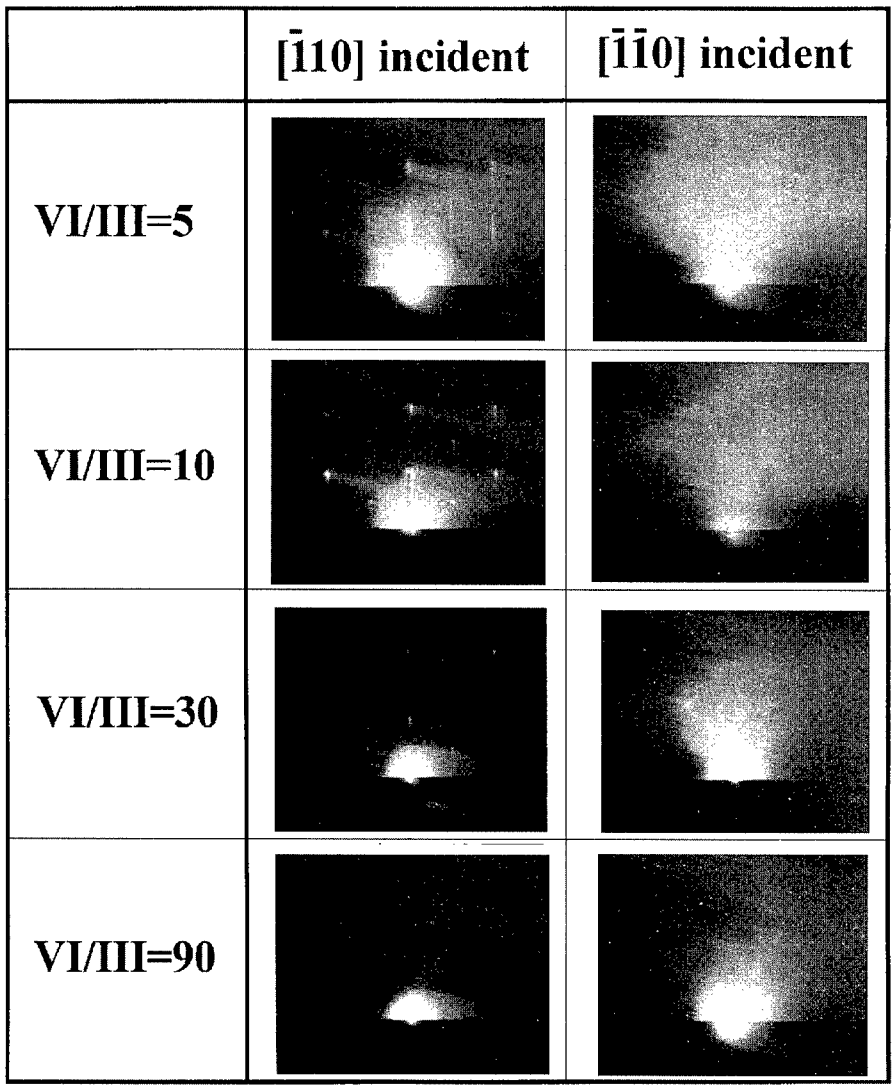

Fig. 1. RHEED patterns of In_2Se_3 films for various VI/III ratios.

epitaxial In_2Se_3 with layered structure on (0 0 1)GaAs substrate is also shown in Fig. 3. In the layered In_2Se_3, *c*-axis corresponds to [1 $\bar{1}$ 1] direction in zincblende structure. In the cross-sectional image, it is found that the layered structure is formed and the direction of *c*-axis corresponds to [$\bar{1}$ 1 1] and [$\bar{1}$ 1 1] direction in the (0 0 1)GaAs substrate. This structure was not observed in (1 $\bar{1}$ 0) cross-sectional image, which indicates that *a*-axis of the layered In_2Se_3 is parallel to [1 1 0] direction. In the surface morphology of the epitaxial In_2Se_3 film, a lot of lines parallel to the [1 1 0] direction are observed. This morphology is considered to be attributed to the *a*-axis direction. These features are similar to the epitaxial GaSe films on (0 0 1)GaAs substrates [11, 12]. We consider that triangular ridges run along [1 1 0] direction and that the anisotropy in the RHEED patterns is attributed to the anisotropic features in the surface structure. The details are still under study.

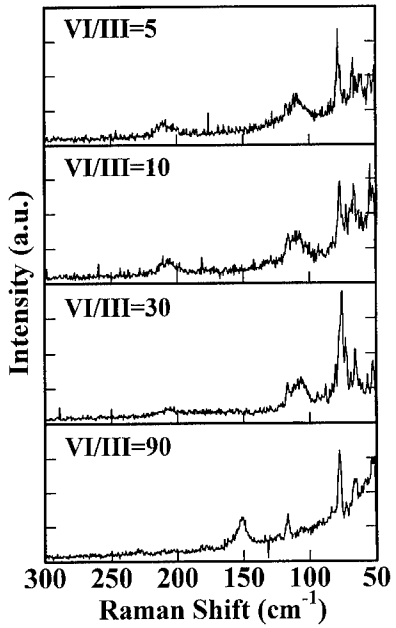

Fig. 2. Raman spectra of In_2Se_3 films for various VI/III ratios.

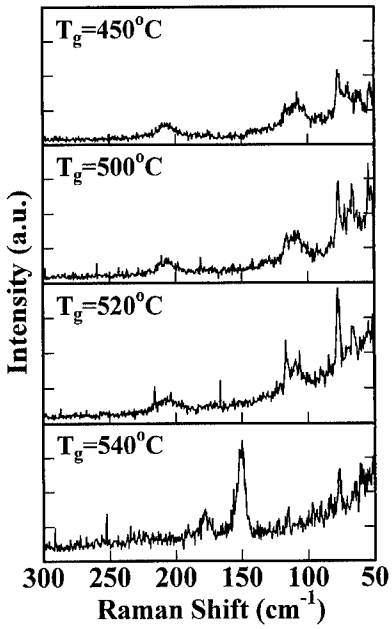

Fig. 4. Raman spectra of In_2Se_3 films for various growth temperatures.

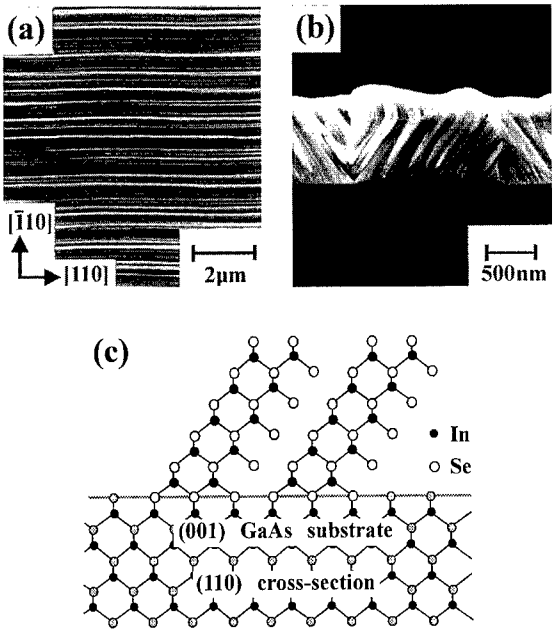

Fig. 3. (a) Surface morphology, (b) (1 1 0) cross-sectional SEM image and (c) a schematic drawing of (1 1 0) cross-sectional view of the epitaxial In_2Se_3 with layered structure on (0 0 1)GaAs substrate.

Next, we investigated growth temperature dependence. Fig. 4 shows the dependence of Raman spectrum on growth temperature. VI/III ratio was kept at 10. At the temperatures below 520°C, the peak located at 108 cm^{-1}, which originates in In_2Se_3 with layered structure, is observed. In these films, spot pattern based on zincblende structure was observed in RHEED patterns. These results suggest that epitaxial In_2Se_3 films with layered structure based on zincblende structure are formed at the temperature below 520°C. On the other hand, the peak located at 151 cm^{-1}, which originates in In_2Se_3 with defect wurtzite structure is observed at the temperature of 540°C. A peak located at around 180 cm^{-1} was also observed in the Raman spectrum of the bulk γ-In_2Se_3 [10]. In this film, ring pattern was observed in RHEED pattern, which indicates that the polycrystalline In_2Se_3 with defect wurtzite structure is obtained at high temperature. From these results, it is found that the epitaxial In_2Se_3 films with layered structure are obtained at low temperatures and low VI/III ratios and that the polycrystalline In_2Se_3

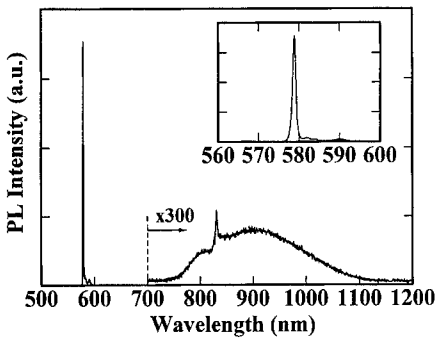

Fig. 5. Photoluminescence spectrum of the In_2Se_3 epitaxial film at 4.2 K.

films with defect wurtzite structure are obtained at high temperatures and high VI/III ratios.

Furthermore, we investigated the optical properties of the epitaxial In_2Se_3 films by PL measurement at 4.2 K. Fig. 5 shows PL spectrum of the In_2Se_3 epitaxial film grown at 520°C with VI/III ratio of 10. Detailed spectrum in the band edge region is shown in the inset. A sharp peak located at around 579 nm (2.14 eV) is observed in the epitaxial In_2Se_3 films. This peak is also observed in the polycrystalline γ-In_2Se_3 films. In order to clarify the origin of the PL emission, we measured wavelength dependence of photoconductivity of the polycrystalline γ-In_2Se_3 film on glass substrate at 4.2 K. It was found that a peak due to an exciton absorption was observed near absorption edge in the wavelength dependence profile and that the wavelength of the exciton absorption peak was almost the same as that of the PL emission peak. Therefore, the PL emission peak located at around 579 nm is found to be exciton emission. Furthermore, intensity of deep level emission peak observed at around 900 nm is very weak. A peak located at around 830 nm is an emission from GaAs substrate. These results suggest that the quality of the In_2Se_3 films is quite good in terms of optical properties. This is the first report on the exciton emission in the In_2Se_3. Moreover, the band gap of In_2Se_3 estimated from Fig. 5 is about 2.15 eV at 4.2 K. This value is larger than the reported band gap of the bulk α-In_2Se_3 with layered structure ($E_g \approx 1.4$ eV) [13, 14], but almost the same as the reported γ-In_2Se_3 films with defect wurtzite structure ($E_g \approx 2.0$ eV) [15]. Therefore, we can consider that the band gap of In_2Se_3 with layered structure is larger than the reported value.

4. Conclusions

We attempted the structural control of In_2Se_3 films by molecular beam epitaxy (MBE). In_2Se_3 epitaxial films with layered structure based on zincblende structure were successfully grown on (0 0 1)GaAs substrates at low temperatures ($T_g \leqslant 520$°C at VI/III ratio of 10) and at low VI/III ratios (VI/III $\leqslant 30$ at 500°C), and polycrystalline In_2Se_3 films with defect wurtzite structure were grown at high temperatures ($T_g \geqslant 540$°C at VI/III ratio of 10) and high VI/III ratios (VI/III $\geqslant 90$ at 500°C). In the epitaxial In_2Se_3 films with layered structure, the direction of c-axis corresponded to [1 $\bar{1}$ 1]and [$\bar{1}$ 1 1] direction in the (0 0 1)GaAs substrates. Furthermore, exciton emission located at around 579 nm was observed in the photoluminescence spectra of the In_2Se_3 films at 4.2 K. This is the first report on the exciton emission in the In_2Se_3.

References

[1] N. Teraguchi, F. Kato, M. Konagai, K. Takahashi, Y. Nakamura and N. Otsuka, Appl. Phys. Lett. 59 (1991) 567.
[2] N. Teraguchi, M. Konagai, F. Kato and K. Takahashi, J. Crystal Growth 115 (1991) 798.
[3] T. Okamoto, N. Kojima, A. Yamada, M. Konagai, K. Takahashi, Y. Nakamura and O. Nittono, Jpn. J. Appl. Phys. 31 (1992) L143.
[4] T. Okamoto, M. Konagai, N. Kojima, A. Yamada, K. Takahashi, Y. Nakamura and O. Nittono, J. Electron. Mater. 22 (1993) 229.
[5] T. Okamoto, A. Yamada, M. Konagai and K. Takahashi, J. Crystal Growth 138 (1994) 204.
[6] T. Okamoto, T. Takegami, A. Yamada and M. Konagai, Jpn. J. Appl. Phys. 34 (1995) 5984.
[7] J. van Landuyt, G. van Tendeloo and S. Amelinckx, Phys. Status Solidi (a) 30 (1975) 299.
[8] K. Osamura, Y. Murakami and Y. Tomiie, J. Phys. Soc. Jpn. 21 (1966) 1848.
[9] J. Ye, T. Yoshida, Y. Nakamura and O. Nittono, Appl. Phys. Lett. 67 (1995) 3066.

[10] K. Kambas, C. Julien, M. Jouanne, A. Likforman and M. Guittard, Phys. Status Solidi (b) 124 (1984) K105.
[11] N. Kojima, K. Sato, A. Yamada, M. Konagai and K. Takahashi, Jpn. J. Appl. Phys. 33 (1994) L1482.
[12] N. Kojima, K. Sato, M. Budiman, A. Yamada, M. Konagai, K. Takahashi, Y. Nakamura and O. Nittono, J. Crystal Growth 150 (1995) 1175.
[13] P. Becla, Z. Gumienny, J. Misiewicz and J.M. Pawlikowski, Opt. Appl. 12 (1982) 143.
[14] C. Julien, M. Eddrief, K. Kambas and M. Balkanski, Thin Solid Films 137 (1986) 27.
[15] M. Yudasaka, T. Matsuoka and K. Nakanishi, Thin Solid Films 146 (1987) 65.

ELSEVIER

Journal of Crystal Growth 175/176 (1997) 1051–1056

JOURNAL OF CRYSTAL GROWTH

Effects of strain on the growth and properties of $CuInSe_2$ epitaxial films

S. Niki[a,*], P.J. Fons[a], H. Shibata[a], T. Kurafuji[a], A. Yamada[a], Y. Okada[a], H. Oyanagi[a], W.G. Bi[b], C.W. Tu[b]

[a] *Optoelectronics Division, Electrotechnical Laboratory, 1-1-4 Umezono, Tsukuba, Ibaraki 305, Japan*
[b] *Department of Electrical and Computer Engineering, University of California at San Diego, La Jolla, California 92093, USA*

Abstract

$CuInSe_2$ films have been grown on both GaAs(0 0 1) and $In_{0.29}Ga_{0.71}As$ *pseudo*-lattice-matched substrates by solid-source molecular beam epitaxy and the effects of strain on the properties of epitaxial films have been investigated. For $CuInSe_2$ epitaxial films grown on GaAs(0 0 1), the intensities of excitonic emissions become stronger and the line widths of the predominant defect-related emissions become smaller on increasing the thickness of the films from 0.4 to 2 μm, suggesting that the defect density decreases with the film thickness. Drastic improvements in optical and transport properties have been achieved by using $In_{0.29}Ga_{0.71}As$ *pseudo*-lattice-matched substrates; free-exciton emissions were predominantly observed, indicating that high-quality $CuInSe_2$ epitaxial films have been grown by controlling the misfit strain between the substrates and the epitaxial films.

PACS: 68.55.Bd; 78.55.Hx; 61.72.Ff

Keywords: Molecualr beam epitaxy; Photoluminescence; X-ray diffraction; Transmission electron microscopy; $CuInSe_2$

1. Introduction

$CuInSe_2$ (CIS)-based chalcopyrite semiconductor solar cells have already demonstrated high conversion efficiencies of up to $\eta = 17.7\%$ [1]. Thin films with thickness of only 2–3 μm are required to absorb sun light effectively and no degradation of solar cell performance for more than 4 years has been reported [2], suggesting that CIS-based solar cells are promising for practical low-cost thin film solar cells. CIS-based poly-crystalline solar cells typically consist of a ZnO window layer, a CdS buffer layer, and a CIS or $CuInGaSe_2$ (CIGS) absorber layer grown, in turn, on Mo- coated soda-lime glass substrates [1]. Significant mismatch in lattice constants, thermal expansion coefficients as well as crystalline structure still exist among the layers as shown in Table 1 despite a remarkable improvement reported in solar cell performance. The effects of such a mismatch on the properties of CIS and consequently on the characteristics of the

* Corresponding author.

0022-0248/97/$17.00 Copyright © 1997 Elsevier Science B.V. All rights reserved
PII S0022-0248(96)01213-4

Table 1
Crystalline structure, lattice constants, and thermal expansion coefficients of the materials used for fabricating $CuInSe_2$-based solar cells

Material	Crystalline structure	Lattice constants (Å)	Thermal expansion coefficients ($\times 10^{-6}\,K^{-1}$)
$CuInSe_2$	Chalcopyrite	$a = 5.7821$, $c = 11.6191$	$\alpha_a = 11.4$, $\alpha_c = 8.6$
CdS	Zincblende	$a = 5.825$	
	Wurtzite	$a = 4.136$, $c = 6.714$	$\alpha_a = 6.5$, $\alpha_c = 4.0$
ZnO	Wurtzite	$a = 3.252$, $c = 5.213$	$\alpha_a = 4.75$, $\alpha_c = 2.92$

solar cells cannot be ignored for further extending the solar cell performance and for manufacturing large-size reproducible modules.

In our earlier work, we have reported the growth and properties of CIS films grown by molecular beam epitaxy (MBE) [3]. Sharp photoluminescence (PL) spectra including near-band-edge emissions have been observed from the CIS epitaxial films grown on GaAs(0 0 1) though defect-related emissions were still dominant [4]. CIS has a chalcopyrite structure with the lattice constants of a-axis (a) and c-axis (c) being $a = 5.7821$ Å and $c = 11.6191$ Å based upon the JCPDS standards. A significant lattice mismatch of $\Delta a/a = 2.2\%$ at room temperature (RT) is present between GaAs and CIS (a-axis); therefore, a large number of defects were observed both at the CIS/GaAs interface and in the active CIS layers [3]. Strain-induced novel phenomena such as the formation of interfacial layer caused by strain-induced interdiffusion between GaAs and CIS have been observed [5]. In addition, a significant mismatch in thermal expansion coefficients exists between $11.4 \times 10^{-6}\,K^{-1}$ for CIS (a-axis) and $6.86 \times 10^{-6}\,K^{-1}$ for GaAs, therefore the lattice mismatch at growth temperature becomes more significant than $\Delta a/a =$ 2.2% at RT.

In this work, effects of strain on the properties of CIS epitaxial films have been investigated by changing the film thickness and by using two kinds of substrates with different lattice mismatch. As shown in Fig. 1, lattice constants of the ternary alloy, $In_xGa_{1-x}As$, can be controlled between those of two binary alloys, GaAs and InAs, as a function of InAs mole fraction (x); lattice constant of $In_xGa_{1-x}As$ is described as $a_{InGaAs}(x) = 5.6533 +$ $0.4051x$ Å based upon the Vegard's law [6]. Use of a linearly or step-graded buffer layer in order to provide nearly 100% strain relaxation and a reduction in threading dislocation densities below $10^6\,cm^{-2}$ has produced promising results and has been applied for large lattice-mismatched systems such as SiGe/Si [7], $In_xGa_{1-x}As$/GaAs [8, 9], etc. A similar technique was applied to investigate the strain effects on film properties and to grow high-quality CIS films.

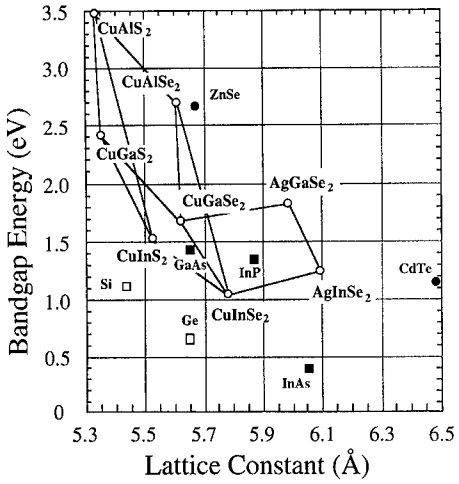

Fig. 1. Band gap and latice constant of several I–III–VI_2 chalcopyrite semiconductors and substrates.

2. Experimental procedure

CIS epitaxial films with a range of growth parameters have been grown by solid-source molecular

beam epitaxy on both GaAs(0 0 1) (CIS/GaAs) and *pseudo*-lattice-matched $In_{0.29}Ga_{0.81}As$ substrates (CIS/InGaAs) at the growth temperatures T_s = 350–600°C. More detailed growth procedures can be found elsewhere [3]. For CIS/GaAs, the S-passivated (2 × 1) GaAs surface has been used, and epitaxial growth with the *c*-axis normal to the substrate has been demonstrated. Thickness of the films was varied from 0.4 to 2.0 μm which is significantly thicker than the calculated critical layer thickness limit of ~80 Å for CIS on GaAs [5].

Pseudo-lattice-matched substrates (*Pseudo*-substrates) were prepared by gas-source MBE using elemental In, Ga, and gas-source As (AsH_3) [10]. A 200 Å GaAs buffer was first grown on a semi-insulating GaAs(0 0 1) substrate, followed by a linearly composition-graded $In_xGa_{1-x}As$ buffer layer, where the In composition was varied linearly with the depth from $x = 0$ to 0.29 at a grading rate of ~1% In/400 Å. A final 1 μm-thick $In_{0.29}Ga_{0.71}As$ layer was grown as a *pseudo*-substrate layer. The surface of the *pseudo*-substrate was passivated by As_2 before removal from the vacuum chamber for transport to the CIS growth system.

The results using various characterization methods such as low-temperature PL, cross-sectional transmission electron microscopy (TEM) and high-resolution X-ray diffraction (HRXRD) will be discussed in comparison with those of the CIS films grown directly on GaAs(0 0 1) (CIS/GaAs). X-ray rocking curves have been obtained using a triple-axis configuration and a high-resolution four-crystal Ge(2 2 0) X-ray diffractometer (Philips: Materials Research Diffractometer). A two bounce Ge(2 2 0) channel cut analyzer crystal was also placed between the CIS films and the detector in order to improve the resolution of the measurements. Typical resolution in the ω direction was ~0.003° and ~0.006° in the 2θ direction. PL experiments were carried out at 2 K with a 1 m single-pass monochromator, Ar^+-laser (λ = 514.5 nm) excitation, and a liquid nitrogen-cooled Ge detector (North Coast: Model EO-817L). Cross-sectional TEM images were taken using a JEOL 4000 F/X microscope operating at 350 kV.

3. Results and discussion

Fig. 2 shows the PL spectra of CIS/GaAs grown at T_s = 450°C as a function of film thickness. The appearance of more distinct near-band-edge emissions with increasing film thickness indicates a reduction in defect density. Fig. 3 shows the dependence of the measured *c*/*a* ratio of CIS films as measured by X-ray diffraction and the line width of the conduction band to acceptor transition (peak 'c') by PL measurements on film thickness. The line width of peak 'c' decreases from 12.0 meV at 0.4 μm to 6.5 meV at 2.0 μm consistent with the above results, on the other hand, the *c*/*a* ratio deviates further from the JCPDS standard value of *c*/*a* = 2.0095; tensile strain along the direction parallel to the surface becomes larger with increasing film thickness. This tensile strain is attributed to the difference in thermal expansion coefficients between the CIS layer and the substrate of about a factor of two. This leads to a large, but imperfect lattice relaxation near the CIS/GaAs interface and is thought to appear during the cooling process [11].

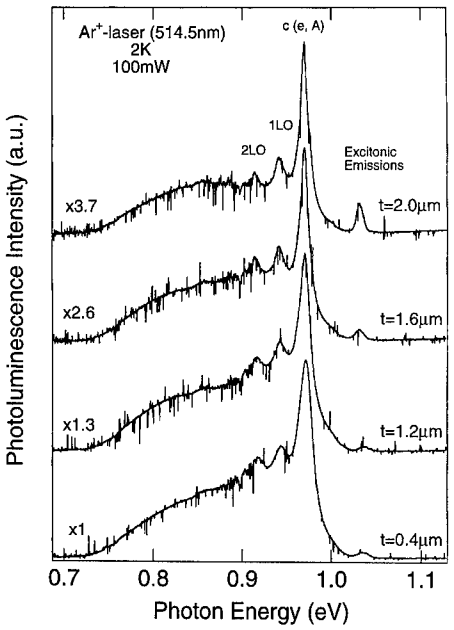

Fig. 2. Photoluminescence specra of CIS/GaAs grown at T_s = 450°C as a function of film thickness.

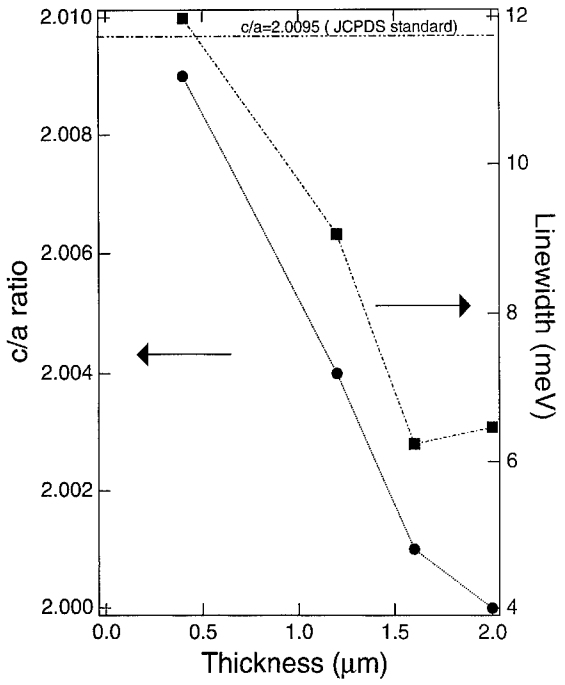

Fig. 3. Dependence of the measured c/a ratio of the CIS films by means of X-ray diffration and the line width of peak 'c' by PL measurements on film thickness.

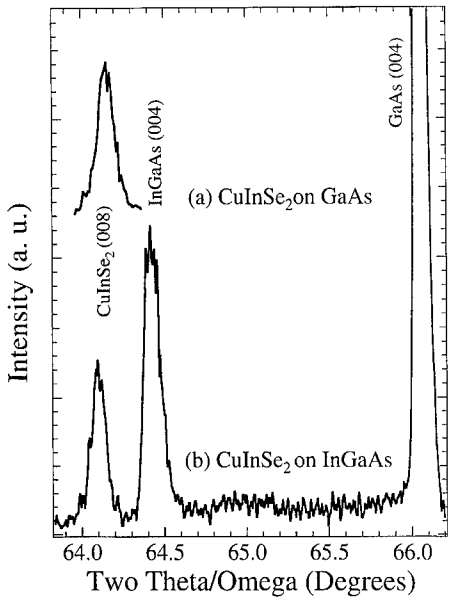

Fig. 4. X-ray scan in the [0 0 1]* direction of the $CuInSe_2$ (0 0 8) grown on both (a) GaAs and (b) $In_{0.29}Ga_{0.71}As$ *pseudo*-lattice-matched substrates.

The c/a ratio changes substantially from $c/a = 2.009$ at 0.4 μm to 2.000 at 2.0 μm, and the expected change in crystal field, Δ_{cf}, with respect to the change in the c/a ratio is calculated to be about 4 meV, using the equation, $\Delta_{cf} = \frac{3}{4}b(2 - c/a)$ where b is the deformation potential [12]. However, peak 'c' showed an energy shift of only less than 1.1 meV for varying film thicknesses from 0.4 to 2.0 μm. The band gap of CIS (E_g) can be defined from the energy of peak 'c' (E_A) using the relation $E_g = E_A + E_i$, provided that the ionization energy (E_i) is independent of the c/a ratio. The c/a ratios in the CIS films were measured at RT, thus the data may not be directly compared with the PL data obtained at 2 K. Assuming that a similar difference in the c/a ratio is sustained at 2 K, the band gap of CIS is likely to be insensitive to a change in the crystal field in this range of c/a ratios.

Fig. 4 shows the X-ray scan in the [0 0 1] direction of the CIS(0 0 8) and the GaAs(0 0 4) reflections for both (a) GaAs and (b) InGaAs

Table 2
List of lattice parameters by means of high resolution X-ray diffraction

Substrate	a-axis (Å)	c-axis (Å)	FWHM (degrees)
GaAs	5.7920	11.6149	0.117
InGaAs	5.7835	11.6175	0.106
Standard (JCPDS)	5.7821	11.6191	–

pseudo-substrates. The results of XRD are also listed in Table 2. It is clear from the figure that the CIS layer was grown epitaxially on the *pseudo*-substrate. Somewhat unexpectedly, no noticeable improvement in the line width of CIS(0 0 8) reflection of CIS/InGaAs has been observed in comparison with that of CIS/GaAs; the line width of the CIS(0 0 8) peak of CIS/InGaAs is apparently limited by the mosaic of the *pseudo*-substrate layer. The measured lattice constants for CIS/InGaAs were in good agreement with the JCPDS standard values, while substantial tensile strain along the surface was present in CIS/GaAs consistent with the results discussed in the earlier paragraph.

A more significant difference in the in-plane lattice constants along two $\langle 1\,0\,0\rangle$ orthogonal directions of $\Delta a/a_{AVE} \sim 0.2\%$ was observed in CIS/InGaAs with respect to $\Delta a/a_{AVE} \sim 0.1\%$ for CIS/GaAs. This difference may be due to the existence of a tilt in the *pseudo*-substrate; however it is not considered to be sufficient to dominate the film properties.

Fig. 5 shows a cross-sectional TEM image of CIS/InGaAs grown at $T_s = 550°C$. Most of the plastic deformation takes place in the linearly composition-graded buffer layer. Such a large relaxation is substantial enough to isolate the upper layers from the GaAs substrate reducing the residual strain in the upper layers. It also shows that the number of misfit dislocations is significantly reduced in the $In_{0.29}Ga_{0.71}As$ and CIS layers.

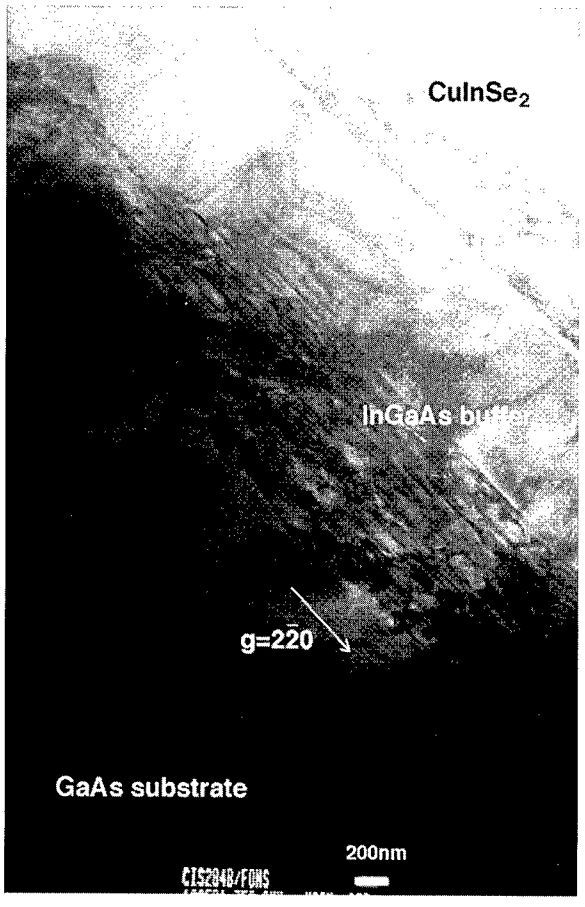

Fig. 5. Cross-sectional image of $CuInSe_2$ grown on $In_{0.29}Ga_{0.71}As$ *pseudo*-lattice-mached substrates.

PL spectra obtained from CIS/GaAs and CIS/InGaAs grown at 550°C are shown in Fig. 6a and Fig. 6b, respectively. Peak 'c' (0.970 eV) is dominant in Fig. 6a, which is typical for near stoichiometric and Cu-rich CIS epitaxial films grown on GaAs. Distinct but weak free-exciton emissions, E_{X1} (1.039 eV) and E_{X2} (1.045 eV), are present, and an emission due to an exciton–donor complex, I_{X0} (1.031 eV), can also be observed [4, 13]. Strong defect-related emission lines (peaks 'c' and 'd') indicate the presence of a large number of point defects in CIS/GaAs.

On the other hand, emissions due to free excitons (E_{X1} and E_{X2}) were predominantly observed in Fig. 6b; the density of optically active residual defects has been substantially reduced. The decrease in the intensity of the defect-related peak 'c' made possible the observation of new emission lines such as peaks 'b', I_{X2} and I_{X3}. Temperature-dependent PL analysis on E_{X1} and E_{X2} confirmed our

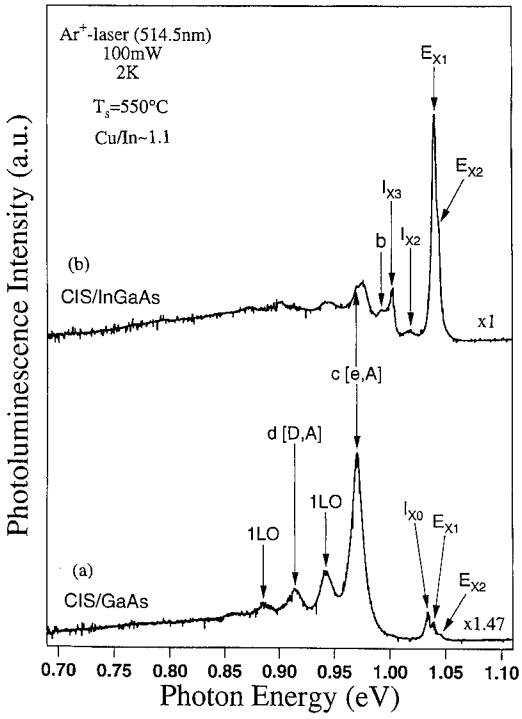

Fig. 6. Photoluminescence spectra at 2 K obstained from $CuInSe_2$ grown on (a) GaAs and (b) $In_{0.29}Ga_{0.71}As$ *pseudo*-lattice-matched substrates.

assignment of these peaks to the free exciton emissions. I_{X2} and I_{X3} are attributed tentatively to emissions associated with an exciton-defect complex from their temperature dependence. Electrical characterization of the CIS/InGaAs (CIS/GaAs) film showed $\mu \sim 110\ \mathrm{cm^2/V\ s}$ ($\mu \sim 38.6\ \mathrm{cm^2/V\ s}$) with a hole concentration of $p \sim 1.5 \times 10^{17}\ \mathrm{cm^{-3}}$ ($p \sim 3.4 \times 10^{17}\ \mathrm{cm^{-3}}$) at RT, also suggesting improvement in crystalline quality consistent with the PL results. Further improvement in the film quality can make possible the control of transport and optical properties of the material extrinsically by intentionally incorporating impurities.

4. Summary

Defects in CIS were found to be strongly sensitive to the misfit strain with respect to the substrate, suggesting that the residual defects created during the process of solar cell fabrication can be further controlled by minimizing the strains among the substrate, absorber and window layers, and metal contacts as well as the surface strain at the grain boundaries. In addition, such high-quality CIS epitaxial films can make possible the investigation of the properties of intrinsic defects as well as the behavior of impurities which are critical parameters to be controlled for device applications.

Acknowledgements

S.N. and T.K greatly appreciate useful discussions and comments by Professor H.H. Wieder regarding the effects of strain on the properties of the CIS films. S.N., P.J.F., and A.Y. would like to thank Dr. H. Yajima and Dr. Y. Makita for their continuous support. One of the authors (C.W.T.) gratefully acknowledges the support of the NSF-Japan Center for Global Partnership Program.

References

[1] J.R. Tuttle, J.S. Ward, A. Duda, T.A. Berens, M.A. Contreras, K.R. Ramanathan, A.L. Tennant, J. Keane, E.D. Cole, K. Emery and R. Noufi, in: Proc. Materials Research Society Spring Meeting J 1.2, April 5–8, San Francisco (1996), to be published.
[2] K. Zweibel, H.S. Ullal, B.G. Roedcrn, R. Noufi, T.J. Coutts and M.M. Al-Jassim, Proc. 23rd IEEE Photovoltaic Specialists Conf. (1993) p. 1073.
[3] S. Niki, Y. Makita, A. Yamada, O. Hellman, P.J. Fons, A. Obara, Y. Okada, R. Shioda, H. Oyanagi, T. Kurafuji, S. Chichibu and H. Nakanishi, J. Crystal Growth 150 (1995) 1201.
[4] S. Niki, H. Shibata, P.J. Fons, A. Yamada, A. Obara, Y. Makita, T. Kurafuji, S. Chichibu and H. Nakanishi, Appl. Phys. Lett. 67 (1995) 1289.
[5] P.J. Fons, in: Proc. Materials Research Society Spring Meeting, Boston (1995), to be published.
[6] S. Adachi, J. Appl. Phys. 53 (1982) 8775.
[7] See, for example: E.A. Fitzgerald, Y.-H. Xie, M.L. Green, D. Brasen, A.R. Kortan, J. Michel, Y.-J. Mii and B.E. Beir, Appl. Phys. Lett. 59 (1991) 811.
[8] J.C.P. Chang, J.J. Chen, J.M. Fernandez, H.H. Wieder and K.L. Kavanagh, Appl. Phys. Lett. 60 (1992) 1129.
[9] J.C.P. Chang, T.P. Chin, C.W. Tu and K.L. Kavanagh, Appl. Phys. Lett. 63 (1993) 500.
[10] S. Niki, P.J. Fons, A. Yamada, T. Kurafuji, S. Chichibu, H. Nakanishi, W.G. Bi and C.W. Tu, Appl. Phys. Lett. 69 (1996) 647.
[11] Y. Okada, P.J. Fons, R. Shioda, H. Oyanagi, S. Niki, A. Yamada and Y. Makita, Crystal Res. Technol. 31 (1996) 285.
[12] H. Neuman, Solar Cells 16 (1986) 317.
[13] S. Niki, Y. Makita, A. Yamada, H. Shibata, P.J. Fons, A. Obara, T. Kurafuji, S. Chichibu and H. Nakanishi, in: Proc. 1st World Conf. on Photovoltaic Energy Conversion (1995) p. 132.

ELSEVIER

Journal of Crystal Growth 175/176 (1997) 1057–1062

JOURNAL OF CRYSTAL GROWTH

MBE growth of PbSe/CaF2/Si(1 1 1) heterostructures

P.J. McCann[a,*], X.M. Fang[a], W.K. Liu[b], B.N. Strecker[a], M.B. Santos[b]

[a] *School of Electrical and Computer Engineering and Laboratory for Electronic Properties of Materials, University of Oklahoma, Norman, Oklahoma 73019, USA*

[b] *Department of Physics and Astronomy and Laboratory for Electronic Properties of Materials, University of Oklahoma, Norman, Oklahoma 73019, USA*

Abstract

Successful epitaxial growth of PbSe/CaF_2/Si(1 1 1) heterostructures using just one growth chamber of a molecular beam epitaxy system is described. Sharp (1 × 1) streaks in the RHEED pattern confirm the high structural quality of PbSe, and SEM and Nomarski microscopy reveal smooth PbSe surfaces. The PbSe epilayers show mobilities as high as 23 200 $cm^2 V^{-1} s^{-1}$ and electron concentrations of $1–2 \times 10^{17} cm^{-3}$ at 77 K. In addition, observation of RHEED intensity oscillations confirm layer-by-layer growth modes for both CaF_2 and PbSe. The PbSe/CaF_2 interface has also been characterized by using X-ray photoelectron spectroscopy. All the Ca 2p, F 1s, Pb 4f and Se 3d peaks show chemical shifts as PbSe coverage on CaF_2 increases. Results show that the PbSe/CaF_2 interface consists of a thin transition layer dominated by Pb–F and Ca–Se bonds.

1. Introduction

Despite the large thermal expansion mismatch between PbSe and silicon, high-quality epitaxial layers of PbSe can be grown on (1 1 1)-oriented silicon substrates when fluoride buffer layers are used [1, 2]. Dislocation glide along {1 0 0} slip planes, which can preserve the crystalline quality of the PbSe epilayer, appears to be responsible for this thermal strain relief [3]. Such heteroepitaxial growth offers a number of benefits that can lead to fabrication of improved infrared optoelectronic devices (PbSe has a band gap of 175 meV at 77 K.) such as photovoltaic infrared sensor arrays [4]. Initial work in this area focused on using a stacked BaF_2/CaF_2 buffer layer [5], but recent work has shown that just a thin CaF_2 layer produces good PbSe epitaxy [6]. This fluoride buffer layer, even when as thin as 50 Å, does appear to be necessary for good PbSe epitaxy since attempts to grow PbSe directly on Si(1 1 1) have resulted in poor layer quality [7]. In this work, we show that high quality PbSe/CaF_2/Si(1 1 1) heterostructures can be grown using just one growth chamber of a molecular beam epitaxy system. In addition, we present reflection high energy electron diffraction (RHEED) intensity oscillation data that confirm layer-by-layer growth

* Corresponding author. E-mail: mccann@mailhost.ecn.uoknor.edu.

0022-0248/97/$17.00 Copyright © 1997 Elsevier Science B.V. All rights reserved
PII S0022-0248(96)00913-X

modes for both CaF_2 and PbSe. We so present X-ray photoelectron spectroscopy (XPS) data which show that the PbSe/CaF_2 interface consists of a thin transition layer dominated by Pb–F and Ca–Se bonds.

2. MBE growth procedures and results

Epitaxial growth of CaF_2 on Si commonly employs a high-temperature ($> 850°C$) oxide desorption step. High temperatures in the presence of a selenium background pressure, as is the case when both CaF_2 and PbSe are grown in the same chamber, are a cause for concern since unwanted reactions between selenium and silicon or calcium may occur. Reactions between silicon and group-VI elements are possible [8], and prior work [9] has shown that selenium vapor does react with BaF_2 forming a BaSe compound at moderate temperatures and a selenium-rich Ba_2Se_3 compound at temperatures above 690°C. Formation of similar reaction products involving selenium and calcium, and/or silicon, would certainly interfere with the silicon–calcium bonding that is required for good CaF_2 epitaxy on Si(1 1 1) [10]. It is therefore desirable to reduce processing temperatures to as low a value as possible such that unwanted reactions are inhibited. Accordingly, we have reduced the silicon preparation temperature more than 300°C by adding an HF : H_2O (1 : 10 in volume) dipping step to the standard Shiraki cleaning procedure [11]. This produces a hydrogen-passivated silicon surface [12], which can be thermally cleaned at a much lower temperature than an oxide-passivated surface. Successful preparation of three inch diameter Si(1 1 1) wafers was confirmed by observing sharp (7×7) streaks in the RHEED patterns after they were annealed for 20 min at 520°C.

CaF_2 growth was accomplished by heating bulk CaF_2 in a dual zone effusion cell held at 1280°C. This cell temperature produces a beam equivalent pressure for CaF_2 of 6.4×10^{-8} Torr and a growth rate of 0.07 ML/s. A two-stage procedure [13] was used to grow approximately 100 Å of CaF_2 for subsequent PbSe epitaxy. Two monolayers of CaF_2 were first grown on the thermally-cleaned Si(1 1 1) at 700°C, and then the substrate temperature was lowered to $\leqslant 250°C$ where additional CaF_2 growth occurred. To minimize the extent of any unwanted reactions, the total time for the initial growth step, which includes: (1) heating up, (2) about 30 s of growth, and (3) cooling down, is kept to less than 15 min. Fig. 1 shows RHEED intensity oscillation data for growth at the second stage temperatures. As the substrate temperature is lowered, the number of intensity oscillations increases showing that layer-by-layer growth continues longer at lower temperatures. As many as ten oscillations are observed for a substrate temperature of 70°C, an indication that the surface migration length for CaF_2 molecules is large, as expected for an ionic compound. Observation of RHEED intensity oscillations is a useful technique for determining epilayer quality during CaF_2 growth since

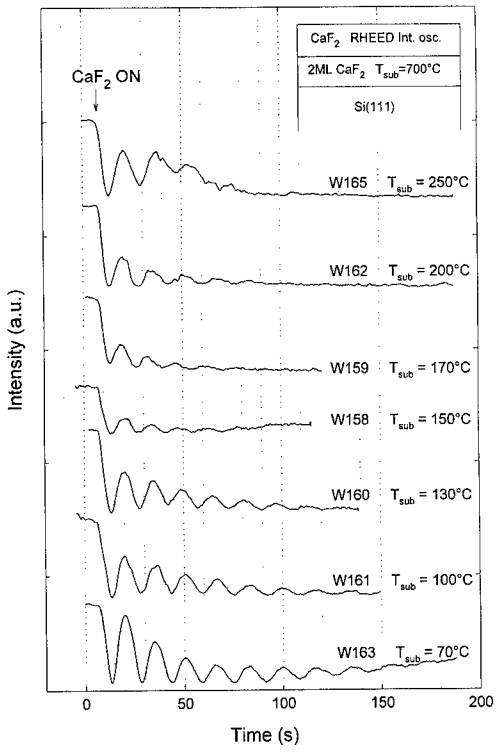

Fig. 1. RHEED intensity oscillations for MBE growth of CaF_2 on Si(1 1 1). Enhanced layer-by-layer growth at low temperatures is the evidence of large surface migration length of CaF_2 molecules.

surface reconstruction does not occur with this material and is thus not available as a technique for determining epilayer quality. Moreover, observing RHEED oscillations allows accurate growth rate calibration.

PbSe growth was accomplished by heating bulk PbSe in a low-temperature effusion cell held at 605°C. This cell temperature produces a beam equivalent pressure for PbSe of 6.1×10^{-7} Torr and a growth rate of 0.26 ML/s. For this work, PbSe layers of approximately 2.3 μm thickness were grown at 310°C on 100 Å of CaF_2 on Si(1 1 1). A small amount of additional PbSe was then grown at various substrate temperatures ranging from 310°C to 210°C for RHEED intensity oscillation experiments, see Fig. 2. Our results are in general agreement with those of Fuchs et al. [14] who observed optimal PbSe growth temperatures above 220°C, where surface diffusion is sufficient for layer-by-layer growth, but below 260°C, where step propagation is not enhanced. However, our results show that layer-by-layer growth below 200°C may be possible since no degradation in RHEED oscillations is seen down to 210°C. This would be consistent with recent results for growth of PbTe where as many as 155 RHEED oscillations have been observed at temperatures as low as 95°C [15]. RHEED oscillation data therefore suggest that both CaF_2 and PbSe may grow via a layer-by-layer mechanism at substrate temperatures below 200°C. Overlap in optimal growth temperatures for CaF_2 and PbSe, as well as accurate growth rates provided by the RHEED intensity oscillation frequencies, will facilitate the fabrication of heterostructure devices composed of thin layers of CaF_2 and PbSe.

Fig. 3 is a Nomarski micrograph showing the surface morphology of a typical PbSe layer. The smooth, featureless surface indicates that unwanted reactions such as those observed by Mathet et al. [2] did not occur during the growth procedure. Hall-effect measurements show that our PbSe layers are n-type and have mobilities as high as 23 200 $cm^2\ V^{-1}\ s^{-1}$ at 77 K, which are comparable to those obtained by Zogg et al. [16]. Even though the layers are undoped, electron concentrations are in the range of $1–2 \times 10^{17}\ cm^{-3}$ due to native defects in the form of selenium vacancies, which each

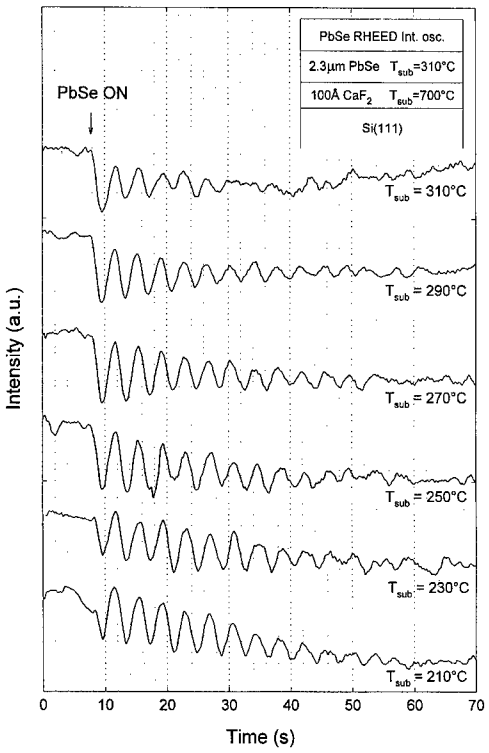

Fig. 2. RHEED intensity oscillations for MBE growth of PbSe on PbSe/CaF_2/Si(1 1 1). Substrate temperatures between 220°C and 260°C are optimal for layer-by-layer growth. Note that a 30°C process window exists where both CaF_2 and PbSe can grow via a layer-by-layer mechanism.

donate two electrons to the conduction band [17]. These vacancies are believed to be created by selenium evaporation after PbSe molecules condense on the substrate surface. Although the concentrations reported here may seem large, they are more than an order of magnitude smaller than electron concentrations for undoped IV–VI semiconductor layers grown by liquid phase epitaxy (LPE) on BaF_2 substrates [18]. It is possible to control selenium vacancy concentration during MBE growth by providing an additional source of selenium as shown by Mathet et al. [2] who demonstrated that even p-type PbSe layers, corresponding to a condition of lead vacancies, could be obtained by increasing the selenium flux. We have just begun experiments in controlling selenium vacancy concentrations using a selenium flux provided by

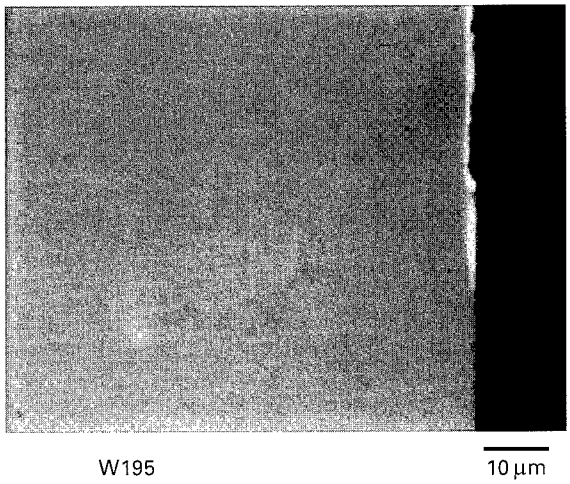

Fig. 3. Nomarski optical micrograph showing the surface morphology of a 2.6 μm thick PbSe layer grown on a buffer layer of CaF_2 on Si(1 1 1). Note the sharp (1 1 1) cleave at the sample edge in the lower right-hand corner.

an EPI Inc. valved-cracker source. Initial results suggest that carrier type and concentration can be controlled by varying the PbSe to Se flux ratio.

3. XPS characterization of the PbSe/CaF_2 interface

Earlier work involving LPE growth of PbSe on BaF_2 substrates revealed that selenium vapor reacts with BaF_2 to form a BaSe reaction layer [9]. Evidence for interfacial reactions between IV–VI semiconductors and group-II-A fluorides has also been seen in MBE growth of PbSe on BaF_2/CaF_2 buffer layers on silicon; blisters are observed to occur when the CaF_2 layer is greater than the critical thickness of 20 Å [2]. It was suspected that reaction with BaF_2 allowed migration of selenium to the CaF_2 layer where it penetrated threading dislocations and reduced the layer's plasticity. Possible reaction product formation at the PbSe/CaF_2 interface is worth investigating since the chemistry is similar to the PbSe/BaF_2 interface. In addition, it is important to know whether the PbSe/CaF_2 interface is structurally abrupt. If so, these materials could be used to fabricate quantum effect heterostructure devices having band edge discontinuities greater than 3 eV.

The PbSe/CaF_2 interface was studied using an XPS analysis chamber attached via a buffer chamber to our MBE growth chamber. XPS spectra were taken using an $AlK\alpha_{1,2}$ source ($h\nu$ = 1486.6 eV) at a potential of 15 kV and with an emission current of 10 mA. Spectra of sample surfaces were taken following growth at 220°C of small amounts of PbSe onto 100 Å of CaF_2 on Si(1 1 1). Fig. 3 shows several XPS spectra for various amounts of PbSe coverage ranging from 0.27 to 26 ML. Monolayer coverage is calculated from the known PbSe growth rate as determined from the RHEED intensity oscillation frequency, see Fig. 4. Shifts of 1.65 eV and 1.70 eV, for the Pb $4f_{7/2}$ and Se 3d binding energies are seen, respectively, as PbSe coverage increases. Note that most of the chemical shift occurs between 0.81 and 6.5 ML and that photoelectron peak energies for Pb and Se shift in tandem. This shows that both Pb and Se interact with the CaF_2 surface and that this interaction extends for only a short distance into the PbSe layer. Binding energies for Ca $2p_{3/2}$ and F 1s are also observed to shift in tandem as PbSe coverage increases, although the amount of shift is less, 1.25 eV for both elements.

Our XPS results do not provide any evidence for the existence of a reaction product at the PbSe/CaF_2 interface. The fact that all photoelectron peak energies shift in tandem implies that there is an orderly compositional transition through the interface. The thickness of this transition layer, about 6.5 ML, can be partially accounted for by the open three-dimensional structure of the CaF_2(1 1 1) surface. Three layers of atoms are available for bonding with deposited material: (1) a layer of fluorine at the surface, (2) a layer of calcium 0.79 Å below the surface, and (3) another layer of fluorine 1.58 Å below the surface. This structure allows interpenetration of the PbSe and CaF_2 layers, which necessarily results in a thin compositional transition layer.

Based on electrostatic arguments, it is reasonable to assume that only Pb–F and Ca–Se bondings occur at the PbSe/CaF_2 interface. This leaves two possible bonding arrangements for the interface. The first one consists of lead atoms residing directly over and bonding to the top layer of fluorine atoms and of selenium atoms residing directly over the

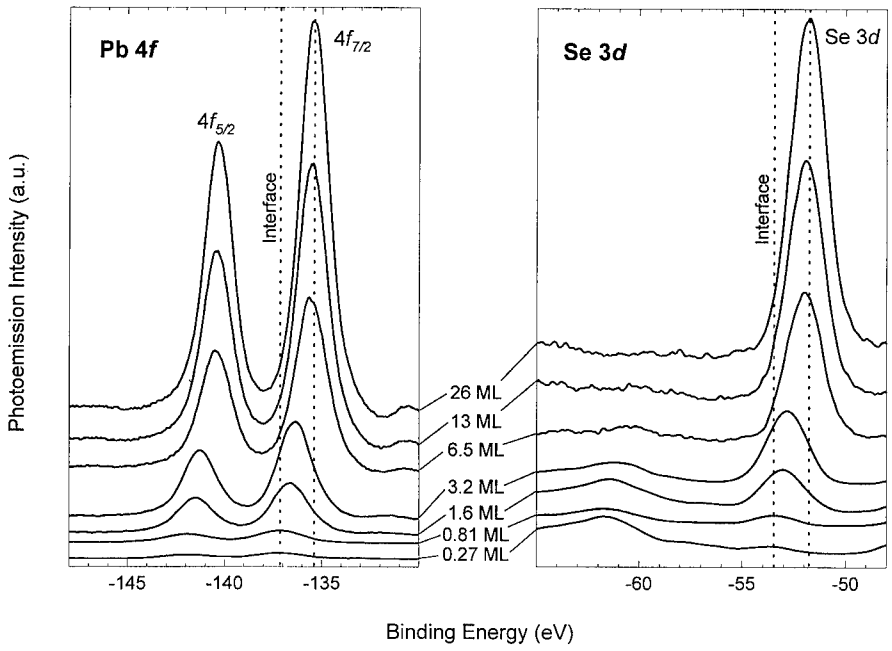

Fig. 4. XPS spectra showing the shifts in Pb $4f_{7/2}$ and Se 3d binding energies for various monolayer coverages of PbSe on CaF_2. In-tandem chemical shifts indicate that both elements interact with the CaF_2 surface.

lower layer of fluorine atoms but bonding to the three surrounding calcium atoms. The second consists of lead atoms residing directly over and bonding to the lower layer of fluorine atoms and of selenium atoms residing directly over and bonding to the layer of calcium atoms. Coexistence of these two bonding arrangements results in the growth of PbSe epilayers with twinned domains azimuthally rotated by $(2n\text{-}1)\pi/3$ with respect to each other. Diffraction from such a layer would show sixfold symmetry. This was not observed in our RHEED patterns showing that only one bonding arrangement exists for our structures. It is not clear from the XPS data which of the two bonding arrangements exists; both are supported by the data. It has, however, been suggested that equilibrium interactions favor the second bonding arrangement [19].

4. Summary

In summary, we have grown high-quality PbSe layers on silicon substrates using 100 Å thick CaF_2 buffer layers, where both materials were grown in the same MBE chamber. SEM and Nomarski microscopy show that the layers are smooth with no evidence of unwanted reactions associated with a selenium background pressure. RHEED intensity oscillations were observed during growth of both the CaF_2 and the PbSe showing that both materials have layer-by-layer growth modes. Hall mobilities for the PbSe layer were as high as 23 200 $cm^2\ V^{-1}\ s^{-1}$. XPS data showed that the PbSe/CaF_2 interface consists of a thin transition layer and lacks any distinct interfacial compound. Our results show that this materials system is a promising candidate for fabrication of infrared optoelectronic devices on silicon substrates.

Acknowledgements

This work was supported by NSF EPSCoR under Cooperative Agreements OSR-9108771 and OSR-9550478.

References

[1] H. Zogg, S. Blunier, A. Fach, C. Maissen, P. Miller, S. Teodoropol, V. Meyer, G. Kostorz, A. Dommann and T. Richmond, Phys. Rev. B 50 (1994) 10801.

[2] V. Mathet, P. Galtier, F. Nguyen-Van-Dau, G. Padeletti and J. Olivier, J. Crystal Growth 132 (1993) 241.

[3] H. Zogg, C. Maissen, S. Blunier, S. Teodoropol, R.M. Overney, T. Richmond and H. Haefke, J. Crystal Growth 127 (1993) 668.

[4] A. Fach, C. Maissen, J. Masek, S. Teodoropol and H. Zogg, Mater. Res. Soc. Symp. Proc. 229 (1994) 279.

[5] H. Zogg, C. Maissen, J. Masek, T. Hoshino, S. Blunier and A.N. Tiwari, Semicond. Sci. Technol. 6 (1991) C36.

[6] H. Zogg, A. Fach, J. John, J. Masek, P. Müller, C. Paglino, Narrow Gap Semiconductors, 1995 (Institute of Physics, London, 1995) p. 160.

[7] P. Müller, A. Fach, J. John, A.N. Tiwari, H. Zogg and G. Kostorz, J. Appl. Phys. 79 (1996) 1911.

[8] R.D. Brigans and M.A. Olmstead, Phys. Rev. B 39 (1989) 12985.

[9] P.J. McCann and C.G. Fonstad, J. Electron. Mater. 20 (1991) 915.

[10] L. Schowalter and R. Fathauer, CRC Critical Rev. Solid State Mater. Sci. 15 (1989) 367.

[11] A. Ishizaka and Y. Shiraki, J. Electrochem. Soc. 133 (1986) 666.

[12] M. Niwano, Y. Takeda, Y. Ishibashi, K. Kurita and N. Miyammoto, J. Appl. Phys. 71 (1992) 5646.

[13] N.S. Sokolov, J.C. Alverez and N.L. Yakovlev, Appl. Surf. Sci. 60/61 (1992) 421.

[14] J. Fuchs, Z. Feit and H. Preier, Appl. Phys. Lett. 53 (1988) 894.

[15] G. Springholz and G. Bauer, J. Crystal Growth 144 (1994) 157.

[16] H. Zogg and M. Hüpi, Appl. Phys. Lett. 47 (1985) 133.

[17] G.W. Pratt, J. Nonmetals 1 (1973) 103.

[18] P.J. McCann, S.K. Aanegola and J.E. Furneaux, Appl. Phys. Lett. 65 (1994) 2185.

[19] D.K. Hohnke, H. Holloway and M.D. Hurley, Thin Solid Films 38 (1976) 49.

ELSEVIER

Journal of Crystal Growth 175/176 (1997) 1063–1068

JOURNAL OF CRYSTAL GROWTH

(GaMn)As: GaAs-based III–V diluted magnetic semiconductors grown by molecular beam epitaxy

T. Hayashi[a], M. Tanaka[a,b,*], T. Nishinaga[a], H. Shimada[c], H. Tsuchiya[c], Y. Otuka[c]

[a] *Department of Electronic Engineering, The University of Tokyo, 7-3-1 Hongo, Bunkyo-ku, Tokyo 113, Japan*
[b] *PRESTO, Research and Development Corporation of Japan, Sakigake 21, Japan*
[c] *Cryogenic Center, The University of Tokyo, 2-11-16 Yayoi, Bunkyo-ku, Tokyo 113, Japan*

Abstract

We have grown novel III–V diluted magnetic semiconductors, $(Ga_{1-x}Mn_x)As$, on GaAs substrates by low-temperature molecular beam epitaxy using strong nonequilibrium growth conditions. When the Mn concentration x is relatively low ($\lesssim 0.08$), homogeneous alloy semiconductors, GaMnAs, are grown with zincblende structure and slightly larger lattice constants than that of GaAs, whereas inhomogeneous structures with zincblende GaMnAs (or GaAs) plus hexagonal MnAs are formed when x is relatively high. Magnetization measurements indicate that the homogeneous GaMnAs films have ferromagnetic ordering at low temperature.

PACS: 75.70. – i; 68.55.Bd; 73.61.Ey; 61.72.Vv

Keywords: GaMnAs; Diluted magnetic semiconductor; Low temperature MBE; Ferromagnetic order

1. Introduction

Molecular beam epitaxy (MBE) has made it possible to grow a variety of new heterostructures and alloy semiconductors with novel properties. Among them, diluted magnetic semiconductors (DMS) have attracted much interest, because they are expected to combine the properties both of magnetic materials and of semiconductors. DMSs are alloy semiconductors in which a fraction of cations are replaced by magnetic ions (transition metals or rare earths). So far, the studies of DMSs were mainly concentrated on II–VI-based materials [1], because some magnetic ions, particularly Mn^{2+}, can be easily incorporated into II–VI compounds by substituting group-II cations. In II–VI DMSs such as CdMnTe and related heterostructures, magneto-optical properties were extensively studied, and recently optical isolators were fabricated utilizing their large Faraday effect [2].

* Corresponding author. Fax: + 81 3 3816 4996; e-mail: masaaki@ee.t.u-tokyo.ac.jp.

0022-0248/97/$17.00 Copyright © 1997 Elsevier Science B.V. All rights reserved
PII S0022-0248(96)00937-2

On the other hand, the study of III–V based DMSs has been limited to InMnAs [3, 4], in which some interesting properties associated with carrier induced magnetism were found in p-type samples. Since these InAs-based DMSs have very narrow band gap (~ 0.36 eV) and much larger lattice constant (~ 0.605 nm) than that of GaAs, the applications to III–V electronics and optoelectronics will be limited. For a wide range of application in III–V systems, a new type of DMS based on GaAs, which is the most widely used and well understood III–V semiconductor, is needed to be prepared. Very recently, De Boeck et al. [5, 6] reported that ferromagnetic MnAs particles were controllably embedded in GaAs by annealing homogeneous GaMnAs layers. However, little is known so far on the epitaxial growth, structure, and magnetic properties of GaMnAs [7, 8]. This paper presents the study of MBE growth and properties of this new class of GaAs based DMS.

2. Molecular beam epitaxial growth

MBE growth of $(Ga_{1-x}Mn_x)As$ thin films on semi-insulating (0 0 1) GaAs substrates were performed with our ULVAC MBC-508 system using solid sources of Ga, As, and Mn. After growing a GaAs buffer layer at 600°C under normal growth conditions, the substrate temperature was cooled to 200–300°C while the As_4 flux was kept on. The reflection high-energy electron diffraction (RHEED) pattern changed from (2×4) to $c(4\times4)$. Then Ga and Mn shutters were successively opened to grow $(Ga_{1-x}Mn_x)As$ at 200–300°C with various Mn content x ranging from 0 to 0.17. The growth rate and the film thickness of GaMnAs were 0.35–0.5 μm/h and 0.5–1.4 μm, respectively. The Mn flux was determined from the growth rate of epitaxial MnAs thin films grown on GaAs and/or on Si, which was already established by our group [9]. All the homogeneous GaMnAs samples were grown under the As-rich conditions at low temperature, as will be described later. Although equilibrium solubility of transition metals in GaAs is generally limited to the order of doping levels ($\sim 10^{19}\,cm^{-3}$), this low-temperature MBE realizes strong nonequilibrium growth conditions, allowing a large amount of Mn atoms to be incorporated into the host GaAs lattice far above its solubility.

We found that homogeneous $(Ga_{1-x}Mn_x)As$ ternary alloys were grown when the Mn content x and growth temperature were relatively low. Fig. 1a shows a typical RHEED pattern of the homogeneous samples, which was taken during the growth of GaMnAs ($x = 0.007$) at 250°C with the azimuth of [1 1 0]. At the growth temperatures of 250°C and of 300°C, homogeneous GaMnAs alloys were obtained with x up to 0.078 and 0.005, respectively. In this case the RHEED patterns were very streaky like Fig. 1a, with (1×2) reconstruction (twofold streaks were weak). RHEED observations with various azimuths,

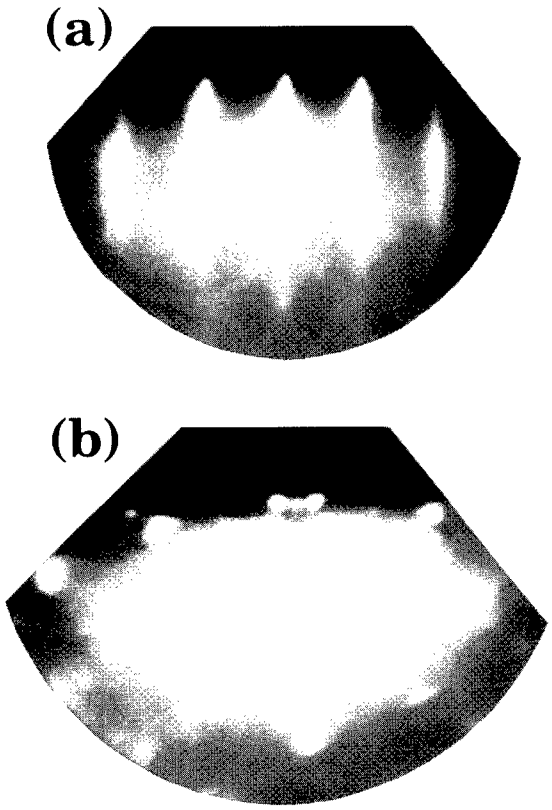

Fig. 1. RHEED patterns during the growth of (Ga, Mn)As with the azimuth of [1 1 0]: (a) the Mn content $x = 0.007$ grown at 250°C, (b) $x = 0.10$ grown at 300°C.

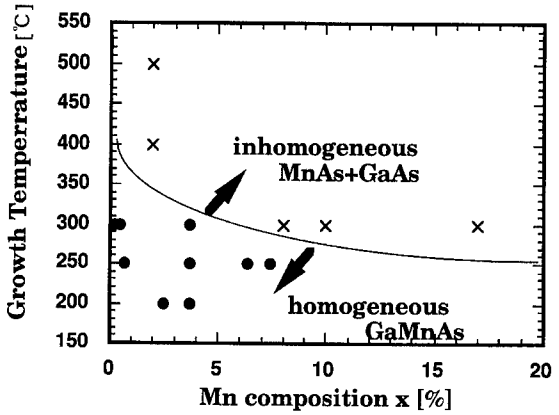

Fig. 2. Diagram of the (Ga, Mn)As film properties in relation to the two growth parameters (Mn content x and growth temperature). Solid circles and crosses denote homogeneous and inhomogeneous structures, respectively.

together with X-ray measurements, indicate that zincblende structure was epitaxially grown. At 300°C, RHEED intensity oscillations were clearly observed at the initial stage of the GaMnAs growth, indicating that epitaxial growth proceeds layer by layer.

In contrast, when the Mn content x and growth temperature were relatively high, clustering of hexagonal MnAs in the GaMnAs layer became significant. Fig. 1b shows a RHEED pattern during the growth of (Ga, Mn)As at $x = 0.10$ grown at 300°C. Diffractions from hexagonal MnAs were observed as well as those of zincblende GaAs (or GaMnAs). Analyzing the RHEED patterns with various azimuths, the most frequently observed epitaxial orientations were $(\bar{1}\,1\,0\,1)$MnAs$\|(0\,0\,1)$GaAs, $[\bar{1}\,\bar{1}\,2\,0]$MnAs$\|[1\,1\,0]$GaAs, similar to the "type-B" MnAs/GaAs heterostructures [10]. Though we have not studied in detail the properties of these inhomogeneous films of GaMnAs (or GaAs) + MnAs, the structure is probably similar to that reported in the Refs. [5, 6]. This shows the limitation of the Mn solubility in GaAs by low-temperature MBE. In Fig. 2, we summarized our results of homogeneous and inhomogeneous film properties in relation to the two important growth parameters (growth temperature and Mn composition).

3. Structural characterizations

To characterize the structure of the (Ga, Mn)As films, X-ray diffraction measurements were done on all the samples. Fig. 3a–Fig. 3c shows θ–2θ spectra of the various homogeneous $Ga_{1-x}Mn_xAs$ films grown at 250°C: (x, thickness) = (0.037, 1.4 μm), (0.064, 0.44 μm), (0.074, 1.4 μm). The peaks of GaMnAs were observed very close to the peak of GaAs (4 0 0) reflection. The splittings are due to Cu-Kα1 and Cu-Kα2. One can see that the lattice constants of the GaMnAs films are slightly larger than that ($a_0 = 0.56533$ nm) of GaAs. No indication of MnAs formation was seen in these samples. From double-crystal X-ray diffraction measurements, the values of lattice mismatch $\Delta a/a_0$ to the GaAs substrate were estimated to be 0.59% at $x = 0.074$. The values of lattice mismatch measured by X-ray at various x are plotted by the solid circles in Fig. 3d. Here, we plotted the data of some samples for which we measured x by EMPA (the data of other samples that we not measured by EMPA are not plotted, and the values of x of those samples were estimated by the experimental formula derived from Fig. 3d). The line-widths of the GaMnAs peaks were ~ 150 s, only a little wider than that of GaAs substrate. The narrow line width of the GaMnAs peaks indicates high epitaxial quality. The GaMnAs films on GaAs substrates are under the compressive strain, therefore, the lattice spacing of these sample is extended in the vertical direction. We calculated intrinsic lattice constants of cubic GaMnAs assuming that the Poisson's ratio of GaMnAs is equal to that of GaAs, as plotted by the crosses in Fig. 3d. The intrinsic lattice constants are on a nearly straight line, i.e. following Vegard's law.

In contrast, for the inhomogeneous samples whose RHEED patterns showed MnAs clustering like Fig. 1b, MnAs formation was also observed in X-ray spectra, as shown in Fig. 3e which was taken from the sample with nominal x of 0.08 grown at 300°C. One can see an intense peak of MnAs$(\bar{1}\,1\,0\,1)$ as well as that of GaAs (2 0 0). A small peak of MnAs$(\bar{1}\,1\,0\,0)$ was also seen. This indicates that the crystal orientation of the MnAs clusters in GaAs (or possibly GaMnAs) is mainly the $(\bar{1}\,1\,0\,1)$ of the

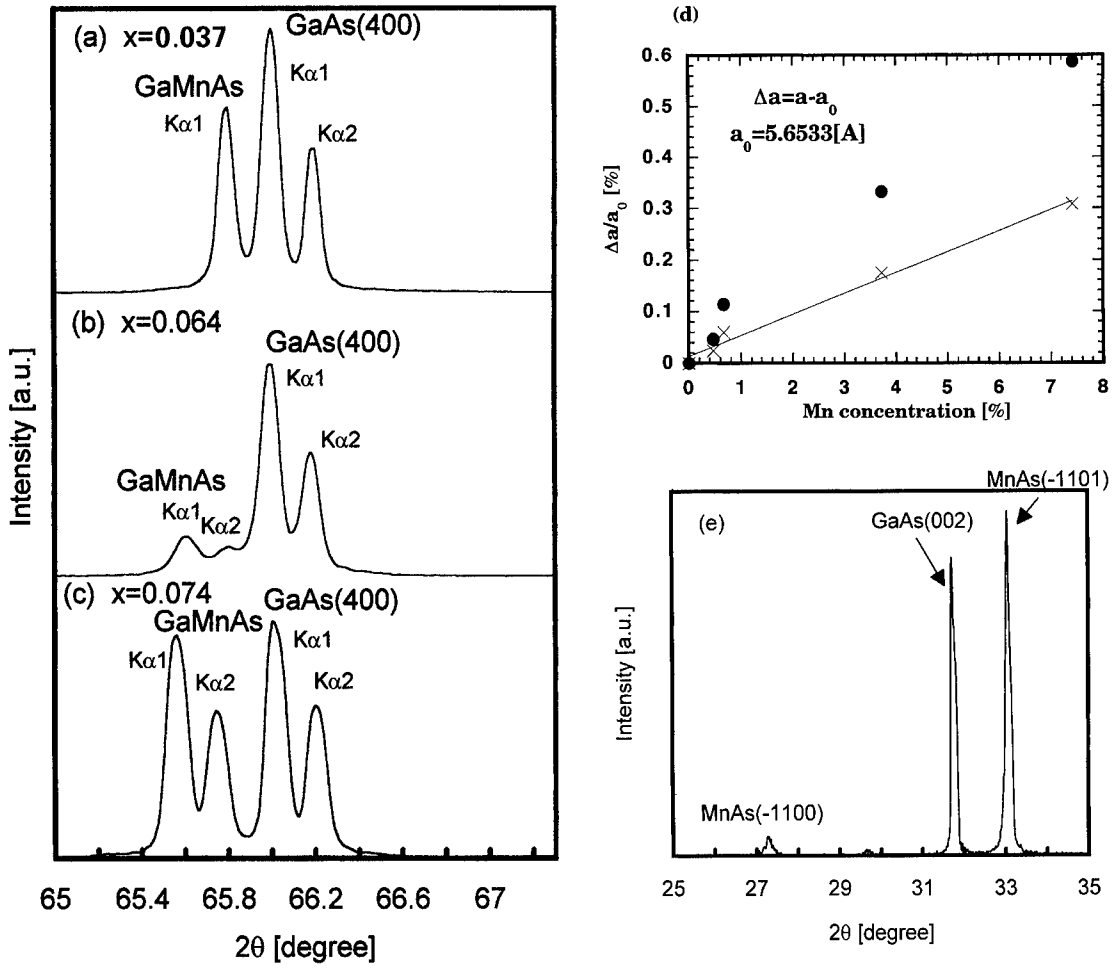

Fig. 3. X-ray diffraction (θ–2θ) spectra of various (Ga, Mn)As films grown on (0 0 1) GaAs: (a)–(c) homogeneous $Ga_{1-x}Mn_xAs$ films grown at 250°C; (a) $x = 0.037$, (b) $x = 0.064$, (c) $x = 0.074$. (d) The lattice mismatch of GaMnAs to GaAS substrate at various Mn content x, investigated with double crystal X-ray diffraction measurements. The values of x were estimated by EMPA. Solid circles are experimental values, and crosses are calculated values, assuming the GaMnAs films are fully strained. (e) X-ray spectrum of an inhomogeneous film of GaAs (or GaMnAs) + MnAs with the nominal value of $x = 0.08$ grown at 300°C.

hexagonal structure, in agreement with the results of RHEED.

4. Magnetic properties

First, magnetotransport properties were studied for the homogeneous GaMnAs samples. In Hall measurements at room temperature and at 77 K, all samples showed p-type conduction with the hole concentration of $3.8 \times 10^{17}\,cm^{-3}$ (Mn composition $x = 0.004$, $T_g = 300°C$) – $2.6 \times 10^{20}\,cm^{-3}$ (Mn composition $x = 0.074$, $T_g = 250°C$) with no ferromagnetic behavior. Within our experiments, there was no special correlation between the hole concentration and their growth parameters. At low temperature range (4.2 K or below), however, clear hysteretic behaviors have appeared in magnetoresistance (R_{xx}–H) measurements, and Hall resistance (R_{xy}–H) measurements showed extraordinary Hall effect (EHE), suggesting the presence of ferromagnetic ordering.

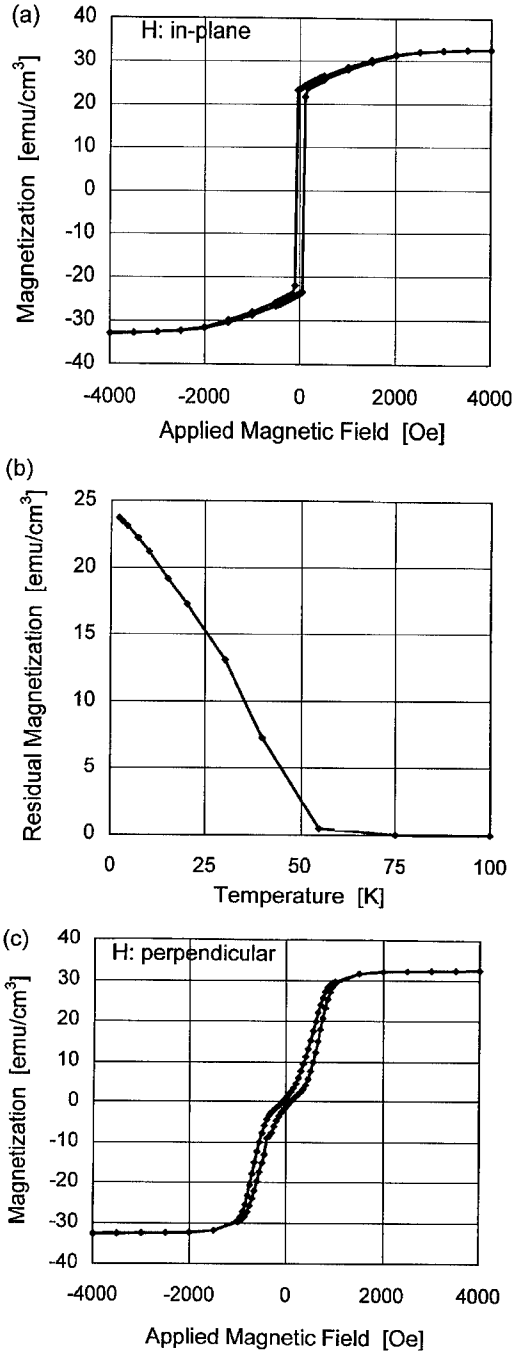

Fig. 4. (a) Magnetization (M–H) curve of a 1.4 μm-thick GaMnAs ($x = 0.074$, grown at 250°C) measured by SQUID at 1.9 K, when the magnetic field was applied in plane. (b) Temperature dependence of the residual magnetization of the same sample, indicating the Curie temperature of this sample is 55–60 K. (c) Magnetization (M–H) curve of the same sample at 1.9 K, when the magnetic field was applied perpendicular to the film plane.

Magnetization measurements were performed on the homogeneous GaMnAs films using a superconducting quantum interference device (SQUID). Fig. 4a shows a magnetization (M–H) curve of a 1.4 μm-thick $(Ga_{1-x}Mn_x)As$ film with $x = 0.074$ measured at 1.9 K, when the magnetic field H was applied in plane along the $\langle 110 \rangle$ axis. The hole concentration and mobility of this sample at room temperature were $2.6 \times 10^{20}\ cm^{-3}$ and $7.24\ cm^2/V \cdot s$, respectively. A square-like hysteresis in the M–H characteristics directly indicates the presence of ferromagnetic ordering. The values of coercive field H_c and saturation magnetization M_s were estimated to be 56 Oe and 33 emu/cm^3, respectively. The clear hysteresis behavior remained when the temperature was increased up to 55 K, above which the hysteresis behavior disappeared. Fig. 4b shows the temperature dependence of residual magnetization M_r, indicating that the Curie temperature of this sample is 55–60 K, much higher than that (7.5 K) of p-type InMnAs [4].

To characterize the magnetic anisotropy, we have done magnetization measurements on the same sample with the magnetic field H applied perpendicular to the film plane. Fig. 4c shows the result of M–H characteristics measured at 1.9 K, exhibiting much higher saturation field (1500–2000 Oe). Though a little hysteresis behavior was observed, its shape is far from square. The results of Fig. 4a and Fig. 4c indicate that the easy magnetization axis of the present GaMnAs film is not perpendicular but aligned in the film plane.

5. Summary

We have grown new GaAs-based diluted magnetic semiconductors (Ga, Mn)As by low-temperature MBE. Homogeneous ternary alloys were obtained when the Mn content x and growth temperature were relatively low. The crystal structure was zincblende with slightly larger lattice constants than that of GaAs. All the GaMnAs samples showed p-type conduction with the hole concentration of 3.8×10^{17}–$2.6 \times 10^{20}\ cm^{-3}$. The homogeneous GaMnAs film with $x = 0.074$ was shown to have ferromagnetic ordering at low temperature

with the easy magnetization axis in plane, and its Curie temperature was estimated to be 55–60 K.

References

[1] J.K. Furdyna and J. Kossut, Eds., Semiconductors and Semimetals, Vol. 25, Diluted Magnetic Semiconductors (Academic Press, Boston, 1986).
[2] K. Onodera, T. Matsumoto and M. Kimura, Electron. Lett. 30 (1994) 1954.
[3] H. Munekata, H. Ohno, S. von Molnar, A. Segmuller, L.L. Chang and L. Esaki, Phys. Rev. Lett. 63 (1989) 1849.
[4] H. Ohno, H. Munekata, S. von Molnar and L.L. Chang, J. Appl. Phys. 69 (1991) 6103.
[5] J. De Boeck, R. Oesterholt, A. Van Esch, H.Bender, C. Bruynseraede, C. Van Hoof and G. Borghs, presented at the 2nd Int. Symp. on Metallic Multilayers, Cambridge, UK, September 1995; J. Magn. Magn. Mater. 156 (1996) 148.
[6] J. De Boeck, R. Oesterholt, A. Van Esch, H. Bender, C. Bruynseraede, C. Van Hoof and G. Borghs, Appl. Phys. Lett. 68 (1996) 2744.
[7] T. Hayashi, M. Tanaka, T. Nishinaga and H. Shimada, presented at the Spring Meeting of the Japan Society of Applied Physics (JSAP) 29aw-1, March 1996; T. Hayashi, M. Tanaka, T. Nishinaga, H. Shimada, H. Tsuchiya and Y. Otuka, Proc. 9th Int. Conf. on Molecular Beam Epitaxy, Malibu, USA, August (1996).
[8] We notice that other group are also studying GaMnAs independently: F. Matsukura, A. Shen, A. Oiwa, H. Ohno, S. Katsumoto, H. Iye, S. Sugano and Y. Sugawara, The Spring Meeting of JSAP 29aw-3, March 1996; H. Ohno, A. Shen, F. Matsukura, A. Oiwa, A. Endo, S. Katsumoto and H. Iye, Appl. Phys. Lett. 69 (1996) 363; Y. Nishikawa and J. Yoshino, Proc. 15th Electronic Materials Symp., Paper-J3 Izu-Nagaoka, July (1996); J. De Boeck, A. Van Esch and G. Borghs, Proc. 9th Int. Conf. on Molecular Beam Epitaxy, Malibu, USA, August (1996).
[9] M. Tanaka, J.P. Harbison, T, Sands, T.L. Cheeks, V.G. Keramidas and G.M. Rothberg, J. Vac. Sci. Technol. B 12 (1994) 1091; K. Akeura, M. Tanaka, M. Ueki and T. Nishinaga, Appl. Phys. Lett. 67 (1995) 3349.
[10] M. Tanaka, J.P. Harbison, M.C. Park, Y.S. Park, T. Shin and G.M. Rothberg, Appl. Phys. Lett. 65 (1994) 1964.

ELSEVIER

Journal of Crystal Growth 175/176 (1997) 1069–1074

JOURNAL OF CRYSTAL GROWTH

Epitaxy of (Ga, Mn)As, a new diluted magnetic semiconductor based on GaAs

A. Shen[a,*,1], H. Ohno[a,b], F. Matsukura[a], Y. Sugawara[a], N. Akiba[a], T. Kuroiwa[a], A. Oiwa[c], A. Endo[c], S. Katsumoto[c], Y. Iye[c]

[a] *Laboratory for Electronic Intelligent Systems, Research Institute of Electrical Communication, Tohoku University, Sendai 980-77, Japan*
[b] *Research Development Corporation of Japan (JRDC), Japan*
[c] *Institute for Solid State Physics, University of Tokyo, Tokyo 106, Japan*

Abstract

GaAs-based diluted magnetic semiconductor, (Ga, Mn)As, with Mn composition x up to 0.07 was prepared by molecular-beam epitaxy on GaAs substrate at temperatures ranging from 160 to 320°C. Clear reflection high-energy electron diffraction oscillations were observed at the initial growth stage, indicating that the growth mode is two-dimensional. The lattice constant of (Ga, Mn)As films determined by X-ray diffraction showed a linear increase with the increase of Mn composition. Well-aligned in-plane ferromagnetic order was observed by magnetization measurements. Magnetotransport measurements also revealed the presence of ferromagnetic order in the (Ga, Mn)As layer. The easy axis of magnetization can be reversed by changing the strain direction in (Ga, Mn)As. GaAs/(Ga, Mn)As superlattice structures with high crystal perfection and good interface quality were also prepared.

PACS: 68.55.Bd; 75.58.Pp; 73.61.Ey; 75.30.Gw

Keywords: Molecular-beam epitaxy; III–V compounds; Diluted magnetic semiconductors; Ferromagnetic order; Magnetic anisotropy; Superlattice

1. Introduction

Due to the limited low solubility of magnetic ions in III–V semiconductors [1–3] the study of diluted magnetic semiconductors (DMSs) has long been concentrated mostly on the II–VI-based materials [4]. By using non-equilibrium growth conditions of low-temperature molecular-beam epitaxy (LT-MBE), a III–V-based DMS, (In, Mn)As, was successfully prepared in 1989 [5] and substitution of Mn atoms for the In sites was found in homogenous (In, Mn)As films by X-ray-absorption fine-structure measurements [6]. Detailed magnetotransport study of p-type homogeneous

* Corresponding author. Fax: +81 22 217 5555; e-mail: shen@riec.tohoku.ac.jp.

[1] Permanent address: Shanghai Institute of Optics and Fine Mechanics, Chinese Academy of Sciences, Shanghai 201800, People's Republic of China.

0022-0248/97/$17.00 Copyright © 1997 Elsevier Science B.V. All rights reserved
PII S0022-0248(96)00967-0

(In, Mn)As films revealed the presence of carrier-induced ferromagnetic ordering at low temperatures [7]. The study of III–V DMSs, however, has so far been limited mostly to (In, Mn)As [5–11], except for the works on (Ga, Mn)Sb [12] and on the formation of MnAs clusters in GaAs host [13]. Recently, we have successfully prepared a new III–V-based DMS, (Ga, Mn)As [14], which is based on the most well understood and extensively used III–V compound, GaAs. Here we report in detail the MBE growth and properties of the (Ga, Mn)As films.

2. MBE growth of (Ga, Mn)As films

The (Ga, Mn)As films were grown by solid-source MBE on semi-insulating (0 0 1) GaAs substrates using constituent elements of Ga, Mn, and As. All the growth was carried out under As stabilized condition with the growth rate of 0.6–0.8 μm/h. The Mn content x in the $(Ga_{1-x}, Mn_x)As$ was calibrated by electron probe microanalysis measurements. Reflection high-energy electron diffraction (RHEED) was used for in situ monitoring of the growth procedures.

At a substrate temperature $T_s = 250°C$, (Ga, Mn)As films were obtained with x varying from 0.015 to 0.071. At a fixed $x = 0.035$ epitaxial (Ga, Mn)As layers can be grown at T_s ranging from 160°C to 320°C. Hereafter we will concentrate mostly on the samples grown at $T_s = 250°C$. A 100 nm GaAs layer was first grown at $T_s = 700°C$. After lowering T_s to 250°C, another 100 nm GaAs was grown prior to the growth of 150 nm thick (Ga, Mn)As. The first GaAs layer grown at 700°C showed the well-known (2×4) surface reconstruction, which changed to $c(4 \times 4)$ when T_s was lowered to 480–520°C and remained $c(4 \times 4)$ below. The surface reconstruction of LT GaAs and that of (Ga, Mn)As were (1×1) and (1×2), respectively, as shown in Fig. 1.

Clear RHEED oscillations were observed at the initial growth stage, indicating that the growth mode is two-dimensional. Fig. 2 shows the RHEED specular beam intensity oscillations for GaAs grown at 600°C and 250°C and for (Ga, Mn)As. One striking feature is that GaAs grown at 250°C can still keep the layer-by-layer growth. At first, we thought the oscillation of GaAs at LT might be caused by Mn, which acted as a surfactant. But the results are reproducible even

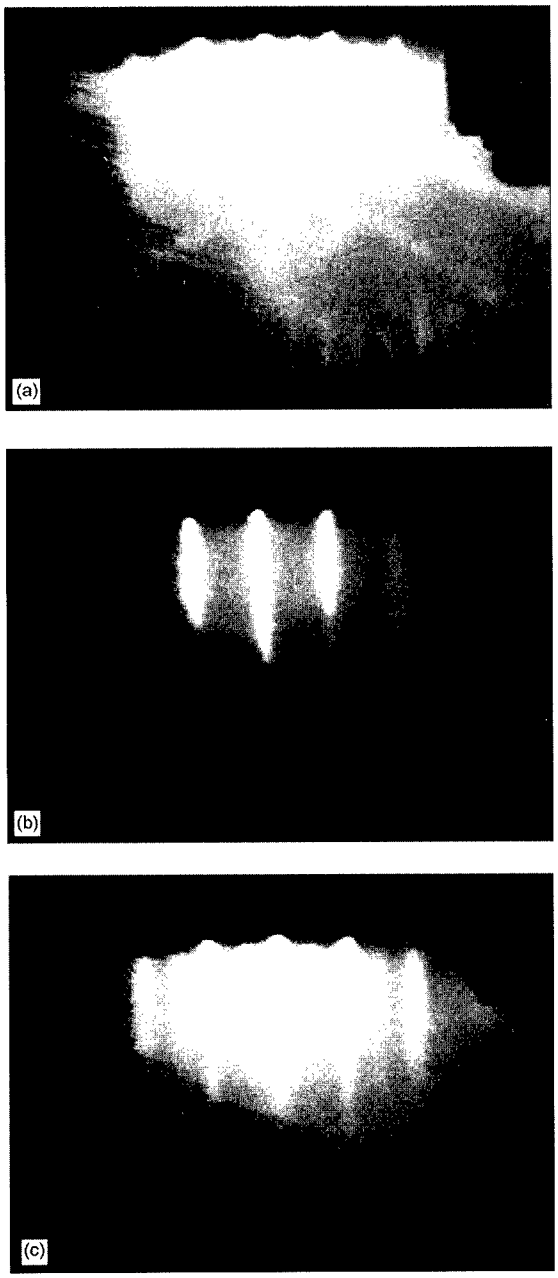

Fig. 1. RHEED patterns of (a) GaAs before the growth of LT GaAs, (b) LT GaAs, and (c) (Ga, Mn)As, taken from [$\bar{1}$ 1 0] azimuth, showed the $c(4 \times 4)$, (1×1) and (1×2) surface reconstruction, respectively.

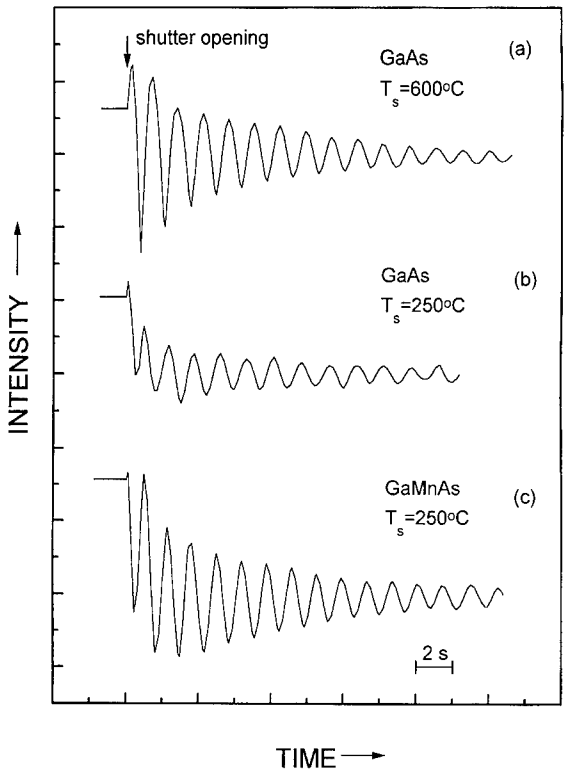

Fig. 2. Temporal evolution of RHEED specular beam intensity (along [1 1 0] azimuth) for (a) GaAs grown at 600°C, (b) GaAs grown at 250°C, and (c) (Ga, Mn)As grown at 250°C.

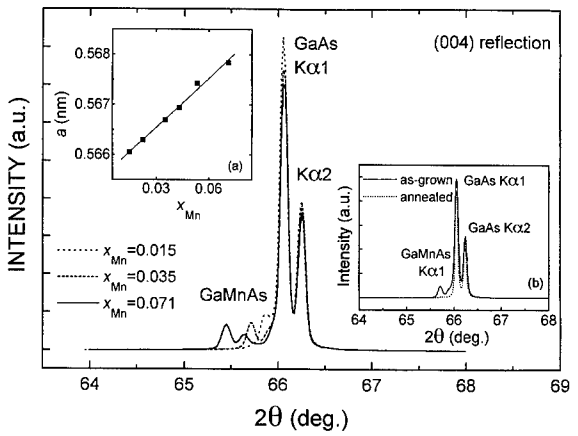

Fig. 3. X-ray diffraction curves for (Ga, Mn)As films, obtained by θ–2θ scans using Cu Kα radiation. Inset (a) shows lattice constant a vs. Mn composition x in the $(Ga_{1-x}, Mn_x)As$ films. Inset (b) shows the comparison of X-ray diffraction curves for (Ga, Mn)As films before and after annealing. The disappearing of (Ga, Mn)As peak in the annealed sample is an indication of the formation of MnAs clusters in the sample by the annealing process.

in the growth chamber without Mn cell. We have done works on the RHEED oscillations of GaAs systematically and found that GaAs can keep the layer-by-layer growth throughout the temperature range from 150°C to 730°C. Detailed results on RHEED oscillation of GaAs will be published elsewhere.

3. Metallurgical evaluations

θ–2θ scans of X-ray diffraction were performed at room temperature using Cu Kα radiation. Clear diffraction peaks from (Ga, Mn)As were observed for all the samples along with diffraction peaks from the underneath GaAs. Fig. 3 shows the diffraction curves of three samples with $x = 0.015$, 0.035 and 0.071. As can be seen from the figure, the peak position of (Ga, Mn)As shifts to lower angle as x increases, indicating that the lattice constant a increases with the increase of x. Dependence of a on the Mn composition x of (Ga, Mn)As is shown in the inset (a) of Fig. 3. a was calculated from the peak position of (Ga, Mn)As (0 0 4) diffraction assuming that (Ga, Mn)As is fully strained and that (Ga, Mn)As has the same elastic constant as GaAs. The assumption that (Ga, Mn)As is fully strained on GaAs was further confirmed by asymmetric X-ray diffraction by using a double crystal diffractometer with (1 1 5) reflection. As can be seen from inset (a), a increases linearly with x, showing that it follows Vegard's law. The extrapolated lattice constants for GaAs (0.566 nm) and MnAs (0.598 nm) are in good agreement with the known GaAs lattice constant (0.56533 nm) and with the MnAs lattice constant extrapolated from the (In, Mn)As work (0.601 nm) [5], suggesting that all the Mn atoms were incorporated in the zincblende alloy. There is no indication of the formation of the second-phase MnAs in the film from the X-ray diffraction measurements.

Inset (b) of Fig. 3 shows the diffraction curves from two samples with the same nominal Mn composition $x = 0.035$. One sample was annealed at

700°C for 2 min, the other one is the as-grown sample. The annealing was done in situ under As_4 flux. The complete disappearing of (Ga, Mn)As peaks in the annealed sample suggests the formation of MnAs clusters in GaAs host [13].

4. Magnetic and magnetotransport properties

Magnetization measurements done by SQUID (superconducting quantum interference device) magnetometer showed the presence of a ferromagnetic order in the (Ga, Mn)As films. Fig. 4 shows the magnetic field dependence of the magnetization of a sample with $x = 0.035$ at 5 K, with magnetic field B applied both parallel and perpendicular to the sample surface. A clear square hysteresis was observed when B was applied parallel to the sample surface, indicating the existence of a well-ordered ferromagnetic structure in the film. On the other hand, when B was applied perpendicular to the surface the hysteresis is less pronounced, suggesting that the magnetic anisotropy favors in-plane direction. From the vanishing of the remanent magnetization, which was obtained by temperature-dependent measurements, the Curie temperature of the sample was determined to be 60 K. Absence of remanence above 75 K also confirms that the concentration of MnAs, whose Curie temperature is 310 K, is extremely low.

Magnetotransport measurements were performed at temperatures ranging from 1.5 to 300 K under magnetic field up to 9 T. All samples showed p-type conduction. At low temperatures, the Hall resistivity ρ_{Hall} is dominated by the anomalous Hall effect and the B dependence of ρ_{Hall} showed a hysteresis loop very similar to what was observed in magnetic measurements when B was applied perpendicular to the sample surface. The carrier concentration in the sample with $x = 0.035$ was determined to be $3\text{–}4 \times 10^{20}\ cm^{-3}$ from the high magnetic field region ($6\ T < B < 9\ T$) at 1.5 K, which is of the same order as the Mn concentration ($7.7 \times 10^{20}\ cm^{-3}$). The inset of Fig. 4 shows the magnetization M determined by SQUID measurement and that deduced from magnetotransport measurement by taking $\rho_{Hall} = c\rho M$ (where ρ is the resistivity, c a constant). Very good agreement was

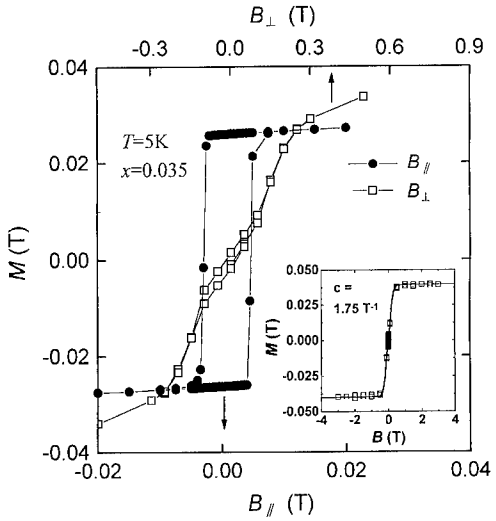

Fig. 4. Magnetic field dependence of magnetization M at 5 K for a (Ga, Mn)As film with $x = 0.035$, with the field applied parallel (solid circle) and perpendicular (open square) to the sample surface. Inset shows a comparison of B dependence of M between SQUID measurement (open square, at 5 K) and magnetotransport measurement (solid line, at 4.2 K).

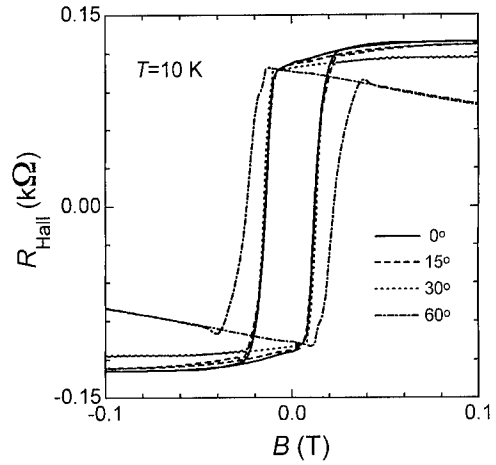

Fig. 5. Hall resistance, R_{Hall}, of (Ga, Mn)As/(In, Ga)As heterostructure as a function of B with an angle between B and the sample surface normal as a parameter. A square hysteresis loop was observed. The coercive field changes with the angle while the height of the hysteresis loop keeps unchanged, suggesting the easy axis of magnetization is perpendicular to the sample surface.

obtained with $c = 1.75\ T^{-1}$. The Curie temperature T_c was also obtained from the temperature dependence of susceptibility determined from the transport measurements in the paramagnetic region

($T > 120$ K), where the susceptibility fellows the Curie–Weiss law. T_c determined from transport measurements for the samples with $x = 0.035, 0.043$ and 0.053 are 83, 99 and 97 K, respectively.

The in-plane easy axis of magnetization in the (Ga, Mn)As grown on GaAs was thought to be induced by a compressive strain present in the film, although in general the easy axis favors in-plane direction due to the demagnetization field. By growing (Ga, Mn)As on a relaxed (In, Ga)As buffer layer with larger lattice constant than that of (Ga, Mn)As, which makes the (Ga, Mn)As under tensile strain, the easy axis was changed to be perpendicular to the plane, as demonstrated in Fig. 5.

5. GaAs/(Ga, Mn)As superlattice structures

GaAs/(Ga, Mn)As superlattice structures were also prepared by MBE. The introduction of superlattice structures is expected to provide additional parameters for controlling the spatial confinement of both carriers and magnetic ions, possibly involving dimensional effects. The nonmagnetic/ferromagnetic multilayer system is also an interesting system for studying the exchange coupling between the ferromagnetic layers by adjusting the thickness of the nonmagnetic layers.

Double crystal X-ray diffraction measurements were performed for the superlattice samples. Clear satellite peaks were observed, indicating the existence of a periodic structure in the samples. The high perfection of the structure was confirmed by the observation of thickness fringes due to perfect crystal diffraction from thin films. Magnetotransport measurements revealed the existence of ferromagnetic order in the current superlattice structures. Detailed results concerning the superlattice structures will be published elsewhere [15].

6. Summary

In summary, we have successfully prepared a new GaAs-based III–V DMS, $(Ga_{1-x}, Mn_x)As$, by MBE, with x varying from 0.015 to 0.07. Clear RHEED oscillations were observed at the initial growth stage, indicating that the growth mode is two-dimensional. X-ray diffraction measurements showed that the lattice constant of the (Ga, Mn)As films increases linearly with Mn composition, suggesting homogenous incorporation of Mn atoms in the zinc-blende alloy. Well-aligned in-plane ferromagnetic order was observed by SQUID measurements. Magnetotransport measurements revealed the occurrence of the anomalous Hall effect in the (Ga, Mn)As layer and the hole concentration to be of the order of Mn concentration. The easy axis of magnetization was found to be reversible by changing the strain direction in the (Ga, Mn)As films. GaAs/(Ga, Mn)As superlattice structures were also prepared.

Acknowledgements

This work was partly supported by a Grant-in-Aid for the Scientific Research from the Ministry of Education, Science, Sports, and Culture, Japan. The partial support from the Mitsubishi Foundation is also acknowledged. The authors thank Professor Y. Horikoshi at Waseda University for the discussion about the RHEED oscillation results of LT GaAs. We also thank Professor H. Takagi at University of Tokyo for his help in magnetization measurements. One of the authors (A.S.) acknowledges JSPS for awarding him the fellowship to conduct research in Japan.

References

[1] M. Ilegems, R. Dingle and L.W. Rupp, Jr., J. Appl. Phys. 46 (1975) 3059.
[2] Th. Frey, M. Maier, J. Schneider and M. Gehrke, J. Phys. C 21 (1988) 5539.
[3] D.G. Andrianov, V.V. Karataev, G.V. Lazareva, Yu.B. Muravlev and A.S. Savel'ev, Sov. Phys. Semicond. 11 (1977) 738.
[4] J.K. Furdyna and J. Kossut, Eds., Semiconductor and Semimetals, Vol. 25 (Academic, New York, 1988)
[5] H. Munekata, H. Ohno, S. von Molnár, A. Segmüller, L.L. Chang and L. Esaki, Phys. Rev. Lett. 63 (1989) 1849.
[6] Y.L. Soo, S.W. Huang, Z.H. Ming, Y.H. Kao, H. Munekata and L.L. Chang, Phys. Rev. B 53 (1996) 4905.

[7] H. Ohno, H. Munekata, T. Penney, S. von Molnár and L.L. Chang, Phys. Rev. Lett. 68 (1992) 2664.
[8] H. Ohno, H. Munekata, S. von Molnár and L.L. Chang, J. Appl. Phys. 69 (1991) 6103.
[9] H. Munekata, A. Zaslavsky, P. Fumagalli and R.J. Gambio, Appl. Phys. Lett. 63 (1993) 2929.
[10] H. Ohno, F. Matsukura, H. Munekata, Y. Iye and J. Nakahara, in: Proc. 22nd Int. Conf. on Physics of Semiconductors , Ed. D.J. Lockwood (World Scientific, Singapore, 1995) p. 2605.
[11] H. Ohno, Mater. Sci. Forum 182–184 (1995) 443.
[12] S. Basu and T. Adhikari, Solid State Commun. 95 (1995) 53; T. Adhikari and S. Basu, Jpn. J. Appl. Phys. 33 (1994) 4581.
[13] J. De Boeck, R. Oesterholt, A. Van Esch, H. Bender, C. Bruynseraede, C. Van Hoof and G. Borghs, Appl. Phys. Lett. 68 (1996) 2744.
[14] H. Ohno, A. Shen, F. Matsukura, A. Oiwa, A. Endo, S. Katsumoto and Y. Iye, Appl. Phys. Lett. 69 (1996) 363.
[15] A. Shen, H. Ohno, F. Matsukura, Y. Sugawara, Y. Ohno, N. Akiba and T. Kuroiwa, unpublished.

ELSEVIER

Journal of Crystal Growth 175/176 (1997) 1075–1080

JOURNAL OF CRYSTAL GROWTH

Growth parameter dependence of step patterns in AlGaAs molecular beam epitaxy on vicinal GaAs(1 1 0) inclined toward (1 1 1)A[1]

Shigehiko Hasegawa*, Kazuki Sato, Satoshi Torii, Hisao Nakashima

The Institute of Scientific and Industrial Research, Osaka University, 8-1 Mihogaoka, Ibaraki, Osaka 567, Japan

Abstract

We have studied growth parameter dependence of macrostep patterns in AlGaAs molecular beam epitaxial (MBE) growth using As_2 molecular beams with the use of atomic force microscopy. It is found that MBE growth by using As_2 molecular beams leads to the formation of coherently aligned macrosteps. From the analysis of the macrostep patterns, we deduce the characteristic that increasing growth temperatures leads to the formation of wider macrosteps. In contrast, MBE growth using solid As source (As_4) gives rise to highly connected zigzag networks of macrosteps. We will discuss the difference in macrostep patterns between MBE growth using As_2 and As_4 in terms of the presence of As_4 physisorption states and the difference in the diffusion length of As species.

1. Introduction

We have demonstrated that molecular beam epitaxial (MBE) growth on vicinal GaAs(1 1 0) induces macrosteps several tens of nm high [1], and that such macrostep system is one of fairly good candidates as substrates for fabricating nanostructures such as quantum wires, since macrosteps formed by MBE using AsH_3 gas source are coherently aligned along [$\bar{1}$ 1 0] direction perpendicular to the misorientation direction of the vicinal (1 1 0) substrates [2]. However, MBE growth by using solid As source (As_4) produces rather fluctuated macrostep patterns. In order to fabricate excellent nanostructures, it is necessary to control macrostep patterns, i.e, to know what growth parameters make straight and uniform macrosteps stable.

Mainly, there are two differences between MBE growth by using AsH_3 and As_4: one is the presence of atomic hydrogen and/or hydrogen molecules, the other is the difference in the constituent of arsenic molecules (i.e. As_2 and As_4). Recently, Takeuchi [3] using conventional MBE plus hydrogen

* Corresponding author. Fax: + 81 6 879 8414; e-mail:hasegawa@sanken.osaka-u.ac.jp.

[1] The misorientation direction of (1 1 1)B in our previous papers [1, 10] is incorrect. It should be corrected to (1 1 1)A.

0022-0248/97/$17.00 Copyright © 1997 Elsevier Science B.V. All rights reserved
PII S0022-0248(96)00929-3

source showed that MBE growth under atomic hydrogen and/or hydrogen molecules leads to little improvement of the macrostep patterns. He also reported that cracking of AsH_3 produces As_2 and hydrogen, while the generation of AsH_x is negligible.

In this paper, we present growth parameter dependence of macrostep patterns in AlGaAs MBE growth using As_2 molecular beams with the use of atomic force microscopy (AFM). In particular, our interest is concentrated both on how the macrostep patterns are changed by varying growth temperature and V/III ratio and on what leads to the difference in the resulting step patterns when compared with the results using As_4 molecular beams.

2. Experimental procedure

$Al_{0.5}Ga_{0.5}As$ layers of 400 nm thickness were grown by MBE on vicinal GaAs(1 1 0) substrates inclined by 3° toward (1 1 1)A using the following arsenic sources: one, a tetrameric arsenic (As_4) beam sublimated from solid arsenic source, the other a dimeric arsenic (As_2) beam produced by dissociating GaAs polycrystalline at temperatures ranging from 860 to 890°C using Knudsen cell. Dissociation of GaAs at these temperatures produces arsenic beams almost consisting only of As_2 (As_2/As_4 is usually larger than 1 0 0) [4–7]. Simultaneously, Ga beams are apparently produced by the dissociation of GaAs but negligible order of below one 10th of its As_2 flux. Growth temperature T_G was varied from 430 to 580°C. V/III pressure ratio $R_{V/III}$ for AlGaAs growth using As_2 and As_4 beams was also varied in the range of 20–80 and 50–260, respectively. Growth rate of AlGaAs layers was 200 nm/h. Before AlGaAs growth, chemically etched substrates were thermally cleaned at 630°C for 20 min under As_4 flux, then buffer layers of 200 nm thick GaAs were grown at 580°C by using As_2 beams. This growth condition for GaAs buffer layers was found to provide atomically smooth growth surfaces consisting of diatomic steps. All AFM measurements were carried out in air in contact mode.

3. Results and discussion

To demonstrate how the difference between As_2 and As_4 beams affects patterns of macrosteps formed by MBE growth, shown in Fig. 1a and Fig. 1b are typical 5 μm × 5 μm AFM images of AlGaAs surfaces grown by using As_2 and As_4 molecular beams, respectively. They were taken for the AlGaAs films grown at 580°C by using As_2 beams at $R_{V/III} = 30$ and As_4 beams at $R_{V/III} = 152$. From the AFM image shown in Fig. 1a, it can be seen that macrosteps formed by using As_2 beam are coherently aligned along [$\bar{1}$ 1 0] direction, and that their terrace width and step height are 300 nm

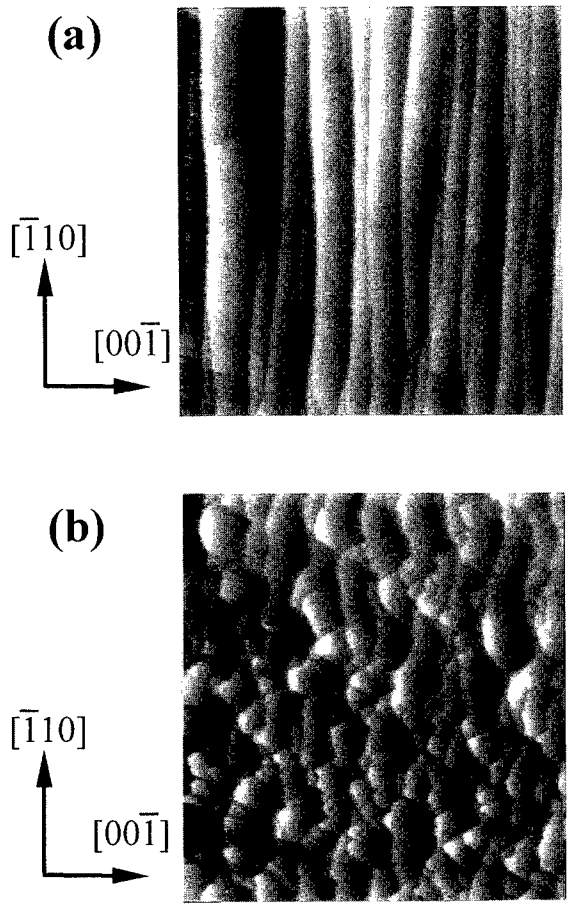

Fig. 1. AFM images (5 μm × 5 μm) of AlGaAs films grown by MBE at 580°C on vicinal GaAs(1 1 0) substrates when using (a) As_2 molecular beams and (b) As_4 molecular beams.

wide and 15 nm high on an average, respectively. This macrostep pattern is very similar to those formed by gas source (AsH_3) MBE [1, 2]. In contrast, MBE growth by using As_4 produces highly connected zigzag networks of macrosteps, as shown in Fig. 1b. We, therefore, consider that MBE growth by using As_2 is essential for the formation of fairly straight and uniformly spaced macrosteps on vicinal GaAs (1 1 0) substrates.

Next, to make clear the growth parameter dependence of the macrostep patterns when using As_2, we have carried out AFM measurements for the AlGaAs films grown at various growth condition (T_G = 430–580°C, $R_{V/III}$ = 20–80).

The AFM images for the films grown at 480–580°C showed that AlGaAs growth leads to the formation of macrosteps similar to the one shown in Fig. 1a, while such macrosteps were not observed for the films grown at 430°C. To deduce the characteristics of the macrosteps formed at 480–580°C, we plotted the growth temperature dependence of the average terrace widths $\langle W \rangle$ and the terrace width distribution $\langle W \rangle P(W/\langle W \rangle)$ scaled to the average terrace width shown in Fig. 2. On the micrographs, we measured the local distance between adjacent steps along [0 0 1] direction. The present analysis allows us to deduce the following two characteristics of the macrosteps. Firstly, it is clear from Fig. 2a that with increasing growth temperature, the average terrace width increases showing little dependence on the V/III ratio. Secondly, it is obvious from Fig. 2b that all the terrace width distributions plotted for the AlGaAs film surfaces fall on the same curve regardless of the growth temperature and the V/III ratio. In an equilibrium picture, the terrace width distribution for a given vicinal surface is determined by energetic interactions between steps. Bartelt et al. [8] and Joós et al. [9] have theoretically derived the relationship between the terrace width distributions and the strength of step-step interactions. The solid curve shown in Fig. 2b is the scaled terrace width distribution calculated for many non-interacting wandering steps except for the non-crossing condition for the steps, i.e. the free-fermion model. Surprisingly, the observed distributions $\langle W \rangle P(W/\langle W \rangle)$ almost fit the solid curve,

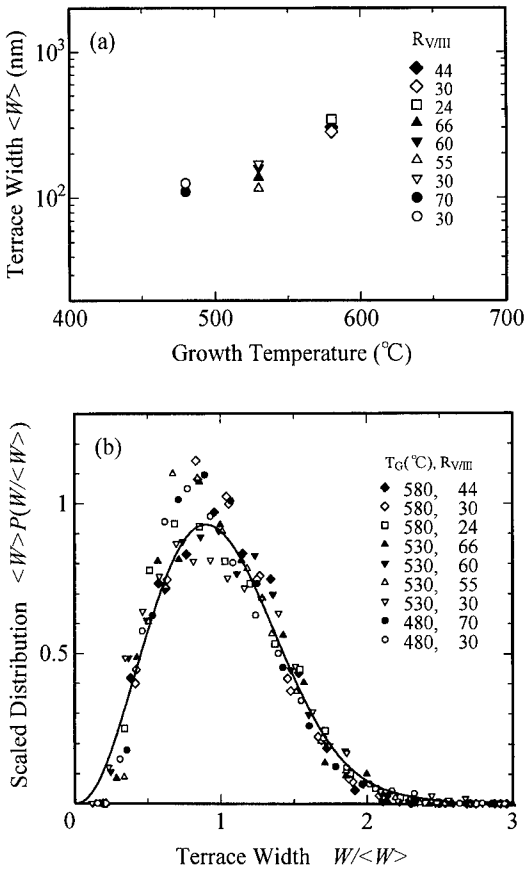

Fig. 2. (a) Growth temperature dependence of the average terrace width $\langle W \rangle$ and (b) scaled terrace width distribution for AlGaAs films grown by using As_2. The solid curve is the distribution for the free-fermion model [8, 9].

although some data are scattered around the curve. In other words, the present results for the macrosteps formed by using As_2 seem to be well described by the model that the steps do not interact with each other except that they cannot cross. Of course, macrosteps formed by MBE growth do not represent equilibrium structures. However, the above analysis is still useful for deducing the characteristics of step patterns, as will be discussed later.

As for AlGaAs growth by using As_4, the surface morphologies including the step patterns show rather complicated dependence both on the growth

temperature T_G and on the V/III ratio $R_{V/III}$. From the AFM and reflection high-energy electron diffraction (RHEED) observations, the T_G–$R_{V/III}$ growth parameter plane (T_G = 430–630°C, $R_{V/III}$ = 50–260) seems to be divided into the 5 regions (A–E) in terms of the surface morphologies. The characteristic surface morphologies corresponding to the regions (A–E) are as follows. AlGaAs growth under the parameter of the regions (A: $T_G \geqslant 530$°C, $R_{V/III} \geqslant 200$ or $R_{V/III} \sim 50$ and $T_G \sim 580$°C, $R_{V/III} \geqslant 150$) and (B: T_G = 450–550°C, $R_{V/III} \sim 150$) leads to the macrosteps shown in Fig. 1b and Fig. 3b, respectively. For the growth under the region (C: $T_G \geqslant 630$°C, $R_{V/III} \geqslant 150$) of high-growth temperatures and sufficient V/III ratio, rather smooth surface morphologies were observed by AFM. In addition, RHEED observations suggested that the growing surfaces consist of diatomic steps, as previously reported [10], although such diatomic steps were not observed in the AFM images. In the region (D: $T_G \geqslant 580$°C, $R_{V/III} \leqslant 50$) of high-growth temperatures but low V/III ratio, however, the surface morphology became macroscopically rough. For the growth under the region (E: $T_G \leqslant 430$°C) of low growth temperatures, flat surface morphologies were observed by AFM, while the growing surface displayed the non-splitted (1 × 1) RHEED patterns. Judging from the AFM and RHEED observations, it is thought that the growth under the region (E) causes multi-atomic steps of several tens of nm wide. Among these five regions, contrasted with the growth by using As_2 are the results for the regions (A) and (B). As mentioned above, the growth under the parameter of the region (A) causes highly connected zigzag macrosteps. Obviously, the terrace width distributions for such macrostep patterns are different from the distribution shown in Fig. 2b. It is peaked near the half of the average terrace width, then almost linearly decreases with increasing the normalized terrace width $W/\langle W\rangle$. On the other hand, the macrosteps formed under the parameter of the region (B) yields the terrace width distribution very similar to the one for the macrosteps formed by using As_2. If we now look over the AFM images shown in Fig. 3a and Fig. 3b, however, we note that there is the difference between the macrosteps formed by using As_2 and As_4. Almost all the

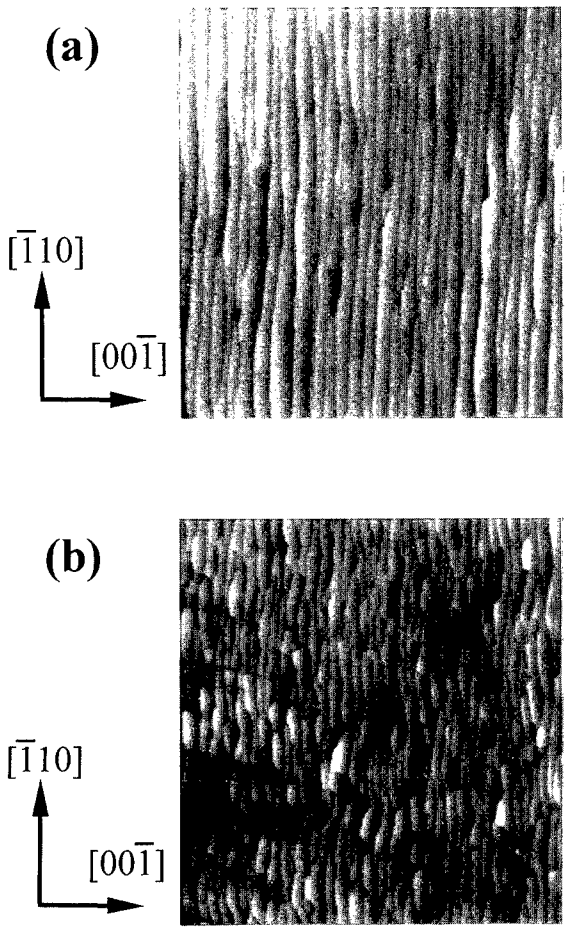

Fig. 3. AFM images (5 μm × 5 μm) of AlGaAs films grown by MBE at 530°C on vicinal GaAs(1 1 0) substrates when using (a) As_2 molecular beams ($R_{V/III}$ = 66) and (b) As_4 molecular beams ($R_{V/III}$ = 152).

As_2 steps run along [$\bar{1}$ 1 0] direction perpendicular to the miscut direction over 5 μm without touching each other, while the macrosteps formed by using As_4 just extend to at most 1 or 2 μm along [$\bar{1}$ 1 0] direction. Analyzing the distance between step–step collisions would extract a characteristic of those macrostep patterns. However, it is hard to obtain such data because of the complicated connected patterns. Instead, we measured the terrace *length* distributions along [$\bar{1}$ 1 0] direction. As a result, it turns out that the terrace length distributions for all macrosteps formed by using As_4 fall on the same

exponentially decay curves with increasing terrace length. This indicates that the macrostep patterns formed by using As_4 are characterized by the terrace length distribution. In other words, the macrosteps formed by using As_4 have the same fluctuation in terrace length. We, therefore, consider that complex and highly connected zigzag networks of steps result from the fluctuation along the step edges originating in the use of As_4 beams.

In order to deduce the origin of the fluctuation along the step edges leading to complex and highly connected networks of steps, we summarize the difference between As_2 and As_4 molecular beam. Firstly, the sticking coefficient of As_2 to Ga-rich GaAs(0 0 1) surface tends to unity [11, 12] while that of As_4 never exceeds the value of 0.5 [13, 14]. Secondly, there exists the physisorption state for As_4 molecules even at high temperatures [15]. Finally, As_4 and As_2 differ in the mass and the temperature of the molecular source. It is expected that this affects thermalization process of As species, i.e., energy transfer between As molecules and substrate atoms, and energy conversion process of adsorbing molecules such as translational to vibrational energy transfer.

Based on the present results and the above-mentioned difference between As_2 and As_4 molecules, one possible explanation is that the formation of zigzag steps originates in the presence of the physisorption state of As_4 and fluctuates along the step edges. It is conceivable that step motion is influenced by the presence of such physisorbates. In other words, the physisorbates act as impurities and impede the step motions. Recently, Kandel and Weeks [16] have studied the impurity-induced step bunching suggested by Frank [17] using two-dimensional models that allow fluctuations along the step edges. Their Monte Carlo simulation shows that impurity-induced step bunching leads to the formation of very complex and highly connected step patterns which resemble the present AFM image shown in Fig. 1b very much.

Another explanation is that the observed morphological difference comes from the difference in the diffusion length between the As species, which is expected from the third difference between As_2 and As_4 mentioned above. Consider the initial stages of AlGaAs growth proceeding in step-flow mode on the diatomic steps of GaAs(1 1 0) surfaces. Taking account of the direction of Ga–As bonding and step structures of the surface, AlGaAs growth is considered to proceed along step edges directed toward $[\bar{1}\,1\,0]$. Initially, Al(Ga)As nuclei stick to GaAs diatomic step edges. An average distance between the adjacent nuclei usually depends on the diffusion length of As and/or Ga atoms. This means that when the diffusion length is short, diatomic steps largely meander on the surface because of the short average distance between nuclei. In fact, the RHEED observation of the surfaces grown at 630°C on the vicinal GaAs(1 1 0) inclined toward (1 1 1)A by 6° revealed that diatomic steps formed by using As_4 wander largely [10]. We, therefore, expect that such fluctuation along the step edges affects the macrostep pattern.

4. Conclusions

We have studied growth parameter dependence of macrostep patterns in AlGaAs MBE growth using As_2 molecular beams with the use of AFM. It is found that MBE growth by using As_2 leads to the formation of coherently aligned macrosteps, as is in the case of MBE growth by using AsH_3. From the growth temperature dependence of the average terrace width and the terrace width distribution, we deduce the characteristic that increasing growth temperatures leads to the formation of wider macrosteps regardless of V/III ratio. Besides, the terrace width distribution for these macrosteps is well described by the free-fermion model. In contrast, MBE growth by using As_4 leads to highly connected zigzag networks of macrosteps. By analyzing the macrostep patterns it is found that its patterns are characterized by the terrace length distribution showing the exponentially decay with increasing terrace length. These characteristics of the macrostep patterns indicate that complex and highly connected zigzag networks of steps result from the fluctuation along the step edges originating in the use of As_4 beams.

Acknowledgements

This work is partially supported by a Grant-in-Aid for Scientific Research on Priority Areas "Quantum Coherent Electronics" and Monbusho International Scientific Research: Joint Research from the Ministry of Education, Science, Sports and Culture, Japan.

References

[1] S. Hasegawa, M. Sato, K. Maehashi, H. Asahi and H. Nakashima, J. Crystal Growth 111 (1991) 371.
[2] M. Takeuchi, K. Shiba, K. Sato, H.K. Huang, K. Inoue and H. Nakashima, Jpn. J. Appl. Phys. 34 (1995) 4411 and references therein.
[3] M. Takeuchi, Doctoral Dissertation, Osaka University (1996).
[4] T. Foxon, J.A. Harvey and B.A. Joyce, J. Phys. Chem. Solids 34 (1973) 1693.
[5] R. Arthur, J. Phys. Chem. Solids 28 (1967) 2257.
[6] Y. Cho, J. Appl. Phys. 42 (1971) 2074.
[7] B. Panish and R.A. Hamm, J. Crystal Growth 78 (1986) 445.
[8] C. Bartelt, T.L. Einstein and E.D. Williams, Surf. Sci. 240 (1990) L591.
[9] B. Joós, T.L. Einstein and N.C. Bartelt, Phys. Rev. B 43 (1991) 8153.
[10] S. Hasegawa, K. Kimura, M. Sato, K. Maehashi and H. Nakashima, Surf. Sci. 267 (1992) 5.
[11] T. Foxon and B.A. Joyce, Surf. Sci. 64 (1977) 293.
[12] R. Arthur, Surf. Sci. 43 (1974) 449.
[13] T. Foxon and B.A. Joyce, Surf. Sci. 50 (1975) 434.
[14] Y. Tsao, T.M. Brennan and B.E. Hammons, Appl. Phys. Lett. 53 (1988) 288.
[15] C. García, C. Neri and J. Massies, J. Crystal Growth 98 (1989) 511.
[16] D. Kandel and J.D. Weeks, Phys. Rev. Lett. 72 (1994) 1678.
[17] C. Frank, in: Growth and Perfection of Crystals, Eds. R. Doremus, B. Roberts and D. Turnbull (Wiley, New York, 1958) p. 411.

ELSEVIER

Journal of Crystal Growth 175/176 (1997) 1081–1086

JOURNAL OF CRYSTAL GROWTH

Effects of tensile strain and substrate off-orientation on the growth of GaInAs/InP multiple quantum well structures by CBE

T. Marschner[a,*], R.T.H. Rongen[a], M.R. Leys[a], F.D. Tichelaar[b], H. Vonk[a], J.H. Wolter[a]

[a] *COBRA Inter-University Research Institute, Eindhoven University of Technology, Semiconductor Physics, P.O. Box 513, 5600 MB Eindhoven, The Netherlands*

[b] *Laboratory of Metallurgy, Delft University of Technology, Rotterdamseweg 137, 2628 AL Delft, The Netherlands*

Abstract

GaInAs/InP multiple quantum well (MQW) layers with high tensile strain in the GaInAs layers have been grown by chemical beam epitaxy (CBE). The samples were analysed by high-resolution X-ray diffraction (XRD), photoluminescence (PL) spectroscopy and transmission electron microscopy (TEM). The influence on layer properties of the tensile strain and the substrate off-orientation of the (100) InP substrates is investigated. XRD studies reveal that the growth rate of GaInAs as well as that of InP is larger for off-oriented substrates than for exactly oriented substrates. This behaviour is independent of the strain in the GaInAs layers and of the growth temperature in the chosen range between 485°C and 545°C. We attribute the observed changes of the growth rate to the different growth modes on exact (100) and off-oriented substrates. MQW structures grown on off-oriented substrates show a linear increase of the PL line width of the GaInAs MQW peak with increasing tensile strain in the GaInAs layers. In contrast, it stays constant for exactly oriented substrates. This increase in the PL line width for off-oriented substrates is explained by the lattice tilting occurring when strained layers are deposited on stepped surfaces. The tilt angle is proportional to the amount of incorporated elastic strain as shown by the azimuthal dependence of the position of the zeroth-order satellite reflection in XRD.

1. Introduction

$Ga_xIn_{1-x}As$/InP multiple quantum well (MQW) layers are becoming increasingly important for applications in optical telecommunications in the near infrared region (1.3–1.5 μm). For many applications it is highly desirable to realize polarization-independent optical components. This can possibly be achieved by growing GaInAs superlattice structures with high tensile strain, i.e. with high Ga content in the GaInAs well layers [1, 2].

For strained MQW structures, however, the critical thickness for misfit dislocation generation has to be taken into account. Additionally, the thicknesses of wells and barriers as well as the Ga

* Corresponding author. Fax: + 31 40 2453587; e-mail: t.marschner@phys.tue.nl.

0022-0248/97/$17.00 Copyright © 1997 Elsevier Science B.V. All rights reserved
PII S0022-0248(96)00930-X

content of the GaInAs layers have to be controlled precisely. Also a smooth surface morphology over large areas is necessary.

Therefore, it is of importance for device applications to investigate the influence of the epitaxial growth parameters on the structural and optical properties of strained structures and optimize the epitaxial growth with respect to these results.

We present here results obtained on a series of 10-period MQW structures grown by chemical beam epitaxy (CBE) in the growth temperature range between 485°C and 545°C. We discuss the effect of tensile strain and substrate off-orientation on the growth rate and on the structural and optical properties. Such test structures provide valuable insight in the relevant properties of highly strained MQW structures, which have to be taken into account for designing MQW-based device structures.

2. Experimental procedure

The samples were grown in a Riber CBE 32P system using triethylgallium (TEGa), trimethylindium (TMIn), arsine (ASH_3) and phosphine (PH_3). The TEGa and TMIn flows were combined without carrier gas in a low temperature (LT) injector to form a single emerging beam. Arsine and phosphine were introduced through a high-temperature (HT) cracker. The growth temperature varied between 485°C and 545°C and was measured with an optical pyrometer. The V/III ratio was 3.8 for the InP barriers and 1.75 for the GaInAs wells. The (100) InP substrates were either exactly oriented ($\pm$ 0.2°) or 2° off-oriented towards the [110]-direction. As test structure a MQW structure consisting of 10 periods nominally 5 nm GaInAs/5 nm InP/1 monolayer (ML) InAs/5 nm InP with various Ga concentrations (x_{Ga}) was chosen. The compressively strained InAs ML was obtained by exposing the InP surface to a beam of AsH_3 during 1 s [3] to provide some strain compensation for the tensile-strained GaInAs layers. The growth interruption sequence was chosen in a way that the upper and the lower interface of the GaInAs layer were symmetrically strained in compression [3]. Therefore, the interfacial layers also contribute to the compensation of the tensile strain in the GaInAs layers. X-ray diffraction studies show that at the bottom and at the top of the GaInAs layers 1 ML $InAs_{0.5}P_{0.5}$ is formed. Details about the interface structure have been published elsewhere [3–5].

The epitaxial layers were investigated by high-resolution X-ray diffraction (XRD), low-temperature photoluminescence (PL) and cross-sectional transmission electron microscopy (TEM). The XRD studies were performed by using a Bede model 200 double-crystal diffractometer (Bede Scientific, UK). The PL spectra were recorded at 5 K at a power density of 20 mW/cm^2 of the 514 nm Ar-ion laser line. A CCD camera was used as detector. The cross-sectional TEM images were taken in a Philips CM30T electron microscope operating at 300 kV.

3. Results and discussion

3.1. XRD characterization

The thicknesses of the individual MQW layers as well as the Ga concentration (x_{Ga}) in the GaInAs layers could directly be calculated from the XRD rocking curves by using the previously mentioned interface structure and the relation $v_{InAs} = v_{InP}$, which is valid for the same TMIn flow. v_{InAs} and v_{InP} are the binary growth rates of InAs and InP, respectively. To verify these calculations the measured rocking curves of the samples were compared to dynamical simulations using the simulation package RADS (Bede Scientific, UK). Both measurements and simulations show good correspondence up to $x_{Ga} = 0.77$. This corresponds to a lattice mismatch perpendicular to the surface $(\Delta d/d)^{\perp} = -4 \times 10^{-2}$ in the individual GaInAs layers and an average mismatch of the whole MQW structure $\overline{(\Delta d/d)^{\perp}} = -1.1 \times 10^{-2}$. The values of the layer thickness and strain for the individual MQW layers as well as for the entire MQW structure are approximately equal to the critical thickness for misfit dislocation generation [6, 7]. However, the good agreement of the linewidth of the MQW satellite reflections of approximately 110 arcsec between measurement and

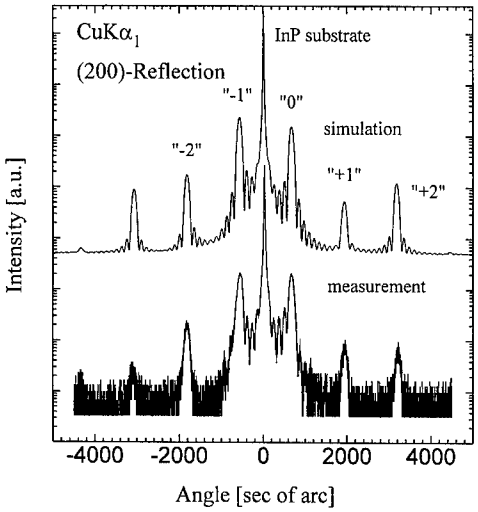

Fig. 1. Comparison of an experimental (bottom) and a simulated (top) XRD pattern of a MQW structure with $x_{Ga} = 0.74$. For clarity the patterns are shifted on the intensity scale.

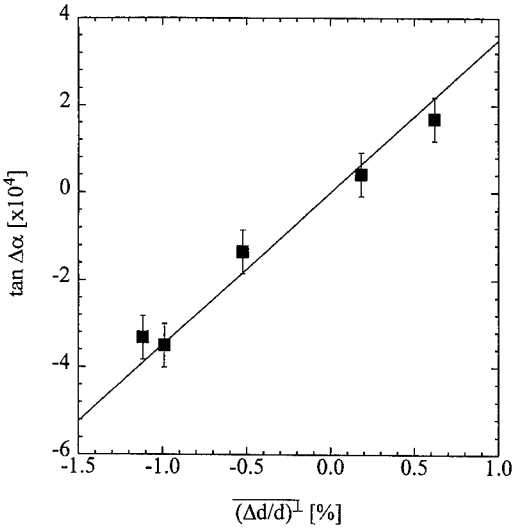

Fig. 2. Dependence of tan $\Delta\alpha$ on the average lattice mismatch $\overline{(\Delta d/d)^{\perp}}$ using the relationship $\tan\Delta\alpha = \overline{(\Delta d/d)^{\perp}} \tan\alpha$ [8]. $\Delta\alpha$: tilt angle, α: substrate off-orientation angle (here: 2°). The measured data and the theoretical relation show good correspondence.

simulation indicates that no relaxation of the layers by formation of misfit dislocations has occurred. This becomes clear from Fig. 1 giving an example of a measured and a simulated XRD rocking curve for $x_{Ga} = 0.74$.

To investigate a possible tilting of the MQW layers the dependence of the XRD peak positions on the azimuthal angle Φ was analysed. The tilt was determined by the dependence of the distance between the substrate reflection and the zeroth-order satellite reflection on the azimuthal angle Φ following [8, 9]. Fig. 2 shows the dependence of the tilt of the structures grown on off-oriented substrates on the average lattice mismatch $\overline{(\Delta d/d)^{\perp}}$ of the respective MQW structures. For an increase of $\overline{(\Delta d/d)^{\perp}}$ the tilt increases linearly. Additionally, the relationship Nagai [8] derived for an elastically strained layer, namely $\tan\Delta\alpha = \overline{(\Delta d/d)^{\perp}} \tan\alpha$, where $\Delta\alpha$ is the angle of tilt and α the substrate off-orientation angle, is included into Fig. 2 as solid line. The measured values show good correspondence to the theory again confirming that the samples are not relaxed by dislocations. Because the tilt is a direct consequence of surface steps due to substrate off-orientation [8, 9] the samples grown on exactly oriented substrates show no lattice tilting.

3.2. *Dependence of the growth rate of InP and GaInAs on growth temperature and substrate off-orientation*

Fig. 3 shows the InP (Fig. 3a) and GaInAs (Fig. 3b) growth rates v_{InP} and v_{GaInAs} and the Ga content (x_{Ga}) in the GaInAs well layers (Fig. 3c) in dependence of the growth temperature for 2° off-oriented substrates (solid circles) and for exactly oriented substrates (open circles). The growth rates v_{InP} and v_{GaInAs} were obtained by dividing the layer thicknesses determined by XRD by the respective growth times in CBE. For all temperatures in the range between 485°C and 545°C the growth rate for InP v_{InP} as well as for GaInAs v_{GaInAs} is larger for the off-oriented substrates than for the exactly oriented substrates, although the individual values are dependent on the growth temperature. The Ga content in the GaInAs well layers also changes with temperature, but is almost independent of the substrate off-orientation in agreement with Ref. [10]. Simultaneously, as noted in Ref. [11] the use of off-oriented substrates improves the surface morphology. Details about the influence of the substrate off-orientation on the surface morphology will be published elsewhere.

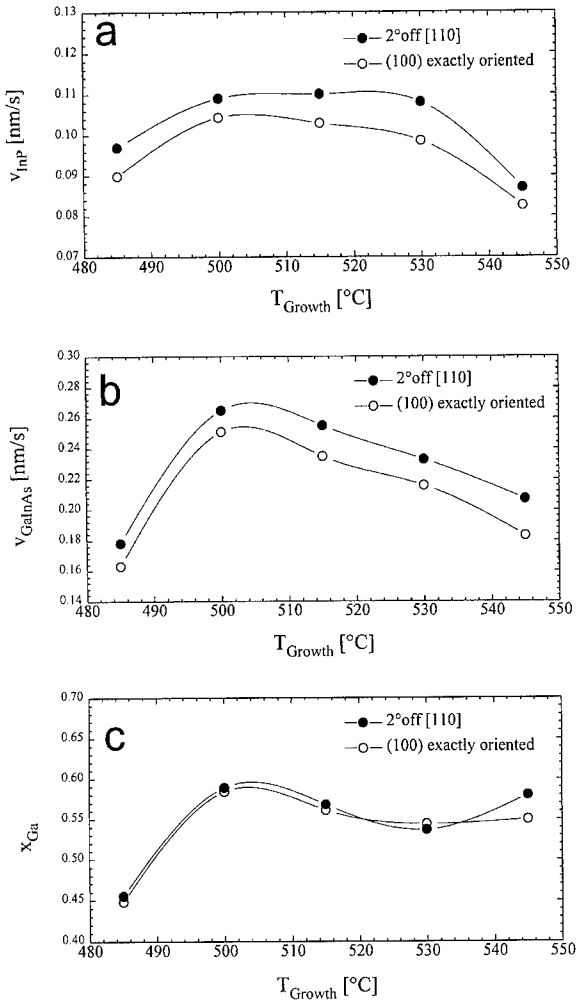

Fig. 3. InP growth rate v_{InP} (a), GaInAs growth rate v_{GaInAs} (b) and Ga content (x_{Ga}) in the GaInAs well layers (c) for off-oriented (solid markers) and exactly oriented (open markers) (100) InP substrates as a function of the growth temperature.

The InP growth rate v_{InP} is almost constant for growth temperatures from 500°C to 530°C and shows a slight decrease for temperatures beyond this temperature range. For high temperatures this decrease is due to the desorption of In species from the surface [12]. For low growth temperatures v_{InP} is reduced because of an incomplete dissociation of TMIn [13].

The variations of v_{GaInAs} with the growth temperature are mainly due to changes in the GaAs growth rate for temperatures below 545°C. This is indicated by the temperature dependence of x_{Ga} (Fig. 2c) which shows a similar dependence as the GaInAs growth rate. For temperatures above 500°C v_{GaInAs} is reduced by increased DEGa desorption from the surface whereas the decrease in v_{GaInAs} for temperatures below 500°C is caused by the blocking of free surface sites by adsorbed ethyl groups [14]. For $T = 545$°C the desorption of DEGa is lower than the evaporation of In causing the slight increase of x_{Ga} although v_{GaInAs} is further reduced.

The differences in the growth rates between off-oriented substrates and exactly oriented substrates can be explained by the different growth modes taking place on either type of substrate. For off-oriented substrates mainly step flow growth can be assumed while for exactly oriented substrates layer by layer growth takes place. The then required nucleation of 2D islands of a critical size leads to a higher probability of evaporation of group-III atoms and therefore to a reduced growth rate on exactly oriented substrates.

Additionally, Fig. 3a shows that for off-oriented substrates v_{InP} decreases only for $T > 530$°C and stays almost constant between 500°C and 530°C. For exactly oriented substrates, however, v_{InP} already starts to decrease within this temperature range. This indicates a continuous In evaporation with increasing temperature for exactly oriented substrates, while for off-oriented substrates the surface steps act as a barrier retarding the In evaporation up to a critical temperature $T > 530$°C in our case.

From Fig. 3c it becomes clear that for our growth conditions the evaporation rate of In and Ga atoms is approximately the same for off-oriented and exactly oriented substrates. Only at $T = 545$°C the Ga content is higher on off-oriented than on exactly oriented substrates suggesting a delayed Ga evaporation from off-oriented substrates. Our results additionally indicate that v_{GaInAs} is independent of the incorporated strain and simply remains proportional to the total group-III flux at a given temperature.

3.3. *Effects of tensile strain on the optical properties of the structures*

Fig. 4 shows the dependence of the PL line width of the MQW peak on the tensile strain in the

GaInAs well layers for exactly and off-oriented substrates. The energy of the respective transitions is approximately 1 eV and depends on the thickness and Ga content of the individual MQW structures.

For exactly oriented substrates the line width does not change up to the maximum Ga content $x_{Ga} = 0.77$. For off-oriented substrates the PL line width is the same as for exactly oriented substrates for lattice matched structures ($(\Delta d/d)^{\perp}_{GaInAs} = 0$), but increases linearly with the strain. Note that the PL line width shows no dependence of the growth temperature in the range from 500°C to 530°C.

The increase in the PL line width can be caused by a number of effects such as changes in alloy distribution, roughening of the interfaces or lateral well thickness fluctuations. However, the very clear trend shown in Fig. 4 leads us to the conclusion that the strain induced lattice tilting is the dominant contribution on substrates with a relatively high step density. Due to the different step heights for materials with different lattice constants a pure tetragonal distortion at the step edges is not possible. This leads to the formation of local strain fields being highest at the step edges with increasing strain in the GaInAs layers. Thus, the layers show lateral and periodic strain fluctuations. The nontetragonal distortion at the step edges eventually leads to the lattice tilt [8].

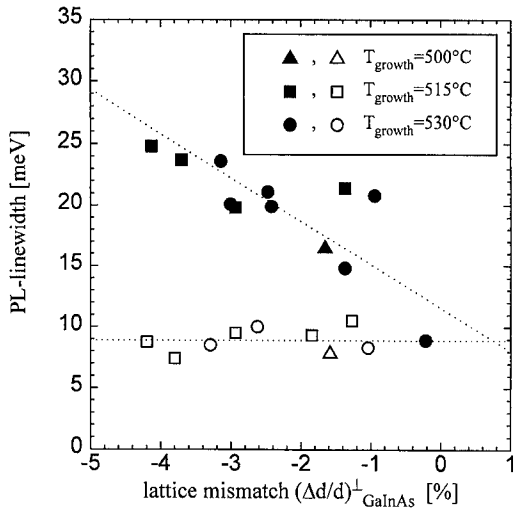

Fig. 4. Photoluminescence line width of the GaInAs MQW peak as a function of the lattice mismatch $(\Delta d/d)^{\perp}$ of the GaInAs layers for off-oriented (solid markers) and exactly oriented (open markers) (100) InP substrates. The included lines are guides to the eye.

From literature it is known that GaInAs layers with high tensile strain can have a wavy surface [15]. Such surface undulations are known to decrease the strain by elastic deformation. However, cross-sectional TEM reveals that this applies for both exactly and off-oriented substrates in our case. Therefore, these quantum well thickness variations cannot explain the trend observed in Fig. 4, although they might also lead to a broadening of the PL peaks. Further investigations are necessary, how the PL line width is affected by the undulations. Details about the layer morphology of the structures in dependence of strain and substrate off-orientation will be published elsewhere.

4. Summary

We have investigated the influence of the process parameters on the CBE growth of tensile-strained GaInAs/InP MQW structures. The samples were characterized by HR-XRD, PL and cross-sectional TEM. The exact layer structure was obtained by comparing XRD measurements to simulations. The GaInAs as well as InP growth rate on off-oriented substrates is found to be higher than on exactly oriented substrates. This is attributed to the fact that for off-oriented substrates mainly step flow growth can be assumed while for exactly oriented substrates layer by layer growth takes place. The then required nucleation of 2D islands of a critical size leads to a higher degree of evaporation of group-III atoms and, therefore, to a lower growth rate for exactly oriented substrates over the whole temperature range under investigation.

PL measurements on samples grown on exactly oriented substrates show that the line width of the GaInAs MQW peak stays constant with increasing tensile strain. For off-oriented substrates the line width increases linearly with the tensile strain in the GaInAs layers. This strain-induced broadening of the PL peaks is explained by the increase of the lattice tilt with increasing strain for epitaxial growth on off-oriented, i.e. stepped substrates

leading to an increase of the local strain fields at the step edges. These strain fields eventually causes the observed broadening of the PL peaks.

Our results indicate that for high-quality devices based on highly strained MQW structures the substrate off-orientation has to be reduced as far as possible.

Acknowledgements

The authors would like to thank T.R. de Kruijff (TU Delft) for TEM sample preparation. This work was supported by the Dutch Ministry of Economic Affairs (IOP).

References

[1] C.G.M. Vreeburg, C.R. de Boer, Y.S. Oei, B.H. Verbeek, R.T.H. Rongen, M.R. Leys, H. Vonk, J.H. Wolter, F.H. Groen and J.J.G.M. van der Tol, Proc. 7th Eur. Conf. on Int. Opt. (ECIO 1995) p. 284.
[2] P. Wiedemann, G. Laube, J. Weber and E. Lach, J. Crystal Growth 170 (1997) 117.
[3] R.T.H. Rongen, M.R. Leys, H. Vonk, J.H. Wolter and Y.S. Oei, J. Crystal Growth 164 (1996) 263.
[4] M.R. Leys, R.T.H. Rongen, J. Hopkins, H. Vonk, C.M. van Es, J.H. Wolter and F.D. Tichelaar, J. Crystal Growth 150 (1993) 633.
[5] J. Hopkins, M.R. Leys, R.T.H. Rongen, H. Vonk and J.H. Wolter, J. Crystal Growth, submitted.
[6] J.W. Matthews and A.E. Blakeslee, J. Crystal Growth 27 (1974) 118.
[7] D.C. Houghton, M. Davies and M. Dion, Appl. Phys. Lett. 64 (1994) 505.
[8] H. Nagai, J. Appl. Phys. 45 (1974) 3789.
[9] F. Riesz, J. Crystal Growth 140 (1994) 213.
[10] H. Heinecke, B. Baur, R. Höger, B. Jobst and A. Miklis, J. Crystal Growth 124 (1992) 170.
[11] J.L. Benchimol, F. Alaoui, Y. Gao, G. Le Roux, E.V.K. Rao and F. Alexandre, J. Crystal Growth 105 (1990) 135.
[12] R.T.H. Rongen, M.R. Leys, P.J. van Hall, C.M. van Es, H. Vonk and J.H. Wolter, J. Electron. Mater. 24 (1995) 1391.
[13] W.T. Tsang, J. Electron. Mater. 15 (1986) 235.
[14] C.L. French and J.S. Foord, J. Crystal Growth 120 (1992) 63.
[15] A. Ponchet, A. Le Corre, A. Godefroy, S. Salaun and A. Poudoulec, J. Crystal Growth 153 (1995) 71.

ELSEVIER

Journal of Crystal Growth 175/176 (1997) 1087–1091

JOURNAL OF CRYSTAL GROWTH

Organized growth of GaAs/AlAs lateral superlattices on vicinal surfaces: where are the limits?

F. Laruelle*, F. Lelarge, Z.Z. Wang, T. Mélin, A. Cavanna, B. Etienne

Laboratoire de Microstructures et de Microélectronique (L2M), CNRS, B.P. 107, F-92225 Bagneux Cedex, France

Abstract

We report on three issues concerning the growth of GaAs/AlAs lateral superlattices on vicinal surfaces to obtain quantum wires with negligible inter-wire tunnel coupling. We show that the ledge roughness increases with increasing terrace length and decreases for slower growth rates. The tilt angle of lateral superlattices is not the relevant parameter as long as electronic properties are concerned: one has to consider the product of the coverage error by the lateral superlattice thickness. The Ga flux stability is a critical parameter to be controlled. The use of dual-filament cells improves it by a factor two compared to single-filament ones.

1. Introduction

Despite an efficient Al/Ga vertical atomic exchange [1], ordered GaAs/AlAs growth on vicinal surfaces is now a well-recognized approach leading to one-dimensional electron systems (1D ES) with new and fascinating electronic properties [2]. The strength of the lateral potential modulation is of the order of the Fermi energy (20 meV) whereas the lateral period is of the order of the Fermi wavelength (30 nm). Electronic properties are described in a lateral superlattice (LSL) picture, i.e., multiple quantum wires with significant inter-wire tunnel coupling. In order to investigate such 1D ES without inter-wire tunnel coupling, one has to increase the potential energy over confinement energy ratio either by increasing the LSL Al content or by increasing the lateral period using vicinal surfaces with smaller misorientation angle.

Increasing the terrace length of the vicinal surface up to 80 nm raises several problems concerning the LSL growth. The first issue is related to the morphology of the step array, the periodicity of which has to be optimized. The second issue concerns the LSL tilt. Indeed, if the LSL coverage (GaAs and AlAs) differs from one by ε then the LSL tilt angle β is given by $\beta = \arctan \varepsilon/\alpha$ where α is the misorientation angle. Since $1/\alpha$ is typically 200–300, one would think that vertical LSL cannot be made. We will show here that the relevant parameter is not β but the product $N\varepsilon$ as far as electronic properties are concerned (here N is the number of LSL

* Corresponding author. Fax: + 33 1 42 31 73 78; e-mail: francois.laruelle@bagneux.cnet.fr.

0022-0248/97/$17.00 Copyright © 1997 Elsevier Science B.V. All rights reserved
PII S0022-0248(96)00890-1

MonoLayers (ML)). Since N is typically 20–30, this makes the flux control ten times easier! A third issue concerning LSL growth lies around the flux stability so that the Ga and Al fluxes are constant throughout the LSL. This is to prevent the formation of LSL with random tilt variations. With respect to this, we will show that the proper use of a dual-filament Ga cell improves the flux stability compared to a single-filament one.

2. Steps periodicity at low misorientation angles

Our purpose is not to discuss the reasons of the build-up of a periodic step array (presented elsewhere [3]) but to investigate the limits for such a build-up, the adjustable parameter being the misorientation angle. Fig. 1 shows AFM images of GaAs surfaces misoriented toward [1 1 0] by 0.2° and 0.3°. These images are obtained in a N_2 dry box in less than 1 h after being taken out of the molecular beam epitaxy (MBE) system. The epitaxy consists of a 1 μm GaAs buffer grown at 2 Å/s with a substrate temperature $T_{sub} = 620$°C followed by 200 nm of GaAs grown at 0.5 Å/s with $T_{sub} = 580$°C. For these two temperatures, the As_4 flux is minimized in order to keep an As-rich surface during MBE. To enhance surface diffusion, migration enhanced epitaxy (MEE) (alternate supply of element III and V) [4] has been used to grow the last 10 nm of GaAs in one sample at a growth rate of 0.1 Å/s while keeping T_{sub} at 580°C.

For the two MBE grown samples, step edges along [1 $\bar{1}$ 0] are not straight because steps move by incorporating GaAs islands that develop on large terraces under these growth conditions. The ledge roughness is more pronounced for lower misorientation (0.2°) because nucleated islands are larger on wider terraces. The improvement of the surface of the MEE grown sample is readily apparent in Fig. 1, where the ledge roughness is considerably reduced, whereas the step periodicity is know well-defined at 50 nm. On this MEE sample, regions with periodicities close to 60 nm are observed with rough ledges so that 50 nm is considered as the largest terrace width for which we obtain smooth ledges and periodic steps at 580°C by MEE.

3. Scaling laws in tilted LSL

As LSL are designed to be active regions so as to confine 1D ES, it is of primary importance to understand the effect of an imperfect coverage of the surface by LSL layers in order to specify flux control. Fig. 2 depicts a tilted LSL in which each LSL ML covers a fraction $1 + \varepsilon$ of the surface. As

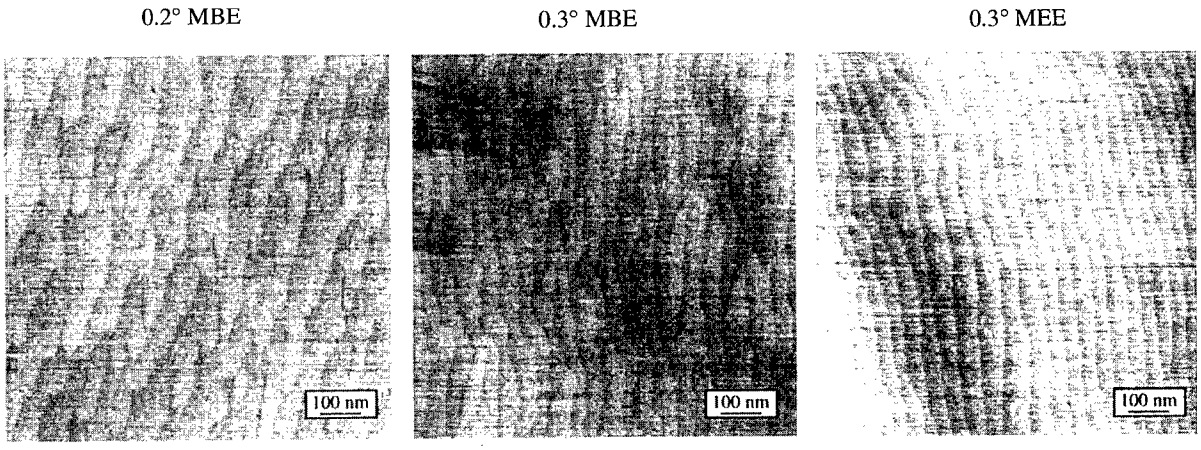

Fig. 1. Atomic force microscopy of GaAs vicinal surfaces. The misorientation and the final growth mode (MBE or MEE) used prior to sample cooling are indicated.

mentioned above, the tilt angle is given by $\beta = \arctan \varepsilon/\alpha$. If we consider that in each LSL ML the Al composition along [1 1 0] (or x) is given by a cosine law, the stacking of N such MLs results in the following lateral Al content:

$$X_\varepsilon^{\mathrm{Al}}(x, z) = X_{\mathrm{av.}}\left[1 + \lambda \cos\left(2\pi\frac{x}{L_x} + 2\pi\varepsilon\frac{z}{a}\right)\right], \quad (1)$$

where $X_{\mathrm{av.}}$ is the LSL mean Al content and λ describes the amplitude of lateral ordering ($\lambda = 0$ in the case of a random growth, $\lambda = (2/\pi X_{\mathrm{av.}}) \sin \pi X_{\mathrm{av.}}$ in the case of a perfectly ordered growth). In Eq. (1), the tilt or imperfect coverage acts through the phase term $2\pi\varepsilon(z/a)$. If the product $N\varepsilon$ is much smaller than 1, all LSL layers are considered in-phase so that the LSL can be treated as a vertical one at least as far as electronic properties are concerned. If $N\varepsilon$ is much larger than one, the electronic envelope wave function will average the tilted LSL composition profile to $X_{\mathrm{av.}}$ so that the modulated part goes to zero.

To estimate this averaging effect quantitatively, we insert this LSL potential in an infinite square quantum well (QW) and compute matrix elements between envelope functions associated to the subband defined by the infinite QW. Envelope functions $\Psi_n(z)$ are of the form:

$$\Psi_n(z) = \sqrt{\frac{2}{Na}} \sin\left(\frac{n\pi z}{Na}\right). \quad (2)$$

Matrix elements $V_\varepsilon^{m,n}(x)$ can be considered as effective potentials scattering an electron of the subband n into the m one. We get

$$V_\varepsilon^{m,n}(x) = -\frac{V_0\lambda}{\pi} A_\varepsilon^{m,n} \times \cos\left[\frac{2\pi x}{L_x} + \pi N\varepsilon + (m+n)\frac{\pi}{2}\right], \quad (3)$$

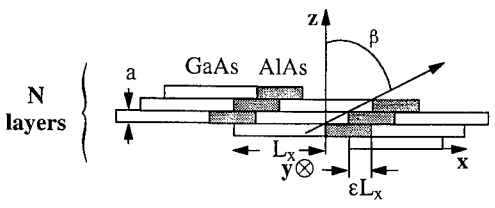

Fig. 2. Schematic view of a tilted lateral superlattice.

$$A_\varepsilon^{m,n} = \frac{16mn\,N\varepsilon}{[(m-n)^2 - 4N^2\varepsilon^2][(m+n)^2 - 4N^2\varepsilon^2]} \times \sin\left[\pi N\varepsilon + (m+n)\frac{\pi}{2}\right], \quad (4)$$

where V_0 is a term related to the band offset and proportional to $X_{\mathrm{av.}}$. Matrix elements preserve the $2\pi/L_x$ periodicity defined by the step array as it appears in Eq. (3). The phase term $\pi N\varepsilon + (m+n)\pi/2$ is of no importance in Eq. (3), whereas it governs the dependence of the effective lateral potential amplitude $A_\varepsilon^{m,n}$ in Eq. (4). This amplitude in Eq. (4) depends only on ε and not on α or L_x unlike the tilt angle β. This demonstrates that the relevant scaling parameter for the electronic properties is $\pi N\varepsilon$ not β.

Alternatively, if a large and constant tilt angle is chosen, let us say $\beta = 80°$, a large lateral potential is obtained only if N is smaller than $1/\varepsilon$. This means that the LSL has to be thin in order to exhibit 1D electronic properties, with a thickness smaller than $N_c = \cot\beta/\alpha$ with $N_c = 10$ for $\alpha = 1°$ and $\beta = 80°$.

Fig. 3 shows the variations of $A_\varepsilon^{m,n}$ with $N\varepsilon$ for $\{m, n\} = \{1, 2\}$. It is clear that the intra-subband potential ($m = n$) decreases for large $N\varepsilon$, whereas the first inter-subband potential exhibit a resonance for $N\varepsilon = 1$. This inter-subband coupling resonance has been recently evidenced in optical experiments performed on doped tilted LSL [5]. This demonstrates that a tilted LSL cannot be considered as a vertical one of smaller amplitude: a vertical LSL provides a separable potential

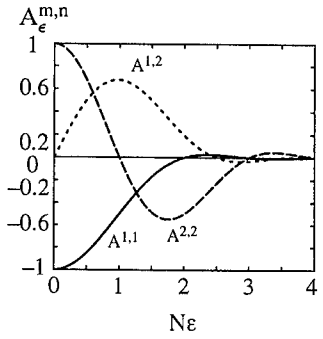

Fig. 3. Universal amplitude of the effective potential for the first two subbands.

(i.e. depending only on x), whereas a tilted LSL does not.

4. Ga flux stability

From the previous considerations it is clear that the coverage should be constant throughout the LSL growth. This requires highly stable Ga and Al fluxes. It is widely accepted that the main emphasis should be put on the former. Dual filament effusion cells allow to operate a Ga cell with the tip of the crucible heated independently and hotter than the base of the crucible to prevent accumulation of Ga droplets at the tip. This avoids cold droplets to change the thermal equilibrium of the Ga bath when they flow from the tip to the base of the crucible. This mechanism is the main source of flux instability in Ga effusion cells. We show here that the use of a dual filament cell requires an adequate regulation strategy of both tip and base filaments to get highly stable fluxes. These fluxes are measured by reflection high-energy electron diffraction (RHEED) oscillations on a 2×2 mm GaAs substrate at $T_{sub} = 560°C$ to ensure a unity Ga sticking coefficient. The RHEED oscillation trace is then analyzed by mean of Fourier transform in order to get the frequency with a high accuracy. Then the dispersion of the data is analyzed over almost an hour.

Fig. 4a shows flux measurements starting 1 h after outgassing Ga cells 100°C above their operating temperature. The single-filament cell displays a noisy flux (statistical standard deviation $\sigma = 0.25\%$), whereas the dual-filament one is less noisy but shows a systematic drift ($\sigma = 0.2$–0.6%). Fig. 4b displays similar measurements recorded 4 h after outgassing. The systematic drift of the dual-filament cell has disappeared and the stability is excellent ($\sigma = 0.1\%$ or less), whereas the stability of

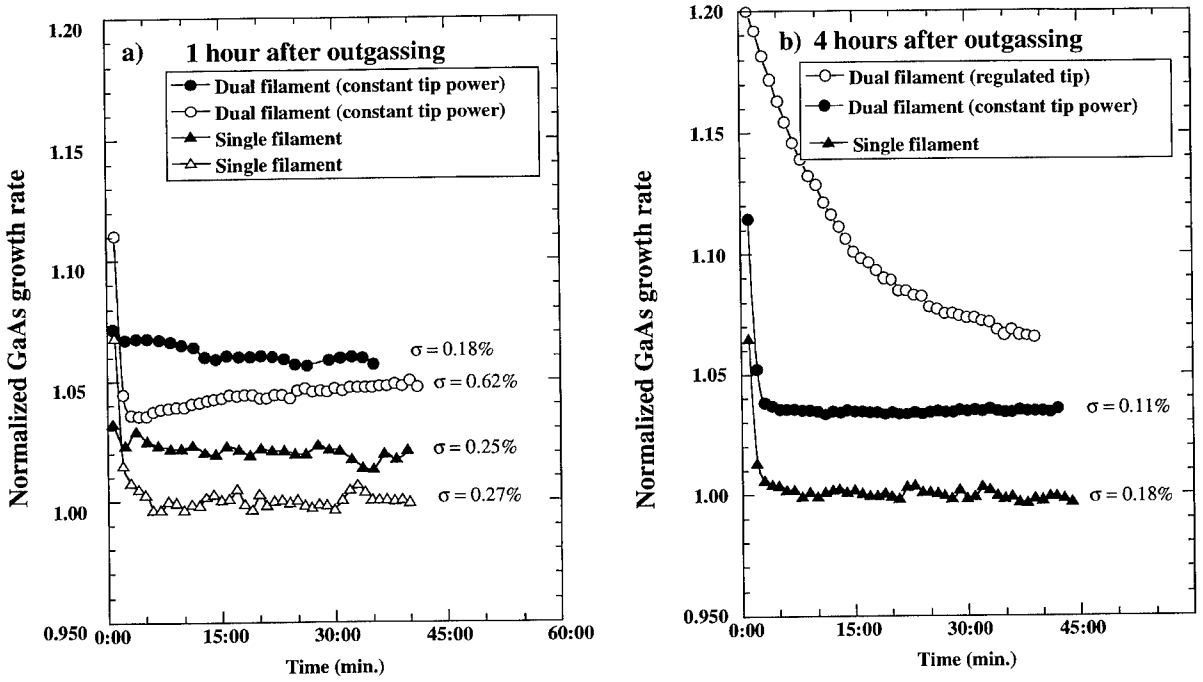

Fig. 4. (a) Ga flux is plotted versus time after shutter opening for two different cells (circles and triangles) and two different runs (open and filled symbols). Each set of data is normalized to 1 and shifted vertically for clarity. (b) Ga flux is plotted versus time for two different cells (filled circles and triangles). Open circles show the Ga flux when the tip power is regulated with the tip thermocouple.

the single-filament cell has only slightly improved ($\sigma = 0.18\%$). This confirms that Ga droplets at the crucible tip are the main source of Ga flux instability since visual inspection of both crucibles reveals a large Ga accumulation at the tip of the single-filament cell and the absence of any Ga droplet at the tip of the dual-filament one.

Concerning the regulation strategy we omitted to say that the dual-filament cell was operated with a base filament regulated with the base thermocouple and a constant power injected in the tip filament to ensure identical temperatures on both base and tip thermocouples when the cell shutter is closed. This strategy yields the most stable fluxes. As a matter of comparison we display on Fig. 4b the measured fluxes when both filaments are regulated on their respective thermocouple with identical set-points. We observe then a very long transient: the Ga flux never stabilizes at a given value over 45 min! This is certainly due to the change in the Ga bath thermal equilibrium when the power increases in the tip filament after the shutter is opened. When operating this cell with a constant power in the tip filament (i.e. with a tip 30°C colder than the base) we never detected any Ga droplets accumulation provided the cell is outgassed every day with a tip at the same temperature than the base.

5. Conclusion

We have considered three important issues related to LSL growth on vicinal surfaces. To obtain periodic step arrays with large periodicities requires to grow GaAs and AlAs in the MEE mode. Even if large periodicities (i.e. small misorientation angles) would lead to strongly tilted LSLs we have shown that the flux control is determined only by the LSL thickness probed by the electronic wave function as long as electronic properties are concerned. This makes the flux control ten times easier. Finally, the use of dual-filament Ga cell improves the flux stability compared to single-filament ones provided a constant power and not a regulated one is injected in the filament heating the tip of the crucible.

References

[1] B. Etienne and F. Laruelle, J. Crystal Growth 127 (1993) 1056.
[2] B. Etienne, F. Laruelle, J. Bloch, L. Sfaxi and F. Lelarge, J. Crystal growth 150 (1995) 336.
[3] F. Lelarge, Z.Z. Wang, F. Laruelle and B. Etienne, J. Crystal Growth 175 (1997) xxx.
[4] Y. Horikoshi, M. Kawashima and H. Yamaguchi, Jpn. J. Appl. Phys 25 (1986) L868.
[5] T. Mélin and F. Laruelle, Phys. Rev. Lett. 76 (1996) 4219.

ELSEVIER

Journal of Crystal Growth 175/176 (1997) 1092–1096

JOURNAL OF CRYSTAL GROWTH

Formation of multi-atomic steps and novel n-AlGaAs/GaAs heterojunctions on vicinal (1 1 1)B substrates by MBE and anisotropic transport of 2D electrons

Y. Nakamura[a,b,*], S. Koshiba[a,b], H. Sakaki[a,b]

[a] *Quantum Transition Project, JRDC, 4-7-6 Komaba, Meguro-ku, Tokyo 153, Japan*
[b] *RCAST, University of Tokyo, 4-6-1 Komaba, Meguro-ku, Tokyo 153, Japan*

Abstract

We have investigated the MBE growth of GaAs on vicinal (1 1 1)B substrates and examined in detail the multi-atomic step structures appearing at the growth front as well as at the n-AlGaAs/GaAs heterojunction. It has been found that the uniformity and periodicity of such steps depend strongly on the growth condition, especially As_4 flux, and that their morphology drastically affects transport of electrons flowing along heterojunctions. The use of high As_4 flux is effective in improving the step uniformity, and in drastically reducing the channel resistance perpendicular to the steps. Key factors for the fabrication of high-quality devices such as quantum wires on (1 1 1)B planes have been discussed.

To fabricate several semiconductor devices, it is important to prepare GaAs/AlGaAs structures with very smooth (1 1 1)B surfaces and interfaces. For example, quantum wells (QWs) on (1 1 1)B are useful to reduce the threshold current of lasers due to its unique valence band structure [1]. As for piezo-electric effect, it becomes maximum on the (1 1 1) plane among low-index planes [2]. To fabricate very narrow quantum wires (QWRs), this plane is attractive, since ridge QWRs and edge QWRs can be fabricated on GaAs/AlGaAs-facet structures having two (1 1 1)B side planes and (0 0 1) plane [3–5].

Especially for the edge QWRs, the smoothness on (1 1 1)B facets is essential to make high-quality wires. Earlier, we investigated the morphology of slightly misoriented (1 1 1)B facet by atomic force microscopy (AFM) and detected multi-atomic steps with ~ 30 nm periodicity [6]. In making the edge QWR, one must clarify the role of such steps and the way to control them, since electrons flow across these steps.

In this paper, we investigate these issues to show that very regular steps can be prepared on vicinal (1 1 1)B planes and that a highly conductive channel can be formed for electrons flowing across these steps. In particular, we study by AFM how multi-atomic steps on vicinal (1 1 1)B substrates depend on As_4 flux. We also investigate how the morphology of these steps affects the transport of

* Corresponding author. Fax: +81 3 3460 9026; e-mail: nakamura@kyokusho.rcast.u-tokyo.ac.jp.

0022-0248/97/$17.00 Copyright © 1997 Elsevier Science B.V. All rights reserved
PII S0022-0248(96)00963-3

two-dimensional (2D) electrons in selectively doped n-AlGaAs/GaAs heterojunctions [7].

In this work, we use GaAs substrates having vicinal (1 1 1)B plane with misorientation angle $\Delta\theta$ of 2° toward the nearest $(\bar{1}\,0\,\bar{1})$ plane. Fig. 1a is an illustration of the top view of $(\bar{1}\,\bar{1}\,\bar{1})$, or (1 1 1)B orientation with respect to other orientations. Fig. 1b shows the cross-sectional view cut along line α–β in (a) and also the misorientation $\Delta\theta$. As will be described later, multi-atomic steps are parallel to the intersection of $(\bar{1}\,\bar{1}\,\bar{1})$ and the $(\bar{1}\,0\,\bar{1})$ plane [6, 7]. If another misorientation direction is used, (1 1 1)B surfaces will be rough due to faceting.

We have studied first how the morphology of 0.6 μm-thick GaAs layer grown at 580°C depends on As_4 fluxes. The As_4/Ga flux ratios of beam-equivalent pressure were set 50 or 130, respectively. GaAs growth rate is 0.26 μm/h. Fig. 2a and Fig. 2b show AFM images of a GaAs surface grown with low As_4 flux. In the height image (a), the height of the structure is indicated by the brightness. In the derivative image (b), dark lines and bright regions correspond to multi-atomic steps and flat terraces, respectively. Note that the step periodicity is not uniform. For the sample grown with high As_4 flux, however, steps are quite straight and uniformly spaced with the main period of ~ 20 nm as shown in Fig. 2d and Fig. 2e.

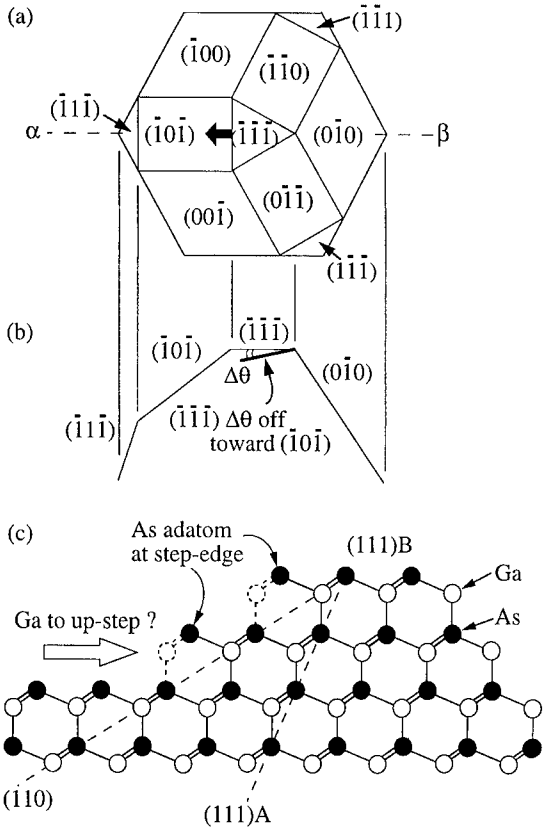

Fig. 1. (a) Top view of crystal orientations near $(\bar{1}\,\bar{1}\,\bar{1})$, or (1 1 1)B plane. The cross-sectional view seen at line α–β of (a) is shown in (b) together with the misorientation angle $\Delta\theta$. (c) Atomic-scale structure of the step on the vicinal (1 1 1)B plane.

We plot the cross-sectional height profiles of these two samples in Fig. 2c and Fig. 2f, where two distinctive differences are noteworthy. Large amplitude steps having the height of 3 nm and the long spacing of several hundred nanometers are seen only in Fig. 2c, whereas regular steps with the average height of 0.4–0.7 nm are seen in Fig. 2f. Thus, steps of Fig. 2f are about two monolayers in height. The other point to note is the presence of very steep steps in Fig. 2c, whose slope is as large as 20°. In contrast, no such steps are seen in Fig. 2f with the slopes being several degrees at most. As will be discussed later, a large anisotropy in electron transport appears only in the presence of high-amplitude steps.

We discuss the relation between As_4 flux and the step uniformity. It has been pointed out that step bunching will appear when adatoms are incorporated preferentially at down-steps. The spacing of steps will be equalized when adatoms are incorporated selectively at up-steps. In case of vicinal (1 1 1)B plane, As atoms stick with single bond at step edges as shown in Fig. 1c, since the surface orientation at the step is close to (1 1 0) or (1 1 1)A. The probability of an As atom to occupy this site at the step edges may not be high as the site is unstable but it can be enhanced by increasing the As_4 flux. Hence, the existence of these As atoms at the step edges may enhance the possibility of Ga-atom incorporation at up-steps as indicated by open arrow in Fig. 1c and may contribute to an equalization of the step spacing.

To investigate how the morphology of steps affects the transport of electrons, we deposited an n-type AlGaAs layer on two kinds of GaAs layers

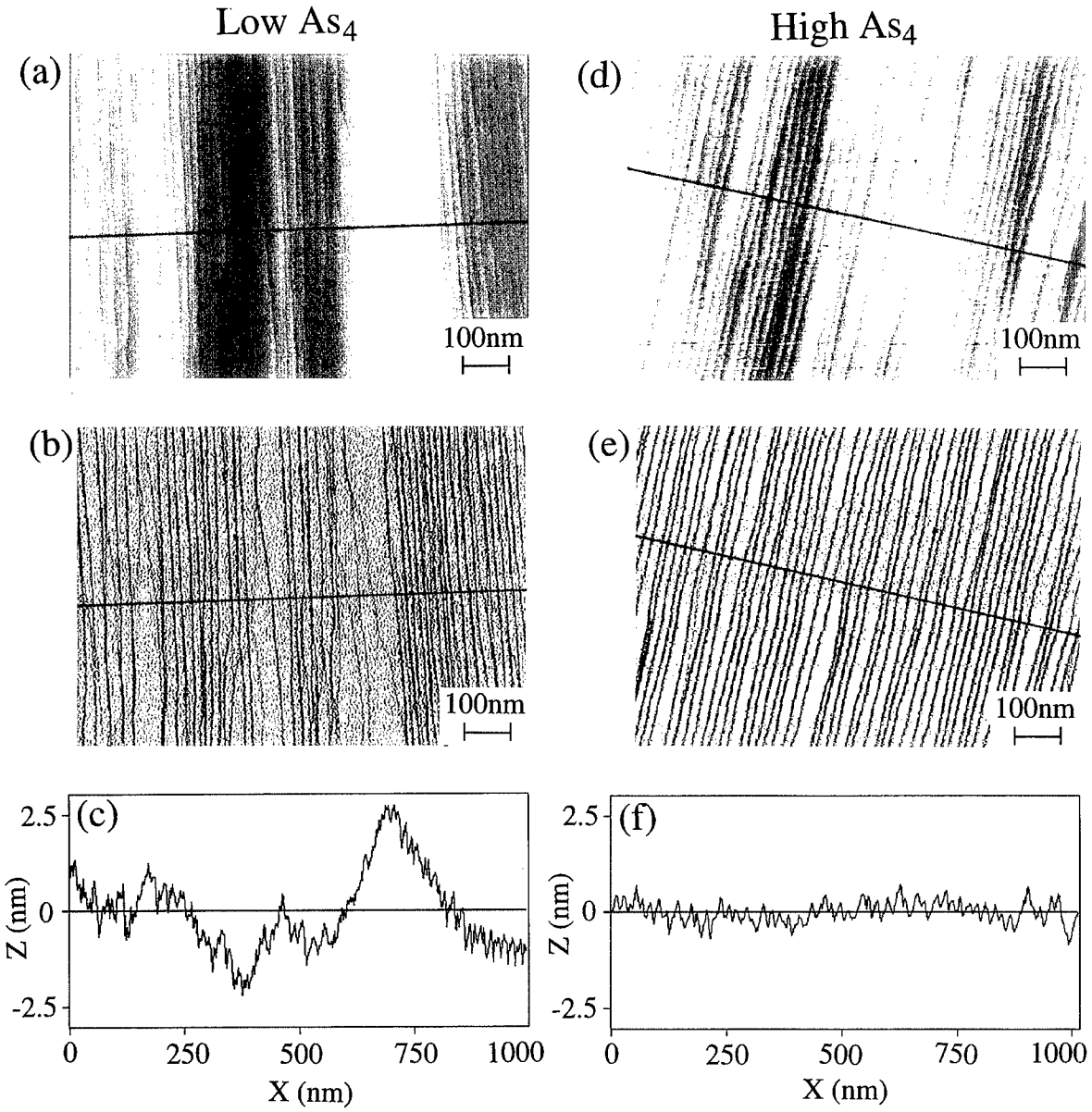

Fig. 2. AFM images (a) and (b) of a GaAs (1 1 1)B surface grown with low As_4 flux and its cross-sectional height profile (c). Corresponding results on the sample grown with high As_4 flux are given in (d), (e), and (f). Note that images are given in height mode for (a) and (d), and in derivative mode for (b) and (e).

having multi-atomic steps, as shown in Fig. 3a. After growing a 0.6 μm GaAs, we grew a 20 nm-thick undoped $Al_{0.33}Ga_{0.67}As$ spacer layer, a 90 nm-thick Si-doped $Al_{0.33}Ga_{0.67}As$ with the dopant density of 6×10^{17} cm^{-3}, and a 20 nm-thick GaAs cap layer. The growth condition was similar to that for the earlier study, where As_4/Ga flux ratios of beam-equivalent pressure were 55 and 170 for the two samples. By using each of these wafers, two kinds of FETs with the channel of 50 μm in width and 600 μm in length were formed as shown in Fig. 4a. Note that 2D electrons at these

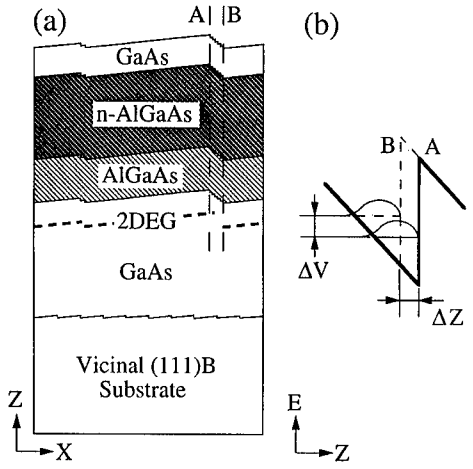

Fig. 3. Cross-sectional diagram (a) of modulation doped n-AlGaAs/GaAs heterojunction with a corrugated interface. Potential profiles (b) at points A and B, indicating the appearance of a potential barrier at the steps.

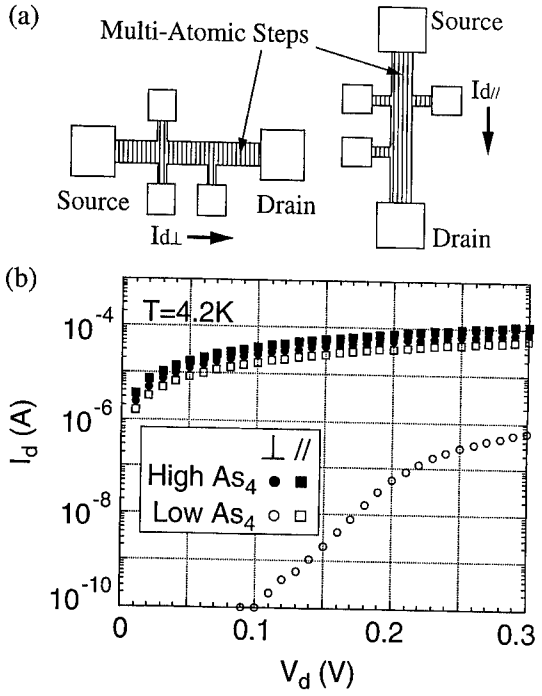

Fig. 4. FET patterns (a) to measure the current $I_{d\perp}$ perpendicular to and that $I_{d\parallel}$ parallel to the steps. The drain current $I_{d\perp}$ and $I_{d\parallel}$ were measured at 4 K as a function of V_d. The data for the sample prepared under high As_4 flux are shown by solid circles ($I_{d\perp}$) and squares ($I_{d\parallel}$). The data of the sample grown under the low As_4 flux are shown by open circles ($I_{d\perp}$) and squares ($I_{d\parallel}$).

corrugated heterojunctions will flow either perpendicular ($\perp$) to or parallel ($\parallel$) to the multi-atomic steps. The Hall measurement done at 14 K on a sample grown with high As_4 flux has shown that the mobility μ and concentration N_s of 2D electrons are 80 000 $cm^2/V\,s$ and $1.9\times10^{11}\ cm^{-2}$, respectively. From the Shubnikov de Haas measurement on this sample, N_s was found to be $3.6\times10^{11}\ cm^{-2}$, though the origin for this difference is not clear yet. Hall measurement on the other sample will be described elsewhere, since their behavior is complicated as shown below.

Fig. 4b shows current I_d – voltage V_d characteristics of these devices measured at 4 K for the two current directions. In the sample grown with low As_4 flux, the current $I_{d\parallel}$ flowing parallel to the steps (blank squares) is high but current $I_{d\perp}$ perpendicular to the steps is extremely small and nonlinear for V_d as shown by blank circles, indicating an extremely large anisotropy. Only the current $I_{d\perp}$ perpendicular to the steps is blocked, probably by large potential barriers. Here, we confirmed that source and drain electrodes are good and ohmic by measuring the channel conductance parallel to the steps. When high As_4 flux is used, currents for both directions are linear and almost isotropic, and are as large as the parallel current $I_{d\parallel}$ of the sample grown with low As_4. These results indicate that very smooth (1 1 1)B planes can be prepared and that highly conductive channels can be formed even for the direction perpendicular to the steps. Hence, high-quality transport devices and QWRs can be prepared on (1 1 1)B planes.

In the sample grown with low As_4, potential barriers appear for electron motion perpendicular to the multi-atomic steps as mentioned above. Mechanisms of the barrier formation are not clear yet, but it should be related to the presence of large steps or steep steps as shown in Fig. 2c. One possible reason is the roughness itself at the heterojunction. As illustrated in Fig. 3a, 2D-electrons flowing across the steps will be reflected at the steps, since the potential $V(x, z)$ at points A and B are displaced as shown by solid and dashed lines in Fig. 3b. Although the details of potential profile

is not known, earlier models on interface roughness scattering have shown that the effective potential ΔV caused by the interface displacement is of the order of the interface electric field F multiplied by the roughness height Δz. Hence, by setting $\Delta z = 3$ nm and $F = 50$ kV/cm at sheet electron density N_s of 3.6×10^{11} cm^{-2} [8], we estimate that the effective potential ΔV introduced by roughness may be of the order of 15 meV. Since this value overestimates the effect of roughness, a more rigorous analysis is certainly required not only by refining the mathematical model but also by considering the possible variations of spacer layer thickness and the donor concentrations.

Another possible reason for the appearance of potential barriers is the anomalous incorporation of Si atoms in the region of multi-atomic steps. Since (1 1 0), (1 1 1)A, and crystallographic planes other than (1 1 1)B show up at the steps of our sample as shown in Fig. 1c, some fraction of Si atoms, which fall directly on or migrate to these planes, can be either inactivated or incorporated into acceptor sites. If such processes take place, the local potential near the steps is raised and the electron concentration is locally lowered, resulting in a kind of potential barriers. This anomalous incorporation of Si dopants is quite probable, since Si atoms on (1 1 1)A and related planes of GaAs are known to work as acceptors [9], unless the layer is grown with very high As_4 flux at low temperatures.

In summary, it is shown that the growth of GaAs with low As_4 flux on vicinal (1 1 1)B planes results in aperiodic multi-atomic step structures. When the layer is grown with high As_4 flux, multi-atomic step become evenly spaced with typical period of 20 nm. The transport of electrons is found to be scarcely affected by evenly spaced step structures but strongly blocked by aperiodic steps with high amplitude, leading to a huge in-plane anisotropy of conductance in excess of 100. The key factor for high-quality QWRs using (1 1 1)B facets is clarified.

We wish to express our sincere gratitude to Professor Petroff, Dr. Ichiro Tanaka, and Dr. Metzner for the very useful discussions. We thank Professor Shiraki and Mr. Usami of University of Tokyo for their help in AFM observation.

References

[1] T. Hayakawa, M. Kondo, T. Suyama, K. Takahashi, S. Yamamoto and T. Hijikata, Jpn. J. Appl. Phys. 26 (1987) L302.
[2] M. Ilg, K.H. Ploog and A. Trampert, Phys. Rev. B 50 (1994) 17111.
[3] S. Koshiba, H. Noge, H. Akiyama, T. Inoshita, Y. Nakamura, A. Shimizu, Y. Nagamune, M. Tsuchiya, H. Kano and H. Sakaki, Appl. Phys. Lett. 64 (1994) 363.
[4] Y. Nakamura, S. Koshiba, M. Tsuchiya, H. Kano and H. Sakaki, Appl. Phys. Lett. 59 (1991) 700.
[5] Y. Nakamura, M. Tsuchiya, S. Koshiba, H. Noge and H. Sakaki, Appl. Phys. Lett. 64 (1994) 2552.
[6] Y. Nakamura, I. Tanaka, N. Takeuchi, S. Koshiba, H. Noge and H. Sakaki, Jpn. J. Appl. Phys. 35 (1996) 4038.
[7] Y. Nakamura, S. Koshiba and H. Sakaki, Appl. Phys. Lett. 69 (1996) 4093.
[8] K. Hirakawa, H. Sakaki and J. Yoshino, Appl. Phys. Lett. 45 (1984) 253.
[9] Y. Kadoya, A. Sato, H. Kano and H. Sakaki, J. Crystal Growth 111 (1991) 280.

ELSEVIER

Journal of Crystal Growth 175/176 (1997) 1097–1101

JOURNAL OF CRYSTAL GROWTH

MBE growth of two-dimensional electron gases on (110) GaAs

C.B. Sørensen[a,*], H. Gislason[b], J.M. Hvam[b]

[a] *Niels Bohr Institute, Ørsted Laboratory, University of Copenhagen, Universitetsparken 5, DK-2100 Copenhagen Ø, Denmark*
[b] *Mikroelektronik Centret, The Technical University of Denmark, bld. 345 East, DK-2800 Lyngby, Denmark*

Abstract

We have studied the influence of growth temperature on the electrical properties of two-dimensional electron gases, grown by molecular beam epitaxy on (1 1 0) oriented GaAs. The mobility and carrier density of the grown layers depend strongly on the chosen substrate temperature, having a narrow maximum around 470°C. Growth at 10–20°C below the optimum temperature results in insulating layers. We show that this steep drop in mobility and carrier density is strongly correlated with the carbon incorporation observed in photoluminescence. In the temperature range 480–520°C the mobility is only about 60% of the peak value and both mobility and carrier density change only slightly. Above 520°C the mobility drops again whereas the carrier density stays virtually unchanged. We believe this to be caused by interface roughness.

1. Introduction

Motivated by the current strong interest in low-dimensional systems, grown by cleaved edge overgrowth (CEO) [1], we have investigated how the properties of two-dimensional electron gases (2DEG's) grown by molecular beam epitaxy (MBE) on (1 1 0) GaAs are influenced by the substrate temperature.

For the realization of high-quality one-dimensional (1D), or modulated 2DEG samples, by CEO [2], one has to grow a good-quality 2DEG on the cleaved (1 1 0) edge of an already grown GaAs/AlGaAs structure.

The growth of high-quality material on the (1 1 0) surface has already been reported [3–8]. The optimal growth conditions for the (1 1 0) surface use a high V/III flux ratio and a low substrate temperature compared to growth on a conventional (1 0 0) surface. These conditions compensate for the low incorporation coefficient of the As to the non-polar (1 1 0) surface. An additional improvement in the quality of the grown layers can be achieved by using As_2 instead of As_4 [6–8]. In this paper we investigate a total of 16 2DEG samples grown in the temperature range 440–595°C. We find that the low-temperature transport properties are very sensitive to small variations ($\pm$ 10°C) in the growth temperature. The grown layers were also characterized by low-temperature photoluminescence (PL), and in the temperature range 440–480°C we find a strong correlation with the transport properties.

* Corresponding author.
Fax: + 45 35 32 04 60; e-mail: cbs@fys.ku.dk.

0022-0248/97/$17.00 Copyright © 1997 Elsevier Science B.V. All rights reserved
PII S0022-0248(96)00964-5

2. Experimental procedures

The layers were grown in a Varian Modular Gen II, 3-inch MBE machine using a Varian cracker source for the arsenic (As_2).

The (1 1 0) oriented substrates used were semi-insulating GaAs 'epi-ready' 2 in. diameter wafers, cut with an orientational accuracy of $\pm$ 0.25°, from American Xtal Technology.

The growth rates used were about 0.2 μm/h for AlAs and 0.5 μm/h for GaAs, as measured by RHEED oscillations on a (1 0 0) calibration wafer prior to growth. The V/III beam equivalent pressure (BEP) ratio was 20–30. A more detailed description of the system and growth procedure can be found in Ref. [6].

All substrate temperatures in this work are the temperatures indicated by the thermocouple (T_{TC}), located behind the wafer. Using an IRCON series V infrared pyrometer we obtain the following relation between the temperatures read by the pyrometer (T_{pyro}) and the thermocouple (T_{TC}): $T_{pyro} = 0.78T_{TC} + 56.4$ (emissivity set to 0.7).

All 16 samples were grown with an identical structure schematically shown in Fig. 1.

The structure used was not designed for obtaining maximum mobility [9], but instead designed as a test structure, insuring a high carrier density in the 2DEG under the growth conditions used in this work. We have employed the technique of δ-doping in these structures to reduce the effect of autocompensation [6].

After growth the samples were cut in 5 × 5 mm pieces, and in order to make electrical measurements, ohmic contacts were formed by alloying small Sn beads at 300°C for 1 min, in an atmosphere of dry N_2.

The sample configuration used was a standard van der Pauw square sample, with a contact in each corner.

3. Electrical characterization

Of the 16 samples we succeeded in contacting 13, grown in the temperature range 440–560°C. Two samples grown at 582°C and 595°C were insulating. The samples grown at 440°C and 560°C were difficult to contact, giving non-linear I/V charcteristics, and the exact values of electron mobility and

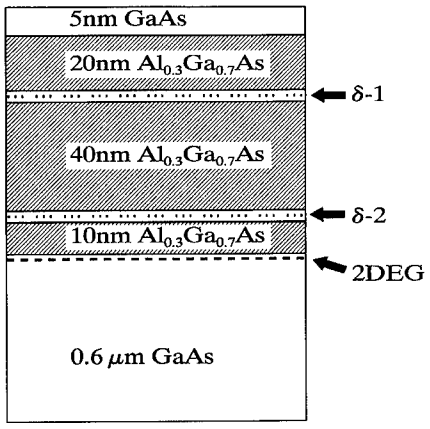

Fig. 1. Schematic view of δ-doped 2DEG structure. δ-1 and δ-2 are Si delta-doped layers with densities of 3.5×10^{12} and 1.5×10^{12} cm^{-2}.

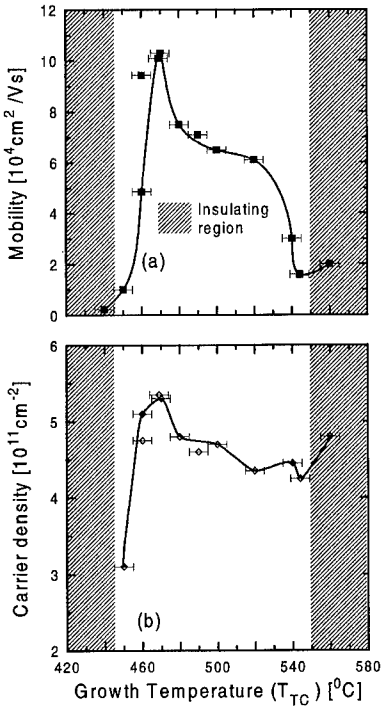

Fig. 2. Electron mobility (a) and carrier concentration (b) as a function of substrate growth temperature. Measurement temperature is 10 K.

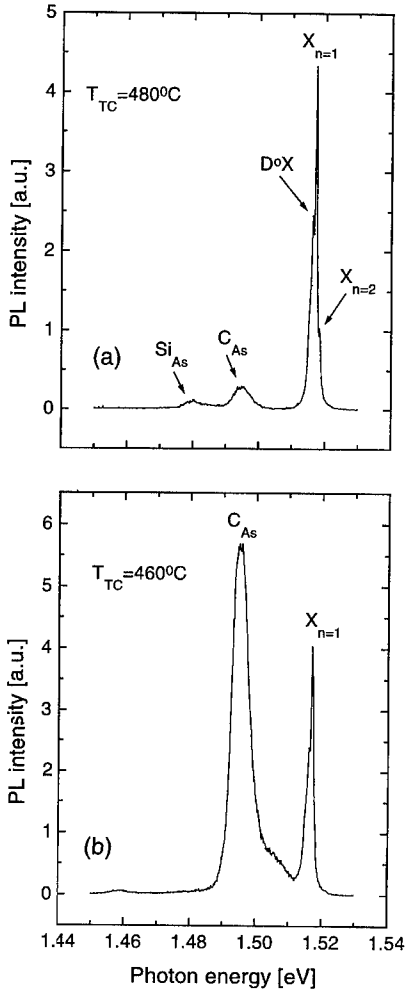

Fig. 3. Photoluminescence spectra of two structures grown at $T_{TC} = 480°C$ (a) and $T_{TC} = 460°C$ (b). Excitation intensity is 4 W/cm^2.

carrier density are therefore uncertain. Fig. 2 shows mobility and carrier density as measured at 10 K in the dark. The two shaded regions indicate where the samples gradually become insulating. The curves are intended to guide the eye only.

As seen in the plot of mobility versus growth temperature (Fig. 2a), the mobility has a maximum around a temperature of 470 ± 5°C. At lower temperatures the mobility drops drastically, and at 440°C the samples become insulating. The drastic drop in mobility is followed by an equally steep drop in the carrier concentration. This drop in mobility is correlated with the PL measurements which are discussed in detail in Section 4 (Fig. 3).

In the temperature range 480–520°C the mobility and carrier density change only little. The mobility is, however, only about 60% of the peak mobility.

At temperatures higher than 520°C there is again a steep drop in mobility. However, in this range the carrier concentration stays virtually unchanged, and we see no significant changes in the PL spectra.

The surface morphology is excellent and mirror like for the samples grown at temperatures below 470°C, while the surfaces of the samples grown in the range 480–520°C show a gradual increase in the number and size of facets, as also observed by others [8–10]. At temperatures higher than 520°C the surface displays a clear faceting, indicating a Ga-rich growth caused by a poor As sticking coefficient. The limiting factor of the 2DEG mobility at the high growth temperatures thus seems to be the roughness of the GaAs/AlGaAs interface.

For reference, we have also grown the same 2DEG structure on a (1 0 0) oriented substrate, under optimum (1 0 0) conditions ($T_{TC} = 730°C$ and minimally As rich). This sample had a carrier density of 6.0×10^{11} cm^{-2} and a mobility of 300.000 cm^2/(V s). The carrier densities of the best (1 1 0) samples are thus only about 10% lower than the (1 0 0) reference. The mobility, however, is only one third of the (1 0 0) mobility.

4. Optical characterization

The optical quality of the (1 1 0) layers was investigated by low-temperature photoluminescence. The samples were mounted in a continuous-flow cryostat using liquid He as coolant. During the measurements the sample temperature was kept at 4 K, and the luminescence was excited by the 632.8 nm line of a HeNe laser (intensity 4 W/cm^2). A 0.66 m focal length spectrometer was used to disperse the luminescence. The signal was detected by a GaAs photomultiplier and recorded using lock-in techniques.

From the total of 16 samples, we chose nine samples grown in the temperature range 440–560°C for elaborate PL characterization. All

nine samples were characterized using three different excitation intensities: 4, 0.4 and 0.04 W/cm^2, thus obtaining a total of 27 spectra.

In Fig. 3, we display two representative spectra, one taken at the high-temperature side of the mobility peak and one taken on the low-temperature side.

The spectrum in Fig. 3a is taken from the sample grown at 480°C and shows a single dominant line at 1.5152 eV with a width of 1.0 meV. This is assigned to the emission from the $n = 1$ state of the free exciton, and is labeled by $X_{n=1}$. The peak at 1.5183 eV, on the high-energy side of the free exciton, indicates the $n = 2$ state of the free exciton ($X_{n=2}$). At the low-energy side we observe a peak, which we attribute to excitons bound to neutral donors (D°X)

The signal at 1.495 eV has an intensity 15 times lower than the dominant free-exciton line. It is assigned to transitions involving carbon acceptor states, as commonly observed in PL of MBE-grown GaAs material [11] and labeled C_{As} in the figure.

The spectrum taken from the sample grown at 460°C is quite different as seen in Fig. 3b. In this sample the peak related to carbon acceptor states is the dominant one. The intensity ratio of the free-exciton line to the carbon-related luminescence ($X_{n=1}/C_{As}$) is in this case 0.7.

As can be seen, there is a substantial difference in the two spectra, the spectrum from the sample grown at 480°C indicates a high-quality material, whereas the spectrum from the 460°C sample is dominated by the carbon-related impurities. This is, as mentioned earlier, strongly correlated with the drop in carrier concentration and mobility.

We have also investigated the samples grown at higher temperatures and in this case the spectra remain virtually unchanged, even past the point where the mobility displays a steep drop. However, for the samples grown at 480°C and higher we start to see a small signal at 1.48 eV (Fig. 3a), which we attribute to Si acceptors. At higher temperatures the sticking coefficient of As starts to drop, and the chance of Si incorporating as an acceptor on an As site increases. This is also consistent with the observed small drop in carrier concentration as seen in Fig. 2b.

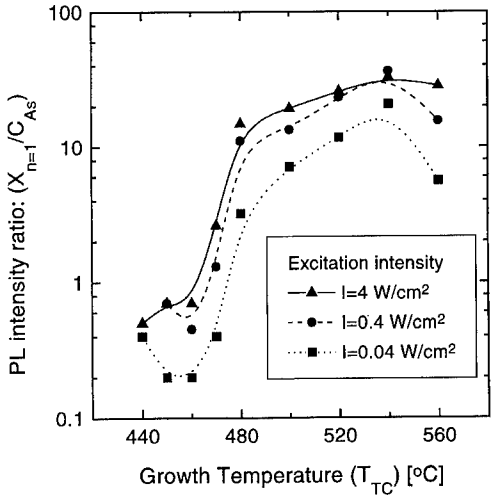

Fig. 4. PL intensity ratio between the $n = 1$ free exciton and the carbon-related luminescence versus sample growth temperature. Data is shown for three different excitation intensities.

Fig. 4 shows the ratio of PL intensity between the free-exciton emision ($X_{n=1}$) and the carbon related transitions (C_{As}) versus growth temperature. Data from all of the 27 spectra are shown.

The three curves, taken at different excitation intensities (4, 0.4 and 0.04 W/cm^2), all show the same general tendency, namely that the intensity ratio $X_{n=1}/C_{As}$ changes drastically when the growth temperature is reduced from 480°C to 460°C. All spectra taken from samples grown at temperatures $\geqslant$ 480°C are dominated by the free-exciton emision, whereas all spectra taken from samples grown at temperatures $\leqslant$ 460°C are dominated by the emission from the carbon-related transistions.

5. Conclusion

We have shown that using the optimum growth temperature is extremely important for the quality of 2DEG's on (1 1 0) GaAs. A growth temperature which is 10–20°C below the optimum temperature, yields an almost insulating layer. In CEO, it is common practice to mount the samples to be cleaved, on a bracket, mounted on a modified

substrate holder [12, 13]. This bracket sticks out 3–5 mm from the holder at an angle of 90° towards the sources. This mounting procedure will inherently lead to a lower temperature of the cleaved surface, as compared to a reference sample mounted in the normal position [13].

As we have shown, this difference in temperature will affect the low-temperature transport properties of the CEO samples seriously.

The cause of the drop in mobility and carrier density at temperatures lower than 470°C has been shown to be related to the enhanced incorporation of carbon, at the low growth temperature used, whereas the drop in mobility at temperatures higher than 520°C is probably related to the roughness of the grown layers.

Acknowledgements

This work was supported by the Danish Ministries of Research and Industry in the framework of CNAST (Center for Nanostructures), and all samples were grown and processed at the III–V Nanolab.

References

[1] L. Pfeiffer, K.W. West, H.L. Störmer, J.P. Eisenstein, K.W. Baldwin, D. Gershoni and J. Spector, Appl. Phys. Lett. 56 (1990) 1697.
[2] H.L. Störmer, L.N. Pfeiffer, K.W. West and K.W. Baldwin, in: Nanostructures and Mesoscopic Systems, Eds. W.P. Kirk and M.A. Reed (Academic Press, Boston, 1992) ch. 3, p. 51.
[3] J. Zhou, Y. Huang, Y. Li and W.Y. Jia, J. Crystal Growth 81 (1987) 221.
[4] L.T.P. Allen, E.R. Weber, J. Washburn and Y.C. Pao, Appl. Phys. Lett. 51 (1987) 670.
[5] E.F. Schubert, L. Pfeiffer, K.W. West, H.S. Luftman and G.J. Zydzik, Appl. Phys. Lett. 64 (1994) 2238.
[6] C.B. Sørensen, H. Gislason, D. Birkedal and J.M. Hvam, Microelectron. J. 26 (1995) 767.
[7] H. Gislason, C.B. Sørensen and J.M. Hvam, Appl. Phys. Lett. 69 (1996) 800.
[8] M.C. Holland, A.H. Kean and C.R. Stanley, J. Crystal Growth 150 (1995) 455.
[9] B. Etienne and E. Paris, J. Phys. 48 (1987) 2049.
[10] L.T.P. Allen, E.R. Weber, J. Washburn, Y.C. Pao and A.G. Elliot, J. Crystal Growth 87 (1988) 193.
[11] L. Pavesi, in: Properties of Aluminum Gallium Arsenide, Ed. S. Adachi (INSPEC, London, 1993) ch. 9, p. 245.
[12] L. Pfeiffer, H.L. Störmer, K.W. West, A.R. Goñi, A. Pinczuk, R.C. Ashoori, M.M. Dignam and W. Wegscheider, J. Crystal Growth 127 (1993) 849.
[13] T. Someya, H. Akiyama and H. Sakaki, J. Appl. Phys. 79 (1996) 2522.

ELSEVIER

Journal of Crystal Growth 175/176 (1997) 1102–1107

JOURNAL OF CRYSTAL GROWTH

The building up of terrace periodicity by MBE growth on (0 0 1) GaAs vicinal surfaces

F. Lelarge*, Z.Z. Wang, A. Cavanna, F. Laruelle, B. Etienne

Laboratoire de Microstructures et de Microélectronique, CNRS, B.P. 107, F-92225 Bagneux Cedex, France

Abstract

The morphology of MBE grown GaAs vicinal surfaces is studied using ex situ AFM. Analysing the statistical distribution of terrace width, we succeed in explaining our measurements either by a thermodynamical equilibrium model taking into account the step by step interaction or by a 2D Monte Carlo simulation of the growth. In the latter case, an anisotropic Schwoebel barrier at the step edge has to be introduced in order to get a good agreement. We argue that growth is the efficient process to get a low disordered step array at the usual time scale and temperature range of MBE. In addition the effect of a GaAs/AlAs buffer superlattice, or of pure AlAs layer, or of Si doping in GaAs is also discussed.

PACS: 68.55.Eg; 68.35.Bs; 61.16.Ch; 61.20.Ja

Keywords: Molecular beam epitaxy; Vicinal surfaces; Monte Carlo simulation; Atomic force microscopy

1. Introduction

Organized growth on vicinal surfaces appears as a simple and attractive way to realize, in a single technological step, high quality 1D GaAs/AlAs quantum structures [1] with novel and interesting optical [2] and electrical [3] properties. A necessary requirement is obviously to get and to keep a surface with a nearly periodic arrangement of the step array. In this work we use vicinal surfaces with monomolecular Ga terminated steps (type A) for a large range of misorientation angle (the corresponding mean terrace length L varies from 8 to 75 nm). We used solid source MBE (Riber 2300) and a commercially available Atomic Force Microscope (Nanoscope III). The AFM measurements are performed outside the MBE system with the entire scanning unit placed in a plexiglass glove box purged with pure and dry nitrogen gas. We worked with a silicium cantilever in the contact mode and the applied force is less than 10 nN [4].

* Corresponding author. Fax: + 33 1 42 31 73 78; e-mail: francois.lelarge@bagneux.cnet.fr.

0022-0248/97/$17.00 Copyright © 1997 Elsevier Science B.V. All rights reserved
PII S0022-0248(96)00910-4

2. Building up of terrace periodicity

Before any growth, but after oxide sublimation and a 5 mn thermal annealing at 650°C under As_4 flux in the growth chamber, although the RHEED pattern is 2D-like and reconstructed, the AFM scan reveals that the substrate surface is in fact very rough and exhibits large anisotropic structures elongated along [1 $\bar{1}$ 0] (they are typically 100 nm wide, 500 nm long, 3–6 nm deep). During subsequent GaAs buffer growth, the splitting of the RHEED specular spot (observed for misorientation angle $\alpha > 0.5°$) appears rapidly (20–60 monolayers (ML)) indicating that some nice terrace periodicity is recovered. An AFM scan made after 180 s growth at 620°C and 2 Å/s gives a confirmation to this, although some deeper holes still remain. Note that the post-growth oxydation during the transfer of the sample limits the AFM lateral resolution (4 nm here instead of better than 1 nm on a Au surface) and kinks on step edges are not resolved. After a thicker buffer grown with weak As/Ga flux ratio (the surface is reconstructed 3×1) and a reduced growth rate (0.5 Å/s at 620°C), a peaked terrace distribution is obtained for terrace length L below 50 nm ($L = a/\tan\alpha$, $a = 2.83$ Å in GaAs). On low misoriented substrates ($\alpha = 0.2°$), the growth is indeed not in the step flow mode and the partial island nucleation on terrace disrupt the periodicity. No step bunching occurs in our growth conditions (see $\alpha = 1°$ data on Fig. 1), at variance with previous reports [5]. The terrace width

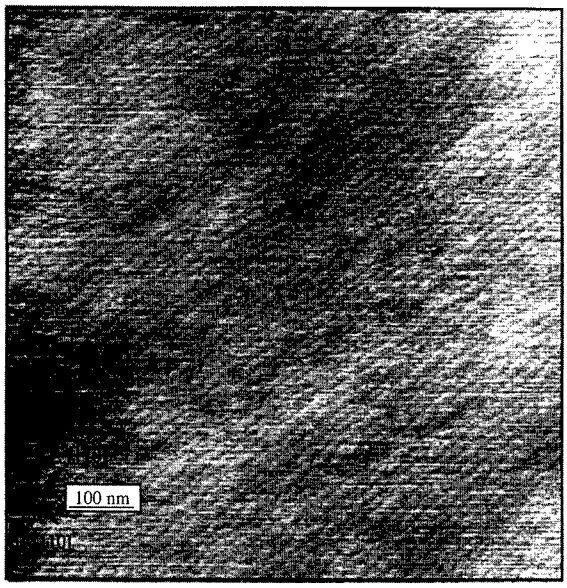

Fig. 1. AFM scan of a vicinal surface misoriented by an angle of 1° towards [1 1 0] (Ga step) after the growth of a GaAs buffer.

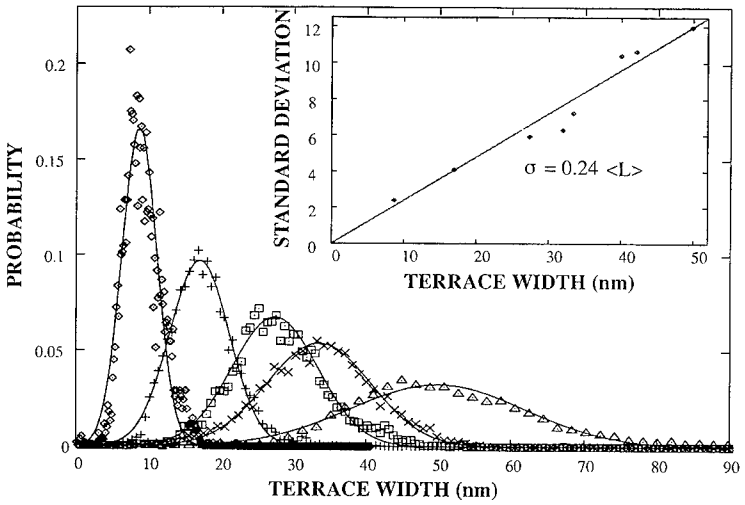

Fig. 2. Distribution of terrace width for five misorientation angles (nominal values: 2°, 1°, 0.5°, 0.5°, 0.3°) obtained from the analysis of an area comprising 4000–10 000 terraces. The two sets of data for 0.5° are within the accuracy of the misorientation. In the insert, variation of the standard deviation with mean terrace length for 8 samples.

distributions obey to a Gaussian law with a mean value close to the nominal terrace periodicity (misorientation accuracy $\pm 0.1°$). A nearly linear relationship between the standard deviation and the mean value of the Gaussian ($\sigma = 0.24 \pm 0.04 \langle L \rangle$) is obtained as shown in Fig. 2. There is no reduction in σ by including a superlattice GaAs/AlAs in the buffer. Our results are very similar to vicinal Si (1 1 1) where it was founded $\sigma = 0.25 \langle L \rangle$ [6]. This close identity with Si is really surprising if we consider the conditions used in that case (a few hours at $T = 900°C$) which are far away from ours ($T = 580°C$ and 2000 Å grown at 0.18 ML/s).

3. Equilibrium models

In Si, the results have been explained by thermodynamical equilibrium between interacting steps. In order to understand how this works, we have considered four equilibrium models based on: (i) straight noninteracting steps, (ii) single step meandering between fixed walls, (iii) terrace-step-kink (TSK) model taking into account only entropic repulsion, (iv) entropic and energetic step-step repulsion. Fig. 3 displays the terrace width distributions observed on Ga (and also on As terminated steps misoriented by 0.5°) and the distributions predicted by the different equilibrium models. In these models, the step configuration is only determined by the state of lower energy without any consideration of the kinetics of the incorporation at the step edges. For a sequence of straight noninteracting steps, an exponential distribution is expected. The distribution, obtained for a single step confined between two rigid walls separated by $2 \langle L \rangle$ [7], already captures most of the physics of the entropic repulsion which drastically reduces the probability of finding small terraces. For purely entropic interactions, the distribution obeys the "universal law" calculated by Joos et al. in the one-dimensionnal free fermion model [8]. If entropic and energetic repulsion coexist, the distribution is narrow and obeys to a Gaussian law when energetic repulsion outweighs the entropic one. An energetic repulsion with a L^{-2} decay, as in the last model, is needed to explain the linear relationship between the standard deviation and the mean value of the Gaussian observed on Ga surfaces. For As terminated steps, note that the observed distribution is skewed (with a peak value slighty below the mean terrace width) and that the step edges are more disordered. Some terraces are as large as twice the nominal periodicity. But the probability of finding a terrace narrower than 10 nm remains small.

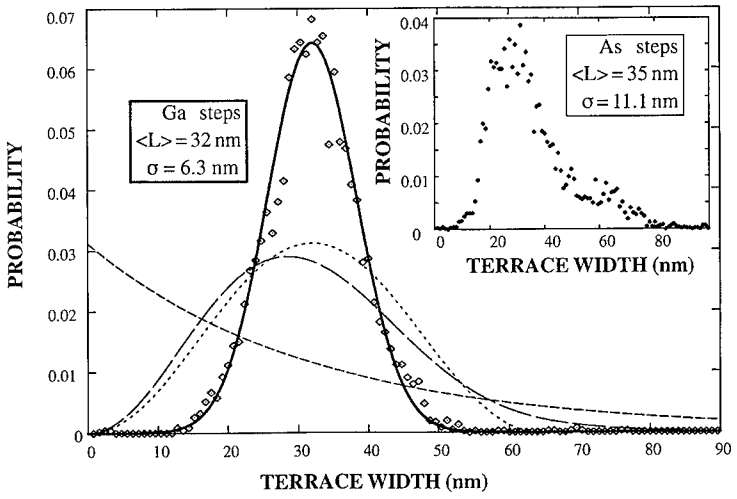

Fig. 3. Fit of the data obtained on a 0.5° A (Ga step) sample using four equilibrium models discussed in the text: short dashes (model i), long dashes (model ii), dots (model iii), plain line (model iv). The insert shows the data for a 0.5° B (As step) sample.

4. Role of the kinetics

In GaAs around 600°C, thermal annealing is not efficient to get a periodic step array and growth is unavoidable. Although this is partly due to the fact that the starting surface is very far from a smooth surface, we believe that the atom kinetics on the surface will be more important to determine the terrace distribution rather than the minimization of a free energy accounting only for the interactions discussed above. In our growth conditions, weakly bound mobile atoms are mainly provided by impinging atoms rather than by atoms thermally excited out of the surface.

In order to determine the critical parameters of the step array ordering, we have grown on 0.5° A misoriented samples a GaAs buffer in the conditions optimized for the terrace periodicity and then we have studied the change of the surface morphology as a function of specific growth conditions. Thus, a 60 nm thick GaAs layer growth at a much lower temperature (540°C) leads to the formation of mounds elongated in the [1 $\bar{1}$ 0] direction (4ML's high, 60 nm wide and 300 nm long). These results are in good agreement with those observed by Orme et al. [9] on nominal surfaces. In the [1 1 0] direction, the terrace width defined by these structures ($\sim$ 6 nm) is approximatively equal to the diffusion length at 540°C if we refer to the transition temperature, between island nucleation and step flow, measured by RHEED on 2° A ($\langle L \rangle = 8$ nm).

Growing a $Ga_{1-x}Al_xAs$ ($x = 0.33$) barrier, the step periodicity remains quite good despite the lower lateral resolution of the AFM measurement ($\sim$ 6 nm) due to the stronger surface oxydation. On AlAs layer (900 Å at 0.25 Å/s), buried by 20 Å of GaAs to avoid the AlAs oxydation, the step array is more disordered in spite of a sharper specular spot splitting in RHEED. The surface morphology is explained by a partial incorporation at the step edge for pure AlAs growth, in agreement with the fact that RHEED oscillations can always be resolved during AlAs homoepitaxy. A surprising point is that we did not observe any mounds after the epitaxy of AlAs grown at low temperature (100 nm at 500°C). We are led to the conclusion that the Schwoebel barrier evidenced on GaAs is much weaker on an AlAs surface. This agrees with the well-known fact that AlAs layers grown at low temperature are mirror like, but not with the impossibility to smooth out a rough surface by AlAs growth at higher temperature. We believe that then impurities (O, C) floating on the AlAs surface hamper the adatom diffusion.

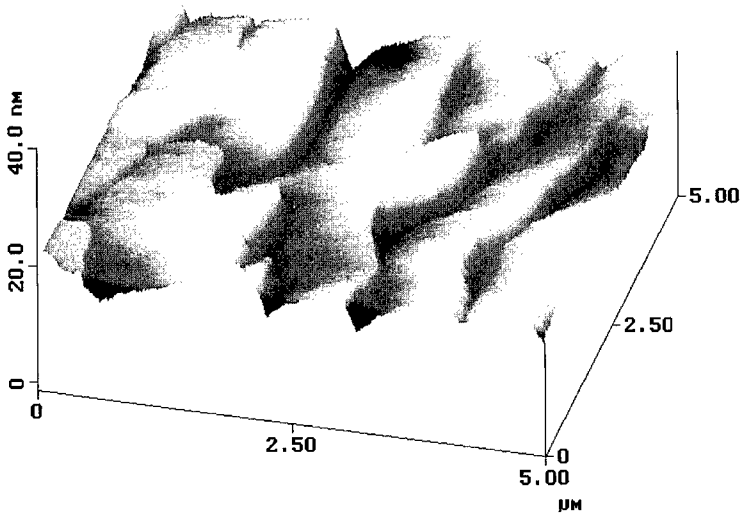

Fig. 4. AFM scan of a GaAs : Si surface showing step bunching. The substrate is a 0.5° A surface.

To evidence the role of impurities in the building up of the terrace periodicity, we have grown Si doped GaAs layers at 580°C. After the growth of a 200 nm GaAs layer at low doping (2×10^{17} cm^{-3} which is typically used in order to provide STM measurements on GaAs), we observe a more irregular step array ($\sigma = 0.31\langle L\rangle$, i.e. 25–30% larger) and some elongated islands on the terraces. The poor terrace periodicity observed in ultra-vacuum STM measurements [5] can be explained by impurity step pinning. However no difference with pure GaAs growth can be evidenced on the RHEED oscillations (the transition temperature to step flow is just the same) but this can be fortuitous and misleading because of these islands. For very high Si concentration (2×10^{19} cm^{-3}), irregular macrosteps (up to 30 ML's high for 60 nm thick layers) which might be unresolved step bunching are observed (Fig. 4). The surface morphology is quite different from the mounds. We have not yet a clear understanding of how to explain this. At this high doping level the surface As coverage is lower [10] and a change of the surface reconstruction from 3×1 to a 3×2 is observed.

5. 2D Monte Carlo simulation

We developed a Monte Carlo simulation to mimic the MBE growth and to understand the results observed on pure GaAs. Our model is very close to that developed by Vvendensky et al. [11]. Only 5 parameters are introduced: the binding energy to the substrate ($E_s = 1.58$ eV), the binding energy to in-plane nearest neighbour ($E_n^{(A)} \sim 0.16$ eV along [1 1 0] and $E_n^{(B)} \sim 0.32$ eV along [1 $\bar{1}$ 0]) and a Schwoebel barrier ($E_b^{(A)}$ and $E_b^{(B)}$). E_s is determined by the temperature required for step flow growth mode whereas the anisotropy ratio $E_n^{(A)}/E_n^{(B)}$ is determined by the anisotropy of islands nucleating on the terraces. The values of the parameters are those taken in Ref. [12] but we have then to increase the temperature of the calculation by 50°C. We did not use additional rule such as the instantaneous search by impinging atoms of the most favourable site in a given area. This rule destroys at once any roughness at low temperature which does not corresponds to experimental observation. Our calculations are done on a 100×100 array of "GaAs site" (400 Å $\times$ 400 Å) with periodic boundary conditions. We investigated the smoothing of initial rough surfaces and the step array ordering on 2° misoriented substrates.

We are able to account for all the observations using an anisotropic Schwoebel barrier: (i) the formation of the mounds observed at low growth temperature requires this barrier [9], (ii) it is impossible to smooth out a rough surface if this barrier is strong in both directions [13], (accepting this, the barrier anisotropy is consistent with the mound anisotropy) and (iii) as will be discussed next, the terrace periodicity is not good enough without a Schwoebel barrier. We do not claim that we are able to distinguish between an anisotropic Schwoebel barrier and an anisotropic diffusion: either the barrier is weaker or the hopping rate is larger in the [1 $\bar{1}$ 0] direction. The published results on the hopping rate anisotropy are somehow contradictory [14, 12]. So far we have decided to ignore it. In order to minimize the number of parameters we took $E_b^{(B)} = 0$. With $E_b^{(A)} = 0.175$ eV, it is possible to smooth a 10 ML's deep hole in 20 ML's at 650°C and 0.1 ML/s and to develop mounds at 500°C. Simulation at low temperature (500–550°C) without any Schwoebel barrier followed by 60 s relaxation showed a surface morphology similar to our AFM study of AlAs growth (to simplify the analysis the other parameters remained unchanged).

To study the terrace ordering, our array comprised 5 steps which are bunched together (4 nm apart each other) and separated by a large terrace (24 nm wide) as initial conditions. The error function $f(t) = 1/N\sqrt{\sum_i (L_i - \langle L\rangle)^2}$, where N is the number of steps and L_i the mean distance between two neighbouring steps, gives us a quick quantitative estimation of the ordering ($f(t) = 0$ for a perfectly ordered surface). f(0) is close to 1 in our initial conditions and $f(t)$ should become smaller than $\sigma/\langle L\rangle = 0.24$ to reproduce AFM measurements. Without any Schwoebel barrier this is not possible. With an isotropic barrier, if some island nucleation occurs on the large terrace then the roughness develops further and $f(t)$ increases. But with an

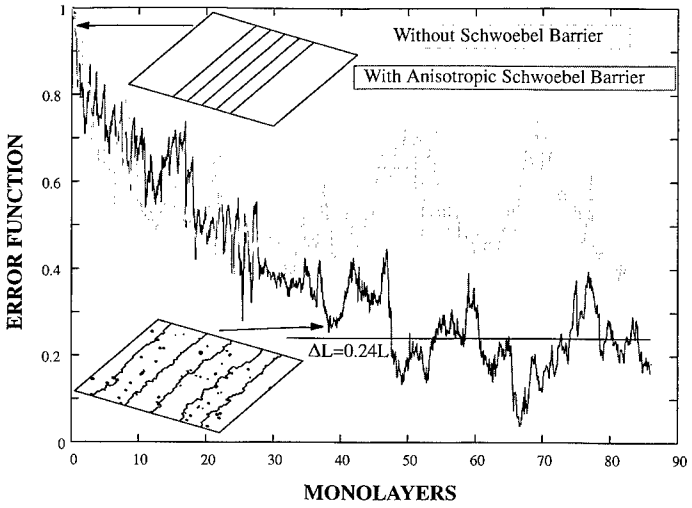

Fig. 5. Time evolution of the error function f(t) (used to have a quick estimation of the terrace ordering) as a function of the number of monolayers for two cases: no Schwoebel barrier and anisotropic Schwoebel barrier. The initial and a typical final surfaces are also shown.

anisotropic barrier, $f(t)$ decreases below the required value in less than 60 ML's as shown in Fig. 5. The time scale is then also correct. The oscillations of $f(t)$ could be reduced if the step interactions were taken in account.

6. Conclusions

Studying by AFM the terrace distribution of misoriented substrates after MBE growth of undoped or doped GaAs and undoped AlAs, we report several new results. Step bunching on GaAs vicinal surfaces can be avoided in the usual growth conditions but can be induced at high Si doping. In optimized conditions the terrace distribution of pure GaAs is sharply peaked around the mean value for a large range of misorientation angle. The results can be well explained quantitatively by equilibrium and dynamical models (Monte Carlo simulation). Lower migration length (AlAs or moderate Si doping) increases the terrace disorder. We give also some evidence that the Schwoebel barrier at step edges is strongly anisotropic in GaAs and negligible in AlAs.

References

[1] B. Etienne, F. Laruelle, J. Bloch, L. Sfaxi and F. Lelarge, J. Crystal Growth 150 (1995) 336.
[2] J. Bloch, U. Bockelmann and F. Laruelle, Europhys. Lett. 501 (1994) 28.
[3] B. Etienne, M. Hayne, F. Petit, F. Lelarge and F. Laruelle, The Physics of Semiconductors, Eds. M. Scheffler and R. Zimmermann (World Scientific, Singapore, 1996) p. 1137.
[4] F .Lelarge, C. Lebreton and Z.Z. Wang, STM '95, Aspen, USA (unpublished).
[5] K. Pond, A. Lorke, J. Ibbetson, V. Bressler-Hill, R. Maboudian, W.H. Weinberg, A.C. Gossard and P.M. Petroff, J. Vac. Sci. Technol. B 12 (1994) 2689.
[6] X.S. Wang, J.L. Goldberg, N.C. Bartelt, T.L. Einstein and E.D. Williams, Phys. Rev. Lett. 65 (1990) 2430.
[7] E.E. Gruber and W.W. Mullins, J. Phys. Chem. Solids 28 (1967) 875.
[8] B. Joos, T.L. Einstein and N.C. Bartelt, Phys. Rev. B 43 (1991) 8153.
[9] C. Orme, M.D. Johnson, K.T. Leung and B.G. Orr, Appl. Phys. Lett. 64 (1993) 860.
[10] V. Thierry-Mieg, F. Laruelle and B. Etienne, J. Crystal Growth 127 (1993) 1022.
[11] D. Vvedensky and S. Clarke, Surf. Sci. 25 (1990) 373.
[12] T. Shitara, D.D. Vvedensky and M.R. Wilby, Phys. Rev. B 46 (1992) 6825.
[13] I. Elkinani and J. Villain, J. Phys. I France 4 (1994) 949.
[14] K. Ohta, T. Koshima and T. Nakagawa, J. Crystal Growth 95 (1989) 71.

ELSEVIER

Journal of Crystal Growth 175/176 (1997) 1108–1113

JOURNAL OF CRYSTAL GROWTH

Photoluminescence investigation of p-type Si-doped AlGaAs grown by molecular beam epitaxy on (1 1 1)A, (2 1 1)A and (3 1 1)A GaAs surfaces

M. Henini[a], N. Galbiati[b], E. Grilli[b], M. Guzzi[b], L. Pavesi[c]

[a] *Department of Physics, University of Nottingham, Nottingham NG7 2RD, UK*
[b] *Istituto Nazionale per la Fisica della Materia, Dipartimento di Fisica, Universita di Trento, Via Sommarive 14, I-38050 Povo, Trento, Italy*
[c] *Istituto Nazionale per la Fisica della Materia, Dipartimento di Fisica, Universita degli Studi, Via Celoria 16, I-20133 Milano, Italy*

Abstract

A systematic study of Si-doped AlGaAs grown on (1 1 1)A, (2 1 1)A, and (3 1 1)A GaAs surfaces by molecular beam epitaxy is reported. Both electrical and photoluminescence measurements have been carried out to investigate the physics of the Si incorporation. The optical identification of the incorporated impurities together with the determination of free carrier concentration and mobility allowed us to suggest a simple kinetic model for the Si incorporation in AlGaAs grown on substrates with different orientations.

1. Introduction

The possibility of exploiting in device manufacturing the amphoteric character of the Si impurity in (Ga,Al)As by simply using different planes has recently attracted great interest. It has been demonstrated that under identical growth conditions Si incorporates preferentially as a donor for growth on (N 1 1)B and as an acceptor on (N 1 1)A surfaces ($N = 1, 2, 3$) [1, 2]. However, Si is mainly a donor when the growth is on the conventional (1 0 0) plane.

This has opened the possibility to realise lateral p-n junction and field-effect transistors [3] on patterned substrates with the use of a single dopant species. Moreover, the study of the molecular beam epitaxy (MBE) growth on substrates with different orientations could provide useful information on the epitaxial growth mechanism and on the physics of dopant incorporation.

Here, we will report on a systematic study of the optical properties of AlGaAs samples grown on (1 1 1)A, (2 1 1)A and (3 1 1)A surfaces with different Si doping levels.

2. Experimental details and samples

The epitaxial layers have been grown on GaAs substrates oriented to within $\pm 0.5°$ for the (2 1 1)A and (3 1 1)A planes and 3° off towards (1 0 0) for the (1 1 1)A surface using a Varian Gen-II MBE system. The growth temperature and rate were 630°C and 1.5 monolayer/s, respectively. The As/(Ga,Al)

0022-0248/97/$17.00 Copyright © 1997 Elsevier Science B.V. All rights reserved
PII S0022-0248(96)00974-8

beam-equivalent pressure ratio determined by an ionisation gauge was ~ 12. After growth the epitaxial surfaces were examined using a Nomarski phase-contrast optical microscope and were found to be mirror smooth and nearly defect free, except for the (1 1 1)A surface which had a milky finish. This bad morphology is expected for the growth on the (1 1 1)A orientation under the above growth conditions. In this study the samples were grown simultaneously adopting the growth parameters which gave optimal electrical properties of (3 1 1)A and (1 0 0) heterostructures [4]. For each substrate orientation a set of samples with four different silicon dopings has been grown: the silicon flux was set in order to give intended free carrier concentrations, N_I, of 1.0×10^{15}, 2×10^{16}, 1.3×10^{17}, and 1.3×10^{18} cm^{-3} in (1 0 0) oriented AlGaAs. These were characterised at 77 K and 300 K using Hall measurements (see Table 1 for details).

The photoluminescence (PL) was excited by the 488 nm line of an Ar^+ laser with an excitation power density (J_{exc}) in the 2×10^{-5} W/cm^2 to 20 W/cm^2 range. The temperature (T) of the samples has been varied between 12 K and 300 K using a cryocooler. The luminescence was analyzed by a single grating monochromator and detected by a photomultiplier tube with a cooled GaAs photocathode followed by a lock-in amplifier.

The sample characteristics and the electrical measurements results are summarized in Table 1. All the samples show a p-type conductivity and the room temperature Hall mobility μ_H does not show a significant dependence on the substrate orientation [5]. In Ref. [5] we reported that carbon was present in high concentration in (2 1 1)A and (311)A samples and not in (1 1 1)A surfaces.

3. Photoluminescence spectra

The energy gap (E_g) and hence the Al mole fraction x (see Table 1) were determined by PL measurements at different values of T and J_{exc}. By comparing the spectral position and the evolution with J_{exc} and T of the various PL bands with the literature [6], we identified the responsible impurities. More data and details are reported in Ref. [7].

In Fig. 1 the spectra at $T = 12$ K of the (3 1 1)A samples are shown. The spectrum of sample e1 ($N_I = 1.0\times10^{15}$ cm^{-3}) is characterized by several overlaping transitions broadened by the alloy

Table 1
Main characteristics of the samples: d = thickness, N_I = intended doping concentration, p_H = Hall hole concentration, μ_H = Hall hole mobility, x = Al mole fraction, E_g = energy gap at $T = 12$ K

Sample	Surface orientation	d (μm)	N_I (cm^{-3})	p_H (cm^{-3})		μ_H ($cm^2/V\cdot s$)		x	E_g (eV)
				300 K	77 K	300 K	77 K		
c1	(1 1 1)A	6	1.0×10^{15}	insulating	insulating	insulating	insulating		
c2		2	2.0×10^{16}	3.0×10^{15}	1.0×10^{14}	143	1136		
c3		2	1.3×10^{17}	8.9×10^{16}	3.9×10^{15}	129	2712		
c4		2	1.3×10^{18}	6.3×10^{17}	1.8×10^{16}	57	896		
d1	(2 1 1)A	6	1.0×10^{15}	5.0×10^{16}	1.3×10^{16}	121	576	0.272	1.922
d2		2	2.0×10^{16}	4.9×10^{16}	3.9×10^{15}	148	2132	0.284	1.939
d3		2	1.3×10^{17}	1.7×10^{17}	3.3×10^{15}	120	2565	0.276	1.928
d4		2	1.3×10^{18}	7.0×10^{17}	2.0×10^{16}	62	480	0.257	1.900
e1	(3 1 1)A	6	1.0×10^{15}	3.4×10^{16}	3.4×10^{15}	100	997	0.278	1.931
e2		2	2.0×10^{16}	2.9×10^{16}	1.3×10^{15}	158	3977	0.291	1.950
e3		2	1.3×10^{17}	1.6×10^{17}	2.8×10^{15}	119	3059	0.286	1.943
e4		2	1.3×10^{18}	4.8×10^{17}	4.3×10^{15}	82	2183	0.282	1.937

disorder: the bound exciton (BE) recombination at 1.919 eV, the free electron to bound hole recombination (e,C) at 1.907 eV and the donor–acceptor pair transition (D,C) at 1.894 eV involving the C acceptor. The same transitions involving Si, namely (e,Si) and (D,Si), are peaked at 1.876 and 1.854 eV, respectively. The spectrum of sample e2 ($N_I = 2.0 \times 10^{16}$ cm^{-3}) consists of a wide band from which at least two structures can be resolved by varying T or J_{exc}: the (e,C) and (e,Si) transitions. In the spectrum of sample e3 ($N_I = 1.3 \times 10^{17}$ cm^{-3}) we only observe the (e,Si) recombination. Finally, the band in the spectrum of sample e4 ($N_I = 1.3 \times 10^{18}$ cm^{-3}) is peaked at the (D,Si) transition. In all the observed donor to acceptor transitions the donor is likely to be Si on the Ga (or Al) site.

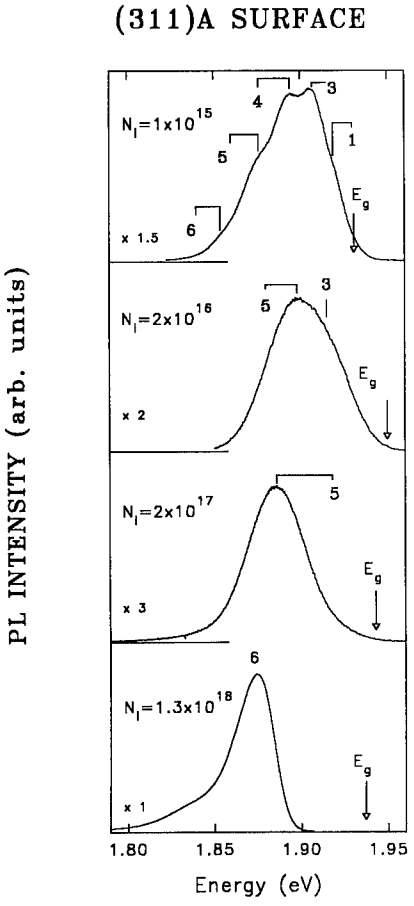

Fig. 1. Photoluminescence spectra of the (3 1 1)A samples at different doping levels measured at 12 K with an excitation power density of 20 W/cm^2. For each sample the intended doping N_I (in cm^{-3}) is given. The relative sensitivity factor is given on the left and the energy gap (E_g) values are indicated by the hollow arrows. The numbers on the spectra stand for the following processes: (1) bound exciton recombination; (3) free electron to carbon acceptor transition; (4) donor to carbon acceptor pair transition; (5) free electron to silicon acceptor transition; (6) donor to silicon acceptor pair transition.

The low temperature spectra of the (2 1 1)A samples are shown in Fig. 2. The spectra of d1 ($N_I = 1.0 \times 10^{15}$ cm^{-3}) and d2 ($N_I = 2.0 \times 10^{16}$ cm^{-3}) samples consist of a single narrow band, peaked at an energy lower than that of the BE, which shifts to higher energies by increasing J_{exc}. Thus the narrow peak in the spectra of samples d1 and d2 could be attributed to the overlap of the BE and the defect bound excitons (d,X) recombinations. The variation of the relative intensity of the two transitions with J_{exc} may be responsible for the energy shift. The (d,X) transitions have been tentatively associated with complexes consisting of impurities and intrinsic defects, such as vacancies and interstitials [8]. In the spectrum of sample d3 ($N_I = 1.3 \times 10^{17}$ cm^{-3}) the main peak has the same attribution as that of the samples d1 and d2 and the presence of Si acceptors is revealed by a weak (D,Si) emission band at 1.866 eV. Decreasing J_{exc}, the main peak shifts to 1.899 eV corresponding to the (e,C) recombination and the (D,Si) band intensity rises. The spectrum of sample d4 ($N_I = 1.3 \times 10^{18}$ cm^{-3}) is characterized by an asymmetric band with a long low energy tail. Increasing T the peak energy follows the thermal energy gap shift as given by the Varshni equation [9]. This suggests that free hole with free electron recombinations (BB) are responsible for this emission. Moreover, some weak low energy structures which could be attributed to (d,X) and C acceptor related transitions, can be resolved with increasing T.

The PL spectra of the (1 1 1)A samples shown in Fig. 3 consist either of a single peak at an energy much lower than that of the C or Si related emissions (samples c1 and c3) or of a wide band (samples c2 and c4). We argue that these PL spectra are attributed to the low sample quality due to the growth conditions used, which are not the optimal for the (1 1 1)A oriented substrates [2].

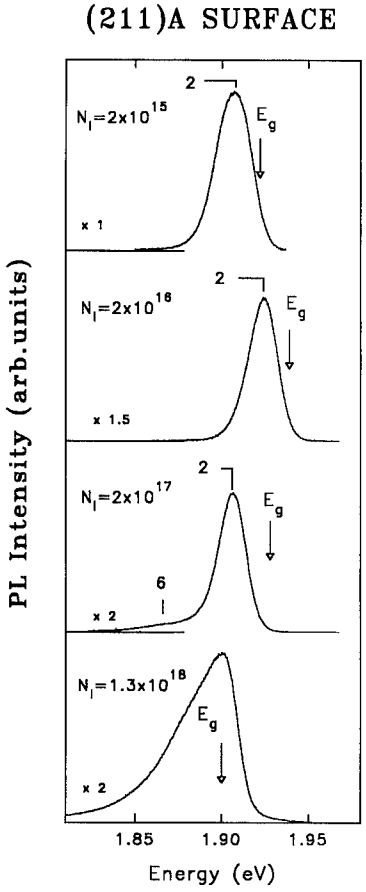

Fig. 2. Photoluminescence spectra of the (2 1 1)A samples at different doping levels measured at 12 K with an excitation power density of 20 W/cm^2. For each sample the intended doping N_I (in cm^{-3}) is given. The relative sensitivity factor is given on the left and the energy gap (E_g) values are indicated by the hollow arrows. The numbers on the spectra stand for the following processes: (2) superposition of bound exciton and defect bound exciton recombinations; (6) donor to silicon acceptor pair transition.

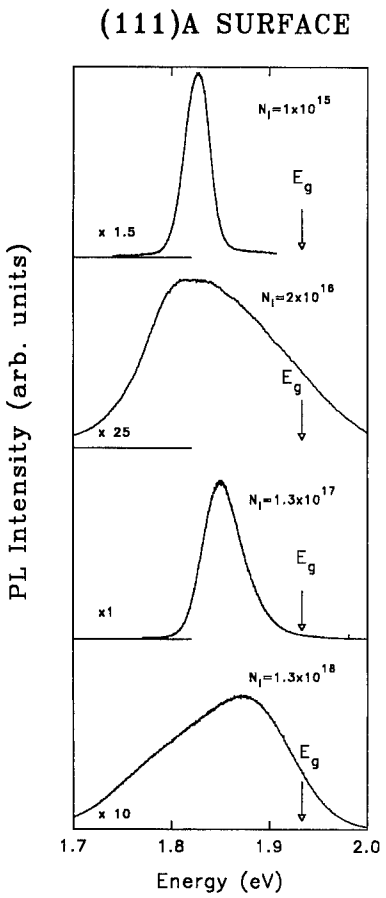

Fig. 3. Photoluminescence spectra of the (1 1 1)A samples at different doping levels measured at 12 K with an excitation power density of 20 W/cm^2. For each sample the intended doping N_I (in cm^{-3}) is given. The relative sensitivity factor is given on the left and the energy gap (E_g) values are indicated by the hollow arrows.

4. Discussion

Since the samples were grown simultaneously, it is not possible to make a direct comparison between our PL data and those published in the literature. The latter in fact generally refer to samples grown using conditions optimized for a given substrate orientation.

We found that the morphological and optical quality continuously improve by changing the substrate orientation from (1 1 1)A, to (2 1 1)A and to (3 1 1)A. However, in spite of the differences in the PL lineshapes at $T = 12$ K, the luminescence efficiency, taken as the integral of the luminescence spectrum at $T = 300$ K, is comparable for all the samples and increases with increasing p_H. The nearly equal luminescence intensities are reflected in the mobility values of all the samples which compare reasonably well with each other. On the other hand, the low temperature PL spectra are rather different. This is not surprising. In fact, small

concentrations of efficient radiative channels can dominate the optical properties without affecting the electrical ones.

A clear dependence of the acceptor incorporation in the samples on the substrate orientation has been found. The (1 1 1)A samples show a relevant Si incorporation on As sites without evidence of other unwanted acceptors. In fact, the free carrier concentration increases markedly with increasing N_I. These conclusions cannot be supported by the PL data because the spectra are dominated by unresolved bands and deep transitions.

The acceptor incorporation in (3 1 1)A samples is different. Firstly, the electrical measurements of the samples with low N_I reveal the presence of a residual acceptor impurity. From PL this impurity can be identified as carbon. Secondly, the PL spectra show that the (D,Si) transitions become more and more evident by increasing N_I revealing the presence of Si self-compensation.

The electrical data of the (2 1 1)A samples have a similar trend as those of the (3 1 1)A ones but the PL spectra show a more relevant defectiveness of the former as revealed by the presence of the (d,X) recombination.

The phenomenology of the incorporation of silicon on III or V sites in AlGaAs has been described in a previous work [2]. However the physics of such incorporation is still a matter of debate. To our knowledge, no detailed theoretical work is present in the literature. Only a phenomenological model, which has been applied in different cases [3, 10], has been developed to explain the amphoteric behaviour of group IV impurities in GaAs grown on high index surfaces [11, 12]. This model does not take into account the surface reconstruction. However, it works quite well and we use it for the discussion of our data. The main point of the model is that, among the different (N 1 1)A surfaces, the efficiency of the Si incorporation on the As site varies due to the specific bonding geometry of each of the surfaces, in particular to the different single to double dangling bonds ratio. For surfaces with a higher density of double dangling bonds, As predominates in the competition with the Si for the group V site occupation. For instance, the (1 1 1)A plane presents on the Al/Ga rich surface only single dangling bonds for the As incorporation. Hence a good incorporation efficiency of Si in As site is expected. Also a lower quality of the grown epilayers follows [13].

In terms of single to double dangling bonds ratio, the (1 0 0) and the (1 1 1)A surfaces present the two extreme situations (Fig. 4). Going from the (1 1 1)A to the (1 0 0) surface one passes through the (2 1 1)A and the (3 1 1)A ones, which have a periodic step structure with As step edge atoms and Al/Ga terrace atoms. This structure can be viewed as a sequence of (1 0 0)-like surfaces with double dangling bonds and (1 1 1)A-like surfaces with single dangling bonds. Let us consider, for example, the growth on the (2 1 1)A plane (Fig. 4). A newly chemisorbed Al/Ga atom in position (2) together with the preexisting Al/Ga atom in position (1) makes two dangling bonds available for the incorporation of an As atom in position (3). In proximity of these sites the As_4 molecule easily decomposes [11] and the As incorporation is favoured with respect to the Si one.

The observed differences in the Si incorporation between the (2 1 1)A and the (3 1 1)A grown samples are explained by the extent of the (1 1 1)A-like terraces which increases from the (3 1 1)A

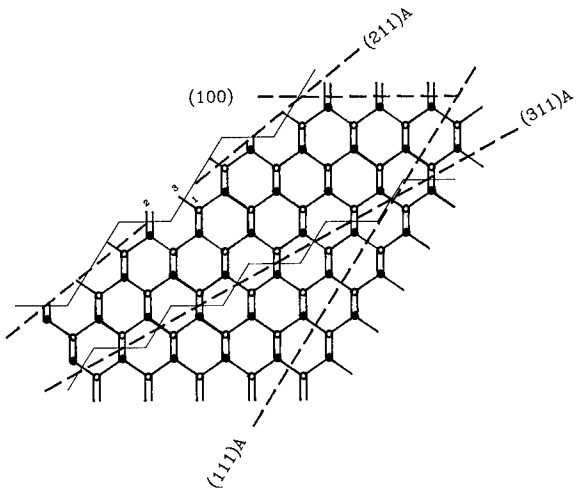

Fig. 4. Atomic arrangement projected on the (1 1 0) plane of the ideal (1 0 0), (1 1 1)A, (2 1 1)A and (3 1 1)A surfaces for the zinc blende crystal structure showing the single and double dangling bonds sites. Full dots and open dots are the group V atoms and the group III atoms, respectively. During the growth, a newly chemisorbed Al/Ga atom in position (2) together with the preexisting Al/Ga atom in position (1) makes two dangling bonds available for the incorporation of an As atom in position (3).

surface to the (2 1 1)A one. Hence, passing from (1 1 1)A to (2 1 1)A and finally to (3 1 1)A surfaces the Si incorporation in As sites is less and less favoured by the increasing As competition and the Al/Ga sites occupation by Si is more and more probable.

It is tempting to apply this simple model also to the incorporation of C. It is well known that C incorporates quite easily in the MBE growth of (1 0 0) layers while we have found that in the (1 1 1)A layers it does not. Thus it is expected that the C incorporation is favoured in presence of (1 0 0)-like steps. This is confirmed by the PL data giving a clear evidence of C in the (3 1 1)A samples while no strong evidence of C presence is found in the spectra of the (2 1 1)A samples.

5. Conclusions

We have observed that the (1 1 1)A surfaces incorporate less carbon than the (2 1 1)A and the (3 1 1)A ones, which need a higher silicon flux before the presence of Si clearly manifests itself in the electrical and optical measurements. We have found a lower optical and morphological quality in the (1 1 1)A samples; however this does not affect markedly the values of the Hall mobility, free carrier concentration and PL efficiency.

Our results can be explained using a simple model in which the single to double dangling bond ratio characterizing the different planes mainly determines the impurities incorporation.

Acknowledgements

M.H. wishes to acknowledge the UK EPSRC. L.P. thanks the Consorzio CRSC for a scholarship. L.P. has been supported by GaAsNet of CNR. Finally the authors would like to thank the NATO for funds enabling the collaboration.

References

[1] W.I. Wang, E.E. Mendez, T.S. Kuan and L. Esaki, Appl. Phys. Lett. 47 (1985) 826.
[2] L. Pavesi, M. Henini, D. Johnston and I. Harrison, Semicond. Sci. Technol. 10 (1995) 49.
[3] W.Q. Li, P.K. Bhattacharya, S.H. Kwok and R. Merlin, J. Appl. Phys. 72 (1992) 3129.
[4] M. Henini, P.J. Rodgers, P.A. Crump, B.L. Gallagher and G. Hill, Appl. Phys. Lett. 65 (1994) 2054.
[5] N. Galbiati, E. Grilli, M. Guzzi, L. Brusaferri, L. Pavesi and M. Henini, Semicond. Sci. Technol., to be published.
[6] L. Pavesi and M. Guzzi, J. Appl. Phys. 75 (1994) 4779.
[7] N. Galbiati, Undergraduate Thesis, Milan University (1994).
[8] M. Mihara, Y. Nomura, M. Mannoh, K. Yamanaka, S. Naritsuka, K. Shinozaki, T. Yuasa and M. Ishii, J. Appl. Phys. 55 (1984) 3765.
[9] Y.P. Varshni, Physica 34 (1967) 149.
[10] S.S. Bose, B. Lee, M.H. Kim, G.E. Stillman and W.I. Wang, J. Appl. Phys. 63 (1988) 743.
[11] S. Subbanna, H. Kroemer and J.L. Merz, J. Appl. Phys. 59 (1986) 488.
[12] B. Lee, S.S. Bose, M.H. Kim, A.D. Reed, G.E. Stillman, W.I. Wang, L. Vina and P.C. Colter, J. Crystal Growth 96 (1989) 27.
[13] M.R. Fahy, K. Sato and B.A. Joyce, Appl. Phys. Lett. 64 (1994) 190.

ELSEVIER

Journal of Crystal Growth 175/176 (1997) 1114–1119

JOURNAL OF CRYSTAL GROWTH

Patterned growth on GaAs (3 1 1)A substrates

Richard Nötzel*, Johann Menniger, Manfred Ramsteiner, Achim Trampert, Hans-Peter Schönherr, Lutz Däweritz, Klaus H. Ploog

Paul-Drude-Institut für Festkörperelektronik, Hausvogteiplatz 5-7, D-10117 Berlin, Germany

Abstract

We report on a new type in the selectivity of growth found during MBE of (AlGa)As on patterned GaAs (3 1 1)A substrates. For mesa stripes oriented along the [0 1 −1] direction a smooth convex curved surface profile develops on one side enclosing thicker regions of GaAs along the sidewall between thinner regions on the mesa top and bottom. Cross-sectional TEM directly images the evolution of this unique profile to rely on the preferential migration of Ga atoms from both sides toward the sidewall (opposite to the case of patterned GaAs (1 0 0) or (1 1 1) substrates), via size reduction of a fast growing side facet close to the next (1 0 0) plane. On the opposite side, a rough slow growing (1 1 1)A side facet is established. Mesa stripes oriented along [−2 3 3] exhibit two slow growing side facets without roughening of the growth front. The surface morphology of the different sidewalls is related to the anisotropy of the surface diffusion length of Ga adatoms along [−2 3 3] and [0 1 −1] determined by AFM linescans from the variation of the GaAs layer thickness close to the edges of shallow square shaped mesas. As confirmed by TEM and CL spectroscopy, the uniformity and the selectivity of the growth mode across the fast growing sidewall is not reduced for step heights in the nanometer range allowing the formation of quasi-planar sidewall quantum-wire arrays.

1. Introduction

We study the selectivity of growth during molecular beam epitaxy (MBE) of (AlGa)As on patterned GaAs (3 1 1)A substrates. As expected from the unique growth modes in MBE and metal-organic vapor phase epitaxy (MOVPE) on planar GaAs(3 1 1)A & B substrates to naturally produce ordered arrays of nanometer-scale quantum structures [1, 2], the selectivity of growth on patterned GaAs (3 1 1)A substrates is qualitatively different from that on patterned low-index GaAs (1 0 0) and (1 1 1) substrates [3, 4]. This offers a new flexibility for the design of devices and quantum structures. During MBE of (AlGa)As on patterned GaAs (3 1 1)A substrates we have found the formation of a fast growing sidewall on one side of mesa stripes oriented along the [0 1 −1] direction [5]. Preferential migration of Ga adatoms from the mesa top and bottom toward the sidewall develops a smooth convex curved surface profile without faceting. This unique growth mode that does not occur for the perpendicular stripe orientation nor on other

* Corresponding author. Fax: + 49 30 20377 201; e-mail: notzel@pdi.wias-berlin.de.

0022-0248/97/$17.00 Copyright © 1997 Elsevier Science B.V. All rights reserved
PII S0022-0248(96)00862-7

patterned GaAs (n 1 1)A&B substrates [6] remains stable for step heights down to the quantum-size regime to produce lateral quasi-planar quantum wires on patterned GaAs (3 1 1)A substrates. The wires exhibit high structural perfection and uniformity, narrow emission lines in photoluminescence (PL) spectroscopy and high PL efficiency up to room temperature [7]. Quantum confinement of excitons in the wires has been demonstrated by the changeover from one-dimensional confinement to magnetic confinement with increasing magnetic field [6]. The PL energy position of the wires critically depends on the initial step height providing an additional parameter to control the size of the wires that has no correspondence in V-groove- or ridge-type structures. Finally, it has been shown that, for a given step height, the wires can be stacked in growth direction without any increase in interface roughness or wire size fluctuations indicating a self-limiting lateral growth mechanism [6].

In this paper we present an atomic force microscopy (AFM) study of the surface profiles across the edges of mesa stripes along [0 1 −1] and [−2 3 3] on patterned GaAs (3 1 1)A substrates after overgrowth. The surface morphology of the convex curved fast growing sidewall is as smooth as that of the flat parts of the mesa. On the other hand, the slow growing (1 1 1) side facet on the opposite side shows pronounced roughening of the growth front. The evolution of the fast growing sidewall is investigated by cross-sectional transmission electron microscopy (TEM). The convex curved surface profile is found to develop via size reduction of a fast growing side facet close to the next (1 0 0) plane. For the perpendicular mesa stripes along [−2 3 3] two symmetrically arranged slow growing side facets close to {3 3 1} planes develop on both sides. Besides macroscopic defects on one side no roughening of the growth front occurs. The surface diffusion lengths of Ga adatoms along the two perpendicular [−2 3 3] and [0 1 −1] azimuths are deduced from the variation of the GaAs layer thickness close to the edges of shallow square shaped mesas. The anisotropy of the diffusion

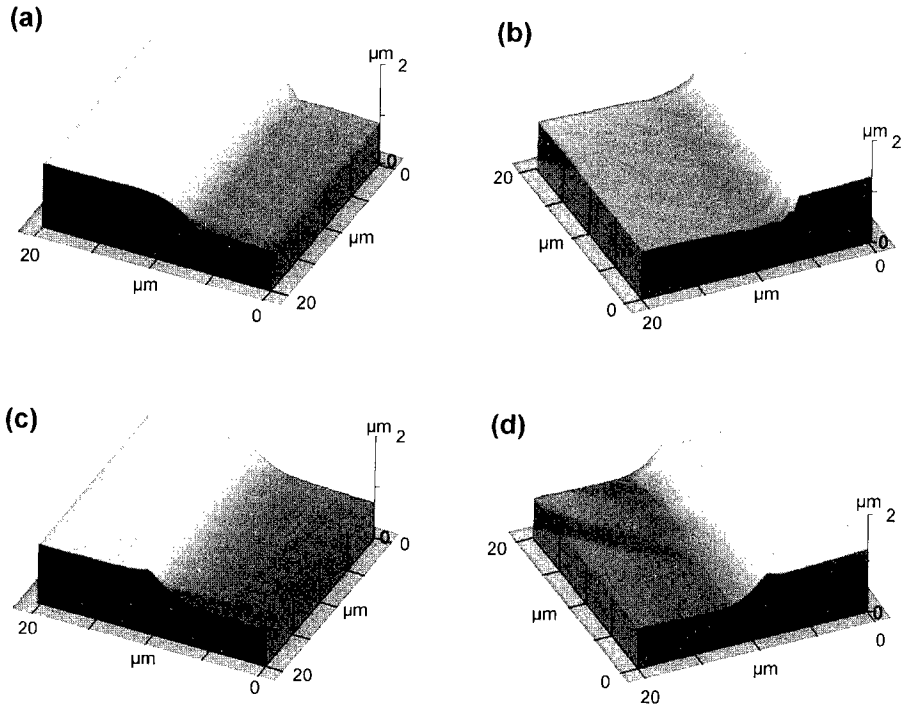

Fig. 1. AFM images of the edges of the 400 nm high mesa stripes after overgrowth. (a) Fast growing sidewall and (b) slow growing sidewall along [0 1 −1]. (c), (d) AFM images of both sidewalls along [−2 3 3].

length is brought in connection with the surface morphology of the slow and fast growing sidewalls of the mesa stripes. For step heights in the quantum-size regime an array of sidewall quantum wires with 4 μm pitch is fabricated and characterized by cathodoluminescence (CL) spectroscopy.

2. Sample preparation and experimental setup

The GaAs (3 1 1)A substrates were patterned by optical lithography and wet chemical etching using the $H_2SO_4 : H_2O_2 : H_2O$ (1 : 8 : 40) preferential chemical etching solution. The mesa stripes were oriented along the two perpendicular [0 1 −1] and [−2 3 3] directions. After cleaning in concentrated H_2SO_4 and rinsing in deionized water the samples were introduced into the MBE growth chamber. The GaAs/$Al_{0.5}Ga_{0.5}As$ multilayer structures (see below) were grown at 620°C while the substrates were rotated with 6 rpm. The growth rates for GaAs and $Al_{0.5}Ga_{0.5}As$ were 0.5 and 1 μm/h, and the group-V-to-III-flux ratio was about 5. The structural and optical properties of the samples were investigated by AFM, TEM, and CL spectroscopy.

3. Results and discussion

Fig. 1a–Fig. 1d show three-dimensional AFM images of the sidewalls of 80 μm wide and 400 nm high mesa stripes along [0 1 −1] Fig. 1a, Fig. 1b, and along [−2 3 3] Fig. 1c, Fig. 1d after overgrowth. The layer sequence comprises 5 periods 100 nm $Al_{0.5}Ga_{0.5}As$/100 nm GaAs. In the center of the fourth (AlGa)As layer a 8 nm thick GaAs layer is inserted. The AFM image in Fig. 1a shows the surface profile of the convex curved fast growing sidewall of the mesa stripe along [0 1 −1] that develops in the sector toward the next (1 0 0) plane. As confirmed by scanning electron microscopy (SEM) [5] the surface is not roughened compared to the flat parts of the mesa. The surface profile in

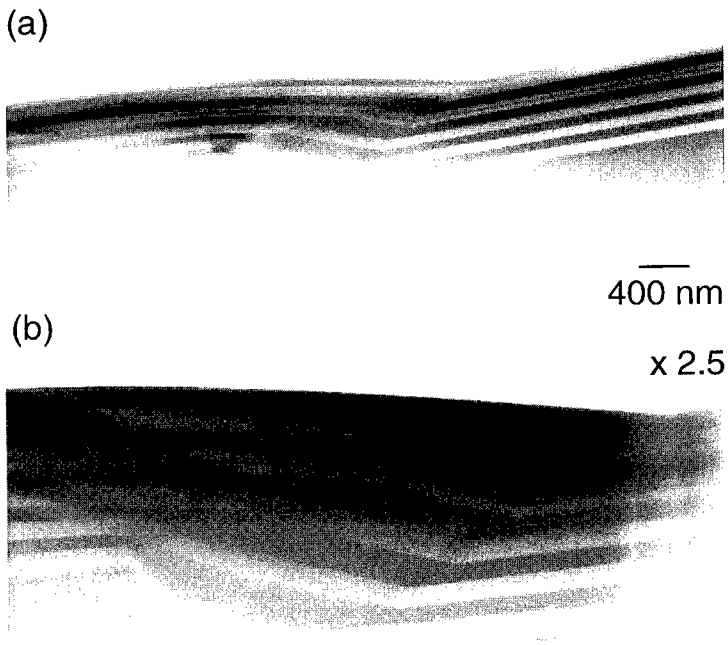

Fig. 2. (a) Cross-sectional TEM image viewed along [0 1 −1] of the fast growing sidewall of the mesa stripe along [0 1 −1]. In (b) the scale is enhanced.

Fig. 1b of the opposite side in the sector toward the next (1 1 1) plane shows the evolution of a rough slow growing (1 1 1) side facet with the characteristic concave curved bottom corner. Smooth slow growing side facets are formed at the sidewalls of the mesa stripes along [−2 3 3] (Fig. 1c and Fig. 1d).

The evolution of the fast growing sidewall is investigated by cross-sectional TEM shown in Fig. 2a and Fig. 2b. At the sidewall, first a fast growing side facet close to the next (1 0 0) plane is developed which reduces in size during growth of GaAs to end up with the convex curved surface profile with a stable bottom step corner. The adjacent areas in the top and bottom areas of the mesa exhibit a reduced layer thickness due to migration of Ga adatoms toward the sidewall as has been confirmed by spatially resolved CL from the quantum-well layer [5]. For (AlGa)As almost no variation of the layer thickness and contrast across the step is observed due to the small surface diffusion length of Al suggesting an almost uniform Al composition.

Lateral growth can be obtained also in MOVPE and metalorganic MBE, in particular, on patterned GaAs (1 1 1)A&B substrates [8, 9] due to the dependence of the chemical reactivity of the precursors on different crystallographic planes and growth conditions. The shape of the side facets, however, that is determined by the migration of adatoms, has a concave curved surface profile at the bottom corner of the mesas similar to that of slow growing side facets. Hence, also in these cases the surface diffusion of adatoms is away from the side facets highlighting the unique growth mode on patterned GaAs (3 1 1)A substrates.

Shallow mesas, 30 nm high, have been prepared to determine the surface diffusion lengths $L_{[-2\,3\,3]}$ and $L_{[0\,1\,-1]}$ of Ga adatoms along the perpendicular [−2 3 3] and [0 1 −1] directions. As the mesa height is more than one order of magnitude smaller than usual surface diffusion

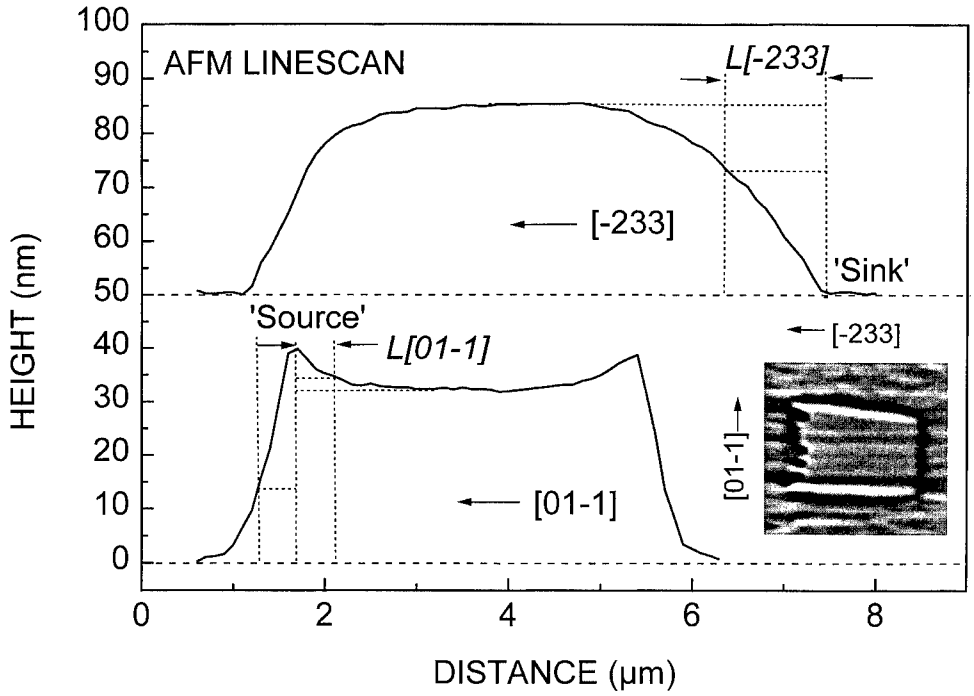

Fig. 3. AFM linescans along [−2 3 3] and [0 1 −1] across shallow square shaped mesas after overgrowth. The arrows mark the diffusion lengths determined from the exponential variation of the layer thickness close to the edges of the mesa. The inset shows the AFM top view of the mesa.

lengths, the shape of the sidewalls is essentially determined by the diffusion length that can then be measured from the exponential variation of the layer thickness, i.e., the growth rate close to the edges of the mesa in analogy to the experiments using μ-RHEED [10, 11]. Fig. 3 shows the AFM linescans along $[-2\,3\,3]$ and $[0\,1-1]$ across the mesa depicted in the inset. The thickness of the GaAs layer grown over the mesa is 70 nm. From the exponential variation of the layer thickness in the linescan along $[-2\,3\,3]$ close to the bottom corner of the convex curved surface profile acting as a sink for Ga atoms, $L_{[-2\,3\,3]}$ amounts to 1–1.5 μm. The linescan along $[0\,1\,-1]$ close to the top of the mesa acting as a source of Ga atoms gives $L_{[0\,1-1]}$ to be 0.3–0.5 μm. The anisotropy of the diffusion length suggests a relationship with the surface morphology of the sidewalls. Smooth surface profiles are obtained for either a slow growing side facet together with the larger diffusion length parallel to the step or a fast growing sidewall with the larger diffusion length perpendicular to the step. A slow growing sidewall with the larger diffusion length perpendicular to the step produces a rough surface morphology. This finding is essential for choosing the optimum pattern alignment on arbitrarily oriented substrates. The anisotropy of the diffusion length, however, is comparable to that on (1 0 0) surfaces [10, 11]. Hence, on patterned GaAs (3 1 1)A substrates the highly anisotropic microscopic surface corrugation along $[-2\,3\,3]$ [1] is assumed to stabilize the respective growth fronts additionally.

The preservation of the convex curved surface profile for step heights in the quantum-size regime with a stable bottom step corner allows the formation of lateral quantum wires along the single fast growing sidewall [7]. In order to increase the in-plane density of the wires, an array of mesa stripes 20 nm high and 2 μm wide with spacings of 2 μm is prepared. The mesa structure is overgrown by a 50 nm thick GaAs buffer layer followed by a 6 nm thick GaAs layer sandwiched between 50 nm thick lower and upper $Al_{0.5}Ga_{0.5}As$ barrier layers capped with 20 nm GaAs. For this layer sequence the height and width of the lateral quantum wire have been determined by TEM to about 12 and 50 nm, respectively [7]. A lateral potential barrier of the

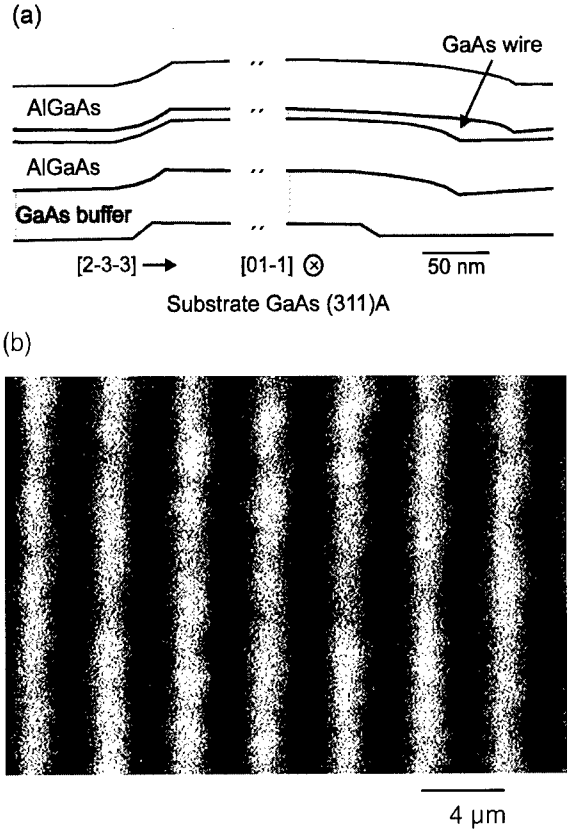

Fig. 4. (a) Schematic of the growth mode on shallow mesa stripes along $[0\,1\,-1]$ to form lateral quantum wires at the fast growing sidewall. (b) Filtered CL intensity mapping detected at the wire peak position at 1.540 eV of the array of sidewall quantum wires with 4 μm pitch.

wire around 60 meV has been estimated from the red shift of the PL from the wire compared to that of the adjacent wells. Fig. 4a presents a schematic of the quantum wire formation deduced from TEM. The high uniformity of the wire array over a large area is demonstrated by the filtered CL intensity mapping detected at the wire peak position at 1.540 eV shown in Fig. 4b.

4. Conclusion

We have investigated the MBE growth of (AlGa)As on patterned GaAs (3 1 1)A substrates. On one side of mesa stripes along $[0\,1-1]$ a fast growing sidewall with a smooth convex curved

surface profile is developed. On the opposite side a slow growing (1 1 1) side facet with pronounced roughness is formed. Smooth slow growing surface profiles are formed at the sidewalls of the mesa stripes along [−2 3 3]. Cross-sectional TEM has shown the convex curved surface profile to evolve during size reduction of a fast growing side facet close to the next (1 0 0) plane due to preferential migration of Ga adatoms from both sides toward the sidewall. The surface diffusion lengths of Ga adatoms along [−2 3 3] and [0 1 −1] have been determined from AFM linescans and related to the surface morphology of the sidewalls. For step heights in the quantum-size regime an array with 4 μm pitch of lateral quantum wires along the fast growing sidewalls has been fabricated that exhibits high uniformity over a large surface area.

Acknowledgements

The work was supported in part by the Bundesministerium für Bildung, Wissenschaft, Forschung und Technologie.

References

[1] R. Nötzel, N. Ledentsov, L. Däweritz, M. Hohenstein and K. Ploog, Phys. Rev. Lett. 67 (1991) 3812.
[2] R. Nötzel, J. Temmyo and T. Tamamura, Nature 369 (1994) 131.
[3] E. Kapon, M.C. Tamargo and D.M. Hwang, Appl. Phys. Lett. 50 (1987) 347.
[4] T. Takebe, M. Fujii, T. Yamamoto, K. Fujta and K. Kobayashi, J. Crystal Growth 127 (1993) 937.
[5] R. Nötzel, J. Menniger, M. Ramsteiner, A. Ruiz, H.P. Schönherr and K.H. Ploog, Appl. Phys. Lett. 68 (1996) 1132.
[6] R. Nötzel, M. Ramsteiner, J. Menniger, A. Trampert, H.P. Schönherr, L. Däweritz and K.H. Ploog, J. Appl. Phys. 80 (1996) 4108.
[7] R. Nötzel, M. Ramsteiner, J. Menniger, A. Trampert, H.P. Schönherr, L. Däweritz and K.H. Ploog, Jpn. J. Appl. Phys. 35 (1996) L297.
[8] S.H. Jones, L.K. Seidel, K.M. Lau and M. Harold, J. Crystal Growth 108 (1991) 73.
[9] Y. Nomura, Y. Morishita, S. Goto, Y. Katayama and T. Isu, Jpn. J. Appl. Phys. 30 (1991) 3771.
[10] M. Hata, T. Isu, A. Watanabe and Y. Katayama, J. Vac. Sci. Technol. B 8 (1990) 692.
[11] X.Q. Shen and T. Nishinaga, Jpn. J. Appl. Phys. 32 (1993) L1117.

ELSEVIER

Journal of Crystal Growth 175/176 (1997) 1120–1125

JOURNAL OF CRYSTAL GROWTH

Strain-balanced AlGaInAs/InP heterostructures with up to 50 QWs by MBE

H. Hillmer*, R. Lösch, W. Schlapp

Deutsche Telekom, Technologiezentrum, P.O. Box 100003, D-64276 Darmstadt, Germany

Abstract

Using solid-source MBE, strain-balanced quaternary AlGaInAs/AlGaInAs multiple quantum well (MQW) strucures have been grown and studied by photoluminescence (PL) and X-ray diffraction (XRD) measurements, showing high epitaxial quality and excellent homogeneity in growth direction. The PL linewidths are low and almost independent of the number of QWs ($1 \leqslant N_{QW} \leqslant 50$). With respect to photonic device applications at 1.55 μm, structures with quaternary QWs seem to be superior compared to structures with ternary QWs: structures with quaternary QWs enable more degrees of freedom in device design and reveal a five times larger lateral wafer area in which the PL wavelength is constant.

PACS: 68.55.Bd; 73.20.Dx; 78.65.F; 42.60.By

From the epitaxial point of view and for applications in advanced optoelectronic and electronic devices, strain-balanced QWs are very attractive. For the Bragg reflectors of surface emitting lasers, e.g., high-quality multiple heterostructures with a large refractive index contrast and a large number of periods are required. Strain-balanced structures allow numerous periods, although highly strained layers are involved [1–5]. Furthermore, for the active layers of lasers, multiple QW structures are desirable, allowing as many degrees of freedom as possible in selecting compositions, well widths and number of wells. E.g., in order to obtain ultra-high modulation bandwidths, a sufficiently high number of wells is required in order to guarantee high differential gain. In recent years, QW structures including quaternary material in both wells and barriers have been grown and studied several times using the rather well known GaInAsP/GaInAsP/InP material system (see, for example, Refs. [4–9]). In contrast, AlGaInAs/AlGaInAs/InP heterostructures have been grown, investigated and applied only occasionally [10–14].

Using a Modular GEN II solid source MBE, we have grown AlGaInAs/AlGaInAs MQW structures on semi-insulating, n- and p-doped (1 0 0)-oriented InP-substrates. We used two In-furnaces and one furnace, respectively, for the Al, Ga and As source

* Corresponding author. Fax: + 49 6151 83 4912; e-mail: hillmer@fz.telekom.de.

0022-0248/97/$17.00 Copyright © 1997 Elsevier Science B.V. All rights reserved
PII S0022-0248(96)00825-I

materials at 510°C substrate temperature. In the structures studied here, no growth interruptions were applied at the QW heterostructure interfaces. During the growth of the MQW structure the Al-flux and the Ga-flux are kept constant. The variation of the well and barrier compositions is realized by changing the In-fluxes (switching between the In-I and In-II furnace) at the interfaces, respectively. Combining XRD studies, low temperature PL measurements and corresponding simulations, respectively, we determined the well widths, barrier widths and compositions of all layers involved, using also results from wafers with isolated bulk layers grown under nominally identical conditions. To obtain strain-balanced structures, this procedure was used to adjust the geometric and compositional parameters such as the In-content in the wells and barriers (lattice mismatch) as well as the Al-content in the wells and barriers. The number of QWs is defined by the number of reproductions of a unit cell in growth direction. The unit cell consists of an $Al_{0.093}Ga_{0.197}In_{0.71}As$ well (width L_z) embedded by two $Al_{0.208}Ga_{0.445}In_{0.347}As$ barriers of thickness $L_B/2$. This enables a strain-balancing of the compressively strained well ($\Delta a/a \sim +1.2\%$) by two symmetrically positioned tensile strained barrier parts ($\Delta a/a \sim -1.4\%$) of widths $L_B/2$. A strain-compensation can also be obtained where the product of barrier lattice mismatch and the barrier width L_B is about the well lattice mismatch times L_z. Finally, there are lattice-matched $Al_{0.227}Ga_{0.243}In_{0.53}As$ layers ($\lambda_{PL} \sim 1.21$ μm) cladding the two bordering barrier layers asymmetrically on both sides. The inset of Fig. 3 schematically displays the variation of the conduction band edge of our samples. In Ref. [12] we have studied several single QW samples having the same compositions and identical ratio of L_z/L_B, but different well widths. These samples show a variation of the PL linewidths as a function of well width which can be attributed to the changing influence of interface roughness and alloy disorder broadening mechanisms.

To investigate the stability of the strain-balanced MQW structures, samples containing different numbers of wells ($1 \leqslant N_{QW} \leqslant 50$) were grown. Fig. 1 depicts a scanning electron microscope (SEM) image of a cleaved strain-balanced MQW structure, containing 50 compressively strained quaternary wells (light stripes), 49 tensile strained barriers of width L_B (dark stripes) and 2 barriers of the same composition but half the width L_B (thin dark stripes, first and last of the stack). The geometrical parameters (L_B, L_z) and compositional parameters (In-content, Al-content, ...) are intended for a laser structure emitting at 1.55 μm.

The corresponding PL spectrum is displayed in Fig. 2. We measured a PL linewidth of 9.3 meV at 10 K which can quantitatively be attributed to broadening mechanisms involving interface

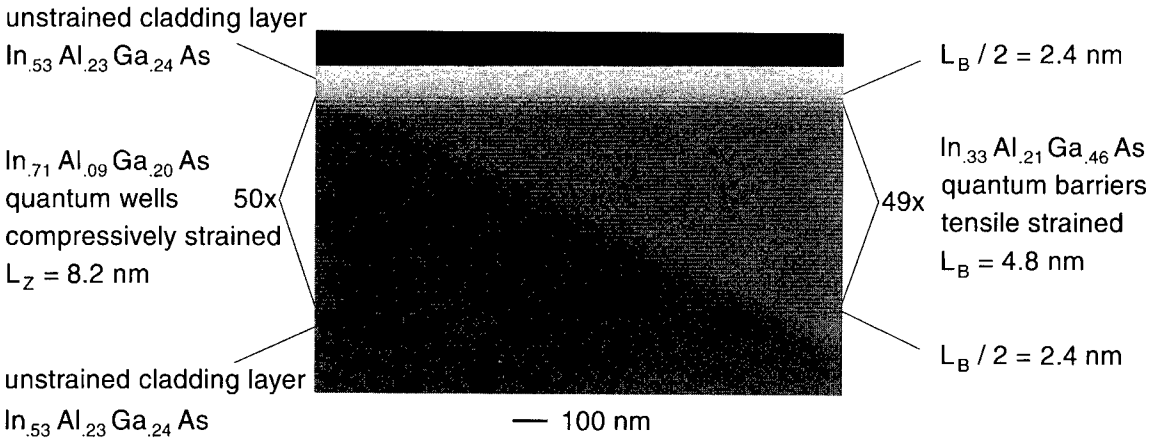

Fig. 1. SEM micrograph of a cleaved strain-balanced heterostructure including 50 QWs.

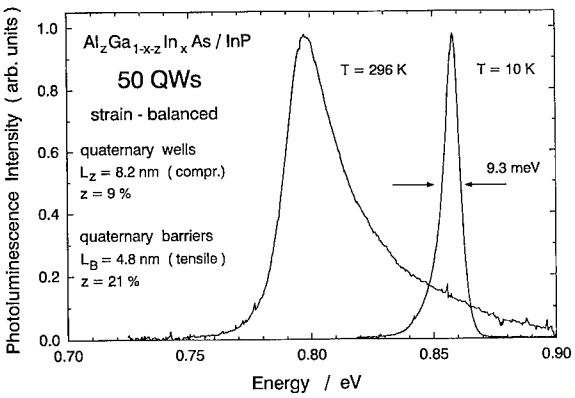

Fig. 2. Experimental photoluminescence (PL) spectra of the structure shown in Fig. 1 at 10 K and 300 K.

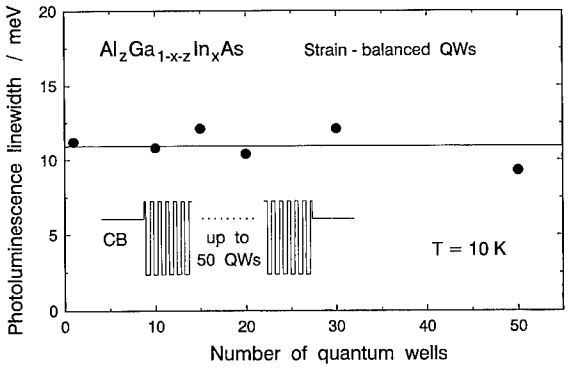

Fig. 3. Linewidth of PL spectra at 10 K as a function of the number N_{QW} of QWs. The variation of the conduction band edge is schematically shown in the inset.

roughness and alloy disorder. This low value indicates that the variations in both compositional and geometrical parameters from well to well are very low. The emission at room temperature is thermally broadened and shifted to longer wavelengths according to the temperature dependence of the fundamental band gaps of the individual layers.

Fig. 3 depicts the experimental PL linewidth at 10 K as a function of N_{QW}. The layer widths of these structures are $L_z = 7.2$ nm and $L_B = 5.8$ nm (for $N_{QW} = 1, 10, 15, 20$) as well as $L_z = 8.2$ nm and $L_B = 4.8$ nm (for $N_{QW} = 30$ and 50). We observe no dependence of the PL linewidth on the number of QWs for $N_{QW} \leqslant 30$, except for statistical fluctuations. It is interesting to observe that the lowest linewidth is measured for $N_{QW} = 50$, which might originate from a smaller influence of interface roughnesses, since the well width is slightly higher than in the structures with $1 \leqslant N_{QW} \leqslant 20$. However, we suppose another physical reason for this low PL linewidth as explained below. For the barrier widths considered here tunneling processes through the potential barriers play a minor role. However, reducing the barrier width, the two-dimensional character of the carriers slightly weakens due to increasing coulomb interaction towards a growing three-dimensional character [15]. Therefore, the sensitivity of the wave functions to interface roughnesses is decreased, causing a slight reduction of the interface roughness induced PL linewidth broadening.

Fig. 4 depicts a measured XRD rocking curve of a structure containing 50 QWs. The corresponding simulated spectrum, which is obtained from dynamical linewidth theory, is shown below and is in good agreement. This indicates that the geometrical and compositional parameters as well as the material properties give a good description of the system. Fig. 5a displays a blow-up of Fig. 4 indicating the $50 - 2 = 48$ side-maxima corresponding to 50 wells. Note that the total strained stack has a very large width of 0.65 μm. A blow-up of an XRD spectrum measured for a sample including 30 wells is shown in Fig. 5b. Also in this case the number of wells (30) can be identified by the number of side-maxima. Between the 1st and the 2nd satellite reflection we observe $30 - 2 = 28$ side-maxima. In Fig. 5a the resolution of all structures is affected by the final resolution of the quadruple-monochromator and the noise at low count rates. All our samples containing different numbers of wells ($1 \leqslant N_{QW} \leqslant 50$) show a very good crystalline quality and excellent homogeneity in growth direction with respect to layer thicknesses and compositions (Figs. 2–5).

Finally, the homogeneity of our structures is studied in lateral direction on the wafer, which is essential for device yield and the reproducibility of specific device properties. PL scans at 300 K were performed on several uncleaved 2″-wafers. Fig. 6 displays the wavelength of the PL maximum in [0 −1 1] direction on (1 0 0) oriented surfaces.

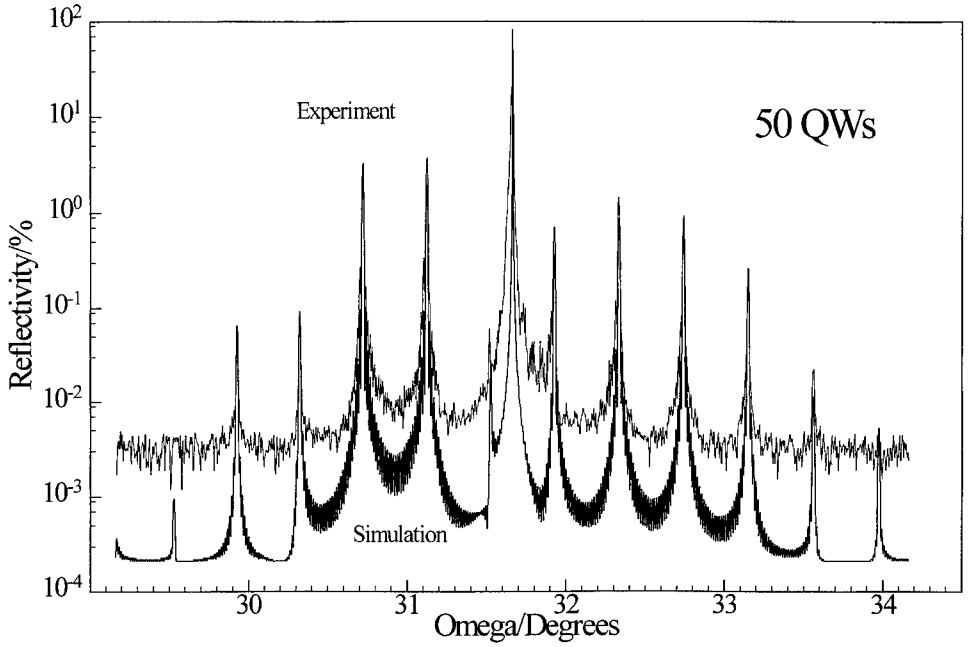

Fig. 4. Experimental and simulated XRD-rocking curves of a strain-balanced heterostructures including 50 QWs. The lower curve is vertically shifted.

MQW structures with 10 ternary and 10 quaternary wells are compared, having an absolute emission wavelength of $\lambda_0 = 1.55\ \mu m$ at 300 K. Note that the profiles are vertically shifted and the vertical scale is blown up (one tick corresponds to a wavelength variation of 0.06%). The two lower profiles correspond to compressively strained $Ga_{0.29}In_{0.71}As$ wells ($L_z = 3$ nm) and lattice matched $Al_{0.225}Ga_{0.25}In_{0.525}$ As barriers ($L_B = 8$ nm). The two upper profiles correspond to compressively strained $Al_{0.093}Ga_{0.197}In_{0.71}As$ wells ($L_z = 7.2$ nm) and tensile strained $Al_{0.208}Ga_{0.445}In_{0.347}As$ barriers ($L_B = 5.8$ nm). The lateral wavelength variations of all samples with ternary wells are similar. Two typical examples are shown in Fig. 6. All structures with quaternary wells also show a similar behaviour among each other, which is reverse, however, to the ternary wells. With respect to device fabrication it is important to note that the structures with quaternary wells show a much larger part in the center of the 2″ wafer where the wavelength is almost constant. For structures with quaternary wells this area exceeds 5 cm^2 and, thus, is five times larger than for ternary wells. That difference seems to be partly influenced by the ratio of the well widths of 3 nm/7.2 nm. Assuming in both cases an identical absolute fluctuation in well width, the emission wavelength of the wider wells is less sensitive to these changes. For the second profile from the top the standard deviation is only 0.065 nm in the central region.

In the following, possible explanations will be given for the different radial variations of the wavelength profiles of the ternary and quaternary wells. Since variations in the layer thickness and composition of the well materials cause much larger changes in the quantization energies, we do not consider the respective changes in the barriers. Now, we list possible mechanisms which in combination may explain the observed lateral wavelegth variations in Fig. 6.

(i) Compositional changes due to slightly varying desorption rates may be caused by a possible small temperature gradient in radial direction. Since the desorption of Al is negligible, no gradient in the Al-content will occur. In contrast, the desorption

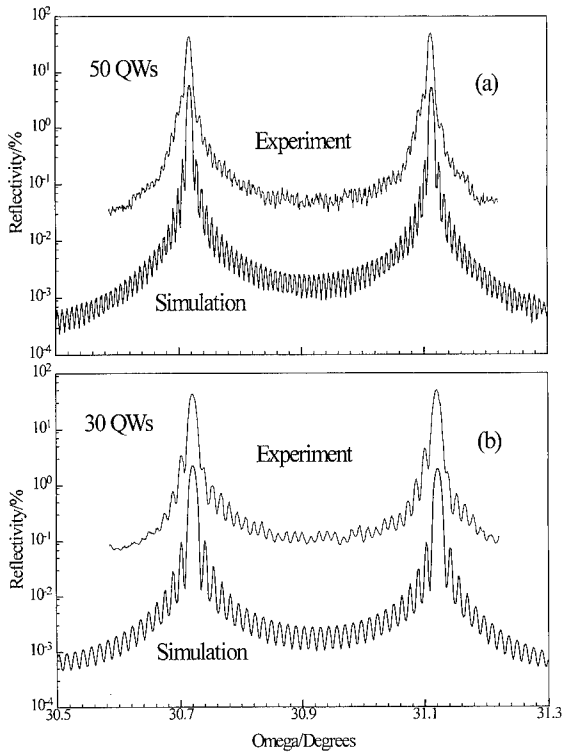

Fig. 5. Blow-ups of experimental and simulated XRD-rocking curves of strain-balanced heterostructures including 50 QWs (a) and 30 QWs (b).

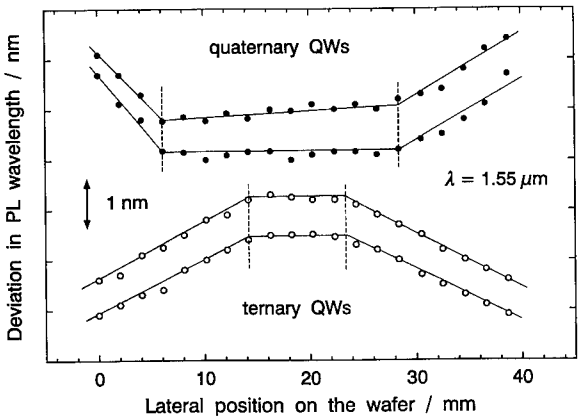

Fig. 6. Variation of the wavelength of the PL maximum at 300 K in lateral direction for (1 0 0) oriented wafers. The lasers structures include 10 ternary wells (open symbols) or quaternary wells (closed symbols) and have an emission wavelength of $\lambda \sim 1.55$ μm. For a better destinction the profiles are vertically shifted.

rates of In and Ga are considerably higher. For a given substrate temperature AlGaInAs shows a weaker In desorption than GaInAs, due to the presence of Al. However, we believe that this effect is still very small for 510°C.

(ii) The layer thicknesses are mainly determined by the fluxes of the molecular beams, and possible radial temperature gradients do not have a significant influence. We believe that the differences in the profiles of structures with ternary and quaternary wells most likely result from spatial flux variations (the centers of the beam characteristics probably do not coincide with the center of the wafer, i.e. the rotation axis).

The use of quaternary QWs in photonic devices allows strain and well width to be varied independently of each other while maintaining e.g. 1.55 μm emission wavelength. The use of strain compensation overcomes the total critical layer thickness restrictions and enables a free choice of the number of QWs in photonic device design. Recently, we obtained a record modulation bandwith of 26 GHz for 1.55 μm AlGaInAs lasers [16–18] with either ternary or quaternary QWs.

In conclusion, strain-balanced high-quality AlGaInAs/AlGaInAs MQW structures were grown by solid source MBE. The PL linewidths are low and do not vary with the number of QWs ($1 \leqslant N_{QW} \leqslant 50$). With respect to photonic device applications, structures with quaternary QWs seem to be superior compared to structures with ternary QWs, e.g. due to more efficient carrier capture from the cladding layers [19] and due to a five times larger lateral wafer area in which the PL wavelength is constant.

We wish to thank H. Burkhard, F. Steinhagen, R. Zimmermann and M. Walter for stimulating discussions, A. Pöcker and H. Schwinn for X-ray diffraction measurements and W. Betz for the SEM micrographs.

References

[1] E.P. O' Reilly, Semicond. Sci. Technol. 4 (1989) 121.
[2] G. Allen Vawter and D.R. Myrs, J. Appl. Phys. 65 (1989) 4769.

[3] S.C. Jain, M. Willander and H. Maes, Semicond. Sci. Technol. 11 (1996) 641.
[4] C.P. Seltzer, S.D. Perrin, M.C. Tatham and D.M. Cooper, Electron. Lett. 27 (1991) 1268.
[5] R.W. Glew, K. Scarrott, A.T.R. Briggs, A.D. Smith, V.A. Wilkinson, X. Zhou and M. Silver, J. Crystal Growth 145 (1994) 764.
[6] L.M. Woods, P. Silvestre, P. Thiagarajan, G.A. Patrizi and G.Y. Robinson, J. Electron. Mater. 23 (1994) 1229.
[7] A. Hamoudi, A. Ougazzaden, Ph. Krauz, E.V.K. Rao, M. Juhel and H. Thibierge, Appl. Phys. Lett. 66 (1995) 718.
[8] E. Kuphal, H. Burkhard and A. Pöcker, Jpn. J. Appl. Phys. 34 (1995) 3487.
[9] O. Issanchou, J. Barrau, E. Idart-Alhor and M. Quillec, J. Appl. Phys. 76 (1995) 3925.
[10] W.-Y. Choi and C.G. Fonstad, J. Crystal Growth 127 (1993) 555.
[11] Ch. Zah, R. Bhat, B.N. Pathak, F. Favire, W. Lin, M.C. Wang, N.C. Andreadakis, D.M. Hwang, M.A. Koza, T.-P. Lee, Z. Wang, D. Darby, D. Flanders and J.J. Hiesh, IEEE J. Quantum Electron. 30 (1994) 511.
[12] H. Hillmer, R. Lösch, F. Steinhagen, W. Schlapp, A. Pöcker and H. Burkhard, Electron. Lett. 31 (1995) 1346.
[13] M.C. Wang, W. Lin, T.T. Shi and Y.K. Tu, Electron. Lett. 31 (1995) 1584.
[14] M.J. Moudry, E.J. Tarsa and L.A. Coldren, J. Electron. Mater. 25 (1996) 948.
[15] P.S. Jung, J.M. Jacob, J.J. Song, Y.C. Chang and C.W. Tu, Phys. Rev. B 40 (1989) 6454.
[16] F. Steinhagen, H. Hillmer, R. Lösch, W. Schlapp, H. Walter, R. Göbel, E. Kuphal, H.L. Hartnagel and H. Burkhard, Electron. Lett. 31 (1995) 274.
[17] H. Hillmer, A. Greiner, F. Steinhagen, R. Lösch, W. Schlapp, T. Kuhn, H. Burkhard, Hot Carriers in Semiconductors (Plenum, New York, 1996) p. 581; Presentation at 9th Int. Conf. on Hot Carriers in Semiconductors, Chicago (1995).
[18] H. Hillmer, A. Greiner, F. Steinhagen, H. Burkhard, R. Lösch, W. Schlapp and T. Kuhn, SPIE Proc., Vol. 2693, Physics and Simulation of Optoelectronic Devices IV, Bellingham (1996) 352.
[19] S. Marcincevicius, H. Hillmer, R. Lösch and H. Olin, Appl. Phys. Lett. 69 (1996) 1101.

ELSEVIER

Journal of Crystal Growth 175/176 (1997) 1126–1130

JOURNAL OF CRYSTAL GROWTH

New route to reduce ionized impurity scattering in modulation-doped GaAs quantum wells

R. Hey*, K.-J. Friedland, H. Kostial, R. Klann, H.K. Ploog

Paul-Drude-Institut für Festkörperelektronik, Hausvogteiplatz 5–7, D-10117 Berlin, Germany

Abstract

We propose a new concept for the reduction of impurity scattering in remotely doped GaAs single quantum wells by using heavy-mass X-electrons in the short-period AlAs/GaAs superlattice barriers which smooth the potential fluctuations of the ionized Si dopants. Electron mobilities as high as 120 $m^2/V \cdot s$ and electron densities of 1.6×10^{16} m^{-2} are obtained in 10 nm GaAs single quantum wells in the one-subband occupation mode without any parallel conductance. To demonstrate the applicability of our concept magnetotransport and photoluminescence measurements together with self-consistent calculations are presented. Limitations of the effectiveness of the reduction of impurity scattering by impurity segregation and intermixing in the superlattice are discussed.

PACS: 73.20.Dx; 73.50.Bk; 73.61.Ey; 81.05.Ea; 81.15.Hi

Keywords: Electronic materials; Heterojunctions; Quantum wells; Superlattices; Molecular beam epitaxy

1. Introduction

For the application in low-noise and high-frequency devices a high conductivity of the two-dimensional electron gas (2DEG) in a heterojunction is required. Material combinations providing high barriers allow for high 2DEG concentrations n and make the devices work at higher temperatures [1–4]. However, in a given material system the scope to increase the conductivity either by simply increasing the dopant density or decreasing the dopant sheet-conductive channel separation is limited. The occurrence of parallel conductivity in the doping channel as well as the population of excited subbands with additional intersubband scattering [5] and, most importantly, the increased remote impurity scattering [6, 7] result in a lowering of the electron mobility μ and hence, the conductivity. In addition, in high mobility samples other limitations of the mobility such as interface roughness scattering in (Al,Ga)As systems [8] and alloy disorder scattering in ternary systems [9] become important. Recently, low temperature experiments with a high electron mobility of about 400 $m^2/V \cdot s$ in the (Al,Ga)As system with densities

* Corresponding author.

0022-0248/97/$17.00 Copyright © 1997 Elsevier Science B.V. All rights reserved
PII S0022-0248(96)00950-5

of 0.64×10^{15} m^{-2} per quantum well [2] or up to 3×10^{15} m^{-2} have been reported [3]. In the pseudomorphic (AlGa)As/(InGa)As material system conductivities approaching $n \times \mu = 9 \times 10^{16}$ /V·s up to temperatures as high as $T = 77$ K have been obtained [4] by optimizing the quantum well thickness and the dopant separation from the quantum well.

In this work we propose a new concept for both the enhancement of the carrier concentration and the reduction of remote impurity scattering (RIS) in GaAs single quantum wells (SQW), thereby significantly increasing the $n \times \mu$ product, i.e., the conductivity. The concept is based on the occurrence of heavy-mass X-electrons in short-period superlattices (SPSL) barriers, which are located near to the dopant sheet and are very effective in smoothing potential fluctuations caused by randomly distributed dopant atoms. The barriers for the GaAs SQW are formed by AlAs/GaAs SPSL. We present magnetotransport experiments in order to confirm the applicability of this concept. Results of photoluminescence (PL) measurements show the presence of X-electrons in our structures.

2. Experimental procedure

The structures under investigation are grown by solid-source molecular beam epitaxy on semiinsulating GaAs (0 0 1) substrates. The free carriers in the 10 nm GaAs SQW are provided by remote δ-doping with Si at a distance of 14 or 10 nm. The barriers consist of 60 periods of a 4 monolayers (ML) AlAs/8ML GaAs SPSL. Single Si δ-doping sheets with a dopant concentration of $N^{2D} = 2.5 \times 10^{16}$ m^{-2} are placed on both sides of the SQW into a GaAs layer of the SPSL. The growth temperature of the lower barrier and the SQW is 580°C, whereas the temperature for the δ-doping sheet and its vicinity is 510°C to suppress Si segregation into the SQW. The growth rate and the beam-equivalent As_4-to-Ga pressure ratio are 0.66 μm/h and 8, respectively. SPSL and SQW are grown in the two-dimensional island nucleation growth mode as was proven by atomic force microscopy and by reflection high-energy electron diffraction in additional experiments. For comparison structures doped on one side as well as on both sides of the SQW are grown at a constant temperature of 580°C. For more flexibility in placing the doping sheet at certain distances to the SQW in these stuctures the SPSL period is decreased from 12 ML to 6 ML. We study the low-temperature magnetotransport properties of samples with a Hall-bar geometry. A Ti/Au gate electrode is used to change the electron density. In all measurements the magnetic field was perpendicular to the SQW interfaces.

3. Results and discussion

The dependence of the parallel ρ_{xx} and transverse ρ_{xy} components of the resistivity tensor on the magnetic field of a remotely doped SQW with SPSL barriers is shown in Fig. 1. A very high mobility at surprisingly high electron densities is observed. The one-subband occupation is manifested by the one frequency Shubnikov–de-Haas (SdH) oscillation of the corresponding σ_{xx} component of the conductivity tensor up to the highest gate voltages. We use the procedure described in [10] to derive the electron densities n_{SdH} from the SdH frequency. These values are equal to the carrier

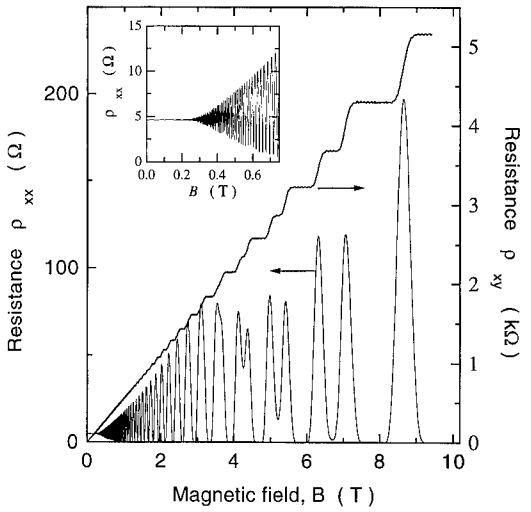

Fig. 1. Magnetic field dependence of ρ_{xx} and ρ_{xy} at $T = 0.33$ K for a remotely doped SQW with a spacer thickness of 14 nm.

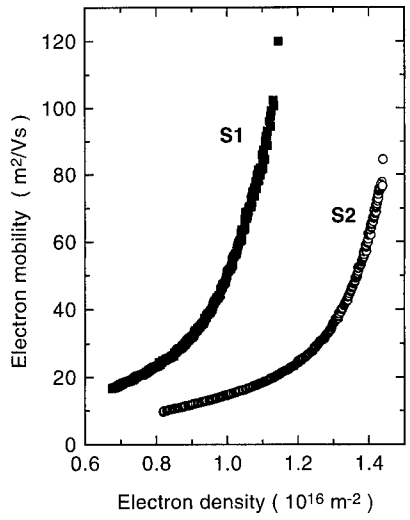

Fig. 2. Dependence of the electron mobility μ_H on the electron density n_H obtained at $T = 0.33$ K and $B = 0.1$ T of two gated samples. The single maximum mobility in both curves is measured on the same samples without any gate. S1 and S1 denote samples with 14 and 10 nm spacer thicknesses, respectively.

densities n_H calculated from the low field Hall-effect $\rho_{xy} = \gamma/(en_H)$ using a Hall-factor $\gamma = 1$. Together with the exact value $\rho^{\nu}_{xy} = h/(e^2\nu)$ and $\rho^{\nu}_{xx} = 0$ in the quantum Hall regime for the integer filling factor ν these results demonstrate the absence of any parallel conductance in the doping region. The conductance is determined exclusively by electrons in the lowest 2DEG subband of the SQW. Therefore, we can determine the Hall mobilities of the 2DEG as $\mu_H = \rho_{xy}/\rho_{xx}$ at low magnetic fields. Fig. 2 reveals an unusual dependence of μ_H on the electron density n_H. While we observe a power-like dependence $\mu_H \sim (n_H)^k$ with $1.5 < k < 2$ at lower densities (for example $n_H < 0.95 \times 10^{16}$ m^{-2} in sample S1 in Fig. 2) the mobility increases drastically up to 120 m^2/V·s for $n_H > 0.95 \times 10^{16}$ m^{-2} within a very narrow electron density region. The power-like behaviour of μ_H at lower densities is usually related to the remote impurity scattering (RIS) by randomly distributed impurities in the doping plane [9]. At higher densities the power k exceeds 8, which is difficult to model by scattering theories based on random potentials. We find that the maximum product $n \times \mu = 1.35 \times 10^{18}$/V·s and

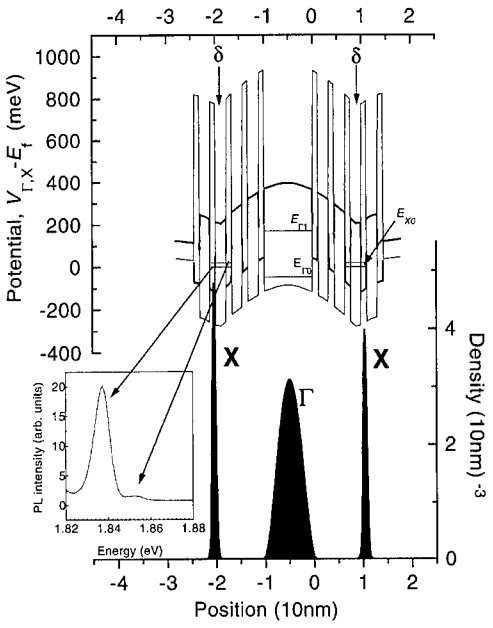

Fig. 3. Calculated potential (upper part) and distribution (lower part) of the the X- and Γ-carriers, bold line – V_X, thin line – V_Γ. Thin horizontal lines represent the subband edge energies. Note the level-splitting of the X-band electrons. The inset shows a typical PL-spectrum for the type-II recombination (original spectrum, the spectral region of the optical phonon replica is not shown).

4.20×10^{17}/V·s at temperatures $T = 0.3$ and 77 K, respectively. These values are comparable to the highest conductivities in experiments with SQW's at low temperatures, $T < 1$ K [2, 3]. The $n \times \mu$ product at $T = 77$ K in this work is even several times larger than the highest reported value for 2DEG [4]. To explain the increased mobility in our system we adopt a RIS model with reduced fluctuating scattering potential at higher densities and take into account additional carriers with very low mobilities in the SPSL very close to the doping layers. By voltage dependent capacitance measurements we found that additional low mobility carriers are present in the SPSL nearby the doping plane [11]. To clarify the nature of the additional carriers we show in Fig. 3 the results of model calculations of the potential and charge distribution in our structures [12]. These calculations account for two different kinds of electrons. First, we

consider the usual Γ-electrons with the isotropic effective mass $m_\Gamma/m_e = 0.07$ which form the 2DEG ground subband. These electrons with high mobility are located in the SQW. The edge of the higher Γ-electron subbands in the SQW as well as in the SPSL is more than 170 meV above the Fermi-energy and, therefore, these subbands cannot be occupied at low temperatures. This is the reason for the possible enhancement of the electron density in the SQW up to $1.6 \times 10^{16}\ m^{-2}$ without causing any parallel conductance. The maximum density for single subband occupation is not yet known. Our model calculations show this value to be much higher than $2 \times 10^{16}\ m^{-2}$. Next we have to include the higher conduction band minima of the AlAs/GaAs SPSL system into the calculation. It is known from experiments with AlGaAs/AlAs multiple quantum wells [13] that at AlAs-thicknesses $d_{AlAs} < 3$–4 nm the X_z-electrons govern the transport properties. These are electrons with the lower in-plane effective mass of about $m_{eff}/m_0 = 0.25$ while the heavy mass component $m_{Xl}/m_e = 1.1$ in AlAs accounts for the subband quantization. The period in our SPSL is well below the Γ–X crossover and our calculations show that states with the lower in-plane mass component are occupied first. The subband edge of states with the heavy in-plane mass is too high to be occupied by electrons at low temperatures. Our simple calculations do not account for any spatial lateral relief in the SPSL, but show quantitatively that in this system the X-electrons appear in the AlAs 'well' closest to the δ-doped GaAs sheet. Their density and spatial distribution, however, depend sensitively on the interface structure and the lateral potential fluctuations. Our results show conclusively that with X-electrons in the SPSL the mobility of the electrons in the GaAs SQW is considerably increased. The explanation follows directly from our calculations. Fig. 3 shows that the X-electrons are located in the AlAs 'well' on one side of the doped GaAs sheet in the SPSL. Their expected Bohr radius $a_B^X \approx 2$–3 nm as well as their nominal distance from the doping layer $d \approx 1.7$ nm is considerably smaller than the average distance between the Si-dopant atoms $d_D = 1/\sqrt{N_D} \approx 8$–9 nm. Therefore, the X-electrons can be very easily localized at the minima of the fluctuating potential caused by the randomly distributed dopant atoms. This localization explains the absence of any parallel conductance. The high effective mass of the X-electrons results in a screening parameter which is several times larger than that of the Γ-electrons. Therefore, the X-electrons screen the fluctuating potential of the ionized Si impurities more effectively and selectively, leading to an increase of the mobility of the Γ-electrons in the GaAs SQW.

Mobility enhancement is not observed in similar samples which are δ-doped only on one side. Obviously, deep trap centers are present at the SPSL interfaces which now decrease the mobility. Their potential fluctuations cannot be smoothed because of the missing X-electrons on this side.

To study the energy spectrum of the X-electrons we have carried out photoluminescence (PL) measurements. In all our samples the PL spectra for the type-II recombination region show two peaks (see inset in Fig. 3). This structure follows directly from the subband-splitting of the X-electrons in the SPSL, which is caused by the electric field of the separated X- and Γ-electrons. The indirect recombination is possible from AlAs-'wells' on both sides of the GaAs-'well' with a small energy difference. According to our calculations this subband-splitting with an energy separation of nearly 20 meV depends weakly on the position and the doping density (see Fig. 3). This splitting is close to the observed peak separation in the PL. The higher density of X-electrons at the lower energy sublevel explains the higher intensity of the low-energy side peak in the PL-spectra.

This new route to reduce RIS in modulation-doped GaAs QW is effective unless dopant segregation and intermixing of the SPSL barrier take place. In order to be more flexible in placing the dopant sheet at discrete separations to the well, the SPSL period is reduced from 12 ML to 6 ML. The carrier concentration is not effected, but the mobility decreases by a factor of about 8. This mobility reduction is probably caused by intermixing and dopant segregation. It is known that there is a unidirectional segregation of Ga from GaAs into AlAs at the GaAs/AlAs interface [14]. This segregation leads to an intermixing of the SPSL components. The intermixing process develops inhomogeneously depending on the actual defect structure of the

surface (terrace-step edge structure). The process will be more pronounced the smaller the individual SPSL layers are. As a consequence the dopant segregation towards the SQW interface in the growth direction is enhanced leading to an increase of RIS. Additionally, strong intermixing can lift the type II SPSL character. Growing the whole structure at a constant substrate temperature (580°C) also leads to a loss of the extreme high electron mobility because of similar reasons. Therefore, the achievement of smooth SQW interfaces and the suppression of dopant segregation in combination with intermixing effects should be balanced by an adequate choice of growth temperatures.

4. Conclusions

In conclusion, we have shown that the impurity scattering in remotely doped GaAs SQWs can be reduced effectively by the presence of heavy-mass X-electrons in the direct vicinity of the dopant atoms in the SPSL barriers. These X-electrons exhibit an extremely high screening capability and are able to smoothen the potential fluctuations caused by the random distribution of the dopant atoms. They are localized and do not contribute to the conductivity. PL studies as well as self-consistent calculations confirm the existence of X-electrons in the AlAs/GaAs SPSL barriers. The high electron conductivity is lost by dopant segregation in combination with intermixing effects in ultra-short period superlattices. With an adequate choice of the growth procedure these detrimental effects can be minimized.

Acknowledgements

The authors wish to thank M. Höricke for the MBE growth and A. Riedel for assistance with the sample preparation.

References

[1] G. Tränkle, H. Rothfritz, R. Müller and R. Weimann, J. Crystal Growth 120 (1992) 240.
[2] L.N. Pfeiffer, K.W. West, J.P. Eisenstein, K.W. Baldwin and P. Gammel, Appl. Phys. Lett. 61 (1992) 1211.
[3] B.E. Kane, L.N. Pfeiffer and K.W. West, Appl. Phys. Lett. 67 (1995) 1262.
[4] M. Blumina, I.O. Lelong, R. Sarfaty and D. Fekete, J. Appl. Phys. 75 (1994) 357.
[5] R.A. Mena, S.E. Schacham, E.J. Haugland, S.A. Alterovitz, S.B. Bibyk and S.A. Ringel, J. Appl. Phys. 78 (1995) 3940.
[6] K. Suzuki, K. Saito, T. Saku, A. Sugimura, Y. Horikoshi and S. Yamada, J. Crystal Growth 150 (1995) 1266; T. Saku, Y. Horikoshi and S. Tarucha, Jpn. J. Appl. Phys. 33 (1994) 4837.
[7] S. Hiyamizu, J. Saito, K. Nanbu and T. Ishikawa, Jpn. J. Appl. Phys. 22 (1983) L609.
[8] U. Bockelmann, G. Abstreiter, G. Weimann and W. Schlapp, Phys. Rev. B 41 (1990) 7864.
[9] A. Gold, Phys. Rev. B 38 (1988) 10798.
[10] J.P. Harrang, R.J. Higgins, R.K. Goodall, P.R. Jay, M. Laviron and P. Delescluse, Phys. Rev. B 32 (1985) 8126.
[11] K.-F. Friedland, R. Hey, H. Kostial, R. Klann and K.H. Ploog, Phys. Rev. Lett. 77 (1996) 4616.
[12] K.-J. Friedland and R. Zimmermann, unpublished. The calculations are performed by the one-dimensional self-consistent solution of the Schrödinger and Poisson equations in the effective mass aproximation, including exchange and correlation interaction energy.
[13] S. Yamada, K. Maezawa, W.T. Yuen and R.A. Stradling, Physica B 201 (1994) 295.
[14] W. Braun and K.H. Ploog, J. Appl. Phys. 75 (1994) 1993.

ELSEVIER

Journal of Crystal Growth 175/176 (1997) 1131–1137

JOURNAL OF CRYSTAL GROWTH

The growth of AlGaAs–InGaAs quantum-well structures by molecular beam epitaxy: observation of critical interdependent effects utilizing the design of experiments approach

Robert N. Bicknell-Tassius*, Kyeong Lee, April S. Brown, Georgianna Dagnall, Gary May

School of Electrical Engineering and Computer Science, Georgia Tech Research Institute, Georgia Institute of Technology, Atlanta, Georgia 30332-0250, USA

Abstract

The traditional approach to determine relationships between growth conditions and material properties has rested on the standard experimental approach – varying one parameter while holding all others constant. This technique does not effectively allow the observation of important interactions in complicated multilayer structures. Critical interdependent effects have been observed in the growth of AlGaAs/InGaAs quantum-well structures by molecular beam epitaxy (MBE). It is shown that statistical experimental design is an effective method for optimizing complex multilayer structures quickly. This technique is very useful for the optimization of processes with a large number of interdependent parameters and allows for the clear visualization and separation of complex interwoven effects. In the present work, we show for the first time the importance of the oxide desorption process for the optimal growth of AlGaAs-containing structures. The choice of an optimized oxide desorption process can lead to a decrease in the interfacial oxygen by almost two orders of magnitude.

1. Introduction

Molecular beam epitaxy (MBE) is a well developed and versatile technique for the growth of compound semiconductor heterostructures and devices. Although this process has the capability for stringent control of layer composition, purity, and thickness [1], the process optimization for a given device structure is complicated by a large number of coupled control parameters, such as the substrate temperature, V/III flux ratio, growth rates of alloys, etc. For this reason the optimization of a new device structure can often take tens to hundreds of growth runs.

The traditional approach to determine relationships between growth conditions and material properties has rested on the standard experimental approach – varying one factor while holding the

* Corresponding author. Fax: + 1 404 8944832; e-mail: rb91@prism.gatech.edu.

0022-0248/97/$17.00 Copyright © 1997 Elsevier Science B.V. All rights reserved
PII S0022-0248(96)01210-9

others constant. The basic assumption of this approach is that the coupling of the various growth parameters is small. This technique does not effectively allow the observation of important interactions in device structures. For example, growing high-quality AlGaAs requires high substrate temperature, unless other parameters are important, such as the minimization of dopant diffusion, which requires lower substrate temperature. The results of such approaches have been reported in the literature, where the effect of growth temperature on the quality of AlGaAs epitaxial layers has been correlated to growth temperature [2, 3] and possibly interfacial oxygen [4], which leads to a dramatic decrease in the recombination lifetime in these materials [5, 6].

Response surface modeling is a powerful technique for process optimization [7] and has been used to optimize the growth of InGaAs by chemical beam epitaxy [8] and is now standard practice in the silicon processing industry. In the present work, we have utilized a Resolution IV, 2^{6-2} fractional factorial experimental design (with 16 trials) to ascertain important interactions in a generic AlGaAs/InGaAs single-quantum-well structure. We have observed interactions which have never been quantified before. In addition, we show, for the first time, the importance of effective oxide removal techniques for the growth of high-quality structures. These results clearly show that the optimum growth conditions are strongly coupled, and for this reason the traditional approach of varying one parameter while holding all others constant is ineffective.

2. Experimental procedure

The structure investigated in the present work consisted of a 0.1 μm GaAs interface layer, a 0.5 μm AlGaAs buffer layer followed by a 75 Å InGaAs quantum well, which was capped by 0.25 μm AlGaAs cap layer. All samples in this study were grown in a solid source Varian Gen II MBE system using solid As_4 as the arsenic species. Samples were grown on 1/4 of a 2″ semi-insulating GaAs wafer that was briefly etched in 5 : 1 : 1 $H_2SO_4 : H_2O : H_2O_2$ before being indium-mounted on a standard molybdenum sample holder. In the 16 trial runs the following factors were varied: oxide removal temperature from 580 to 650°C, oxide removal time from 30 to 300 s; AlGaAs growth temperature from 580 to 630°C, InGaAs growth temperature from 480 to 520°C, the interface

Table 1
Summary of the growth experiments performed

	Desorb temperature (T0X)	Desorb time (T1_OX)	AlGaAs temperature (TAL)	InGaAs temperature (TIN)	Arsenic temperature (PAS)	Interrupt time (INT_TIME)
ATDC-1	580	300	580	520	340	30
ATDC-2	580	30	580	520	325	90
ATDC-3	580	30	630	450	340	90
ATDC-4	580	30	580	450	325	30
ATDC-5	580	30	630	520	340	30
ATDC-6	580	300	580	450	340	90
ATDC-7	650	300	580	450	325	90
ATDC-8	650	30	630	520	325	30
ATDC-9	580	300	630	520	325	90
ATDC-10	650	30	580	450	340	30
ATDC-11	580	300	630	450	325	30
ATDC-12	650	300	580	520	325	30
ATDC-13	650	30	630	450	325	90
ATDC-14	650	300	630	450	340	30
ATDC-15	650	30	580	520	340	90
ATDC-16	650	300	630	520	340	90

interrupt time from 30 to 90 s, and the arsenic cell temperature from 325 to 340°C ($1, 2 \times 10^{-5}$ Torr). The 16 sample runs and the order in which they were performed are summarized in Table 1. It is important to note that the RHEED pattern indicated complete oxide removal for all the 16 samples in the experiments.

All 16 samples were characterized by surface defect density, AlGaAs structural and optical quality, and InGaAs optical quality by 77 K photoluminescence (PL) and double-crystal X-ray diffraction (DCRC).

3. Results and discussion

The chosen factors were all found to be statistically significant and large variations in material properties were observed. For example, the defect density varied by one order of magnitude, the AlGaAs PL full-width at half-maximum (FWHM) varied by a factor of six, the AlGaAs X-ray FWHM varied by a factor of two, and the InGaAs PL FWHM varied by a factor of six. The experimental data were analyzed using the RS/Discover commercial software package [9]. Table 2 shows the main effects and two-factor interactions found to be significant at a 95% confidence level using the Student's *t*-test statistic [7]. This table shows one of the significant advantages over the statistically designed experiment approach: it not only allows the visualization of the results, but also provides a numerical estimate to the reliability of the results.

The results for the InGaAs photoluminescence (PL) full-width at half-maximum (FWHM) as a function of the InGaAs growth temperature and arsenic cell temperature is shown in Fig. 1. The narrowest photoluminescence linewidths are obtained at the lowest substrate temperature and the highest arsenic fluxes. This observation is in agreement with results published in the literature [10], and gives confidence that our approach agreement with the known phenomena.

We also observe a strong relationship between the growth temperature of the AlGaAs buffer layer and the resultant quality of the InGaAs quantum wells. The InGaAs PL FWHM as a function of the AlGaAs buffer layer growth temperature and the

Table 2
Summary of the effects of growth parameters on the epilayer characteristics

	Defects	X-ray			Photoluminescence			
		GaAs	AlGaAs	SEP	InGaAs		AlGaAs	
		FWHM	FWHM		FWHM	Pos	FWHM	Pos
TOX	X	X	X	X	X	X	X	X
TL_OX	X		X	X		X		X
TAL	X	X		X		X		X
TIN	X							
PAS	X				X			
INT_TIME	X					X		
TOX*TAL			X					
TOX*TIN								
TOX*PAS			X					
TL_OX*TIN			X				X	
TL_OX*PAS				X			X	X
TAL*TIN				X			X	X
TAL*PAS				X			X	X
TIN*PAS		X		X			X	X
TIN*INT_TIME	X						X	X
PAS*INT_TIME							X	X

arsenic cell temperature is shown in Fig. 2. The best InGaAs photoluminescence is obtained when the AlGaAs buffer layer is grown at the higher end of the range of the AlGaAs growth temperatures investigated. This is consistent with the observation that a higher AlGaAs growth temperature improves surface morphology, which, in turn, should improve quantum-well interface smoothness.

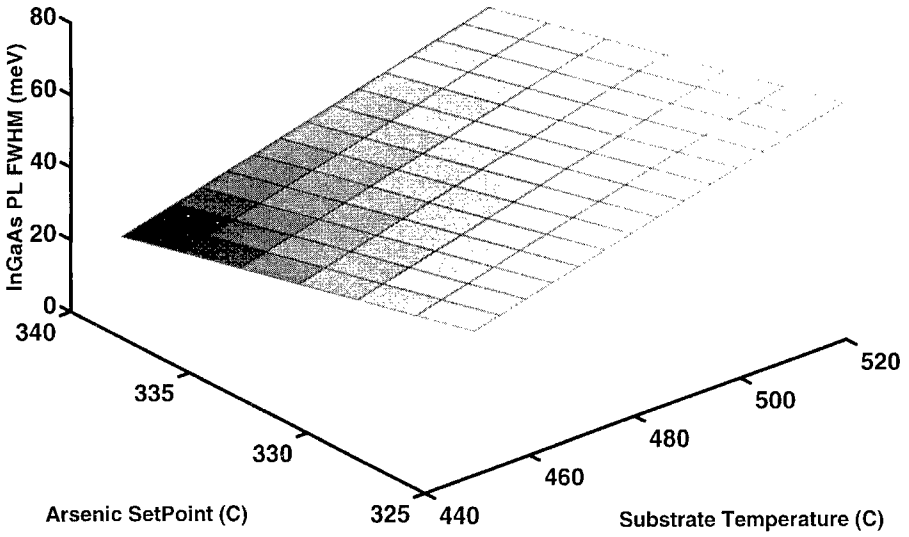

Fig. 1. InGaAs photoluminescence FWHM as a function of substrate temperature during the InGaAs growth and arsenic flux.

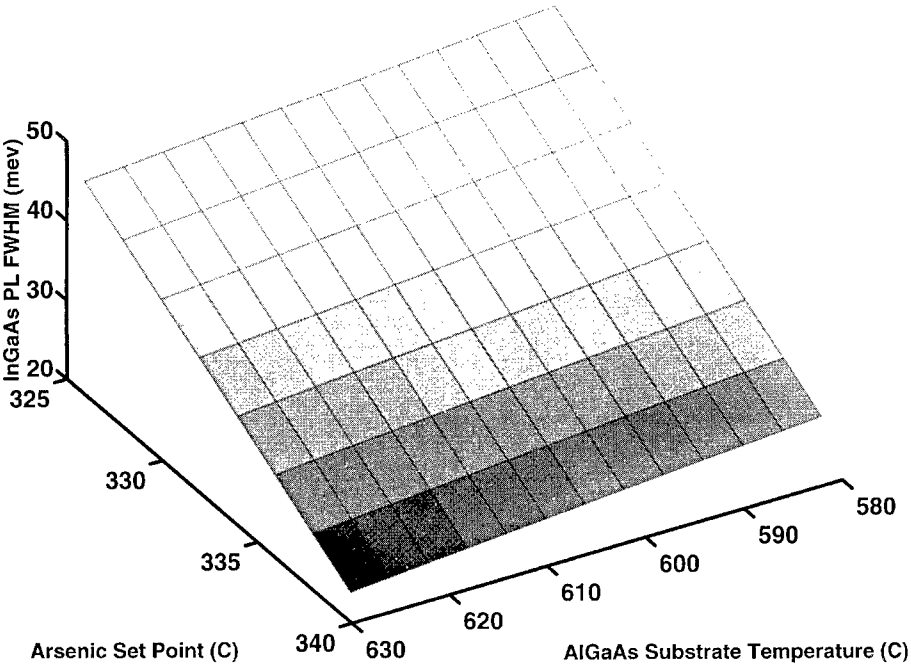

Fig. 2. AlGaAs photoluminescence FWHM as a function of substrate temperature during the growth of the AlGaAs and arsenic flux.

The effect of the oxide desorption process prior to the initiation of growth on the quality of the AlGaAs buffer layer is shown in Fig. 3, wherein the AlGaAs PL FWHM is plotted as a function of the desorption temperature and time. As can be seen, the quality of the AlGaAs epitaxial layer is dramatically affected by the exact desorption process. To our knowledge, this is the first quantitative observation of the critical importance of the oxide removal conditions on AlGaAs quality.

Not only are the temperature and time of the desorption process important, but as can be seen in Fig. 4, there is a coupling between the desorption temperature and the arsenic flux. The photoluminescence FWHM of the AlGaAs buffer is shown as a function of the desorption temperature and arsenic flux. This relationship maybe due to growth kinetic processes during the AlGaAs growth and/or changes in surface roughness during the oxide desorption process which are arsenic-flux-dependent.

Secondary ion mass spectrometery measurements (SIMS) have confirmed that the higher desorption temperatures lead to films with lower oxygen content. The oxygen concentration at the substrate/GaAs buffer layer interface as a function of oxide desorption temperature and time is shown in Fig. 5. The critical nature of the oxide desorption is readily evident. At low oxide desorption temperatures (580°C) a decrease in the interfacial oxygen concentration by also two orders of magnitude can be obtained by increasing the hold time before the initiation of growth from 30 to 300 s. Increasing the temperature at which the oxide desorption takes place also reduces the amount of interfacial oxygen to a lesser extent.

The exact oxide desorption process employed not only affects the amount of oxygen at the film/substrate interface, but also has a dramatic effect on the oxygen incorporation in the AlGaAs buffer layer. The oxygen concentration in AlGaAs buffer layer as determined by SIMS is shown in Fig. 6 as a function of the desorption temperature and desorption time. Similar to the results for the interfacial oxygen, a strong decrease in the concentration of oxygen in AlGaAs buffer layer is seen upon increasing the hold time at the oxide desorption temperature. It is also observed that the concentration of oxygen in AlGaAs buffer layer actually increases slightly as the oxide desorption temperature is raised from 580 to 650°C. This may be due to the oxygen segregation at the growth front and/or increased outgassing of the surrounding growth environment.

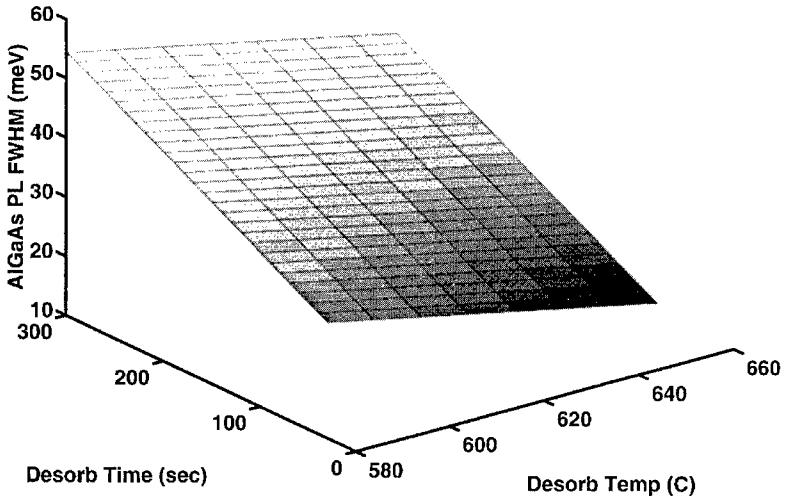

Fig. 3. AlGaAs photoluminescence FWHM as a function of oxide removal temperature and time for a growth temperature of 630°C.

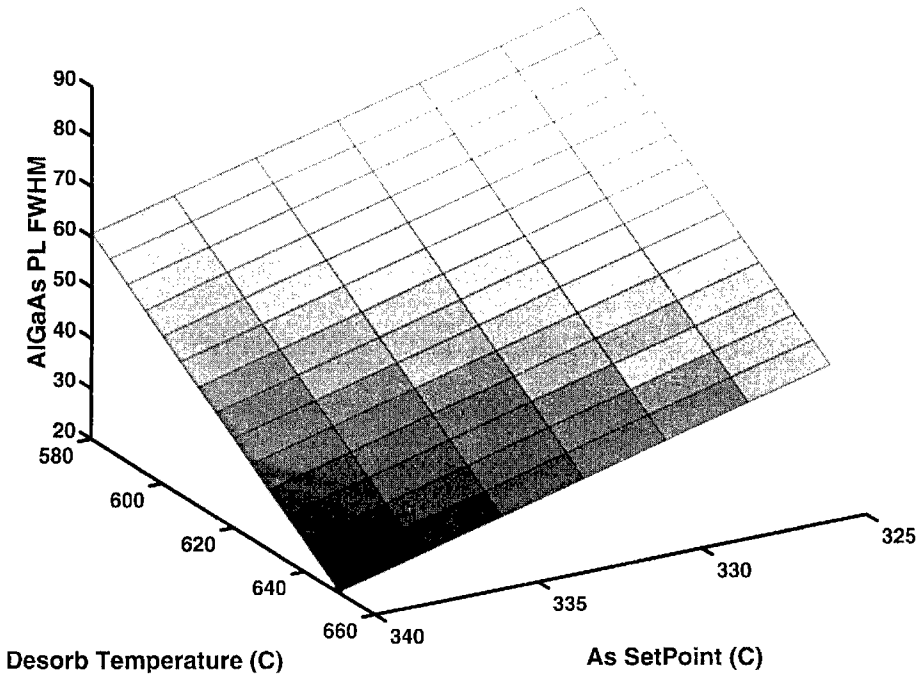

Fig. 4. AlGaAs photoluminescence FWHM as a function of oxide removal temperature and arsenic flux.

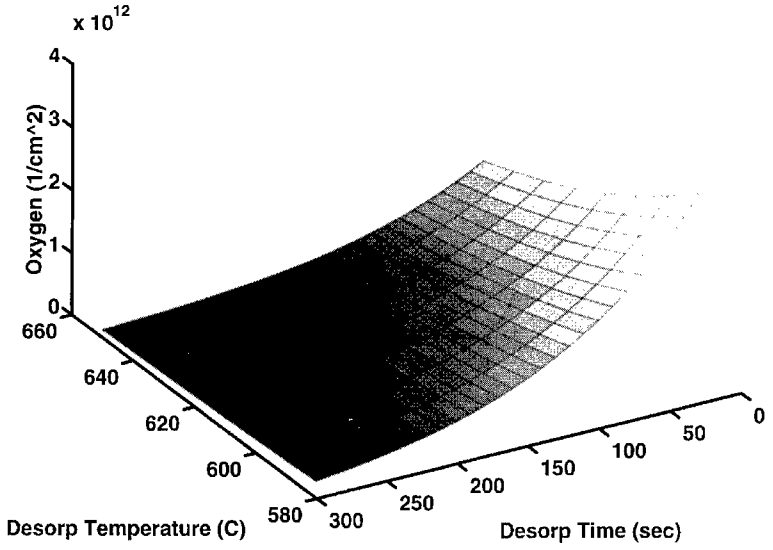

Fig. 5. Substrate/GaAs interfacial oxygen concentration as a function of the oxide desorption temperature and desorption time as determined by SIMS.

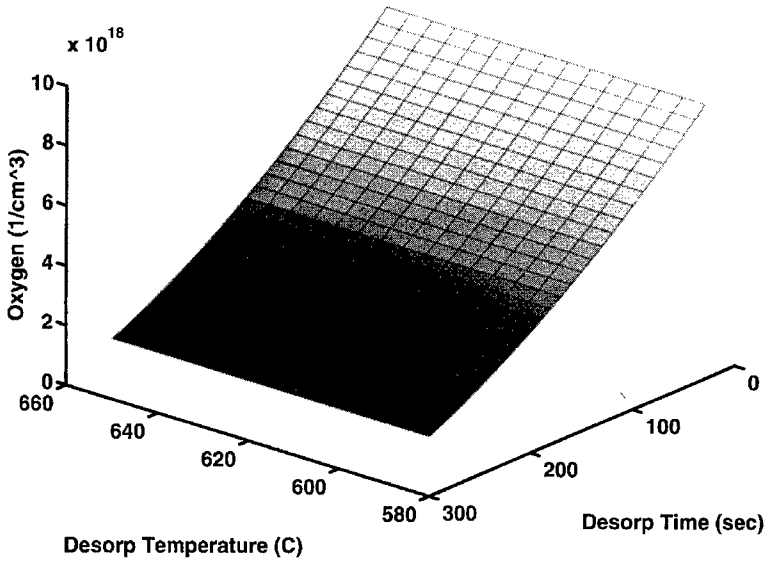

Fig. 6. Concentration of oxygen in the AlGaAs buffer layer as a function of the oxide desorption temperature and desorption time as determined by SIMS.

4. Summary

In summary, we have observed and quantified significant interactions in the growth of AlGaAs–InGaAs quantum-well structures. We have shown that statistical experimental design is an efficient means for optimizing growth conditions for a given device structure. In addition, we quantify, for the first time, the important interactions between effective substrate oxide desorption and AlGaAs and InGaAs growth conditions.

Acknowledgements

The authors would like to thank the Georgia Advanced Technology Development Center for supporting of this work.

References

[1] A. Brown, in: Encylopedia of Advanced Materials, Eds. Bloor, Brook, Flemings and Mahajan (Pergamon, Oxford, 1989).
[2] T. Achtnich, G. Burri and M. Ilegems, J. Vac. Sci. Technol. A 7 (1989) 2537.
[3] K. Yamanaka, S. Naritsuka, K. Kanamoto, M. Mihara and M. Ishii, J. Appl. Phys. 61 (1987) 5062.
[4] C.T. Foxon, T.S. Cheung, P. Dawson, D.E. Lacklison, J.W. Orton, V.v.d. Vleuten, O.H. Hughes and M. Henini, J. Vac. Sci. Technol. B 12 (1994) 1026.
[5] J.W. Orton, P. Dawson, D.E. Lacklison, T.S. Cheng and C.T. Foxon, Semicond. Sci. Technol. 9 (1994) 1616.
[6] T.S. Cheng, P. Dawson, D.E. Lacklison, C.T. Foxon, J.W. Orton and O.H. Hughes, J. Crystal Growth 127 (1993) 841.
[7] G.E.P. Box, W.G. Hunter and J.S. Hunter, Statistics for Experimenters (Wiley, New York, 1978).
[8] M.E. Sherwin, G.O. Munns, M.E. Elta, E.G. Woelk, S.B. Crary, F.L. Terry and G.I. Haddad, J. Crystal Growth 111 (1991) 594.
[9] RS/Discover, BBN Software Products Corporation.
[10] P.R. Berger, K. Chang, P. Battacharya and J. Singh, J. Vac. Sci. Technol. 5 (1987) 1162.

ELSEVIER

Journal of Crystal Growth 175/176 (1997) 1138–1143

JOURNAL OF CRYSTAL GROWTH

MBE growth and physics of strongly coupled p-type double quantum wells showing correlated $\nu = 1$ quantum Hall state

M. Henini*, R.J. Hyndman, T. Ihn, B.L. Gallagher, T.J. Foster, J.S. Chauhan, J.R. Middleton

Department of Physics, University of Nottingham, Nottingham NG7 2RD, UK

Abstract

We present a systematic magnetotransport study of high mobility (3 1 1)A strongly coupled p-type double quantum wells which demonstrate the existence of a correlated $\nu = 1$ quantum Hall state in the limit of weak tunnelling. Our results are in good agreement with the finite temperature phase transition predicted for this state.

Keywords: Two-dimensional hole gas; Molecular beam epitaxy; Gallium aluminium arsenide; Tunnelling

1. Introduction

Until recently, it has not been possible to realize a two-dimensional hole gas (2DHG) with high mobility using Be-doped GaAs/(AlGa)As heterostructures. Mobility enhancement of 2DHG has been observed by Henini et al. [1] in modulated p-type GaAs/(AlGa)As heterostructures on the (3 1 1)A GaAs surface using Si as the acceptor. A 2DHG with low temperature mobility as high as 1.2×10^6 cm^2 V^{-1} s^{-1} was obtained. Such high-quality samples allowed them to study the fractional quantum Hall effect for holes, a fundamental physical phenomenon which has been intensively investigated in the two-dimensional electron gas (2DEG) in n-type GaAs/(AlGa)As heterostructures with mobilities exceeding 10^7 cm^2 V^{-1} s^{-1}. Using the same growth procedure as those of Ref. [1] we have recently grown a series of very closely spaced p-type double quantum wells.

In this article we report the MBE growth of high-quality p-type modulated double quantum wells on (3 1 1)A using Si as the p-type dopant. We will show that the p-type double quantum wells exhibit interesting phenomena compared to the n-type double quantum well samples which have recently attracted considerable interest [2–4].

In single-layer, two-dimensional (2D) conductors the integer quantum Hall effect (IQHE) is a single particle phenomenon which arises when the Fermi energy lies in the region of localised states between Landau levels. The FQHE is a many-body phenomenon which arises from the intra-layer

* Corresponding author. Fax: + 44 115 951 5180; e-mail: ppzmh@ppn1.nott.ac.uk.

0022-0248/97/$17.00 Copyright © 1997 Elsevier Science B.V. All rights reserved
PII S0022-0248(96)01212-2

Coulombic interaction. This leads to transitions into correlated liquid-like ground states when the Landau level filling factor, ν, has particular odd denominator fractional values. In these cases, there exists a finite gap separating the ground state from the lowest-lying excited state. When two such 2D layers are in close proximity, the inter-layer Coulombic interaction can lead to new FQHE states when the filling factor in each layer is an *even* denominator fraction [2].

In a double layer system the quantum Hall effect at a total Landau level filling factor $\nu = 1$ (i.e., $\nu = \frac{1}{2}$ in each layer) can arise in two ways. If tunnelling is strong a single particle state can occur in which the energy gap is that separating the lowest symmetric and antisymmetric states of the system (Δ_{SAS}). A many body $\nu = 1$ state is also possible for strong inter-layer Coulombic interaction even in the absence of tunnelling [2]. The $\nu = 1$ state is expected to occur when the width of the barrier between the two quantum wells, d, is comparable with the magnetic length, ℓ_B. An explanation to the origin of the $\nu = 1$ state has been treated theoretically [2] by considering that the carriers in the two quantum wells have a fictional spin of $\pm \frac{1}{2}$.

The lowest energy charged excitations of the bi-layer correlated $\nu = 1$ states are merons which can be pictured as vortices in the spin orientation and which carry a charge of $\pm e/2$. At low enough temperatures, these objects are bound together in vortex–antivortex pairs with a total charge of 0 or $\pm e$ (a closely bound meron pair carrying charge $\pm e$ can be viewed as a skyrmion). At a finite temperature, T_{KT}, a Kosterlitz–Thouless transition is predicted to occur. At T_{KT} the pairs unbind and the energy gap to charge excitations disappears. It is predicted [2] that the bi-layer $\nu = 1$ state should only be stable for $d/\ell_B < 1.6$, since T_{KT} tends to zero at this value.

In n-type GaAs/GaAlAs double layer systems at small layer separation, when the inter-layer Coulombic energy is large, tunnelling also tends to be strong due to the small electron effective mass. Due to the added effect of tunnelling of the carriers between the two quantum wells the assignment of the origin of the $\nu = 1$ state becomes difficult. States for $\nu = 1$ showing behaviour consistent with that predicted for the correlated state have been observed in a series of n-type double quantum wells which have Δ_{SAS} values as low as 0.8 K [3]. However, in these samples tunnelling still plays an important role as is shown in tilted field experiments [3]. Complex behaviour has also been observed in very wide quantum wells which have some bi-layer character, but which also have very large Δ_{SAS} [4]. It is clear from these studies that inter-layer correlations are important in stabilising the observed $\nu = 1$ states. However, the prediction of a $\nu = 1$ state in the limit of small Δ_{SAS} has still not been directly demonstrated experimentally. In this paper we will concentrate on results for high mobility p-type double quantum wells for samples from one MBE grown wafer (NU1174), though the $\nu = 1$ state is observed in samples with appropriate densities from several wafers.

2. Experimental procedure

The structures were grown by MBE on 2-in liquid-encapsulated Czochralski semi-insulating substrates oriented within $\pm 0.5°$ of (3 1 1)A. The growth parameters were: substrate temperature of 630°C, beam equivalent pressure of As/Ga = 12, and a preferred growth rate of one monolayer per second and half a monolayer per second for GaAs and AlAs, respectively. The As_4 beam was generated using an Intevac Cracker cell filled with arsenic lumps from Preussag.

The preparation procedures of the MBE equipment broadly followed the method adopted by various groups and recommended by Intevac, and the growth parameters used above were those which gave us optimal electrical properties of (3 1 1)A heterostructures [1]. As we reported in Ref. [1] we used silicon as a p-type dopant for the (3 1 1)A orientation.

The modulation-doped samples consisted of a buffer layer followed by two GaAs quantum wells bounded on each side by an undoped $Al_{0.33}Ga_{0.67}As$ spacer layer, and lightly silicon-doped $Al_{0.33}Ga_{0.67}As$ layer. The whole structure was terminated by a 17 nm GaAs capping layer. The buffer layer consisted of 1 μm thick undoped GaAs followed by a superlattice $20 \times$ (2.5 nm $Al_{0.33}Ga_{0.67}As$ + 2.5 nm GaAs) and 0.5 μm un-

doped GaAs. A two-dimensional hole gas (2DHG) is confined at each of the $GaAs/Al_{0.33}Ga_{0.67}As$ interfaces. Each quantum well is 100 Å wide and they are separated by a 30 Å AlAs barrier as is shown in the insert of Fig. 2. The layer structure is almost symmetrical with Si-doped layers with the same doping density and the same thickness on each side of the quantum wells. However, it has been found necessary to make the lower spacer layer thicker (650 Å) than the upper spacer (600 Å) to compensate for the upward drift of the dopant with the growth surface.

The epitaxial layers were processed into Hall bars orientated along the $[\bar{2}\,3\,3]$ direction, by means of conventional photolithography and wet etching. The contacts consisted of 5 nm of Au, 10 nm of Zn, and 200 nm of Au annealled for sixty seconds at 510°C.

3. Results and discussion

The total carrier density and the relative densities in the two wells can be controlled using front and back gates. This is illustrated in Fig. 1 where the low field Shubnikov–de Hass oscillations for a series of different front gate biases are shown. Off balance a complex beating is seen while at balance one observes a single oscillatory period at the lowest fields before the spin-splitting is resolved at slightly higher fields. The density can be accurately determined from the Fourier transform of the low field Shubnikov–de Haas oscillations. As grown the carrier density in each well for NU1174 samples is within 5% of $1.1 \times 10^{15}\ m^{-2}$ and the average mobility is $400\,000\ cm^2\ V^{-1}\ s^{-1}$. The mobility is found to be a very weak function of carrier density as is the case for p-type heterostructures [1]. The potential and density distribution for this structure, shown in Fig. 2, was obtained by solving the Poisson equation and the one-electron Schrödinger equation self-consistently. A parabolic dispersion with a mass of $0.45m_0$ was used and many-body effects were included in the local-density-approximation. This yields a weakly hole-density-dependent Δ_{SAS} of ~ 70 mK. This very small value is the result of the very weak tunnelling for the high mass holes.

Fig. 2 shows the typical behaviour of the longitudinal resistance, R_{xx}, and the Hall resistance,

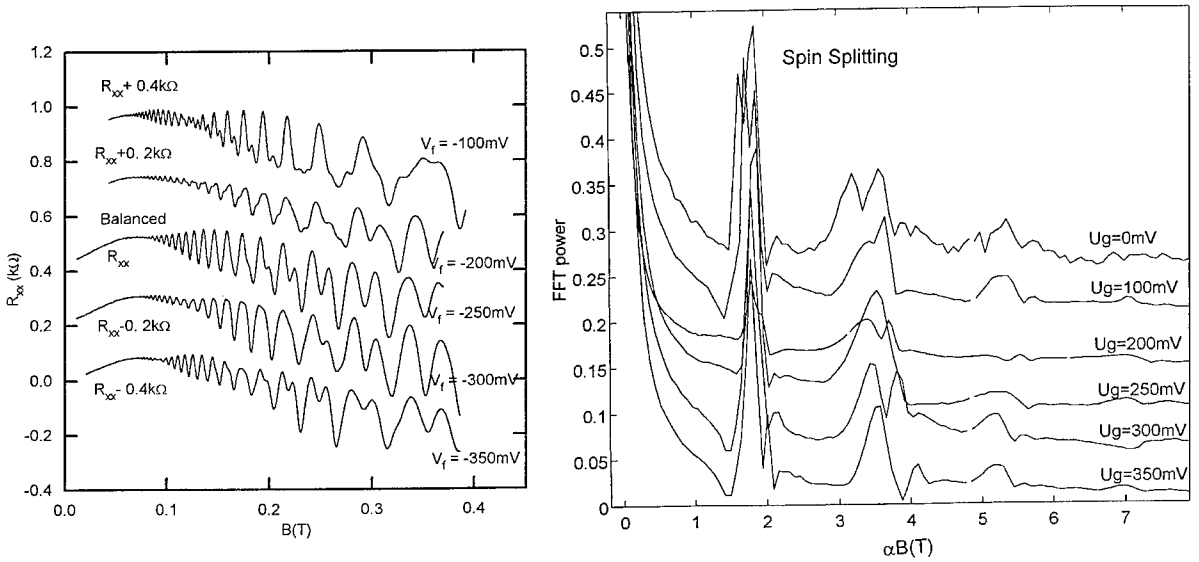

Fig. 1. Dependence of the Shubnikov–de Haas oscillations at zero back gate bias on applied front gate bias. Beating is seen when the hole densities in each well are not equal.

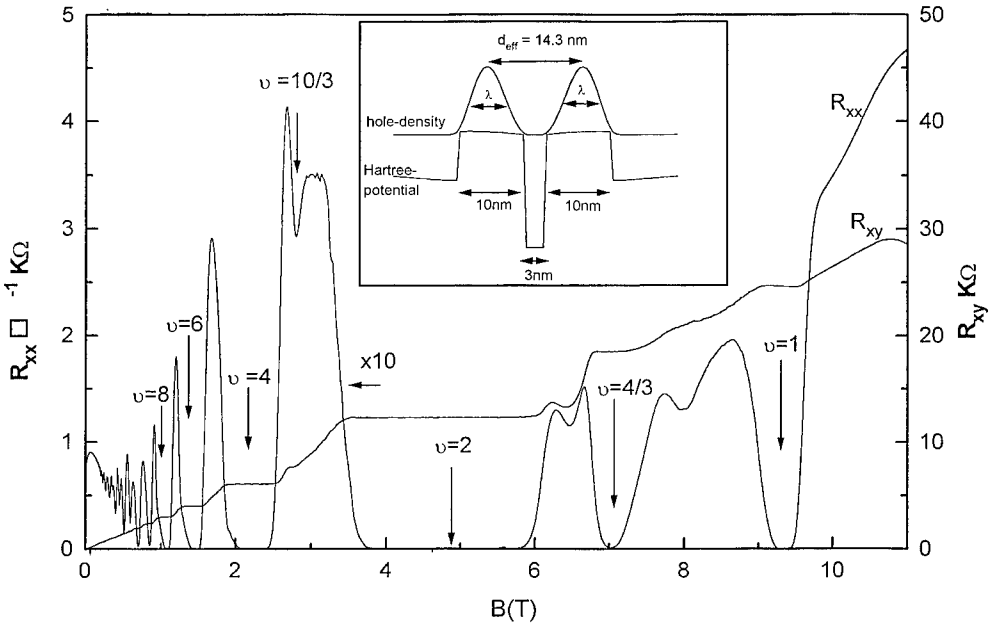

Fig. 2. Typical R_{xx} and R_{xy} results (at 60 mK) for equal hole number densities of 1.1×10^{11} cm^{-2} in each well. The insert shows the calculated potential profile and hole density distribution.

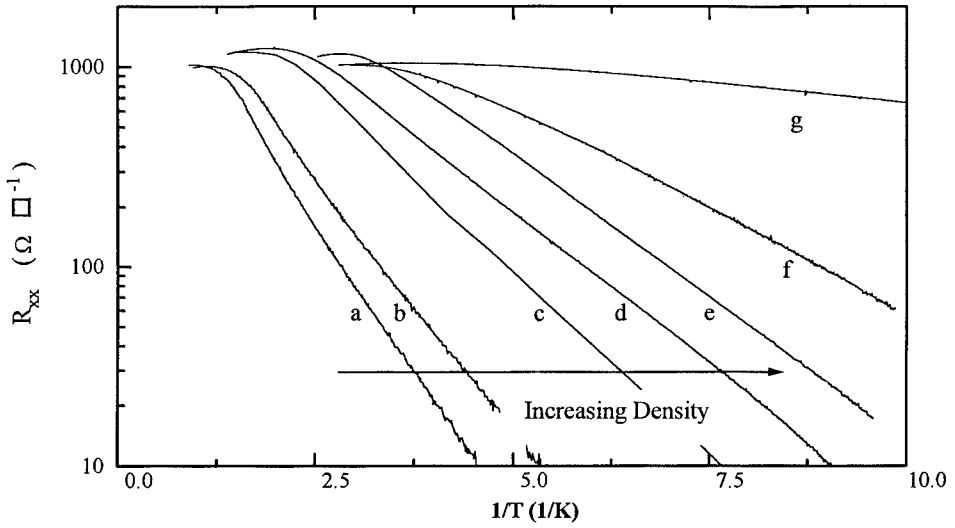

Fig. 3. Activation plots at $\nu = 1$ ($\nu = \frac{1}{2}$ in each well) for a series of total number densities with activation energies in Kelvin given in the bracket. (a) 1.61×10^{11} cm^{-2} (2.9 K) (b) 2.08×10^{11} cm^{-2} (1.9 K) (c) 2.23×10^{11} cm^{-2} (1.7 K) (d) 2.29×10^{11} cm^{-2} (1.4 K) (e) 2.33×10^{11} cm^{-2} (1.3 K) (f) 2.54×10^{11} cm^{-2} (0.54 K) (g) 2.63×10^{11} cm^{-2} (0.2 K).

R_{xy} when the hole number densities in the two wells are balanced. As we will show, strong $\nu = 1$ quantum Hall states are observed which have activation energies of up fifty times Δ_{SAS}. The states at $\nu = 3, 5, 7, \ldots$ are all absent as expected for weak tunnelling. This is direct unambiguous proof of the existence of the correlated $\nu = 1$ state in the limit of weak tunnelling.

Activation plots of ℓnR_{xx} against $1/T$ are given in Fig. 3. This shows very unusual behaviour since at low enough temperature one observes normal activated behaviour indicating the presence of an energy gap, ΔE. But as the temperature is raised the activated behaviour is terminated rather abruptly and no minimum in R_{xx} is observable above a temperature T^* which is much smaller than ΔE. This is in contrast to the behaviour of the adjacent $\nu = \frac{4}{3}$ state, which shows normal behaviour. This behaviour is predicted from the well-known Kosterlitz–Thouless transition in which one has the disappearance of the energy gap for charged excitations at a finite temperature, T_{KT}. It is worth noting that, surprisingly, similar behaviour has been seen [5] in very wide quantum wells despite the very strong tunnelling.

In Fig. 4 we present the dependence of the activation energy and our T^* values as a function of d/ℓ_B. T^* steadily falls towards zero as d/ℓ_B approaches ~ 1.7, while ΔE falls rapidly to zero at this value. The predicted values [2] of ΔE are ~ 10 K. However, it is expected that finite thickness corrections, Landau level mixing and disorder will all tend to reduce this value. Our values are, therefore, not inconsistent with expectation. A more useful comparison can be made between our values of T^* and the predicted behaviour of T_{KT} since this transition temperature should be less influenced by disorder. To do so, we have taken the prediction of Ref. [1] for the behaviour at a fixed ℓ_B as a function of d and scaled them by the intra-layer Coulombic energy. In Fig. 4 we have plotted the expected T_{KT} against our upper $(d/\ell_B)_{eff}$ scale. Good agreement in functional form but a disagreement by a factor of ~ 2 in magnitude is found. Given the uncertainties in the calculated magnitude and in our scaling procedure, this disagreement in magnitude is not surprising.

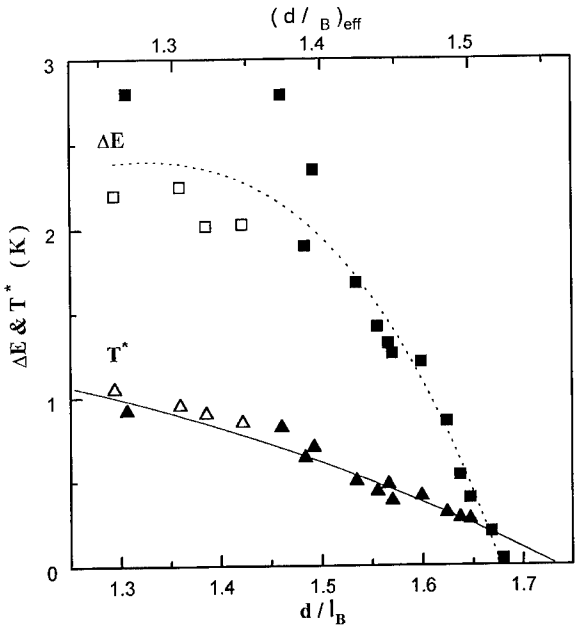

Fig. 4. Dependence of the activation energy ΔE and critical temperature T^* on d/ℓ_B obtained for the same densities as those of Fig. 2. T^* is taken as the point where the extrapolated activation line crossed the horizontal line through the saturation resistance value.

4. Conclusion

We have shown that samples of Si-doped GaAs/AlGaAs coupled 2DHGs structures with mobilities as high as 400 000 $cm^2\ V^{-1}\ s^{-1}$ can be achieved on the (3 1 1)A GaAs surface. Furthermore we have observed correlated $\nu = 1$ bi-layer states in the limit of weak tunnelling and find evidence of a finite temperature phase transition. The nature of the state is clear from the fact that it systematically *weakens* with increasing carrier density, and is destroyed for $d/\ell_B > 1.7$. Our results are in good agreement with recent theoretical predictions.

Acknowledgements

This work is supported by the United Kingdom Engineering and Physical Sciences Research Council (EPSRC).

References

[1] M. Henini, P.J. Rodgers, P.A. Crump, B.L. Gallagher and G. Hill, Appl. Phys. Lett. 65 (1994) 2054.

[2] K. Moon, H. Mori, K. Yang, S.M. Girvin, A.A.H. MacDonald, L. Zheng, D. Yoshioka and S.C. Zhang, Phys. Rev. B 51 (1995) 5138, and references therein.
[3] S.Q. Murphy, J.S. Einsenstein, G.S. Boebinger, L.N. Pfeiffer and K.W. West, Phys. Rev. Lett. 72 (1994) 728.
[4] Y.W. Suen, H.C. Manoharan, X. Ying, M.B. Santoz and M. Shayegan, Phys. Rev. Lett. 72 (1994) 3405.
[5] T.S. Lay, Y.W. Suen, H.C. Manoharan, X. Ying, M.B. Santoz and M. Shayegan, Phys. Rev. B 50 (1994) 17725.

ELSEVIER

Journal of Crystal Growth 175/176 (1997) 1144–1151

JOURNAL OF CRYSTAL GROWTH

Photoluminescence study of Si/SiGe multiple quantum wells grown by MBE

D. Grützmacher[a,*], R. Hartmann[a], E. Müller[a], U. Gennser[a], A. Dommann[b]

[a] *Paul Scherrer Institute, Micro- and Nanostructures Laboratory, CH-5232 Villigen PSI, Switzerland*
[b] *Neutechnikum Buchs, Laboratory for Vacuumtechnology, CH-9470 Buchs, Switzerland*

Abstract

Pseudomorphic Si/SiGe multiple quantum well (MQW) structures were grown by solid source molecular beam epitaxy (MBE). The optical and structural properties of MQWs grown with and without bias applied to the substrate during the deposition were studied in detail. SiGe phonon resolved band-edge luminescence of as-grown samples is found only for MQWs deposited with a positive bias at the substrate. Subsequent rapid thermal annealing improves the photoluminescence properties of films grown with zero or positive bias, whereas for samples grown with a negative bias a broad deep luminescence band is observed. A strong correlation between the observation of the deep luminescence and the appearance of defects in the SiGe layers is established. It is most likely that these defects originate from ion bombardment of the growing film during e-beam evaporation in solid source MBE.

PACS: 78.66. – w; 81.15.Hi; 78.55. – m

Keywords: Quantum well structures; Photoluminescence; SiGe alloys; Molecular beam epitaxy

1. Introduction

Molecular beam epitaxy (MBE) is a key technology for the development of Si/Ge-based material systems. In fact it is the only epitaxial system which permits a controlled growth of structurally perfectionized Si/Ge superlattices (SL) [1] and more recently, of coupled $Si_{1-x-y}Ge_xC_y/Si_{1-y}C_y$ quantum wells (QWs) [2]. Both structures are of particular interest for the development of an efficient silicon-based electrically pumped light emitter. For the SL structures intense luminescence is predicted due to zone folding effects and symmetry breaking of states at the interfaces [3], whereas for the coupled QWs the enhancement is attributed to spatially indirect (type II) transitions of electrons and holes confined in neighbouring quantum wells [2]. Besides a well-resolved band-edge-related luminescence spectra consisting of a no-phonon (NP) peak and phonon replicas, the luminescence of samples

* Corresponding author.

0022-0248/97/$17.00 Copyright © 1997 Elsevier Science B.V. All rights reserved
PII S0022-0248(96)00992-X

grown by solid source MBE frequently show a deep luminescence, 80–120 meV below the band-edge related luminescence [4, 5]. In particular for SiGe QWs grown at low temperatures (<700°C) this broad band is often observed, whereas band-edge luminescence is observed typically for samples either grown at higher temperatures [6–8] or subsequently annealed above 700°C [9]. The physical origin of this deep luminescence is still a matter of controversy. Several suggestions, including an optically active defect [5], donor acceptor pairs [10] and Ge-rich platelets [11], have been put forward to explain the phenomena. More recently, Sturm et al. [12] were able to create deep photoluminescence by ion implantation of Si into Si/SiGe QWs grown by rapid thermal chemical vapor deposition. They were able to recover the band-edge luminescence by annealing at 800°C. This result suggests that the deep luminescence of MBE grown samples is related to ion bombardment during growth. Some initial results using a substrate bias during the growth by MBE also point towards this model [13].

In this study we report on the optical properties (low-temperature photoluminescence (PL)) in relation with the structural properties, analysed by transmission electron microscopy and X-ray diffraction, of SiGe/Si multiple QWs. The deposition temperature, the substrate bias and the time and temperature of an subsequent rapid thermal annealing (RTA) of the QW samples were chosen as variables.

2. Experimental procedure

The SiGe/Si structures were grown in a solid source MBE chamber containing e-beam evaporators for Si and Ge, a pyrolitic graphite filament for C sublimation and effusion cells for B and Sb. A schematic view of the chamber is shown in Fig. 1. The distance between the e-beam evaporators and the substrate is approximately 0.5 m, which gives on the one hand good uniformity, but on the other hand requires quite high electron emission currents of the e-beam evaporators to achieve reasonable growth rates for the Si and SiGe layers (0.1–0.2 nm/s). In turn, this high emission current will also lead to enhanced generation of secondary

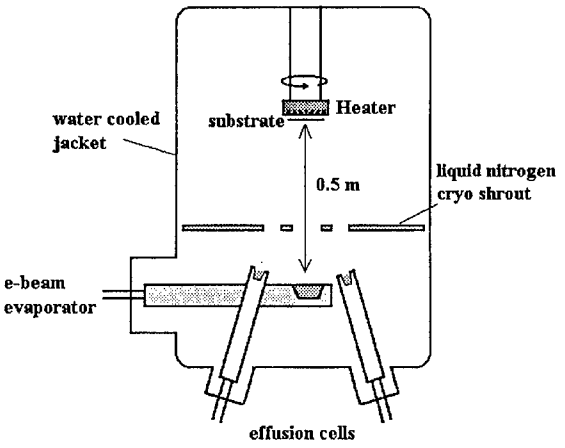

Fig. 1. Schematic view of the solid source MBE system used in the study.

and scattered electrons. For the Ge source a custom made Si crucible was used. The Si and the Ge source were shielded by Si walls to reduce the amount of scattered and secondary electrons traveling throughout the chamber. The flux of the e-beam evaporators is feedback controlled by a mass spectrometer.

The samples discussed were grown on undoped Si(1 0 0) substrates with a resistance of >400 Ω cm at temperatures ranging from 550°C to 750°C. The temperature was measured by a thermocouple close to the filament, the actual temperature of the wafer was probably lower. The QW structures were grown on a 100 nm thick Si buffer layer. The QW structures contained 10 periods with 10 nm-wide Si barriers and SiGe wells of typically 2–8 nm and Ge concentrations between 5% and 30%. The composition and thicknesses of the wells were determined by X-ray diffraction and cross-sectional TEM.

Prior to growth the substrate bias was adjusted between −1500 and + 1500 V. After the e-beam evaporators were powered the + 1500 V bias dropped to about + 200 V. The currents between the substrate and the ground was measured to be 60–70 nA.

After the growth, the QW structures were thermally treated by a RTA process in the temperature range from 750–950°C for 240 s, in a N_2/H_2 gas mixture as well as in pure N_2. PL spectra were taken before and after the RTA treatment. The

spectra were recorded at 2.4 K using an Ar^+ laser at 488 nm for excitation (excitation power: 6 mW) and a cooled Ge photoconductor for detection.

3. Results and discussion

The dependence of low-temperature (2.4 K) PL spectra on the substrate bias is shown in Fig. 2.

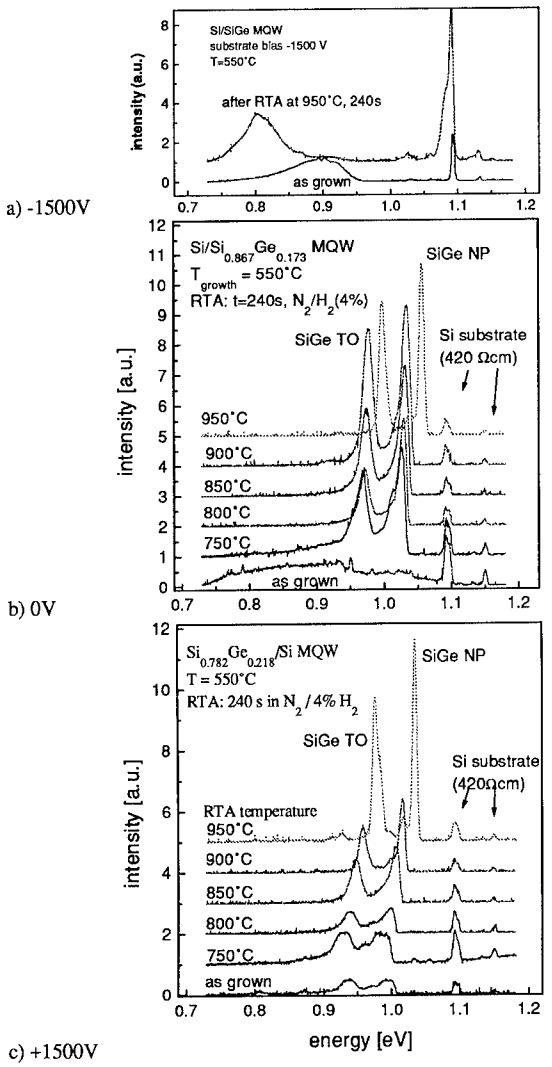

Fig. 2. 2.4 K photoluminescence (PL) spectra of Si/SiGe MQWs grown at 550°C with (a) negative bias (-1500V), (b) zero bias and (c) positive bias (+1500 V). For each sample PL spectra of the as- grown MQW and after a RTA at 750–950°C is shown.

Fig. 2b depicts the PL spectra of a sample grown at 550°C with 0 V bias, i.e. with a floating substrate, and subsequently annealed at temperatures ranging from 750°C to 950°C. The as-grown sample shows besides the Si PL lines of the substrate a broad-band luminescence. This broad band gets even more pronounced when a substrate bias of −1500 V is applied to the sample as shown in Fig. 2a. The PL spectra of the sample shown in Fig. 2c is grown with a substrate bias of + 1500 V. In this case the broad-band luminescence is suppressed and band-edge luminescence of the SiGe QWs is visible. After the sample anneals at temperatures above 750°C the multiple quantum wells (MQWs) grown with positive and no bias show only band-edge luminescence and the broad-band luminescence vanishes. With increasing RTA temperatures the NP lines get more intense and the line width decreases. These results are observed independently of the gas ambient, pure N_2 or N_2/H_2 mixtures, indicating that the effect cannot be attributed to hydrogen passivation of defects in the QWs. It is remarkable that the PL lines of the MQW grown with the substrate bias of + 1500 V shift continuously with temperature to higher energies, indicative of Ge diffusion from the wells into the Si barriers. In contrast, the MQW grown with floating bias shows only very a small shift up to RTA temperatures of 900°C and then a significant shift at 950°C. The MQW grown with the negative bias (−1500 V) shows no band-edge luminescence after RTA processing and the broad-band luminescence remains quite significant.

A possible interpretation of the result is the following. During e-beam evaporation of Si and Ge, many secondary and scattered electrons hit the substrate thus charging it negatively. Due to this negative charge, positive Si and Ge ions are accelerated towards the substrate damaging the growing layer. By applying a positive bias to the substrate the effect is suppressed, whereas a negative bias enhances the damage caused by the ions.

In order to obtain more information about the structural properties of these defects, a careful analysis by TEM of as-grown MQW deposited with and without bias as well as after RTA processing has been done. Before discussing the results in detail, a few general comments about the TEM

analysis are warranted. Fig. 3a shows a cross-sectional bright field image of an as-grown MQW containing 5 nm wide SiGe quantum wells (dark layers in the image) with a Ge concentration of 21.8%. A bias of + 1500 V was applied before starting the growth. The image reveals no extended defects, no interface contamination and smooth interfaces. Fig. 3b and Fig. 3c show high resolution images of the same sample investigated with (b) 300 keV and (c) 200 keV electrons in the TEM. In both images small defects show up as dark shadows, with extensions not larger than 5 nm. In the case of 300 kV conditions they show up in some cases with a stronger contrast. The defocus conditions optimized for these defects result in a rather weak contrast between Si and SiGe layers.

To insure that the defects are grown in defects, and are not created by the ion milling during the preparation of the TEM samples, or stem from electron bombardment during examination, the preparation and examination parameters were varied, and samples grown by other techniques, like atmospheric pressure chemical vapor deposition, were examined. The defects are found independent of the electron energies and of the dose, rendering damage during examination rather unlikely. However, the defects are only found in samples grown by solid source MBE, and not in samples grown by other techniques and prepared and examined with the same parameters. This gives strong indications that the defects are present in the as-grown film, although they might be point defects which get enlarged during preparation and examination.

In the next paragraph we demonstrate that these defects can be correlated with the PL features. As discussed in Fig. 2 the PL spectra of MBE grown Si/SiGe MQWs show band-edge luminescence after the RTA step at temperatures > 750°C or by applying a positive substrate bias. For this reason we carefully prepared TEM samples of MQWs which were grown under different bias conditions and with different subsequent annealing steps.

Fig. 4 compares TEM micrographs of a MQW with 5 nm wide $Si_{0.83}Ge_{0.17}$ wells separated by 10 nm-thick barriers grown at 550°C before and after annealing at 950°C and a MQW sample

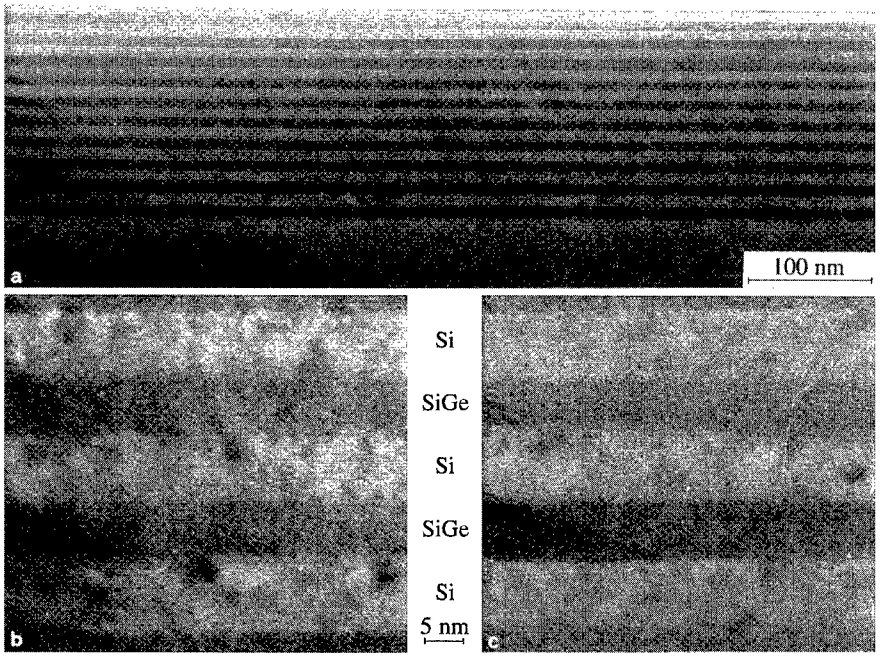

Fig. 3. Cross-section TEM micrographs of a Si/SiGe MQW structure, (a) bright field TEM image, (b) high-resolution TEM taken at 200 kV and (c) taken at 300 kV.

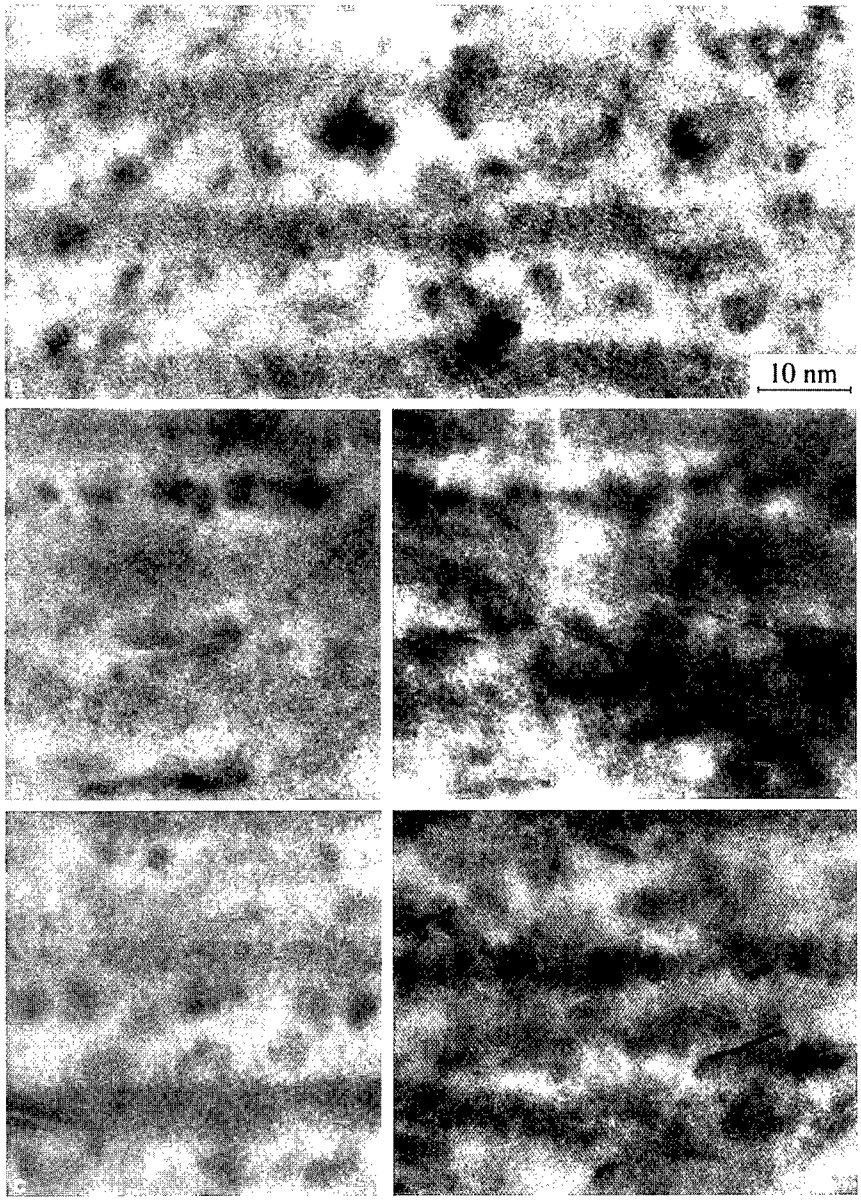

Fig. 4. Comparison of 2.4 K photoluminescence and cross-sectional TEM of Si/SiGe MQWs (a) before and (b) after RTA processing at 950°C for 240 s.

grown at 750°C. Whereas the TEM micrograph of the as-grown (550°C) sample (Fig. 4a) shows defects distributed throughout the wells and the barriers, the TEM micrograph of the annealed sample (Fig. 4b) exhibits defects only in the Si barriers. For clarity, the latter TEM micrograph is divided into two parts taken with different defocus conditions giving different contrasts for the defects. They are visible as dark spots lined up in the otherwise rather bright area of the Si wells. The SiGe layers are visible as gray bands of quite uniform color. For the sample grown at 750°C a similar behavior is

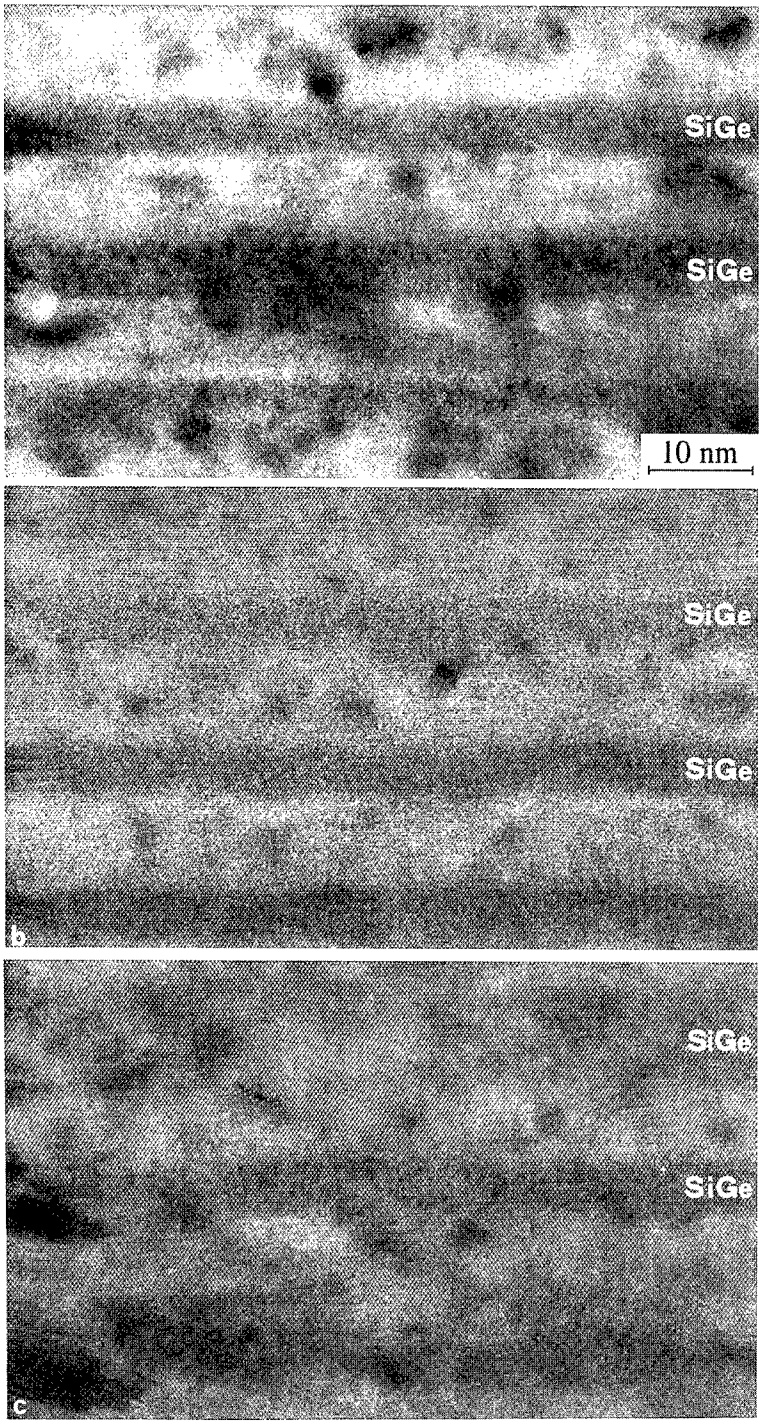

Fig. 5. High-resolution TEM micrographs of samples grown with (a) negative (-1500 V), (b) zero and (c) positive (+1500 V) substrate bias.

observed, the defects are lined up in the Si barriers. Notice that for the annealed sample, where the defects are found only in the Si barriers, intense phonon resolved luminescence of the SiGe wells is observed. In contrast, the as-grown sample reveals only a broad deep PL band, and at the same time the defects can be found in the SiGe as well as in the Si layers. This result gives clear proof of a correlation between the defects and the broad-band luminescence. Apparantly the annealing leads to an outdiffusion of the defects from the SiGe layers into the Si. This diffusion process may be strain driven, i.e. the defects lower overall strain in the system by moving from the SiGe into the Si layer. The diffusion behavior agrees well with the PL results of Sturm et al. [12] for CVD-grown Si/SiGe heterostructures subsequently implanted with Si and annealed at 600–800°C. It is also noteworthy that defects are only obtained in the Si barriers even without subsequent annealing for the samples grown at elevated temperatures ($>$ 700°C). Typically, at these growth temperatures phonon resolved PL is observed for MBE-grown SiGe quantum wells [6].

Since band-edge luminescence is observed also for samples grown at low temperatures (550°C) which were deposited with a negative bias, it is interesting to do the same careful TEM analysis with those samples. Fig. 5 compares TEM micrographs of MQWs grown with (a) positive bias (+ 1500 V), (b) zero bias and (c) negative bias (−1500 V). All samples have 17–21% Ge in the wells, a barrier width of 10 and well widths of 5 nm. The negative applied bias lead to a very defective sample throughout all layers. In addition, samples grown with a negative bias show contaminated substrate interfaces and rather large precipitate-like defects in the layers. Apparently the negatively biased substrate attracts positively charged particles in the MBE chamber.

The difference in the TEM cross-sectional micrographs for the positively and zero biased samples is not obvious. However, there are significantly less defects in the SiGe wells as in the Si barriers in the biased sample, whereas in the sample grown on the floating substrate the defects are more equally distributed. This result indicates that the activation energy to create a defect in the SiGe layer is lower than in a Si layer, which may again be an effect of the build in strain of the SiGe layers. This result agrees with the observation made for the photoluminescence of the samples. MQWs grown on floating substrates showed a broad deep luminescence, whereas the MQWs deposited on positively biased samples exhibit in no case broad luminescence but frequently phonon resolved band-edge luminescence.

4. Conclusions

Si/SiGe MQWs were grown by solid source MBE using different growth temperatures and substrate bias conditions. The samples were analyzed by TEM and PL before and after RTA at temperatures ranging from 750°C to 950°C. Our results give clear proof of an correlation between the appearance of defects in the SiGe wells and broad band PL. In addition, our results indicate that the defects are caused by ion bombardment during e-beam evaporation in solid source MBE. A positive substrate bias reduces the damage, particularly in the SiGe films. Subsequent annealing of the QW structures strongly improves the photoluminescence of the Si/SiGe MQWs by driving the defects out of the SiGe wells into the Si barriers.

References

[1] R. Zachai, K. Eberl, G. Abstreiter, E. Kasper and H. Kibbel, Phys. Rev. Lett. 64 (1990) 1055.
[2] K. Brunner, K. Eberl and W. Winter, Appl. Phys. Lett. 69 (1996) 1279.
[3] I. Morrison and M. Jaros, Phys. Rev. B 37 (1988) 916.
[4] J.-P. Nöel, N.L. Rowell, D.C. Houghton and D.D. Perovic, Appl. Phys. Lett. 57 (1990) 1037.
[5] K. Terashima, M. Tajima, N. Ikarashi, T. Niino and T. Tatsumi, Jpn. J. Appl. Phys. 30 (1991) 3601.
[6] J. Brunner, U. Menczigar, M. Gail, E. Friess and G. Abstreiter, J. Crystal Growth 127 (1993) 443.
[7] H.P. Zeindl, S. Nilsson, J. Klatt, D. Krüger and R. Kurps, J. Crystal Growth 157 (1995) 31.
[8] G. Otha, S. Fukatsu, N. Usami, Y. Shiraki and T. Hattori, J. Crystal Growth 157 (1995) 36.
[9] N. Rowell, J.-P. Nöel, D.C. Houghton, A. Wang, L.C. Lenchyshyn, M.L.W. Thewalt and D.D. Perovic, J. Appl. Phys. 74 (1993) 2790.

[10] E.R. Glaser, T.A. Kennedy, D.J. Godbey, P.E. Thompson, K.L. Wang and C.H. Chern, Phys. Rev. B 47 (1993) 1305.
[11] J.-P. Nöel, N.L. Rowell, D.C Houghton, A. Wang and D.D. Perovic, Appl. Phys. Lett. 61 (1992) 690.
[12] J.C. Sturm, A.St. Amour, Y. Lacroix and M.L.W. Thewalt, Appl. Phys. Lett. 64 (1994) 2291.
[13] I.A. Buyanova, A. Henry, W.M. Chen, W.X. Ni, G.V. Hansson and B. Monemar, Appl. Phys. Lett. 67 (1995) 1642.

ELSEVIER

Journal of Crystal Growth 175/176 (1997) 1152–1156

JOURNAL OF CRYSTAL GROWTH

Photoluminescence spectra of shadow masked multiple quantum wells

S. Sopitpan*, P. Cheewatas, S. Thainoi, S. Ratanathammaphan, S. Panyakeow

Semiconductor Device Research Laboratory, Chulalongkorn University, Bangkok 10330, Thailand

Abstract

Lines of local epitaxy of GaAs/GaAlAs multiple quantum wells with linewidth of 7 and 5 μm having line separation of 250 μm were fabricated by molecular beam epitaxy (MBE) using shadow masking technique. Photoluminescence (PL) measurements at 10 K were performed by using an argon laser with cylindrical lens producing line focus and with circular lens producing point focus for the excitation. The focussed line and focussed point of laser beam were ~100 μm and could be aligned to the stripes of MQW. The PL spectrum characteristics reflect the quantum well structure as well as the crystal quality of shadow masked epitaxy layers. The PL spectrum shows double PL peaks at 758 and 774 nm with nearly equal intensity when the exciting beam lined parallel to the stripes of MQW have a 7 μm window and quantum well width of 30 monolayers. Overlapping PL peaks at 810 and 818 nm were observed from MQW having 5 μm window and quantum well width of 60 monolayers. Similar results were obtained by point focussed laser beam and by line focussed laser beam at perpendicular configuration. A stronger PL peak at 818 nm was clearly emphasized by strip-off MQW samples having 5 μm stripes. The PL peak from a shadow masked MQW sample was sharp having spectral FWHM of 14 nm and was relatively stronger than that obtained from conventional MQW samples. These experimental data indicated that MBE grown MQW mesa using shadow masking technique is suitable for quantum device fabrication.

Keywords: Photoluminescence; Shadow mask; Molecular beam epitaxy

1. Introduction

Mesa structures of GaAs/GaAlAs multiple quantum well (MQW) have been widely used in many quantum device fabrications. Generated or injected carriers could be easily confined in this mesa structure. Vertical switching device could be designed and realized by the mesa structuring technique. Photolithography and chemical etching are conventional processing steps of the mesa structure. However, chemical etching creates many defects on the etched surfaces affecting active MQW layers. These defects degrade device performance and cause low yield of device mass production. In addition, chemical etching does not allow a reproducible control of the layer thickness of an atomic scale which is needed for three dimensional integration of complex devices having MQW structure.

* Corresponding author. Fax: + 66 2 2518991; e-mail: fengdkg@chulkn.car.chula.ac.th.

0022-0248/97/$17.00 Copyright © 1997 Elsevier Science B.V. All rights reserved
PII S0022-0248(96)01220-1

Direct preparation of mesa structure by molecular beam epitaxy (MBE) growth is preferable [1] to avoid any chemical etching of active MQW layers. A novel method for mesa growth of epitaxial GaAs layers by MBE technique using patterned shadow masks was investigated [2] and was demonstrated in fabricating GaAlAs/GaAs hetero-*nipi* structure [3].

This research paper is an attempt to apply the shadow masking technique in growing GaAs/GaAlAs mesa epitaxy MQW by MBE technology. Shadow masked MQW samples were examined by photoluminescence (PL) measurement to confirm the quantum well phenomenon and its sharpness. The successful MBE grown mesa MQW using shadow masks gives stronger PL than a conventional MBE sample. An experiment of PL measurement on a strip-off sample having mesa MQW structure was also conducted to ensure the result. It is found that PL peaks from mesa MQW by shadow masking technique are three times stronger than a reference plain surface MQW and the PL spectrum has an acceptable sharpness of quantum effect (14 nm). This shadow masking technique is suitable for fabricating of MQW having complex structures.

2. Shadow mask preparation

The shadow masks consisted of MBE grown $Ga_{0.5}Al_{0.5}As$ and GaAs layers. The $Ga_{0.5}Al_{0.5}As$ layer, so-called *mask spacer* is grown on (1 0 0) semi-insulator GaAs substrate for 3.5 μm thickness. The GaAs layer is then consecutively grown over the top surface of the mask spacer for about 1 μm thickness. This GaAs layer is called a *mask layer*.

A shadow mask preparing process is adapted from Gulden et al. [2] by using $H_3PO_4 : H_2O_2 : H_2O = 1 : 1 : 10$ (by volume) to open the windows on the mask layer instead of $NH_4OH : H_2O_2 : H_2O$ solution for reducing shadow effect due to the space between an edge of the mask and the surface during the MBE growing process. Line shaped window patterns of 7 and 5 μm width and 250 μm separation were provided for the experiment. The micrograph cross-sectional view of shadow mask is shown in Fig. 1. The

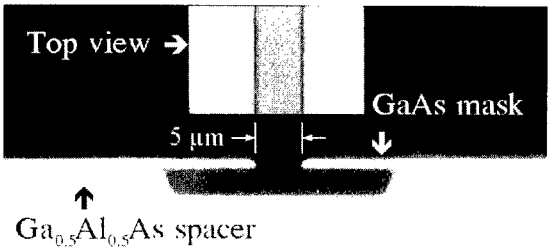

Fig. 1. Cross-sectional view of the shadow mask by an optical microscope.

masked sample is ready to be epitaxially grown in MBE machine for patternized MQW mesa structure.

3. Growth of multiple quantum wells through shadow mask

There were three samples fabricated in this experiment.

- Sample #1: This is a reference sample to test the conditions of MQW growth. The MQW structure was grown on the plain (1 0 0) GaAs substrate.
- Sample #2: The sample which was prepared with 7 μm wide line patterns.
- Sample #3: The sample which was prepared with 5 μm wide line patterns.

A conventional MBE method was used to fabricate series of $GaAs/Ga_{0.8}Al_{0.2}As$ to form a structure of 10 identical unit quantum wells. There are two different well widths, 60 monolayers and 30 monolayers. Samples #1 and #3 have 60 monolayers well width and sample #2 has 30 monolayers well width. The barrier thickness of all samples are 180 monolayers. Clean surfaces of GaAs mask layers and GaAs substrate under shadow masks is confirmed by RHEED pattern before each MBE growth. Substrate temperature during the growths was 650°C while the substrates were rotated at 4 rpm for uniformity. Figs. 2 and 3 show the cross-sectional views of shadow masked mesa MQW by an optical microscope and a scanning electron microscope, respectively.

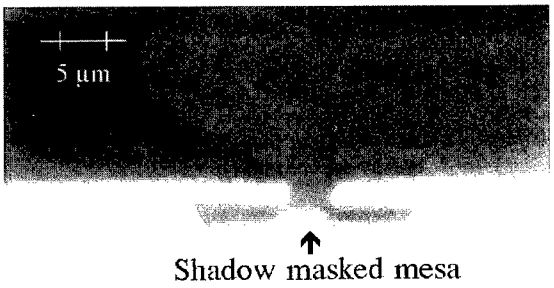

Fig. 2. Cross-sectional view of shadow masked mesa MQW by an optical microscope.

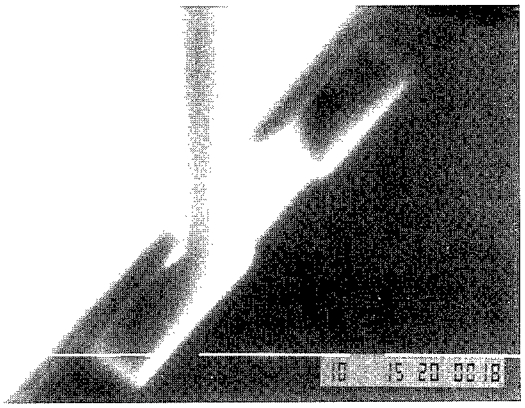

Fig. 3. Perspective cross-sectional view of shadow masked mesa MQW by SEM.

Furthermore, after MBE growth process, a part of sample #3 was passed through a *strip-off* procedure by second reverse photolithography. The mesa-line structures were protected by photoresist after the photolithography process. Shadow masks and GaAs/$Ga_{0.8}Al_{0.2}As$ quantum well structure grown over the masks were then partially removed with $NH_4OH : H_2O_2 : H_2O = 3 : 1 : 15$ (by volume). Fig. 4 shows a cross-sectional view of mesa-MQW after the strip-off to eliminate the shadow masks for effectiveness of MQW signal.

4. Photoluminescence results

The photoluminescence (PL) measurements were conducted by using 50 mW Ar^{-1} laser as the excitation of all samples set up in 10 K cryogenic system. The laser beam was point focussed by a circular lens and was line focussed by a cylindrical lens onto the stripes of MQW. The line focus could be aligned parallel to the stripes (0°) and perpendicular to the stripes (90°) for analysis of the PL results. The focussing dimension was ~ 100 μm for spot and line. PL signals were collected by a set of collimated lens and passed through a monochromator. Spectral PL data were detected by a photomultiplier and recorded in a computer for analytical works.

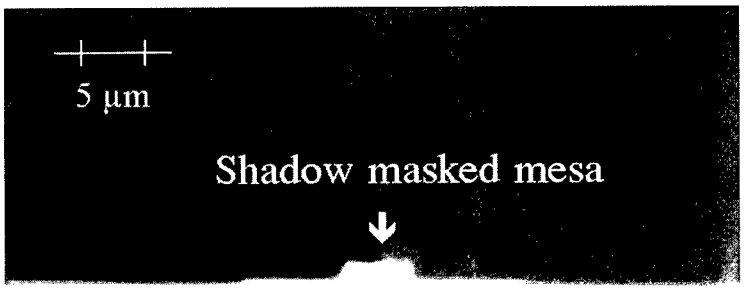

GaAs substrate

Fig. 4. Cross-sectional view of mesa-MQW after strip-off process.

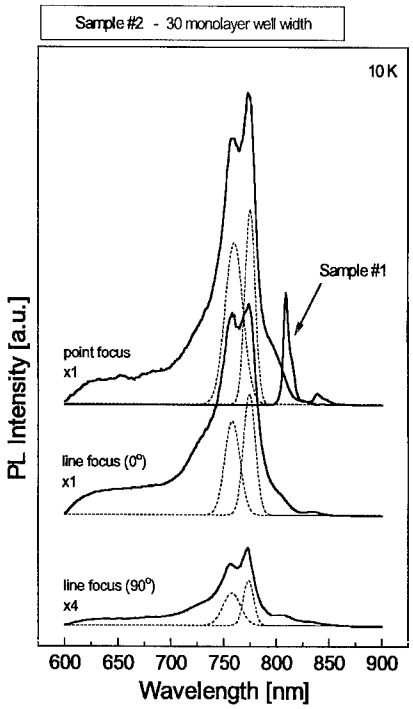

Fig. 5. PL spectra at 10 K of shadow masked mesa-MQW stripe 7 μm wide (Sample #2).

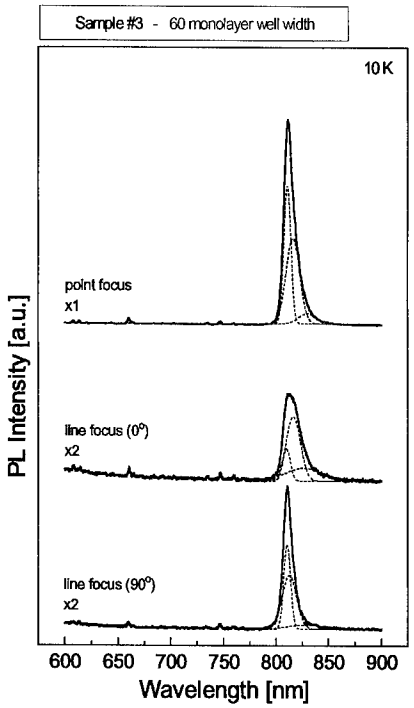

Fig. 6. PL spectra at 10 K of shadow masked mesa-MQW stripe 5 μm wide (Sample #3).

Fig. 5 shows PL spectra of shadow masked mesa-MQW stripes with 7 μm width (Sample #2) when the sample was excited by point and line of laser beams both at 0° and 90° configurations. The dash lines in the figures were created by using the *Multiple Gauss fitting* utility in Origin™ plotting program. Double PL peaks at 758 and 774 nm were observed in all cases. The strongest PL peaks were obtained by point focus due to the most intense excitation laser beam. In case of line focus, at 0° configuration, the sample gave nearly equal intensity of double PL peaks but less strong signals due to shadow mask effect in optical alignment of the PL experimental setup. At 90° configuration, PL peaks become weaker due to the smaller effective area. The separation of these double PL peaks (about 16 nm) could be explained by the variation of narrow quantum well widths between MQW on shadow mask and mesa MQW under shadow mask. The quantized states of electrons in quantum wells are defined by well thickness [4].

Fig. 6 shows PL results from sample #3. An objective for preparing this sample is to provide a tunability of the quantized state in the shadow masked MQW. Overlapping of PL peaks at 810 and 818 nm were observed and referred to the previous experiment [5]. Small variations occur due to broader quantum well width. The strongest PL peaks were again observed by point focus due to the most intense excitation of laser beam. However, line focus at 0° configuration gave lowest PL peaks due to narrower window and this made PL alignment more difficult. When the sample was rotated to 90° configuration, PL alignment became easier and better PL signals were detected.

To ease the PL alignment, shadow masks of sample #3 were partially stripped-off and were studied under the same conditions. The only strongest PL peak was always at 818 nm which corresponded to the mesa-MQW stripe while the PL peak at 810 nm was comparatively much smaller. The best configuration for the stripped-off sample

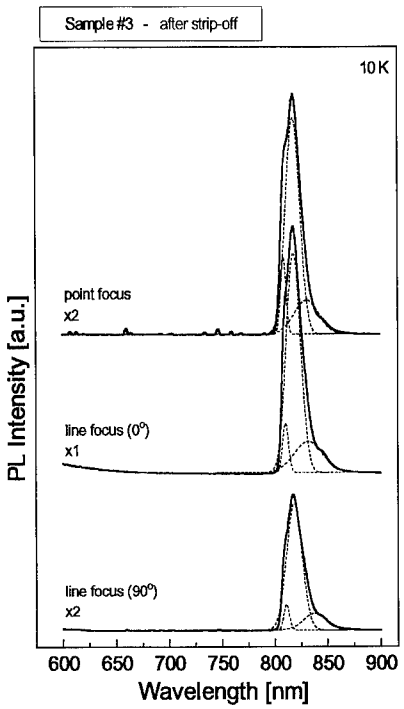

Fig. 7. PL spectra at 10 K of strip-off mesa-MQW stripe 5 μm wide (Sample #3).

was line focus at 0° position due to efficient PL alignment which becomes more effective than point focus excitation. The line focus at 90° configuration still gave weak PL peaks, but PL signals from strip-off sample were always stronger than those from shadow masked samples as shown in Fig. 7. PL peaks were about 3 times stronger after the strip-off process.

All PL spectra from both samples #2 and #3 had nearly the same *full width at half maximum* (FWHM) of 14 nm which was reasonably sharp compared to that obtained from the reference PL peaks from a plain surface MQW sample (Sample #1).

5. Conclusions

The 10 MQW mesa structures were grown through shadow masks onto the GaAs substrates by MBE technology. The structures were self-organized by the mesa shapes grown. PL spectra indicate that the mesa structures consist of multiple quantum wells as in the previous study. PL peaks from the MQW can be tuned by varying the well layer thickness. The sharpness of PL peaks reflects the mesa crystal quality. The experimental results showed that the shadow mask technique was suitable for future patternized MQW device fabrications.

Acknowledgements

The research work was financially supported by the Royal Thai Government Research Fund and the National Science and Technology Development Agency of Thailand. Part of the initial research investigation was conducted at Universität der Bundeswehr München, Germany under Professor I. Eisele's supervision with the scholarship support from DAAD sandwich program.

References

[1] E. Hammerl, F. Wittmann, J. Messarosch, I. Eisele, V. Huber and H. Oppolzer, Mater. Res. Soc. Symp. Proc. 220 (1991) 27.

[2] K.H. Gulden, X. Wu, J.S. Smith, P. Kiesel, A. Höfler, M. Kneissl, P. Riel and G.H. Döhler, Appl. Phys. Lett. 62 (1993) 3180.

[3] X. Wu, K.H. Gulden, M. Thomas, J.S. Smith, J.R. Whinnery, S. Malzer, P. Kiesel, M. Kneissl and G.H. Döhler, Appl. Phys. Lett. 62 (1993) 152.

[4] R.L. Liboff, Introductory Quantum Mechanics, (Addison-Wesley, New York, 1991) p. 92.

[5] S. Sopitpan, S. Thainoi, P. Cheewatas, S. Ratanathammapan, T. Cholapranee, M. Sawadsaringkarn and S. Panyakeow, Proc. 18th Conf. on Electrical Engineering, Cholburi, Thailand (1995) p. 566.

ELSEVIER

Journal of Crystal Growth 175/176 (1997) 1157–1161

JOURNAL OF CRYSTAL GROWTH

Radiative decay in type-II GaP/AlP/GaP quantum wells

S. Nagao[a,*], K. Fujii[a], T. Fujimori[a], H. Gotoh[a], H. Ito[b], F. Minami[b]

[a] *Opto-electronics Laboratory, Mitsubishi Chemical Corporation, 1000, Higashi-mamiana, Ushiku, Ibaraki 300-12, Japan*
[b] *Department of Applied Physics, Tokyo Institute of Technology, Meguro-ku, Tokyo 152, Japan*

Abstract

We have studied time-resolved photoluminescence (PL) of type-II GaP/AlP/GaP quantum wells with different well widths and acquired detailed information concerning the mechanisms of the radiative recombination. At low temperatures, the PL spectra consist mainly of a no-phonon line. The decay of the no-phonon line was slow and nonexponential. The decay curves could be fitted to a model which assumes that the radiative recombination occurs as the result of both incoherent and coherent Γ–X scattering due to disorder at the interface. The fit revealed that the dominant Γ–X mixing mechanism was random scattering caused by fluctuations in the potential at the interface. Based on simple perturbation theory, the observed increase in the radiative decay rate with decreasing well width was explained by the increase of overlap of the electron envelope wave functions as well as the decrease of Γ–X energy separation. The model suggests that the magnitude of the potential responsible for the Γ–X mixing is considerably greater than those observed in the type II GaAs/AlAs heterostructures.

Keywords: Time-resolved photoluminescence; Type-II quantum wells; Localized indirect excitons; Γ–X mixing

1. Introduction

Lattice matched GaP and AlP are both indirect bandgap compound semiconductors with conduction band minima at the X points where the band lineup is type-II at the AlP/GaP heterointerface [1]. The schematic band alignment of a GaP/AlP/GaP quantum well (QW) is shown in Fig. 1. In such type-II (staggered) band lineups, the AlP well layer only confines the electrons at the X minima; the holes lie on the band edge at the zone center in the GaP layers. Thus in the type-II configuration, electrons and holes are separated both in real and in k-space, and one can expect no oscillator strength for the optical transition if there are no momentum mixing mechanisms. In the type-II GaAs/AlAs heterostructures, however, there have been a number of studies showing the presence of a finite oscillator strength caused by Γ–X mixing effects [2–14]. The Γ–X mixing can arise purely from a potential step at the heterointerface without any zone folding effects associated with the periodicity of the superlattice [9].

This paper reports on our study of radiative decay in type-II GaP/AlP/GaP QWs with different well widths. Highly efficient continuous-wave (cw)

* Corresponding author. E-mail: nagao@rc.m-kagaku.co.jp.

0022-0248/97/$17.00 Copyright © 1997 Elsevier Science B.V. All rights reserved
PII S0022-0248(96)01006-8

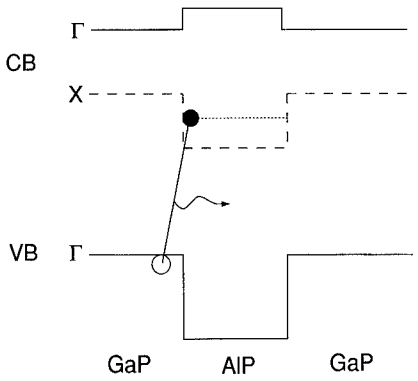

Fig. 1. Schematic type II band alignment at GaP/AlP/GaP heterointerfaces. Solid lines represent the Γ extrema of conduction and valence band. Dashed line is the X minima of conduction band and dotted line indicates the X confined electron state.

photoluminescence (PL) is obtained at low temperatures from GaP/AlP/GaP QW structures with simple type-II configurations [15]. Time-resolved PL has been employed to clarify the recombination mechanism. A slow and nonexponential decay of the luminescence was explained by the emission of the localized indirect excitons at the interface. We analyzed the decay data based on simple perturbation theory.

2. Experimental procedure

The GaP/AlP/GaP multiple QW (MQW) structures were grown on GaP (0 0 1) substrates by gas source MBE (VG Semicon V80H) using PH_3 and elemental Ga and Al. The MQW structures consist of 5 periods of AlP layers separated from each other by 30-nm thick GaP layers. The AlP layer thicknesses were varied with the samples (1, 2, 3, 5, and 8 monolayers (ML)). After thermal cleaning of the surface and subsequent growth of a 250-nm GaP buffer layer, the MQW structures were grown at 620°C. The growth rates of AlP and GaP were 0.25 and 0.5 ML/s, respectively. During the growth of the GaP and AlP layers, reflection high energy electron diffraction (RHEED) showed intense and sharp spots on the Laue rings and long lasting intensity oscillations in specular beams, indicating the progression of layer-by-layer growth [16]. Especially for the AlP layers, very precise ML growth control was performed by means of RHEED intensity oscillations so as to reduce the effect of the fluctuations of the Al molecular beams just after opening of the effusion cell shutter.

Cw PL spectra were excited with the 325 nm line from a He–Cd laser and detected via a spectrometer by a photomultiplier using lock-in techniques. The excitation power density was 0.3 W/cm^2. For time-resolved measurement, the excitation source was the second harmonic light of a Ti:sapphire laser, pumped by a frequency-doubled Q-switched Nd:YAG laser. The repetition rate, pulse width and pulse energy of the excitation pulse were 3 kHz, 100 ns and 0.3 μJ, respectively. The luminescence was detected by a gated photon counter. The temporal resolution of the detector was ~5 ns.

3. Results and discussion

Fig. 2 shows the cw PL spectrum from the 2 ML AlP wells measured at 4.2 K. This spectrum is typical of the samples studied, consisting of a strong no-phonon line and a weak phonon sideband

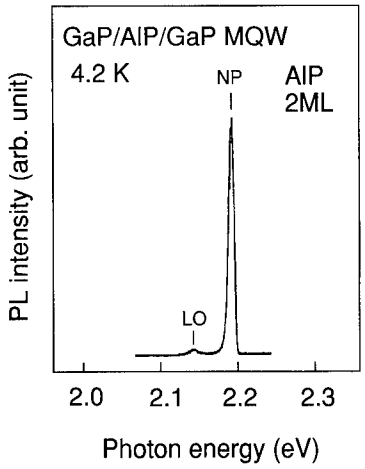

Fig. 2. Cw PL spectra at 4.2 K from a GaP/AlP/GaP MQW structure with well width of 2 ML.

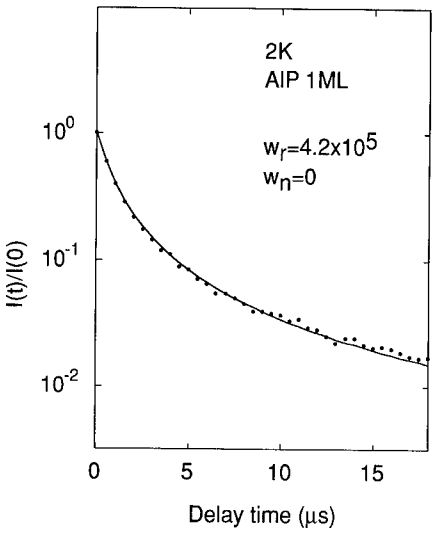

Fig. 3. Luminescence decay curve of the no-phonon line for the 1 ML AlP wells at 2 K. Full curve is Eq. (2), with $w_r = 4.2 \times 10^5\ s^{-1}$ and $w_n = 0\ s^{-1}$.

50 meV lower in energy, very close to the Γ-point LO phonon energy of GaP. The no-phonon line is derived from the transition between the confined AlP X_z and the GaP Γ state [15]. The presence of the strong no-phonon line and the GaP LO (Γ) phonon satellite suggests that there are significant momentum mixing mechanisms between the X and Γ electron states, which result in a finite oscillator strength. The possible sources are coherent and incoherent scatterings by the heterointerface. Coherent scattering is expected to occur due to breakdown of symmetry at the interfaces by the presence of ultra-thin AlP layers in the GaP bulk crystalline structure. Incoherent scattering is induced by roughness at the interface, which gives rise to random potential fluctuations.

The decay after pulsed excitation is slow and nonexponential, as shown for 1 ML AlP wells in Fig. 3. This temporal behavior can be explained by a model which assumes Γ–X mixing mechanisms for localized indirect excitons by disorder at the interface [17, 18, 6]. According to the model, for localized indirect excitons at the zone boundary, whose decay is permitted by scattering to Γ by a random potential, the time decay of the

Table 1
Sample parameters, where Δ is the energy separation between the GaP Γ and AlP X electron states, and $\langle \phi_C^{AlP(X)} | \phi_C^{GaP(\Gamma)} \rangle$ is the overlap integral of the two electron envelop wave functions; the parameters w_r and w_n are random and non-random average decay rates, respectely, obtained from fits to the PL decay curves

AlP (ML)	Δ (eV)	$\langle \phi_C^{AlP(X)} \vert \phi_C^{GaP(\Gamma)} \rangle$ ($\times 10^{-2}$)	w_r ($10^5\ s^{-1}$)	w_n ($10^5\ s^{-1}$)
1	0.62	6.4	4.2	< 0.01
2	0.70	4.3	0.38	< 0.01
3	0.77	3.6	0.33	< 0.001
5	0.85	3.0	0.28	< 0.01
8	0.90	2.6	0.12	< 0.001

no-phonon line is given by

$$I(t)/I(0) = (1 + 2w_r t)^{-3/2}, \tag{1}$$

where w_r is the average radiative decay rate due to random potential scattering. If in addition to random (incoherent) scattering, there is a non-random (coherent) contribution w_n to the decay rate, Eq. (1) is modified [6] as

$$I(t)/I(0) = e^{-w_n t}[1 + 2w_n t/(1 + w_n/w_r)](1 + 2w_r t)^{-3/2}. \tag{2}$$

The experimental data fitted the time dependence predicted from this model. The best fit was obtained with $w_r = 4.2 \times 10^5\ s^{-1}$ and $w_n = 0\ s^{-1}$ for 1 ML AlP wells, as shown in Fig. 2. The fitted values of w_r and w_n are given in Table 1. The parameter w_r increased with decreasing AlP well width. In all the samples w_n was considerably small and could be zero. The dominant mixing mechanism is therefore considered to be random scattering.

For the no-phonon transitions of indirect excitons, the $\boldsymbol{k}$-selection rule requires there to be mixing between the X and Γ states. In the first-order perturbation theory for Γ–X mixing by a potential V [10], the matrix element for electric dipole transitions between conduction and valence bands is given by

$$M_{c,v} = \frac{\langle \psi_C^{AlP(X)} | V | \psi_C^{GaP(\Gamma)} \rangle \langle \psi_C^{GaP(\Gamma)} | p | \psi_V^{GaP(\Gamma)} \rangle}{\Delta}, \tag{3}$$

where ψ_C and ψ_V are wave functions at the conduction and valence-band extrema, Δ is the Γ–X splitting ($E_\Gamma - E_X$), and p is the dipole operator. The mixing is assumed to occur only between the AlP X states and the lowest Γ states in GaP. The oscillator strength for radiative transition is proportional to the square of the matrix element. The mixing factor in Eq. (3) can be transformed as follows [9]:

$$\langle \psi_C^{AlP(X)} | V | \psi_C^{GaP(\Gamma)} \rangle = \langle u_C^{AlP(X)} | V | u_C^{GaP(\Gamma)} \rangle \langle \phi_C^{AlP(X)} | \phi_C^{GaP(\Gamma)} \rangle, \quad (4)$$

where u is the Bloch part of the wave function and ϕ is the slowly varying envelope wave function. The radiative decay rate is thus given by

$$w_{X-\Gamma} = w_{\Gamma-\Gamma}(V_{mix}\langle \phi_C^{AlP(X)} | \phi_C^{GaP(\Gamma)} \rangle / \Delta)^2, \quad (5)$$

where $w_{\Gamma-\Gamma}$ is $\langle \psi_C^{GaP(\Gamma)} | p | \psi_V^{GaP(\Gamma)} \rangle^2$, and V_{mix} is $\langle u_C^{AlP(X)} | V | u_C^{GaP(\Gamma)} \rangle$. Table 1 gives the energy separation between the Γ and X electron states and the overlap integral of the electron envelope wave functions as calculated using a Kronig–Penney model. In spite of the large energy separation between the X and Γ electron states and the small overlap integral due to the sample structure, we obsereved finite radiative decay rates in the range of 10^4–10^6 s^{-1}. This suggests that the GaP/AlP heterostructure has a considerably large mixing potential V_{mix}. In the direct bandgap semiconductors, the radiative decay rate is larger than 1×10^9 s^{-1}, so we assume a value of 10^9–10^{10} s^{-1} for $w_{\Gamma-\Gamma}$. The resulting V_{mix} from Eq. (5) is of the order of 10–10^2 meV, which is far greater than those obtained in the type-II GaAs/AlAs system [9, 13].

Fig. 4 shows the radiative decay rate w_r as a function of $(\langle \phi_C^{AlP(X)} | \phi_C^{GaP(\Gamma)} \rangle / \Delta)^2$. The linear relationship seen in Fig. 4 shows that the model can well explain the dependence of w_r on AlP well width. The increase in w_r with decreasing AlP well width results from an increase in the overlap integral of the electron envelope functions as well as a decrease in the energy splitting Δ. The mixing potential V_{mix} is almost completely independent of AlP well width.

One might expect a coherent contribution to the radiative decay rate due to the abrupt potential step along the growth direction at the heterointerface. The absence of such a coherent contribution is attributed to the small lateral scale of roughness at the interface. In the samples, the lateral scale of roughness is far smaller than the lateral size of excitons and the effective interface roughness is much less than one atomic layer [15]. In GaAs/AlAs QWs, the lateral size of roughness on AlAs-on-GaAs interfaces is close to or larger than exciton diameter, whereas on GaAs-on-AlAs interfaces, it is so small as compared with exciton diameter that they act as a smooth interface [19]. This is due to a far small diffusion length of the Al atoms along the AlAs surface in contrast to that of the Ga atoms along the GaAs surface. In the GaP/AlP system which is being grown in this study, both of the AlP-on-GaP and GaP-on-AlP interfaces have such a "pseudo-smooth" nature. Diffusion of both the Ga atoms along the GaP surface and the Al atoms along the AlP surface is expected to be very small. Since this pseudo-smooth interface has a stochastic variation in the distribution of microsteps, excitons localized in different regions would experience different effective well widths. Thus the pseudo-smooth interface would act as an effective and random scattering source due to its abruptness and random fluctuations of average local potential.

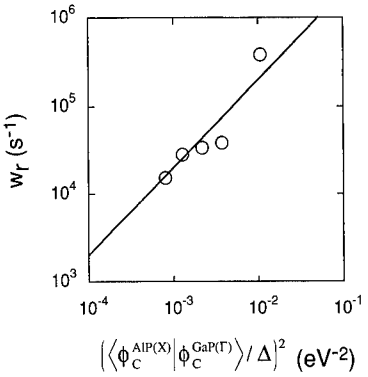

Fig. 4. Average random decay rates (w_r) obtained from fits to the PL decay curves, plotted as a function of $(\langle \phi_C^{AlP(X)} | \phi_C^{GaP(\Gamma)} \rangle / \Delta)^2$, where Δ is the energy separation between the GaP Γ and AlP X electron states, and $\langle \phi_C^{AlP(X)} | \phi_C^{GaP(\Gamma)} \rangle$ is the overlap integral of the two electron envelope wave functions.

4. Conclusions

We investigated radiative decay in type-II GaP/AlP/GaP quantum wells with thickness of 1, 2, 3, 5, and 8 ML. The no-phonon line at 2 K showed a slow and nonexponential decay. This temporal behavior was interpreted as the emission from the localized indirect excitons scattered by random fluctuations in potential at the GaP/AlP interface. The average random radiative decay rate increased with decreasing well width, which was interpreted to be the result of the increase of overlap between the X and Γ electron envelope wave functions as well as the decrease of Γ–X energy splitting. The simple perturbation theory suggested that the Γ–X mixing potential at the GaP/AlP heterointerface was far larger than that observed in the type-II GaAs/AlAs system.

References

[1] K. Adomi, N. Noto, A. Nakamura and T. Tanaka, J. Crystal Growth 124 (1992) 570.
[2] P. Dawson, B.A. Wilson, C.W. Tu and R.C. Miller, Appl. Phys. Lett. 48 (1986) 541.
[3] E. Finkman, M.D. Sturge and M.C. Tamargo, Appl. Phys. Lett. 49 (1986) 1299.
[4] G. Danan, B. Etienne, F. Mollot, R. Planel, A.M. Jean-Louis, F. Alexandre, B. Jusserand, G. Le Roux, J.Y. Marzin, H. Savary and B. Sermage, Phys. Rev. B 35 (1987) 6207.
[5] F. Minami, K. Hirata, K. Era, T. Yao and Y. Masumoto, Phys. Rev. B 36 (1987) 2875.
[6] E. Finkman, M.D. Sturge, M.-H. Meynadier, R.E. Nahory, M.C. Tamargo, D.M. Hwang and C.C. Chang, J. Lumin. 39 (1987).
[7] M.-H. Meynadier, R.E. Nahory, J.M. Worlock, M.C. Tamargo, J.L. De Miguel and M.D. Sturge, Phys. Rev. Lett. 60 (1988) 1338.
[8] B.A. Wilson, Carl E. Bonner, R.C. Spitzer, P. Dawson, K.J. Moore and C.T. Foxon, J. Vac. Sci. Technol. B 6 (1988) 1156.
[9] P. Dawson, K.J. Moore, C.T. Foxon, G.W. 't Hooft and R.P. Van Hal, J. Appl. Phys. 65 (1989) 3606.
[10] M.S. Skolnick, G.W. Smith, I.L. Spain, C.R. Whitehouse, D.C. Herbert, D.M. Whittaker and L.J. Reed, Phys. Rev. B 39 (1989) 11191.
[11] B.A. Wilson, Carl E. Bonner, R.C. Spitzer, R. Fischer, P. Dawson, K.J. Moore, C.T. Foxon and G.W. 't Hooft, Phys. Rev. B 40 (1989) 1825.
[12] J. Feldmann, J. Nunnenkamp, G. Peter, E. Göbel, J. Kuhl, K. Ploog, P. Dawson and C.T. Foxon, Phys. Rev. B 42 (1990) 5809.
[13] M. Nakayama, K. Imazawa, K. Suyama, I. Tanaka and H. Nishimura, Phys. Rev. B 49 (1994) 13564.
[14] W.R. Tribe, P.C. Klipstein, R.A. Woolley and J.S. Roberts, Phys. Rev. B 51 (1995) 9735.
[15] S. Nagao et al., J. Appl. Phys., to be published.
[16] T. Fujimori, S. Nagao and H. Gotoh, J. Crystal Growth 127 (1993) 213.
[17] M.V. Klein, M.D. Sturge and E. Cohen, Phys. Rev. B 25 (1982) 4331.
[18] M.D. Sturge, E. Cohen and R.A. Logan, Phys. Rev. B 27 (1983) 2362.
[19] M. Tanaka and H. Sakaki, J. Crystal Growth 81 (1987) 153.

ELSEVIER

Journal of Crystal Growth 175/176 (1997) 1162–1166

JOURNAL OF CRYSTAL GROWTH

Temperature-insensitive photoluminescence above 300 K in strained $Ga_xIn_{1-x}As$ multiple quantum wire heterostructures

D.E. Wohlert, S.T. Chou[1], K.Y. Cheng*

Department of Electrical and Computer Engineering and Microelectronics Laboratory, University of Illinois at Urbana-Champaign, Urbana, Illinois 61801, USA

Abstract

Stable peak wavelength photoluminescence (PL) spectra has been observed in $Ga_xIn_{1-x}As$ strained multiple quantum wire (MQWR) heterostructures over a temperature range between 250 and 380 K. The MQWR samples were grown in situ by molecular beam epitaxy using the strain-induced lateral-layer ordering (SILO) process to create the quantum wires. The formation of the strained $Ga_xIn_{1-x}As$ quantum wires and the amount of the strain associated with the wires depends on the growth conditions and structural configuration of the MQWR active region. Samples grown near a substrate temperature of 500°C show a negligible net PL peak wavelength shift between 77 and 380 K. Red shifts and blue shifts of PL peak wavelengths between 77 and 380 K are observed in samples grown at temperatures less than and greater than 500°C, respectively. Due to the multi-axial strain fields induced by the SILO process in the MQWR active regions, the PL peak wavelength of all the MQWR samples stabilize at ~ 1.61 μm for temperatures above 250 K. The temperature dependent shift of peak PL wavelength between room temperature and 72°C for these MQWR heterostructures is as low as 0.2 Å/°C.

PACS: 68.65. + g; 81.15.Hi; 78.66.Fd

Keywords: QWR; PL; PPL; Multi-axial strain; MBE; SILO

1. Introduction

The well documented improvements in performance of quantum well (QW) lasers over double heterostructure lasers serve as motivation to develop quantum wire (QWR) lasers in the hope of attaining further improvements. The superior characteristics of QW devices such as lower threshold currents, decreased temperature sensitivity, higher differential gain, and a narrower gain spectrum are mainly due to the localized step-like nature of the density of states (DOS) function for QWs [1]. Since the DOS function for QWRs is even more localized, QWR lasers are expected to out perform their QW

* Corresponding author. Fax: + 1 217 244 6375; e-mail: k-cheng@uiuc.edu.

[1] Present address: Electrical Engineering Department, Chung-Cheng Institute of Technology, Ta-Hsi, Tao-Yuan, Taiwan 335, Taiwan, ROC.

0022-0248/97/$17.00 Copyright © 1997 Elsevier Science B.V. All rights reserved
PII S0022-0248(96)01032-9

counterparts. However, due to limitations in current QWR fabrication technology it is very difficult to physically realize nanometer-size wires with uniform cross-sections. As a consequence of wire imperfection, the DOS function is QW-like making the theoretically predicted advantages of QWRs not noticeable [2]. Nevertheless, many interesting properties have already been observed in these non-ideal QWR device structures [3–5].

Recently, we discovered a unique temperature insensitive photoluminescence (PL) behavior in strained $Ga_xIn_{1-x}As/InP$ multiple quantum wire (MQWR) heterostructures prepared by the strain induced lateral-layer ordering (SILO) process [6]. The PL peak wavelength would either not shift between 77 K and room temperature or would blue shift with increasing temperature depending on the MQWR layer structure. Furthermore, the peak PL wavelength converges to about 1.61 μm at 300 K for every sample. In order to utilize such strained MQWR structures in high speed fiber optical communication systems, the PL peak wavelength needs to be tuned to 1.55 μm and maintained at that value for temperatures greater than 300 K. It is plausible to meet these requirements based on the results presented in Ref. [6] since the PL wavelength shift was found to be a function of the strain distribution within the MQWR active region where the multi-axial strain itself is controlled by the layer structure in the active region and the growth conditions [6, 7]. Therefore, to further pursue strained $Ga_xIn_{1-x}As$ MQWR structures as stable emitters for high speed fiber optical communication systems we have investigated the multi-axial strain which exists in the MQWR active regions. Specifically, in this study, we report on the growth temperature effect on the PL peak wavelength shift as well as the high temperature (~100°C) PL behavior in strained $Ga_xIn_{1-x}As$ MQWR structures.

2. Experimental procedure

Strained $Ga_xIn_{1-x}As$ MQWR heterostructures have been grown in situ on (1 0 0) on-axis InP substrates by MBE using the SILO process. The details of the growth conditions have been described in a previous publication [7]. To have precise control of the layer composition, the Ga, In, and Al fluxes were calibrated using reflection high energy electron diffraction intensity oscillations. Different growth temperatures were examined as well as different structural configurations to see what effect they had on wire formation and the corresponding PL spectra. Typical structures examined here contain a 1200 Å $Al_{0.48}In_{0.52}As$ buffer, and a 1200 Å $Al_{0.24}Ga_{0.24}In_{0.52}As$ cladding region, followed by the strained $Ga_xIn_{1-x}As$ MQWR active region, another 1200 Å $Al_{0.24}Ga_{0.24}In_{0.52}As$ cladding region, and a 500 Å $Al_{0.48}In_{0.52}As$ cap. The active region consists of one to five 100 Å conventional QWs separated by 75–150 Å $Al_{0.24}Ga_{0.24}In_{0.52}As$ barriers. A schematic of a typical MQWR structure with 5 QWs is shown in Fig. 1. Each QW contains 8 pairs of $(GaAs)_m/(InAs)_n$ short period superlattice (SPS) grown at a fixed ratio of $m : n \approx 2 : 2.2$ where m and n are the number of monolayers of GaAs and InAs, respectively. Within these QWs a composition modulation perpendcular to the growth direction is induced by the strain associated with the small non-zero values of mismatch $\Delta T = \Delta T(m, n, a_0, a_{GaAs}, a_{InAs})$ between the SPS layers and the substrate, and global average strain $\Delta S = \Delta S(m, n, a_0, a_{GaAs}, a_{InAs})$ within the SPS [3, 8]. The quantities a_o, a_{GaAs}, and a_{InAs} correspond to the

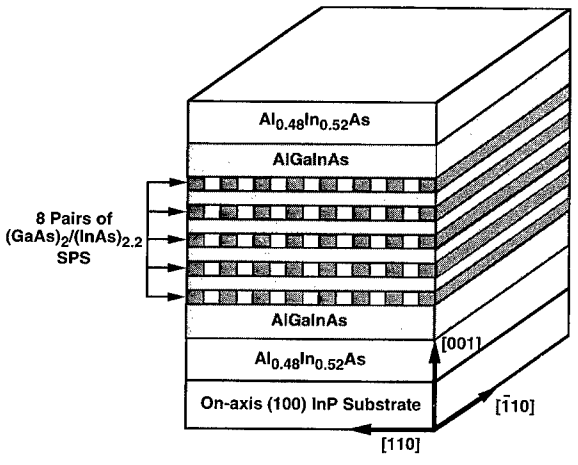

Fig. 1. The schematic diagram of a typical $Ga_xIn_{1-x}As$ strained MQWR heterostructure used in this study.

lattice constants of InP, GaAs, and InAs, respectively. Since the lateral composition modulation is formed within conventional QWs in the [1 0 0] direction, two-dimensional quantum confinement is attained resulting in QWRs.

To investigate the effect of strain on the MQWR region and the resulting PL spectra, samples with differing amounts of strain were studied by preparing samples at different substrate temperatures T_g, using the desorption temperature of InP, $\sim 540°C$, as a reference. For comparison, a multiple quantum well (MQW) sample with latticed matched GaInAs QWs was prepared.

The luminescence properties of the strained MQWR samples were studied using standard PL measurement techniques. The samples were mounted in a liquid nitrogen cooled dewar for measurements between 77 and 300 K. To measure the PL spectrum of the sample for temperatures greater than 300 K, a hot plate was used to heat the sample and a thermocouple monitored the temperature of the crystal. The heterostructures were excited using the 5145 Å line of an Ar^+ laser with an excitation intensity of approximately 100 W/cm^2. The collected light was dispersed in a 0.5 m focal length grating spectrometer and detected with a liquid nitrogen cooled Ge detector using the lock-in technique. To examine the wire formation of the heterostructures, polarized photoluminescence (PPL) spectra were taken. This was done using the same setup as for PL measurements but with a polarization analyzer located in front of the spectrometer and orienting it either parallel or perpendicular to the [$\bar{1}$ 1 0] direction (e.g., the QWR axis) of the sample [3, 7]. A depolarizer is placed in front of the spectrometer to remove any possible grating polarizations.

3. Results and discussion

The existence of the lateral composition modulation in the strained $Ga_xIn_{1-x}As$ MQWR structures was examined by cross-sectional transmission electron microscopy (TEM). The results indicate that a composition modulation consisting of alternating larger band gap Ga-rich regions and smaller band gap In-rich regions on the order of 100 Å has been formed [7, 9]. In addition to TEM, confirmation of wire formation is provided by the observation of PPL spectra. It is expected that the PL emitted from the [1 0 0] direction will appear to be polarized when the polarization analyzer located in front of the spectrometer is oriented parallel and perpendicular to the wires. The polarization effect reflects the existence of QWRs formed by the SILO process and the strain fields associated with the lateral composition modulation. The magnitude of polarization is proportional to the degree of the lateral composition modulation [3]. Fig. 2 shows the PPL spectra of a strained $Ga_xIn_{1-x}As$ MQWR heterostructure at 77 K. The peak intensities at 1.61 μm are highly polarized whereas the PL from the AlGaInAs cladding and barrier layers display the usual small preferential polarization for bulk crystals with a zinc-blende type cubic symmetry [10]. It is thus concluded that the peak PL wavelength at 1.61 μm emanates from the MQWR active region within the sample.

In a previous study, the influence of QWRs on the PL behavior of strained $Ga_xIn_{1-x}As$ MQWR heterostructures measured at temperatures between 77 and 300 K was reported [6]. It was found that the temperature dependence of the peak PL wavelength for samples with 2 QWs in the MQWR region differed from that of samples with 5 QWs.

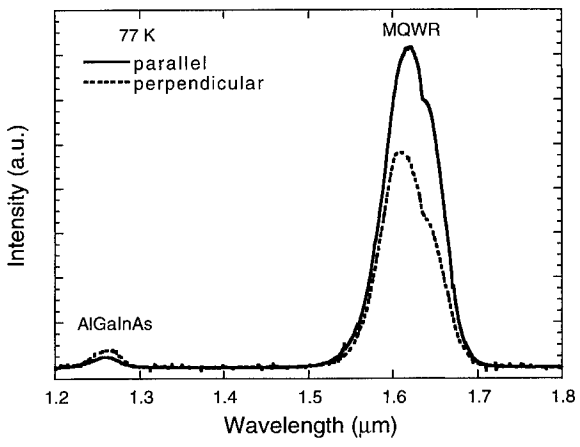

Fig. 2. The 77 K PPL spectra of the $Ga_xIn_{1-x}As$ strained MQWR heterostructures. The solid and dashed lines denote the orientation of the polarization analyzer with respect to the quantum wire axis for the PPL measurement.

This structural difference manifests itself as differing strain fields in the MQWR active region. Since the strain induced by the SILO process is a cumulative effect [7], the highly strained structures with 5 QWs will have a stronger lateral composition modulation than those with 2 QWs. This is supported by the fact that the PL emitted from the 5 QW sample has a stronger polarization than that observed from the 2 QW sample. The samples with 2 QWs show no net shift in peak PL wavelength for temperature ranging from 77 to 300 K, whereas the 5 QW sample has a net blue shift of peak PL wavelength with increasing temperature up until 300 K. This effect was attributed to the multi-axial strain distribution which exists in the MQWR active region [6].

To further examine this effect, the PL behavior of strained $Ga_xIn_{1-x}As$ MQWR heterostructures with 5 QWs grown under different substrate temperatures T_g is examined in this study. The PL spectrum of these samples was observed to be polarized indicating QWR formation in each sample. In Fig. 3 the resulting trend in temperature dependence of peak PL wavelength shift between 77 and 300 K for various values of T_g is given. It has been shown that the lateral composition modulation is optimized in $Ga_xIn_{1-x}As$ MQWRs grown at a temperature above and near 500°C [7]. At growth temperatures lower than 500°C, a less regular weaker lateral composition modulation occurs resulting in irregular QWRs, whereas samples grown above and near 500°C have a stronger composition modulation which allows for the formation of regular arrays of QWRs. Thus, Fig. 3 indicates that strained $Ga_xIn_{1-x}As$ MQWR samples with a stronger lateral composition modulation have a larger blue shift with respect to increasing cryostat temperatures. However, for samples grown at lower values of T_g, the magnitude of the blue shift decreases until the shift of peak PL wavelengths approaches the expected red shift value of approximately 1000 Å for the lattice matched GaInAs MQW control sample.

The high temperature properties of the strained $Ga_xIn_{1-x}As$ MQWR samples were studied using PL spectroscopy. Fig. 4 compares the temperature dependence of peak PL wavelengths of strained MQWR heterostructures and the MQW control

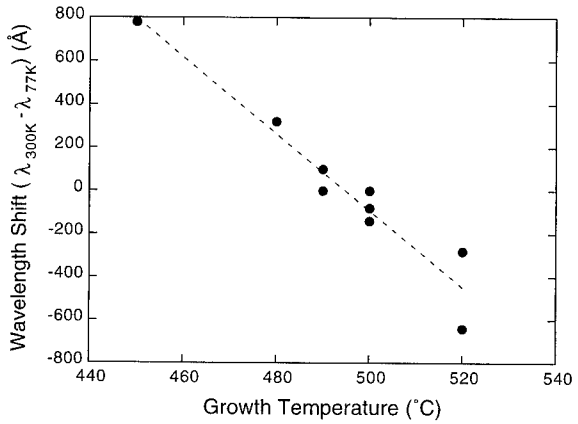

Fig. 3. The net peak wavelength shift between 77 and 300 K of the $Ga_xIn_{1-x}As$ strained MQWR heterostructures as a function of the growth temperature. The dashed line represents the best linear fit to the data.

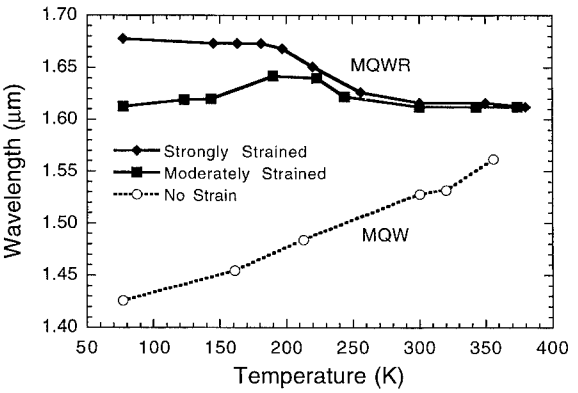

Fig. 4. The peak wavelength of PL spectra between 77 and 380 K for a strongly strained MQWR heterostructure, a moderately strained MQWR heterostructure, and an unstrained MQW sample.

sample from 77 to 380 K. Two types of strained MQWR samples are shown here, those that are strongly strained and those that are moderately strained. The strongly strained samples correspond to samples with five conventional QWs grown above and near 500°C. Moderately strained samples refer to samples with 2 QWs or samples with 5 QWs prepared at temperatures less than 500°C.

Two very interesting features can be seen in Fig. 4. First of all, the overall shift in wavelength of the strained MQWR samples is less than the MQW control sample. In fact, the moderately strained MQWR samples tend to have no net effective temperature dependence where the strongly strained MQWR samples have a net blue shift with increasing temperature. Both of these trends are in stark contrast to the expected net red shift of 1000 Å depicted by the MQW control sample. Most importantly, the peak PL wavelengths of both strained MQWR heterostructures are relatively stable at 1.61 μm for temperatures between 250 and 380 K. In the temperature range of room temperature to 72°C, the wavelength shifts with a dependence as low as 0.2 Å / °C. This thermal induced wavelength drift rate is only 4% of that in conventional MQWs (~5 Å / °C). Furthermore, we conclude that the stable peaks originate from the MQWR region since the PL at 1.61 μm is coincident with the polarized peaks seen in Fig. 2.

The samples studied in Fig. 4 correspond to samples grown under different substrate temperatures and to samples with different structural configurations. Thus, it is clear that by varying T_g and by making structural modifications, the strain in the $Ga_xIn_{1-x}As$ MQWR active region can be manipulated. The resultant effect is apparent in the temperature behavior of the peak PL wavelength where, most importantly, it is stable above room temperature.

4. Conclusions

It has been shown that the peak PL wavelength of strained $Ga_xIn_{1-x}As$ MQWR heterostructures is stable for temperatures ranging from 250 to 380K. It has a temperature dependence as low as 0.2 Å / °C between room temperature and 72°C. This is over a 25 time improvement over the conventional MQW structures. The PL behavior of these samples between 77 and 300 K varies depending on the amount of strain induced in the MQWR active region by the SILO process. The strain in the MQWR regions, which directly effects the PL peak wavelength shift, can be controlled by the growth temperature and structural configuration. Between 250 and 380 K, all samples show a nearly stable PL peak wavelength near 1.61 μm. The fact that the wavelength is stable above 300 K is of paramount importance to the continued pursuit of QWR technology since QWRs with a stable emission wavelength could be used as the active region of lasers, thus, improving the temperature characteristics of emitters for communication and information systems.

Acknowledgements

The authors wish to thank L.J. Chou and Professor K.C. Hsieh for technical discussions. This work was supported by the National Science Foundation (ECD-89-43166 and ECS-92-02294) and Joint Services Electronics Program (N00014-96-1-0129).

References

[1] Y. Arakawa and A. Yariv, IEEE Quantum Electron. QE-22 (1986) 1887.
[2] H. Zarem, K. Vahala and A. Yariv, IEEE J. Quantum Electron. QE-25 (1989) 705.
[3] P.J. Pearah, A.C. Chen, A.M. Moy, K.C. Hsieh and K.Y. Cheng, IEEE J. Quantum Electron. QE-30 (1994) 608.
[4] S.T. Chou, K.Y. Cheng, L.J. Chou and K.C. Hsieh, Appl. Phys. Lett. 66 (1995) 2220.
[5] U.A. Griesinger, H. Schwezer, V. Harle, J. Hommel, F. Barth, B. Hohing, B. Klepser and F. Scholz, IEEE Photon. Lett. 7 (1995) 953.
[6] D.E. Wohlert, S.T. Chou, A.C. Chen, K.Y. Cheng and K.C. Hsieh, Appl. Phys. Lett. 68 (1996) 2386.
[7] S.T. Chou, K.Y. Cheng, L.J. Chou and K.C. Hsieh, J. Appl. Phys. 78 1995 6270.
[8] K.Y. Cheng, K.C. Hsieh and J.N. Baillargeon, Appl. Phys. Lett. 60 (1992) 2892.
[9] S.T. Chou, K.C. Hsieh, K.Y. Cheng and L.J. Chou, J. Vac. Sci. Technol. B13 (1995) 650.
[10] K.Y. Cheng, K.C. Hsieh, J.N. Baillargeon and A. Mascarenhas, Proc. 1991 Int. Symp. GaAs and related Compounds, Inst. Phys. Ser., Vol. 120 (Seattle, WA, USA, 1992) p. 589.

ELSEVIER

Journal of Crystal Growth 175/176 (1997) 1167–1172

JOURNAL OF CRYSTAL GROWTH

Growth-mode-induced surface morphology and its relation to optical properties of GaAs single quantum wells

R. Hey*, I. Gorbunova, M. Ramsteiner, M. Wassermeier, L. Däweritz , K.H. Ploog

Paul-Drude-Institut für Festkörperelektronik, Hausvogteiplatz 5–7, D-10117 Berlin, Germany

Abstract

Quantum wells with short period superlattice barriers are grown by molecular beam epitaxy in growth modes which range from two-dimensional island nucleation to step flow. These different growth modes result in different surface morphologies as imaged by atomic force microscopy. Micro-photoluminescence of the quantum wells and of their barriers reveal spectra with a rich fine structure. These narrow lines in the micro-photoluminescence spectra are attributed to exciton localization by potential fluctuations at the interface. The formation of a pronounced roughening of step edges for samples grown either at high As_4-partial pressure or on misoriented substrates with As-terminated steps is observed, which is accompanied by the appearance of a pronounced fine structure in photoluminescence and a broadening of its distribution.

PACS: 68.35.Ct; 78.66.Fd; 81.05.Ea; 81.15.Hi

Keywords: Superlattices; Quantum wells; Molecular beam epitaxy; AlAs/GaAs

1. Introduction

The electrical transport and the optical properties of novel devices with reduced dimensionality are sensitively influenced by the defect structure of the interfaces including the geometrical and the chemical profile across the interfaces [1] because the magnitude of these defects is on a length scale comparable to, e.g., the extension of the confined wave function of electrons. However, it is not clear which kind of imperfections govern the local physical properties–defects on an atomic scale as revealed by scanning tunneling microscopy [2] or those on a submicron scale already visualized by atomic force microscopy [3]. For a better understanding of these phenomena, a detailed characterization with high spatial resolution is required. Spatially resolved photoluminescence studies of thin quantum wells (QW) have revealed that the radiation emitted from localized areas [4, 5] reflects potential fluctuations due to well thickness inhomogeneities and compositional transients at

*Corresponding author. Fax: +49 30 20377201; e-mail: hey@pdi.wias-berlin.de.

0022-0248/97/$17.00 Copyright © 1997 Elsevier Science B.V. All rights reserved
PII S0022-0248(96)01039-1

interfaces. Furthermore, the interfaces of a quantum well (normal and inverted) are inequivalent as manifested by, e.g., a unidirectional segregation [6].

In this paper we present results of micro-photoluminescence (μ-PL) and atomic force microscopy (AFM) investigations of a series of QWs. They were prepared under extremely different growth conditions in order to examine the influence of growth-mode-induced morphologies on the optical properties of these structures.

2. Experimental procedure

GaAs single quantum wells with a thickness of 16 monolayers (ML) embedded in short period superlattice (SPSL) barriers consisting of 8 ML GaAs/4 ML AlAs are grown by solid-source molecular beam epitaxy. The temperatures and As_4-to-Ga beam-equivalent pressure (BEP) ratios are varied in a range from 550°C to 640°C and 8 to 30, respectively. Almost exactly oriented GaAs(0 0 1) substrates and those with misorientations up to 2° towards (1 1 1) Ga and 2° towards (1 $\bar{1}$ 1) As are used. The upper barrier is capped with GaAs of the same thickness as the QW. For growth rates of about 300 nm/h the above-mentioned growth conditions allow the adjustment of the (2 × 4) or (3 × 1) surface reconstructions and growth modes ranging from two-dimensional island nucleation to step flow. Growth is interrupted for 40 s after the deposition of the 16 ML QW. The samples are cooled down at a rate of 20°C/min in an As_4 atmosphere, thereby maintaining the (2 × 4) surface reconstruction. AFM investigations are performed in ambient in the constant force contact mode. Low-temperature μ-PL studies (8 K) are performed with a confocal imaging system using a microscope objective lens together with a fixed diaphragm. The area of excitation and detection is confined to about 2 μm^2.

3. Results and discussions

The use of an air AFM for the study of surface morphologies in the GaAs/AlAs material system is restricted to the steady-state GaAs surfaces. For comparability of surface and interface morphologies we ensured that under identical growth conditions the buffer layer, the QW and the cap layer surface show identical terrace width distribution and step edge profiles which remain unchanged within a few minutes, the time needed to quench the surface. Fig. 1 displays AFM micrographs of homoepitaxial GaAs layers annealed under As_4 atmosphere at the growth temperature (T_s = 610°C). A well-developed step array corresponding to the 0.2° misorientation is maintained after 2 min annealing (Fig. 1a) which is nearly identical to that obtained for unannealed samples (not shown). After 5 min of annealing the surface starts to change by the onset of increased step bunching (Fig. 1b)

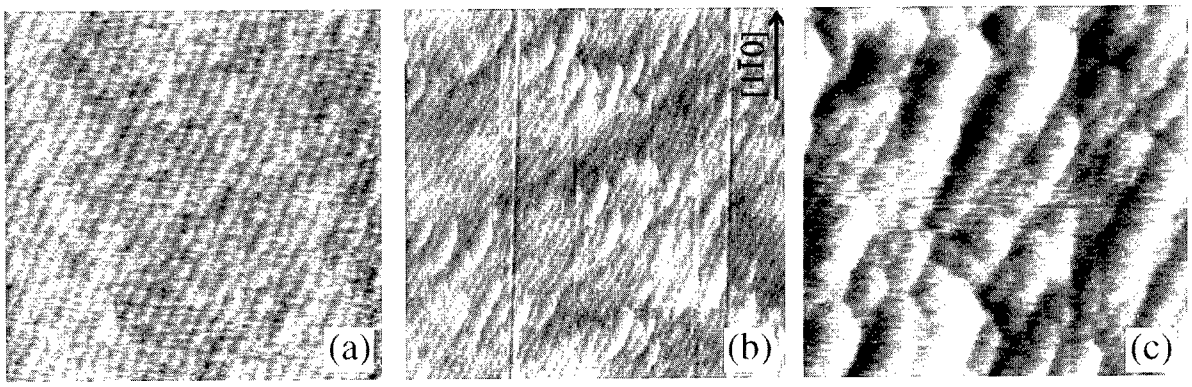

Fig. 1. AFM micrographs (3 μm × 3 μm) of homoepitaxial layers grown on 0.2° misoriented (0 0 1) GaAs after annealing for 2 min (a), 5 min (b) and 20 min (c) at T_s = 610°C in As_4 ambient. The initially well-ordered monolayer step system is progressively disturbed by increased step bunching.

which is initiated predominantly at multikinks in the step edges. Prolonged annealing totally changes the initial appearance of the surface (Fig. 1c) by the formation of very narrow terraces or even multilayer steps [7] with abruptly changing step edge directions.

Fig. 2 shows AFM micrographs of the cap layer surface of QW structures grown in the two-dimensional island nucleation mode (Fig. 2a), predominantly in the step flow mode (Fig. 2b), in the pure step flow mode (Fig. 2c) and in a modified step flow mode (incomplete condensation at high growth temperature) (Fig. 2d). The surfaces display a $(2\times4)\alpha$ (Fig. 2a and Fig. 2b) or a weak (3×1) (Fig. 2c and Fig. 2d) reconstruction during growth. Details of growth parameters are listed in Table 1. Caused by an unintentional miscut of the substrates and due to the distinct growth conditions, the step systems exhibit very different terrace and step edge profiles. High arsenic partial pressures p_{As_4} and high substrate temperature T_s lead to a pronounced step edge roughening by the formation of larger Ga- and As-terminated step segments (Fig. 2b). Thus, the total length of the step edge segments between a fixed distance is maximized compared to the case of reduced arsenic flux which results in less roughened step edges (Fig. 2c). At $T_s = 640°C$, the surface of the layer contains a high number of holes and islands on the terraces (Fig. 2d) indicating a collapse of the pure step flow

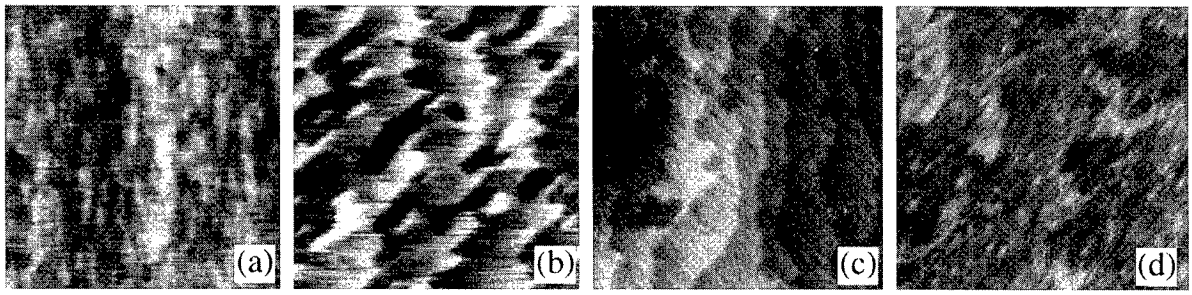

Fig. 2. AFM micrographs (2 μm × 2 μm) of the cap layer surfaces of QW structures prepared under different growth conditions. T_s and As_4/Ga-BEP ratios were 550°C/10 (#1) (a), 610°C/30 (#3) (b), 610°C/10 (#4) (c) and 640°C/10 (#6) (d). Substrates are unintentionally misoriented by about 0.03°–0.05° towards (0 1 1). Growth is performed in the two-dimensional island nucleation mode (a), predominantly in the step flow mode (b), pure step flow mode (c) and step flow mode with incomplete condensation (d).

Table 1
Compilation of substrate misorientations α, growth rates R, BEP-ratios, growth temperatures T_s, surface reconstructions SR, growth modes M and FWHM of QW and SPSL emission

#	α (°)	R (nm/h)	BEP As_4/Ga	T_s (°C)	SR	M	FWHM	
							QW (meV)	SPSL (meV)
1	0	310	10	550	2×4	2DN	6.3	10.3
2	0	310	10	580	2×4	2DN	6.7	9.7
3	0	310	30	610	2×4	SF[a]	6.9	13.5
4	0	310	10	610	3×1	SF	7	9
5	0.35A	310	10	610	3×1	SF	5.7	8.5
6	0	310	10	640	3×1	SF[b]	8	10.2
7	2A	310	8	610	1×1	SF	6.1	9.6
8	2B	310	8	610	1×1	SF	9	11.2

[a] Denotes predominantly step flow mode.
[b] Step flow mode at incomplete condensation, 2DN the two-dimensional island nucleation mode.

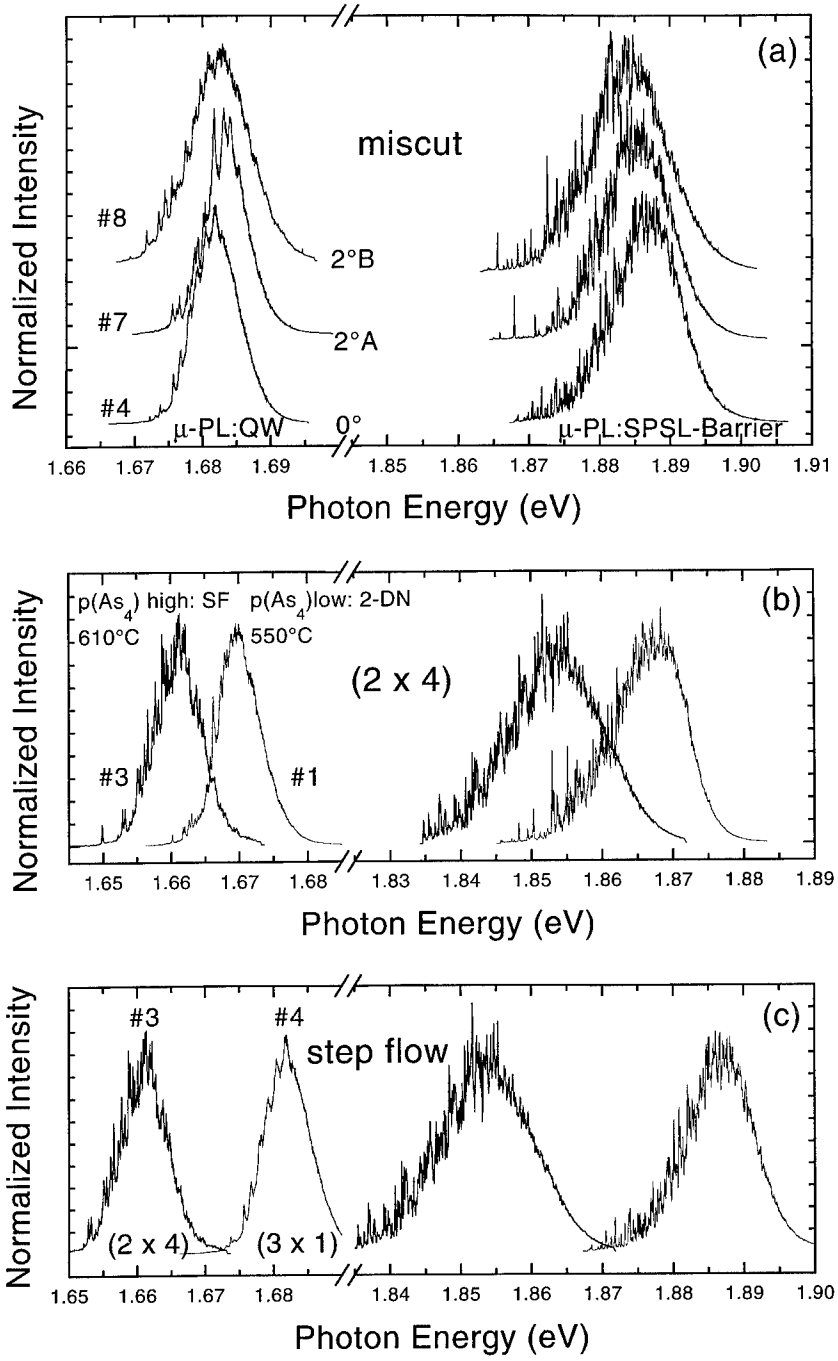

Fig. 3. Micro-PL spectra of the QW emission (1.66–1.68 eV) and SPSL emission (1.85–1.885 eV) of samples grown on different misoriented substrates (2°B, 2°A, 0° denote miscut towards (1 $\bar{1}$ 1)As (#8), (1 1 1)Ga (#7) and no intentional miscut (#4)) (a), with the (2 × 4) surface reconstruction at T_s = 550°C in the two-dimensional island nucleation mode (#1) and T_s = 610°C in the step flow mode (#3) (b) and in the step flow mode at T_s = 610°C with different surface reconstructions (#3, 4) (c).

mode due to an incomplete GaAs condensation. At lower T_s, layers grow in the 2D-nucleation mode (Fig. 2a).

The optical characterization of the layer system is performed by μ-PL. The spectra of all QW and all SPSL emission show a rich fine structure and the envelopes of which correspond to the conventional PL spectra with full-width at half-maximum (FWHM) values of 6–8 and 8–14 meV, respectively, (Fig. 3a and Fig. 3c). The spikes in the μ-PL spectra are very narrow (FWHM $\leqslant$ 0.1 meV).

Fig. 3a shows μ-PL spectra from the QW and the SPSL of samples all grown in the step flow mode at the same T_s but on differently misoriented substrates. The reconstruction during growth for larger miscuts is (1×1), whereas for small miscuts an asymmetrical (3×1) is maintained. For misorientations between 0° and 2° towards (1 1 1) Ga, no quantitative variation in the PL spectra is observed while misorientation towards (1 $\bar{1}$ 1) As results in a broadening of the spike distribution. In Fig. 3b we compare PL spectra of two samples grown both with a (2×4) surface reconstruction but at different T_s and p_{As_4}. Obviously, with increasing arsenic partial pressure the fine structures in the QW and SPSL spectra become more pronounced. The SPSL emission is asymmetrical for the sample grown at lower T_s and narrower compared to the one grown under high p_{As_4}. This asymmetry reflects exciton transfer into local potential minima at the interface defects. Fig. 3c shows PL spectra of two samples grown in the same growth mode and at the same T_s but with different reconstructions due to different p_{As_4}. Again we observe a remarkable broadening of the SPSL emission in the case of excessive As incidence.

Growth mode, growth rate, T_s, p_{As_4} and surface reconstruction are interrelated, and thus, they cannot be adjusted independently. Even when taking into account this difficulty, we neither recognize a systematic influence of the growth mode nor the reconstruction on the PL properties (Fig. 3b and Fig. 3c). However, a high p_{As_4} leads to a remarkable broadening of the PL spectra. The same broadening is observed for samples grown on vicinal substrates with As-terminated steps. By comparing this finding with AFM images (Fig. 2b) we conclude that the total length of step edge segments is maximized for the above mentioned growth conditions which seems to assist the formation of localization sites. The generally observed undulation of the surface or interface in the 1 μm range [2] is not responsible for the occurance of numerous spikes because of the limited probe area (1.5 μm in diameter).

The spikes in the PL spectra are attributed to the localization of excitons at potential fluctuations due to topological defects at step edges or compositional gradients across the interfaces. From present results it is not justified to correlate exciton localization sites to morphological features. However, it is reasonable to assume that local potential minima for excitons are preferentially formed by intermixing which is mainly caused by Ga segregation at step edges or boundaries of the surface reconstruction domains on the terraces. Therefore, strong step edge roughening favors the formation of localization sites.

4. Summary

A series of GaAs single quantum wells are prepared on almost exactly and on misoriented GaAs (0 0 1) substrates by solid-source MBE with the aim to examine the impact of surface morphologies on the optical properties of the layer system. The samples are grown under controlled conditions giving rise to distinct surface reconstructions and growth modes and studied in combination of AFM and μ-PL. For all structures the optical emission from the QW and from the AlAs/GaAs SPSL barriers show a pronounced fine structure in the μ-PL spectra which is attributed to exciton localization. Direct correlations to either growth mode or surface reconstruction to PL properties are not found. However, As-rich growth conditions lead to enforced roughening of step edges which is concomitant with a broadening of the PL emission distribution. The latter is also observed when As-terminated misorientations steps are involved. It is supposed that this step edge roughening increases the probability of local intermixing, and thus the formation of additional exciton localization sites.

Acknowledgements

We appreciate the experience and assistance of M. Höricke in MBE growth.

References

[1] K.A. Mäder, L.-W. Wang and A. Zunger, J. Appl. Phys. 78 (1995) 6639.
[2] M.D. Pashley, K.W. Haberen and J.M. Gaines, Appl. Phys. Lett. 58 (1991) 406.
[3] R. Hey, M. Wassermeier, J. Behrend, L. Däweritz, K.H. Ploog and H. Raidt, J. Crystal Growth 154 (1995) 1.
[4] H.F. Hess, E. Betzig, T.D. Harris, L.N. Pfeiffer and K.W. West, Science 264 (1994) 1740.
[5] K. Brunner, G. Abstreiter, G. Böhm, G. Tränkle and G. Weimann, Appl. Phys. Lett. 64 (1994) 3320.
[6] W. Braun and K.H. Ploog, J. Appl. Phys. 75 (1994) 1993.
[7] K Ohkuri, J. Ishizari, S. Hara and T. Fukui, J. Crystal Growth 160 (1996) 235.

ELSEVIER

Journal of Crystal Growth 175/176 (1997) 1173–1177

JOURNAL OF CRYSTAL GROWTH

Photoluminescence of low-temperature AlGaAs/GaAs multiple quantum wells

W. Feng*, F. Chen, Q. Huang, J.M. Zhou

Institute of Physics, Chinese Academy of Sciences, P.O. Box 603-36, Beijing 100080, People's Republic of China

Abstract

The photoluminescence (PL) of low-temperature-grown AlGaAs/GaAs multiple quantum wells (LT-MQWs) has been investigated and compared with a normal-temperature-grown AlGaAs/GaAs MQW structure (NT-MQWs) implanted with protons. The as-grown LT-MQWs show much more intensive PL than the as-implanted NT-MQWs. Upon anneal, the PL from the LT-MQWs and the NT-MQWs exhibits different behaviors. For the NT-MQWs, the PL intensity increases monotonously with rising annealing temperature due to the decrease of implantation-induced defects. By contrast, the PL from the LT-MQWs is drastically quenched, and the PL intensity drops nearly three orders of magnitude after anneal at 600°C. The annealing behavior of the PL from the LT-MQWs is attributed to the formation of As clusters that act as deep trap centers for the photoexcited carriers and cause the quenching of the PL intensity. After anneal, enhanced interface intermixing and roughening have been observed in the LT-MQWs.

PACS: 68.55.Bd; 78.55.Cr; 71.55.Eq; 78.66.Fd

Keywords: Molecular beam epitaxy; Photoluminescence; Multiple quantum wells

1. Introduction

GaAs grown by molecular beam epitaxy (MBE) at low temperatures (LT-GaAs) has generated great scientific and technological interest since the report of Smith et al. [1]. LT-GaAs is highly non-stoichiometric, containing up to 1–2% excess As in the form of As antisite (As_{Ga}), As interstitial and Ga vacancy [2–5]. It exhibits extremely short carrier lifetimes [6, 7], and when annealed, very high resistivity. Upon anneal, the point defect densities in LT-GaAs are dramatically reduced, and the excess As collects in As clusters. Now, there exist two models explaining the electrical properties of LT-GaAs, i.e., the "antisite defect compensation" model and the "buried Schottky barrier" model. The former explains the electrical properties of LT-GaAs by the role of As_{Ga} defects in compensation and hopping conduction [3], while the latter attributes the semi-insulating properties to overlapping depletion regions around As clusters [8].

On the other hand, ion implantation is a well-established technique to introduce traps or recombination centers in semiconductors. Very high

* Corresponding author. Fax: + 86 10 62562605; e-mail: wfeng@aphy02.iphy.ac.cn.

0022-0248/97/$17.00 Copyright © 1997 Elsevier Science B.V. All rights reserved
PII S0022-0248(96)01041-X

resistivity and subpicosecond carrier lifetimes can also be realized by ion implantation. In this work, we investigated the effect of annealing on the PL of the LT-MQWs and the proton-implanted NT-MQWs. The variations of PL reflect the changes of defect concentrations in samples upon annealing. By comparing the annealing temperature dependence of PL of the LT-MQWs and the proton implanted NT-MQWs, anomalous annealing behavior of PL for the LT-MQWs was found, and explained by the formation of As clusters after annealing.

2. Experimental procedure

The samples were grown on semi-insulating GaAs(100) substrates in a V80H MBE machine with uncracked As_4. During growth, the As_4/Ga beam equivalent pressure (BEP) ratio was kept at 10. A standard MQW sample consists of 1 μm of GaAs buffer layer, 500 Å of AlAs, 1500 Å of $Al_{0.3}Ga_{0.7}As$, and 75 periods of $Al_{0.3}Ga_{0.7}As$ (100 Å)/GaAs (70 Å), as illustrated in Fig. 1. Two MQW samples were grown in this study, one at 310°C (referred to as LT-MQWs) and the other at normal temperature (referred to as NT-MQWs). After growth, the NT-MQWs was implanted with protons at 180 keV to a dosage of 10^{14} cm^{-2}. Such an implantation will create 10^{19} defects per cm^3 in the sample. Two samples were then cut into pieces and each piece was subjected to 30 s isochronic annealing at 500–900°C. The PL measurements were made at 77 K. The 5145 Å line of an Ar^+ laser was used as an excitation optical source. The PL from the samples was dispersed by a focus length $f = 0.5$ m monochromater and detected by a photomultiplier tube coupled to a lock-in amplifier.

3. Results and discussion

Shown in Fig. 2 are the PL spectra for two MQW samples at several annealing temperatures. The PL peaks are due to the $n = 1$ heavy-hole transitions in the AlGaAs/GaAs MQWs. As is seen, the PL spectra of the LT-MQWs and the NT-MQWs exhibit different dependences on annealing temperature. The integrated PL intensity as a function of annealing temperature is given in Fig. 3. For the NT-MQWs, the PL intensity increases monotonously with increasing annealing temperature,

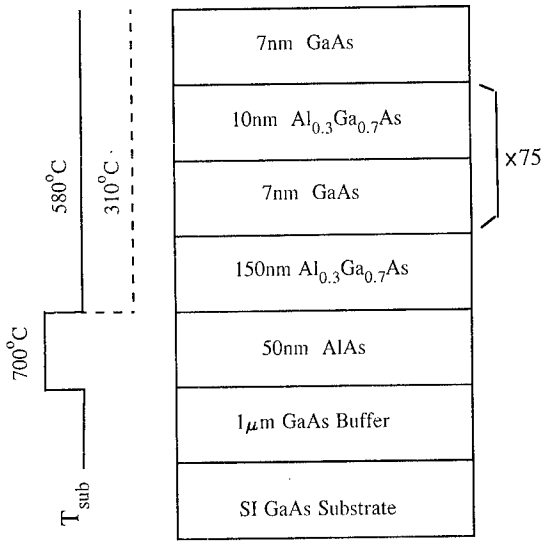

Fig. 1. Schematic structure of the MQW samples. On the left are shown the substrate temperature profiles used in the growth of the LT-MQWs (dash line) and the NT-MQWs (solid line).

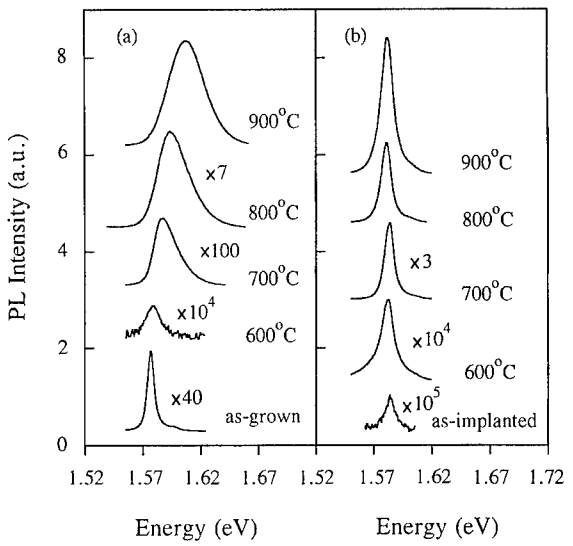

Fig. 2. PL spectra at various annealing temperatures for (a) LT-MQWs and (b) NT-MQWs.

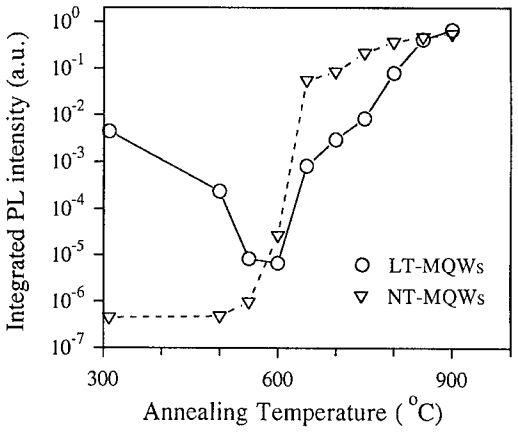

Fig. 3. The integrated PL intensity as a function of annealing temperature for the LT-MQWs and the NT-MQWs.

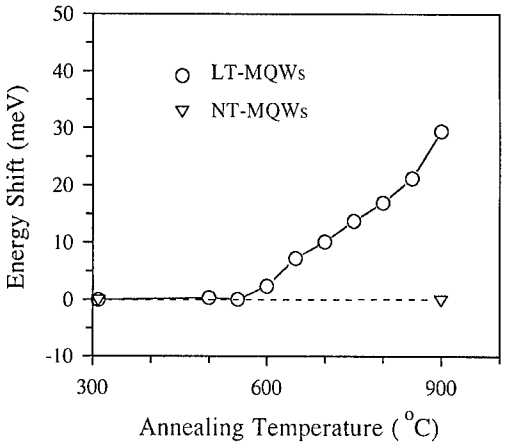

Fig. 4. The PL energy shift versus annealing temperature for the LT-MQWs and the NT-MQWs.

due to the gradual decrease of concentration of defects created by implantation which act as nonradiative recombination centers for photoexcited carriers. For annealing temperatures above 600°C, the PL intensity becomes saturated, indicating a nearly complete recovery of implantation-induced damage. By contrast, the relatively strong PL for the as-grown LT-MQWs is dramatically quenched after annealing at 600°C. The PL intensity first decreases nearly three orders of magnitude, and then recovers gradually as the annealing temperature is raised above 600°C. At 900°C anneal, the PL intensity of the LT-MQWs becomes comparable with that of the NT-MQWs. There have been many reports that annealing at 600°C or below can greatly reduce point defect densities in LT-GaAs [3, 9]. Since the deep defects can act as nonradiative recombination centers, the reduction in defect densities after annealing should lead to an enhancement in the PL intensity, as is observed for the NT-MQWs. However, we observe an opposite trend in the PL spectra of the LT-MQWs annealed at 600°C and below. This anomalous annealing behavior of PL intensity for the LT-MQWs is believed to be related to the formation of As clusters, and will be discussed later.

The PL peak energy shift versus annealing temperature is shown in Fig. 4. No change in the peak energy is observed for the NT-MQWs with annealing up to 900°C. The PL peak energy of the LT-MQWs also shows no visible change with annealing below 600°C. For annealing above 600°C, the PL peak begins to move toward higher energy. The energy shift reaches 30 meV with annealing at 900°C. The observed energy shift for the LT-MQWs is attributed to Al-Ga interdiffusion at AlGaAs/GaAs interfaces. The Al–Ga intermixing changes square wells into parabolic ones, and raises the subband energy levels in the wells. The large energy shifts indicate that strong Al–Ga interdiffusion occurs at the AlGaAs/GaAs interfaces. The enhancement of intermixing can be ascribed to the high density of V_{Ga} vacancies in the LT-MQWs, which assist the diffusion of atoms on the Ga sublattice [10]. The Al–Ga interdiffusion also results in interface roughening that broadens the PL peaks. Fig. 5 shows the full width at half maximum (FWHM) of PL peak as a function of annealing temperature. The increasing PL linewidths indicate that the interfaces are heavily roughened for the LT-MQWs after annealing.

There are two possible explanations for the sharp decrease in the PL intensity for the LT-MQWs annealed at 600°C or below. One is that after annealing, some new point defects and/or defect complexes appear which act as more effective nonradiative recombination centers than those in the as-grown sample. From a detailed study on the annealing-temperature dependence of PL intensity for LT samples grown at various temperatures, we

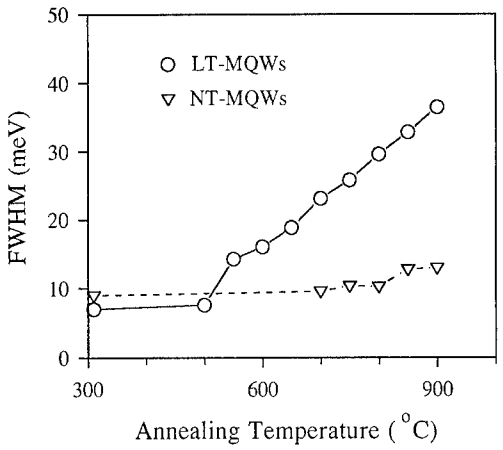

Fig. 5. The full-width at half-maximum as a function of annealing temperature for the LT-MQWs and the NT-MQWs.

found that the annealing temperature at which the PL intensity of a LT sample is quenched the most is dependent on its growth temperature. The higher the growth temperature, the higher the annealing temperature required to quench the PL intensity. For example, the annealing temperature corresponding to the minimum PL intensity is 800°C for the samples grown at ·350°C, and 550°C for the samples grown at ~ 300°C or below. These facts imply that the supposed new defects should appear for annealing temperatures ranging from 550°C to 800°C, i.e., they can withstand annealing at temperatures up to 800°C. However, it is seen in Fig. 2 that the PL intensity increases by about four orders of magnitude from 600°C to 800°C. Such an increase in PL intensity indicates that the new defects, if they exist, cannot withstand annealing at temperatures up to 800°C. Therefore, the quenching of PL intensity cannot be explained by the formation of new point defects (or defect complexes).

The second explanation is evidently related to the formation of As clusters in the annealed LT-MQWs. The As/GaAs interfaces exhibit very high nonradiative recombination rates [6]. The photoexcited carriers are fast trapped by As clusters. Thus, the radiative recombination probabilities and carrier lifetimes are drastically reduced, causing the quenching of PL intensity. With further increase of annealing temperature, the As cluster coarsening process results in a lower cluster density and larger spacing between As clusters. The trapping probabilities for photoexcited carriers at the As clusters decrease. Therefore, the radiative recombination probabilities and thereby the PL intensities increase. The above-mentioned annealing-temperature dependence of the PL intensity on growth temperature can be explained as follows: Under the same As_4/Ga BEP ratio, less excess As will be incorporated into the LT sample grown at higher temperature, and therefore annealing at higher temperature is needed to form sizable As clusters.

Upon annealing, the line shapes of PL spectra of the LT-MQWs also show different changes than the NT-MQWs. From Fig. 2, it is seen that the PL peaks for the NT-MQWs keep Gaussian line shapes with annealing at 500–900°C. On the other hand, the PL line shapes for the LT-MQWs become strongly asymmetric upon annealing. The higher energy tail gets more prominent with increasing annealing temperature up to 700°C. With further increase of annealing temperature from

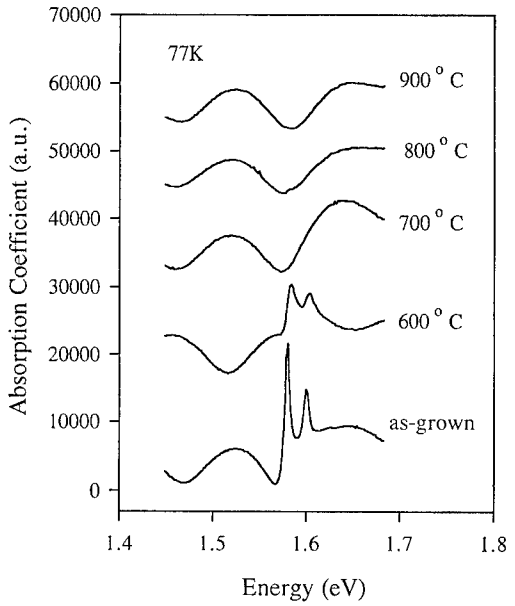

Fig. 6. The absorption spectra for the LT-MQWs annealed at several temperatures. The spectra are vertically shifted for clarity.

700°C to 900°C, a Gaussian line shape gradually recovers. The changes in PL line shape have relation with the quenching of excitons in the LT-MQWs, as can be seen from the optical absorption shown in Fig. 6. The excitonic features trail off with increasing annealing temperature, and become fully quenched at 700°C. For annealing temperatures 700–900°C, only the interference fringes can be seen in the absorption spectra. For annealing temperatures below 700°C, PL of the LT-MQWs changes from exciton-dominated to band-to-band-recombination-dominated, resulting in asymmetric PL line shapes. For annealing temperatures higher than 700°C, strong interface intermixing and roughening occur. The increasing statistical broadening in the LT-MQWs makes the band-to-band-recombination line shape become more and more a Gaussian [11].

4. Summary

In summary, the effects of thermal annealing on the optical emission properties of the LT-MQWs and the NT-MQWs have been studied and compared. Upon annealing, the PL of the LT-MQWs and the NT-MQWs show different annealing behaviors. This difference clearly reveals out the role of As clusters in determining the optical properties of the LT-MQWs.

Acknowledgements

This work was supported by the National Foundation of Natural Sciences under Grant No. 69478001.

References

[1] F.W. Smith, A.R. Calawa, C.L. Chen, M.J. Manfra and L.J. Mahoney, IEEE Electron. Device Lett. EDL-9 (1988) 77.
[2] M.R. Melloch, J.M. Woodall, E.S. Harmon, N. Otsuka, F.H. Pollak, D.D. Nolte, R.M. Feenstra and M.A. Lutz, Annu. Rev. Mater. Sci. 25 (1995) 547.
[3] C. Look, Thin Solid Films 231 (1993) 61.
[4] M. Kaminska, Z. Liliental-Weber, E.R. Weber, T. George, J.B. Kortright, F.W. Smith, B.-Y. Tsaur and A.R. Calawa, Appl. Phys. Lett. 54 (1989) 1881.
[5] M.O. Manasreh, D.C. Look, K.R. Evans and C.E. Stutz, Phys. Rev. B 41 (1990) 10272.
[6] R.E. Viturro, M.R. Melloch and J.M. Woodall, Appl. Phys. Lett. 60 (1992) 3007.
[7] S. Gupta, M.Y. Frankel, J.A. Valdmanis, J.F. Whitaker, F.W. Smith and A.R. Calawa, Appl. Phys. Lett. 59 (1991) 3276.
[8] A.C. Warren, J.M. Woodall, J.L. Freeouf, D. Grischkowsky, D.T. Mclnturff, M.R. Melloch and N. Otsuka, Appl. Phys. Lett. 57 (1990) 1331.
[9] X. Liu, A. Prasad, W.M. Chen, A. Kurpiewski, A. Stoschek, Z. Liliental-Weber and E.R. Weber, Appl. Phys. Lett. 65 (1994) 3002.
[10] D.E. Bliss, W. Walukiewicz, J.W. Ager III, E.E. Haller, K.T. Chan and S. Tanigawa, J. Appl. Phys. 71 (1992) 1699.
[11] J. Christen and D. Bimberg, Phys. Rev. B 42 (1990) 7213.

ELSEVIER

Journal of Crystal Growth 175/176 (1997) 1178–1185

JOURNAL OF CRYSTAL GROWTH

Surface chemistry during metalorganic molecular beam epitaxy studied by pulsed molecular beam scattering

Masahiro Sasaki[a,*], Seikoh Yoshida[b]

[a] *Institute of Applied Physics, University of Tsukuba, Tennoudai, Tsukuba, Ibaraki 305, Japan*
[b] *The Furukawa Electric Co. Ltd., Yokohama R&D Laboratories, Okano, Nishi-ku, Yokohama 220, Japan*

Abstract

The surface chemistry during metalorganic molecular beam epitaxy (MOMBE) is discussed on the basis of the time-of-flight (time-of-arrival) distributions of trimethylgallium (TMG) molecules scattered from structure-controlled GaAs(1 0 0), GaAs(1 1 0) and GaAs(1 1 1)B surfaces as well as oxidized GaAs surfaces. The scattering (adsorption and desorption) of TMG from GaAs surfaces, the initial stage of the surface chemistry, is interpreted within the framework of precursor-mediated chemisorption, where the precursor state is deepened by the charge distribution of the relaxed or reconstructed GaAs surface and the dissociative chemisorption is suppressed on the surface with the highly stabilized structure. The growth suppression on oxidized GaAs surface is due to the absence of the deep precursor states, implying the mechanism of selective area growth. The growth suppression on an As-excess GaAs(1 1 1)B surface, by which the GaAs lateral growth is realized on a grooved GaAs(1 1 1)B substrate, is explained by neutral As trimers which geometrically hinder the TMG trapping in the precursor state. It is also found that the TMG scattering varies with the surface preparation method even if electron diffraction shows similar reconstructions, which suggests that TMG molecules diffuse over the wide area during trapping in the precursor state.

1. Introduction

It is well known that the growth rate of metalorganic molecular beam epitaxy (MOMBE) drastically varies with the growth condition. By utilizing this behavior of MOMBE, we can three-dimensionally control the epitaxial growth. For example, GaAs can be selectively grown on window areas opened on mask materials, such as oxides and nitrides, where MOMBE growth is highly suppressed [1–3]. Atomic layer epitaxy (ALE) is realized by alternately supplying source gases, since the MOMBE growth is limited to one atomic monolayer under single source gas supply [4, 5]. Furthermore, using the behavior that the growth rate is very low on the GaAs(1 1 1)B surface under a high As flux [6, 7], we can laterally grow GaAs on a grooved GaAs(1 1 1)B substrate [8]. However, the mechanism governing the drastically varying

* Corresponding author. Fax: +81 298 53 5205; e-mail: sasaki@bk.tsukuba.ac.jp.

0022-0248/97/$17.00 Copyright © 1997 Elsevier Science B.V. All rights reserved
PII S0022-0248(96)00871-8

MOMBE growth rate has not been well understood so far.

In order to clarify the mechanism, the growth rate as a function of growth condition has been investigated in detail [9–12]. Several analytical methods such as reflection difference spectroscopy [13], surface photo-absorption measurement [14], grazing incidence X-ray diffraction [15], have been applied. Mass spectrometry of desorbed species enable us to in situ observe the surface chemistry during MOMBE [16–19]. These studies implied the mechanism in ALE. Furthermore, it is demonstrated that the GaAs growth selectivity in selective area growth is attributed to the difference in the decomposition rate of such Ga source gases as trimethylgallium (TMG) and triethylgallium (TEG) from the mass spectrometric analysis of the desorbed species [2]. The decomposition suppression of source gases on the As-rich GaAs(1 1 1)B surface was also found by mass spectrometry [6], which is against the expectation that the As-containing species promote TMG decomposition as is known in the vapor-phase reaction [20]. Also on the GaAs(1 0 0) surface, we found that the surface reaction of TMG is not influenced by the As density on surface but by the surface structure; TMG decomposition is suppressed on a GaAs(1 0 0)-(2 × 4) surface with a specific As coverage, which has a highly stabilized structure [21].

As mentioned above, great effort has been done to understand the mechanism of the surface-reaction. However, within static behaviors of MOMBE growth, the mechanism of the surface-dependent reaction has not been clear. In order to extract the essential factors in the surface-dependent reaction, the information beyond the static behaviors has been required.

Pulsed molecular beam scattering is a powerful technique to observe the dynamical behavior of the surface reaction, especially of the adsorption and desorption of gases [22]. Recently, we demonstrate that the surface residence time and the energy relaxation of TMG during scattering can be directly evaluated from the time-of-arrival distributions of TMG scattered from well-defined GaAs surfaces and that the surface scattering of TMG is interpreted within the framework of precursor-mediated chemisorption mechanism [23–25].

In this paper, we discuss the surface chemistry during MOMBE on the basis of the results of the pulsed TMG beam scattering from the well-defined GaAs surfaces which carefully prepared by epitaxial growth and subsequent treatments, focusing on the mechanism of selective area growth and lateral growth of GaAs. Furthermore, we examine the TMG scatterings from GaAs surfaces with similar reconstructions which are prepared by different methods.

2. Experimental procedure

The experiments were carried out in a multichamber system comprising an MOMBE growth facility, a pulsed molecular beam scattering chamber, and a surface treatment chamber, which have already been described elsewhere [23–25].

We generated pulsed TMG beams using a rotating chopper with two slits of 2 mm in width and a synchronized high-speed pulsed valve with a 0.5 mm nozzle. The pulse shape of incident TMG beams was well reproduced by the velocity distribution of translationally shifted Maxwell–Boltzmann with a translational shift velocity of 457 m/s and a velocity spread of 103 m/s. Using a cryoshrouded quadrupole mass spectrometer, we measured the time-of-arrival (time-of-flight) distributions of TMG molecules scattered from GaAs surfaces prepared in the MOMBE growth facility and the surface treatment chamber.

GaAs surface has variously reconstructed or relaxed structures, depending on the surface stoichiometry as well as the surface orientation. Furthermore, surface properties are known to vary with the surface preparation method even if the reconstructions are similar [26]. In this study, we compared the TMG scatterings from differently prepared GaAs surfaces, containing epitaxially prepared GaAs(1 0 0), GaAs(1 1 0), and GaAs(1 1 1)B surfaces with controlled structures as well as As-desorption-prepared GaAs surfaces. We also examined the scattering from the oxidized GaAs surface, where TMG decomposition is known to be suppressed. The oxidized GaAs surfaces were prepared by oxygen exposure under no light irradiation.

3. Results and discussion

3.1. Scattering of TMG from oxidized GaAs surfaces

First, we examined the scattering of TMG molecules from oxidized GaAs surfaces in order to study the mechanism of selective area growth of GaAs.

The time-of-arrival distributions of TMG molecules scattered from oxidized GaAs surfaces were found to be broader than those expected from the velocity distribution of the incident TMG beams. This broadening is due to the relaxation of translational energy of TMG molecules during scattering. From the analysis of the time-of-arrival distributions, we can evaluate the relaxation of the translational energy of TMG molecules. These time-of-arrival distributions were well reproduced by the convolution of the velocity distributions of incident and scattered TMG, where the velocity distribution of scattered TMG molecules were assumed to be of shifted Maxwell–Boltzmann, while the velocity distribution of incident TMG molecules are directly measured [24].

From the curve-fitting of the time-of-arrival distributions, we extracted two parameters in the velocity distribution of scattered TMG molecules, velocity spread and shift velocity. Fig. 1 shows these parameters as functions of the surface temperature.

If there is no energy relaxation during scattering, the velocity distribution of the scattered TMG molecules would be equal to that of the incident TMG molecules. On the other hand, if TMG scattering occurs under thermal equilibrium at the surface temperature, the velocity spread would be equal to the solid line and the shift velocity would be zero. It is noticed from Fig. 1 that the parameters extracted from time-of-arrival distributions trace the values corresponding to those under thermal equilibrium. According to the mass spectrometric study of desorbed species, TMG molecules do not decompose on this oxidized GaAs surface [27]. Therefore, it is considered that TMG molecules are not decomposed even when TMG molecules obtain thermal energy from surface during scattering under thermal equilibrium. It should be noted that TMG

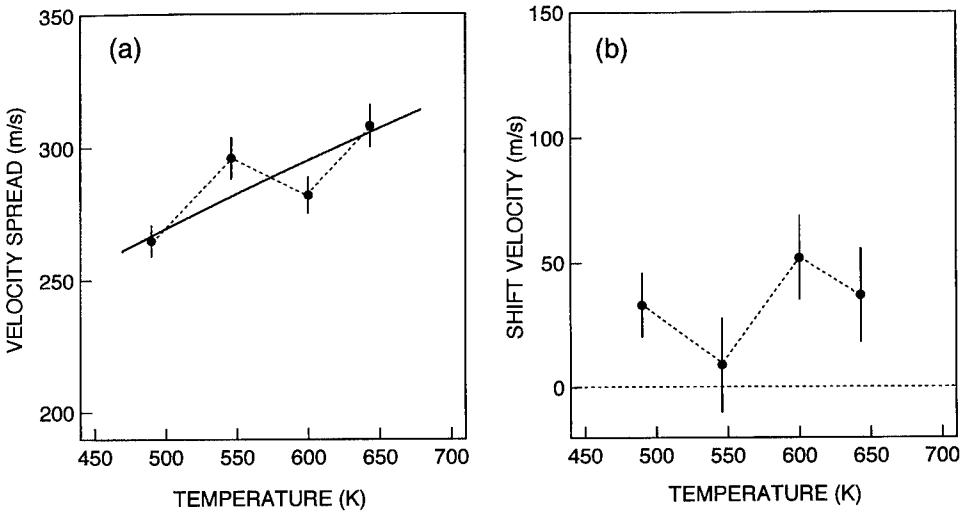

Fig. 1. (a) Velocity spread and (b) shift velocity in velocity distribution of TMG scattered from oxidized GaAs surface as functions of the surface temperature. These values were obtained by curve-fitting of time-of-arrival distributions of scattered TMG to the convolution formula of velocity distributions of incident and scattered TMG. The velocity distributions are assumed to be of shifted Maxwell–Boltzmann. If there is no energy relaxation during scattering, the velocity distribution of the scattered TMG molecules would be equal to that of the incident TMG molecules; that is, velocity spread and shift velocity would be 457 and 103 m/s, respectively. On the other hand, if TMG molecules are completely thermalized by the substrate surface, the velocity spread would be equal to the solid line ($\sqrt{2kT}$ s/m) and the shift velocity would be zero.

molecules are efficiently decomposed on the GaAs surface at the same temperature. The result suggests that the difference in the TMG decomposition rate is not attributed to the difference in the amount of the energy transfer from GaAs surface to TMG molecules during scattering.

3.2. Scattering of TMG from GaAs surfaces

According to the TMG decomposition rate on GaAs(1 0 0) surface as a function of surface As coverage, the TMG decomposition is anomalously suppressed on a specific GaAs(1 0 0)-(2 × 4) surface ($\theta_{As} = 0.75$), which is reproducibly obtained by a controlled cooling process after GaAs epitaxy [21]. Since the structure of this surface is known to be highly stabilized, we presume that TMG decomposition is suppressed when the structure stability is sufficiently high.

In the case of the TMG scattering from the specific GaAs(1 0 0)-(2 × 4) surface, the time-of-arrival distribution was found to be much broader and cannot be interpreted only by the translational energy relaxation. This distribution was well reproduced by adding a component for scattering with a trapping during scattering for such a long period that we can directly observe within the time resolution of the system we used. Fig. 2 shows the result of the curve-fitting of the time-of-arrival distribution of TMG to the sum of the components for scatterings with and without surface residence. This indicates that there exists a precursor state, where TMG molecules are temporarily trapped in the initial stage of scattering. From the temperature dependence of the reciprocal surface residence time (TMG escape rate from the precursor state to vacuum), the depth of the precursor state is estimated to be 0.85 eV [28]. Although TMG molecules are dominantly trapped in the deep precursor state, almost all the TMG molecules are desorbed without a permanent sticking (the sticking probability is nearly zero).

This behavior was also observed on the GaAs(1 1 0) and GaAs(1 1 1)B-($\sqrt{19} \times \sqrt{19}$) surfaces. It has been established that the GaAs(1 1 0) surface is stabilized [29]. From the temperature programmed desorption study, the stability of the GaAs(1 1 1)B-($\sqrt{19} \times \sqrt{19}$) structure is considered

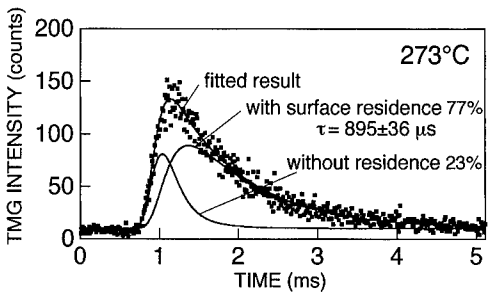

Fig. 2. The result of the curve-fitting of the time-of-arrival distribution of TMG scattered from the TMG-decomposition-suppressed GaAs(1 0 0)-(2 × 4) surface at 273°C to the sum of the components of scatterings with and without a surface residence during scattering, where the relaxation of translational energy during scattering was taken into account. The obtained result shows that 77% of TMG molecules are desorbed after trapping for a surface residence time of about 0.9 ms in the precursor state without dissociative chemisorption.

to be high [25]. Therefore, we conclude that this behavior is common for the scattering of TMG from the highly stabilized GaAs surfaces.

From the temperature dependence of the surface residence time during scattering, the depths of the precursor states for GaAs(1 1 0) and GaAs(1 1 1)B-($\sqrt{19} \times \sqrt{19}$) surfaces are estimated to be 0.32 and 0.35 eV, respectively [30].

In order to explain the depth of precursor states, we simply examine the charge distribution of the relaxed or reconstructed GaAs surface structures. The electrons of dangling states in Ga are completely moved to As to maintain a semiconducting surface [31]. Therefore, in the buckled picture of the GaAs(1 1 0) surface [29], the topmost Ga–As pair generates a sufficiently large electrostatic dipole moment outside the crystal, which can polarize TMG molecules coming near to the surface, resulting in the TMG trapping in the deep precursor states observed here [25]. In the case of the GaAs(1 1 1)B-($\sqrt{19} \times \sqrt{19}$) surface [32], the electrostatic behavior is considered to be similar to that for the (1 1 0) surface. The deeper precursor state for the GaAs(1 0 0)-(2 × 4) surface is explained by the higher density of the Ga–As pairs in the proposed (2 × 4) structure [33]. Therefore, the surface electrostatic behavior explains well the depth of the precursor state [30].

In the case of the scattering from less stabilized GaAs surfaces such as GaAs(1 0 0)-c(4 × 4), GaAs(1 0 0)-(1 × 6), and GaAs(1 1 1)B-(1 × 1) surfaces, where high TMG decomposition rate is observed [6, 21], the time-of-arrival distributions were observed to have no component for the scattering with a long surface residence, as shown in Fig. 3. The small amount of scattered TMG corresponds to the large amount of TMG dissociatively chemisorbed [25]. We consider that there exists a precursor state also on the GaAs surface with less stability, since the surfaces have As–Ga pairs generating the large electric dipole, and that TMG trapped in the precursor state is efficiently decomposed, providing such a high TMG decomposition rate as about 0.5.

From the comparison of the scatterings from clean GaAs and oxidized GaAs surfaces, it is concluded that the TMG decomposition suppression on the oxide is attributed to the lack of the precursor state [24].

3.3. TMG decomposition suppression by excess As

TMG decomposition is highly suppressed on the As-excess GaAs(1 1 1)B surface with (2 × 2) reconstruction, resulting in the lateral growth of GaAs on a grooved GaAs(1 1 1)B substrate by controlling As flux [8]. We examined pulsed TMG beam scattering also on the GaAs(1 1 1)B-(2 × 2) surface. The TMG scattering was found to be very similar to that from the oxidized GaAs surfaces; that is, all the TMG molecules are scattered without trapping in a deep precursor state although the energy relaxation occurs.

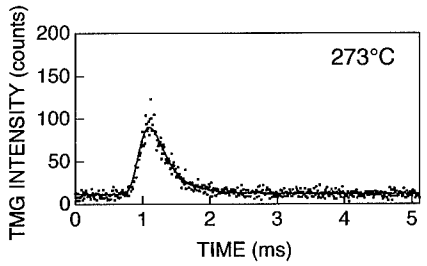

Fig. 3. The time-of-arrival distribution of TMG scattered from a reactive GaAs(1 0 0)-(1 × 6) surface at 273°C, which is well reproduced by the single component of scattering without surface residence, where translational energy relaxation during scattering is taken into account. The smaller signal corresponds to the higher sticking probability of TMG.

This feature is interpreted by the reconstructed surface structure. The GaAs(1 1 1)B-(2 × 2) surface consists of As-trimers on As-terminated GaAs(1 1 1)B surface [32]. According to the simple estimation of electron distribution similar to that for the above-mentioned GaAs surfaces, the topmost As trimers on As-terminated surface are neutral [30]. The As–Ga pairs in the second and third atomic layers, where electrons are biased, certainly generate large electric dipole moments. However, the space between As trimers where TMG molecules can approach is small compared with the TMG molecular size. We consider that TMG trapping is hindered geometrically by such neutral adatoms as topmost As-trimers on the As surface. This mechanism is consistent with the results on the super-As-rich GaAs(1 0 0)-c(4 × 4) that TMG sticking probability decrease as the As coverage further increases [25].

3.4. Surface preparation dependence of the TMG scattering

The above-mentioned GaAs(1 0 0)-(2 × 4) surface, where TMG decomposition is suppressed, was prepared by controlling As flux during the cooling process after GaAs epitaxial growth (referred to as epitaxially prepared surface). A GaAs(1 0 0) surface showing (2 × 4) reconstruction can also be obtained by another method such as a process containing As desorption from an As-covered GaAs surface (referred to as As-desorption-prepared surface). It has been reported that the work function of the epitaxially prepared GaAs(1 0 0)-(2 × 4) surface is largely different from that of the As-desorption prepared GaAs(1 0 0)-(2 × 4) surface [26]. This demonstrates that these surfaces are not the same. Here, we examine the scatterings of pulsed TMG beam from these surfaces.

Fig. 4 shows the temperature-programmed desorption (TPD) spectrum of As_2 from an As-rich GaAs(1 0 0)-c(4 × 4) surface, in which observed reconstructions are also given. The ramp rate is set at 0.1°C/s. It is considered that the bottom of the deep valley at 480°C in Fig. 4 corresponds to the

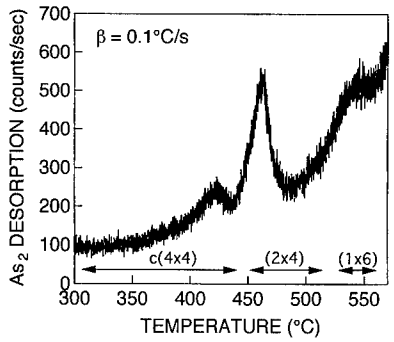

Fig. 4. Temperature programmed desorption spectrum of As_2 from an As-excess GaAs(1 0 0)-c(4 × 4) surface. The ramp rate is 0.1°C/s. The reconstructions observed by RHEED during the temperature programmed desorption measurement are given.

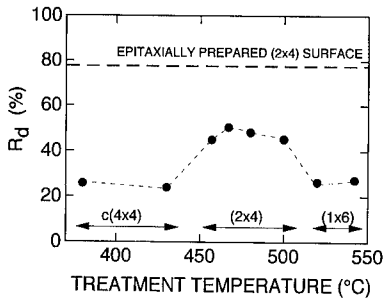

Fig. 5. The ratio (R_d) of the amount of TMG molecules in the component for the scattering with the surface residence time to the total amount of TMG scattered from As-desorption prepared GaAs(1 0 0) surfaces as a function of the treatment temperature. These amounts were evaluated by integrating the fitted distributions; $R_d = \int F_d(t)\,dt / \int F(t)\,dt$, where $F_d(t)$ and $F(t)$ are the fitted time-of-arrival distribution for the component for the scattering with surface residence and the fitted total time-of-arrival distribution, respectively. The dashed line indicates the R_d value for the scattering from the epitaxially prepared GaAs(1 0 0)-(2 × 4) surface (Fig. 2).

GaAs(1 0 0) surface with the highest stability among the As-desorption-prepared (2 × 4)-reconstructed surfaces.

For TMG scattering experiments, we prepared GaAs(1 0 0) surfaces by heating the As-rich GaAs(1 0 0)-c(4 × 4) surface up to different treatment temperatures (T_t's) at a ramp rate of 0.1°C/s and quenching it. The time-of-arrival distributions of TMG molecules scattered from these surfaces were analyzed by curve-fitting to the sum of the components for scatterings with and without surface residence during scattering in the same manner as in the cases of the Fig. 2.

Fig. 5 shows the ratio (R_d) of the amount of TMG molecules in the component for scattering with a long surface residence to the total amount of scattered TMG as a function of T_t. The R_d value was evaluated by integrating the fitted time-of-arrival distribution. The dashed line in Fig. 5 indicates the R_d value for the scattering from the epitaxially prepared GaAs(1 0 0)-(2 × 4) surface (Fig. 2).

We found in Fig. 5 that R_d's for the As-desorption-prepared surfaces are much smaller than that for the epitaxially prepared surface. This result indicates that TMG surface chemistry varies with the surface preparation even if the reconstructions observed by low-energy electron diffraction (LEED) or reflection high-energy electron diffraction (RHEED) are similar. The component for the scattering with the surface residence corresponds to the TMG molecules which survive dissociative chemisorption in the precursor states for a long period. The dissociative chemisorption on GaAs surface is considered to occur at the surface sites with less stabilized structure (referred to as active sites). Therefore, high R_d indicates a low density of active sites. This results suggests that the density of active sites on As-desorption-prepared surface is higher than that on the epitaxially prepared surface.

As can be seen in Fig. 5, R_d is relatively high when the surface shows (2 × 4) reconstruction. However, we cannot observe a tendency that R_d become larger at the treatment temperature corresponding to the valley bottom in the TPD spectrum. Here the difference in As desorption rate in the TPD spectrum suggests the difference in the stability of the surface. This discrepancy is explained by taking into account the surface diffusion, which enables TMG efficiently to reach to active sites even if the number of the active site is very small. This behavior is consistent with the As coverage dependence of the TMG decomposition rate [21].

The GaAs surface during MOMBE growth is considered to be different from the static surfaces

we examined in this study, even if the surface reconstructions are observed to be similar. During growth, surface atoms are not necessarily in the most stable sites but moving dynamically. Then, the density of active sites is probably higher. Therefore, it is expected that MOMBE growth is not so strongly suppressed by the surface stability. In fact, it was observed that the As-coverage dependence of MOMBE growth rate on GaAs(1 0 0) is not so drastic as that of TMG scattering in this study [10], although the growth rate decrease due to the high surface stability, which is well explained by the mechanism proposed in this study, is clearly observed.

4. Summary

We measured the time-of-arrival distributions of TMG scattered from variously reconstructed or relaxed GaAs(1 0 0), GaAs(1 1 0) and GaAs(1 1 1)B surfaces as well as oxidized GaAs surface. The initial stage of the TMG surface chemistry on GaAs is interpreted within the framework of precursor-mediated chemisorption. We discussed the TMG decomposition suppression in the cases of the selective area growth and the lateral growth of GaAs. The growth suppression on oxidized GaAs surfaces during the selective area epitaxy of GaAs is due to the absence of the deep precursor states, rather than smaller energy that TMG obtains during scattering from substrate surface. On the other hand, the growth suppression on the As-excess GaAs(1 1 1)B surface during the lateral growth of GaAs is originated from neutral As-trimers geometrically hindering TMG trapping. It was also found that TMG scattering was so sensitive that it varies with the surface preparation method even if the diffraction patterns are similar. This suggests that TMG diffuse over wide area during trapping in the precursor states.

Acknowledgements

This work was carried out at Optoelectronics Technology Research Laboratory (OTL). The authors would like to thank Dr. Y. Katayama, Dr. C. Yamada, Dr. M. Yamada, Dr. I. Hayashi and Dr. M. Tamura for their fruitful discussion and continuous encouragement.

References

[1] E. Tokumitsu, Y. Kudou, M. Konagai and K. Takahashi, J. Appl. Phys. 55 (1983) 3163.
[2] Y. Hiratani, Y. Ohki, Y. Sugimoto, K. Akita, M. Taneya and H. Hidaka, Jpn. J. Appl. Phys. 29 (1990) L1360.
[3] S. Yoshida and M. Sasaki, in: Proc 19th Int. Symp. GaAs and Related Compounds, Karuizawa, Japan, 1992, Eds. T. Ikegami, H. Hasegawa, and Y. Takeda, Inst. Phys. Conf. Ser. No. 129 (1993) p. 49.
[4] J. Nishizawa, H. Abe and T. Kurabayashi, J. Electrochem. Soc. 132 (1985) 1197.
[5] A. Watanabe, T. Isu, M. Hata, T. Kamijo and Y. Katayama, Jpn. J. Appl. Phys. 28 (1989) L1080.
[6] Y. Ohki, Y. Hiratani and M. Sasaki, Appl. Phys. Lett. 59 (1991) 2538.
[7] Y. Ohki and Y. Hiratani, Appl. Organometal. Chem. 5 (1991) 277.
[8] Y. Nomura, Y. Morishita, S. Goto and Y. Katayama, J. Electron. Mater. 23 (1994) 97.
[9] T.H. Chiu, J.E. Cunningham and A. Robertson, J. Crystal Growth 95 (1989) 136.
[10] T. Isu, M. Hata and A. Watanabe, J. Crystal Growth 105 (1990) 209.
[11] T. Kaneko, H. Asahi and S. Gonda, J. Crystal Growth 120 (1992) 39.
[12] T. Kaneko, O. Naji, T.S. Jones and B.A. Joyce, J. Crystal Growth 127 (1993) 1059.
[13] D.E. Aspnes, I. Kamiya, H. Tanaka and R. Bhat, J. Vac. Sci. Technol. B 10 (1992) 1725.
[14] N. Kobayashi and Y. Horikoshi, Jpn. J. Appl. Phys. 30 (1991) L319.
[15] D.W. Kisker, G.B. Stephensen, P.H. Fuoss, F.J. Lamelas, S. Brennan and P. Imperatori, J. Crystal Growth 124 (1992) 1.
[16] J. Nishizawa, T. Kurabayashi, H. Abe and A. Nozoe, Surf. Sci. 185 (1987) 249.
[17] J.R. Creighton, K. Lykke, V.A. Shamamian and B.D. Kay, Appl. Phys. Lett. 57 (1990) 279.
[18] J.R. Creighton, Surf. Sci. 234 (1990) 287.
[19] M.L. Yu, J. Appl. Phys. 73 (1993) 716.
[20] M. Mashita, Jpn. J. Appl. Phys. 29 (1990) 813.
[21] M. Sasaki and S. Yoshida, J. Vac. Sci. Technol. B 10 (1992) 1720.
[22] M. Asscher and G.A. Somorjai, in: Atomic and Molecular Beam Methods, Vol. 2, Ed. G. Scole (Oxford University Press, New York, 1992) p. 488.
[23] M. Sasaki and S. Yoshida, Jpn. J. Appl. Phys. 33 (1994) L884.
[24] M. Sasaki and S. Yoshida, Surf. Sci. 315 (1994) L964.
[25] M. Sasaki and S. Yoshida, Surf. Sci. 356 (1996) 233.

[26] R. Duszak, C.J. Palmstrøm, L.T. Florez, Y.-N. Yang and J.H. Weaver, J. Vac. Sci. Technol. B 10 (1992) 1891.
[27] Y. Hiratani and Y. Ohki, unpublished.
[28] M. Sasaki and S. Yoshida, Jpn. J. Appl. Phys. 34 (1995) 1113.
[29] C.B. Duke, J. Vac. Sci. Technol. A 10 (1992) 2032.
[30] M. Sasaki and S. Yoshida, Surf. Sci. 357/358 (1996) 863.
[31] D.J. Chadi, J. Vac. Sci. Technol. A 5 (1987) 834.
[32] D.K. Biegelsen, R.D. Bringans, J.E. Northrup and L.-E. Swartz, Phys. Rev. Lett. 65 (1990) 452.
[33] M.D. Pashley, Phys. Rev. B 40 (1989) 10481.

ELSEVIER

Journal of Crystal Growth 175/176 (1997) 1186–1194

JOURNAL OF CRYSTAL GROWTH

Lateral coupling of InP/GaInAsP/InP structures by selective area MOMBE

M. Wachter[a], U. Schöffel[a], M. Schier[b], H. Heinecke[a,*]

[a] *University of Ulm, Department of Semiconductor Physics, D-89069 Ulm, Germany*
[b] *Siemens AG, Corporate Research and Development, D-81730 Munich, Germany*

Abstract

Lateral couplings of InP/GaInAsP/InP structures selectively grown by metalorganic molecular beam epitaxy (MOMBE) are presented. The heterostructures were grown by either using the hydrides AsH_3 and PH_3 or tertiarybutylphosphine and tertiarybutylarsine as group V precursors in a prototype multiwafer (MOMBE) system. The base heterostructures of the first epitaxy were patterned with SiO_2 mask stripes and trenches were reactive-ion etched. Heterostructures were selectively filled in by a second growth run forming lateral heterojunctions of different quaternary materials. The structures exhibit a bright photoluminescence and a sharp transition at the boundary of the locally grown material indicating a high crystal quality up to the lateral junction with only a minor change in the PL wavelength (< 2 nm). These optimized lateral couplings were applied to laser/waveguide butt-couplings. Optical coupling losses were determined by means of reactive-ion etched waveguides across cascades of coupled GaInAsP layers with an emission wavelength of $\lambda_G \approx 1050$ nm. Values as low as 0.12 dB/coupling were determined in cut-back measurements.

1. Introduction

The realization of photonic integrated circuits (PICS) is a field of growing interest [1–3]. The monolithic integration of devices like lasers, waveguides and photodetectors require some lateral coupling of heterostructures. Lateral couplings can be achieved by overgrowth of patterned semiconductor surfaces [4, 5]. A more attractive pathway for the production of PICS with lateral couplings is the embedded selective-area epitaxy (SAE), due to the planarity of the structures and a higher degree of freedom in the design of the device structures [1, 2, 6].

The true SAE of InP/GaInAsP heterostructures is only achieved in metalorganic growth systems [2, 7]. The lateral couplings of heterostructures by SAE have been realized in metalorganic vapour phase epitaxy (MOVPE) [1, 8–10] and in metalorganic molecular beam epitaxy (MOMBE) [3, 11].

In MOVPE the gas-phase-concentration gradients and diffusion processes lead to a growth-rate enhancement and to a change of the material composition starting at a distance larger than 50 μm from the masked area. This behaviour is a function of the growth parameters and depends on the mask

* Corresponding author: Fax: + 49 731 502-6106; e-mail: heinecke@sunrise.e-technik.uni-ulm.de.

0022-0248/97/$17.00 Copyright © 1997 Elsevier Science B.V. All rights reserved
PII S0022-0248(96)01027-5

geometry and the aspect ratio of the masked to the unmasked area [2, 12–14].

In MOMBE the growth is determined by the adsorption, diffusion and desorption processes of the molecules on the semiconductor surface only. The variation of the material composition on the (1 0 0) surface at a transition of a growth to a non-growth area is not significantly affected [6] and is rather independent of the aspect ratio [2, 15]. In the case of embedded SAE, the growth starts in a tub at various crystal planes. The growth rate on these side walls has to be optimized for planar infills. The published couplings achieved by selective area MOMBE so far were all grown by using a tilted molecular beam geometry for the group III precursors [3, 11]. Due to shadowing and side wall growth effects there is only a small growth parameter window to achieve a good lateral contact without gaps or planar layers with no growth rate enhancement at the transition area for the use of a tilted beam geometry. Therefore, we have here applied a perpendicular molecular beam geometry for reducing the lateral growth rate [16].

In terms of production, the replacement of hydrides by less dangerous precursors like tertiarybutylarsine (TBAs) and tertiarybutylphosphine (TBP) is of growing interest [17, 18]. High-quality heterostructure couplings are obtained with both classes of precursors. The optimization of the embedded SAE-process yields extremely low-loss waveguide couplings applicable in PICs.

2. Experimental procedure

The samples were grown in a multiwafer production-type MOMBE system (Riber Epineat).

The precursors trimethylindium (TMI), triethylgallium (TEG) for the group III elements, and thermally precracked arsine (AsH_3) or TBAs and phosphine (PH_3) or TBP for the group V elements are injected into the growth chamber. The group III molecular beams are created by gas injectors having an angle of 90° or 50° with respect to the substrate surface. Due to the lower lateral growth all the growth experiments presented in this study were carried out by using the perpendicular molecular beam geometry [16].

In the first epitaxy an InP/GaInAsP/InP double hetero(DH)structure was grown on a 2 inch InP wafer misoriented 2° towards the nearest (1 1 0) plane. This base structure was covered by different 120 nm-thick SiO_2 masks. The mask consists either of SiO_2 stripes with a width between 4 and 100 μm and a periodicity of 500 μm or of 15 μm wide SiO_2 twin stripes separated by a gap ranging from 1.5 to 5 μm with a periodicity of 250 μm. Trenches up to 2.7 μm in depth were reactively ion etched into the base structure of the first epitaxy. Prior to the second SAE growth run, the samples were etched in $H_2SO_4 : H_2O_2 : H_2O$ (3 : 1 : 6 in volume ratio) for 5 to 20 s just before introduction into the loading chamber. DH structures were filled in by the second growth run with a typical V/III input ratio of 10, a growth temperature of 495°C and a vertical growth rate of 0.5 μm/h.

We have investigated lateral couplings between InP/GaInAsP/InP base structures with an emission wavelength of $\lambda_G \approx 1550$ or 1050 nm and a filled in DH structure with $\lambda_G \approx 1550$ or 1050 nm. All the couplings were oriented in the [0 1 1] or [0 $\bar{1}$ $\bar{1}$] direction, which is the standard orientation for laser cavities in the production.

3. Results and discussion

The test structure for the integration of lasers and waveguides is the coupling of a DH structure with $\lambda_G \approx 1550$ nm and the infill DH structure with $\lambda_G \approx 1050$ nm.

The scanning electron microscopy (SEM) cross-section view in Fig. 1a shows a 5 μm wide selective infill ($\lambda_G = 1048$ nm) in between two 15 μm wide masked DH base structures ($\lambda_G = 1510$ nm). The SEM investigations reveal planar infill-layers and smooth contacts with lateral heterojunctions of the quaternary layer. The selective infill was grown under conditions where the (0 1 1) and (0 $\bar{1}$ $\bar{1}$) planes are kinetically stable in planar SAE [7, 16, 19]. The perpendicular molecular beam geometry ensures a low lateral growth rate. In the case of a high lateral growth rate, the infilled layers are curved and the vertical growth rate enhancement in the vicinity of the junction facet leads to the formation of the significant "ears" in

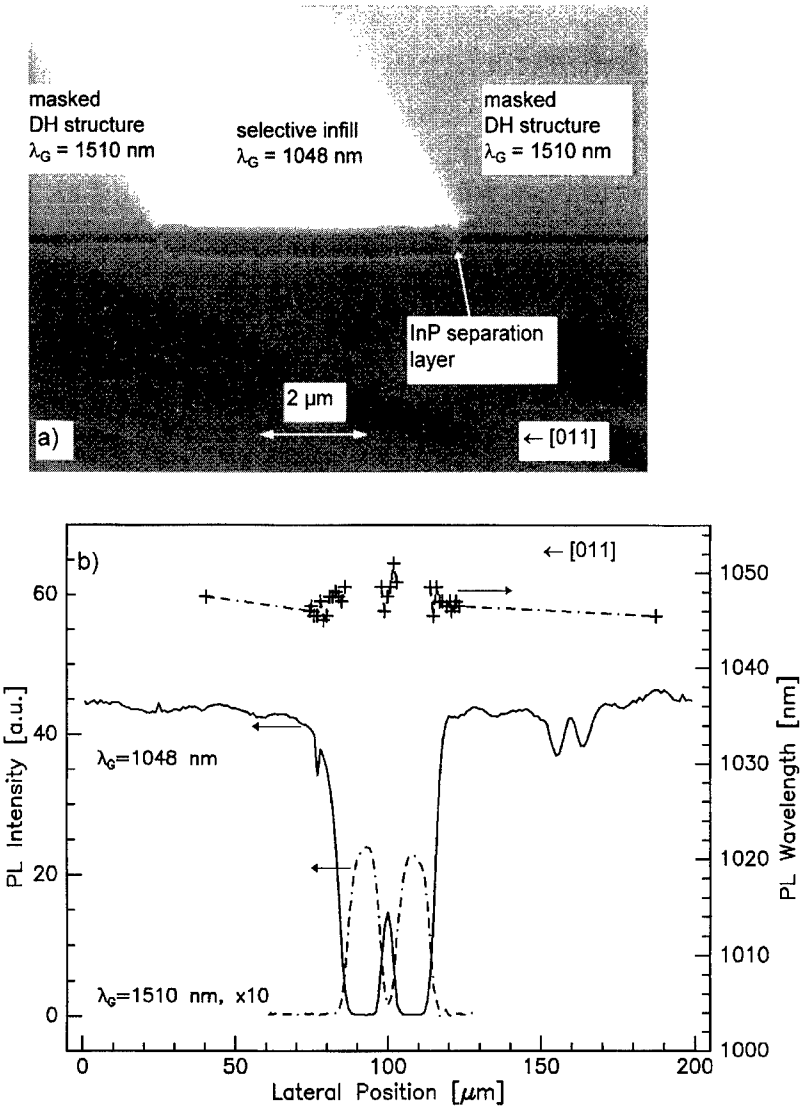

Fig. 1. Lateral junctions between selective infill [InP(d = 0.15 µm)/GaInAsP(d = 0.5 µm, λ_G = 1048 nm)/InP(d = 0.15 µm)] and masked DH structure [InP(d = 0.8 µm)/GaInAsP(d = 0.2 µm, λ_G = 1510 nm)/InP(d = 0.2 µm)] grown by using AsH_3 and PH_3. (a) SEM cross-section view; (b) Spatially resolved PL measurements at 300 K. Linescans of the PL intensity at the PL wavelength of the maximum and PL wavelength versus the lateral position of the laser spot.

the transition area [2]. Anyhow the lateral growth rate has to be high enough to avoid gaps between the infill and the side wall of the masked base structure. The planarity of the SAE layers shown is independent of the aspect ratio (here investigated from 2 to 22%) of the masked to the unmasked surface and of the width of the masked ridges or the width of the etched trenches.

During the growth of the InP buffer layer a vertical InP separation layer was grown at the side wall of the tub (see Fig. 1a). This InP separation layer is adjustable in the thickness in the range from 10%

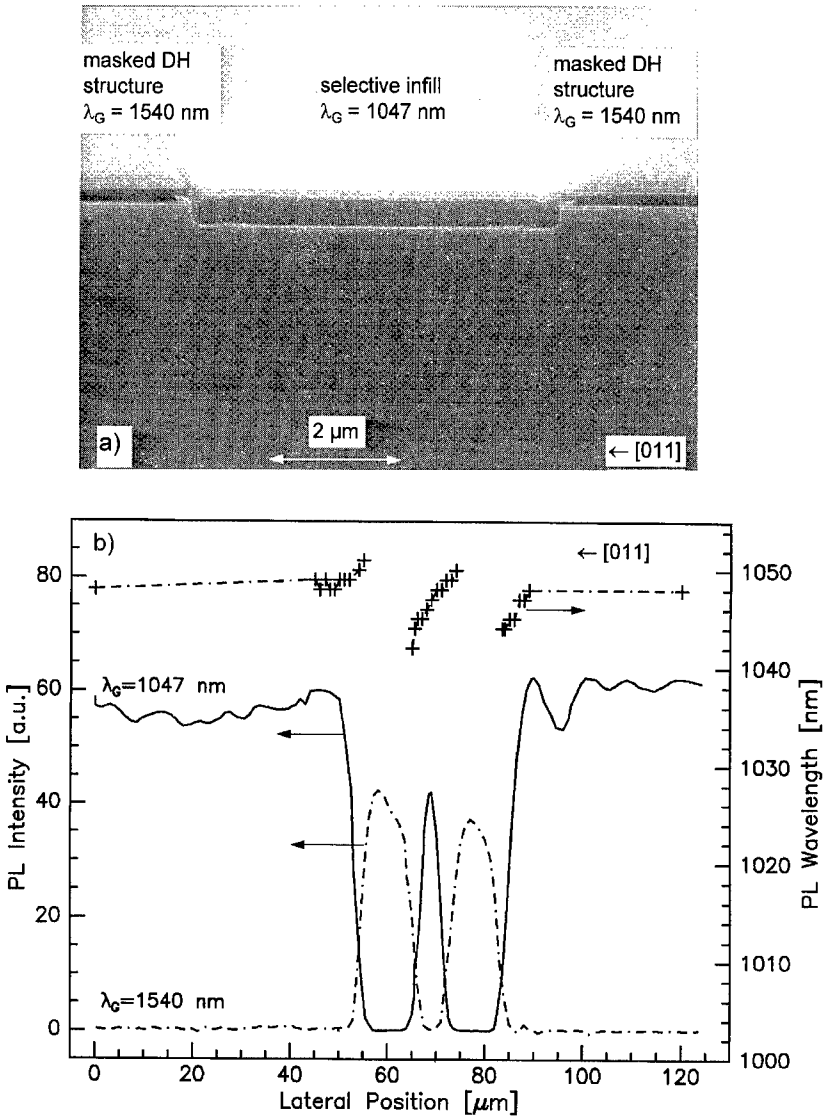

Fig. 2. Lateral junctions between selective infill [InP(d = 0.15 µm)/GaInAsP(d = 0.4 µm, λ_G = 1047 nm)/InP(d = 0.15 µm) and masked DH structure [InP(d = 0.8 µm)/GaInAsP(d = 0.2 µm, λ_G = 1540 nm)/InP(d = 0.2 µm)] grown by using TBAs and TBP. (a) SEM cross-section view; (b) Spatially resolved PL measurements at 300 K. Linescans of the PL intensity at the PL wavelength of the maximum and PL wavelength versus the lateral position of the laser spot.

to 90% of the InP buffer thickness by changing the growth parameters of the buffer layer and the molecular beam geometry. In the micrograph shown in Fig. 1a this lateral thickness is 50%. The thickness of the InP separation layer is reduced for a lower vertical growth rate and a lower growth temperature. For comparison, when using the tilted injection geometry the thickness of the InP separation layer is increased up to a factor of 2.

An efficient butt-coupling of two DH structures requires a constant material composition of the quaternary infill up to the mask edge. We have

investigated the material quality at the transition area by means of spatial-photoluminescence (μ-PL) measurements at room temperature. The plot in Fig. 1b shows linescans of the PL intensity dependent on the lateral position of the excitation laser spot (spot size 5 μm in diameter) on the (1 0 0) surface of the sample. The SAE quaternary layer exhibits a bright luminescence and a sharp decay at the boundary of the locally grown structure. This decay of the PL intensity at $\lambda_G = 1048$ nm coincides spatially with the increase at $\lambda_G = 1510$ nm and vice versa. The measured decay /increase length of 4 – 5 μm coincides with the spot size of the excitation laser beam. Consequently, a sharp transition boundary is realized. The measured maximum PL wavelength at the lateral heterojunction in the coupling zone is very stable. The small deviation of ± 2 nm is in the order of the wavelength error using 300 K PL for the rapidly decreasing intensity at the junction. At a distance of 5 μm, the PL wavelength of the infill is identical to the emission wavelength of a large-area-grown reference sample emphasizing the independence of the aspect ratio of the mask.

Previous investigations by spatially resolved X-ray diffraction of heterostructures selectively grown by MOMBE have shown a change of the lattice mismatch of less than 1.0×10^{-4} in a transition width of 6 μm. μ-PL measurements at these samples have demonstrated low variations in the PL wavelength too [20, 21]. We conclude from this knowledge and our PL results that the quaternary material composition with a high crystal quality is not affected up to the lateral junction and that the composition of the infill is identical to the reference sample.

In comparison to the sample presented in the SEM micrograph in Fig. 1a, the filled in DH structure ($\lambda_G = 1047$ nm) in Fig. 2a was grown using TBAs and TBP as group V precursors. This infill shows a slight ear formation. The linescans of the PL intensity in the plot in Fig. 2b exhibits again a sharp transition of the quaternary materials with emission wavelengths of $\lambda_G = 1047$ (infill) and 1540 nm (base structure). The measured wavelength shift of ± 4 nm of the quaternary infill at the junction is slightly higher for the infill grown with TBAs and TBP. This example was grown with a vertical growth rate of 1 μm/h instead of the standard growth rate for SAE of 0.5 μm/h.

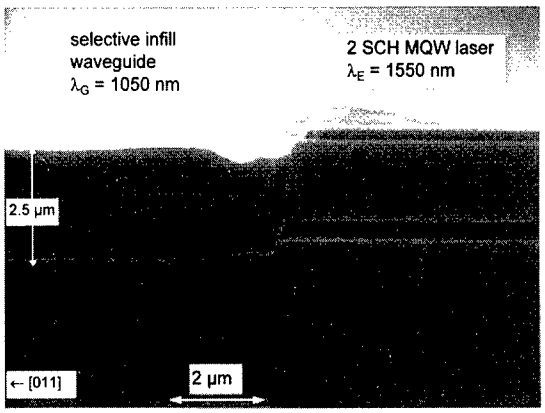

Fig. 3. Lateral butt-coupling of a 2 SCH-MQW ($\lambda_E = 1550$ nm) laser with a waveguide ($\lambda_G = 1050$ nm) structure.

Further experiments with the growth rate of 0.5 μm/h have shown a slight growth rate enhancement at the mask boundary too. This overgrowth and wavelength shift is probably caused by different surface diffusion processes, so that an individual optimization for the TBP/TBAs-process is required.

The results of the optimization in the hydride process of the selective infill were applied for laser/waveguide butt-couplings. Fig. 3 presents a cross-section of a laser/waveguide butt-coupling grown with the conventional hydrides. There is a smooth contact between the strained multiquantum-well laser structure with two separate confinement layers (2 SCH MQW) [22] and the waveguide infill [23]. The infill with a height of 2.5 μm shows neither any overgrowth over the mask nor ears at the junctions. During the growth of the entire selective infill the growth rate, the growth temperature and the V/III ratio was kept constant. This convenient growth procedure is only applicable in the perpendicular geometry [16, 24].

Masked islands of 100 μm × 600 μm were embedded by the waveguide DH structure with $\lambda_G = 1050$ nm forming lateral couplings. Laser-waveguide chips were cleaved. The lasers (400 μm in length) are surrounded on three sides by the waveguide DH structure. The threshold current

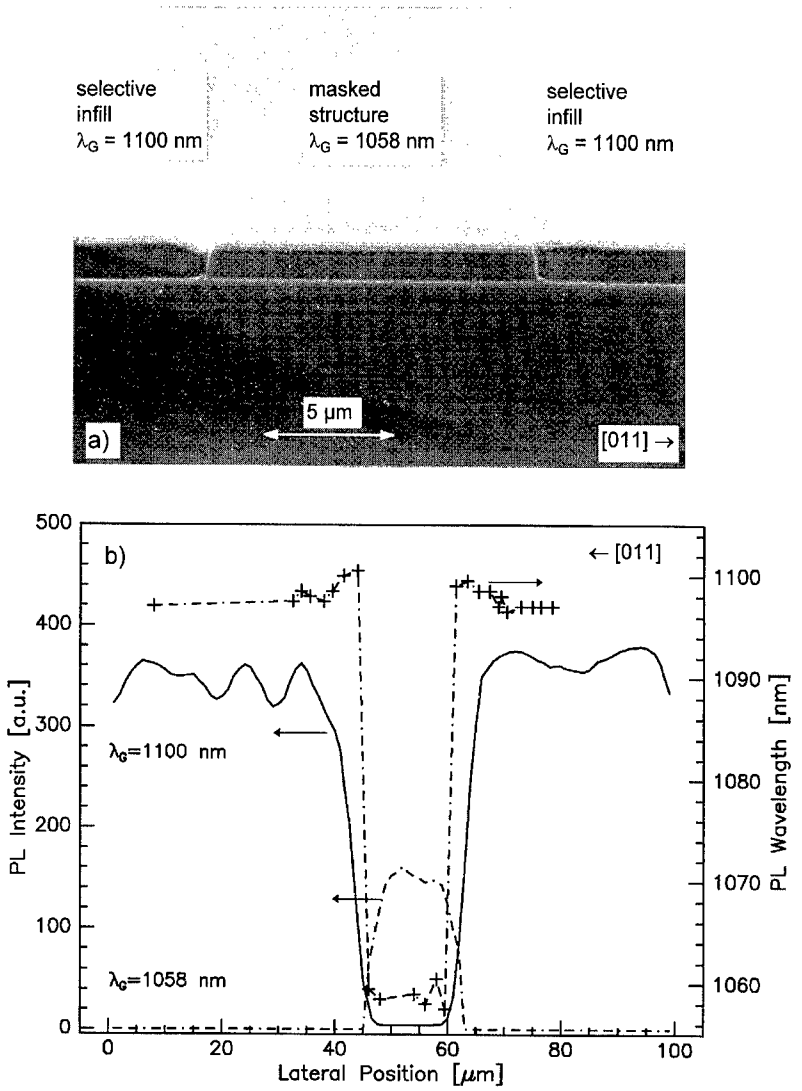

Fig. 4. Lateral junctions between selective infill [InP(d = 0.25 µm)/GaInAsP(d = 1.15 µm, λ_G = 1100 nm)/InP(d = 0.4 µm)] and masked DH structure [InP(d = 0.5)/GaInAsP(d = 1.1 µm, λ_G = 1058 nm)/InP(d = 0.45 µm)] (a) SEM cross-section view; (b) Spatially resolved PL measurements at 300 K. Linescans of the PL intensity at the PL wavelength of the maximum and PL wavelength versus the lateral position of the laser spot.

density of a laser/waveguide combination with a 300 µm-long waveguide-DH structure is j_{th} = 1.28 kA/cm^2. The threshold current density decreases to j_{th} = 880 A/cm^2 if the waveguide-DH structure in the direction of the laser cavity is cleaved off. This threshold current density is identical with the value of a reference sample before selective-area-growth processing [22, 23]. Consequently, the etching and SAE growth of the waveguide have not degraded the laser performance. In order to determine quantitatively the optical losses at such lateral couplings a waveguide/waveguide integration was processed.

The SEM cross-section view in Fig. 4a gives an example of a coupling of an InP/GaInAsP(λ_G = 1058 nm)/InP and an InP/GaInAsP(λ_G =

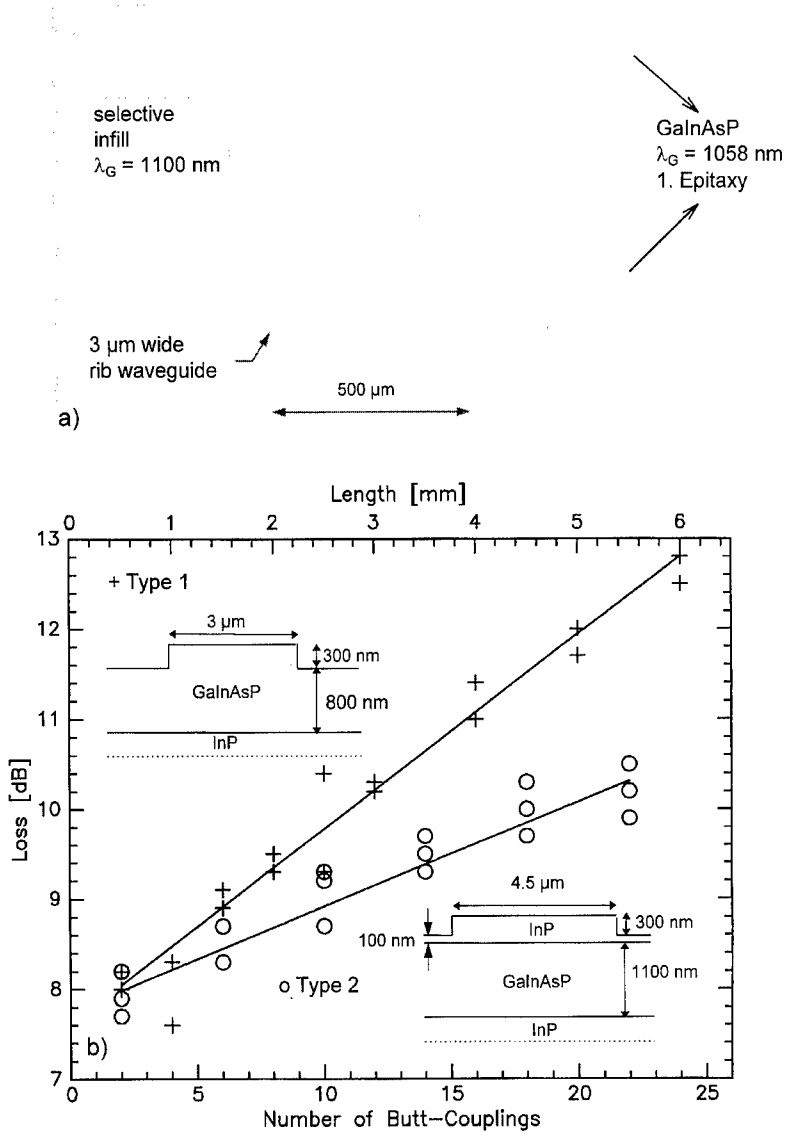

Fig. 5. Cascades of waveguide/waveguide butt-couplings. (a) Interference contrast micrograph of a top view on a coupling cascade and (b) optical loss versus the number of butt-couplings of two different types of rib waveguides.

1100 nm)/InP. In this example the masked structure was grown with TBAs and TBP.

Such a structure allows for the investigation of the material composition at the transition areas by µ-PL due to a difference in λ_G higher than the full width of maximum of the PL peak at 300 K and for the precise loss measurements at the butt-couplings due to an approximately identical refractive index of both quaternary materials. This SAE infill exhibits absolutely planar layers, a thin InP separation layer (10% of the buffer layer thickness) and a smooth contact to the masked quaternary material. The µ-PL data in Fig. 4b are comparable to the data of the example in Fig. 1b, except for the lateral

transition of an emission wavelength of $\lambda_G = 1058$ to 1100 nm. Again, there is only a shift of the PL wavelength at the junction of less than ± 2 nm. These properties promise highly efficient butt-couplings.

Fig. 5a gives a Nomarski interference micrograph of a top view on a series of reactive-ion-etched-rib waveguides perpendicular across the lateral heterojunctions. The horizontal 8 and 12 μm-wide lines represent the heterostructure with $\lambda_G = 1058$ nm from the first grown structure. In between, there is an infill of the DH structure with $\lambda_G = 1100$ nm. We have etched two different types of rib waveguides as shown in the inset of Fig. 5b. In type 1 the wave is guided by a 3 μm wide reactive-ion-etched ridge in the quaternary material. The second type of waveguide is obtained by a 4.5 μm-wide ridge etched in the InP cap layer.

The precise determination of the loss of the waveguide/waveguide butt-couplings was achieved with the cut-back method using the TE polarized laser light with a wavelength of 1540 nm. In Fig. 5b, the coupling loss of these different types of waveguides versus the number of butt-couplings is plotted. The small spread of data points for the two different waveguides of the same type in the case of type 1 and three in the case of type 2 over 12 cut-backs illustrates the high uniformity of the couplings. Some scatter of cleaved edge surface gives the major source of error in the measurement. Type 1 shows an optical loss of (0.22 ± 0.05) dB/coupling in the cut-back measurements for a series of 24 butt-couplings and type 2 the best value of (0.12 ± 0.04) dB/coupling for a series of 22 butt-couplings. The propagation loss of identical waveguides on a reference sample without any couplings was measured to be (0.59 ± 0.06) dB/cm by the Fabry–Perot resonance method [25]. This low propagation loss of the waveguides are comparable to the best published data [26, 27] and is still included in the cut-back measurements.

4. Conclusion

The embedded SAE grown lateral couplings of InP/GaInAsP/InP-DH structures have a constant material composition up to the lateral contact. The PL intensity is high up to the junction with a rapid decay at the junction given by the resolution of the laserspot of about 5 μm. We have presented the first lateral coupling of GaInAsP/InP heterostructures selectively grown by using the replacement precursors TBAs and TBP.

The reactive ion etching process and the selective regrowth of waveguides in MOMBE allow for a high quality butt-coupling of laser and waveguides and does not degrade the threshold current densities of the MQW lasers.

The butt-coupling efficiency of 97% measured at a cascade of 22 couplings on a length over 5.5 mm, which is in the order of the dimensions of chips incorporating PICs, is very attractive for applications in the integration of photonic devices.

Acknowledgements

The authors would like to thank E. Veuhoff, H. Baumeister, S. Illek, B. Schmidt from Siemens AG, P. Albrecht from Heinrich Hertz Institute, M. Popp and M. Keidler from University of Ulm for their support in processing and stimulating discussions. This work was partly funded by the German Ministery of Education and Research (BMBF) under contracts 01 BP 468/8 and 01 BM 412/2.

References

[1] R.C. Goodfellow, Mater. Sci. Eng. B 9 (1991) 1.
[2] G.J. Davies, W.J. Duncan, P.J. Skevington, C.L. French and J.S. Foord, Mater. Sci. Eng. B 9 (1991) 93.
[3] H. Heinecke and E. Veuhoff, Mater. Sci. Eng. B 21 (1993) 120.
[4] A. Ougazzaden, R. Mellet, A. Mircea and A. Affonso, Jr., Mater. Sci. Eng. B 9 (1991) 69.
[5] B. Baur, H. Heinecke, M. Schier and N. Emeis, J. Crystal Growth 127 (1993) 175.
[6] H. Heinecke, J. Crystal Growth 136 (1994) 18.
[7] H. Heinecke and E. Veuhoff, in: Proc. 6th Int. Conf. on Indium Phosphide and Related Materials, Santa Barbara, CA, USA (1994) Proc. IEEE Catalog No. 4CH3369-9, pp. 636–639.
[8] R. Strzoda, G. Ebbinghaus, T. Scherg and N. Emeis, J. Crystal Growth 154 (1995) 27.
[9] J.-H. Ahn, K.R. Oh, J.S. Kim, S.W. Lee, H.M. Kim, K.E. Pyun and H.M. Park, IEEE Photon. Technol. Lett. 8 (1996) 200.

[10] D. Trommer, Proc. 7th Eur. Conf. on Int. Opt. (ECIO) (1995) p. 93.
[11] P. Legay, F. Alexandre, J.L. Benchimol, M. Allovon, F. Laune and S. Fouchet, J. Crystal Growth 164 (1996) 314.
[12] H. Heinecke, A. Brauers, F. Grafahrend, C. Plass, N. Pütz, K. Werner, M. Weyers, H. Lüth and P. Balk, J. Crystal Growth 77 (1986) 303.
[13] E.J. Thrush, M.A. Gibbon, J.P. Stagg, C.G. Cureton, C.J. Jones, R.E. Mallard, A.G. Norman and G.R. Booker, J. Crystal Growth 124 (1992) 249.
[14] M. Gibbon, J.P. Stagg, C.G. Cureton, E.J. Thrush, C.J. Jones, R.E. Mallard, R.E. Pritchard, N. Collis and A. Chew, Semicond. Sci. Technol. 8 (1993) 998.
[15] H. Heinecke, Mater. Sci. Eng. B 9 (1991) 83.
[16] M. Wachter and H. Heinecke, J. Crystal Growth 164 (1996) 302.
[17] C.H. Chen, C.A. Larsen and G.B. Stringfellow, Appl. Phys. Lett. 50 (1987) 218.
[18] M. Keidler, M. Popp, D. Ritter, B. Marheineke and H. Heinecke, J. Crystal Growth 170 (1997) 161.
[19] R. Matz, H. Heinecke, B. Baur, R. Primig and C. Cremer, J. Crystal Growth 127 (1993) 230.
[20] A. Iberl, M. Schuster, H. Göbel, A. Meyer, B. Baur, R. Matz, A. Snigirev, L. Snigireva, A. Freund, B. Lengeler and H. Heinecke, J. Phys. D 28 (1995) A200.
[21] A. Iberl, H. Göbel and H. Heinecke, J. Phys. D 28 (1995) A172.
[22] M. Popp, H. Heinecke, H. Baumeister and E. Veuhoff, J. Crystal Growth 175/176 (1997) 1247.
[23] M. Keidler, M. Wachter, M. Popp, H. Baumeister, E. Veuhoff and H. Heinecke, to be published.
[24] H. Heinecke, Phys. Scr. T 55 (1994) 14.
[25] R.G. Walker, Electron. Lett. 21 (1985) 581.
[26] H. Künzel, P. Albrecht, R. Gibis, M. Hamacher and S. Schelhase, J. Crystal Growth 164 (1996) 449.
[27] J.H. Angenent, M. Erman, J.M. Auger, R. Gamonal and P.J.A. Thijs, Electron. Lett. 25 (1989) 628.

ELSEVIER

Journal of Crystal Growth 175/176 (1997) 1195–1199

JOURNAL OF CRYSTAL GROWTH

New semiconductors TlInGaP and their gas source MBE growth

H. Asahi[a,*], M. Fushida[a], K. Yamamoto[a], K. Iwata[a], H. Koh[a], K. Asami[a], S. Gonda[a], K. Oe[b]

[a] *The Institute of Scientific and Industrial Research, Osaka University, 8-1, Mihogaoka, Ibaraki, Osaka 567, Japan*
[b] *NTT Opto-electronics Laboratories, Morinosato Wakamiya Atsugi, Kanagawa 243-01, Japan*

Abstract

New III–V compound semiconductors $Tl_xIn_{1-x-y}Ga_yP$ (thallium indium gallium phosphide), which we proposed recently for 0.9 μm to over 10 μm laser diodes, are grown by gas source molecular beam epitaxy on InP and GaAs substrates for the first time. They have a potential to exhibit a temperature-independent band-gap energy. Grown layers exhibit (2 × 4) surface reconstruction. X-ray diffraction measurements show the successful growth of TlInP, TlGaP and TlInGaP, although phase separation is observed in TlGaP grown on GaAs. Photoluminescence emission is observed for TlInP and TlInGaP grown on InP. Hall measurements show n-type conduction with a room temperature electron concentration of 6.3×10^{15} cm^{-3} and an electron mobility of 2 500 cm^2/V·s.

PACS: 68.55.Bd; 78.65.Fa

Keywords: Thallium alloy; TlInP; TlGaP; TlInGaP; Infrared; Mid-infrared; Temperature-independent band gap; Gas source MBE

1. Introduction

Recently, we have proposed the new III–V compound semiconductors $Tl_xIn_{1-x-y}Ga_yP$ (thallium indium gallium phosphide) as an active layer for 0.9 μm to over 10 μm wavelength range laser diodes [1]. TlInGaP can be lattice-matched to InP as well as GaAs. This material system can cover the wavelength range from 0.92 μm (InP) to over 10 μm (TlInP) and is suitable for optical devices, especially for 1 μm range laser diodes (LDs) for optical fiber communications and mid-infrared (longer than 2 μm) LDs. Furthermore, these LDs can have the potential to operate without changing the wavelength with ambient temperature variation. TlInGaP can also be lattice-matched to GaAs, covering wavelengths from 0.65 μm (InGaP) to about 1.24 μm (TlGaP).

The estimated band gap energy variation with alloy composition is shown in Fig. 1 [1]. The line

* Corresponding author. E-mail: asahi@sanken.osaka-u.ac.jp.

0022-0248/97/$17.00 Copyright © 1997 Elsevier Science B.V. All rights reserved
PII S0022-0248(96)00936-0

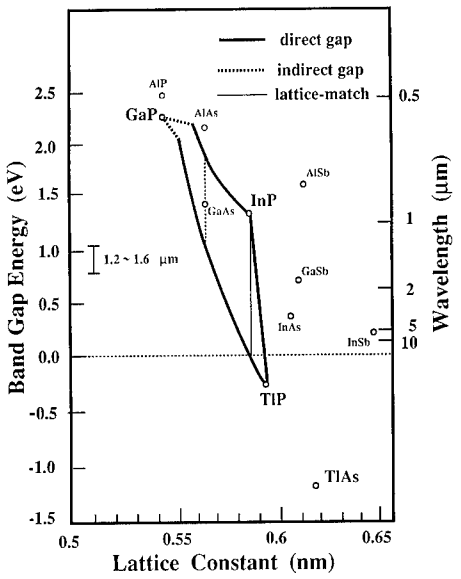

Fig. 1. Band gap energy versus lattice constant for TlInGaP (see text). Compositions for the lattice-matching to InP and GaAs are indicated by vertical solid line and vertical dashed line, respectively.

for InGaP is based on experimental data, the line for TlInP is from theoretical calculation [2], while the line for TlGaP is only estimated. These semiconductor materials are alloys consisting of the semiconductor InGaP and the semimetal TlP. This alloy system has only one group V atom and the type-I band lineup having a wider conduction band discontinuity than that of valence band is expected. This characteristics is very suitable for the optical devices. Furthermore, the semiconductors whose band gap does not change with ambient temperature are expected because of the alloy of semiconductor and semimetal similar to $Hg_xCd_{1-x}Te$, where the temperature-independent band-gap energy at a Hg composition of 0.4 was observed [3]. This characteristics is very promising to fabricate semiconductor lasers whose wavelength does not change with ambient temperature variation, which is very important for the advance in WDM (wavelength division multiplexing) optical fiber communication, because one problem in using InGaAsP/InP LDs in WDM system is that the lasing wavelength fluctuates with ambient temperature variation due to the temperature dependence of band gap energy and LDs in WDM system must be equipped with Peltier elements that works to stabilize LD temperature.

In this paper, we report the first successful growth of this material system by using gas source molecular beam epitaxy (MBE) on both InP and GaAs substrates. Preliminary results on optical and electrical properties are also described.

2. Experimental procedure

The growth was conducted in a gas source MBE apparatus (ANELVA GBE-830), which was evacuated by an oil diffusion pump with liquid-nitrogen trap [4]. Elemental Tl (5N), In (7N) and Ga (7N) were used as group III sources and thermally cracked PH_3 was used as a group V source. The substrates used were Fe-doped (100) InP and Cr-doped (1 0 0) GaAs. The substrate temperature was monitored with an optical pyrometer calibrated by the melting point of InSb at 525°C. PH_3 flow rate was 0.5–1.5 SCCM. The vapor pressure of Tl is similar to that of Sb (antimony) at low cell temperatures and lower at high cell temperatures, and Tl vaporizes from melt. Therefore, the Tl flux controllability is much better than that of Sb. The toxicity of Tl is known to be higher than that of As, so that extreme care during treatment must be taken. Tl or Tl contaminated surfaces should not be touched with bare hands and Tl flakes or vapors should not be inhaled: lethal intake is documented to be at 600 mg.

Grown surfaces were studied by reflection high energy electron diffraction (RHEED). Crystallographic quality and mole fraction of layers were evaluated by X-ray diffraction. Electrical properties were studied by van der Pauw Hall measurement. Photoluminescence (PL) measurement was conducted with an Ar ion laser (488 nm) as an excitation source.

3. Results and discussion

3.1. Growth on InP

The InP substrate surface was thermally cleaned at 480°C under a PH_3 flow rate of 1.0 SCCM. After

thermal cleaning, an InP buffer layer (0.1 μm thick) was grown at a substrate temperature of 350–450°C with a PH_3 flow rate of 0.3–0.5 SCCM. RHEED patterns showed (2 × 4) phosphorus-stabilized reconstruction. On these InP buffer layers, TlP binary, TlInP ternary and TlInGaP quaternary layers were grown (thickness: about 0.5 μm). Tl composition of TlInP was 0–1, while Tl and Ga compositions of TlInGaP were about 0.05–0.2 and 0.1–0.2, respectively.

RHEED patterns for TlP and TlInP revealed (2 × 4) reconstruction at substrate temperatures of 400–450°C showing phosphorus-stabilized surfaces. The surface exhibited mirror-like. During the growth of TlInP, RHEED intensity oscillation was observed as shown in Fig. 2. By the addition of Tl flux during the growth of InP, the oscillation period was decreased indicating the growth of TlInP. At lower temperatures RHEED pattern showed phosphorus-excess (2 × 2) reconstruction.

Fig. 3 shows the double crystal (monochromatic) X-ray diffraction rocking curves for TlP/InP and TlInP/InP samples. In addition to the peak from InP, those from TlP and TlInP are clearly visible, indicating the successful growth of TlP and TlInP. TlInP alloys with various Tl compositions were also grown by varying Tl flux during growth and the alloy composition of TlInP was found to vary with Tl flux [5]. Therefore, it was shown that the entire range of TlInP can be grown by gas-source MBE. Recently, phase separation was reported in the MOVPE growth of TlInSb (thallium indium antimonide) [6]. However, in the present study we observed no phase separation in TlInP grown on InP by gas-source MBE, though phase separation was observed in the TlGaP growth as described below.

PL emission was detected from the TlInP layers grown on InP substrates. Fig. 4 shows the 77 K PL spectra from TlInP and InP. The PL shift to lower energy is small in Fig. 4 because of low Tl composition. PL study on TlInP with larger Tl composition is in progress, and results will be reported in the separate paper. Preliminary Hall measurement data on TlInP showed n-type conduction with an electron concentration of 6.3×10^{15} (3.9×10^{15}) cm^{-3} and an electron mobility of 2 500 (22 000) $cm^2/V \cdot s$ at room temperature (77 K) for TlInP with a Tl composition of 5%.

Fig. 5 shows the double crystal X-ray diffraction rocking curves for the TlInGaP quaternary layer grown on InP. The peaks from InP and TlInGaP are clearly observed. The shifts to the lower diffraction angle for the TlInGaP peak with increasing Tl flux and to the higher angle with increasing Ga flux were observed. These shifts agree with the increase of Tl mole fraction and Ga mole fraction, respectively. This indicates that quaternary TlInGaP

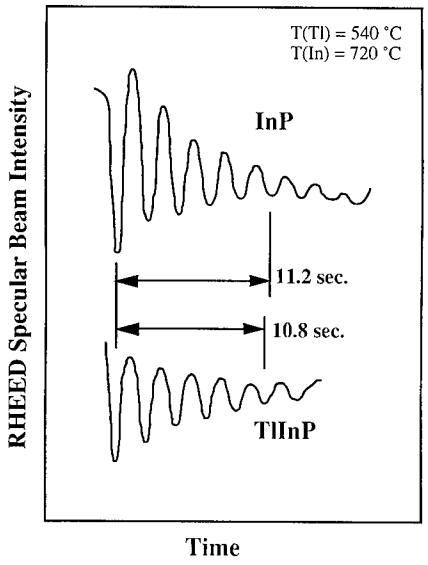

Fig. 2. RHEED intensity oscillations during the growth of InP and TlInP.

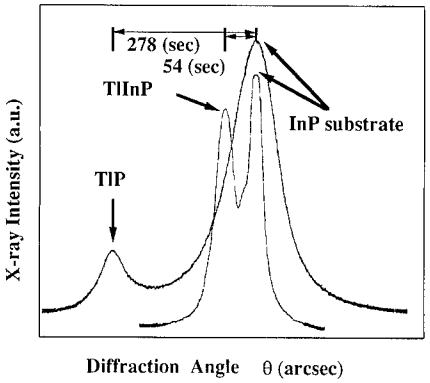

Fig. 3. Double crystal X-ray diffraction rocking curves for TlP/InP and TlInP/InP.

layers can also be grown by gas-source MBE. Reduction of full width at half maximum (FWHM) was also observed by decreasing the degree of lattice-mismatch for TlInGaP as can be seen in Fig. 5. No phase separation was also observed. This result indicates that the TlInGaP alloy on InP substrate is promising from the viewpoint of crystal growth. We have observed the PL (not shown) only from the TlInGaP with a composition close to InP at present.

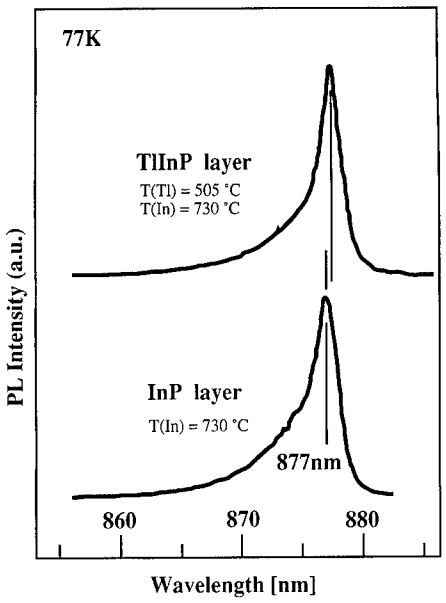

Fig. 4. Photoluminescence spectra from InP and TlInP grown on InP.

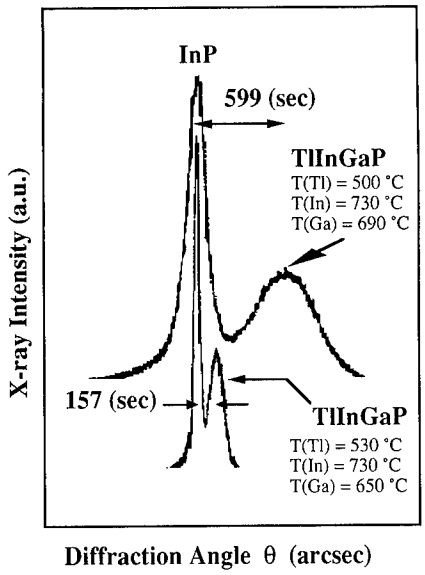

Fig. 5. Double crystal X-ray diffraction rocking curves for TlInGaP on InP.

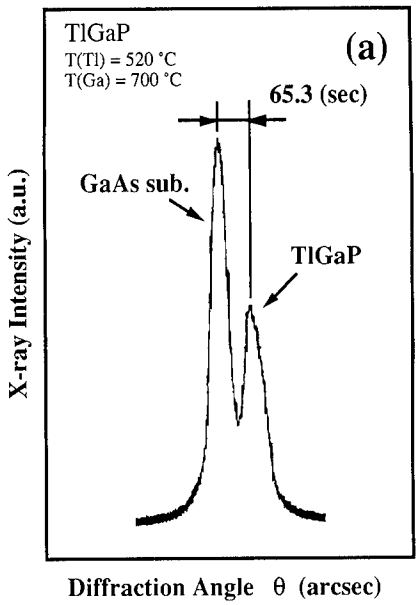

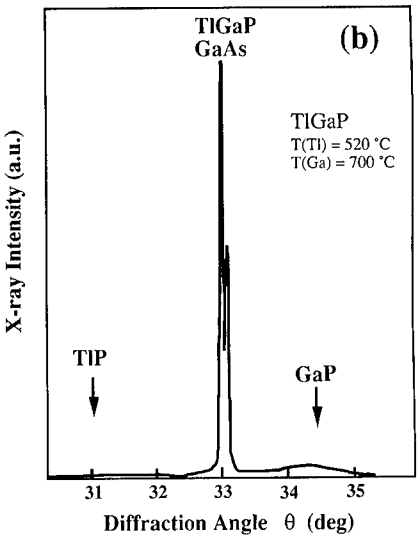

Fig. 6. (a) Double crystal (monochromatic) X-ray diffraction rocking curve for TlGaP on GaAs around the angle of GaAs. Peak from TlGaP is observed as well as that of GaAs. (b) Powder (unmonochromatic) X-ray diffraction rocking curve for the same sample. Phase separation is observed.

3.2. Growth on GaAs

We have also grown TlGaP layers on GaAs substrates. TlGaP layers (thickness: about 0.5 μm) were grown after the growth of GaAs buffer layer. Fig. 6 shows (a) double crystal (monochromatic) X-ray diffraction rocking curve and (b) conventional powder (unmonochromatic) X-ray diffraction rocking curve from TlGaP/GaAs. Two peaks are observed in Fig. 6a. Lower and higher angle peaks are confirmed to come from GaAs substrate and TlGaP layer, respectively, by selective etching of TlGaP layer with HCl. This means that the nearly lattice-matched TlGaP was grown here. However, as shown in Fig. 6b, phase separation was also observed. In addition to the diffraction peaks from GaAs and nearly lattice-matched TlGaP at around 33.06° where the Kα1 and Kα2 peaks are resolved, the broad peak at the angle for GaP (34.45°) is also observed. The broad peak is also visible at the angle for TlP (31°), though weak for this sample. This observation indicates the occurrence of phase separation and is contrast to the result for TlInP on InP. This difference seems to be due to the difference in lattice-mismatch between the two systems. Tl comopsition of phase separated TlGaP having lattice constant close to GaAs ranged from about 0.47–0.53 in the present study. More detailed results will be reported elsewhere.

4. Summary

We have, for the first time, studied the growth of new semiconductor TlInGaP, which we recently proposed as an active layer of 0.9 μm to over 10 μm laser diodes, by gas source MBE on (1 0 0) InP and GaAs substrates. Grown layers exhibited (2×4) surface reconstruction. RHEED intensity oscillation was observed during the growth of TlInP as well as InP indicating the layer by layer growth. X-ray diffraction measurements showed the successful growth of TlInP, TlGaP and TlInGaP. No phase separation was observed in TlInP and TlInGaP grown on InP substrate, while the phase separation was observed in TlGaP grown on GaAs. PL emission was observed for TlInP and TlInGaP grown on InP, though composition was close to InP. The layers showed n-type conduction with an electron concentration of 6.3×10^{15} (3.9×10^{15}) cm^{-3} and an electron mobility of 2 500 (22 000) $cm^2/V \cdot s$ at room temperature (77 K) for TlInP with a Tl composition of 5%. It is concluded that the gas source MBE is a promising method for the growth of TlInGaP.

References

[1] H. Asahi, K. Yamamoto, K. Iwata, S. Gonda and K. Oe, Jpn. J. Appl. Phys. 35 (1996) L876.
[2] M. van Schilfgaarde, A.B. Chen, S. Krishnamurthy and A. Sher, Appl. Phys. Lett. 65 (1994) 2714.
[3] D. Long, Energy Bands in Semiconductors (Wiley, New York, 1968).
[4] H. Asahi, K. Asami, T. Watanabe, S.J. Yu, T. Kaneko, S. Emura and S. Gonda, Appl. Phys. Lett. 58 (1991) 1407.
[5] K. Yamamoto, H. Asahi, M. Fushida, K. Iwata and S. Gonda, J. Appl. Phys. 81 (1997), in press.
[6] K.T. Huang, R.M. Cohen and G.B. Stringfellow, J. Crystal Growth 156 (1995) 320.

ELSEVIER

Journal of Crystal Growth 175/176 (1997) 1200–1204

JOURNAL OF CRYSTAL GROWTH

CBE of 1.55 μm (GaIn)(AsP) lasers for monolithic integration

A. Nutsch[a,b,*], B. Torabi[a,b], H. Kratzer[b], G. Tränkle[a], G. Weimann[a]

[a] *Fraunhofer-Institut für Angewandte Festkörperphysik, Tullastrasse 72, D-79108 Freiburg, Germany*
[b] *Walter Schottky Institut, Am Coulombwall, D-85748 Garching, Germany*

Abstract

Chemical beam epitaxy is well suited for monolithic integration due to its mask selective growth. We have grown embedded GaInAsP/GaInAsP SCH MQW laser structures in grooves in InP substrates etched by ECR-RIE using CH_2/H_2 with Si_3N_4 masks, both, for etching and selective growth. Our laser structure consisted of six compressively strained quaternary MQWs, quaternary barriers ($\lambda = 1.2$ μm) and confinement layers ($\lambda = 1.1$ μm). Selectively grown stripe lasers in 4 μm wide grooves showed threshold currents of 16 mA for a length of 280 μm. No change in composition of the quaternary core appeared for lasers in 7 and 30 μm wide grooves, when compared with lasers on planar substrates. Quantum wells grown in narrow 4 μm wide grooves, on the other hand showed wavelength shifts depending on substrate misorientation. A 10 nm redshift is observed on (1 0 0) substrates oriented 2° off towards the next [1 1 0] direction, whereas a slight blueshift on (1 0 0) exact oriented substrates occurred.

1. Introduction

The monolithic integration of differing photonic devices requires selective area epitaxy. Chemical beam epitaxy (CBE) allows selective growth of (GaIn) (AsP) layers on structured and masked substrates, thus the integration of lasers, waveguides, etc. become possible. The growth is restricted to non-masked areas, as no nucleation takes place on dielectric masks, e.g. Si_3N_4. We describe the realisation of strained 1.55 μm laser structures for monolithic integration. Filling the laser into a groove on the substrate reduces the number of regrowths, lowering the thermal stress on the laser structure.

Best device performance is usually obtained with compressively strained GaInAsP/GaInAsP SCH MQW structures [1, 2]. The use of quaternary wells gives an additional degree of freedom, allowing a variation of strain at a fixed well width to obtain the required wavelength of 1.53 μm. It is essential in view of monolithic integration to grow these complicated laser structures selectively on Si_3N_4 masked and patterned InP substrates.

2. CBE of high quality GaInAsP

Epitaxy was performed on sulfur-doped (1 0 0) InP substrates oriented 2° off towards the nearest

* Corresponding author. Fax: + 49 89 3206 620; e-mail: arn@e26.physik.tu-muenchen.de.

0022-0248/97/$17.00 Copyright © 1997 Elsevier Science B.V. All rights reserved
PII S0022-0248(96)01205-5

[1 1 0] direction. The precursors were pure trimethylindium and triethylgallium as group-III sources. A high temperature (1050°C) injector decomposed arsine and phosphine as group-V sources. We investigated the epitaxial growth of lattice matched quaternary compounds and found only very narrow parameter windows suited for high crystal quality, essentially if growth temperatures are kept constant to avoid growth interruptions at the interfaces of the MQW structure.

Fig. 1 emphasizes the viable V/III_{BEP} ratios for our rather high growth temperature of 543°C as a function of the emission wavelength, characterizing the composition. Increasing In and P content, i.e. decreasing wavelength, requires higher supply of hydrides, changing from a V/III_{BEP} ratio of 3 for long wavelength GaInAsP to 8.5 and 10 for compositions corresponding to wavelengths of 1.2 and 1.1 μm, respectively.

GaInAsP layers (300 nm thick), lattice matched to InP, grown with the above parameters, always had high luminescence yield and mirror-like surface morphology. For long wavelength GaInAsP the typical 4.2 K photoluminescence linewidth was 3–4 meV. The compositions used for confinement and barriers showed slightly higher values of 5 meV. The linewidths were nearly independent of the strain, ranging from $(\Delta a/a)_{relax.} = -1.5 \times 10^{-3}$ to 1.5×10^{-3}. Photoluminescence linewidths obtained at 300 K are typically 40 meV. These results emphasize the high quality of GaInAsP in the narrow growth window.

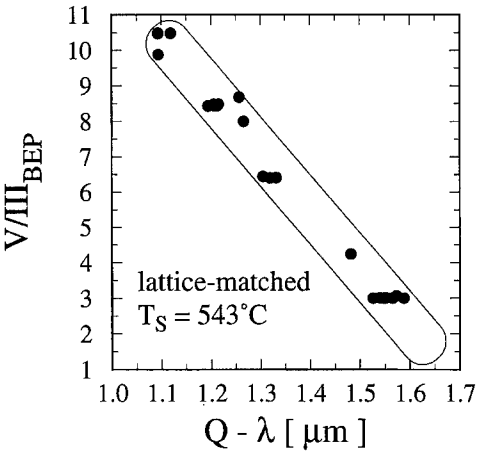

Fig. 1. Optimized V/III_{BEP} ratio as a function of GaInAsP composition for growth at $T_S = 543$°C, with an accurate control of the V/III_{BEP} ratio. With increasing Ga and As content the V/III_{BEP} ratio has to be lowered.

3. Planar growth of quaternary lasers

A typical MQW structure consisted of 6 compressively strained GaInAsP quantum wells and barriers with a material composition of $\lambda = 1.2$ μm. The MQW was embedded in-between two 1.2 and 1.1 μm GaInAsP separate confinement heterostructure layers with thicknesses of 35 and 100 nm, respectively. The n and p cladding layers with thicknesses of 1000 and 1600 nm were doped with elemental Si and Be.

These all quaternary MQWs showed an intense and narrow photoluminescence at 300 K ($E_{PL} = 0.81$ eV for laser emission at 0.80 eV) and 4.2 K, with FWHM values of 24 and 6.4 meV, respectively. The well width was 5.4 nm and the strain of the QW was $(\Delta a/a)_{relax.} = 6.5 \times 10^{-3}$, determined by XRD measurements. All other quaternary layers were lattice matched within $|\Delta a/a|_{relax.} < 0.25 \times 10^{-3}$. Broad area laser diodes processed from these structures [3] had extrapolated threshold current densities of 410 A cm^{-2} and internal losses of 12 cm^{-1}. These extremely low threshold current densities of 68 A cm^{-2} per quantum well clearly demonstrate the high quality of quaternary laser structures grown with CBE. Ternary lasers with equal well widths and half strain for the identical emission wavelength showed higher values of 78 A cm^{-2}, indicating the influence of higher strain for the reduction of threshold current densities.

4. Selective growth of laser structures

Having established optimized growth and material parameters on planar, i.e. nonstructured substrates, we used these growth conditions for the epitaxy of SCH MQW structures in grooves, 1.5 μm deep with varying widths. To obtain planar growth at the bottom of the groove, we modified

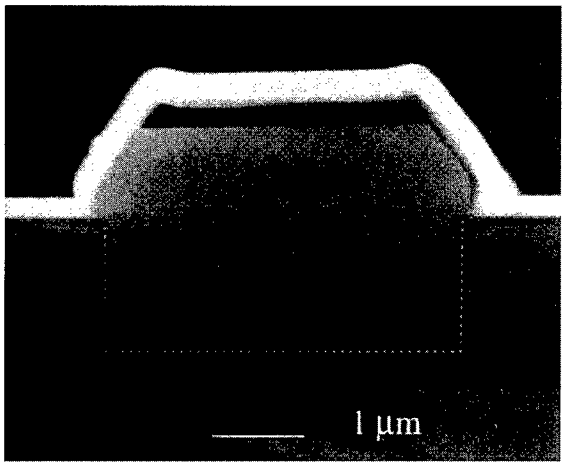

Fig. 2. SEM picture of the facet of a selectively grown MCRW Laser.

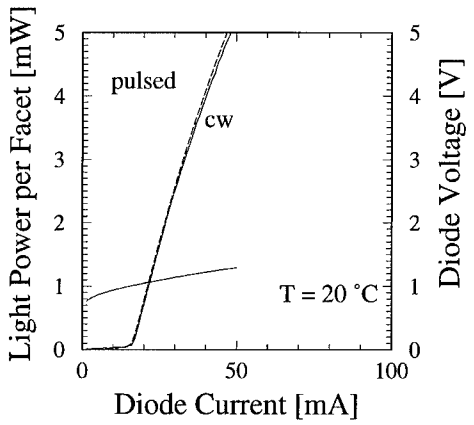

Fig. 3. Light power output characteristic of a (GaIn) (AsP) SCH MQW laser selectively grown in an InP groove. The identical threshold current is 16 mA, for pulsed and cw operation.

the growth rates for the InP : Si cladding layer, however. Reducing the growth rate $\alpha_{(1\ 0\ 0)}$ from the usual 0.4 nm s^{-1} to 0.1 nm s^{-1} and simultaneously increasing the V/III_{BEP} ratio from 4.5 to 18 resulted in planar growth without marked edge distortions, e.g. {1 1 1} facets. Once planar growth was achieved we grew the SCH MQW structure under optimized "material-quality" conditions maintaining nearly planar growth.

Fig. 2 presents the SEM picture of a cleaved facet. Due to the high growth rate of the GaInAsP layers (0.4 nm s^{-1}), small {1 1 1} facets at the edge of the SCH MQW layer appeared. Growth of 1.4 μm thick InP : Be cladding layers with $\alpha_{(100)} = 0.4$ nm s^{-1} to a height above the groove edge, resulted in a faceted ridge. This guaranteed an excellent coverage with the evaporated metallisation for contacting. Laser facets were obtained by cleaving perpendicular to the grooves. Fig. 3 shows the light power output-current characteristics for a 280 μm long, 4 μm broad device. The lasers show a low threshold current of 16 mA and an external quantum efficiency of 47% for both facets.

5. Selective growth on 2° misoriented substrates

Compositional changes of homogeneous thick GaInAsP layers and quaternary SCH MQW structures were investigated with cathodoluminescence for different groove widths. The laser core and thick GaInAsP layers did not change in composition in 7 and 30 μm wide grooves, compared to the planar growth. In narrow, 4 μm wide grooves the energy shift was − 5 meV for quaternary and − 13 meV for ternary quantum wells (see Fig. 4).

The decrease in emission energy of 1.2 μm wavelength, thick GaInAsP was found to be 10 meV. For GaInAs the energy shift indicates an increase in compressive strain. The relative

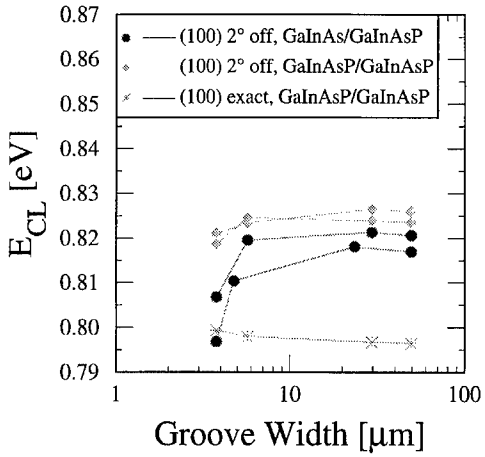

Fig. 4. Cathodoluminescence measurements for different groove widths. For 4 μm wide grooves on (1 0 0) 2° misoriented substrates a redshift is observed. For the same grooves on exactly oriented (1 0 0) substrates a blueshift occurs.

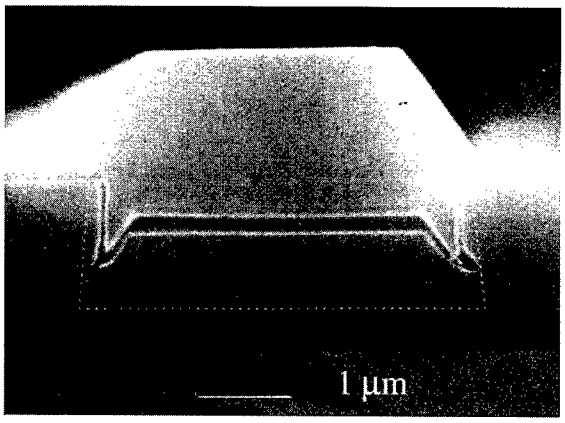

Fig. 5. SEM picture of the cleaved facet of a selective grown laser structure on a (1 0 0) oriented substrate.

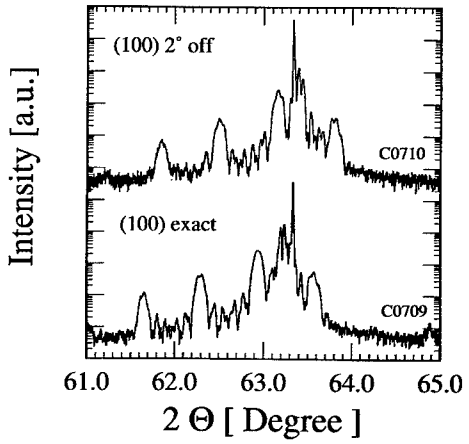

Fig. 6. XRD spectra of wide area selectively grown SCH MQW structures on (1 0 0) substrates, oriented exactly and 2° off.

incorporation ratio In/Ga during planar growth for quaternary and ternary compositions showed a constant value of 2.5, independent of composition. Due to the observed equal incorporation ratio In/Ga at planar growth for quaternary and ternary compositions the energy shift indicated a lower Ga incorporation for GaInAs and for GaInAsP. In the case of the GaInAsP ($\lambda = 1.2$ µm) the energy shift linked with a reduced phosphorus incorporation.

With decreasing misorientation of the substrate, i.e. lower surface step density, the gallium and the phosphorus incorporation of GaInAsP ($\lambda = 1.05$ µm) were found to decrease [4]. In our case, we observed a tilted surface in the 4 µm wide grooves, corresponding to the misorientation of the substrate. These phenomena did not occur when using exactly oriented (1 0 0) InP substrates as shown in Fig. 5. The SEM picture shows the facet of a selectively grown laser in a groove on a substrate with an exact (1 0 0) surface orientation. Here the energy shifted to slightly higher values (+3 meV) as shown in Fig. 4.

Growth of laser structures yielded higher compressive strain when using (1 0 0) oriented substrates in comparison to structures grown at the same temperature and material fluxes on 2° misoriented substrates. XRD spectra show this clearly in Fig. 6. The upper spectrum is that of a SCH MQW structure on a misoriented substrate, the lower spectrum shows the same structure grown on a (1 0 0) exactly oriented substrate. Especially, the peaks attributed to the confinement layers shifted to lower angles indicating a change in lattice mismatch of $\Delta(\Delta a/a) = 3 \times 10^{-3}$ for $\lambda = 1.1$ µm and 1.2 µm GaInAsP. For the long wavelength GaInAsP of the quantum wells the change of mismatch was half with $\Delta(\Delta a/a) = 1.5 \times 10^{-3}$. The photoluminescence energy rose by 25 meV on the misoriented substrate, while the superlattice period was constant within 0.2 nm, indicating unchanged growth rates.

The energy shift to lower values in narrow grooves during selective growth on 2° misoriented substrates was due to lower step densities, by reconstruction of the (1 0 0) plane in the groove. Investigations of wide area selective growth on (1 0 0) oriented substrates substantiated this result.

6. Summary

The presented results show the capability of chemical beam epitaxy for monolithic integration of optoelectronic devices. The optimized growth parameters of planar grown laser structures allow the selective growth of high quality lasers with threshold currents as low as 16 mA. The redshift of the emission wavelength for narrow 4 µm wide devices in grooves on 2° misoriented substrates indicate a reconstruction of the (1 0 0) plane during selective growth.

For geometrical reasons (lateral symmetries of infilled structure) the growth on exactly oriented substrates has to be preferred, especially as the 4.2 K photoluminescence linewidth of 5 meV was the best one achieved during this work. On the other hand it is easy to suppress {1 1 1} facets in grooves on misoriented substrates. However, growth parameters on exact oriented substrates a re more sensitive, especially control of InP growth is difficult at our rather high growth temperatures.

Acknowledgements

This work was supported by Bundesministerium für Bildung, Wissenschaft, Forschung und Technologie (BMBF) under the joint project Photonik II.

References

[1] M. Silver and E.P. O'Reilly, IEEE J. Quantum Electron. 31 (1995) 1193.
[2] P.J.A. Thijs, L.F. Tiermeijer, J.J.M. Binsma and T. van Dongen, IEEE J. Quantum Electron. 30 (1994) 477.
[3] B. Torabi, A. Nutsch, H. Kratzer, G. Tränkle and G. Weimann, 8th Int. Conf. on Indium Phosphide and Related Materials, Schwäbisch Gmünd (1996) pp. 773–776.
[4] H. Heinecke, B. Baur, R. Röger, B. Jobst and A. Miklis, J. Crystal Growth 124 (1992) 170.

ELSEVIER

Journal of Crystal Growth 175/176 (1997) 1205–1209

JOURNAL OF CRYSTAL GROWTH

MOMBE growth of highly tensile-strained InGaAsP MQWs and their applications to 1.3-μm wavelength low threshold current lasers

H. Sugiura*, M. Ogasawara, M. Mitsuhara, N. Yamamoto, M. Itoh

NTT Opto-electronics Laboratories, 3-1, Morinosato Wakamiya, Atsugi-shi, Kanagawa, 243-01, Japan

Abstract

We have studied metalorganic molecular beam epitaxy (MOMBE) of InGaAsP multi-quantum wells (MQWs) with 0.5–1.8% tensile-strained well layers. The MQW photoluminescence intensity depends significantly on the barrier layer strain to compensate well layer strain. Optimizing the strain compensation conditions, i.e., keeping the net strain less than 0.3%, makes it possible to grow high optical quality MQWs with 1.8%-strained, 10-well layers. A critical thickness-net strain (t_c–ε^*) curve for the tensile-strained MQWs has been experimentally determined by analyzing more than 50 samples with various strains and total thicknesses. The t_c–ε^* curve fairly agrees with the one calculated by the Matthews formula for more 0.5% net strain, but the t_c values are much higher than the expected ones below that range. For 6-well MQW lasers, the threshold current densities, J_{th}'s, decrease with increasing tensile strain; the minimum J_{th} obtained is 0.6 kA/cm^2 at 1.3% strain.

1. Introduction

Strained multi-quantum well (MQW) lasers emitting at 1.3 μm wavelength are of interest for optical communication and optical interconnection systems [1]. Theoretical studies [2, 3] predict that tensile-strained MQW lasers have even better performance than compressive ones. Little work, however, has been carried out for tensile-strained MQWs owing to the difficulty of growing them.

The theoretical studies show that, in order to extract the beneficial effects of tensile-strained MQWs, the well layer must be more than 100 Å thick and have more than 1% strain. The stacking of such thick and highly strained layers easily generate misfit dislocations. For example, photoluminescence intensity of 1.1% tensile-strained MQWs grown by metalorganic chemical vapor deposition (MOCVD) remains strong for up to three wells but drastically degrades for four wells. The threshold current density of the MQW lasers decreases with increasing tensile strain in less than the 1% range as predicted, but it increases with over 1% strain [4, 5]. Increasing the strain and well number is expected to improve the laser performance.

The growth of strained MQWs with high optical quality requires a knowledge of the critical

* Corresponding author. Fax: +81 462 40 4301; e-mail: sugiura@aecl.ntt.jp.

0022-0248/97/$17.00 Copyright © 1997 Elsevier Science B.V. All rights reserved
PII S0022-0248(96)00887-1

thickness over which misfit dislocation are generated. Houghton et al. [6] derived a theoretical formula for MQWs using the Matthews model [7]: the Matthews formula holds for MQWs by replacing strain and layer thickness with net strain [8] and MQW total thickness. Many researchers have reported that strain compensation to reduce net strain is effective for growing highly strained MQWs and improving laser performance [5, 9]. However, there has been no systematic study on the experimentally determined critical thickness for tensile-strained MQWs.

Recently, one of the authors reported that metalorganic molecular beam epitaxy (MOMBE) enables the growth of 1.45%, 6-well strained MQWs [10] without generating misfit dislocations. In this letter, we describe how to grow tensile-strained InGaAsP MQWs with many well layers and show what parameters determine critical thickness of the strained MQWs grown by MOMBE. The strain effect on the MQW laser performance is also mentioned.

2. Experimental procedure

We used the Vacuum Generators V-400 CBE system. Triethylgallium (TEG) and trimethylindium (TMI) were the group III sources, and AsH_3 and PH_3 the group V sources. The hydride gases were decomposed in a low-pressure cracker cell heated at 905°C. Substrate temperature was kept at 520°C for InGaAsP films. The temperature was calibrated with the InSb melting point. Solid Be and Sn were used as p- and n-type dopants, respectively. Pre-etched (1 0 0)-oriented substrates purchased from Sumitomo were used without any chemical treatment.

Typical MQWs consisted of tensile-strained InGaAsP (equivalent wavelength $\lambda = 1.5$ μm) as well layers and compressive-strained InGaAsP ($\lambda = 1.13$ μm) as barrier layers. The well layer thickness L_w and the barrier thickness L_b were kept at 100 and 140 Å, respectively. Double-crystal X-ray diffraction spectra of the MQWs were analyzed with a kinematic step model to determine the lattice constants of the unrelaxed well and barrier layers. The strain values used in this paper represent the lattice mismatch to InP. The tensile strain ε_w in the wells was varied from 0.5% to 1.8% while the compressive strain ε_b in the barriers was varied from 0% to 0.5%. Each value contains an ambiguity of $\pm 0.03\%$. Hereafter, we refer to the MQWs with 1.3% tensile strained layer simply as 1.3% strained MQWs. A plan-view transmission electron microscopy (TEM) study was carried out to observe directly misfit dislocations. Microphotoluminescence (μ-PL) [11] was measured with a Waterloo Scientific SPM-2000 to observe misfit dislocations in a 2×2 mm^2 area. Conventional PL measurements were performed at room temperature using a YAG laser as an excitation source.

The MQW lasers had separate confinement double heterostructures (SCH) with MQWs. Using MOMBE, we grew a structure consisting of a 5000 Å thick n-type InP buffer layer, 1000 Å thick undoped InGaAsP ($\lambda = 1.13$ μm), the undoped MQWs mentioned above, 1000 Å thick undoped InGaAsP ($\lambda = 1.13$ μm), a p-type 0.5 μm thick InP, and an InGaAs cap layer. After removing the cap layer, a p-type 2 μm thick InP layer and a p-type InGaAs contact layer were sequentially overgrown at 620°C by MOCVD. The SCH structure was processed into broad lasers with a 40 μm wide stripe.

3. Results

Fig. 1 plots the MQW PL intensity against barrier layer compressive strain as a parameter of well tensile strain. The well number was fixed at six. The tensile strain values were 1.3%, 1.45%, and 1.6% while the barrier strain was varied from 0% to 0.5%. The figure indicates two important features. First, the PL intensity of the MQWs remarkably improves by increasing the barrier strain. Though not shown for 1.8% tensile strain, a similar curve was obtained. This means that the strain compensation technique is still effective in the growth of MQWs consisting of such highly strained and thick well layers. Second, the barrier strain needed for obtaining strong PL intensity must be increased for larger tensile strain.

We have studied the MQWs in Fig. 1 from structural property point of view. Cross-sectional TEM study showed that the thickness modulation of the well layers due to spinodal decomposition was about 10 Å which did not depend on barrier strain

values. Plain-view TEM and μ-PL measurement revealed that the low PL intensity MQWs had misfit dislocation as shown in Fig. 2a and Fig. 2b, respectively. The misfit dislocation generation is the cause of reducing the PL intensity [12]. By using μ-PL, we classified the samples used in Fig. 1 into two groups, i.e., with and withot misfit dislocations. The results are summarized in Fig. 3. The vertical axis shows the net strain ε^* calculated using the formula of $\varepsilon^* = (L_w\,\varepsilon_w + L_b\,\varepsilon_b)/(L_w + L_b)$. The

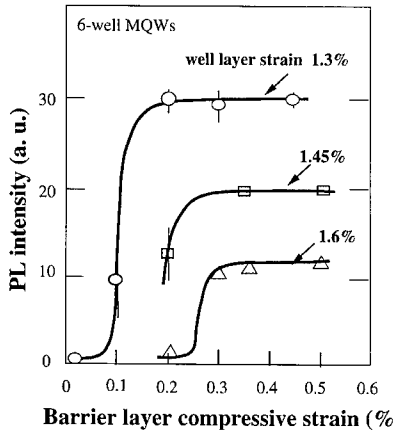

Fig. 1. Dependence of MQW PL intensity on barrier layer compressive strain as a parameter of well layer tensile strain. The barrier strain needed for obtaining strong PL intensity must be increased for larger tensile strain.

figure clearly shows that misfit dislocations are generated when the net strain exceeds 0.43% irrespective of well tensile strain. This fact strongly suggests that MQW strain condition reflects net strain, not well layer strain. Since the MQWs have a total thickness of 1440 Å, we can say that the critical thickness t_c for 0.43% net strain is 1440 Å.

In order to determine experimentally the critical thicknesses of MQWs in a wide net strain range, we grew more than 50 MQWs with various total thicknesses and net strains. The results are summarized in Fig. 4, where the data are classified into two groups, i.e., with and without misfit dislocations. The solid squares represent the MQWs with tensile-strained InGaAsP well layers in which misfit dislocations are generated while the open squares represent those in which dislocations are not generated. The solid circles represent the MQWs with compressively strained InAsP well layers containing misfit dislocations while the open circles are for those not containing dislocations [13]. The solid line is the border dividing the two classes of the MQWs. In other words, the solid line is the experimentally determined critical thickness–net strain curve. The figure shows that the curve is almost the same for the MQWs with either tensile- or compressive-strained well layers. The gray line in the figure is a theoretical curve calculated using the Matthews formula applied for MQWs [6]. Comparing the two curves, we can extract two

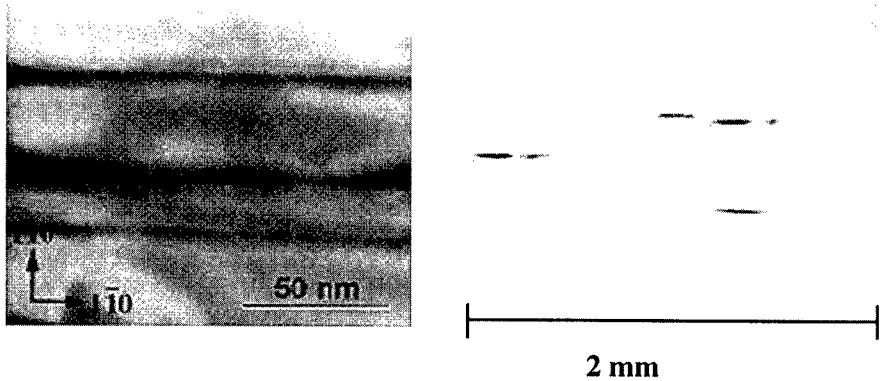

Fig. 2. (a) and (b) Misfit dislocation patterns of a tensile strained MQW obtained by plan-view TEM (a) and μ-PL (b). The misfit dislocations orient to [1 1 0]. The μ-PL observed area was $2 \times 2\ mm^2$.

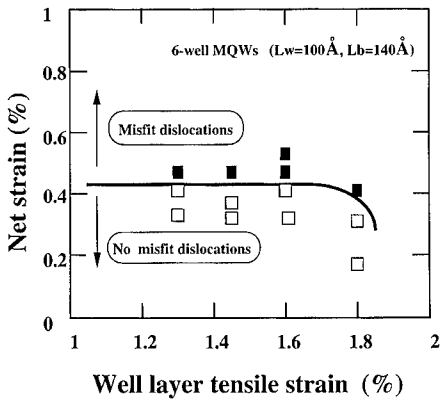

Fig. 3. Relation between the net strain and well layer strain of the MQWs with respect to misfit dislocations. The samples are used in Fig. 1. Misfit dislocations are generated for net strains over 0.43%.

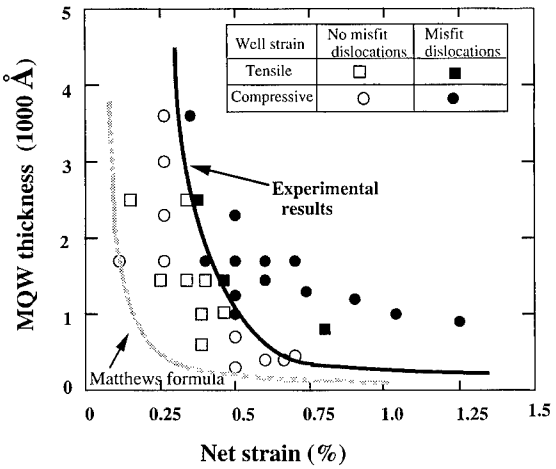

Fig. 4. Map of MQWs for various MQW total thicknesses and net strains in which misfit dislocations are and are not generated. The solid and gray lines are respectively the experimental and theoretical critical thickness–net strain curves.

important features. First, the tendency for critical thickness to decrease with increasing net strain is the same for the two curves. Second, the experimentally determined critical thickness is much larger than the theoretical values in the low net stain range, i.e., less than 0.5%. This latter result suggests that the Matthews formula needs modification in the low net strain range.

Here, we compare our critical thickness results with those for MQWs grown by MOCVD. According to Refs. [4, 5], the critical thickness at 0.47% net strain for the tensile strained MQWs is about 330 Å. This value is much smaller than our value of 1440 Å and is rather close to the expected value calculated by the Matthews formula (see Fig. 4). The critical thickness difference can be explained in terms of the growth temperature difference between the two growth methods; 650°C for MOCVD and 520°C for MOMBE. Using a modified Matthews model, Price [14] theoretically indicated that the critical thickness can be increased when temperature is lowered. Low-temperature growth might prevent the motion of dislocation due to low lattice vibration.

We conducted an experiment to see how many well layers can be grown for tensile-strained MQWs without generating misfit dislocations. The results are summarized in Fig. 5 as a map of MQWs for various well numbers and tensile strains. Solid and open circles are for the MQWs with and without misfit dislocations, respectively. The well layer tensile strain was varied from 0.5% to 1.8%. Each MQW was designed to have a net strain between 0.2 and 0.3 except for the 1.45% MQWs, whose net strain was 0.37%. From the figure, the maximum well number below which dislocations are not generated is more than ten throughout the tensile strain range from 0.5% to 1.8%. This value is more than twice that obtained in MOCVD growth.

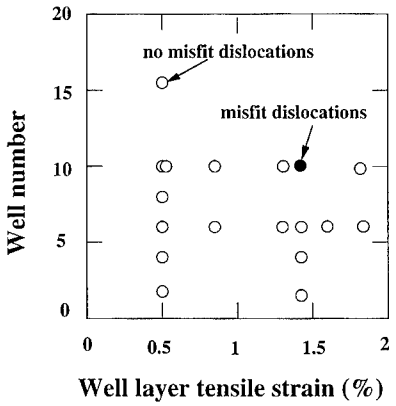

Fig. 5. Map of the MQWs for various well numbers and tensile strains in which misfit dislocations are and are not generated. Each MQW had a net strain between 0.2 and 0.3 except for the 1.45% strained MQWs.

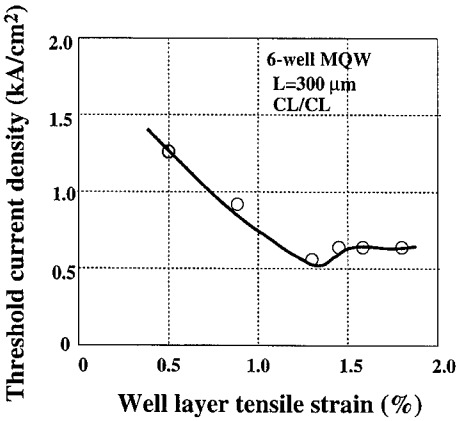

Fig. 6. Dependence of the threshold current density on the well strain for the 6-well MQW lasers.

Finally, we describe the laser characteristics of the tensile strained MQWs emitting at 1.3 μm wavelength. Misfit-dislocations free MQWs were processed into broad area lasers with a cavity length of 300 μm. All the lasers operated in TM mode. For a fixed strain value of 1.45%, the threshold current density J_{th} decreased from 2 to 0.7 kA/cm^2 by increasing the well number from 2 to 6. Fig. 6 shows the dependence of the threshold current density on the well strain for the 6-well MQW lasers. The J_{th}'s decrease with increasing tensile strain from 0.5% to 1.3%, but they slightly increase or remain rather constant in the 1.45 –1.8% strain range; the minimum J_{th} is 0.6 kA/cm^2 at 1.3%. This value is the smallest ever reported for tensile strained 1.3 μm wavelength lasers for such a cavity length. The optimum strain of 1.3% is slightly different from the reported values of about 1% in MOCVD [4, 5].

The reduction of J_{th} with the larger strain can be explained in terms of a greater separation between the light-hole and the heavy-hole energy band. The saturation of the J_{th} in the 1.45 –1.8% strain range may be related to the well layer microstructure caused by spinodal decomposition, which was revealed by cross-sectional TEM microscopy [15].

4. Summary

We have systematically studied strain compensation conditions for the MOMBE-grown tensile strained MQWs. The net strain must be kept less than 0.3% in order to obtain MQWs with strong PL intensity. As a result, a 10-well, 1.8% tensile-strain MQW can be grown without generating misfit dislocations. The experimentally determined critical thickness–net strain curve for the strained MQWs agrees with the one calculated by the Matthews formula except in the net strain range of less than 0.5%, which suggests that modification of the formula is required in the low strain range. The threshold current density of the 6-well MQW lasers decreases with increasing well layer strain; the lowest J_{th} is 0.6 kA/cm^2 at 1.3% strain.

References

[1] T. Tsuchiya, M. Komori, K. Uomi, A. Oka, T. Kawano and A. Oishi, Electron. Lett. 30 (1994) 788.
[2] E.P. O'Reilly, G. Jones, A. Ghiti and A.R. Adams, Electron. Lett. 27 (1991) 1417.
[3] S. Seki, T. Yamanaka, W. Lui, Y. Yoshikuni and K. Yokoyama, IEEE J. Quantum Electron. 30 (1994) 500.
[4] N. Yokouchi, N. Yamanaka, N. Iwai and A. Kaskawa, IEEE Photon. Tech. Lett. 7 (1995) 842.
[5] P.J.A. Thijs, T. van Dongen, L.F. Tiemeijer and J.J.M. Binsma, J. Lightwave Technol. 12 (1994) 28.
[6] D.C. Houghton, M. Davies, T. Sudersens Rao and M. Dion, J. Crystal Growth 136 (1994) 56.
[7] J.W. Matthews and A.E. Blakeslee, J. Crystal Growth 27 (1974) 118.
[8] C.P. Seltzer, S.D. Perrin, M.J. Harlow, R. Studd and P.C. Spurdens, Electron. Lett. 30 (1994) 227.
[9] T. Takagi, K. Goto, M. Takemi, A. Takemoto, T. Aoyagi, H. Watanabe, Y. Mihashi, S. Takamiya and S. Mitui, J. Crystal Growth 145 (1994) 892.
[10] H. Sugiura, M. Itoh, N. Yamamoto, M. Ogasawara, K. Kishi and Y. Kondo, Appl. Phys. Lett. 68 (1996) 3213.
[11] M. Nakao, H. Oohashi, T. Hirono, H. Kamada and H. Sugiura, J. Appl. Phys. 78 (1995) 3462.
[12] X. Zhou, P. Charsley, A.D. Smith and A.T.R. Brigss, in: Electron Microscopy and Analysis Group Conf., Inst. Phys. Conf. Ser., Vol. 138 (Inst. Phys., Bristol, 1993) p. 321.
[13] H. Sugiura, M. Ogasawara, M. Mistuhara, H. Oohashi and T. Amano, J. Appl. Phys. 79 (1996) 1233.
[14] G.L. Price, Phys. Rev. Lett. 66 (1991) 469.
[15] H. Sugiura, M. Mistuhara, M. Ogasawara, M. Itoh and H. Kamada, J. Appl. Phys. (1997), in press.

ELSEVIER

Journal of Crystal Growth 175/176 (1997) 1210–1216

JOURNAL OF CRYSTAL GROWTH

Growth and transformation of ultra-thin InAs/InP layers obtained by chemical beam epitaxy

N. Lebouché-Girard, A. Rudra*, E. Kapon

Institut de Micro et Optoélectronique, Département de Physique, Ecole Polytechnique Fédérale de Lausanne, CH-1015 Lausanne, Switzerland

Abstract

We have studied the morphology of InAs layers grown on InP epitaxial surfaces and their evolution under cracked arsine anneal using atomic force microscopy. On an exactly oriented (0 0 1) surface, a 2 ML InAs layer annealed under arsine breaks into elongated dots oriented along the [$\bar{1}$ 1 0] direction. During annealing, the dot density first increases, then decreases, pointing to stages dominated by nucleation and by coalescence, respectively. Nucleation and filamentary growth of InAs is observed along the steps of a step-bunched InP surface, with an average misorientation of 0.8° towards [1 1 0], while no localization can be achieved on surfaces tilted towards [$\bar{1}$ 1 0]. A more homogeneous population of isotropic InAs dots with a base size dispersion as low as $\pm$ 10% is obtained when a silicon-doped InP buffer layer is used.

Keywords: InAs; InP; Quantum dots; Self-organization; Chemical beam epitaxy

1. Introduction

InGaAs/GaAs and InGaAs/InP low-dimensional nanostructures, particularly quantum wires and dots, have interesting optical properties which could make them good candidates for use in novel optoelectronic devices, for instance as the active layer of improved lasers [1]. However, these applications require a high density of very small and regular wires or dots. An efficient way to fabricate such dot structures is to take advantage of the Stranski–Krastanow (SK) growth mode in lattice-mismatched systems like InAs/GaAs [2, 3].

More recently, the compressively strained InAs/InP system has been drawing attention. A thin InAs layer grows in a two-dimensional (2D) way, but a few seconds anneal under cracked arsine triggers an evolution from a two to a three-dimensional (3D) surface as seen by reflection high energy electron diffraction [4, 5]. Transmission electron microscopy confirmed the formation of InAs dots following this procedure [6]. However, no direct observation of this surface was carried out so far.

In the present paper, we report the atomic force microscopy (AFM) investigation of the surface of InP and InAs/InP epilayers grown by chemical beam epitaxy (CBE). We demonstrate the influence of the substrate miscut and its doping on the surface structure and its evolution under arsine anneal.

* Corresponding author. Fax: + 41 21 693 54 80; e-mail: rudra@dpmail.epfl.ch.

0022-0248/97/$17.00 Copyright © 1997 Published by Elsevier Science B.V. All rights reserved
PII S0022-0248(96)00955-4

2. Experimental procedure

The samples discussed here were grown by CBE using pure trimethylindium, cracked arsine, cracked phosphine and a solid Si source for n-type doping. We used exactly oriented (0 0 1)InP substrates as well as misoriented ones with various miscuts in both [1 1 0] and [$\bar{1}$ 1 0] directions (with an orientation tolerance smaller than $\pm$ 0.1°). The layer structures consisted of a 4000 Å InP buffer grown at a rate of 1 μm/h at a temperature of 500°C for exactly oriented substrates and 520°C for misoriented ones, and subsequently annealed for 5 min under phosphine flux. After optimization of the InP layer morphology, we have grown between 0.3 and 2 monolayers (ML) InAs, at a growth rate of 0.3 ML s^{-1} and a temperature of 500°C. Next, an anneal under arsine for a few seconds and an anneal under phosphine to quench the process were performed. The samples were finally investigated at atmospheric pressure using a digital instrument nanoscope III AFM.

3. Exactly oriented surfaces

After growth of a 4000 Å thick InP layer at 1 μm/h and 500°C, the surface shows a fragmented topography with a patchwork of 2D islands 5000 Å wide and 1 ML high, as expected under these conventional CBE growth conditions for InP [7]. Having this surface anneal under phosphine was found to smoothen it and create large atomically flat terraces (Fig. 1).

Fig. 2 is an AFM picture corresponding to the case of a 2 ML thick InAs layer annealed for 1 min under arsine. It reveals a high density (4.6×10^9 cm^{-2}) of dots oriented along the [$\bar{1}$ 1 0] direction. A cross-section study reveals a grossly pyramidal dot shape; their main sidewall facets are close to {1 1 5} planes. Their average length, width and thickness are 1165, 367 and 53 Å, respectively, with dot-to-dot variations of less than $\pm$ 20% for the lateral dimensions, but as high as $\pm$ 30% for their height. The main difference between these dots and the InAs dots obtained by gas source molecular beam epitaxy and arsine anneal [6] is in the stronger anisotropy observed in our case and

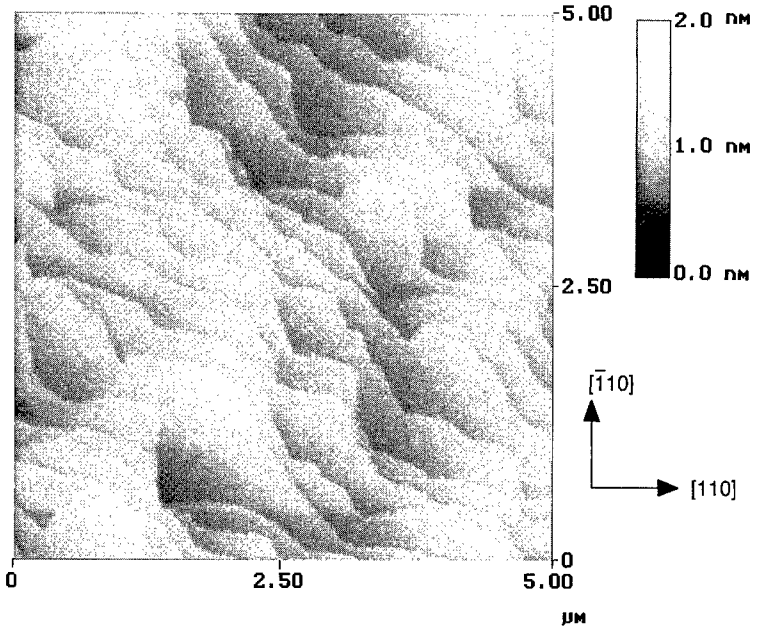

Fig. 1. AFM image of a 4000 Å InP buffer grown at 500°C on an exactly oriented substrate and annealed under cracked phosphine for 5 min.

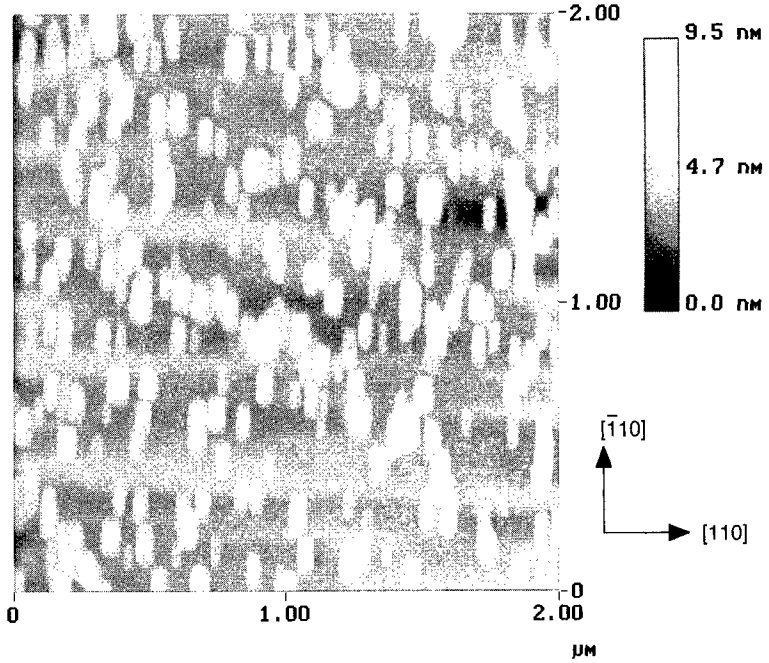

Fig. 2. AFM image of a 2 ML InAs layer grown at 500°C on an exactly oriented substrate and annealed under cracked arsine for 1 min.

also observed for InAs dots obtained by the SK growth mode on InP by molecular beam epitaxy [8].

The effect of annealing time t_a is shown in Fig. 3 which presents the evolution of the dots density (D), average dot volume and shape versus t_a. For $15\,s \leqslant t_a \leqslant 300\,s$, the dots density lies in the 1×10^9–$7 \times 10^9\ cm^{-2}$ range (Fig. 3a). First, D increases to a maximum value of $6.75 \times 10^9\ cm^{-2}$ corresponding to $t_a = 30\,s$, then it monotonically decreases showing dot gathering. Fig. 3a also shows the dots volume evolution which presents an almost monotonous increase with t_a. The dot shape variations are shown in Fig. 3b which presents the width, length and height evolution with t_a. For $t_a = 15\,s$, the dots are small and well oriented along the [1̄ 1 0] direction. When t_a increases to 300 s, the average dot length hardly changes, while both their width and height slightly increase. The dot size regularity is not varying when $t_a \leqslant 60\,s$ and is about $\pm 20\%$ for the lateral dimensions and $\pm 30\%$ for the height. For $t_a > 60\,s$ the regularity of dot size deteriorates drastically (the height variations are more than $\pm 50\%$ for $t_a = 300\,s$). This is probably the result of random coalescence.

These results show several regimes in the dot evolution with t_a. At the beginning of the anneal under arsine, small, regular and very elongated dots are formed. The orientation, along the [1̄ 1 0] direction, could be explained by the surface dimerisation which induces a higher binding energy in this direction [9, 10]. The total volume of these dots (V_{3D}) is less than the total deposited InAs volume which means, since In reevaporation is negligible at 500°C, that there is still a 2D InAs layer under the dots. When the annealing time increases, the dot size and particularly their density increase to reach a maximum. This might be called the *nucleation* step. During the anneal under arsine, there is a surface reorganization which creates spatial fluctuations of the 2D layer thickness. The critical thickness is thus *locally* exceeded and some dots nucleate [11]. On the other hand, there is a minimum distance between the dots which is a consequence of the repulsion between them [12] and the dot density increases until this minimum is reached.

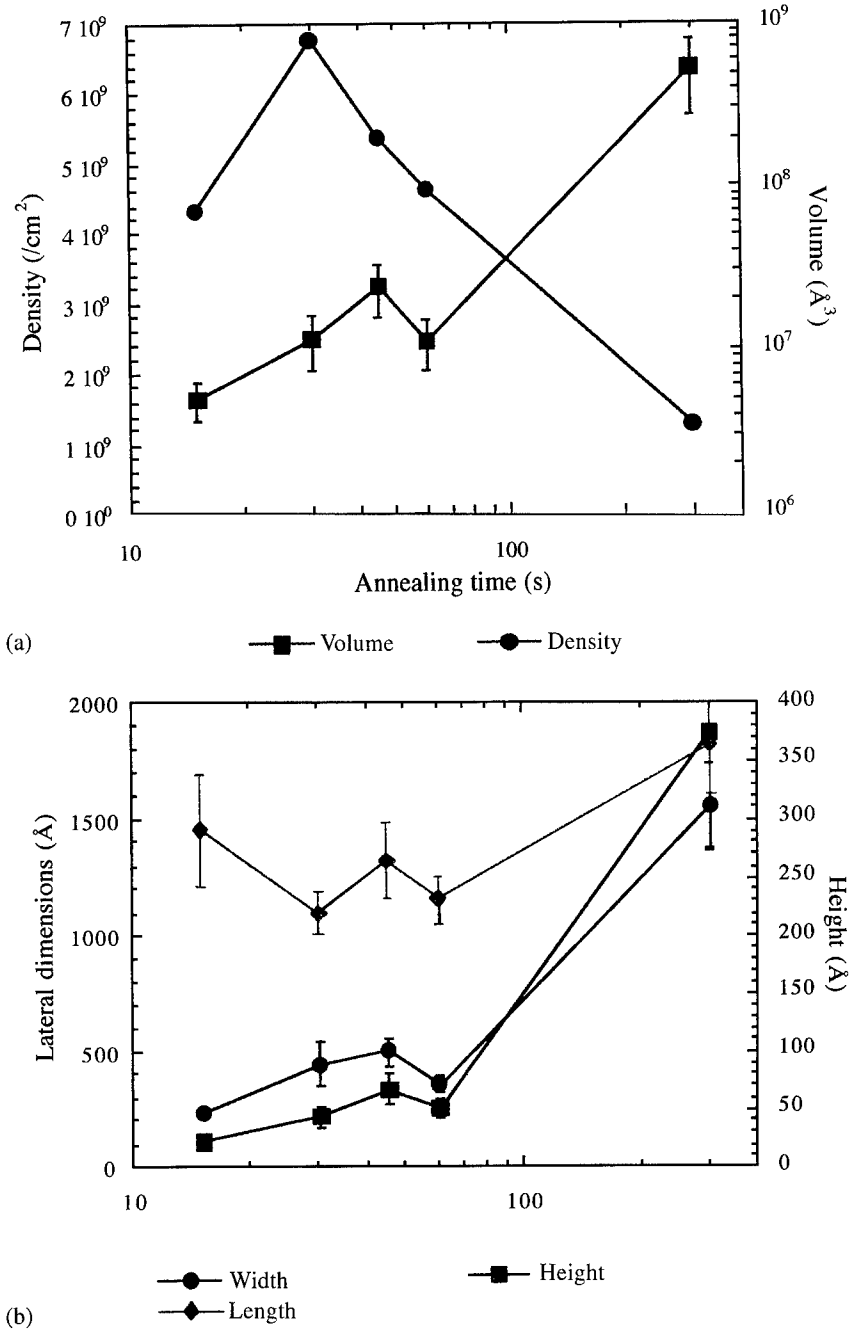

Fig. 3. (a) Evolution of the density and volume of InAs islands (corresponding to 2 ML) versus the annealing time under cracked arsine. (b) Evolution of width, length and height of the islands versus the annealing time. The lines are for the guidance of the eye only.

During this step, V_{3D} increases but is still less than the total InAs volume. When t_a increases further, the dot density decreases and the dot size increases; the dots touch each other and start to gather in a regular way (their size regularity does not deteriorate). During this *growth* stage, however, they

become less elongated and thicker. It is important to notice that the dot size variations do not increase during the *nucleation* and *growth* stages because their gathering is regulated by the consumption of the 2D layer. Finally, when $t_a > 60$ s the dots exhibit a random *coalescence* step which deteriorates their size regularity (the 2D layer is already consumed).

We want to stress that our nominal InAs layer is below the critical thickness (at which the 2D growth is replaced by a 3D one) which is 3 ML for the InAs/InP system [13] and that the formation of our dots is clearly different from the SK mode. However, the evolution with annealing time under arsine shows features which are similar to the formation of the InAs/GaAs dots by the SK growth mode [3, 12].

4. Vicinal surfaces

As we have seen, the size variations of our dots are larger than for InAs/GaAs dots [14]. To further investigate this point, we have studied the substrate influence on the dot formation and size regularity. As we know that the dot density and positioning play a key role in self-assembly processes [3] and that defects on the surface drive the dot nucleation [15, 16], we optimized the morphology of the InP layer (underneath the dots) creating purposely "organized" surface defects. For this purpose, we have used misoriented substrates with different miscuts and various growth parameters in order to obtain *multiatomic steps* using the step bunching phenomenon [17–20]. We have systematically studied the morphology of InP layers grown on substrates tilted towards [1 1 0] (A) and [$\bar{1}$ 1 0] (B), with the growth temperature in the range of 490–520°C. The layers grown on the A steps were more regular than those grown on the B steps. The 0.8°-tilt surface was finally selected because the steps were the most regular at a temperature of 520°C and we obtained 5 Å high double-steps separated by 440 Å wide terraces, oriented along [$\bar{1}$ 1 0]. On these optimized surfaces, we have grown a thin InAs layer with different thickness from 0.2 ML to 0.6 ML and then annealed them under arsine for 1 min.

Our main results are shown in Fig. 4. For a 0.3 ML InAs thick layer and on the exactly oriented substrate there is no dot formation (Fig. 4a). The InAs film can be distinguished from the InP background as it is composed of small 2D islands which are typical of an incomplete layer [12]. On the 0.8°-off (0 0 1) misoriented surface (Fig. 4b), elongated dots oriented along the step direction are formed on the numerous steps which serve as preferential nucleation sites [21]. This means that for such a thin InAs layer and during this short annealing time, kinetics does not allow the formation of dots on a surface without defect, but the multisteps are efficient nucleation sites which favor dot formation. When the InAs layer thickness increases the dots become wider, higher but especially longer along the steps, becoming short wires (Fig. 4c).

It is interesting to note that for similar experiments on a surface with B steps, the multisteps along the [1 1 0] direction do not influence much the dot shape which is still elongated and oriented along [$\bar{1}$ 1 0].

5. Influence of silicon doping

Another approach for creating surface defects for dot nucleation is to dope the buffer layer. We have studied by AFM the morphology of a Si-doped InP layer with a doping concentration of 3×10^{18} cm^{-3} grown on (0 0 1)InP surface. It reveals that, in addition to large terraces present on the undoped InP layer surface, there are numerous 2D islands. As we can see in Fig. 5, the Si-doping of the InP buffer influences the InAs dots morphology (cf. with Fig. 2). For the same InAs layer thickness (2 ML), the dots are not elongated anymore, but are pyramid or cone shaped. In addition, they exhibit a higher density; 1.6×10^{10} cm^{-2} instead of 4.6×10^{9} cm^{-2} and they are bigger (87 Å high and 687 Å wide on average). Moreover, the Si presence significantly improves the dot size regularity; $\pm 10\%$ instead of $\pm 20\%$ for the width, $\pm 20\%$ instead of $\pm 30\%$ for the height. This size dispersion is as good as that observed for the InAs/GaAs system which is twice as much strained as the InAs/InP one.

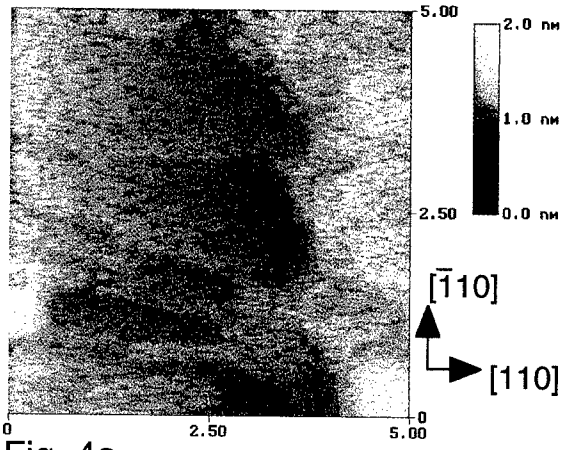

Fig. 4a

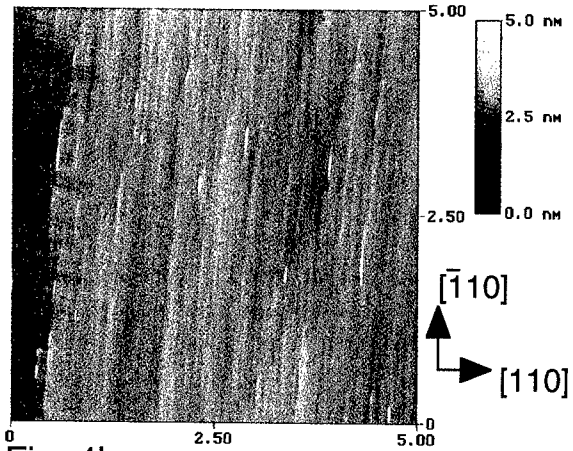

Fig. 4b

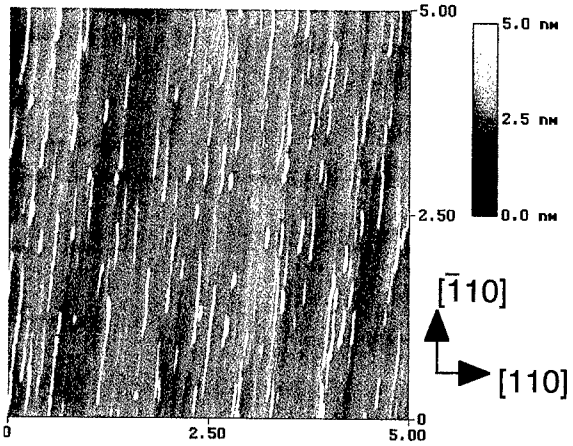

Fig. 4c

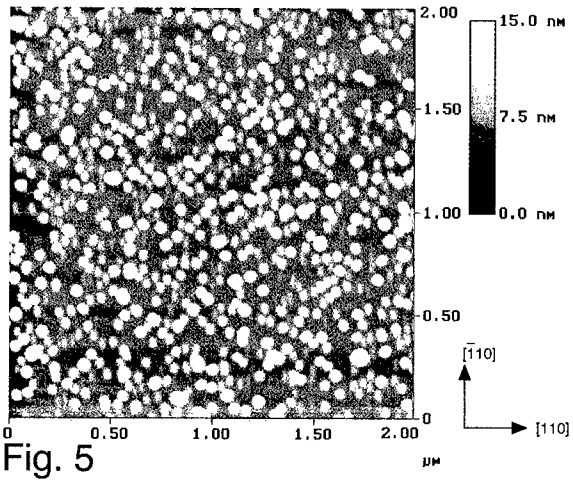

Fig. 5

Fig. 4. AFM image of an InAs film after cracked arsine anneal for 1 min. (a) 0.3 ML on exactly oriented substrate, (b) 0.3 ML on 0.8° off [1 1 0] substrate, (c) 0.6 ML on 0.8° off [1 1 0] substrate.

Fig. 5. AFM image of a 2 ML InAs layer grown at 500°C on a Si-doped InP layer (exactly oriented substrate) and annealed under cracked arsine for 1 min.

Concerning the isotropic shape of the InAs dots, it is well known that the presence of Si in a GaAs layer can modify the surface structure, even leading to Ga rich reconstruction [22]. As we have seen previously, the elongated shape of the dots nucleated on an undoped InP buffer can be correlated with the surface reconstruction. If this reconstruction changes, the dot shape could change as well.

Since Si doping of the InP buffer was found to strongly influence the dot formation on exactly oriented substrates, we also extended this experiment to vicinal surfaces. However, there was no dramatic influence on the features of the step-bunched InP surface.

6. Summary

The direct observation by AFM of the surface of thin InAs films grown as 2D layers on InP surfaces confirms that arsine anneal induces a surface reorganization leading to the formation of InAs dots.

This behavior can be modified by introducing perturbations on the surface. For instance, a significantly better size uniformity and an isotropic island shape are observed on a Si-doped surface as compared with an undoped layer. Moreover, nucleation and growth along steps on vicinal surfaces tilted toward [1 1 0] was observed, while such preferential growth could not be obtained when the tilt was toward [$\bar{1}$ 1 0]. Further investigations are needed in order to improve the size distribution of such dots for applications in long wavelengths optoelectronic devices.

Acknowledgements

The authors wish to thank J.F. Carlin for the Si concentration measurements and J.M. Moison from the Centre National d'Etudes des Télécommunications, Laboratoire de Bagneux (France) for the dots size measurements software. This work is supported by the Fonds National Suisse de la Recherche Scientifique.

References

[1] M. Asada, Y. Miyamoto, Y. Suematsu, Jpn. J. Appl. Phys. 24 (1985) L95.
[2] L. Goldstein, F. Glas, J.Y. Marzin, M.N. Charasse, G.L. Roux, Appl. Phys. Lett. 47 (1985) 1099.
[3] J.M. Moison, F. Houzay, F. Barthe, L. Leprince, Appl. Phys. Lett. 64 (1994) 196.
[4] J.F. Carlin, R. Houdré, A. Rudra, M. Illegems, Appl. Phys. Lett. 59 (1991) 3018.
[5] A. Rudra, R. Houdré, J.F. Carlin, M. Illegems, J. Crystal Growth 136 (1994) 278.
[6] A. Ponchet, A.L. Corre, H. l'Haridon, B. Lambert, S. Salaün, Appl. Phys. Lett. 67 (1995) 1850.
[7] J.F. Carlin, Thèse de Doctorat de l'Ecole Polytechnique Fédérale de Lausanne (1993) 17.
[8] G. Hollinger, M. Gendry, J.L. Duvault, C. Santinelli, Appl. Surf. Sci. 56–58 (1991) 665.
[9] T. Shitara, D.D. Vvedensky, M.R. Wilby, J. Zhang, J.H. Neave, B.A. Joyce, Phys. Rev. B 46 (1992) 6815.
[10] T. Shitara, D.D. Vvendesky, M.R. Wilby, Phys. Rev. B 46 (1992) 6825.
[11] J.M. Gérard, J.B. Genin, J. Lefebvre, J.Y. Marzin, J.M. Moison, N. Lebouché, F. Barthe, J. Crystal Growth 150 (1995) 351.
[12] N. Lebouché, Thèse de Doctorat de l'Université Paris VII (1995) 35.
[13] N. Grandjean, J. Massies, F. Raymond, Jpn. J. App. Phys. 33 (1994) L1427.
[14] C.W. Snyder, D. Barlett, B.G. Orr, P.K. Bhattacharya, J. Singh, J. Vac. Sci. Technol. B 9 (1991) 2189.
[15] D. Leonard, K. Pond, P.M. Petroff, Phys. Rev. B 50 (1994) 11687.
[16] N. Ikoma, S. Ohkouchi, Jpn. J. Appl. Phys. 34 (1995) L724.
[17] T. Nishida, M. Shinohara, N. Inoue, J. Appl. Phys. 78 (1995) 2854.
[18] M. Shinohara, N. Inoue, Appl. Phys. Lett. 66 (1995) 1936.
[19] V. Merlin, T.M. Duc, G. Younes, Y. Monteil, V. Souliere, P. Regreny, J. Appl. Phys. 78 (1995) 5048.
[20] H. Yamaguchi, Y. Homma, Y. Horikoshi, Appl. Phys. Lett. 66 (1995) 1626.
[21] M. Kitamura, N. Nishioka, J. Oshinowo, Y. Arakawa, Appl. Phys. Lett. 66 (1995) 3663.
[22] M. Wassermaier, J. Behren, L. Däweritz, K. Ploog, Phys. Rev. B 52 (1995) R2269.

ELSEVIER

Journal of Crystal Growth 175/176 (1997) 1217–1222

JOURNAL OF CRYSTAL GROWTH

Transient surface states during the CBE growth of GaAs

T. Farrell[a], D. Hill[a], T.B. Joyce[a], T.J. Bullough[a], P. Weightman[b,*]

[a] *Department of Materials Science and Engineering, The University of Liverpool, P.O. Box 147 Liverpool L69 3BX, UK*
[b] *Interdisciplinary Research Centre in Surface Science, The University of Liverpool, P.O. Box 147 Liverpool L69 3BX, UK*

Abstract

We report the occurrence of a transient surface state during the initial stages of CBE GaAs(0 0 1) growth. The state was detected in real-time reflectance (R) and reflectance anisotropy spectroscopy (RAS) growth monitoring. At low growth rates, less than 1 μm/h, beam equivalent pressure (BEP) of triethylgallium (TEG) $< 2.5 \times 10^{-5}$ mbar there was no change in R and the RAS signal changed from its pre-growth value under arsenic stabilisation at the growth temperature to its "during growth" value upon admission of the TEG, with the familiar monolayer oscillations. At higher TEG BEPs there was a rapid increase in R at all monitoring wavelengths, followed by a monotonic decay to its pre-growth value. This transient increase in R was accompanied by a change in the RAS signal, the magnitude and sign of which varied with wavelength. The initial increase in R is shown to be associated with the development of a metallic-like surface whereas the changes in the RAS signal are consistent with the formation of Ga dimers.

Keywords: CBE growth; GaAs; RAS

1. Introduction

Optical monitoring of epitaxial growth is gaining wide-spread acceptance as a valuable aid in understanding growth processes. Optical techniques are relatively insensitive to the growth pressure, and whilst this is not particularly important in MBE growth, it is of tremendous benefit for higher-pressure growth environments such as MOVPE. One such optical technique is reflectance anisotropy spectroscopy (RAS) [1, 2], which measures $\Delta R/R$, the ratio of the difference, ΔR, in normal incidence reflectance for light linearly polarised along two orthogonal directions in a sample surface to the average normal incidence reflectance, R, as a function of photon energy. RAS is sensitive to short-range order (bond energies and directions) in the material under investigation. For a cubic material such as GaAs with isotropic bulk optical properties, RAS gives a direct measure of surface optical anisotropy, primarily arising from the surface reconstructions. Indeed, RAS has been applied with considerable success in the study of MOVPE growth, in particular, in mapping out surface reconstructions as a function of III/V ratio and temperature for MOVPE grown GaAs [3, 4] from correlations of simultaneous RAS and RHEED measurements on MBE [3, 5, 6] and CBE [3] grown GaAs.

* Corresponding author.

0022-0248/97/$17.00 Copyright © 1997 Elsevier Science B.V. All rights reserved
PII S0022-0248(96)00962-1

Like RHEED, RAS has also been used to study the dynamics of the growth. For such measurements the monitoring is undertaken at a fixed photon energy, the energy often being that where the difference in the pre-growth RAS and the RAS determined during growth is maximum [7]. For GaAs this energy is 2.6 eV. However, this is not a necessary condition for a dynamic study of GaAs growth using RAS; such studies have been reported at photon energies down to 1.85 eV [8]. Monolayer period oscillations are readily observed in the dynamic RA traces of GaAs and AlAs CBE growth [9] at relatively low group III BEPs corresponding to growth rates up to ~ 1 ML/s. The purpose of this study was to use RAS to probe the growth dynamics at the higher group III BEPs normally used in our CBE GaAs growth.

2. Experimental procedure

The CBE growth experiments were carried out in a VG80H growth system fitted with gas lines which has been described elsewhere [10]. The precursors were thermally pre-cracked arsine (AsH3) and triethylgallium (TEG). The real-time RAS monitoring system was based on the photo-elastic modulator design reported by Aspnes [2].

The RAS measurements are calculated and displayed in real time as $\Delta R/R$. Thus, any temporal changes in the surface anisotropy (ΔR) can be correlated with changes in R.

Typically, a spectrum (1.5–4.0 eV) with data points at every 0.02 eV took 2 min to acquire. In the single wavelength dynamic mode, measurements were taken and displayed in real time at intervals down to 20 ms.

The experiments were carried out at temperatures where the CBE growth rate of GaAs is maximum for a given group III beam equivalent pressure (BEP), that is over the range 510–560°C [11]. Spectral and dynamic R and RAS measurements were made with the group III and group V BEPs over the ranges 3.0×10^{-5}–4.5×10^{-5} mbar and 10^{-4}–4×10^{-4} mbar, respectively, where the GaAs growth rate is in the range 1.5–2 ML/s.

3. Results and discussion

RAS spectra over the range 1.5–4.0 eV for temperatures of 510°C and 535°C are shown in Fig. 1 in the pre-growth (PG) condition (group III BEP = 0) and during growth (DG) with a group III BEP of 3×10^{-5} mbar; the group V BEP was 10^{-4} mbar in all cases. From correlations with previous simultaneous RHEED and RAS measurements on our CBE growth equipment [3] these spectral RAS traces show the 510°C pre-growth surface reconstruction to be $c(4\times4)$, changing to 2×4 during growth, whilst the 535°C pre-growth reconstruction can be approximately represented as a linear combination of $c(4\times4)$ and 2×4, also changing to 2×4 during growth. During growth at higher temperatures and for pre-growth the RAS signal is that of the 2×4 surface [3].

Upon admission of TEG at BEPs up to 2.5×10^{-5} mbar, there was no change in R and the dynamic RAS trace changed from the pre-growth

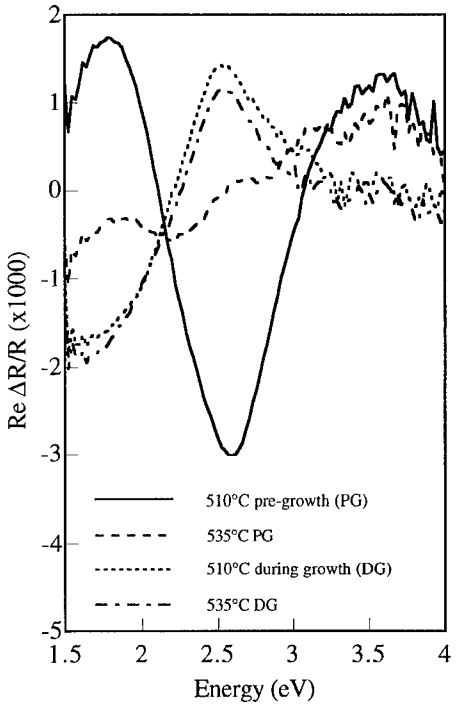

Fig. 1. RA spectra of GaAs at different temperatures in the pre-growth and during growth conditions.

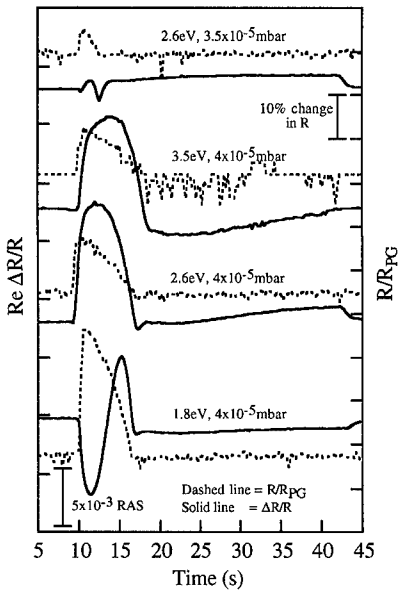

Fig. 2. Transients in R and $\Delta R/R$ as a function of monitoring energy and group III BEP.

to the "during growth" value with the familiar oscillatory behaviour. The period of the oscillations corresponded to the growth of 1 ML of GaAs and the oscillations damped out to the during growth RAS value. When the group III BEP was higher than $\sim 3 \times 10^{-5}$ mbar, immediately upon admission of the TEG, there was a rapid *increase* in the value of R at all monitoring energies followed by a decay to the pre-growth value of R. At these higher BEPs the oscillatory behaviour of the dynamic RAS trace disappeared and transients were observed in the RAS trace in the interval between the pre-growth and the during-growth conditions. Examples of the transients are shown in Fig. 2, in which the RAS traces have been shifted in the $\Delta R/R$ axis but the scale has been preserved. Likewise, the reflectance traces have been shifted whilst maintaining the scale and have been normalised to the pre-growth value, R_{PG}; they therefore appear as a percentage change.

In all transients the maximum in R occurred some 0.8–1.0 s after the admission of the TEG. However, the decay time, back to the pre-growth value, increased with increasing group III BEP (for a constant group V BEP). The magnitude of the increase in R depended on both energy and group III BEP (again at a constant group V BEP). Fig. 2 shows that the increase in R was 27% at 1.8 eV falling through 12% at 2.6 eV to 9% at 3.5 eV when the group III and group V BEPs were 4×10^{-5} and 10^{-4} mbar, respectively; reducing the group III BEP to 3.5×10^{-5} mbar had the effect of reducing the increase in R to 6%.

Using a bilayer model (ambient/addlayer/bulk GaAs) the change in R with thickness can be estimated, provided the optical constants (refractive index, n, and extinction coefficient, k) of the addlayer and GaAs are known. Over the spectral range of interest, the refractive index of GaAs, n_{GaAs}, is ~ 4 and the extinction coefficient, k_{GaAs}, is in the range 0.2–2.5 [12]. Over this short period of time the maximum amount of material that may have been added to the substrate is ~ 2 ML and thus the increase in R requires either $n_s \gg n_{GaAs}$ or $k_s \gg k_{GaAs}$ or both, where n_s and k_s are the optical constants of the surface addlayer. The refractive index of GaAs is high and it is unlikely that n_s can be much greater than nGaAs. Large values of the extinction coefficient ($k \gg 1$) occur in metals, the magnitude falling with energy over the spectral range of this study. A bilayer simulation assuming the addlayer to have a thickness of 2 monolayers for the group III BEP of 4×10^{-5} mbar and taking a range of values of n_s from 1 to n_{GaAs} at the monitoring wavelength indicated that k_s would have the values 16 ± 2 at 1.8 eV, 9 ± 1 at 2.6 eV and 6 ± 1 at 3.5 eV. Thus, the increase in R upon admission of the TEG is consistent with the addlayer being metallic in terms of its optical behaviour. The bilayer model predicts an oscillatory behaviour in R with thickness if the addlayer remained as deposited. The monotonic decay back to the original value of R and the absence of oscillations indicates that the addlayer becomes incorporated into the growing GaAs.

Fig. 2 demonstrates that the transient in R was always accompanied by a transient in the dynamic RAS trace, the duration of the two transients being similar. As the RAS signal is presented as $\Delta R/R$ then any changes in R will automatically be manifest as a change in $\Delta R/R$. A given percentage *increase* in R will cause the magnitude of $\Delta R/R$ to

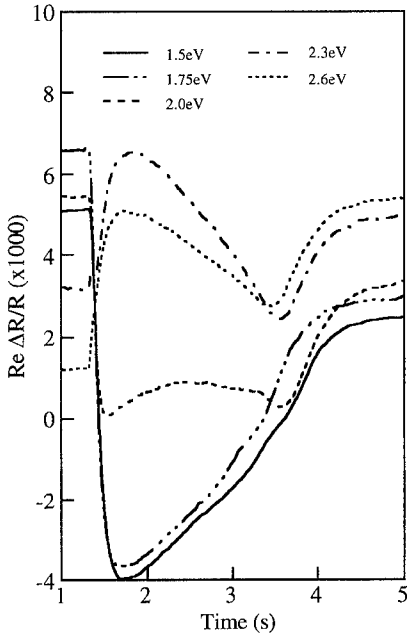

Fig. 3. Transient RAS traces at different energies during the initial stages of GaAs growth. Group III BEP $= 3.8 \times 10^{-5}$ mbar, group V BEP $= 10^{-4}$ mbar.

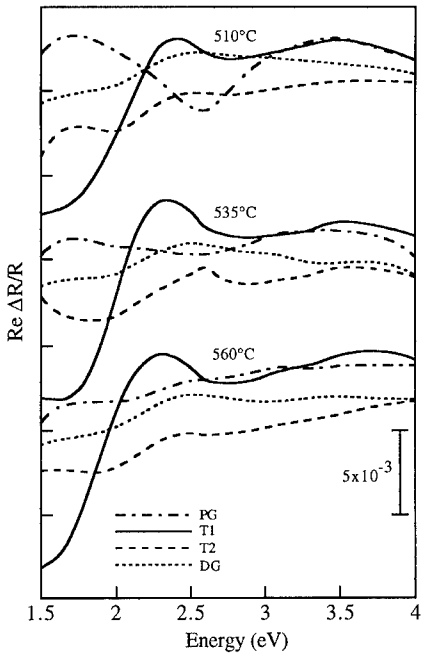

Fig. 4. RAS spectra obtained from dynamic traces before growth (PG) at different times during the transient (T1 & T2) and during steady state growth (DG).

fall by a corresponding fraction. As can be seen from Fig. 2 the magnitude of the changes in $\Delta R/R$ does not correspond in percentage terms with the fractional increase in R; depending on the monitoring energy $\Delta R/R$ may increase or decrease during the transient. This demonstrates that there is a change in the surface optical anisotropy over the duration of the transient.

The changing surface optical anisotropy was investigated by monitoring the period immediately after the admission of TEG with fixed photon energies over the range 1.5 to 4.0 eV. Examples of the dynamic RAS traces are given in Fig. 3 for BEPs of 3.8×10^{-5} mbar (group III) and 10^{-4} mbar (group V) at 510°C. This enabled RAS spectra to be derived at various times during the dynamic RAS monitoring. The results are shown in Fig. 4 for the pre-growth and steady-state during growth conditions along with two points in the transient. The spectra indicated as T1 in Fig. 4, which are similar at each temperature, correspond to the peak in the reflectance transient whilst those marked T2 correspond to the feature at 3.6 s in Fig. 3. The similarity in the derived PG and DG spectra (Fig. 4) and the directly determined PG and steady state DG spectra (Fig. 1) is evident.

We have established that at point T1 in the transient the surface is metallic, the metallic nature probably arising from a high Ga content in the surface addlayer. To generate a *steady-state* Ga rich surface, the temperature was reduced to 300°C with the group III BEP = 0, and the group *V* supply switched off. RAS spectra were taken as the group V BEP was reduced from 10^{-5} to 10^{-8} mbar, Fig. 5. At 10^{-5} mbar, the RAS spectrum is typical of the $d(4 \times 4)$ reconstruction, indicating that the surface is still As rich. However, with a group V BEP in the range 10^{-7}–10^{-8} mbar the spectra (Fig. 5) show the development of a trough below 2 eV which deepens and shifts to lower energies as the group V BEP falls, consistent with the development of the Ga rich 4×2 reconstruction [5]. The T1 spectra of Fig. 4 exhibit some common features

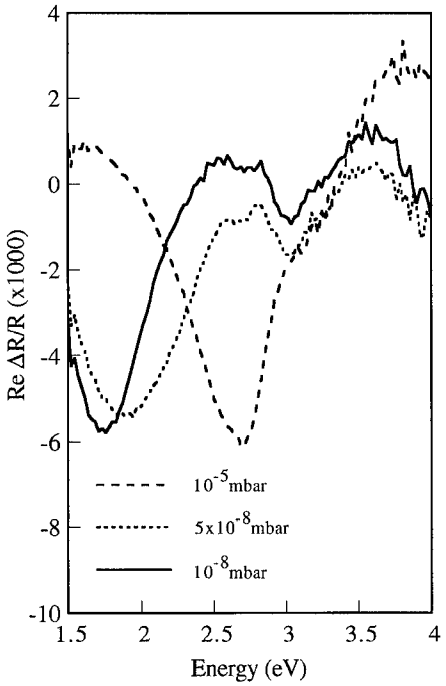

Fig. 5. RA spectra of GaAs as a function of group V BEP at 300°C with the group III BEP = 0.

with the lower temperature Ga rich spectra (Fig. 5) especially the large trough in the region below 2.0 eV, where the Ga dimers are known to dominate the RAS of GaAs, and the peak developing at ~ 2.4 eV.

The dynamic RAS measurements suggest that the transient addlayer initially comprises Ga dimers, whereas the reflectivity measurements demonstrate it is initially metallic, at least in terms of its optical properties. It has been shown [13] that when metal atoms are deposited on semiconductor surfaces, metallisation may occur with coverage of between 0.5 and 1 ML. Indeed, there are calculations which indicate that the deposition of ~ 1 ML of alkali metals on GaAs(0 0 1) produces a metallic surface [14] and that the As saturated GaAs(0 0 1) (2 × 4) surface, in which six As atoms form three dimers in the unit cell and there are no Ga atoms in the outermost layer, is also metallic [15]. However, we have not found any theoretical work on the nature of the Ga rich GaAs(0 0 1) 4 × 2 surface. Our results suggest that this surface is metallic also.

It therefore appears that the initial part ($t < 1.0$ s) of the transient is due to the rapid dissociation of the TEG molecule leaving Ga on the surface, which is yet to be incorporated as GaAs. Thus, with the group III BEP greater than 3.5×10^{-5} mbar the net deposition rate of Ga is initially too high, in relation to the As flux, to be incorporated into the growing structure. Decreasing the III/V ratio has the effect of reducing the overall duration of the transient by accelerating the rate of incorporation. Transitory behaviour has been observed in a RHEED study of the MOMBE growth of GaAs with TEG and As_4 as precursors [16] with a high TEG flux. The reconstruction of the transients was Ga rich 4 × 2 and the authors [16] suggested that Ga was initially deposited as clusters subsequently being incorporated on the arrival of the As. This suggests that there may be a different growth rate over the duration of the transient than in the steady state when equilibrium is established. It was further reported that the growth rate was lower during the transient [16]. By observing the transient in both RAS and R during the growth of GaAs on a GaAs(0 0 1) substrate incorporating a thin layer of AlGaAs, we were able to study the growth rate over the duration of the transient via multiple reflection interference [17]. The results [18] indicate that the growth is slower over the transient in agreement with Ref. [16].

4. Conclusion

At group III BEPs greater than 3.5×10^{-5} mbar there exists a transient surface state in the initial stages of the CBE growth of GaAs. The surface reconstruction changes over the duration of the transient. Initially it appears to be 4 × 2 Ga rich and metallic and is due to the deposition of Ga on to the surface faster than it can be incorporated as growth of GaAs is initiated. After about 1 s the Ga begins to be incorporated and after a further few seconds, depending on the III/V ratio, the growth continues as normal.

Acknowledgements

We wish to acknowledge the assistance given to us by Professor W. Richter and his group at the Technical University of Berlin, especially Jens Rumberg, in connection with the RAS equipment.

References

[1] D.E. Aspnes and A.A. Studna, Phys. Rev. Lett. 54 (1985) 1956.
[2] D.E. Aspnes, J.P. Harbison, A.A. Studna and L.T. Florez, J. Vac. Sci. Technol. A 6 (1988) 1327.
[3] J. Rumberg, PhD Thesis, Technical University of Berlin (1996).
[4] W. Richter, Philos. Trans. Roy. Soc. London A 344 (1993) 453.
[5] I. Kamiya, D.E. Aspnes, L.T. Florez and J.P. Harbison, Phys. Rev. B 46 (1992) 15894.
[6] S.M. Sholz, A.B. Muller, W. Richter, D.R.T. Zahn, D.I. Westwood, D.A. Woolf and R.H. Williams, J. Vac. Sci. Tehnol. B 10 (1992) 1710.
[7] J.P. Harbison, D.E. Aspnes, A.A. Studna, L.T. Florez and M.K. Kelly, J. Appl. Phys. Lett. 52 (1988) 2046.
[8] S.R. Armstrong, R.D. Hoare, M.E. Pemble, I.M. Povey, A. Stafford, A.G. Taylor, B.A. Joyce, J.H. Neave, D.R. Klug and J. Zhang, Surf. Sci. 274 (1992) 263.
[9] J. Rumberg, F. Reinhardt, W. Richter, T. Farrell and J. Armstrong, J. Vac. Sci. Technol. B 13 (1995) 88.
[10] T.B. Joyce, J. Crystal Growth 105 (1990) 299.
[11] T.B. Joyce, T. Bullough, P. Kightley, C.J. Kiely, Y.R. Xing and P.J. Goodhew, J. Crystal Growth 120 (1992) 206.
[12] D.E. Aspnes, S.M. Kelso, R.A. Logan and R.J. Bhat, J. Appl. Phys. 6 (1986) 754.
[13] G.P. Srivastava and Inder P. Batra, in: Proc. NATO Advanced Workshop on Metallisation and Metal–Semiconductor Interfaces, Munich, Germany (1988), NATO ASI Series 195 (Plenum, New York, 1989) p. 289.
[14] R. Rincon, J. Ortega, F. Flores, A. Levy Yeyati and A. Martin-Rodero, Phys. Rev. B 52 (1995) 16345.
[15] R. Rincon, R. Saiz-Pardo, R. Perez and F. Flores, in: Proc ICFSI-4, Julich, June (1993), Eds. B. Lengeler, H. Luth, W. Monch and J. Pollmann (World Scientific, Singapore, 1994) p. 293.
[16] H.K. Dong, S.C.H. Hung and C.W. Tu, Mater. Res. Soc. Symp. Proc. 340 (1994) 193.
[17] T. Farrell and J.V. Armstrong, Appl. Surf. Sci. 86 (1995) 582.
[18] T. Farrell, D. Hill, T.J. Bullough, T.B. Joyce and P. Weightman, to be submitted.

ELSEVIER

Journal of Crystal Growth 175/176 (1997) 1223–1230

JOURNAL OF CRYSTAL GROWTH

Be redistribution in InGaAs and InP grown by gas source molecular beam epitaxy

Teruo Mozume*, Kazuhiko Hosomi

Central Research Laboratory, Hitachi, Ltd., Kokubunji, Tokyo 185, Japan

Abstract

The redistribution of Be during the growth of InGaAs and InGaAs/InP heterostructures by gas source molecular beam epitaxy has been studied using secondary ion mass spectrometry. Be deposition to the InP layer grown next to the highly Be-doped InGaAs layer has been shown to cause significant Be segregation. Although the growth temperature and AsH_3 flux dependence of Be redistribution in InGaAs layers can be explained by the substitutional–interstitial (S–I) diffusion mechanism, no enhancement of Be redistribution in InGaAs is observed by n^+ doping in nearby layers, inconsistent with previous results of Zn diffusion. The temperature dependence of Be profiles in InP layers follows the S–I diffusion mechanism, however the PH_3 flow rate dependence is inconsistent with the model.

1. Introduction

To achieve the full potential of heterojunction bipolar transistors (HBTs) in terms of high-speed performance, rigorous control of doping profiles in the base region is necessary. Specifically, device performance can be improved through heavy p-type doping of the transistor base region to reduce base resistance while maintaining narrow abrupt base-doping profiles to keep the minority-carrier transit time through this region short. For the acceptor-doped base layer, beryllium (Be) and zinc (Zn) have been the conventional dopants used in molecular beam epitaxy (MBE) and organometallic vapor-phase epitaxy (OMVPE) because of their high doping efficiency, good hole transport properties, and acceptable diffusion rate at moderate doping levels. However, for doping levels in the $10^{19}\ cm^{-3}$ range, concentration-dependent diffusion has been reported to be a serious problem [1].

Be and Zn diffusion in GaAs has been extensively studied for many years [1–6]. A model of diffusing interstitial impurity which is captured on a group-III lattice site has proved successful in explaining results. The substitutional-interstitial (S–I) diffusion mechanism [6, 7] is based on the reaction equation

$$A_i^{m+} + V_{Ga}^0 \Leftrightarrow A_s^- + (m+1)h, \quad (1)$$

where A stands for a Be or Zn atom with A_s^- being the singly ionized substitutional species and A_i^{m+} the interstitial species with charge m^+. Here, V_{Ga}^0 is the neutral Ga vacancy, and h is the hole.

* Corresponding author. Fax: +81 298 47 4417; e-mail: mozume@festa.or.jp.

0022-0248/97/$17.00 Copyright © 1997 Elsevier Science B.V. All rights reserved
PII S0022-0248(96)01211-0

The diffusivity of interstitial Be or Zn is assumed to be much larger than that of substitutional Be or Zn or of a lattice vacancy.

It is also well known that the diffusion of Zn is enhanced by nearby highly n-type layers, as in HBT structures [4, 5, 8], and this was explained by Deppe [9] in terms of nonequilibrium point defects induced by a combination of surface pinning of the Fermi level and n^+ doping. On the other hand, Be diffusion is suppressed by the presence of nearby n^+ layer [10–12]. A satisfactory model of Zn and Be diffusion should be able to account for these experimental characteristics. The above-described objective is yet to be attained.

Up to now, Be diffusion has been extensively studied in GaAs/AlGaAs systems. There are few reports on Be redistribution in InGaAs/InP.

In this article, to gain a better understanding of the processes involved in Be redistribution in InGaAs and InGaAs/InP heterostructures, we have investigated the effects of growth temperature, group V flux, and n-type doping concentrations in nearby layers by studying secondary ion mass spectrometry (SIMS) depth profiles.

2. Experimental procedure

All studied layers were grown in a gas source molecular beam epitaxy (GSMBE) system. Details of this system were reported in Ref. [13]. Elemental Ga and In were used for the group-III growth species derived from effusion cells. 100% AsH_3 and PH_3 were decomposed in a low-pressure thermal cracker cell maintained at 900°C. The substrate temperature was determined using an Ircon, Model-V, pyrometer.

In order to investigate the effects of growth temperature, group-V flux, and n-type doping to nearby layer, we grew three types of samples as shown in Fig. 1. Fig. 1a and Fig. 1b show an InGaAs n-i-p-n structure and a n-InP/i-InGaAs/p-InGaAs/n-InP heterostructure. Be- and Si-doping concentrations for these samples were set around $1–3 \times 10^{19}$ and $1–2 \times 10^{17}\ cm^{-3}$, respectively. In the course of growing samples (a) and (b), 400 s growth interruptions were introduced prior to growing the intentionally Be-doped InGaAs layer to raise Be cell temperature. After the Be-doped InGaAs layer was grown, Be cell temperature was lowered by 200 to 650°C and no growth interruption was introduced. Fig. 1c shows the InGaAs pn-junction structure used to study the effect of n-type doping in nearby layers. In this sample Be concentration was set around $2 \times 10^{19}\ cm^{-3}$ and Si concentration was varied from 7×10^{17} to $3 \times 10^{19}\ cm^{-3}$. A 30 nm low Si-doped InGaAs layer was introduced between each highly Be- and Si-doped layer. 200 s growth interruptions were introduced to set the Si and Be temperatures. After

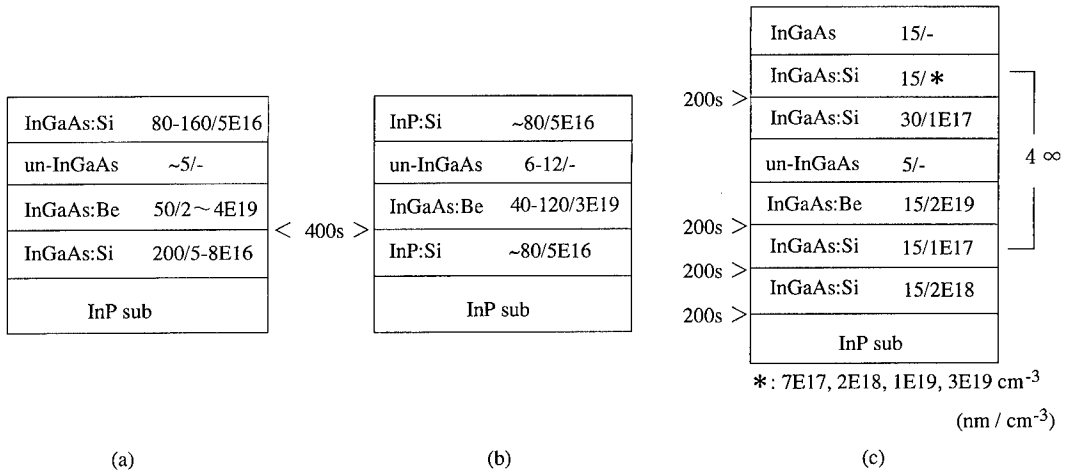

Fig. 1. Sample structures. (a) InGaAs pn-junction structure. (b) InGaAs/InP double heterostructures. (c) InGaAs stacked pn-junction structure.

growing Be-doped layers, no growth interruptions were introduced, while Be cell temperature was lowered by 200°C.

SIMS measurements were provided by Evans East from their Physical Electronics 6600 SIMS system. Cesium ions and oxygen ions were used as primary ions and the primary ion acceleration potential used was 3 and 6 kV, respectively.

3. Results and discussion

3.1. Effects of Be-cell temperature profile

Anomalous Be redistribution towards the surface was observed in samples grown at 460°C by keeping the Be cell temperature constant throughout the growth (samples (a) and (b) in Fig. 2). We found that the extended growth of high-concentration Be-doping layers causes Be deposition even when the Be shutter is closed, as was previously observed by Panish et al. [14], and this unintentional Be doping causes significant Be segregation into the Si-doped InP-layer grown next to them. The term "segregation" will be used for dopants moving predominantly towards the surface during crystal growth. The unintentional Be-doping level is around 1×10^{17} cm^{-3}, as is seen in the undoped InGaAs layer in Fig. 2. Be accumulation during growth interruption is also observed (sample (b)). The full-width at half-maximum (FWHM) of the Be peak in sample (a) is about 58 nm. Considering the SIMS depth resolution, the measured FWHM is in good agreement with the intended thickness of 50 nm. Therefore, the unintentional Be-doping seems to cause no effect on the top profile of the Be peak. This is probably because the unintentional doping density is more than two-orders of magnitude smaller than the peak concentration. The origin of the unintentional Be-doping is probably the re-evaporation of Be from the shutter.

Therefore, in the course of the experiments, Be cell temperature was lowered by 200 to 650°C before and after the Be-doping layers were grown. When the Be temperature was lowered, a sharp Be profile was obtained on both sides of the intentionally Be-doped region (sample (c)). The asymmetry found in the Be profile (c) is probably due to the well known knock-on effect.

Schubert et al. [15] explained Be surface segregation in MBE grown GaAs by taking into account Fermi-level pinning at the semiconductor–vacuum interface. Using this model, the segregation velocity of the dopants is given by

$$v_d = \frac{De}{kT}\frac{eN_A^{2D}}{\varepsilon}, \tag{2}$$

where v_d is the growth rate and N_A^{2D} is two-dimensional doping density. Suppose the diffusion coefficient of InGaAs is the same as that of GaAs, the diffusion coefficient $D < 10^{-16}$ cm^2/s yields a negligible segregation velocity at 460°C. Therefore, for samples grown at low growth temperature, segregation does not dominate as was pointed out by these researchers.

3.2. InGaAs pn-junction structures

The Be-profiles of InGaAs pn-junction samples (Fig. 1a) are shown in Figs. 3 and 4 . The influence of growth temperature on Be redistribution in InGaAs pn-junction structures grown using an AsH_3 flow rate of 10 sccm is given in Fig. 3. The Si-SIMS profile is also shown as a layer marker. When the growth temperature is set between 400–460°C, sharp Be profiles are obtained on both sides of the doping peaks. When the AsH_3 flow rate is reduced to 1.5 sccm, although the substrate side of the Be profile is the same as samples grown with a higher AsH_3 flow rate, the surface side tail of the profile shows clear Be-segregation (Fig. 4).

AsH_3 flow rate dependence can be explained on the basis of the S–I diffusion mechanism, in which a positively ionized Be interstitial (Be_i^{m+}) rapidly diffuses until it encounters a group III vacancy site (V_{III}), which it may then occupy, thereby becoming negatively charged (Be_{III}^{-}). For an interstitial diffusion controlled process, the criterion of the process is $(m+1)D_iC_i \gg D_sC_s$, where m is the charge state of the interstitials, D is the diffusion coefficient, C is the diffusion source concentration, and i and s stand for interstitial and substitutional species. The difference in the diffusivities can be as much as six orders of magnitude faster than known

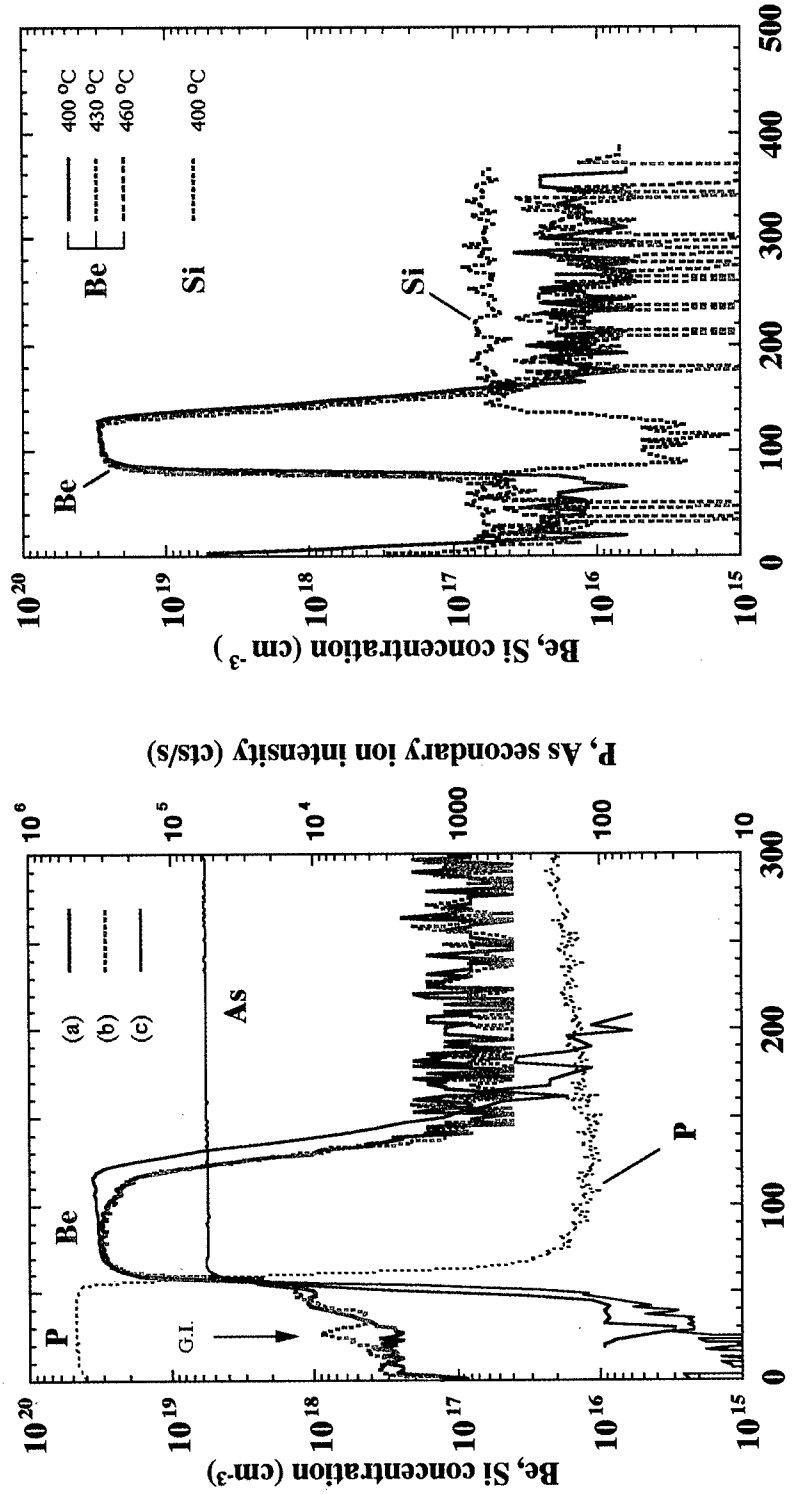

Fig. 2. Be cell temperature dependence of Be-SIMS profiles in gas source MBE grown InGaAs/InP heterostructures. (a) and (b) are samples grown by keeping Be cell temperature high. Growth interruption of 200 s is introduced during InP layer growth of sample (b). (c) A sample grown by setting Be cell temperature 200°C lower to 650°C before and after the Be-doping layer was grown. G.I. stands for growth interruption.

Fig. 3. Growth temperature dependence of Be-SIMS profiles in InGaAs pn-junction structures grown with an AsH_3 flow rate of 10 sccm.

substitutional impurities, therefore this difference in diffusion coefficients is expected to be able to offset the concentration difference which is estimated to be two to three orders of magnitude [15]. This mechanism implies that Be diffusion can be enhanced by decreasing the number of V_{III}. A decrease in V_{III} can be accomplished by decreasing the V/III flux ratio during growth, or by raising the growth temperature while keeping the arsenic flux constant.

3.3. InGaAs/InP heterostructures

Figs. 5–7 show the Be-profiles in the InGaAs/InP double-heterostructures shown in Fig. 1b. When the flow rates of AsH_3 and PH_3 are 6 sccm (Fig. 5), although the Be profiles in InGaAs show no growth temperature dependence, the profile in the InP layers of the sample grown at 490°C is considerably broader. The FWHM of the Be peak in sample grown at 400°C is about 58 nm, which is almost coinciding with the intended thickness of 52 nm. Therefore, it can be concluded that, when the AsH_3 flow rate is 6 sccm, the Be-profile can be tailored in InGaAs layers even at higher growth temperature, as is shown in Figs. 3–5, while significant redistribution of Be occurs in InP layers for sample grown at 490°C. When the PH_3 flow rate is reduced to 4 sccm while keeping AsH_3 flow rate constant, Be redistribution observed in the tail region of sample grown at 490°C is reduced (Fig. 6). The substrate side of the profiles show no temperature dependence. Fig. 7 shows the PH_3 flow rate dependence for samples grown at 490°C. In samples grown with PH_3 flow rates of 6 and 8 sccm, the Be profiles in the InP layers broaden inconsistently with the above-mentioned S–I diffusion mechanism. From Figs. 5–7, it is confirmed that, for Be redistribution in InP, the PH_3 flow rate dependence is inconsistent with the proposed S–I diffusion model, although the temperature dependence follows the S–I diffusion mechanism. From the facts that the thermal cleaning of InP in GSMBE under high PH_3 flow rate results in roughened surface, and exposure to H_2 plasma leads to the roughened surface by preferential desorption of P [16], the PH_3 flow rate dependence of Be redistribution seems to be due to hydrogen assisted preferential desorption of P at the InP surface. Further investigations, particularly PH_3 flow rate dependence of the InP surface structure is necessary to understand the Be redistribution characteristics in InP.

3.4. n-type doping dependence

It has been reported that an abnormal Zn redistribution into the AlGaAs emitter and the GaAs collector in the HBT structure takes place when all the layers except the base are doped with Si [4, 5]. In the case of Zn diffusion in InGaAs/InP heterostructures grown by OMVPE, Kurishima et al. [17] pointed out that, at lower growth temperature, high n^+ doping in the subcollector layer in a heterojunction bipolar transistor structure is the main cause of enhanced Zn diffusion. The basis for explaining Zn diffusion is that a high concentration of nonequilibrium group-III interstitials generated in the n^+ layer move toward both the surface and the underlying layers, and kick-out the Zn from substitutional to interstitial sites via the reaction

$$Zn_{III}^{-} + IIIi + 2h^{+} \leftrightarrow Zn_i^{+}.$$

The interstitial Zn then rapidly diffuses towards both the surface and the underlying layers.

We have examined the effects of Si-doping in adjoining layers to Be-doped layers in the InGaAs stacked pn-junction structure shown in Fig. 1c. Si doping density was varied from 7×10^{17} to 3×10^{19} cm^{-3}. No Be diffusion was observed even for layers with the highest Si doping concentrations (Fig. 8). The Fermi level in InGaAs is reported to be pinned close to the conduction band [18]. On the basis of Deppe's model [9], it is clear that if the Fermi level is not pinned close to mid gap at the surface, then the number of group-III interstitials in n-type layer ($N_{I_{III}}^{n}$) is same as that in intrinsic layer ($N_{I_{III}}^{i}$). Therefore, the number of interstitial Be is reduced and Be redistribution should be suppressed.

4. Summary

In conclusion, we have shown that unintentional Be doping to the InP layer grown next to the highly

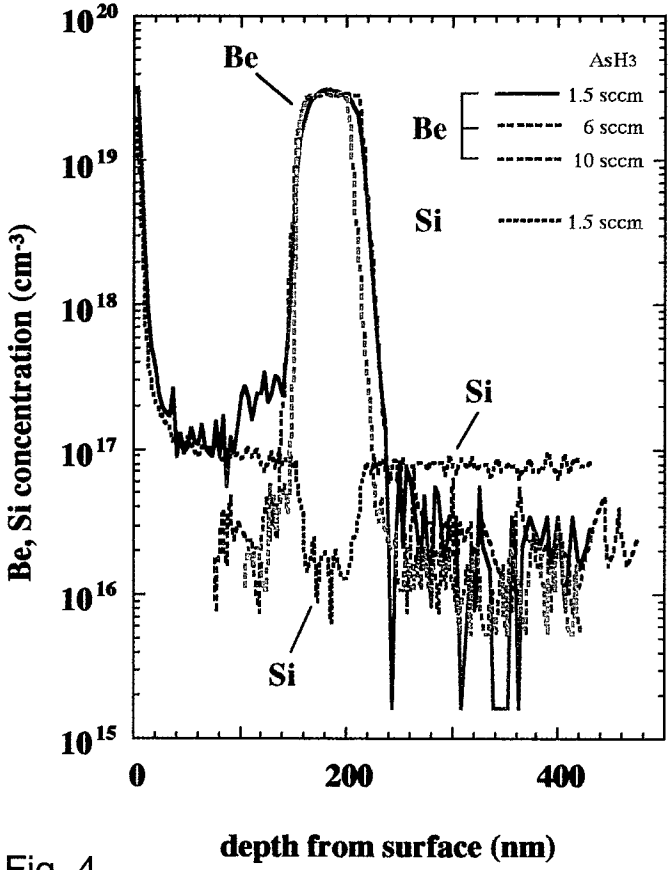

Fig. 4

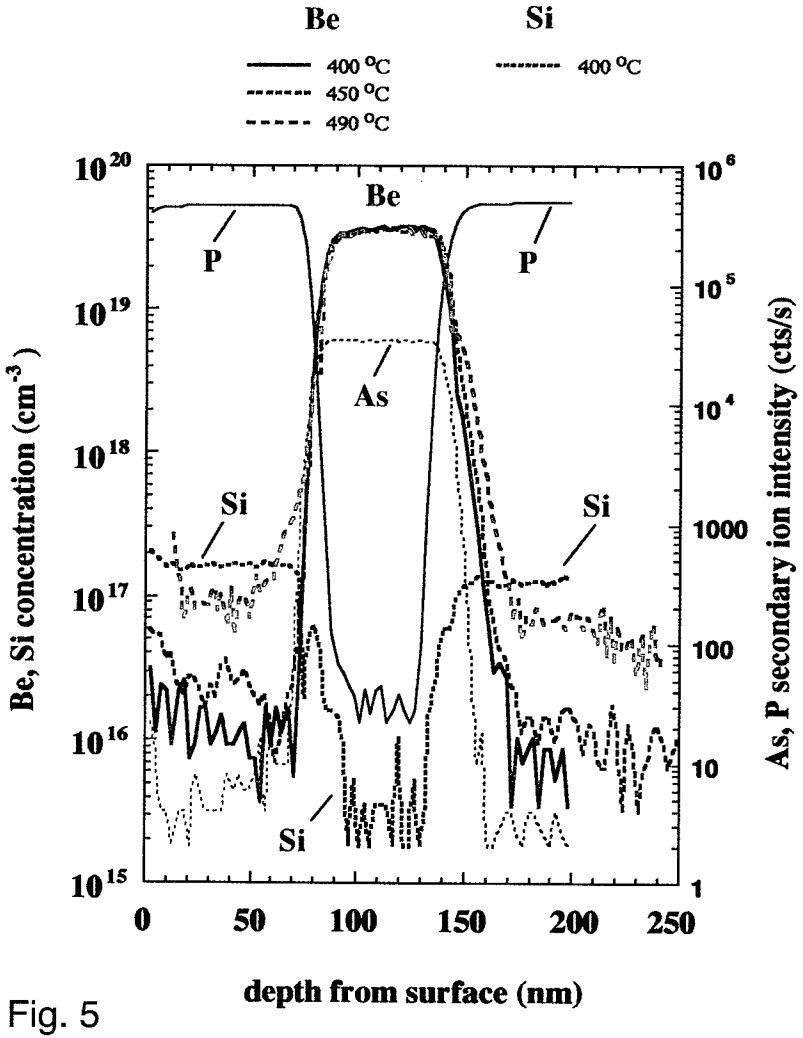

Fig. 5

Fig. 4. AsH_3 flow rate dependence of Be-SIMS profiles in InGaAs pn-junction structures grown at around 440°C.
Fig. 5. Growth temperature dependence of Be-SIMS profiles in InGaAs/InP double heterostructures grown with AsH_3 and PH_3 flow rates of 6 sccm.

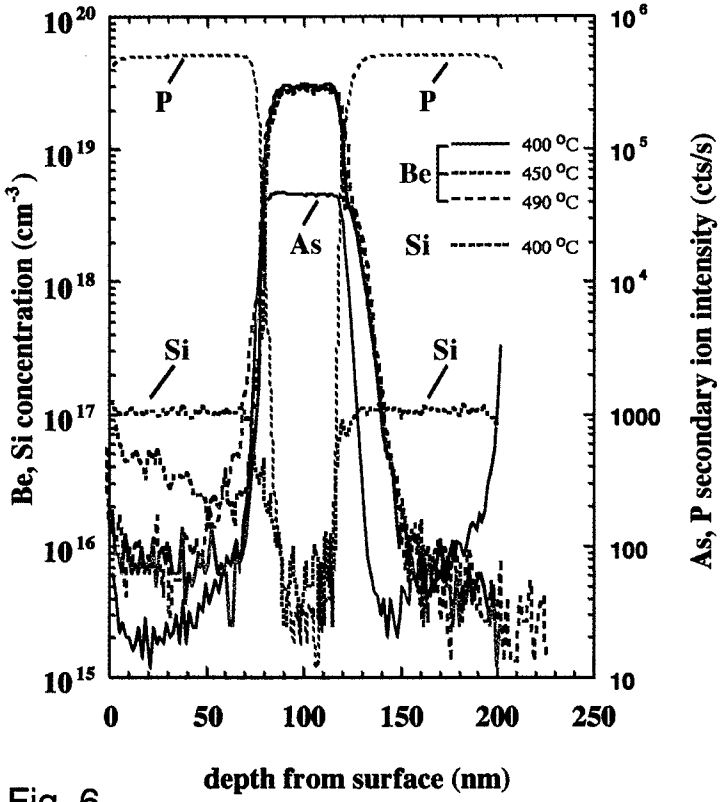

Fig. 6

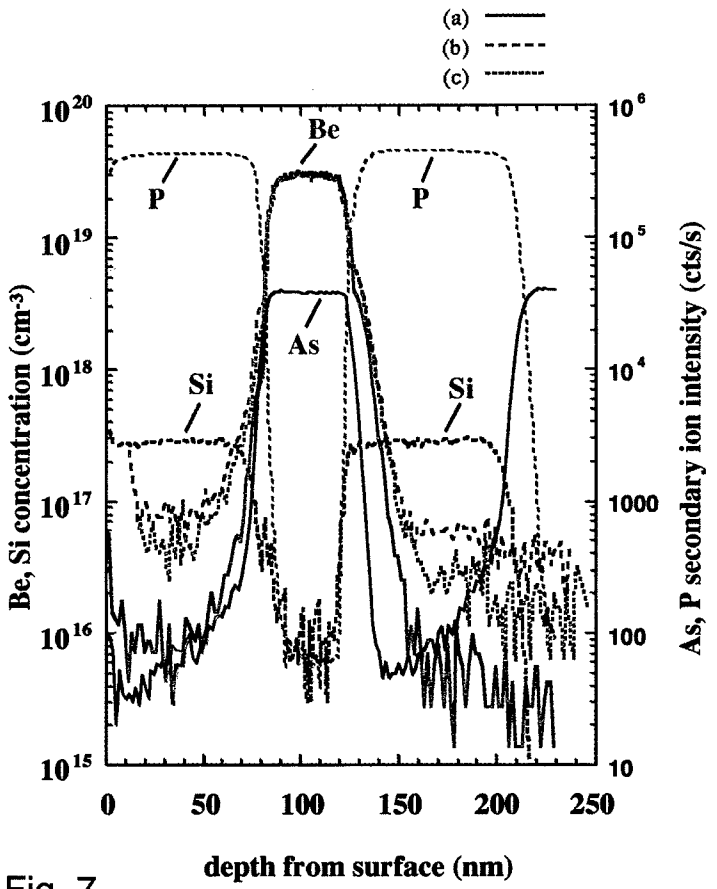

Fig. 7

Fig. 6. Growth temperature dependence of Be-SIMS profiles in InGaAs/InP double heterostructures grown with AsH_3 and PH_3 flow rate of 6 and 4 sccm.
Fig. 7. PH_3 flow rate dependence of Be-SIMS profiles in InGaAs/InP double heterostructures grown at 490°C. AsH_3 flow rate was set at 6 sccm. (a), (b) and (c) are samples grown with PH_3 flow rates of 4, 6 and 8 sccm, respectively. The Si profile shown in the figure is taken from the sample grown with a PH_3 flow rate of 4 sccm.

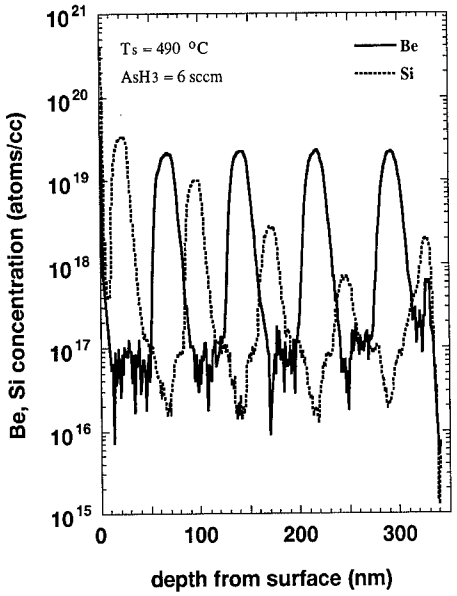

Fig. 8. Be-SIMS profile of a stacked InGaAs pn-junction structure with varying Si concentrations from 7×10^{17} to 3×10^{19} cm^{-3}. The sample was grown at 490°C with an AsH_3 flux ratio of 6 sccm.

Be-doped InGaAs layer causes significant Be redistribution, and we have also shown that the growth temperature and AsH_3 flux dependence of Be redistribution in InGaAs layers can be explained by the S–I diffusion mechanism. However, in InP/InGaAs heterostructures, although the temperature dependence of the Be profile follows the S–I diffusion mechanism, the PH_3 flow rate dependence is inconsistent with the model. Regarding the effects of n^+ doping in nearby layers, no enhancement of Be redistribution in InGaAs was observed, which is inconsistent with previous results. This can be explained in the framework of Depp's model if the Fermi level of InGaAs is pinned close to the conduction band.

Acknowledgements

The authors gratefully acknowledge the contributions of K. Ouchi, H. Masuda, T. Oka, and T. Tanoue. Thanks are also due to C.W. Magee of Evans East and K. Shingu of Nano Science Co. for the SIMS measurements and their fruitful discussions.

References

[1] P.M. Enquist, G.W. Wicks, L.F. Eastman and C. Hitzman, J. Appl. Phys. 58 (1985) 4130.
[2] D.L. Miller and P.M. Asbeck, J. Appl. Phys. 57 (1985) 1816.
[3] E.F. Schubert, J.M. Kuo, R.F. Kopf, H.S. Luftman, L.C. Hopkins and N.J. Sauer, J. Appl. Phys. 67 (1990) 1969.
[4] P.M. Enquist, J. Crystal Growth 93 (1988) 637.
[5] W.S. Hobson, S.J. Peaton and A.S. Jordan, Appl. Phys. Lett. 56 (1990) 1251.
[6] S. Yu, T.Y. Tan and U. Gösele, J. Appl. Phys. 69 (1991) 3547.
[7] R.S. Longini, Solid State Electron. 5 (1962) 127.
[8] R. Bhat, M.A. Koza, J.I. Song, S.A. Schwarz, C. Caneau and W.P Hong, Appl. Phys. Lett. 65 (1994) 338.
[9] D.G. Deppe, Appl. Phys. Lett. 56 (1990) 370.
[10] E.G. Scott, D. Wake, G.D.T. Spiller and G.J. Davies, J. Appl. Phys. 66 (1989) 5344.
[11] V. Swaminathan, N. Chand, M. Geva, P.J. Anthony and A.S. Jordan, J. Appl. Phys. 72 (1992) 4648.
[12] M.J. Tejwani, H. Kanber, B.M. Paine and J.M. Whelan, Appl. Phys. Lett. 53 (1988) 2411.
[13] T. Mozume, H. Kashima, K. Hosomi, K. Ogata, K. Suenaga and A. Nakano, Appl. Surf. Sci. 75 (1994) 233.
[14] M.B. Panish, R.A. Hamm, D. Ritter, H.S. Luftman and C.M. Cotell, J. Crystal Growth 112 (1991) 343.
[15] S.N.G. Chu, R.A. Logan, M. Geva and N.T. Ha, J. Appl. Phys. 78 (1995) 3001.
[16] T. Sugino, H. Yamamoto and J. Shirafuji, Jpn. J. Appl. Phys. 30 (1991) L984.
[17] K. Kurishima, T. Kobayashi, H. Ito and U. Gösele, J. Appl. Phys. 79 (1996) 4017.
[18] H. Hasegawa, M. Akagawa, H. Iwadate and E. Ohne, Extended Abstract of the 7th International Workshop on Future Electron Devices, Toba, Japan, Oct. 1989, P223.

ELSEVIER

Journal of Crystal Growth 175/176 (1997) 1231–1235

JOURNAL OF CRYSTAL GROWTH

Growth temperature-dependent conduction-type inversion of C-doped InGaAs grown by chemical beam epitaxy

Jeong-Rae Ro[a,*], Sung-Bock Kim[a], Seong-Ju Park[b], El-Hang Lee[a]

[a] *Electronics and Telecommunications Research Institute, Taejon 305-600, South Korea*
[b] *Kwangju Institute of Science and Technology, Kwangju 506-303, South Korea*

Abstract

We report for the first time on the growth temperature-dependent conduction-type transition of carbon-doped InGaAs grown by chemical beam epitaxy (CBE) using triethylgallium (TEGa), trimethylindium (TMIn), precracked arsine (AsH_3), and unprecracked monoethylarsine (MEAs). The hole concentration of InGaAs layers decreased with increasing growth temperature and conductivity changed from p to n at around 450°C. The conduction-type inversion of InGaAs layer is attributed to the surface segregation of indium and decomposition and incorporation kinetics of group-III source materials on the surface depending on the growth temperatures. The variations of indium composition and the V/III ratio did not affect the growth temperature-dependent conduction-type inversion of carbon-doped InGaAs. This behavior is attributed to the effect of surface segregation of indium on the carbon incorporation during the growth of InGaAs.

1. Introduction

The behavior of dopants in semiconductor is of basic interest and its understanding is fundamental for device applications. Electrical and optical device performances are influenced by properties of dopants, such as the incorporation efficiency or activation energy of free carriers. Carbon, a p-type dopant in the GaAs/AlGaAs material system, has been of great interest and widely investigated [1–4]. GaAs films with carrier concentrations of 1×10^{20} and 1×10^{21} cm^{-3} have been demonstrated by metal-organic chemical vapor deposition (MOCVD) [5] and metalorganic molecular beam epitaxy (MOMBE) [4] or chemical beam epitaxy (CBE), respectively. The main advantage of carbon in these materials is the low diffusivity [6, 7] that accompanies the high dopant activity, permitting thin, highly conducting layers to be used in devices such as the heterojunction bipolar transistors (HBTs). However, the behavior of carbon as an intentional dopant in III–V materials has not been sufficiently understood. Until recently, carbon had been regarded as an undesirable residual impurity in III–V materials for the MOMBE, CBE, and MOCVD methods.

InGaAs is a promising material for high-speed device applications owing to its high electron

* Corresponding author.

0022-0248/97/$17.00 Copyright © 1997 Elsevier Science B.V. All rights reserved
PII S0022-0248(96)00966-9

mobility and high peak electron drift velocity. The behavior of carbon in InGaAs is not well characterized at present, but the use of a p-type carbon-doped InGaAs base in InP/InGaAs HBTs would be of great interest if high doping levels can be obtained, and if carbon similarly shows low diffusivity in InGaAs. However, it is more difficult to achieve a high p-type doping level in InGaAs with carbon, because the carbon incorporation efficiency decreases with an increase in indium mole fraction [8, 9], and the amphoteric behavior of carbon produces n-type or p-type InGaAs, depending on growth conditions [10]. Up to now, p-type $In_xGa_{1-x}As$ was obtained only when trimethylgallium (TMGa) together with solid In and solid As, CCl_4, or CBr_4 was used for carbon dopant sources. Also, the p–n conversion occurs at $x = 0.8$ for InGaAs films grown by MOMBE [11], whereas it occurs at $x = 0.6$ for those grown by conventional molecular beam epitaxy (MBE) with a heated graphite filament as a carbon source [10]. This paper reports the growth temperature-dependent conduction-type transition of carbon-doped InGaAs on GaAs grown by CBE using trimethylindium (TMIn), triethylgallium (TEGa), precracked arsine (AsH_3), and unprecracked monoethylarsine (MEAs). To the best of our knowledge, no work has been known to report on the growth temperature-dependent conduction-type inversion of carbon-doped InGaAs. In our previous work, p-type carbon-doped InGaAs was successfully grown at low growth temperature by CBE using TEGa, TMIn, and MEAs [12]. In this work, we extended our investigation on the effect of hydride source gases, indium compositions, and V/III ratios on the growth temperature-dependent conduction-type inversion of carbon-doped InGaAs layers.

2. Experimental procedure

Growth of InGaAs was done in a modified CBE apparatus which consists of an ultrahigh vacuum growth chamber and a gas source control system [13]. TMIn, TEGa, precracked AsH_3, and unprecracked MEAs were used as the source materials. All growths of InGaAs were carried out on Cr-doped GaAs(100) with 2° off toward (110). Prior to the growth, the substrate was heated to remove adsorbed impurity and surface oxide layers. The growth temperature of InGaAs was in the range of 340–550°C, as measured by optical pyrometer. The In compositions of grown layers, determined by photoluminescence (PL) and double-crystal X-ray diffraction (DCXD), agreed to within 5%. Layer thicknesses were determined by scanning electron microscope (SEM) on stained and etched cleavage planes. The epilayer thicknesses used in the experiment were 0.5 to 1.5 μm. Some of the samples had some surface morphology due to the lattice mismatch. The carrier concentration and mobility were determined by van der Pauw–Hall effect measurement at room temperature. The Hall samples were cleaved $6 \times 6\ mm^2$ squares with indium ohmic contacts at the sample corners.

3. Results

Fig. 1 shows the growth temperature-dependent carrier concentration of InGaAs layers obtained from van der Pauw method. The In composition of InGaAs layers were about 0.2. The hole concentration of InGaAs using TEGa, TMIn, and MEAs decreased with increasing growth temperature and the conductivity type changed from p to n at around 450°C. Above 460°C, the conduction type of grown layer shows n and the electron concentration of InGaAs layer decreases with increasing growth temperature. As shown in Fig. 1, the growth temperature-dependent type conversion of InGaAs layer with precracked arsine is similar to that of InGaAs with MEAs. This suggests that group-III source material is influencing the growth temperature-dependent type transition rather than group-V source gases in the growing film. In Fig. 1, two different characteristics of carbon incorporation are observed depending on growth temperature. The amphoteric nature of carbon dopant consistently explains the behavior of carbon incorporation in InGaAs. The average bond strengths for $Ga–C_2H_5$, $As–CH_3$, and $In–CH_3$ are 57, 55, and 47 kcal/mol, respectively [14]. Although these values do not represent actual binding energies for precursors on the epilayer surface during growth, the relative amplitudes are considered to be still

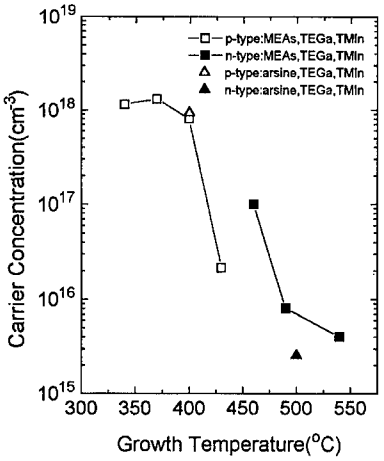

Fig. 1. Dependence of carrier concentration and conduction type in InGaAs layer on the growth temperature (V/III = 10).

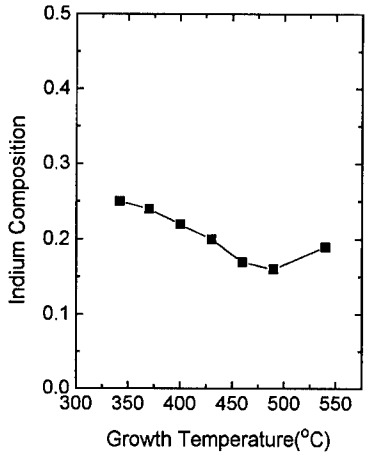

Fig. 2. Effect of growth temperature on indium fraction in InGaAs layers (V/III = 10).

valid in the comparison of the binding energies between carbon and metals. Below 450°C, the observed p-type conduction is due to the carbon which may be incorporated as a Ga–C bond into the growing layer and can be activated effectively at As site. The binding energy for Ga–C is larger than that for As–C. This may be attributed to the fact that carbon preferably occupy As sites. Above 460°C, a conductivity inversion from p- to n-type was observed without a much variation of indium composition in InGaAs grown layers. It was mentioned in a previous work [15] that the dissociation kinetics of precursors is not changed during growth of InGaAs at these temperatures. It is well known that even small amounts of lattice indium have such a pronounced effect on the growth characteristics of InGaAs. This appears to stem from the occurrence of surface segregation of indium. Although indium is fairly immobile in the lattice at low temperatures, rapid segregation from bulk to surface occurs as the substrate temperature is raised above 450°C [16]. This phenomenon results in an increase in the surface concentration of indium, until it decreases at much higher temperatures as a result of indium evaporation [17]. As a result, the surface adatom population of indium is increased with growth temperature. As mentioned above, the binding energy of In–C is smaller than that of As–C. This should cause carbon atoms to preferably occupy indium sites at the growth front of InGaAs layer. If the conduction-type inversion is originated from the self-compensation of carbon in InGaAs, a reduction of carrier concentration and mobility should be observed around the conduction-type inversion border. But, a significant reduction of carrier concentration was not observed at this growth temperature region, where the conduction-type inversion occurs, as shown in Fig. 1. These results imply that the growth temperature-dependent conduction-type inversion is not due to the self-compensation of carbon in this material. Our result suggests that the dissociation kinetics of precursors and the surface segregation of indium critically change the lattice site of carbon in the InGaAs material system, depending on the growth temperature.

Fig. 2 shows the dependence of the indium composition in InGaAs layer on the growth temperature. The InGaAs layers were grown on the GaAs substrate with beam equivalent pressure flux ratios of TEGa to TMIn of 7 : 3. Unlike the MOMBE-grown samples [11], severe temperature-dependent variations of the indium composition were not observed in CBE-grown InGaAs using unprecracked MEAs. It may be due to the different growth mechanism of InGaAs using unprecracked MEAs compared to that of elemental arsenic. Here, the surface segregation of indium depending on the growth

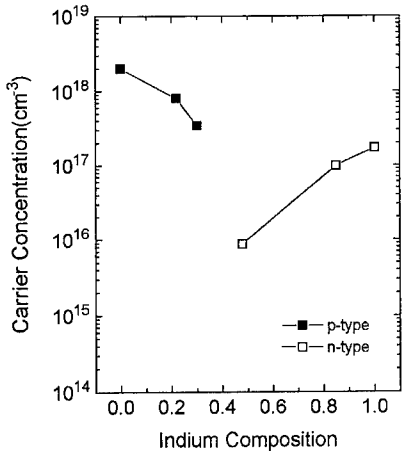

Fig. 3. Dependence of carrier concentration and conduction type in InGaAs layer on the indium composition ($T = 400$°C, V/III = 10).

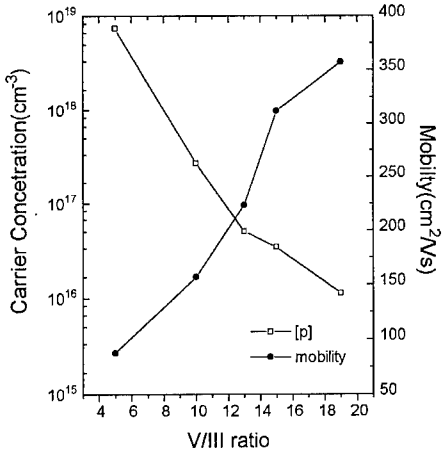

Fig. 4. Effect of V/III ratio on carrier concentration and mobility ($T = 400$°C).

temperature does not seem to significantly influence the bulk composition of indium in InGaAs grown layers. These results indicate that the inversion of conductivity type with increasing growth temperature as shown in Fig. 1 is not resulted from the variation of indium composition.

Fig. 3 shows the dependence of free carrier concentration of carbon-doped $In_xGa_{1-x}As$ on the InAs mole fraction grown at the temperature of 400°C. The beam equivalent pressure flux ratio of TEGa to TMIn was varied from 0 to 1 with fixed MEAs beam flux and substrate temperature. The conductivity-type changes from p to n between $x = 0.3$ and 0.45. The p–n inversion occurs between $x = 0.3$ and 0.45 for the $In_xGa_{1-x}As$ layers grown by CBE using unprecracked MEAs, whereas it occurs at $x = 0.6$ and 0.8 for those grown by MOMBE [11] and solid-source MBE with heated graphite filament [10], respectively. It is worth noting that the hole concentration of InGaAs layers grown by CBE using TEGa, TMIn, and unprecracked MEAs is comparable to that of the carbon-doped InGaAs layers grown by conventional MBE with heated graphite filament. The conduction-type inversion with indium composition usually accompanies the decrease of free carrier concentration and mobility [10]. As carbon can occupy both donor and acceptor sites, strong carrier compensation causes a large increase in ionized impurity scattering. A significant reduction of carrier concentration is shown around the border as shown in Fig. 3. These results imply that the indium composition-dependent conduction-type inversion is due to the self-compensation of carbon in InGaAs. Therefore, the mechanism of conduction-type inversion with indium composition is different from that with growth temperature. A reduction of electron mobility was observed in InAs samples. We believe that it results from the defects occurring in InAs due to the large lattice mismatch between GaAs and InAs. The growth temperature-dependent conduction-type inversion of InGaAs layers occurred at the indium compositions less than 0.3, as shown in Figs. 1 and 2. Therefore, the growth temperature-dependent conduction-type transition is not attributed to an increase of the indium composition with growth temperature.

Fig. 4 shows the dependence of carrier concentration of InGaAs epilayers on V/III ratio obtained at the growth temperature of 400°C. All samples grown under the conditions of various V/III ratios and low growth temperature show p-type conduction, which is consistent with the results shown in Fig. 1. The surface segregation of indium during the growth of InGaAs is suppressed by increasing the arsenic pressure [17]. As shown in Fig. 4, samples under the condition of low V/III ratios were

measured as p-type conduction. The elementary process of carbon incorporation at low temperatures is governed by dissociation kinetics of source materials on the surface and the effect of surface segregation of indium on the carbon incorporation is negligible in this region. Therefore, the growth temperature-dependent conduction-type transition is not attributed to the variation of V/III ratio. Furthermore, the carrier concentration and mobility of grown layer depended distinctly on the partial pressure of MEAs. Therefore, it is believed that the presence of partially cracked arsine radical and hydrogen atom dissociated from MEAs on the growing surface can inhibit the incorporation of hydrocarbon, since the surface can play a key role in inhibiting hydrocarbon pyrolysis due to an available surface population of arsine radical and atomic hydrogen.

4. Summary

We have examined for the first time the growth temperature-dependent conduction-type inversion of carbon-doped InGaAs on GaAs grown by CBE using TMIn, TEGa, precracked AsH_3, and unprecracked MEAs. A conduction-type inversion from p to n is found to occur in the InGaAs layers with increasing growth temperature. This phenomenon can be understood by considering surface segregation of indium during InGaAs growth at high growth temperatures and different decomposition and incorporation kinetics of carbon-containing source materials on the surface at low growth temperatures. From the investigation on the effects of V/III ratio and indium composition, the growth temperature-dependent conduction-type inversion is not attributed to the influence of V/III ratio and the variation of indium composition. From this work, it is suggested that the surface segregation of indium has a significant effect on the dopant incorporation and activation behavior in the growth of indium-containing compound semiconductor, for example InGaAs or InAlAs. These results suggest that p–n junction of indium-containing materials can be fabricated by the control of growth temperature without introduction of dopants.

Acknowledgements

This work was sponsored by the Ministry of Information and Communications, South Korea.

References

[1] C.R. Abernathy, S.J. Pearton, R. Caruso, J. Ren and J. Kovalchik, Appl. Phys. Lett. 55 (1987) 1750.
[2] R.J. Malik, R.N. Nottenberg, E.F. Schubert, J.F. Walker and R.W. Ryan, Appl. Phys. Lett. 53 (1988) 2661.
[3] T.J. de Lyon, N.I. Buchan, P.D. Kirchner, J.M. Woodall, G.J. Scilla and F. Cardone, Appl. Phys. Lett. 58 (1991) 517.
[4] M. Konagai, T. Yamada, T. Akatsuka, K. Saito, E. Tokumitsu and K. Takahashi, J. Crystal Growth 98 (1989) 167.
[5] P.M. Enquist, Appl. Phys. Lett. 57 (1990) 2348.
[6] T.J. Kuech, M.A. Tischler, P.J. Wang, G. Scilla, R. Potemski and F. Cardone, Appl. Phys. Lett. 53 (1988) 1377.
[7] B.T. Cunningham, L.J. Guido, J.E. Baker, J.S. Major, Jr., N. Holonyak, Jr. and G.E. Stillman, Appl. Phys. Lett. 55 (1989) 687.
[8] J. Shirakashi, T. Yamada, M. Qi, S. Nozaki, K. Takahashi, E. Tokumitsu and M. Konagai, Jpn. J. Appl. Phys. 30 (1991) L1609.
[9] S.A. Stockman, A.W. Hanson and G.E. Stillman, Appl. Phys. Lett. 60 (1992) 2903.
[10] H. Ito and T. Ishibashi, Jpn. J. Appl. Phys. 30 (1991) L944.
[11] E. Tokumitsu, J. Shirakashi, M. Qi, T. Yamada, S. Nozaki, M. Konagai and K. Takahashi, J. Crystal Growth 120 (1992) 301.
[12] J.R. Ro, S.J. Park, S.B. Kim and E.H. Lee, J. Crystal Growth 150 (1995) 627.
[13] S.J. Park, J.R. Ro, J.K. Sim and E.H. Lee, ETRI J. 16 (1994) 1.
[14] G.B. Stringfellow, Organometallic Vapor-Phase Epitaxy, (Academic Press, San Diego, 1989) p. 21.
[15] J.R. Ro, S.J. Park, S.B. Kim and E.H. Lee, J. Crystal Growth 150 (1995) 627.
[16] N.K. Singh, J.S. Ford, P.J. Skevington and G.J. Davies, J. Crystal Growth 120 (1992) 33.
[17] Y. Iimura, K. Nagata, Y. Aoyagi and S. Namba, J. Crystal Growth 105 (1990) 230.

ELSEVIER

Journal of Crystal Growth 175/176 (1997) 1236–1241

JOURNAL OF CRYSTAL GROWTH

Selective area etching of III–V semiconductors using TDMAAs and TDMASb in metalorganic molecular beam epitaxy chamber

K. Yamamoto, H. Asahi*, T. Hayashi, K. Hidaka, S. Gonda

The Institute of Scientific and Industrial Research, Osaka University, 8-1, Mihogaoka, Ibaraki, Osaka 567, Japan

Abstract

Selective area etching of SiO_2-masked GaAs using trisdimethylaminoarsenic (TDMAAs) is studied. GaAs substrates are partly masked with stripe shaped SiO_2 films along the [0 1 1] and [0 $\bar{1}$ 1] directions. Cross-sectional scanning electron microscopy observation shows that the etched shape depends on both the direction of the mask and substrate temperature, and is almost independent of the TDMAAs flow rate. At low substrate temperatures, the (1 1 1)B surface is preferentially formed and a V-shaped groove is formed for the [0 1 1] mask direction. With increasing substrate temperature, the V-groove changes to the channel with vertical side walls due to the drastic increase of the etching rate of (1 1 1)B. For the [0 $\bar{1}$ 1] mask direction, the vertical (0 1 1) plane is formed at all temperatures. It is found that etched shapes are determined by the difference of etching rates and that etching rates are influenced by the crystal structure on the surface. On the other hand, the etching rate of GaSb by TDMASb is independent of substrate surface orientation. This is because the bond strength of GaSb is weak and the etching proceeds along the direction of molecular beams. Enhanced etching rate is observed for InP by TDMAAs, which is explained by the formation of thin InAs layer on InP due to the irradiation of As released from TDMAAs.

1. Introduction

Selective area etching and regrowth using patterned substrates are emerging as a very promising technique for the fabrication of nanoscale structures, such as quantum dots or wires [1]. Considering these multiple processes, the clean environment is required since the optical and electrical properties of devices will be affected by a contamination due to an air exposure or surface residues. Furthermore, the accurate control of etched profiles with a minimal damage is necessary. For this purpose, metalorganic molecular beam epitaxy (MOMBE) is a useful method because the etching and regrowth can be conducted in the same vacuum chamber by switching from etching to growth and vice versa as described below.

An As precursor, trisdimethylaminoarsenic $\{As[N(CH_3)_2]_3$, TDMAAs$\}$, has been proposed as an alternative candidate in the MOMBE growth of

* Corresponding author. E-mail: asahi@sanken.osaka-u.ac.jp.

0022-0248/97/$17.00 Copyright © 1997 Elsevier Science B.V. All rights reserved
PII S0022-0248(96)00863-9

GaAs and AlGaAs [2–9] instead of the extremely toxic and high thermally stable hydride-like AsH_3. Since TDMAAs releases As atoms even at low temperatures (300–450°C) compared with other precursors [5, 6], thermal precracking in a gas cell before the supply on the substrate surface is not needed. This leads to a low carbon incorporation by TDMAAs in the growth of GaAs with both triethylgallium (TEGa) and trimethylgallium (TMGa) [3, 7].

It was also reported that GaAs and GaSb substrates are etched by TDMAAs and by trisdimethylaminoantimony $\{Sb[N(CH_3)_2]_3$, TDMASb$\}$ [9–12]. The etching by these metalorganics was considered to be due to the reaction of surface Ga atoms with TDMAAs and TDMASb related species (probably, amine species) resulting in the formation of volatile Ga species although the exact mechanism has not been understood yet. The etching proceeds in the monolayer-by-monolayer mode, which was confirmed by the reflection high-energy electron diffraction (RHEED) intensity oscillations [12].

For the regrowth, TDMAAs is also a suitable As source because the selective area epitaxy of GaAs was easily achieved by the combination of TEGa and TDMAAs at lower temperatures than by the use of TEGa and solid As [8].

In this paper, we report on the metalorganic molecular beam etching of SiO_2-masked GaAs substrates by TDMAAs and discuss the mechanism of the formation of etched shapes. In addition, the dependence of etching characteristics on etched substrate (GaSb, GaAs, GaP, InP) and metalorganic molecules (TDMAAs, TDMASb) is also described.

2. Experimental procedure

The etching experiments were conducted using a modified ULVAC MBE 300 apparatus equipped with gas cells for TDMAAs and TDMASb. The growth chamber was evacuated by an oil diffusion pump with a liquid nitrogen trap, yielding a pressure of less than 5×10^{-6} Torr during etching. Non-precracked TDMAAs and TDMASb were directly introduced into the growth chamber through mass flow controllers (MFCs) without any carrier gases. Source cylinder, gas line and gas cell were heated at proper temperatures in order to avoid their condensation and to get reasonable gas flow rates. The substrates used were (1 0 0)-GaAs partly masked with SiO_2 films for selective area etching, and non-masked (1 0 0) and (n 1 1) $\{n = 5, 4, 3, 2, \frac{7}{5}, 1\}$, GaAs and GaSb. Stripe mask patterns aligned along [0 1 1] and [0 $\bar{1}$ 1] directions were formed by a conventional photolithography and a wet chemical etching. The substrate temperature (T_{sub}) was monitored by an optical pyrometer calibrated by the melting point of InSb at 525°C. The substrate holder was rotated intermittently during etching. Cross-sectional etched profiles were studied by the scanning electron microscopy (SEM).

3. Results and discussion

3.1. Selective area etching on SiO_2-masked GaAs substrate

Selective area etching using TDMAAs was performed on SiO_2-masked GaAs substrates. Fig. 1 shows typical cross-sectional SEM photographs of etched substrates with a stripe mask aligned along the [0 1 1] and [0 $\bar{1}$ 1] directions. It was found that etched shapes were influenced by the direction of a stripe mask and T_{sub}. At T_{sub} lower than 550°C, for the [0 1 1] mask direction, only (1 1 1)B surfaces were observed and the V-shaped groove was formed (Fig. 1a). With elevating T_{sub} up to 600°C, (1 1 1)B surfaces disappeared and only vertical (0 1 1) side walls emerged (Fig. 1b). On the other hand, for the [0 $\bar{1}$ 1] mask direction, the etched side walls were a combination of (1 1 1)A and vertical (0 1 1) at low temperatures (Fig. 1c), and in addition to these surfaces (4 1 1)A facets emerged at T_{sub} higher than 600°C (Fig. 1d). But etched shapes were almost independent of a TDMAAs flow rate. These results indicate the possibility of controlling the etched profiles by selecting the etching condition.

In order to study the mechanism for the formation of etched side walls, the ER variations with T_{sub} were measured for (1 0 0), (4 1 1), and (1 1 1)

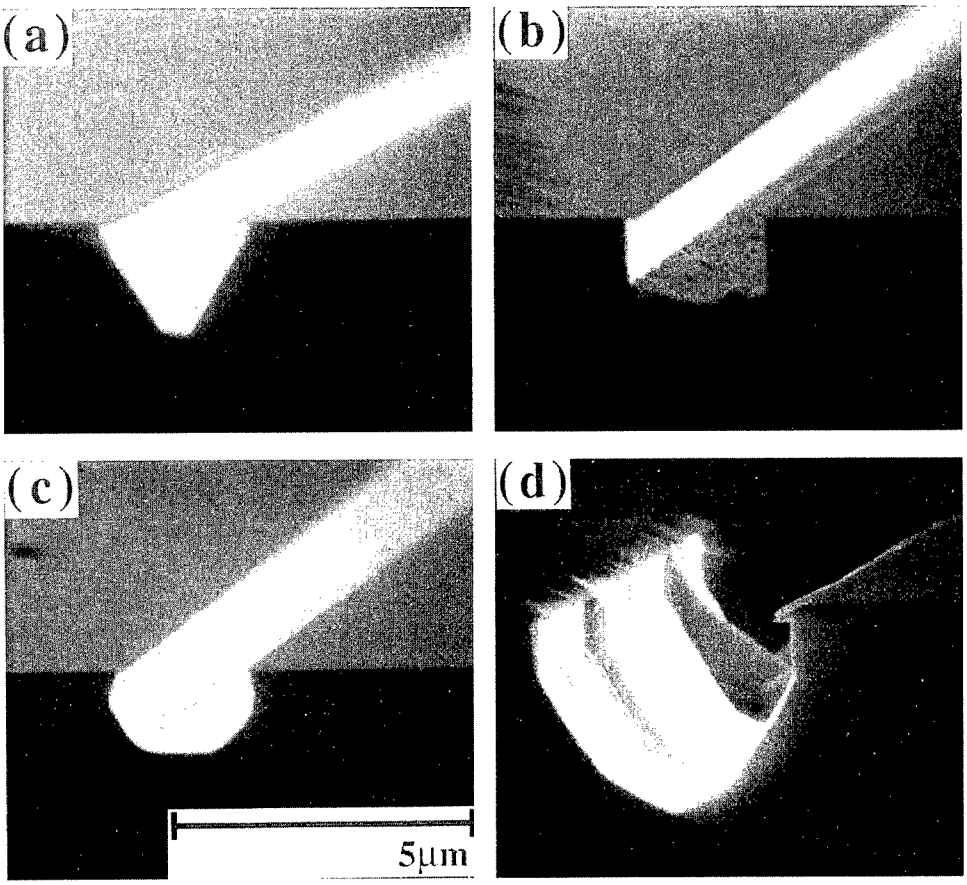

Fig. 1. Cross-sectional SEM photographs of GaAs with (a), (b) [0 1 1] and (c), (d) [0 $\bar{1}$ 1] oriented SiO_2 stripe masks after etching by TDMAAs at (a), (c) low and (b), (d) high T_{sub}.

surfaces as shown in Fig. 2. These (n 1 1) substrates were mounted on a same Mo holder, and the etched thickness (or etching rate (ER)) was measured by the step height between the etched area and the masked one with a small Ta metal strip. As can be seen, ERs were increased with T_{sub} for all surfaces. Our previous work [12] showed that the etching occurs when amino-species react with surface Ga atoms, which are formed by the desorption of outermost As atoms from the surface. This suggests that the ER increases at higher T_{sub} due to the the low surface coverage of group V atoms, where the desorption of As is enhanced.

Now, we consider the dependence of the ER on the substrate orientation. At low T_{sub}, the ER of the (1 1 1)B was smallest, indicating that the (1 1 1)B is

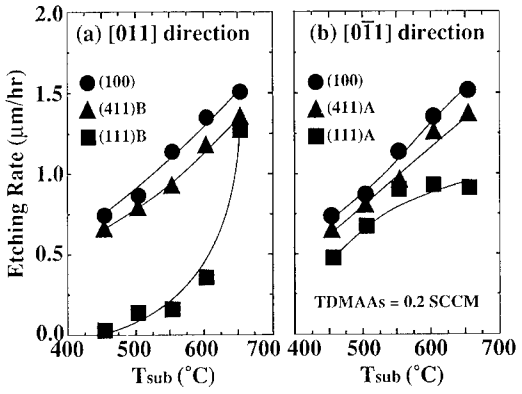

Fig. 2. Etching rate dependence of GaAs by TDMAAs on T_{sub} as a function of surface orientation.

difficult to be etched. However, by increasing T_{sub}, it drastically increased and approached those for other surfaces. On the other hand, that of the (1 1 1)A was slightly smaller than that of the (1 0 0) at all T_{sub}, but did not increase above 600°C. These differences in ERs are explained by taking into account the crystal structure of three surfaces, i.e., (1 1 1)A, (1 0 0) and (1 1 1)B. Although the ERs for other (n 1 1) surfaces were not considered here, they are assumed to be similar to those for the (100) and (1 1 1) surfaces because the (n 1 1) surfaces are composed of (1 0 0) and (1 1 1) surfaces. The (1 1 1)A and (1 1 1)B are terminated by Ga and As atoms, respectively. That is, As atoms on the (1 1 1)B surface are strongly bound with three back-bonds to the underlying Ga atom, whereas those on the (1 0 0) and (1 1 1)A have two and only one back-bonds, respectively. At low T_{sub}, the surface coverage of As on the (1 1 1)B surface is highest due to the strong strength of As-bonds and a little desorption of As, resulting in the slow ER. From the above discussion, the surface coverage of As on the (1 1 1)A is lowest and the ER is considered to be the highest. However, the ER of (1 1 1)A surface was lower than that of the (1 0 0) surface. This discrepancy might be due to the strong bonding of Ga atoms on the (1 1 1)A surface, where Ga atoms have three back-bonds to the underlying As atoms. At higher T_{sub} above 600°C, the RHEED pattern indicated that the desorption of As molecules is enhanced and that the surface is terminated by the Ga surface or covered with Ga droplets. Therefore, ERs are independent of the surface coverage of As and depend on only the strength of Ga atoms. It is also understood that the ER of (1 1 1)B, where Ga atoms are bound to surface As atoms with only one bond, drastically increases with increasing T_{sub} and that the ER of (1 1 1)A, where Ga atoms with three back-bonds, is lower than those of the other surfaces.

Now, we discuss the dependence of etched profiles on the etching condition (Fig. 1). For the [0 1 1] mask direction, the (1 1 1)B surface are selectively formed due to the low ER of the (111)B at low T_{sub}. However, as the T_{sub} increases, ER for the (1 1 1)B plane increases rapidly and approaches those for the other planes. Therefore, at higher T_{sub}, vertical (0 1 1) side walls are formed because the etching proceeds along the direction of molecular beams which is perpendicular to the surface. On the other hand, for the [0 $\bar{1}$ 1] mask direction, the ER of the (1 1 1)A plane is slightly smaller than those for the other surfaces at all T_{sub}. Therefore, vertical etching is mainly expected, but (1 1 1)A planes are also formed at the bottom region of the etched walls due to the low etching rate of (1 1 1)A. But (4 1 1)A planes also appeared at the base of the walls. This is not clear, but it might be related to the reflection of TDMAAs molecules from the (1 1 1)A planes inside the etched channel or to the higher stability of the (4 1 1)A surface [13].

3.2. Comparison of etching rates between GaAs and GaSb

We investigated the etching process on GaAs and GaSb substrates. The ER of GaAs by TDMAAs increased with T_{sub} for all surface orientations. In addition, the (1 0 0) surface was etched with the highest ER and the ER was decreased in accordance with an increase of the tilt angle ((1 0 0) > (4 1 1) > (1 1 1)) as shown in Fig. 2. From the decomposition study of TDMAAs, it is completely pyrolized above 350°C [5, 6]. Since etching experiments here were conducted at T_{sub} higher than 450°C, the decomposition efficiency is almost unity, producing no orientation dependence. Therefore, ERs on high index substrates are considered to be determined by the crystal structure of the surface.

Fig. 3 shows the substrate orientation (tilt angle) dependence of the ER of GaSb by TDMASb as a function of T_{sub}. As can be seen in this figure, the ER is almost independent of the tilt angle. Solid circles in Fig. 4 show the ER of (1 0 0)-GaSb by TDMASb. The ER of GaSb saturated at T_{sub} 550°C, whereas that of GaAs by TDMASb increased with T_{sub} as shown in Fig. 4. This saturation of the ER is caused by the weak bond of GaSb compared with that of GaAs. In the case of GaSb, Sb atoms are easily desorbed from the top surface and Ga droplets exist on the Sb sublayer at T_{sub} higher than 500°C [14]. On the surface with Ga droplets, the ER depends neither on the surface coverage of Sb, nor on the tilt angle because TDMASb easily reacts with Ga droplets on the surface under the Sb free condition. Furthermore,

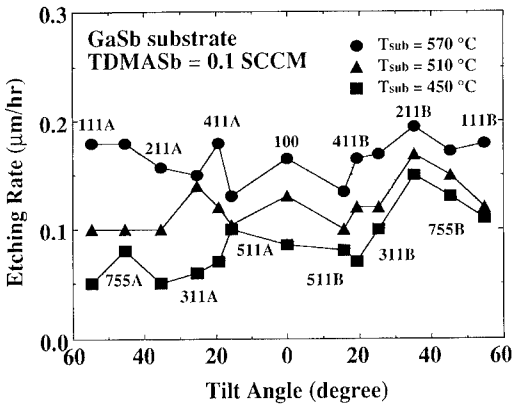

Fig. 3. Etching rate dependence of GaSb by TDMASb on surface orientation as a function of T_{sub}.

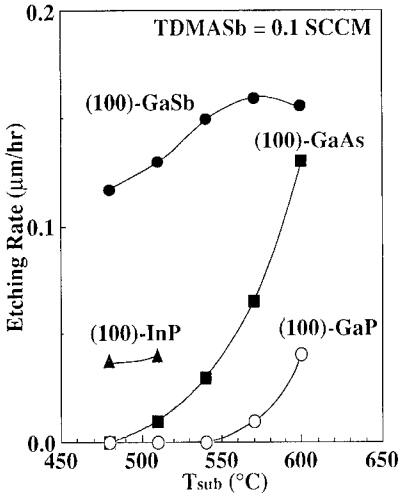

Fig. 4. Etching rate dependence of (1 0 0)-GaSb, GaAs, GaP and InP on T_{sub} for the etching by TDMASb.

the ER is limited by the supply of TDMASb, resulting in the saturation of the ER.

3.3. Etching of different substrates by TDMAAs and TDMASb

We studied the influence of the ER on the etched material, (1 0 0)-GaSb, GaAs, GaP and InP substrates. Fig. 4 shows the ER dependence of various substrates etched by TDMASb on the T_{sub}. All substrates were etched and the order of the ER is

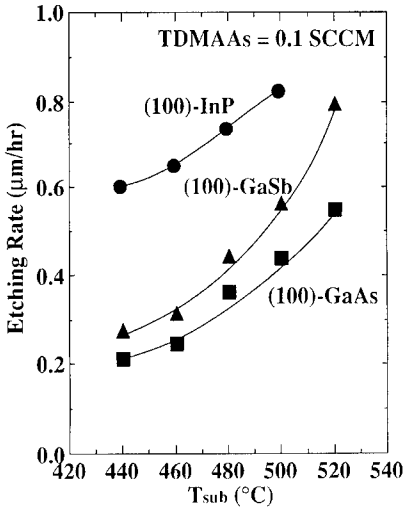

Fig. 5. Etching rate dependence of (1 0 0)-GaSb, GaAs, and InP on T_{sub} for the etching by TDMAAs.

GaSb > InP > GaAs > GaP. In order to explain this result, we consider the difference of bond strength. The bond of GaSb (45.9 kcal/mol) is the weakest among them, resulting in the highest etching rate, while the etching rate of GaP is relatively low because of the strongest bond strength (54.9 kcal/mol) [15]. Therefore, the order of bond strength, which is Ga–Sb < In-P (47.3 kcal/mol) < Ga–As (50.1 kcal/mol) < Ga–P, corresponds to the order of the ER. However, the ER of InP is higher than that of GaSb when TDMAAs was used for etching instead of TDMASb as shown in Fig. 5. The SEM observation indicated that surface morphologies of InP were rough after etching. In solid source MBE, it has been known that the surface of InP is replaced by thin InAs layers by the irradiation of As beam due to the high vapor pressure of P [16]. Hence, the surface of InP is exchanged into InAs by As atoms released from TDMAAs, followed by etching by amino-groups. Therefore, the ER of InP substrates increases due to the etching of InAs instead of InP.

4. Summary

Selective area etching of SiO_2-masked GaAs using TDMAAs was studied. Cross-sectional SEM

observation showed that the etched shape depends on both the direction of the mask and the substrate temperature, and is almost independent of the TDMAAs flow rate. It was found that these etched shapes are determined by the ER for each surfaces and that the ER is influenced by the crystal structure on the surface. Therefore, it is possible to control the etched profiles by choosing etching conditions. TDMAAs is not only a promising arsenic source for growth but also is a quite useful in situ etching gas source. In contrast, the ER of GaSb etched by TDMASb was independent of the crystal structure and was similar for all high index substrates. This is due to the weak bond strength of GaSb. When the InP substrate was etched by TDMAAs, the surface of InP was replaced by thin InAs layers due to the irradiation of As released from TDMAAs and the growth rate of InP was enhanced.

Acknowledgements

This work was supported in part by the Scientific Research Grant-in-Aid #07650014 from the Ministry of Education, Sport, Science and Culture of Japan, and the Research and Development Association for Future Electron Devices.

References

[1] W.T. Tsang, R. Kapre and P.F. Sciortino, Jr., J. Crystal Growth 136 (1994) 42.
[2] C.R. Abernathy, P.W. Wisk, S.J. Pearton, F. Ren, D.A. Bohling and G.T. Muhr, J. Crystal Growth 124 (1992) 64.
[3] C.R. Abernathy, P.W. Wisk, D.A. Bohling and G.T. Muhr, Appl. Phys. Lett. 60 (1992) 2421.
[4] G. Zimmermann, H. Protzmann, T. Marschner, O. Zsebök, W. Stolz, E.O. Göbel, P. Gimmnich, J. Lorberth, T. Filz, P. Kurpas and W. Richter, J. Crystal Growth 129 (1993) 37.
[5] K. Hamaoka, I. Suemune, K. Fujii, T. Koui, A. Kiahimoto and M. Yamanishi, Jpn. J. Appl. Phys. 30 (1991) L1579.
[6] S. Salim, J.P. Lu, K.F. Jensen and D.A. Bohling, J. Crystal Growth 124 (1992) 16.
[7] S. Goto, Y. Nomura, Y. Morishita, Y. Katayama and H. Ohno, J. Crystal Growth 149 (1995) 143.
[8] X.F. Liu, H. Asahi, K. Inoue, D. Marx, K. Asami, K. Miki and S. Gonda, J. Appl. Phys. 77 (1995) 1952.
[9] H. Asahi, X.F. Liu, K. Inoue, D. Marx, K. Asami, K. Miki and S. Gonda, J. Crystal Growth 145 (1994) 668.
[10] X.F. Liu, H. Asahi, K. Inoue, D. Marx, K. Asami, K. Miki and S. Gonda, Appl. Phys. Lett. 65 (1994) 1027.
[11] D. Marx, H. Asahi, X.F. Liu, M. Higashiwaki, A.B. Villaflor, K. Miki, K. Yamamoto, S. Gonda, S. Shimomura and S. Hiyamizu, J. Crystal Growth 150 (1995) 551.
[12] A.B. Villaflor, H. Asahi, D. Marx, K. Miki, K. Yamamoto and S. Gonda, J. Crystal Growth 150 (1995) 638.
[13] S. Shimomura, A. Wakejima, A. Adachi, Y. Okamoto, N. Sano, K. Murase and S. Hiyamizu, Jpn. J. Appl. Phys. 32 (1993) L1728.
[14] M. Yano, K. Yamamoto, T. Utatsu and M. Inoue, J. Vac. Sci. Technol. B 12 (1994) 1133.
[15] CRC Handbook of chemistry and Physics, 70th ed. (CRC Press, Boca Ration, 1990) p. 197.
[16] M. Yano, H. Yokose, Y. Iwai and M. Inoue, J. Crystal Growth 111 (1991) 609.

ELSEVIER

Journal of Crystal Growth 175/176 (1997) 1242–1246

JOURNAL OF CRYSTAL GROWTH

Indium surface segregation during chemical beam epitaxy of $Ga_{1-x}In_xAs/GaAs$ and $Ga_{1-x}In_xP/GaAs$ heterostructures

M. Mesrine*, J. Massies, C. Deparis, N. Grandjean, E. Vanelle, M. Leroux

Centre de Recherche sur l'Hétéro-Epitaxie et ses Applications, CNRS, Sophia-Antipolis, Rue Bernard Gregory, F-06560 Valbonne, France

Abstract

We report on the investigation of In surface segregation in GaInP/GaAs and GaInAs/GaAs heterostructures grown by chemical beam epitaxy (CBE). Owing to the peculiarities of CBE growth, it is shown that In segregation can be quantitatively evaluated in real-time by using reflection high-energy electron diffraction (RHEED). A segregation coefficient and its variation with the growth temperature is extracted from the RHEED data. It is used to determine the In composition profiles at the interfaces of GaInAs/GaAs quantum well (QW) structures as a function of the growth temperature. A good agreement is found between optical transition energies calculated from these profiles and the experimental photoluminescence (PL) energies. PL energy shifts observed in GaInP/GaAs QW's as a function of the growth temperature are qualitatively explained by In segregation.

PACS: 68.55.Bd; 68.35.Fx; 61.14.Hg

Keywords: Chemical beam epitaxy; Surface segregation; Photoluminescence; $Ga_{1-x}In_xP$; $In_xGa_{1-x}As$

1. Introduction

It is now recognized that surface segregation is a severe limitation to the building of perfectly abrupt III–V semiconductor interfaces. However, most of the available data are mainly concerned with $Ga_{1-x}In_xAs/GaAs$ grown by standard solid source molecular beam epitaxy (MBE) and only a few results have been reported for other III–V materials [1] as well as for different growth methods such as chemical beam epitaxy (CBE) [2–4]. Also, only scarce reports concern real-time investigations during growth [5]. In a previous paper, we have reported on the study of In surface segregation during CBE growth of $Ga_{1-x}In_xP/GaAs$ heterostructures [6]. We have demonstrated that In segregation at both normal and inverted interfaces can be evidenced in real-time by reflection high-energy electron diffraction (RHEED) via growth rate variations observed in the first stages of the growth. In the present paper, we investigate in the same way the temperature dependence of the In segregation in GaAs. The validity of our method of in situ determination of In

* Corresponding author.

0022-0248/97/$17.00 Copyright © 1997 Published by Elsevier Science B.V. All rights reserved
PII S0022-0248(96)00919-0

segregation is demonstrated by correctly predicting from the RHEED data the transition energies experimentally observed by photoluminescence (PL) in GaInAs/GaAs QW's grown at various temperatures. Finally, the variation of PL energies of GaAs/GaInP QW's as a function of growth temperature is discussed in the framework of In segregation.

2. Experimental details

Growth was carried out in an ultra-high vacuum reactor especially designed for CBE (RIBER-EPINEAT) and which has been described elsewhere [7]. Triethylgallium (TEG) and trimethylindium (TMI) were used as group III-element precursors. Group V-element fluxes were provided by high temperature cracking (950°C) of AsH_3 and PH_3. All the samples were grown on GaAs (0 0 1) substrates. The temperature was controlled using an infrared pyrometer calibrated with the melting point of InSb (525°C). For the GaInP/GaAs heterostructures, GaInP was grown at 550°C with a growth rate of 0.92 monolayers per second (ML/s), while GaAs was grown at various temperatures with a constant growth rate of 0.82 ML/s. The temperature was varied during the growth interruptions at the direct and inverted interfaces, while the surface was stabilized under cracked PH_3 and AsH_3 for GaInP and GaAs, respectively. The growth of GaInP on GaAs was performed by switching all the precursors in the same time, in order to minimize the formation of GaP at this interface [8]. At the GaAs on GaInP interface, the growth was interrupted for 1 s under cracked AsH_3 leading to a partial substitution of the phosphorus atoms of the surface layer by arsenic ones [9]. However, it has to be noted here that different growth interruption sequences were investigated at the beginning of this study in order to check that the growth interruption procedure has no influence on the growth rate of the following layers. Growth at the interfaces of GaInAs/GaAs heterostructures is less critical, so standard growth interruptions were performed (30 s growth interruption under As_2 flux at both interfaces) in order to smooth the interfaces between the two materials. Photoluminescence was excited with a 4880 Å line of an argon laser and measured at 9 K in a closed-cycle He cryostat.

3. Results

3.1. Correlation between growth rate transient and In surface segregation

During the early stages of the growth of GaInP on GaAs, the growth rate deduced from RHEED specular beam intensity variation decreases before reaching a steady state value (Fig. 1a). With the assumption that the decomposition of TEG, and as a consequence the incorporation rate of Ga, is decreased by the presence of In on the growth front, this particular feature of the RHEED oscillatory period can be explained by a gradual increase of the In composition at the beginning of the growth up to a steady state value reached after few monolayers [2, 6]. The observed growth rate transient is in fact the signature of In surface segregation. At the inverted interface, i.e. GaAs on GaInP (Fig. 1b), an increase of the growth rate is now observed at the beginning of the growth. It can be explained in the same way by considering now the incorporation of the surface segregated excess In atoms at the GaInP surface into the GaAs growing layer [6].

The In profile calculation from these data is straightforward assuming that the growth rate

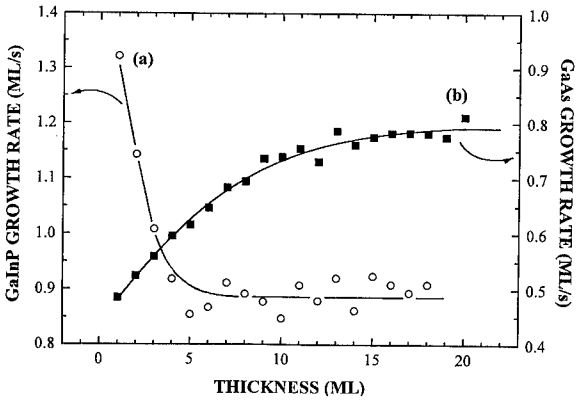

Fig. 1. Growth rate variations deduced from RHEED specular beam intensity oscillations of (a) $Ga_{0.51}In_{0.49}P$ on GaAs and (b) GaAs on $Ga_{0.51}In_{0.49}P$. The growth temperature is 550°C.

difference between one of the layers in the transient regime (nth layer) and the steady state growth rate is proportional to the difference of In surface population of the (n-1)th layer and layers at the steady state. The simple model of Muraki et al. [10] is then used to quantify the segregation process. This model needs the determination of two experimental data, x_0 and x_{ss}, which are respectively the In bulk and surface layer compositions when the steady state of GaInP growth is reached. The x_{ss} value is assumed to be given by the monolayer fraction of InP which is necessary to predeposit onto GaAs in order to eliminate the growth rate transient of GaInP [5, 11, 6]. It allows us to determine the exchange coefficient R in GaInP, which is the fraction of In atoms on the topmost layer segregating to the next layer. It can be obtained following the expression:

$$\Delta r_n/\Delta r_{n'\neq n} = \left(x_{ss} - x_0 \sum_{i=0}^{n-1} R^i\right) \Big/ \left(x_{ss} - x_0 \sum_{i=0}^{n'-1} R^i\right),$$

where Δr_n is the growth rate difference between the nth layer and layers at the steady state.

With the previous assumptions, R for GaAs is extracted from the growth rate variation (Δr_n) between the nth layer and pure GaAs: $R = (\Delta r_n/\Delta r_{n'})^{1/n-n'}$.

We have applied the same method for the In segregation in GaInAs/GaAs by considering the growth rate transient observed at both interfaces through the RHEED specular beam intensity oscillations.

3.2. Influence of the growth temperature

In this part, we first investigate the growth temperature (T_s) dependence of the In surface segregation in GaAs grown on $Ga_{0.51}In_{0.49}P$. For this study, the GaInP growth conditions were kept constant (550°C and 0.92 ML/s) and only the GaAs growth temperature was varied. The R values corresponding to the In surface segregation in GaAs grown on GaInP as a function of T_s were determined as discussed above and are shown in Fig. 2 (closed squares). Between 500°C and 560°C, these values are well fitted by an Arrhenius law, indicating that the segregation process has a temperature dependent behavior with an activation energy of ≈ 0.23 eV. In the low temperature range (below 500°C), R becomes more sensitive to the growth temperature. This behavior is similar to the one observed by Iimura et al. [2] for the GaInAs growth rate variation as a function of the temperature. It can be explained by an increasing coverage of the growth front by alkyl species when the growth temperature is decreased. The growth front is in fact encapsulated by the remaining alkyl radicals which may finally act as surfactant-like species and decrease the In surface segregation phenomenon [12, 13].

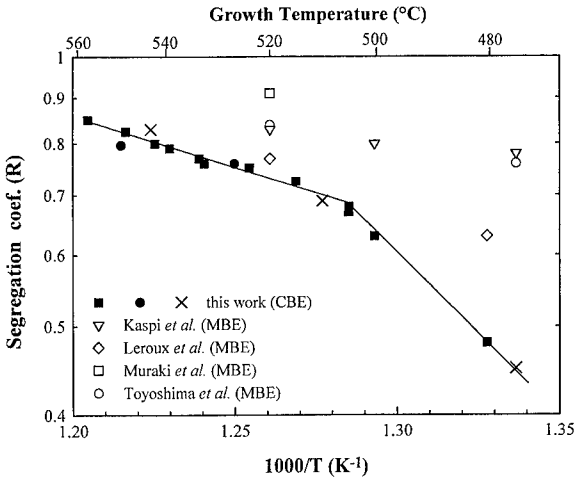

Fig. 2. In surface segregation coefficient in GaAs (R) as a function of growth temperature, deduced from the growth rate transient of GaAs grown by CBE on $Ga_{0.51}In_{0.49}P$ (closed squares) and on $Ga_{0.8}In_{0.2}As$ (closed circles). The crosses correspond to the R values obtained by fitting the optical transition energies of $Ga_{0.65}In_{0.35}As$/GaAs QW's grown at different temperatures (see Fig. 3). The open symbols are for GaInAs grown by MBE and are taken from Refs. [10, 14, 16, 17].

The R values have been determined as a function of the growth temperature for the growth of GaAs on $Ga_{0.8}In_{0.2}As$ and are also reported in Fig. 2 (closed circles). This figure clearly shows that, as expected, there is no difference in the segregation process of In when growing GaAs on top of GaInP or on top of GaInAs layers.

The knowledge of the temperature dependence of R can be very useful to predict the transition energy of QWs. In fact, the best way to demonstrate this, but also to validate our in situ method for

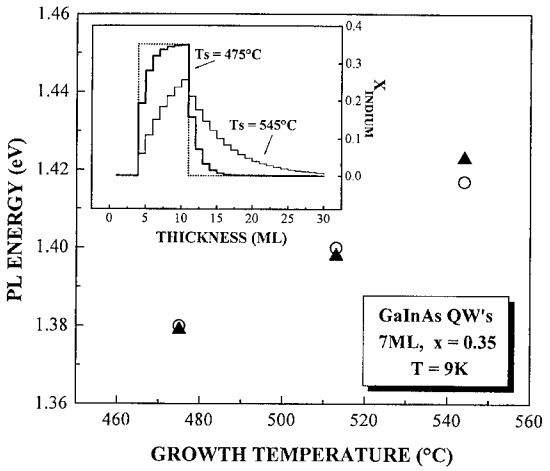

Fig. 3. Experimental PL transition energies of a 7 ML wide $Ga_{0.65}In_{0.35}As$/ GaAs QW grown by CBE as a function of growth temperature (closed triangles). Open circles correspond to transition energies calculated using R values from the data of Fig. 2 (straight lines). The inset is the In composition profile determined using R values (Fig. 2 data) at 545°C (full line) and at 475°C (darkest line). The dashed line corresponds to the ideal QW profile (without segregation).

determining R, is to use Fig. 2 data (straight lines) to calculate the optical transition energies of QWs in the well known GaInAs/GaAs system and to compare them with experimental results. With this aim, a sample containing three 7 MLs wide QW's of $Ga_{0.65}In_{0.35}As$ separated by 500 Å GaAs barriers was grown with decreasing the temperature, in such a way that the three QWs correspond to a growth temperature of 545°C, 510°C and 475°C, respectively. The R segregation coefficients, deduced from the fit of Fig. 2 data, are 0.81, 0.70 and 0.45, respectively. In Fig. 3, are reported the theoretical transition energies obtained using the potential profiles determined with these R coefficients (open symbols) and the experimental transition energies obtained at 9 K by PL (closed symbols) (the insert shows the In composition profiles deduced from the R values at 475°C and 545°C). A very good agreement is obtained between both sets of data. On the other hand, the QW PL energy can also be fitted by using R as an adjustable parameter [14, 15]. The corresponding R values are reported as crosses in Fig. 2. It can be seen that they agree well with the data obtained through RHEED real-time measurements, confirming once more the validity of this new in situ method for determining In segregation coefficient. We can then compare with confidence the R values determined in this study with the values reported in the literature for MBE growth of GaInAs/GaAs heterostructures (plotted in Fig. 2 with open symbols) [10, 14, 16, 17]. It should be emphasized that for similar growth parameters, the R values corresponding to CBE growth are always lower than that generally reported for MBE experiments, as previously noted by Leymarie et al. [15] from optical spectroscopy results. This can be tentatively attributed to the effect of a kinetic limitation specific to the CBE growth environment (due, for example, to the hydrogen or other radical adsorption at the growing surface).

Finally, in order to complete the comparison between GaInAs/GaAs and GaAs/GaInP heterostructures, we have grown four samples, each containing two GaAs/GaInP QWs of 25 and 6 ML, respectively, separated by 500-Å-thick $Ga_{0.51}In_{0.49}P$ barriers (the well thicknesses are determined by RHEED oscillations and therefore take into account the growth rate transient). For each sample, the 6 ML-thick QW is grown at various temperatures (respectively 480°C, 505°C, 525°C and 550°C), while the wide QW (25 ML), which is first grown, corresponds to a fixed temperature of

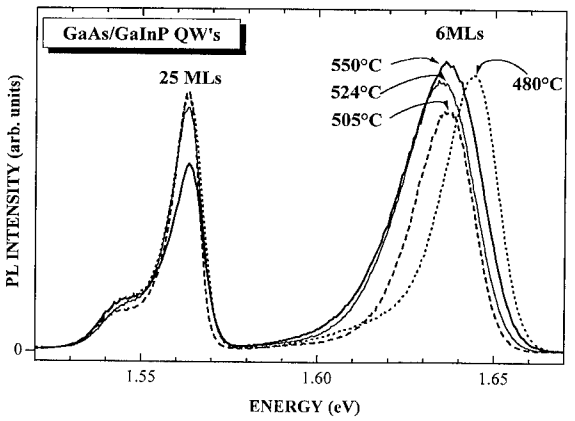

Fig. 4. Photoluminescence (9 K) of $Ga_{0.51}In_{0.49}P$/GaAs QW structures containing a wide QW (25 ML) grown at 550°C (reference QW) and a 6 ML QW grown at different temperatures.

550°C in order to check the reproducibility of the growth conditions from sample to sample. The growth temperature for the GaInP barriers is kept constant (550°C). Fig. 4 displays the PL spectra of these four samples. The first point to note is that the energy shift of the 6 ML GaAs QW as a function of the growth temperature is less important than the shift observed for GaInAs (7 ML)/GaAs QW's (Fig. 3). Actually, a significant red shift occurs when increasing the growth temperature from 480°C to 505°C and then saturates (note that the slope of the R variation with temperature decreases drastically above 505°, Fig. 2). This red shift can be, at least partly, explained by considering that In is incorporated in the GaAs QW. In fact, above a R (growth temperature) value of ≈ 0.7 (≈ 510°C), this red shift saturates as In escapes from the thin GaAs well at the GaInP on GaAs interface. Nevertheless, a quantitative description of this phenomenon is a complex problem due to additional effect of As–P intermixing at the interfaces which is poorly known but has a dramatic influence on the optical properties of the QWs. Further investigations are therefore necessary to correctly understand the energy shifts observed in GaAs/GaInP QW structures.

4. Conclusions

In conclusion, it is shown that In surface segregation in III–V compounds, such as GaInP and GaInAs, can be quantitatively evaluated in real-time during CBE growth. This is possible owing to the growth rate transients due to the variation of the In surface composition in the first stages of the growth, which can be measured through RHEED intensity oscillations. Following this, we have determined the temperature variation of the segregation coefficient of In in GaAs. The validity of our approach is demonstrated by correctly predicting the photoluminescence energies of GaInAs/GaAs QWs, grown at different temperatures, using In composition profiles deduced from the in situ determined segregation coefficient. The influence of In segregation on optical transition energies in the GaInP/GaAs system has also been evidenced, though the quantitative interpretation of the results is not as straightforward as in the GaInAs/GaAs system, presumably due to the group V element interfacial intermixing.

Acknowledgements

The authors would like to thank J.C. Garcia (THOMSON CSF/LCR) for useful discussions, J.C. Gillon and M. Ancilotti (RIBER-SA) for technical support and D. Le Cheviller for his invaluable help during the growth experiments. This work was supported in part by the Ministère de la Défense (DGA/DRET) under Contract No. 94486 and by EEC Contract No. CHRX CT 94.

References

[1] J.M. Moison, F. Houzay, F. Barthe, J.M. Gerard, B. Jusserand, J. Massies and F.S. Turco-Sandroff, J. Crystal Growth 111 (1991) 141 and references therein.
[2] Y. Iimura, K. Nagata, Y. Aoyagi and S. Namba, J. Crystal Growth 105 (1990) 230.
[3] H.S. Hansen, A. Bensaoula, S. Tougaard, J. Zborowski and A. Ignatiev, J. Crystal Growth 116 (1992) 271.
[4] J.P. Landesman, J.C. Garcia, J. Massies, G. Jezequel, P. Maurel, J.P. Hirtz and P. Alnot, J. Vac. Sci. Technol. B 10 (1992) 1761.
[5] J.M. Gérard, Appl. Phys. Lett. 61 (1992) 2096.
[6] M. Mesrine, J. Massies, C. Deparis, N. Grandjean and E. Vanelle, Appl. Phys. Lett. 68 (1996) 3579.
[7] B. Courboulès, J. Massies, C. Deparis, N. Grandjean, J. Leymarie, C. Monier, A.M. Vasson and A. Vasson, Appl. Phys. Lett. 64 (1994) 1523.
[8] A. Freundlich, A. Bensaoula, A.H. Bensaoula and V. Rossignol, J. Vac. Sci. Technol. B 11 (1993) 843.
[9] M. Tabuchi, N. Yamada, K. Fujibayashi, Y. Takeda and H. Kamei, J. Electron. Mater. 25 (1996) 671.
[10] K. Muraki, S. Fukatsu, Y. Shiraki and R. Ito, Appl. Phys. Lett. 61 (1992) 557.
[11] J. Nagle, J.P. Landesman, M. Larive, C. Mottet and P. Bois, J. Crystal Growth 127 (1993) 550.
[12] K. Sato, T. Kitani, T. Matsuyama, H. Ikeda, S. Zaima and Y. Yasuda, J. Crystal Growth 150 (1995) 944.
[13] K. Nakagawa, A. Nishida, Y. Kimura and T. Shimada, J. Crystal Growth 150 (1995) 939.
[14] M. Leroux, N. Grandjean, C. Deparis, J. Massies, C. Lopez, R. Mayoral and F. Meseguer, Jpn. J. Appl. Phys. 34 (1995) 3437.
[15] J. Leymarie, C. Monier, A. Vasson, A.M. Vasson, M. Leroux, B. Courboules, N. Grandjean, C. Deparis and J. Massies, Phys. Rev. B 51 (1995) 13274.
[16] R. Kaspi and K.R. Evans, Appl. Phys. Lett. 67 (1995) 819.
[17] H. Toyoshima, T. Niwa, J. Yamazaki and A. Okamoto, Appl. Phys. Lett. 63 (1993) 821.

ELSEVIER

Journal of Crystal Growth 175/176 (1997) 1247–1253

JOURNAL OF CRYSTAL GROWTH

Full gaseous source growth of separate confinement MQW 1.55 μm laser structures in a production MOMBE

M. Popp[a], H. Heinecke[a,*], H. Baumeister[b], E. Veuhoff[b]

[a] *Department of Semiconductor Physics, University of Ulm, Albert-Einstein-Allee 45, D-89069 Ulm, Germany*
[b] *Siemens AG, ZFE T KM 3, D-81730 Munich, Germany*

Abstract

The feasibility of metalorganic molecular beam epitaxy (MOMBE or CBE) as a production process is studied with respect to flexibility, uniformity, long term stability and device quality. Gaseous doping sources were used for growth of GaInAsP/InP device structures: For n and p type doping disilane and diethylzinc (DEZn), respectively, were injected. The importance of precracking for efficient dopant incorporation is described. For uniform growth across larger areas the dependence of layer composition on growth temperature is critical. Therefore this effect along with the effect of V/III ratio have been studied in detail, and the optimum growth conditions are discussed. It is demonstrated that composition uniformity and long term stability can be obtained leading to variations of emission wavelength and lattice mismatch below $\pm$ 1.5 nm and $\pm 1.5 \times 10^{-4}$, respectively. These material properties are found across an area of about 90% of a 2 in wafer revealing the high yield of this process. As a device test vehicle, strained layer MQW laser structures were grown, and data on broad area threshold current densities are compared with state of the art results from structures grown by metalorganic vapour phase epitaxy (MOVPE).

1. Introduction

It has been demonstrated that metalorganic molecular beam epitaxy has the potential to deliver state-of-the-art InP-based device structures for the fabrication of lasers, photodetectors, modulators and HBTs [1–4]. The flexibility of MOMBE is in addition enhanced by the unique material qualities obtained in the selective area epitaxy process (SAE) which enables a high quality of device integration like lasers and waveguides [5, 6]. First reports on the development of production type MOMBE setups are recently presented [7, 8]. However, the growth chemistry of the GaInAsP on InP is ruled by a complex dependence on growth temperature, V/III ratio and absolute injection fluxes [9–12]. In order to obtain an excellent lateral and vertical uniformity, an optimization process concerning the temperature sensitivity for all quaternaries having a gap wavelength between 1.05 and 1.65 μm is performed and an accurate temperature control with time and across the wafers is absolutely required [8].

* Corresponding author. Fax.: + 49 0731 502 6106; e-mail: heinecke@sunrise.e-technik.uni-ulm.de.

0022-0248/97/$17.00 Copyright © 1997 Elsevier Science B.V. All rights reserved
PII S0022-0248(96)00945-1

There are instabilities due to passivation of the solid dopant Be and Si in MOMBE. The implementation of cooled baffles can suppress this aging process of the dopant [13], but this hinders an uniform upscaling for large area growth or multi-wafer production. As a consequence and in order to move all sources for growth *and* doping out of the growth chamber several doping gases for donor and acceptor incorporation have been investigated [14–19].

In this communication we concentrate on the important issues for the upscaling of the MOMBE process. The quaternary growth in the wavelength range from 1.05 to 1.65 μm is investigated targeting for stable growth conditions with optimized parameter dependencies. The doping is achieved by using the identical doping gases DEZn and disilane as in MOVPE. This selection of dopants enables steep dopant profiles in InP-based heterostructures and is of major importance for the acceptance in the production. The stability and flux uniformity of this full gaseous MOMBE process is finally tested by the fabrication of strained MQW lasers with double separate confinement layers. This test bed for our production type MOMBE incorporates as well several quaternary layers as p- and n-type doped films.

2. Experimental procedure

The experiments were carried out in a 3×2 in multi-wafer production type MOMBE system. As precursors trimethylindium (TMI), triethylgallium (TEG), AsH_3, PH_3, diethylzinc and disilane were used. The system is equipped with two equivalent high temperature cells each with one AsH_3 and PH_3 line and a third high temperature cell for the disilane injection. In this investigation only one high temperature cell for the group V elements was used. The group III elements were injected via a low temperature central- and a low temperature off axis cell, each connected to a TEG and TMI line. For Zn-doping the system was equipped additionally with a low temperature dopant cell [19]. Details about system layout and gas injection were given in ref. [8, 19, 20].

InP : Fe and InP : S-doped (1 0 0)-substrates with 2° misorientation towards the (1 $\bar{1}$ 0) direction were used. A growth rate between 1.0 and 1.3 μm/h was selected depending on the material. The quaternary layers were mainly grown at a constant V/III ratio of 3.7, in selected cases the V/III ratio was increased to 6.8 for optimized surface smoothening. The layers were characterized by room temperature photoluminescence (PL) and high resolution X-ray-diffraction. The growth temperature was accurately ($\pm$ 1°C) controlled in the center of the 2 in wafer via a two channel optical infrared pyrometer in the range between 450°C and 530°C. The Si and Zn doped InP layers were characterized by Hall measurement and secondary ion mass spectrometry (SIMS).

Separate confinement MQW laser structures were grown at an optimized growth temperature of 510°C for the active region. The Zn doped cladding layers were grown at an optimized growth temperature of 450°C [19]. The Zn doping starts after a recess in the InP cladding layer of 120 nm undoped InP. The test structures were characterized by PL, X-ray diffraction transmission electron spectroscopy (TEM) and SIMS. The emission wavelength yields 1.55 μm. The layer sequence was processed as broad area laser ($50/100 \times 400\ \mu m^2$). For the ohmic contact a sequence of Au/Zn/Au was used on the p-side, the n-contact is made of Au/AuSn/Au.

3. Results and discussion

3.1. Growth of GaInAsP

To investigate the temperature dependence of the composition in the GaInAsP-alloys, *single quaternary GaInAsP layers* in the wavelength ranges of 1.05 (Q-1.05), 1.25 (Q-1.25), 1.55 (Q-1.55) and 1.65 μm (GaInAs) were grown in the temperature range of 460–530°C with a thickness of 0.3–1.3 μm. Generally we used an input V/III ratio of 3.7 at a constant growth rate. The TEG, TMI, AsH_3 and PH_3 fluxes were precisely kept constant for each wavelength range. The material composition in GaInAsP was calculated according the references [21, 22]. At lower temperatures (< 490°C) the

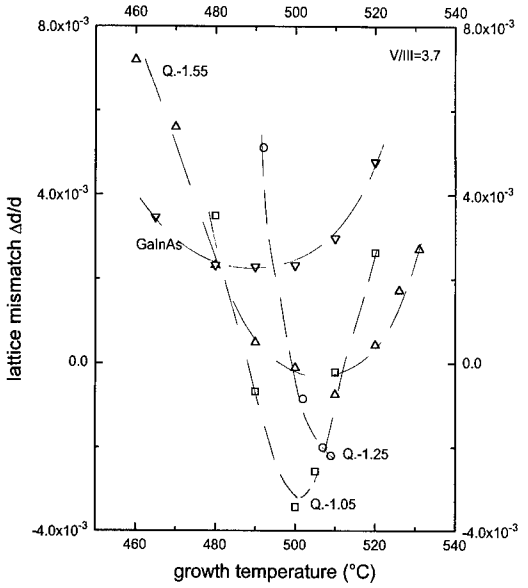

Fig. 1. Effect of the growth temperature on the lattice mismatch $\Delta d/d$ (V/III ratio = const.) for GaInAs(P): Q-1.05 μm, Q-1.25 μm, Q-1.55 μm, GaInAs.

thermal dissociation of the TEG molecules is the limiting factor whereas at higher temperatures (> 490°C) a Ga molecule loss is observed [11, 23, 24]. This leads to the typical u-curve in the plot of the measured lattice mismatch $\Delta d/d$ versus growth temperature (Fig. 1) in the wavelength range of 1.05–1.65 μm. The minimum of these u-curves is observed at 490°C for GaInAs, at 505°C for Q-1.55 layers, at 513°C for Q-1.25 layers and then 500°C for Q-1.05 layers. The Q-1.05 process has the strongest temperature dependence, whereas GaInAs reveals the weakest dependence in the temperature range of 460–530°C.

Around the most practical growth temperature of 510°C the optimum room temperature photoluminescence was achieved for all quaternary materials. At this growth temperature we observe a change in lattice mismatch $\Delta a/a$ – which is half of the measured value $\Delta d/d$ – of 95 ppm/°C for GaInAs, for Q-1.55 material this coefficient is reduced to 85 ppm/°C and for the Q-1.25 material this coefficient is negative (− 130 ppm/°C). The coefficient for Q-1.05 layers is positive again (150 ppm/°C). Consequently, this optimum temperature enables coefficients of $< |150$ ppm$|$/°C for all GaInAsP compositions. The maximum of Ga incorporation is observed at 490°C for GaInAs and at 500°C for the other quaternary materials, which is represented in the Ga/In ratio in Fig. 2a. Above a temperature of 490°C we observe an increasing P uptake in GaInAsP (see Fig. 2b). The shift of the minimum in lattice mismatch for the Q-1.25 material towards higher temperatures (see Fig. 1) is a consequence of the strong increase of the P incorporation as shown on Fig. 2b. The comparison of the data from Fig. 2 reveals that the increase in the P uptake at higher temperatures (Fig. 2b) always is accompanied by a decrease of the Ga uptake at higher temperatures. Changing the composition from GaInAs to InP at the constant temperature of 510°C a drastically decrease of the Ga and P incorporation efficiencies is observed. This can be evaluated from the data in Fig. 2 by plotting the Ga/In (P/As) ratio in the solid layer versus the Ga/In (P/As) ratio in the beam flux (not shown here). A similar correlation was found earlier for the GaInAsP growth on vicinal surfaces [10]. It was speculated that the Ga molecule loss is due to a mutual effect between the higher P content and the Ga molecules.

This is in line with the results from Refs. [10, 25], but in contrast to the data from Ref. [9], where a higher Ga incorporation was reported for quaternary materials near InP. This discrepancy is not clear at the moment, but the difference might be originating from the fact that in Ref. [9] the layers for each material were grown in a stack of quaternary layers grown at different growth temperatures. Our procedure using single layers allows for a detailed and independent determination of the absolute Ga and P incorporation in GaInAsP by PL and X-ray-diffraction.

3.2. *Uniformity and reproducibility*

For device structure production vertical as well as lateral uniformity over a 2 in wafer is required. Therefore single quaternary layers Q-1.55 were grown with a thickness of 1.3 μm. Uniformity of the layer in vertical direction was achieved using an automated optical pyrometer system [8] for the

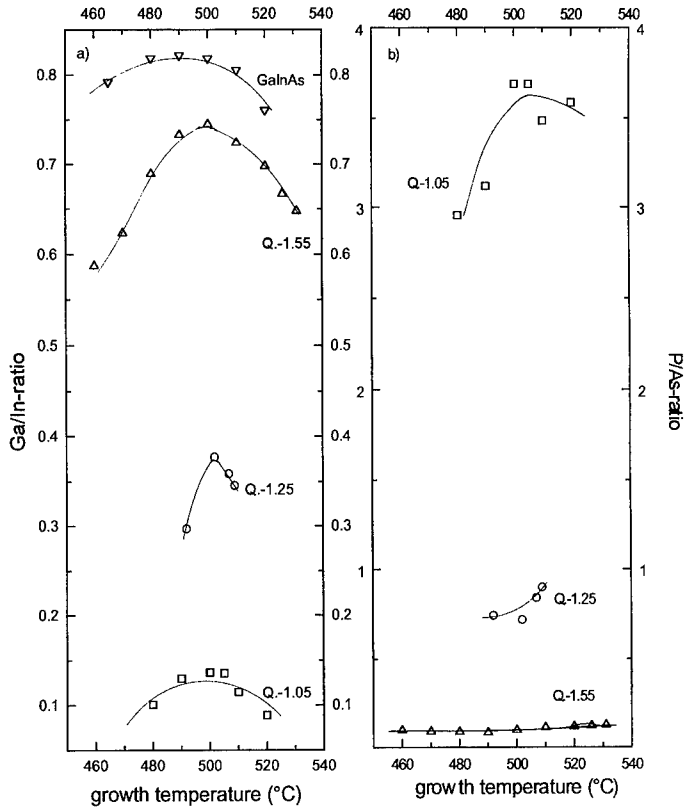

Fig. 2. Effect of the growth temperature on the Ga/In ratio and the P/As ratio.

growth temperature measurement. Fig. 3 gives the lateral dependence of the wavelength variation and the variation in lattice mismatch $\Delta a/a$ across a single 2 in wafer. The wavelength uniformity is better than $\pm$ 1.5 nm and in lattice mismatch a uniformity of $\pm$ 150 ppm is achieved. On the basis of the data in Figs. 1 and 2 it can be calculated that the growth temperature at the edge of the 2 in wafer is 3°C higher than in the center. Notice that more than 90% of the wafer area is suitable for device fabrication in this production type MOMBE system. The reproducibility measured for 10 samples during a period of $1\frac{1}{2}$ month was $\pm$ 1.5 nm in wavelength and $\pm$ 150 ppm in lattice mismatch for the Q-1.55 material. These stability data are comparable to those reported earlier by Heinecke et. al. [4] and within the scatter of the 2 in uniformity shown in Fig. 3.

3.3. Doping using disilane

As in MOVPE Si_2H_6 for the n doping of InP layers has been used. For the application in device structures a sufficient uniformity in the doping process is required. In order to avoid clogging a high conductance, high temperature cell was used. The injector is comparable to the hydride cracker yielding a good 5 in uniformity. The growth temperature was set to 510°C. The layer thickness was 1.3 μm (growth rate 1.3 μm/h, V/III = 4.5). Fig. 4 gives the dependence of the precracking temperature on the net electron concentration in InP using 5% disilane diluted in H_2 and pure disilane. The dopant gas flux was held constant. The Si incorporation in InP starts at 600°C precracking temperature. A maximum of the net electron concentration is observed for 5% disilane at 900°C

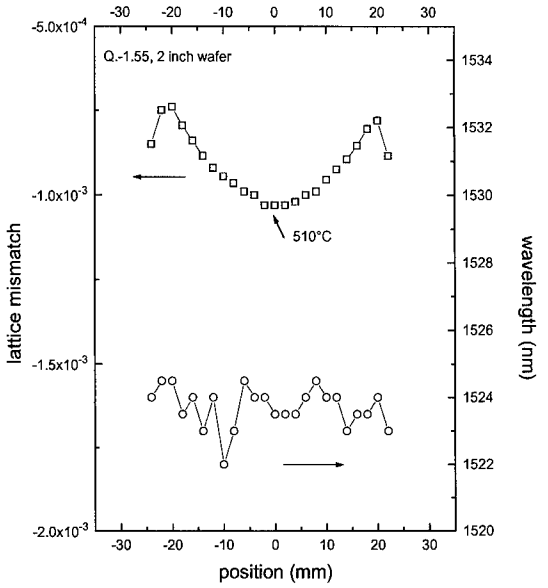

Fig. 3. Lattice mismatch $\Delta a/a$ and PL wavelength across a single 2 in wafer.

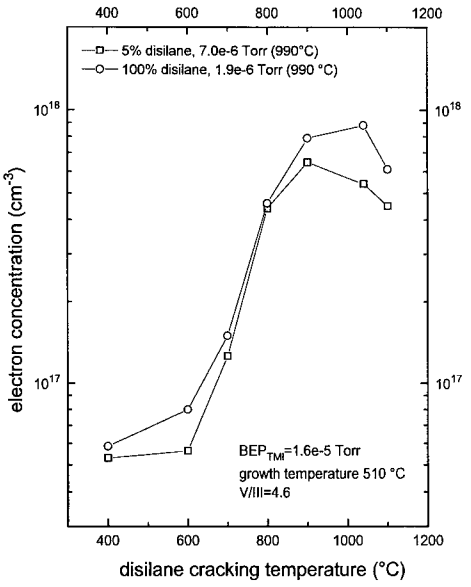

Fig. 4. Effect of the disilane cracking temperature on the electron concentration in Si doped InP.

precracking temperature and for undiluted disilane at 1000°C precracking temperature. Above 1000°C in the cracker the electron concentration in the layer is reduced. We assume, that at lower cracking temperatures (600–1000°C) the disilane is not completely precracked (SiH_2 formation supports the Si-incorporation in InP [26]). Above 1000°C the disilane decomposes and Si deposits in the HTD-injector, but the vapour pressure of Si at this temperature is too low to achieve significant dopant fluxes. The electrical activation calculated by the comparison of SIMS and Hall data is independent of the precracking temperature between 400 and 1100°C and reaches 85–90%. At a growth temperature of 450°C the electrical activation is reduced to 46%. Furthermore, as expected a linear dependence of the electron concentration on the Si_2H_6 flux is measured in the range of 10^{16}–$7x10^{17}/cm^3$.

3.4. Separate confinement MQW-laser structures

The basic layer sequence for the laser structures was 1000 nm Si-doped InP cladding layer/100 nm Si doped Q-1.15 confinement/30 nm Q-1.25/MQW with 5 wells/30 nm Q-1.25/100 nm Q-1.15/120 nm undoped InP spacer layer/1600 nm Zn-doped InP-cladding/200 nm Zn-doped GaInAs. In the MQW the lattice matched Q-1.25-material was used as barrier (thickness 10 nm) and unstrained GaInAs or 0.6%/0.8%/1.0% compressively strained quaternary layers as wells (thickness 6 nm). Fig. 5 presents the SIMS-measurement of a double separate confinement MQW laser structure. On the basis of the results achieved earlier [19] the spacer thickness of 120 nm at the p-side cladding layer is sufficient to avoid Zn diffusion into the quaternary MQW region, which is located 2 μm from the surface on the SIMS data and bounded by the slight decrease in the Ga and the P signals. The decrease of the Zn signal in the SCH layers is more rapid than 30nm/decade indicative of minimal Zn diffusion. Table 1 shows the results of the threshold current densities using GaInAs or 0.6%/0.8%/1.0% compressive strained quaternary wells. The lowest threshold current densities with $100 \times 400\ \mu m^2$ broad area test structures are observed with 1.0% strained wells. Under optimized growth conditions we achieve 640 A/cm^2 for the 400 μm long devices, which is comparable with lasers grown by CBE and MOVPE [1, 27].

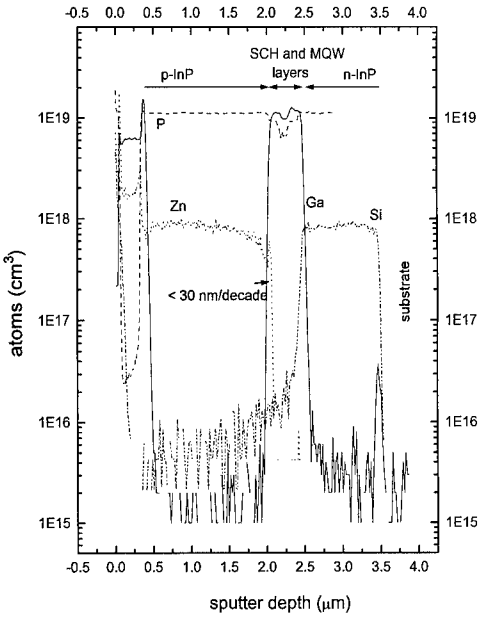

Fig. 5. SIMS profile of a double SCH MQW laser structure.

Table 1
Threshold current densities of the 1.55 μm broad area lasers (50/100 μm × 400 μm)

Quantum wells	j_{th} (A/cm^2)
(a) unstrained-GaInAs	1600
(b) 0.6% strained-GaInAsP	1040
(c) 0.8% strained-GaInAsP	1040
(d) 1.0% strained-GaInAsP	880
(e) 1.0% strained-GaInAsP optimized	640

Table 2
Uniformity of threshold current density across a 2 in. wafer (from (d) in Table 1)

Distance from center (mm)	j_{th} (A/cm^2)
0	880
10	800/780/680
18	760/880/800/640
24	670/670

The uniformity of the threshold current densities across a 2 in wafer varies in the range of 750 ± 110 A/cm^2 with the lowest threshold current densities at the outer diameters of the wafer (Table 2).

4. Conclusions

This study has shown that for growth of InP based device material even for n and p type doping the identical precursors can be used in MOMBE as in MOVPE. The gaseous dopant sources disilane and diethylzinc, which are qualified precursors in MOVPE production lines, were successfully applied in a MOMBE process. It has been demonstrated that for doping with disilane a high temperature cracking cell is required, whereas diethylzinc can be injected without precracking. With both precursors steep dopant profiles were achieved.

From a detailed study of the effect of growth temperature on quaternary layer composition the optimum temperature range for good layer uniformity has been elaborated. A temperature around 510°C should be chosen to maximize the useful wafer area (yield = 90%) for device applications with respect to composition uniformity and high optical quality.

The recipe of a constant growth temperature along with a fixed V/III-ratio reduces extensive optimization work for the growth of quaternary layers of any desired composition.

As a device test vehicle the strained layer MQW laser was chosen. Our MOMBE results from the full 2 in wafer process are comparable with state-of-the-art MOVPE data. This investigation clearly reveals that the MOMBE process has taken a further step on its way towards production maturity with the option of multi-wafer processing.

Acknowledgements

This work was partly supported by the German Ministry of Education and Research (BMBF) under contract 01BP467/7 and 01BP468/8 of the Photonics Program.

References

[1] W.T. Tsang, J. Crystal Growth 120 (1992) 1.
[2] W.T. Tsang, J. Crystal Growth 105 (1990) 1.
[3] W.T. Tsang, F.S. Choa, M.C. Wu, Y.K. Chen, A.M. Sergent and P.F. Sciortino, Jr., Appl. Phys. Lett. 58 (1991) 2610.
[4] H. Heinecke, B. Baur, N. Emeis and M. Schier, J. Crystal Growth 120 (1992) 140.
[5] H. Heinecke and E. Veuhoff, Mater. Sci. Eng. B 21 (1993) 120.
[6] M. Wachter, U. Schöffel, M. Schier and H. Heinecke, J. Crystal Growth 175/176 (1997) 1186.
[7] H. Ando, S. Yamaura and T. Fujii, J. Crystal Growth 164 (1995) 1.
[8] B. Marheineke, M. Popp and H. Heinecke, J. Crystal Growth 164 (1996) 16.
[9] T.H. Chiu, M.D. Williams, T.K. Woodward, J.E. Cunningham, J.E. Zucker, T. Sizer, F.G. Storz and J.F. Ferguson, J. Crystal Growth 124 (1992) 165.
[10] H. Heinecke, B. Baur, R. Höger, B. Jobst and A. Miklis, J. Crystal Growth 124 (1992) 170.
[11] J.L. Benchimol, G. Le Roux, H. Thibierge, C. Daguet, F. Alexandre and F. Brillouet, J. Crystal Growth 107 (1991) 978.
[12] H.P. Meier, R.F. Broom, P.W. Epperlein, S. Hausser, A. Jakubowicz and W. Walter, J. Crystal Growth 127 (1993) 165.
[13] K. Beer, B. Baur, H. Heinecke and R. Treichler, J. Crystal Growth 120 (1992) 312.
[14] H. Heinecke, K. Werner, M. Weyers, H. Lüth and P. Balk, J. Crystal Growth 81 (1987) 270.
[15] H. Ando, N. Okamoto, A. Sandhu and T. Fujii, Jpn. J. Appl. Phys. 30 (1991) L1696.
[16] K. Kimura, S. Horiguchi, K. Kamon, M. Shimazu, M. Mashita, M. Mihara and M. Ishii, J. Crystal Growth 81 (1986) 276.
[17] T. Sudersena Rao, C. Lacelle, S.J. Rolfe, M. Dion, J. Thompson, P. Marshall, P. Chow-Chong, D. Ross, M. Davies and A.P. Roth, Appl. Phys. Lett. 65 (8) (1994) 1015.
[18] W.T. Tsang, F.S. Choa, R.A. Logan, T. Tanbum-Ek and A.M. Sergent, Appl. Phys. Lett. 59 (9) (1991) 1008.
[19] E. Veuhoff, H. Baumeister, R. Treichler, M. Popp and H. Heinecke, J. Crystal Growth 164 (1996) 402.
[20] M. Wachter and H. Heinecke, J. Crystal Growth 164 (1996) 302.
[21] E. Kuphal, J. Crystal Growth 67 (1984) 441.
[22] H. Asai and K. Oe, J. Appl. Phys. 54 (1983) 2052.
[23] T. Martin, C.R. Whitehouse and P.A. Lane, J. Crystal Growth 107 (1991) 969.
[24] A. Robertson, Jr., T.H. Chiu, W.T. Tsang and J.E. Cunningham, J. Appl. Phys. 65 (1988) 877.
[25] H. Heinecke, J. Crystal Growth 127 (1993) 126.
[26] C. Blaauw, F.R. Shepherd, C.J. Miner and A.J. Springthorpe, J. Electron. Mater. 19 (1990) 1.
[27] B. Stegmüller, E. Veuhoff, J. Rieger and H. Hedrich, Electron. Lett. 29 (19) (1993) 1691.

ELSEVIER

Journal of Crystal Growth 175/176 (1997) 1254–1258

JOURNAL OF CRYSTAL GROWTH

GSMBE growth and characterization of $In_xGa_{1-x}As/InP$ strained-layer MQWs in a P-i-N Configuration

Wang Xiaoliang[a,*], Sun Dianzhao[a], Kong Meiying[a], Hou Xun[b], Zeng Yiping[a]

[a] *Institute of Semiconductors, Chinese Academy of Sciences, P.O. Box 912, Beijing 100083, People's Republic of China*
[b] *Xi'an Institute of Optics and Precision Mechanics, Chinese Academy of Sciences, P.O. Box 80, Xi'an 710068, People's Republic of China*

Abstract

$In_xGa_{1-x}As/InP$ ($0.39 \leqslant x \leqslant 0.68$) strained-layer quantum wells having 20 wells with thickness of 50 Å in a P-i-N configuration were grown by gas source molecular beam epitaxy (GSMBE). High-resolution X-ray diffraction rocking curves show the presence of up to seven orders of sharp and intense satellite reflection, indicative of the structural perfection of the samples. Low-temperature photoluminescence and low-temperature absorption spectra were used to determine the exciton transition energies as a function of strain. Good agreement is achieved between exciton transition energies obtained experimentally at low temperature with those calculated using the deformation potential theory.

PACS: 68.65. + g; 68.55.Bd; 78.66.Fd; 73.20.Dx

Keywords: Quantum wells; Molecular beam epitaxy; InGaAs/InP; Optical properties

1. Introduction

Strained layer quantum wells (QWs) are of considerable interest due to the added flexibility in controlling their optical and electrical transport properties. The biaxial in-plane strain caused by lattice constant mismatch has been used to optimize device performance such as reduced threshold current densities in strained quantum well lasers [1–3] and reduced switching times of high electron mobility devices [4]. The $In_xGa_{1-x}As/InP$ ($0 \leqslant x \leqslant 1$) quantum well structure, with relative lattice mismatch -3.8% for $x = 0$ to $+3.2\%$ for $x = 1$, is one of the most important material systems for device applications such as long wavelength lasers [1, 2], high electron mobility transistors [5] and electro-optic modulators and switching devices [6–9]. Although many investigations on this structure have been conducted [10–15], optical absorption characteristics [12–15] have not sufficiently been clarified, in particular, for strained QWs.

In this work, we report the growth of the strained layer InGaAs/InP multiple quantum wells (MQWs) with P-i-N configuration using a home-made GSMBE system and the use of optical techniques to

* Corresponding author. Fax: + 86 10 62562389; e-mail: xlwang@red.semi.ac.cn.

0022-0248/97/$17.00 Copyright © 1997 Elsevier Science B.V. All rights reserved
PII S0022-0248(97)00921-9

study on the excitonic transition energies in the InGaAs/InP MQWs as a function of strain.

2. Experimental procedure

The epitaxial growth was carried out in a home-made GSMBE system equipped with a low-pressure hydride gas-cracking cell for As_2 and P_2 molecular beams. These were supplied as 100% arsine and phosphine. Control of flow rates was achieved using mass flow controllers. The Group-III elements were produced from two indium and one gallium conventional effusion cells. The pressure in the growth chamber during growth was usually between 5×10^{-5} and 1×10^{-4} Torr. The growth rates of GaAs, InP and InGaAs were calibrated with in situ observations of the intensity oscillations of reflection high-energy electron diffraction (RHEED). The growth temperature was determined by a thermocouple located just behind the molybdenum sample holder and calibrated by an pyrometer.

To optimize the growth parameters such as growth temperature and V/III ratio, two series of InGaAs epilayers were grown, one with different growth temperatures, and the other with different AsH_3 flow rates. The growth rate for all samples was 1 ML/s. The double-crystal X-ray diffractions were used to determine the InGaAs lattice-mismatch relative to InP substrates, and the results show that the lattice mismatch for all samples was small than 1×10^{-3}. The low-temperature (10 K) photoluminescence spectra (PL) measurements were carried out for InGaAs/InP heterostructure samples. The results show that when the growth rate is 1 ML/s, the optimized growth conditions were such that the AsH_3 flow rate was 8–10 sccm and the growth temperature was about 500°C, i.e., when the growth rate is 1 ML/s, the arsine flow rate is between 8 and 10 sccm, and the growth temperature is about 500°C, the grown InGaAs epilayer has the most intense and narrowest PL peak. The obtained optimized growth parameters were used to grow InGaAs/InP strained MQWs in a P-i-N configuration.

The structures grown in our experiments are described in Fig. 1. The InGaAs/InP MQWs were grown on (0 0 1)-oriented InP substrates in a P-i-N configuration. The undoped MQWs in the i-region was prepared on a 0.2 μm-thick unintentionally doped InP layer under which a 0.2 μm n-InP buffer layer was first grown. It consists of 20 InGaAs quantum wells with thickness of 50 Å separated by 200 Å-thick InP barrier. On the MQWs a 0.2 μm thick undoped InP and then a 0.5 μm-thick p-InP were deposited. Five samples were grown and studied, one lattice matched with $x = 0.53$ (sample C), two under compression with $x = 0.63$ (sample D) and $x = 0.68$ (sample E), and the reminder under tension with $x = 0.39$ (sample A) and $x = 0.50$ (sample B). The indium concentration x was varied from $x = 0.39$ to 0.68.

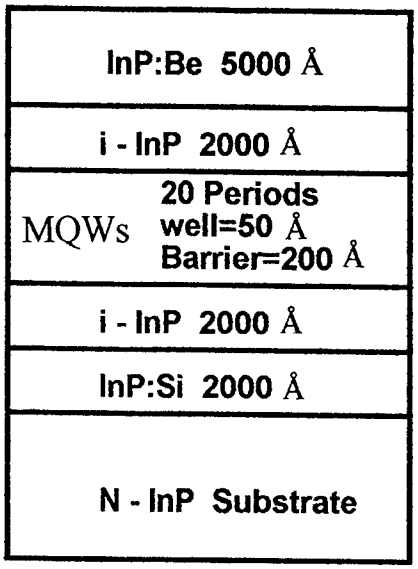

Fig. 1. Schematic diagram of the strained layer InGaAs/InP multiple quantum wells in a P-i-N configuration.

The gas switching procedure used for growing MQWs is shown on Fig. 2. Two indium conventional effusion cells were used, one (denoted by In(1)) for growing InP barriers, the other (denoted by In(2)) for InGaAs wells. To improve interface quality, the growth interruption was used at each interface. At the InP/InGaAs interface, the surface was first stabilized under cracked PH_3 (mainly P_2) during time T_1, then under cracked AsH_3 (mainly As_2) during time T_2. At the InGaAs/InP interface, the reverse procedure was employed using times

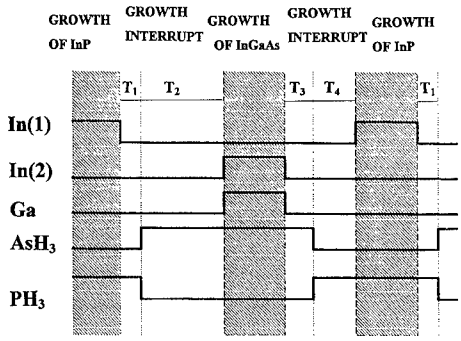

Fig. 2. Switching sequence carried out for the growth of strained InGaAs/InP MQWs.

T_3 and T_4. Considering that As_2 has a higher sticking coefficient than P_2, we choose growth interruption times of 5 s at the InP/InGaAs interface and 10 s at the InGaAs/InP interfaces.

3. Results and discussion

Fig. 3 presents the high-resolution Cukα_1 X-ray diffraction (HRXRD) scans of five samples with different quantum well compositions (therefore with different strains). The rocking curves show the presence of up to seven orders of satellite reflection, indicative of the structural perfection of the samples. The satellite reflections of the lattice-matched sample (sample C) show a highly symmetric intensity distribution on both sides of the (0 0 4) InP peak as expected from strain-free layers. In comparison, the asymmetric shape of the two upper traces (sample D and E) with their enhanced left-hand-side diffraction intensity, is indicative of in-plane compressive strain, resulting in lattice tension in the growth direction. The opposite sign of the strain (in-plane tensile strain) results in the enhanced right-hand-side diffraction intensity of the two lower traces (sample A and B). Despite the lattice mismatch, however, the strained samples retain their structural integrity, as judged by the sharpness and intensity of the satellite reflection.

To determine the $n = 1$ exciton recombination energies in the InGaAs MQWs, the 10 K photoluminescence measurements were performed. For each of the five samples, we observed a sharp and

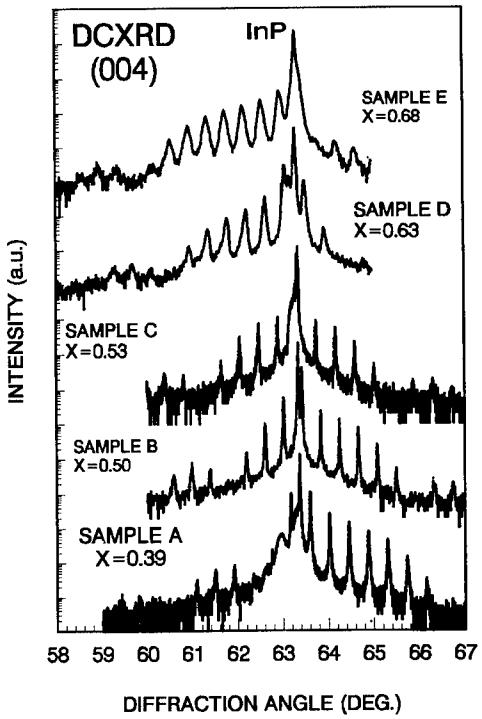

Fig. 3. The high-resolution X-ray diffraction rocking curves for five InGaAs/InP MQWs with different quantum well indium composition x.

intense PL peak, which is due to the excitonic recombination of electron and hole from the $n = 1$ subband level. The peak energies obtained are shown in Fig. 5 by triangle data points.

Fig. 4 represents the 10 K optical absorption spectra for the five samples A, B, C, D and E. The number indicates sublevels, and the letters H and L denote an electron to heavy-hole and electron to light-hole transition, respectively. From Fig. 4 we can see that the samples exhibit well-shaped excitonic transitions. The characteristic step-like structure, which reflects their two-dimension nature, are clearly shown with the exception of sample A. For sample B, C, D, and E, the spectra show two clear excitonic absorption peaks at the absorption edge, one corresponding to the $n = 1$ heavy-hole excitonic transition (1 1 H), the other corresponding to the $n = 1$ light-hole excitonic transition (1 1 L). For sample A, the spectrum show only one broader absorption peak, which is due to the $n = 1$ light-hole excitonic transition. The above assignment has

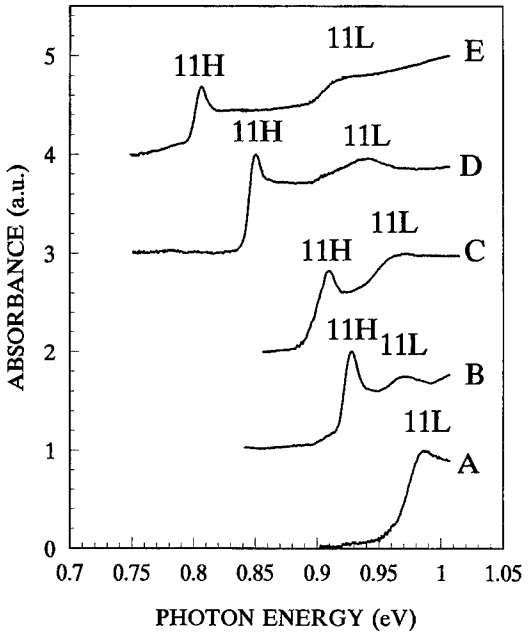

Fig. 4. Absorption spectra for five samples. The indium composition of sample A, B, C, D and E are, respectively, 0.39, 0.50, 0.53, 0.63 and 0.68.

been made on the basis of an energy shift calculation using the deformation potential model [15]. In the calculation, the heavy- and light-hole energy split at a Γ point due to the strain effect has been taken into account. The numerical parameters used in the calculation of the band structure are taken from Ref. [15]. The parameters of InGaAs are calculated using the well-known Vegard's law between GaAs and InAs. For all five samples, due to the InGaAs quantum wells are thin (50 Å), only the first level in the conduction band is allowed. Therefore, no other absorption peak can be seen as in the Fig. 4.

The curve shown in Fig. 5 is the calculated $n = 1$ excitonic transition energies as a function of InGaAs quantum well indium composition using the deformation potential model [15]. The data points on the same plot are the experimental results obtained by PL and absorption measurements for four strained and one lattice-matched InGaAs/InP MQWs in a P-i-N configuration. From Fig. 5, we can see that the experimental results agree well with those of calculation. As indium composition x increases, the transition energies corresponding to $1\,1\,H$ and $1\,1\,L$ decreases and the separation between $1\,1\,H$ and $1\,1\,L$ absorption peaks vary. When $x < 0.42$, the $1\,1\,H$ energy is larger than $1\,1\,L$ energy for a given indium composition x, indicating that the first light-hole sublevel is above the first heavy-hole sublevel due to biaxial in-plane tensile strain. When $x = 0.42$, the $1\,1\,H$ energy is equal to the $1\,1\,L$ energy, showing that the first light-hole sublevel and the first heavy-hole sublevel degenerate at this quantum well composition. When $x > 0.42$, the $1\,1\,L$ energy is larger than $1\,1\,H$ energy, indicating that the first light-hole sublevel is below the first heavy-hole sub level for a given x due to quantum size and strain effects.

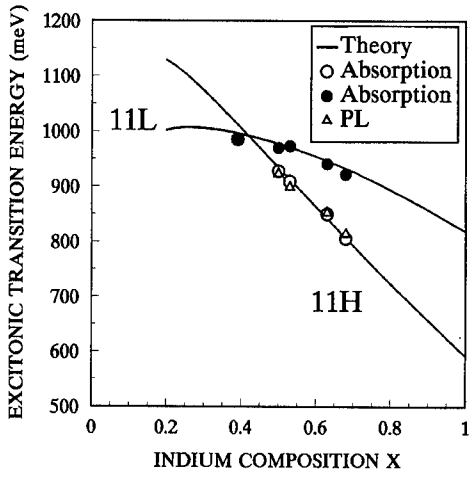

Fig. 5. Experimental and theoretical excitonic transition energies as a function of indium composition.

4. Summary

We have grown a series of $In_xGa_{1-x}As/InP$ strained quantum wells with x varying from $x = 0.39$ to 0.68 using a home-made GSMBE system. High-resolution X-ray diffraction patterns show the presence of up to seven orders of sharp and intense satellite reflection, indicative of the structural perfection of the samples. The low-temperature PL and absorption spectrum are used to determine the exciton transition energies as a function of strain. The agreement between transition

energies obtained experimentally at low temperature with calculated results using the deformation potential theory is good.

References

[1] Ming C. Wu, N.A. Ollson, D. Sivco and A.Y. Cho, Appl. Phys. Lett. 56 (1990) 221.
[2] H. Temkin, T. Tanbun-Ek and R.A. Logan, Appl. Phys. Lett. 56 (1990) 1210.
[3] P.J.A. Thijs, F. Luuk, P.I. Kuindersma, J.J.M. Binsma and T. van Dongen, IEEE J. Quantum Electron. QE-27 (1991) 1426.
[4] J. Chen, J.M. Fernandez and H.H. Wieder, Appl. Phys. Lett. 61 (1992) 1116.
[5] R.M. Kapre, A. Madhukar and S. Goha, Appl. Phys. Lett. 58 (1991) 2255.
[6] K.W. Goossen, E.A. Caridi, T.Y. Chang, J.B. Stark, D.A.B. Miller and R.A. Morgan, Appl. Phys. Lett. 56 (1990) 715.
[7] D. Gershoni, R.A. Hamm, M.B. Panish and D.A. Humphrey, Appl. Phys. Lett. 56 (1990) 1347.
[8] U. Koren, B.I. Miller, T.L. Koch, C. Eisenstein, R.S. Tucker, I. Bar-Joseph and R.S. Chemla, Appl. Phys. Lett. 51 (1987) 1132.
[9] N. Agrawal, D. Hoffmann, D. Franke and K.C. Li, Appl. Phys. Lett. 61 (1992) 249.
[10] R.E. Cavicchi, D.V. Lang, D. Gershoni, A.M. Sergent, J.M. Vandenberg, S.N.G. Chu and M.B. Panish, Appl. Phys. Lett. 54 (1989) 739.
[11] T.Y. Wang and G.B. Stringfellow, J. Appl. Phys. 67 (1990) 344.
[12] H. Temkin, M.B. Panish and S.N.G. Chu, Appl. Phys. Lett. 49 (1986) 859.
[13] M. Razeghi, J. Nagle, P. Maurel, F. Omnes and J.P. Pochoue, Appl. Phys. Lett. 49 (1986) 1110.
[14] Y. Kawaguchi and H. Asahi, Appl. Phys. Lett. 50 (1987) 1243.
[15] D. Gershoni, H. Temkin, M.B. Panish and R.A. Hamm, Phys. Rev. B 39 (1989) 5531.

ELSEVIER

Journal of Crystal Growth 175/176 (1997) 1259–1264

JOURNAL OF CRYSTAL GROWTH

Symmetric triangular-barrier optoelectronic switch (S-TOPS) by gas source MBE

H. Sakata*, Y. Nagao, Y. Matsushima

KDD, R&D Laboratories, 2-1-15 Ohara, Kamifukuoka-shi, Saitama 356, Japan

Abstract

We report a novel optical functional device, a symmetric triangular-barrier optoelectronic switch (S-TOPS), which consists of a symmetric n^+–i–δp^+–i–n^+ structure of $In_{0.53}Ga_{0.47}As$, grown by a gas source molecular beam epitaxy (GSMBE). We fabricated the S-TOPS by changing the sheet-carrier concentration of the δp^+ gate layer to introduce an avalanche multiplication for positive feedback in the operation. In the current vs. voltage characteristics of the S-TOPS under illumination of 1.55 μm wavelength light, we successfully confirmed a bipolar S-shaped negative differential resistance (NDR) characteristics on a certain range of sheet-carrier concentration of the δp^+ gate layer. Clear latch characteristics in the input-light power vs. current characteristics were also obtained in both the positive and negative biased conditions. We found that it is very important to optimize the sheet-carrier concentration to fabricate the S-TOPS.

PACS: 73.40.Kp; 85.60.Dw

Keywords: Optical functional device; Gas source MBE; Negative differential resistance; Avalanche multiplication

1. Indroduction

For optical signal processing, various kinds of functions are needed for optical devices such as logic, memory, and so on. For these purposes, an optoelectronic switch showing nonlinear optical response is quite promising, and several kinds of devices have been studied to date [1–6]. Especially the devices which use S-shaped negative differential resistance (NDR) are very attractive [1–4]. Among them devices such as the p–n–p–n structure [1, 2], p^+–n^+–i–δp^+–i–n^+ structure [3], and the heterojunction bipolar phototransistor (HPT) with n^+–p^+–i–n^+ structure [4] have been studied. These devices utilize the avalanche multiplication phenomena in the reverse-biased condition for switching.

We have already proposed a novel device, triangular-barrier optoelectronic switch (TOPS) [7].

* Corresponding author. Fax: + 81 492 78 7516; e-mail: sakata@lab.kdd.co.jp.

0022-0248/97/$17.00 Copyright © 1997 Elsevier Science B.V. All rights reserved
PII S0022-0248(96)01016-0

It consisted of an n^+–i–δp^+–i–n^+ doping profile in $In_{0.53}Ga_{0.47}As/In_{0.52}Al_{0.48}As$ heterostructure and showed clear S-shaped NDR. By utilizing this S-shaped NDR, we successfully obtained differential gain, bistable and latch characteristics by simply changing the bias voltages [8]. This device also showed good characteristics such as high-sensitivity, high-gain and high-contrast outputs. TOPS was grown by a gas-source molecular beam epitaxy (GSMBE), which is a promising technique for realizing sharp interfaces and good δ-doped layers [9]. We confirmed optoelectronic logic operations such as AND and OR operations by a single TOPS, and NOT, NAND, NOR, XOR operations by dual TOPS [10]. It is noted that these logic gates can be implemented by using only one or two devices, and that these operations can be realized without any optical or electrical reset signals. However, TOPS has only unipolar S-shaped NDR due to its asymmetric heterostructure. Flexibility of the circuit structure of TOPS is limited by its unipolarity when it is used in the arrayed structure. If TOPS has a bipolar S-shaped NDR, we can use the functions of TOPS at both polarities. Therefore, it is expected to extend the flexibility of the circuit structure of TOPS in the arrayed structure by using bipolar type.

In this paper, we propose a novel symmetric structure triangular-barrier optoelectronic switch (S-TOPS) for 1 μm wavelength-range operation by GSMBE, and demonstrate the optically controllable bipolar S-shaped NDRs. To our knowledge, this is the first demonstration of optically controllable bipolar S-shaped NDRs using n^+–i–δp^+–i–n^+ structure.

2. Growth and measurement

The devices were grown by GSMBE. Group III elements of In and Ga and respective p- and n-type dopants of Be and Si were used. As for the group V sources, 100% AsH_3 and PH_3 with cracking at 1000°C were used. The flow rates of AsH_3 and PH_3 were 4.0 and 10.0 sccm, respectively. The background pressures during the growth were 6×10^{-5} Torr for AsH_3 and 2×10^{-4} Torr for PH_3. PH_3 was used for InP buffer layer. The device was grown on an (1 0 0) semi-insulating InP substrate. The typical growth temperature and the growth rate were 420°C and 0.4 μm/h, respectively, for InGaAs. We obtained the proper sheet-carrier concentration of the δp^+ layer by precise control of Be cell temperature. The devices were formed into a mesa structure with 60 μm diameter. Contact with the top layer was achieved by evaporating Au / Sn to form an open-ring structure using the lift-off technique.

The input light was introduced at the top of the device with a lensed fiber, and the wavelength of the input light was 1.55 μm. *I–V* characteristics were measured under positive and negative bias of the substrate side, separately.

3. Results and discussion

To clear the difference between a unipolar NDR and a bipolar NDR characteristics, a brief summary of the TOPS is described first [7]. Fig. 1 shows a band diagram of the TOPS, in which the bias voltage is applied. It had n^+–i–δp^+–i–n^+ structure of $In_{0.53}Ga_{0.47}As/In_{0.52}Al_{0.48}As$ for 1.5 μm wavelength-range operation. The sheet-carrier concentration of δp^+-$In_{0.53}Ga_{0.47}As$ layer was 9.8×10^{11} cm^{-2}. The avalanche multiplication occurs in the drain region as the bias voltage is increased. As a result, electrons and holes are generated in the drain, and the holes move to the gate layer and accumulate in it. Resultant lowering

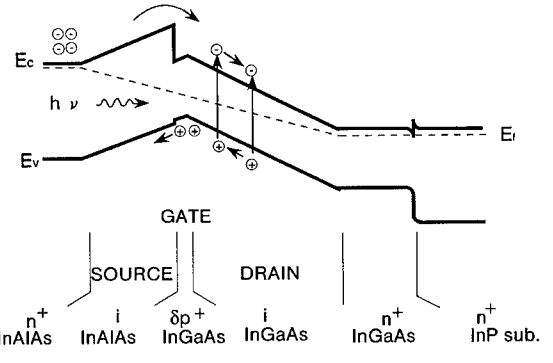

Fig. 1. Band diagram of the TOPS with a bias voltage.

of the gate-potential barriers increases the majority-carrier flow of electrons over the potential barrier from the source to the drain region with a thermionic emission. Multiplied holes lower the potential barrier further, so the majority-carrier flow increases. This positive feedback phenomenon gives rise to S-shaped NDR. It should be noted that the avalanche multiplication can be stopped by decreasing the input-light power, and the various functions can be realized by only changing bias voltages. Experimental I–V characteristics of the TOPS at different input-light powers observed at room temperature are shown in Fig. 2. Here, a significant S-shaped negative differential resistance (NDR) was observed in forward bias when the input-light power was less than 2 μW. However, in the reverse bias condition no NDR characteristics were observed, though a small change in I–V characteristics with low input-light power.

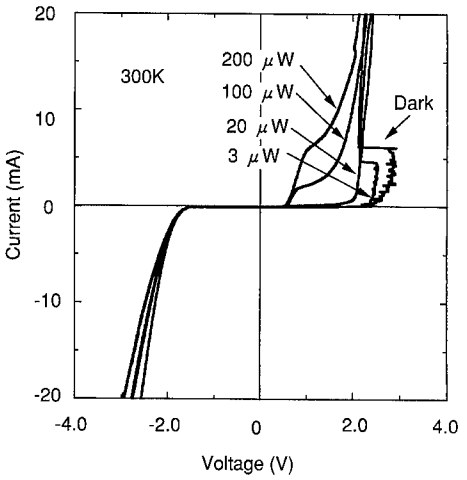

Fig. 2. I–V characteristics at different input-light powers of the TOPS.

To realize a bipolar NDR characteristics, we propose a novel device, S-TOPS. Fig. 3 shows the device structure of the S-TOPS. The device structure consisted of n^+-InP buffer layer (0.64 μm, 1.9×10^{18} cm^{-3}), n^+-$In_{0.53}Ga_{0.47}As$ (0.098 μm, 2.2×10^{18} cm^{-3}), i-$In_{0.53}Ga_{0.47}As$ (0.39 μm), δp^+-$In_{0.53}Ga_{0.47}As$ (98 Å, n_{sp+}), i-$In_{0.53}Ga_{0.47}As$ (0.39 μm) and n^+-$In_{0.53}Ga_{0.47}As$ (0.098 μm, 2.2×10^{18} cm^{-3}). Here, n_{sp+} is the sheet-carrier concentration of the δp^+ layer. The δp^+-InGaAs region was designated as the gate and both the i-InGaAs regions were designated as the source or drain region determined by the polarity of the bias voltage. An S-shaped NDR is expected to occur due to avalanche multiplication in both i-InGaAs drain regions. The parameters of the δp^+ layer were critical to attain the NDR operation, which was caused by the avalanche multiplication near the δp^+ layer. We fabricated the S-TOPS devices which have the same sheet-carrier concentration as

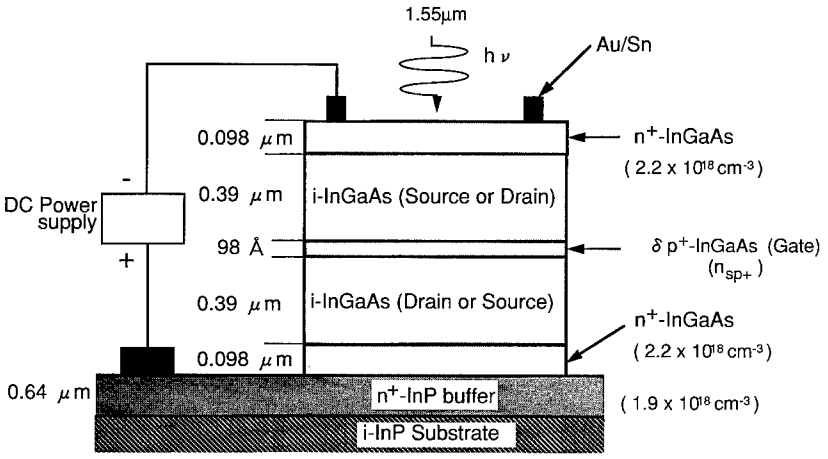

Fig. 3. Device structure of the S-TOPS.

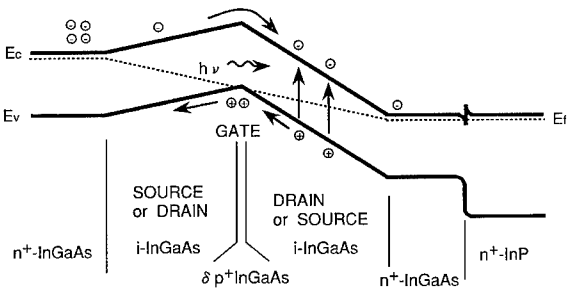

Fig. 4. Band diagram of the S-TOPS with a bias voltage.

that of the δp^+ gate layer. Fig. 4 shows a band diagram of the S-TOPS under biased condition. The major difference of the S-TOPS from a conventional TOPS is the symmetric structure.

Experimental I–V characteristics of S-TOPS at different input-light powers are shown in Fig. 5a–Fig. 5c, in which the sheet-carrier concentration n_{sp+} of δp^+ layer were varied as follows:

(a) $n_{sp+} = 3.8 \times 10^{11}\ \mathrm{cm}^{-2}$,
(b) $n_{sp+} = 1.4 \times 10^{12}\ \mathrm{cm}^{-2}$,
(c) $n_{sp+} = 1.1 \times 10^{13}\ \mathrm{cm}^{-2}$.

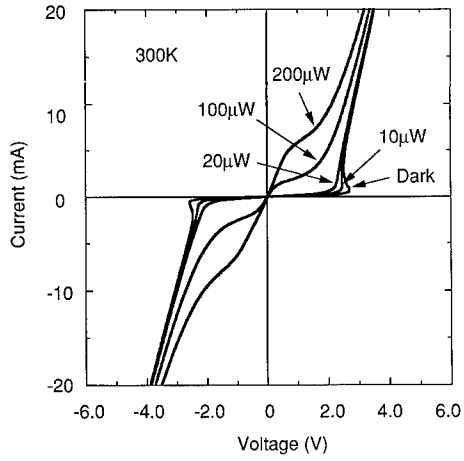

(a) n_{sp+}= 3.8 x 10^{13} cm^{-2}

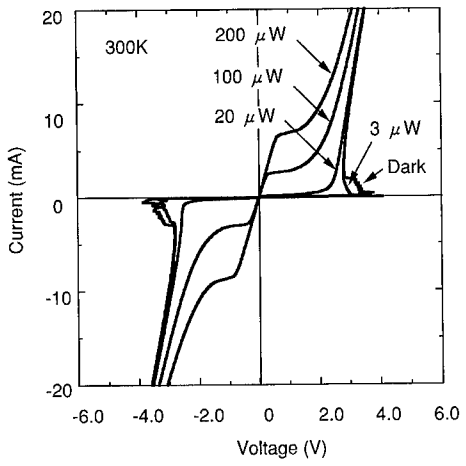

(b) n_{sp+}= 1.4 x 10^{13} cm^{-2}

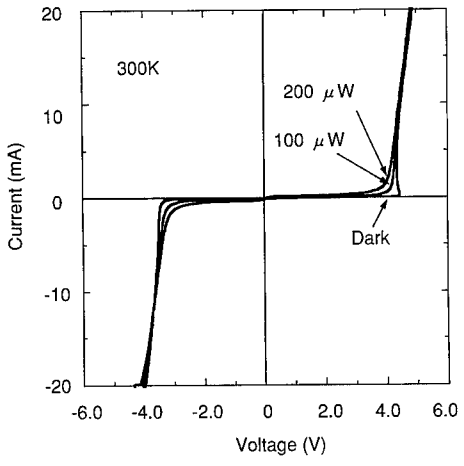

(c) n_{sp+}= 1.1 x 10^{14} cm^{-2}

Fig. 5. I–V characteristics of the S-TOPS at different input-light powers by changing the sheet carrier concentration n_{sp+}. (a) $n_{sp+} = 3.8 \times 10^{11}\ \mathrm{cm}^{-2}$. (b) $n_{sp+} = 1.4 \times 10^{12}\ \mathrm{cm}^{-2}$. (c) $n_{sp+} = 1.1 \times 10^{13}\ \mathrm{cm}^{-2}$.

In Fig. 5a, we obtained only gain characteristic because electrons in i-layer can easily flow over the potential barrier when the photo-generated hole accumulate in the gate layer and lower the potential barrier. The avalanche multiplication, however, does not occur in this case due to low-potential height made by the δp^+ doping. On the other hand, we obtained clear bipolar S-shaped NDRs and gain characteristic simultaneously in Fig. 5b. It is because of the positive feedback due to the avalanche multiplication and gain characteristic. In the case of further high doping such as in Fig. 5c, we could not obtain the gain characteristic any more. Photocurrent was only obtained on this condition that electrons could not flow over the potential barrier.

It is noted that there is a certain range of sheet-carrier concentration n_{sp+} of the δp^+ gate layer for positive feedback to occur. The reason is described as follows. The potential-barrier height depends on the thickness and the sheet-carrier concentration of the δp^+ layer, and the widths of the source and the drain. Since the parameters except the sheet-carrier concentration n_{sp+} of these samples were not changed, the barrier height depends only on the sheet-carrier concentration. When the sheet-carrier concentration n_{sp+} is large enough, the electric field in the drain becomes large enough for the avalanche multiplication. Here it is important that the majority-carriers, electrons, flow over the potential barrier when the bias voltage and/or the input-light power is increased. When the sheet-carrier concentration n_{sp+} is extremely large, electrons cannot easily flow over the potential barrier. If the electrons do not flow from the source at all, positive feedback does not occur in the drain. When the positive feedback does not occur in the drain, it is possible to have two types of operation. One is the phototransistor type which has a gain without NDR in Fig. 5a, the other is the photodiode type which has only photocurrent without a gain and NDR in Fig. 5c. Therefore, we must determine the potential-barrier height to satisfy both, electron flow and avalanche multiplication. For example, the parameters of $n_{sp+} = 1.4 \times 10^{12}$ cm^{-2}, in which bipolar S-shaped NDR was obtained as shown in Fig. 5b, corresponds to about 3.9 eV for the barrier height, and 1.0×10^5(V/cm) for the electric field. We can also observe a slight asymmetric NDR characteristics in Fig. 5b. It is likely that the quantity of the majority carriers, which are generated in the i-InGaAs source layer by the absorption of the input-light, is different by the polarity of the bias voltage because the input-light is incident on the surface of the devices.

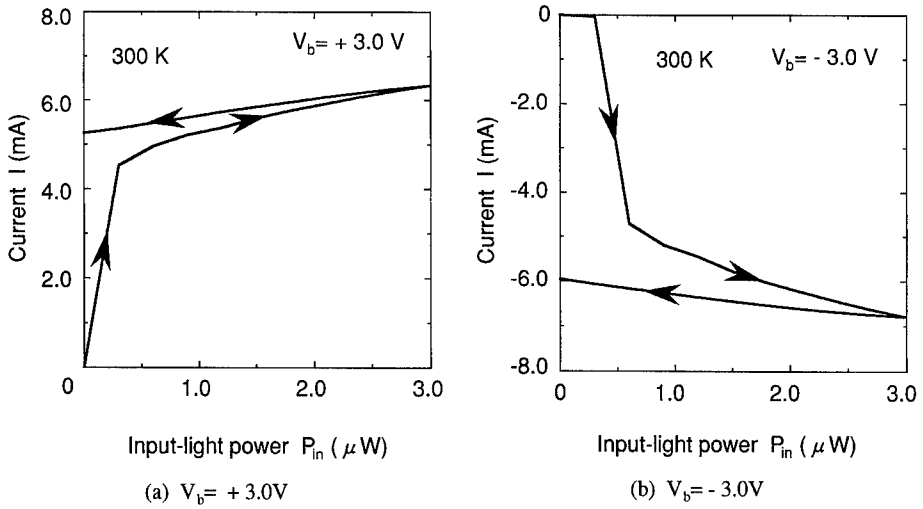

Fig. 6. Input-light power versus output-current characteristics of the S-TOPS by changing the bias voltages V_b. (a) $V_b = +3.0$ V. (b) $V_b = -3.0$ V.

Fig. 6a and Fig. 6b shows input-light power versus current characteristics by changing the bias voltages V_b in the device of Fig. 5b. We obtained latch characteristic with positive bias condition in Fig. 6a. We also obtained nearly the same latch characteristics with negative bias in Fig. 6b, therefore, we can use this device as a bipolar optoelectronic switch. We can also observe the difference in the input-light power threshold between the polarities of the bias voltage. This, as also the small difference in I–V characteristics mentioned above, is due to the difference in the number of the photogenerated carriers in the i-InGaAs source layers. From these results, we confirmed that it is important to optimize the sheet-carrier concentration of δ-doped layer for the S-TOPS operations.

4. Conclusions

We fabricated and examined a novel symmetric triangular-barrier optoelectronic switch (S-TOPS) by GSMBE, which consisted of a symmetric n^+–i–δp^+–i–n^+ structure. Bipolar S-shaped NDR and clear latch characteristics were obtained in both positive and negative biased condition. We also found that it was very important to optimize the sheet-carrier concentration of the δp^+ gate layer to realize the S-TOPS operation. These characteristics also show the high potential of GSMBE for fabricating well-controlled δ-doped structure. We can apply this S-TOPS device to optical functional devices such as optical logic devices and optical memories as well as two-dimensional optical signal processing.

Acknowledgements

The authors would like to thank Dr. H. Murakami for his encouragement and Mr. K. Osawa for technical assistance.

References

[1] G.W. Taylor, J.G. Simmons, A.Y. Cho and R.S. Mand, J. Appl. Phys. 59 (1986) 596.
[2] K. Kasahara, Y. Tashiro, N. Hamao, M. Sugimoto and T. Yanase, Appl. Phys. Lett. 52 (1988) 679.
[3] R.S. Mand, Y. Ashizawa and M. Nakamura, Electron. Lett. 22 (1986) 952.
[4] F.Y. Huang and H. Morkoç, Appl. Phys. Lett. 64 (1994) 405.
[5] C. Amano, S. Matsuo and T. Kurokawa, IEEE Photon. Technol. Lett. 3 (1991) 736.
[6] Y. Kawamura, H. Asai, S. Matsuo and C. Amano, IEEE J. Quantum Electron. QE-28 (1992) 308.
[7] H. Sakata, K. Utaka and Y. Matsushima, J. Crystal Growth 150 (1995) 1384.
[8] H. Sakata, K. Utaka and Y. Matsushima, Electron. Lett. 30 (1994) 1792.
[9] L. Goldstein, J. Crystal Growth 105 (1990) 93.
[10] H. Sakata, Y. Nagao and Y. Matsushima, Proc. Int. Conf. on Optical Computing '96, Optical Review 3 (1996) 433.

ELSEVIER

Journal of Crystal Growth 175/176 (1997) 1265–1269

JOURNAL OF CRYSTAL GROWTH

Chemical beam epitaxy growth of tensile-strained GaAsP/GaAlAs quantum well heterostructures for laser application

J.Ch. Garcia[a,*], A. Lebkiri[a], A. Fily[a], Ph. Collot[a], J. Massies[b], M. Leroux[b]

[a] *Laboratoire Central de Recherches, Thomson CSF, F-91404 Orsay, Cedex, France*
[b] *CRHEA/CNRS, Rue Bernard Grégory, F-06560 Valbonne, France*

Abstract

We report on the chemical beam epitaxy growth conditions of high-quality $Ga_{1-x}Al_xAs$ (x: 0.2–0.6) and tensile-strained $GaAs_{1-y}P_y$ quantum wells (y: 0.05–0.29) on GaAs(0 0 1) surfaces using trimethylamine alane and alternative precursors of group V elements (tertiarybutylarsine (TBAs) and tertiarybutylphosphine (TBP)). Cracking conditions of TBAs and TBP have been improved in order to reduce the carbon incorporation. Low levels of carbon and oxygen were detected by SIMS analysis of AlGaAs layers, independent of the aluminum concentration used ($[O] \approx 6\text{–}8 \times 10^{17}$ cm^{-3}, $[C] \approx 4\text{–}5 \times 10^{17}$ cm^{-3}). GaAsP quantum wells have been grown exhibiting high luminescence efficiency and full-width at half-maximum of 10 meV for 30 Å thick quantum well. The QW photoluminescence of E1-HH1, E1–LH1 energy transitions as a function of P mole fraction is well accounted for by envelope function calculations including strain effects. Preliminar results concerning laser diodes are discussed in the light of laser structure designs.

PACS: 78.66.Fd; 68.55.Bd

1. Introduction

AlGaAs-based high-power laser diodes (LDs) emitting in the 0.8 μm range have key applications in the field of optical information processing and solid state laser pumping. Up to now, these laser diodes have been fabricated using metal-organic chemical-vapor deposition (MOCVD) [1, 2] or molecular beam epitaxy (MBE) [3]. Although chemical beam epitaxy (CBE) is comparatively a recently developed technique, it is very promising for low-cost mass production devices with a reduced environmental impact compared to MOCVD. On the other hand, the use of gases as material sources adds versatility to the conventional solid sources MBE technology. Using this technique, it is, for example, easy to incorporate tensile strain in the active region of AlGaAs-based LD structures by inserting GaAsP pseudomorphic quantum well (QW) layers. This is an important point since

* Corresponding author.

0022-0248/97/$17.00 Copyright © 1997 Elsevier Science B.V. All rights reserved
PII S0022-0248(96)01017-2

tensile strain has been shown to improve LDs characteristics [4–6]. However, the growth of high-quality AlGaAs material by CBE has been hindered for years by the lack of a suitable metalorganic (MO) Al starting source. Owing to the recent progress in the development and synthesis of Al containing MO precursors, such as trimethylamine-alane (TMAAl) or dimethylethylamine-alane (DMEAAl), it is now possible to obtain high purity CBE AlGaAs material [7]. However, these advances have been mainly used to realize bipolar or two-dimensional electron gas transistors [8, 9] and there is only a few reported results on the optical properties of CBE grown AlGaAs-based QW structures (see Ref. [10] and references therein).

The aim of this paper is to report on the CBE growth conditions of high-quality LD structures combining $Al_xGa_{1-x}As$ ($x = 0.2$–0.6) and tensile strain $GaAs_{1-y}P_y$ QWs ($y = 0.05$–0.25) using TMAAl and low toxicity alternative precursors of group V elements (tertiarybutylarsine and tertiarybutylphosphine).

2. Experimental procedure

The experiments have been carried out in a all gaseous sources 3X2″ VG90 machine. The gas source configuration is the following: group III atoms are provided by organometallic sources (triethylgallium (TEGa) and trimethylamine-alane (TMAAl)); precracked tertiarybutylphosphine (TBP), tertiarybutylarsine (TBAs) and uncracked tridimethylaminoarsenic (tDMAAs) are the group V starting sources. Uncracked hydrogen sulfide (H_2S) and trimethylgallium (TMGa) were used for n- and p-type doping, respectively. All the gas sources are regulated using a two valves pressure control system which permits a very high level of reliability but also of flux reproducibility. As an example, over a period of 6 months, Al compositions variation did not exceed $\pm 1\%$ for fixed TEGa, TMAAl setpoint pressures and substrate temperature.

Thanks to the relatively high vapor pressure of TBAs and TBP, it has been possible to use a high-pressure type cracker cell design previously developed for arsine and phosphine. The optimum cracking temperature for TBAs is 760°C leading to a complete decomposition of TBAs into As_2, CH_4 and butene radicals. Increasing the cracking temperature results in an increase of carbon incorporation in GaAs up to $10^{18}\,cm^{-3}$ (to compare with $10^{16}\,cm^{-3}$ under optimal conditions). The cracking of phosphorus containing products is more difficult and less efficient. A complete cracking of the TBP molecule without production of PH_3, which represents the limiting step of the reaction, is obtained at a cracker temperature of 1000°C. However, this temperature results in high levels of carbon incorporation, in particular for ternary $Ga_{0.5}In_{0.5}P$ compounds, degrading the growth front and then the surface morphology. In fact, the optimum cracking temperature in terms of epilayer structural quality and carbon incorporation is found to be 950°C. Under these conditions, the cracking of the TBP molecule is uncomplete [11] but allows the growth of phosphorus-based compounds (InP, GaIn(As)P) at a growth rate of about 1 μm/h.

3. Assessment of high purity GaAlAs materials

To our knowledge, no informations have been reported, up to now, on the growth of GaAlAs by CBE using the TMAAl, TBAs source combination. Smooth surface morphology and low defect densities ($<10\,def/cm^2$) have been obtained in the 520–600°C growth temperature range even for aluminum concentration exceeding 55%. The use of tDMAAs as a starting source leads to rough GaAlAs surface mainly due to the relatively poor purity (solvant traces) of the source resulting in high oxygen incorporation ($>5\times10^{18}\,cm^{-3}$). Carbon and oxygen incorporation have been characterized as a function of growth temperature and V/III ratio. Growth temperature has been found to have little effect on both oxygen and carbon incorporation in the epilayers. The carbon concentration determined by SIMS versus the V/III ratio is shown in Fig. 1. The carbon concentration is reduced to $4\times10^{17}\,cm^{-3}$ with increasing the V/III ratio (i.e., TBAs flux) with no significant variation of the oxygen doping level lying at $6\times10^{17}\,cm^{-3}$. These values are not influenced by the aluminum concentration up to 55%. Residual doping level for

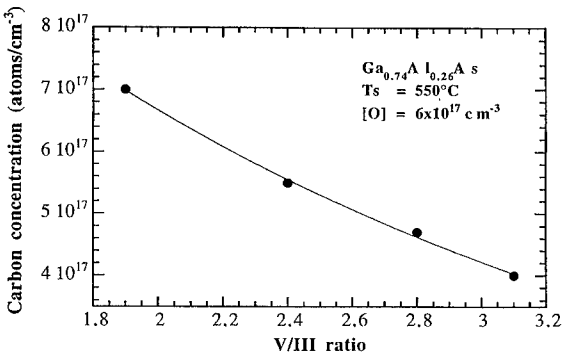

Fig. 1. SIMS carbon concentration in $Ga_{0.74}Al_{0.26}As$ as a function of V/III ratio.

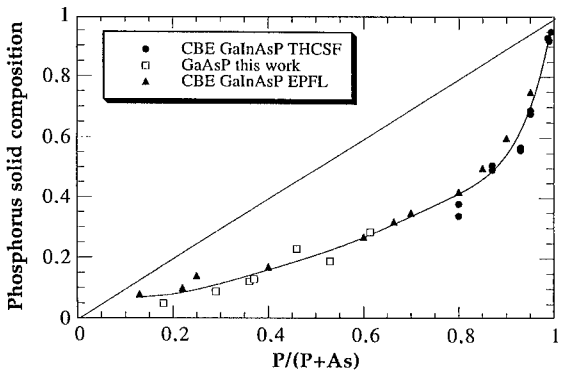

Fig. 2. P composition in GaAsP determined by RHEED intensity oscillations under group V limited growth versus the relative phosphorus composition of the gas phase. Note the good agreement between ex situ phosphorus composition measurements in quaternary alloys grown on InP [15] or GaAs [14] substrates with those obtained for GaAsP.

bulk $Ga_{0.65}Al_{0.35}As$ is p-type in the low 10^{16} cm^{-3} range.

4. GaAsP phosphorus composition control

GaAsP bulk layers can be grown in the full temperature range 500–600°C using TBAs and TBP group V starting sources. The P mole fraction has been tentatively determined by using group V induced RHEED intensity oscillations [12] as proposed by Hou et al. [13]. Indeed, these authors have shown that the phosphorus composition deduced under these conditions (excess of Ga) is the same as that obtained under a V/III ratio higher than 1. Consequently, they concluded that, even under a V/III ratio < 1, the incorporation of phosphorus is partially hindered by the presence of As. Fig. 2 shows the phosphorus concentration in $GaAs_{1-y}P_y$ deduced from the measurement of arsenic and (As + P) incorporation rate under V/III ratio less than 1 compared to phosphorus concentration in the solid determined from ex situ X-ray diffraction measurements. In the same plot, P solid concentrations in GaInAsP/GaAs [14] and GaInAsP/InP [15] versus the gas phase P/(As + P) ratio are reported. The same behavior for the incorporation of the group V elements is observed when comparing GaAsP and quaternary GaInAsP alloys lattice matched on InP and GaAs. It can then be suggested that group III elements play a minor role in the incorporation mechanisms of As and P. Besides that, it is clear that the P compositions determined from RHEED intensity oscillations under Ga excess conditions do not reveal the real solid P composition. Then, it can be concluded that the interaction between As and P must be negligible under these conditions and consequently, the phosphorus composition deduced from group V induced RHEED oscillations represents, in fact, the phosphorus to arsenic flux ratio P/(As + P) in the gas phase. These results give evidence of the important parameter which is the displacement of phosphorus by arsenic and vice versa under group V rich growth conditions. Nevertheless, it should be pointed out that, if both arsenic and phosphorus fluxes are significantly lower than the Ga one, the condition V/III >1 being filled by the sum of As and P fluxes, the in situ P determination would be valid [16]. However, in case where As or P individual flux is able to maintain a group V rich growth front, again, the in situ measurements diverge from ex situ composition values.

5. Optical properties of GaAsP QWs

Optical properties of separate confinement heterostructure GaAsP/GaAlAs QWs have been characterized by room temperature photolumine-

Table 1
Parameters for $GaAs_{(1-y)}P_y$ [18]

a(A°)	$5.6533 - 0.2021y$
m_c^*/m_0	$0.069 + 0.023y$
γ_1	$6.85 - 2.75y$
γ_2	$2.1 - 1.61y$
γ_3	$2.9 - 1.65y$
E_g(eV) at 300 K	$1.424 + 1.174y + 0.186y^2$
C_{11} (10^{11} dyn/cm^2)	$11.88 + 2.24y$
C_{12} (10^{11} dyn/cm^2)	$5.38 + 0.87y$
a (eV)	$-9.77 + 0.47y$
b (eV)	$-1.7 + 0.2y$
ΔE_v	$100\%\Delta E_g^{\text{unstrain}}$

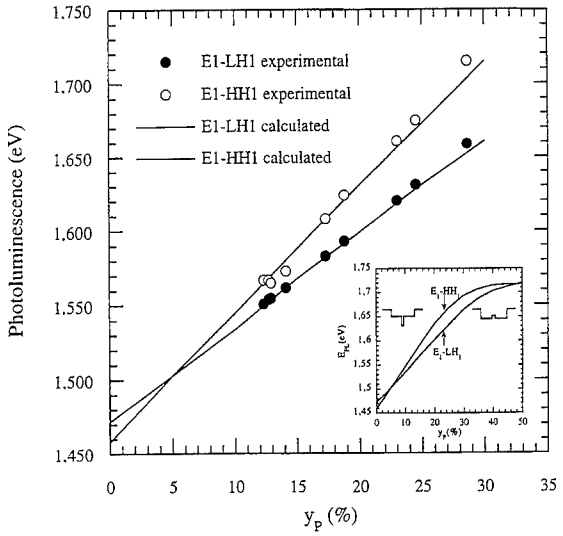

Fig. 3. Experimental photoluminescence energies as a function of phosphorus composition in 100 Å GaAsP QW. The plot shows also the calculated energies (solid lines) for aluminum composition in the barriers of 25%. The insert displays the theoritical trend for a wider range of P composition.

scence. The structure is composed of two cladding 1.2 μm thick $Ga_{0.56}Al_{0.44}As$ layers, an optical $Ga_{0.75}Al_{0.25}As$ cavity of 2000 Å with a single 100 Å GaAsP quantum well, the P composition being varied from 0 to 30%. Double X-ray measurements have been used to determine the phosphorus concentration with a precision of ±1%. For phosphorus concentrations higher than 10% two well-defined luminescence peaks have been observed corresponding to the heavy hole and light hole transitions. These measurements indicated a lowest HH1 transition energy for the low P compositions and a lowest LH1 transition energy for the high P compositions. The subband edges were calculated using a standard transfer matrix method [17]. The parameters [18] taken for the simulation are listed in Table 1. Due to the tensile strain in the GaAsP layer the HH1 and LH1 levels are splitted by the shear energy which increases with increasing the phosphorus concentration. For the lower P composition, the HH1 level is more confined than the LH1 level due to the difference in effective masses. For higher P composition the shear energy overcomes this effect so that we observe a higher transition energy for E1–HH1 transition than for E1–LH1 transition as soon as phosphorus composition is greater than 5%. Fig. 3 shows the variation of E1–HH1 and E1–LH1 energy transitions as a function of phosphorus composition for 100 Å thick quantum wells. A good agreement is obtained between experimental and calculated results. Note that we used a band offset between GaAsP and GaAlAs which affects 100% of the unstrained gap difference to the valence band discontinuity. The inset in Fig. 3 shows that above 30% of phosphorus, the difference (E1–LH1) – (E1–HH1) decreases and nearly vanishes above 44%. This reflects the shrinkage of the carriers confinement in the well and their progressive delocalisation in the whole cavity.

To complete this study, we report preliminar results concerning tensile-strained separate confinement heterostructure double quantum well (SCH-DQW) lasers. The P composition in the GaAsP quantum wells is 14% leading to an emission wavelength of 780 nm, the Al composition is 25% in the barriers and 44% in the cladding regions. Broad area lasers operate with a threshold current density of 1.6 kA/cm^2 and an external quantum efficiency 0.45 W/A for 0.7 mm long devices. The internal waveguide losses are of about 6 cm^{-1} which are typical for this kind of device. These results compare favourably with laser performances on single quantum well structures reported

by Agahi et al. [19] except for the threshold current density. These laser structures [19] were grown by MOVPE but with an Al content in the barrier of 34%. The lower threshold current density reported by Agahi et al. can be explained by an increase of Al content in the barrier which decreases both population of hole and conduction electron in the cavity and so the current losses due to radiative and non-radiative recombinations in the cavity. Note that the population inversion depends mainly on the properties of the QW layers, so the gain threshold condition is unchanged for both cases. In conclusion, the Al fraction in the cavity material has to be increased up to 30% while the GaAlAs confinement barrier has to be consequently increased to at least 55% in order to maintain a significant optical confinement.

6. Conclusion

In summary, we have demonstrated the possibility of using alternative group V organometallic precursors (TBAs, TBP) for the growth by CBE of GaAlAs/GaAsP quantum well structures. Carbon and oxygen concentrations in GaAlAs layers are in the mid-10^{17} cm^{-3} range whatever the aluminum composition used ($<55\%$). In situ measurements of P and As incorporation rates under Ga excess conditions did not appear suitable for the determination of group V alloy composition. Finally, GaAsP QW structures have been grown exhibiting high luminescence efficiency for P compositions ranging from 5 to 28%. The QW photoluminescence energy as a function of P mole fraction is found to be well accounted for by envelope function calculations including strain effects. At least for $y_P \leqslant 25\%$, a good agreement is obtained between experimental and calculated E1–HH1 and E1–LH1 energy transitions. These calculations have been used to optimize GaAlAs/GaAsP laser structure designs.

Acknowledgements

Acknowledgements are due to J. Nagle, C. Dua and Y. Cordier for fruitful discussions as well as to D. Leguen for growth technical assistance.

References

[1] J. Luft and E. Wudy, Thin Solid Films 175 (1989) 213.
[2] A. Shima, M. Miyashita, T. Miura, T. Kadowaki, N. Hayafuji, M. Aiga and W. Susaki, IEEE J. Quantum Electron. 30 (1994) 24.
[3] T. Hayakawa, K. Matsumoto, M. Morishima, M. Nagai, H. Horie, Y. Ishigame, A. Isoyama and Y. Niwata, Appl. Phys. Lett. 63 (1993) 1718.
[4] C.J. Van der Poel, H.P.M. Ambrosius, R.W.M. Linders, R.M.L. Peeters, G.A. Acket and M.P.C.M. Krijn, Appl. Phys. Lett. 63 (1993) 2312.
[5] F. Agahi, K.M. Lau, H.K. Choi, A. Baliga and N.G. Anderson, Photon Technol. Lett. 7 (1995) 140.
[6] D. Sun and D.W. Treat, IEEE Photon Technol. Lett. 8 (1996) 13.
[7] R.W. Freer, T. Martin, P.A. Lane, C.R. Whitehouse, T.J. Whitaker, M. Houlton, P.D.J. Calcott, D. Lee, A.C. Jones and S.A. Rushworth, J. Crystal Growth 150 (1995) 539.
[8] C.R. Abernathy, F. Ren, S.J. Pearton, T.R. Fullowan, R.K. Montgomery, P.W. Wisk, J.R. Lothian and P.R. Smith, J. Crystal Growth 120 (1992) 234.
[9] H. Rothfritz, R. Müller, G. Tränkle, R. Kempter, J. Plauth and G. Weimann, J. Crystal Growth 127 (1993) 179.
[10] B. Courboules, C. Deparis, J. Massies, M. Leroux and C. Grattepain, Appl. Phys. Lett. 65 (1994) 836.
[11] J.Ch. Garcia, C. Dua, M. Saeed and D. Pavlidis, Proc. Electronic Material Conference, Santa Barbara, USA (1996), J. Electon. Mater., to be published
[12] J.Ch. Garcia, C. Neri and J. Massies, J. Crystal Growth 98 (1989) 511.
[13] H.Q. Hou, B.W. Liang, T.P. Chin and C.W. Tu, Appl. Phys. Lett. 59 (1991) 292.
[14] J.Ch. Garcia and Y. Cordier, Int. Semiconductor Heteroepitaxy Conf., Montpellier, France, 4–7 July, 1995, Eds. B. Gil and R.L. Aulombard (World Scientific, Singapore, 1995) p. 618.
[15] J.F. Carlin, A. Rudra and M. Illegems, J. Crystal Growth 131 (1993) 387.
[16] H.Q. Hou and C.W. Tu, Appl. Phys. Lett. 60 (1992) 1872.
[17] S.L. Chuang, Phys. Rev. B 43 (1991) 9649.
[18] K.H. Hellwege, Ed., Numerical Data and Functional Relationship, in: Science and Technology, Landolt-Bornstein, New Series, Group III, Vol. 22A (Springer, Berlin, 1986).
[19] F. Agahi, K.M. Lau, H.K. Choi, A. Baliga and N.G. Anderson, IEEE Photon. Technol. Lett. 7 (1995) 1041.

ELSEVIER

Journal of Crystal Growth 175/176 (1997) 1270–1277

JOURNAL OF CRYSTAL GROWTH

Contamination in molecular beam epitaxy: the role of arsenic drag effect

Z.R. Wasilewski[a,*], S.J. Rolfe[a], R.A. Wilson[b]

[a] *Institute for Microstructural Sciences, National Research Council of Canada, Montreal Road, Ottawa, Ontario, Canada, K1A 0R6*
[b] *Laboratory for Physical Sciences, University of Maryland, College Park, Maryland 20740, USA*

Abstract

We have measured levels of Al, In and Si in nominally pure GaAs layers grown by molecular beam epitaxy as a function of arsenic flux for a number of different combinations of idling temperatures of Al, In and Si cells, using either As_2 or As_4 arsenic molecules. We find that a considerable number of atoms find their way to the growing layer in spite of closed shutters and no direct line of sight from their effusion cell to the wafer surface. The number of these atoms is proportional to the arsenic flux used and to the equilibrium vapor pressure over the considered element. We present arguments for the existence of the "arsenic drag" effect which deflects a fraction of the atoms that by-passed their effusion cell shutter towards the wafer.

PACS: 68.55.Bd; 34.50. – s

Keywords: MBE; Contamination; Molecular scattering

1. Introduction

Much progress has been made in the field of purification of elements used for molecular beam epitaxy (MBE) with the result that in many areas quality of sources available in the market is no longer the limiting factor. In spite of that, large gaps still exist between the quality of the best and "typical" layers grown in any given class. In order to bridge this gap, a better understanding of the remaining factors is needed in areas such as MBE system design, its preparation, and growth procedures. In the present work, we examine a contamination source which for the past four years has been controversial, namely unintentional doping with elements from idling effusion cells. Proposed mechanisms ranged from suboxide transport [1] to direct re-evaporation from coated shutters and inadequately cooled cell ports [2]. Although plausible under some circumstances, none of the proposed mechanisms explains the growing evidence

* Corresponding author. Fax: + 1 613 941 4557; e-mail: zbig.wasilewski@nrc.ca.

0022-0248/97/$17.00 Copyright © 1997 Elsevier Science B.V. All rights reserved
PII S0022-0248(96)01229-8

that such contamination is quite common, even in the absence of either of the conditions considered. In the present paper, we demonstrate that this contamination is linked to the direct interaction between molecular beams traversing the chamber, a process which has been regarded so far as negligible in the typical MBE environment.

2. Experimental procedure

The experiment was performed using a modified [3] V80H VG-Semicon MBE machine with effusion cells configuration as shown in Fig. 1a. The wafer temperature in the growth chamber is monitored using an infrared pyrometer calibrated against melting point of InSb. Molecules desorbing from the central 2 cm^2 of the wafer can be monitored with the narrow-acceptance angle, ion-counting Quadrupole Mass Spectrometer (QMS) located in the vicinity of the In cell port. The shutters in Fig. 1a are shown in the positions used for the "collecting planes" (to be defined later) and the "dark" ports indicate cells not used in the present experiment. Fig. 1b shows the 3D perspective view of the shutters within the cell ports. The system of tantalum panels shown, which isolates the effusion cells, is in good thermal contact with the bottom of the cryoshroud. This minimizes potential thermal cross-talk and cross-contamination between the cells. With shutters in closed position, no point on a 3″ substrate lies in a direct line of sight from the emitting surfaces of any effusion cells. The shutters, however, do not provide a tight seal of the cell compartment, leaving considerable gaps through which some of the flux can enter the growth chamber. Examples of such peripheral molecular beams are shown in Fig. 1c–Fig. 1e. Fig. 1c shows the approximate intersection of the As beam with the peripheral In beam. A high-capacity EPI valved cracker cell was used as a source for both As_2 and As_4. The composition of the flux leaving this cell was determined by the temperature of its Rhenium cracking zone, giving predominantly As_2 flux at 950°C, and predominantly As_4 flux at 400°C. To quantify the arsenic flux incident on the wafer surface, we have calibrated the background pressure readings of the ion gauge placed between the growth chamber and one of the two cryopumps. A reading during typical growth should be proportional to the arsenic flux used. For the calibration purpose, while growing GaAs at 2 Å/s and 600°C, the arsenic flux (As_2 or As_4) was decreased gradually until the transition to 4×2 Ga-stabilized surface reconstruction had been detected with RHEED. This transition occurs very abruptly and can be clearly detected even with wafer rotation. At this point [4] sticking coefficients are equal to 1 and 0.5 for As_2 and As_4, respectively. With GaAs grown at the rate of 2 Å/s, the gallium flux at the surface is 4.42×10^{14} atoms/cm^2 s. This offers reference points at molecular fluxes of 2.21×10^{14} molecules/cm^2 s for both As_2 and As_4. The background pressures we registered for such conditions were 5.5×10^{-8} and 2.0×10^{-7} mbar for As_2 and As_4, respectively. Using this calibration we converted the background pressure P_{bkd} to the As flux Φ incident on the wafer using the following formula:

$$\Phi = \begin{cases} 2.21 \times 10^{14} \left(\dfrac{P_{bkg}}{5.5 \times 10^{-8}} \right) \dfrac{\text{molecules}}{\text{cm}^2\,\text{s}} & \text{for } As_2, \\ 2.21 \times 10^{14} \left(\dfrac{P_{bkg}}{2.0 \times 10^{-7}} \right) \dfrac{\text{molecules}}{\text{cm}^2\,\text{s}} & \text{for } As_4. \end{cases} \quad (1)$$

Fig. 2 shows the functional diagram of the growth recipe designed to test Al, Si and In cells for their ability to deliver their respective elements to the wafer surface in spite of the closed shutters. The schematic of the layer grown is shown on the right-hand side of the figure (growth progresses in the bottom-top direction). The information to the left of the layer schematic shows, for different segments of the layer deposited, the type of molecules leaving the arsenic cell, its valve setting (3, 2, 1 squares[1] and closed), as well as the Al, Si and In nominal[2] fluxes. To overcome SIMS sensitivity problems and to minimize the sputtering time, the previously

[1] We use here the "square" unit for simplicity. For the actual valve controller the 3, 2, 1 squares and closed translate to 180, 120, 60 and 0 setting, respectively. The arsenic flux leaving the cell is approximately proportional to these settings.

[2] By "nominal" we mean here the flux which would be incident on the wafer surface if the cell shutter was open.

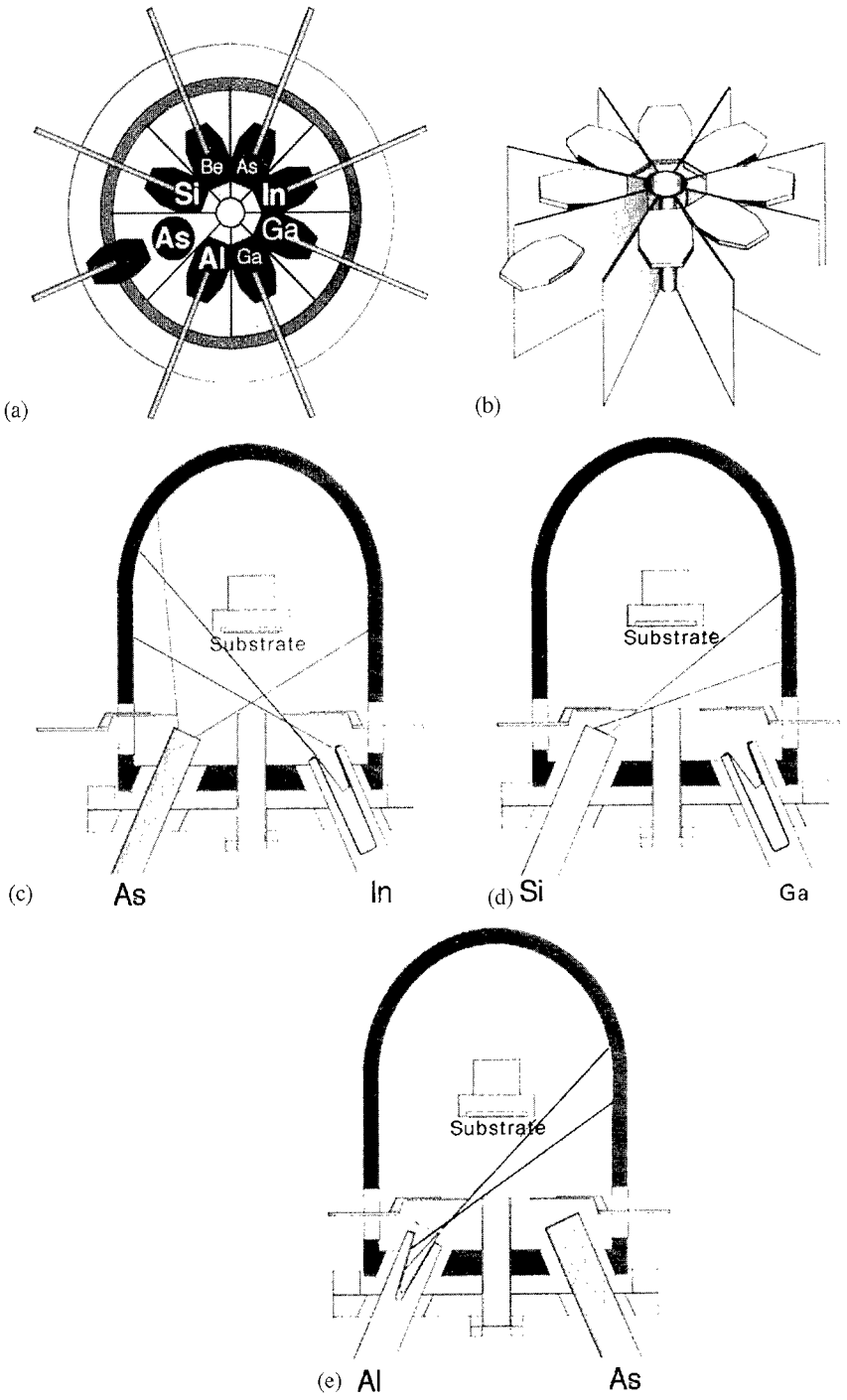

Fig. 1. Effusion cell configurations in the growth chamber: (a) Relative placement of the effusion cells with respect to each other. The shutters are drawn in the positions used for the "collecting planes" and the "dark" ports indicate cells not used in the present experiment. (b) 3D perspective view of the shutters within the cell ports. The system of tantalum panels shown isolates the effusion cells from each other. (c)–(e) Cross sections through the growth chamber showing the cell designs and their positioning with respect to the shutters as well as the peripheral beams which enter the chamber via the gaps between the shutters and the panels.

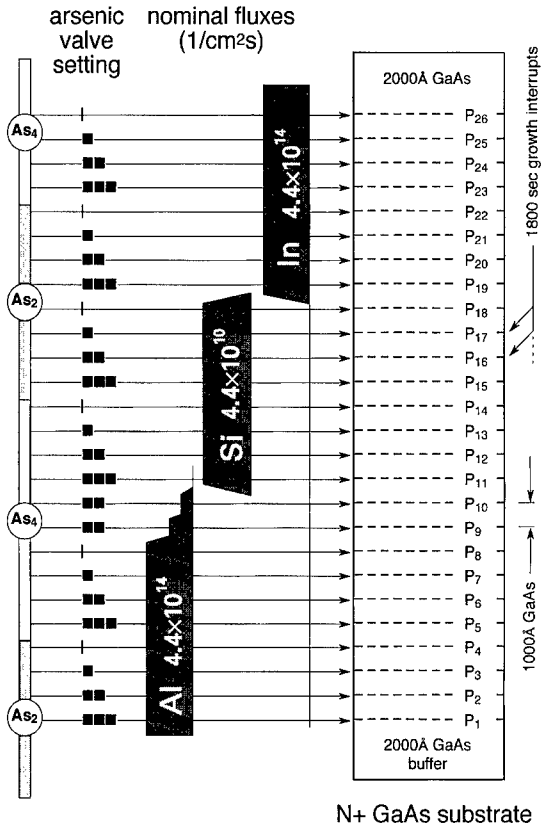

Fig. 2. Functional diagram of the growth recipe used. The schematic of the layer grown is shown on the right-hand side of the figure (growth progresses in the bottom-top direction). The information to the left of the layer schematic shows, for different segments of the layer deposited, the type of molecules leaving the arsenic cell, its valve setting (3, 2, 1 squares and closed). The height of the banners representing the Al, Si and In nominal fluxes is proportional to the vapor pressures over the respective elements.

mentioned collecting planes were introduced. At this stage GaAs growth was interrupted for 30 min (the planes are indicated with the dashed lines). The arsenic valve settings shown are the settings used during corresponding growth interrupts. For the 1000 Å GaAs spacing layers, an arsenic valve setting of 0.5 (in the "square" units) was used (not indicated in Fig. 2). The nominal fluxes for Al, Si and In were calculated from their respective cell temperatures using typical calibration procedures. Note that the Al flux was reduced in steps for the P_9 and P_{10} collecting planes (keeping the As_4 flux constant). This was done to measure the influence of the nominal Al flux value on the contamination of the layer with Al atoms. The vertical line that extends down from the In-related flux marker indicates that, even for this over 100 times lower setting (flux of 2.9×10^{12} 1/cm^2 s), considerable In contamination was subsequently measured with SIMS.

The growth was performed on N + (0 0 1)GaAs 2″ epi-ready substrates. The wafer was mounted in 3″ molybdenum holder using an In-free mounting technique. Prior to transferring into the growth chamber, the wafer was outgassed for 2 h in the preparation chamber at 600°C, as indicated by the outgassing stage thermocouple (the actual wafer temperature is 50–70°C lower). In order to remove possible remains of oxide, the wafer was further annealed for 30 min at 650°C in the growth chamber under arsenic flux. Subsequently, the substrate temperature was lowered to 600°C and a buffer layer of 500 Å GaAs was grown followed by smoothing superlattice of ten periods of 20 Å GaAs/20 Å AlAs and 2000 Å GaAs layer. During the growth of the 2000 Å GaAs layer the substrate temperature was lowered to 500°C in order to limit diffusion and/or segregation of the contaminants deposited on the collecting planes.

SIMS profiles of Al, In and Si were performed ex-situ with Cameca IMS 4f secondary ion mass spectrometer. Si was detected as the negative ion with 14.5 keV Cs^+ primary beam, while In and Al were both detected as positive ions with 2.75 keV O_2^+ primary beam. The primary beam was rastered over 350×350 μm area and a 63×63 μm was analyzed. The calibration of the absolute Si concentration was done with an implant standard. The In standard was obtained by profiling $In_{0.17}Ga_{0.83}As$/GaAs multiple quantum well (3 periods of 430 Å GaAs/70 Å InGaAs) where the total amount of In was derived independently from X-ray rocking curve measurement. To calibrate the Al contamination level, we have normalized the SIMS counts to the total amount of Al expected in the buffer AlAs/GaAs superlattice of the structure studied.

The top three panels in Fig. 3 show the results of SIMS profiles for Al, Si and In plotted using linear scale. Note that the profiles are plotted with the substrate on the left-hand side of the plot. The amounts of respective elements deposited on each collecting plane are proportional to the shaded

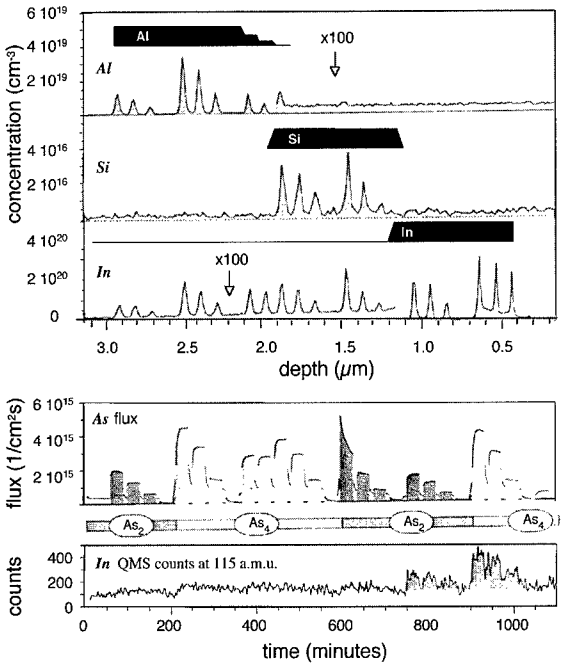

Fig. 3. From top to bottom: Results of SIMS profiles for Al, Si and In. Note that the profiles are plotted with the substrate on the left-hand side. Dark-shaded banners included in each panel indicate the nominal flux for the given element as used in Fig. 2, Arsenic fluxes incident on each collecting plane are shown below the three SIMS profiles. The 30 min growth interrupts are marked by the shading under corresponding stretches of the recordings. The bottom panel shows the QMS readings at 115 a.m.u. (In^+). Note that the last two panels are plotted versus time, while the first three are plotted versus the distance from the surface.

areas under the corresponding peaks. Dark-shaded banners included in each panel indicate the nominal flux for the given element (proportional to the banner height) as used in Fig. 2. Below the SIMS profiles are shown the arsenic fluxes incident on each collecting plane. The fluxes were calculated directly from the recordings of the background pressure in the growth chamber using Eq. (1). The arsenic fluxes are also plotted using linear scale, and the 30 min growth interrupts are marked by the shading under corresponding stretches of the recordings. The bottom panel in Fig. 3 shows the QMS readings at a.m.u. of 115, which corresponds to single ionized atomic In. Note that the last two panels are plotted versus time, while the first three are plotted versus the distance from the surface. In spite of this disparity, the periodic nature of the structure (1800 s interrupt/500 s of GaAs growth) allowed us to align the SIMS peaks with corresponding arsenic flux traces. The strong correlations between the *amount of contamination* on each collecting plane with the product of the *arsenic flux* and the respective *element nominal flux*, can be seen in the figure without any numerical analysis. As mentioned earlier, traces of In are found on all collection planes, even those where In was idling at over 200°C lower than the nominal setting of 932°C used to test its contaminating potential. On the other hand, the QMS counts of the atomic In, showing clear correlation with the arsenic flux, are seen only for the high nominal In flux. In this case, however, we are detecting only In atoms which by-passed the cell shutter and were back-scattered into the narrow acceptance angle of QMS before reaching the LN_2-cooled shroud (see Fig. 1c).

3. Analysis and discussion

Fig. 4 shows the results of analysis of the experimental data discussed above. To facilitate comparison between the three elements studied, the data are plotted on a log–log scale. On the X-axes we plot the average As flux impinging the wafer surface during the given growth interrupt. The closed symbols represent the data obtained with As_2, while the open symbols correspond to the data obtained with As_4. The Y coordinates were obtained in the following way. First the surface density of the element on the collecting plane was calculated by integrating the area under the SIMS profile of the corresponding region. This quantity was then converted into the effective contamination flux by dividing the calculated density over the 1800 s it took to accumulate it. The *flux leakage rate* plotted is the ratio of this contamination flux to the nominal flux of the element (flux which would be arriving at the surface if the shutter was opened). In much simplified but practical terms this ratio may be looked upon as the shutter-effective transparency. The lines plotted through the points (note the log–log scale) are of the form $Y = \alpha X$, where the coefficient α was fitted using the least-squares algorithm applied to the

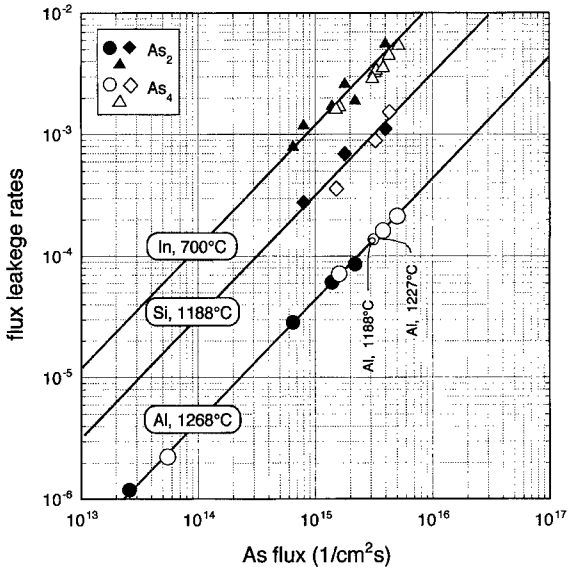

Fig. 4. Results of analysis of the experimental data from the Fig. 3 with appropriate labeling. The *flux leakage rate* plotted is the ratio of contamination flux to the nominal flux of the element. The lines plotted through the points (note the log–log scale) are of the form $Y = \alpha X$.

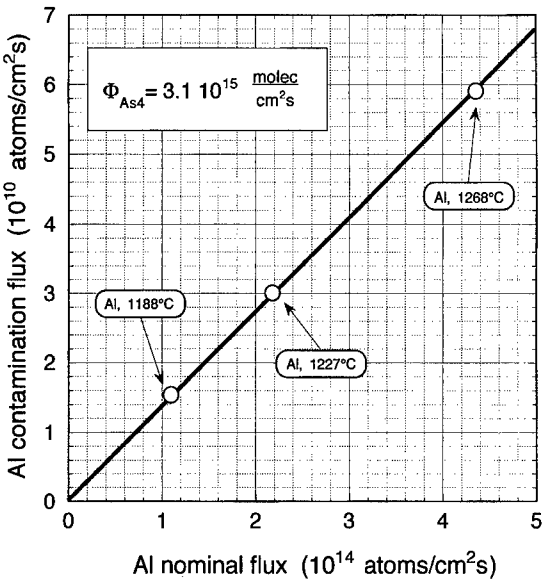

Fig. 5. The Al contamination flux for three different nominal Al fluxes using the same As_4 flux of 3.1×10^{15} molecules/cm^2 s.

experimental data separately for every element, but combining As_2 and As_4 points. It is clear that such a simple relationship describes experimental results[3] very well, proving that for all the cells investigated, the leakage rates are proportional to the arsenic flux used. The most complete set of data is available for Al, which follows such proportional behavior for over two orders of magnitude change in the incident As flux. Fig. 5 shows the Al contamination flux for three different settings of the Al cell temperature using the same As_4 flux of 3.1×10^{15} molecules/cm^2 s. It is clear that the Al contamination is proportional to the Al nominal flux, indicating that no intermediate steps in the Al transport are present (such as re-evaporation from the shutter edges). Qualitatively, we see the same behavior for In and Si.

The experimental results discussed above provide a solid evidence that the *direct* interaction between the peripheral molecular beams from Al, In and Si cells with the arsenic molecules traversing the growth chamber is responsible for deflecting trajectories of these atoms towards the substrate and towards the source flange. Since the correlation was established by monitoring the As flux using the background pressure, the actual proportion of scattering events caused by the direct arsenic beam and those caused by the background arsenic molecules remains speculative. The direct arsenic molecular beam likely plays the dominant role in deflecting other atoms towards the substrate, because within its range (i) the beam-equivalent pressure is

[3] The only points used in this plot for the case of In are those obtained with lower In flux because the In "leakage" was so big that at the higher In temperature more than 4 monolayers of InAs were deposited on the collecting planes during each growth interrupt. Deposition of more than 2 monolayers of InAs on GaAs changes the layer-by-layer growth mode to Stranski–Krastanov growth mode with additional InAs forming dots. We see evidence of the formation of such dots particularly clearly on the logarithmic scale of the SIMS profile for In (not shown). This effect, along with In-segregation, makes SIMS data from this region unsuitable for the kind of comparison which is shown in Fig. 4. Qualitatively, however, the behavior is similar to that observed for the lower In temperature.

considerably higher than that of the background arsenic and (ii) the beam is very directional, thus providing efficient momentum transfer in the direction of the substrate. This resembles the mechanism of a UHV diffusion pump [5], where heated vapor is injected into high-vacuum region through a system of narrow nozzles. Rapid expansion gives rise to the supersonic jets, that provide enough downward molecular "drag" to sustain a very large differential pressure between the high- and low-vacuum regions within the pump. This resemblance is particularly striking for the case of the cracker design used in our system, where the arsenic molecules are rapidly decompressed from relatively high-pressure bulk evaporator region (pressure approaching 1 mbar) into the UHV chamber through a very narrow (a couple of millimeters in diameter) nozzle. On the other hand, for the case of the atoms deflected towards the source flange (as demonstrated by correlations of the QMS reading at 115 a.m.u. with the arsenic background pressure), significant role is likely played by other arsenic molecules bouncing around the chamber, particularly the excess arsenic re-evaporated from the substrate. The process of redirecting the atoms back to the source flange has been used in the past to study flux transients of group III atoms with QMS [6]; however, the mechanism responsible was not identified at that time. The same phenomenon explains also many of the elusive memory effects and cross-contamination problems in MBE systems. Indeed, with the aid of arsenic scattering, material from one cell can contaminate another cell. The level of such contamination can build up over time and will be particularly aggravated if high arsenic fluxes are used and many shutters are opened at the same time.

Another issue which cannot be conclusively resolved at present is the relative contributions of the nonreactive (elastic and inelastic) scattering events to the reactive processes, where as a result of collision a new molecule is formed (say $As_2 + In \rightarrow As_2In$). The dominant role of the *nonreactive* scattering in the observed wafer contamination finds indirect support in the very similar values for the scattering efficiencies measured for As_2 and As_4 molecular beams (see Fig. 4). Indeed, the arsenic dimer and tetramer show very different behavior in coating MBE chamber parts, as well as interact in a different way with the growing layer surface [7, 8]. Thus, it is reasonable to expect that they should also show much different reactiveness when it comes to bonding single group IV or group III atom in the process of collision. A simple estimate shows that in our experiments the average momentum of As_2 molecule is very close to that of As_4 (As_2 is half the mass, but it leaves the cracking zone with roughly twice the speed). Since the total momentum is conserved in the reactive collision, it would require very similar reactivity of As_2 and As_4 to explain the similarity of measured dependences. However, since the complexity of atomic scattering mechanisms is considerable [9], a dedicated study on crossed molecular beams would have to be performed to shed more light on this issue.

Note that In leakage rate is about 40 times larger than that measured for Al, while Si is in between the two. Such large differences in the flux leakage rates measured for different effusion cells can be understood qualitatively by examining the individual cell designs and locations (see Fig. 1c and Fig. 1d). Indeed, the direction of the "stray" In beam and its overlap with the direct As flux ensures the maximum momentum transfer between the two. Also, the In cell is a dual filament "hot-lip" design which will give relatively strong flux at large angles to the cell axis. In contrast, the Al cell is of a "cold lip" design which minimizes the risk of Al "creeping out" of the crucible. In our case the "cold lip" protection is supplemented by the dual crucible arrangement which minimizes the risk to the cell in the event of the crucible cracking. The final result is that the top portions of the walls for Al crucible emits very little, and the rings of Al which accumulate there further reduce the flux leaving the cell at large angles, thus strongly reducing the Al peripheral beam. The Si cell is most conveniently compared to the Al cell. Indeed, both cells are located symmetrically on each side of the arsenic cracker cell; thus, one would expect similar effective intersection of their respective "stray" beams with the arsenic beam. The Si cell, however, is located higher up in the source flange and its 5 cm^3 conical crucible is loaded with strips of cleaved Si wafer. The orientation of the strips within the crucible is such that its emission profile should be much closer to

that characteristic of the hot-lip cell, giving a considerably stronger peripheral beam than that for Al cell.

In summary, we find that hot effusion cells can contaminate the wafer surface with their respective elements in spite of the closed shutter and no direct line-of-sight from the crucible to the wafer. The amount of such contamination is proportional to both the arsenic flux used and the element vapor pressure over the crucible. The efficiency of such process is similar for As_2 and As_4 molecules, regardless of the contaminating material. All these observations are qualitatively consistent with the model where the peripheral atomic beams traversing the growth chamber are scattered towards the wafer surface by the arsenic molecular flux. The scattering efficiency is sufficient to redirect a fraction of the atoms back to source flange before they are chemisorbed at the shroud walls. We present arguments in support of a model in which the process is dominated by the nonreactive scattering; however, this particular issue can be resolved only through further dedicated experiments. Most of the problems related to the effects described are best taken care of by proper MBE system design. However, with existing systems many of the negative consequences can be avoided by altering certain growth procedures or simple modification of the flux blocking structures adjacent to the cell ports.[4]

Although the experimental results presented pertain to scattering by arsenic molecules, the physics behind this phenomenon is very general. The importance of the effect for other material systems and molecular beams will depend on the growth conditions and design of the apparatus used.

Acknowledgements

Helpful discussions with Dr. Keith Evans and Dr. Frederick Johnson are gratefully acknowledged.

References

[1] C.E.C. Wood and R.A. Wilson, J. Vac. Sci. Technol. B 11 (1993) 1036.
[2] A.J. SpringThorpe, W.T. Moore, A. Majeed and R.W. Streater, J. Vac. Sci. Technol. B 11 (1993) 1275.
[3] Z.R. Wasilewski, G.C. Aers, A.J. SpringThorpe and C.J. Miner, J. Vac. Sci. Technol. B 9 (1991) 120.
[4] T.M. Brennan, J.Y. Tsao and B.E. Hammons, J. Vac. Sci. Technol. B 10 (1991) 33.
[5] H.G. Nöller, in: Handbook of Vacuum Physics, Vol. 1, Ed. A.H.W. Beck (Pergamon, Oxford, 1966) p. 321.
[6] F.G. Celii, Y.C. Kao, I. Beam E.A., W.M. Duncan and T.S. Moise, J. Vac. Sci. Technol. B 11 (1993) 1018.
[7] C.T. Foxon and B.A. Joyce, Surf. Sci. 50 (1975) 434.
[8] C.T. Foxon and B.A. Joyce, Surf. Sci. 64 (1977) 293.
[9] R.B. Bernstein, Proc. 3rd Int. Conf. on the Physics of Electronic and Atomic Collisions, London (1963) p. 895.
[10] P.T. Coleridge, Z.R. Wasilewski and P. Zawadzki, J. Vac. Sci. Technol. B (1996) 2290.

[4] For instance, by employing appropriate growth procedures, we have been able to grow reproducibly in our system AlGaAs/GaAs ultra-high mobililty two-dimensional electron gas structures (peak mobilities up to 6 400 000 cm^2/V s [10]) while the same structures grown without the corrective measures are significantly worse (peak mobilities up to 1 000 000 cm^2/V s).

ELSEVIER

Journal of Crystal Growth 175/176 (1997) 1278–1283

JOURNAL OF CRYSTAL GROWTH

Photoluminescence and X-ray characterization of relaxed $Si_{1-x}Ge_x$ alloys grown on silicon on insulator (SOI) and implanted SOI substrates

Michael A. Chu[a,*], Martin O. Tanner[a], Fengyi Huang[a], Kang L. Wang[a], Gordon G. Chu[b], Mark S. Goorsky[b]

[a] *Device Research Laboratory, Department of Electrical Engineering, University of California, Los Angeles, California 90095-1594, USA*
[b] *Department of Materials Science and Engineering, University of California, Los Angeles, Californai 90095, USA*

Abstract

Boron and oxygen were implanted into the SiO_2 region of a thin silicon on insulator (SOI) substrate to form borosilicate glass and reduce the reflow temperature needed for compliant substrates. The effect of lowering the reflow temperature was examined by characterizing a strained $Si_{0.7}Ge_{0.3}$ layer which was grown on the implanted compliant substrate by molecular beam epitaxy. Photoluminescence (PL) and triple-axis X-ray diffraction were used to characterize film quality, Ge concentration and percent relaxation. A marked decrease in the annealing temperature required (roughly a difference of 300°C) to relax the $Si_{0.7}Ge_{0.3}$ layer was fully observed. The PL spectra show a broad band around 800 meV that is believed to be related to the relaxation of the SiGe layer. The intensity of this peak first increases and then decreases dramatically when the annealing temperature reaches the point when the SiGe layer begins to relax or the underlying glass begins to flow. For the sample grown on the boron and oxygen implanted BESOI, this low-energy peak is shown to disappear completely at an annealing temperature of 900°C. Above 900°C, we begin to see the evolution of near band-gap luminescence for the $Si_{0.7}Ge_{0.3}$ layer grown on implanted BESOI. An energy peak which shifts to higher energies, from 970 to 1025 meV, with greater relaxation is only observed for the sample grown on the implanted substrate. It is believed that the observation of near band-gap luminescence is primarily due to the reduced reflow temperature and a low-defect dislocation concentration in the $Si_{0.7}Ge_{0.3}$ film.

PACS: 68.55. – a; 78.55. – m; 68.60. – p

Keywords: Thin film growth technique; Epitaxy; Moecular beam epitaxy

* Corresponding author. Fax: + 1 310 206 8495; e-mail: mchu@ee.ucla.edu.

0022-0248/97/$17.00 Copyright © 1997 Published by Elsevier Science B.V. All rights reserved
PII S0022-0248(96)00933-5

1. Introduction

Recently, there has been an interest in achieving high-mobility *n*-channel field-effect transistors by using tensilely strained silicon for the electron channel [1, 2]. Electron mobilities greater than 520 000 cm^2/V s at 4.2 K have been reported [2] for tensilely strained silicon on relaxed $Si_{1-x}Ge_x$. Another application of such a high-quality relaxed SiGe buffer layer is for optical devices where dislocations are of important concern [3, 4]. Normally, relaxed $Si_{1-x}Ge_x$ films have been grown on abrupt or more recently graded buffer layers [5]. The major drawbacks have been high dislocation densities for the former and the extremely large buffer thicknesses for the latter.

In 1994, Powell et al. [6] proposed a novel approach in which a very thin 'free-floating' buffer layer is allowed to absorb most of the strain of a SiGe epilayer grown on top of it. The dislocations develop in the buffer layer and allow the epilayer to fully relax its strain without formation of dislocations. The 'compliant substrate' may consist of a thin monocrystalline Si layer on top of a SiO_2 layer on top of a silicon substrate. In this approach, the surmised mechanism leading to the reduced dislocation density is the viscous flow of the buried SiO_2 layer, which allows the Si to float and the strain in the SiGe layer to be relaxed by the introduction of dislocations primarily in the thin Si layer. Recently, we have investigated the quality of annealed $Si_{0.86}Ge_{0.14}$ films grown on thin Bond-Etchback silicon on insulator (BESOI) wafers using photoluminescence and X-ray diffraction techniques [7]. We presented evidence for partial strain relaxation of these layers, resulting in higher film quality than for the same layers grown on bulk Si. However, the temperatures required for strain relaxation of the $Si_{0.86}Ge_{0.14}$ film were high (in the range of 950°C–1100°C). Such a high temperature would cause the strained epitaxial film to develop dislocations before the substrate becomes 'free-floating'. In this paper, we present an approach using low-temperature glasses formed by ion implantation to lower the reflow temperature of the buried oxide layer such that the strain may be relaxed before unwanted dislocations develop in the epifilm.

2. Experimental procedure

Phosphosilicate (PSG) or borosilicate (BSG) is known to have a lower reflow temperature than SiO_2 [8]. By implanting SiO_2 with phosphorous and a subsequent implant of oxygen to activate the phosphorous, these glasses can be formed [9]. Likewise, borosilicate glass can be formed in a similar manner. The main advantage for the latter is that the boron ion is smaller than the phosphorous ion and hence will result in smaller surface damage. Thus, annealing or recrystallization will be easier from the surface, in view of the fact that there is the absence of a bulk 'seed'. This lower reflow temperature offers several important advantages. First, it allows strain relaxation at lower temperatures which would precede mechanisms likely to occur at higher temperatures, like Ge segregation, surface roughening, and dislocation formation. Second, it allows for the possibility of in-situ reflow annealing and thus allows for better control over the growth conditions of SiGe epilayers.

The BESOI substrates in this work were produced by Sibond, Inc. [10]. The silicon and silicon dioxide layers were initially 200 and 230 nm thick, respectively. The silicon film was subsequently etched using an anisotropic etchant, tetra-methyl ammonium hydroxide (TMAH) to roughly 60 nm. One of the BESOI substrates was then implanted first with boron and then oxygen. The implant fluences were determined by the stoichiometrical ratio of B_2O_3 and the targeted concentration of 5% by weight. We determined the implanting energies by setting the projected range, R_p, to approximately the center of the SiO_2 layer. The actual energies and fluences were 40 keV and 9.1×10^{15} cm^{-2} for boron and 50 keV and 1.4×10^{16} cm^{-2} for oxygen, respectively, [11]. After the implant and a 800°C anneal for 30 min, the top Si layer was thinned down further to the desired thickness ($\sim$ 20 nm). This extra step not only allows the top thin Si layer to be strained or relaxed easily but also allows us to etch off some of the Si surface damaged by the implantation process. The final thicknesses of the Si and the SiO_2 were confirmed using an ellipsometer. The surface roughness was characterized by an atomic force microscope and the root mean squared roughness was measured to be about 11 Å.

After the substrates were cleaned using a modified Ishizaka and Shiraki cleaning procedure [12], they were attached to a single holder and loaded into a Perkin-Elmer Model 430S MBE system. The substrates consisted of a p-Si substrate, an unimplanted BESOI substrate, and a B and O implanted BESOI substrate. Following a 10 min. thermal cleaning at 900°C, 10 nm of Si, 120 nm of $Si_{0.7}Ge_{0.3}$ and 5 nm of Si were deposited consecutively at 475°C. All photoluminescence (PL) measurements were measured at 4.2 K with an excitation wavelength of 488 nm from an Ar laser. The actual Ge concentration was verified by high resolution triple-axis X-ray diffraction (TAD) using both symmetric [0 0 4] and asymmetric [2 2 4] scans.

3. Results and discussion

Figs. 1–3 show PL spectra as a function of annealing temperature for the $Si_{0.7}Ge_{0.3}$ layer grown on the plain p-silicon substrate (Sample A), unimplanted BESOI (Sample B), and B and O implanted BESOI (Sample C), respectively. From the as-grown spectra in all cases Fig. 1a, Fig. 2a and Fig. 3a, we can see luminescence attributed to the substrates which are the peaks above 1 eV and a lower-energy broad peak sometimes seen on MBE grown samples [13–15]. For Sample A, as we slowly increase the annealing temperatures from 800°C, we see that the luminescence of the broad peak increases in intensity relative to the p-substrate lumine scence in Fig. 1, which is to be expected since this broad energy peak is usually associated with dislocations. For sample B, the layers grown on the unimplanted BESOI substrate, we see an increase and then a decrease of the broad energy peak intensity. The intensity begins to decrease around 1100°C. This low-energy broad-band luminescence appears to be related to the T-band luminescence as seen by others [15] since it has the same temperature and band-gap dependences as the T-band. Its relationship to D1 or D2, whose energies are similar to this broad luminescence, is unknown at this time. For Sample C, the broad peak is more noticeable after a 800°C annealing. However, at temperatures above 900°C the broad peak disappears and a higher-energy peak begins to appear (900 meV–1.04 eV).

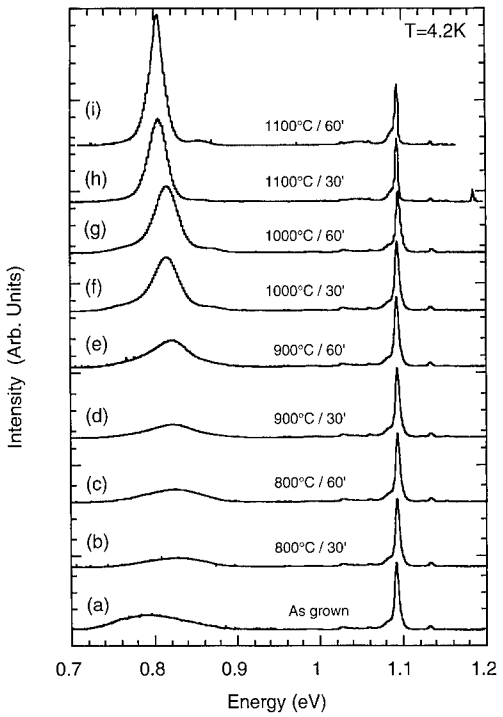

Fig. 1. PL Spectra of Sample A as a function of annealing temperature and time – $Si_{0.70}Ge_{0.30}$ alloy layer on a p-Si substrate; (a) as grown, (b) 800°C–30 min, (c) 800°C–60 min, (d) 900°C–30 min, (e) 900°C–60 min, (f) 1000°C–30 min, (g) 1000°C–60 min, (h) 1100°C–30 min, (i) 1100°C–60 min.

As confirmed by high-resolution triple axis X-ray diffraction (TAD), the evolution of the low-energy peak in the luminescence demonstrates the relaxation mechanism. It can be seen for Sample C that the temperature at which this band reaches the maximum intensity occurs when annealed around 800–850°C for 30 min. Whereas for the unimplanted Sample B, this temperature and time are around 1100°C for 60 min. For Sample A, which is grown on a conventional p-silicon substrate, the peak never decreases in the annealing temperature range examined. It is assumed that if it does begin to decrease, it is obviously at a higher temperature and may be attributed to other mechanisms due to its extreme temperature. Hence, we can see that we have effectively lowered the reflow temperature by about 300°C by the use of implantation. This lower energy broad band also appears to correspond to

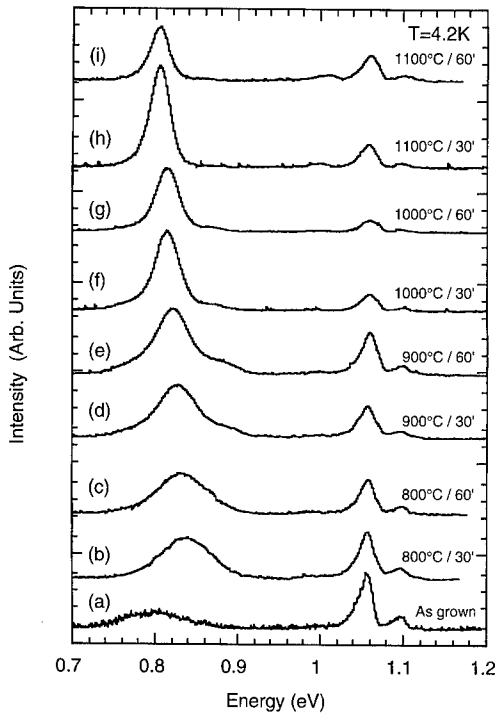

Fig. 2. PL Spectra of Sample B as a function of annealing temperature and time – $Si_{0.70}Ge_{0.30}$ alloy layer on unimplanted BESOI substrate; (a) as grown (b) 800°C–30 min, (c) 800°C–60 min, (d) 900°C–30 min, (e) 900°C–60 min, (f) 1000°C–30 min, (g) 1000°C–60 min, (h) 1100°C–30 min, (i) 1100°C–60 min.

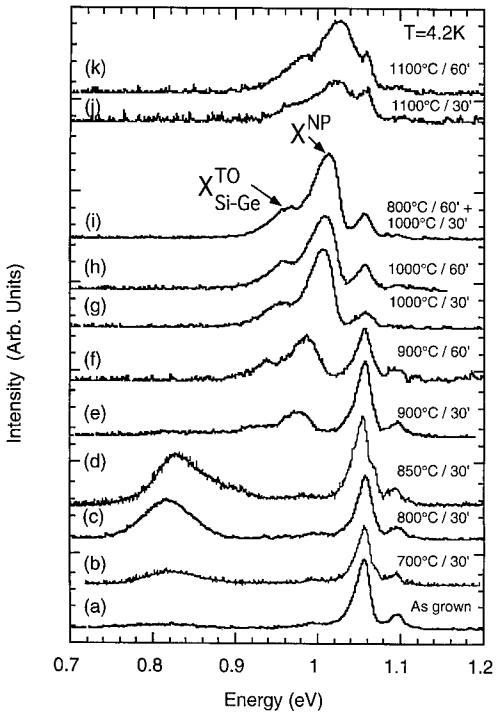

Fig. 3. PL Spectra of Sample C as a function of annealing temperature and time – $Si_{0.70}Ge_{0.30}$ alloy layer on a boron and oxygen implanted substrate; (a) as grown (b) 700°C–30 min, (c) 800°C–30 min, (d) 850°C–30 min, (e) 900°C–30 min, (f) 900°C–60 min, (g) 1000°C–30 min, (h) 1000°C–60 min, (i) 800°C–60 min and 1000°C–30 min, (j) 1100°C–30 min, (k) 1100°C–60 min.

the mosaic spread in the high-resolution X-ray spectra observed from the sample (not shown) and in Ref. [7]. The decrease in the mosaic spread in the TAD spectrum can be explained by noting that when the strain of the SiGe layer is transferred to the thin Si layer fully or partially (with and without accompanying dislocations), the $Si_{0.7}Ge_{0.3}$ layer is 'smoother'. The disappearance of this broad low-energy luminescence peak can be directly attributed to the relaxation of the $Si_{0.7}Ge_{0.3}$ without accompanying dislocations and to the subsequent transfer of the strain to the thin silicon layer fully or partially. Assuming no dislocation formation, the equilibrium relaxation of the finite bilayer system should be roughly 75% using the formulation of Huang et al. [16]. This 75% relaxation (confirmed by TAD) of the top SiGe layer, for example in the case of Sample C, occurs at an annealing temperature of 850°C when the broad low energy luminescence peak reaches a maximum. However, after further annealing (1000°C or above), the layer fully relaxes (95%). This can be attributed to the fact that the bottom thin silicon layer relaxes by way of dislocations. At higher temperatures, the thickness of the thin Si layer (~ 20 nm), will surpass the critical thickness determined by the $Si_{0.7}Ge_{0.3}$ 'substrate' and the thin Si film will be dislocated to relieve the strain. Hence, the $Si_{0.7}Ge_{0.3}$ layer is free to relax without formation of misfit dislocations in the $Si_{0.7}Ge_{0.3}$ layer itself. The disappearance of the broad low-energy luminescence peak also supports the notion that this peak does not arise from the dislocations themselves, but rather from the strain field around the SiGe/Si interface. This is especially

true in the case of the compliant substrates since it would not be expected that the dislocations will disappear at higher temperatures. Hence, in the case of the compliant substrates, the low-energy luminescence may arise due to the strain field around the interface.

Fig. 3 also shows the evolution of several higher energy peaks (900 meV–1040 meV) for Sample C at annealing temperatures of 900°C and above. We attribute these peaks to band-gap related luminescence both the NP and TO_{Si-Si} phonon replica. The energy values of 1.015 and 0.955 eV from Fig. 3(i) correspond well to published reports [17, 18], particularly if we use the 95% relaxation value from TAD. The temperature dependence of these peaks follows the same temperature dependence as reported by others for SiGe near band-gap luminescence [19]. The 1.015 eV peak disappears around 55 K and shifts to lower energies with increasing temperature. The strain relaxation dependence discussed previously also supports our assignment of these peaks since we expect that at higher annealing temperatures the SiGe layer will relax more and that the SiGe band-gap will shift to higher energies as illustrated in Fig. 3.

The energy peaks around 900–1040 meV in Fig. 3 are shown to broaden as the annealing temperature increases beyond 900°C. The reason for the broadening is not fully understood at this time but may be related to Ge segregation at higher temperatures or more likely some relaxation distribution in the SiGe layer. Etching of the SiGe layer confirms that the near band-gap luminescence does indeed come from the SiGe layer and not from the thin silicon layer, nor the substrate. The fact that this near band-gap luminescence is not evident in the PL spectra of Samples A and B, may be attributed to the presence of dislocations or other mechanisms which compete for the recombination of the same carriers. We should also note that since the $Si_{0.7}Ge_{0.3}$ layer is 1200 Å, it is larger than the conventional critical thickness for a pseudomorphic growth of $Si_{0.7}Ge_{0.3}$ on Si. Augmentation of the pseudomorphic thickness may be expected since, for lower reflow temperatures, the thin silicon layer of the BESOI substrate should accommodate some of the strain within the thin silicon layer [16].

4. Conclusions

We have successfully demonstrated the lowering of the reflow temperature of BESOI by about 300°C by implanting the SiO_2 layer with both boron and oxygen. Near band-gap luminescence from the relaxed $Si_{0.7}Ge_{0.3}$ layers grown on implanted BESOI was observed. In addition, we showed the decrease and disappearance of a low energy ($\sim$ 0.80 eV) broad feature in the PL spectra. This low energy feature was shown to be directly related to the relaxation of the $Si_{0.7}Ge_{0.3}$ layer and possibly the generation of dislocations in the underlying Si layer. It may be possible to further lower the reflow temperature of the SiO_2 layer by implanting the region with a higher concentration of boron and oxygen. The approach described in this paper may be used to grow high-quality strained Si/SiGe on SOI. Likewise, this approach may be extended to other strained layer systems, such as GaAs on Si, etc.

Acknowledgements

This work was supported in part by the Semiconductor Research Corporation (SRC) under Dr. W. Lynch and the National Science Foundation under Dr. Le Verne Hess. The authors also wish to thank Dr. S.S. Iyer of Sibond, Inc. for the BESOI wafers used in this study.

References

[1] K.L. Wang, S.G. Thomas and M.O. Tanner, J. Mater. Sci.: Mater. Electron. 6 (1995) 311.
[2] K. Ismail, M. Arafa, K.L. Saenger, J.O. Chu and B.S. Meyerson, Appl. Phys. Lett. 66 (1995) 1077.
[3] E. Kasper, H. Kibbel and H. Presting, Thin Solid Films 183 (1989) 87.
[4] D.K. Nayak, N. Usami, S. Fukatsu and Y. Shiraki, Appl. Phys. Lett. 63 (1993) 3509.
[5] E.A. Fitzgerald, Y.-H. Xie, M.L. Green, D. Brasen, A.R. Kortan, J. Michel, Y.-J. Mii and B.E. Weir, Appl. Phys. Lett. 59 (1991) 811.
[6] A.R. Powell, S.S. Iyer and F.K. LeGoues, Appl. Phys. Lett. 64 (1994) 1856.
[7] M.O. Tanner, M.A. Chu, K.L. Wang, M. Meshkinpour and M.S. Goorsky, J. Crystal Growth 157 (1995) 121.

[8] N.P. Bansal and R.H. Doremus, in: Handbook of Glass Properties (Academic Press, New York, 1986).
[9] K. Oyoshi, T. Tagami, K. Yamashita and S. Tanaka, Nucl. Instrum. Methods B 59/60 (1991) 1324.
[10] Sibond L.L.C. Hudson Valley Research Park, Hopewell Junction, NY, 12533–6531.
[11] J.F. Ziegler and J.P. Biersack, Energies and Fluences Calculated by TRIM-90 (Pergamon, New York, 1985).
[12] A. Ishizaka and Y. Shiraki, J. Electrochem. Soc. 133 (1986) 666.
[13] J.-N. Noel, N.L. Rowell, D.C. Houghton, A. Wang and D.D. Perovic, Appl. Phys. Lett. 61 (1992) 690.
[14] E.R. Glaser, T.A. Kennedy, D.J. Godbey, P.E. Thompson, K.L. Wang and C.H. Chern, Phys. Rev. B 47 (1993) 1305.
[15] A. Souifi, G. Bremond, T. Benyattou, G. Guillot, D. Dutartre and I. Berbezier, J. Vac. Sci. Technol. B 10 (1992) 2002.
[16] F.Y. Huang and K.L. Wang, Philos. Mag. Lett. 72 (1995) 231.
[17] J. Weber and M. Alonso, Phys. Rev. B 40 (1989) 5683.
[18] R. Braunstein, A. Moore and F. Herman, Phys. Rev. 109 (1958) 695.
[19] G.S. Mitchard and T.C. McGill, Phys. Rev. B 25 (1982) 5351.

ELSEVIER

Journal of Crystal Growth 175/176 (1997) 1284–1288

JOURNAL OF CRYSTAL GROWTH

Modulated-beam studies of the layer-by-layer etching of GaAs(0 0 1) using $AsBr_3$: identification of the reaction mechanism

J. Zhang[1,a,*], O.P. Naji[2,a], P. Steans[2,a], P. Tejedor[a], T. Kaneko[b], T.S. Jones[2,a], B.A. Joyce[a]

[a] *IRC for Semiconductor Materials, Blackett Laboratory, Imperial College of Science, Technology and Medicine, Prince Consort Road, London SW7 2BZ, UK*

[b] *Max-Planck-Institut für Festkörperforschung, Heisenbergstrasse 1, D-70569 Stuttgart, Germany*

Abstract

Modulated-beam mass spectroscopy (MBMS) has been used to study the reaction mechanism of the layer-by-layer etching of GaAs(0 0 1) using $AsBr_3$ under molecular beam epitaxy conditions. It is shown that GaBr is the main etching product and its "delay" time with respect to the incident $AsBr_3$ flux exhibits a strong dependence on substrate temperature, changing from 12 ms in the reaction limited regime at 387°C to less than 0.5 ms at 560°C. Desorbing As-containing species appear to have very short surface lifetimes throughout the temperature range investigated and the additional As_2 flux supplied from a solid source has no effect on the etching rate. The results suggest a reaction pathway where the rate limiting step is the formation or desorption of GaBr and not the decomposition of $AsBr_3$.

PACS: 81.65.Cf; 81.15.Hi

1. Introduction

It has recently been demonstrated that III–V semiconductor materials such as GaAs and InP can be chemically etched in an ultrahigh vacuum (UHV) chamber using molecular beams of group-V halides, e.g. $AsCl_3$ [1, 2], PCl_3 [3] and $AsBr_3$ [4]. The etching process on GaAs(0 0 1) has been monitored by reflection high-energy electron diffraction (RHEED) [1, 4]. Specular beam RHEED intensity oscillations were observed over a wide temperature range indicating that the etching process occurs on a layer-by-layer basis, similar to the corresponding growth processes that are well known on this surface [5]. The combination of atomic controlled etching and growth in the same UHV chamber offers considerable promise for the fabrication of novel low-dimensional semiconductor heterostructures [6].

* Corresponding author. E-mail: jing.zhang@ic.ac.uk.

[1] Also at: Department of Physics, Imperial College, London, UK.

[2] Also at: Department of Chemistry, Imperial College, London, UK.

0022-0248/97/$17.00 Copyright © 1997 Elsevier Science B.V. All rights reserved
PII S0022-0248(96)00831-7

Kinetic information regarding the etching rates using $AsBr_3$ and their dependence on flow rate and substrate temperature has been obtained from RHEED intensity oscillation measurements on GaAs(0 0 1) [4, 7]. Oscillations were observed over a wide range of substrate temperatures, between 350 and 650°C, and the etching rate was found to be constant above 460°C but decreased significantly at lower temperatures. Two etching regimes were therefore identified, a supply-rate-limited regime at high temperatures (> 460°C) and a reaction-rate-limited regime at low temperatures (<460°C) [4]. Furthermore, measurements have been made across AlGaAs/GaAs heterojunctions and the etching rate was found to be determined by the surface composition of the group-III elements [7].

Although RHEED intensity oscillation measurements can provide information regarding the rates of the etching process, it is not a species-specific technique and provides no direct information on reaction pathways. In contrast, modulated beam mass spectroscopy (MBMS) is ideally suited for detailed kinetic studies and it has been used successfully as a probe of reaction mechanisms in the growth of GaAs by molecular beam epitaxy (MBE) [8, 9] and metalorganic molecular beam epitaxy (MOMBE) [10, 11]. In common with other modulation-based techniques, MBMS has the advantage that it allows the detection of small signals over a large background. Modulation of the desorbing beam enables the species leaving the surface to be identified, whereas modulation of the incident beam allows the determination of reaction orders and surface residence times [8].

In this paper, we present MBMS measurements for the in situ etching of GaAs(0 0 1) using $AsBr_3$. We find the dominant etching product to be GaBr and its delay time with respect to the incident $AsBr_3$ is measured over a wide range of temperature. Our results suggest a reaction pathway where the rate-limiting step is the formation or desorption of GaBr and not the decomposition of $AsBr_3$ at the surface.

2. Experimental procedure

The experiments were performed in a purpose built metalorganic MBE system with additional group-V halide gas source and solid group III sources [12]. The growth chamber is also equiped with MBMS and RHEED systems. Epi-ready, singular GaAs(0 0 1) substrates were used and the initial oxide was removed in the growth chamber at 610°C in the presence of an As_2 flux supplied from a solid source cracker cell. Buffer layers of GaAs were grown using solid sources at 580°C to ensure that each subsequent etching experiment would not remove material and expose the underlying interface. The $AsBr_3$ gas source was maintained at 80°C to avoid condensation in the gas line and the $AsBr_3$ flow rate was 0.03 SCCM. A concomitant As_2 flux was used throughout all etching experiments to maintain an As-rich surface condition.

The MBMS system consists of a quadrupole mass spectrometer with a cross beam ioniser and two modulators. The ioniser of the mass spectrometer was surrounded by a liquid nitrogen tank, except for a solid angle directly facing the sample. The modulators were positioned in front of the entrance to the ioniser and the gas cell, to provide modulation of the molecular (atomic) fragments desorbing from the sample into the ioniser, or $AsBr_3$ molecules incident on the sample. A multichannel scaler (MCS) was used to collect the modulated signal which allows digital processing of the signal. This is a significant advantage over the conventional lock-in amplifer instrumentation as a number of parameters can be obtained using digital methods in addition to the phase angle and amplitude. It also allows signal averaging as the spectra is obtained through accumulation over many scans, thus improving the signal to noise ratio. The methods of obtaining these additional parameters, such as orders of reaction, can be found in the work of Foxon and Joyce [8, 9].

3. Results and discussion

The reaction products were identified by monitoring the desorbing beam during etching of GaAs(0 0 1) with $AsBr_3$ in both the supply- and reaction-limited regimes, as indicated by RHEED intensity oscillation studies. Modulated signals were detected in both regimes at mass–charge ratios (m/e) of 69 (Ga^+), 148 ($GaBr^+$), but no signals

were identified at 158 (Br_2^+) and 227 ($GaBr_2^+$). The specific mass charge ratios were chosen after consideration of the isotope distribution and the need to separate each species in the mass spectrometer. The intensity of the modulated signals at 69 and 148, determined from the amplitude at the fundamental modulation frequency, exhibited the same temperature dependence as the etching rate. Since the vapour pressure of Ga over GaAs is very low, it can be concluded that the main desorbing neutral species must be GaBr, and that the modulated signal at 69 derives purely from the cracking pattern of GaBr. There is, however, a possiblity that the ionisation fragmentation patterns of $GaBr_x$ ($x > 1$) may not give a significant contribution to the signal at $m/e = 227$.

Modulation of the incident $AsBr_3$ flux allows determination of a number of kinetic parameters. Fourier analysis of modulated signals obtained at $m/e = 69, 75$ (As^+), 148, 150 (As_2^+) and 237 ($AsBr_2^+$) show characteristics of a linear response (zero even harmonics in Fourier analysis of the spectra) with respect to the incident $AsBr_3$ flux [8] in both supply-rate and reaction-rate-limited regimes. This is consistent with the linear analysis using the convolution between the odd drive function and the impulse response, indicating that the apparent etching reaction is first order. This is in agreement with the etching-rate measurements obtained by RHEED in the supply-rate-limited regime due to the linear dependence of the etching rate on the incident $AsBr_3$ flux. However, rate measurements (using RHEED) in the reaction-rate-limited regime show a negligible dependence on the incident flux, i.e. the reaction is pseudo-zeroth order with respect to the $AsBr_3$ flux. The apparent discrepancy between results obtained from the two techniques can be explained as follows. A zeroth order reaction would not generate a modulated signal in an MBMS experiment. The zeroth order shown in rate measurements (RHEED) reflects saturation of the surface by $AsBr_3$. This would not be true if the $AsBr_3$ flux is reduced below a *threshold* value. Under the conditions used for MBMS, the $AsBr_3$ flux is modulated between zero and a designated flux which is higher than the *threshold* value. The part below this *threshold* value would give rise to the modulated signal detected in MBMS. Therefore, the first order indicated by the MBMS results reflects the condition when there is no saturation of $AsBr_3$ on the surface.

The surface delay time (lifetime) of the detected species can be obtained using a number of methods [8]. Fig. 1 shows the MCS spectrum obtained at an m/e ratio of 69 and at a substrate temperature of 387°C. Since the signal at $m/e = 69$ was due to the fragmentation of GaBr in the ioniser, the information obtained arises solely from GaBr. For a first-order reaction, the impulse response is an exponentially decaying function. Also shown in Fig. 1 are several examples of simulated spectra taking into account the flight time of the incident (mass = 312 amu) and desorbing neutrals (mass = 148 amu) and impulse response functions with different decay constants. Comparison of the simulated and experimental data indicates a surface delay time for GaBr of approximately 12 ms. This decreases with increasing temperature to a value of about 2 ms at 526°C. At a temperature of 560°C, the surface delay time is below the resolution of the instrument (0.5 ms) for the modulation frequency used.

The surface lifetime of the As-containing species are all very short compared to the resolution of the instrument at the modulation frequency used. Fig. 2 shows the temperature dependence of the etching rate at two different As_2 fluxes supplied from a solid source. The etching rate is identical under the two conditions indicating that As_2 has a negligible effect on the rate-limiting step of the etching reaction (at least within the range of As_2 flux used). The very short surface lifetime of the As-containing species over the temperature range studied suggests that dissociation of $AsBr_3$ is unlikely to be the rate-limiting step in the etching reaction. In contrast, the surface delay time of the etching product GaBr changes drastically as a function of substrate temperature in the reaction-limited regime. It is clear that either the formation or desorption of GaBr must be the rate-limiting step in the etching reaction. This result is entirely in agreement with previous RHEED studies which have looked at the effect on the etching rate of the surface composition [12], and results obtained from etching across AlGaAs/GaAs heterojunctions [7], where the etching rate was determined by the

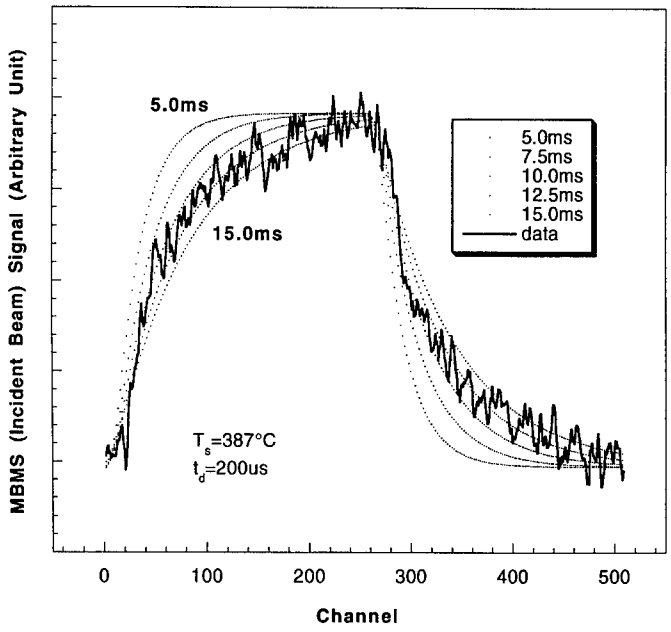

Fig. 1. MCS spectrum obtained at 387°C for $m/e = 69$ and various simulated curves with increasing delay time.

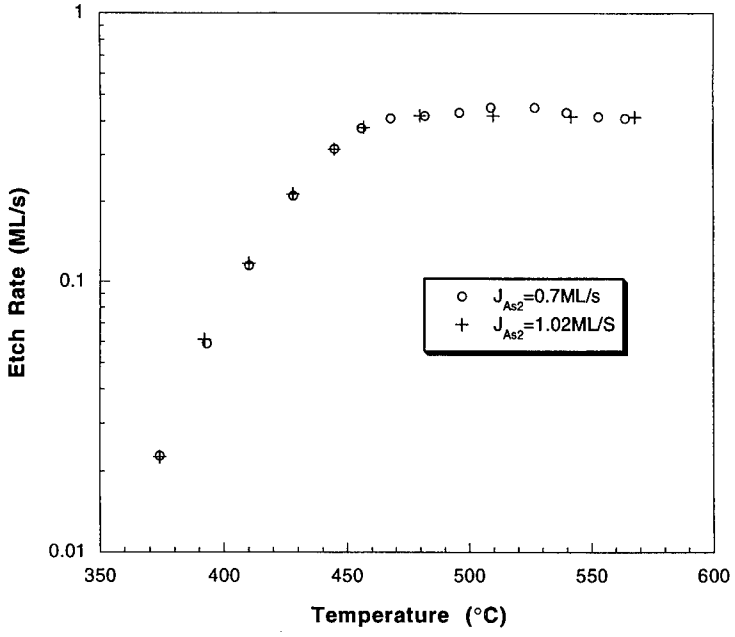

Fig. 2. Etch rate as a function of substrate temperature at two different As_2 flux.

surface composition of the group-III elements. The As_2 flux supplied from the solid source has no effect on the etching rate or the position of the transition region between the supply-rate and reaction-limited regime. Clearly, the rate-limiting step is unlikely to depend on the surface As concentration.

4. Conclusions

MBMS has been used to obtain important kinetic information, complimentary to that obtained from RHEED intensity oscillations, concerning the layer-by-layer etching reaction of GaAs(0 0 1) using $AsBr_3$ in an MBE growth system. The underlying etching reaction is first order with respect to the incident $AsBr_3$ flux. The main reaction product has been identified as GaBr and the rate-limiting step in the etching reaction involves either the formation of GaBr or its desorption from the surface. A concomitant As_2 flux supplied from a solid source to maintain an As-rich reconstruction has little effect on the etching rate and suggests that the rate-limiting step does not depend on the surface As concentration.

Acknowledgements

The authors wish to thank Jim Neave for practical help and stimulating discussion on numerous occasions. This work was funded by Engineering and Physical Science Research Council, under grant No. GR/J 97540. One of us (P.T.) acknowledges gratefully the financial support from the Spanish Ministry of Education and Science.

References

[1] W.T. Tsang, T.H. Chiu and R.M. Kapre, Appl. Phys. Lett. 63 (1993) 3500.
[2] T.H. Chiu, W.T. Tsang, M.D. Williams, C.A.C. Mendonca, K. Dareyer and F.G. Storz, Appl. Phys. Lett. 65 (1994) 3368.
[3] W.T. Tsang, R.M. Kapre and P.F. Sciortino, Jr., J. Crystal Growth 136 (1994) 42.
[4] T. Kaneko, P. Smilaure, B.A. Joyce, T. Kawamura and D.D. Vvedensky, Phys. Rev. Lett. 74 (1995) 3289.
[5] J.H. Neave, B.A. Joyce, P.J. Dobson and N. Norton, Appl. Phys. A 31 (1983) 1.
[6] T. Kaneko, T. Sager and K. Eberl, Mater. Res. Soc. Proc. 405 (1995), in press.
[7] T. Kaneko and K. Eberl, Phys. Rev. Lett., submitted.
[8] C.T. Foxon, M.R. Boudry and B.A. Joyce, Surf. Sci. 44 (1974) 69.
[9] B.A. Joyce, Report Progr. Phys. 48 (1985) 1637.
[10] T. Martin and C.R. Whitehouse, J. Crystal Growth 105 (1990) 57.
[11] E.M. Gibson, C.T. Foxon, J. Zhang and B.A. Joyce, J. Crystal Growth 105 (1990) 81.
[12] T. Kaneko, O. Naji, T.S. Jones and B.A. Joyce, J. Crystal Growth 136 (1994) 99.

ELSEVIER

Journal of Crystal Growth 175/176 (1997) 1289–1293

JOURNAL OF CRYSTAL GROWTH

Morphology of MBE grown InAs films studied by atomic force microscope

Y. Wang[a,*], Y.N. Sheng[a], Weikun Ge[a], Jiannong Wang[a], L.L. Chang[a], Jie Xie[b], Jianxing Ma[c], Jianbin Xu[c]

[a] *Department of Physics, The Hong Kong University of Science and Technology, Clear Water Bay, Kwoloon, Hong Kong*
[b] *Material Characterization and Praparation Center, The Hong Kong University of Science and Technology, Clear Water Bay, Kwoloon, Hong Kong*
[c] *Department of Electrical Engineering, The Chinese University of Hong Kong, Shatin, Hong Kong*

Abstract

The morphology of MBE grown InAs films on GaSb buffered GaAs(0 0 1) substrates with miscuts ranging between 0.2° and 4° has been studied by atomic force microscope (AFM). Step flow growth mode on nominal singular (1 0 0) substrates has been observed for samples grown at substrate temperatures higher than 500°C and for samples on miscut substrates grown at temperatures between 400°C and 530°C. Unstable growth mode has been observed on nominal singular (0 0 1) substrates when substrate temperatures are lower than 450°C. Relatively high density pits have also been observed on InAs surfaces with nucleation temperatures above 450°C.

PACS: 61.16.Ch; 68.55.Bd

Keywords: InAs; Morphology; Atomic force microscopy

Molecular beam epitaxy (MBE) is a widely employed technique for growing III–V compound semiconductor materials and heterostructures. Because of its technical and scientific importance, MBE grown surfaces have been widely studied by a variety of techniques, such as reflection high energy electron deflection (RHEED), scanning tunneling microscope (STM), and atomic force microscope (AFM). RHEED has proven to be a powerful tool providing a lot of real time information, including growth mode transition, surface diffusion length, and surface reconstruction during the film deposition. However, RHEED can only provide averaged coherent diffraction information, failing to give local topographic information. More recently, STM and AFM have been employed to study the MBE grown films at various points during the evolution of the surfaces [1, 2], which have

* Corresponding author.

0022-0248/97/$17.00 Copyright © 1997 Elsevier Science B.V. All rights reserved
PII S0022-0248(96)00959-1

provided more detailed information about local noncoherent structures. However, among a large number of publications on STM and AFM studies on MBE growth of III–V semiconductors, most of them concentrate on GaAs [3, 4]. InAs is another III–V semiconductor with relatively narrow band gap (0.354 eV at room temperature). The novel broken-gap alignment with GaSb and small lattice mismatch between InAs and GaSb make the material very promising in infrared applications. In this paper we will report our AFM results of morphology of MBE grown InAs films on GaSb buffered GaAs substrates

Our samples were grown on (1 0 0)GaAs substrates with a variety of miscuts ranging between 0.2° (nominally singular) and 4°. The As_2 was used as the As source. The typical As/In pressure ratio is about 15 for the sample grown at temperatures higher than the surface phase transition temperature [5], and 10 for the samples grown at relatively lower temperatures, the growth rate was approximately 0.3 μm/h. In order to make the substrate temperature measurements more reliable, the surface phase transition temperature during growth was employed as a calibration point. If the As/In beam flux ratio is high enough, the hysteretic range for this phase transition can be smaller than 2°C. The substrate temperatures during the growth was varied between 530 and 430°C. The samples consist of a 500 nm GaSb buffer layer grown at 500°C on GaAs substrates, a 10 nm InAs nucleation layer grown at either 430°C or higher temperatures, and an InAs layer with a thickness variating from 200 to 500 nm grown at different temperatures. Strong RHEED intensity oscillations were observed for the InAs films grown at temperatures higher than 500°C. However, these oscillations were absent for samples grown at temperatures lower than 460°C, even after 5 min annealing at 520°C.

The AFM measurements were conducted under ambient conditions. Although a native oxide layer has been formed, which is believed to be a few nm thick, the monolayer steps and terraces remain clearly observable. The sample grown on nominal singular (0 0 1) substrates show very large differences in surface morphology for different growth temperatures. As shown in Fig. 1a, for samples

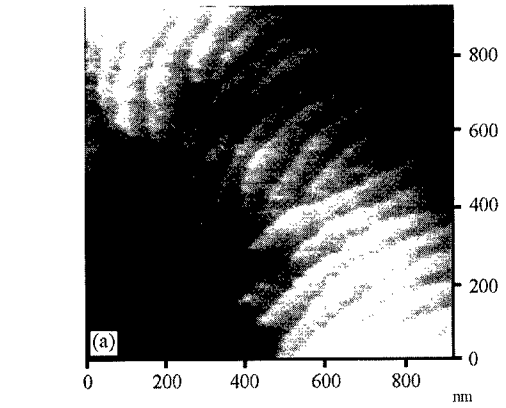

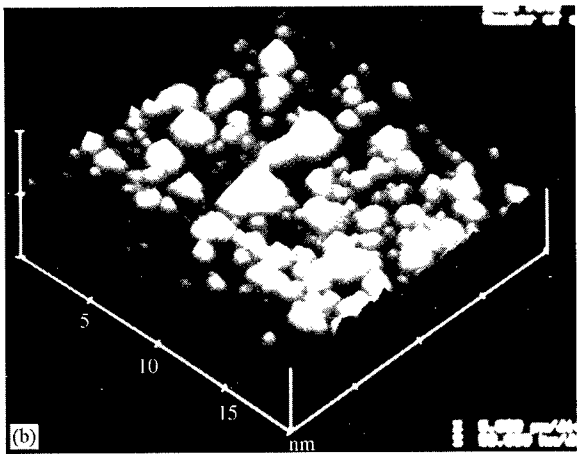

Fig. 1. AFM images of the surface morphology of InAs films on GaSb buffered GaAs substrates: (a) image of 0.9×0.9 μm^2 on (0 0 1) singular substrates grown at 510°C; (b) three dimensional image of 20×20 μm^2 on (0 0 1) singular substrates grown at 430°C, z-axis scale is 50 nm.

grown at 520°C, the surfaces are quite smooth and regular monolayer step edges with terrace widths of about 80 nm have been measured. However, in comparison with the samples grown at temperatures higher than 500°C, the surfaces of samples grown at temperatures below 450°C are relatively rough, as shown in Fig. 1b. Detailed examination of the surface reveals that the surface is formed by approximately circular shaped mounds with different sizes and heights. The very interesting feature of these mounds is that their slopes are approximately identical. The typical sizes of mounds are between a few hundred nm to a few μm. Their slope is

slightly larger than 1°. We have studied films grown at the same substrate temperature but with different thickness of InAs from 200–500 nm. The feature of the surfaces is almost the same as what has been shown in Fig. 1b. This means that the surfaces have reached a steady state after 200 nm growth at this substrate temperature.

This type of surface feature represents an unstable growth mode. It means that the growth on the singular surface is unstable. The growth will evolute into step flow growth mode through kinetic roughening. This kind unstable growth mode occurs when the competition between step flow and nucleation favors the nucleation of new islands. This happens when the terrace width is larger than the typical length of the adatoms travel before nucleating an island. However, this is not a sufficient condition for this unstable mode growth. For two dimension islands turning into multilayer mounds, the adatoms need to stay at the top of the islands rather than to jump off the terraces. Therefore, in order to sustain the unstable mode growth, the material should exhibit an energy barrier (Schwoebel barrier [6]) to prevent the adatoms from jumping off the terraces.

On a (0 0 1) singular GaSb surface which was grown on a GaAs(0 0 1) substrate, as shown in Fig. 2, the typical terraces width are larger than the distance of In adatoms traveling before nucleating an island on InAs surface. Therefore, it is very likely that the first few InAs layers take a two dimensional island nucleation growth mode. Once the islands have grown large enough, Schwoebel barrier will be formed to prevent the adatoms jumping off the terraces. The adatoms will be bounced back from the step edges, which will initiate the unstable growth.

In comparison with GaAs unstable mode growth, unstable mode growth on InAs surfaces exhibits a different feature. In the case of GaAs growth, the mounds are observed to be anisotropic [1, 7]. The STM and laser light scattering experiments show that the enlongated mounds tend to take their main axis along the [$\bar{1}$ 1 0] direction. In their experiments, the ratio between the length and the width of the mounds is about 4. In our case for InAs growth, the mounds exhibit an isotropic feature. This means that the Schwoebel barrier,

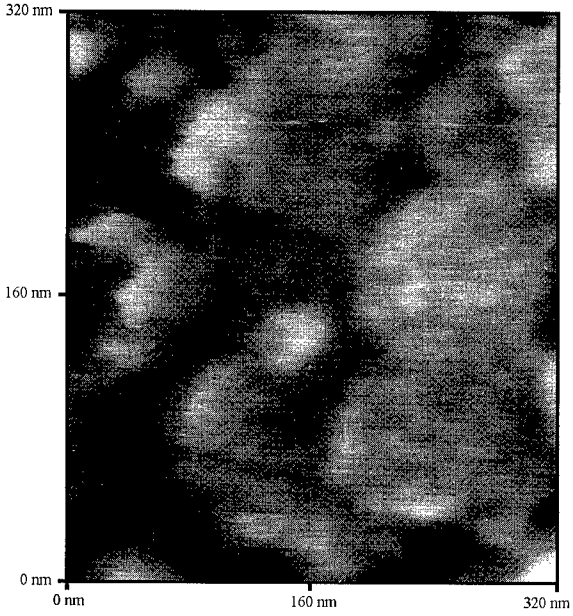

Fig. 2. Image of $320 \times 320\ nm^2$ of the typical surface morphology of GaSb (0 0 1) singular surface before InAs epilayer growth.

sticking probabilities, and adatom diffusion on InAs(0 0 1) surface are isotropic. On the other hand, some of them are anisotropic on a GaAs(0 0 1) surface.

In order to further confirm the above argument, we have also studied the surface morphology of InAs films grown on miscut substrates at different substrate temperatures. Fig. 3 shows the morphology of InAs films on 3° off GaSb buffered GaAs substrates. The films grown at temperatures of 430 and 520°C exhibit the similar morphology with high density of monolayer step edges. The film growth takes the step flow growth mode. The tilting angle of the miscut substrates is larger than the slope of the mounds which have been observed on the films grown on singular substrates. In other words, the average terrace width is smaller than the distance of the adatoms traveling before the nucleate islands. Therefore, the films growth favorite step flow growth mode.

The influence of the nucleation temperature on InAs growing on GaSb has also been studied. Fig. 4 shows a typical AFM image of the surface of

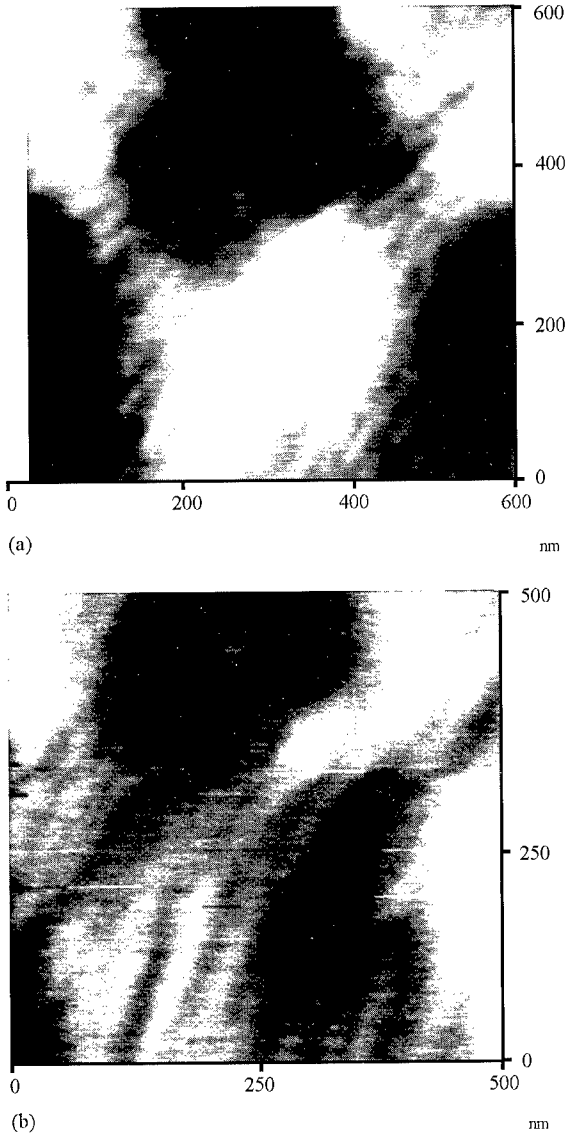

Fig. 3. AFM images of InAs films grown on miscut substrates: (a) grown at 510°C and (b) grown at 430°C.

an InAs film with a thickness of 500 nm grown at 460°C. The InAs nucleation temperature is also at 460°C. The surfaces are relatively rough and with a relatively high density of deep pits (more than 200 nm in depth) surrounded by terraces (about 40 nm high). This phenomenon is consistent with that observed in the case of unstable growth. These

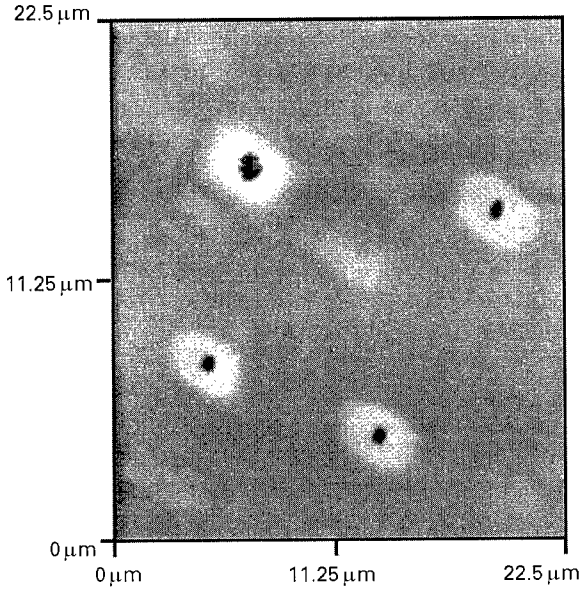

Fig. 4. AFM image of an InAs surface grown at 460°C with a nucleation temperature of 460°C.

facts can be explained on the basis of (l) insufficient and anisotropic In diffusions due to the Schwoebel barrier at the step edges, and (2) step pinning by surface defects, such as highly strained GaAs clusters which we believe to be generated on the GaSb surface by exposing the surface to As_2 beam flux during the nucleation process of InAs layer.

In summary, the surface morphology of InAs films grown on GaSb buffered GaAs substrates has been studied. Unstable mode growth has been observed on films grown on singular substrates at relatively low substrate temperatures. Unlike what has been observed on MBE grown GaAs films, the mounds on an InAs singular surface which formed due to growth instability were found to be isotropic. This means that the adatom diffusion, sticking probabilities, and Schwoebel barriers on InAs(0 0 1) surface are isotropic. The higher nucleation temperature (above 460°C) will result in relatively high density pits which we believe are due to the surface defects, such as highly strained GaAs clusters generated on the GaSb surface by exposing the surface to As_2 beam flux during the nucleation process of InAs layer.

This work has been supported by RGC Competitive Earthmarked Research Grant: grant No. HKUST6 1 3/95P and by MFG grant: grant No. MFG94/95.SC03.

References

[1] C. Orme, M. Johnson, J.L. Sudijono, K.T. Leung and B.G. Orr, Appl. Phys. Lett. 64 (1994) 860.

[2] Makoto Kasu and Naofi Kobayashi, Jpn. Appl. Phys. 33 (1994) 712.

[3] A.W. Hunt, C. Orme, D.R.M. Williams, B.G. Orr and L.M. Sander, Europhys. Lett. 27 (1994) 611.

[4] Junmimg Zhou, Qikun Xue, Hideo Chaya, Tomihiro Hashizume and Toshio Sakurai, Appl. Phys. Lett. 64 (1994) 583.

[5] H. Yamaguchi and Y. Horikoshi, Appl. Phys. Lett. 64 (1994) 2572.

[6] R.L. Schwoebel and E.J. Shipsey, J. Appl. Phys. 37 (1966) 3682.

[7] F. Borions, D. Golmayo, L. Gonzales and J.L. de Miguel, Jpn. Appl. Phys. 24 (1985) L478.

ELSEVIER

Journal of Crystal Growth 175/176 (1997) 1294–1298

JOURNAL OF CRYSTAL GROWTH

Luminescence anomaly in band gap tailored $In_{0.53}(Ga_xAl_{1-x})_{0.47}As$ quaternary alloy grown by molecular beam epitaxy

A. Ramam*, S.J. Chua

Department of Electrical Engineering, Centre for Optoelectronics, National University of Singapore, 10 Kent Ridge Crescent, Singapore 119260, Singapore

Abstract

$In_{0.53}(Ga_xAl_{1-x})_{0.47}As$ epilayers with band gap energy varying from 0.78 to 1.42 eV are grown lattice matched to InP substrate by MBE technique. The lattice mismatch and crystalline quality of the layers are assessed by the double crystal X-ray diffraction and the lattice vibrations due to the three binary compounds in the alloy are observed in the Raman spectra. Photoluminescence studies in the range 4–100 K showed an anomalous "inverted S" shaped variation in the PL energy versus temperature plot for epilayers with Al mole fraction less than 0.2. For mole fraction greater than 0.2, the characteristic dip in the energy values disappears and the normal band gap energy versus temperature relation is restored. Strong localization of excitons is associated with such a behavior in Al rich InGaAlAs epilayers.

PACS: 81.05.Ea; 81.15.Hi; 78.55.Cr

Keywords: Molecular beam epitaxy; Photoluminescence; Exciton; Quaternary alloy; Lattice matching

1. Introduction

The III–V group of semiconductors are of potential importance in high-speed electronics and optoelectronics applications. The "arsenide" based ternaries ($Al_{0.48}In_{0.52}As$ and $Ga_{0.47}In_{0.53}As$) and quaternary ($In_{0.53}(Ga_xAl_{(1-x)})_{0.47}As$) alloy materials are an attractive alternative to the phosphide based (InGaAsP) material system covering the wavelength range of 1.1–1.7 μm. The band gap of InGaAlAs alloy can be engineered between the emission wavelengths of the two bounding ternary alloys namely: $In_{0.53}Ga_{0.47}As$ (0.76 eV, 1.63 μm) and $In_{0.52}Al_{0.48}As$ (1.46 eV, 0.85 μm), and can be an alternative to the InGaAsP quaternary material. With the conventional solid source MBE technique, the growth of InGaAlAs alloy is relatively easier than InGaAsP due to the following reasons: (a) only one group V element (As) is incorporated, avoiding the problem of As/P ratio control, (b) composition of the layer is controlled by each constituent element's flux intensity, as noted by Ohno

* Corresponding author. Fax: + 65 7791103; e-mail: elera@leonis.nus.sg.

0022-0248/97/$17.00 Copyright © 1997 Elsevier Science B.V. All rights reserved
PII S0022-0248(96)01036-6

et al. [1] and (c) near-unity sticking coefficients of the three group III elements facilitate reproducibility of composition. The growth of lattice matched InGaAlAs alloy on InP substrates by MBE technique was first reported by Barnard et al. [2] and subsequently, the material was improved in its optical and crystal properties by other workers [3–6]. Olego et al. [7] developed an empirical expression between the band gap and composition of the alloy, suggesting that the alloy is a pseudo-binary of the two ternary materials. Most of the previous works on the MBE growths, incorporated pulse techniques [8] or two In/two Al cells [9, 10]. In our present work we have used one cell for each element and grown state-of-the art epilayers of InGaAlAs, as indicated by photoluminescence (PL) and double crystal X-ray diffraction (DCXD) results. These well characterized epilayers are studied under a temperature variation of 4–300 K at varying excitation power levels in PL experiments.

2. Experimental procedure

The quaternary alloy epilayers of $In_{0.53}(Ga_xAl_{1-x})_{0.47}As$ were grown in a solid source MBE system (RIBER 32P model), with source elements of purity greater than 5 N. The In Beam Equivalent Pressure (BEP) was kept constant at 3.3×10^{-7} mbar and Ga/Al BEP ratio was varied such that the band gap energy of the layers could be tailored, whilst keeping them lattice matched to the InP substrate. All the epilayers are grown to a constant thickness of 1.5 μm and at a constant substrate temperature of 510°C. The layers were characterized for lattice mismatch and crystalline quality on a double crystal X-ray diffractometer and the Raman spectra were observed on a Renishaw micro Raman system fitted with a high sensitive Charge Coupled Device (CCD) detector. The PL studies were made in a low-temperature closed loop He cryostat with argon laser as the exciting source and with Photo-Multiplier Tube (PMT), lock-in amplifier comprising the measurement setup for detecting the PL signal.

3. Results

$In_{0.53}(Ga_xAl_{1-x})_{0.47}As$ epilayers with Al composition varying from 0.05 to 0.45 were grown lattice matched to InP substrate under a normalized In flux of 0.46. The normalized In flux is defined as the ratio of In flux to the total group III fluxes. The lattice mismatch obtained for the independently grown InGaAlAs epilayers is within 0.03%, with FWHMs in the range 20–35 arcsec. The band gap of the material was estimated from the RT photoluminescence (PL) peaks, as shown in Fig. 1, and were observed to vary from 0.78 eV to 1.42 eV with FWHMs in the range 30–100 meV. Peaks at 1.35 and 1.42 eV, however, are not shown in the figure due to their broad FWHMs. Table 1 shows the various growth parameters used for forming the varying band gap energy InGaAlAs epilayers.

The results obtained by DCXD and PL characterization indicate high crystalline and optical quality of the $In_{0.53}(Ga_xAl_{1-x})_{0.47}As$ epilayers. Raman spectra of the samples showed distinct phonon vibrational mode peaks of the three binary (InAs, GaAs and AlAs) compounds with the intensity ratios being equivalent to the mole fraction of the elements in the alloy. Fig. 2. shows the Raman spectra of various epilayers with a noticeable shift in the peak positions due to the variation in alloy composition.

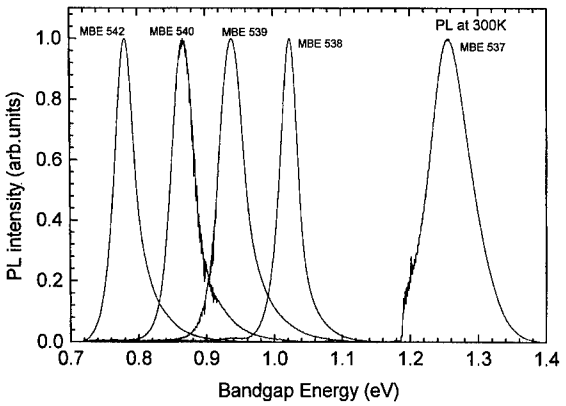

Fig. 1. Room temperature photoluminescence peaks of band gap engineered samples. The peak values vary from 0.78 to 1.26 eV.

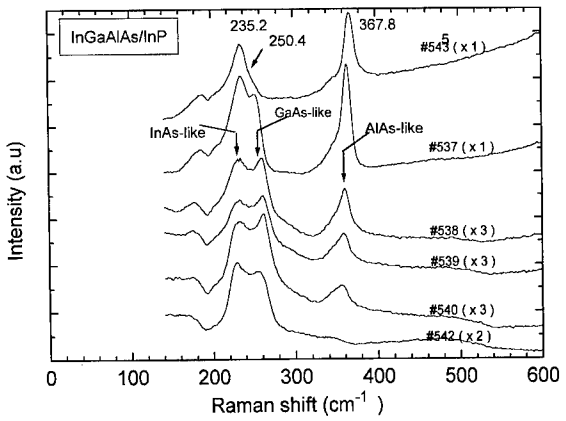

Fig. 2. Raman spectra of various InGaAlAs samples for different Al mole fraction in the alloy.

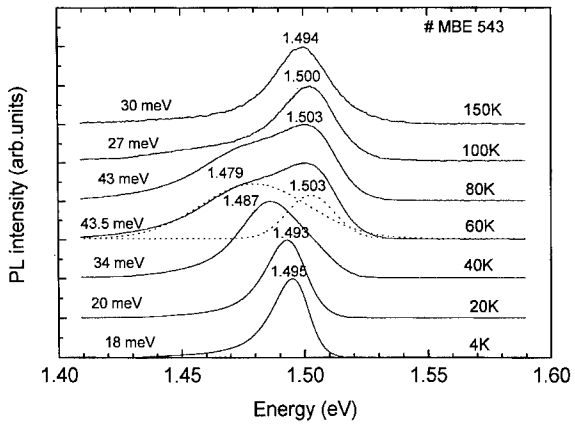

Fig. 3. PL spectra of sample # 543 at temperatures < 150 K and constant excitation power.

In the PL spectra, an interesting phenomenon of "inverted S" shaped behavior is observed in the variation of PL energy with temperature in the range 4–100 K. Initially as the temperature is raised from 4 to 30 K, a red shift is observed in the energy peaks. Between 30 and 80 K a blue shift occurs and beyond that the normal red shift takes over following the Varshni's equation [11] for band-to-band transition. This anomalous temperature dependence was first observed by Kondow and Minagawa [12] in $Ga_{0.5}In_{0.5}P/GaAs$ samples and the probable cause was related to the crystal defects in the epilayer. Olsthoorn et al. [13] and Ferguson et al. [14] observed similar phenomena in lattice matched InAlAs material and called the anomaly as "inverted S" shaped dependence. However, in this case the observations were related to the localization of excitons.

For sample #543 with Al = 0.42 and Ga = 0.05, the 4K PL spectrum shows a strong peak due to the bound exciton transition, at 1.495 eV with a FWHM of 18 meV. Deconvolution of the single peak suggests that in addition to the bound exciton transition, impurity levels, free exciton and band-to-band transitions are also built in. With increase in excitation power the peak intensities rise with the peak position remaining at a constant value. However, at high power levels a small peak develops at the high-energy side of the spectrum due to free exciton or band-to-band transitions with the bound exciton intensity tending to saturate. In Fig. 3, the PL spectra of sample #543 at variable temperatures are shown. On varying the temperature from 4 to 40 K the peak energy position is observed to shift to lower energy values. At 40 K

Table 1
Various growth parameters used for growing InGaAlAs epilayers BEPs given in the units of mbar

Sample	Ga	Al	In	J_{Ga}/J_{Al}	E_g (eV)
#543	1.3×10^{-8}	1.0×10^{-7}	4.3×10^{-7}	0.07	1.42
#364	4.0×10^{-8}	9.4×10^{-8}	4.3×10^{-7}	0.23	1.34
#537	5.2×10^{-8}	8.0×10^{-8}	4.3×10^{-7}	0.35	1.26
#538	1.2×10^{-7}	5.0×10^{-8}	4.3×10^{-7}	1.28	1.02
#539	1.3×10^{-7}	3.9×10^{-8}	4.3×10^{-7}	1.80	0.94
#540	1.6×10^{-7}	2.6×10^{-8}	4.3×10^{-7}	3.20	0.87
#542	1.4×10^{-7}	9.0×10^{-9}	3.3×10^{-7}	8.40	0.78

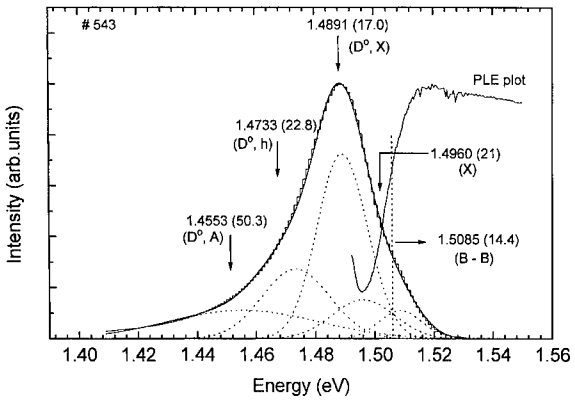

Fig. 4. PL and PLE spectra superimposed for sample # 543 at $T = 4$ K.

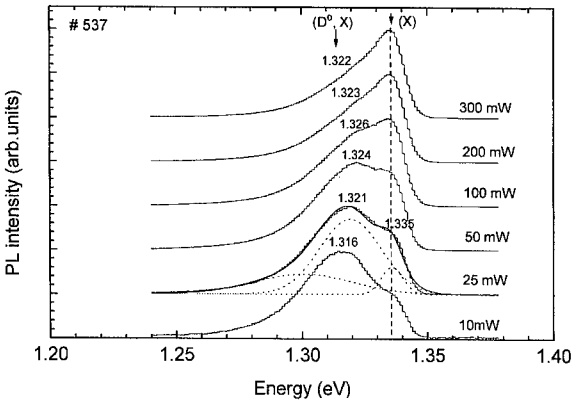

Fig. 5. PL spectra of sample # 537 at $T = 4$ K for variable excitation power levels.

the bound exciton partially converts to free exciton and a sudden shift towards the higher energy is observed. During this temperature range the free and bound excitons co-exist and two distinct peaks can be visualized. Up to about 80 K the free exciton dominates over the bound exciton and finally the latter quenches off at about 100 K. Beyond this temperature up to 300 K the band-to-band transition takes over and the Varshni's equation is obeyed.

The difference in energies at 4 K, between the observed values and that obtained by Varshni's equation is about 28.3 meV. The binding energies calculated by the expressions given by Goetz et al. [15] can account for only 11 meV ($E_x = 4.2$ meV, $E_D = 6.8$ meV). The excess energy of 17.3 meV is thus associated with the localization of excitons to some unknown energy levels. Fig. 4 shows the superposition of PL spectrum and the PLE spectrum which is detected at the emission peak of bound exciton. The absorption threshold in the PLE spectrum is attributed to the band edge transition which corresponds to the high energy peak of the deconvoluted PL spectrum. In sample #538 (Al = 0.2, Ga = 0.26) the energy peak observed at 4 K is due to the free (carrier) exciton and does not show any dip in energy values with the variation of temperature up to 300 K. At low excitation power levels the bound and free excitation transitions co-exist, but at high power levels the peak observed is completely dominated by free

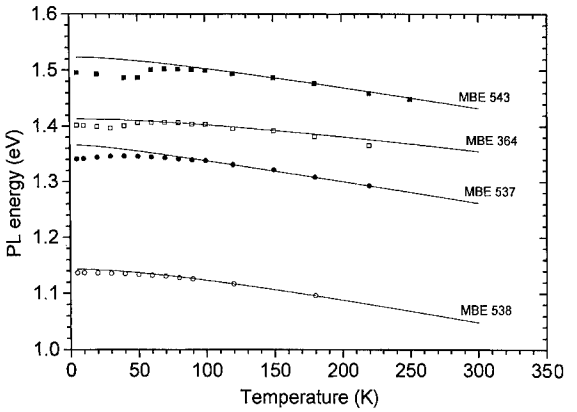

Fig. 6. Combined plot of PL energy versus temperature of samples indicating the progressive change in the "inverted S" behavior.

exciton transition. In Fig. 5 the PL spectra of #538 at different excitation power levels are shown. Finally in sample #539 (Al = 0.17, Ga = 0.30), the peak observed at 4 K is due to the band-to-band transition and hence in the temperature variation upto 300 K, the trend follows the Varshni's band gap versus temperature relation. Fig. 6 shows the combined plot of all the samples in the PL energy versus temperature. For high Al content layers, the tendency to localize exciton strongly to an energy level below the excitonic levels is high due to the highly reactive nature of Al. It is estimated that for Al < 0.2 the characteristic dip in energy totally disappears.

4. Conclusions

InGaAlAs epilayers are grown lattice matched to InP substrate with band gap tailored between 0.78 and 1.42 eV. For Al rich layers strong localization of excitons is proposed since the energy discrepency at 4 K between the observed values and that predicted by the unknown excitonic energies is large. Due to the highly reactive nature of Al, certain energy levels are formed in Al rich InGaAlAs layers which tend to localize the excitons.

References

[1] H. Ohno, J. Bernard, C.E.C. Wood and L.F. Eastman, IEEE Electron. Dev. Lett. 1 (1980) 154.
[2] J.A. Barnard, C.E.C. Wood and L.F. Eastman, IEEE Electron Dev. Lett. 3 (1982) 318.
[3] Kazuya Masu, Tomoyoshi Mishima, Shin-ichiro Hiroi, Makoto Konagai and Kiyoshi Takahashi, J. Appl. Phys. 53 (1982) 7558.
[4] J.P. Praseuth, M.C. Joncour, J.M. Gerard, P. Henoc and M. Quillec, J. Appl. Phys. 63 (1988) 400.
[5] F. Genova, G. Moello and C. Rigo, J. Vac. Sci. Technol. B 5 (1987) 811.
[6] Albert Chin, Pallab Bhattacharya, Won-Pyo and Wei-Qi Li, J. Vac. Sci. Technol. B 6 (1988) 665.
[7] D. Olego, T.Y. Chang, E. Silberg, E.A. Caridi and A. Pinczuk, Appl. Phys. Lett. 41 (1982) 476.
[8] Toshio Fuji, Yoshiaki Nakata, Yoshihiro Sugiyama and Satoshi Hiyamizu, Jpn. J. Appl. Phys. 25 (1986) L254.
[9] L. Goldstein, J.P. Praseuth, M.C. Joncour, J. Primot and P. Henoc, J. Crystal Growth 81 (1987) 396.
[10] M. Quillec, M. Allovon, F. Brillouet, A. Gloukhian, J.P. Praseuth and B. Sermage, Electron. Lett. 25 (1989) 1731.
[11] Y.P. Varshni, Physica 34 (1967) 149.
[12] Masahiko Kondow and Shigekazu Minagawa, Appl. Phys. Lett. 54 (1989) 1760.
[13] S.M. Olsthoorn, F.A.J.M. Driessen, A.P.A.M. Eijkelenboom and L.J. Giling, J. Appl. Phys. 73 (1993) 7798.
[14] I.T. Ferguson, T.S. Cheng, C.M. Sotomayor Torres and R. Murray, J. Vac. Sci. Technol. B 12 (1994) 1319.
[15] K.H. Goetz, D. Bimberg, H. Jurgensen, J. Selders, A.V. Solomonov, G.F. Glinski and M. Razeghi, J. Appl. Phys 54 (1983) 4542.

ELSEVIER

Journal of Crystal Growth 175/176 (1997) 1299–1302

JOURNAL OF CRYSTAL GROWTH

Full wafer optical characterisation of resonant tunnelling structures using photoluminescence excitation spectroscopy

P.D. Buckle[a,*], P. Dawson[a], M. Missous[b], W.S. Truscott[b]

[a] *Department of Physics, Institute of Science and Technology (UMIST), University of Manchester, P.O. Box 88, Manchester M60 1QD, UK*
[b] *Department of Electrical Engineering and Electronics, Institute of Science and Technology (UMIST), University of Manchester, P.O. Box 88, Manchester M60 1QD, UK*

Abstract

We report on a novel optical technique for accurately characterising unprocessed GaAs/AlGaAs tunnelling structures having two or more thin barriers and thick, heavily doped, contact layers. The results from photoluminescence excitation spectroscopy measurements are presented in which the intensity of the photoluminescence from the heavily doped contact layers rather than photoluminescence from the quantum wells is monitored. This method gives essential information for growth and quality control of "as-grown" layers prior to device fabrication. The usefulness and precision of this technique is illustrated by the measurement of a 0.3% variation in layer thickness from the centre to the edge of an as-grown wafer, and a 1% wafer to wafer variation in layer thickness in a series of triple barrier resonant tunnelling structures that have been designed for use at THz frequencies.

PACS: 73.20.Dx; 71.55.Eq; 71.70. – d

1. Introduction

The capability of molecular beam epitaxy (MBE) for high precision growth of thin film structures has enabled the fabrication of many types of complex tunnelling structures. The ease with which such structures can be exploited commercially will be improved when it is possible for the as-grown wafers to be accurately and non-destructively characterised, without expensive, time-consuming processing and electrical measurements. As-grown wafer characterisation should provide essential feedback as rapidly as possible in order to control the growth of subsequent wafers. In particular, the accurate determination of quantum well thicknesses is extremely important, as device designs seek to exploit the full capability of MBE growth [1, 2]. Low-temperature photoluminescence spectroscopy has been shown to be a powerful tool for studying various characteristics of resonant tunnelling devices [3–6], but the problem of measuring as-grown (no applied bias) wafer material remains problematic. In general at low temperatures, for as-grown structures which contain a small number

* Corresponding author. Fax: + 44 161 2004770; e-mail: buckle@fs4.ee.umist.ac.uk.

0022-0248/97/$17.00 Copyright © 1997 Elsevier Science B.V. All rights reserved
PII S0022-0248(96)01038-X

of quantum wells and thin barriers, very little or no photoluminescence is observed from the quantum well regions. This is because photo-injected carriers rapidly escape from the quantum well before any significant recombination can occur. For example, the electron escape time for a 70 Å GaAs quantum well confined by 50 Å $Al_{0.3}Ga_{0.7}As$ barriers is of the order of 1 ps, whereas the exciton recombination time is of the order of 1 ns [7].

This paper presents results of a novel variant of photoluminescence excitation spectroscopy for characterising as-grown wafers that are to be processed into triple barrier tunnelling devices. The technique involves monitoring the luminescence intensity from the contact layers of the wafer instead of from the well regions. Strong well-resolved exciton transitions were observed from the quantum wells. These spectra were used to determine quantum well widths prior to processing and to monitor the uniformity of quantum well thickness across 50 mm diameter wafers.

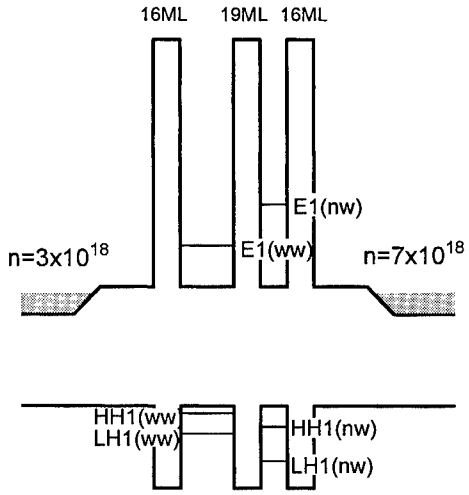

Fig. 1. Schematic potential profile showing lowest lying electron and hole subband levels within the active region of a triple barrier resonant tunnelling structure. The shaded regions indicate the heavily doped layers.

2. Experimental procedure

The samples studied come from a set of closely related triple-barrier resonant tunnelling structures that have been designed for use as ultra high speed devices (THz) which demand very high precision growth for successful operation [2]. The electron energy subband spacing in these devices, for THz operation, must be the order of only 4 meV. Therefore, sharply defined energy states with minimal broadening are critical. The structures were grown without interruption at 0.85 μm/h on 50 mm semi-insulating GaAs substrates in a VG Semicon V90H system using conventional Ga and Al cells and a solid source cracker producing As_2. The layer sequence was as follows: (i) 1 μm n^+ ($N_{Si} = 3\times10^{18}\,cm^{-3}$) GaAs lower contact layer (ii) 100 Å n($N_{Si} = 3\times10^{17}\,cm^{-3}$) GaAs layer (iii) 100 Å undoped GaAs spacer (iv) 16 monolayer (ML) $Al_{0.33}Ga_{0.67}As$ barrier (v) undoped wide GaAs quantum well (WW) (vi) 19 ML $Al_{0.33}Ga_{0.67}As$ barrier (vii) undoped GaAs quantum well with either the same thickness as the WW or a narrower quantum well (NW) (viii) 16 ML $Al_{0.33}Ga_{0.67}As$ barrier (ix) 200 Å GaAs spacer layer (x) $5\times10^{12}\,cm^{-2}$ Si δ-doped GaAs (xi) 0.5 μm n^+ ($N_{Si} = 7\times10^{18}\,cm^{-3}$) upper contact layer. For the purposes of this discussion, the structures grown with both quantum wells of the same nominal thickness are referred to as symmetric structures, while those with quantum wells with different thicknesses are referred to as anti-symmetric structures. The growth temperature was 580°C for layers (i)–(ix) and was reduced to 540°C for layers (x) and (xi). A schematic of the band alignment for these structures is shown in Fig. 1, which includes the $n = 1$ electron, heavy hole and light hole confined states, and an indication of the heavily doped contact regions.

For the optical measurements the as-grown wafers were mounted on the cold finger of a variable temperature closed cycle helium cryostat. Light from a chopped Ar^+ pumped Ti : Sapphire laser was focused onto the wafer (spot size ~100 μm diameter) with typical power densities of 50 W/cm². The power density was small enough that no sample heating effects were observed, nor was there any change in the current through 80 μm square mesa devices with 50 μm square windows. The resulting luminescence was dispersed by a 0.75 m double grating spectrometer (SPEX 1404) and

detected by a thermoelectrically cooled GaAs photomultiplier. The signal was then processed by a conventional lock-in amplifier.

3. Results and discussion

In Fig. 2a is shown a photoluminescence spectrum from an as-grown wafer containing a symmetric well triple barrier structure with both quantum wells having a nominal thickness of 23 ML. We would expect the WW quantum well emission to occur at an energy around 1.580 eV. As can be seen from the spectrum we observe no emission from the quantum well due to the fast carrier escape discussed earlier but we observe strong emission bands at 1.530 and 1.490 eV. The broad emission at 1.530 eV is identified as being due to band-to-band recombination from the heavily doped n-type contact layers, with a clearly defined Fermi-energy labelled E_f. The emission process at 1.495 eV is identified as band-to-acceptor recombination. When excitation spectroscopy measurements are made on this sample over an energy range 1.550–1.660 eV, while detecting the band-to-band recombination from the contact layers, we observe the spectrum as shown in Fig. 2(b). The form of this spectra is not sensitive to the detection energy across the whole broad band–band luminescence

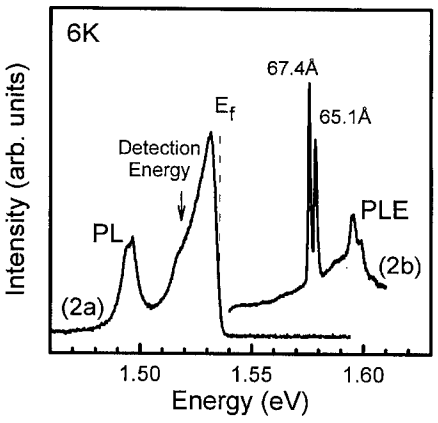

Fig. 2. (a) Photoluminescence spectrum of the nominally 23/23 ML structure wafer. (b) Photoluminescence excitation spectrum of the nominally 23/23 ML wafer, detected on the GaAs contact, band–band luminescence.

feature. The two groups of lines around 1.578 and 1.600 eV are identified as involving $n = 1$ electron to $n = 1$ heavy hole transitions and $n = 1$ electron to $n = 1$ light hole transitions, respectively. The mechanism for the observation of these signals is that photocreated electron/hole pairs and excitons in the quantum wells escape rapidly to the doped contact layers, resulting in an increase of the luminescence from the heavily doped contact region. The precise nature of the splitting of the two groups in this symmetric well sample is not yet clear. The splitting could be associated with symmetric and antisymmetric states of the $n = 1$ electron state or could be due to the two quantum wells having an effective well thickness different by 2.3 Å. The precise identification of these features is not as important as the main issue of this paper, which is that although it is not possible to detect photoluminescence from the quantum wells in an as-grown wafer, it is possible to measure quantum well optical transitions by using excitation spectroscopy and detecting luminescence from the contact layers. The usefulness of this characterisation technique is shown in Fig. 3. In this figure are shown a series of eleven PLE spectra taken in a uniformly spaced scan at radii from 5 to 22 mm on a 50 mm diameter wafer incorporating an asymmetric well triple barrier tunnelling structure. The peaks correspond to the $n = 1$ electron-heavy hole exciton transitions in each of the wells whose widths are calculated to be 69.1 Å and 66.2 Å. Further peaks are observed, attributed to $n = 1$ electron-light hole exciton transitions, but are not shown in Fig. 3. The extreme variation in the position of the lowest energy peak over the scan is 0.3 meV (average line width of 1.05 meV). This corresponds to a variation in the effective width of the quantum wells of only 0.3%. These data demonstrate the high uniformity afforded by the V90H MBE system, originally designed for multiple 2″ or single 4″ wafers, in growing uniform structures over large areas. The uniformity demonstrated (0.3%) is to an extent well below what is required by device processors (typically $\pm$ 1%). For a series of eight TBRTS, where the WW quantum well was maintained at a nominal 23 ML and the NW quantum well ranged from 23 ML down to 16 ML the wafer-to-wafer variation in WW width was only 1%.

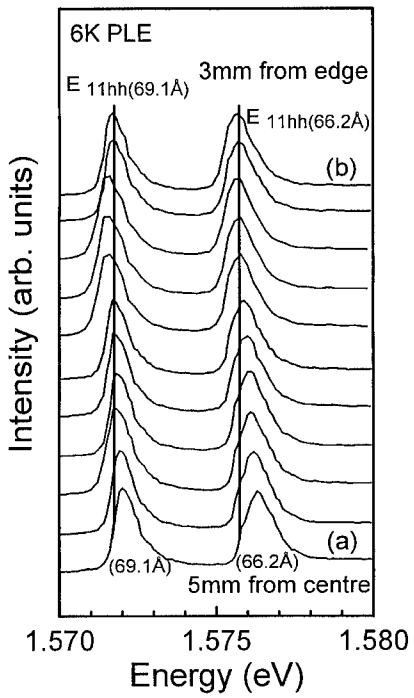

Fig. 3. A series of photoluminescence excitation spectra obtained from different points across a 50 mm diameter wafer. Spectrum (a) is taken at a point 5 mm from the centre and spectrum (b) is taken at a point 3 mm from the edge.

To emphasise the significance of this data it demonstrates:

(1) The uniformity of the quantum well thickness across the majority of the slice.

(2) The usefulness of the technique in that accurate characterisation of multi barrier tunnelling structures can be applied to whole wafers without any sample processing.

This technique has been successfully used for a variety of triple barrier resonant tunnelling structures with differing well widths ranging from 24 ML (68 Å) down to as low as 9 ML (25 Å), and differing barrier aluminium concentrations of 33%, 29.5% and 26%. In the case of these highly asymmetrical narrow well structures, $n = 1$ electron-heavy hole transitions are observed at energies up to 1.725 eV.

4. Conclusion

We have demonstrated a high-resolution method for characterising multiple barrier resonant tunnelling structure wafer material. By monitoring the photoluminescence intensity from the heavily doped contact region we have used PLE on wafers to determine the quantum well transition energies. The important point to emphasise is that without any sample processing it is not possible to detect any photoluminescence from the quantum wells of such structures. The sensitivity of this technique has been demonstrated by conducting a detailed characterisation of a series of unprocessed wafers which include high-quality triple barrier resonant tunnelling devices. The measurements have been used to give valuable information about wafer uniformity and quality together with an accurate measurement of the lowest lying electron-heavy hole and electron-light hole transition energies.

References

[1] J. Faist, F. Capasso, C. Sirtori, D.L Sivco, A.L. Hutchinson, S.N.G. Chu and A.Y. Cho, Electron. Lett. 29 (1993) 2230; J. Faist, F. Capasso, D.L. Sivco, A.L. Hutchinson and A.Y. Cho, Science. 264 (1994) 553; J. Faist, F. Capasso, C. Sirtori, D.L. Sivco, A.L. Hutchinson, M. Hybertsen and A.Y. Cho, Phys. Rev. Lett. 76 (1996) 411.

[2] W.S. Truscott, Solid State Electron. 37 (1994) 1235.

[3] J.F. Young, B.M. Wood, G.C. Aers, R.L. Devine, H.C. Liu, D. Landheer, M. Buchanan, A. Springthorpe and J. Mandeville, Phys. Rev. Lett. 60 (1988) 2085.

[4] M.S. Skolnick, D.G. Hayes, P.E. Simmonds, A.W. Higgs, G.W. Smith, H.J. Hutchinson, C.R. Whitehouse, L. Eaves, M. Henini, O.H. Hughes, M.L. Leadbeater and D.P. Halliday, Phys. Rev. B. 41 (1990) 10754.

[5] M.S. Skolnick, P.E. Simmonds, D.G. Hayes, A.W. Higgs, G.W. Smith, A.D. Pitt, C.R. Whitehouse, H.J. Hutchinson, C.R.H. White, L. Eaves, M. Henini and O.H. Hughes, Phys. Rev. B. 42 (1990) 3069.

[6] T.K. Woodward, D.S. Chemla, I. Bar-Joseph, H.U. Baranger, D.L Sivco and A.Y. Cho, Phys. Rev. B. 44 (1991) 1353.

[7] J. Feldmann, G. Peter, E.O. Göbel, P. Dawson, K. Moore, C. Foxon and R.J. Elliot, Phys. Rev. Lett. 59 (1987) 2337.

ELSEVIER

Journal of Crystal Growth 175/176 (1997) 1303–1308

JOURNAL OF CRYSTAL GROWTH

Scanning tunneling spectroscopy and first-principles investigation on GaAs(0 0 1)(2 × 6)-S surface formed by molecular beam epitaxy

Shiro Tsukamoto*, Takahisa Ohno, Nobuyuki Koguchi

National Research Institute for Metals, 1-2-1 Sengen, Tsukuba, Ibaraki 305, Japan

Abstract

The surface reconstruction of, in situ prepared, S-terminated GaAs (0 0 1) is studied by scanning tunneling microscopy and a first-principles pseudopotential method. According to an electron counting model, in order to form this (2 × 6)-S on GaAs (0 0 1) surface, one electron needs to be transferred from each S dimer to the Ga dangling bonds on the missing dimer region. As a result of the first-principles investigation on the S–S bond length of one S dimer, the separations are calculated as 0.2370 nm and 0.3897 nm, with and without one electron transfer, respectively. Experimental result agreed well with the former condition. This indicates that there may be a long-range electron transfer on this (2 × 6) structure. Moreover, the calculated electronic structure of this S dimer with one electron transfer shows a flat unoccupied band which is mainly caused by the antibonding band of the S–S bond. This result also agreed well with conductivity spectrum of this (2 × 6) surface by scanning tunneling spectroscopy, which shows a peak on the conduction band side.

PACS: 81.65. – b; 07.79.Cz; 31.15.Ar; 73.20.At

Keywords: Gallium arsenide; (2 × 6)-S; Multi-step; Sulfur termination; In vacuum; Annealing; Scanning tunneling microscopy; Scanning tunneling spectroscopy; Molecular beam epitaxy; Density functional calculations; Surface energy; Surface relaxation and reconstruction

1. Introduction

The sulfur-terminated (S-terminated) GaAs (0 0 1) surface is an important factor in droplet epitaxy which is a useful technique for fabricating quantum dot structures [1]. In order to establish this technique and to understand the droplet growth mechanism, the details of the S-terminated surface reconstruction needs to be investigated.

The (2 × 1) surface reconstruction is generally understood to be that of the S-terminated GaAs (001) surface as measured by low-energy electron diffraction (LEED) and reflection high-energy electron diffraction (RHEED) studies [2, 3]. However, this 2 × 1 reconstruction is a rather diffused streaky pattern with diffused transmission spots, which is due to the surface roughness caused by the etching

* Corresponding author. Fax: + 81 298 53 1093; e-mail:tsuka@nrim.go.jp.

0022-0248/97/$17.00 Copyright © 1997 Elsevier Science B.V. All rights reserved
PII S0022-0248(96)01183-9

effect of a sulfide solution such as Na_2S [4], $(NH_4)_2S$ [5, 6], and $(NH_4)_2S_X$ [6]. Moreover, there are few reports of scanning tunneling microscopy (STM) images of such a surface [7, 8]. Therefore, under these conditions, it is unwise to say that the (2×1) surface reconstruction is dominant on the S-terminated GaAs(0 0 1) surface.

Recently, we have developed a novel fabrication method for the S-terminated GaAs (0 0 1) surface, with exposure to S vapor in a molecular beam epitaxy (MBE) system [9, 10]. Using this method, the S-terminated GaAs surface is formed without exposure to air or etching the surface. In this case, a diffused (2×1) structure is not observed in RHEED, only the (2×6) forms are observed after exposure to S vapor and annealing [9, 10]. Moreover, we have demonstrated that a (2×6) is dominant on the S-terminated GaAs (0 0 1) surface by STM [11, 12] and high-temperature STM observations [13]. Even on the $(NH_4)_2S_X$ treated [12] and H_2S irradiated [14] GaAs (0 0 1) surfaces, (2×6) structure was observed. Despite all these experimental works, the passivation mechanism of the GaAs surface is still not clearly understood. Knowledge of the actual atomic configurations at the S-terminated surface and the corresponding electronic structures remains insufficient.

Therefore, in this paper, we study this (2×6) structure with a scanning tunneling spectroscopy (STS) technique and a first-principles pseudopotential method. The structural and electronic properties of GaAs(0 0 1) surfaces covered with an adsorbed monolayer of S atoms are discussed with the experimental and theoretical results.

2. Termination process

In this study, the two vacuum systems, MBE and STM, are separated by air. The MBE system is a conventional ANELVA-620 with a sample introduction chamber, in which a valved knudsen cell charged with elemental S is installed. The background pressure of the sample introduction chamber is 6×10^{-6} Pa.

The Si-doped GaAs(001) 1° off $\langle 1\,1\,1 \rangle$A ($n = 2 \times 10^{18}\ cm^{-3}$) sample is prepared by standard solvent cleaning and etching procedures, and then loaded into the MBE chamber. An undoped GaAs buffer layer of 0.2 μm was grown at 590°C, resulting in smooth one-monolayer-stepped terraces. Then, the sample was processed with multi-step S termination method [15]. This method reduces the ununiformity of surface reconstructions, realizing the S-termination on the Ga-stabilized surface with a coverage of 1 [13]. The process of this method is as follows. First, the substrate temperature has decreased to room temperature with c (4×4) As-adsorbed surface shown in the Fig. 1a. Next, the sample was immediately transferred into the MBE sample introduction chamber and exposed to the S vapor, which generates a chamber pressure of 4×10^{-4} Pa for 3 min (Fig. 1b). Then,

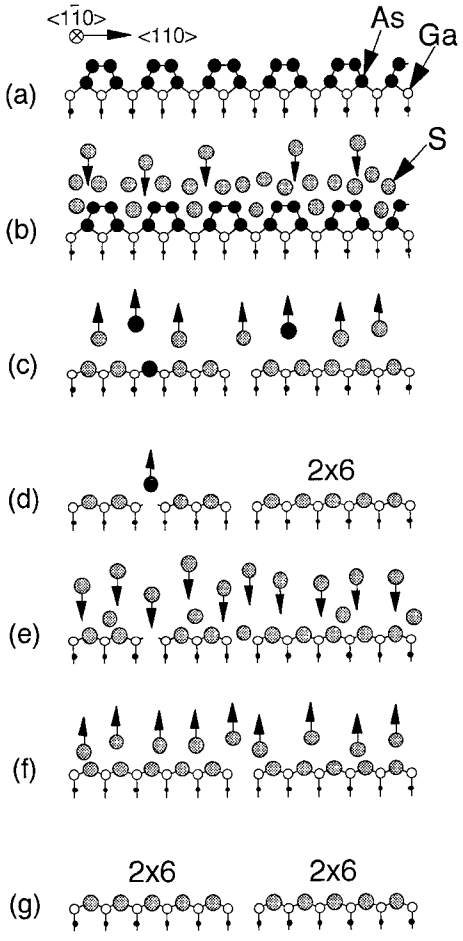

Fig. 1. Multi-step S termination process.

the sample was transferred into the MBE growth chamber and annealed at 370°C for 30 min without the As molecular-beam flux (Fig. 1c). Because of the difference of bond energies of S–Ga and As–Ga, at this temperature, only the As atoms remaining upon the Ga layer were desorbed (Fig. 1d). Then, again, repeating the same process, the sample was cooled down, exposed to the S vapor (Fig. 1e), and annealed at 370°C for 30 min (Fig. 1f). This second step of the S-termination filled the escaped holes of As atoms and realized the highly uniform (2×6) surface reconstruction (Fig. 1g). After the sample was cooled down to about 10°C and again transferred into the MBE sample introduction chamber, it was exposed to the S vapor, which generates a chamber pressure of 8×10^{-3} Pa, at room temperature for 5 min, forming the thick S protective layer [13]. The sample was then transferred from the MBE system through air to the STM apparatus.

The STM (JEOL-JSTM4500VT) is a multichamber UHV system. There are a sample introduction chamber, a treatment chamber with RHEED, and a STM main chamber. The background pressure of both the treatment chamber and the STM main chamber is 1×10^{-8} Pa. In the STM main chamber, the sample was directly heated by an electric current and the temperature was measured with an optical pyrometer having a detection wavelength of 2 μm. The removal process of the protective layer has been described elsewhere [11, 13]. The STM measurements were performed in the constant current mode and the STM images were taken at a sample bias voltage of -3 V relative to the tip and a constant tunneling current of 0.2 nA. The tips are electrochemically etched tungsten wires.

3. Calculation methods

We performed total-energy calculations by using the local density functional (LDF) approach. The total energy function is minimized with respect to both the plane-wave coefficients of the occupied orbitals and the ionic degrees of freedom by using the conjugate-gradient technique [16]. The pseudo wavefunctions are expanded in terms of a plane-wave basis set corresponding to a kinetic-energy

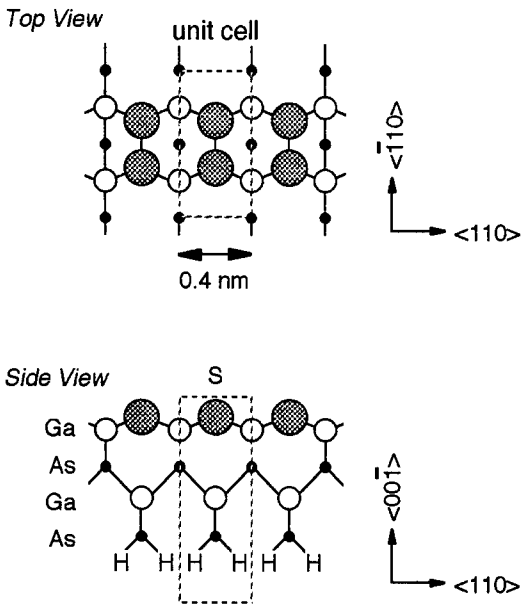

Fig. 2. A slab geometry for first-principles pseudopotential calculation. S–S bond length with and without one electron transfer in one S dimer was investigated.

cutoff of 7.29 Ry. Four special k points are employed to sample the primitive surface Brillouin zone. The surface is simulated by a slab geometry shown in Fig. 2. This model uses supercells containing one sulfur layer, two layers of GaAs, and one layer of hypothetical hydrogen used for the surface termination [17]. It is found that the energy cutoff of 7.29 Ry and the supercell containing five atomic layers are sufficient to achieve the convergence of energy differences within 0.1 eV. Here, we only focus on a (2×1) unit because a (2×6) unit is too large for the calculation. Then, with and without one electron transfer from this (2×1) unit, the (2×6) and (2×1) cases are discussed, respectively.

4. Results and discussion

At first, in order to evaluate the slab geometry for calculation, we compared an S–S bond length from STM results with that from the theoretical calculation. From the STM observation, it was found

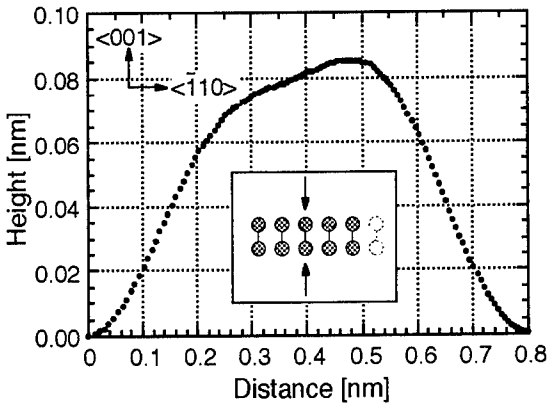

Fig. 3. Cross-section of S dimer in (2 × 6)-S at a sample bias voltage of −3V relative to the tip and a constant tunneling current of 0.2 nA.

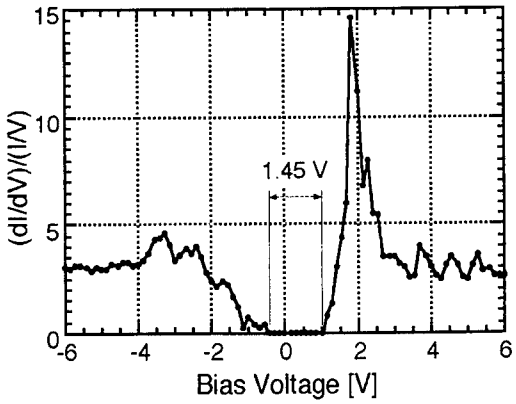

Fig. 4. Conductivity spectrum of (2 × 6)-S surface by STS measurements.

that the separation between the S atoms of the S dimer was about 0.23 nm as shown in Fig. 3. According to the electron counting model, in order to form this (2 × 6)-S on GaAs(0 0 1) surface, one electron needs to be transferred from each S dimer to the Ga dangling bonds on the missing dimer region [11]. Thus, we investigate the S–S bond length with and without one electron transfer using the first-principles pseudopotential method. As a result, the separations are calculated as 0.2370 and 0.3897 nm, with and without one electron transfer, in the case of (2 × 6) and (2 × 1), respectively. Experimental results agreed well with the former condition. This indicates that this slab geometry is only a part of the (2 × 6) structure but able to describe the whole structure with fulfillment of the electron counting (local-charge neutrality) heuristics.

By the STS measurement on this (2 × 6) structure, a conductivity spectrum as shown in Fig. 4 was obtained. The spectrum is an average of several spectra taken from a well ordered region of a (2 × 6) surface. No spatial variation was observed in the spectra. The voltage width of $dI/dV = 0$ indicates the energy band gap of GaAs (1.45 V) which is reasonable at room temperature, showing that the S layer does not significantly affect the band gap. There is a peak on the conduction band side. The GaAs(0 0 1) (2 × 1)-Se surface does not show such a peak in STS [18]. In order to understand this spectrum, the electronic structure of this S dimer with and without one electron transfer was calculated using the same slab geometry as in Fig. 2. The effective band gap obtained by this method of calculation is shown in Fig. 5. The discrepancy between this effective band gap and the experimental value (1.45 V) is about 47%. In the case of the one electron transfer, (2 × 6) case, it exhibits an unoccupied flat band which is mainly caused by the antibonding band of the S–S bond shown in Fig. 5a. This result agreed well with the sharpness and energetic position of the peak in Fig. 4. Therefore, this peak should be related to the S dimers.

Moreover, in the case of no electron transfer, (2 × 1) case, there are several surface state bands associated with the surface S atoms in the energy gap region (Fig. 5b). But, in the case of the one electron transfer, there are no surface state bands in that region (Fig. 5a). This indicates that the one electron transfer can noticeably reduce the surface state density in the gap region.

Even though we need to confirm that these electrons from S dimers should transfer to the missing dimer region by a calculation of the complete (2 × 6) structure as well as the detailed STS mapping of the (2 × 6) structure. It is suggested by these theoretical and the experimental results that there are long-range electron transfers on this (2 × 6) structure.

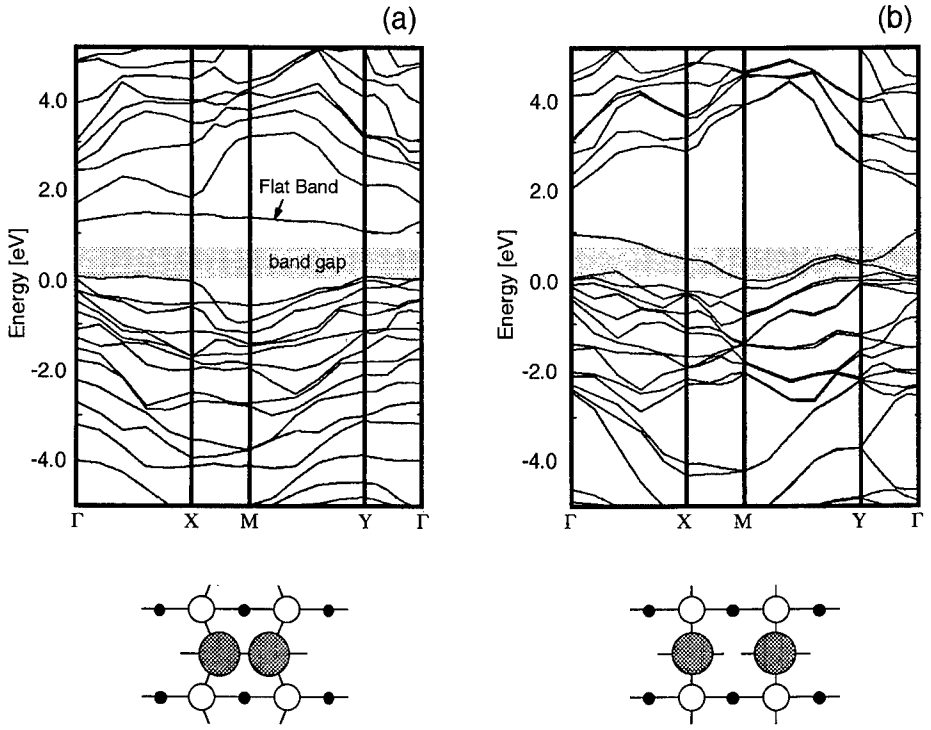

Fig. 5. Calculated electronic structures (a) with and (b) without one electron transfer. Shown band gap is an effective value by this calculation method.

These transfers may change the surface charge density on an atomic scale. We believe that these missing dimer regions will become the first growth sites when Ga atoms are deposited.

5. Conclusions

We have studied the (2×6) structure with the STS technique and the first-principles pseudopotential method. The structural and electronic properties of GaAs(0 0 1) surfaces covered with an adsorbed monolayer of S atoms were discussed with the experimental and theoretical results. By comparing the experimental results with the theoretical calculation, it was found that there was agreement between them, indicating that there are long-range electron transfers on this (2×6) structure and these transfers may change the surface charge density in the atomic scale. Therefore, when Ga atoms are deposited on this (2×6) structure, this changed surface charge density may determine the first growth sites of the Ga atoms.

References

[1] N. Koguchi and K. Ishige, Jpn. J. Appl. Phys. 32 (1993) 2052.
[2] J. Massies, F. Dezaly and N.T. Linh, J. Vac. Sci. Technol. 17 (1980) 1134.
[3] H. Oigawa, J.-F. Fan, Y. Nannichi, K. Ando, K. Saiki and A. Koma, Jpn. J. Appl. Phys. 28 (1989) L340.
[4] C.J. Sandroff, R.N. Nottenburg, J.C. Bischoff and R. Bhat, Appl. Phys. Lett. 51 (1987) 33.
[5] M.S. Carpenter, M.R. Melloch, M.S. Lundstrom and S.P. Tobin, Appl. Phys. Lett. 52 (1988) 2157.
[6] J.-F. Fan, H. Oigawa, Y. Nannichi, Jpn. J. Appl. Phys. 27 (1988) L1331, L2125.
[7] M. Tanimoto, H. Yokoyama, M. Shinohara and N. Inoue, Jpn. J. Appl. Phys. 33 (1994) L279.
[8] N. Yokoi, H. Andoh and M. Takai, Appl. Phys. Lett. 64 (1994) 2578.
[9] N. Koguchi, K. Ishige and S. Takahashi, J. Vac. Sci. Technol. B 11 (1993) 787.

[10] N. Koguchi, K. Ishige and S. Tsukamoto, Mater. Res. Soc. Symp. Proc. 326 (1994) 269.
[11] S. Tsukamoto and N. Koguchi, Jpn. J. Appl. Phys. 33 (1994) L1185.
[12] S. Tsukamoto and N. Koguchi, Appl. Phys. Lett. 65 (1994) 2199.
[13] S. Tsukamoto and N. Koguchi, J. Crystal Growth 150 (1995) 33.
[14] J. Suda, R. Tokutome, Y. Kawakami, Sz. Fujita and Sg. Fujita, J. Crystal Growth 175/176 (1997) 593.
[15] S. Tsukamoto and N. Koguchi, in: Ext. Abs. of 3rd Asia–Pacific Workshop on Intel. Mat., Tokyo (1995).
[16] M.P. Teter, M.C. Payne and D.C. Allan, Phys. Rev. B 40 (1989) 12255.
[17] T. Ohno and K. Shiraishi, Phys. Rev. B 42 (1991) 11194.
[18] M.D. Pashley and D. Li, J. Vac. Sci. Technol. A 12 (1994) 1848.

ELSEVIER

Journal of Crystal Growth 175/176 (1997) 1309–1315

JOURNAL OF CRYSTAL GROWTH

Does scanning tunnelling microscopy provide a realistic picture of the step array of vicinal GaAs(0 0 1) surfaces grown at high temperature?

L. Däweritz[a,*], H. Nörenberg[b], P. Schützendübe[a], K.H. Ploog[a]

[a] *Paul-Drude-Institut für Festkörperelektronik, Hausvogteiplatz 5–7, D-10117 Berlin, Germany*
[b] *Department of Materials, University of Oxford, Parks Road, Oxford OX1 3PH, UK*

Abstract

A 90° double reflection high-energy electron diffraction (RHEED) set-up was used to perform a two-dimensional (2D) study of the morphology of vicinal GaAs(0 0 1) surfaces during molecular beam epitaxy, in particular at high temperatures where the quenching for scanning tunnelling microscopy studies (STM) is a problem. In the transition range between 2D and step flow growth the terrace width fluctuation is found to increase on the B-surface (2° misorientation towards (1 $\bar{1}$ 1)As), whereas the A-surface (2° misorientation towards (1 1 1)Ga) becomes more uniformly stepped. This is discussed in terms of different barrier heights for downward diffusion of Ga adatoms over A- and B-type steps. For the A-surface different apparent transition temperatures between 2D and step flow growth are found in the [$\bar{1}$ 1 0] and [1 1 0] azimuths. In accordance with STM results this is explained by an increasing elongation of islands in [$\bar{1}$ 1 0] direction with increased substrate temperature. Above 580°C kinetically smoothed A and B surfaces transform after growth interruption rapidly to less ordered equilibrium surfaces. On the A-surface in addition the adatom concentration changes rapidly. Both processes occur in less than 1 s which creates problems to properly quench such surfaces for STM studies.

PACS: 61.14.Hg; 68.35.Bs; 68.35.Fx; 81.15.Hi; 81.05.Ea

Keywords: Kinetics of growth; Morphological stability of GaAs(0 0 1); Molecular beam epitaxy

1. Introduction

Step arrays on vicinal GaAs(0 0 1) surfaces have attracted considerable interest in molecular beam epitaxy (MBE) growth studies. The growth on regularly stepped surfaces leads to an improved surface/interface morphology which is reflected in improved device quality [1]. For novel concepts, such as quantum wire growth [2], the requirements on the regularity of the step array are much more stringent and a deeper understanding of the surface processes is needed. The recording of RHEED

* Corresponding author. Fax: + 49 30 203 77 201; e-mail: daeweritz@pdi.wias-berlin.de.

0022-0248/97/$17.00 Copyright © 1997 Elsevier Science B.V. All rights reserved
PII S0022-0248(96)01040-8

intensity oscillations as a widely used technique to control the transition from 2D to step flow growth [3] and the measurements of intensity profiles for an assessment of terrace width fluctuation and step edge straightness [4] in principle provide 1D information, whereas the morphology of the real surface [5–7] and kinetic processes on it have 2D character. Real space imaging by STM showed quite different step structures for the vicinal surface misoriented towards [$\bar{1}$ 1 0] (A-surface) and towards [1 1 0] (B-surface), respectively. Ga terminated (A) steps on the A-surface are smoother compared with As terminated (B) steps on the B-surface, but the terrace width is less homogeneous [5]. From RHEED [8] and in situ scanning electron microscopy studies [9] it became evident that the transition between 2D and step flow growth is not abrupt. STM investigations after quenching showed islands elongated in [$\bar{1}$ 1 0] direction [10–14]. When high substrate temperatures are used, which are of interest for the growth of laterally ordered structures, quenching the actual structure of the growth surface becomes a real problem.

In this work, we use a 90° double RHEED set-up for a 2D real-time study of the GaAs(0 0 1) growth surface. The intensity behaviour during growth and after growth interruptions is discussed in terms of competition between kinetic processes and thermodynamic equilibrium. In particular, we consider an anisotropic barrier for downward diffusion of adatoms over A and B steps. Finally it is pointed out that in situ RHEED and room temperature STM results can differ considerably due to fast changes from local to global thermodynamic equilibrium.

2. Experiment

The experimental set-up for the double RHEED experiments (Fig. 1) comprises two RHEED guns installed in such a way that the two 20 keV electron beams intersect on the sample at an angle of 90°. The incidence angle was 0.4°. The intensity of the specular beam was simultaneously monitored in both ⟨110⟩ azimuths parallel and perpendicular to the steps with two CCD cameras connected to two independent image processing systems. Small substrate pieces of $10 \times 10\,mm^2$ from epiready GaAs(0 0 1) wafers with 2° misorientation towards (1 1 1)Ga or (1 $\bar{1}$ 1)As were used. The substrate temperature measured with a thermocouple pressed to the backside of the substrate was calibrated to the oxide desorption temperature (580°C). The accuracy of temperature differences for experiments on the same sample is supposed to be better than 5°C, whereas the accuracy of the absolute temperature measurement for different samples has an error margin of up to 20°C. In order to avoid systematic structural changes, measurements at higher and lower substrate temperatures were carried out at random. The growth rate was 0.7 ML s^{-1} and the As_4:Ga beam equivalent pressure ratio was 15 in all experiments to maintain a (2×4) reconstruction during growth.

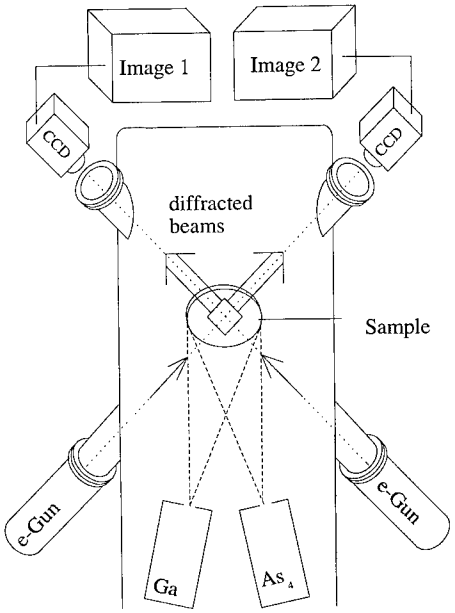

Fig. 1. Experimental set-up for simultaneous recording of RHEED intensity oscillations in two perpendicular azimuths.

3. Results and discussion

Fig. 2 shows recordings of the specular beam RHEED intensity for GaAs growth on A- and

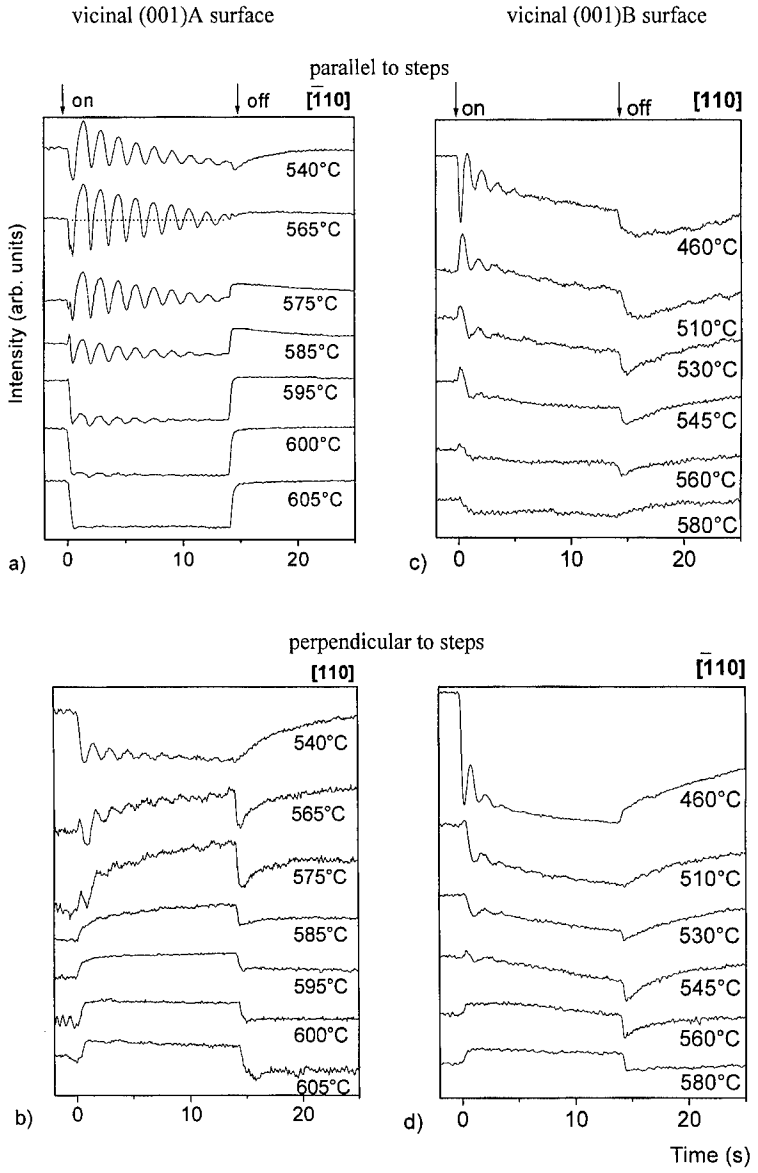

Fig. 2. Intensity of the specular RHEED beam during and after growth on vicinal GaAs(0 0 1)A surface (a, b) and on vicinal GaAs(0 0 1)B surface (c, d) for different substrate temperatures, recorded *simultaneously* in the azimuth parallel (a, c) and perpendicular to the misorientation steps (b, d). The dotted line in the second trace of (a) defines the average intensity.

B-surfaces. Their comparison allows us to check whether the curves are directly correlated with changes in distribution and shape of atomic steps. At high substrate temperatures, where the growth proceeds entirely in the step flow mode and therefore no intensity oscillations are visible, a striking difference is observed between the intensity behaviour in the two azimuths. For the A-surface the intensity decreases after growth initiation in the [$\bar{1}$ 1 0] azimuth (Fig. 2a) whereas it increases in the

[1 1 0] azimuth (Fig. 2b). The opposite behaviour is found for the B-surface, where the intensity decreases in [1 1 0] azimuth (Fig. 2c) and increases in [$\bar{1}$ 1 0] azimuth (Fig. 2d). Both surfaces show, however, a similar intensity behaviour for the direction parallel to the steps (compare Fig. 2a and Fig. 2c) and for the direction perpendicular to the steps (compare Fig. 2b and Fig. 2d). Consequently, the intensity behaviour is dominated by the evolution of the step structure. If it would be governed by changes in surface reconstruction one should expect a similar intensity behaviour in the same azimuths of the different vicinal surfaces. This is not the case. Therefore, it is justified to assume in the later discussion that intensity recordings in the azimuths parallel and perpendicular to the nominal step direction are sensitive to step edge roughness and terrace width fluctuation, respectively. This is based on general belief that the intensity is mainly affected by the step component perpendicular to the direction of the incident beam [12, 15]. In addition, changes in adatom density will affect the intensity in particular in the azimuth parallel to the step edges. The latter explains that under the regime of entire step flow the intensity decay and rise after growth initiation and interruption, respectively, in the azimuth parallel to the step edges is different for A- and B-surfaces (Fig. 2a and Fig. 2c). This is attributed to the build-up of a higher adatom density on the growing A-surface compared to the B-surface due to a higher incorporation rate into B-type steps and/or preferred migration along [$\bar{1}$ 1 0].

At substrate temperatures of $\sim$580°C for the B-surface and $\sim$600°C for the A-surface, the specular RHEED beam intensity reaches constant values for the non-growing and growing surfaces within less than 1 s. This proves that the kinetic processes are rapid so that the system can approach a local thermodynamic equilibrium on the length scale probed by RHEED.

Below these substrate temperatures the competition between kinetic processes and the system's desire to reach the thermodynamic equilibrium is shifted in favour of the kinetics. A striking difference in the intensity behaviour during growth is observed between A- and B-surfaces. For the A-surface, the average intensity as defined in Fig. 2a, is approximately constant in the azimuth parallel to the steps. In the perpendicular azimuth (Fig. 2b), however, it increases for temperatures > 540°C. In the case of the B-surface the average intensity decreases continuously during growth in both azimuths (Fig. 2c and Fig. 2d). This opposite behaviour of A- and B-surfaces in the azimuth perpendicular to the steps can be understood within models considering the barrier for downward diffusion over steps [16, 17]. If the Schwoebel barrier is large or infinite for downward flow, the preferential adatom attachment to the upper step edge will lead to a terrace width equalisation because the step velocity is directly proportional to the size of the feeding range. In the opposite case atoms arriving on the terrace can approach the step with a higher probability from the upper terrace and hence the terrace width fluctuation will increase. Supposing that the ordered step array leads to a higher specular beam RHEED intensity, the intensity increase observed during growth on the A-surface suggests terrace width equalisation whereas the intensity decrease in case of the B-surface is explained by increased terrace width fluctuation. Therefore, we conclude that the diffusion over the steps is anisotropic, with a higher barrier for A-type steps than for B-type steps.

For the A-surface the transition temperature from 2D to step flow growth is 605°C in the [$\bar{1}$ 1 0] azimuth parallel to the steps (Fig. 2a) and 585°C in the [1 1 0] azimuth perpendicular to the steps (Fig. 2b), as indicated by the disappearance of the oscillations. This difference between the transition temperatures in the two azimuths can be explained in terms of a changing shape of the growing island when the transition temperature is approached. Following the assumptions that the specular beam RHEED intensity and the step length per area (which for an islanded surface is a better measure than step edge roughness and terrace width fluctuation) are correlated and that the step length per area normal to the electron beam is mainly responsible for the oscillation in this azimuth [12], we must conclude that the step length per area reaches its steady-state value in the [1 1 0] azimuth at a lower substrate temperature than in the [$\bar{1}$ 1 0] azimuth. In particular at higher temperatures the preferred Ga atom migration along [$\bar{1}$ 1 0] [18]

(which is disputed by some authors [19]) and/or the higher sticking probability on B-type steps than on A-type steps [19, 20] leads to anisotropic island growth (for an illustration of the surface processes see Fig. 3). At lower substrate temperature the elongated islands preserve their axis ratio more or less during growth leading to periodic changes in step length per area in both the [1 1 0] and [$\bar{1}$ 1 0] azimuth. With increasing substrate temperature the island elongation is not only influenced by the factors already considered. The tendency to anisotropic growth will even be increased by the downward diffusion over B steps. During island growth and coalescence the length of the A-steps approaches a steady-state value whereas the B-steps are still changing their length per area periodically. Accordingly, intensity oscillations occur in the [$\bar{1}$ 1 0] azimuth but can no longer be observed in the [1 1 0] azimuth.

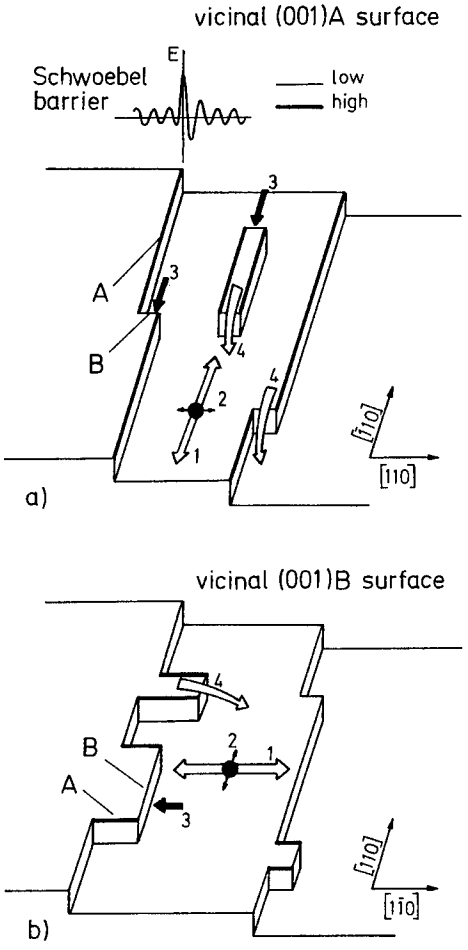

Fig. 3. Schematic representation of the evolution of the surface morphology due to anisotropic Ga adatom migration along [$\bar{1}$ 1 0] (1) and [1 1 0] (2), preferred incorporation in B-type steps (3), and downward diffusion over B-type steps (4). (a) Vicinal GaAs(0 0 1)A surface with straight steps and elongated islands on the terraces, (b) vicinal GaAs(0 0 1)B surface with strong step meandering.

For the B-surface (Fig. 2c and Fig. 2d) the oscillations are less pronounced. A strong meandering of the B-steps during growth is evident from the continuously decreasing intensity in the [1 1 0] azimuth. The simultaneous decrease of the specular beam intensity in the [$\bar{1}$ 1 0] azimuth indicates that the step meandering is coupled with an increase in terrace width fluctuation. Assuming at least two distinguishable intensity maxima to be present, the temperature for transition from 2D to step flow growth is estimated to 560°C for both the [1 1 0] azimuth and the [$\bar{1}$ 1 0] azimuth. It is obvious that due to step meandering the B-surface is more isotropic regarding the surface roughness than the A-surface. The surface evolution below the transition to step flow is well explained by the preferential adatom migration along the [$\bar{1}$ 1 0] direction, the higher sticking probability of Ga atoms at B-type steps and a high probability of an adatom crossing downward B-type steps (Fig. 3b).

Above the transition to step flow ($\geqslant$ 560°C), the RHEED intensity behaviour in the [1 1 0] azimuth indicates that after growth initiation the step edge roughness increases but reaches a steady-state value within 1 s (Fig. 2c). Surprisingly, the rapid intensity increase after growth initiation to a constant value in the [$\bar{1}$ 1 0] azimuth (Fig. 2d) suggests "kinetic smoothing" due to terrace width equalisation. Therefore, in this temperature range another mechanism than adatom crossing downward B-steps must be effective. The fractional-order beams disappear during growth, indicating that the ordering (unbunching) of steps and disordering on terraces are linked and that the energetics of the resulting metastable surface is significantly changed. It is the same mechanism that becomes operative on the vicinal Si(1 1 1) surface in a narrow temperature range beneath the equilibrium

faceting temperature [21]. In this case the kinetic smoothing of the equilibrium faceted surface is accompanied by the disappearance of the (7×7) reconstruction. In contrast to the metastable smoothed vicinal Si(1 1 1) surface which is remarkably robust, the kinetically smoothed vicinal GaAs(0 0 1)B surface transforms to the equilibrium bunched surface within less than 1 s.

RHEED and STM are complementary methods that differ condiderably in sample handling. It is, therefore, challenging to relate results of the present experiments with the double RHEED geometry to results from STM investigations. For growth on the A-surface it has been concluded from the intensity oscillation behaviour that the island elongation along $[\bar{1}\,1\,0]$ increases in the 2D growth regime with substrate temperature not only due to anisotropy in adatom migration and attachment on A-type and B-type steps but in particular due to downward diffusion over B-type steps. The transition in growth mode from 2D to step flow is completed at 605°C, i.e. in a temperature range for which we expect near equilibrium conditions. To verify this, Fig. 4 summarises data on the axis ratio of islands derived from STM (or atomic force microscopy [7]) studies by several authors for the nominal singular (0 0 1) surface (near A-type steps). If not given by the authors, we have estimated the axis ratios from the smaller islands. For substrate temperatures $\leqslant 590$°C the data show a linear increase of the axis ratio with temperature. At a substrate temperature of 590°C the island axis ratio increases from ~4 for rapidly cooled samples [11] up to ~10 for annealed samples (indicated by arrow) [11, 13]. A shape anisotropy of ~10 has been found also for sample growth and 15 min annealing at 610°C suggesting that this represents the equilibrium anisotropy [14]. This agrees well with our conclusion that the island shape anisotropy increases with temperature until a constant value is reached at near-equilibrium conditions. In agreement with our real-time study on vicinal surfaces, the STM analysis of the morphology on the singular surface at near-equilibrium conditions [14] indicated a barrier for transport at least over A steps and a possible anisotropy in the barrier.

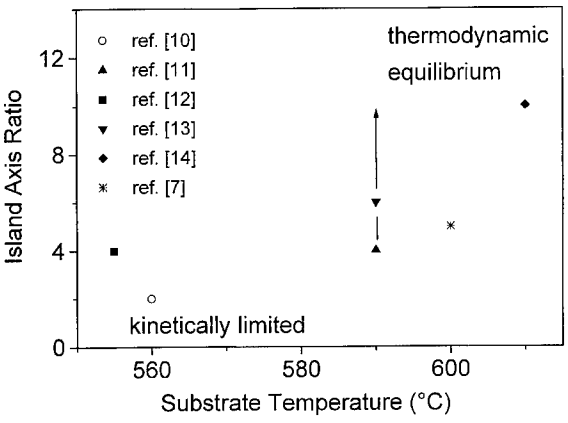

Fig. 4. Axis ratio determined by STM/AFM for GaAs islands on nominal singular GaAs(0 0 1) surfaces with A-type steps (solid symbols) and on a vicinal GaAs(0 0 1)B surface (open symbol) for different substrate temperatures.

The present study shows that at near-equilibrium conditions dramatic changes between the structure of the dynamic and static surface occur in less than 1 s. A change between kinetic smoothing and equilbrium bunching is observed on the A- as well as on the B-surface. On the A-surface we find in addition an abrupt increase and decrease in adatom density after growth initiation and interruption, respectively, indicated by a sudden RHEED intensity change in the $[\bar{1}\,1\,0]$ azimuth (Fig. 2a). This on a first glance unexpected high adatom concentration and its rapid reordering with changed surface conditions is evident also from recent STM work [22]. For a 0.15° misoriented surface quenched within 2.0 s from 600°C (faster than in usual MBE/STM work) it has been found that a concentration equivalent to a coverage as high as 0.18 ML was frozen into small islands.

4. Conclusions

Using a 90° double RHEED set-up a 2D analysis of the evolution of the morphology on vicinal GaAs(0 0 1) surfaces during growth and after growth interruption has been performed. On the A-surface the disappearance temperature of the RHEED intensity oscillations is about 20°C higher in $[\bar{1}\,1\,0]$ azimuth than in [1 1 0] azimuth due to the formation of elongated islands which change

their axis ratio in the transition range between 2D and step flow growth. During growth under kinetically controlled conditions the A-surface becomes more uniformly stepped whereas on the B-surface the terrace width fluctuation increases. This is explained by an asymmetry in the step attachment with a downward diffusion of Ga adatoms over B-type steps. A kinetic smoothing observed at near equilibrium conditions above $\sim 580°C$ also on the B-surface is linked with a disordering of the reconstruction and therefore not the result of the step attachment asymmetry but rather a consequence of the energetics. This unbunched surface is metastable and recovers after growth interruption within less than 1 s to the equilibrium bunched surface, which is faster than realizable freezing times in STM studies. On the A-surface in addition a rapid change in the adatom concentration occurs after growth interruption. Our results demonstrate that the 90° double RHEED technique can be advantageously used to study metastable surfaces that are difficult to quench in from high growth temperature for STM studies at room temperature. But even in this case the imaging by STM is valuable for the detailed interpretation of the RHEED results, provided differences due to a transition from local to global thermodynamic equilibrium are taken into account.

Acknowledgements

The authors gratefully acknowledge the valuable technical assistance by K. Hagenstein and H.P. Schönherr.

References

[1] See, e.g.: H.Z. Chen, A. Ghaffari, H. Morkoç and A. Yarif, Appl. Phys. Lett. 51 (1987) 2094.
[2] J.M. Gaines, P.M. Petroff, H. Kroemer, R.J. Simes, R.S. Geels and J.H. English, J. Vac. Sci. Technol. B 6 (1988) 1378.
[3] H. Neave, P.J. Dobson, B.A. Joyce and J. Zhang, Appl. Phys. Lett. 47 (1985) 100.
[4] P.R. Pukite, P.I. Cohen and S. Batra, in: Reflection High Energy Electron Diffraction and Reflection Imaging of Surfaces, Eds. P.K. Larsen and P.J. Dobson (Plenum, New York, 1988) p. 427.
[5] M.D. Pashley, K.W. Haberern and J.M. Gaines, Appl. Phys. Lett. 58 (1991) 406.
[6] K. Pond, A. Lorke, J. Ibbetson, V. Bressler-Hill, R. Maboudian, W.H. Weinberg, A.C. Gossard and P.M. Petroff, J. Vac. Sci. Technol. B 12 (1994) 2689.
[7] R. Hey, M. Wassermeier, J. Behrend, L. Däweritz, K. Ploog and H. Raidt, J. Crystal Growth 154 (1995) 1.
[8] T. Shitara, J. Zhang, J.H. Neave and B.A. Joyce, J. Crystal Growth 127 (1993) 494.
[9] N. Inoue, J. Crystal Growth 146 (1995) 334.
[10] M. Tanimoto, J. Osaka, T. Takigami, S. Hirono and K. Kanisawa, Ultramicroscopy 42–44 (1992) 1275.
[11] T. Ide, A. Yamashita and T. Mizutani, Phys. Rev. B 46 (1992) 1905.
[12] J. Sudijono, M.D. Johnson, C.W. Snyder, M.B. Elowitz and B.G. Orr, Phys. Rev. Lett. 69 (1992) 2811.
[13] L. Tanaka, S. Ohkouchi and A. Hashimoto, Jpn. J. Appl. Phys. 31 (1992) 2216.
[14] E.J. Heller and M.G. Lagally, Appl. Phys. Lett. 60 (1992) 2675.
[15] M.G. Lagally, D.E. Savage and M.C. Tringides, in: Reflection High Energy Electron Diffraction and Reflection Imaging of Surfaces, Eds. P.K. Larsen and P.J. Dobson (Plenum, New York, 1988) p. 139.
[16] R.L. Schwoebel, J. Appl. Phys. 40 (1969) 614.
[17] S.A. Chalmers, J.Y. Tsao and A.C. Gossard, J. Appl. Phys. 73 (1993) 7351.
[18] See, e.g.: K. Shiraishi, Appl. Phys. Lett. 60 (1992) 1363.
[19] See, e.g.: T. Shitara, D.D. Vvedensky, M.R. Wilby, J. Zhang, J.H. Neave and B.A. Joyce, Phys. Rev. B 46 (1992) 6825.
[20] K. Miwa and T. Nishinaga, J. Crystal Growth 146 (1995) 177.
[21] R.J. Phaneuf, H.-C. Kan and E.D. Williams, in: Low Dimensional Structures Prepared by Epitaxial Growth on Patterned Substrates, Eds. K. Eberl, P.M. Petroff and P. Demester (Kluwer, Dordrecht, 1995) p. 185.
[22] M.D. Johnson, K.T. Leung, A. Birch, B.G. Orr and J. Tersoff, Surf. Sci. 350 (1996) 254.

ELSEVIER

Journal of Crystal Growth 175/176 (1997) 1316–1320

JOURNAL OF CRYSTAL GROWTH

Substrate temperature change in III–V molecular beam epitaxy

K.R. Evans[1,a,*], J.E. Ehret[a], C.R. Jones[b], R. Kaspi[b]

[a] *Avionics Directorate, Wright Laboratory, Wright-Patterson Air Force Base, Ohio 45433, USA*
[b] *University Research Center, Wright State University, Dayton Ohio 45435, USA*

Abstract

The surface temperature (T_s), as inferred by desorption mass spectrometric determination of the Ga desorption rate, was followed in time after instantaneous changes were made in the setpoint temperature (T_{stpt}) during molecular beam epitaxy (MBE) growth of GaAs. Comparison between the time-evolution of T_s and that of the non-contact thermocouple-indicated temperature (T_{TC}) shows that large T_s overshoot is likely to occur under typical MBE growth conditions. Such T_s overshoot can lead to significant compositional grading at nominally abrupt heterojunctions. Details of how T_s evolves in time are found to depend on substrate conductivity, temperature controller settings (proportional band, integral, derivative), and maximum heater current setpoint.

1. Introduction

The ability to control substrate temperature during molecular beam epitaxy (MBE) is critical for realizing high quality semiconductor heterostructures. The most common substrate temperature sensor is the non-contact thermocouple, which is inexpensive and simple to implement. However, its use is prone to large systematic errors, both under nominally constant temperature conditions and when implementing intentional temperature changes. Intentional temperature changes are often implemented at a heterointerface (e.g., growth of GaAs at 600°C followed by growth of AlGaAs at 700°C). In the present work the relationship between the actual surface temperature and the thermocouple-indicated temperature is determined when implementing a stepwise increase in the setpoint temperature. The goal is to examine how closely the thermocouple temperature follows that of the wafer surface; i.e., to determine time-lags and overshoot phenomena. Effects of substrate conductivity and substrate temperature-controller settings are investigated.

2. Experimental procedure

The experiments were performed on a Gen II equipped with an apertured line-of-sight mass spectrometer on the center port of the source flange. The commercial substrate temperature sensing

* Corresponding author.
[1] Present Address: Semiconductor Laser International, 421 E. Main Street, Endicott, New York 13760, USA.

0022-0248/97/$17.00 Copyright © 1997 Elsevier Science B.V. All rights reserved
PII S0022-0248(96)00866-4

thermocouple floats in vacuum between the heater filaments and the substrate and is radiatively shielded from the heater filaments. Further details in the experimental arrangement can be found in Ref. [1].

The relationship between the thermocouple-indicated temperature (T_{TC}) and the GaAs surface temperature (T_s) was followed in time after instantaneous changes were made in the controller setpoint temperature (T_{stpt}). The GaAs surface temperature was inferred from the Ga desorption rate [F_d(Ga)], which was measured by desorption mass spectrometry (DMS). Fig. 1 shows how F_d(Ga) and T_{TC} respond to a stepwise increase in T_{stpt} (dashed line) from 615 to 727°C at $t = 100$ s during growth of GaAs on a semi-insulating (SI) wafer. The Ga flux and As_2 beam equivalent pressure were 0.75 ML/s and 5×10^{-6} torr, respectively. The behavior of T_{TC} (right) relative to T_{stpt} is characterized by an initial ~70 s lag, with little if any overshoot. In contrast, F_d(Ga) (left) overshoots to a value which is about 500% of its eventual steady-state value at the new setpoint. The overshoot in F_d(Ga) corresponds to an overshoot in T_s of approximately 35°C [2] and the peak magnitude of F_d(Ga) is equal to 75% of the magnitude of the incident Ga flux. Additionally, the maximum in F_d(Ga) occurs roughly at a time at which T_{TC} settles to the new T_{stpt}.

Similar data was taken for a variety of temperature setpoints, substrate conductivity, and temperature controller (PID and maximum current) settings.

3. Results and discussion

The effect of maximum heater current was examined by repeating the experiment for maximum heater current settings of 7 and 8 A; the results are shown in Fig. 2. (All other conditions were held constant.) The higher maximum current setting, which corresponds to the data displayed in Fig. 1, is seen to give rise to approximately a threefold larger overshoot in F_d(Ga) and a significantly more rapid settling time than the smaller maximum current setting. It is concluded that large stepwise increases in heater current provide large and rapid overshoots in T_s. It is also clear that low maximum current settings are consistent with minimization of the overshoot magnitude but not necessarily the time to settle to the new setpoint. Note that the thermocouple response time is most sluggish for the lower current setting, as one would expect. Additionally, the maximum in F_d(Ga) occurs roughly at a time at which T_{TC} settles to the new T_{stpt}, regardless of the maximum current setting.

It is common practice for the MBE grower to alter or tune the proportional band, integral, and

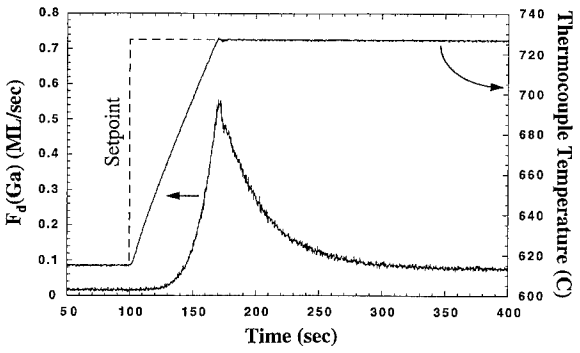

Fig. 1. Variation of thermocouple output temperature (right axis) and Ga desorption rate (left axis) as a function of time as a stepwise increase in the setpoint temperature (dashed line) is implemented.

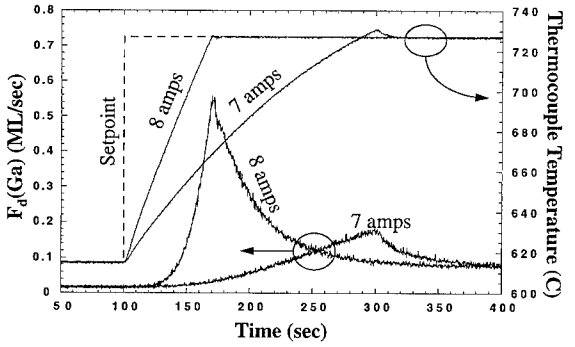

Fig. 2. Variation of thermocouple output temperature (right axis) and Ga desorption rate (left axis) as a function of time as a stepwise increase in the setpoint temperature (dashed line) is implemented. Results are shown for two different cases corresponding to maximum heater current settings of 7 and 8 A.

derivative settings of the temperature controller. The data displayed in Fig. 3 is a comparison of two different integral times of 3 and 50 s, with all other conditions held constant. The lower integral setting leads to a larger magnitude of overshoot but gives rise to a similar rise time and eventual settling time for T_{TC} to reach the new T_{stpt}. Also, the response of F_d(Ga) for the lower integral setting shows significantly under-damped behavior, which also is observed in the thermocouple output, although not as pronounced.

The parameter space of temperature controller settings for experiments such as those under investigation is rather large. However, it is thought that careful examination of various combinations of proportional band, integral, derivative, and maximum heater settings would likely result in the determination of conditions giving rise to reasonably rapid response times with minimal T_s overshoot. However, such an investigation would be very time-consuming and the information obtained would not be easily transferred to another set of growth conditions and temperature setpoint changes.

Since non-contact-mounted substrates are heated largely through radiative coupling, the substrate bandgap is an important issue in determining the fraction of heater radiation which is absorbed. One might expect to observe different responses between conductive and semi-insulating substrates since the effective bandgap of the former is smaller. In Fig. 4 we compare the responses of a SI substrate with that of a conductive n^+ substrate. The different stepwise changes in T_{stpt} effected for the two different substrates, as shown by the dashed lines, were chosen to yield the same magnitude of F_d(Ga) after full settling, in order to show the difference in setpoints required to yield the same steady-state surface temperature. Consistent with the effective bandgap argument are the following observations: (1) F_d(Ga) rises more rapidly for the n^+ substrate, (2) the time it takes for F_d(Ga) to peak is shorter; and (3) the setpoint required to reach the same settling value of F_d(Ga) is lower for the n^+ substrate than for the SI substrate. One conclusion from these observations is that one must be careful when setting growth parameters for a given substrate conductivity if they were determined or optimized while growing on a substrate of different conductivity.

Thus, heater controller settings and substrate conductivity all affect the relationship between the surface temperature and the thermocouple output when effecting stepwise temperature changes during MBE growth. These observations are the result of the relatively loose coupling between T_s and T_{TC}. What is needed is a way of controlling T_s directly. One way of achieving that is by decoupling the

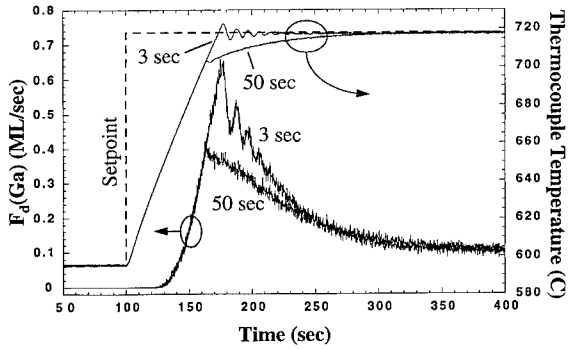

Fig. 3. Variation of thermocouple output temperature (right axis) and Ga desorption rate (left axis) as a function of time as a stepwise increase in the setpoint temperature (dashed line) is implemented. Results are shown for two different cases corresponding to temperature controller integral settings of 3 and 50 s.

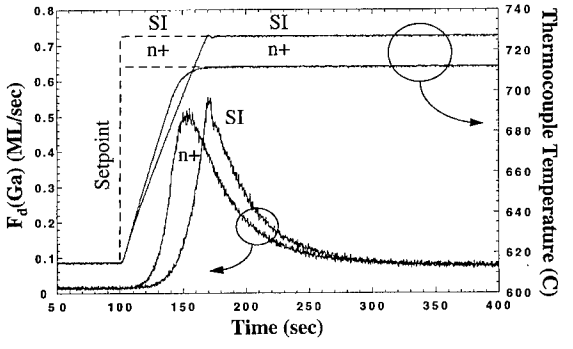

Fig. 4. Variation of thermocouple output temperature (right axis) and Ga desorption rate (left axis) as a function of time as a stepwise increase in the setpoint temperature (dashed line) is implemented. Results are shown for two different substrates: one is conductive (n^+) and one is semi-insulating (SI).

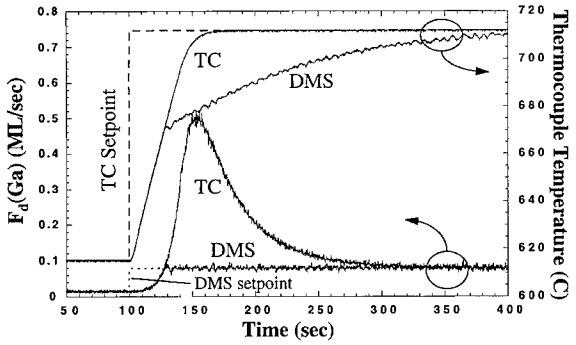

Fig. 5. Variation of thermocouple output temperature (right axis) and Ga desorption rate (left axis) as a function of time as a stepwise increase in the setpoint temperature (dashed line – TC control) or Ga desorption rate setpoint (dashed line – DMS control) is implemented.

thermocouple output from the temperature controller and, instead, directly coupling the signal corresponding to F_d(Ga) [1]. In Fig. 5 we compare the responses of T_{TC} and F_d(Ga) to stepwise changes in their respective setpoints, during normal thermocouple control (TC control) and desorption rate control (DMS control), respectively. The temperature controller settings used were identical for the two data sets; the desorption signal was appropriately conditioned to fall into the appropriate input voltage range for the temperature controller for the case of DMS control. The data show that DMS control provides a rapid time response with very minimal overshoot of T_s, in marked contrast to the significant overshoot and long settling time associated with TC control.

Note that, in the case of DMS control (Fig. 5), the thermocouple output rises in a nearly two-step linear-grade fashion. Thus, another potentially useful approach to improving the time response and overshoot characteristics of the time evolution of T_s during normal TC control would be to ramp up the setpoint temperature instead of increasing it in a stepwise fashion. This may be especially useful if the luxury of implementing DMS control is not available.

It is important to note that related difficulties in controlling surface temperature can also affect heterostructure growth when purposely reducing the substrate temperature. Previous measurements [3] on MBE growth of (Al,Ga)As/InGaAs structures have shown that significant In desorption can occur even when the thermocouple output temperature indicates that it should not. This comes about when dropping the substrate temperature from that used for AlGaAs growth to that used for InGaAs growth. Since one typically tries to avoid desorptive loss of In, the drop in temperature is implemented during growth of the last portion of AlGaAs. We have found that under typical growth conditions for our system, the thermocouple temperature settles to its new (lower) setpoint more rapidly than the actual surface temperature, and thus it is propitious to allow extra settling time.

4. Conclusions

The relatively loose relationship between the surface temperature and the non-contact thermocouple-indicated temperature gives rise to significant overshoot in surface temperature when effecting temperature setpoint increases under normal thermocouple control. The response time and the magnitude of overshoot associated with the surface temperature, when effecting stepwise changes in setpoint temperature, are dependent on the substrate conductivity and on the temperature controller settings, including the maximum current setting. By decoupling the thermocouple output from the temperature controller and, instead, coupling to it the suitably conditioned output of the desorption sensor, direct feedback control of the substrate surface temperature is effected, giving rise to a rapid response of the surface temperature with very little temperature overshoot.

Since the optimum growth temperature is generally different for adjacent epitaxial layers in a semiconductor heterostructure, stepwise changes in substrate temperature are routinely implemented during MBE growth. The results of the present study indicate that significant variation of growth rate and layer composition at heterointerfaces are likely to result if the temperature ramping is done in an uncontrolled fashion.

Acknowledgements

The authors thank C. Huang, L. Kyle and C. Litton for technical support. R.K. and C.R.J. were supported by US Air Force Contract # F33615-95-C-1765. This work was partially supported by the US Air Force Office of Scientific Research (AFOSR).

References

[1] K.R. Evans, R. Kaspi, C.R. Jones, V. Jogai and R. Sherriff, J. Crystal Growth 127 (1993) 523.
[2] J.M. Van Hove and P.I. Cohen, Appl. Phys. Lett. 47 (1985) 726.
[3] K.R. Evans and J.E. Ehret, private communication.

ELSEVIER

Journal of Crystal Growth 175/176 (1997) 1321–1340

JOURNAL OF CRYSTAL GROWTH

Author index

Abernathy, C.R., see MacKenzie, J.D. 175/176 (1997) 84
Adachi, A., see Tomita, N. 175/176 (1997) 809
Adachi, A., see Higashiwaki, M. 175/176 (1997) 814
Adachi, A., see Shinohara, K. 175/176 (1997) 924
Adams, S.J., see Eyink, K.G. 175/176 (1997) 262
Ahn, C.C., see Croke, E.T. 175/176 (1997) 486
Aiba, Y., see Hashimoto, A. 175/176 (1997) 129
Akasaki, I. and H. Amano, Progress and prospect of group-III nitride semiconductors 175/176 (1997) 29
Akiba, N., see Shen, A. 175/176 (1997) 1069
Akimoto, K., see Cho, S.H. 175/176 (1997) 112
Alferov, Zh.I., see Ustinov, V.M. 175/176 (1997) 689
Allegri, P., see Bosacchi, A. 175/176 (1997) 771
Alperin, J., see Du, Q. 175/176 (1997) 849
Amano, H., see Akasaki, I. 175/176 (1997) 29
Andersson, T.G., K. Nozawa and Y. Horikoshi, Studies of GaN layers grown on sapphire using an RF-source 175/176 (1997) 117
Andersson, T.G., see Thordson, J.V. 175/176 (1997) 234
Andersson, T.G., see Roslund, J.H. 175/176 (1997) 883
Andersson, T.G., see Wang, S.M. 175/176 (1997) 1016
Antipov, V.G., see Nikishin, S.A. 175/176 (1997) 139
Aqariden, F., see Wijewarnasuriya, P.S. 175/176 (1997) 647
Arain, O., see Li, Y. 175/176 (1997) 250
Araki, T., see Inoue, N. 175/176 (1997) 286
Armelles, G., see Postigo, P.A. 175/176 (1997) 298
Arnoult, A., see Tatarenko, S. 175/176 (1997) 682
Asahi, H., see Iwata, K. 175/176 (1997) 150
Asahi, H., see Kim, S.J. 175/176 (1997) 754
Asahi, H., M. Fushida, K. Yamamoto, K. Iwata, H. Koh, K. Asami, S. Gonda and K. Oe, New semiconductors TlInGaP and their gas source MBE growth 175/176 (1997) 1195
Asahi, H., see Yamamoto, K. 175/176 (1997) 1236
Asami, K., see Iwata, K. 175/176 (1997) 150
Asami, K., see Kim, S.J. 175/176 (1997) 754
Asami, K., see Asahi, H. 175/176 (1997) 1195
Asbeck, P.M., see Li, N.Y. 175/176 (1997) 387
Asonen, H., see Toivonen, M. 175/176 (1997) 37
Avanzini, V., see Bosacchi, A. 175/176 (1997) 771
Averbeck, R., H. Tews, A. Graber and H. Riechert, Blue and green electroluminescence from GaN/InGaN heterostructures 175/176 (1997) 122
Bacher, K., S. Massie and M. Seaford, Molecular beam epitaxy of strain-compensated InGaAs/GaAsP quantum-well intersubband photodetectors 175/176 (1997) 977
Bacon, D.D., see Kuo, J.M. 175/176 (1997) 971
Baillargeon, J.N., see Faist, J. 175/176 (1997) 22
Bair, A.E., see Croke, E.T. 175/176 (1997) 486
Baldasaro, P., see Uppal, P.N. 175/176 (1997) 877
Bambha, N., see Zeng, L. 175/176 (1997) 541
Bambha, N., see Cavus, A. 175/176 (1997) 558
Baron, T., see Tatarenko, S. 175/176 (1997) 682
Basmaji, P., see González-Borrero, P.P. 175/176 (1997) 765
Bauer, G., see Zerlauth, S. 175/176 (1997) 459
Bauer, G., see Ueta, A.Y. 175/176 (1997) 1022
Baumeister, H., see Popp, M. 175/176 (1997) 1247
Beere, H.E., J.H. Thompson, G.A.C. Jones and D.A. Ritchie, Selective area epitaxy of GaAs using very low energy Ga^+ focused ion beam deposition combined with molecular beam epitaxial growth 175/176 (1997) 398
Behrend, J., M. Wassermeier, W. Braun, P. Krispin and K.H. Ploog, Real space imaging of GaAs/AlAs (0 0 1) heterointerfaces 175/176 (1997) 178
Beltram, F., see Lazzeri, M. 175/176 (1997) 603
Bennett, B.R., see Thibado, P.M. 175/176 (1997) 317
Bennett, B.R., B.V. Shanabrook, P.M. Thibado, L.J. Whitman and R. Magno, Stranski–Krastanov growth of InSb, GaSb, and AlSb on GaAs: structure of the wetting layers 175/176 (1997) 888
Benson, J.D., A.B. Cornfeld, M. Martinka, J.H. Dinan, B. Johs, P. He and J.A. Woollam, Ellipsometric analysis of CdZnTe preparation for HgCdTe MBE growth 175/176 (1997) 659

Benz, II, R., see Menkara, H.M. 175/176 (1997) 983
Bergh, M., see Wang, S.M. 175/176 (1997) 1016
Bert, N.A., see Ustinov, V.M. 175/176 (1997) 689
Beton, P.H., see Henini, M. 175/176 (1997) 782
Bhattacharya, P., see Linder, K.K. 175/176 (1997) 499
Bhattacharya, P., see Kamath, K. 175/176 (1997) 720
Bhattacharya, P., see Kamath, K. 175/176 (1997) 935
Bi, W.G. and C.W. Tu, N incorporation in GaN_xP_{1-x} and InN_xP_{1-x} using a RF N plasma source 175/176 (1997) 145
Bi, W.G., see Niki, S. 175/176 (1997) 1051
Bicknell-Tassius, R.N., see Fournier, F. 175/176 (1997) 203
Bicknell-Tassius, R.N., see Kromann, R.F. 175/176 (1997) 334
Bicknell-Tassius, R.N., see Menkara, H.M. 175/176 (1997) 983
Bicknell-Tassius, R.N., K. Lee, A.S. Brown, G. Dagnall and G. May, The growth of AlGaAs–InGaAs quantum-well structures by molecular beam epitaxy: observation of critical interdependent effects utilizing the design of experiments approach 175/176 (1997) 1131
Bimberg, D., see Ustinov, V.M. 175/176 (1997) 689
Blank, H.-R., see Thomas, M. 175/176 (1997) 894
Block, T.R., J. Cowles, L. Tran, M. Wojtowicz, A.K. Oki and D.C. Streit, MBE growth of quaternary InGaAlAs layers in InGaAs/InAlAs HBTs to improve device performance 175/176 (1997) 903
Block, T.R., see Wojtowicz, M. 175/176 (1997) 930
Böhm, G., see Sexl, M. 175/176 (1997) 915
Böhrer, J., see Ustinov, V.M. 175/176 (1997) 689
Bonanni, A., see Lazzeri, M. 175/176 (1997) 603
Boney, C., see Hughes, W.C. 175/176 (1997) 546
Boonzaayer, M.D., see Kuo, C.H. 175/176 (1997) 281
Bosacchi, A., P. Frigeri, S. Franchi, P. Allegri and V. Avanzini, InAs/GaAs self-assembled quantum dots grown by ALMBE and MBE 175/176 (1997) 771
Bosacchi, A., A.C. De Riccardis, P. Frigeri, S. Franchi, C. Ferrari, S. Gennari, L. Lazzarini, L. Nasi, G. Salviati, A.V. Drigo and F. Romanato, Continuously graded buffers for InGaAs/GaAs structures grown on GaAs 175/176 (1997) 1009
Böttcher, J., see Künzel, H. 175/176 (1997) 411
Böttcher, J., see Künzel, H. 175/176 (1997) 940
Bower, J.E., see Hong, M. 175/176 (1997) 422
Bowers, J.E., see Mirin, R.P. 175/176 (1997) 696
Brandt, O., H. Yang, A. Yamada and K.H. Ploog, Relation between surface reconstruction transitions and growth kinetics of zincblende (0 0 1) GaN 175/176 (1997) 134
Braun, W., A. Trampert, L. Däwerzitz and K.H. Ploog, Laterally nonuniform Ga segregation at GaAs/AlGaAs interfaces during MBE growth 175/176 (1997) 156
Braun, W., see Behrend, J. 175/176 (1997) 178
Briones, F., see Postigo, P.A. 175/176 (1997) 298
Briones, F., see Utzmeier, T. 175/176 (1997) 725
Bronner, W., see Gaymann, A. 175/176 (1997) 898
Brown, A.S., see Fournier, F. 175/176 (1997) 203
Brown, A.S., see Kromann, R.F. 175/176 (1997) 334
Brown, A.S., see Bicknell-Tassius, R.N. 175/176 (1997) 1131
Brown, S.J., P.D. Rose, E.H. Linfield, D.A. Ritchie, V. Drouot and G.A.C. Jones, In situ STM characterisation of Ga^+ focused ion beam interactions with MBE grown GaAs(1 0 0) 175/176 (1997) 346
Brunet, P., see Tournié, E. 175/176 (1997) 577
Brunner, K., W. Winter, K. Eberl, N.Y. Jin-Phillipp and F. Phillipp, Fabrication and band alignment of pseudomorphic $Si_{1-y}C_y$, $Si_{1-x-y}Ge_xC_y$ and coupled $Si_{1-y}C_y/Si_{1-x-y}Ge_xC_y$ quantum well structures on Si substrates 175/176 (1997) 451
Buchholz, D.B., see Kuo, J.M. 175/176 (1997) 971
Buckle, P.D., P. Dawson, M. Missous and W.S. Truscott, Full wafer optical characterisation of resonant tunnelling structures using photoluminescence excitation spectroscopy 175/176 (1997) 1299
Bullough, T.J., see Joyce, T.B. 175/176 (1997) 377
Bullough, T.J., see Farrell, T. 175/176 (1997) 1217
Burke, T.M., E.H. Linfield, D.A. Ritchie, M. Pepper and J.H. Burroughes, Hydrogen radical surface cleaning of GaAs for MBE regrowth 175/176 (1997) 416
Burroughes, J.H., see Burke, T.M. 175/176 (1997) 416

Cai, W.Z., see Micovic, M. 175/176 (1997) 428
Campbell, B., see Uppal, P.N. 175/176 (1997) 877
Capasso, F., see Faist, J. 175/176 (1997) 22
Carter-Coman, C., see Fournier, F. 175/176 (1997) 203
Cavanna, A., see Laruelle, F. 175/176 (1997) 1087
Cavanna, A., see Lelarge, F. 175/176 (1997) 1102
Cavus, A., see Zeng, L. 175/176 (1997) 541
Cavus, A., L. Zeng, B.X. Yang, N. Dai, M.C. Tamargo, N. Bambha and F. Semendy, Optimized growth of lattice-matched ZnCdSe epilayers on InP substrates 175/176 (1997) 558
Chaichimansour, M., see Schön, S. 175/176 (1997) 598
Chandrasekhar, D., see Croke, E.T. 175/176 (1997) 486
Chang, L.L., see Wang, Y. 175/176 (1997) 1289
Chang, P.C., see Lin, C.-H. 175/176 (1997) 955
Chang, W.S.C., see Mei, X.B. 175/176 (1997) 994
Chapman, G.R., see Rajavel, R.D. 175/176 (1997) 653
Charache, G., see Uppal, P.N. 175/176 (1997) 877

Chauhan, J.S., see Henini, M. 175/176 (1997) 782
Chauhan, J.S., see Henini, M. 175/176 (1997) 1138
Chavarkar, P., D.S.L. Mui, T. Strand, L.A. Coldren and U.K. Mishra, Analysis of in-situ etched and regrown AlInAs/GaInAs interfaces 175/176 (1997) 393
Cheewatas, P., see Sopitpan, S. 175/176 (1997) 1152
Chen, A.C., see Moy, A.M. 175/176 (1997) 819
Chen, F., see Feng, W. 175/176 (1997) 1173
Chen, G.T., see Li, A.Z. 175/176 (1997) 873
Chen, H., X.G. Xie, W.Q. Cheng, Q. Huang and J.M. Zhou, The growth and luminescence of SiGe dots 175/176 (1997) 524
Chen, P., see Ramachandran, T.R. 175/176 (1997) 216
Chen, P., see Konkar, A. 175/176 (1997) 741
Chen, W.S., see Sou, I.K. 175/176 (1997) 632
Chen, X.Q., see He, L. 175/176 (1997) 677
Chen, Y., see Zhang, Y.-H. 175/176 (1997) 833
Chen, Y.J., see Johnson, F.G. 175/176 (1997) 46
Chen, Y.P., see Kim, C.C. 175/176 (1997) 328
Chen, Y.P., see Kim, C.C. 175/176 (1997) 613
Cheng, K.Y., see Moy, A.M. 175/176 (1997) 819
Cheng, K.Y., see Wohlert, D.E. 175/176 (1997) 1162
Cheng, W.Q., see Chen, H. 175/176 (1997) 524
Chew, A., see Joyce, T.B. 175/176 (1997) 377
Chin, A., C.C. Liao, J. Chu and S.S. Li, Investigation of Si-doped p-type AlGaAs/GaAs, AlGaAs/InGaAs quantum well infrared photodetectors and multiquantum wells grown on (3 1 1)A GaAs 175/176 (1997) 999
Chirovsky, L.M.F., see Kuo, J.M. 175/176 (1997) 971
Cho, A.Y., see Faist, J. 175/176 (1997) 22
Cho, H.D., see Yoo, M.C. 175/176 (1997) 100
Cho, H.D., N.H. Ko, S.H. Park, T.W. Kang, J.W. Han, K.S. Eom, S.H. Won and K.S. Jung, Zinc blende GaN grown by radio frequency plasma assisted molecular beam epitaxy 175/176 (1997) 125
Cho, S.H., U. Tanaka, T. Maruyama, K. Akimoto, H. Okumura and S. Yoshida, Cathodoluminescence of GaN films grown under Ga and N rich conditions by radio-frequency-molecular beam epitaxy 175/176 (1997) 112
Choi, H.K., see Turner, G.W. 175/176 (1997) 825
Chou, L.J., see Moy, A.M. 175/176 (1997) 819
Chou, S.T., see Wohlert, D.E. 175/176 (1997) 1162
Chow, D.H., see Zinck, J.J. 175/176 (1997) 323
Chow, P.P., K.R. Evans, A.J. Spring-Thorpe, P. Fisher, J.J. Klaassen, A. Wowchak and J. Van Hove, Sensor controlled linear motion oven (S-LIMO) for group III flux operation 175/176 (1997) 61
Chow, P.P., see Van Hove, J.M. 175/176 (1997) 79
Christiansen, K., see Schmitt, J. 175/176 (1997) 528
Christiansen, S., see Schmitt, J. 175/176 (1997) 528
Chu, C.C., see Ng, T.B. 175/176 (1997) 552
Chu, G.G., see Chu, M.A. 175/176 (1997) 1278
Chu, J., S.S. Li and P. Ho, The growth and characterization of two new P-type compressively strained layer InGaAs/AlGaAs/GaAs quantum well infrared photodetectors for mid- and long-wavelength infrared detection 175/176 (1997) 964
Chu, J., see Chin, A. 175/176 (1997) 999
Chu, M.A., M.O. Tanner, F. Huang, K.L. Wang, G.G. Chu and M.S. Goorsky, Photoluminescence and X-ray characterization of relaxed $Si_{1-x}Ge_x$ alloys grown on silicon on insulator (SOI) and implanted SOI substrates 175/176 (1997) 1278
Chu, S.-N.G., see Faist, J. 175/176 (1997) 22
Chua, S.J., see Ramam, A. 175/176 (1997) 1294
Chyi, Jen-Inn, Tzer-En Nee, Ching-Ting Lee, Jia-Lin Shieh and Jen-Wei Pan, Formation of self-organized $In_{0.5}Ga_{0.5}As$ quantum dots on GaAs by molecular beam epitaxy 175/176 (1997) 777
Cibert, J., see Tatarenko, S. 175/176 (1997) 682
Coldren, L.A., see Jackson, A. 175/176 (1997) 244
Coldren, L.A., see Chavarkar, P. 175/176 (1997) 393
Colin, T., T. Skauli and S. Løvold, Elastic and plastic deformation in low mismatched $Cd_xHg_{1-x}Te/Cd_{1-y}Zn_yTe$ 175/176 (1997) 670
Collot, Ph., see Garcia, J.Ch. 175/176 (1997) 1265
Colombo, P., see Sacks, R.N. 175/176 (1997) 66
Connors, M.K., see Turner, G.W. 175/176 (1997) 825
Cook, Jr., J.W., see Johnson, M.A.L. 175/176 (1997) 72
Cook, Jr., J.W., see Hughes, W.C. 175/176 (1997) 546
Cornfeld, A.B., see Benson, J.D. 175/176 (1997) 659
Cowles, J., see Block, T.R. 175/176 (1997) 903
Croke, E.T., A.T. Hunter, C.C. Ahn, T. Laursen, D. Chandrasekhar, A.E. Bair, D.J. Smith and J.W. Mayer, Control of composition and crystallinity in the molecular beam epitaxy of strain-compensated $Si_{1-x-y}Ge_xC_y$ alloys on Si 175/176 (1997) 486
Croswell, D.R., see Van Hove, J.M. 175/176 (1997) 79
Cunningham, J.E., see Kuo, J.M. 175/176 (1997) 971

D'Asaro, L.A., see Kuo, J.M. 175/176 (1997) 971
Dagenais, M., see Johnson, F.G. 175/176 (1997) 46
Dagnall, G., see Bicknell-Tassius, R.N. 175/176 (1997) 1131
Dahringer, D., see Kuo, J.M. 175/176 (1997) 971
Dai, N., see Cavus, A. 175/176 (1997) 558
Daraselia, M., see Kim, C.C. 175/176 (1997) 328
Darhuber, A.A., see Zerlauth, S. 175/176 (1997) 459
David, J.P.R., see Hopkinson, M. 175/176 (1997) 1033
Davidson, B.R., see Joyce, T.B. 175/176 (1997) 377

Däweritz, L., see Braun, W. 175/176 (1997) 156
Däweritz, L., K. Stahrenberg, P. Schützendübe, J.-T. Zettler, W. Richter and K.H. Ploog, Evolution of short- and long-range order during Si incorporation on GaAs(0 0 1) observed by RAS and RHEED during MBE 175/176 (1997) 310
Däweritz, L., see Nötzel, R. 175/176 (1997) 1114
Däweritz , L., see Hey, R. 175/176 (1997) 1167
Däweritz, L., H. Nörenberg, P. Schützendübe and K.H. Ploog, Does scanning tunnelling microscopy provide a realistic picture of the step array of vicinal GaAs(0 0 1) surfaces grown at high temperature? 175/176 (1997) 1309
Dawson, P., see Buckle, P.D. 175/176 (1997) 1299
De Melo, O., see Hernández-Calderón, I. 175/176 (1997) 571
De Riccardis, A.C., see Bosacchi, A. 175/176 (1997) 1009
DeHerrera, M.F., see Kuo, C.H. 175/176 (1997) 281
Deparis, C., see Mesrine, M. 175/176 (1997) 1242
Díaz, P., see Hernández-Calderón, I. 175/176 (1997) 571
DiLorenzo, J.V., B. Lauterwasser and M.P. Zaitlin, Applications of MBE grown PHEMTs 175/176 (1997) 1
Dinan, J.H., see Benson, J.D. 175/176 (1997) 659
Ding, R.J., see He, L. 175/176 (1997) 677
Dion, M.M., see Wasilewski, Z.R. 175/176 (1997) 238
Döhler, G.H., see Malzer, S. 175/176 (1997) 960
Dommann, A., see Grützmacher, D. 175/176 (1997) 1144
Doolittle, A., see Fournier, F. 175/176 (1997) 203
Dorsey, D.L., see Mahalingam, K. 175/176 (1997) 211
Dorsey, D.L., see Venkatasubramanian, R. 175/176 (1997) 224
Dorsey, J.F., see Kromann, R.F. 175/176 (1997) 334
Drigo, A.V., see Bosacchi, A. 175/176 (1997) 1009
Drouot, V., see Brown, S.J. 175/176 (1997) 346
Du, Q., J. Alperin and W.I. Wang, Molecular beam epitaxial growth of GaInSbBi for infrared detector applications 175/176 (1997) 849

Eaves, L., see Henini, M. 175/176 (1997) 782
Eaves, L., see Henini, M. 175/176 (1997) 919
Eberl, K., see Brunner, K. 175/176 (1997) 451
Eberl, K., A. Kurtenbach, M. Zundel, J.Y. Jin-Phillipp, F. Phillipp, A. Moritz, R. Wirth and A. Hangleiter, Self-assembling InP quantum dots for red lasers 175/176 (1997) 702
Edmond, J.A., see Johnson, M.A.L. 175/176 (1997) 72
Egorov, A.Yu., see Ustinov, V.M. 175/176 (1997) 689
Ehret, J.E., see Evans, K.R. 175/176 (1997) 1316
Endo, A., see Shen, A. 175/176 (1997) 1069
Eom, K.S., see Cho, H.D. 175/176 (1997) 125
Etienne, B., see Laruelle, F. 175/176 (1997) 1087
Etienne, B., see Lelarge, F. 175/176 (1997) 1102
Evans, K.R., see Chow, P.P. 175/176 (1997) 61
Evans, K.R., see Jenny, J.R. 175/176 (1997) 89
Evans, K.R., see Mahalingam, K. 175/176 (1997) 211
Evans, K.R., see Kaspi, R. 175/176 (1997) 838
Evans, K.R., J.E. Ehret, C.R. Jones and R. Kaspi, Substrate temperature change in III–V molecular beam epitaxy 175/176 (1997) 1316
Eyink, K.G., J.K. Patterson, S.J. Adams, T.W. Haas and W.V. Lampert, Use of optical fiber pyrometry in molecular beam epitaxy 175/176 (1997) 262

Faist, J., F. Capasso, C. Sirtori, D.L. Sivco, J.N. Baillargeon, A.L. Hutchinson, S.-N.G. Chu and A.Y. Cho, High power mid-infrared quantum cascade lasers with a molecular beam epitaxy grown InP cladding operating above room temperature 175/176 (1997) 22
Fang, W.Z., see He, L. 175/176 (1997) 677
Fang, X.M., see Liu, W.K. 175/176 (1997) 853
Fang, X.M., see McCann, P.J. 175/176 (1997) 1057
Farrell, T., see Joyce, T.B. 175/176 (1997) 377
Farrell, T., D. Hill, T.B. Joyce, T.J. Bullough and P. Weightman, Transient surface states during the CBE growth of GaAs 175/176 (1997) 1217
Faurie, J.P., see Tournié, E. 175/176 (1997) 577
Faurie, J.P., see Wijewarnasuriya, P.S. 175/176 (1997) 647
Felix, C.L., see Lin, C.-H. 175/176 (1997) 955
Feng, W., F. Chen, Q. Huang and J.M. Zhou, Photoluminescence of low-temperature AlGaAs/GaAs multiple quantum wells 175/176 (1997) 1173
Fernier, B., see Pagnod-Rossiaux, Ph. 175/176 (1997) 948
Ferrari, C., see Bosacchi, A. 175/176 (1997) 1009
Feuillet, G., see Hacke, P. 175/176 (1997) 94
Fily, A., see Garcia, J.Ch. 175/176 (1997) 1265
Fischer, F., G. Landwehr, Th. Litz, H.J. Lugauer, U. Zehnder, Th. Gerhard, W. Ossau and A. Waag, II–VI light-emitting devices based on beryllium chalcogenides 175/176 (1997) 532
Fischer, F., see Lugauer, H.-J. 175/176 (1997) 619
Fisher, P., see Chow, P.P. 175/176 (1997) 61
Flack, F., see Micovic, M. 175/176 (1997) 428
Fons, P.J., see Niki, S. 175/176 (1997) 1051
Foster, T.J., see Henini, M. 175/176 (1997) 1138
Fournier, F., R.A. Metzger, A. Doolittle, A.S. Brown, C. Carter-Coman, N.M. Jokerst and R. Bicknell-Tassius, Growth dynamics of InGaAs/GaAs by MBE 175/176 (1997) 203
Franchi, S., see Bosacchi, A. 175/176 (1997) 771
Franchi, S., see Bosacchi, A. 175/176 (1997) 1009
Franciosi, A., see Lazzeri, M. 175/176 (1997) 603
Friedland, K.-J., see Hey, R. 175/176 (1997) 1126
Frigeri, P., see Bosacchi, A. 175/176 (1997) 771

Frigeri, P., see Bosacchi, A. 175/176 (1997) 1009
Fuentes, J., see Hernández-Calderón, I. 175/176 (1997) 571
Fujii, K., see Nagao, S. 175/176 (1997) 1157
Fujimori, T., see Nagao, S. 175/176 (1997) 1157
Fujita, K., see Tomita, N. 175/176 (1997) 809
Fujita, Sg., see Suda, J. 175/176 (1997) 593
Fujita, Sz., see Suda, J. 175/176 (1997) 593
Fukatsu, S., see Miyake, Y. 175/176 (1997) 465
Fukatsu, S., see Ishikawa, Y. 175/176 (1997) 493
Fukatsu, S., see Kim, E.S. 175/176 (1997) 519
Furuhata, N., see Niwa, T. 175/176 (1997) 441
Furushou, T., see Yano, M. 175/176 (1997) 665
Fushida, M., see Asahi, H. 175/176 (1997) 195
Futatsugi, T., see Nakata, Y. 175/176 (1997) 713

Gaborit, F., see Pagnod-Rossiaux, Ph. 175/176 (1997) 948
Galbiati, N., see Henini, M. 175/176 (1997) 1108
Gallagher, B.L., see Henini, M. 175/176 (1997) 1138
Ganser, P., see Haupt, M. 175/176 (1997) 1028
Garcia, J.Ch., A. Lebkiri, A. Fily, Ph. Collot, J. Massies and M. Leroux, Chemical beam epitaxy growth of tensile-strained GaAsP/GaAlAs quantum well heterostructures for laser application 175/176 (1997) 1265
García, R., see Utzmeier, T. 175/176 (1997) 725
Gastev, S.V., see Novikov, S.V. 175/176 (1997) 514
Gaymann, A., J. Schaub, W. Bronner, N. Grün, J. Hornung and K. Köhler, Molecular beam epitaxy of vertically compact $Al_xGa_{1-x}As/GaAs$ laser-HEMT structures for monolithic integration 175/176 (1997) 898
Ge, W., see Wang, Y. 175/176 (1997) 1289
Geißelbrecht, W., see Malzer, S. 175/176 (1997) 960
Gennari, S., see Bosacchi, A. 175/176 (1997) 1009
Gennser, U., see Grützmacher, D. 175/176 (1997) 1144
Gerhard, T., see Fischer, F. 175/176 (1997) 532
Gerhard, T., see Lugauer, H.-J. 175/176 (1997) 619
Gill, D., see Uppal, P.N. 175/176 (1997) 877
Gislason, H., see Sørensen, C.B. 175/176 (1997) 1097
Giudice, G.E., see Thiagarajan, P. 175/176 (1997) 945
Goetz, P., see Rajavel, R.D. 175/176 (1997) 653
Gonda, S., see Iwata, K. 175/176 (1997) 150
Gonda, S., see Kim, S.J. 175/176 (1997) 754
Gonda, S., see Asahi, H. 175/176 (1997) 1195
Gonda, S., see Yamamoto, K. 175/176 (1997) 1236
Gong, Qian, see Zhu, Donghai 175/176 (1997) 1004
González-Borrero, P.P., E. Marega, Jr., D.I. Lubyshev, E. Petitprez and P. Basmaji, Molecular-beam epitaxy of self-assembled InAs quantum dots on non-(1 0 0) oriented GaAs 175/176 (1997) 765
Goorsky, M.S., see Xiang, Q. 175/176 (1997) 469
Goorsky, M.S., see Chu, M.A. 175/176 (1997) 1278
Goossen, K.W., see Kuo, J.M. 175/176 (1997) 971
Gorbunova, I., see Hey, R. 175/176 (1997) 1167
Gordeev, N.Yu., see Ustinov, V.M. 175/176 (1997) 689
Gösele, U., see Ustinov, V.M. 175/176 (1997) 689
Gossard, A.C., see Jackson, A. 175/176 (1997) 244
Gossard, A.C., see Mirin, R.P. 175/176 (1997) 696
Goto, H., see Kuze, N. 175/176 (1997) 868
Gotoh, H., see Nagao, S. 175/176 (1997) 1157
Graber, A., see Averbeck, R. 175/176 (1997) 122
Grahn, H.T., see Mazuelas, A. 175/176 (1997) 383
Grandjean, N., see Mesrine, M. 175/176 (1997) 1242
Gray, A., see Zeng, L. 175/176 (1997) 541
Greiling, P., Millimeterwave and digital applications of InP-based MBE grown HEMTs and HBTs 175/176 (1997) 8
Grein, C.H., see Wijewarnasuriya, P.S. 175/176 (1997) 647
Grilli, E., see Henini, M. 175/176 (1997) 1108
Grün, M., see Tatarenko, S. 175/176 (1997) 682
Grün, N., see Gaymann, A. 175/176 (1997) 898
Grützmacher, D., R. Hartmann, E. Müller, U. Gennser and A. Dommann, Photoluminescence study of Si/SiGe multiple quantum wells grown by MBE 175/176 (1997) 1144
Gunshor, R.L., see Ng, T.B. 175/176 (1997) 552
Guo, S.P., see He, L. 175/176 (1997) 677
Guzzi, M., see Henini, M. 175/176 (1997) 1108

Haas, T.W., see Eyink, K.G. 175/176 (1997) 262
Hacke, P., G. Feuillet, H. Okumura and S. Yoshida, Stability of surface reconstructions on hexagonal GaN grown by molecular beam epitaxy 175/176 (1997) 94
Han, A.-C., see Wojtowicz, M. 175/176 (1997) 930
Han, J., see Ng, T.B. 175/176 (1997) 552
Han, J.W., see Cho, H.D. 175/176 (1997) 125
Hanamaki, Y., T. Takeuchi, N. Ogasawara and Y. Shiraki, Fabrication of InGaAs vertical-cavity surface-emitting lasers by molecular beam epitaxy on (4 1 1)A GaAs substrates and its room-temperature operation 175/176 (1997) 359
Hangleiter, A., see Eberl, K. 175/176 (1997) 702
Harde, P., see Künzel, H. 175/176 (1997) 940
Harmand, J.C., A. Kohl, M. Juhel and G. Le Roux, Molecular beam epitaxy of AlGaAsSb system for 1.55 μm Bragg mirrors 175/176 (1997) 372
Harris, Jr., J.S., see Solomon, G.S. 175/176 (1997) 707
Harris, Jr., J.S., see Okada, Y. 175/176 (1997) 1039
Hartmann, R., see Grützmacher, D. 175/176 (1997) 1144
Hase, A., see Künzel, H. 175/176 (1997) 411
Hasegawa, S., K. Sato, S. Torii and H. Nakashima, Growth parameter dependence of step patterns in AlGaAs molecular beam epitaxy on vicinal GaAs(1 1 0) inclined toward (1 1 1)A 175/176 (1997) 1075
Hasegawa, Y., see Xue, Q. 175/176 (1997) 174

Hashimoto, A., Y. Aiba, T. Motizuki, M. Ohkubo and A. Yamamoto, Initial growth stage of GaN on Si substrate by alternating source supply using dimethyl-hydrazine 175/176 (1997) 129
Haupt, M., K. Köhler, P. Ganser, S. Müller and W. Rothemund, Molecular beam epitaxy of $Al_{0.48}In_{0.52}As/Ga_{0.47}In_{0.53}As$ heterostructures on metamorphic $Al_xGa_yIn_{1-x-y}As$ buffer layers 175/176 (1997) 1028
Haury, A., see Tatarenko, S. 175/176 (1997) 682
Hayafuji, N., see Izumi, S. 175/176 (1997) 404
Hayashi, T., M. Tanaka, T. Nishinaga, H. Shimada, H. Tsuchiya and Y. Otuka, (GaMn)As:GaAs-based III–V diluted magnetic semiconductors grown by molecular beam epitaxy 175/176 (1997) 1063
Hayashi, T., see Yamamoto, K. 175/176 (1997) 1236
Hayden, R.K., see Henini, M. 175/176 (1997) 919
He, L., J.R. Yang, S.L. Wang, S.P. Guo, M.F. Yu, X.Q. Chen, W.Z. Fang, Y.M. Qiao, Q.Y. Zhang, R.J. Ding and T.L. Xin, A study of MBE growth and thermal annealing of p-type long wavelength HgCdTe 175/176 (1997) 677
He, P., see Benson, J.D. 175/176 (1997) 659
Heinecke, H., see Schneider, J.M. 175/176 (1997) 184
Heinecke, H., see Wachter, M. 175/176 (1997) 1186
Heinecke, H., see Popp, M. 175/176 (1997) 1247
Heiß, H., see Sexl, M. 175/176 (1997) 915
Heitz, R., see Ramachandran, T.R. 175/176 (1997) 216
Helbig, R., see Schmitt, J. 175/176 (1997) 528
Henini, M., I.E. Itskevich, T. Ihn, P. Moriarty, A. Nogaret, P.H. Beton, L. Eaves, P.C. Main, J.R. Middleton and J.S. Chauhan, MBE growth and magnetotunnelling transport properties of a single GaAs/AlAs/GaAs barrier incorporating InAs quantum dots 175/176 (1997) 782
Henini, M., R.K. Hayden, T. Takamasu, N. Miura, L. Eaves and G. Hill, Resonant tunnelling of holes in double barrier heterostructures grown by MBE on (1 1 0) oriented GaAs substrates 175/176 (1997) 919
Henini, M., N. Galbiati, E. Grilli, M. Guzzi and L. Pavesi, Photoluminescence investigation of p-type Si-doped AlGaAs grown by molecular beam epitaxy on (1 1 1)A, (2 1 1)A and (3 1 1)A GaAs surfaces 175/176 (1997) 1108
Henini, M., R.J. Hyndman, T. Ihn, B.L. Gallagher, T.J. Foster, J.S. Chauhan and J.R. Middleton, MBE growth and physics of strongly coupled p-type double quantum wells showing correlated $\nu = 1$ quantum Hall state 175/176 (1997) 1138
Hensel, H.-J., see Künzel, H. 175/176 (1997) 411
Heremans , J., see Partin, D.L. 175/176 (1997) 860
Hernández, L., see Hernández-Calderón, I. 175/176 (1997) 571
Hernández-Calderón, I., E. López-Luna, J. Luyo, M. Meléndez-Lira, O. de Melo, P. Díaz, L. Hernández, J. Fuentes, R. León and H. Sitter, Investigation of the structural properties of MBE grown ZnSe/GaAs heterostructures 175/176 (1997) 571
Hey, R., see Mazuelas, A. 175/176 (1997) 383
Hey, R., K.-J. Friedland, H. Kostial, R. Klann and H.K. Ploog, New route to reduce ionized impurity scattering in modulation-doped GaAs quantum wells 175/176 (1997) 1126
Hey, R., I. Gorbunova, M. Ramsteiner, M. Wassermeier, L. Däweritz and K.H. Ploog, Growth-mode-induced surface morphology and its relation to optical properties of GaAs single quantum wells 175/176 (1997) 1167
Hidaka, K., see Yamamoto, K. 175/176 (1997) 1236
Higashiwaki, M., M. Yamamoto, S. Shimomura, A. Adachi and S. Hiyamizu, High-density GaAs/$(GaAs)_2(AlAs)_2$ quantum wires naturally formed on (7 7 5)B-oriented GaAs substrates by molecular beam epitaxy 175/176 (1997) 814
Hilburger, U., see Malzer, S. 175/176 (1997) 960
Hill, D., see Farrell, T. 175/176 (1997) 1217
Hill, G., see Henini, M. 175/176 (1997) 919
Hillmer, H., R. Lösch and W. Schlapp, Strain-balanced AlGaInAs/InP heterostructures with up to 50 QWs by MBE 175/176 (1997) 1120
Hiraiwa, K., see Nishikata, K. 175/176 (1997) 990
Hiyamizu, S., see Tomita, N. 175/176 (1997) 809
Hiyamizu, S., see Higashiwaki, M. 175/176 (1997) 814
Hiyamizu, S., see Shinohara, K. 175/176 (1997) 924
Ho, E., see Ng, T.B. 175/176 (1997) 552
Ho, E., see Warlick, E.L. 175/176 (1997) 564
Ho, P., see Chu, J. 175/176 (1997) 964
Hoffman, C.A., see Lin, C.-H. 175/176 (1997) 955
Holý, V., see Zerlauth, S. 175/176 (1997) 459
Homma, Y., H. Yamaguchi and Y. Horikoshi, In situ observation of MEE GaAs growth using scanning electron microscopy 175/176 (1997) 292
Homma, Y., see Inoue, N. 175/176 (1997) 286
Hömmerich, U., see MacKenzie, J.D. 175/176 (1997) 84
Hong, M., J.P. Mannaerts, J.E. Bower, J. Kwo, M. Passlack, W-Y. Hwang and L.W. Tu, Novel $Ga_2O_3(Gd_2O_3)$ passivation techniques to produce low D_{it} oxide-GaAs interfaces 175/176 (1997) 422

Hopkinson, M. and J.P.R. David, Incorporation of As_2 in $InAs_xP_{1-x}$ and its application to $InAs_xP_{1-x}$/InP quantum well structures 175/176 (1997) 1033
Horikoshi, Y., see Andersson, T.G. 175/176 (1997) 117
Horikoshi, Y., see Muraki, K. 175/176 (1997) 162
Horikoshi, Y., see Homma, Y. 175/176 (1997) 292
Horikoshi, Y., see Kanisawa, K. 175/176 (1997) 304
Hornung, J., see Gaymann, A. 175/176 (1997) 898
Horst, S., see Johnson, F.G. 175/176 (1997) 46
Hosomi, K., see Mozume, T. 175/176 (1997) 1223
Hou Xun, see Wang Xiaoliang 175/176 (1997) 1254
Houng, Y.M. and M.R.T. Tan, MBE growth of highly reproducible VCSELs 175/176 (1997) 352
Hsieh, K.C., see Moy, A.M. 175/176 (1997) 819
Hsin, Y.M., see Li, N.Y. 175/176 (1997) 387
Hua, G.C., see Ng, T.B. 175/176 (1997) 552
Huang, F., see Chu, M.A. 175/176 (1997) 1278
Huang, Q., see Chen, H. 175/176 (1997) 524
Huang, Q., see Feng, W. 175/176 (1997) 1173
Hughes, W.C., see Johnson, M.A.L. 175/176 (1997) 72
Hughes, W.C., C. Boney, M.A.L. Johnson, J.W. Cook, Jr. and J.F. Schetzina, Surface preparation of ZnSe substrates for MBE growth of II–VI light emitters 175/176 (1997) 546
Hui, S.P., see Kuo, J.M. 175/176 (1997) 971
Hunter, A.T., see Croke, E.T. 175/176 (1997) 486
Hutchinson, A.L., see Faist, J. 175/176 (1997) 22
Hvam, J.M., see Sørensen, C.B. 175/176 (1997) 1097
Hwang, W-Y., see Hong, M. 175/176 (1997) 422
Hyndman, R.J., see Henini, M. 175/176 (1997) 1138

Ibbetson, J.P., see Mirin, R.P. 175/176 (1997) 696
Ihn, T., see Henini, M. 175/176 (1997) 782
Ihn, T., see Henini, M. 175/176 (1997) 1138
Iizuka, K., K. Matsumaru, T. Suzuki, Y. Takahira, T. Nishioka and H. Okamoto, High-temperature surface cleaning of AlGaAs without As flux for MBE regrowth 175/176 (1997) 447
Ikeda, M., see Okuyama, H. 175/176 (1997) 587
Inoue, N., Y. Kawamura, Y. Homma, J. Osaka, T. Araki and T. Ito, Two-dimensional to one-dimensional mode change in GaAs molecular beam epitaxy revealed by in situ scanning electron microscopy 175/176 (1997) 286
Irikawa, M., see Nishikata, K. 175/176 (1997) 990
Ishibashi, A., see Okuyama, H. 175/176 (1997) 587
Ishikawa, T., see López-López, M. 175/176 (1997) 799
Ishikawa, Y., N. Shibata and S. Fukatsu, Stratified suspension of highly ordered Si nanoparticles in SiO_2 created by Si MBE with oxygen coimplantation 175/176 (1997) 493
Isoya, T., see Yamamoto, M. 175/176 (1997) 191
Ito, H., see Nagao, S. 175/176 (1997) 1157
Ito, T., see Yamamoto, M. 175/176 (1997) 191
Ito, T., see Inoue, N. 175/176 (1997) 286
Itoh, M., see Sugiura, H. 175/176 (1997) 1205
Itskevich, I.E., see Henini, M. 175/176 (1997) 782
Iwabuchi, T., see Yamamoto, M. 175/176 (1997) 191
Iwata, K., H. Asahi, K. Asami and S. Gonda, Gas source MBE growth of GaN rich side of $GaN_{1-x}P_x$ using ion-removed ECR radical cell 175/176 (1997) 150
Iwata, K., see Asahi, H. 175/176 (1997) 1195
Iye, Y., see Shen, A. 175/176 (1997) 1069
Izumi, S., Y. Yamamoto, T. Kunii, S. Miyakuni, N. Hayafuji, K. Sato and M. Otsubo, Selective area chemical beam epitaxial regrowth of Si-doped GaAs by using silicon tetraiodide for field effect transistor application 175/176 (1997) 404

Jackson, A., P. Pinsukanjana, L. Coldren and A. Gossard, Monitoring Ga and In desorption and In surface segregation during MBE using atomic absorption 175/176 (1997) 244
Jamba, D.M., see Rajavel, R.D. 175/176 (1997) 653
Jan, W.Y., see Kuo, J.M. 175/176 (1997) 971
Janiak, K., see Künzel, H. 175/176 (1997) 411
Jenny, J.R., R. Kaspi and K.R. Evans, Growth kinetics of GaN grown by gas-source molecular beam epitaxy 175/176 (1997) 89
Jensen, J.E., see Rajavel, R.D. 175/176 (1997) 653
Jeon, Min-Hyon, see Kim, Moon-Deock 175/176 (1997) 637
Jeppesen, S., see Miller, M.S. 175/176 (1997) 747
Ji, Jeong-Keun, see Kim, Moon-Deock 175/176 (1997) 637
Jiang, S., see Zhou, X. 175/176 (1997) 624
Jin-Phillipp, J.Y., see Eberl, K. 175/176 (1997) 702
Jin-Phillipp, N.Y., see Brunner, K. 175/176 (1997) 451
Johnson, E.A., see Vögele, B. 175/176 (1997) 229
Johnson, F.G., O. King, F. Seiferth, S. Horst, D.R. Stone, R.D. Whaley, M. Dagenais and Y.J. Chen, Solid source MBE growth and regrowth of 1.55 μm wavelength GaInAsP/InP ridge lasers 175/176 (1997) 46
Johnson, M.A.L., W.C. Hughes, W.H. Rowland, Jr., J.W. Cook, Jr., J.F. Schetzina, M. Leonard, H.S. Kong, J.A. Edmond and J. Zavada, Growth of GaN, InGaN, and AlGaN films and quantum well structures by molecular beam epitaxy 175/176 (1997) 72
Johnson, M.A.L., see Hughes, W.C. 175/176 (1997) 546
Johnson, S.R. and T. Tiedje, Effect of substrate thickness, back surface texture, reflectivity, and thin film interference on optical band-gap thermometry 175/176 (1997) 273

Johs, B., see Kuo, C.H. 175/176 (1997) 281
Johs, B., see Benson, J.D. 175/176 (1997) 659
Jokerst, N.M., see Fournier, F. 175/176 (1997) 203
Jones, C.R., see Evans, K.R. 175/176 (1997) 1316
Jones, G.A.C., see Brown, S.J. 175/176 (1997) 346
Jones, G.A.C., see Beere, H.E. 175/176 (1997) 398
Jones, T.S., see Zhang, J. 175/176 (1997) 1284
Joyce, B.A., see Zhang, J. 175/176 (1997) 477
Joyce, B.A., see Mizushima, K. 175/176 (1997) 509
Joyce, B.A., see Zhang, J. 175/176 (1997) 1284
Joyce, T.B., T.J. Bullough, T. Farrell, B.R. Davidson, D.E. Sykes and A. Chew, Carbon delta doping in chemical beam epitaxy using CBr_4 175/176 (1997) 377
Joyce, T.B., see Farrell, T. 175/176 (1997) 1217
Juhel, M., see Harmand, J.C. 175/176 (1997) 372
Jung, K.S., see Cho, H.D. 175/176 (1997) 125

Kalburge, A., see Ramachandran, T.R. 175/176 (1997) 216
Kamath, K., P. Bhattacharya and J. Phillips, Room temperature luminescence from self-organized $In_xGa_{1-x}As/GaAs$ ($0.35 < x < 0.45$) quantum dots with high size uniformity 175/176 (1997) 720
Kamath, K., P. Bhattacharya and J. Singh, Multispectral InGaAs/GaAs/AlGaAs laser arrays by MBE growth on patterned substrates 175/176 (1997) 935
Kamiya, I., see Koshiba, S. 175/176 (1997) 804
Kaneko, T., see Zhang, J. 175/176 (1997) 1284
Kaneko, Y., see Mars, D.E. 175/176 (1997) 365
Kang, S.K., see Yoo, M.C. 175/176 (1997) 100
Kang, T.W., see Cho, H.D. 175/176 (1997) 125
Kanisawa, K., H. Yamaguchi and Y. Horikoshi, Electronic properties of monolayer steps on GaAs (0 0 1) surfaces studied by scanning tunneling microscopy 175/176 (1997) 304
Kapon, E., see Lebouché-Girard, N. 175/176 (1997) 1210
Karlsson, C., see Wang, S.M. 175/176 (1997) 1016
Kasahara, K., see Shinohara, K. 175/176 (1997) 924
Kaspi, R., see Jenny, J.R. 175/176 (1997) 89
Kaspi, R. and K.R. Evans, Sb-surface segregation and the control of compositional abruptness at the GaAsSb/GaAs interface 175/176 (1997) 838
Kaspi, R., see Evans, K.R. 175/176 (1997) 1316
Kasukawa, A., see Nishikata, K. 175/176 (1997) 990
Katsumoto, S., see Shen, A. 175/176 (1997) 1069
Kawabe, M., see Okada, Y. 175/176 (1997) 1039
Kawakami, Y., see Suda, J. 175/176 (1997) 593
Kawamura, Y., see Inoue, N. 175/176 (1997) 286
Kawasumi, T., see Okuyama, H. 175/176 (1997) 587
Kiesel, P., see Malzer, S. 175/176 (1997) 960
Kilpelä, O., see Novikov, S.V. 175/176 (1997) 514
Kim, Bong-Jin, see Kim, Moon-Deock 175/176 (1997) 637
Kim, C.C., Y.P. Chen, M. Daraselia, S. Sivananthan, S.-C.Y. Tsen and D.J. Smith, Reflectivity difference spectroscopy study of thin film ZnSe grown on GaAs by molecular beam epitaxy 175/176 (1997) 328
Kim, C.C., Y.P. Chen, S. Sivananthan, S.-C.Y. Tsen and D.J. Smith, Molecular beam epitaxial growth of ZnSe on GaAs substrates: influence of precursors on interface quality 175/176 (1997) 613
Kim, E.S., N. Usami, H. Sunamura, S. Fukatsu and Y. Shiraki, Luminescence study on Ge islands as stressors on $Si_{1-x}Ge_x/Si$ quantum well 175/176 (1997) 519
Kim, J.Y., see Miyake, Y. 175/176 (1997) 465
Kim, Jin-Suck, see Kim, Moon-Deock 175/176 (1997) 637
Kim, M., see Lippert, G. 175/176 (1997) 473
Kim, Moon-Deock, Bong-Jin Kim, Min-Hyon Jeon, Jeong-Keun Ji, Sang-Dong Lee, Eun-Soon Oh, Jin-Suck Kim, Hae-Sung Park and Tae-Il Kim, Room-temperature continuous-wave operation of ZnSe-based blue–green laser diode grown by molecular beam epitaxy 175/176 (1997) 637
Kim, S.J., H. Asahi, M. Takemoto, K. Asami, J.H. Noh and S. Gonda, Self-organized quantum dot structures in strained $(GaP)_n(InP)_m$ short period superlattices grown on GaAs (N 1 1) by gas-source MBE 175/176 (1997) 754
Kim, Sung-Bock, see Ro, Jeong-Rae 175/176 (1997) 1231
Kim, Tae-Il, see Kim, Moon-Deock 175/176 (1997) 637
Kimura, Y., see Nakagawa, K. 175/176 (1997) 481
King, O., see Johnson, F.G. 175/176 (1997) 46
Kirk, W.P., see Zhou, X. 175/176 (1997) 624
Kishi, T., see Tomita, N. 175/176 (1997) 809
Kiyama, H., see Xue, Q. 175/176 (1997) 174
Klaassen, J.J., see Chow, P.P. 175/176 (1997) 61
Klaassen, J.J., see Van Hove, J.M. 175/176 (1997) 79
Klann, R., see Hey, R. 175/176 (1997) 1126
Kneissl, M., see Malzer, S. 175/176 (1997) 960
Ko, N.H., see Cho, H.D. 175/176 (1997) 125
Kobayashi, N.P., see Ramachandran, T.R. 175/176 (1997) 216
Koch, M.W., see Wamsley, C.C. 175/176 (1997) 42
Koguchi, N., see Tsukamoto, S. 175/176 (1997) 1303
Koh, H., see Asahi, H. 175/176 (1997) 1195
Kohl, A., see Harmand, J.C. 175/176 (1997) 372
Köhler, K., see Gaymann, A. 175/176 (1997) 898
Köhler, K., see Haupt, M. 175/176 (1997) 1028
Köhler, R., see Parthier, L. 175/176 (1997) 642
Koike, K., see Yano, M. 175/176 (1997) 665
Kolodziejski, L.A., see Ng, T.B. 175/176 (1997) 552
Kolodziejski, L.A., see Warlick, E.L. 175/176 (1997) 564
Komarov, S., see Solomon, G.S. 175/176 (1997) 707
Konagai, M., see Okamoto, T. 175/176 (1997) 1045
Kong, H.S., see Johnson, M.A.L. 175/176 (1997) 72
Kong, M.Y., see Pan, D. 175/176 (1997) 760

Kong Meiying, see Wang Xiaoliang 175/176 (1997) 1254
Konkar, A., H.T. Lin, D.H. Rich, P. Chen and A. Madhukar, Growth controlled fabrication and cathodoluminescence study of 3D confined GaAs volumes on non-planar patterned GaAs(0 0 1) substrates 175/176 (1997) 741
Kop'ev, P.S., see Ustinov, V.M. 175/176 (1997) 689
Kosai, K., see Rajavel, R.D. 175/176 (1997) 653
Koshiba, S., see Noda, T. 175/176 (1997) 787
Koshiba, S., I. Tanaka, Y. Nakamura, I. Kamiya, T. Someya, T. Ngo and H. Sakaki, UHV-AFM study of MBE-grown 10 nm scale ridge quantum wires 175/176 (1997) 804
Koshiba, S., see Nakamura, Y. 175/176 (1997) 1092
Kosogov, A.O., see Ustinov, V.M. 175/176 (1997) 689
Kossives, D., see Kuo, J.M. 175/176 (1997) 971
Kostial, H., see Hey, R. 175/176 (1997) 1126
Kovsh, A.R., see Ustinov, V.M. 175/176 (1997) 689
Kowalski, B., see Miller, M.S. 175/176 (1997) 747
Kratzer, H., see Nutsch, A. 175/176 (1997) 1200
Kraus, S., see Sexl, M. 175/176 (1997) 915
Krispin, P., see Behrend, J. 175/176 (1997) 178
Kroemer, H., see Thomas, M. 175/176 (1997) 894
Kromann, R.F., R.N. Bicknell-Tassius, A.S. Brown, J.F. Dorsey, K. Lee and G. May, Real-time monitoring of RHEED using machine vision techniques 175/176 (1997) 334
Kudo, M. and T. Mishima, MBE growth of Si-doped InAlAsSb layers lattice-matched with InAs 175/176 (1997) 844
Kudo, M., H. Matsumoto, T. Tanimoto, T. Mishima and I. Ohbu, Improved hole transport properties of highly strained $In_{0.35}Ga_{0.65}As$ channel double-modulation-doped structures grown by MBE on GaAs 175/176 (1997) 910
Kunii, T., see Izumi, S. 175/176 (1997) 404
Künzel, H., J. Böttcher, A. Hase, H.-J. Hensel, K. Janiak, G. Urmann and A. Paraskevopoulos, MBE regrowth on AlGaInAs DFB gratings using in-situ hydrogen radical cleaning 175/176 (1997) 411
Künzel, H., J. Böttcher, P. Harde and R. Maessen, MBE growth of high-quality InP for GaInAs/InP heterostructures using incongruent evaporation of GaP 175/176 (1997) 940
Kuo, C.H., M.D. Boonzaayer, M.F. De-Herrera, D.K. Schroder, G.N. Maracas and B. Johs, Real time in-situ thickness control of Fabry–Perot cavities in MBE by 44 and 88 wavelength ellipsometry 175/176 (1997) 281
Kuo, J.M., Y.C. Wang, K.W. Goossen, L.M.F. Chirovsky, S.P. Hui, B.T. Tseng, J. Walker, A.L. Lentine, R.E. Leibenguth, G. Livescu, W.Y. Jan, J.E. Cunningham, L.A. D'Asaro, A. Ron, D. Dahringer, D. Kossives, D.D. Bacon, R.L. Morrison, R.A. Novotny, D.B. Buchholz and W.E. Mayo, Large array of GaAs modulators and detectors flip-chip solder bonded to silicon CMOS using InGaP as the selective etch stop for GaAs substrate removal 175/176 (1997) 971
Kurafuji, T., see Niki, S. 175/176 (1997) 1051
Kuroiwa, T., see Shen, A. 175/176 (1997) 1069
Kurtenbach, A., see Eberl, K. 175/176 (1997) 702
Kuze, N., H. Goto, M. Matsui, I. Shibasaki and H. Sakaki, Molecular beam epitaxial growth of high electron mobility InAs/AlGaAsSb deep quantum well structures 175/176 (1997) 868
Kwo, J., see Hong, M. 175/176 (1997) 422

Lampert, W.V., see Eyink, K.G. 175/176 (1997) 262
Landin, L., see Miller, M.S. 175/176 (1997) 747
Landwehr, G., see Fischer, F. 175/176 (1997) 532
Landwehr, G., see Lugauer, H.-J. 175/176 (1997) 619
Laruelle, F., F. Lelarge, Z.Z. Wang, T. Mélin, A. Cavanna and B. Etienne, Organized growth of GaAs/AlAs lateral superlattices on vicinal surfaces: where are the limits? 175/176 (1997) 1087
Laruelle, F., see Lelarge, F. 175/176 (1997) 1102
Laursen, T., see Croke, E.T. 175/176 (1997) 486
Lauterwasser, B., see DiLorenzo, J.V. 175/176 (1997) 1
Lazzarini, L., see Bosacchi, A. 175/176 (1997) 1009
Lazzarino, M., see Lazzeri, M. 175/176 (1997) 603
Lazzeri, M., V. Pellegrini, F. Beltram, M. Lazzarino, J.J. Paggel, L. Sorba, S. Rubini, A. Bonanni and A. Franciosi, Electrical characterization of engineered ZnSe–GaAs heterojunction diodes 175/176 (1997) 603
Le Roux, G., see Harmand, J.C. 175/176 (1997) 372
Lebkiri, A., see Garcia, J.Ch. 175/176 (1997) 1265
Lebouché-Girard, N., A. Rudra and E. Kapon, Growth and transformation of ultra-thin InAs/InP layers obtained by chemical beam epitaxy 175/176 (1997) 1210
Ledentsov, N.N., see Ustinov, V.M. 175/176 (1997) 689
Lee, Ching-Ting, see Chyi, Jen-Inn 175/176 (1997) 777
Lee, El-Hang, see Ro, Jeong-Rae 175/176 (1997) 1231
Lee, H.P., see Zhou, J.J. 175/176 (1997) 52
Lee, H.P., see Li, Y. 175/176 (1997) 250
Lee, J.W., see Yoo, M.C. 175/176 (1997) 100
Lee, K., see Kromann, R.F. 175/176 (1997) 334
Lee, K., see Bicknell-Tassius, R.N. 175/176 (1997) 1131

Lee, Sang-Dong, see Kim, Moon-Deock 175/176 (1997) 637
Lees, A.K., see Zhang, J. 175/176 (1997) 477
Leibenguth, R.E., see Kuo, J.M. 175/176 (1997) 971
Lelarge, F., see Laruelle, F. 175/176 (1997) 1087
Lelarge, F., Z.Z. Wang, A. Cavanna, F. Laruelle and B. Etienne, The building up of terrace periodicity by MBE growth on (0 0 1) GaAs vicinal surfaces 175/176 (1997) 1102
Lentine, A.L., see Kuo, J.M. 175/176 (1997) 971
León, R., see Hernández-Calderón, I. 175/176 (1997) 571
Leonard, M., see Johnson, M.A.L. 175/176 (1997) 72
Leroux, M., see Mesrine, M. 175/176 (1997) 1242
Leroux, M., see Garcia, J.Ch. 175/176 (1997) 1265
Lew, A., see Zhang, Y.-H. 175/176 (1997) 833
Leys, M.R., see Marschner, T. 175/176 (1997) 1081
Li, A.Z., Y. Zhao, Y.L. Zheng, G.T. Chen, G.P. Ru, W.Z. Shen and J.Q. Zhong, MBE growth and characterization of high-quality GaInAsSb/AlGaAsSb strained multiple quantum well structures 175/176 (1997) 873
Li, J.M., see Pan, D. 175/176 (1997) 760
Li, N.Y., Y.M. Hsin, P.M. Asbeck and C.W. Tu, Improving the etched/regrown GaAs interface by in-situ etching using tris-dimethylaminoarsenic 175/176 (1997) 387
Li, S., see Xiang, Q. 175/176 (1997) 469
Li, S.S., see Chu, J. 175/176 (1997) 964
Li, S.S., see Chin, A. 175/176 (1997) 999
Li, Shengying, see Zhu, Donghai 175/176 (1997) 1004
Li, Y., see Zhou, J.J. 175/176 (1997) 52
Li, Y., J.J. Zhou, P. Thompson, D. Pacheco, D.L. Sato, O. Arain and H.P. Lee, Simultaneous in situ measurement of substrate temperature and layer thickness using diffuse reflectance spectroscopy (DRS) during molecular beam epitaxy 175/176 (1997) 250
Liang, Jiben, see Zhu, Donghai 175/176 (1997) 1004
Liao, C.C., see Chin, A. 175/176 (1997) 999
Lin, C.-H., S.J. Murry, D. Zhang, P.C. Chang, Y. Zhou, S.S. Pei, J.I. Malin, C.L. Felix, J.R. Meyer, C.A. Hoffman and J.F. Pinto, MBE grown mid-infrared type-II quantum-well lasers 175/176 (1997) 955
Lin, H.T., see Konkar, A. 175/176 (1997) 741
Linder, K.K., F.C. Zhang, J.-S. Rieh and P. Bhattacharya, Characterization of mismatched SiGe grown on low temperature Si buffer layers by molecular beam epitaxy 175/176 (1997) 499
Linfield, E.H., see Brown, S.J. 175/176 (1997) 346
Linfield, E.H., see Burke, T.M. 175/176 (1997) 416
Lippert, G., P. Zaumseil, H.J. Osten and M. Kim, Enhancement of substitutional carbon incorporation in hydrogen-mediated pseudomorphic growth of strained alloy layers on Si(0 0 1) 175/176 (1997) 473
Litz, Th., see Fischer, F. 175/176 (1997) 532
Litz, Th., see Lugauer, H.-J. 175/176 (1997) 619
Liu, W.K., X.M. Fang, J. Winesett, W. Ma, X. Zhang, M.B. Santos and P.J. McCann, Large mismatch heteroepitaxy of InSb on Si(1 1 1) substrates using CaF_2 buffer layers 175/176 (1997) 853
Liu, W.K., see McCann, P.J. 175/176 (1997) 1057
Liu, X., see Zhou, J.J. 175/176 (1997) 52
Livescu, G., see Kuo, J.M. 175/176 (1997) 971
Lockwood, D.J., see Wasilewski, Z.R. 175/176 (1997) 238
Loi, K.K., see Mei, X.B. 175/176 (1997) 994
Long, A.R., see Vögele, B. 175/176 (1997) 229
López-López, M. and T. Ishikawa, Vertically stacked quantum wires fabricated by an in situ processing technique 175/176 (1997) 799
López-Luna, E., see Hernández-Calderón, I. 175/176 (1997) 571
Lösch, R., see Hillmer, H. 175/176 (1997) 1120
Loughin, S., see Uppal, P.N. 175/176 (1997) 877
Løvold, S., see Colin, T. 175/176 (1997) 670
Lubyshev, D.I., see Micovic, M. 175/176 (1997) 428
Lubyshev, D.I., see González-Borrero, P.P. 175/176 (1997) 765
Lugauer, H.J., see Fischer, F. 175/176 (1997) 532
Lugauer, H.J., Th. Litz, F. Fischer, A. Waag, T. Gerhard, U. Zehnder, W. Ossau and G. Landwehr, p-Type doping of beryllium chalcogenides grown by molecular beam epitaxy 175/176 (1997) 619
Luther, S., see Parthier, L. 175/176 (1997) 642
Luyo, J., see Hernández-Calderón, I. 175/176 (1997) 571

Ma, J., see Wang, Y. 175/176 (1997) 1289
Ma, W., see Liu, W.K. 175/176 (1997) 853
Ma, Z., see Sou, I.K. 175/176 (1997) 632
Machel, G., see Parthier, L. 175/176 (1997) 642
MacKenzie, J.D., C.R. Abernathy, S.J. Pearton, U. Hömmerich, X. Wu, R.N. Schwartz, R.G. Wilson and J.M. Zavada, Er doping of III-nitrides during growth by metalorganic molecular beam epitaxy 175/176 (1997) 84
Madhukar, A., see Ramachandran, T.R. 175/176 (1997) 216
Madhukar, A., see Konkar, A. 175/176 (1997) 741
Maeda, T., see Niwa, T. 175/176 (1997) 441
Maessen, R., see Künzel, H. 175/176 (1997) 940
Magno, R., see Bennett, B.R. 175/176 (1997) 888
Mahalingam, K., D.L. Dorsey, K.R. Evans and R. Venkatasubramanian, A Monte Carlo study of gallium desorption kinetics during MBE of (1 0 0)-GaAs/AlGaAs heterostructures 175/176 (1997) 211

Mahalingam, K., see Venkatasubramanian, R. 175/176 (1997) 224
Main, P.C., see Henini, M. 175/176 (1997) 782
Malin, J.I., see Lin, C.-H. 175/176 (1997) 955
Malzer, S., W. Geißelbrecht, U. Hilburger, M. Kneissl, P. Kiesel, R. Mayer and G.H. Döhler, Waveguide modulator structures with soft optical confinement grown by the epitaxial shadow mask (ESM) MBE-technique 175/176 (1997) 960
Manfra, M.J., see Turner, G.W. 175/176 (1997) 825
Mannaerts, J.P., see Hong, M. 175/176 (1997) 422
Mao, J., see Sou, I.K. 175/176 (1997) 632
Maracas, G.N., see Kuo, C.H. 175/176 (1997) 281
Marega, Jr., E., see González-Borrero, P.P. 175/176 (1997) 765
Markov, V.A., A.I. Nikiforov and O.P. Pchelyakov, In situ RHEED control of direct MBE growth of Ge quantum dots on Si (0 0 1) 175/176 (1997) 736
Mars, D.E., S.J. Rosner, Y. Kaneko, S. Nakagawa, T. Takeuchi and N. Yamada, Growth of vertical cavity surface emitting laser material on (3 1 1)B GaAs by MBE 175/176 (1997) 365
Marschner, T., R.T.H. Rongen, M.R. Leys, F.D. Tichelaar, H. Vonk and J.H. Wolter, Effects of tensile strain and substrate off-orientation on the growth of GaInAs/InP multiple quantum well structures by CBE 175/176 (1997) 1081
Martinka, M., see Benson, J.D. 175/176 (1997) 659
Maruyama, T., see Cho, S.H. 175/176 (1997) 112
Massie, S., see Bacher, K. 175/176 (1997) 977
Massies, J., see Mesrine, M. 175/176 (1997) 1242
Massies, J., see Garcia, J.Ch. 175/176 (1997) 1265
Matsui, M., see Kuze, N. 175/176 (1997) 868
Matsukura, F., see Shen, A. 175/176 (1997) 1069
Matsumaru, K., see Iizuka, K. 175/176 (1997) 447
Matsumoto, H., see Kudo, M. 175/176 (1997) 910
Matsumura, N., T. Matsuoka, H. Shimakawa and J. Saraie, Molecular beam epitaxial growth of ZnSe(1 1 1) films on GaAs(1 1 1)B substrates and nitrogen doping 175/176 (1997) 608
Matsuoka, T., see Matsumura, N. 175/176 (1997) 608
Matsushima, Y., see Sakata, H. 175/176 (1997) 1259
Maximov, I., see Miller, M.S. 175/176 (1997) 747
Maximov, M.V., see Ustinov, V.M. 175/176 (1997) 689
May, G., see Kromann, R.F. 175/176 (1997) 334
May, G., see Bicknell-Tassius, R.N. 175/176 (1997) 1131
Mayer, J.W., see Croke, E.T. 175/176 (1997) 486
Mayer, R., see Malzer, S. 175/176 (1997) 960
Mayo, W.E., see Kuo, J.M. 175/176 (1997) 971
Mazuelas, A., R. Hey, M. Wassermeier and H. T. Grahn, Strain compensation in highly carbon doped GaAs/AlAs distributed Bragg reflectors 175/176 (1997) 383
McCann, P.J., see Liu, W.K. 175/176 (1997) 853
McCann, P.J., X.M. Fang, W.K. Liu, B.N. Strecker and M.B. Santos, MBE growth of $PbSe/CaF_2/Si(1\,1\,1)$ heterostructures 175/176 (1997) 1057
Mei, X.B., K.K. Loi, W.S.C. Chang and C.W. Tu, Improved electroabsorption properties in 1.3 μm MQW waveguide modulators by a modified doping profile 175/176 (1997) 994
Meléndez-Lira, M., see Hernández-Calderón, I. 175/176 (1997) 571
Mélin, T., see Laruelle, F. 175/176 (1997) 1087
Menkara, H.M., R.N. Bicknell-Tassius, R. Benz, II and C.J. Summers, MBE growth and characterization of doped multiple quantum well avalanche photodiodes 175/176 (1997) 983
Menniger, J., see Nötzel, R. 175/176 (1997) 1114
Merkulov, A.V., see Nikishin, S.A. 175/176 (1997) 139
Merle d'Aubigné, Y., see Tatarenko, S. 175/176 (1997) 682
Mesrine, M., J. Massies, C. Deparis, N. Grandjean, E. Vanelle and M. Leroux, Indium surface segregation during chemical beam epitaxy of $Ga_{1-x}In_xAs/GaAs$ and $Ga_{1-x}In_xP/GaAs$ heterostructures 175/176 (1997) 1242
Metzger, R.A., see Fournier, F. 175/176 (1997) 203
Meyer, J.R., see Lin, C.-H. 175/176 (1997) 955
Meyer, T., see von Känel, H. 175/176 (1997) 340
Micovic, M., D. Lubyshev, W.Z. Cai, F. Flack, R.W. Streater, A.J. Spring-Thorpe and D.L. Miller, Iodine-assisted molecular beam epitaxy 175/176 (1997) 428
Middleton, J.R., see Henini, M. 175/176 (1997) 782
Middleton, J.R., see Henini, M. 175/176 (1997) 1138
Miller, D.L., see Micovic, M. 175/176 (1997) 428
Miller, M.S., L. Landin, S. Jeppesen, A. Petersson, I. Maximov, B. Kowalski and L. Samuelson, Manipulating InAs island sizes with chemical beam epitaxy growth on GaAs patterns 175/176 (1997) 747
Minami, F., see Nagao, S. 175/176 (1997) 1157
Mirin, R.P., J.P. Ibbetson, J.E. Bowers and A.C. Gossard, Overgrowth of InGaAs quantum dots formed by alternating molecular beam epitaxy 175/176 (1997) 696
Mishima, T., see Kudo, M. 175/176 (1997) 844
Mishima, T., see Kudo, M. 175/176 (1997) 910
Mishra, U.K., see Chavarkar, P. 175/176 (1997) 393
Missous, M. and S. O'Hagan, Low temperature (LT) and stoichiometric low temperature (SLT) MBE GaAs and related compounds: improved structural, electrical and optical properties 175/176 (1997) 197

Missous, M., see Buckle, P.D. 175/176 (1997) 1299
Mitsuhara, M., see Sugiura, H. 175/176 (1997) 1205
Miura, N., see Henini, M. 175/176 (1997) 919
Miyake, Y., J.Y. Kim, Y. Shiraki and S. Fukatsu, Why is a quantum-confined Stark shift absent in type-I strained $Si_{1-x}Ge_x/Si$ symmetric quantum wells? 175/176 (1997) 465
Miyakuni, S., see Izumi, S. 175/176 (1997) 404
Miyao, M., see Nakagawa, K. 175/176 (1997) 481
Mizushima, K., D.D. Vvedensky, P. Šmilauer, A. Zangwill, J. Zhang and B.A. Joyce, Effect of Hydrogen on the growth kinetics of Si(0 0 1) during GSMBE from disilane 175/176 (1997) 509
Morhain, C., see Tournié, E. 175/176 (1997) 577
Moriarty, P., see Henini, M. 175/176 (1997) 782
Moritz, A., see Eberl, K. 175/176 (1997) 702
Morrison, R.L., see Kuo, J.M. 175/176 (1997) 971
Motizuki, T., see Hashimoto, A. 175/176 (1997) 129
Moy, A.M., A.C. Chen, K.Y. Cheng, L.J. Chou and K.C. Hsieh, Growth of GaInAsP quantum wire heterostructures using the strain-induced lateral-layer ordering process 175/176 (1997) 819
Mozume, T. and K. Hosomi, Be redistribution in InGaAs and InP grown by gas source molecular beam epitaxy 175/176 (1997) 1223
Mui, D.S.L., see Chavarkar, P. 175/176 (1997) 393
Müller, E., see Grützmacher, D. 175/176 (1997) 1144
Müller, S., see Haupt, M. 175/176 (1997) 1028
Muraki, K. and Y. Horikoshi, Suppression of AlGaAs/GaAs superlattice intermixing by p-type doping 175/176 (1997) 162
Murry, S.J., see Lin, C.-H. 175/176 (1997) 955
Muto, S., see Nakata, Y. 175/176 (1997) 168

Nagamune, Y., see Noda, T. 175/176 (1997) 787
Nagao, S., K. Fujii, T. Fujimori, H. Gotoh, H. Ito and F. Minami, Radiative decay in type-II GaP/AlP/GaP quantum wells 175/176 (1997) 1157
Nagao, Y., see Sakata, H. 175/176 (1997) 1259
Naji, O.P., see Zhang, J. 175/176 (1997) 1284
Nakagawa, K., Y. Kimura and M. Miyao, Reduction of SiGe heterointerface mixing by atomic hydrogen irradiation during molecular beam epitaxy and its mechanism 175/176 (1997) 481
Nakagawa, S., see Mars, D.E. 175/176 (1997) 365
Nakamura, Y., see Koshiba, S. 175/176 (1997) 804
Nakamura, Y., S. Koshiba and H. Sakaki, Formation of multi-atomic steps and novel n-AlGaAs/GaAs heterojunctions on vicinal (1 1 1)B substrates by MBE and anisotropic transport of 2D electrons 175/176 (1997) 1092
Nakashima, H., see Hasegawa, S. 175/176 (1997) 1075
Nakata, Y., O. Ueda, Y. Nishikawa, S. Muto and N. Yokoyama, InAs/GaAs in-plane strained superlattices grown on slightly misoriented (1 1 0) InP substrates by molecular beam epitaxy 175/176 (1997) 168
Nakata, Y., Y. Sugiyama, T. Futatsugi and N. Yokoyama, Self-assembled structures of closely stacked InAs islands grown on GaAs by molecular beam epitaxy 175/176 (1997) 713
Nasi, L., see Bosacchi, A. 175/176 (1997) 1009
Ndap, J.O., see Tournié, E. 175/176 (1997) 577
Nee, Tzer-En, see Chyi, Jen-Inn 175/176 (1997) 777
Ng, T.B., C.C. Chu, J. Han, G.C. Hua, R.L. Gunshor, E. Ho, E.L. Warlick, L.A. Kolodziejski and A.V. Nurmikko, Reduction of extended defects in II–VI blue–green laser diodes 175/176 (1997) 552
Ngo, T., see Koshiba, S. 175/176 (1997) 804
Niki, S., P.J. Fons, H. Shibata, T. Kurafuji, A. Yamada, Y. Okada, H. Oyanagi, W.G. Bi and C.W. Tu, Effects of strain on the growth and properties of $CuInSe_2$ epitaxial films 175/176 (1997) 1051
Nikiforov, A.I., see Markov, V.A. 175/176 (1997) 736
Nikishin, S.A., G.A. Seryogin, H. Temkin, V.G. Antipov, S.S. Ruvimov and A.V. Merkulov, Gas source molecular beam epitaxy of cubic GaN/GaAs (0 0 1) using hydrazine 175/176 (1997) 139
Nishikata, K., H. Shimizu, K. Hiraiwa, S. Yoshida, N. Yamanaka, M. Irikawa and A. Kasukawa, Low dark current AlGaInAs/InP waveguide photodiodes using hybrid MBE and MOCVD growth 175/176 (1997) 990
Nishikawa, Y., see Nakata, Y. 175/176 (1997) 168
Nishinaga, T., see Hayashi, T. 175/176 (1997) 1063
Nishioka, T., see Iizuka, K. 175/176 (1997) 447
Niwa, T., N. Furuhata and T. Maeda, Formation of an n-GaAs/n-GaAs regrowth interface without carrier depletion using electron cyclotron resonance hydrogen plasma 175/176 (1997) 441
Noda, T., Y. Nagamune, Y. Ohno, S. Koshiba and H. Sakaki, Selective MBE growth of GaAs wire and dot structures using atomic hydrogens and their electronic properties 175/176 (1997) 787
Nogaret, A., see Henini, M. 175/176 (1997) 782
Noh, J.H., see Kim, S.J. 175/176 (1997) 754
Nörenberg, H., see Däweritz, L. 175/176 (1997) 1309

Nötzel, R., J. Menniger, M. Ramsteiner, A. Trampert, H.-P. Schönherr, L. Däweritz and K.H. Ploog, Patterned growth on GaAs (3 1 1)A substrates 175/176 (1997) 1114
Novikov, S.V., J. Sinkkonen, O. Kilpelä and S.V. Gastev, Visible light emission from MBD-grown Si/SiO_2 superlattices 175/176 (1997) 514
Novotny, R.A., see Kuo, J.M. 175/176 (1997) 971
Nozawa, K., see Andersson, T.G. 175/176 (1997) 117
Nurmikko, A.V., see Ng, T.B. 175/176 (1997) 552
Nutsch, A., B. Torabi, H. Kratzer, G. Tränkle and G. Weimann, CBE of 1.55 μm (GaIn)(AsP) lasers for monolithic integration 175/176 (1997) 1200

O'Hagan, S., see Missous, M. 175/176 (1997) 197
Oe, K., see Asahi, H. 175/176 (1997) 1195
Ogasawara, M., see Sugiura, H. 175/176 (1997) 1205
Ogasawara, N., see Hanamaki, Y. 175/176 (1997) 359
Ogino, T., see Xue, Q. 175/176 (1997) 174
Oh, Eun-Soon, see Kim, Moon-Deock 175/176 (1997) 637
Ohbu, I., see Kudo, M. 175/176 (1997) 910
Ohkubo, M., see Hashimoto, A. 175/176 (1997) 129
Ohno, H., see Shen, A. 175/176 (1997) 1069
Ohno, T., see Tsukamoto, S. 175/176 (1997) 1303
Ohno, Y., see Noda, T. 175/176 (1997) 787
Ohshima, N., see Yokozeki, M. 175/176 (1997) 435
Oiwa, A., see Shen, A. 175/176 (1997) 1069
Okada, Y., J.S. Harris, Jr., A. Sutoh and M. Kawabe, Growth of abrupt GaAs/Ge heterointerfaces by atomic hydrogen-assisted molecular beam epitaxy 175/176 (1997) 1039
Okada, Y., see Niki, S. 175/176 (1997) 1051
Okamoto, H., see Takahira, Y. 175/176 (1997) 267
Okamoto, H., see Iizuka, K. 175/176 (1997) 447
Okamoto, T., A. Yamada and M. Konagai, Growth and characterization of In_2Se_3 epitaxial films by molecular beam epitaxy 175/176 (1997) 1045
Oki, A.K., see Block, T.R. 175/176 (1997) 903
Okumura, H., see Hacke, P. 175/176 (1997) 94
Okumura, H., see Cho, S.H. 175/176 (1997) 112
Okuyama, H., T. Kawasumi, A. Ishibashi and M. Ikeda, Growth mechanism of II–VI compound semiconductors by molecular beam epitaxy 175/176 (1997) 587
Olsson, E., see Wang, S.M. 175/176 (1997) 1016
Ongaretto, C., see Tournié, E. 175/176 (1997) 577
Osaka, J., see Inoue, N. 175/176 (1997) 286
Ossau, W., see Fischer, F. 175/176 (1997) 532
Ossau, W., see Lugauer, H.-J. 175/176 (1997) 619
Osten , H.J., see Lippert, G. 175/176 (1997) 473
Otsubo, M., see Izumi, S. 175/176 (1997) 404
Otuka, Y., see Hayashi, T. 175/176 (1997) 1063
Oyanagi, H., see Niki, S. 175/176 (1997) 1051

Pacheco, D., see Zhou, J.J. 175/176 (1997) 52
Pacheco, D., see Li, Y. 175/176 (1997) 250
Paggel, J.J., see Lazzeri, M. 175/176 (1997) 603
Pagnod-Rossiaux, Ph., F. Gaborit, N. Tscherptner, L. Roux, C. Starck and B. Fernier, High temperature (Ga)InAsP/high band gap GaInAsP barriers 1.3 μm SL-MQW lasers grown by gas source MBE 175/176 (1997) 948
Pan, D., Y.P. Zeng, J.M. Li, C.H. Zhang, M.Y. Kong, H.M. Wang, C.Y. Wang and J. Wu, Intersubband absorption from $In_{0.26}Ga_{0.74}As/GaAs$ quantum dot superlattice 175/176 (1997) 760
Pan, Jen-Wei, see Chyi, Jen-Inn 175/176 (1997) 777
Panyakeow, S., see Sopitpan, S. 175/176 (1997) 1152
Paraskevopoulos, A., see Künzel, H. 175/176 (1997) 411
Park, Hae-Sung, see Kim, Moon-Deock 175/176 (1997) 637
Park, M.Y., see Yoo, M.C. 175/176 (1997) 100
Park, S.H., see Cho, H.D. 175/176 (1997) 125
Park, Seong-Ju, see Ro, Jeong-Rae 175/176 (1997) 1231
Park, W., see Schön, S. 175/176 (1997) 598
Parthier, L., H. Wißmann, S. Luther, G. Machel, M. Schmidbauer, R. Köhler and M. von Ortenberg, Growth and characterization of lattice-matched HgSe 175/176 (1997) 642
Partin, D.L., J. Heremans and C.M. Thrush, Indium antimonide doped with manganese grown by molecular beam epitaxy 175/176 (1997) 860
Pascua, D., see Wojtowicz, M. 175/176 (1997) 930
Passlack, M., see Hong, M. 175/176 (1997) 422
Patten, E.A., see Rajavel, R.D. 175/176 (1997) 653
Patterson, G.A., see Sacks, R.N. 175/176 (1997) 66
Patterson, J.K., see Eyink, K.G. 175/176 (1997) 262
Pavesi, L., see Henini, M. 175/176 (1997) 1108
Pchelyakov, O.P., see Markov, V.A. 175/176 (1997) 736
Pearton, S.J., see MacKenzie, J.D. 175/176 (1997) 84
Pei, S.S., see Lin, C.-H. 175/176 (1997) 955
Pellegrini, V., see Lazzeri, M. 175/176 (1997) 603
Pensl, G., see Schmitt, J. 175/176 (1997) 528
Pepper, M., see Burke, T.M. 175/176 (1997) 416
Pessa, M., see Toivonen, M. 175/176 (1997) 37
Petersson, A., see Miller, M.S. 175/176 (1997) 747
Petitprez, E., see González-Borrero, P.P. 175/176 (1997) 765
Petrich, G.S., see Warlick, E.L. 175/176 (1997) 564
Phillipp, F., see Brunner, K. 175/176 (1997) 451
Phillipp, F., see Eberl, K. 175/176 (1997) 702
Phillips, J., see Kamath, K. 175/176 (1997) 720
Pietralla, J.-T., see Schneider, J.M. 175/176 (1997) 184
Pinsukanjana, P., see Jackson, A. 175/176 (1997) 244
Pinto, J.F., see Lin, C.-H. 175/176 (1997) 955
Ploog, K.H., see Brandt, O. 175/176 (1997) 134
Ploog, K.H., see Braun, W. 175/176 (1997) 156
Ploog, K.H., see Behrend, J. 175/176 (1997) 178
Ploog, K.H., see Däweritz, L. 175/176 (1997) 310

Ploog, K.H., see Nötzel, R. 175/176 (1997) 1114
Ploog, H.K., see Hey, R. 175/176 (1997) 1126
Ploog, K.H., see Hey, R. 175/176 (1997) 1167
Ploog, K.H., see Däweritz, L. 175/176 (1997) 1309
Poole, P., see Wasilewski, Z.R. 175/176 (1997) 238
Popp, M., H. Heinecke, H. Baumeister and E. Veuhoff, Full gaseous source growth of separate confinement MQW 1.55 μm laser structures in a production MOMBE 175/176 (1997) 1247
Postigo, P.A., T. Utzmeier, G. Armelles and F. Briones, A new in situ III–V surface characterization technique: chemical modulation spectroscopy 175/176 (1997) 298
Postigo, P.A., see Utzmeier, T. 175/176 (1997) 725

Qiao, Y.M., see He, L. 175/176 (1997) 677

Radford, W.A., see Rajavel, R.D. 175/176 (1997) 653
Rajavel, R.D., D.M. Jamba, O.K. Wu, J.E. Jensen, J.A. Wilson, E.A. Patten, K. Kosai, P. Goetz, G.R. Chapman and W.A. Radford, High performance HgCdTe two-color infrared detectors grown by molecular beam epitaxy 175/176 (1997) 653
Ramachandran, T.R., R. Heitz, N.P. Kobayashi, A. Kalburge, W. Yu, P. Chen and A. Madhukar, Re-entrant behavior of 2D to 3D morphology change and 3D island lateral size equalization via mass exchange in Stranski–Krastanow growth: InAs on GaAs(0 0 1) 175/176 (1997) 216
Ramam, A. and S.J. Chua, Luminescence anomaly in band gap tailored $In_{0.53}(Ga_xAl_{1-x})_{0.47}As$ quaternary alloy grown by molecular beam epitaxy 175/176 (1997) 1294
Ramsteiner, M., see Nötzel, R. 175/176 (1997) 1114
Ramsteiner, M., see Hey, R. 175/176 (1997) 1167
Ratanathammaphan, S., see Sopitpan, S. 175/176 (1997) 1152
Rich, D.H., see Konkar, A. 175/176 (1997) 741
Richter, W., see Däweritz, L. 175/176 (1997) 310
Riechert, H., see Averbeck, R. 175/176 (1997) 122
Rieh , J.-S., see Linder, K.K. 175/176 (1997) 499
Ringel, S.A., see Sieg, R.M. 175/176 (1997) 256
Ritchie, D.A., see Brown, S.J. 175/176 (1997) 346
Ritchie, D.A., see Beere, H.E. 175/176 (1997) 398
Ritchie, D.A., see Burke, T.M. 175/176 (1997) 416
Ro, Jeong-Rae, Sung-Bock Kim, Seong-Ju Park and El-Hang Lee, Growth temperature-dependent conduction-type inversion of C-doped InGaAs grown by chemical beam epitaxy 175/176 (1997) 1231
Robinson , B.J., see Wang, J. 175/176 (1997) 793
Robinson, G.Y., see Thiagarajan, P. 175/176 (1997) 945
Rolfe, S.J., see Wasilewski, Z.R. 175/176 (1997) 1270
Romanato, F., see Bosacchi, A. 175/176 (1997) 1009
Ron, A., see Kuo, J.M. 175/176 (1997) 971
Rongen, R.T.H., see Marschner, T. 175/176 (1997) 1081
Rorsman, N., see Wang, S.M. 175/176 (1997) 1016
Rosamond, M.F., see Van Hove, J.M. 175/176 (1997) 79
Rose, P.D., see Brown, S.J. 175/176 (1997) 346
Roslund, J.H., O. Zsebők, G. Swenson and T.G. Andersson, Molecular-beam-epitaxial growth of $Ga_{1-x}In_xSb$ on GaAs substrates 175/176 (1997) 883
Rosner, S.J., see Mars, D.E. 175/176 (1997) 365
Rothemund, W., see Haupt, M. 175/176 (1997) 1028
Roux, L., see Pagnod-Rossiaux, Ph. 175/176 (1997) 948
Rowland, Jr., W.H., see Johnson, M.A.L. 175/176 (1997) 72
Ru, G.P., see Li, A.Z. 175/176 (1997) 873
Rubini, S., see Lazzeri, M. 175/176 (1997) 603
Rudra, A., see Lebouché-Girard, N. 175/176 (1997) 1210
Ruvimov, S.S., see Nikishin, S.A. 175/176 (1997) 139

Sacks, R.N., P. Colombo, G.A. Patterson and K.A. Stair, Improved MBE-grown GaAs using a novel, high-capacity Ga effusion cell 175/176 (1997) 66
Sacks, R.N., see Sieg, R.M. 175/176 (1997) 256
Sakaki, H., see Yusa, G. 175/176 (1997) 730
Sakaki, H., see Noda, T. 175/176 (1997) 787
Sakaki, H., see Koshiba, S. 175/176 (1997) 804
Sakaki, H., see Kuze, N. 175/176 (1997) 868
Sakaki, H., see Nakamura, Y. 175/176 (1997) 1092
Sakamoto, K., see Xiang, Q. 175/176 (1997) 469
Sakata, H., Y. Nagao and Y. Matsushima, Symmetric triangular-barrier optoelectronic switch (S-TOPS) by gas source MBE 175/176 (1997) 1259
Sakurai, T., see Xue, Q. 175/176 (1997) 174
Salviati, G., see Bosacchi, A. 175/176 (1997) 1009
Saminadayar, K., see Tatarenko, S. 175/176 (1997) 682
Samuelson, L., see Miller, M.S. 175/176 (1997) 747
Sano, N., see Shinohara, K. 175/176 (1997) 924
Santos, M.B., see Liu, W.K. 175/176 (1997) 853
Santos, M.B., see McCann, P.J. 175/176 (1997) 1057
Saraie, J., see Matsumura, N. 175/176 (1997) 608
Sasaki, M., see Yoshida, S. 175/176 (1997) 107
Sasaki, M. and S. Yoshida, Surface chemistry during metalorganic molecular beam epitaxy studied by pulsed molecular beam scattering 175/176 (1997) 1178
Sato, D.L., see Li, Y. 175/176 (1997) 250
Sato, K., see Izumi, S. 175/176 (1997) 404
Sato, K., see Hasegawa, S. 175/176 (1997) 1075
Savolainen, P., see Toivonen, M. 175/176 (1997) 37
Schadt, M., see Schmitt, J. 175/176 (1997) 528
Schäffler, F., see Zerlauth, S. 175/176 (1997) 459

Schaub, J., see Gaymann, A. 175/176 (1997) 898
Schetzina, J.F., see Johnson, M.A.L. 175/176 (1997) 72
Schetzina, J.F., see Hughes, W.C. 175/176 (1997) 546
Schier, M., see Wachter, M. 175/176 (1997) 1186
Schlapp, W., see Hillmer, H. 175/176 (1997) 1120
Schmidbauer, M., see Parthier, L. 175/176 (1997) 642
Schmitt, J., T. Troffer, K. Christiansen, M. Schadt, S. Christiansen, R. Helbig, G. Pensl and H.P. Strunk, Characterization of homoepitaxial SiC layers 175/176 (1997) 528
Schneider, J.M., J.-T. Pietralla and H. Heinecke, Control of chemical composition and band gap energy in $Ga_xIn_{1-x-y}Al_yAs$ on InP during molecular beam epitaxy 175/176 (1997) 184
Schöffel, U., see Wachter, M. 175/176 (1997) 1186
Schön, S., M. Chaichimansour, W. Park, T. Yang, B.K. Wagner and C.J. Summers, Homogeneous and δ-doped ZnS:Mn grown by MBE 175/176 (1997) 598
Schönherr, H.-P., see Nötzel, R. 175/176 (1997) 1114
Schroder, D.K., see Kuo, C.H. 175/176 (1997) 281
Schützendübe, P., see Däweritz, L. 175/176 (1997) 310
Schützendübe, P., see Däweritz, L. 175/176 (1997) 1309
Schwartz, R.N., see MacKenzie, J.D. 175/176 (1997) 84
Seaford, M., see Bacher, K. 175/176 (1997) 977
Segawa, Y., see Yasuda, T. 175/176 (1997) 583
Seiferth, F., see Johnson, F.G. 175/176 (1997) 46
Semendy, F., see Zeng, L. 175/176 (1997) 541
Semendy, F., see Cavus, A. 175/176 (1997) 558
Seryogin, G.A., see Nikishin, S.A. 175/176 (1997) 139
Sexl, M., G. Böhm, D. Xu, H. Heiß, S. Kraus, G. Tränkle and G. Weimann, MBE growth of double-sided doped InAlAs/InGaAs HEMTs with an InAs layer inserted in the channel 175/176 (1997) 915
Shanabrook, B.V., see Thibado, P.M. 175/176 (1997) 317
Shanabrook, B.V., see Bennett, B.R. 175/176 (1997) 888
Shen, A., H. Ohno, F. Matsukura, Y. Sugawara, N. Akiba, T. Kuroiwa, A. Oiwa, A. Endo, S. Katsumoto and Y. Iye, Epitaxy of (Ga, Mn)As, a new diluted magnetic semiconductor based on GaAs 175/176 (1997) 1069
Shen, W.Z., see Li, A.Z. 175/176 (1997) 873
Sheng, Y.N., see Wang, Y. 175/176 (1997) 1289
Shernyakov, Yu.M., see Ustinov, V.M. 175/176 (1997) 689
Shibasaki, I., Mass production of InAs Hall elements by MBE 175/176 (1997) 13
Shibasaki, I., see Yamamoto, M. 175/176 (1997) 191
Shibasaki, I., see Kuze, N. 175/176 (1997) 868
Shibata, H., see Niki, S. 175/176 (1997) 1051
Shibata, N., see Ishikawa, Y. 175/176 (1997) 493
Shieh, Jia-Lin, see Chyi, Jen-Inn 175/176 (1997) 777
Shimada, H., see Hayashi, T. 175/176 (1997) 1063
Shimakawa, H., see Matsumura, N. 175/176 (1997) 608
Shimizu, H., see Nishikata, K. 175/176 (1997) 990
Shimomura, S., see Tomita, N. 175/176 (1997) 809
Shimomura, S., see Higashiwaki, M. 175/176 (1997) 814
Shimomura, S., see Shinohara, K. 175/176 (1997) 924
Shinohara, K., K. Kasahara, S. Shimomura, A. Adachi, N. Sano and S. Hiyamizu, GaAs/AlAs resonant tunneling diodes with super-flat interfaces grown on (4 1 1)A GaAs substrates by MBE 175/176 (1997) 924
Shiraki, Y., see Hanamaki, Y. 175/176 (1997) 359
Shiraki, Y., see Miyake, Y. 175/176 (1997) 465
Shiraki, Y., see Yutani, A. 175/176 (1997) 504
Shiraki, Y., see Kim, E.S. 175/176 (1997) 519
Sieg, R.M., R.N. Sacks and S.A. Ringel, Application of pyrometric interferometry to the in situ monitoring of $In_{0.52}Al_{0.48}As$, $In_{0.53}Ga_{0.47}As$, and quaternary alloy growth on InP substrates 175/176 (1997) 256
Simmons, J.G., see Wang, J. 175/176 (1997) 793
Singh, J., see Kamath, K. 175/176 (1997) 935
Sinkkonen, J., see Novikov, S.V. 175/176 (1997) 514
Sirringhaus, H., see von Känel, H. 175/176 (1997) 340
Sirtori, C., see Faist, J. 175/176 (1997) 22
Sitter, H., see Hernández-Calderón, I. 175/176 (1997) 571
Sivananthan, S., see Kim, C.C. 175/176 (1997) 328
Sivananthan, S., see Kim, C.C. 175/176 (1997) 613
Sivananthan, S., see Wijewarnasuriya, P.S. 175/176 (1997) 647
Sivco, D.L., see Faist, J. 175/176 (1997) 22
Skauli, T., see Colin, T. 175/176 (1997) 670
Skuras, E., see Vögele, B. 175/176 (1997) 229
Šmilauer, P., see Mizushima, K. 175/176 (1997) 509
Smith, D.J., see Kim, C.C. 175/176 (1997) 328
Smith, D.J., see Croke, E.T. 175/176 (1997) 486
Smith, D.J., see Kim, C.C. 175/176 (1997) 613
Sobiesierksi, Z., see Zhang, J. 175/176 (1997) 477
Södervall, U., see Thordson, J.V. 175/176 (1997) 234
Solomon, G.S., S. Komarov, J.S. Harris, Jr. and Y. Yamamoto, Increased size uniformity through vertical quantum dot columns 175/176 (1997) 707
Someya, T., see Koshiba, S. 175/176 (1997) 804
Sopitpan, S., P. Cheewatas, S. Thainoi, S. Ratanathammaphan and S. Panyakeow, Photoluminescence spectra of shadow masked multiple quantum wells 175/176 (1997) 1152
Sorba, L., see Lazzeri, M. 175/176 (1997) 603
Sørensen, C.B., H. Gislason and J.M. Hvam, MBE growth of two-dimensional electron gases on (110) GaAs 175/176 (1997) 1097
Sou, I.K., J. Mao, Z. Ma, W.S. Chen, Z. Yang, K.S. Wong and G.K.L. Wong, Blue-light emission from ZnSTe-based EL devices 175/176 (1997) 632
Springholz, G., see Ueta, A.Y. 175/176 (1997) 1022

SpringThorpe, A.J., see Chow, P.P. 175/176 (1997) 61
SpringThorpe, A.J., see Wasilewski, Z.R. 175/176 (1997) 238
SpringThorpe, A.J., see Micovic, M. 175/176 (1997) 428
Stahrenberg, K., see Däweritz, L. 175/176 (1997) 310
Stair, K.A., see Sacks, R.N. 175/176 (1997) 66
Stangl, J., see Zerlauth, S. 175/176 (1997) 459
Stanley, C.R., see Vögele, B. 175/176 (1997) 229
Starck, C., see Pagnod-Rossiaux, Ph. 175/176 (1997) 948
Steans, P., see Zhang, J. 175/176 (1997) 1284
Stone, D.R., see Johnson, F.G. 175/176 (1997) 46
Strand, T., see Chavarkar, P. 175/176 (1997) 393
Streater, R.W., see Wasilewski, Z.R. 175/176 (1997) 238
Streater, R.W., see Micovic, M. 175/176 (1997) 428
Strecker, B.N., see McCann, P.J. 175/176 (1997) 1057
Streit, D.C., see Block, T.R. 175/176 (1997) 903
Streit, D.C., see Wojtowicz, M. 175/176 (1997) 930
Strunk, H.P., see Schmitt, J. 175/176 (1997) 528
Suda, J., R. Tokutome, Y. Kawakami, Sz. Fujita and Sg. Fujita, Hydrogen sulfide treatment of GaAs substrate and its effects on initial stage of ZnSe growth 175/176 (1997) 593
Sugawara, Y., see Shen, A. 175/176 (1997) 1069
Sugiura, H., M. Ogasawara, M. Mitsuhara, N. Yamamoto and M. Itoh, MOMBE growth of highly tensile-strained InGaAsP MQWs and their applications to 1.3-μm wavelength low threshold current lasers 175/176 (1997) 1205
Sugiyama, Y., see Nakata, Y. 175/176 (1997) 713
Summers, C.J., see Schön, S. 175/176 (1997) 598
Summers, C.J., see Menkara, H.M. 175/176 (1997) 983
Sun Dianzhao, see Wang Xiaoliang 175/176 (1997) 1254
Sunamura, H., see Kim, E.S. 175/176 (1997) 519
Sutoh, A., see Okada, Y. 175/176 (1997) 1039
Suzuki, T., see Iizuka, K. 175/176 (1997) 447
Svensson, S., see Uppal, P.N. 175/176 (1997) 877
Swenson, G., see Thordson, J.V. 175/176 (1997) 234
Swenson , G., see Roslund, J.H. 175/176 (1997) 883
Sykes, D.E., see Joyce, T.B. 175/176 (1997) 377

Takahira, Y. and H. Okamoto, Measurement of MBE substrate temperature by photoluminescence 175/176 (1997) 267
Takahira, Y., see Iizuka, K. 175/176 (1997) 447
Takamasu, T., see Henini, M. 175/176 (1997) 919
Takekawa, K., see Tomita, N. 175/176 (1997) 809
Takemoto, M., see Kim, S.J. 175/176 (1997) 754
Takeuchi, T., see Hanamaki, Y. 175/176 (1997) 359
Takeuchi, T., see Mars, D.E. 175/176 (1997) 365
Tamargo, M.C., see Zeng, L. 175/176 (1997) 41
Tamargo, M.C., see Cavus, A. 175/176 (1997) 558
Tamayo, J., see Utzmeier, T. 175/176 (1997) 725
Tan, M.R.T., see Houng, Y.M. 175/176 (1997) 352
Tanaka, I., see Koshiba, S. 175/176 (1997) 804
Tanaka, M., see Hayashi, T. 175/176 (1997) 1063
Tanaka, U., see Cho, S.H. 175/176 (1997) 112
Tanimoto, T., see Kudo, M. 175/176 (1997) 910
Tanner, M.O., see Chu, M.A. 175/176 (1997) 1278
Tatarenko, S., T. Baron, A. Arnoult, J. Cibert, M. Grün, A. Haury, Y. Merle d'Aubigné, A. Wasiela and K. Saminadayar, Nitrogen doping of Te-based II–VI compounds 175/176 (1997) 682
Taylor, A.G., see Zhang, J. 175/176 (1997) 477
Tejedor, P., see Zhang, J. 175/176 (1997) 1284
Temkin, H., see Nikishin, S.A. 175/176 (1997) 139
Temkin , H., see Thiagarajan, P. 175/176 (1997) 945
Tews, H., see Averbeck, R. 175/176 (1997) 122
Thainoi, S., see Sopitpan, S. 175/176 (1997) 1152
Thiagarajan, P., G.E. Giudice, H. Temkin and G.Y. Robinson, Gas-source molecular beam epitaxial growth of low threshold current 1.3 μm InAsP/InGaAsP lasers 175/176 (1997) 945
Thibado, P.M., B.R. Bennett, B.V. Shanabrook and L.J. Whitman, A RHEED and STM study of Sb-rich AlSb and GaSb (0 0 1) surface reconstructions 175/176 (1997) 317
Thibado, P.M., see Bennett, B.R. 175/176 (1997) 888
Thomas, M., H.-R. Blank, K.C. Wong and H. Kroemer, Buffer-dependent mobility and morphology of InAs/(Al,Ga)Sb quantum wells 175/176 (1997) 894
Thompson, D.A., see Wang, J. 175/176 (1997) 793
Thompson, J.H., see Beere, H.E. 175/176 (1997) 398
Thompson, P., see Li, Y. 175/176 (1997) 250
Thordson, J.V., T.G. Andersson, G. Swenson and U. Södervall, Two-dimensional limitations when increasing the Si-concentration from δ-doping to thin Si-layers in GaAs 175/176 (1997) 234
Thrush, C.M., see Partin, D.L. 175/176 (1997) 860
Tichelaar, F.D., see Marschner, T. 175/176 (1997) 1081
Tiedje, T., see Johnson, S.R. 175/176 (1997) 273
Toivonen, M., P. Savolainen, H. Asonen and M. Pessa, Solid-source MBE for growth of laser diode materials 175/176 (1997) 37
Tokutome, R., see Suda, J. 175/176 (1997) 593
Tomita, N., T. Kishi, K. Takekawa, K. Fujita, T. Watanabe, A. Adachi, S. Shimomura and S. Hiyamizu, Improved optical qualities of GaAs/$Al_{0.3}Ga_{0.7}As$ tilted T-shaped quantum wires fabricated by glancing-angle molecular beam epitaxy 175/176 (1997) 809
Torabi, B., see Nutsch, A. 175/176 (1997) 1200
Torii, S., see Hasegawa, S. 175/176 (1997) 1075
Tournié, E., P. Brunet, C. Ongaretto, C. Morhain, J.-P. Faurie, R. Triboulet and J.O. Ndap, ZnSe homoepitaxial growth on solid-phase recrystallized substrates 175/176 (1997) 577

Trampert, A., see Braun, W. 175/176 (1997) 156
Trampert, A., see Nötzel, R. 175/176 (1997) 1114
Tran, L., see Block, T.R. 175/176 (1997) 903
Tränkle, G., see Sexl, M. 175/176 (1997) 915
Tränkle, G., see Nutsch, A. 175/176 (1997) 1200
Triboulet, R., see Tournié, E. 175/176 (1997) 577
Troffer, T., see Schmitt, J. 175/176 (1997) 528
Truscott, W.S., see Buckle, P.D. 175/176 (1997) 1299
Tsatsul'nikov, A.F., see Ustinov, V.M. 175/176 (1997) 689
Tscherptner, N., see Pagnod-Rossiaux, Ph. 175/176 (1997) 948
Tsen, S.-C.Y., see Kim, C.C. 175/176 (1997) 328
Tsen, S.-C.Y., see Kim, C.C. 175/176 (1997) 613
Tseng, B.T., see Kuo, J.M. 175/176 (1997) 971
Tsuchiya, H., see Hayashi, T. 175/176 (1997) 1063
Tsuji, T., see Yokozeki, M. 175/176 (1997) 435
Tsukamoto, S., T. Ohno and N. Koguchi, Scanning tunneling spectroscopy and first-principles investigation on GaAs(0 0 1)(2 × 6)-S surface formed by molecular beam epitaxy 175/176 (1997) 1303
Tu, C.W., see Bi, W.G. 175/176 (1997) 145
Tu, C.W., see Li, N.Y. 175/176 (1997) 387
Tu, C.W., see Mei, X.B. 175/176 (1997) 994
Tu, C.W., see Niki, S. 175/176 (1997) 1051
Tu, L.W., see Hong, M. 175/176 (1997) 422
Turner, G.W., M.J. Manfra, H.K. Choi and M.K. Connors, MBE growth of high-power InAsSb/InAlAsSb quantum-well diode lasers emitting at 3.5 μm 175/176 (1997) 825

Ueda, O., see Nakata, Y. 175/176 (1997) 168
Ueta, A.Y., G. Springholz and G. Bauer, Improved nucleation and spiral growth of PbTe on BaF_2 (1 1 1) 175/176 (1997) 1022
Uppal, P.N., G. Charache, P. Baldasaro, B. Campbell, S. Loughin, S. Svensson and D. Gill, MBE growth of GaInAsSb p/n junction diodes for thermophotovoltaic applications 175/176 (1997) 877
U'Ren, G., see Xiang, Q. 175/176 (1997) 469
Urmann, G., see Künzel, H. 175/176 (1997) 411
Usami, N., see Kim, E.S. 175/176 (1997) 519
Ustinov, V.M., A.Yu. Egorov, A.R. Kovsh, A.E. Zhukov, M.V. Maximov, A.F. Tsatsul'nikov, N.Yu. Gordeev, S.V. Zaitsev, Yu.M. Shernyakov, N.A. Bert, P.S. Kop'ev, Zh.I. Alferov, N.N. Ledentsov, J. Böhrer, D. Bimberg, A.O. Kosogov, P. Werner and U. Gösele, Low-threshold injection lasers based on vertically coupled quantum dots 175/176 (1997) 689
Utzmeier, T., see Postigo, P.A. 175/176 (1997) 298
Utzmeier, T., J. Tamayo, P.A. Postigo, R. García and F. Briones, Growth and characterization of self-organized InSb quantum dots and quantum dashes 175/176 (1997) 725

Van Hove, J.M., see Chow, P.P. 175/176 (1997) 61
Van Hove, J.M., P.P. Chow, A.M. Wowchak, J.J. Klaassen, M.F. Rosamond and D.R. Croswell, Optimization of AlGaN films grown by RF atomic nitrogen plasma using in-situ cathodoluminescence 175/176 (1997) 79
Vanelle, E., see Mesrine, M. 175/176 (1997) 1242
Venkatasubramanian, R., see Mahalingam, K. 175/176 (1997) 211
Venkatasubramanian, R., D.L. Dorsey and K. Mahalingam, Heuristic rules for group IV dopant site selection in III–V compounds 175/176 (1997) 224
Veuhoff, E., see Popp, M. 175/176 (1997) 1247
Vögele, B., C.R. Stanley, E. Skuras, A.R. Long and E.A. Johnson, Surface segregation of Si in δ-doped $In_{0.53}Ga_{0.47}As$ grown by molecular beam epitaxy 175/176 (1997) 229
Von Känel, H., T. Meyer and H. Sirringhaus, In-situ BEEM study of interfacial dislocations and point defects 175/176 (1997) 340
Von Ortenberg, M., see Parthier, L. 175/176 (1997) 642
Vonk, H., see Marschner, T. 175/176 (1997) 1081
Vvedensky, D.D., see Mizushima, K. 175/176 (1997) 509

Waag, A., see Fischer, F. 175/176 (1997) 532
Waag, A., see Lugauer, H.-J. 175/176 (1997) 619
Wachter, M., U. Schöffel, M. Schier and H. Heinecke, Lateral coupling of InP/GaInAsP/InP structures by selective area MOMBE 175/176 (1997) 1186
Wagner, B.K., see Schön, S. 175/176 (1997) 598
Walker, J., see Kuo, J.M. 175/176 (1997) 971
Wamsley, C.C., M.W. Koch and G.W. Wicks, Low threshold 1.3 μm InAsP/GaInAsP lasers grown by solid-source molecular beam epitaxy 175/176 (1997) 42
Wang, C.Y., see Pan, D. 175/176 (1997) 760
Wang, D., see Xiang, Q. 175/176 (1997) 469
Wang, H.M., see Pan, D. 175/176 (1997) 760
Wang, J., D.A. Thompson, B.J. Robinson and J.G. Simmons, Molecular beam epitaxial growth of InGaAs/InGaAsP quantum wires on V-grooved InP substrates with (1 1 1) sidewalls 175/176 (1997) 793
Wang, J., see Wang, Y. 175/176 (1997) 1289

Wang, K.L., see Xiang, Q. 175/176 (1997) 469
Wang, K.L., see Chu, M.A. 175/176 (1997) 1278
Wang, S.L., see He, L. 175/176 (1997) 677
Wang, S.M., C. Karlsson, N. Rorsman, M. Bergh, E. Olsson, T.G. Andersson and H. Zirath, Molecular beam epitaxy growth and characterization of $In_xGa_{1-x}As$ ($0.57 \leqslant x \leqslant 1$) on GaAs using InAlAs graded buffer 175/176 (1997) 1016
Wang, W.I., see Du, Q. 175/176 (1997) 849
Wang Xiaoliang, Sun Dianzhao, Kong Meiying, Hou Xun, Zeng Yiping, GSMBE growth and characterization of $In_xGa_{1-x}As/InP$ strained-layer MQWs in a P-i-N Configuration 175/176 (1997) 1254
Wang, Y., Y.N. Sheng, W. Ge, J. Wang, L.L. Chang, J. Xie, J. Ma and J. Xu, Morphology of MBE grown InAs films studied by atomic force microscope 175/176 (1997) 1289
Wang, Y.C., see Kuo, J.M. 175/176 (1997) 971
Wang, Z.Z., see Laruelle, F. 175/176 (1997) 1087
Wang, Z.Z., see Lelarge, F. 175/176 (1997) 1102
Wang, Zhanguo, see Zhu, Donghai 175/176 (1997) 1004
Warlick, E.L., see Ng, T.B. 175/176 (1997) 552
Warlick, E.L., E. Ho, G.S. Petrich and L.A. Kolodziejski, Reducing the defect density in MBE-ZnSe/III–V heterostructures 175/176 (1997) 564
Wasiela, A., see Tatarenko, S. 175/176 (1997) 682
Wasilewski, Z.R., M.M. Dion, D.J. Lockwood, P. Poole, R.W. Streater and A.J. SpringThorpe, Determination of $Al_xGa_{(1-x)}As$ composition: the MBE perspective 175/176 (1997) 238
Wasilewski, Z.R., S.J. Rolfe and R.A. Wilson, Contamination in molecular beam epitaxy: the role of arsenic drag effect 175/176 (1997) 1270
Wassermeier, M., see Behrend, J. 175/176 (1997) 178
Wassermeier , M., see Mazuelas, A. 175/176 (1997) 383
Wassermeier, M., see Hey, R. 175/176 (1997) 1167
Watanabe, T., see Tomita, N. 175/176 (1997) 809
Weightman, P., see Farrell, T. 175/176 (1997) 1217
Weimann, G., see Sexl, M. 175/176 (1997) 915
Weimann, G., see Nutsch, A. 175/176 (1997) 1200
Werner, P., see Ustinov, V.M. 175/176 (1997) 689
Westwood, D.I., see Zhang, J. 175/176 (1997) 477
Whaley, R.D., see Johnson, F.G. 175/176 (1997) 46
Whitman, L.J., see Thibado, P.M. 175/176 (1997) 317
Whitman, L.J., see Bennett, B.R. 175/176 (1997) 888
Wicks, G.W., see Wamsley, C.C. 175/176 (1997) 42
Wijewarnasuriya, P.S., F. Aqariden, C.H. Grein, J.P. Faurie and S. Sivananthan, p-Type doping with arsenic in (2 1 1)B HgCdTe grown by MBE 175/176 (1997) 647
Wilson, J.A., see Rajavel, R.D. 175/176 (1997) 653
Wilson, R.A., see Wasilewski, Z.R. 175/176 (1997) 1270
Wilson, R.G., see MacKenzie, J.D. 175/176 (1997) 84
Winesett, J., see Liu, W.K. 175/176 (1997) 853
Winter, W., see Brunner, K. 175/176 (1997) 451
Wirth, R., see Eberl, K. 175/176 (1997) 702
Wißmann, H., see Parthier, L. 175/176 (1997) 642
Wohlert, D.E., S.T. Chou and K.Y. Cheng, Temperature-insensitive photoluminescence above 300 K in strained Ga_xIn_{1-x} As multiple quantum wire heterostructures 175/176 (1997) 1162
Wojtowicz, M., see Block, T.R. 175/176 (1997) 903
Wojtowicz, M., D. Pascua, A.-C. Han, T.R. Block and D.C. Streit, Photoluminescence characterization of MBE grown AlGaAs/InGaAs/GaAs pseudomorphic HEMTs 175/176 (1997) 930
Wolter, J.H., see Marschner, T. 175/176 (1997) 1081
Won, S.H., see Cho, H.D. 175/176 (1997) 125
Wong, G.K.L., see Sou, I.K. 175/176 (1997) 632
Wong, K.C., see Thomas, M. 175/176 (1997) 894
Wong, K.S., see Sou, I.K. 175/176 (1997) 632
Woollam, J.A., see Benson, J.D. 175/176 (1997) 659
Wowchak, A.M., see Chow, P.P. 175/176 (1997) 61
Wowchak, A.M., see Van Hove, J.M. 175/176 (1997) 79
Wu, J., see Pan, D. 175/176 (1997) 760
Wu, O.K., see Rajavel, R.D. 175/176 (1997) 653
Wu, X., see MacKenzie, J.D. 175/176 (1997) 84

Xiang, Q., S. Li, D. Wang, K. Sakamoto, K.L. Wang, G. U'Ren and M. Goorsky, Sidewall faceting and inter-facet mass transport in selectively grown epitaxial layers on SiO_2-masked Si(1 1 0) substrates 175/176 (1997) 469
Xie, J., see Wang, Y. 175/176 (1997) 1289
Xie, M.H., see Zhang, J. 175/176 (1997) 477
Xie, X.G., see Chen, H. 175/176 (1997) 524
Xin, T.L., see He, L. 175/176 (1997) 677
Xu, Bo, see Zhu, Donghai 175/176 (1997) 1004
Xu, D., see Sexl, M. 175/176 (1997) 915
Xu, J., see Wang, Y. 175/176 (1997) 1289
Xue, Q., T. Ogino, H. Kiyama, Y. Hasegawa and T. Sakurai, Surface reconstruction and morphology evolution in highly strained InAs epilayer growth on GaAs(0 0 1) surface 175/176 (1997) 174

Yamada, A., see Brandt, O. 175/176 (1997) 134
Yamada, A., see Okamoto, T. 175/176 (1997) 1045
Yamada, A., see Niki, S. 175/176 (1997) 1051
Yamada, N., see Mars, D.E. 175/176 (1997) 365
Yamaguchi, H., see Homma, Y. 175/176 (1997) 292
Yamaguchi, H., see Kanisawa, K. 175/176 (1997) 304
Yamamoto, A., see Hashimoto, A. 175/176 (1997) 129

Yamamoto, K., see Asahi, H. 175/176 (1997) 1195

Yamamoto, K., H. Asahi, T. Hayashi, K. Hidaka and S. Gonda, Selective area etching of III–V semiconductors using TDMAAs and TDMASb in metalorganic molecular beam epitaxy chamber 175/176 (1997) 1236

Yamamoto, M., T. Iwabuchi, T. Ito, T. Yoshida, T. Isoya and I. Shibasaki, Properties of InAs thin films grown on (1 0 0)-oriented GaAs substrate with various tilted angles and directions of misorientation 175/176 (1997) 191

Yamamoto, M., see Higashiwaki, M. 175/176 (1997) 814

Yamamoto, N., see Sugiura, H. 175/176 (1997) 1205

Yamamoto, Y., see Izumi, S. 175/176 (1997) 404

Yamamoto, Y., see Solomon, G.S. 175/176 (1997) 707

Yamanaka, N., see Nishikata, K. 175/176 (1997) 990

Yang, B.X., see Zeng, L. 175/176 (1997) 541

Yang, B.X., see Cavus, A. 175/176 (1997) 558

Yang, H., see Brandt, O. 175/176 (1997) 134

Yang, J.R., see He, L. 175/176 (1997) 677

Yang, T., see Schön, S. 175/176 (1997) 598

Yang, Z., see Sou, I.K. 175/176 (1997) 632

Yano, M., K. Koike, T. Furushou and T. Yodo, Molecular beam epitaxial growth of the CdMnTe/CdTe superlattices on (100) GaAs substrates 175/176 (1997) 665

Yasuda, T., B.-P. Zhang and Y. Segawa, MBE growth of n-type ZnSe and ZnS using ethylchloride as a dopant 175/176 (1997) 583

Yodo, T., see Yano, M. 175/176 (1997) 665

Yokoyama, N., see Nakata, Y. 175/176 (1997) 168

Yokoyama, N., see Nakata, Y. 175/176 (1997) 713

Yokozeki, M., H. Yonezu, T. Tsuji and N. Ohshima, Passivation of misfit dislocations by atomic hydrogen irradiation in lattice-mismatched heteroepitaxy 175/176 (1997) 435

Yonezu, H., see Yokozeki, M. 175/176 (1997) 435

Yoo, M.C., M.Y. Park, S.K. Kang, H.D. Cho and J.W. Lee, Growth and p-type doping of GaN on c-plane sapphire by nitrogen plasma-assisted molecular beam epitaxy 175/176 (1997) 100

Yoshida, S., see Hacke, P. 175/176 (1997) 94

Yoshida, S. and M. Sasaki, Surface crystal-structure of a GaN film as an in situ mask using MOMBE 175/176 (1997) 107

Yoshida, S., see Cho, S.H. 175/176 (1997) 112

Yoshida, S., see Nishikata, K. 175/176 (1997) 990

Yoshida, S., see Sasaki, M. 175/176 (1997) 1178

Yoshida, T., see Yamamoto, M. 175/176 (1997) 191

Yu, E., see Zhang, Y.-H. 175/176 (1997) 833

Yu, M.F., see He, L. 175/176 (1997) 677

Yu, W., see Ramachandran, T.R. 175/176 (1997) 216

Yusa, G. and H. Sakaki, MBE growth of novel GaAs/n-AlGaAs field-effect transistor structures with embedded InAs quantum traps and their transport characteristics 175/176 (1997) 730

Yutani, A. and Y. Shiraki, Hybrid MBE growth and mobility limiting factors of *n*-channel Si/SiGe modulation-doped systems 175/176 (1997) 504

Zaitlin, M.P., see DiLorenzo, J.V. 175/176 (1997) 1

Zaitsev, S.V., see Ustinov, V.M. 175/176 (1997) 689

Zangwill, A., see Mizushima, K. 175/176 (1997) 509

Zaumseil, P., see Lippert, G. 175/176 (1997) 473

Zavada, J.M., see Johnson, M.A.L. 175/176 (1997) 72

Zavada, J.M., see MacKenzie, J.D. 175/176 (1997) 84

Zehnder, U., see Fischer, F. 175/176 (1997) 532

Zehnder, U., see Lugauer, H.-J. 175/176 (1997) 619

Zeng, L., A. Cavus, B.X. Yang, M.C. Tamargo, N. Bambha, A. Gray and F. Semendy, Molecular beam epitaxial growth of lattice-matched $Zn_xCd_yMg_{1-x-y}Se$ quaternaries on InP substrates 175/176 (1997) 541

Zeng, L., see Cavus, A. 175/176 (1997) 558

Zeng, Y.P., see Pan, D. 175/176 (1997) 760

Zeng Yiping, see Wang Xiaoliang 175/176 (1997) 1254

Zerlauth, S., J. Stangl, A.A. Darhuber, V. Holý, G. Bauer and F. Schäffler, MBE growth and structural characterization of $Si_{1-y}C_y/Si_{1-x}Ge_x$ superlattices 175/176 (1997) 459

Zettler, J.-T., see Däweritz, L. 175/176 (1997) 310

Zhang, B.-P., see Yasuda, T. 175/176 (1997) 583

Zhang, C.H., see Pan, D. 175/176 (1997) 760

Zhang, D., see Lin, C.-H. 175/176 (1997) 955

Zhang, F.C., see Linder, K.K. 175/176 (1997) 499

Zhang, J., A.K. Lees, A.G. Taylor, M.H. Xie, B.A. Joyce, Z. Sobiesierksi and D.I. Westwood, New hydrogen desorption kinetics from vicinal Si(0 0 1) surfaces observed by reflectance anisotropy spectroscopy 175/176 (1997) 477

Zhang, J., see Mizushima, K. 175/176 (1997) 509

Zhang, J., O.P. Naji, P. Steans, P. Tejedor, T. Kaneko, T.S. Jones and B.A. Joyce, Modulated-beam studies of the layer-by-layer etching of GaAs(0 0 1) using $AsBr_3$: identification of the reaction mechanism 175/176 (1997) 1284

Zhang, Jun, see Zhu, Donghai 175/176 (1997) 1004

Zhang, Q.Y., see He, L. 175/176 (1997) 677

Zhang, X., see Liu, W.K. 175/176 (1997) 853

Zhang, Y.-H., A. Lew, E. Yu and Y. Chen, Microstructural properties of $InAs/InAs_xSb_{1-x}$ superlattices and $InAs_xSb_{1-x}$ ordered alloys grown by modulated molecular beam epitaxy 175/176 (1997) 833

Zhao, Y., see Li, A.Z. 175/176 (1997) 873
Zheng, Y.L., see Li, A.Z. 175/176 (1997) 873
Zhong, J.Q., see Li, A.Z. 175/176 (1997) 873
Zhou, J.J., Y. Li, D. Pacheco, H.P. Lee and X. Liu, Virtual control simulator for closed-loop epitaxial growth 175/176 (1997) 52
Zhou, J.J., see Li, Y. 175/176 (1997) 250
Zhou, J.M., see Chen, H. 175/176 (1997) 524
Zhou, J.M., see Feng, W. 175/176 (1997) 1173
Zhou, X., S. Jiang and W.P. Kirk, Molecular beam epitaxy of BeTe on vicinal Si(1 0 0) Surfaces 175/176 (1997) 624
Zhou, Y., see Lin, C.-H. 175/176 (1997) 955
Zhu, Donghai, Zhanguo Wang, Jiben Liang, Bo Xu, Zhanping Zhu, Jun Zhang, Qian Gong and Shengying Li, 808 nm high-power laser grown by MBE through the control of Be diffusion and use of superlattice 175/176 (1997) 1004
Zhu, Zhanping, see Zhu, Donghai 175/176 (1997) 1004
Zhukov, A.E., see Ustinov, V.M. 175/176 (1997) 689
Zinck, J.J. and D.H. Chow, Effects of morphology on photoemission oscillation measurements during growth of resonant tunneling devices 175/176 (1997) 323
Zirath, H., see Wang, S.M. 175/176 (1997) 1016
Zsebők, O., see Roslund, J.H. 175/176 (1997) 883
Zundel, M., see Eberl, K. 175/176 (1997) 702

ELSEVIER

Journal of Crystal Growth 175/176 (1997) 1341–1343

JOURNAL OF CRYSTAL GROWTH

Subject index

Apparatus
– for in situ device processing in molecular beam epitaxy
– – of gallium arsenide 799

Characterization
– by atomic absorption
– – of gallium and indium desorption 244
– by atomic force microscopy
– – of aluminum gallium arsenide 334
– – of gallium arsenide ridge quantum wire 804
– – of indium gallium arsenide 334
– by ballistic electron emission spectroscopy
– – of cobalt silicide 340
– by cathodoluminescence
– – of III-nitrides growth 72, 79
– by diffuse reflectance spectroscopy
– – of simultaneous temperature and thickness measurements 250
– by ellipsometry
– – of cadmium zinc telluride 659
– – of thickness control 281
– by optical anisotropy
– – of gallium arsenide 310
– – of silicon 477
– by optical bandgap thermometry
– – of surface temperature in molecular beam epitaxy growth 273
– by optical fiber pyrometry
– – of substrate temperature in molecular beam epitaxy growth 262
– by photoluminescence
– – of surface temperature in molecular beam epitaxy growth 267
– by reflection high energy electron diffraction
– – of gallium arsenide 310
– by scanning electron microscopy
– – of migration enhanced epitaxy 292
– by scanning tunneling microscopy
– – of gallium arsenide 346
– by surface chemical modulation spectroscopy
– – of surface composition 298

Computer simulation
– of closed loop epitaxial growth 52
– of molecular beam epitaxy of III–V compounds 211
– of probability density of carrier states 809

Device characterization
– Bragg mirrors 372, 383
– diodes 340, 499, 532, 603, 632, 637, 653, 677, 849, 877, 919, 924, 983, 990, 1033, 1299
– electronic materials 84, 197, 229, 377, 398, 532, 903, 960, 1126, 1299
– heterojunction 122, 393, 532, 603, 844, 903, 910, 915, 919, 940, 945, 955, 1028, 1092, 1097, 1138, 1242, 1254
– lasers 22, 37, 42, 46, 352, 365, 532, 637, 689, 825, 898, 935, 948, 1004, 1120, 1186, 1200,
– low dimensional quantum structures (wells, wires, dots, dashes) 37, 72, 197, 459, 465, 519, 524, 532, 637, 682, 689, 702, 707, 720, 725, 736, 741, 754, 760, 765, 771, 777, 782, 787, 793, 799, 809, 814, 844, 868, 873, 910, 919, 948, 964, 977, 983, 994, 1009, 1033, 1081, 1114, 1120, 1126, 1138, 1144, 1152, 1157, 1162, 1200, 1205, 1249, 1265
– wave guides 960, 990
Diffusional control
– of beryllium in III–V compounds 1004
– of heterointerfaces 162
Diodes, see Device characterization

Electronic materials, see Device characterization
Etching
– by hydrogen radicals 411, 416, 435, 441
– chemical 387, 428, 441, 799, 983, 1284
– thermal 393, 447, 799

Heat flow control, of
– gallium arsenide surfaces 1316
Heterojunction, see Device characterization

Kinetics
– of contamination 1270

– of growth 89, 94, 134, 156, 174, 184, 211, 216, 224, 229, 244, 286, 304, 310, 323, 328, 473, 477, 486, 509, 541, 838, 888, 1039, 1075, 1081, 1186, 1265, 1309
– of interface control 94, 129, 178, 459, 486, 838, 1039, 1167

Lasers, see Device characterization
Lasers, crystals for
– aluminum arsenide 359
– aluminum gallium arsenide 359
– gallium arsenide 359
– indium arsenide phosphide 945
– indium gallium arsenide 359
– indium gallium arsenide phosphide 945, 948
– zinc cadmium selenide 558
– zinc magnesium sulphide selenide 552
– zinc selenide 552
– zinc sulphide selenide 552

Morphological stability
– of aluminum antimonide 888
– of gallium antimonide 888
– of gallium arsenide 1309
– of indium antimonide 888
– of indium arsenide layers 216, 747
– of silicon germanium carbon 486

Nucleation
– of aluminum antimonide 888
– of gallium antimonide 888
– of gallium arsenide 292, 310
– of indium antimonide 888
– of lead telluride 1022
– of III-nitrides 139

Superlattices, multilayers
– of IV–IV compounds 459
– of III–V compounds 156, 162, 178, 411, 447, 754, 760, 782, 799, 833, 898, 1009, 1081, 1167, 1173, 1254
– of II–VI compounds 564, 571, 665
Surface energy, determination
– of gallium arsenide by ab initio calculations 1303
Surface preparation
– of cadmium zinc telluride 659
– of gallium arsenide 593
– of zinc selenide 546
Surface structure
– of aluminum arsenide 310, 323
– of gallium antimonide 310, 323
– of gallium arsenide 304, 310, 1167, 1183, 1303
– of gallium nitride 94, 139
– of indium arsenide 174, 323
– of irradiated gallium arsenide 346
– of vicinal orientation 1087

Thin film growth, epitaxy
– by atomic layer epitaxy
– – of gallium arsenide 771, 1009
– – of indium arsenide 771
– – of indium gallium arsenide 1009
– by chemical beam epitaxy
– – of aluminum gallium arsenide 404
– – of gallium aluminum arsenide 1265
– – of gallium arsenide 377, 404, 1217, 1236
– – of gallium arsenide phosphide 1265
– – of gallium indium arsenide 1200
– – of gallium indium arsenide phosphide 1200
– – of indium arsenide 747, 1210
– – of indium gallium arsenide 1254, 1259
– – of indium phosphide 1200, 1210
– – of silicon 469, 477, 509
– – of III-nitrides 89, 139
– – of zinc phosphide 1254, 1259
– – of zinc sulphide 598
– by low energy ion implantation
– – of silicon dioxide 493
– by metalorganic molecular beam epitaxy
– – of gallium indium arsenide phosphide 1186, 1205, 1231, 1247
– – of indium phosphide 1186, 1247
– – of III-nitrides 84, 107, 129
– by molecular beam epitaxy
– – of aluminum antimonide 317, 888, 955
– – of aluminum arsenide 52, 156, 178, 238, 250, 267, 323, 359, 365, 383, 782, 804, 924, 1087
– – of aluminum arsenide antimonide 825
– – of aluminum gallium arsenide 61, 162, 197, 238, 352, 359, 365, 387, 416, 428, 447, 689, 730, 741, 809, 814, 894, 898, 930, 935, 960, 964, 971, 983, 999, 1004, 1016, 1075, 1092, 1097, 1108, 1114, 1126, 1131, 1138, 1152, 1299
– – of aluminum gallium arsenide antimonide 372, 868, 873
– – of aluminum gallium indium arsenide 411
– – of aluminum gallium nitride 72, 79
– – of aluminum indium arsenide 393
– – of aluminum nitride 72, 79
– – of aluminum phosphide 1157
– – of beryllium chalcogenides 619
– – of beryllium telluride 624
– – of cadmium magnesium telluride 682
– – of cadmium manganese telluride 665
– – of cadmium telluride 665, 682
– – of cadmium zinc telluride 670, 682
– – of calcium fluoride 853, 1057
– – of cobalt silicide 340
– – of copper indium diselenide 1051
– – of gallium antimonide 317, 323, 888
– – of gallium arsenide 1, 52, 66, 156, 162, 168, 178, 197, 203, 234, 238, 250, 267, 286, 292, 304, 310, 346, 352, 365, 383, 398, 411, 416, 422, 428, 435, 441, 447, 707, 730, 741, 760, 782, 787, 799, 804, 809, 814, 838, 898, 924, 930, 935, 960, 971, 983, 1004, 1039, 1075, 1087, 1092, 1097, 1102, 1126, 1138, 1152, 1242, 1270, 1284, 1299, 1303, 1309, 1316
– – of gallium arsenide antimonide 838
– – of gallium arsenide phosphide 977
– – of gallium gadolinium oxide 422
– – of gallium indium arsenide 184, 1162

– – of gallium indium nitride 122
– – of gallium nitride 29, 72, 79, 94, 100, 112, 117, 122, 125, 134, 150
– – of gallium nitride phosphide 145, 150
– – of gallium phosphide 754, 1157
– – of germanium 736
– – of indium aluminum arsenide 197, 903, 915, 1016, 1028
– – of indium aluminum arsenide antimonide 825, 844
– – of indium antimonide 725, 853, 860, 883, 888
– – of indium arsenide 13, 168, 174, 191, 216, 323, 359, 435, 707, 713, 765, 777, 825, 833, 868, 894, 915, 955, 1289
– – of indium arsenide antimonide 825, 833
– – of indium arsenide phosphide 945, 948, 1033
– – of indium gallium aluminum arsenide 184, 903 990, 1028, 1120, 1294
– – of indium gallium antimonide 955
– – of indium gallium antimonide bismuth 849
– – of indium gallium arsenide 197, 203, 229, 250, 262, 365, 393, 428, 689, 696, 720, 760, 793, 903, 910, 915, 930, 935, 940, 977, 999, 1016, 1028, 1081, 1131
– – of indium gallium arsenide antimonide 873, 877
– – of indium gallium arsenide phosphide 793, 819, 945, 948, 994
– – of indium gallium phosphide 702, 971, 994, 1242
– – of indium nitride phosphide 145
– – of indium phosphide 8, 22, 411, 702, 725, 754, 940, 1033, 1081
– – of indium selenide 1045
– – of lead selenide 1022
– – of mercury cadmium telluride 647, 653, 670, 677
– – of mercury selenide 642
– – of silicon 465, 486, 493, 499, 504, 514, 519, 1144
– – of silicon carbide 528
– – of silicon carbon 451, 459
– – of silicon germanium 459, 465, 473, 481, 499, 504, 519, 524, 1278
– – of silicon germanium carbon 451, 486, 1138
– – of thallium gallium phosphide 1195
– – of thallium indium gallium phosphide 1195
– – of thallium indium phosphide 1195
– – of thallium phosphide 1195
– – of zinc beryllium selenide 532
– – of zinc cadmium magnesium selenide 541
– – of zinc cadmium selenide 541, 558
– – of zinc magnesium sulphide selenide 552, 637
– – of zinc manganese telluride 682
– – of zinc selenide 328, 532, 552, 564, 571, 577, 583, 593, 608, 613, 637
– – of zinc sulphide 583, 598
– – of zinc sulphide telluride 632
– – of zinc sulphoselenide 552, 637
– – of zinc telluride 682
– – theory of growth 224
– – theory of II–VI compounds growth 587
– by solid source molecular beam epitaxy
– – of aluminum gallium arsenide 334
– – of gallium arsenide 1009
– – of indium aluminum arsenide 256
– – of indium gallium aluminum phosphide 37
– – of indium gallium arsenide 256, 334, 1009
– – of indium gallium arsenide phosphide 37, 42 46
– – of zinc selenide 603
– by vapor phase epitaxy
– – through metalorganic chemical vapor deposition
– – – of indium gallium aluminum arsenide 600